SLAC-267
CONF-8307109
UC-34d
(T/E)

PROCEEDINGS

OF

SUMMER INSTITUTE ON PARTICLE PHYSICS

July 18 - 29, 1983

DYNAMICS AND SPECTROSCOPY AT HIGH ENERGY

Program Directors

Frederick J. Gilman

David W. G. S. Leith

Ed. by Patricia M. McDonough

Sponsored by Stanford University and Stanford Linear Accelerator Center under contract with the U.S. Department of Energy. Contract DE-AC03-76SF00515.

January 1984

Printed in the United States of America. Available from National Technical Information Service, U.S. Department of Commerce, 5285 Port Royal Road, Springfield, VA 22161.

PREFACE

The eleventh SLAC Summer Institute on Particle Physics was held from July 18 to July 29, 1983. The main topic was "Dynamics and Spectroscopy at High Energy," and the traditional format was followed of having the first seven days as a "Summer School" and the last three as a "Topical Conference." The school portion was devoted to lectures on spectroscopy of heavy quark systems and jets from both an experimental and theoretical point of view together with lectures on the physics and technology of charged particle tracking and calorimetry. The Topical Conference highlights included reports on the discovery of the W and Z at the CERN $\bar{p}p$ collider. The attendance of 327 physicists from 15 countries, the excellent lectures, and the exciting physics made for a very interesting and lively meeting.

We thank Anne Mosher for her help in the early planning, and Patricia McDonough, the Coordinator of the Institute and Editor of these Proceedings, who took over in mid-course and carried the task through as if she had done it for years. The smooth running and success of the meeting was in large part due to her careful planning and preparation.

Frederick J. Gilman

David W. G. S. Leith

Program Directors

TABLE OF CONTENTS

Part I. LECTURES **page**

S. ELLIS
"Jets in QCD: A Theorist's Perspective" 1

R. HOLLEBEEK
"Jets in e^+e^- Annihilation" 53

R. F. SCHWITTERS
"Jet Production in High Energy Hadron Collisions" 115

M. E. PESKIN
"Aspects of the Dynamics of Heavy-Quark Systems" 151

M. G. D. GILCHRIESE
"Heavy Particle Spectroscopy and Dynamics B's to Z's" 191

J. ELLIS
"... And for Our Next Spectroscopy?" 239

A. H. WALENTA
"Review of the Physics and Technology of Charged Particle Detectors" 275

P. M. MOCKETT
"A Review of the Physics and Technology of High-Energy Calorimeter Devices" 335

Part II. SEMINARS

G. PREPARATA
"Partons vs. Hadrons: A Physical Theory of Fragmentation" 395

V. ZAMBETAKIS
"Magnetic Dipole Transitions in Onia" 409

Part III. TOPICAL CONFERENCE

J. E. GAISER
"Results from the Crystal Ball at Doris II" 421

R. D. EHRLICH
"Heavy Quark Decays: Recent Results from CLEO" 433

J. LEE-FRANZINI
"Recent CUSB Results on Upsilon Spectroscopy and B Physics" 445

W. TOKI
"Mark III Results from SPEAR" 471

page

E. EICHTEN
"Quarkonium: From the Bottom Up" 497

J. WOTSCHACK
"First Results from the CDHS υ Oscillation Experiment at CERN" 517

M. OREGLIA
"Results the CCFR Neutrino Oscillation Experiment" 527

L. R. SULAK
"Recent Results from the IMB Detector" 545

D. P. STOKER
"Search for Right-Handed Currents in Muon Decay" 551

E. LOHRMANN
"Review of e^+e^--Physics with PETRA" 560

C. YOUNG
"Recent Results from DELCO" 607

W. HOFMANN
"Recent Results from the PEP4-TPC on Quark Fragmentation" 623

J. M. WEISS
"Results from HRS at PEP" 643

M. PICCOLO
"Recent Results from MAC" 673

N. LOCKYER
"Latest Results from the Mark II at PEP" 689

D. LISSAUER
"Jets in High Transverse Energy Events Produced in pp Collisions at the CERN ISR" 715

A. HONMA
"A Study of Jet Production and Jet Properties by the UA1 Experiment at the CERN $p\bar{p}$ Collider" 729

T. HANSL-KOZANECKA
"Search for W and Z^0 at the CERN $p\bar{p}$ Collider" 741

J. P. REPELLIN
"Latest Results from the UA2 Experiment at the CERN $\bar{p}p$ Collider: Hadron Jets, $W \to e\upsilon$, $Z^0 \to e^+e^-$" 763

M. JACOB
"Collider Physics-Present and Prospects" 787

APPENDIX

List of Participants 813
Previous SLAC Summer Institute Titles and Speakers 823

JETS IN QCD: A THEORIST'S PERSPECTIVE

Stephen D. Ellis
University of Washington
Seattle, WA 98195

ABSTRACT

The theoretical basis for hadronic JETS is discussed in the context of Quantum Chromodynamics. After a brief historical review, fixed order perturbative structure is discussed. The various results of all orders perturbative analyses are then summarized. The lectures close with a brief treatment of certain nonperturbative issues.

I. INTRODUCTION

One of the most striking phenomenological developments of the last few years has been the clear emergence [1,2] of the long [3] sought after JETS as features of hadronic final states in various types of reactions. These lectures are intended as an introduction to and review of the theoretical understanding of and expectations for these JETS in the context of Quantum Chromodynamics (QCD). Unfortunately space does not allow a truly comprehensive review. [4] There will be little pretext of rigorous derivation. Instead the intent will be to motivate the results in such a fashion as to offer at least a "pictorial" understanding. Also, for obvious geographical reasons, the phenomenological part of the discussion will focus on e^+e^- annihilation reactions. For explicit discussion of experimental data see the companion experimental lectures. [1,2]

The remainder of the Introduction will focus on briefly answering the four basic questions:

(1) What is a JET?

(2) Why look for JETS?

(3) Where are JETS?

(4) How are JETS seen?

© S. Ellis 1983

The rest of the lectures will treat the first two of these questions in more detail proceeding in the direction of decreasing rigor. Section II will deal with fixed order perturbative results, corresponding to the correlations between JETS, and focus on the "antenna pattern" [5] and Energy-Energy Correlation (EEC) [6] in e^+e^- annihilation. The third Section will discuss the all orders "leading logarithm" perturbative analysis of the internal structure of JETS. Section IV will deal with the issues of the nonperturbative corrections to the previously discussed results. The concluding remarks in Section V will consist largely of a summary of important unanswered questions. For more detailed discussions of Questions (3) and (4) above the interested student is referred to the more experimentally [1,2] and detector [7] oriented lectures elsewhere in this Institute.

What is a JET? In the language of a well known fantasy, [8] a JET may be viewed as the smile of the QCD "Cheshire Cat." While the Cat itself (read quark or gluon) cannot be seen explicitly, its presence can be detected via its visible smile (read JET). In terms of a more technical (but still loose) analogy one may consider a JET as the "bubble chamber track" left by an isolated quark as its motion disturbs the "QCD vacuum." Actually this analogy is best thought of as applying in momentum space rather than in coordinate space as will be illustrated below.

These considerations lead directly to the second question, why look for JETS? Clearly by detecting JETS, one is, in some sense, detecting quarks and gluons. In this way one may isolate the elementary interactions of the quarks and gluons and most directly test QCD. To see the connection between these ideas most clearly it is helpful to review the dogma. [9] It is interesting to note that historically much of the framework used below arose in the "dark ages" of the parton model before the "enlightenment" of QCD. While a good deal can now be derived in the context of QCD, [10] there are still several important questions begging to be answered, as will be noted. The basic features of the dogma are the following:

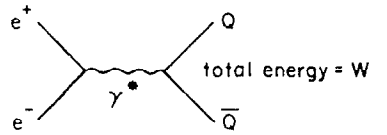
(1) Quarks are the correct algebraic (static quantum numbers) degrees of freedom and all (presently observed) matter is composed of them. This is the basic starting point.

(2) Approximately free quarks and gluons are the correct dynamical degrees of freedom at short distances/large momentum transfers. This is asymptotic freedom which follows from the assumption that quarks interact as prescribed by QCD and renders perturbative QCD relevant at some scale.

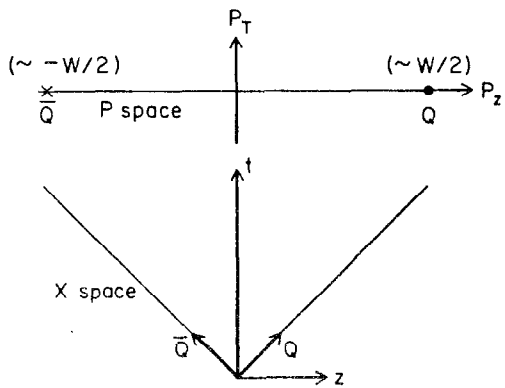
(3) Quarks never "get out", i.e., are never further than approximately one Fermi from an antiquark or from another pair of quarks. This is the concept of confinement and, while an increasing coupling at large distances (infrared slavery) is certainly a property of perturbative QCD and much has been learned from lattice calculations and other techniques, [11] considerable work is needed to allow a complete and useful understanding. This topic is considered in much more detail elsewhere in this Institute. [12]

(4) The confining forces required by (3) are soft. The processes (both perturbative and nonperturbative) which result in confinement and produce $Q\overline{Q}$ pairs out of the vacuum dominantly involve only small momentum transfers. Thus the produced quark pairs and resultant hadrons have small transverse momentum with respect to initial energetic parton direction, i.e., the JET direction. At the present this is simply a belief. It is essential to the observability of JETS. To the extent that JETS are experimentally observed [1,2] the validity of this assumption is confirmed. The observed transverse width of JETS is approximately 350 MeV/c.

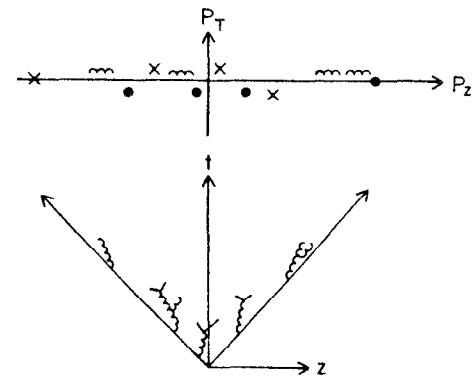
These ideas [13] are represented pictorially in Fig. 1 for the simplest case of electron-positron annihilation at total energy W (Fig. 1(a)). The situation just after the virtual photon produces a $Q\overline{Q}$ pair separating in the z direction is illustrated in Fig. 1(b), both in momentum space and in configuration space (in light cone notation). Note that in momentum space the quarks are initially isolated while in coordinate space they start together but tend to separate as time passes. For short space-time separations (as observed in any frame) the quarks evolve as described by perturbation theory. Gluons are emitted (and sometimes reabsorbed) and result in further quark pairs or more gluons as noted in Fig. 1(c). The emission of energetic, wide angle gluons or quarks is the precursor of N-JET final states (N > 2). Note that, as viewed in momentum space, the region between the initially isolated quarks begins to be populated by this process (the vacuum is ionized). The initial quarks themselves lose energy via this process (they move along paths which curve away from the light cone if they have nonzero masses). At some space-time distance scale explicitly nonperturbative physics sets in (in a Lorentz invariant fashion) as indicated by the hyperbolic boundary in Fig. 1(d). The precise value of the scale describing this transition is presently unknown (see below) but is surely bound above by 1 Fermi. There is further nonperturbative quark pair production and



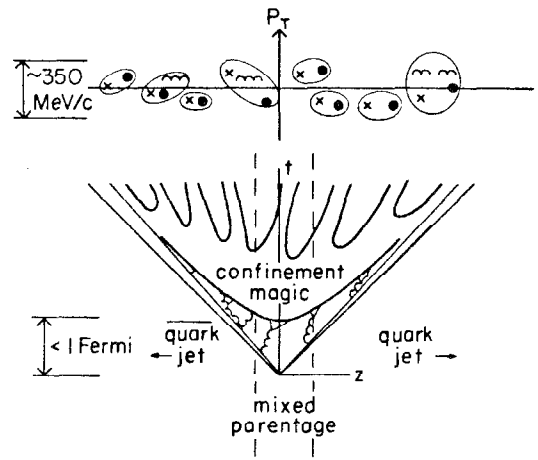
(a)



(b)



(c)



(d)

Fig. 1 Idealized picture of process $e^+e^- \to$ *hadrons*. (a) Lowest order Feynman graph, $e^+e^- \to \gamma^* \to Q\bar{Q}$. (b) Initial situation in momentum space and configuration space. (c) Situation at intermediate time. (d) Situation at long times.

finally, at long distances, organization into color singlet hadrons occurs as illustrated. Note that, in accordance with assumption (4) above, the distribution of final hadrons in momentum is limited in the transverse direction leading to the canonical two-JET structure. In an admittedly pictorial, nonrigorous language, the "string" which confines the initial two quarks is not strong but rather breaks easily, producing quark pairs, and subsequently hadrons, moving generally in the initial direction. Note that a picture with "strong strings" and high mass, narrow resonances, which decays via sequential, uncorrelated decays, will not yield JETS.

While only pieces of this simple picture are derived from QCD at present, it is clearly suggested by data. The procedure is to treat as much as possible by perturbative methods in the context of QCD and deal with the long distance nonperturbative physics via models which are fitted to low energy data. The central outstanding issue is then to determine the distance/momentum scale which characterizes the boundary between perturbative and nonperturbative physics. While the concept of this scale should be clear, a precise definition is possible only within the context of a specific experimentally measurable quantity. The essential phenomenological issue is to what extent our ignorance of this scale affects our ability to understand experimental results and to explicitly test QCD. Note, for example, that any attempt to associate the final state hadrons with specific JETS as illustrated in Fig. 1(d) is bound to suffer ambiguity for the "soft" hadrons. While the energetic hadrons are clearly associated with a specific JET, the necessary sharing of color quantum numbers between the JETS guarantees a mixed parentage for at least some of the slow hadrons as illustrated. The precise definition of the scale of "softness" where this effect becomes important is exactly the major issue noted above: What is the range in momentum space of the correlations which couple different JETS? This ambiguity will play a substantial role in the discussion on how to see JETS.

The example of JETS in e^+e^- annihilation offers a partial answer to Question (3), "Where are JETS?". There are at least two other standard reactions where JET structure is anticipated in the hadronic final state as suggested by Fig. 2. The simplified view of deep inelastic lepton (electron, muon or neutrino)-hadron scattering exhibited in Fig. 2(a) illustrates how the "struck quark" is expected to yield a large angle (with respect to the initial hadron direction in the overall CM frame) JET while the remaining, "spectator" quarks yield a beam oriented JET. For the case of a baryon target (with three quarks), this simple picture suggests that the latter JET is a "diquark" JET. The

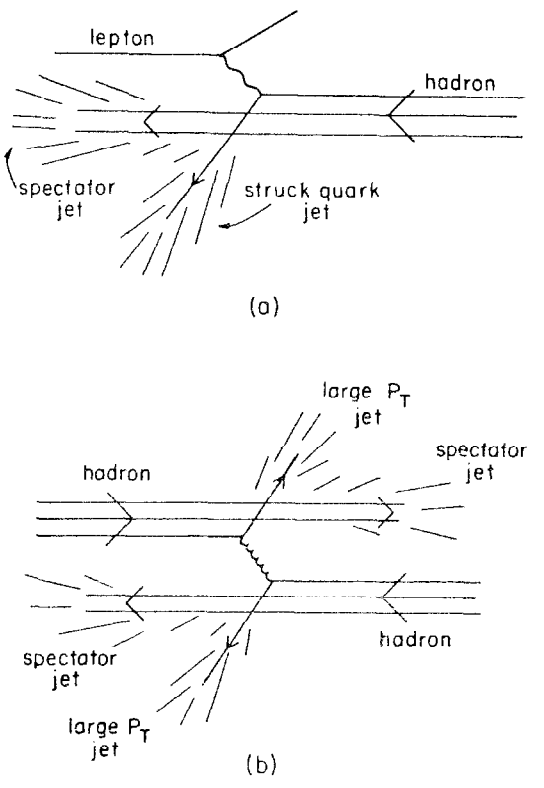


Fig. 2 Other deep inelastic processes with JETS expected in the final state. (a) Lepton-hadron scattering to yield a struck quark JET and a spectator JET. (b) Hadron-hadron scattering to yield 2 large P_T JETS and 2 spectator JETS.

same ideas are easily transferred to the case of deep inelastic hadron-hadron scattering, [14] also referred to as large P_T (transverse momentum) physics, as illustrated in Fig. 2(b). Note in particular the characteristic 4-(or more)-JET structure of the final state in this case. The quite spectacular recent data on this process are discussed elsewhere. [2,14]

The last topic to be treated in the Introduction is the question of how JETS can be detected experimentally. This issue is discussed more expertly elsewhere. [1,2,7] Here there will appear only a theorist's warning. The difficulty arises because (grasping for quasi-poetic analogies) like "true love," a JET is impossible to define precisely, but YOU KNOW IT WHEN YOU SEE IT. Thus, while events which contain JETS are, after the fact, obvious, the game of explicitly triggering on JETS is filled with pitfalls. [14,15] Such a trigger must necessarily define the "size" of the JETS to be detected. However, as noted earlier, there are always some hadrons present in a given event which, even in principle, cannot be uniquely associated with a specific JET. Thus there is always some ambiguity in such a definition. This means theoretically a sensitivity to details which are not under complete control, in particular, the soft, nonperturbative structure of the JET and the correlations between JETS as discussed above. Experimentally the difficulty can be characterized as another attack of the dreaded "trigger bias", [16] YOU SEE WHAT YOU LOOK FOR! Small calorimeters will detect narrow JETS while large detectors will see broader JETS. This means including in the JET fewer or more of the soft hadrons of ambiguous parentage. Thus there is, in principle, an uncertainty in JET energies of approximately $\pm 500 MeV$ which, due to the steeply falling cross sections, can mean a sizeable uncertainty in the magnitude of the JET production cross section in hadronic reactions. At small total JET energy ($E_T \sim 5 - 10 GeV$), where the cross section is approximately exponentially behaved, this uncertainty can be as large as a factor 5. However, at the large E_T's now observed [2] ($E_T \gg 10 GeV$) where the cross section is power behaved ($\sim {E_T}^{-n}, n \geq 5$), the uncertainty in the magnitude of the JET cross section is a rapidly decreasing function of E_T, $\sim \pm n(500 MeV)/E_T$. It will likely be negligible in future experiments.

Due to the difficulties just discussed, it is important to distinguish the various types of JET-measures and JET-properties. Inclusive quantities [17] suffer the least from trigger bias problems and can be treated at fixed order in perturbation theory. These quantities offer the best hope of detailed tests of perturbative QCD. More exclusive quantities, like specific JET triggers, require all order perturbative analyses and are likely to be sensitive also to nonperturbative effects, as noted above. The remainder of these lectures will proceed in this direction of decreasing simplicity and rigor, from fixed order studies to all order renormalization group improved perturbation theory to nonperturbative questions.

II. FIXED ORDER PERTURBATION THEORY

The present review of perturbation theory will necessarily be rather brief. The interested student is encouraged to perform the suggested homework problems with some help from the Appendices and to consult the several good reviews [4] now available. As an example (beloved by the author) of inclusive experimental quantities which can be studied with perturbation theory in fixed order, consider the various energy weighted measures of hadronic final states in e^+e^- annihilation, [5,6] corresponding crudely to measures of JETS and their correlations. The simplest and most inclusive quantity is, of course, the total annihilation cross section, but it carries no information about "jettiness." To understand why such quantities are (and others are not) well behaved in perturbation theory it is sufficient to understand the basic singularity structure of perturbative QCD. For this purpose it is possible to divide the singularities into three varieties.

(1) Ultraviolet:

It is these short distance/large momentum singularities which, when summed to all orders, lead to the renormalization of the coupling. The types of graphs which yield the leading contributions (in an appropriate gauge) are illustrated in Fig. 3. The form of the running (renormalized) coupling including both the leading and first subleading (two loop) contributions (the $\overline{MS}$ subtraction scheme is used throughout) is

$$\frac{\alpha_s(Q^2)}{2\pi} = \frac{1}{b_0 \ln \frac{Q^2}{\Lambda^2} + (b_1/b_0) \ln \ln \frac{Q^2}{\Lambda^2}} \qquad (II.1)$$

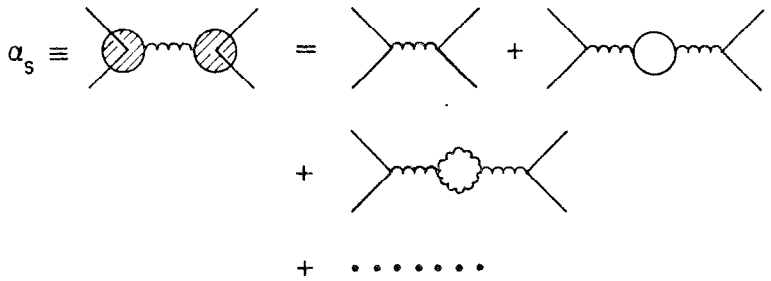


Fig. 3 Sample of Feynman graphs "summed" to yield the renormalized, running coupling.

where

$$b_0 = (11C_A - 2N_f)/6$$
$$b_1 = (17/6){C_A}^2 - (5/6)C_A N_f - C_F N_f/2 \qquad (II.2)$$

and $C_F = ({N_C}^2 - 1)/(2N_C) = 4/3$ is the value of the Casimir operator in the fundamental fermion representation (a measure of the strength of the color coupling to the fermions), $C_A = N_C = 3$ is the Casimir value in the adjoint representation, and N_f is the number of fermion (quark) flavors. The dimensionful parameter Λ characterizes the scale at which the strong interactions are truly strong (experimentally $\Lambda \sim 150 \pm 100 MeV$). In what follows this renormalization (summation of perturbative contributions) will be assumed and the running coupling used explicitly without further comment. Ultraviolet divergences also lead to wave function renormalizations but these will play no explicit role in the present discussions.

(2) Collinear:

These singularities arise in perturbative graphs when, for example, a gluon is emitted by a quark in a direction collinear with the quark as illustrated in Fig. 4, which is to be thought of as embedded in a larger graph. To see an explicit divergence consider massless quarks and gluons ($(k)^2 = (p')^2 = 0$) and evaluate the mass of the initial quark

$$p^2 = (p')^2 + (k)^2 + 2p' \cdot k \quad . \qquad (II.3)$$

Clearly this quark also goes "on shell" in the collinear limit, $p_\mu \parallel k_\mu$, yielding a divergent contribution in this limit.

(3) Infrared:

If the gluon emitted in Fig. 4 is instead (or also) soft, i.e., in the limit $k_\mu \to 0$, the quark of Eq. (II.3) can again go on shell and yield a divergent contribution.

The basic structure of all the perturbative results that follow can be simply under-

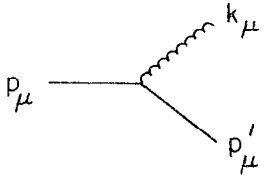


Fig. 4 Generic gluon emission vertex.

stood if these fundamental properties of the theory are remembered. To this end a helpful homework exercise (#I) is to calculate the cross section describing the inclusive production of a quark from the annihilation of an e^+e^- pair (recall Fig. 1(a)) at a specific angle with respect to the lepton beam direction. This should be performed both at order $(\alpha_s)^0$ and order $(\alpha_s)^1$. Since this second quantity will exhibit the divergences just discussed, it is necessary to regulate the divergences in some fashion so as to obtain an explicit result. A plebian but straightforward procedure is to award the gluon a nonzero mass μ. This will, of course, break the formal gauge symmetry but will cause no difficulties in the present calculations. The more purist minded students are encouraged to calculate instead in ν ($\neq 4$) dimensions and change logarithms of the gluon mass (see below) into poles in the quantity $\epsilon = \nu - 4$. Helpful hints and results are found in Appendix A.

The next homework exercise (#II), to be discussed explicitly in the lectures, is to evaluate in the same way the energy weighted cross section, the "antenna pattern" [5] with the geometry illustrated in Fig. 5. This will serve not only to illustrate again the divergences already present in Exercise I but also to demonstrate how the singularities cancel in appropriately defined quantities. The antenna pattern is defined by

$$\frac{1}{\sigma}\frac{d\Sigma}{d\sigma} = \frac{1}{N}\sum_{A=1}^{N}\sum_{a=1}^{n}\left(\frac{E_{Aa}}{W}\right) \quad , \qquad (II.4)$$

where E_{Aa} is the energy of the ath particle in event A. When applied to perturbative calculations the sum is over quarks and gluons (an approximation to be treated later), while in real experiments the sum is over the observed hadrons or simply the observed energy for purely calorimetric experiments. The idea is that, while exclusive cross sections, e.g., the quark cross section, exhibit singularities in perturbation theory, inclusive cross sections such as the energy flow in a specified direction will be singularity free (more on this later). The analogy is that an electrical engineer would never discuss an antenna in terms of its efficiency to broadcast individual photons, but would rather discuss the energy broadcast as a function of direction.

At order $(\alpha_s)^0$ the antenna pattern is easily obtained from the result of the previous exercise. Since the quark and antiquark each carry one half of the total energy W, the

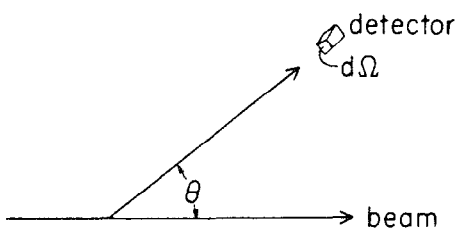


Fig. 5 Geometry of the antenna pattern experiment.

energy weighting introduces a factor 1/2. The sum over the quark and antiquark in turn produces a factor 2. Thus the antenna pattern is identical to the quark cross section at this order in perturbation theory,

$$\frac{1}{\sigma_0}\frac{d\Sigma^0}{d\Omega} = \frac{3}{16\pi}(1+\cos^2\theta). \qquad (II.5)$$

This result illustrates the normalization condition implicit in Eq. (II.4)

$$\int d\Omega \frac{1}{\sigma}\frac{d\Sigma}{d\Omega} = 1. \qquad (II.6)$$

At next order the perturbative diagrams corresponding to "real" gluon emission are illustrated in Fig. 6(a). The contribution to the antenna pattern arising from these graphs when it is the quark or antiquark which is observed is straightforward to evaluate (do it!) and is very similar to the order $(\alpha_s)^1$ result in Exercise I. The result is

$$\frac{1}{\sigma_0}\frac{d\Sigma^{Q+\overline{Q}}_{REAL}}{d\Omega} = \frac{3}{16\pi}\frac{\alpha_s C_F}{2\pi}\left[\left(\ln^2\frac{1}{\epsilon} - \frac{13}{3}\ln\frac{1}{\epsilon} - \frac{\pi^2}{3} + \frac{80}{9}\right)(1+\cos^2\theta) + \frac{1}{2}(1-3\cos^2\theta)\right] + O(\epsilon) \qquad (II.7)$$

where $\epsilon = \mu^2/W^2$. This result clearly illustrates the first perturbative

LESSON: There are up to 2 divergent logarithms per factor of α_s, having already summed the UV divergences.

The appearance of two logarithms simply corresponds to the overlap of the collinear and infrared conditions discussed above. The graphs corresponding to virtual gluons

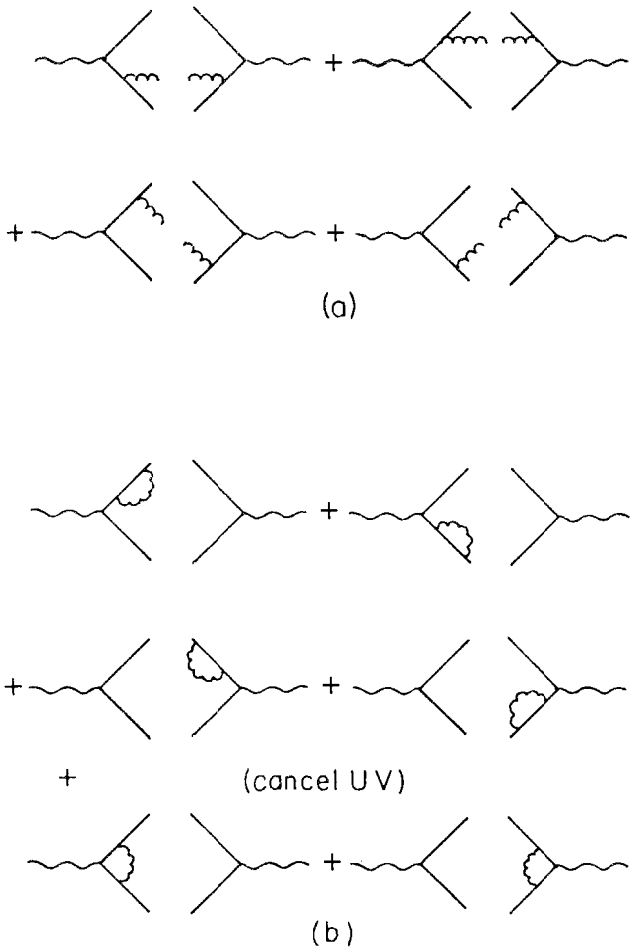


Fig. 6 Feynman graphs for the first order contributions. (a) "Real" gluon emission. (b) Virtual gluon contributions.

are exhibited in Fig. 6(b) where, when the two distinct types are summed, the inherent UV singularities in the loops cancel. Again the contribution to the antenna pattern corresponding to observing the quark and antiquark is trivially related to the result of Exercise I,

$$\frac{1}{\sigma_0}\frac{d\Sigma^{Q+\overline{Q}}_{VIRT}}{d\Omega} = -\frac{3}{16\pi}\frac{\alpha_s C_F}{2\pi}\left[\left(\ln^2\frac{1}{\epsilon} - 3\ln\frac{1}{\epsilon} - \frac{\pi^2}{3} + \frac{7}{2}\right)(1+\cos^2\theta)\right] + O(\epsilon). \tag{II.8}$$

Adding these two expressions yields

$$\frac{1}{\sigma_0}\frac{d\Sigma^{Q+\overline{Q}}_{SUM}}{d\Omega} = \frac{3}{16\pi}\frac{\alpha_s C_F}{2\pi}\left[\left(-\frac{4}{3}\ln\frac{1}{\epsilon} + \frac{97}{18}\right)(1+\cos^2\theta) + \frac{1}{2}(1-3\cos^2\theta)\right] + O(\epsilon). \tag{II.9}$$

Note that the double logarithm has cancelled, leaving only a single logarithm corresponding to a collinear configuration. This is the second perturbative

LESSON: Infrared divergences cancel when real and virtual contributions are added in an unrestricted fashion.

It is also useful for subsequent discussions to note that sums of collinear divergences will be generically of the maximally divergent form ${\alpha_s}^n \ln^n \frac{1}{\epsilon}$ order by order in perturbation theory.

Now consider the possibility of observing the energy carried by the gluon. This contribution clearly arises at first order in the graphs of Fig. 6(a). The corresponding contribution to the antenna pattern is easily found to be

$$\frac{1}{\sigma_0}\frac{d\Sigma^G}{d\Omega} = \frac{3}{16\pi}\frac{\alpha_s C_F}{2\pi}\left[\left(\frac{4}{3}\ln\frac{1}{\epsilon} - \frac{35}{9}\right)(1+\cos^2\theta) + (1-3\cos^2\theta)\right] + O(\epsilon). \qquad (II.10)$$

Summing all the contributions (and setting ϵ to 0) yields the full antenna pattern

$$\frac{1}{\sigma_0}\frac{d\Sigma}{d\Omega} = \frac{3}{16\pi}\left[\left(1+\frac{\alpha_s}{2\pi}\frac{3}{2}C_F\right)(1+\cos^2\theta) + \frac{\alpha_s}{2\pi}\frac{3}{2}C_F(1-3\cos^2\theta)\right]. \qquad (II.11)$$

This illustrates the third and perhaps most important perturbative

LESSON: All divergences cancel for properly chosen quantities.

Since the antenna pattern (or any energy weighted quantity) is insensitive to soft, infrared emissions and does not distinguish between a quark and a quark accompanied by a collinear gluon, the divergences have cancelled in the final result. This is analogous to, but not identical with, the cancellations which occur in QED as summarized in the KLN theorem. [18] The result will be restated and reinterpreted in a more modern language below. The final conclusion from these exercises is that, by using perturbatively finite, energy weighted measures, it should be possible to study JETS perturbatively.

As an example consider the JET-JET angular correlation in e^+e^- annihilation as measured by the Energy-Energy Correlation [6] (EEC). It is simplest to first study the EEC only as a function of χ, the angle between the two "calorimeters" as illustrated in Fig. 7. In this case, when all external angles have been summed over, the EEC is defined by

$$\frac{\sin\chi\,\Delta\chi}{\sigma}\frac{d\Sigma}{d\cos\chi} = \frac{2}{N}\sum_{\substack{events\\A=1}}^{N}\sum_{\substack{pairs\ ab\\a\neq b}}\frac{E_{Aa}E_{Ab}}{W^2} + \frac{1}{N}\sum_A\sum_a\frac{E_{Aa}{}^2}{W^2}\delta(1-\cos\chi) \quad ,$$

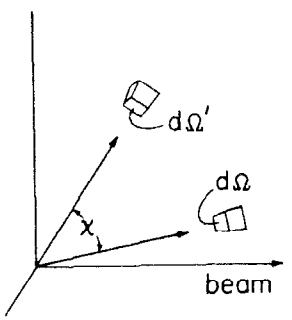


Fig. 7 Geometry for the Energy-Energy Correlation experiment.

$$\cos\left(\chi+\frac{\Delta\chi}{2}\right)\leq\hat{a}\cdot\hat{b}\leq\cos\left(\chi-\frac{\Delta\chi}{2}\right)\quad . \tag{II.12}$$

Due to the inclusion of the second, self-correlation term the EEC has normalization (similar to the antenna pattern)

$$\int d\cos\chi\frac{1}{\sigma}\frac{d\Sigma}{d\cos\chi}=\frac{1}{NW^2}\sum_A\left[\sum_a {E_{Aa}}^2+2\sum_{\substack{pairs\ ab\\ a\neq b}}E_{Aa}E_{Ab}\right]=1\quad . \tag{II.13}$$

As Exercise III evaluate this quantity at order $(\alpha_s)^1$. At angles other than 0°or 180°, only the "real" emission graphs of Fig. 6(a) contribute with the angle χ serving as a physical cutoff. To understand the structure of this quantity in perturbation theory and for the purposes of later discussion, it is useful to isolate the two types of perturbative contributions. When it is the quark and antiquark whose energies are being observed, the EEC has the following form in terms of the natural angular variable $\varsigma = (1-\cos\chi)/2$

$$\frac{1}{\sigma_0}\frac{d\Sigma^{Q+\overline{Q}}}{d\cos\chi}=\frac{\alpha_s}{2\pi}\frac{C_F}{2}\left[\frac{4-3\varsigma}{\varsigma^5}\ln\frac{1}{1-\varsigma}-\frac{4}{\varsigma^4}+\frac{1}{\varsigma^3}+\frac{1}{6\varsigma^2}\right]\quad . \tag{II.14}$$

To understand a little about why it has this form consider the limit $\chi\rightarrow 180°, \varsigma\rightarrow 1$. In this limit, this piece of the EEC behaves as

$$\begin{aligned}\frac{1}{\sigma_0}\frac{d\Sigma^{Q+\overline{Q}}}{d\cos\chi}\quad &\underset{\chi\rightarrow 180°}{\rightarrow}\quad \frac{\alpha_s}{2\pi}\frac{C_F}{2}\left[\frac{1}{1-\varsigma}\ln\frac{1}{1-\varsigma}-\frac{17/6}{1-\varsigma}\right]\\ &\sim\quad \frac{\partial}{\partial(1-\varsigma)}\frac{\alpha_s}{2\pi}\frac{C_F}{2}\left[\frac{1}{2}\ln^2(1-\varsigma)-\frac{17}{6}\ln(1-\varsigma)\right]\end{aligned} \tag{II.15a}$$

where the appearance of the logarithms is easily understood as the footprint of the singularities due to the emission of collinear and/or soft gluons discussed above. Since in this back-to-back configuration both types of emissions are possible kinematically, there are potentially two powers of logarithms per power of α_s. The study of this Double Leading Logarithm Approximation (DLLA) structure is an extremely interesting field in its own right. [19] Unfortunately it is not possible to pursue it further here.

Now consider the opposite limit $\chi\rightarrow 0°, \varsigma\rightarrow 0$ where the quark contribution to the EEC behaves as

$$\frac{1}{\sigma_0}\frac{d\Sigma^{Q+\overline{Q}}}{d\cos\chi}\quad \underset{\chi\rightarrow 0°}{\rightarrow}\quad \frac{\alpha_s}{2\pi}\frac{C_F}{2}\frac{1}{20}\quad , \tag{II.15b}$$

i.e., the gluon can be neither soft nor collinear in this configuration and this contribution is finite in this limit.

Contrast this behavior with that for the contribution when it is a quark (or antiquark) and gluon which are observed. This piece of the EEC has the form

$$\frac{1}{\sigma_0}\frac{d\Sigma^{Q+G}}{d\cos\chi}=\frac{\alpha_s}{2\pi}\frac{C_F}{2}\left\{\frac{1}{1-\varsigma}\frac{1}{\varsigma^5}\left(13-\frac{41}{2}\varsigma+\frac{53}{6}\varsigma^2\right)+\left(\frac{13-14\varsigma+4\varsigma^2}{\varsigma^5}\right)\ln(1-\varsigma)\right\}\quad , \tag{II.16}$$

with corresponding limits

$$\begin{aligned}\frac{1}{\sigma_0}\frac{d\Sigma^{Q+G}}{d\cos\chi}\quad &\underset{\chi\rightarrow 180°}{\rightarrow}\quad \frac{\alpha_s}{2\pi}\frac{C_F}{2}\frac{4}{3}\frac{1}{1-\varsigma}\\ &\sim\quad \frac{\partial}{\partial(1-\varsigma)}\frac{\alpha_s}{2\pi}\frac{C_F}{2}\left[\frac{4}{3}\ln(1-\varsigma)\right]\quad ,\end{aligned} \tag{II.17a}$$

and

$$\frac{1}{\sigma_0}\frac{d\Sigma^{Q+G}}{d\cos\chi} \underset{\chi\to 0^\circ}{\longrightarrow} \frac{\alpha_s}{2\pi}\frac{C_F}{2}\frac{3}{4}\frac{1}{\zeta} \sim \frac{\partial}{\partial\zeta}\frac{\alpha_s}{2\pi}\frac{C_F}{2}\left[\frac{3}{4}\ln\zeta\right] \quad . \tag{II.17b}$$

In this case the gluon, since it is observed, cannot be soft but can be collinear either with the unobserved quark (back-to-back configuration) or with the observed quark (front-to-front configuration). Thus, as expected, there is the derivative of a single logarithm in each limit. In fact the collinear front-to-front logarithm corresponds to the perturbative structure within a JET. This subject will be discussed in some detail in Section III.

For now consider the total first order perturbative EEC [the sum of (II.14) and (II.16)]

$$\frac{1}{\sigma_0}\frac{d\Sigma^{QCD}}{d\cos\chi} = \frac{\alpha_s}{2\pi}\frac{C_F}{4}\left[\frac{3-2\zeta}{\zeta^5(1-\zeta)}\right]\left[3\zeta(2-3\zeta)+2(3-6\zeta+2\zeta^2)\ln(1-\zeta)\right] \quad . \tag{II.18}$$

Written in this form the general behavior discussed above is less than transparent. Consider instead the simple analytic form obtained by fitting the above expression (good to a few percent) in the range $|\cos(\chi)| < 0.9$,

$$\frac{1}{\sigma_0}\frac{d\Sigma^{QCD}}{d\cos\chi} \simeq \frac{\alpha_s}{\pi}\left[\frac{1.21}{\sin^{2.5}\chi} - \frac{0.38\cos\chi}{\sin^3\chi}\right] \quad . \tag{II.19}$$

Perhaps the most dramatic result illustrated by this form (and already suggested by the differences between Eqs. (II.15a,17a) and (II.15b,17b) above) is the significant asymmetry of the perturbative result. For angles χ less than 90° the asymmetry is defined as the difference between the EEC at $180^\circ - \chi$ and that at χ which, from Eq.(II.19), is given approximately by

$$A(\chi) \equiv \frac{1}{\sigma_0}\left[\frac{d\Sigma}{d\cos\chi}(180^\circ-\chi) - \frac{d\Sigma}{d\cos\chi}(\chi)\right] \simeq \frac{\alpha_s}{\pi}\frac{0.76}{\sin^3\chi}\cos\chi \quad . \tag{II.20}$$

This general structure is clearly present in the data. [1,20,21,22]

From the standpoint of fixed order perturbation theory the next step is clear—calculate the second order contributions to the EEC. This computation has in fact been performed [21,22] with interesting results. The general behavior of the EEC is invariant under the inclusion of the next order contributions suggesting that, at least from the standpoint of perturbation theory, it is a useful quantity for testing QCD. In particular, the second order results [21] can be characterized by the replacement $(\sigma_0 \to \sigma_0\left[1+\frac{3}{4}C_F\frac{\alpha_s}{\pi}\right]$ on the lefthand side and)

$$\frac{\alpha_s}{\pi} \to \frac{\alpha_s}{\pi}\left(1+R(\chi)\frac{\alpha_s}{\pi}\right) \tag{II.21}$$

on the righthand side in the first order results. Here α_s is explicitly the two loop form of Eq. (II.1). It turns out that $R(\chi)$ is essentially constant for $|\cos(\chi)| < 0.8$. For the asymmetry the magnitude of R is about 3 indicating that second order fits to data for the asymmetry yield values of α_s which are smaller than the first order result by approximately 15%. The small size of this change again suggests that measurements of such JET correlations may offer a reliable way to determine α_s and test QCD. The issue of nonperturbative corrections to this approach will be treated in Section IV. First consider the internal structure of JETS as implied by the perturbative collinear singularities seen already in Eq. (II.17b). This is the topic of Section III.

III. PERTURBATIVE STRUCTURE OF JETS

The study of the structure of JETS using perturbative techniques in the context of QCD is already a fairly mature field [4,23-29] and the discussion here will cover only the high points with special emphasis on the recent developments. Derivations and insights will be of a "pictorial" rather than detailed and rigorous nature. It is hoped that this introduction will induce the avid student to consult the original papers and/or the excellent reviews [4] available for further details. Before reviewing this wealth of knowledge it is extremely important to preface the discussion with the warning that the results discussed below only become correct asymptotically. Furthermore, there is an ambiguity about when asymptotia sets in which cannot be treated by perturbative techniques alone.

To introduce the relevant concepts rewrite Eq. (II.17b) in the suggestive form

$$\begin{aligned} \frac{1}{\sigma_0}d\Sigma \quad &= \quad \frac{d\varsigma}{\varsigma}\frac{\alpha_s}{2\pi}C_F\int dz\frac{1+z^2}{1-z}zx + \left[\begin{matrix}\text{nonsingular}\\ \varsigma\to 0\end{matrix}\right]d\varsigma \\ &\underset{\varsigma\to 0}{\to} \quad \frac{d\varsigma}{\varsigma}\cdot\frac{\alpha_s}{2\pi}C_F\cdot\frac{3}{4} \quad , \end{aligned} \qquad (III.1)$$

where $z = E_Q/E_{JET}$ and $x = E_G/E_{JET} = 1 - z$ with $E_{JET} \simeq W/2$. The explicit factor of $1/\varsigma$ exhibits the presence of the collinear singularity already discussed. The numerical factor 3/4 arises from the indicated integral over the longitudinal structure within the JET. Note the factor $1/(1-z)$ which is the previously discussed soft singularity. The relationship between these factors will be discussed in more detail shortly. For the moment the important feature of (III.1) is that the presence of the collinear singularity renders fixed order perturbation theory inappropriate for the analysis of the internal structure of JETS. This was already indicated in the previous section where the EEC was singular in the small χ limit. To deal with this problem the most singular contributions, order by order, must be summed to all orders. Furthermore it is ONLY the singular contributions which are included correctly in the following analysis. This improved version of perturbation theory will serve to renormalize the structure of the JET, the so called fragmentation function, and will exhibit the usual nonscaling behavior of QCD.

To make these concepts more concrete note that in the small ς limit, due to these collinear singularities, the EEC will have the general form

$$\varsigma\frac{1}{\sigma}\frac{d\Sigma}{d\varsigma} \quad \underset{\varsigma\to 0}{\sim} \quad \varsigma\frac{d}{d\varsigma}\sum_{n=1}^{\infty}\sum_{m=0}^{n}C_{nm}\left(\frac{\alpha_s}{2\pi}\right)^n\left(\ln\frac{1}{\varsigma}\right)^{n-m} \quad , \qquad (III.2)$$

as suggested by Eq. (III.1) (and indicated in the explicit second order results of Ref. [21]). Here the terms with $m = 0$ correspond to the leading collinear singularities (the leading single logarithms), order by order, $m = 1$ the next-to-leading singularities and so on. As noted earlier these singularities arise from the propagation of nearly onshell quanta and hence might be thought of as corresponding to the "long-time/distance" perturbative structure of the JET (a rather different language from the "short distance" emphasis in deep inelastic scattering). Thus it is perhaps not surprising, but still difficult to prove in general [29] (and will not be demonstrated here), that the singular collinear perturbative structure of the JET factors from the rest of the specific process. This important result is the next perturbative

> *LESSON: The (singular) perturbative structure of (quark and gluon) JETS is universal.*

Note that the coefficients C_{nm}, in fact, depend on the specific quantity calculated but can be easily obtained from the universal structure of JETS as illustrated below. Strictly speaking the C_{nm} can depend on the dimensional scale used to define the JETS but here there is a single natural scale, W, and the C_{nm} are simply numbers.

While the details of the analysis outlined above may appear complicated, the associated physical picture and interpretation is extremely simple and elegant. With an appropriate choice of gauge (i.e., axial or planar, $A\cdot\hat{n} = 0$, where A_μ is the gluon field), the most singular contributions (i.e.,the leading logarithms) arise from the ladder graphs of the generic form illustrated in Fig. 8 where the various characteristic vertices

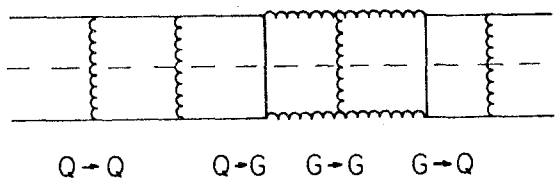


Fig. 8 Illustration of the generic ladder graph structure which yields the leading logarithm approximation.

are labelled. The dashed line is to indicate where the appropriate discontinuity is to be taken and serves to make explicit the important feature that these leading contributions arise (in this gauge) from the square of an amplitude. Thus, at this leading logarithm (one loop) approximation a semiclassical, probabilistic interpretation is possible. To obtain an explicit expression focus first on an individual vertex as in Fig. 9, where the emission of a gluon by a quark is exhibited. To proceed, the emitted gluon (in fact, all quanta cut by the dashed line in Fig. 8) is taken to be "onshell" with mass Q_0^2. This scale supplies the necessary "unphysical" cutoff and will play an essential role in the subsequent discussion. Recall that for the EEC in Eq. (III.1) there is a natural "physical" cutoff, ςQ^2. It is also explicitly assumed in the following analysis that only perturbative QCD contributions are relevant for $Q^2 \geq Q_0^2$, i.e., that nonperturbative effects are negligible. It is further assumed that in this regime a perturbative expansion is appropriate (i.e., $\frac{\alpha_s(Q_0^2)}{\pi} \ll 1$). With an appropriate choice of variables the general form of this vertex (i.e., the kinematics) looks like

$$|\text{vertex}|^2 \quad \alpha \quad \int dq'^2 \frac{d^2q'_T}{\pi} dz\, \delta(z(1-z)q^2-(1-z)q'^2-zQ_0^2-(q'_T)^2)\,|\mathcal{M}|^2. \quad (III.3)$$

Here $\mathcal{M}$ represents the appropriate piece of the matrix element (see below), the δ function arises from the onshell δ function of the emitted gluon, z is the momentum fraction of the continuing quark which is generally defined as the "light cone fraction"

$$z = \frac{q'^+}{q^+} = \frac{(q'_0+q'_3)/\sqrt{2}}{(q_0+q_3)/\sqrt{2}} \quad , \qquad (III.4)$$

and q'_T is the transverse momentum and q'^2 the "offshellness" of the continuing quark. The leading contributions turn out to arise from the "strong ordered" phase space for Fig. 8 which, for the single vertex of Fig. 9, means $q'^2 \ll q^2$. If one is calculating a quantity which is insensitive to the region $z \to 0$ (and $z \to 1$), the transverse momentum integral can be performed trivially using the "onshell" constraint delta function. However, it is important to keep in mind the implicit bounds ${q'_T}^2, q'^2 < zq^2$

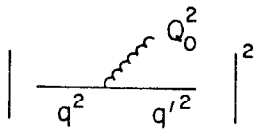


Fig. 9 Vertex for "onshell" gluon emission, the end of a rung in Fig. 8.

which arise from doing the kinematics correctly and which will be essential for questions involving small z. Ignoring momentarily the constants (the C_{nm}) which arise from the z integrals, only the integral over the "offshellness," q'^2, remains. In the strong ordered region mentioned earlier,

$$q^2 \gg q'^2 \gg q''^2 \ldots q^{(n)2} \gg Q_0^2 \quad ,$$

the integrals implicit in the iteration of Fig. 9 and Eq. (III.3) to obtain Fig. 8 decouple. Thus the simple nested form

$$\int^{q^2} \frac{dq'^2}{q'^2} \int^{q'^2} \frac{dq''^2}{q''^2} \cdots \int_{Q_0^2}^{q^{(n-1)2}} \frac{dq^{(n)2}}{q^{(n)2}} \qquad (III.5)$$

is obtained where the well know collinearly singular pieces [the $1/q^2$'s] of the matrix element are explicitly displayed. This clearly leads to the $\ln^n(q^2/Q_0^2)$ structure of Eq. (III.2) and gives the specific form with the substitution $Q_0^2 = \varsigma q^2$.

The "physical" picture is that a quark of initial mass $q^2 \equiv Q^2$ evolves into one of mass Q_0^2 via the perturbative emission of n essentially collinear gluons. It is these collinearly emitted gluons (and quarks) which, when n is summed over, build up the perturbative JET. The treatment of the nonperturbative evolution from the scale Q_0^2 into hadrons will be postponed until Section IV. For the moment note that the essential question is: what is the scale Q_0^2 which characterizes the "size" of nonperturbative effects?

This simple motivation of the form of Eq. (III.2) has ignored the details of the longitudinal structure of the matrix element and the running coupling constant. A more complete analysis is most compactly performed in terms of the fragmentation function, $D(z, Q^2, Q_0^2)$. This function is interpreted as the inclusive distribution of b type partons of mass Q_0^2 in the z range, z to $z + dz$ in a JET due to an a type parton of mass Q^2. As an introduction to this quantity and a warm-up for the QCD JET, consider a goode olde parton model type incoherent JET. [30] Define the distribution

of $b\bar{c}$ type mesons of momentum fraction z in an a type JET as

$$dN_a^{b\bar{c}} \equiv dz\, D_a^{b\bar{c}}(z) \quad . \tag{III.6}$$

As input define the elementary emission process illustrated in Fig. 10(a), the analog of Fig. 9, by

$$dP_a^{b\bar{c}} = \delta_{ab} f_a^c(\eta) d\eta \quad , \tag{III.7}$$

where η is the momentum fraction of the remaining parton and $f(\eta)$ is a given function. The transverse degrees of freedom have been implicitly integrated over. Assuming independent emission and iterating this process generates Fig. 10(b), the analog of Fig. 8. The essential point is that the structure of this physical picture can be summarized by the integral equation

$$dz\, D_a^{b\bar{c}}(z) = \delta_{ab} f_a^c(1-z)dz + \sum_d \int_z^1 d\eta f_a^d(\eta) D_d^{b\bar{c}}\left(\frac{z}{\eta}\right)\frac{dz}{\eta} \quad , \tag{III.8a}$$

or

$$D_a^{b\bar{c}}(z) = \delta_{ab} f_a^c(1-z) + \sum_d \int_z^1 \frac{d\eta}{\eta} f_a^d(\eta) D_d^{b\bar{c}}\left(\frac{z}{\eta}\right) \quad . \tag{III.8b}$$

The inhomogeneous term corresponds to the case where the observed meson is the "first rank" meson which contains the initial quark while the second, integral term summarizes everything else. A pictorial representation of this equation is given in Fig. 10(c).

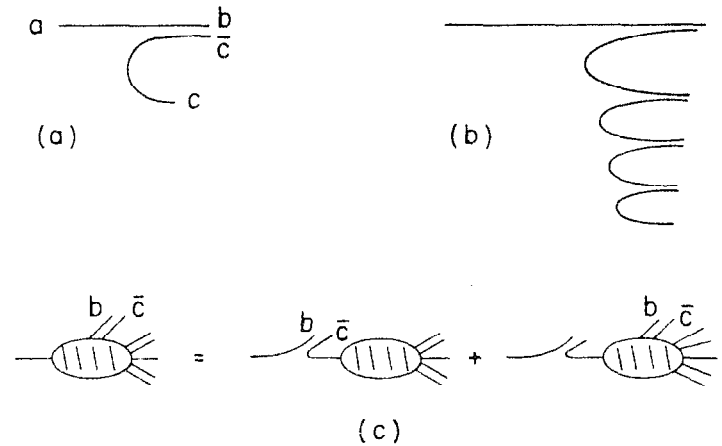


Fig. 10 Idealized structure of a JET in parton picture of Ref. [30]. (a) Basic meson emission vertex. (b) Iteration of the basic vertex. (c) Pictorial representation of the integral equation, Eq. (III.8).

Note that a simple integral equation of this general form must always arise when each of the elementary emission processes is essentially identical and independent, except for the quantum number flow explicitly accounted for by the matrix structure. In particular, something of this form is expected also for the QCD example. However, an essential complication in QCD arises due to the collinear singularities discussed at length above. This difficulty is explicitly indicated by the fact that, unlike Eq. (III.7), the elementary emission process of Eq. (III.3) involves not only an integral over the momentum fraction z but also a SINGULAR integral over the parton mass Q^2. For this reason it is a DIFFERENTIAL integral equation which one studies for QCD JETS. In particular, the SINGULAR part of the matrix element, which is all that is being included here, contains information concerning how the distribution VARIES WITH Q^2 but not about its form at a specific value of Q^2. [This is in contrast with the simple parton model of Eqs. (III.6-III.8) where a specific form of $f(\eta)$ serves to specify $D(z)$ as noted in Appendix B.] At the same time this structure implies that $D(z)$ MUST VARY WITH Q^2, the famous nonscaling of QCD. Said in a more pedestrian fashion, focusing on the derivative with respect to the offshellness Q^2 serves to focus on the collinearly singular piece of the matrix element, i.e., the coefficient of $\ln(Q^2)$.

As a first step toward seeing this structure explicitly rewrite Eq. (III.3) in the form of Eq. (III.7),

$$dP_a^b \equiv P_{a\to c}(x)dx \quad . \qquad (III.9)$$

Here the function $P(x)$ (the "Altarelli-Parisi function" [31]) is the analog of $f(\eta)$ and describes the longitudinal structure of the collinearly singular part of the matrix element in (III.3) (i.e., the coefficient of $1/q^2$). The analog of Eq. (III.8) becomes

$$dN_a^b = dz dD_a^b(z,Q^2,Q_0^2) = \frac{\alpha_s(Q^2)}{2\pi}\frac{dQ^2}{Q^2}\sum_c \int_z^1 dx P_{a\to c}(x) D_c^b\Big(\frac{z}{x},Q^2,Q_0^2\Big)\frac{dz}{x} \quad , \qquad (III.10a)$$

where the Q^2 dependence of the coupling is explicit and where, in perturbative QCD, the indices a, b, c, refer to quarks or gluons $(Q, \overline{Q}, G)$. Now dividing by both dz and $dQ^2/Q^2 = d\ln(Q^2/\Lambda^2) \equiv d\tau$, with $\tau_0 = \ln Q_0^2/\Lambda^2$, yields

$$\frac{\partial}{\partial\tau}D_a^b(z,\tau,\tau_0) = \frac{\alpha_s(\tau)}{2\pi}\sum_c \int_z^1 \frac{dx}{x}P_{a\to c}(x)D_c^b\Big(\frac{z}{x},\tau,\tau_0\Big) \quad . \qquad (III.10b)$$

The analog of Fig. 10c is illustrated in Fig. 11. Note that this equation also exhibits matrix structure, albeit for a somewhat different reason than Eq. (III.8). It is the study of this equation and its implications which constitutes the "JET calculus". [23]

The function $P(x)$ is well defined in the sense that it has a well defined expansion in powers of $\alpha_s/2\pi$,

$$P(x,\alpha_s) = P_{AP}(x) + \frac{\alpha_s}{2\pi}P_{nonleading}(x) + \cdots \quad , \qquad (III.11)$$

in which, at least in principle, all the terms are calculable. The first term is the usual Altarelli-Parisi result, [31] identical for both time-like processes, as here, and space-like processes, e.g., deep inelastic lepton-hadron scattering. It is this term which generates the leading logarithm terms in Eq. (III.2), i.e., $m = 0$. The next term in the expansion (III.11) leads to the next-to-leading logarithms, $m = 1$, and so on. For this reason this expansion is often referred to as a loop expansion corresponding to the topology of the relevant Feynman graphs. The nonsinglet piece of the second term has, in fact, been evaluated. [27]

For the present (abbreviated) purposes it is sufficient to focus on the first term (the leading logarithm approximation-LLA). The specific form of this matrix is (with no sum over flavors)

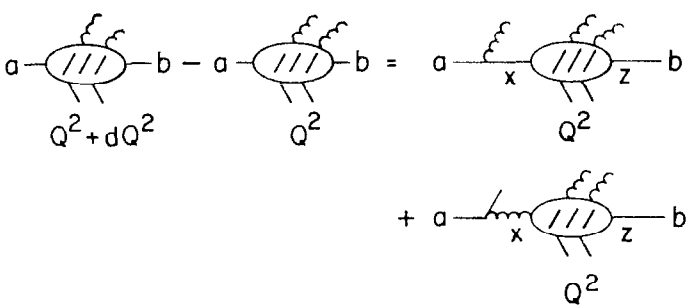


Fig. 11 Pictorial representation of the differential-integral equation, Eq. (III.10).

$$P_{a\to c} = \begin{array}{cc} \overset{(-)}{Q}\to\overset{(-)}{Q} & \overset{(-)}{Q}\to G \\ C_F\left(\frac{1+x^2}{1-x}\right)_+ & C_F\left(\frac{1+(1-x)^2}{x}\right) \\ G\to\overset{(-)}{Q} & G\to G \\ \frac{1}{2}(x^2+(1-x)^2) & 2C_A\left(\frac{1-x}{x}+x(1-x)+\left(\frac{x}{1-x}\right)_+ - \frac{\delta(1-x)}{12}\right)-\frac{N_f}{3}\delta(1-x) \end{array} \qquad (III.12)$$

where the symbol $)_+$ refers to the definition

$$\int dx f_+(x)g(x) \equiv \int dx f(x)[g(x)-g(1)] \quad . \qquad (III.13)$$

This somewhat peculiar definition plus the explicit $\delta(1-x)$ term arise from the fact that the virtual corrections to the matrix have been explicitly included in order to cancel the infrared divergence (recall the second perturbative Lesson) as $x \to 1$.

Since Eq. (III.10b) is an integral equation of the Volterra variety, the standard procedure for solving it is to introduce moments, just as in the case of the structure functions in deep inelastic scattering,

$$M_a^b(r,\tau) \equiv \int_0^1 dz\, z^r D_a^b(z,\tau,\tau_0) \quad , \qquad (III.14a)$$

and

$$A^{(s)}_{a\to b} \equiv \int_0^1 dx\, x^s P_{a\to b}(x) \quad . \qquad (III.14b)$$

As a warm up for what follows the student should perform homework Exercise IV which is to solve Eq. (III.8) using moments as discussed in Appendix B. The moment transform of Eq. (III.10b) is

$$\frac{\partial}{\partial\tau}M_a^b(r,\tau)=\frac{\alpha_s(\tau)}{2\pi}\sum_c A_{a\to c}^{(r)}M_c^b(r,\tau)\quad , \qquad (III.15)$$

which is trivially solved in terms of the matrix

$$[\kappa A]_{a\to c}\equiv\int_{\tau_0}^{\tau}d\tau'\frac{\alpha_s(\tau')}{2\pi}A_{a\to c}\quad , \qquad (III.16)$$

where the $A_{a\to c}$ factor is INSIDE the integral as a reminder that, beyond the leading approximation, $P_{a\to c}$ and thus $A_{a\to c}$ are functions of $\alpha_s(\tau')$ as in Eq. (III.11). In leading order (for both α_s and A) the form is

$$[\kappa A]_{a\to c}=\frac{1}{b_0}\ln\left(\frac{\tau}{\tau_0}\right)A_{a\to c}\quad . \qquad (III.17)$$

The general solution is

$$M_a^b(r,\tau)=\sum_c[exp(\kappa A)]_{a\to c}^{(r)}M_c^b(r,\tau_0)\quad . \qquad (III.18)$$

Note, as mentioned earlier, that in general perturbative QCD specifies only the Q^2 dependence for $Q^2>Q_0^2$ (the factor $exp[\kappa A]$), assuming that nonperturbative contributions are negligible in this region. The moment M at the specific value Q_0^2 enters simply as a constant of integration. It must be determined by other means, e.g., by experiment, if one desires to eventually make contact with the distributions of HADRONS in JETS,i.e., to replace $M_c^b(r,\tau)$ and $M_c^b(r,\tau_0)$ by $M_c^{HADRON}(r,\tau)$ and $M_c^{HADRON}(r,\tau_0)$. If the discussion is limited to only perturbative states, as here, then essentially by definition at $Q^2=Q_0^2$

$$M_c^b(r,\tau_0)=\delta_c^b\quad . \qquad (III.19)$$

As a "cultural" aside note that Eqs. (III.15) to (III.18) can be recaste in the language of a renormalization group equation as discussed briefly in Appendix C.

As homework Exercise V evaluate, in this order, the matrix $A_{a\to c}^{(r)}$, the anomalous dimension matrix. The result is ($NS=nonsinglet$)

$$\begin{aligned}
A_{\substack{(-)\\Q}\to\substack{(-)\\Q}}^{(r)}&=C_F\left[-\frac{1}{2}+\frac{1}{(r+1)(r+2)}-2\sum_{j=2}^{r+1}\frac{1}{j}\right]\equiv A_{NS}^{(r)}\\
A_{\substack{(-)\\Q}\to G}^{(r)}&=C_F\left[\frac{r^2+3r+4}{r(r+1)(r+2)}\right]\\
A_{G\to\substack{(-)\\Q}}^{(r)}&=\frac{1}{2}\left[\frac{r^2+3r+4}{(r+1)(r+2)(r+3)}\right]\\
A_{G\to G}^{(r)}&=C_A\left[-\frac{1}{6}+\frac{2}{r(r+1)}+\frac{2}{(r+2)(r+3)}-2\sum_{j=2}^{r+1}\frac{1}{j}\right]-\frac{N_f}{3}\quad .
\end{aligned} \qquad (III.20)$$

As a cautionary introduction to the following discussion consider, as homework Exercise VI, the following question. In the preceding expressions the argument $\tau=\ln(Q^2/\Lambda^2)$ was used in the quantities α_s and M without discussion. Should it have instead been $\ln(4Q^2/\Lambda^2)$ or, perhaps, $\ln(\frac{1}{3}Q^2/\Lambda^2)$ or even $\ln(f(z)Q^2/\Lambda^2)$? Clearly at least a piece of the answer must arise from the subleading logarithms and the interested student is strongly encouraged to calculate a few! In the following, fairly simple discussion this issue will be treated only for the case $z\to 0$. The avid student who desires the solution to this exercise more generally should consult, for example, Refs. [21,32,33,34], where the latter reference is specifically for the $z\to 1$ case (and actually primarily for structure functions not JETS).

Return now to the results in Eq. (III.20) which supply the formal explanation of a result of the previous section. Recall that the energy weighted quantities calculated there are finite in perturbation theory and require no explicit cutoff nor the all orders analysis employed here. Why is this? The relevant anomalous dimensions, $A^{(r=1)}$, are

$$A^{(1)}_{\substack{(-)\\Q}\to\substack{(-)\\Q}} = -\tfrac{4}{3}C_F \qquad A^{(1)}_{\substack{(-)\\Q}\to G} = \tfrac{4}{3}C_F$$
$$A^{(1)}_{G\to\substack{(-)\\Q}} = \tfrac{1}{6} \qquad A^{(1)}_{G\to G} = -\frac{N_f}{3} \qquad (III.1)$$

Since from the flavor independence of the gluon coupling,

$$\sum_b \sum_i^{2N_f} A_{G\to Q_i} M^b_{Q_i} = 2N_f A_{G\to Q} \sum_b M^b_Q \qquad (III.22a)$$

it follows immediately for the total energy sum rule

$$\frac{\partial}{\partial\tau}\sum_b M^b_a(1,\tau) = \left\{\begin{matrix}\frac{4}{3}C_F, a=Q\\ -N_f, a=G\end{matrix}\right\}\sum_b\left[-M^b_Q(1,\tau)+M^b_G(1,\tau)\right] = 0 \qquad (III.22b)$$

implying energy is conserved,

$$\sum_b M^b_Q(1,\tau) = \sum_b M^b_G(1,\tau) = 1 \qquad (III.2)$$

at some τ where Q represents any flavor quark or antiquark. Since the fact that energy is conserved is unaffected by renormalization, the corresponding anomalous dimensions are zero and energy weighted quantities exhibit none of the cutoff dependent logarithms which are characteristic of those quantities which are renormalized!

It is also possible to rederive the explicit lowest order perturbative result of Eq. (III.1). At this order the parton result of Eq. (III.19) is appropriate and two terms are expected, $Q\to Q$ and $Q\to G$. In each case the weighting factor is $(2E_Q/W)(2E_G/W) = x(1-x)$ (recall that the singular contribution arises from observing the quark and the gluon). Thus the piece with the collinear singularity is given by

$$\varsigma\frac{1}{\sigma_0}\frac{d\Sigma}{d\varsigma} \underset{\varsigma\to 0}{\sim} \frac{\alpha_s}{2\pi}\frac{1}{2}\left\{\int dx P_{Q\to Q}x(1-x) + \int dx P_{Q\to G}x(1-x)\right\} \qquad (III.23)$$
$$\sim \frac{\alpha_s}{2\pi}\frac{1}{2}\left\{A^{(1)}_{Q\to Q}+A^{(1)}_{Q\to G}-A^{(2)}_{Q\to Q}-A^{(2)}_{Q\to G}\right\} .$$

The explicit factor $1/2$ arises because one is observing the internal structure of one JET out of two (recall the normalization of the EEC). From Eq. (III.21) the first two terms in the latter expression cancel, while

$$A^{(2)}_{Q\to Q} = -\frac{25}{12}C_F \quad , \quad A^{(2)}_{Q\to G} = \frac{7}{12}C_F \qquad (III.24)$$

Thus, just as in (III.1),

$$\varsigma\frac{1}{\sigma_0}\frac{d\Sigma}{d\varsigma} \sim \frac{\alpha_s}{2\pi}\frac{1}{2}\left[-A^{(2)}_{Q\to Q}-A^{(2)}_{Q\to G}\right] = \frac{\alpha_s}{2\pi}C_F\frac{3}{4} \quad . \qquad (III.25)$$

Keeping in mind that there are higher order perturbative corrections, which are in principle calculable, and nonperturbative corrections which will be discussed in the next section, the general result of Eq. (III.18) can be interpreted for various r values to yield an enormous number of perturbative expectations for the internal structure of JETS. While this equation is, in principle, a $(2N_f+1)$ dimensional vector equation with $[exp(\kappa A)]$ a $(2N_f+1)$ by $(2N_f+1)$ matrix, this latter matrix is, in fact, flavor and charge conjugation diagonal for $\overset{(-)}{Q}\to\overset{(-)}{Q}$ and flavor and charge conjugation independent for $G\overset{\to}{\leftarrow}\overset{(-)}{Q}$. Thus it collapses to a one dimensional problem for the nonsinglet quantity $M^Q_i - M^{\overline{Q}}_i$. The gluon contribution drops out and the Q (or $\overline{Q}$) function has leading order solution

$$M_Q^Q(r,\tau) - M_Q^{\overline{Q}}(r,\tau) = [exp(\kappa A_{NS})]\Big(M_Q^Q(r,\tau_0) - M_Q^{\overline{Q}}(r,\tau_0)\Big)$$
$$= \left[\frac{\tau}{\tau_0}\right]^{\frac{A_{NS}}{b_0}} \Big(M_Q^Q(r,\tau_0) - M_Q^{\overline{Q}}(r,\tau_0)\Big) \quad , \qquad (III.26)$$

the famous form of the nonscaling behavior. Note that, since the A's are generally nonnegative for small r values, corresponding to small z, and negative for large r, corresponding to $z \to 1$, the characteristic nonscaling behavior is for $D(z,Q^2)$ to decrease at large z and increase at small z as Q^2 increases as illustrated in Fig. 12.

The corresponding singlet problem can be discussed in terms of the average (over Q and $\overline{Q}$ flavors) or singlet quark moment

$$M_{Q_s}^i \equiv \frac{1}{2N_f} \sum_j^{2N_f} M_{Q_j}^i \qquad (III.27)$$

with a corresponding definition of D_Q^i. In this case Eqs. (III.15) and (III.18) become two dimensional as already suggested by the structure of Eqs. (III.12) and (III.20), with index values, Q_s (henceforth labelled simply Q) and G. The previous sum over flavors reduces to the replacement $A_{G\to Q} \to 2N_f A_{G\to Q}$. This system of equations is easily diagonalized and solved as described in Appendix D. As a first example consider the 2 by 2 matrix

$$\overline{A}_{a\to b}^{(r)} \equiv [exp(\kappa A)]_{a\to b}^{(r)} \qquad (III.28)$$

for the case r = 1 as a measure of the momentum of parton b in JET a. In terms of the variable

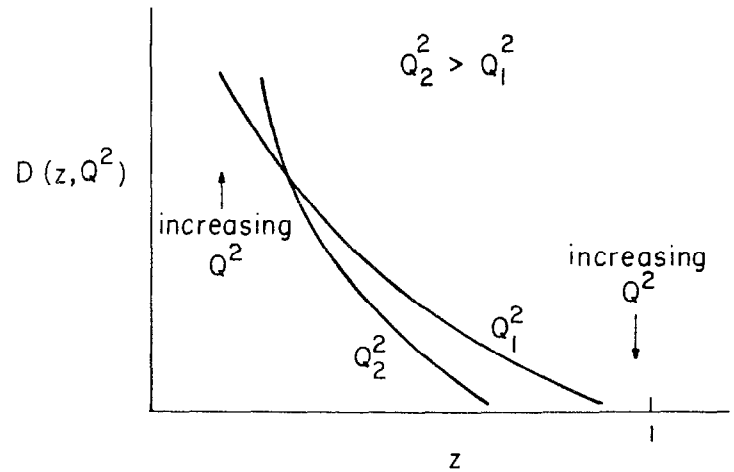


Fig. 12 Pictorial representation of the general nonscaling behavior suggested by Eq. (III.26).

$$\xi = e^{-\kappa(4C_F+N_f)/3} = (\frac{\tau_0}{\tau})^{\frac{8C_F+2N_f}{11C_A-2N_f}} \quad , \qquad (III.29)$$

solve (homework Exercise #VII but see Appendix D) for the corresponding matrix to find

$$\begin{array}{ll} \bar{A}^{(1)}_{Q\to Q} = \frac{N_f+4C_F\xi}{N_f+4C_F} & \bar{A}^{(1)}_{Q\to G} = \frac{4C_F}{N_f+4C_F}(1-\xi) \\ \bar{A}^{(1)}_{G\to Q} = \frac{N_f}{N_f+4C_f}(1-\xi) & \bar{A}^{(1)}_{G\to G} = \frac{4C_F+N_f\xi}{N_f+4C_F} \quad . \end{array} \qquad (III.30)$$

Thus, asymptotically, $\xi \to 0$, for any kind of JET the ratio of the momentum carried by quarks to that carried by gluons is

$$\frac{\bar{A}^{(1)}_{i\to Q}}{\bar{A}^{(1)}_{i\to G}} \underset{\xi\to 0}{\to} \frac{N_f}{4C_F} \quad . \qquad (III.31)$$

This example offers an excellent opportunity to check just how slowly this asymptotic limit is approached. Take, for example, $N_f = 5$ (an admittedly suspect asymptotic choice) for which the $\xi = 0$ limit is 15/16, while for a quark jet the ratio is infinite at $\xi = 1$. As a measure of asymptotia consider the value of Q^2 when the ratio has fallen to the value 15/8. For $\Lambda = 200MeV$ and $Q_0 = 2GeV$ this value is not reached until $Q^2 \simeq 10^6 GeV^2$. This result illustrates the fifth perturbative

LESSON: Asymptotic predictions (even in the contezt of pure perturbation theory) are truly asymptotic, requiring that small powers of logarithms be asymtotically large.

Next consider the limit as the index r of the moment goes to infinity. It is easy to show that this corresponds to studying the fragmentation function in the $z \to 1$ limit, a factor r^{-p-1} in the moment corresponds to a factor $(1-z)^p$ in the fragmentation function. Thus the result

$$\frac{\bar{A}^{(r)}_{i\to G}}{\bar{A}^{(r)}_{i\to Q}} \underset{r\to\infty}{\to} \frac{C_F}{2(C_A-C_F)r\ln r} \qquad (III.32a)$$

suggests

$$\frac{D^G_i(z,\tau)}{D^Q_i(z,\tau)} \underset{z\to 1}{\overset{\alpha}{\to}} \frac{(1-z)}{\ln\frac{1}{1-z}} \quad . \qquad (III.32b)$$

This yields the sixth perturbative

LESSON: The glue distribution in any JET is softer than the quark distribution.

Similarly the result

$$\frac{\bar{A}^{(r)}_{G\to Q}}{\bar{A}^{(r)}_{Q\to Q}} \underset{r\to\infty}{\to} \frac{N_f}{2(C_A-C_F)r\ln r} \qquad (III.33a)$$

suggests

$$\frac{D_G^Q(z,\tau)}{D_Q^Q(z,\tau)} \quad \underset{z\to 1}{\alpha} \quad \frac{1-z}{\ln\frac{1}{1-z}} \qquad (III.33b)$$

and the seventh perturbative

LESSON: Glue JETS are softer than quark JETS.

These last results should be taken only as indicative of the detailed $z \to 1$ behavior. A truly complete analysis of this limit (when $\ln[1/(1-z)]$ is also large) requires the inclusion of terms beyond the LLA. See the analog discussion of $z \to 0$ below and, for example, Reference [33].

In order to give specific meaning to the transverse size of a JET, consider using the EEC to define an angular size. The fraction of a JET's energy contained inside an angle defined by $\varsigma_{MAX} \sim (\chi_{MAX}/2)^2$ is given by

$$\int_0^{\varsigma_{MAX}} d\varsigma \frac{1}{\sigma}\frac{d\Sigma}{d\varsigma}\cdot 2 \equiv \epsilon \quad , \qquad (III.34)$$

where the explicit 2 is the usual two-JET factor. Thus for a specified fraction ϵ the ratio of the required opening angle of a gluon JET versus that of a quark JET is given by

$$\frac{\ln(\chi_{MAX}^{(\epsilon)})\,|_G}{\ln(\chi_{MAX}^{(\epsilon)})\,|_Q} \quad \underset{r\to\infty}{\to} \quad \frac{\frac{3}{2}C_F}{\frac{1}{5}C_A + \frac{1}{10}N_f} \simeq \frac{C_F}{C_A} \quad . \qquad (III.35)$$

Thus with χ_{MAX} less than 1 and C_F/C_A less than 1, it follows that

$$\chi_{MAX}\,|_G \sim (\chi_{MAX}\,|_Q)^{C_F/C_A} \gg \chi_{MAX}\,|_Q \qquad (III.36)$$

This is the eighth perturbative

LESSON: Gluon JETS are fatter than quark JETS.

Now consider the extremely interesting topic of multiplicities, on which there has been considerable work recently (but which can only be briefly sketched here). Note first that the present discussion strictly refers to the multiplicities of quarks and gluons (of "mass" Q_0^2) in a JET. However, it is quite reasonable to expect that this quantity will provide some measure of the multiplicity of hadrons in a JET, at least of the Q^2 dependence of this quantity. Naively one expects that multiplicities are described by the $r = 0$ moment

$$\langle n \rangle = \int dz\, D(z) \equiv M(r=0) \quad . \qquad (III.37)$$

The analysis is complicated by the footprints of the infrared divergences discussed earlier, which reappear here as divergences in the anomalous dimension matrix

$$\begin{array}{ll} A_{Q\to Q}^{(r\to 0)} \to 0 & A_{Q\to G}^{(r\to 0)} \to \frac{2C_F}{r} \\ A_{G\to Q}^{(r\to 0)} \to \frac{2N_f}{3} & A_{G\to G}^{(r\to 0)} \to \frac{2C_A}{r} \end{array} \qquad (III.38)$$

which is clearly ill behaved in the $r \to 0$ limit. However, it is possible to immediately recognize that the dominant contribution to the asymptotic multiplicity arises from the emission of (soft) gluons and that the ratio of the multiplicity of gluons in a gluon JET to that in a quark JET is [recall Eq. (III.19)]

$$\frac{\langle n\rangle_{G\to G}}{\langle n\rangle_{Q\to G}} = \frac{M_G^G(r\to 0)}{M_Q^G(r\to 0)} = \frac{\overline{A}_{G\to G}^{(r\to 0)}}{\overline{A}_{Q\to G}^{(r\to 0)}} \underset{r\to 0}{\to} \frac{C_F}{C_A} < 1 \quad , \qquad (III.39)$$

which is the ninth perturbative

LESSON: Gluon JETS have more soft gluons and therefore, presumably, more soft hadrons.

In the face of these explicit divergences how is the multiplicity to be evaluated? The essential point is to recall the warning given about Eq. (III.3) concerning the $z \to 0$ limit. In this limit the kinematics must be accounted for more carefully [23]. In particular, in the context of Eqs. (III.10) and (III.15), the variables x and z are bounded below by Q_0^2/Q^2 simply from the kinematics and the correct scale on the righthand side of these equations is actually xQ^2 for $x \to 0$ [x here is playing the role of z in Eq. (III.3) and $q'^2 \le xQ^2$]. Thus Eq. (III.15) becomes

$$\frac{\partial}{\partial\tau} M_G^G(r\to 0,\tau) = \lim_{r\to 0} \frac{\alpha_s}{2\pi}\int_{Q_0^2/Q^2} dx \frac{2C_A}{x} x^r M_G^G(r, xQ^2) \quad , \qquad (III.40a)$$

or, changing to a variable $Q'^2 = xQ^2$,

$$\frac{\partial}{\partial\tau} M_G^G(r\to 0,\tau) = \lim_{r\to 0} \frac{\alpha_s}{\pi} C_A \int_{Q_0^2}^{Q^2} \frac{dQ'^2}{Q'^2}\left(\frac{Q'^2}{Q^2}\right)^r M_G^G(r, Q'^2) \quad , \qquad (III.40b)$$

so that taking $r \to 0$ and with $\tau' = \ln(Q'^2/\Lambda^2)$,

$$\frac{\partial}{\partial\tau} M_G^G(0,\tau) = \frac{2C_A}{b_0\tau}\int_{\tau_0}^{\tau} d\tau' M_G^G(0,\tau') \quad . \qquad (III.40c)$$

Taking a second derivative and changing variables to

$$t = \sqrt{\frac{8C_A}{b_0}\tau} \qquad (III.41)$$

yields the equation

$$t^2\frac{\partial}{\partial t^2} M_G^G(0,t) + t\frac{\partial}{\partial t} M_G^G(0,t) - t^2 M_G^G(0,t) = 0 \quad . \qquad (III.42)$$

This is just the differential equation for the modified Bessel function, $I_0(t)$, which yields an asymptotic behavior

$$M_G^G(0,\tau) \underset{\tau\to\infty}{\alpha} exp\left[2\sqrt{(2C_A/b_0)\tau}\right] \quad . \qquad (III.43)$$

Unfortunately this is not yet the entire story.[24,25,26] Since the dominant contribution to the multiplicity comes from the region of phase space where both the collinear singularities and the infrared logarithms arise (the dreaded double leading logarithm regime, recall Ref. [19]), care must be taken to be certain that all such terms are correctly included. Up to now the analysis has focused only on the collinear singularities. Recall that in this leading (single) logarithm approximation (LLA) only the ladder diagrams were required. In the present limit these diagrams yield a contribution of the generic form

$$LLA \sim \sum_n \frac{1}{n!}\left[\frac{C_A \alpha_s}{\pi}\right]^n \ln^n \frac{Q^2}{Q_0^2} \frac{\ln^{n-1} 1/x}{(n-1)!} \quad . \qquad (III.44)$$

Contributions of the form $\ln^{n-1} Q^2/Q_0^2 \ln^n 1/x$, which arise from diagrams with "crossed" rungs, are not included. However, in the present limit, where $\ln(1/x)$ can be of order $\ln(Q^2/Q_0^2)$, these contributions must be included. For example, at order α_s^3, the ladder diagram of Fig. 13a contributes

$$\ln^2 \frac{Q^2}{Q_0^2} \ln \frac{1}{x} - 3 \ln \frac{Q^2}{Q_0^2} \ln^2 \frac{1}{x} + 2 \ln^3 \frac{1}{x} \quad , \qquad (III.45a)$$

while the crossed diagram of Fig. 13(b) contributes

$$- \ln \frac{Q^2}{Q_0^2} \ln^2 \frac{1}{x} + 2 \ln^3 \frac{1}{x} \quad , \qquad (III.45b)$$

yielding a sum

$$\Sigma um = \ln^2 \left(x^2 \frac{Q^2}{Q_0^2} \right) \ln \frac{1}{x} \quad . \qquad (III.45c)$$

Thus the result is as in the LLA except $\ln(Q^2/Q_0^2)$ is replaced by $\ln(x^2 Q^2/Q_0^2)$. It turns out [24] that this form can still be interpreted in terms of the semi-classical, probabilistic language of the ladder diagrams if the strong ordering of "offshellness" is replaced by a strong ordering of emission angles (at least for relativistic particles)

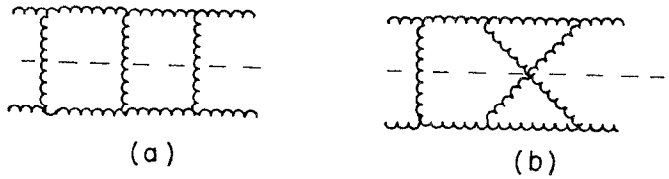


Fig. 13 The order $\alpha_s{}^3$ Feynman graphs relevant to Eq. (III.45). (a) Ladder graph. (b) Crossed rung ladder.

$$1 > \varsigma_1 > \varsigma_2 > \varsigma_3 \ldots > \varsigma_n \quad ,$$

where $\varsigma_i = (1 - \cos\chi_i)/2$ and χ_i is the emission angle of the i^{th} emission as in Fig. 14. The ordering of "offshellness" and the ordering of angles, in fact, yield identical results except in the limit $z, x \to 0$. In the latter limit the coherent (i.e., cancellation) effects of the crossed diagrams can be simply included by ordering the angles. Thus the large angle emission of soft gluons is suppressed by these coherent effects.

The change in the kinematics due to the above angular ordering is easily (or at least heuristically) understood by noting that the limit $z, x \to Q_0^2/Q^2$ relevant to Eq. (III.40) corresponds to backward emission. Recall that for the light cone variables of Eq. (III.4)

$$2q'^{+} \cdot q'^{-} \equiv {q'_0}^2 - {q'_3}^2 \geq Q_0^2$$

so that $q'^{+} \simeq zQ \to Q_0^2/Q$ means $q'^{-} \geq Q/2$. However, the restriction to ordered, forward angles requires $q'^{-} \leq q'^{+}$. Thus small z, x now means both q'^{+} and q'^{-} small ($\sim zQ$) leading to the new constraint $z, x \geq \sqrt{Q_0^2/Q^2} = Q_0/Q$. In the specific example of multiplicity calculations, the result is to replace the scale xQ^2 by x^2Q^2 and the limit Q_0^2/Q^2 by Q_0/Q in Eq. (III.40a) and then to set $Q'^2 = x^2Q^2$ in Eq. (III.38b) and thus $dx/x = (dQ'^2/Q'^2)/2$. Hence Eq. (III.40c) becomes instead

$$\frac{\partial}{\partial\tau} M_G^G(0,\tau) = \frac{C_A}{b_0\tau} \int_{\tau_0}^{\tau} d\tau' M_G^G(0,\tau') \quad , \qquad (III.46)$$

and

$$\langle n \rangle \underset{\tau\to\infty}{\propto} exp\left[2\sqrt{(C_A/b_0)\tau}\right] \quad . \qquad (III.47)$$

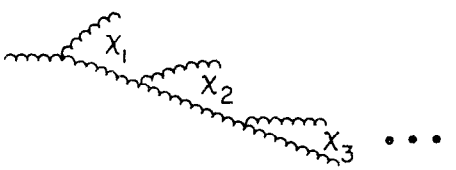


Fig. 14 The angle ordering of emissions characteristic of the result of the coherent summation of leading and subleading contributions as in Fig. 13.

This is easily interpreted in terms of the anomalous dimension

$$\frac{\alpha_s}{2\pi}A^{(r)}_{G\to G} \simeq \frac{1}{4}\left[-r+\sqrt{r^2+\frac{8\alpha_s}{\pi}C_A}\right] \quad , \qquad (III.48a)$$

which for the limit r fixed $\alpha_s \to 0$ behaves as

$$\frac{\alpha_s}{2\pi}A^{(r)}_{G\to G}|^{rfixed}_{\alpha_s\to 0} \quad \sim \quad \frac{\alpha_s C_A}{\pi r} \quad , \qquad (III.48b)$$

while for $r \to 0$ with α_s fixed behaves as

$$\frac{\alpha_s}{2\pi}A_{G\to G}|^{r\to 0}_{\alpha_s fixed} \quad \sim \quad \frac{1}{4}\sqrt{\frac{8\alpha_s C_A}{\pi}} = \sqrt{\frac{C_A}{b_0 \tau}} \quad . \qquad (III.48c)$$

The corresponding exponent for the multiplicity is then

$$\int^{\tau} d\tau' \frac{\alpha_s(\tau')}{2\pi}A^{(r\to 0)}_{G\to G} \quad \to \quad \int^{\tau}\frac{d\tau'}{\sqrt{\tau'}}\sqrt{\frac{C_A}{b_0}} = 2\sqrt{\frac{C_A\tau}{b_0}} \qquad (III.49)$$

as above. The leading behavior of the full distribution can also be calculated [23,25] resulting in

$$zD^G_G(z) \underset{z\to 0}{\sim} \sqrt{\frac{\alpha_s}{2\pi}\frac{\ln(z^2\,Q^2/Q_0^2)}{\ln\,1/z}}\, I_1\left(\sqrt{\frac{4\alpha_s}{2\pi}C_A \ln\frac{1}{z}\left[\ln(z^2Q^2/Q_0^2)\right]}\right) \quad , \qquad (III.50)$$

which suggests an asymptotic distribution which exhibits a peak for z of order $\sqrt{Q_0/Q}$. This in turn suggests a dip at small z. This structure appears to survive the inclusion of subleading perturbative contributions [24] (note the interesting feature that the expansion parameter is $\sqrt{\alpha_s}$) but the influence of nonperturbative effects at reasonable energies has still to be studied in detail. A specific illustration of this structure as realized in the Monte Carlo calculations of Ref. [33] is shown in Fig. 15.

One final topic in the context of multiplicities is both phenomenologically interesting and technically amusing, and thus deserves a brief discussion here. This is the issue of fluctuations in the multiplicity distribution. The observation that these fluctuations are quite large and seem to scale with the average multiplicity (in essentially all reactions involving hadrons) is generally referred to as KNO scaling. [35] More specifically KNO scaling suggests that the quantity $\langle n\rangle P_n$, where P_n is the multiplicity distribution function, i.e., the relative probability of finding multiplicity n, is a function only of the variable $z = n/\langle n\rangle$. To obtain some appreciation of why this issue is interesting, consider some simple models. Consider first an independent emission, Poisson type model (the analog of simple multiperipheral models of hadronic interactions) corresponding to the "one dimensional" structure of Fig. 16. In this case the probability of emission per unit "time" [time here is the analog of $\ln(Q^2/Q_0^2)$] is a fixed constant λ, i.e, the vertex in Fig. 16 is just a constant. The inclusive multiplicity distribution at time t, $P_n(t)$, is then the solution of the differential equation

$$\frac{\partial}{\partial t}P_n(t) = -\lambda P_n(t) + \lambda P_{n-1}(t) \quad . \qquad (III.51)$$

On the righthand side the first term corresponds to the change $n \to n+1$, while the second term gives the $n-1 \to n$ contribution. Note that such a process, where the time derivative of the distribution function depends only on the distribution at that time, belongs to the general class of Markovian processes. [36] This equation is easily solved in terms of the generating function

$$G(\xi,t) \equiv \sum_n \xi^n P_n(t) \quad , \qquad (III.52a)$$

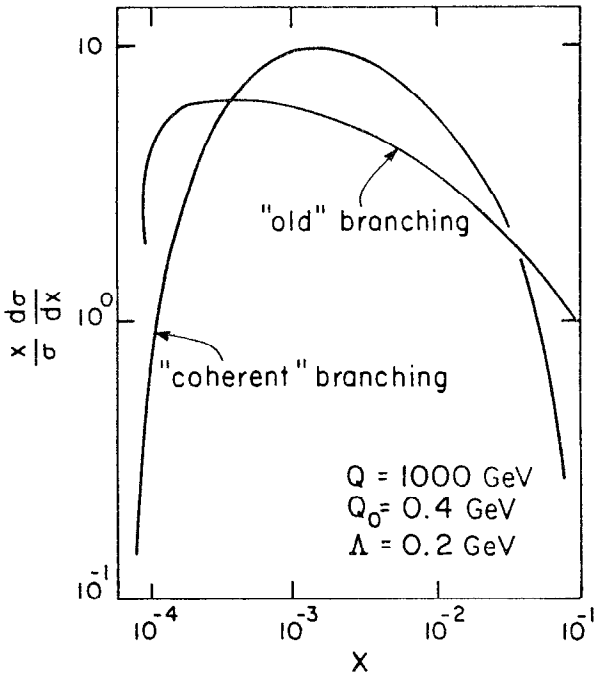


Fig. 15 Illustration of the effects on the x distribution of the angle ordering of emissions of Fig. 14. Figure from the first paper in Ref. [33]. The curve labelled "old" branching refers to strong ordering in the "offshellness" while "coherent" branching refers to ordering of the angles.

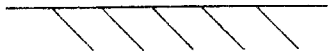


Fig. 16 Illustration of the "linear" structure of emission characteristic of a Poisson type model.

which satisfies boundary conditions

$$G(1,t) = 1 \quad , \quad G(\xi,0) = \xi^{n_0} \quad , \qquad (III.52b)$$

where n_0 is the number of initial particles (but with a single emitter). The various moments of $P_n(t)$ are then easily found as the derivatives of $G(\xi,t)$ with respect to ξ, e.g.,

$$\langle n \rangle = \frac{\partial}{\partial \xi} G \mid_{\xi=1} \quad , \quad \langle n(n-1) \rangle = \frac{\partial^2}{\partial \xi^2} G \mid_{\xi=1} \quad . \qquad (III.53)$$

Rewriting (III.51) as

$$\frac{\partial}{\partial t} G(\xi,t) = -\lambda(1-\xi) G(\xi,t) \quad , \qquad (III.54)$$

the solution is easily found as

$$G(\xi,t) = \xi^{n_0} e^{(\xi-1)\lambda t} \quad . \qquad (III.55)$$

This yields trivially

$$\langle n \rangle = n_0 + \lambda t \quad , \quad \langle n(n-1) \rangle = n_0(n_0-1) + 2n_0\lambda t + \lambda^2 t^2 \quad , \quad (III.56)$$

which then implies

$$\frac{D}{\langle n \rangle} \equiv \sqrt{\frac{\langle n^2 \rangle - \langle n \rangle^2}{\langle n \rangle^2}} \underset{t\to\infty}{\rightarrow} \frac{1}{\sqrt{\lambda t}} \rightarrow 0 \quad . \qquad (III.57)$$

Thus for such processes the fluctuations are asymptotically vanishingly small compared to the average multiplicity (in the usual $1/\sqrt{\langle n \rangle}$ way). As homework Exercise VIII expand G to explicitly derive P_n in this case. The result is

$$P_n = \frac{(n-n_0)^{n-n_0}}{(n-n_0)!} e^{-(n-n_0)} \qquad (III.58)$$

as expected for a Poisson-like system. This is clearly NOT KNO-like.

Consider next the case of processes with the BRANCHING structure as suggested by Fig. 17. Examples of this structure are electromagnetic cascades and populations and, with a little more work, QCD JETS. Since now the probability of emission depends on the number already present, the corresponding differential equation is the "forward" Kolomogorov equation, [36]

$$\frac{\partial}{\partial t} P_n(t) = -\lambda n P_n(t) + \lambda(n-1) P_{n-1}(t) \quad , \qquad (III.59)$$

or

$$\frac{\partial}{\partial t} G(\xi,t) = -\lambda\xi(1-\xi) \frac{\partial}{\partial \xi} G(\xi,t) \qquad (III.60)$$

for the generating function. The solution is now (note that the number of initial particles is the same as the number of initial emitters in this case)

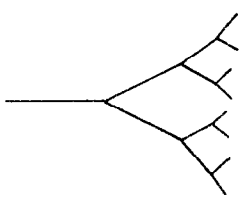


Fig. 17 Illustration of the branching structure characteristic of a cascade type model.

$$G(\xi,t) = \left[\frac{\xi}{\xi + (1-\xi)e^{\lambda t}}\right]^{n_0} \quad , \qquad (III.61)$$

with

$$\langle n \rangle = n_0 e^{\lambda t} \quad , \quad \langle n(n-1) \rangle = n_0(n_0+1)e^{2\lambda t} - 2n_0 e^{\lambda t}$$

and

$$\frac{D}{\langle n \rangle} \underset{t\to\infty}{\rightarrow} \frac{\sqrt{n_0}\, e^{\lambda t}}{n_0 e^{\lambda t}} = \frac{1}{\sqrt{n_0}} \quad . \qquad (III.62)$$

Thus in this case the fluctuations grow asymptotically just as fast as the average multiplicity as in KNO scaling. As homework Exercise IX work out P_n in this case. In particular show that, for $n, \langle n \rangle \gg n_0$ and with $z = n/\langle n \rangle$, the result is

$$\langle n \rangle P_n \sim \frac{{n_0}^{n_0}}{(n_0-1)!} z^{n_0-1} e^{-n_0 z} \quad . \qquad (III.63)$$

To carry this analysis further it is useful to study instead the "backward" Kolomogorov equation which treats the effects on the distribution at time t due to branchings at the beginning, i.e, between $t = 0$ and $t = \Delta t$. This "backward" type structure was, in fact, already encountered in Eqs. (III.10) and (III.15) where the focus was on the variation with Q^2 and not Q_0^2. The corresponding (finite Δt) equation is

$$P_n(t) = (1-\lambda\Delta t)P_n(t-\Delta t) + \lambda\Delta t \sum_{\substack{n_1,n_2 \\ n_1+n_2=n}} P_{n_1}(t-\Delta t)P_{n_2}(t-\Delta t) \quad . \qquad (III.64)$$

The first term on the righthand side describes the contribution of no emission in Δt, while the second term describes one branching such that one branch subsequently emits n_1 particles while the second emits n_2 as illustrated in Fig. 18 (note the explicit choice $n_0 = 1$). The appropriate differential equation is then

$$\frac{\partial}{\partial t}P_n(t) = -\lambda P_n(t) + \lambda \sum_{\substack{n_1,n_2 \\ n_1+n_2=n}} P_{n_1}(t)P_{n_2}(t) \quad , \qquad (III.65a)$$

or, for the generating function,

$$\frac{\partial}{\partial t}G(\xi,t) = \lambda G(\xi,t)[G(\xi,t)-1] \quad . \qquad (III.65b)$$

This is easily solved, $\ln(G/(G-1)) = \exp\left[\lambda t + \ln\left(\frac{\xi-1}{\xi}\right)\right]$, to find

$$G(\xi,t) = \frac{\xi}{\xi + (1-\xi)e^{\lambda t}} \quad , \qquad (III.66)$$

as before for $n_0 = 1$. Now in the interesting case of a gluon JET (but simplified by setting $N_f = 0$) the corresponding equation is [25]

$$\frac{\partial}{\partial \tau}G_G(\xi,\tau) = G_G(\xi,\tau)\left[\frac{\alpha_s C_A}{2\pi}\int d\tau'\left\{G_G(\xi,\tau')-1\right\} + \{1-G_G(\xi,\tau)\}\right] \quad , \qquad (III.67a)$$

or, ignoring the final nonleading term,

$$\frac{\partial}{\partial \tau}\ln G_G(\xi,\tau) \simeq \frac{\alpha_s(\tau)}{2\pi}C_A\int d\tau'\left\{G_G(\xi,\tau')-1\right\} \quad . \qquad (III.67b)$$

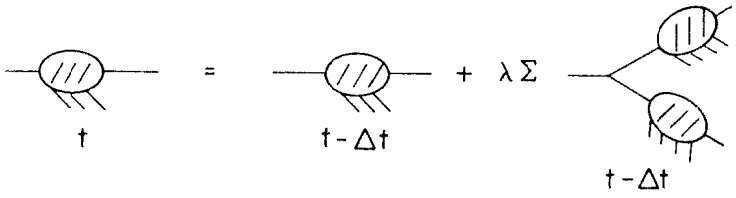


Fig. 18 Pictorial representation of the finite Δt equation, Eq. (III.64).

In this case the general structure is preserved but there is an extra integral due to the infrared singularity present in the gauge theory, plus the emission process now involves a running ("time dependent") coupling. While this equation is no longer trivially solved, one can still proceed by expanding

$$G_G(\xi,\tau)-1 \underset{\xi\to 1}{\sim} \langle n\rangle_G(\xi-1)+\frac{1}{2}\langle n(n-1)\rangle_G(\xi-1)^2+\cdots \quad , \qquad (III.68a)$$

or

$$\ln G_G(\xi,\tau) \underset{\xi\to 1}{\sim} \langle n\rangle_G(\xi-1)+\frac{1}{2}\Big[\langle n(n-1)\rangle_G-\langle n\rangle_G^2\Big](\xi-1)^2+\cdots \quad , \qquad (III.68b)$$

and substituting directly into (III.67). The term proportional to $(\xi-1)$ yields the relation

$$\frac{d}{d\tau}\langle n\rangle_G \simeq \frac{C_A}{b_0\tau}\int d\tau'\langle n\rangle_G \quad . \qquad (III.69)$$

With the ansatz $\langle n(n-1)\rangle_G = C_G\langle n\rangle_G^2$, with C_G a constant, the next term gives

$$\frac{C_G-1}{C_G}\frac{d}{d\tau}\langle n\rangle^2 \simeq \frac{C_A}{b_0\tau}\int d\tau'\langle n\rangle_G^2 \quad . \qquad (III.70)$$

The result, as before, is

$$\langle n\rangle \underset{\tau\to\infty}{\propto} exp\Big[2\sqrt{(C_A/b_0)\tau}\Big] \quad , \qquad (III.71a)$$

but with the added relation

$$\langle n(n-1)\rangle_G \simeq \frac{4}{3}\langle n\rangle_G^2 \qquad \text{or} \qquad \frac{D_G}{\langle n\rangle_G} \simeq \sqrt{C_G-1}=\sqrt{\frac{1}{3}} \quad . \qquad (III.71b)$$

Thus QCD JETS exhibit KNO-type scaling with a form calculable at least in perturbation theory. [37] As a further example, and as homework Exercise X, the interested student is encouraged to show that the corresponding coefficient for a quark jet is

$$C_Q=\frac{1}{3}\frac{C_A}{C_F}+1 \quad , \qquad (III.72)$$

where the relations

$$\langle n\rangle_Q=\frac{C_F}{C_A}\langle n\rangle_G \quad , \qquad \frac{\partial}{\partial\tau}\ln G_Q \simeq \frac{C_F}{b_0\tau}\int d\tau'[G_G-1] \qquad (III.73)$$

are useful. For n_0 independent JETS one performs the following substitutions:

$$G\to G^{n_0} \quad , \quad \langle n\rangle\to n_0\langle n\rangle \quad ;$$

and, for the coefficient C,

$$C\to\frac{n_0-1}{n_0}+\frac{1}{n_0}C \quad . \qquad (III.74)$$

Thus for two quark JETS in e^+e^- annihilation the expected asymptotic result is

$$\frac{D_Q}{\langle n\rangle_Q} \underset{n_0=2}{\rightarrow} \sqrt{\frac{C_Q}{2}-\frac{1}{2}} = \sqrt{\frac{3}{8}} \quad . \qquad (III.75)$$

However, even in perturbation theory the corrections to the leading approximation are down only by $\sqrt{\alpha_s}$. For example the first correction to$C_G = 4/3$ is

$$(-10/9)\Big(1/\sqrt{(48/11)\ln(W/\Lambda)}\Big)$$

as discussed in Ref. [33] (where C_G is labeled R_2). (Note [1,2] that for e^+e^- data this ratio is approximately $\sim$ 0.35 while for pp collisions it seems to be more like $\sim$ 0.6.) Furthermore the Monte Carlo calculation of Ref. [33] indicates sizable other contributions at any foreseeable energy as illustrated in Fig. 19 from that reference.

As a final introduction to the broad existing literature, [25,28] note that approximate solutions to the above equations exhibit the following behavior for the multiplicity distribution for multiplicities far from the average value,

$$\langle n\rangle P_n \underset{n\ll\langle n\rangle}{\sim} \exp\left[-\frac{1}{2}\ln^2\frac{N}{\langle n\rangle}\right] \quad . \qquad (III.76)$$

This corresponds to a damping of low multiplicity, exclusive channels with a generic "form factor,"

$$FF \sim e^{-(1/2)\ln^2\langle n\rangle} \sim e^{-(1/2)(4C_A/b_0)Y} \quad , \qquad (III.77)$$

which is characteristic of all such cascading theories. In particular this leads to a damping of large mass (Q^2) unscreened, i.e., colorful systems of the form

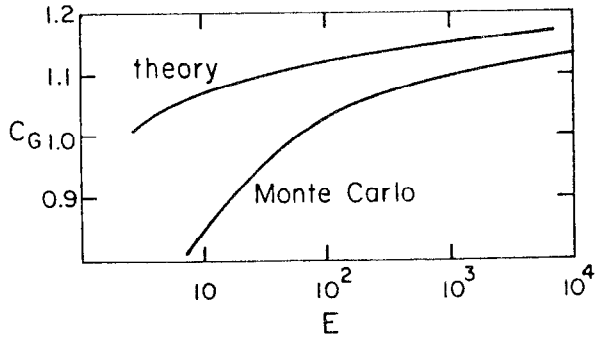


Fig. 19 Monte Carlo results for the coefficient C_G versus the theoretical expectation from the first paper in Ref. [33].

$$\left(\frac{Q_0^2}{Q^2}\right)^{2C_A/b_0} \quad . \qquad (III.78)$$

This structure is the basis of the idea of "preconfinement" [28] whereby, even in perturbation theory, final states tend to organize themselves into relatively low mass color singlet clusters. Naively this conclusion would seem to be rather insensitive to the extra factor of 1/2 in the exponent due to the coherent cancellations discussed earlier [recall (III.46)] although the angular ordering discussed there might be thought [38] to work against such screening. This interpretation appears to be borne out by the Monte Carlo calculations of Reference [33].

To summarize, the truly asymptotic predictions of perturbative QCD are:

(1) the nonscaling behavior of the fragmentation functions;

(2) the behavior $\langle n \rangle \sim \exp\ 2\sqrt{(C_A/b_0)\ln(Q^2/\Lambda^2)}$;

(3) the existence of a dip in $xd\sigma/dx$ for $x < \sqrt{Q/Q_0}$;

(4) that gluon JETS are softer, fatter and exhibit larger multiplicities; and

(5) that KNO scaling hold with predicted values of $\sqrt{(\langle n^2 \rangle - \langle n \rangle^2)/\langle n \rangle^2}$.

Even assuming that the nonleading perturbative corrections, which are often large, have been evaluated, the above discussion provides no insight into the momentum scale at which these predictions become relevant, i.e., what is the scale Q_0 which characterizes nonperturbative contributions?

IV. NONPERTURBATIVE COMMENTS

The simple cascading, semi-classical (i.e., ladder graphs) picture of the evolution of JETS discussed in the previous section is clearly ideal for represention by Monte Carlo simulation. This approach is particularly helpful as the final step, the evolution from the scale Q_0^2 into hadrons, can be included in a fashion which is, at least mathematically, well defined. To be sure, this last step is simply modeled in a more or less ad hoc manner but there is considerable data available to fix the values of the parameters in the models. Unfortunately there still remain unresolved certain essentially technical issues which apparently have phenomenological implications, as will be mentioned later. The initial discussion will focus rather on issues of a more fundamental physics nature.

The logical structure of the picture suggested by the perturbative results of Sections II and III is illustrated in Fig. 20. The basic process is calculated in terms of a finite number on energetic quarks and gluons in finite order perturbation theory. The second step involves the "all orders" perturbative evolution of the quarks and gluons characterized by a scale Q^2 down to those characterized by a scale Q_0^2. This process already results in a JET structure. If the experimental quantity of interest is insensitive to renormalization, for example the energy weighted cross sections of Section II, this step will have no influence on the calculation, as noted earlier. The final step involves the nonperturbative fragmentation into the final hadrons. As underlined several times above, the basic issue is what is the magnitude of the scale Q_0^2 which characterizes the transition from the largely predictive perturbative regime to the largely nonpredictive nonperturbative regime. Clearly the smaller this scale the more hadronic physics is under theoretical control. For the moment this question awaits experimental resolution.

To see that this cannot be a trivial issue, simply note that it is impossible for a color nonsinglet quark or gluon to evolve into only color singlet hadrons in total isolation from the other quarks and gluons present. Thus the picture of completely independent JETS suggested by the naive parton model is, at best, a crude approximation. Correlations induced by the need to conserve color (and energy-momentum, etc.) must appear at some level. In the present discussion the scale Q_0^2 is intended to represent, at least qualitatively (note that it is being used to characterize several different effects), the momentum scale at which the nonperturbative correlations become relevant. The very many distinct efforts [33,39-43] to study these issues in the context of Monte Carlo models can then be generally characterized by differing values of Q_0^2. (This is, of course, an oversimplification of the true situation.) Models with large effective values of Q_0^2, e.g., the Lund String picture, [41] exercisely require that the nonperturbative fragmentation still exhibit many of the features suggested by the perturbation theory applied to the same kinematic regime. The interested reader is referred to the specific

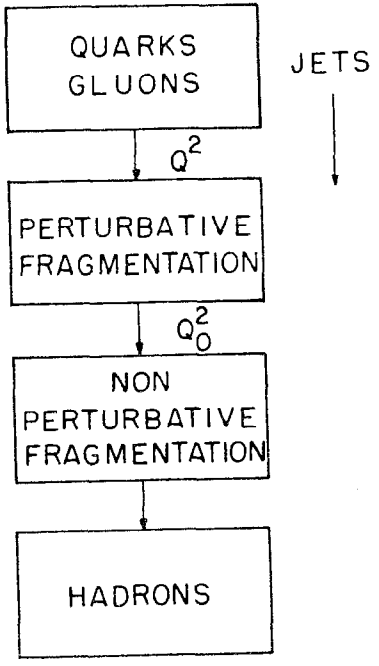


Fig. 20 Idealized representation of the "logical" evolution of JETS from quarks and gluons to hadrons.

references for the details of each model. The present discussion will attempt only to provide an introduction to some of the issues.

As an illustration consider the nonperturbative correlations in two very different models for the (by now very familiar) Energy-Energy Correlation (EEC) in e^+e^- annihilation at first order. Since this quantity is insensitive to renormalization, the differences will arise in the higher "twist corrections" characterized crudely by the magnitude of Q_0/Q. As the first model consider the early Lund String (STR) picture which, in some sense, exhibits a maximal correlation size. In this picture all perturbatively produced gluons are replaced by a quark-antiquark pair (and a leading pion). All quarks and antiquarks are then organized into color singlet strings which fragment independently in their own rest frame. As noted below, this picture will yield a characteristic scale $Q_0 \sim 10GeV$. The contrasting model assumes rather that the perturbative quarks and gluons can fragment in a maximally independent fashion. Such an InCoherent JET (ICJ) picture is a representation of the early parton model motivated pictures [30] and explicitly assumes that *all* quantum numbers are conserved by the correlations of the "wee" or soft partons and hadrons. This feature serves to minimize the influence of such correlations on the EEC. Such a model is characterized by a scale $Q_0 \sim 1GeV$. The major effects arise from the short range correlations due to resonances (or "clusters") long known [44] in soft hadron physics. The contrast between these two is already illustrated qualitatively in Fig. 21. In Fig. 21 on the left an idealized 3 independent JET final state is indicated where the direction and magnitude of the momenta of the partons and the final hadrons are represented by the solid lines. The dashed line is to indicate the general envelope of the hadronic final state in momentum space. Note the differences with the structure on the right of Fig. 21, where the final state contains 2 strings instead. The simple kinematics of the boosts which connect the e^+e^- frame to the two string frames tends to skew the hadron distribution in the fashion indicated.

As an introduction to the results of the Monte Carlo calculation described below, it is both possible and helpful to first discuss the ICJ picture analytically. The distribution of hadrons in such an independent jet is defined as

$$dN \equiv \frac{d^3h}{h_0} f_1(h,p) \quad , \qquad (IV.1)$$

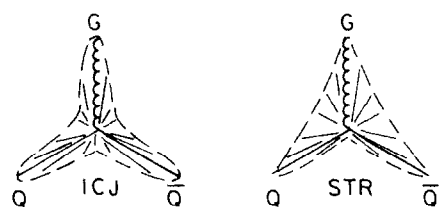


Fig. 21 Idealized representations of the hadronic final state in the InCoherent Jet picture (3 JETS) and the *STRing* picture (2 *strings*). The solid lines represent the momenta of the hadrons while the dashed curves are to imply the "envelope" of the state.

where h is the hadron 4-momentum and p that of the parton, and the geometry is illustrated in Fig. 22. For the present purposes the required quantity is the energy weighted angular distribution defined by

$$F_1(\eta) \equiv \frac{dN}{d\Omega_\eta} \cdot \left(\frac{E}{E_{JET}}\right) = \int \frac{dh h^2}{h_0} \cdot \frac{2h_0}{W} f_1(h,p) \quad , \qquad (IV.2)$$

with normalization

$$\int d\Omega_\eta F_1(\eta) = 1 \quad , \qquad (IV.3)$$

where the total energy of the JET is taken to be $W/2$. As suggested by the parton model the distribution f_1 is assumed to exhibit the following (at least approximate) properties:

(1) It scales in $h_{||}/p$;

(2) It is rapidly cutoff in h_T.

Here parallel and transverse are defined with respect to the JET direction. In the angular range $0° < \eta < 90°$ the angular distribution can be evaluated as an integral over $h_T = h_{||} \cot \eta$,

$$F_1(\eta) = \frac{1}{\pi W} \frac{1}{\sin^3 \eta} \int d^2 h_T f_1\left(\frac{2h_T}{W} \cot \eta, h_T\right) \quad , \qquad (IV.4a)$$

with high energy limit (η fixed)

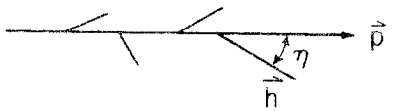


Fig. 22 Geometry of idealized parton JET.

$$F_1(\eta) \underset{0^\circ<\eta\leq 90^\circ}{\overset{W\to\infty}{\longrightarrow}} \frac{1}{\pi W}\frac{1}{\sin^3\eta}\int d^2h_T h_T f(0,h_T) \equiv \frac{C\langle h_T\rangle}{2\pi W\sin^3\eta} \quad , \tag{IV.4b}$$

where $\langle h_T\rangle \sim 350 MeV/c$. The coefficient C defined in (IV.4b) is (assuming a 2-JET structure)

$$C \equiv 2\int d^2h_T f(0,h_T) \simeq \frac{\partial}{\partial \ln W}\langle n\rangle_{TOT} \quad , \tag{IV.5}$$

which, in the context of QCD, can be expected to increase slowly with energy. However, for the present phenomenological purposes, it can be treated as a constant with characteristic value in the range $C \sim 2.5-4$. Using these definitions it is straightforward to show [6] that the leading fragmentation correction to the EEC arises from the order $(\alpha_s)^0$ quark-antiquark final state which in pure perturbation theory contributed only at $\chi = 0^\circ$ and 180°. As homework Exercise XI demonstrate that this correction has the form

$$\begin{aligned}\frac{1}{\sigma}\frac{d\Sigma}{d\cos\chi} &= 2\pi[F_1(\chi)\Theta(90^\circ-\chi)+F_1(180^\circ-\chi)\Theta(\chi-90^\circ)] \\ &= \frac{C\langle h_T\rangle}{W\sin^3\chi} = \frac{C\langle h_T\rangle}{8W}[\zeta(1-\zeta)]^{-3/2} \quad .\end{aligned} \tag{IV.6}$$

This result illustrates several important features. First it is indicative of the fact that such an analysis is performing a simultaneous expansion in two distinct small quantities, $\alpha_s/2\pi$ and Q_0/Q (here $C\langle h_T\rangle/W$). Asymptotically (in this case requiring only that inverse powers of W be small), only the purely perturbative results are relevant but at present energies this is not yet the case. Second it illustrates the expected feature that the EEC is not sensitive to nonperturbative changes in the longitudinal structure of the JET (recall it was insensitive to perturbative, renormalization effects), but is sensitive to smearing due to the transverse size of the final hadronic JET. Finally (IV.6) indicates that the perturbative asymmetry [recall (II.20)] is uncorrected at order $(C\langle h_T\rangle/W)$. This is, of course, simply the result of the inherent symmetry of the

$(C\langle h_T\rangle/W)$. This is, of course, simply the result of the inherent symmetry of the lowest order quark-antiquark final state. The real issue is the magnitude of the order $(\alpha_s \cdot C\langle h_T\rangle/W) \sim (\alpha_s \cdot Q_0/Q)$ correction arising from the fragmentation of the quark-antiquark-gluon final state. It is here that the two models of interest will differ significantly as suggested above.

To study these two extreme pictures calculations [45] were performed using the order $(\alpha_s)^1$ version (4.1) of the Lund Monte Carlo, which has the handy feature that by changing a single parameter the fragmentation scheme can be switched from String to Independent JETS. This implies that in all other ways the final states are treated identically. However, it also means that all the other various parameters have not been fine-tuned to produce identical single particle distributions, for example. For the qualitative conclusions to be drawn here this should not be an issue. Using this Monte Carlo program, 4000 events at $W = 30GeV$ were generated for both of the fragmentation schemes and, using these final states, the EEC was calculated. Actually the final states were generated under various conditions so that the EEC could be evaluated at three distinct stages in the fragmentation process in both cases. These stages are:

(1) Parton level, i.e., no fragmentation;

(2) Primary hadrons but with no transverse momentum with respect to the JET direction for the ICJ case or with respect to the string direction for the STR case, i.e., no transverse momentum either directly from the fragmentation process or from subsequent decays;

(3) Full fragmentation.

The results of these calculations are exhibited in Fig. 23(a) for the ICJ case and 23(b) for the STR case. In both figures the unshaded (largest) histogram corresponds to Stage (3), the righthand hatched (/) histogram is Stage (2) and the lefthand hatched (\) histogram is Stage (1). In both figures the dashed curve is the purely perturbative result corresponding to the chosen value $\Lambda = 0.4GeV$. The full line is the perturbative result including the same kinematic cuts as applied by the Monte Carlo program as outlined briefly in Appendix E. Note that the Monte Carlo is not "capable" of performing the required cancellation between real and virtual perturbative contributions that was discussed in Section II. Instead the offending region containing the infrared singular part of the real contribution is avoided, using a kinematic cut and the known finite part of the real contribution is avoided, using a kinematic cut and the known finite contribution of this region plus the virtual piece appears as a δ function at $\chi = 0°$, not shown explicitly. There is also a further cut specific to the Lund Monte Carlo, as noted in Appendix E. While the effect of these cuts is clearly sizeable at Stages (1) and (2), it is quite minor for Stage (3) (the δ function at $\chi = 0$ is smeared out) and, in any case, does not influence the issues of interest here.

Consider first the simple ICJ results in Fig. 23(a). At the parton level the Monte Carlo results are in agreement with the perturbation theory with cuts—a reassuring check. The size of the fluctuations also indicate the statistical uncertainty with only 4000 events. The important feature is that at Stage (2) nothing has changed, within statistics. This again is really a check since the produced hadrons are collinear with the JETS, i.e., with the quarks and gluons, and thus the energy flow pattern should not change from the parton level. Finally the result of Stage (3) differs from that of Stage (2) by a sizeable, essentially symmetric (see below) contribution of the form indicated in Eq. (IV.6).

As indicated in Fig. 23(b), the STR model at Stage (1) is identical to the ICJ case, again a check on the calculation. The fundamental result is illustrated by the Stage (2) result. The assumption that quarks and gluons fragment into hadrons via a small number of incoherent strings rather than via a slightly larger number of incoherent JETS implies sizeable correlations not present in the simple JET picture at present energies. Note in particular that, with respect to Stage (1), the STR Stage (2) result is larger at small angles and smaller at large angles. It thus will exhibit a smaller asymmetry than at Stage (1). This feature of the STR model can be easily, if qualitatively, understood by studying Fig. 21. A more explicit analytic result comes from applying the simple fragmentation analysis of Eqs. (IV.1) to (IV.5) to the fragmentation of two back-to-back JETS in the string rest frame and then boosting to the e^+e^- rest frame. The correlation between the mass of the string, the opening angle of the string and the requisite boost yields an energy weighted spectrum at Stage (2) of the form

$$\frac{dh_0}{d\cos\chi_1}\Big|_{e^+e^-\,CM} \sim \frac{Cm\sin^2\chi_{QG}}{2\sin^2\chi_1\sin^2\chi_2}\left[\frac{1+\cos\chi_1\cos\chi_2+\sin\chi_1\sin\chi_2}{2\sin\chi_1\sin\chi_2}\right], \qquad (IV.7a)$$

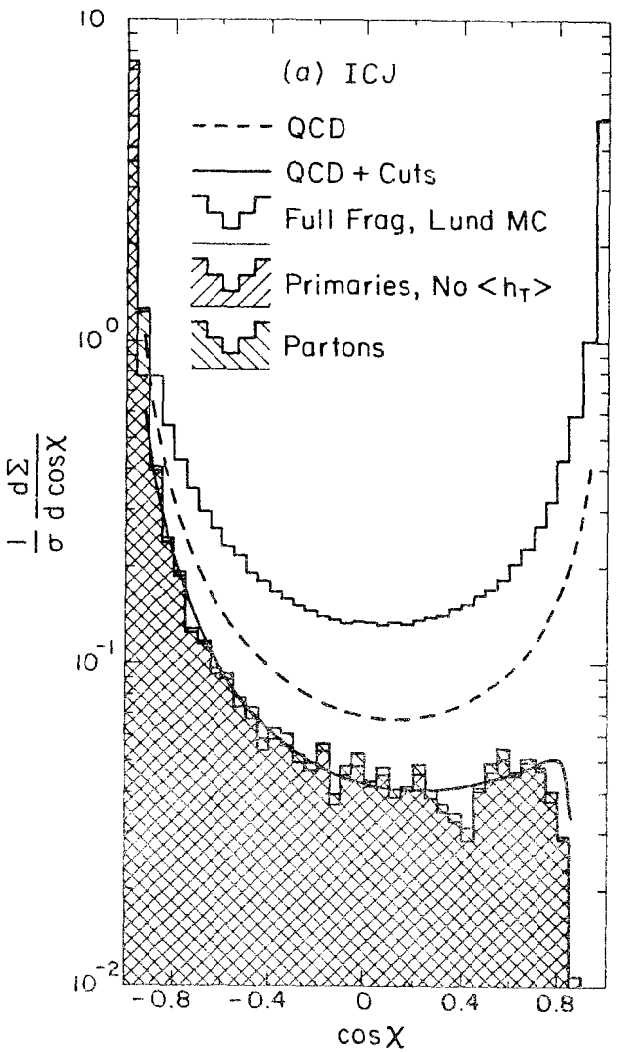


Fig. 23 Result of Monte Carlo calculation of the Energy-Energy Correlation.

(a) InCoherent Jet picture. The data sample was 4000 events at $W = 30GeV$. The three indicated stages of evolution are explained in the text.

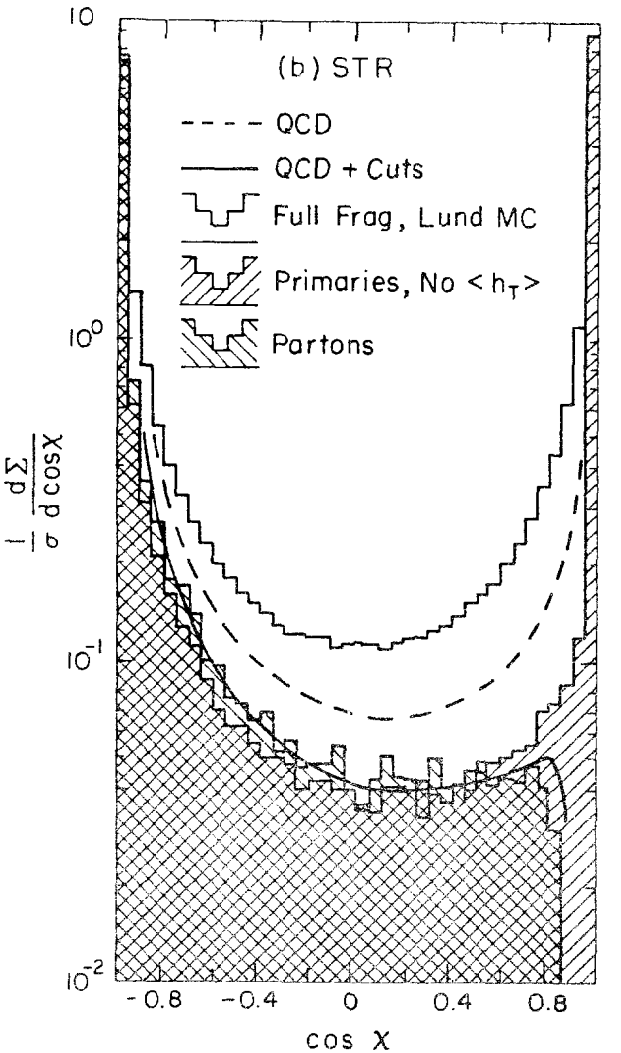


Fig. 23 Result of Monte Carlo calculation of the Energy-Energy Correlation.

(b) STRing picture. The data sample was 4000 events at $W = 30GeV$. The three indicated stages of evolution are explained in the text.

where the angles are defined in Fig. 24, m is the mass of the produced hadron and C is as in Eq. (IV.5). This suggests the useful approximate form

$$\frac{dh_0}{d\cos\chi_1}\Big|_{e^+e^-\,CM} \underset{\chi_1\sim\chi_2\sim\frac{\chi_{QG}}{2}}{\sim} \frac{2Cm\cos^2(\chi_{QG}/2)}{\sin^3(\chi_{QG}/2)} \quad , \qquad (IV.7b)$$

midway along the string, i.e., between the two corresponding JETS. This result clearly suggests that the boosts appropriate to rather low mass, small opening angle strings can lead to sizeable enhancements in the energy carried in the e^+e^- frame by the hadrons which are "wee" in the string frame, as already suggested in Figs. 21 and 23(b). The final step to Stage (3) again produces a smearing of the quark-antiquark final state to yield a large symmetric contribution plus an enhancement of the effect in Eq. (IV.7), because m is now replaced (on average) by $m_T = \sqrt{m^2 + (h_T)^2}$.

Now consider the asymmetries of the results in Fig. 23 which are exhibited in Fig. 25 where, for obvious reasons, the shading rule is inverted. The perturbative result is indicated by the solid curve and is (somewhat miraculously) essentially indistinguishable from the asymmetry of the cross section including the above mentioned cuts (the latter result being smaller approximately uniformly by about 5%). The Stage (1) asymmetry is the unshaded histogram, Stage (2) is righthand hatched (/) while Stage (3) has the lefthand hatch (\). The result in Fig. 25(a) clearly demonstrates the fact that for independent jets the leading fragmentation correction to the asymmetry, order $\alpha_s\, Q_0/W$, is already small at $W = 30$ GeV except near the edges of phase space. The last proviso is, in fact, phenomenologically important. The effects of resonances are certainly important at small angles, and perturbative analyses at present energies are best confined to the region $|\cos(\chi)| \leq 0.7$ even if the JETS are essentially independent. Consider now the histograms of Fig. 25(b). They clearly confirm the discussion above. The long range correlations inherent in string fragmentation can have a sizeable influence on the structure of the hadronic final state. In the present instance they serve to reduce the asymmetry by a factor of approximately two. To summarize the STR result, it is well described by the perturbative form of Eqs. (II.18) and (II.19) plus a symmetric term of the form of Eq. (IV.6) (including also an order $\alpha_s \cdot Q_0/W$ piece), plus an asymmetric fragmentation contribution with asymmetry described satisfactorily numerically by

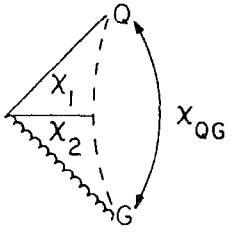


Fig. 24 Geometry of the distribution of hadrons in boosted string as discussed in Eq. (IV.7).

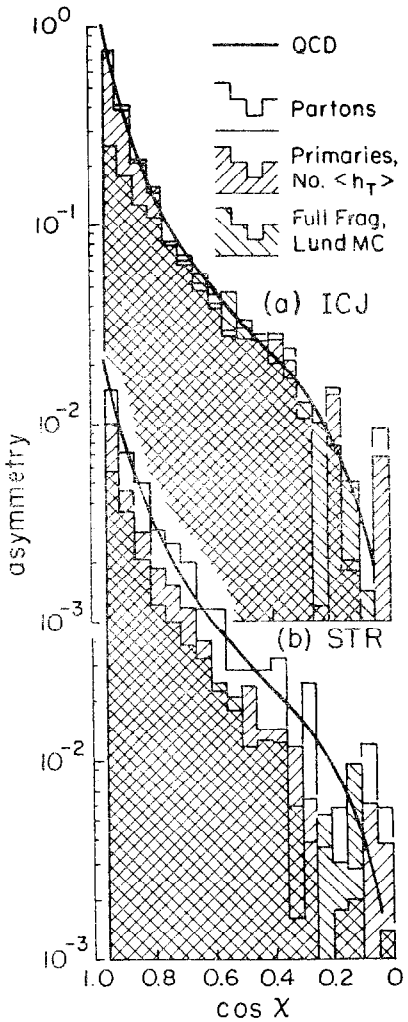


Fig. 25 Asymmetry of the Monte Carlo calculated Energy-Energy Correlation of Fig. 23. (a) InCoherent Jet picture. (b) STRing picture.

$$-\frac{\alpha_s}{\pi}\frac{12.5\text{GeV}}{W}\frac{\cos\chi}{\sin^3\chi} \quad . \qquad (IV.8)$$

This simple and handy approximate analytic form for the asymmetry is already suggested by the fact that the asymmetry of an expression like Eq. (IV.7b) is given by

$$(\sin^5\chi/2 - \cos^5\chi/2)/(\cos^3\chi/2\,\sin^3\chi/2)$$

which is adequately approximated by $-8\cos\chi/\sin^3\chi$ for $10^\circ < \chi < 80^\circ$. Comparison with Eq. (II.20) for $W = 30$ GeV confirms the conclusion mentioned above concerning the decreased asymmetry. The numerical magnitude of the dimensional scale which appears explains the characteristic Q_0 value mentioned at the beginning of the Section. The quality of this simple parameterization is indicated in Fig. 26, where the sum of Eqs. (II.20) and (IV.8) is compared with the asymmetry calculated in the STR model at $W = 30$, 50 and 100 GeV using data sets of 20K events each. It should be noted that for energies much less than 30 GeV the energy dependence of the asymmetry is considerably more complicated.

In summary, the correlations inherent in string-like fragmentation result in events which are much more two-JET-like at present energies than simple independent JET models would predict. This means that care must taken in interpreting various measures of JET cross sections and in attempts to experimentally determine α_s using such cross sections. [45,46] The interested and astute reader might well ask at this point—since the issue of how JETS fragment is so interesting, why can't the existing data be used to distinguish between the various models? While this should in principle be possible (and should be awarded high priority), the present situation is clouded by at least two issues. First the various models [39-43] differ not only on various, sometimes subtle, physics questions but also on certain technical details which are even more obscure but apparently relevant at present energies. For example, if the perturbative final state conserves energy and momentum, the hadronic final state which results from an independent JET fragmentation picture in general will not. This is simply understood as the fact that the JETS acquire a finite mass but generally but do not change their total

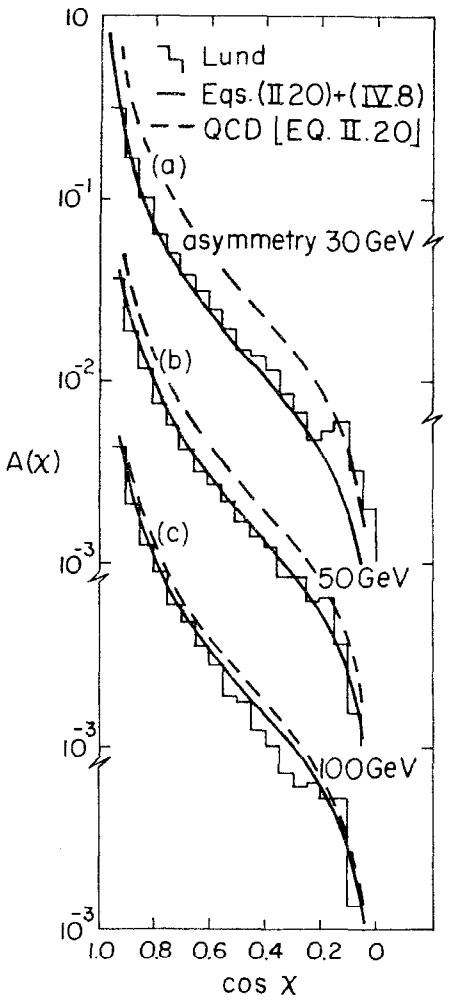


Fig. 26 Energy dependence of asymmetry of Monte Carlo calculated Energy-Energy Correlation compared to analytic results discussed in text. The data sample was 20,000 events at each value of W.

three momentum (i.e., conserve momentum but not energy). Schemes for remedying this situation vary from model to model and apparently are not equivalent. [47] Second the variations of results from one experiment to the next render such relatively subtle questions very difficult to answer at present. [1,2] This situation will surely improve rapidly in the near future.

V. CONCLUSIONS AND QUESTIONS

These lectures will be concluded by simply summarizing at least some of the many outstanding questions concerning JETS.

I. Can the fixed order results of Section II on JET-JET correlations be used to determine α_s and test QCD? (The answer appears to be yes but there is much work yet to be done to make this quantitative.)

II. Are any of the various perturbative predictions for the properties of JETS discussed in Section III, e.g.,

(A) nonscaling,

(B) $\langle n \rangle \sim \exp[c\sqrt{\ln Q}]$,

(C) gluon JETS softer, fatter, with larger $\langle n \rangle$,

(D) dip in $x d\sigma/dx$, and

(E) KNO scaling,

observed and/or observable at present energies? (The answer is, of course, yes and the student is referred to Refs. [1,2] for at least a partial summary of the experimental results.)

III. Do JETS fragment approximately independently or not, i.e., what is Q_0? (This is still largely an open question and deserves much further attention, experimentally and theoretically.)

IV. Are spectator/diquark JETS in deep inelastic scattering and large Pt reactions (recall Fig. 2) the same as e^+e^- JETS? Why or why not? (The preliminary answer to the first question appears to be yes but considerable further detailed work is needed especially with respect to "Why.")

IV. What is the structure of JETS initiated by heavy quarks (a topic not discussed here but of considerable interest—see [48,49])?

JETS are clearly here to stay as an important tool to analyze hadronic final states of all kinds and serve as clear indications of the role of quarks and gluons as dynamical degrees of freedom. While the asymptotic properties of these JETS are precisely predicted by perturbative QCD, there is an enormous quantity of work still to be done. Systematic procedures for evaluating, or at least characterizing the subleading perturbative contributions in the general case must be formulated and studied. Perhaps even more important phenomenologically is the issue of the scale of separation between perturbative and nonperturbative structure, i.e., Q_0. This question must be systematically and quantitatively understood. It is time for theorists, model builders, phenomenologists and experimentalists to do it right!!

ACKNOWLEDGMENTS

The author gratefully acknowledges many helpful discussions with L. Brown, J. Collins, R. Field, A. Mueller, J. Stirling and his fellow lecturers at this Institute. Special thanks go to F. Gilman, D. Leith and especially P. McDonough and her colleagues for organizing and coordinating this outstanding Institute. The author also wishes to acknowledge the support and hospitality of NORDITA, the University of Lund and the University of Helsinki where some of these lectures were prepared. This work was supported in part by the U.S. Dept. of Energy, contract number DE-AC06-81ER-40048.

APPENDIX A

The following comments and formulae are intended to be useful when performing the recommended exercises. Start with the QCD Lagrangian (metric +,-,-,-),

$$\mathcal{L}_{QCD} = -\frac{1}{4}F_{\mu\nu a}F_a^{\mu\nu} + i\bar{\psi}_i D^{\mu}_{ij}\gamma_\mu\psi_j \quad , \tag{A.1}$$

where

$$F_{\mu\nu a} = \partial_\mu A_{\nu a} - \partial_\nu A_{\mu a} + g f_{abc} A_{\mu b} A_{\nu c} \quad , \tag{A.2}$$

and

$$D^{\mu}_{ij} = \partial^\mu \delta_{ij} - igA^\mu_a T_{aij} \quad . \tag{A.3}$$

The matrices (generators) T_a satisfy the algebra

$$[T_a, T_b] = i f_{abc} T_c \quad , \tag{A.4}$$

where

$$TR\sum_a (T_a T_a) = C_F N_c \quad . \tag{A.5}$$

The matrix element squared for the lowest order process, e^+e^-, goes to quark-antiquark as in Fig. 1(a), is then [p_μ = quark 4-momentum, $\bar{p}_\mu$ = antiquark 4-momentum, l_μ = lepton 4-momentum],

$$|M_2|^2 = \frac{4e^2Q_Q^2}{(W^2)^2}[2p\cdot l\bar{p}\cdot l + 2p\cdot\bar{p}\cdot l] = e^2Q_Q^2(1+\cos^2\theta) \quad , \tag{A.6}$$

where θ is the angle between the quark direction and the lepton beam direction. Integration yields the lowest order total cross section, (summing explicitly over color)

$$\sigma_0 = \frac{4\pi\alpha^2}{3W^2}\sum_f \left(\frac{Q_f}{e}\right)^2 \qquad (A.7)$$

The quark differential cross section is

$$\frac{1}{\sigma_0}\frac{d\sigma_Q}{d\Omega} = \frac{3}{16\pi}(1+\cos^2\theta) \qquad (A.8)$$

To discuss the matrix element for the 3 body final state, real gluon emission with "mass" $= \mu$, it is useful to define the variables

$$z = \frac{2E_Q}{W} \qquad \bar{z} = \frac{2E_{\bar{Q}}}{W} \quad , \quad \text{and} \quad \epsilon = \frac{\mu^2}{W^2} \qquad (A.9)$$

The matrix element squared is then

$$|M_3|^2 = \sigma_0\alpha_s(24C_F)(2\pi)^2\left[\frac{z^2(1+\cos^2\theta_Q)+\bar{z}^2(1+\cos^2\theta_{\bar{Q}})}{(1-z)(1-\bar{z})}\right.$$
$$\left. + \frac{\epsilon z}{(1-\bar{z})^2}(z-2-z\cos^2\theta_Q) + \frac{\epsilon\bar{z}}{(1-z)^2}(\bar{z}-2-\bar{z}\cos^2\theta_{\bar{Q}})\right] \quad , \qquad (A.10a)$$

with the constraint

$$0 \le \frac{z+\bar{z}-1+\epsilon}{z\bar{z}} \le 1 \quad , \qquad (A.10b)$$

arising from requiring that the quark-gluon angle be physical and the outgoing particles be "onshell." The allowed region of integration for $z, \bar{z}$ is exhibited in Fig. 27. Performing this integration yields the order α_s quark cross section

$$\frac{1}{\sigma_0}\frac{d\sigma_Q}{d\Omega} = \frac{\alpha_s}{2\pi}C_F\frac{3}{16\pi}\left\{\left[\ln^2\frac{1}{\epsilon} - 3\ln\frac{1}{\epsilon} - \frac{\pi^2}{3} + 5\right](1+\cos^2\theta) + (1-3\cos^2\theta) + O(\epsilon)\right\} \qquad (A.11)$$

The energy weighted cross sections discussed in the text are obtained from similar integrations, including the appropriate factors of $z, \bar{z}$ and $x = 2E_G/W = 2-z-\bar{z}$.

APPENDIX B

Starting from the structure of Eq. (III.8b) with a single flavor

$$D(z) = f(1-z) + \int_z^1 \frac{d\eta}{\eta} f(\eta) D\left(\frac{z}{\eta}\right) \quad , \qquad (B.1a)$$

and with the normalization (one meson per vertex)

$$\int_0^1 d\eta f(\eta) = 1 \quad , \qquad (B.1b)$$

it is useful to define the moments

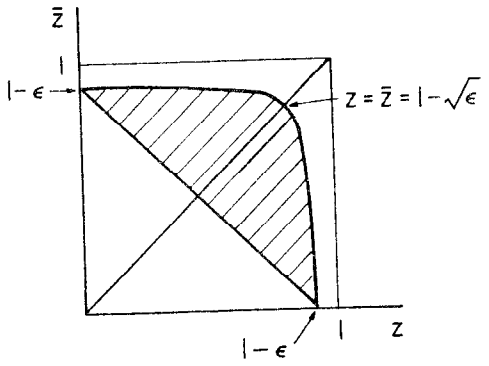


Fig. 27 Region of integration for the matrix element with "gluon mass" cutoff as discussed in Appendix A.

$$M(r) \equiv \int_0^1 dz\, z^r D(z) \quad , \tag{B.2a}$$

$$A(r) \equiv \int_0^1 d\eta\, \eta^r f(\eta) \quad , \tag{B.2b}$$

and

$$C(r) \equiv \int_0^1 dz\, z^r f(1-z) \quad . \tag{B.2c}$$

The normalization condition implies

$$A(0) = C(0) = 1 \quad . \tag{B.3}$$

It also follows trivially that

$$C(1) = A(0) - A(1) \quad , \text{etc.} \tag{B.4}$$

The transform of Eq. (B.1a) is then

$$M(r) = C(r) + A(r)M(r) \quad ,$$

or

$$M(r) = \frac{C(r)}{1-A(r)} = C(r)\left[1 + \frac{A(r)}{1-A(r)}\right] \quad . \qquad (B.5)$$

Thus, if a function $g(\eta)$ is defined by

$$\int_0^1 d\eta\, \eta^r g(\eta) \equiv \frac{A(r)}{1-A(r)} \quad , \qquad (B.6)$$

the solution is

$$D(z) = f(1-z) + \int_z^1 \frac{d\eta}{\eta} g(\eta) f\left(1 - \frac{z}{\eta}\right) \quad . \qquad (B.7)$$

Various results follow immediately. From (B.3) and (B.4) energy is conserved (as it must be),

$$M(1) = \frac{C(1)}{1-A(1)} = 1 \quad . \qquad (B.8)$$

In terms of the finite derivative at $r = 0$,

$$R \equiv \int_0^1 d\eta \ln \frac{1}{\eta} f(\eta) = \frac{d}{dr} A(r)\,|_{r=0} \quad , \qquad (B.9)$$

$A(r)$ has the limit

$$A(r) \underset{r\to 0}{\to} 1 + Rr \quad , \qquad (B.10)$$

and thus

$$M(r) \underset{r\to 0}{\to} \frac{R}{r} \quad . \qquad (B.11)$$

This implies

$$D(z) \underset{z\to 0}{\to} \frac{R}{z} \quad , \qquad (B.12)$$

and thus a multiplicity which behaves as

$$\langle n \rangle \sim \int_{Q_0/Q}^1 dz\, D(z) \underset{Q \gg Q_0}{\sim} R \ln\left(\frac{Q}{Q_0}\right) \quad . \qquad (B.13)$$

As a final observation note that for the physically interesting choice,

$$f(\eta) = (\alpha+1)\eta^\alpha \quad , \qquad (B.14)$$

one has

$$\frac{A(r)}{1-A(r)} = \frac{\alpha+1}{r} \quad . \qquad (B.14)$$

Thus it follows from (B.6) that

$$g(\eta) = \frac{\alpha+1}{\eta} \quad , \qquad (B.15)$$

and thus

$$D(z) = \frac{\alpha+1}{z}(1-z)^{\alpha} \quad . \qquad (B.15)$$

APPENDIX C

To establish a connection with the scaling ideas of the renormalization group note that the moments M can be thought of as depending on a dimensionful scale, in this case Q^2, only through the running coupling $\alpha_s(Q^2)$. Recall that the fragmentation function D has zero "engineering" dimension. This suggests the replacement

$$\frac{d}{d\tau} \quad \rightarrow \quad \frac{d\alpha_s(\tau)}{d\tau}\frac{d}{d\alpha_s} \quad . \qquad (C.1)$$

Furthermore the coupling, $\alpha_s(\tau) \equiv \bar{g}^2(\tau)/4\pi$, changes under rescaling of the momentum $Q \rightarrow \lambda Q$, $\tau \rightarrow \tau + \ln\lambda^2$, as

$$\begin{aligned} \lambda\frac{d\bar{g}(\lambda)}{d\lambda} &\equiv \beta(\bar{g}(\lambda)) \\ &= -\frac{2b_0}{(4\pi)^2}\bar{g}^3 - \frac{4b_1}{(4\pi)^4}\bar{g}^5 + \cdots \quad , \end{aligned} \qquad (C.2)$$

where b_0 and b_1 are given in Eq.(II.2). Thus, since $d\tau \sim 2d\lambda/\lambda$, it follows that

$$\frac{d\alpha_s(\tau)}{d\tau} = \frac{\bar{g}}{4\pi}\beta(\bar{g}(\tau)) \quad , \qquad (C.3)$$

or

$$\frac{d}{d\tau} \quad \rightarrow \quad \frac{1}{2}\beta(\bar{g})\frac{\partial}{\partial\bar{g}} \quad . \qquad (C.4)$$

Hence, if an anomalous dimension γ_n is defined by

$$\gamma_n(\bar{g}) \equiv -\frac{\alpha_s}{\pi}A^{(n)} \quad , \qquad (C.5)$$

then Eq. (III.15) becomes

$$\beta(\bar{g})\frac{\partial M(n,\bar{g})}{\partial\bar{g}} = -\gamma_n(\bar{g})M(n,\bar{g}) \quad , \qquad (C.6a)$$

or, in more standard form,

$$\left[\beta(\bar{g})\frac{\partial}{\partial\bar{g}} + \gamma_n\right]M_n = 0 \quad . \qquad (C.6b)$$

This is equivalent to the statement that the physics is independent of the choice of renormalization scale. The solution to Eq. (C.6) is

$$M_n(\bar{g}) = exp\left[-\int_{\bar{g}_0}^{\bar{g}} d\bar{g}'\frac{\gamma_n(\bar{g}')}{\beta(\bar{g}')}\right]M_n(\bar{g}_0) \qquad (C.7)$$

in direct analogy to Eq. (III.18) with $\overline{g} = \overline{g}(\tau)$ and $\overline{g}_0 = \overline{g}(\tau_0)$. Note that $M_n(\overline{g}_0)$ arises simply as a constant of integration. To compare with the results in the text consider the leading order where

$$
\begin{aligned}
-\int_{\overline{g}_0}^{\overline{g}} dg' \frac{\gamma_n(g')}{\beta(g')} &= -\int_{\overline{g}_0}^{\overline{g}} dg' \frac{\left(-\frac{g'^2}{4\pi^2} A^{(n)}\right)}{\left(\frac{-2b_0}{(4\pi)^2} g'^3\right)} \\
&= -\frac{A^{(n)}}{b_0} \ln\left(\frac{\overline{g}^2}{\overline{g}_0{}^2}\right) = \frac{A^{(n)}}{b_0} \ln\left(\frac{\tau}{\tau_0}\right) ,
\end{aligned}
\tag{C.8}
$$

just as in Eq. (III.17). For a more formal treatment using the techniques of cut vertices see the first paper in Ref. [4] and the next to last papers in Reference [29].

APPENDIX D

In the singlet case Eq. (III.15) becomes

$$
\frac{\partial}{\partial \tau}\begin{pmatrix} M_Q^b(r,\tau) \\ M_G^b(r,\tau) \end{pmatrix} = \frac{\alpha_s(\tau)}{2\pi}\begin{pmatrix} A_{Q\to Q}^{(r)} & A_{Q\to G}^{(r)} \\ 2N_f A_{G\to Q}^{(r)} & A_{G\to G}^{(r)} \end{pmatrix}\begin{pmatrix} M_Q^b(r,\tau) \\ M_G^b(r,\tau) \end{pmatrix} . \tag{D.1}
$$

The matrix in this equation can be easily diagonalized with eigenvalues

$$
A_\pm = \frac{1}{2}\left[A_{Q\to Q} + A_{G\to G} \pm \sqrt{\left(A_{Q\to Q} - A_{G\to G}\right)^2 + 8N_f A_{G\to Q} A_{Q\to G}}\right] . \tag{D.2}
$$

Also useful are the quantities

$$
\begin{aligned}
\alpha(r) &= \frac{A_+^{(r)} - A_{Q\to Q}^{(r)}}{A_+^{(r)} - A_-^{(r)}} , \\
\beta(r) &= \frac{A_{Q\to G}^{(r)}}{A_-^{(r)} - A_+^{(r)}} , \\
\gamma(r) &= \frac{\left(A_+^{(r)} - A_{Q\to Q}^{(r)}\right)\left(A_-^{(r)} - A_{Q\to Q}^{(r)}\right)}{A_{Q\to G}^{(r)}\left(A_+^{(r)} - A_-^{(r)}\right)} .
\end{aligned}
\tag{D.3}
$$

In terms of these quantities the 2 by 2 matrix $\overline{A}$ is

$$
\overline{A}^{(r)} = \begin{pmatrix} (1-\alpha(r))e^{\kappa A_+^{(r)}} + \alpha(r)e^{\kappa A_-^{(r)}} & \beta(r)(e^{\kappa A_-^{(r)}} - e^{\kappa A_+^{(r)}}) \\ \gamma(r)(e^{\kappa A_-^{(r)}} - e^{\kappa A_+^{(r)}}) & \alpha(r)e^{\kappa A_+^{(r)}} + (1-\alpha(r))e^{\kappa A_-^{(r)}} \end{pmatrix} . \tag{D.4}
$$

In particular, using the results of Eq. (III.21) for $r = 1$, the quantities in Eqs. (D.2) and (D.3) become

$$
\begin{aligned}
A_+^{(1)} = 0 \quad &, \quad A_-^{(1)} = -\frac{4}{3}C_F - \frac{1}{3}N_f , \\
\alpha(1) = \beta(1) = \frac{4C_F}{4C_F + N_f} &, \quad \gamma(1) = \frac{N_f}{4C_F + N_f} .
\end{aligned}
\tag{D.5}
$$

Substitution of these results into Eq. (D.4) yields Eqs. (III.29) and (III.30) and the subsequent conclusions.

For the case $r \to 0$ one uses Eq. (III.38) with some care to find for (D.2) and (D.3) the results

$$A_+^{(r\to 0)} \to \frac{2C_A}{r}, \quad A_-^{(0)} = 0,$$
$$\alpha(r\to 0) \to 1 - \frac{C_F N_f r}{3C_A^2}, \quad \beta(0) = -\frac{C_F}{C_A}, \quad \gamma(r\to 0) \to -\frac{N_f}{3C_A} r \quad . \tag{D.6}$$

Thus $\overline{A}$ becomes in this limit

$$\overline{A}^{(r\to 0)} \to \begin{pmatrix} C_F N_f r & 3C_F C_A \\ C_A N_f r & 3C_A^2 \end{pmatrix} \frac{exp[2C_A \kappa / r]}{3C_A^2} \tag{D.7}$$

from which follows Eq. (III.39). The limit $r \to \infty$ can be analyzed in a similar fashion.

APPENDIX E

In order to avoid the singular regions of the 3-body phase space, the Lund Monte Carlo invokes a cut on the invariant mass of the quark-gluon pair, i.e., the "offshellness" of the virtual quark before it emits the gluon. Define this constraint in the form

$$M_{QG}^2 \quad , \quad M_{\bar{Q}G}^2 \geq \mu^2 \quad , \tag{E.1}$$

where μ is a chosen dimensionful parameter.

In the language of Appendix A this corresponds to the constraints

$$1 - z \quad , \quad 1 - \bar{z} \geq \delta \equiv \frac{\mu^2}{W^2} \tag{E.2}$$

on the region of integration in Fig. 27.

This Lund Monte Carlo also requires that, in the frame where the quark-antiquark pair are back-to-back, the gluons have more than a certain amount of transverse momentum. This can be realized in invariant form b constraint,

$$\frac{M_{QG}^2 M_{\bar{Q}G}^2}{M^2 Q\bar{Q}} \geq 8\mu^2 \quad , \tag{E.3}$$

in terms of the quark-gluon, antiquark-gluon and quark-antiquark invariant masses. For simplicity the two dimensionful parameters in Eqs. (E.1) and (E.3) are chosen to be equal. The factor 8 is chosen in an ad hoc fashion to ensure that the program runs in an efficient manner. The corresponding constraint on the integration variables of Appendix A is

$$\frac{(1-z)(1-\bar{z})}{(1-x)} \geq 8\delta \quad . \tag{E.4}$$

Imposing Eqs. (E.2) and (E.4) on the integration of Appendix A for the EEC yields the curve in Fig. 23 for the choice $\delta = 0.0015$, $\mu \sim 1.5$ GeV at $W = 30$ GeV. This analytic procedure is, to some extent, an oversimplification of what actually happens inside the Monte Carlo program but clearly offers a reasonable representation.

REFERENCES

[1] For a summary of the experimental status of JETS in e^+e^- annihilation see the lectures by R. Hollebeek at this Institute.

[2] For a summary of the experimental status of JETS in hadronic reactions see the lectures by R. Schwitters at this Institute.

[3] See, for example, the earlier review by S.D. Ellis, lectures in *Quantum Flavordynamics, Quantum Chromodynamics, and Unified Theories*, Proc. of the NATO Advanced Study Institute in Elementary Particles, July 1979, Boulder, CO (Plenum Press, N.Y.,1980), ed. by K.T. Mahanthappa and J. Randa, page 139. For early discussions of the role of JETS in hadronic physics see J.D. Bjorken, Phys. Rev. *D8*, 4098 (1973); S.D. Ellis and M.B. Kislinger, Phys. Rev. *D9*, 2027 (1974).

[4] A.H. Mueller, Phys. Rep. *73*, 237 (1981); G. Altarelli, Phys. Rep. *81*, 1 (1982); A. Bassetto, M. Ciafaloni and G. Marchesini, preprint SNS 3/1983, UTF 96/83 (to be published in Phys. Rep.).

[5] C.L. Basham, L.S. Brown, S.D. Ellis and S.T. Love, Phys. Rev. *D17*, 2298 (1978).

[6] C.L. Basham, L.S. Brown, S.D. Ellis and S.T. Love, Phys. Rev. Lett. *41*, 1585 (1978); Phys. Rev. *D19*, 2018 (1979).

[7] See the apparatus oriented lectures by A. Walenta and P. Mockett at this Institute.

[8] Lewis Carroll, *Alice's Adventure's in Wonderland*, Chap. VI (1865) .

[9] For a review of parton ideas and JETS see R.P. Feynman, *Photon-Hadron Interactions* (Benjamin, Reading, MA, 1972); J.D. Bjorken, lectures given at the International Summer Institute in Theoretical Physics, DESY, Hamburg, September 1975, preprint SLAC-PUB-1756 (1976).

[10] See, for example, W. Marciano and H. Pagels, Phys. Rep. *36*, 137 (1978); A.J. Buras, Rev. Mod. Phys. *52*, 199 (1980). See also Ref. 4.

[11] For review of the status of lattice calculations see M. Creutz, lectures at the 4th Adriatic Meeting on Particle Physics, Dubrovnik, Yugoslavia, June 1983, Brookhaven preprint BNL-33649 (1983); M. Creutz, L. Jacobs, C. Rebbi, Phys. Rep. *95*, 201(1983). For a discussion of analytic techniques see M. Baker, L. Carson, J.S. Ball and F. Zachariasen, Univ. of Washington preprint DOE/ER/40048-6 P3(1983); M. Baker, J.S. Ball and F. Zachariasen, Nucl. Phys. *B226*, 455(1983).

[12] See the lectures of M. Peskin at this Institute.

[13] J.D. Bjorken, lecture at the 2nd International Conference on Physics in Collision, Stockholm, Sweden, June 1982, preprint FERMILAB-CONF-82/42-THY (1982).

[14] See, for example, M. Jacob, lecture at the 3rd Topical Workshop on Proton-Antiproton Collider Physics, Rome, Italy, January 1983, CERN-TH-3515 (1983); C. Quigg, Summary talk at the Europhysics Study Conference on Multibody Phenomena in Strong, Electromagnetic and Weak Interactions, Erice, Italy, September 1982, preprint FERMILAB-CONF-82/91-THY (1982).

[15] See the review by G. Wolf, Proc. of the 21st International Conference on High Energy Physics, Paris, July 1982 (Journal de Physique, Decembre, 1982), ed. by P. Petiau and M. Porneuf, page C3-525.

[16] See, for example, S.D. Ellis, M. Jacob and P. Landshoff, Nucl. Phys. *B108*, 93 (1976).

[17] This field of study was stimulated to a large extent by the work of G. Sterman and S. Weinberg, Phys. Rev. Lett. *39*, 1436 (1979).

[18] T. Kinoshita, J. Math. Phys. *3*, 650 (1962); T.D. Lee and M. Nauenberg, Phys. Rev. *133*, 1549 (1964).

[19] For a recent review see S.D. Ellis, lecture in the Proc. of the 13th International Symposium on Multiparticle Dynamics, Volendam, the Netherlands, June 1982 (World Scientific Pub. Co., Singapore, 1983), ed. by W. Kittel, W. Metzger and A. Stergiou, page 935. See also the comprehensive approach of J.C. Collins and D.E. Soper discussed, for example, in Nucl. Phys. *B197*, 446(1982); ERRATUM-ibid *B213*, 545(1983).

[20] See, for example, L.S. Brown and S.D. Ellis, Phys. Rev. *D24*, 2383(1981).

[21] D.G. Richards, W.J. Stirling and S.D. Ellis, Phys. Lett. *119B*,193(1982); Nucl. Phys. *B229*, 317(1983).

[22] A. Ali and F. Barreiro, Phys. Lett. *118B*, 155(1982); preprint DESY 83/070(1983).

[23] K. Konishi, A. Ukawa, and G. Veneziano, Phys. Lett. *80B*, 259(1979); Nucl. Phys. *B157*, 45(1979); J. Kalinowski, K. Konishi and T.R. Taylor, Nucl. Phys. *B181*, 221(1981).

[24] A.H. Mueller, Columbia Univ. preprint CU-TP-263(1983); lecture at the Topical Conf. of the 10th SLAC Summer Institute, 1982, Columbia Univ. preprint CU-TP-249(1982); Nucl. Phys. *B213*, 85(1983).

[25] A. Bassetto, M. Ciafaloni and G. Marchesini, Nucl. Phys. *B163*, 477(1980); A. Bassetto, M. Ciafaloni, G. Marchesini and A.H. Mueller, Nucl. Phys. *B207*, 189(1982); D. Amati, A. Bassetto, M. Ciafaloni, G. Marchesini and G. Veneziano, Nucl. Phys. *B173*, 429(1980).

[26] Yu.L. Dokshitzer, V.S. Fadin and Khoze, Phys. Lett. *115B*, 242(1982); Z. Phys. *C15*, 325(1982); Z. Phys. *C18*, 37(1983).

[27] J. Kalinowski, K. Konishi, P.N. Scharbach and T.R. Taylor, Nucl. Phys. *B181*, 253(1981); G. Curci, W. Furmanski and R. Petronzio, Nucl. Phys. *B175*, 27(1980).

[28] D. Amati and G. Veneziano, Phys. Lett. *83B*, 87(1979); A. Bassetto, M. Ciafaloni and G. Marchesini, Phys. Lett. *83B*, 207(1979).

[29] See, for example, D. Amati, R. Petronzio and G. Veneziano, Nucl. Phys. *B140*, 54(1978); Nucl. Phys. *B146*, 29(1978); R.K. Ellis, H. Georgi, M. Machacek, H.D. Politzer and G.C. Ross, Phys. Lett. *78B*, 281(1978); Nucl. Phys. *B152*, 285(1979); S. Libby and G. Sterman, Phys. Rev. *D18*, 3252(1978); C.T. Sachrajda, Phys. Lett. *73B*, 185(1978); Phys. Lett. *76B*, 100(1978). For the more recent work using the powerful techniques of "cut vertices" see A.H. Mueller, the first paper in Ref. [4] and Phys. Rev. *D18*, 3705(1978); S. Gupta and A.H. Mueller, Phys. Rev. *D20*, 118(1979); A. Duncan, S. Gupta and A.H. Mueller, Nucl. Phys. *B175*, 148(1980). For a recent discussion of the "initial state interaction" - factorization controversy see C. Sachrajda, lecture at the 14th International Symposium on Multiparticle Dynamics, Lake Tahoe, CA, June 1983, preprint SLAC-PUB-3181(1983).

[30] R.D. Field and R.P. Feynman, Nucl. Phys. *B136*, 1(1978).

[31] G. Altarelli and G. Parisi, Nucl. Phys. *B126*, 298(1977).

[32] S.J. Brodsky, G.P. Lepage and P.B. Mackenzie, Phys. Rev. *D28*, 228(1983).

[33] G. Marchesini and B.R. Webber, CERN preprint TH-3525(1983). See also B.R. Webber, lecture at the 18th Recontre de Moriond, La Plagne, France, March 1983, CERN preprint TH-3569(1983).

[34] See, for example, G. Parisi, Phys. Lett. *90B*,295(1980); G. Curci and M. Greco, Phys. Lett. *92B*,175(1980); Phys. Lett. *102B*, 280(1981); D. Amati et al., Nucl. Phys. *B173*, 429 (1980); L. Caneschi, Phys. Lett. *98B*, 295(1980); M. Ciafaloni, Phys. Lett. *95B*, 113(1980); M. Ciafaloni and G. Curci, Phys. Lett. *102B*, 352(1981).

[35] Z. Koba, H.B. Nielsen and P. Olesen, Nucl. Phys. *B40*, 317(1972).

[36] See, for example, S. Kidambi Srinivasan, *Stochastic Theory and Cascade Processes*, (American Elsevier Pub. Co., Inc., N.Y., 1969), page 55.

[37] See, for example, F. Hayot and G. Sterman, Phys. Lett. *121B*, 419(1983); and earlier P. Cvitanović, P. Hoyer and K, Zalewski, Nucl. Phys. *B176*, 429(1980). For a different view of the same results see P. Carruthers and C.C. Shih, Phys. Lett. *127B*, 242(1983).

[38] For a fairly complete discussion of several such concerns see Ref. 13.

[39] For Monte Carlo models with "small" Q_0 scales see R.D. Field, G. Fox and R.L. Kelly, preprint CALT-68-927 / UFTP 82-26(1982); Phys. Lett. *119B*, 439(1982); R.D. Field and G.C. Fox, preprint CALT-68-965 / UFTP 82-30(1982). See also R.D. Field, lecture in the Proc. of the 13th International Symposium on Multiparticle Dynamics, Volendam, the Netherlands, June 1982, (World Scientific Pub. Co., Singapore, 1983), ed. by W. Kittel, W. Metzger and A. Stergiou, page 886.

[40] For a Monte Carlo scheme with an "intermediate" Q_0 scale see T.D. Gottschalk, Caltech preprints CALT-68-1030, CALT-68-1052(1983).

[41] For a fragmentation picture with a "large" Q_0 scale see the Lund string in B. Andersson, G. Gustafson and T. Sjöstrand, Nucl. Phys. *B197*, 45(1982); B. Andersson, G. Gustafson, G. Ingelman and T. Sjöstrand, Phys. Rep. *97*, 31(1983); B. Andersson, G. Gustafson and B. Soderberg, Lund Univ. preprint LU-TP-83-2(1983).

[42] For earlier work see A. Ali, E. Pietarinen and J. Willrodt, DESY preprint DESY-T-80/01(1980); P. Hoyer, P. Osland, H.G. Sander, T.F. Walsh and P.M. Zerwas,

Nucl. Phys. *B161*,349(1979); P. Hoyer, C. Peterson, C.-H. Lai and J.L. Peterson, Nucl. Phys. *B151*, 389(1979).

[43] For a different view see R. Odorico, preprints IFUB-83/6(1983); IFUB-82/20(1982); lecture at the Workshop on Drell-Yan Processes, Fermilab, October 1982, preprint IFUB-82/25(1982); Phys. Lett. *102B*, 341(1981); Nucl. Phys. *B172*, 157(1980); Z. Phys. *C4*, 113(1980). See also M. Greco, Phys. Lett. *121B*, 360(1983); lecture at the Workshop on Drell-Yan Processes, Fermilab, October 1982, preprint LNF-82/70-P(1982).

[44] See, for example, C. Quigg, P. Pirilä and G.H. Thomas, Phys. Rev. Lett. *34*, 290(1975); Phys. Rev. *D12*, 92(1975).

[45] S.D. Ellis, Phys. Lett. *117B*, 333(1982).

[46] See, for example, S.D. Ellis, lecture at the 21st International Conference on High Energy Physics, Paris, July 1982, Univ. of Washington preprint DOE/ER/40048-25 P2(1982); CELLO Collaboration, Nucl. Phys. *B218*, 269(1983).

[47] T. Sjöstrand, private communication.

[48] C. Peterson, D. Schlatter, I. Schmitt and P.M. Zerwas, Phys. Rev. *D27*, 105(1983).

[49] L.M. Jones, Phys. Rev. *D28*, 236(1983); L.M. Jones and R. Migneron, Phys. Rev. *D27*, 2063(1983); Z. Phys. *C16*, 217(1983).

SLAC-PUB-3242
October 1983
(T/E)

JETS IN e^+e^- ANNIHILATION*

R. Hollebeek
Stanford Linear Accelerator Center
Stanford University, Stanford, California 94305

Presented at the 11th SLAC Summer Institute on Particle Physics
Stanford, California, July 18-29, 1983

* Work supported by the Department of Energy, contract DE-AC03-76SF00515.

© R. Hollebeek 1983

1. Introduction

Jets in e^+e^- annihilation are either a fantastic surprise or completely expected behavior depending on how strongly one believes in the present quark picture of hadron dynamics. Before embarking on an explanation of what is seen in e^+e^- annihilation from the standard quark picture, let us take a moment to see why the production of jets might be a rather surprising phenomena.

The initial particles are known to be quite small when measured against many of the other mesons and hadrons which we will be talking about. For example, the Bhabha scattering process, $e^+e^- \to e^+e^-$, can be used to test for structure in these leptons since the scattering formula would be modified by the presence of a form factor as shown in Equation (1).

$$F_\pm(q^2) = 1 \pm \frac{q^2}{q^2 - \Lambda_\pm^2} \tag{1}$$

where Λ is a measure of the scale of the electron or positron substructure. When expressed in terms of an rms charge radius, this form factor becomes

$$F_\pm(q^2) = 1 - \frac{q^2\langle R^2\rangle}{6} + \cdots \tag{2}$$

and present limits on Λ_+ of approximately 100 GeV imply a charge radius

$$\langle R^2\rangle \lesssim \frac{6(\hbar c)^2}{\Lambda_+^2} \tag{3}$$

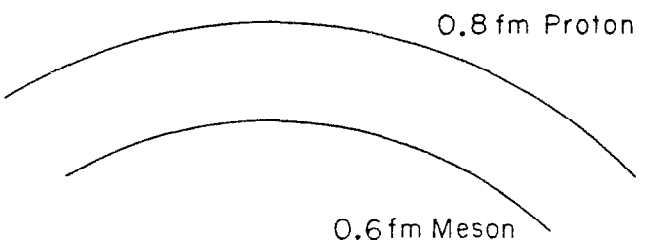
or R less than approximately 5×10^{-16} cm.

The simple quantum numbers of the initial state and standard conservation laws of the interaction greatly simplify the analysis of the final state since we expect that the total charge, baryon number, strangeness, charm, and lepton number of the final state will be zero. An additional simplification comes from the fact that at storage rings (except for radiative corrections) all experiments are done in the center-of-mass frame so that the sum of the final state momenta will be zero and the square of the sums of their individual energies

$$s = (\sum E_i)^2 = (2E_{beam})^2 \tag{4}$$

will be fixed. Values of E_{beam} up to $\sim$ 20 GeV have been achieved.

Now the most fundamental question is how does all this energy, packed into the collision of two extremely small particles, convert itself into hadrons? Figure 1 shows



11-83
4681A1

• Electron upper limit

Figure 1

the relative scales of the upper limit on the lepton when measured against the charge radii of the pi meson and the proton. The lesson to be learned here is that on the scale of what is going to be produced in the final state, electrons are extremely small! As we will see later, the bulk of the data on hadronic final states indicates that the particles emerge in two collimated jets traveling in opposite directions with approximately nine mesons in each jet. Our understanding of the details of this process is very sketchy; we are convinced by the striking two jet structure that the jets arise from the production of an initial state which at least for a time is two-body-like. We have almost no understanding of the detailed mechanism behind quantum number conservation within a jet or between jets.

2. Standard Quark Model

Our standard picture of matter is that it is composed of combinations of the spin 1/2, pointlike constituents called quarks shown in Table 1.

Table 1

Quark Charges and Masses

Quark		Charge	M_Q (GeV)
up	u	2/3	
down	d	-1/3	
strange	s	-1/3	$\sim .4$
charm	c	2/3	~ 1.5
bottom	b	-1/3	~ 5.0
top	t	2/3	?

This picture is supported by the known particles and their quantum numbers, the particle masses and decay branching ratios, and the presence of quark pair bound states such as the $c\bar{c}$ bound state ψ, ψ', at 3.1 GeV, $b\bar{b}$ bound states Υ, Υ' at 10 GeV and to a lesser extent light quark bound states such as the η, η' system $(s\bar{s})$ and the π mesons. Mesons are believed to be integer spin combinations of pairs of quarks while baryons are composed of 1/2-integer combinations of three quarks.

In addition to this basic picture of the composition of mesons and baryons, we believe that in many interactions the constituents interact as if they were *"Quasi-free"*. Scaling in deep inelastic eN scattering for example indicates the presence of three pointlike constituents within the nucleon which interact independently. This extension of the quark composition model to the dynamics of independently interacting constituents (or partons) is often called the quark-parton model.

2.1 Quark-Parton Model of e^+e^- Annihilation

The Feynman diagram for the production of hadrons from e^+e^- annihilation is shown in Figure 2. We can analyze this cross section most easily in terms of another well-known pair production cross section namely $e^+e^- \to \mu^+\mu^-$ (Figure 3). Seen in the center-of-mass system, the cross section is given by

$$\frac{d\sigma}{d\Omega} = \frac{\alpha^2}{4s}\,\beta\left[1+\cos^2\theta+(1-\beta^2)\sin^2\theta+\beta^2P^2\sin^2\theta\cos 2\theta\right] \tag{5}$$

where P is the initial state polarization (usually zero) and θ is the scattering angle between the e^+ and the μ^+. Since the muon is, like the electrons apparently pointlike, the total cross section becomes

$$\sigma_{point-like} = \frac{4}{3}\,\pi\,\frac{\alpha^2}{s} = \frac{86.6nb}{s(GeV^2)}\left(\frac{e_\mu}{e}\right)^2 \tag{6}$$

If we now apply this formula to the production of hadrons, assuming that quarks are also point-like, we find that the total production cross-section for hadrons coming from an initial two-quark state in units of the muon pair cross section will be just

$$R = \frac{\sigma_h}{\sigma_\mu} = 3\sum_i Q_i^2 \tag{7}$$

where Q_i is the quark charge in units of the electron charge, and the sum runs over all quark pairs which can contribute at the available center-of-mass energy. The factor of three comes from the fact that we believe that quarks can come in each of three distinct types. This latter quantum number is called "color".

An additional consequence of this picture is that the quarks will have the angular distribution $1+\cos^2\theta$ characteristic of the production of spin-1/2 objects. If there were additional quarks of spin zero, we would expect a $\sin^2\theta$ distribution with the smaller cross-section

$$\sigma = \frac{\sigma_{point}}{4} \tag{8}$$

since there is no $(2J+1)$ spin sum in the final state of such a system.

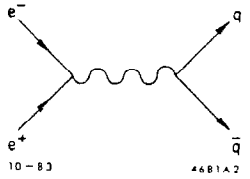


Figure 2

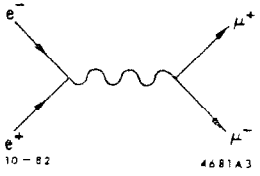


Figure 3

The behavior of R as a function of center-of-mass energy (shown in Figure 4) is in fact one of the most beautiful confirmations of this picture of hadron interactions. Except for the presence of the indicated bound states and resonances, $R(s)$ rises in discrete steps and agrees with the values predicted by the quark-parton picture.

The spin-1/2 nature of the quarks is seen in the fact that the angular distribution of hadrons produced does in fact have a $1 + \cos^2\theta$ distribution. We will come back to the problem of finding the initial quark axis from the directions of the final state particles (the approximately nine mesons in each jet), but if we define the thrust axis θ_T as a measure of the quark axis, then its distribution (Figure 5) shows the required behavior.[1]

A further consequence of the point-like nature of the quarks within the quark-parton picture is that the break-up of the quark into mesons to form a jet should be independent of the center-of-mass scale s. Thus we expect the cross-section to scale, i.e.,

$$\frac{d\sigma}{dx} \sim \frac{1}{s} f(x) \tag{9}$$

where x is the dimensionless ratio

$$x = \frac{2E_h}{\sqrt{s}} \quad .$$

Although small violations of this behavior are seen, this scaling parameterization works well over a large range of energies provided the x value is greater than approximately 0.2 (see Figure 6).

2.2 Phase Space for N Body Final States

We would now like to ask increasingly more detailed questions about what is seen in the final states of these interactions in order to learn more about the dynamics involved in the production of the hadronic matter. But before doing this, it is useful to examine the consequences of a model in which all of the dynamics is determined by the n body phase space integral. The earliest of such models is due to Fermi[2] and with some modifications explains many of the features which we observe. The analysis of the phase space integrals which I am following is due to Lepore and Stuart.[3] The basic principle is to Fourier transform the energy-momentum conserving delta function using

$$\delta = \int_{-\infty}^{\infty} d\alpha \, e^{i(\sqrt{s} - \sum E_i)\alpha} \int_{-\infty}^{\infty} d^3\lambda \, e^{i \sum p_i \lambda} \quad . \tag{10}$$

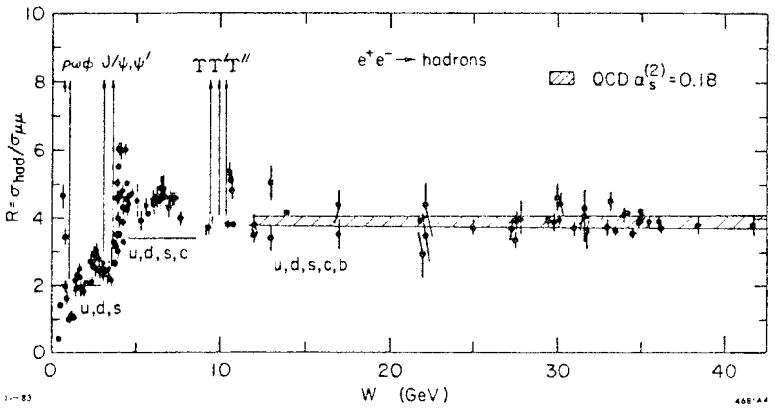


Figure 4

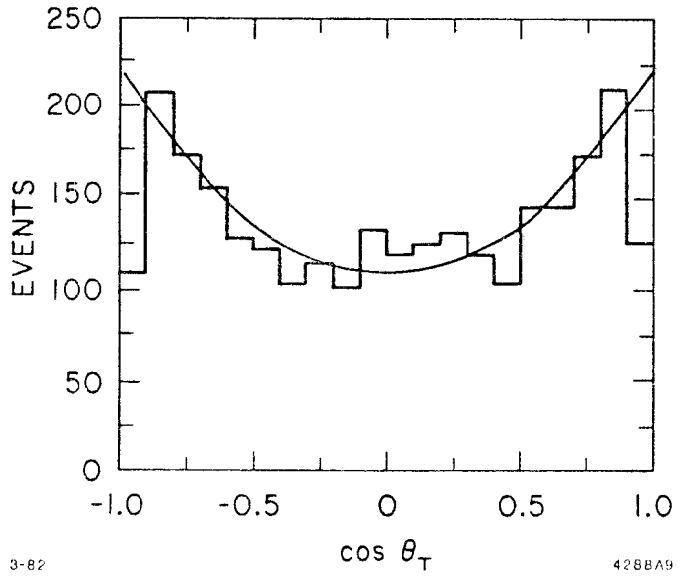


Figure 5

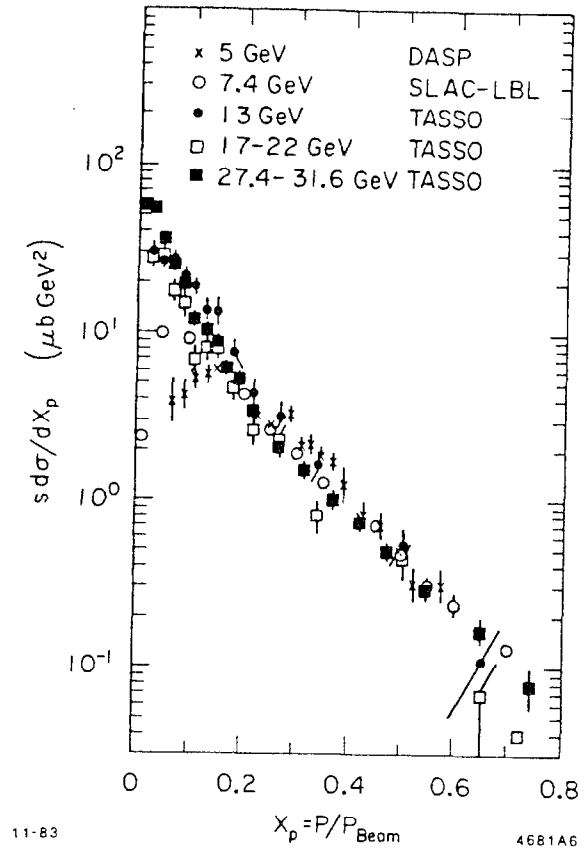


Figure 6

The angular integrals can be done by introducing the variables $p = M \sinh\theta$ and $E = M\cosh\theta$ and we find that the result is of the form

$$\int d^3\lambda \int d\alpha\, e^{i\sqrt{s}\,\alpha} \prod I_i \tag{11}$$

where

$$I_i = \frac{2\pi^2}{i} \frac{M}{(a^2-\lambda^2)^{1/2}} H_1^{(2)}\left[M(a^2-\lambda^2)^{1/2}\right] .$$

Making use of the relation between n and $n-1$ body phase space,

$$E\,\frac{d^3R_n(s)}{dp^3} = \frac{1}{2}\,R_{n-1}(s+m^2-2\sqrt{s}\,E) \tag{12}$$

where each of the final particles is assumed to have mass m, we find that the phase space integrals can be solved in two limits. If the individual particle masses are large compared to the available energy, i.e.,

$$s-(\sum m_i)^2 \ll s \tag{13}$$

we have the nonrelativistic limit to be applied to particle production at low x. This has the form

$$\frac{Ed^3\sigma}{dp^3} \sim e^{-M_x/m} \tag{14}$$

where $M_x^2 = s+m^2-2\sqrt{s}\,E$. At high x where the particle masses are negligible, we have the relativistic limit

$$\frac{Ed^3\sigma}{dp^3} \sim (1-x)^{(2n-6)/2} \tag{15}$$

where $x = 2E_h/\sqrt{s}$.

From Equations (14) and (15) we can see that we expect scaling behavior in this simple model. The slope of $d\sigma/dx$ will be steeper at small x and will be dependent on the masses of the produced particles. At the high x end, the distribution will be determined by the mean multiplicity $\langle n\rangle$ and will scale if $\langle n\rangle$ changes slowly with s. Within statistics, these features are consistent with the data shown in Figure 6. Note that at small x in the figure a correction has to be made for the use of $x_p = p/p_{beam}$.

2.3 How Do We Get Jets?

Despite the fact that the production of two quasi-free quarks seems to explain many of the features of the data, we have still to look closer at the conversion of

these quarks into many hadrons. Up to now we have considered the process of multihadron production as a two-step process as shown in Figure 7. The conversion of the quarks into hadrons was assumed to leave the magnitude of the production cross section unmodified, and the quark axis was found to be preserved in the axis of the jets themselves. The fact that the axis is visible at all, and that jets are seen is actually a consequence of the limited $p_\perp$ behavior of hadronic interactions. The invariant cross section $(Ed^3\sigma)/(dp^3)$ can be rewritten in terms of two new variables: rapidity, defined as

$$y \equiv \frac{1}{2} \ell n \left(\frac{E + p_\parallel}{E + p_\parallel} \right) \quad , \tag{16}$$

and the transverse momentum $p_\perp$ relative to some axis. The relation between these two expressions is just

$$\frac{Ed^3\sigma}{dp^3} = \frac{d^2\sigma}{dy dp_\perp^2} \quad . \tag{17}$$

In hadronic interactions, one usually finds that transverse momenta relative to an incoming quark direction are suppressed so the cross sections have the form

$$\frac{d^2\sigma}{dy dp_\perp^2} \sim e^{-\alpha p_\perp^2} \quad . \tag{18}$$

If we extend this observation to the conversion or fragmentation of the quark into hadrons, we would expect to have to introduce a matrix element

$$|M|^2 = e^{-p_\perp^2/2\sigma_q^2} \quad . \tag{19}.$$

If σ_q is small enough compared to the momenta of the hadrons, this form will result in the preservation of the quark axis in the directions of the final state hadrons. Since there is no modification of the rapidity distribution, we expect this distribution to be flat out to a maximum rapidity y_{MAX} determined by the available energy. Integrating over the inclusive cross section of Equation (17) we also find that the mean multiplicity will be related to y_{MAX} and hence the growth of $\langle n \rangle$ with center-of-mass energy will be just

$$\langle n \rangle \sim y_{MAX} \sim \ell n\, s \quad . \tag{20}$$

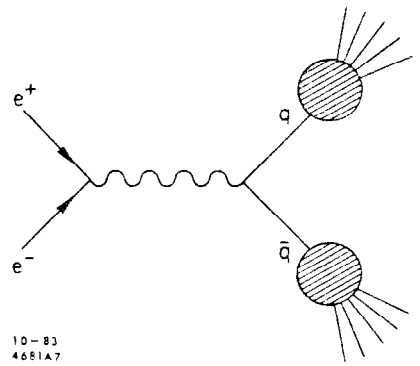


Figure 7

This has the extremely important consequence that since the multiplicity is growing slower than $\sqrt{s}$, the mean energy per particle increases with s. Since the angular deviation of a particle from the quark axis is determined by the ratio between $\langle p_\perp \rangle$ (which is fixed by σ_q) and $\langle E \rangle$, the jets will become more and more collimated and easier to recognize as s increases. The cone angle of the jet will be roughly

$$\delta \sim \frac{\langle p_\perp \rangle}{\langle p_\parallel \rangle} \sim \frac{\ell n\, s}{\sqrt{s}} \quad . \tag{21}$$

Before the advent of machines with available center-of-mass energies in the 30 GeV range, establishing the existence of jet-like behavior required a detailed analysis of the final state structure[4]; however, with present energies, the jets are quite clear. A typical two jet event from the MARK II detector at PEP ($\sqrt{s} = 29$ GeV) is shown in Figure 8.

Figure 9 shows the rapidity distributions as a function of y and $y - y_{MAX}$ for a range of energies. For each energy, there is a wide region where the y distribution is flat, and different energies have similar shapes for the fall off near y_{MAX}. However, there are some problems with our simple picture. First, the cross-section at small y is not the same at all energies indicating that $(d\sigma/dy)|_{y\sim 0}$ is not really constant. While this may not be surprising between 4.8 GeV and 13 GeV due to threshold effects in the production of heavy charmed or bottom mesons, some of the effect remains between 13 GeV and the highest energies. [This effect can be seen in the inset of Figure 9(a).] Second, in the high statistics, high energy data there is perhaps a decrease near $y = o$ which indicates a suppression of production of particles with small $p_\parallel$.

2.4 More Problems with the Simple Two-Jet (Limited $p_\perp$) Picture

Even though the limited $p_\perp$ picture explains the shape of the rapidity and $p_\perp$ distributions reasonably well, we have seen in the last figure that it does not correctly account for the behavior of $d\sigma/dy$ near $y = 0$. This can also be seen by looking at the behavior of the normalization of these curves as a function of center-of-mass energy. If only charged particles are used, (the neutrals have similar behavior) the normalization of $(d^2\sigma)/(dy dp_\perp^2)$ will be the average charged multiplicity $\langle n_{CH} \rangle$. The prediction of the limited $p_\perp$ model was that if σ_q was fixed, this multiplicity would rise like y_{MAX}, namely $\langle n_{CH} \rangle \sim \ell n\, s$. However, from Figure 10 we can see that this is not the case. In the low energy region (1.4 to 7 GeV) the best fit to the data is

$$\langle n_{CH} \rangle = (2.67 \pm 0.04) + (0.48 \pm 0.02)\, \ell n\, s \tag{22}$$

but in the high energy region (7 GeV to 31.6 GeV) this becomes

$$\langle n_{CH} \rangle = (-6.1 \pm 0.4) + (2.79 \pm 0.06)\, \ell n\, s \quad . \tag{23}$$

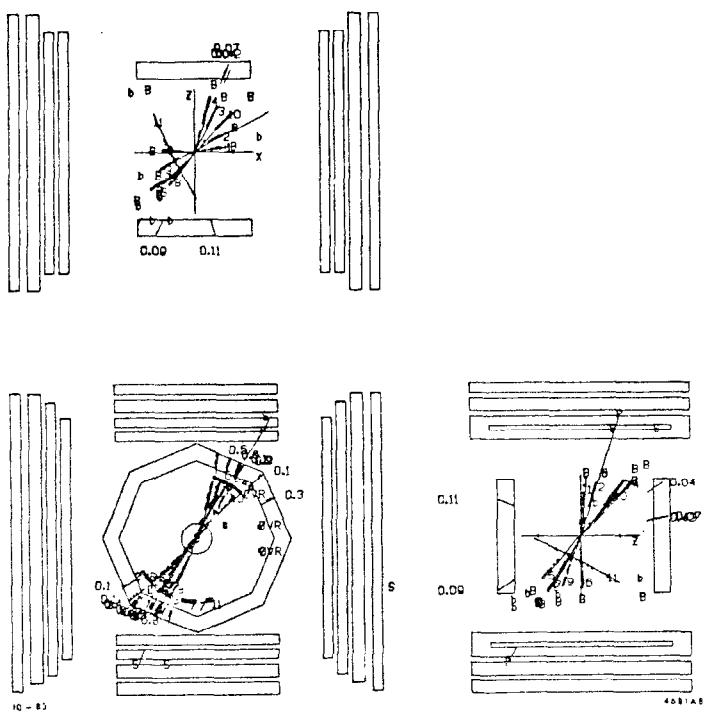


Figure 8

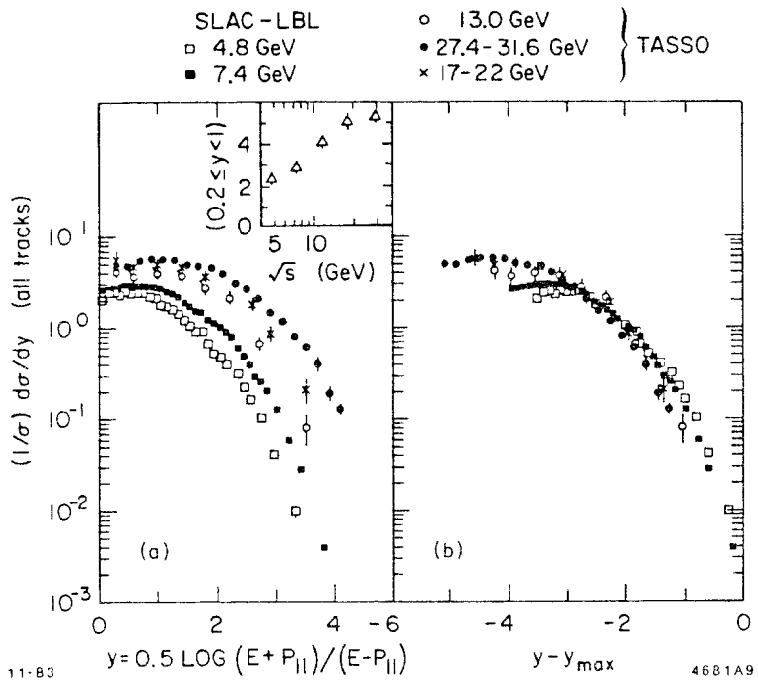


Figure 9

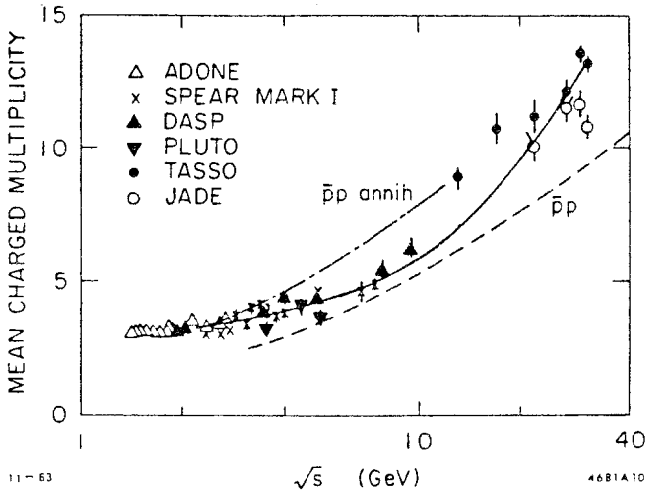


Figure 10

The fit shown in the solid curve[5]

$$\langle n_{CH}\rangle = n_o + a\, exp\left\{b\sqrt{\ell n\,(s/\Lambda^2)}\right\} \tag{24}$$

with $\Lambda = 0.5$ GeV, $n_o = 2.92 \pm 0.04$, $a = 0.0029 \pm 0.0005$ and $b = 2.85 \pm 0.07$, is motivated by QCD or quantum chromodynamics in which three-jet events are expected to contribute to the increase in multiplicity. Simpler forms can also describe the data, of course, and in fact the Fermi statistical model, though it does not predict the two-jet structure of the events, has a variation of $\langle n_{CH}\rangle$ with energy which is

$$\langle n_{CH}\rangle \sim s^{1/4} \tag{25}$$

and is in good agreement with the data. A reasonable fit is also obtained from

$$\langle n_{CH}\rangle = 2. + 0.2\ \ell n\, s + 0.13\ (\ell n\, s)^2 \tag{26}$$

with s in GeV.

The problems with $d\sigma/dy$, the incorrect behavior of $\langle n_{CH}\rangle$ with energy, and tails in the $p_\perp$ distribution (to be discussed later) all lead us to abandon the simplest two-jet picture of hadron events. Additional contributions to the multiplicity and modifications to $d\sigma/dy$ and $d\sigma/p_\perp$ could arise from three-jet production at high energies but we must be careful to add this new process in a way which does not destroy the good agreement which we have found for $R(s)$.

3. Shape Measures

In order to see whether three-jet events or even four-jet events are present in the data, we need to have ways of measuring the hadronic final states and classifying them into two-, three- and four- or more jet samples. One way of doing this is known as the *Momentum Tensor Analysis*[6] and proceeds by finding the eigenvalues of the momentum tensor summed over all particles:

$$M_{\alpha\beta} = \frac{\sum P_{i\alpha} P_{i\beta}}{\sum p_i^2} \qquad \alpha,\ \beta = x,\ y,\ z \tag{27}$$

The solution to the eigenvalue problem for this tensor finds the set of axes which minimizes the relative transverse momentum squared with respect to those axes. The motivation for finding an axis which minimizes $p_\perp^2$ is of course that the limited $p_\perp$ behavior of the quark fragmentation leads us to think that this axis will be a good estimator of the original quark direction. If we order the eigenvalues such that $Q_1 < Q_2 < Q_3$ then the associated eigenvectors $\hat{n}_1$, $\hat{n}_2$, $\hat{n}_3$, of the momentum ellipsoid will be as shown in Figure 11(a). The mean squared momenta relative to the shortest axis is

$$\frac{\langle P_{out}^2\rangle}{\langle P^2\rangle} \equiv \frac{\sum (\underline{p}\cdot\hat{n}_1)^2}{\sum p^2} = Q_1 \tag{28}$$

Similarly for the axis $\hat{n}_2$ we define

$$\frac{\langle P_{in}^2\rangle}{\langle P^2\rangle} = Q_2 \tag{29}$$

For our model of hadron production, we expect that most events will originate from two quarks fragmenting in oppositely directed cones as shown in Figure 11(b). In this case, the eigenvalues Q_1 and Q_2 should be approximately equal, and if the energy is high enough for the mean transverse momentum to be small compared to the mean particle energy, Q_1 will be much less than Q_3. Events with three jets will originate from three partons whose vectors lie in a plane. On average, this plane will be normal to the eigenvector $\hat{n}_1$ if again σ_q is small enough compared to the mean particle energy. In fact, if we assume that the three partons fragment in these events in a way which is similar to two-jet fragmentation, then we would find Q_1 unchanged in three-jet events, but Q_2 somewhat larger.

If there are many jets in an event, or if the energy is low, the event will look spherical, i.e.,

$$Q_1 \sim Q_2 \sim Q_3 = \frac{1}{3} \tag{30}$$

A convenient variable to use for testing for this condition is ***sphericity*** defined as

$$S = \frac{3}{2}(1 - Q_3) = \frac{3}{2}\,\frac{\langle P_{out}^2\rangle + \langle P_{in}^2\rangle}{\langle p^2\rangle} \tag{31}$$

(This was actually one of the original variables used at low energy to establish the existence of two-jet events.) Spherical events will have $S = 1$ and jetty events will have small sphericities. Similarly, we can define ***aplanarity*** in terms of the smallest eigenvalue (which should be the same for two-jet and planar three-jets)

$$A = \frac{3}{2} Q_1 \tag{32}$$

and since this is insensitive to three-jet events and sensitive only to distributions out of the plane normal to $\hat{n}_1$, we can use it to look for heavy particle production or four and more jet events.

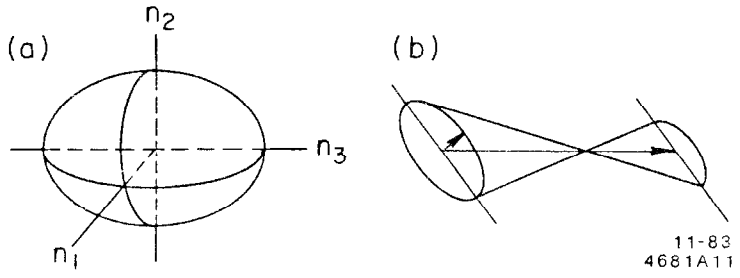


Figure 11

3.1 Linear Shape Variables

There is one major problem in principle with the momentum tensor approach to finding parton directions. Since the eigenvalue problem minimizes the transverse momentum of particles relative to the axes in a least squares sense, the axes and eigenvalues are nonlinear functions of the particle momenta. This makes the theoretical calculation of, for example, the sphericity distribution a difficult task. Worse, however, is the fact that this nonlinearity makes the method sensitive to the details of the quark fragmentation. As an example of this, since $p_\perp^2$ is minimized, if we paired all particles and reminimized using the resultant vectors of these pairs, we would find different eigenvectors. Thus if quarks fragmented a significant fraction of the time into ρ mesons which then decayed into π pairs, this would modify the momentum tensor quantities.

One solution to this dilemma is to linearize the problem. Thus we can define a new axis $\hat{n}_3$ called the thrust axis which maximizes the linear sum of projected momenta along $\hat{n}_3$. A similar extension for the other two axes yields the "eigenvalues"

$$\text{THRUST} \qquad T = \frac{\text{MAX} \sum |p \cdot \hat{n}_3|}{\sum |p|} \tag{33}$$

and

$$\text{MAJOR AXIS} \qquad M_2 = \frac{\text{MAX} \sum |p \cdot \hat{n}_2|}{\sum |p|}$$

where $\hat{n}_2$ is required to be perpendicular to $\hat{n}_3$. The minor axis is defined as the axis perpendicular to the thrust and major axes:

$$\text{MINOR AXIS} \qquad M_1 = \frac{\sum |p \cdot \hat{n}_1|}{\sum |p|} \quad . \tag{34}$$

Deviations from the two-jet hypothesis can be seen by the analog of comparing Q_1 and Q_2 in the momentum tensor analysis. Thus we define the *oblateness* as

$$O = M_2 - M_1 \quad . \tag{35}$$

The analog of sphericity in the linear analysis is *spherocity*[7], defined as

$$S' = \frac{16}{\pi^2} \left[\frac{\sum |p_\perp|}{\sum |p|} \right]^2 \tag{36}$$

and the analog of aplanarity is *acoplanarity*,[8]

$$\mathcal{A} = 4M_1^2 \quad . \tag{37}$$

Triplicity is the sum of the momenta projected along the three axes and approaches one for a perfect three-jet event. When studying the details of three-jet events, it is convenient to look for three axes which minimize the linear sums of transverse momenta with the additional requirement that the three axes must lie in a plane. In this case, the *trijetiness*[9] is defined to be a measure of how well the event conforms to the hypothesis of three planar jets.

As a further extension of these shape measures, standard clustering techniques from numerical analysis can be applied to determine the number of jets in an event. In most previous measures, an assumption has to be made about the number of jets and then tested. If clustering algorithms are used however, criteria can be made for a cluster to be considered a jet, and low energy clusters or other clusters which do not meet these requirements can be removed and/or merged with other clusters. To associate particle groups into clusters requires a metric in momentum and/or position space which defines the "distance" in a clustering sense between any two particles. The easiest way to group the particles is then to use MIN/MAX techniques which start clusters using particles separated by greater than MAX while merging into a cluster all other particles closer than MIN.

While clustering techniques are attractive because they make no *a priori* assumptions about the number of jets, care must be taken in interpreting the results since some metrics are linear and some are not. Nonlinear metrics will have problems with fragmentation similar to those discussed before. In addition to nonlinearities, there may be complicated procedures for merging clusters or associating clusters with jets. However, one of the major strengths of the clustering technique lies in this flexibility since the algorithm can be adjusted and optimized for a particular analysis task using a detailed model or Monte Carlo.[10]

3.2 Energy Dependence of Shape Measures

We now return to the simple model in which the rapidity distribution is flat and the $p_\perp$ is fixed. Since the mean multiplicity is proportional to $\ell n\, s$, the mean momentum is $\langle p \rangle \sim \sqrt{s}\,/\ell n\, s$, and the variation of sphericity with energy will be approximately

$$S = \frac{3}{2}\,\frac{\langle p_\perp^2 \rangle}{\langle p^2 \rangle} \sim \frac{\langle n \rangle^2}{s}\,\langle p_\perp^2 \rangle \sim \frac{(\ell n\, s)^2}{s} \quad . \tag{38}$$

The data[11] are shown in Figure 12 as a function of $\sqrt{s}$, and **do not** fall as sharply as Equation (38) over the whole range.

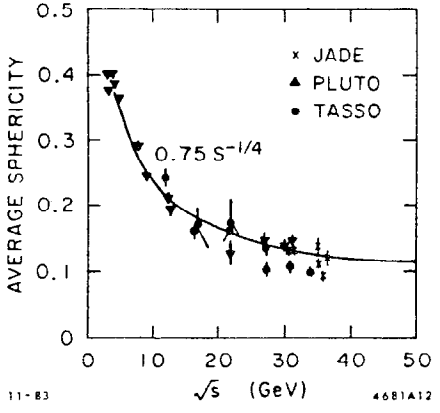


Figure 12

Since the sphericity is related to the eigenvalues Q_1, Q_2, Q_3 by

$$S = 3/2(1 - Q_3) \quad , \tag{39}$$

if we make the assumption that Q_1 and Q_2 are equal and use the fact that

$$Q_1 + Q_2 + Q_3 = 1 \tag{40}$$

we can determine both Q_1 (the shortest axis of the ellipsoid of the average event) and Q_3 (the long axis) for each value of sphericity. The ratio gives the eccentricity of the ellipse

$$\frac{Q_3}{Q_1} = \frac{1 - \frac{2}{3}S}{\frac{1}{3}S} \quad . \tag{41}$$

Table 2 shows this ratio evaluated at low, medium and high energy and illustrates that even though the sphericity does not decrease as rapidly as Equation (38), the events have become much more jet-like at high energies. Figure 13 shows the changes in the distributions for sphericity and aplanarity.[12]

Table 2

Variation of the Maximum to Minimum Axis Ratio with Energy

$\sqrt{s}$	Sphericity	Q_3/Q_1
4	0.4	5.6
10	0.24	10.5
40	0.12	23.0

3.3 Evidence for More Than Two-Jets

The large ratio Q_3/Q_1 makes it rather easy to believe in two-jets at high energy, but as we have seen, the simplest model predicts a too rapid fall off of the sphericity, does not predict the growth of the central region $\{d\sigma/dy\}|_{y\approx 0}$, and does not predict the rapid rise in multiplicity. The most striking evidence that more jets are required, however, comes from looking directly at the $p_\perp$ distributions. Figure 14 compares the normalized distribution of the square of the transverse momentum for charged particles relative to the event axis at low and high energies.[13] While the behavior at low $p_\perp^2$ is similar, there is a substantial change at high $p_\perp^2$. In order to distinguish between an increase in $p_\perp^2$ due to an energy dependent σ_q and the production of planar three-jet events, we compare the behavior of the distributions of the eigenvalues Q_1 and Q_2.

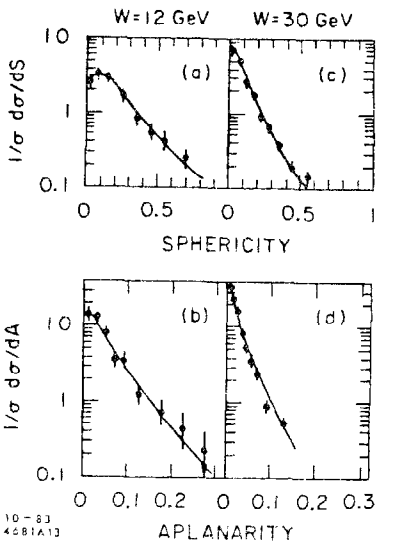


Figure 13

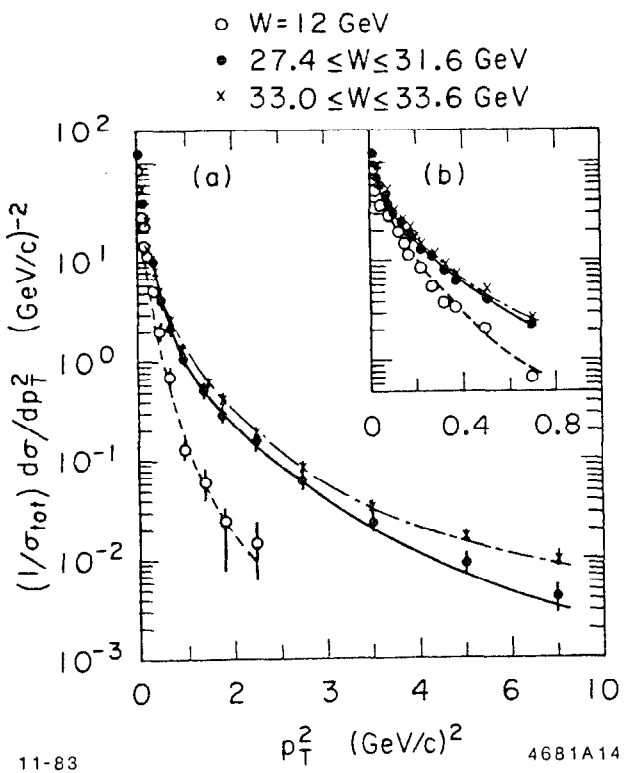


Figure 14

If the change was due to an increase in σ_q, then the events would be faster ellipsoids but with Q_1 still approximately equal to Q_2 The data, however, indicate that the energy behavior of these two quantities is quite different. Figure 15 shows that almost all of the increase in $p_\perp^2$ is coming from an increase in $p_\perp$ **in the plane** of the event.

The curves in Figure 15(a) and (b) indicate the effect of increasing σ_q from 300 MeV/c to 450 MeV/c. While such a modification would be consistent within statistics for the behavior of P_{in}, it fails to describe the long tail in P_{out} at high energy. Figure 15(e) and (d) indicate the quality of the agreement within a model which has a fixed σ_q but a small admixture of planar events at high energy.[13]

4. The Third Jet

We would now like to add a third jet, but in doing so we must be careful not to disturb the basic perturbative picture we have been using which explains the total cross section in terms of quark pair production. If three jet production proceeds through a process like that shown in Figure 16, the coupling constant at the new vertex must be small. A natural candidate for the parton which gives rise to the third jet is the same object which mediates the strong force between quarks. This "gluon", so named because it forms the glue which gives rise to strong binding, must in our case have a coupling constant much less than one.

A consistent picture of these interactions exists in the theory of quantum chromodynamics, which allows the strong interaction to be treated perturbatively in some cases. The coupling constant, α_s, is not constant, but decreases with increasing Q^2. The variation of the coupling constant is given by

$$\alpha_s = \frac{12}{11N_c - 2N_f} \frac{1}{\ell n\, s/\Lambda^2} \tag{42}$$

where N_f is the number of flavors of quarks (u, d, s ...) whose masses are small compared to $\sqrt{Q^2}/2$ and N_c is the number of colors. The constant Λ determines the rate of variation of α_s. It is important to note that α_s and Λ are **not** independent parameters. As shown below, given α_s at a particular Q^2, one can solve for Λ and determine α_s at all Q^2's.

Coupling constants which vary with Q^2 are present even in QED where the sum of the two diagrams shown in Figure 17(a) renormalizes the QED coupling constant α to

$$\alpha(Q^2) = \alpha(\mu_0^2)\left[1 + \frac{\alpha(\mu_0^2)}{3\pi}\, \ell n\, \frac{Q^2}{\mu_0^2}\right] \quad . \tag{43}$$

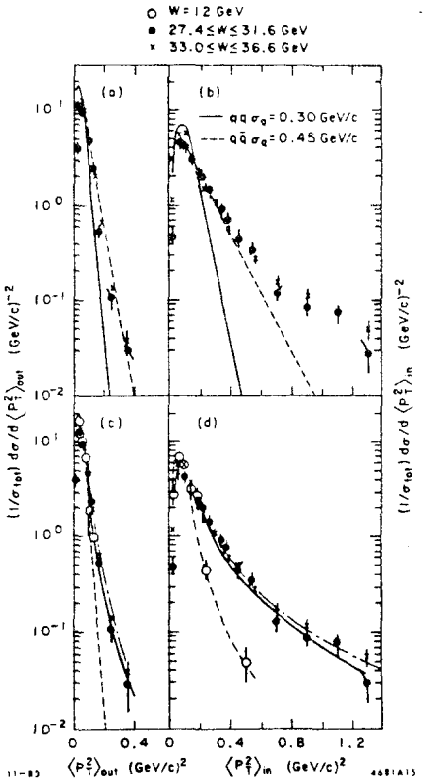


Figure 15

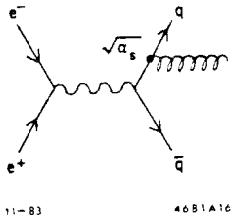


Figure 16

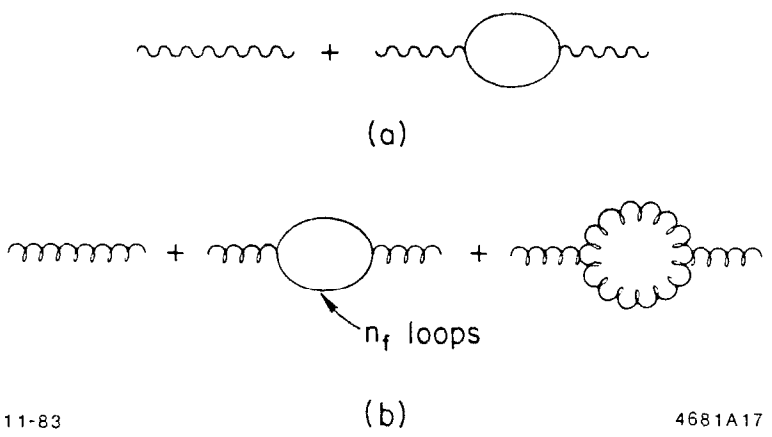


Figure 17

In this case the coupling constant **increases** with Q^2 and since $\alpha(\mu_0^2)$ is very small, the variation is quite small.* A similar analysis in QCD can be carried out provided the lowest order perturbation diagrams are all that need to be summed. In this case, a new diagram enters [see Figure 17(b)] because QCD is a non-Abelian theory so the gluons carry "color" charge and can couple to themselves (just as a photon couples to any charge carrier in QED). The calculation for the diagrams in Figure 17(b) yields a variation of $\alpha_s(Q^2)$ with Q^2 (using $N_c = 3$) given by

$$\alpha_s(Q^2) \sim \alpha_s(\mu_0^2)\left[1 + \frac{\alpha_s(\mu_0^2}{12\pi}\,(2N_f - 33)\,\ell n\,\frac{Q^2}{\mu_0^2}\right] \tag{44}$$

which decreases with Q^2 provided $2N_f$ is less than 33. If Q^2 is sufficiently high, we expect α_s to be small enough for the perturbative calculation to be valid. This property — called asymptotic freedom — is crucial in this application, since without it, we would have no reason to believe that the addition of gluons would not make large changes in the behavior of $R(s)$. In this connection, it is important to keep in mind that the negative term in Equation (44) comes directly from the non-Abelian coupling (gluon self-coupling) diagrams.

The strong coupling constant variation is sometimes expressed in first order QCD as

$$\alpha_s(Q^2) = \frac{12\pi}{11N_c - 2N_f}\left[\ell n\,\frac{Q^2}{\Lambda^2}\right]^{-1} \quad . \tag{45}$$

But note that if $\alpha_s(Q_0^2)$ is known at some Q_0^2, then given N_c and N_f, we know α_s at all Q^2, thus we can solve for the first order Λ parameter. Using Equations (44) and (45) we find

$$\Lambda^2 = Q_0^2\, e^{-b/\alpha_s(Q_0^2)} \tag{46}$$

where

$$b = \frac{12\pi}{11N_c - 2N_f} \quad .$$

In principle, one need never refer to Λ, however, since Equation (44) is just

$$\frac{\alpha_s(Q_0^2)}{\alpha_s(Q^2)} = \left[\frac{\alpha_s(Q_0^2)}{b}\;\ell n\,\frac{Q^2}{Q_0^2} + 1\right] \quad . \tag{47}$$

*For the interested reader, it is amusing to calculate the coupling constant α at the mass of the Z, which will convince you that even in QED the effect is important.

4.1 QCD AND OTHER MODIFICATIONS TO R

Within the framework of QCD, diagrams like that of Figure 16 can be included in the calculation of $R(s)$. The result will be of the form

$$R = 3 \sum e_q^2 \left\{ 1 + C_1 \frac{\alpha_s}{\pi} + C_2 \left(\frac{\alpha_s}{\pi} \right)^2 + \ldots \right\} \quad . \tag{48}$$

The coefficient C_1 is found to be 1 and the coefficient C_2 depends on the renormalization scheme used for the second order calculation.[14] Within the $\overline{MS}$ (minimal subtraction) scheme, the value of C_2 is

$$C_2 = 1.99 - 0.12\ N_f \quad . \tag{49}$$

Since these coefficients are reasonable small, and since as we see later, α_s is somewhere between 0.1 and 0.2, we have succeeded in adding the physics of three-jets without making too large a modification of R. In fact, we have done so well that the QCD modification is small compared to the experimental systematic errors! Table 3 shows recent measurements of R by a number of experimental groups. The weighted average value of R for data taken above 29 GeV is 3.95 ± 0.08 which yields a value for α_s between 0.27 and 0.16.

Table 3

Experimental Measurements of R						
Experiment	$\sqrt{s}$ GeV	R	±	ΔR_{STAT}	±	ΔR_{SYST}
MARK J	12–36.7	3.84	±	0.05	±	0.22
TASSO	14–36.7	4.01	±	0.03	±	0.20
MARKII	29	3.90	±	0.05	±	0.25
MAC	29	3.93	±	0.04	±	0.20
JADE	30–36.7	3.93	±	0.03	±	0.09
TASSO	30–36.7	4.05	±	0.03	±	0.19

If we were to use a different second order subtraction scheme, for example the momentum space scheme where

$$C_2 = -2.19 + 0.16\ N_f \quad , \tag{50}$$

the same experimental measurements would yield α_s values between 0.39 and 0.19. Unfortunately we must conclude from this that present experimental and theoretical uncertainties are too large to **determine** α_s from these measurements. Present experimental errors are also too large to see the expected variation in R (~ 0.03) over the range of available energies.

Even without these problems, there are additional things to consider before converting the measured value of R directly into a value of α_s using Equation (48). The first order QCD correction is approximately seven percent, weak interactions will contribute on the order of three percent corrections at these energies, QED radiative corrections are uncertain to an order of two percent, the variation of α_s with Q^2 is a one percent effect, and finally quark mass effects modify the value of R according to[15]

$$R = \frac{3}{2}\ \beta(3-\beta^2)\ e_Q^2 \left\{ 1 + \frac{4}{3}\ \alpha_s F(\beta) \right\} \tag{51}$$

where

$$F(\beta) = \frac{\pi}{2\beta} - \frac{3+\beta}{4} \left(\frac{\pi}{2} - \frac{3}{4\pi} \right) \quad .$$

While these factors are small near 29 GeV ($\sim 0.1\%$), they are not negligible near 10 GeV. Other effects may also be important in the 10 GeV range. We know for example that the cross section exhibits considerable structure above the $c\bar{c}$ resonances and this may also be true above the $b\bar{b}$ family.

4.2 BACK TO THREE-JETS

Assuming that we can isolate a sample of three-jet events and in some way measure the individual jet properties, let us see what we can learn about α_s and QCD. If the three jets have fractional energies $x_i = E_i/E_b$, and the angle between the gluon and one of the quarks is θ, as shown in Figure 18, at the parton level, the differential cross section will be

$$\frac{d^2\sigma\,(3\,jet)}{dx_1\,dx_2} = \frac{2\alpha_s}{3\pi}\ \sigma\,(2\,jet)\ \frac{x_1^2 + x_2^2}{(1-x_1)(1-x_2)} \tag{52}$$

where $x_1 + x_2 + x_3 = 2$.

Given the rough value of α_s determined before, we can see that roughly five to ten percent of the events should be planar three-jet events. The exact number will depend on the minimum gluon energy and angle with respect to a quark which gives an observable third jet. Obviously as $k = 2 - x_1 - x_2$ becomes small or as θ approaches zero, the event looks more and more like a two-jet event. In fact there is no clear dividing line between the two classes of events. In a way which is reminiscent of the soft photon problem in QED, some $q\bar{q}$ (soft glue) events are indistinguishable from 2 JETS and belong in the calculation of that cross section.

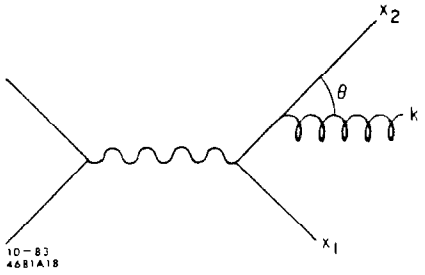


Figure 18

Experimentally, it is convenient to look for three-jets only in those events with a thrust [$T = \text{MAX}(x_1, x_2, x_3)$] of less than some maximum value, typically 0.9. That this does not completely cure the problem of ambiguities about whether the event has two or three jets is shown in Figure 19. A sample of three-jet events has been generated for $T_{\text{MAX}} = 0.95$. All other events are considered to have two-jet kinematics. At the parton level (solid curves) it is quite clear that there are a well-defined number of events with thrust less than 0.95 and hence a well-defined "3 JETS cross section." However, when we consider the effect of fragmentation on the two-jet cross section, it is clear that some of these events, when measured, will have thrust less than 0.95 and appear to be like three-jet events in that respect. As can be seen from the dotted curves in Figure 19, the tail of the two-jet distribution at small thrust is almost as large as the parton level three-jet contribution. Before we can use the thrust distribution to test QCD, we must be quite certain about the tail of the two-jet contributions.

4.3 GLUON SPIN

In discussing two jet events in e^+e^- annihilation, we found that the angular distribution of the jet (thrust) axis reflected the fact that the spin of the quarks was 1/2. We can apply the same principle to the three-jet case to determine the spin of the third jet. Experimentally it is easier to determine the axis of a jet than its total energy. Using energy and momentum conservation, the fractional energies of the three jets can be deduced from their relative angles using

$$x_i = \frac{2\sin\theta_i}{\sin\theta_1 + \sin\theta_2 + \sin\theta_3} \quad . \tag{53}$$

The angular distributions of the jets relative to each other are determined by the spin of the jets; thus if the gluon (jet number 3) is a vector particle, the differential cross section is given by Equation (52) namely

$$\text{Vector gluon}: \quad \frac{d^2\sigma}{dx_1\,dx_2} = \frac{2\alpha_s}{3\pi}\,\sigma_0 \left\{ \frac{x_1^2 + x_2^2}{(1-x_1)(1-x_2)} + \begin{matrix} 1,\,2,\,3 \\ \text{cyclic} \\ \text{permutations} \end{matrix} \right\} . \tag{54}$$

For scalar gluons, the angular distributions are given by

$$\text{Scalar gluon}: \quad \frac{d^2\sigma}{dx_1\,dx_2} = \frac{\tilde{\alpha}_s}{3\pi}\,\sigma_0 \left\{ \frac{x_3^2}{(1-x_1)(1-x_2)} + \begin{matrix} \text{cyclic} \\ \text{permutations} \end{matrix} \right\} \tag{55}$$

where $\tilde{\alpha}_s$ is some effective coupling constant for the scalar theory. Following the method of Ellis and Karliner,[16] the angular distributions can be simplified by looking for the angular distribution of x_2 and x_3 in the rest frame of x_1 as shown in Figure 20. The angle $\tilde{\theta}$ can be determined from the measured jet axes using

$$\cos\tilde{\theta} = \frac{x_2 - x_3}{x_1} = \frac{\sin\theta_2 - \sin\theta_3}{\sin\theta_1} \quad . \tag{56}$$

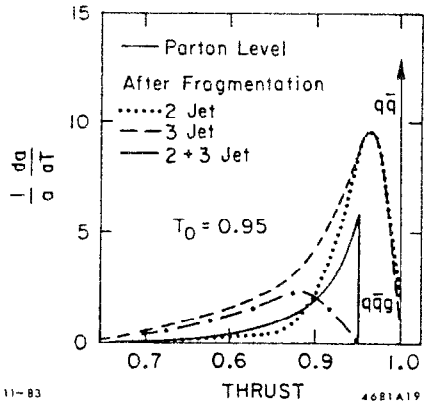


Figure 19

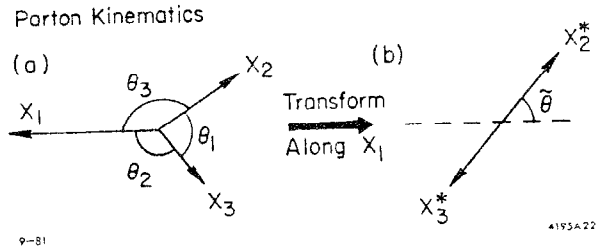


Figure 20

The experimental data from the TASSO detector for energies above 25 GeV and event thrust (x_1) less than 0.9 is shown in Figure 21 and rules out the scalar hypothesis.

4.4 Determining α_s from the Ratio of Jet Cross Sections

Naively, one would expect that Equation (52) would allow one to measure α_s from the ratio of jet cross sections since

$$\frac{\sigma_{3\,\mathrm{JET}}}{\sigma_{2\,\mathrm{JET}}} \sim \alpha_s \qquad \text{and} \qquad \frac{\sigma_{4\,\mathrm{JET}}}{\sigma_{3\,\mathrm{JET}}} \sim \alpha_s \qquad \cdots$$

Of course, the gluon must have some minimum energy to be observable and since the energy spectrum for the gluons will be a bremsstrahlung spectrum

$$\frac{d\sigma}{dE\,d\theta} \sim \frac{\alpha_s}{k\theta} \quad , \tag{57}$$

we need to define a minimum angle θ_{MIN} and energy k_{MIN} above which events will be called three-jet events. Remember, however, that as Q^2 becomes small, α_s becomes larger. For soft and/or collinear gluons, the theory becomes nonperturbative and we do not know the form which corresponds to Equation (57). As shown in Figure 22, this means that we do not know the form of the cross section below θ_{MIN}. The total two-jet and three-jet cross sections are thus given by

$$\begin{aligned} \sigma_{2\,\mathrm{JET}} &\equiv \sigma_2 + \int_0^{E_{\mathrm{MIN}}} \int^{\theta_{\mathrm{MIN}}} \frac{d^2\sigma_3}{dE\,d\theta} \\ \sigma_{3\,\mathrm{JET}} &\equiv \int_{\theta_{\mathrm{MIN}}} \int_{E_{\mathrm{MIN}}} \frac{d^2\sigma_3}{dE\,d\theta} \quad . \end{aligned} \tag{58}$$

Note that at the parton level, the two-jet cross section consists of two parts, the second of which we do not know how to evaluate.

Unfortunately, there is a second complication which comes from the fact that experiments do not see partons (quarks and gluons) directly, but see the hadrons which result from their fragmentation. If we start with an event which at the parton level has two-jets, then each of these jets will result in hadrons spread over some angular range as shown in Figure 23(a), both due to the finite resolution of the detection apparatus and the fragmentation process itself. As a result [Figure 23(b)], some of these events will result in configurations which have energy greater than E_{MIN} and angles greater than θ_{MIN}. The **detected** three-jet cross section is now

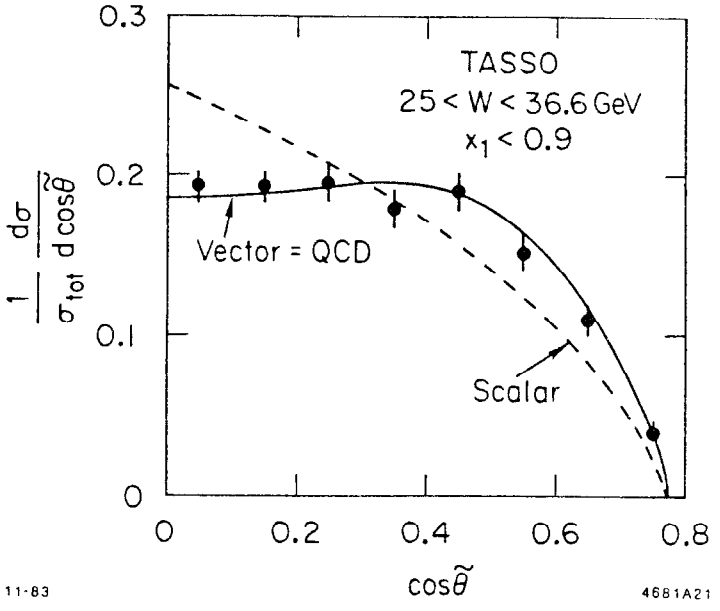


Figure 21

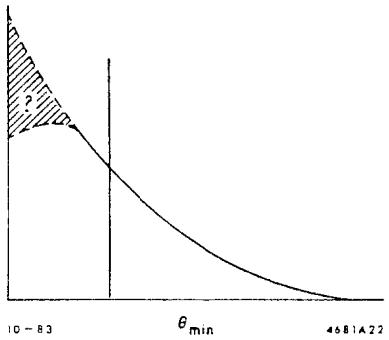


Figure 22

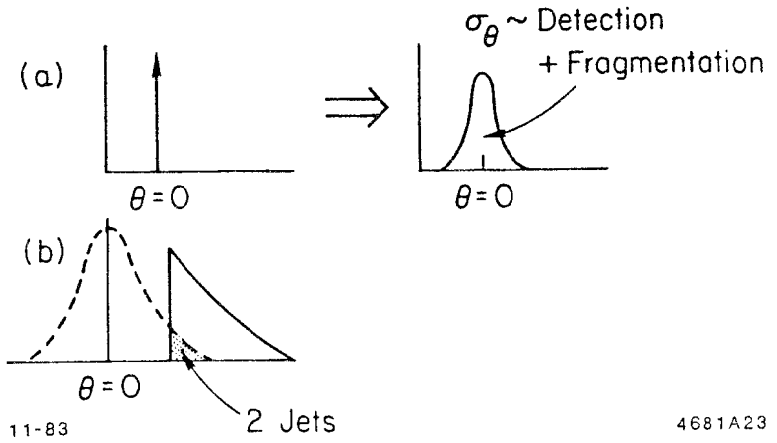


Figure 23

$$\sigma_{3\,\mathrm{JET\ DETECTED}} = (1-\epsilon)\,\sigma_{3\,\mathrm{JET}} + 2\ \mathrm{JET\ TAIL}$$

where ϵ is the fraction of three-jet events which as a result of detector resolution and fragmentation are detected as two-jet events even though at the parton level they might have satisfied the three-jet cuts for E_{MIN} and θ_{MIN}. One of the goals of the experimentalist is of course to design cuts which minimize these problems. This has to be done with the aid of a detailed model of the detector and the fragmentation process. One can typically reduce the contribution of two-parton events which are present in a three-jet sample so that if the efficiency for three-jet detection is such that approximately ten percent of the events are classified as three-jet events, the 2 JET contamination is approximately one percent of the total or ten percent of the 3 JET sample. This is sufficient to get a relatively clean sample of three-jet events for studying particle composition, angular distributions, et cetera. Different models of the fragmentation process, however, disagree about the magnitude of the second term in the two-jet cross section [Equation (58)] and so as yet we cannot use the jet cross section ratios to determine α_s precisely.

5. We Need a Fragmentation Model

It is clear from the preceding discussion that we need a rather detailed fragmentation model to use in extracting information from the data about QCD. Since these models are attempting to parameterize or describe the soft part of QCD which cannot be handled perturbatively, they are somewhat arbitrary. After discussing the more common models, we will return to look at the data and see how we can use the data to constrain the models.

There are at present three major classes of fragmentation models, each of which have been implemented in large Monte Carlo simulation programs for use in e^+e^- annihilation. The *Independent Fragmentation Model* considers the fragmentation process to be independent of the parton production process. In addition each parton fragments independently of the others. Hence quantum number conservation often has to be added in a somewhat *ad hoc* manner. The Hoyer, Ali and Feynman-Field Monte Carlos are all of this type. Figure 24(a) shows an example of this type of process; the fragmentation process may or may not be different for gluons and quarks. *String Models*, studied extensively by the Lund group, are based on the analogy between strong QCD and $1+1D$ QED. The fragmentation process results from $q\bar{q}$ production at breaks in a string (or color flux tube) extending between the partons [Figure 24(b)]. Thus fragmentation within three-parton events may be different from

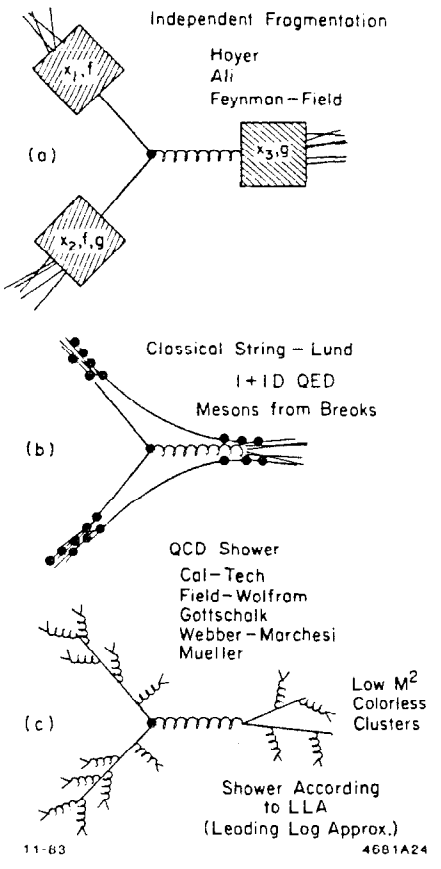


Figure 24

that in two-parton events, and the partons do not fragment independently. Finally, QCD shower Monte Carlos (Field-Wolfram, Gottschalk, Webber-Marchesi, Mueller) generate soft hadronization using a cascade approach which attempts to generate a shower of partons using leading log QCD approximations at each step in the shower [Figure 24(c)].

Each Monte Carlo must first decide how many partons to produce using first or second order QCD matrix elements or possibly leading log approximations. These partons must then be converted into hadrons with an independent/string/shower algorithm which accounts for quantum number conservation. These primary hadrons must then decay into secondary hadrons whenever they are unstable. In some cases these decays are quite straightforward, the angular distributions and branching ratios being taken from Particle Data Group compilations. In other cases, such as the decays of heavy mesons (B, B^*, $F\ldots$) or charmed baryons, the branching ratios can vary from model to model. To complicate the situation further, many groups replace the "standard" decay routines with their own favorite secondary decays and branching ratios! Finally, the response of the detector to the resulting mesons and baryons must be simulated along with the effect of analysis and physics cuts.

5.1 Independent Fragmentation Model

The fragmentation of a quark (or gluon) in this model is defined primarily by the splitting function $f(z)$ which determines the probability that a quark emits a hadron with fractional energy z. As shown in Figure 25, if the original quark has four-momentum, $\mathbb{P}$ then each splitting results in a hadron with four-momentum $z\,\mathbb{P}$ and a residual quark with $(1-z)\,\mathbb{P}$. The earliest form of the splitting function used in these models was

$$f(z) = 1 - a_F + 3a_F(1-z)^2 \tag{59}$$

where

$$z = \frac{(p_{\|} + E)_h}{(p_{\|} + E)_q} \quad .$$

Successive applications of this simple splitting function lead to the final jet, and one can see that the inclusive momentum spectrum of **primary** hadrons is completely determined by $f(z)$. Corrections for secondary decays of course have to be made when comparing to observed distributions. It is an interesting exercise to show that without

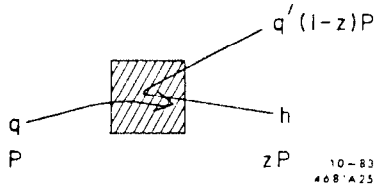


Figure 25

secondary decays, the successive application of $f(z)$ results in an integral equation for the resultant hadron spectrum which is just

$$D(z) = f(z) + \int_z^1 \frac{dz'}{z'} f(1-z') D\left(\frac{z}{z'}\right) \tag{60}$$

where the second term is the feed-down contribution. Furthermore, it is possible to show that

$$D(z) = \frac{f(z)}{z}$$

is a solution for all $f(z)$ of the form

$$f(z) = (m+1)(1-z)^m \quad . \tag{61}$$

The important point to remember is that the hadron spectrum D(z) is an important constraint on the form of f(z).

As we discussed before, the behavior of the hadronic events is characterized by severly limited transverse momentum. This is incorporated into the model by introducing a $q_\perp$ for the hadron relative to the quark axis in each splitting. The probability distribution is given by

$$\frac{dN}{dq_\perp^2} \sim e^{-q_\perp^2/2\sigma_q} \tag{62}$$

with the $q_\perp$ of the hadron being balanced at each splitting by the $q_\perp$ of the recoil quark q' as shown in Figure 26. The spin of the produced hadron is determined at each branching by the ratio of vector (ρ, K^*, ...) to pseudoscalar (π, K, ...) production via the internal parameter

$$\frac{P}{P+V} \quad .$$

The final state multiplicity is very sensitive to this parameter because of the difference between vector and pseudoscalar meson masses and decay multiplicities.

Looking at the branching process in more detail, we can see that the type of hadron produced will depend on the initial quark and the choice of final quark q' as in Figure 27. The meson production results from a series of $q\bar{q}$ pair productions. The type of pair produced is chosen with

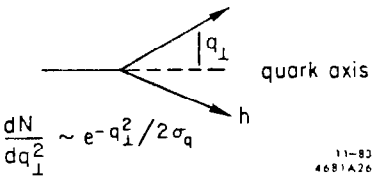


Figure 26

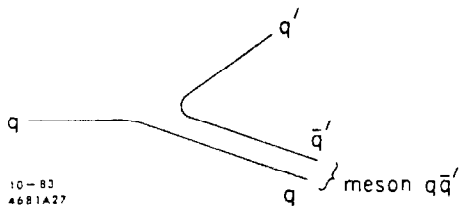


Figure 27

$$u\bar{u} : d\bar{d} : s\bar{s} = a : a : b \tag{63}$$

with $b < a$ to account for the phase space suppression due to the heavier s quark mass. The a/b ratio will determine the $\rho : K^*$ ratio as well as the $\pi : K$ ratio in the final state. As shown in Figure 28, if one starts from a two-parton state, the primary $q\bar{q}$ pair will be $u : c : d : s : b = 4 : 4 : 1 : 1 : 1$. Charmed or bottom mesons or baryons are expected to contain the primary quark, and one pair joins the last q' of the q fragmentation with the last $\bar{q}'$ of the $\bar{q}$ fragmentation.

In principle, the fragmentation of a gluon can be described by a similar process, but first we need to convert each gluon into a quark-antiquark pair. In the Hoyer Monte Carlo, all of the momentum of the gluon is carried by one of these quarks. As a result, gluon fragmentation is indistinguishable from quark fragmentation. In the Ali model, the gluon is split into a quark pair using the Altarelli-Parisi splitting function for gluons:

$$f_g(z) = z^2 + (1-z)^2 \quad . \tag{64}$$

As discussed before for quark jets, $f(z)$ will determine the momentum spectrum of hadrons within the gluon jet.

In the case of heavy meson production, the heavy quark tends to carry away a large fraction of the momentum. Thus the fragmentation function will tend to peak more strongly for heavier quarks. In addition, if heavy quark pair production is strongly suppressed, the heavy meson will always contain the primary quark and hence there will be no feed-down contribution as in Equation (60). The form of the fragmentation function used is

$$D(z) = \frac{k}{z\left(1 - \frac{1}{z} - \frac{\epsilon}{1-z}\right)^2} \quad . \tag{65}$$

The heavier the quark, the smaller the value of ϵ. The constants can be determined from measurements of inclusive D and B meson production.

Baryon production does not fit easily into branching processes of the type shown in Figures 27 and 28, and must be put in phenomenologically. The observed proton fractions in the final states can be roughly explained if there is a probability of order ten percent of producing a diquark-antidiquark pair at each branching in addition to the process in Equation (63). If this is indeed the production mechanism for baryons, we might expect significant $p_\perp$ correlations between baryon pairs[17] and we would also expect baryons to be correlated in rapidity and probably that baryon-antibaryon pairs would tend to lie in the same jet due to local compensation of baryon number.

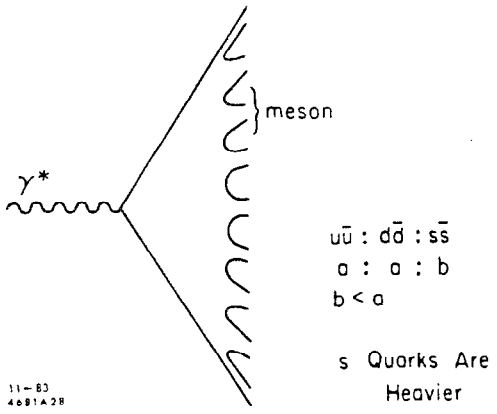


Figure 28

Most of the independent fragmentation models have now been modified to include diagrams arising from higher order corrections in QCD. Figure 29 shows the type of diagrams considered. The earliest Hoyer and Ali models included only diagrams up to order α_s with two and three jets. Subsequent versions of the Ali model included the order α_s^2–four-jet contributions, but did not include virtual corrections to the three-jet processes. The reason the latter processes are difficult to include is that the virtual three-jet corrections cancel divergences in the four-jet processes when one of the four-jets becomes soft. In order to do this properly, one must have a criterion for deciding when a four-jet event contains a parton which is soft enough to make it look like a three-jet event. An event which looks like Figure 30(a) could arise from a diagram like that shown in Figure 30(b). In this case, we can classify the event as a three-jet event provided the invariant mass of the soft parton with the nearest jet is small enough.

Two calculations of the four-jet corrections to the three-jet cross section including virtual corrections originally yielded quite different results. In the first approach,[18] a small invariant mass cut ($M_{ij} \gtrsim 0.1$ GeV) was used and predicted large corrections to the three-jet fraction. A calculation using a larger cutoff[19] ($M_{ij} \gtrsim 5.0$ GeV) gave a ten to twenty percent correction. The discrepancy has been studied by Gottschalk[20] in terms of the variable

$$y = \frac{M_{ij}^2}{s} \quad . \tag{66}$$

In the ERT calculation, the cutoff invariant mass corresponds to a y value of 10^{-5} while in the FKSS approach, the cutoff is approximately 10^{-2}. As a function of y, Figure 31 shows that the four- and three-jet cross sections are both positive only for y values greater that 0.03. In addition, requiring the four-jet contribution to be positive for thrust values less than 0.9 requires a y value of approximately $y \gtrsim 0.04$ (Figure 32).

The total cross section for hadron production is given by

$$\sigma_{\rm TOT} = \sigma_0 \left[1 + \frac{\alpha_s(Q^2)}{\pi} + (1.98 - .115\, N_f)\, \frac{\alpha_s^2(Q^2)}{\pi^2} \right] \tag{67}$$

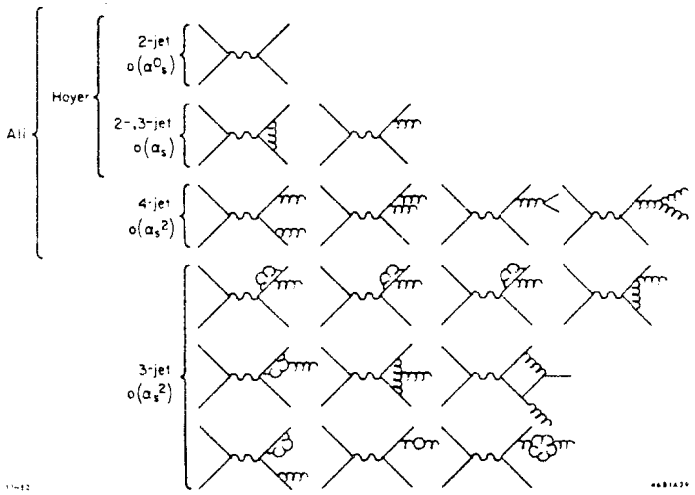


Figure 29

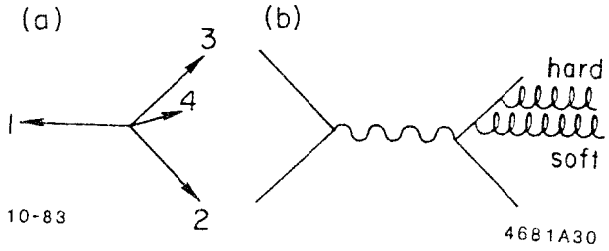


Figure 30

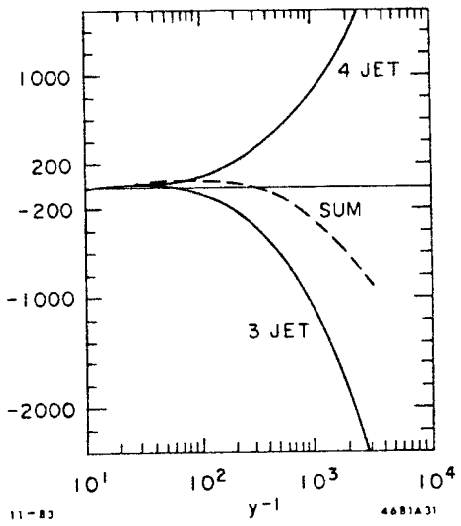


Figure 31

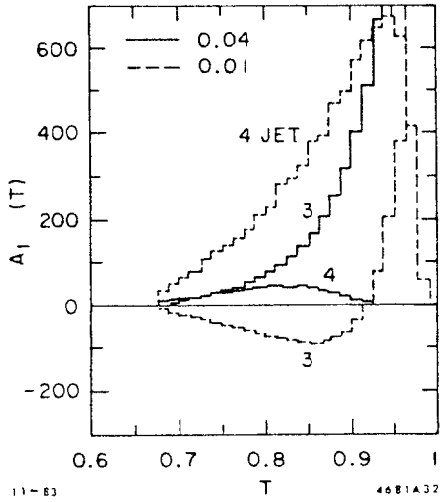


Figure 32

where

$$\sigma_0 = \frac{11}{3}\,\frac{4\pi\alpha^2}{3s} \quad .$$

Because of the physical processes involved in fragmentation, three-jet events are indistinguishable from two-jets when the event thrust is greater than ~ 0.05 and four-jets become indistinguishable from three-jets for acoplanarity less than ~ 0.05, thus the observed three- and four-jet cross sections must be defined as

$$\begin{aligned} \sigma_{3\,\mathrm{JET}} &= \int_{2/3}^{T_{\mathrm{MAX}}} dT\,\frac{d\sigma}{dT}\,(q\bar{q}g) \\ \sigma_{4\,\mathrm{JET}} &= \int_{A_{\mathrm{MIN}}}^{1} dA\,\frac{d\sigma}{dA}\,(q\bar{q}gg + q\bar{q}q\bar{q}) \end{aligned} \tag{68}$$

where, for example[21]

$$\frac{d\sigma}{dT}\,(q\bar{q}g) = \frac{2}{3}\,\frac{\alpha_s}{\pi}\,\sigma_0\left[\frac{2(3T^2-3T-2)}{T(1-T)}\,\ell n\left(\frac{2T-1}{1-T}\right) - \frac{3(3T-2)(2-T)}{1-T}\right] \quad . \tag{69}$$

5.2 The String-Lund Model

In the previous model, a $q\bar{q}$ pair was produced and some time later we imagine that the two quarks are moving apart and that eventually they fragment independently. However, this model violates several things which we know about quarks. Quarks carry color, and this color charge leads to the strong force which binds quarks together to form mesons. From potential models of $q\bar{q}$ bound states, we find that this force is almost constant as a function of the separation between the quarks. This leads to a potential energy between two moving quarks which increases as

$$\begin{aligned} E &\sim Kd \\ K &\sim 1\,\mathrm{GeV/fm} = 0.2\,\mathrm{GeV}^2 \end{aligned} \tag{70}$$

where d is the separation between the two quarks. At some point, we will have an energy larger than the mass of two light quarks, and we could have $q\bar{q}$ pair production from the field between the original pair. Schwinger[22] has shown that the behavior of 3+1 dimensional QCD is very similar to that of 1 + 1 QED in that the force leads to the formulation of a color flux tube with constant energy per unit length between the $q\bar{q}$ pair. If the separation is large enough, this flux tube (or string in 1 + 1 dimensions) will break as shown in Figure 33 leading eventually to the formation of mesons.

This behavior in 1 + 1 dimensions is often depicted by a graph of t versus x as shown in Figure 34. Lines of constant proper time will be hyperbolas in this plot, and the velocity of a quark or meson will be inversely proportional to the slope of its trajectory in the plane. If a string breaks at two places, A and B as in Figure 33, and if the distance between points A and B satisfies

$$(x_A - x_B)^2 - (t_A - t_B)^2 > \frac{m^2}{K^2} \tag{71}$$

a meson can be produced. The fragmentation process generates many such mesons with the slowest mesons being produced first in contrast to the procedure used in the independent models where fragmentation starts with the fastest (primary) quarks. For this reason, this is called an "inside out cascade."

If each meson carries away a random fraction of the energy remaining in a string segment, the longitudinal fragmentation function will be $f(z) = 1$, but this is modified in QCD by the suppression of high z hadrons due to collinear gluon emission and leads to the effective form

$$\begin{aligned} f(z) &= (1+c)(1-z)^c \\ c &= \frac{2}{3}\,\frac{12}{33-2N_f}\left(\ell n\ell n\,\frac{M^2_{\mathrm{upper}}}{\Lambda^2} - \ell n\ell n\,\frac{M^2_{\mathrm{lower}}}{\Lambda^2}\right) \end{aligned} \tag{72}$$

where M^2_{upper} is the invariant mass above which gluons are considered separately and M^2_{lower} is a typical meson mass square. In practice, the c parameters are left as free parameters to be adjusted for each quark type, and are approximately as shown in Table 4.[23]

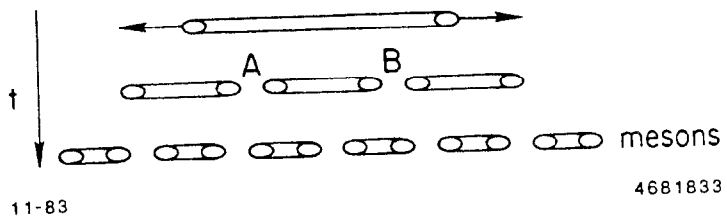


Figure 33

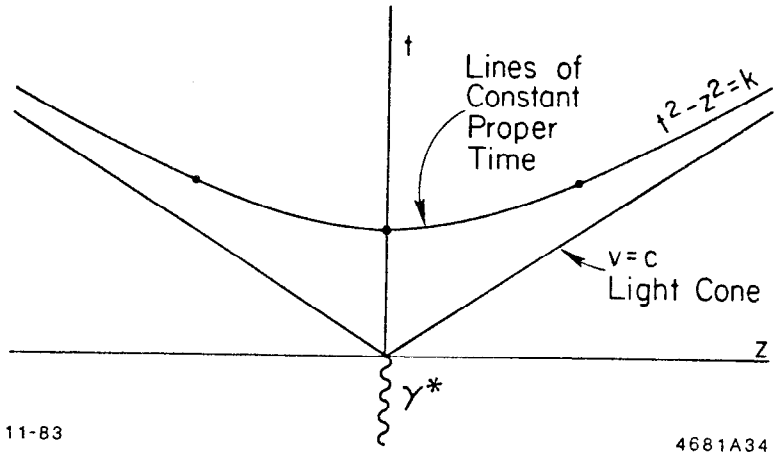


Figure 34

Table 4

Lund Model fragmentation parameters $f(z) = (1+c)(1-z)^c$					
quark	u	d	s	c	b
c	0.5	0.5	0.35	0.15	0.05

Finite meson mass and transverse momentum relative to the flux tube axis can be treated as a tunneling process and lead to production probabilities of the form

$$e^{-\pi(m^2+p_\perp^2)/K} \quad . \tag{73}$$

As a result, heavy quark pair production is suppressed in the ratio

$$u : d : s : c = 1 : 1 : 0.3 : 10^{-11} \quad ,$$

and all mesons have the same $p_\perp$ spectra independent of their flavor content.

Hard gluon emission is added to the model with probabilities taken from perturbative QCD to order α_s. For a three-parton configuration (Figure 35), the string is stretched from quark to gluon to antiquark. The gluon energy is shared equally between two string segments and thus if the number of particles produced per unit of rapidity is a fundamental property of the string (or the color flux tube), the gluon jet will be softer than a quark jet. We would expect to find

$$\frac{dN}{dy}\Big\|_{\text{gluon}} \simeq 2\,\frac{dN}{dy}\Big\|_{\text{quark}} \tag{74}$$

but this effect may be moderated by finite mass effects and the lower mean energy of the gluon jet. This prediction is quite similar to the QCD prediction

$$\langle n\rangle_{\text{glue}} \simeq \frac{9}{4}\,\langle n\rangle_{\text{quark}} \tag{75}$$

where the 9/4 comes from the color factor

$$\frac{2n_c^2}{n_c^2-1} \quad . \tag{76}$$

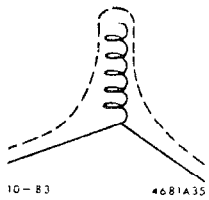


Figure 35

Since particle production occurs along the string, there may be fewer particles produced in the angular region between the q and the $\bar{q}$ than between the quarks and the gluon.[24]

The use of the tunneling hypothesis for quark mass effects has the interesting consequence that flavor production ratios, for example — the K/π ratio, are completely determined by the vertex weighting factor for each string break

$$\frac{(K\tau)^2}{(K\tau)^2 + m_t^2} \quad , \quad m_t^2 = m^2 + p_\perp^2 \quad . \tag{77}$$

All particle and flavor dependent mass effects should result from this simple factor. The model could of course be extended if necessary to include flavor dependent factors other than those predicted by mass dependent suppression of the tunneling probability.

Baryon production is introduced into the model by allowing the string to break into diquark-antidiquark pairs with an adjustable parameter fixed by the proton fraction in the final states. This is similar to what is done in the independent fragmentation models except that again production ratios for different types of baryons (p, Λ, Σ ...) are related in a definite way by the tunneling suppression factors.

Inclusion of higher order QCD effects in the string model raises several interesting questions. In the case of a $q\bar{q}g$ event, there is only one way to stretch the string between the q and the $\bar{q}$. However, with two gluons, there are two possibilities. The "correct" configuration can be chosen provided the gluons do not have the same color and provided the colors of the quarks are known. This requires a modification of the α_s^2 QCD matrix elements.[23,18]

Gluon jets produced using the string fragmentation picture tend to be softer than those produced by the independent fragmentation models, so that with a fixed set of analysis cuts, some three-jet events in the string picture will be lost into the two-jet sample. Qualitatively, this requires an increase in the effective value of α_s in order to produce the same number of observed three-jet events. As will be seen later, this type of effect makes it difficult to determine α_s in a model independent or fragmentation independent way.

5.3 Cascade Models

Cascade models differ from the previous two models in two important ways. First, the evolution of the event is followed using leading log perturbative QCD until there are large numbers of partons in the final state. Soft gluon contributions are eliminated by requiring the parent parton in a branching to have a minimum invariant mass, typically a few GeV. Second, before these partons are converted into hadrons, preconfinement takes over, i.e., as shown in Figure 36, groups of partons combine to form color singlet clusters. This use of preconfinement means that color screening occurs before hadronization. The actual hadronization process must be parameterized from low energy data in terms of the decay of these clusters into smaller mass subclusters.

The joining of various parts of the parton shower together into colorless groups before hadronization is analogous to a model with many strings. The emphasis, unlike the independent fragmentation model, is on incorporating the strong color force as a fundamental feature of the model so that hadronization can be described in terms of the behavior of hadrons and not in terms of the fragmentation functions of colored quarks and gluons. Unlike the string model which generates hadrons from breaks in the string, the hadrons in this model are formed from the combination of leading log QCD showers and low mass hadronization. Perhaps in the future, we will be able to show that these two pictures are equivalent.

6. Can We Measure α_s from Jet Properties?

We now would like to return to the question of measuring the strong coupling constant α_s from properties of the jets observed in the final states. In the earliest measurements (1979-1980) there were several groups with of order 1000 events above $\sqrt{s} = 30$ GeV and there was reasonable agreement using lowest order QCD independent fragmentation models that α_s was approximately 0.17. Table 5 shows the results of these measurements. The MARK J group adjusted the transverse momentum fragmentation parameter σ_q and the coupling constant α_s to fit the oblateness and minor

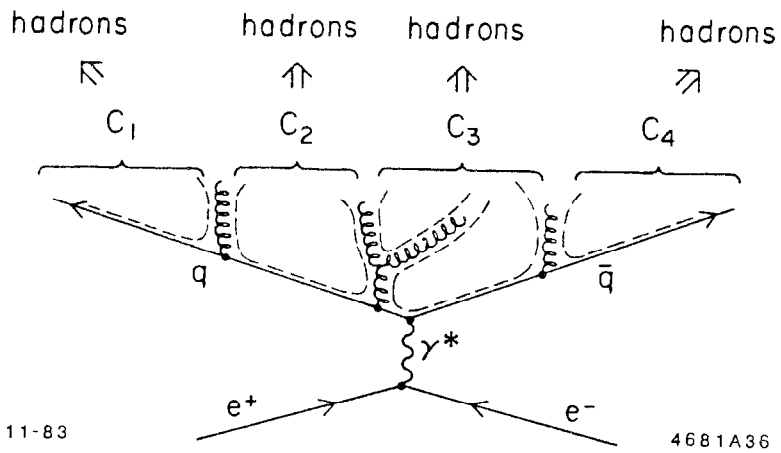


Figure 36

Table 5

Results on α_s (1979/80)					
	Distributions Fitted	Fit Parameter	Model	Higher Orders	α_s ($\pm$ stat $\pm$ syst)
MARK J	0, Minor	σ_q, α_s	Ali	some $O(\alpha_s^2)$	$0.19 \pm 0.02 \pm 0.04$
TASSO	$\frac{dN}{dx}$, p_{out}^2,	a_F, σ_q	Hoyer	$O(\alpha_s)$	$0.19 \pm 0.02 \pm 0.03$
	S, A	$\frac{P}{P+V}$, α_s			
			Ali	some $O(\alpha_s^2)$	$0.17 \pm 0.02 \pm 0.04$
JADE	$\frac{dN}{dx}$, p_{out}^2,	a_F, σ_q	Hoyer	$O(\alpha_s)$	$0.18 \pm 0.03 \pm 0.03$
	S, A	$\frac{P}{P+V}$, α_s			
PLUTO	Number of 3-Cluster Events, x_1	α_s	Hoyer	$O(\alpha_s)$	$0.15 \pm 0.03 \pm 0.02$

axis distributions. The TASSO and JADE groups in addition varied the vector fractions and longitudinal fragmentation and fitted the thrust distributions, the mean transverse momentum out of the plane, the sphericity and the aplanarity. The PLUTO group used a similar method to fit α_s as a function of the number of three-cluster events and the thrust distribution in these events.

The first group to make extensive use of the string model, however, found substantially higher values for α_s.[25] Using five different methods, they found as shown in Table 6 that while they agreed with previous determinations using independent models, the string picture required values of α_s which were higher by ~ 0.08. This could be traced to the tendency of the string model to produce softer fragmentation in the

Table 6

CELLO (1982) $O(\alpha_s)$		
Distribution Fitted	Hoyer Independent Jets	Lund Model String Picture
$N(S > 0.25, A < 0.1)$	$\alpha_s = 0.19 \pm 0.03$	0.28 ± 0.045
$N(O > 0.2)$	$\alpha_s = 0.19 \pm 0.02$	0.26 ± 0.040
N(3 clusters)	$\alpha_s = 0.145 \pm 0.020$	0.235 ± 0.025
dN/dX_1	$\alpha_s = 0.155 \pm 0.015$	0.235 ± 0.025
Energy − Energy Correlation	$\alpha_s = 0.150 \pm 0.020$	0.25 ± 0.04

three-parton final states. These results disagree with a similar determination by the JADE group which fits the number of three-cluster events and the thrust distributions and finds $\alpha_s = 0.20 \pm 0.015 \pm 0.03$ for **both** models.[26]

While the discrepancy is still not resolved, part of the problem may lie in the fact that the CELLO fits using the Hoyer model are not in good agreement with the data for both the thrust distribution and the $p_\perp$ distribution as shown in Figure 37. Clearly it is important to optimize all of the parameters in each of the models to give the best fit to the data before comparing values of α_s. The TASSO group has made a comparison of this type. They modify the longitudinal fragmentation function in the independent fragmentation model which was originally of the form

$$f(z) = 1 - a + 3a(1-z)^2 \tag{78}$$

to be of a form similar to that used in the string models, namely

$$f(z) = (1 + a_L)(1-z)^{a_L} \tag{79}$$

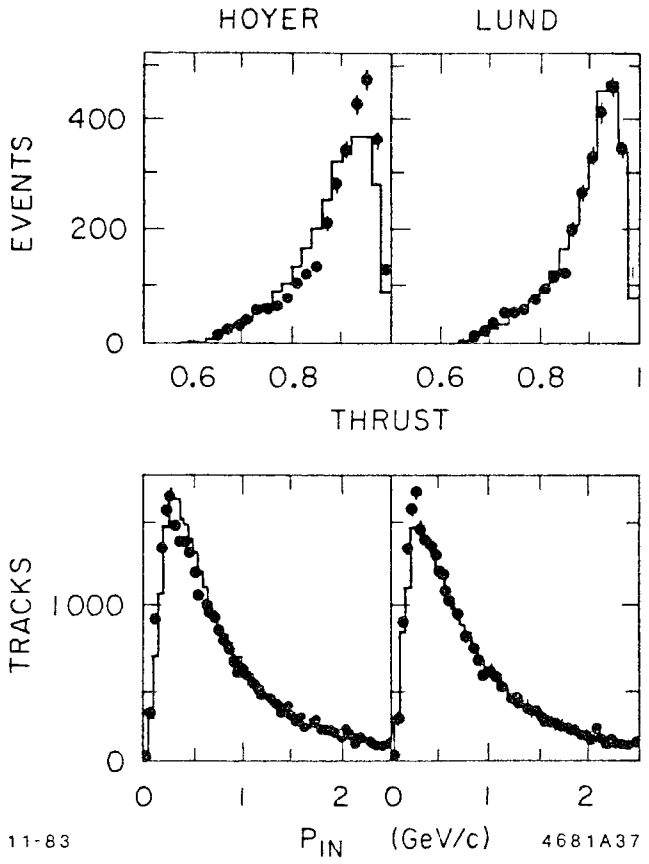


Figure 37

for u, d and s quarks. Heavier quarks are treated with a fragmentation function given by

$$f(z) = \frac{k}{z\left(1-\frac{1}{z}-\frac{\epsilon}{1-z}\right)^2} \tag{80}$$

where $\epsilon = 0.18$ for c quarks and $\epsilon = 0.04$ for b quarks. The ρ to π ratio is used to determine the pseudoscalar fraction and they find

$$\frac{P}{P+V} = 0.42 \quad . \tag{81}$$

The K production fraction determines the strange quark fraction in the sea

$$\frac{s\bar{s}}{u\bar{u}} = \frac{s\bar{s}}{d\bar{d}} = 0.4 \tag{82}$$

and the proton fraction fixes the ratio of baryon to meson plus baryon production

$$\frac{\text{Prob}\,(q \to q' + B)}{\text{Prob}\,(q \to q' + M) + \text{Prob}\,(q \to q' + B)} = 0.1 \quad . \tag{83}$$

This leaves three free parameters a_L, σ_q and α_s which can be used to fit the remaining shape measures. The results of the fit using $O(\alpha_s^2)$ matrix elements (FKSS) are shown in Table 7 and agree qualitatively with the CELLO conclusion, that the value deduced for α_s is model dependent.

Table 7

TASSO $O(\alpha_s^2)$ Measurements of α_s (Preliminary)		
Method	Independent	String
x_p, Q_1, Q_2	0.166	0.216
x_p, P_{out}^2, P_{in}^2	0.155	0.201
3 Clusters, $O(\alpha_s)$	0.170	0.237

A similar study by the MARK J group[27] uses $O(\alpha_s^2)$ matrix elements (ERT) and fits the energy-energy correlations (discussed later) in the range $|\cos x| < 0.72$. In this case they find agreement between the two models on the value of α_s:

$$\alpha_s = 0.14 \pm 0.01 \qquad \text{Lund model}$$

$$\alpha_s = 0.12 \pm 0.01 \qquad \text{Ali model} \quad ,$$

in disagreement with the CELLO $O(\alpha_s)$ result for energy-energy correlations of

$$\alpha_s = 0.15 \pm 0.02 \qquad \text{Hoyer model}$$

$$\alpha_s = 0.25 \pm 0.04 \qquad \text{Lund model} \quad .$$

There is considerable disagreement on the precise value of α_s, and several systematic effects must be taken into account when comparing the different measurements. Different groups use different parameters within the independent models to fit their data. Some of these parameters (particularly σ_q) will affect the value found for α_s. The inclusion of higher order effects tends to decrease the value of α_s, and finally, with each model, determining α_s from the number of three-cluster events or the energy-energy correlation tends to give smaller results than the use of thrust distributions and shape parameters. Hopefully a detailed comparison of all of the parameters used to determine α_s and the sensitivity of α_s to these parameters will eventually allow us to make this measurement. Meanwhile, however, our confidence that this can be done in a truly model independent manner has been considerably shaken.

7. Determining Fragmentation Parameters

From the preceding discussion, it is clear that we need to carefully constrain the fragmentation parameters of the models and test our ideas about this soft physics with the available data before we can make further progress on the perturbative predictions of QCD. There are four ways in which this is currently being done.

* First, the mean multiplicities and momentum spectra of identified particles must be studied to determine the strange quark fraction in the sea, diquark production probabilities, and the spin ratios $\rho : \pi$ and $K^* : K$.

* Second, we should study the way in which quantum numbers are conserved. Are they conserved locally? Is there detailed $p_\perp$ balance between produced baryons? Are strange particles produced in pairs close together in rapidity?
* Third, heavy quark fragmentation must be studied to teach us about quark mass effects and to parameterize $f(z)$ for c and b quarks.
* Finally, we should look for differences between quark and gluon jets to distinguish between models (Hoyer) where their fragmentation is identical and other models (Ali, Lund) where eventually we should see differences in the momentum spectrum of fragmentation products or their multiplicity.

We now discuss the experimental information available on these questions.

New data on particle fractions are available from the TPC detector which uses the 65% truncated mean of 120 samples per track to measure the dE/dx energy loss of particles in the gas of the TPC detector. Different types of particles will have different energy losses depending on the β of the particle. Figure 38 shows the observed bands and allows separation of most particles out to momenta of order 1 GeV. Above 4 GeV, the particle fractions can be determined by fitting the distribution of energy losses. The resultant particle fractions (preliminary) are shown in Figure 39. Similar data are shown in Figure 40(a),(b) and (c), from the HRS, DELCO, and TASSO detectors. The HRS uses time-of-flight techniques to separate the particles, and the DELCO detector uses Čerenkov detectors. The TASSO detector uses a combination of time-of-flight and Čerenkov techniques. The data show good agreement between the different detectors and techniques and indicate that as the particle momenta increase, the difference between π, K and p production diminishes. Extrapolating from the observed behavior, it appears that at momenta of order 20 GeV, we would no longer see any dependence of the production mechanism on either the strangeness or baryon number of the produced particle. At high momenta it is important to remember that the particle fractions are separated statistically by all three methods and hence the fractions have highly correlated errors.

There are still some normalization differences between experiments, particularly in the proton fractions. The original versions of the Lund model adjusted the diquark

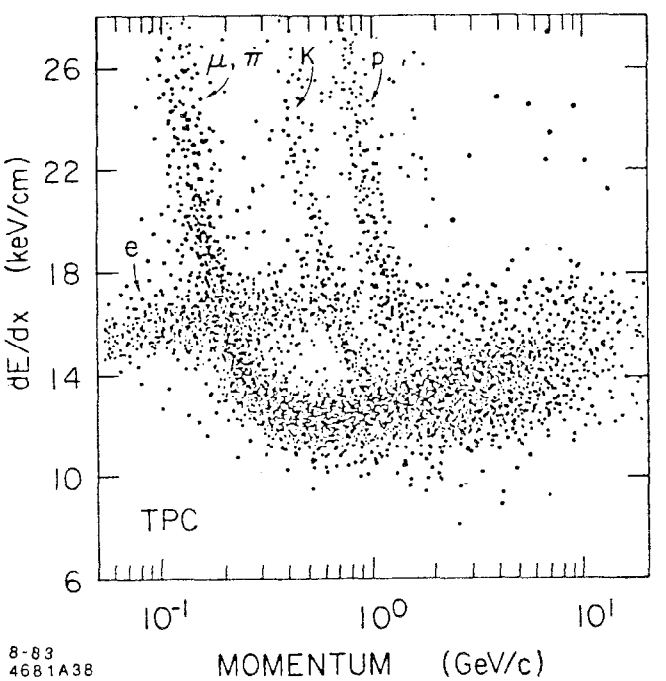


Figure 38

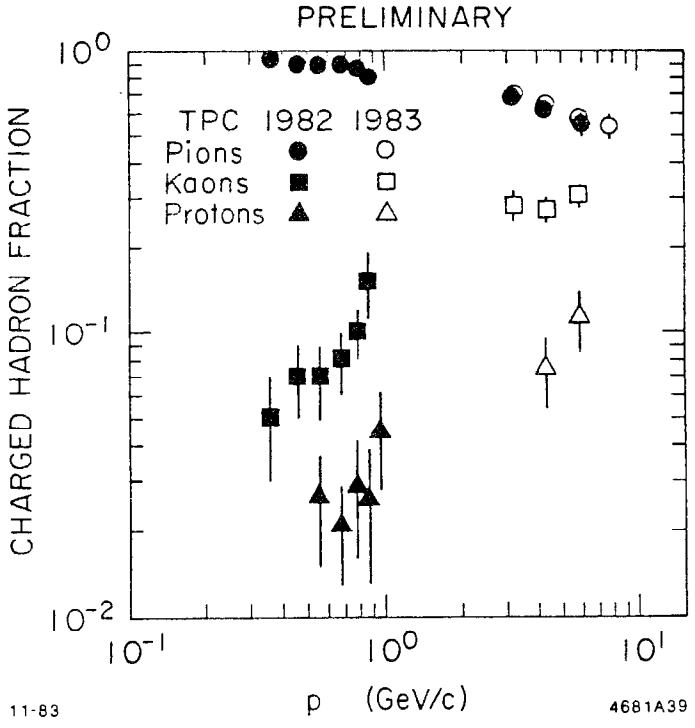


Figure 39

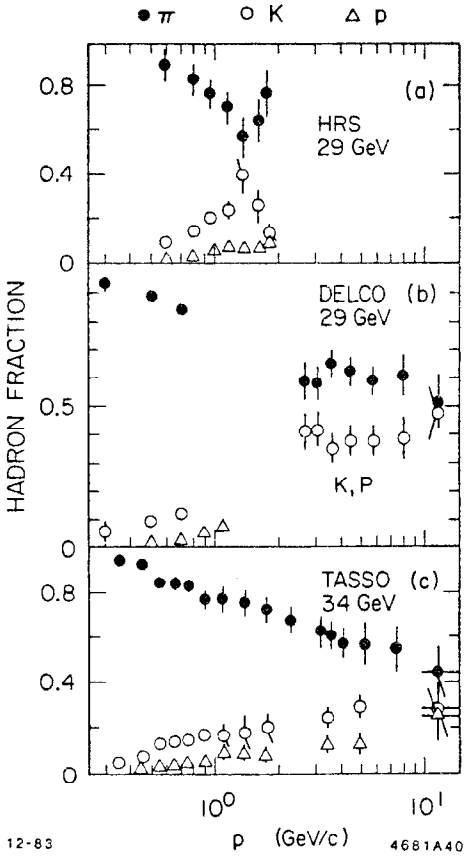


Figure 40

production probabilities to 0.065 using data taken in the SPEAR energy range. Data from the MARK II and TASSO detectors indicate that a higher rate of proton production is seen at higher energy and are consistent with a diquark probability of 0.10. Figure 41, however, shows a comparison of the MARK II data on proton fractions with the recent HRS data. The HRS proton fraction is lower and probably in better agreement with the original 0.065 number.

The CELLO group has compared the production of neutral and charged π mesons. Figure 42 shows that the $\pi^{\pm}$ spectrum is the same within statistics as the π° spectrum. There is little room for significant amounts[28] of η production which would give an enhanced yield of π°'s. The data are in good agreement with simple isospin arguments which predict $2\sigma(\pi^{\circ}) \simeq \sigma(\pi^{+}) + \sigma(\pi^{-})$. When compared to hadrons, it appears that the π mesons (which are lighter) fall somewhat more steeply as expected from phase space arguments. The charged π meson spectra at low and high energies are shown in Figure 43 and show a steeply falling exponential with a slower fall off at high x, again as predicted by our phase space arguments.

Having measured the inclusive distribution for pions which is determined by the longitudinal fragmentation function $f(z)$, we can compare it to the same distribution for K mesons to see if the production dynamics of K's are similar. Figure 44 shows the inclusive distribution of K mesons together with the range of values seen at the same energies for π mesons. At high x, the slopes of the distributions are quite similar indicating similar fragmentation mechanisms. At low x, the suppression of the K mesons is due to the heavier mass of these objects since as shown in Equation (14) we expect the slope of the exponential falloff in the low x region to be smaller for higher masses. Figure 45 compares the behavior of the protons with that of the $K^{\pm}$ mesons and again, the behavior is similar in the high x region, and the slope is somewhat smaller in the low x region for the heavier particle.

In studying particle production ratios, neutral K mesons and Λ baryons are useful because they can be detected over a much larger momentum range than charged K's or protons. The detection technique for these particles is based on finding the two-body decay modes $K^{\circ} \rightarrow \pi^{+}\pi^{-}$ and $\Lambda \rightarrow p\pi^{-}$. With somewhat reduced efficiency, this allows detectors which do not have Čerenkov detectors to study the inclusive

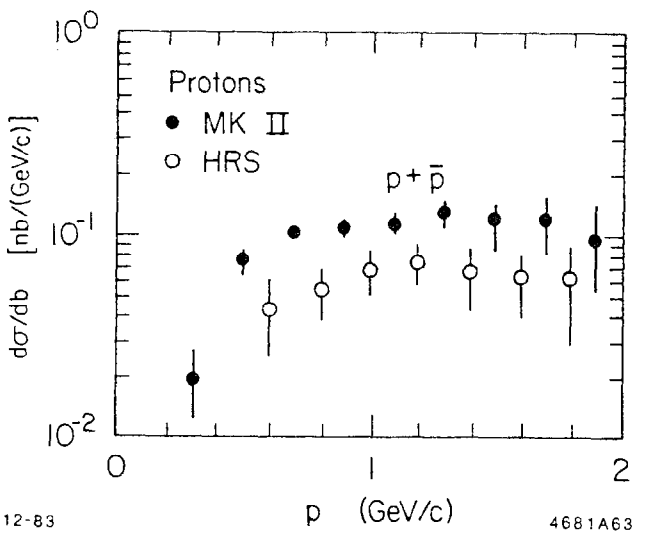


Figure 41

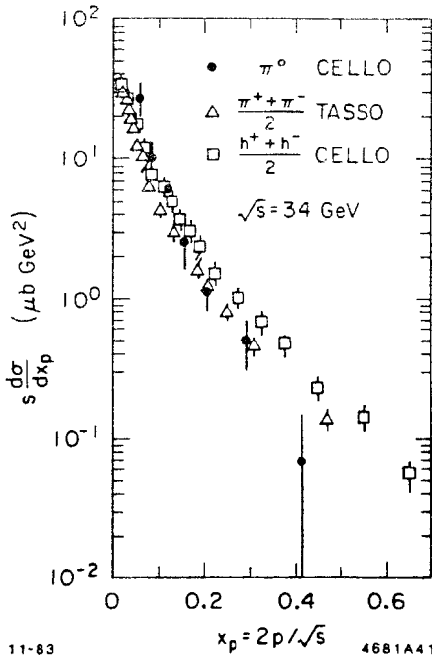


Figure 42

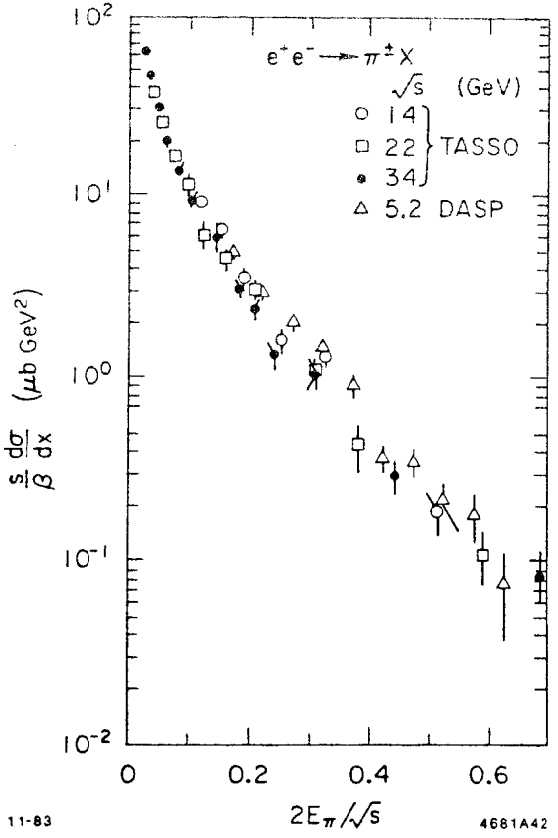


Figure 43

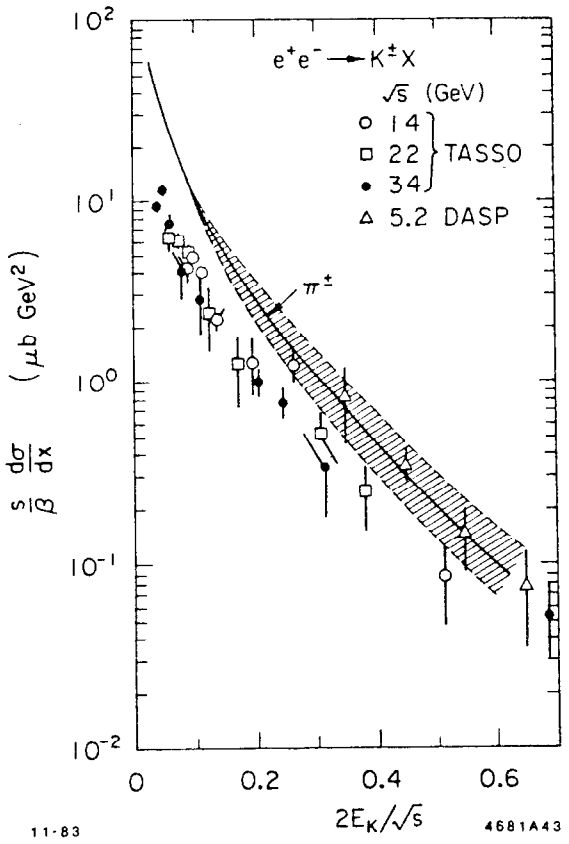


Figure 44

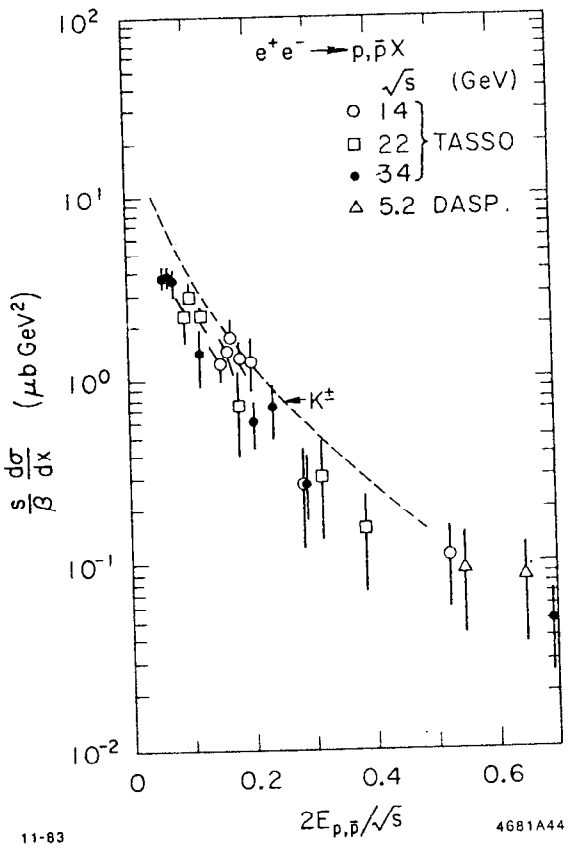


Figure 45

spectra of these particles. Figure 46 shows a comparison of the K° and Λ spectra with the π meson spectra from data taken by the TASSO detector. The ratio of K to Λ production is ~ 2.7 over the range $0.1 < X < 0.3$. This ratio is a free parameter in the independent fragmentation models, but is fixed in the LUND model due to the presence of $e^{-M^2/K}$ vertex factors.

7.1 Energy Dependent Parameters

In making these comparisons, we have so far ignored the fact that the particle fractions are changing as a function of center-of-mass energy. As shown in Figure 47, there is considerable information about the behavior of these fractions, and in principle we should expect that the model used to parameterize the high energy fragmentation behavior would also predict the observed energy dependence. In practice, while many groups have tried to optimize the model parameters at a single energy, very little work has been done to determine whether a single set of parameters also gives a consistent picture of these energy dependent effects.

In fact, we know that at least some of the parameters used in present models are energy dependent. This means that in order to implement a single set of energy independent parameters, the model builders will have to include further dynamical effects. As an example of this energy dependence, we examine the behavior of $s\bar{s}$ production from the sea. In order to determine this parameter, we must fit the observed rate of K° production.

Figure 48 shows that the number of K°'s observed per event changes by ~ 0.4–0.6 when crossing the charm threshold. Thus at ~ 5 GeV, roughly half of the observed rate comes from charm, and half comes from u, d or s quark production. Since the number of K's from charm depends for the most part on decay branching ratios of charm mesons, we ask only that the fragmentation model predict the observed K° rate which **does not** come from charm. For values of the probability of $s\bar{s}$ production between 0.0 and 0.1, the Feynman–Field model predicts noncharm K° rates between 0.57 and 0.92. The observed rate,[29] however, is 0.52 ± 0.05 which gives an estimate of $P_{s\bar{s}}$ of

$$P_{s\bar{s}} < 0.03 \ @ \ 7.3 \text{ GeV} \quad .$$

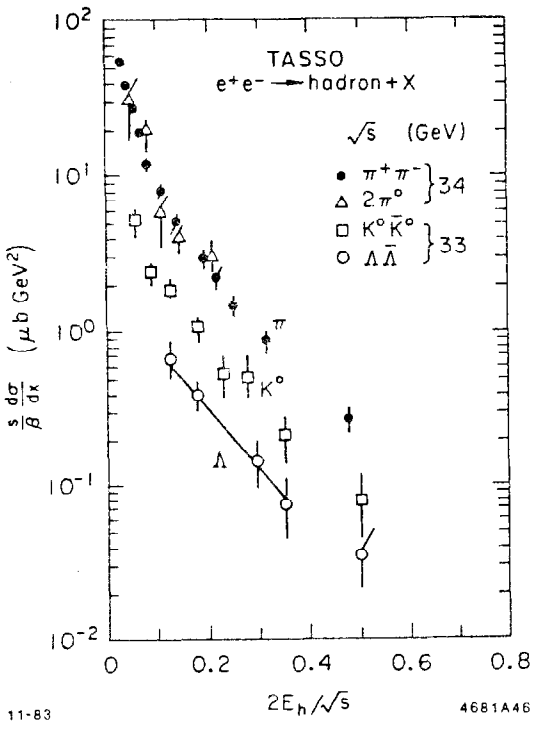


Figure 46

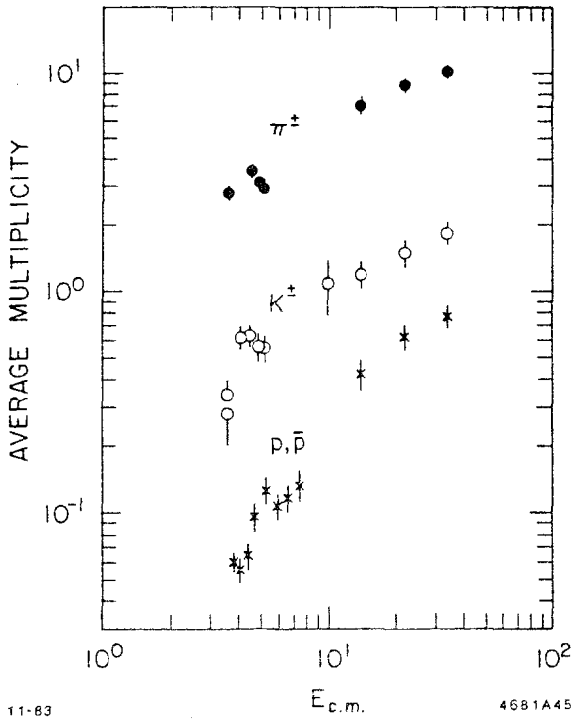


Figure 47

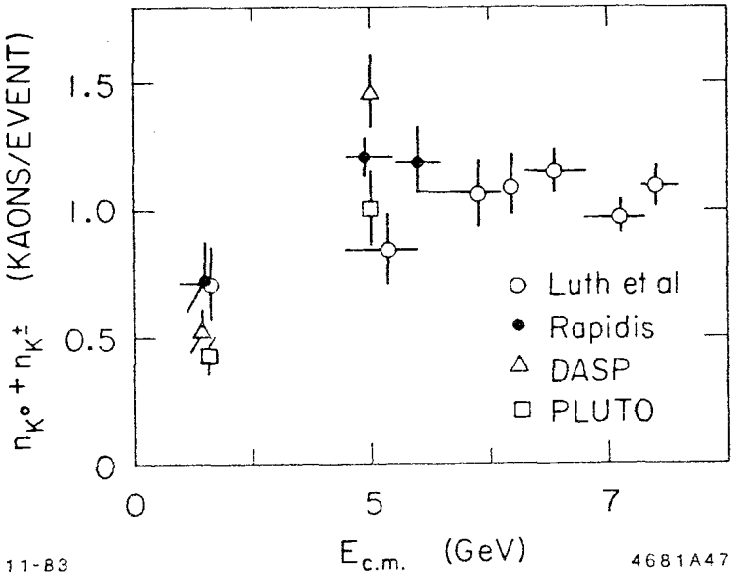


Figure 48

There are several additional uncertainties which must be accounted for in repeating this exercise at higher energy. Both bottom and charm mesons will now contribute to the observed K° rate. Furthermore, the effective branching ratio of b, c quarks to K° will depend on the fraction of D^* and D mesons produced. Figure 49 shows the (preliminary) MARK II rate for K°'s per event together with the prediction of the independent fragmentation model as a function of $P_{s\bar{s}}$ for values of $B(b,c \to K^\circ)$ between 0.36 and 0.56. This yields a value

$$P_{s\bar{s}} = 0.08 \pm 0.04 \quad @ \ 29 \ \text{GeV} \quad .$$

This value of $P_{s\bar{s}}$ assumes that the production of strange baryons proceeds through mechanisms other than strange quark sea production. If, however, Λ production comes predominantly from diquark production with strangeness provided by an $s\,\bar{s}$ from the sea, then $P_{s\bar{s}}$ must be increased by ~ 0.04.

By comparing the low energy value of $P_{s\bar{s}}$ to the high energy value, we see that this parameterization of strange quark production is energy dependent. This is not really surprising since the independent fragmentation model does not explicitly account for quark mass effects and is using the $P_{s\bar{s}}$ parameter to describe the phase space suppression of the heavier strange quark. While the 1 GeV rest mass of the pair is significant at 7.3 GeV, we expect it to be less so at higher energies. It would be an interesting test of the dynamical model of such suppressions in the Lund model (i.e., tunneling) to apply that model to the center-of-mass energy variation of strange meson production.

7.2 Correlations Between Parameters

In addition to being energy dependent, many of the fragmentation model parameters are highly correlated. As an example of this, we now look at the effect of changing the vector fraction on the previous parameter $P_{s\bar{s}}$. If the production probabilities of u and s quarks at each branching are related by $s \simeq .3\,u$, then $P_{s\bar{s}}$ will be given by

$$\frac{s}{\text{TOT}} = \frac{.3}{.3+1+1} = .13 \quad . \tag{84}$$

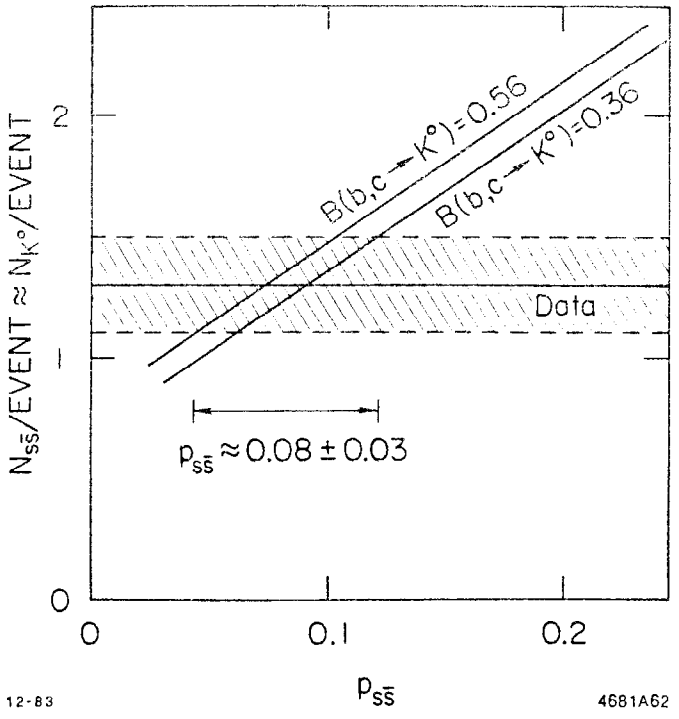


Figure 49

The observable is, however, not $P_{s\bar{s}}$ but the rate of K's per event. If we observe $\sim 1.3K^{\circ}$/event and again assume that 0.4–0.6 comes from charm production, then roughly 1 K°/event is due to $s\bar{s}$ production in the branchings of the fragmentation process. But to convert $P_{s\bar{s}}$ into an observed total rate, we need to know **how many** branches, N_B, there are on average in the fragmentation. This number of branches will of course also determine the final state multiplicity, however, it is only the primary mesons whose multiplicities are directly determined by N_B.

For a fixed secondary meson multiplicity, N_S, the relation between N_B and N_S and hence the relation between $P_{s\bar{s}}$ and N_{K^*} will depend on the vector fraction,V. For example, if $N_S \sim 18$ and the vector fraction is 1, the primary multiplicity is $N_S/2$ because the primary mesons are all ρ mesons and $\rho \to \pi\pi$. Since 1 K°/event will come from one $s\bar{s}$ pair (assuming equal charged and neutral K's), this translates to a $P_{s\bar{s}}$ of

$$\frac{s\bar{s}}{\text{TOT}} \sim \begin{cases} 1/18 & V = 0 \\ 1/9 & V = 1 \end{cases} \quad . \tag{85}$$

The vector fraction can be directly determined by fitting the observed rates for ρ and K^* production. Figure 50 shows the observed $\pi\pi$ mass spectra at 7.3 GeV (MARK I) together with fits for a smooth background and K° and ρ production. The measured ρ° spectra yield 0.4 ± 0.1 ρ°/event which gives a vector fraction

$$\begin{aligned} V &= 0.24 \pm 0.12 \qquad \text{at 7.3 GeV} \quad , \\ P &= 0.76 \pm 0.12 \quad . \end{aligned} \tag{86}$$

A similar measurement has been made by the TASSO group,[30] and is shown in Figure 51 for data taken at 14, 22 and 34 GeV. Figure 52 shows the inclusive cross-section at 34 GeV compared to the π meson distribution with the familiar features of suppression of high mass production at low x and mass independent production at high x. The total number of ρ°/event in the x range $0.2 < x < 0.7$ is shown in Table 8 and determines a pseudoscalar fraction of $P/(P+V) = 0.42 \pm 0.08 \pm 0.15$ or

$$\begin{aligned} V &= 0.58 \pm 0.17 \quad , \\ P &= 0.42 \pm 0.17 \qquad \text{at 34 GeV} \quad . \end{aligned} \tag{87}$$

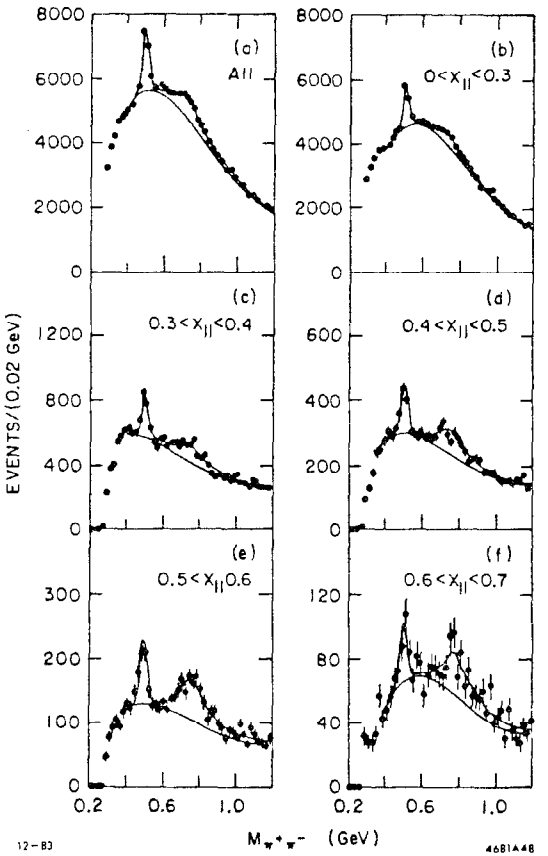


Figure 50

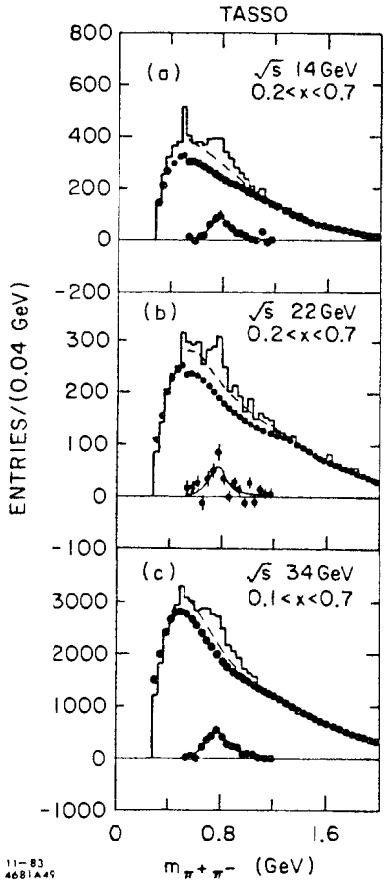


Figure 51

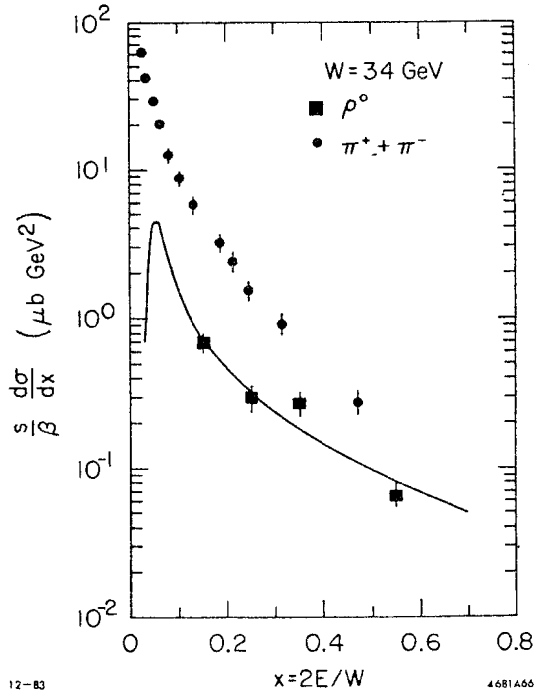


Figure 52

Table 8

TASSO ρ Production	
ρ_0 per event $(0.2 < x < 0.7)$	$\sqrt{s}$ (GeV)
$0.33 \pm 0.06 \pm 0.07$	14
$0.22 \pm 0.06 \pm 0.05$	22
$0.22 \pm 0.02 \pm 0.05$	34

The vector fraction is suppressed at low energies presumably because of the higher mass of vector ρ compared to pseudoscalar π. If there were no mass effects, we would expect the pseudoscalar to vector ratio to be the ratio of number of states

$$\frac{P}{V} = \frac{1}{3} \quad . \tag{88}$$

Although consistent with $V = 3P$, the central values of the TASSO measurements give $P/V \sim 1/1.4$ and the 7.3 GeV measurements give $P/V \sim 3.5/1$.

In summary, the study of perturbative QCD effects such as the determination of α_s requires a detailed parameterization of hadronization. Different models at present seem to give different results, thus we must be sure that each model correctly describes as many features of the data as possible. We already know that models as different as the Ali and Lund approaches can be adjusted at a particular energy to be virtually indistinguishable. Thus, the only possibility to distinguish between different dynamical assumptions appears to be to make use of the center-of-mass dependence of the parameterizations. As we have seen, this is complicated not only by the fact that there are charm and bottom thresholds between the low and high energy regions, but also by the fact that the models rely heavily on the simplifying assumptions of massless quarks and statistical spin ratios and hence cannot be expected to correctly predict low energy phenomena.

7.3 Quantum Number Correlations

So far we have used only the single particle inclusive distributions and particle ratios to test the dynamics of fragmentation. It is also possible to use particle correlations and in particular to look at the details of the ways in which charge, strangeness and baryon number are conserved in the models. In a model of fragmentation which uses the sequential production of $q\bar{q}$ pairs such as that shown in Figure 53 for example, we would expect that strangeness conservation is accomplished locally by the production of $s\bar{s}$ pairs. If the particles from such a pair tend to lie close together in rapidity, then there should be strong rapidity correlations for pairs of strange mesons. Similarly, if baryon production arises from diquark-antidiquark production, baryon-antibaryon pairs should show similar correlations.

Charge is also conserved locally in such a model. Note that if the event is divided into two jets as shown in Figure 53, the charge of each jet is either 0 or ± 1 depending on the flavor of the "last" $q\bar{q}$ pair. Groups of particles separated by $\sim 2y_{\rm MAX}/N_B$ should have zero net charge, and leading particles in each jet should be oppositely charged. The first evidence for this type of behavior was found by the TASSO group.[31] The data in Figure 54 shows the charge compensation probability $\bar{\phi}_r(y, y')$ which is the probability for fixed y' that the particle charge at y' is compensated by an oppositely charged particle at y normalized to the density of particles at y and y'. As can be seen in the figure, the charge of a particle tends to be compensated by a short range correlation with other particles with $\Delta y \sim \pm 1.5$. The open circles compare the results which are obtained using the same events but randomizing all of the charges in the final state. In principle, this randomization should only be applied to primary mesons, since we have already seen, Equation (87), that vector meson production is significant. Nevertheless, the results are in good agreement with an independent fragmentation model of the Ali type. In addition to the short range correlation, the fastest particles $(2.5 \leq |y'| \leq 5.5)$ show a long tail in the charge compensation probability indicating that $\sim 15 \pm 3\%$ of the charge is compensated by particles in the opposite jet. The authors were unable to reproduce this long range correlation using a model which produced neutral partons $[MC(gg)]$ obeying Feynman–Field fragmentation, and interpreted it as evidence for the production of charged primary partons.

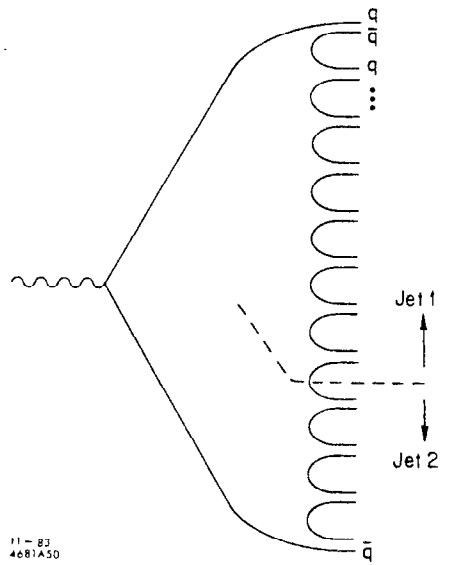


Figure 53

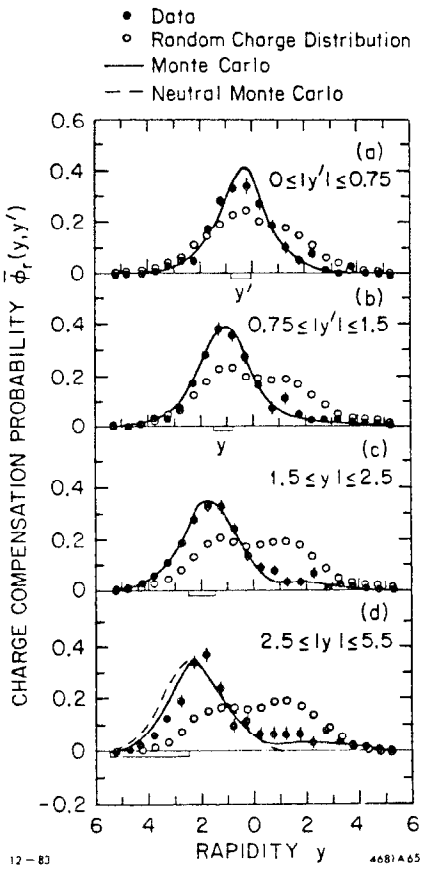


Figure 54

In a similar study of two particle charge correlations, the PLUTO group found[32] that the mean charge of a jet in a two jet event was

$$|Q| = 0.55 \pm 0.25 \quad . \tag{89}$$

This was determined by extrapolating the observed mean jet charge with experimental cuts between the values detected for Feynman–Field jets with charges of zero and one. This value is in good agreement with what would be expected from the simplest model. Let us assume that primary quarks u, d, s, c, b are produced with probabilities $4/11 : 1/11 : 1/11 : 4/11 : 1/11$, and $q\bar{q}$ pairs of the type u, d, s are produced in the ratio $1 : 1 : .3$ or $.43 : .43 : .13$. Then a charge one jet will result from a u quark provided the "last" quark pair is of the $d\bar{d}$ or $s\bar{s}$ type. Similarly, charge one jets will result from d quarks when the last pair is a $u\bar{u}$. Thus the average jet charge is just

$$2 \times \frac{4}{11} \times [.43 + .13] + 3 \times \frac{1}{11} \times [.43] = 0.52 \quad . \tag{90}$$

Figure 55 shows preliminary data from the TPC detector. They measure the product of charges in the two jets with a gap of width Δy excluded from the central region. Thus for $\Delta y \to 0$, this product is the product of jet charges, and for $\Delta y \to 8$, it measures the correlation of the leading particles. The event sample consists of events with sphericity less than 0.25 and charged multiplicity greater than five. Also shown is the fact that the fragmentation parameters for two-jet events in the Lund model reproduce the shape of the observed correlations and that models with random final state charges or randomized charges for the primary mesons do not agree with the data. Similar (preliminary) data are shown in Figure 56 from the MARK II detector (an $x_\perp$ cut is used in place of a rapidity gap) and compared to the behavior of charge one and charge zero jets in the Ali model. As in the case of the PLUTO data, one can extrapolate between the behavior of these two samples to determine the mean charge product of two jets

$$-\langle Q_1 Q_2 \rangle = 0.53 \pm 0.12 \quad . \tag{91}$$

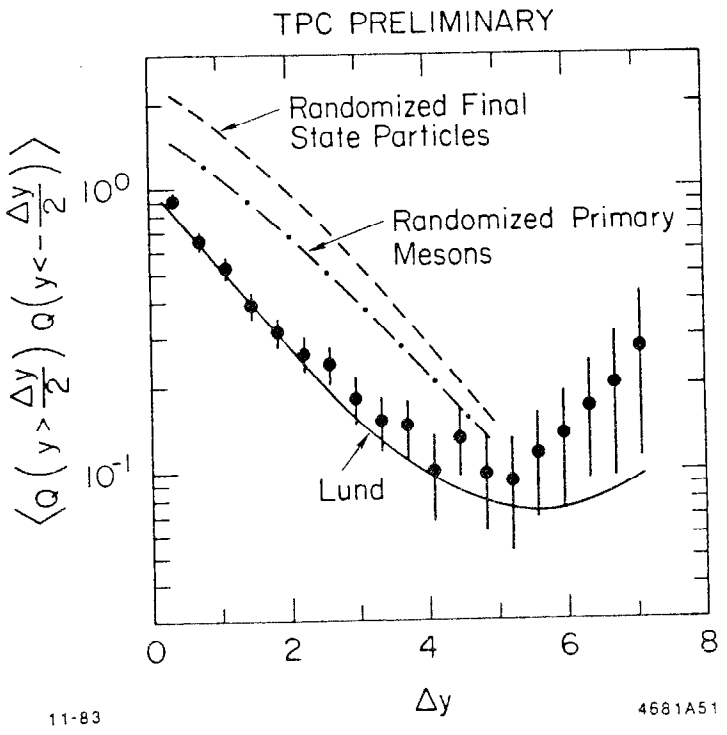


Figure 55

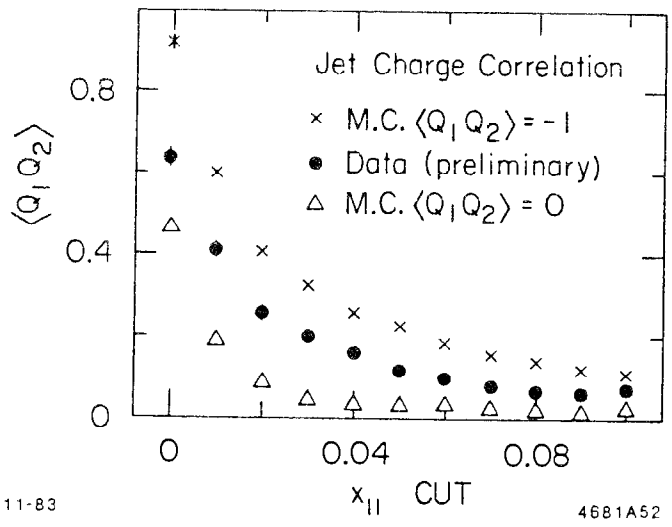


Figure 56

7.4 Baryon Correlations

If the diquark production mechanism is correct, we would expect that baryons would also show short range correlations. Other mechanisms may also lead to such effects; in any case it is interesting to determine whether baryon number is conserved locally or globally. We can study the mechanism of baryon production most easily by comparing the rates of proton-antiproton pairs produced in the same and opposite jets. Early data using time-of-flight techniques in the MARK II detector[33] used pairs of baryons in the region $x < 0.14$ and showed only slight enhancement of same jet $p\bar{p}$'s in the soft region.

This has been extended by the TASSO detector which uses its hadron arms to identify protons in the ranges $1 < p < 2.3$ and $3 < p < 5$ GeV/c. In a sample of 26,376 hadronic events, they find as shown in Table 9 that the observed pairs are predominantly produced in the same jet.

Table 9

TASSO Baryon Pairs (no acceptance corrections)		
	Opposite Jet	Same Jet
$p\bar{p}$	2.2 ± 2.8	15.2 ± 4.6
pp, $\bar{p}\bar{p}$	1.8 ± 2.6	-0.05 ± 2

As improved statistics become available, it will be interesting to test the diquark model assumption that the $p_\perp$ of the diquark (baryon) relative to the fragmentation axis is balanced by the $p_\perp$ of the antidiquark (antibaryon). This question has been examined by Bartl *et al.*, who suggest several tests of this mechanism. These studies should also be extended to pairs of strange mesons, although since the probability of $s\bar{s}$ production in the fragmentation process is higher than diquark production, the increased number of $s\bar{s}$ branchings will make it more difficult to test detailed $p_\perp$ balance and short range correlations.

7.5 Heavy Quark Fragmentation

The presence of heavy quark thresholds considerably complicates the analysis of present data since it means that mass effects which fall off as a power of

$$\frac{2M_Q}{\sqrt{s}} \tag{92}$$

can remain important to quite high energies. It is important then to correctly parameterize the fragmentation functions of heavy B and D mesons. Theoretically we expect the transition probability between a heavy quark Q and a state containing the heavy quark plus a light pair as shown in Figure 57 to be given by

$$P(i \to f) \sim \frac{1}{(\Delta E)^2} \tag{93}$$

where $\Delta E \sim E(Q\bar{q}) + E(q) - E(Q)$. If the heavy meson $Q\bar{q}$ carries a fraction z of the initial quark momentum, ΔE is

$$\left(M_Q^2 + z^2p^2\right)^{1/2} + \left(M_{\bar{q}}^2 + (1-z)^2p^2\right)^{1/2} - \left(M_Q^2 + p^2\right)^{1/2} \sim 1 - \frac{1}{z} - \frac{\epsilon}{1-z} \tag{94}$$

where $\epsilon = (m_q/M_Q)^2$. The resulting transition probability will be[34]

$$D_Q^H(z) = \frac{1}{z}\,\frac{k}{[1 - \frac{1}{z} - \frac{\epsilon}{1-z}]^2} \tag{95}$$

which peaks toward larger z for heavier mesons.

Heavy mesons have been directly detected using the reaction

$$\begin{array}{lll} D^{*+} \to D^0\pi^+ & & \mathrm{BR} = 0.44 \pm 0.1 \\ \quad\ \hookrightarrow \quad K^-\pi^+ & & \mathrm{BR} = 0.03 \pm 0.06\ . \end{array}$$

Due to the small mass difference between the D^* and the D mesons,

$$\begin{aligned} M(D^{*\pm}) - M(D^0) &= 145.3\ \mathrm{MeV} \\ &= m_\pi + 5.7\,\mathrm{MeV} \end{aligned}$$

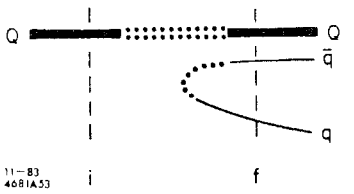


Figure 57

the system is highly constrained and a clean sample can be found without identification of the K meson.[35] Recent data from the DELCO detector uses Čerenkov identified K mesons to search for D^*'s in the mode

$$\begin{array}{lll} D^{*+} \rightarrow & D^\circ \pi^+ & \\ & \hookrightarrow & K\pi \\ & \rightarrow & K\pi x \\ & \rightarrow & K\pi\pi\pi \end{array} .$$

The measured cross sections as a function of the z of the D^* meson are shown in Figure 58, where for comparison all measurements have been normalized to a $D^* \rightarrow D\pi$ branching ratio of 0.44. Table 10 shows the values obtained for the ϵ parameter from fitting the z distributions to a fragmentation function of the form (95) and the total cross-sections and R values for D^* production. The average R value is 1.65 which indicates that D^* production is a significant fraction of the total charm and bottom quark fragmentation

$$\frac{\sigma(D^{*+} + D^{*-})}{2\sigma_{c,\bar{c}} + 2\sigma_{b,\bar{b}}} \sim 0.5 \quad . \tag{96}$$

Table 10

D^* Production Spectra and Cross Sections

Detector	$\sqrt{s}$	ϵ	$\sigma(D^{*\pm})$	R_{D^*}
MARK II	29	0.25	0.25 ± 0.13	2.5 ± 1.3
DELCO	29	0.39 ± 0.16	$0.20 \pm 0.3 \pm 0.07$	2.0 ± 0.8
CLEO	10		1.6 ± 0.6	1.8 ± 0.7
TASSO	34	0.18 ± 0.07	0.094 ± 0.041	$1.25 \pm 0.32 \pm 0.44$

As shown in Figure 59, the HRS detector has detected D° mesons directly in the $K\pi$ mass spectrum. This allows a direct comparison D° and D^* spectra which are found to be similar, and eventually will eliminate uncertainties in the total D^* production rate due to the $D^* \rightarrow D^\circ$ branching ratio.

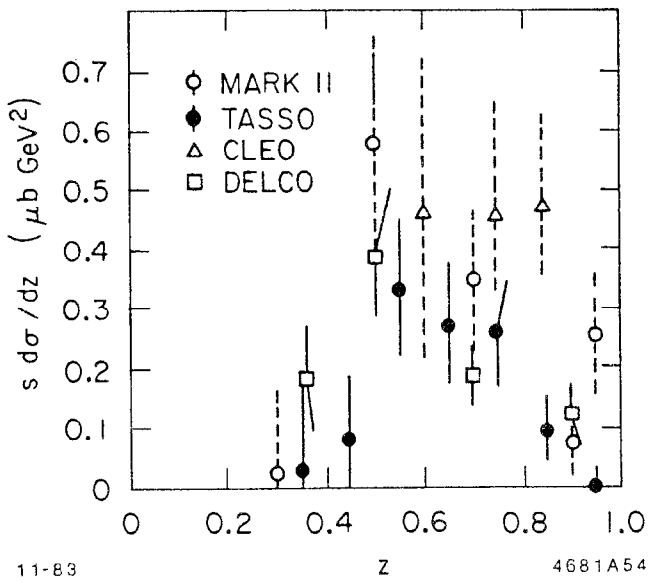


Figure 58

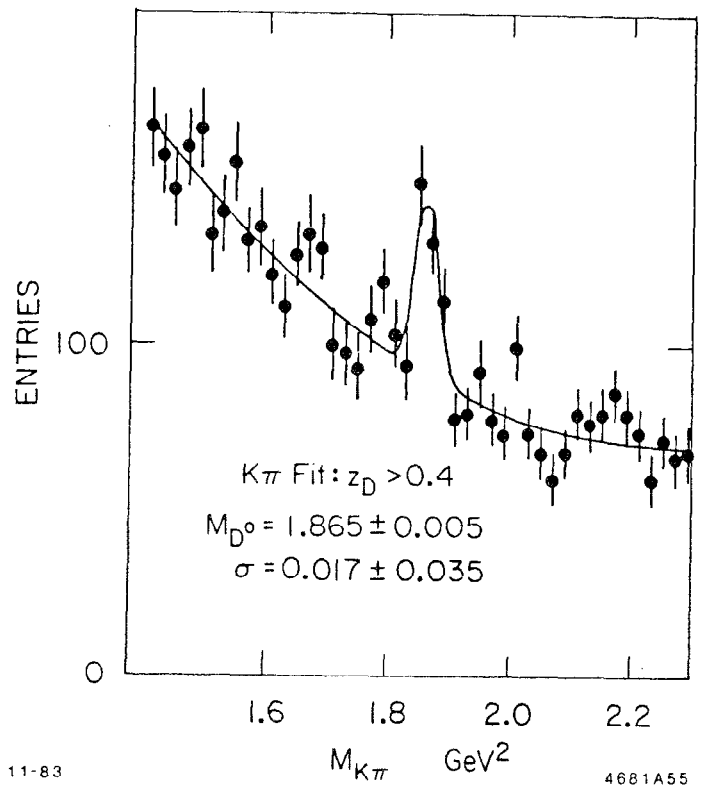


Figure 59

Charm and bottom mesons can also be detected indirectly by fitting the transverse momentum spectra of leptons from the semileptonic decays of these mesons. Detected leptons are binned in momentum and transverse momentum and the spectrum is fit with the semileptonic branching ratios $\mathrm{BR}(c \to e)$, $\mathrm{BR}(b \to e)$ and the shape of the b fragmentation function (ϵ_b) as free parameters. The shape of the c fragmentation function is taken from the D^* cross-section. Since high $p_\perp$ bins are dominated by $b \to e$ and low $p_\perp$ bins are dominated by $c \to e$, the two contributions can be separated. The results of the fit from the MARK II detector[36] give

$$\mathrm{BR}(c \to e) = 7 \pm 2 \pm 2\% \quad ,$$

$$\mathrm{BR}(b \to e) = 11 \pm 3 \pm 3\% \quad ,$$

$$\epsilon_b = 0.04^{+0.35}_{-0.25} \quad .$$

Similar measurements have been done by the MAC detector using the muon spectra. They find[37]

$$\mathrm{BR}(c \to \mu) = 7.6^{+9.7}_{-2.7}\% \quad ,$$

$$\mathrm{BR}(b \to \mu) = 15.5^{+5.4}_{-2.9}\% \quad ,$$

$$\epsilon_b = 0.008^{+0.037}_{-0.008} \quad .$$

Figure 60 shows a comparison of the fragmentation functions for heavy mesons for values $\epsilon_c \sim 0.25$ and $\epsilon_b \sim 0.04$ and indicates that the spectrum from b quarks is considerably harder than that of c quarks. Using a value of $\epsilon_c \sim 0.25$, the expected parameter for b quarks using Equation (94) would be

$$\epsilon_b \sim \epsilon_c \cdot \frac{m_c^2}{m_b^2} \sim 0.03 \qquad (97)$$

in good agreement with the data.

7.6 Gluon Fragmentation

The gluon fragmentation function is believed to behave *asymptotically* in QCD in a way which differs from quark jets. The total multiplicity and mean transverse momentum of gluon jets should be larger. In order to test these predictions, however,

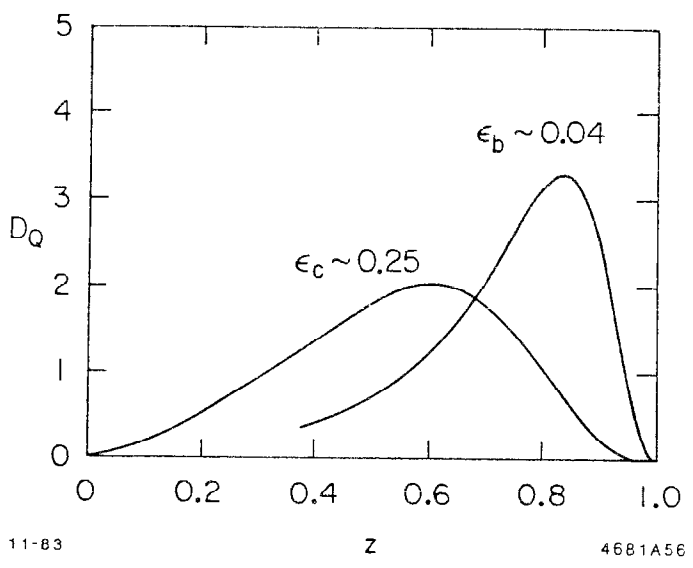


Figure 60

we must be careful since, on average, the energy of gluon jets is much less than that of observed quark jets. Figure 61 shows the energy distributions dN/dx_i of the three jets produced in QCD at the parton level. Note that there is almost no overlap at a fixed center-of-mass energy between the fastest jet (quark) and the slowest jet (gluon). In fact, in the region where they overlap, the confusion about which jet is actually the gluon is maximal! Since we have seen that particle fractions and other jet parameters are energy dependent, we would like to compare jets which we believe to be gluons with quark jets of the **same** energy. This has been done by the JADE group using center-of-mass energies of 22 GeV and 29–36.4 GeV.[38] Gluon jets of energy between 7 and 10 GeV come mainly from the higher center-of-mass data, and can be compared to fast jets coming predominantly from the 22 GeV sample. Figure 62(a) shows the mean transverse momentum of the three jets ($x_1 > x_2 > x_3$) as a function of the detected jet energy. The jet energies are calculated in each event from the angles of the three-jets. The observed distributions are consistent with an independent fragmentation model where σ_q is 500 MeV/c for a gluon and 330 MeV/c for a quark jet. They are also consistent with the Lund model which results in a softer fragmentation function for gluons than for quarks [see Equation (74)]. As shown in Figure 62(b), these differences are not seen in Monte Carlo events where the quark and gluon have identical fragmentation functions (Hoyer model).

In order to eliminate the possibility that the above result arises from incorrect identification of the quark axis for the first and second jets at 22 GeV, the JADE group has also compared the $p_\perp$ spectra of particles seen in a 50° cone around the third jet at 33 GeV with the spectra seen for a similar cone around the axis of two-jet events at 14 GeV.[39] Again, the Monte Carlo shows that there is little relative bias in the two spectra [Figure 63(a)] and that similar spectra are obtained for Monte Carlo data with identical quark and gluon fragmentation functions. The data indicate [Figure 63(b)] again that the gluon jets at 33 GeV are wider than the quark jets.

The particle compositions in the gluon jets could also differ from quark jets. In this respect, since the average gluon jet energy is small, we would expect heavier mass particle production to be suppressed at low energies as it is in quark jets. Gluons, however, are flavor blind. Unlike the fragmentation process which involves very soft gluons

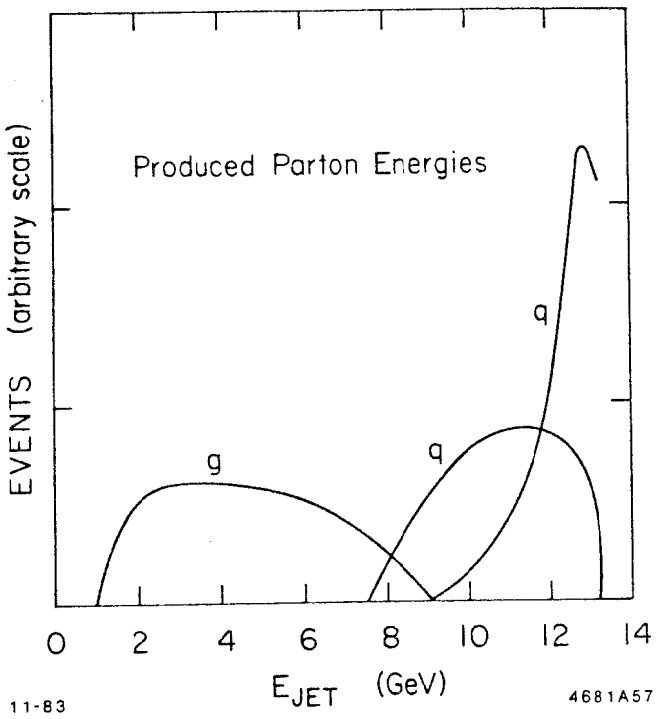


Figure 61

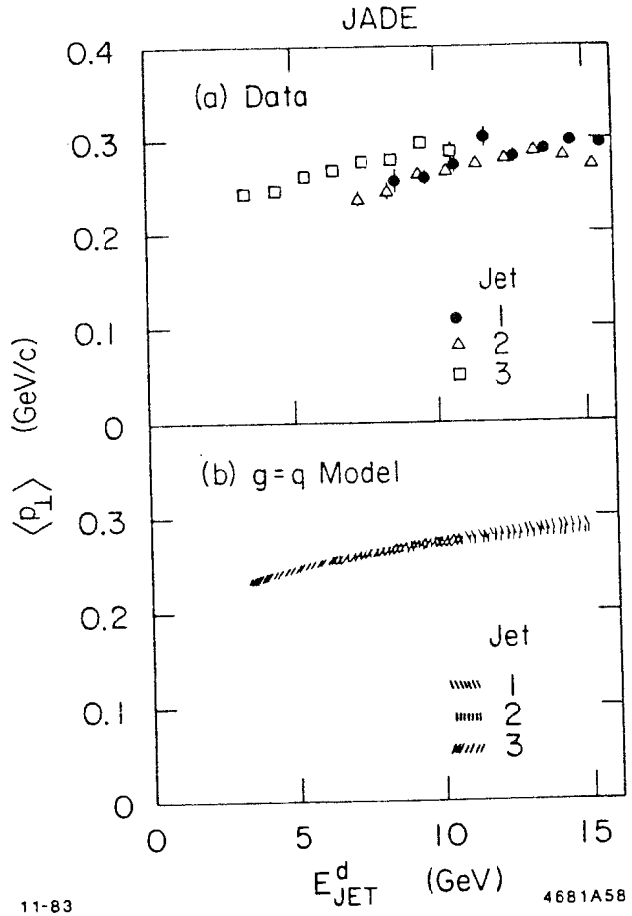


Figure 62

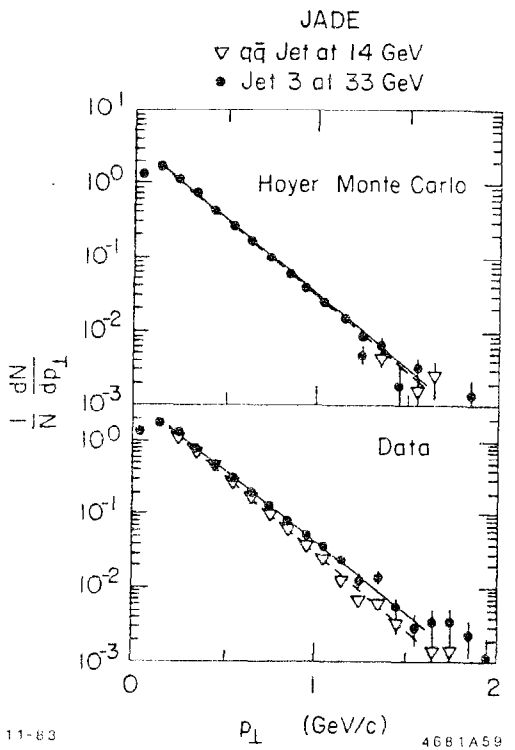


Figure 63

so that strange quarks are suppressed, three-jet events contain hard gluons and hence may result in increased strange particle production.

An interesting hint that this may be the case has been found by the TASSO group which has compared the $\Lambda, \bar{\Lambda}$ yield in three-jet events with that found in the entire event sample. The yield in three-jet events is[40]

$$0.052 \pm 0.010\ \Lambda_s' / \text{event}$$

and in the entire sample it is

$$0.022 \pm 0.003\ \Lambda_s' / \text{event} \quad .$$

Since no correction has been made for the lower average energy of the gluon jet, this may indicate significant enhancement of Λ production for the third jet. A similar enhancement has been seen by the JADE group in the production of η mesons.[41] Events identified at 34 GeV as 2 jets ($S < 0.15$) contain

$$0.22 \pm 0.06 \pm 0.06\ \eta / \text{event}$$

while the event sample as a whole has

$$0.72 \pm 0.10 \pm 0.18\ \eta / \text{event} \quad .$$

In both of these analyses, no corrections have yet been applied for the contribution of b and c quark events to the non-two-jet samples.

8. Energy–Energy Correlations

The parameterization of fragmentation is obviously a difficult and complex task. There are a large number of parameters in any model which must be determined from the data, and as we have seen, most of these parameters are correlated or energy dependent. While some of the fragmentation studies which have been mentioned are interesting tests of soft hadron dynamics (quantum number correlations, particle fractions in the third jet, baryon dynamics), our primary purpose in studying fragmentation was to eliminate uncertainties due to soft corrections to perturbative processes.

It appears at present, for example, that different models make different predictions about the relationship of the perturbative parameter α_s and the observed three-jet fraction.

One can, however, take an entirely different approach, and look for new observables which will be insensitive to fragmentation. This assumes of course that hard and soft processes do in fact factor and that such observables exist. This is by no means a proven conclusion yet in QCD.[42]

One possibility for a fragmentation independent measure of α_s is the behavior of the correlation function between two energy deposits in finite solid angle elements. As shown in Figure 64, one determines the energy weighted cross section for two solid angle elements Ω_1 and Ω_2:

$$\frac{1}{\sigma_0}\frac{d\Sigma}{d\Omega_1\, d\Omega_2} \quad ,$$

$$\Sigma = S_N \int \left(\frac{d^2\sigma}{dx_1\, dx_2}\right) x_1\, x_2\, dx_1\, dx_2 \quad , \tag{98}$$

$$S_N = 1, \quad i = j\,; \qquad S_N = 2, \quad i \neq j \quad .$$

Although this cross section looks quite complicated, it solves a number of QCD problems. Since we look only at the energy deposit, and do not ask whether the parent parton is a gluon or a quark, problems due to collinear gluon emission within a quark jet are eliminated. Furthermore, soft gluon problems are cured by using the energy weighted cross-section.

The energy energy correlation function can be calculated in first order QCD and is of the form[43]

$$\frac{1}{\sigma_0}\frac{d\Sigma}{d\Omega_1\, d\Omega_2} = A(\chi)\,\frac{1}{\sigma}\left(\frac{d\sigma}{d\Omega_1}+\frac{d\sigma}{d\Omega_2}\right) + B(\chi)\,\frac{3}{16\pi}\,(\cos\chi + \cos\theta\cos\theta') \tag{99}$$

where the two elements of solid angle Ω_1, Ω_2 are specified by angles θ, ϕ, θ', ϕ' and χ is the angle between $d\Omega_1$ and $d\Omega_2$. The functions A and B determine the independent and correlated parts of the energy deposit and are given by

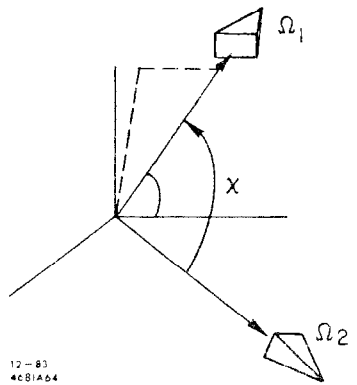


Figure 64

$$A(\chi) = \frac{\alpha_s}{12\pi}\,\frac{1}{1-z}\left[\left(\frac{3}{z^5}-\frac{4}{z^4}\right)\ell n\,(1-z)+\frac{3}{z^4}-\frac{5}{2z^3}-\frac{1}{z^2}\right] \quad ,$$

$$B(\chi) = \frac{\alpha_s}{12\pi}\,\frac{1}{1-z}\left[\left(\frac{12}{z^5}-\frac{16}{z^4}+\frac{4}{z^3}\right)\ell n\,(1-z)+\frac{12}{z^4}-\frac{10}{z^3}\right] \tag{100}$$

where $z = (1/2)(1-\cos\chi)$. Note that both of these functions are proportional to α_s, and therefore if second order corrections[44] are small, one could hope to determine α_s directly from a fit to the energy-energy correlation.

We can also see from the forms above that the perturbative calculations tend to be singular both for large and small χ, ($z = 0, 1$). In these regions, one should not attempt to fit the energy-energy correlation to the perturbative formulae since there are significant logarithmic and fragmentation dependent corrections.[45] In the simplest models of fragmentation, one expects the fragmentation contributions of a single jet to be of the form[43]

$$\frac{c(p_\perp)}{4\pi\sqrt{s}}\,\sin^{-3}\chi \tag{101}$$

where the coefficient $c(p_\perp)$ measures the width of the energy weighted jet, and depends on the jet multiplicity

$$\langle n\rangle \simeq c\,\ell n\,\sqrt{s} + \text{constant} \quad . \tag{102}$$

If the fragmentation is the same for both jets in a two-jet event, then it contributes a symmetric term which will cancel in the asymmetry

$$A(\chi) = \frac{1}{\sigma}\left[\left.\frac{d\sigma}{d\cos\chi}\right|_{\pi-\chi} - \left.\frac{d\sigma}{d\cos\chi}\right|_{\chi}\right] \quad . \tag{103}$$

This cancellation is however, not complete in a three-jet event as illustrated in Figure 65. Jets two and three are not at $\chi = 180°$ and may have widths which differ from those of jet one. Thus we expect some residual fragmentation dependence even in the asymmetry.[46]

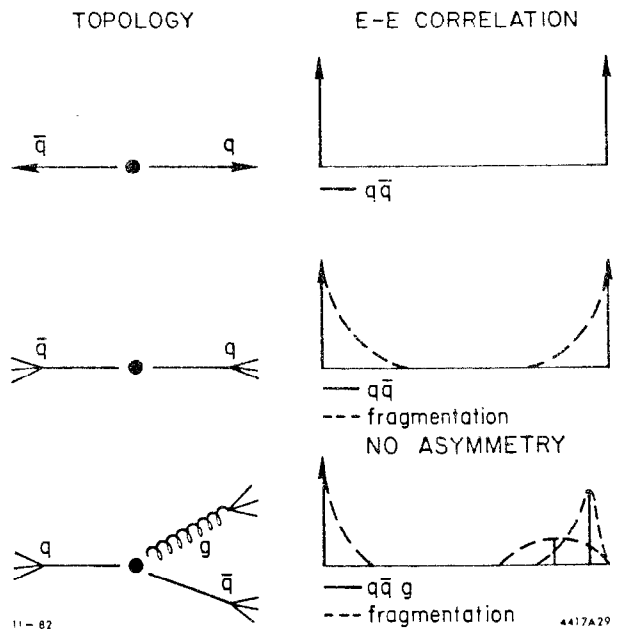


Figure 65

Figure 66 shows the data from the CELLO collaboration[47] for the energy-energy correlation as a function of χ. A fit for α_s yields

$$\begin{aligned} \alpha_s &= 0.21 \pm 0.01 \quad , \\ c\langle p_\perp \rangle &= 1.2 \pm 0.05 \end{aligned} \tag{104}$$

to first order in α_s. Fitting the asymmetry alone gives a value of α_s of

$$\alpha_s = 0.15 \pm 0.02 \quad .$$

A similar fit by the MARK II collaboration[46] gave

$$\alpha_s = 0.19 \pm 0.02 \pm 0.03$$

to first order in α_s and used a fragmentation form

$$\frac{\alpha_s A_1}{\sqrt{s}} \begin{cases} \frac{1}{\sin^3 \chi} & \cos\chi > 0 \\ \sin\chi & \cos\chi < 0 \end{cases} \quad . \tag{105}$$

Data from the MAC detector are shown in Figure 67. The data from different detectors cannot always be compared directly because they may or may not be corrected for experimental acceptances. In addition, the MARK II data are normalized using

$$\frac{E_i E_j}{s}$$

and the MAC data are normalized to

$$\frac{E_i E_j}{(E_{vis})^2} \quad .$$

At the moment, there are still uncertainties of order fifteen percent in the value of α_s determined in this way due to uncertainties in second order corrections, the form of the fragmentation contributions, and the angular range of χ which should be used to

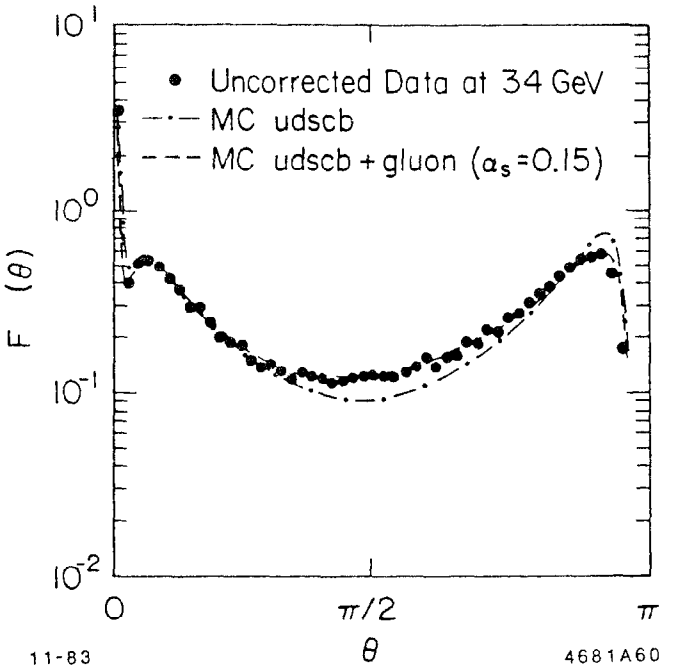


Figure 66

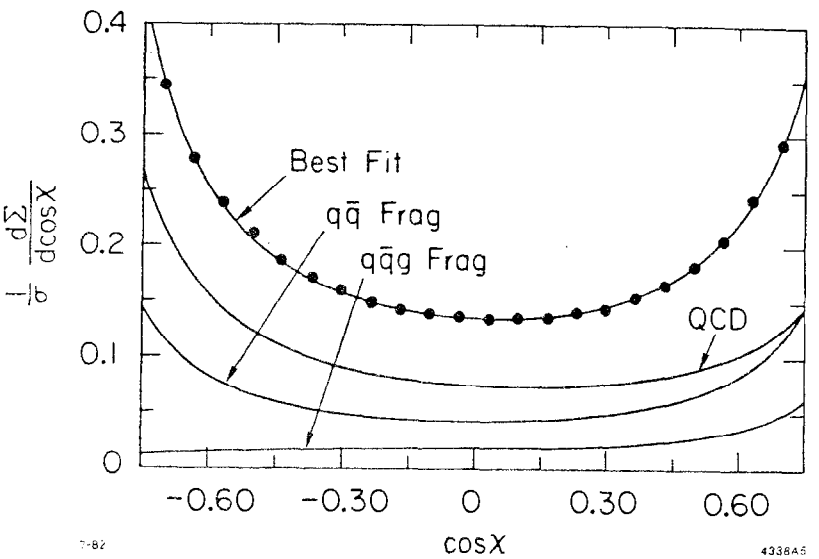


Figure 67

fit for α_s. The technique, however, seems promising, and recent data from the MARK J collaboration[48] indicate that by fitting α_s over the restricted region $|\cos\chi| < 0.72$ and using second order corrections (ERT), the independent and string models give essentially the same result for α_s

$$\alpha_s = 0.14 \pm 0.01 \qquad \text{Lund} \quad ,$$

$$\alpha_s = 0.12 \pm 0.01 \qquad \text{Ali} \quad .$$

9. Summary

We have a simple perturbative picture of the production of hadrons from e^+e^- annihilations which works quite well in predicting the main features of this interaction. It explains the magnitude of the total cross section, the basic two-jet structure, and the final state angular distributions. It is also consistent with our present ideas about the structure of hadronic matter and the requirement that at high enough energies, the corrections due to strong interactions are small and hence treatable in a perturbative sense. We have seen, however, that to progress beyond this point requires a detailed model of fragmentation phenomena and that differences in models prevent us from making clean predictions about QCD. It is therefore important that we continue to study the fragmentation process and try to parameterize it as well as possible. Large amounts of experimental data are now available on this subject, and new tests will become available as experimenters look in more detail at the behavior of quantum number correlations and energy dependent effects. In doing this, it will be important to keep in mind that mass effects can yield significant energy variations in the model parameters.

Our eventual goal should be to find ways of treating the data which will yield quantitative tests of QCD. Studies of three- and four-jet fractions, three-jet fragmentation properties, and energy-energy correlations have begun, and hopefully with improved understanding of fragmentation effects, will yield such tests.

References

1. J. Dorfan, SLAC-PUB-2963, August 1982.
2. E. Fermi, Prog. Theor. Phys. 5, 570 (1950).
3. J. Lepore and R. Stuart, Phys. Rev. 94, 1724 (1954).
4. See for example, G. Hanson *et al.*, Phys. Rev. D26, 991 (1982).
5. R. Brandelik, *et al.*, Phys. Lett. 89B, 418 (1980).
6. See for example, S. Brandt and H. D. Dahmen, Z. Phys. C1, 61 (1979).
7. H. Georgi, M. Machacek, Phys. Rev. Lett. 39, 1237 (1977).
8. A. De Rujula, J. Ellis, E. Floratos, M. Gaillard, Nucl. Phys. B138, 387 (1978).
9. San Lan Wu and Georg. Zobernig, Z. Phys., C2, 107 (1979).
10. See also, H. Daum, H. Meyer, J. Burger, Z. Phys. C8, 167 (1981); J. Dorfan, Z. Phys. C7, 349 (1981); and K. Lanius, DESY 80/36.
11. D. Cords, Proc. XXth Int. Conf. on High Energy Physics, Madison, Wisconsin, DESY 80/92.
12. TASSO, Phys. Lett. 94B, 437 (1980).
13. P. Söding, G. Wolf, Ann. Rev. Nucl. Sci. 31, 231 (1981). Data from TASSO, Phys. Lett. 86B, 243 (1979),
14. See C. H. Llewellyn Smith, Proc. XXth Int. Conf. on High Energy Physics, Madison, Wisconsin, p. 1345.
15. T. Appelquist, H. Politzer, Phys. Rev. Lett. 34, 43 (1975).
16. J. Ellis, I. Karliner, Nucl. Phys. B148, 141 (1979).
17. A. Bartl, SLAC-PUB-3163.
18. R. Ellis, D. Ross and A. Terrano, Nucl. Phys. B178, 421 (1981); J. Vermaseren, K. Gaemers and S. Oldham, Nucl. Phys. B187, 301 (1981).
19. K. Fabricius, G. Kramer, G. Schierholz and I. Schmitt, Z. Phys. C11, 315 (1981).
20. T. Gottschalk, Phys. Lett. 109B, 331 (1982).
21. A. De Rujula *et al.*, Nucl. Phys. B138, 387 (1978).
22. J. Schwinger, Phys. Rev. 82, 664 (1951).
23. For a more detailed discussion of the model parameters see: T. Sjöstrand, Comput. Phys. Commun. 28, 229 (1983) and Comput. Phys. Commun. 27, 243 (1982).
24. B. Andersson, G. Gustafson and T. Sjöstrand, Phys. Lett. 94B, 211 (1980).
25. H. J. Behrend *et al.*, Nucl. Phys. B218, 269 (1983).
26. W. Bartel *et al.*, Phys. Lett. 119B, 239 (1982).
27. B. Adeva *et al.*, Phys. Rev. Lett. 50, 2051 (1983).
28. Direct observation of η's indicates $\sim 0.7\,\eta$'s/event at 34 GeV, JADE, DESY 83-063, July 1983.
29. S. Cooper, LBL-11322, August 1980.
30. TASSO, Phys. Lett. 117B, 135 (1982).
31. TASSO, Phys. Lett. 100B, 357 (1981).
32. Ch. Berger *et al.*, Nucl. Phys. B214, 189 (1983).
33. R. Hollebeek, Int. Symp. on Lepton Photon Interaction at High Energy, Bonn, 1981.
34. C. Peterson, D. Schlatter, I. Schmitt and P. Zerwas, Phys. Rev. D27, 105 (1983).
35. J. Yelton *et al.*, Phys. Rev. Lett. 49, 430 (1982).
36. M. Nelson *et al.*, Phys. Rev. Lett. 50, 1542 (1983).
37. E. Fernandez *et al.*, Phys. Rev. Lett. 50, 2054 (1983).
38. W. Bartel *et al.*, Phys. Lett. 123B, 460 (1983).
39. W. Bartel *et al.*, DESY 82/086, Phys. Lett. 123B, 460 (1983).

40. San Lan Wu, DESY 83-007, February 1983.

41. W. Bartel *et al.*, DESY 83-063, July 1983.

42. H. Quinn, SLAC-PUB-3190, August 1983.

43. C. Basham, L. Brown, S. Ellis and S. Love, Phys. Rev. D17, 2298 (1978).

44. D. Richards, W. Stirling, and S. Ellis, Phys. Lett. 119B, 193 (1982); A. Ali and F. Barreiro, Phys. Lett. 118B, 155 (1982).

45. D. Richards, W. Stirling and S. Ellis, DAMTP 83/1.

46. D. Schlatter, *et al.*, Phys. Rev. Lett. 49, 521 (1982).

47. H. S. Behrend *et al.*, Z. Phys. C14, 95 (1982).

48. B. Adeva *et al.*, Phys. Rev. Lett. 50, 2051 (1983).

JET PRODUCTION IN HIGH ENERGY HADRON COLLISIONS

R. F. Schwitters
Department of Physics, Harvard University*/Fermilab†

INTRODUCTION

Over the past year or two, high energy physics has presented some remarkable images from experiments at the new CERN $S\bar{p}pS$ Collider. Much interest has been generated by the very rare W^{+-} and Z^0 events that were discovered in the CERN experiments, but there are hundreds of thousands of "ordinary" hadronic interactions, that appear quite remarkable when the charged particles are viewed in detectors such as UA-1, giving event pictures similar to the one shown in Fig. 1. A fraction of these events look even more remarkable when the angular distribution of the transverse energy (the energies of the particles in an event weighted by the sine of the respective production angles) is examined as in the event from the UA-2 detector that is shown in Fig. 2. In such events, a sizeable fraction of the available center of mass energy is confined in two narrow clusters that are approximately 180 degrees apart in azimuthal angle. These are the jets.

© R. Schwitters 1983

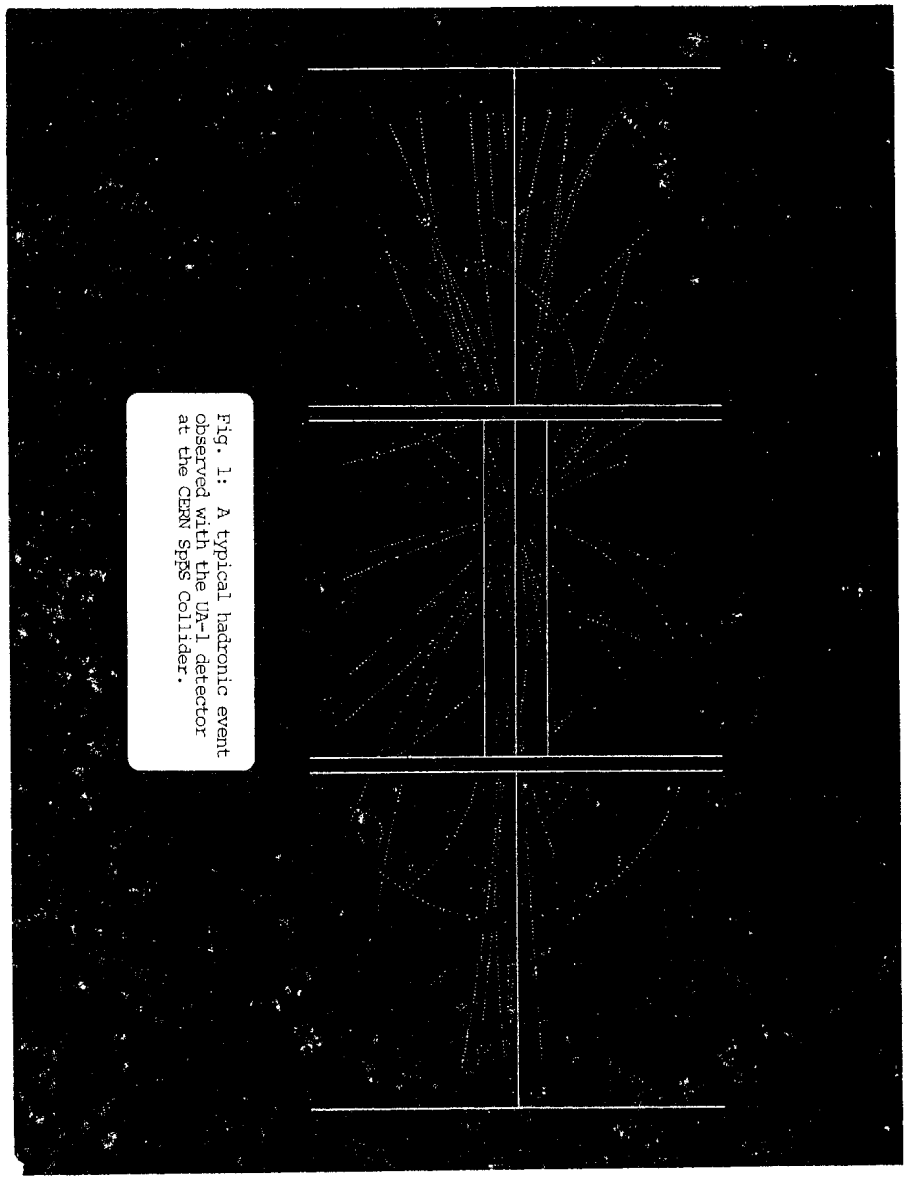


Fig. 1: A typical hadronic event observed with the UA-1 detector at the CERN SpPS Collider.

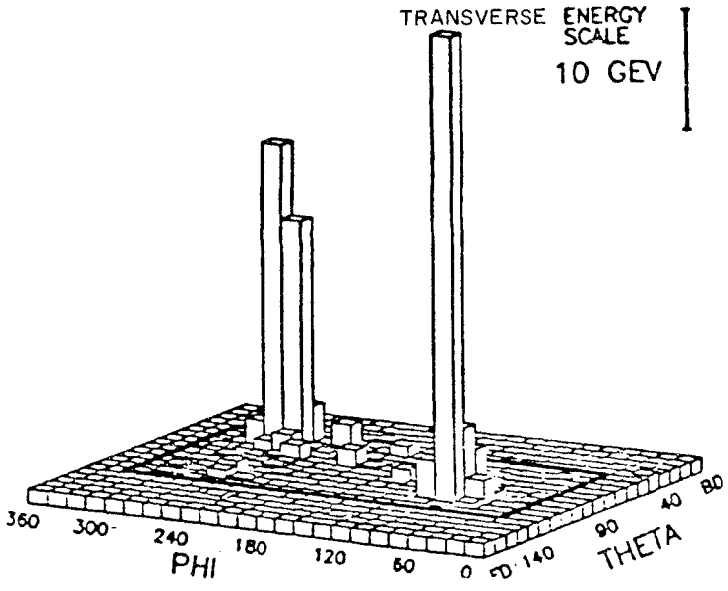


Fig. 2: Transverse energy deposited in UA-2 calorimeters for a jet event observed at the CERN SpPS Collider.

Studies of jets of hadrons at the CERN $Sp\bar{p}S$ Collider are revolutionizing our understanding of hadronic physics. The first, preliminary results indicate that jets may be relatively simple objects that can be treated as single particles for many purposes. This has obvious practical benefit for experimentalists who wish to study physics with high energy hadron colliders and is considered by many to be one of the most important early results to emerge from the CERN collider. Because of the very large rate of change of understanding that is taking place right now, it is inappropriate to present a complete review of what is now known about jets in hadron collisions. Rather, these lectures will attempt to provide a basis for understanding the new results as they become available.

The plan of these lectures is to first estimate what we might expect jets to look like in hadronic interactions. Then, some experimental questions related to detecting jets in high energy hadronic collisions are examined. Next, searches for jet behavior in fixed-target hadron experiments are reviewed. Finally, some of the new colliding beam experiments are described. Because this field is still in such an exploratory phase, the intent is to be qualitative; the days of detailed, quantitative comparisons with theory are in front of us.

The notion that jets of hadrons might play an important role in hadron interactions received wide attention in 1971 through the paper of Berman, Bjorken, and Kogut.[1] They applied the parton model ideas being developed for understanding deep inelastic electron scattering to the problem of high energy hadron collisions. The basic idea was that the partons inside nucleons, responsible for the "large", scaling cross sections in deep inelastic electron scattering, would undergo "hard" collisions with each other when hadrons collide, giving rise to relatively large rates of hadrons produced at large momenta transverse to the initial hadron direction. Shortly thereafter, the first "large-p_t" phenomena were reported by experiments running on the CERN ISR,[2] a set of intersecting storage rings providing proton-proton collisions up to about 63 GeV center of mass energy. Subsequently, reactions studied in fixed target experiments at the new 400 GeV Fermilab synchrotron and later at the CERN SPS were shown to have relatively large yields of hadrons and photons at large-p_t. These measurements were interpreted as arising from hard scattering of partons, but they did not provide a definitive proof of this picture. During this same period of time, the theory of quantum chromodynamics (QCD) superseded the parton

model to become the standard theoretical description of strong interactions.[3] In 1975, experiments at the SLAC electron-positron collider SPEAR[4] found that hadrons are produced in high energy electron-positron collisions as jets of particles emanating from spin-1/2 parton-like objects, presumably the quarks of QCD. Between 1973 and about 1980 many experiments were performed at Fermilab and the CERN SPS and ISR to test the validity of QCD by studying large-p_t yields of hadrons and searching for jets of hadrons. This large, important body of work has been reviewed extensively (Ref.2). By 1979, it had become apparent that there needed to be developed "jet" triggers for detecting all hadrons coming from a given parton because single particle yields were sufficiently remote from the underlying parton or quark distributions. The era of jet triggers began with fixed target experiments at Fermilab and the SPS operating at center of mass energies near 25 GeV. Improved detectors at the ISR were upgraded principally to add jet triggers for finding hadronic jet phenomena at center of mass energies up to 63 GeV. The large detectors at the $Sp\bar{p}S$ Collider, UA-1 and UA-2, were designed with triggers sensitive to jets produced in 540 GeV p-p collisions.

EXPECTATIONS FOR HIGH ENERGY HADRON COLLISIONS

The parton model picture of hadron production at large-p_t is extremely simple. The incident hadrons are viewed as collections of nearly free, low mass, point-like constituents that carry the initial hadron's momentum and energy. Hadrons are produced at large-p_t when a parton from one hadron suffers a hard collision with a parton in the second incident particle. A hard collision means that the two partons carry a large fraction of the initial energy and they scatter at large angles in their common center of momentum frame. After the hard collision, the scattered partons "dress" themselves into tight bundles or jets of hadrons that should retain information about the directions and energies of the parent partons. The unscattered partons continue in the directions of the initial hadrons and also dress themselves into jets of hadrons known as the target and projectile fragments. Thus the parton model predicts that large-p_t hadrons arise from events with four jets. Two of the jets are at large angles with respect to the incident direction, while the other two jets follow the initial hadron directions. The two large-p_t jets are not generally collinear because the rest frame of the scattered partons need not coincide with the center of mass frame

of the incident hadrons. The motion of this rest frame is, however, essentially along the direction of the initial hadrons and the large-p_t jets should be approximately coplanar.

This qualitative picture of large-p_t hadron production makes an important quantitative prediction, namely the scaling of single particle, inclusive cross sections. Because the partons have no intrinsic scale size, at p_t values larger than a few GeV/c (the scale of the nuclear force) the only relevant scale is given by p_t itself. Thus, the invariant single-particle inclusive cross section must have the following functional dependence on p_t:

$$E \frac{d\sigma}{d^3p} = \frac{1}{p_t^4} f(x_t, \cos\theta) \qquad (1)$$

where f is an unspecified function of the dimensionless quantities, x_t the fraction of the maximum possible p_t and the cosine of the production angle θ.

One of the most complete experimental tests of scaling is provided by the classic results on single π^0 production near 90 degrees at the ISR by the CCR group.[5] This experiment found some of the first evidence for large-p_t phenomena and has since collected data at center of mass energies $\sqrt{s}$ between 23 GeV and 63 GeV. A summary of their results is given in Fig. 3.

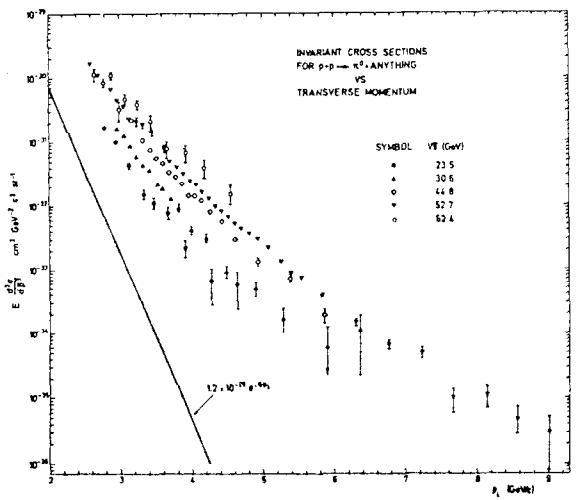


Fig. 3: Inclusive π^0 cross sections measured by the CCR collaboration (Ref.5) for various center of mass energies at the CERN ISR.

First note that the cross sections for $p_t > 3$ GeV are orders of magnitude larger than an exponential extrapolation of low-p_t data; this is what is called large-p_t production. A fit to these data using a scaling cross section where the power of p_t was allowed to vary gives an excellent description of all the data shown in Fig. 3. The fitted invariant cross section is:

$$E\frac{d\sigma}{d^3p}\Big|_{\pi^0} \propto p_t^{-(8.24\pm0.05)} \times \exp\left[-(26.1\pm0.5)x_t\right] \quad . \quad (2)$$

While these data exhibit a kind of scaling, they are in serious disagreement with the prediction of the simple parton model, Eq. (1).

Other experiments have attempted to observe the jets directly by examining the hadrons recoiling ("away-side" jet) against a large-p_t single particle ("trigger" particle). An example of this kind of study is shown in Fig. 4, where the phase-space density of charged particles in events where the trigger particle has a p_t in the range 3-4.5 GeV/c is plotted. These results are from the BFS Collaboration at the ISR.[6] No dramatic jet-like structures are evident in this kind of study. Indeed, it is often very difficult to disentangle possible structures arising simply from energy-momentum conservation from true multi-particle

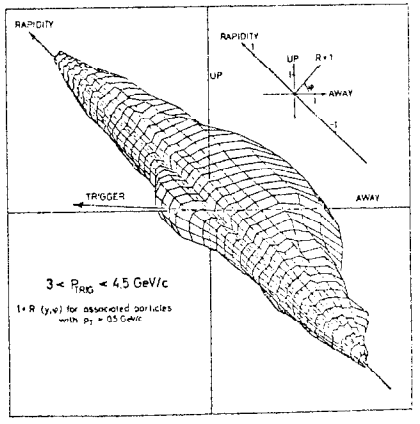


Fig. 4: Phase-space density for events triggered by a large p_t particle measured by the BFS collaboration (Ref. 6) at the ISR.

correlations such as jets.

The discrepancies between simple parton model predictions and observations of large-p_t hadron production are thought to arise from "QCD-effects". In QCD, we have a fundamental theory of hadrons and it is expected that several elementary sub-processes are involved in large-p_t phenomena. Some of these are: quark-quark scattering, quark-gluon scattering, gluon-gluon scattering, and quark-antiquark production by gluons. The physical picture of a hard scattering event is very much like the parton model, except for the color fields that connect the quarks or gluons participating in the hard collision with the other constituents of the initial hadrons. This complication is not expected to alter the expectation that for hard-enough collisions, a four-jet event structure should obtain, with two of the jets being nearly collinear with the original hadron direction and with the other two jets being coplanar and balancing transverse momentum. Furthermore, the individual jets should appear much like the jets seen in $e^+ e^-$ collisions, because the underlying fragmentation processes are expected to be similar.

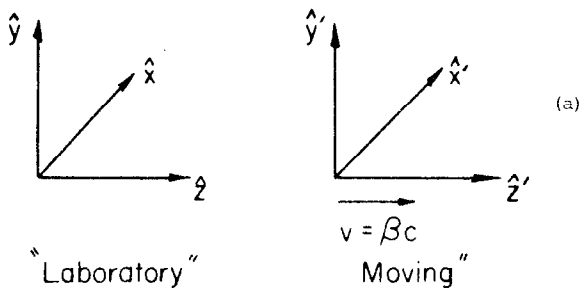
More quantitative tests of QCD are made involving single particle spectra, two-particle correlations, etc.; these tests are summarized in References 2,7. To estimate fragmentation of gluons and quarks to hadrons and other so-called non-pertubative effects, elaborate Monte Carlo programs have been written.[8] These involve fitting parameters to data in combination with the predicted behavior of the elementary subprocesses. A survey of these tests of QCD is beyond the scope of these lectures, but in general, rather satisfactory agreement exists. The main question remains, however: Are there really jets produced in hadron collisions and, if so, can they be used to find new physics?

KINEMATICS

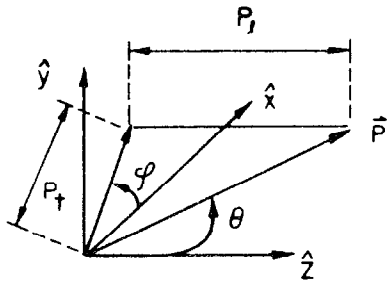
Before proceeding, we shall digress into kinematics to find convenient variables for describing high energy hadron collisions. Consider a Lorentz transformation between the laboratory frame and a frame moving along the z-axis with speed βc as indicated in Fig. 5a. The usual Lorentz transformation is given by:

$$\begin{pmatrix} t \\ z \end{pmatrix} = \begin{pmatrix} \gamma & \gamma\beta \\ \gamma\beta & \gamma \end{pmatrix} \begin{pmatrix} t' \\ z' \end{pmatrix} \qquad \gamma = \frac{1}{\sqrt{1-\beta^2}} \ . \tag{3}$$

It is usually very convenient to transform to "light-cone" variables, t+z and t-z. With these variables, the Lorentz transformation is written:



(a)



(b)

Fig. 5: a) Definition of Lorentz frames. b) Definition of momentum components and angles.

$$\begin{pmatrix} t+z \\ t-z \end{pmatrix} = \begin{bmatrix} \gamma(1+\beta) & 0 \\ 0 & \gamma(1-\beta) \end{bmatrix} \begin{pmatrix} t'+z' \\ t'-z' \end{pmatrix} . \qquad (4)$$

The "rapidity" y is defined by:

$$y = \frac{1}{2} \ln\left(\frac{1+\beta}{1-\beta}\right) . \qquad (5)$$

With this definition of the rapidity, the Lorentz transformation for light-cone variables becomes:

$$\begin{pmatrix} t+z \\ t-z \end{pmatrix} = \begin{pmatrix} e^{y} & 0 \\ 0 & e^{-y} \end{pmatrix} \begin{pmatrix} t'+z' \\ t'-z' \end{pmatrix} . \qquad (6)$$

In addition to the diagonal form, this representation has the advantage that for successive Lorentz transformations along the same axis, the rapidities add.

Fig. 5b shows the momentum vector of some particle in the laboratory frame and indicates its transverse and longitudinal components, p_t and p_l, as well as the polar and azimuthal angles, θ, ϕ. Rather than using (p_l, p_t, ϕ) or (p, θ, ϕ) to describe the particle, it is often convenient to use the rapidity y of the particular frame where $p_l = 0$ as the longitudinal variable. Application of a Lorentz transformation from the $p_l = 0$ frame to the laboratory frame gives the following relation between y and the laboratory frame

energy E and longitudinal momentum:

$$y = \frac{1}{2} \ln\left(\frac{E+p_l}{E-p_l}\right) . \qquad (7)$$

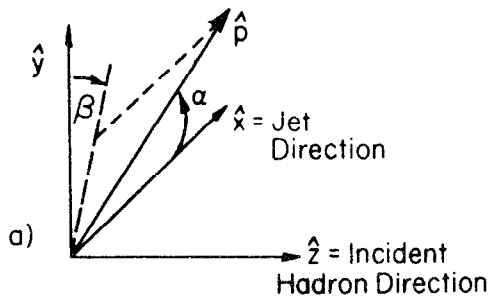
In the limit where $E >> m$, the particle's rest mass, this expression can be simplified to read:

$$y \simeq \ln(\cot \theta/2) \qquad (8)$$

$$E \simeq \frac{1}{2} e^y \sqrt{m^2+p_t^2} .$$

Why should we bother with this variable rapidity? As the previous expression indicates, y can be determined for high energy particles by just measuring angles. Furthermore, the geometry of particle momenta in y-ϕ space is quite simple. Near 90 degrees, y-ϕ space and θ-ϕ space are very similar, but at small angles, y-ϕ space becomes very distorted with respect to θ-ϕ space. Finally, y is a very simple phase-space variable.

To see how rapidity can provide a very simple and convenient description of relativistic particles in jets, consider a jet produced at 90 degrees such that its principal axis is along the x-axis as depicted in Fig. 6a. We have not yet defined precisely what is a jet, but for this exercise it is sufficient to treat



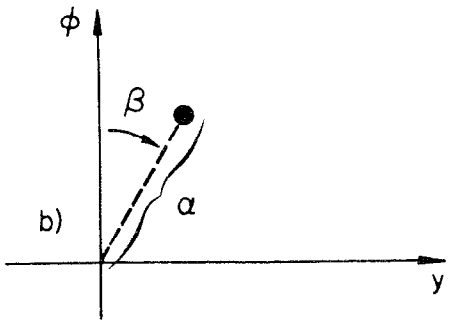


Fig. 6: a) Definition of angles relative to the jet axis, b) Coordinate of a particle on y-ϕ plot.

the jet axis as some preferred direction about which one measures the momenta and directions of high energy particles. Suppose a relativistic particle in the jet has momentum $\hat{p}$ and polar angle α with repect to the jet axis. The azimuthal angle in the y-z plane measured from the y-axis is β. These quantities are indicated in Fig. 6a. In this discussion, it is assumed that $\alpha<<1$. In terms of the usual laboratory frame variables, y, ϕ, and p_t, this particle has coordinates,

$$y = \alpha\sin\beta \ , \ \phi = \alpha\cos\beta \ , \ p_t = \hat{p}.$$

The coordinates of this particle can be plotted as a point in y-ϕ space as shown in Fig. 6b. The point is at a radius α from the origin and is rotated by β from the ϕ axis. Now we can see the usefulness of this parameterization: if the initial jet axis was produced at some arbitrary rapidity and azimuth, y_0-ϕ_0, then the coordinates of the observed prong would simply be translated by y_0, ϕ_0 in the y-ϕ plane. The third independent variable, p_t, is invariant to translations in the y-ϕ plane.

These points bear repeating: the particles associated with jets are conveniently described in a reference frame, where the net longitudinal momentum of the jet system is zero. If the original hadrons collide along the z-axis, the jet system is described with respect to the x-axis of a frame moving along the initial hadron direction at a velocity such that the net z component of momentum of the jet system is zero. To take an extreme example, if all the particles associated with the jet fell on a cone of half-angle α with respect to the jet axis, then their coordinates plotted on the laboratory y-ϕ plane would fall on a circle of radius α. The center of this circle would correspond to the rapidity and azimuth of the jet and the transverse momenta of the particles would equal the momenta of the particles in the jet frame. Following the earlier discussion, the polar angle α of particles with respect to the jet axis can be written in terms of the equivalent rapidity with respect to the jet axis, $\hat{y}$. For relativistic particles near the jet axis, the approximate relationship is:

$$\alpha \simeq 2 \exp(-\hat{y}). \qquad (9)$$

Regardless of the precise definition of jets, we see that if particles in high energy hadron collisions tend to cluster about some preferred axis, then the particles will show up as a cluster in y-ϕ space. The centroid of the observed cluster is directly related to the direction of the preferred axis and the size of the cluster in y-ϕ space is a measure of the tightness of the clustering in the jet reference frame.

For completeness, we note that the invariant phase space element can be written as:

$$\frac{d^3p}{E} = \frac{1}{2}\, d\phi\, dp_t^2\, dy\ . \qquad (10)$$

Therefore, the Lorentz-invariant single-particle inclusive cross section is given by:

$$E\,\frac{d\sigma}{d^3p} = \frac{1}{\pi}\,\frac{d\sigma}{dy\, dp_t^2} \qquad (11)$$

where it is assumed that one is always dealing with cylindrically symmetric systems. This form is particularly useful because in many cases of interest, the inclusive cross section factors approximately into a product of a function of y and a function of p_t. The distribution function in y is usually relatively smooth and broad, while p_t distributions are usually rapidly falling functions. This general behavior is characteristic of wide classes of multihadronic systems and reflects the strong correlations imposed by energy-momentum conservation, as well as the underlying dynamics of the particular system. Examples of these distribution functions for quite different physical systems are given in Figures 7-10. In the case of hadron jet production by $e^+ e^-$ annihilation,[9] Figs. 7 and 8, y and p_t are measured with respect to the jet

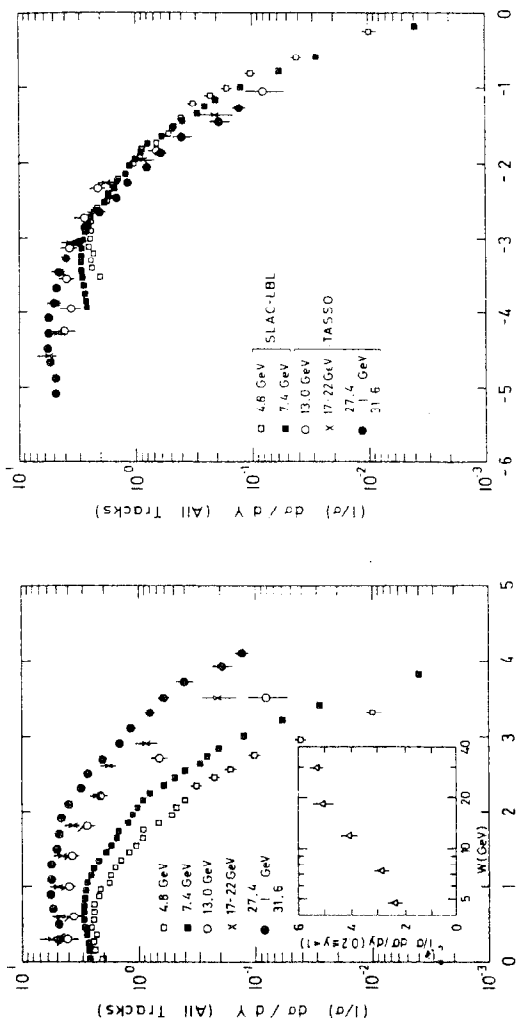


Fig. 7: Rapidity distributions for charged hadrons from e^+e^- jets.

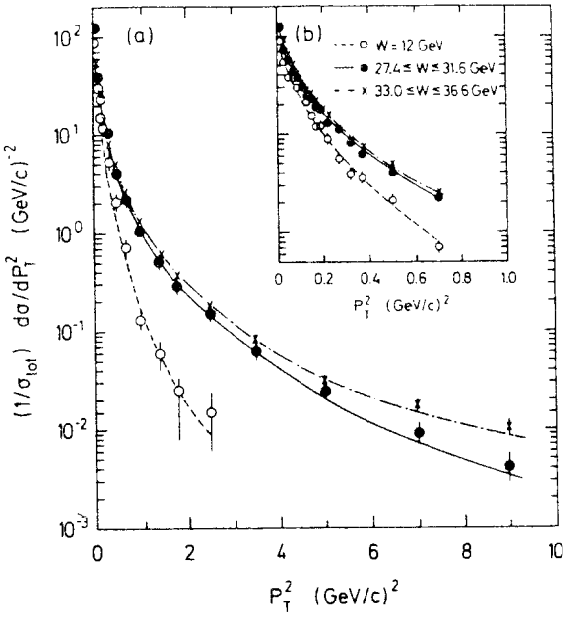


Fig. 8: Transverse momentum distribution for charged hadrons from e^+e^- jets.

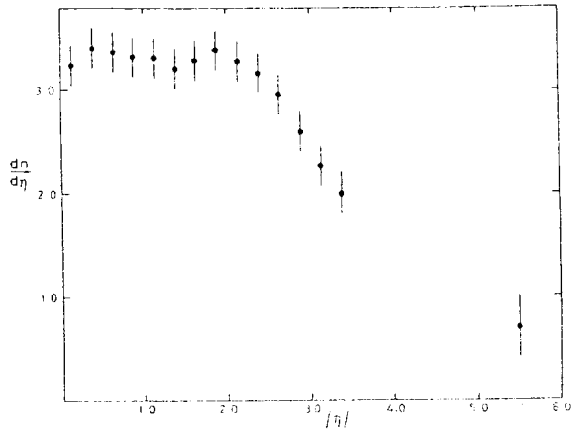
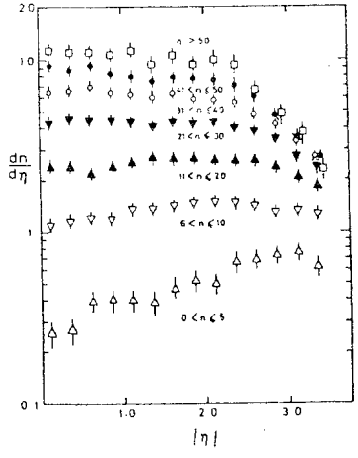
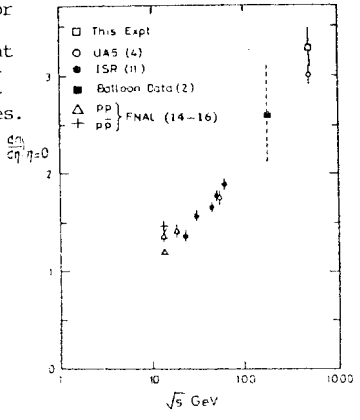


Fig. 9: Rapidity distributions for hadrons produced in the CERN $S\bar{p}pS$ Collider at $\sqrt{s}$=540 GeV. The plot at the lower left gives rapidity distributions for events with different charged particle multiplicities.





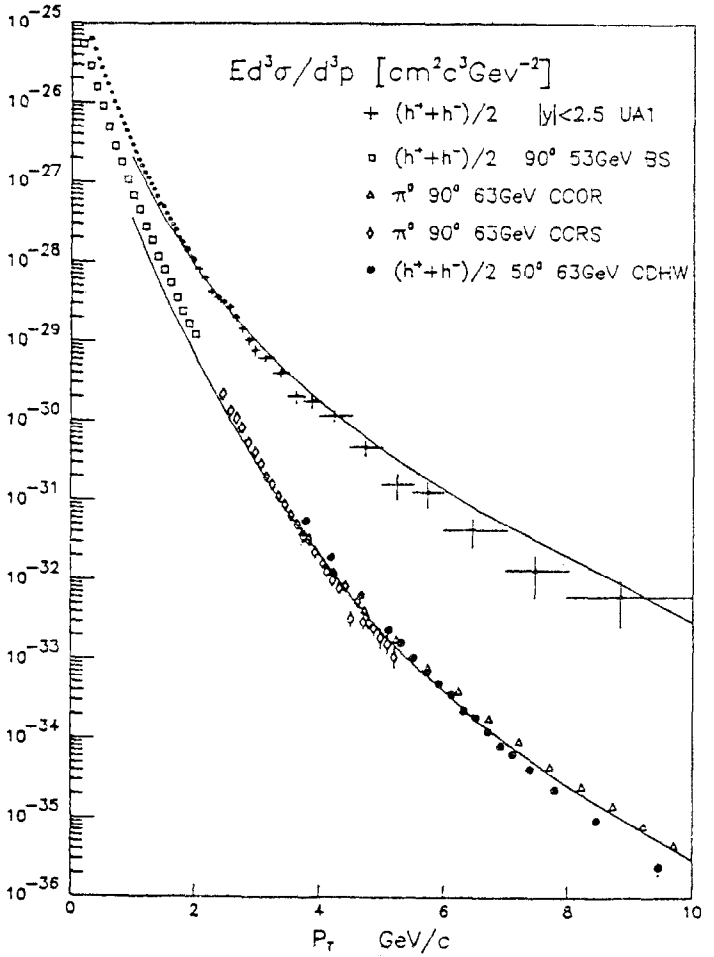


Fig. 10: Transverse momentum distribution for hadrons produced at the $Sp\bar{p}S$ Collider and at the ISR.

axis of the events. Representative distributions for "minimum-bias" events in hadron-hadron collisions[10,7] are presented in Figs. 9, 10. The term minimum-bias loosely refers to the entire inelastic cross section for a given reaction.

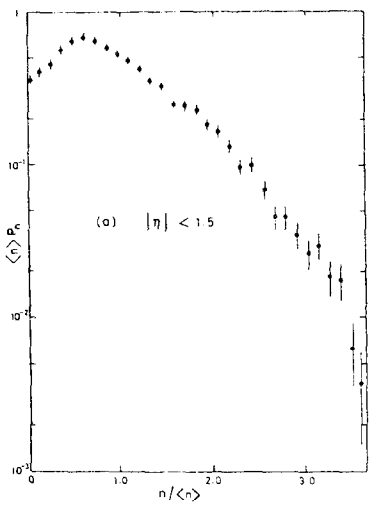
As discussed above, measurements of single particle spectra in hadron collisions have seen evidence for large-p_t phenomena that are most likely due to hard collisions between the constituents of hadrons, but they have not given an incisive picture of the underlying structure and forces. This is because a single large-p_t particle is expected to carry a variable fraction of the parent parton (quark or gluon in the language of QCD) momentum in a direction that may not coincide with the parton direction. In addition, the energy and momentum of a large-p_t particle must be balanced by the other particles in the event which gives rise to multiparticle correlations that may confuse the interpretation of these events. The way around these problems is to try to measure all the particles in hadronic events and to attempt to assign them to jets. This approach presents new experimental challenges that will be discussed next.

EXPERIMENTAL QUESTIONS

The goal of detecting as many of the particles as possible in hadronic collisions and assigning them to jets makes many difficult demands on the experimental apparatus. The most obvious requirement is the need for large solid angle acceptance. Essentially 4π coverage is required. In fixed-target experiments, large fractions of the center of mass solid angle can be covered by relatively simple walls of detectors because of the relativistic transformations to the laboratory frame. Detectors for colliding beam experiments must be built to cover as much of the full laboratory solid angle as possible. As we shall see, kinematic limits for hadron reactions of interest can stretch to several units of rapidity which translates to a need for detecting particles at angles of order one degree or less in existing or planned hadron colliders.

Detectors for measuring jet behavior must be capable of handling very large multiplicities of charged and neutral particles. For example, the UA-5 experiment[11] at the CERN $Sp\bar{p}S$ Collider measures a mean charged multiplicity of approximately 27 particles. Presumably, there is a similar number of neutral particles in these events. Experimental difficulties may also arise from the fact that there are very large, non-Poisson, fluctuations in the multiplicity distribution. This effect is related to KNO scaling which is indicated by the CERN $Sp\bar{p}S$ Collider data[10] shown in Fig. 11. This effect means that to a good approximation the multiplicity distribution in hadron collisions is a universal function of the observed multiplicity relative to its mean value for a wide range of center of mass energies.

The only practical means for detecting all these particles is to use fine-grained calorimeters. The calorimeters must be capable of measuring energies of photons and both charged and neutral hadrons with good spatial resolution and energy resolution so that clusters of particles arising from jets will be seen. A common method for achieving good spatial resolution is by dividing the calorimeters into subunits called towers. Figure 12 shows one tower of the UA-2 calorimeter system.[12] As is done in several detectors, the UA-2 group chose to divide their calorimeter system in depth with a lead-scintillator shower counter in the front, followed by an iron-scintillator hadron calorimeter which is sampled over two regions in depth. The front shower counter responds mainly to photons and electrons, while hadrons shower through the full depth of the calorimeter. In UA-2, 200 of these towers, each



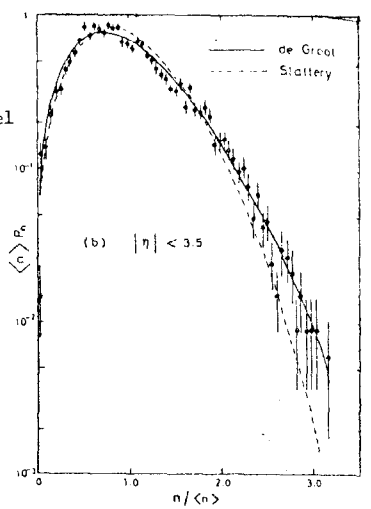


Fig. 11: Observed multiplicity distributions plotted in KNO scaling variables for two different ranges of rapidity. The curves through the data are model fits (see Ref.10).

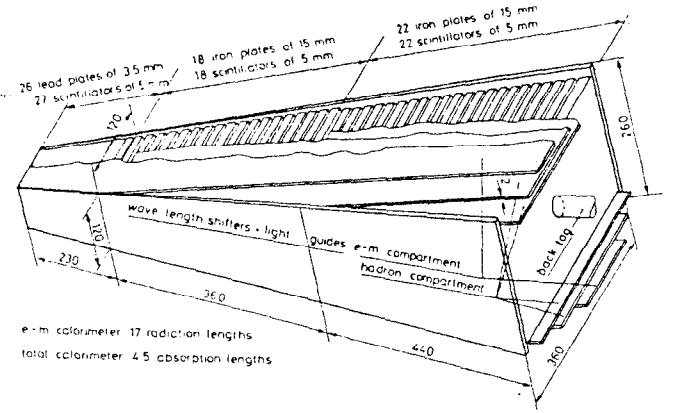


Fig. 12: Exploded view of a UA-2 central calorimeter tower.

covering 10 degrees in θ by 15 degrees in ϕ, are packed together to make up the major part of their detector for jet studies.

One of the simplest calorimetric detectors for jet experiments was used at Fermilab[13] and is shown in Fig. 13. This is a calorimeter wall for fixed target measurements. One of the largest calorimeter systems planned is for the CDF detector[14] being built to study 2 TeV $p-\bar{p}$ collisions at Fermilab. This device, shown in Fig. 14, will cover the range $-4<y<4$ with towers of electromagnetic shower counters and hadron calorimeters employing various technologies depending on angular region. The towers in CDF will occupy 0.1 units of rapidity and approximately 5 degrees in azimuth.

Calorimeters are not capable of making perfect measurements of energy flow in hadronic events. Typical shower counter resolutions are of order, $\delta E/E \sim 15\%-20\%/\sqrt{E}$ where E is expressed in GeV. Most hadron calorimeters have energy resolutions in the range:

$$\delta E/E \sim 60\%-100\%/\sqrt{E}.$$

The best sampling calorimeter for measuring hadron energy flow uses uranium plates in an experiment using the Axial Field Spectrometer[15] at the ISR. The energy resolution of this device is almost a factor of two

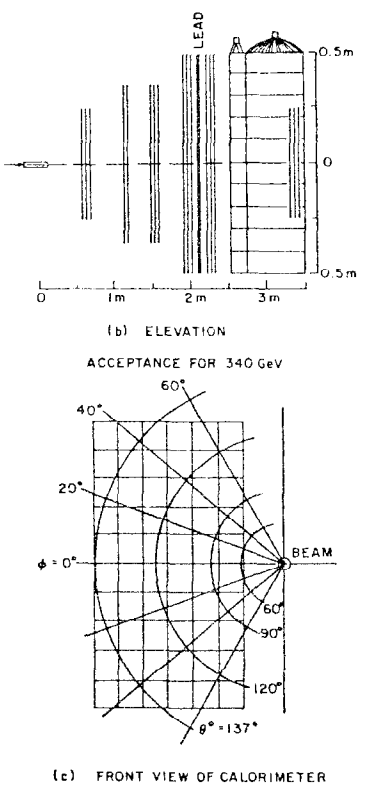


Fig. 13: Calorimeter for early Fermilab fixed target jet experiment (Ref.13). Curves give center-of-mass polar angle acceptance.

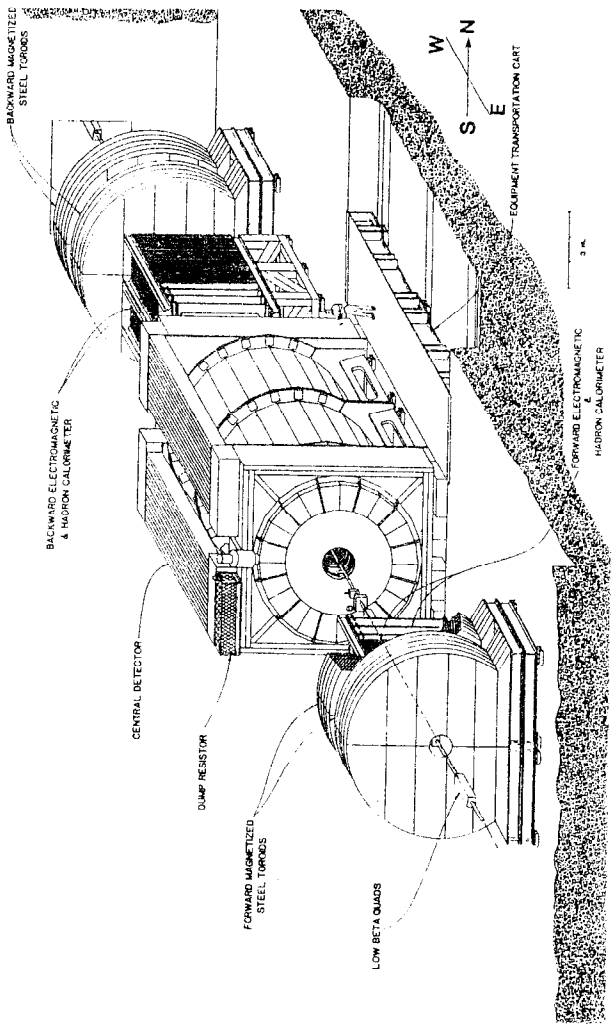


Fig. 14: Isometric drawing of the CDF detector being built for Fermilab Tevatron Collider.

better than the best hadron calorimeters employing iron plates.

Beyond questions of energy resolution, these calorimetric detectors may introduce systematic uncertainties because their response may be different depending on the type of incident hadron. Significant energy can leak out the back of hadron calorimeters, another source of systematic errors. Calibrating these devices is a major undertaking. The basic problem is that there are virtually no "standard candles" naturally available in hadron collisions for calibrating the calorimeters. Thus, one must provide redundant means for maintaining the calibration. Examples are to use radioactive sources, standard light flashing or charge injection systems, and muons penetrating the calorimeters. Usually, the experimenters try to make a direct calibration by measuring all of the calorimeter units in test beams and transferring the calibrations with some of the methods just described. Generally, one is doing very well if the shower counters can be calibrated with systematic errors less than about 2%. Hadron calorimeter systems usually have somewhat larger systematic uncertainties.

Another problem encountered in hadron jet experiments is the large event rate. Total cross sections are large and experiments must use restrictive triggers to reduce event rates to manageable levels. In many cases, more than one interaction may occur during the resolving time of the detector. It is clearly important to find reliable ways to eliminate multiple interactions as they could easily bias the results. An example of pile-up is shown in Fig. 15 for the COR experiment[16] at the ISR. The multiple-event background can easily dominate the rate for single good events.

THE FIXED TARGET EXPERIMENTS

The first detectors equipped with jet triggers looking for jet production in hadron collisions were designed for fixed target experiments run at Fermilab in the late 1970's in a variety of hadron beams. The experiment of V. Cook et al.[13] used a "1/2-wall" array of calorimeters and studied p-p collisions at beam energies between 100 and 340 GeV. C. Bromberg et al.[17] used two small calorimeters and magnetic analysis for measurements at 130 and 200 GeV in a variety of hadron beams. M. D. Corcoran et al.[18] published results from a two-arm calorimeter experiment run at 130 GeV and 200 GeV with pions and protons. The most

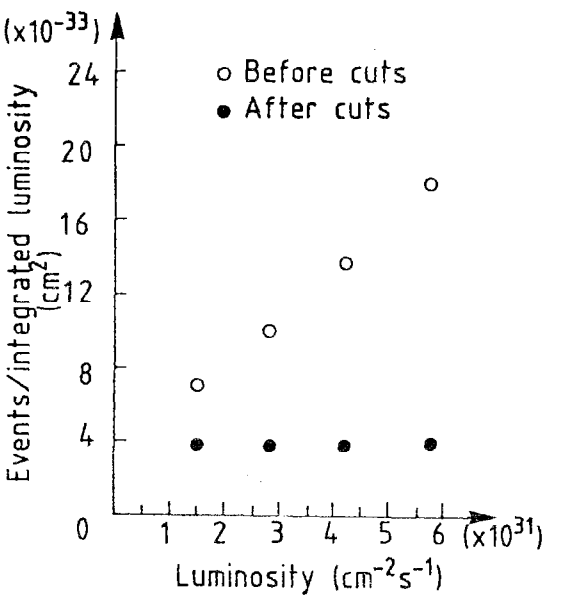


Fig. 15: Normalized event rate vs luminosity for the COR experiment at the ISR showing pile-up effects.

significant result of these early experiments was the observation of substantially larger cross sections for multiparticle transverse energy flow as compared to single particle production at the same value of transverse momentum or energy. The multiparticle cross sections were typically two orders of magnitude larger than the corresponding single particle cross sections. No conclusive evidence for jet production was uncovered by these experiments.

Following this first round of fixed target jet experiments, second generation experiments were performed at Fermilab and CERN using improved detectors. The Fermilab experiments were called E557[19] and E609[20] and they were run at 400 GeV which corresponds to 27 GeV center of mass energy; the CERN experiment was NA-5[21] and it studied 150 GeV and 300 GeV p-p and π-p collisions. The NA-5 apparatus is shown in Fig. 16. The major component is a cylindrical calorimeter wall consisting of 240 towers that have lead-scintillator shower counters followed by iron-scintillator hadron calorimeters. The acceptance of each tower is 9 degrees in center of mass polar angle by 15 degrees in azimuth. The complete acceptance is $-0.88 < y < 0.67$ and 2π radians in ϕ.

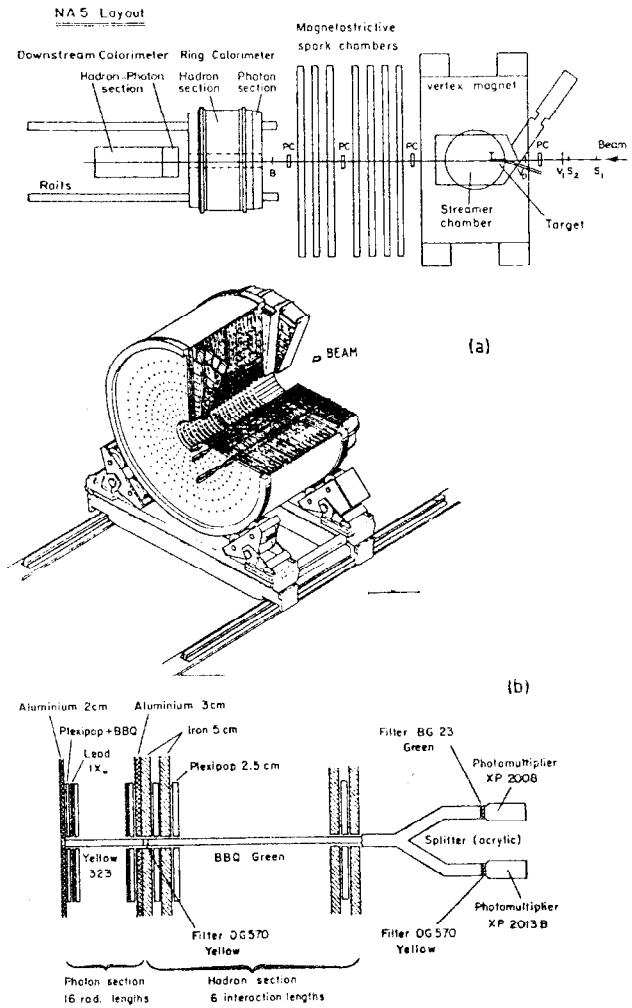


Fig. 16: Apparatus used for the NA-5 fixed target jet experiment.

The energies measured by the towers were weighted in proportion to their radius and summed, giving the total transverse energy of events. Separate triggers were formed using different azimuthal regions of the calorimeter. One trigger was based on the full azimuthal acceptance. The second trigger summed the transverse energy for two opposite azimuthal quadrants of the calorimeter. The third trigger summed the transverse energy for just one azimuthal quadrant. In a highly exaggerated jet picture where just two coplanar, very highly collimated jets give rise to all the transverse energy, one would expect the first trigger to have twice the rate of the second trigger and both the second and third triggers would count the same rate.

Differential cross sections in transverse energy measured by NA-5 for these three trigger conditions are shown in Fig. 17. At a given value of E_t, the cross sections for the different triggers differ by several orders of magnitude, in contradiction to the simplest jet picture. Furthermore, there is no evidence of a large-E_t tail that might indicate some kind of new jet processes in these data. Indeed, as the solid curves drawn in Fig. 17 indicate, a reasonable model of the beam jets associated with the initial hadron fragments are sufficient to describe these data. The

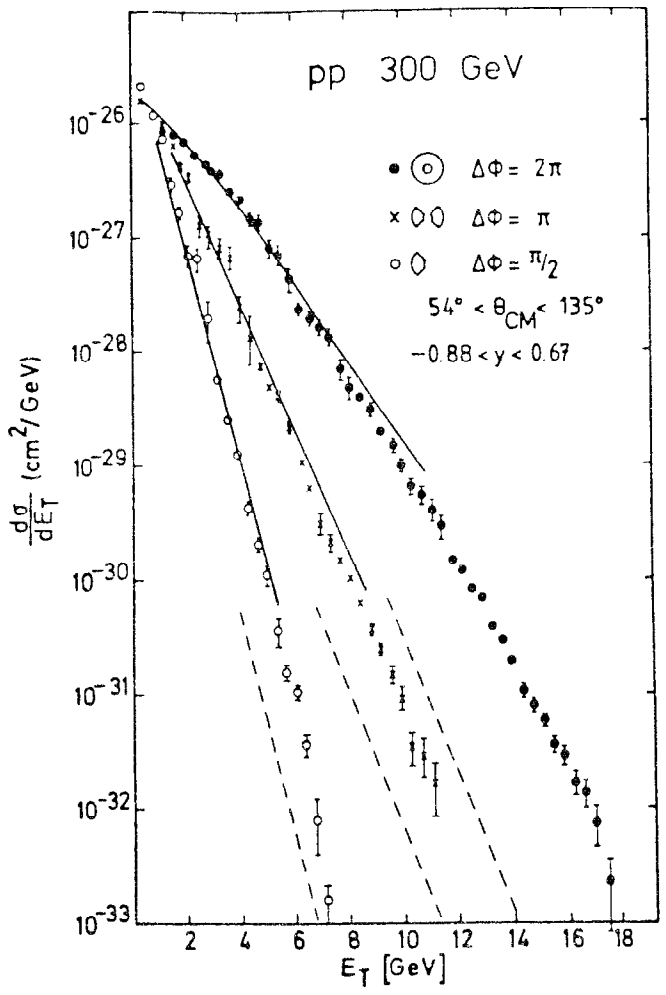


Fig. 17: Transverse energy distributions for different trigger configurations in the NA-5 experiment. Solid and dashed curves described in text.

contributions due to the hard scattering of partons expected from QCD are indicated by the dashed lines on the figure and these are well below the data, presumably swamped by the spectator or beam jets.

To search for coplanar structure in these events, the NA-5 group computed a quantity P, the planarity, for each event. P is defined by:

$$P = \frac{\Sigma\, p_{t\ in}^2 - \Sigma\, p_{t\ out}^2}{\Sigma\, p_{t\ in}^2 + \Sigma\, p_{t\ out}^2} \qquad (12)$$

where the summations are over the squares of the components of the transverse energy measured by the calorimeter towers relative to an orthogonal set of axes, the "in"-"out" axes, in the transverse plane. The orientation of the in-out axes is chosen to maximize P. A jet-like event will have P near 1, while an azimuthally symmetric event will have P=0. Planarity distributions for different values of E_t are given in Fig. 18. There is no dramatic shift toward jet-like events in these distributions.

Experiments E557 and E609 give results that are completely consistent with the NA-5 results, although E609 claims to have isolated a small jet component in the planarity distributions at large E_t. A small jet component is not ruled out by any of the experiments. The lack of a clear jet signal in these fixed target

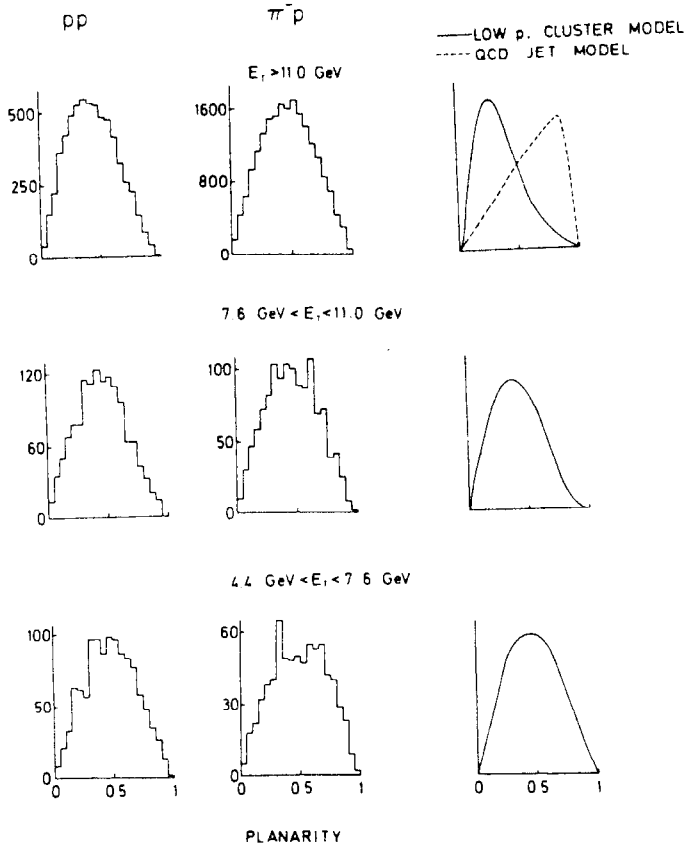


Fig. 18: Planarity distributions from NA-5 measurements for different values of transverse energy and incident hadron type. The right-hand column gives calculated planarities for two different models.

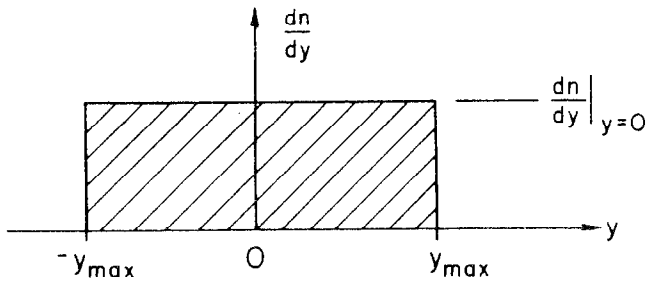
experiments poses several questions: Should we have seen jets in these experiments? If not, under what conditions can we expect to see convincing evidence for jets in hadron collisions?

A SIMPLE-MINDED JET MODEL

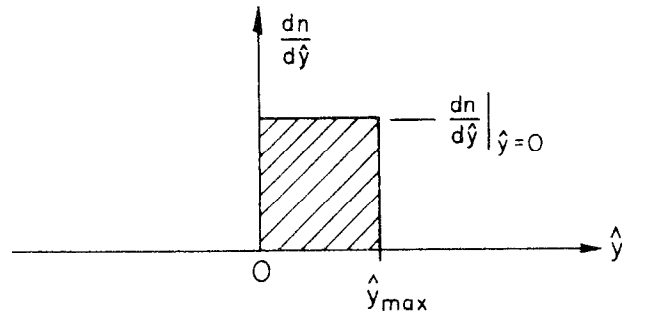
To gain an intuitive understanding of what jets might look like in hadronic interactions, we shall develop a simple analytical jet model based on the average behavior of minimum-bias hadronic events to simulate beam jets and the average behavior of jets produced by $e^+ e^-$ annihilation for modeling the parton jets. The basic picture is that the events should show a 4-jet structure with two beam jets along the initial hadron directions and two parton jets that are coplanar, conserving transverse momentum. We imagine plotting all the particles in an event on a y-ϕ plot and looking for the parton jets as dense clusters in the number of particles or transverse energy in this space, relative to the density of particles or transverse energy coming from the beam jets.

The fragmentation of both kinds of jets is assumed to be described by some steeply falling function of p_t relative to the jet axis and a flat rapidity distribution up to some maximum value of rapidity set by energy conservation. These rapidity distributions are indicated schematically in Fig. 19. The densities of particles per unit rapidity and mean values of transverse momentum for both types of jets are found empirically from the minimum-bias and $e^+ e^-$ jet data shown in Figs. 7-10.

For describing the parton jets, we shall estimate the opening angle of the cone that contains one-half the prongs in the jet. As discussed in the section on kinematics, when transformed to the laboratory frame, this cone will form a circle in y-ϕ space that also contains one-half the jet particles, but more than one-half the transverse energy of the jet. This cone angle is easily found: it corresponds to the median rapidity of the particles associated with the parton jet in the jet reference frame (the x-axis of Fig. 6). But, in this simple model where the rapidity distribution is a box, the median rapidity is one-half the maximum rapidity. Finally, the maximum value of rapidity for both types of jets is related to the mean transverse momentum per particle and the rapidity distribution by energy conservation. The total energy of the beam jets is approximated by the center of mass energy of the hadron collision, $\sqrt{s}$. The transverse energy of each parton jet is called E.



a) Beam Jets



b) Parton Jets

Fig. 19: Rapidity distributions assumed for beam jets and parton jets in the "simple-minded" jet model.

From very crude "eyeball" fits of the data in Figs. 7-10, we find that the mean transverse momentum per particle in both the beam jets and parton jets is 1/2 GeV. It is also assumed that one-half the particles are charged and one-half are neutral in both kinds of jets. The rapidity density of particles in the beam jets is numerically equal to $\ln\sqrt{s}$; that of the parton jets is 4 lnE. In all these expressions and those following, $\sqrt{s}$ and E are to be evaluated in units of GeV.

From this information, the model gives the maximum rapidity for the beam jet particles as:

$$y_{max} = \ln\left(\frac{2\sqrt{s}}{\ln\sqrt{s}}\right). \qquad (13)$$

Note that strictly speaking this model does not conserve energy because the parton jet energy is not subtracted from the beam jets. The polar angle of the cone containing one-half the jet particles, which is also the radius of the median circle on y-ϕ plot is given by:

$$\theta_{1/2} = 2\sqrt{\frac{\ln E}{E}}. \qquad (14)$$

The mean number of charged particles in the two beam jets is:

$$n_b = \ln \sqrt{s} \times \ln\left(\frac{2\sqrt{s}}{\ln \sqrt{s}}\right) \qquad (15)$$

and the mean number of charged particles per parton jet is:

$$n_p = 2 \ln E \times \ln\left(\frac{E}{\ln E}\right). \qquad (16)$$

Numerical results from this simple-minded jet model are summarized in the following tables:

The Beam Jets

$\sqrt{s}$ (GeV)	y_{max}	$\langle E_t \rangle$ (GeV)	Density of charged particles per unit y-ϕ
25	2.7	8.8	0.26
63	3.4	14	0.33
540	5.1	32	0.50

The Parton Jets

E_t per jet (GeV)	$\theta_{1/2}$	E_t inside $\theta_{1/2}$ (GeV)	Density of charged particles inside $\theta_{1/2}$ per unit y-ϕ
5	1.1	2.5	0.47
10	0.96	5.0	1.17
20	0.77	12.	3.1
40	0.61	28.	7.5

The striking thing about these numbers is the dramatic increase in the particle density per unit y-ϕ bin for parton jets with transverse energies above about 20 GeV. The density of particles in the lower energy parton jets are not too dissimilar from the beam jets. Thus, the jets that could be produced at fixed target energies do not contribute significantly larger charged particle densities or transverse energy over the normal minimum-bias events. At ISR energies, the parton jets should become visible. For example, two parton jets of 15-20 GeV transverse energy each will contribute approximately 16-24 GeV of transverse energy in clusters along with the transverse energy of the beam jets, giving a total E_t of roughly 30 GeV. The charged particle density in the jet clusters in these events is almost an order of magnitude larger than that in minimum bias events. Jets should become clear by ISR energies and spectacular by Sp$\bar{p}$S energies. This behavior is indicated schematically in Fig. 20.

EXPERIMENTS WITH COLLIDING BEAMS

The most extensive measurements of jet production at the ISR have been made by the Axial Field Spectrometer and reported in a series of papers by T. Åkesson et al.[22] A schematic drawing of the AFS is shown in Fig. 21. It consists of a solenoid magnetic

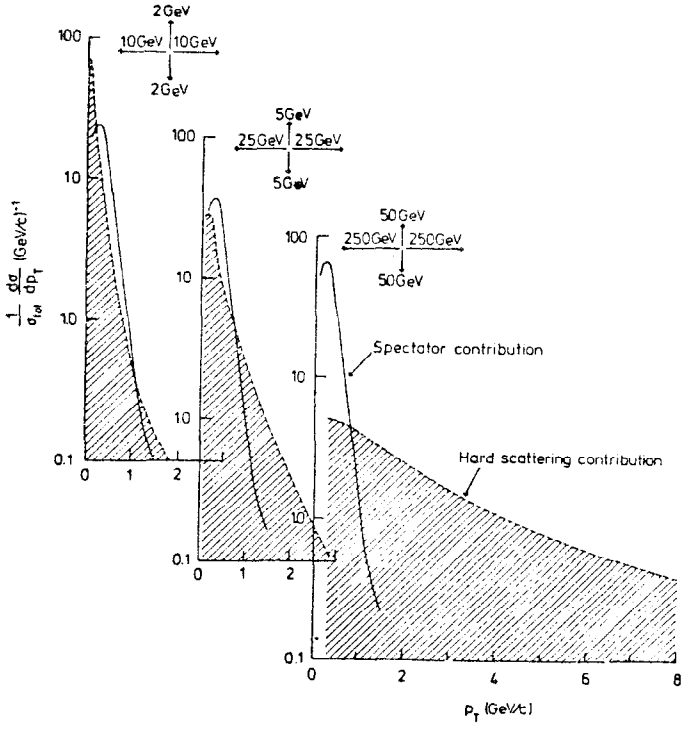


Fig. 20: Schematic representation of the relative contributions to large p_t production by beam and parton jets at c.m. energies of 25, 60, and 600 GeV (from Ref. 7).

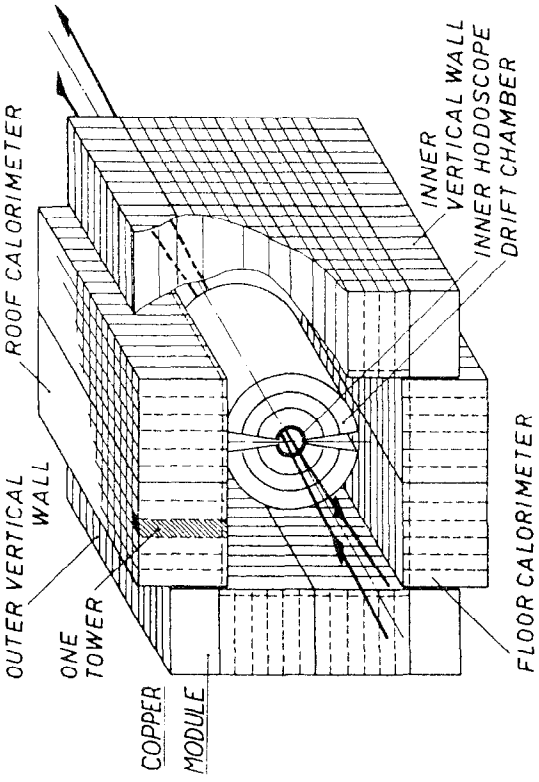


Fig. 21: Schematic drawing of the AFS detector at the ISR.

tracking detector surrounded by walls of fine-grained calorimeters arranged in a tower geometry. The calorimeters employ uranium and copper plates and have excellent energy resolution. The acceptance is approximately ±1 unit of rapidity and 2π radians in ϕ. Triggers weighted by transverse energy are available.

Some of the earlier measurements using a partial calorimeter were consistent with QCD jet production and the most recent data with the full calorimeter system give convincing evidence for jets. The observed transverse energy distribution from the AFS operating with the full calorimetry is given in Fig. 22. The data extend to E_t values beyond 40 GeV, but the distribution is steeply falling with no obvious structure. To look for planar event structure, the group plots a quantity called Circularity, C, which is just 1 - Planarity as defined by Equation 12. Jets should show up with small values of C. The AFS measurements of Circularity are plotted in Fig. 23 for various values of the observed transverse energy and center of mass energy. For $E_t > 25$ GeV, there is a distinct shift to lower values of C. This effect is seen more clearly in Fig. 24a where the mean value of C drops significantly beyond E_t 25 GeV, but it shows very little variation with center of mass energy. Notice that the data at the lowest c.m. energy, 30

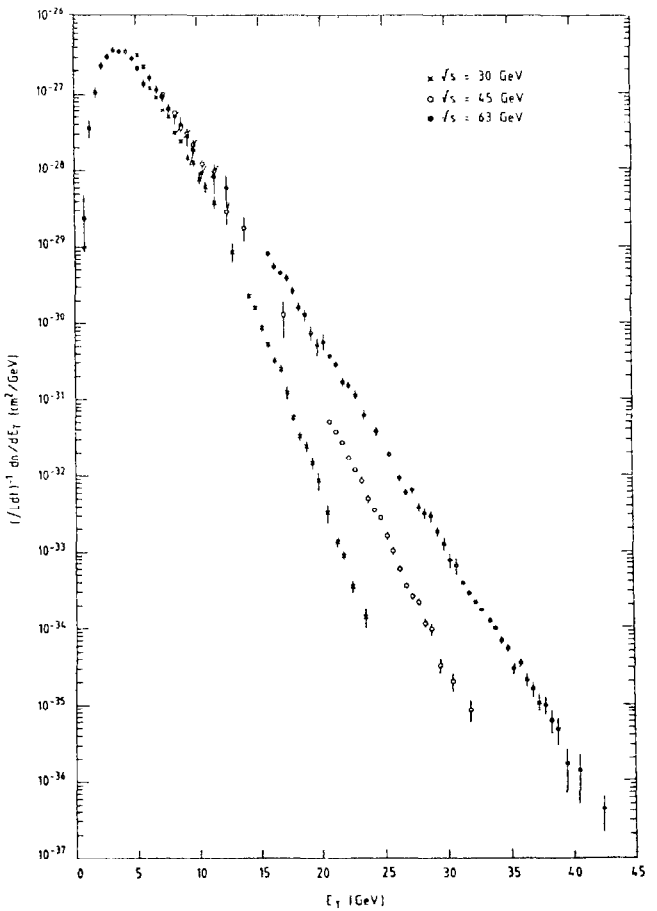


Fig. 22: Transverse energy distributions measured by the AFS group for different values of center of mass energy.

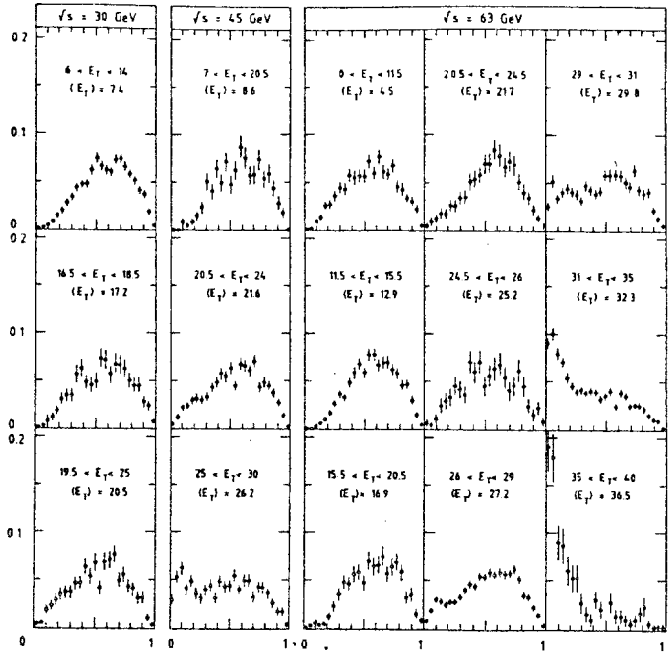


Fig. 23: Circularity distributions measured by the AFS group for different values of center of mass energy and observed transverse energy, E_t.

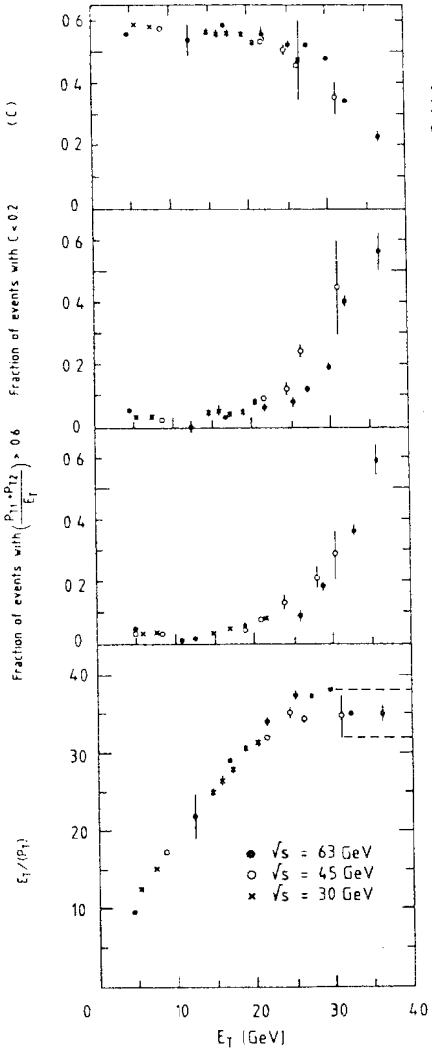


Fig. 24:

a) Mean circularity vs E_t from the AFS results of Fig. 23.

b) Fraction of low circularity events vs E_t.

c) Fraction of events where the majority of the observed E_t is contained in two clusters vs E_t.

d) A measure of the observed particle multiplicity vs E_t.

GeV, do not extend to large enough E_t to see the effects of the jets, consistent with the fixed target measurements discussed previously. The other plots in Fig. 24 show the same general trend in somewhat different ways.

The COR collaboration[16] has also published evidence for jet production at the ISR. Their detector consists of an array of lead-glass shower counters surrounding a solenoidal tracking detector. The detector is optimized for measuring π^0's and gamma rays in the shower counters and charged particle momenta in the solenoid magnet. The experiment was triggered on the neutral transverse energy E_t^0. A clustering algorithm was used to combine the observed neutral energy into contiguous blocks of clusters. Figure 25 shows the fraction of the detected E_t^0 that is contained in the two most energetic clusters and the single most energetic cluster. These fractions rise somewhat above $E_t^0 > 20$ GeV, indicating the emergence of a two-jet structure. In events where $E_t^0 > 24$ GeV, the charged particle momenta were combined with the shower counter energy and algorithms were used to split the events into two spatial hemispheres normal to two jet axes that were not necessarily back to back. It was found that these jet axes were nearly always back to back in azimuth, however. Given the two jet axes and the

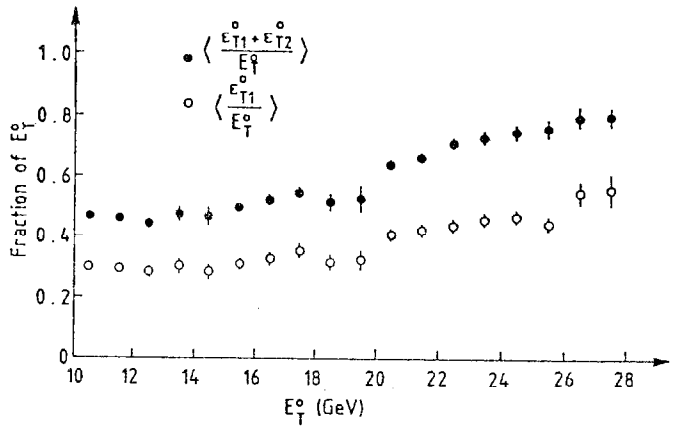


Fig. 25: Fraction of the observed neutral transverse energy carried by the highest energy single cluster and two clusters of highest energy vs E_t^0 as measured by the COR experiment at the ISR.

particle momentum information, the sphericity (same definition as $e^+ e^-$ case)[4] for the two jets was computed and added to give an event sphericity. Sphericity distributions for different values of E_t^0 are shown in Fig. 26. Events with large E_t^0 have significantly lower sphericities, consistent with the two-parton jet picture.

Other experiments at the ISR have reported observation of jets, notably the CDHW collaboration[23] using the SFM detector. This experiment has rather graphic evidence for the full 4-jet (i.e., 2 portion jet - 2 beam jet) structure of these events, but the triggers involved single particles and the results are somewhat more complicated to analyze compared to the calorimetric jet triggers of the newer experiments.

The first overwhelming evidence for jets in hadron collisions came from the UA-2 collaboration[24] running on the CERN $Sp\bar{p}S$ Collider. The apparatus is shown in Fig. 27. For the jet studies, the main components were the 200 shower counter and hadron calorimeter towers that occupied ±1 unit of rapidity and 300 degrees in azimuth. The calorimeter gains were adjusted to provide outputs proportional to transverse energy and these outputs were summed in the trigger. Typical trigger cuts required E_t > 20 GeV. The two-jet nature of the large-E_t particles in these 540 GeV p-p

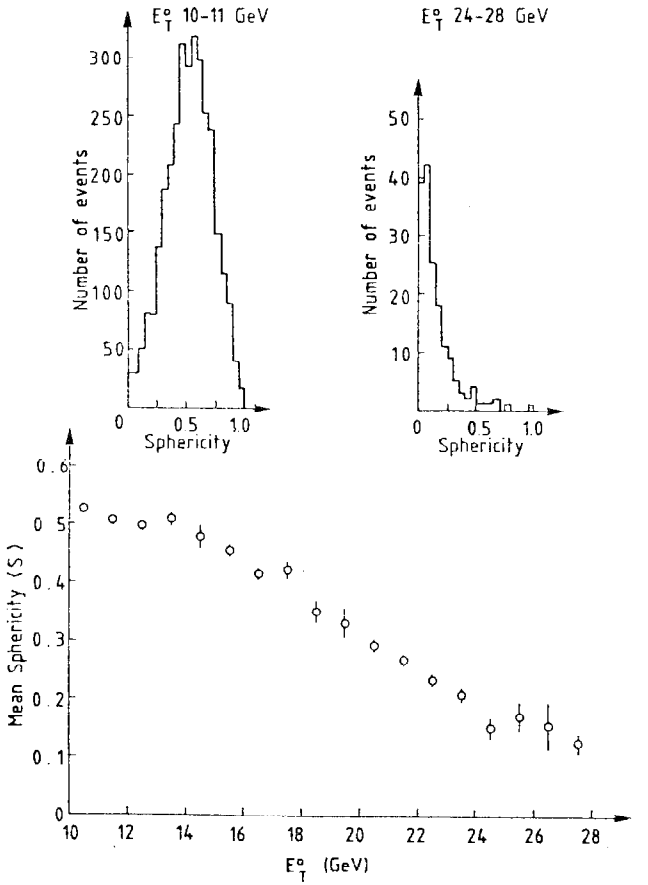
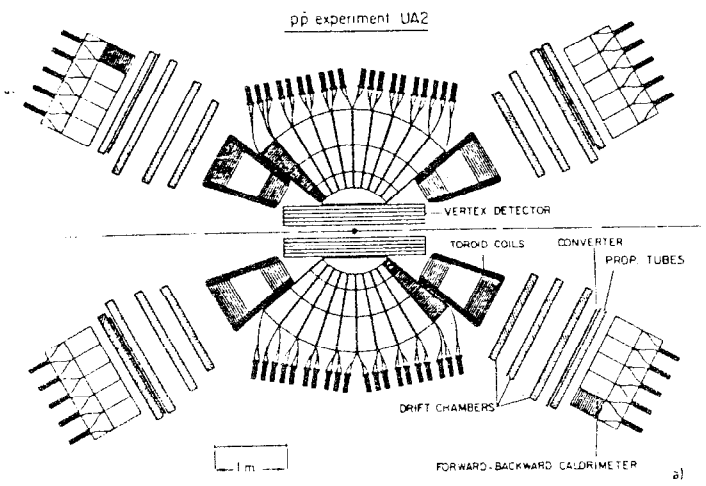


Fig. 26: Sphericity distributions for various values of neutral transverse energy from the COR experiment.



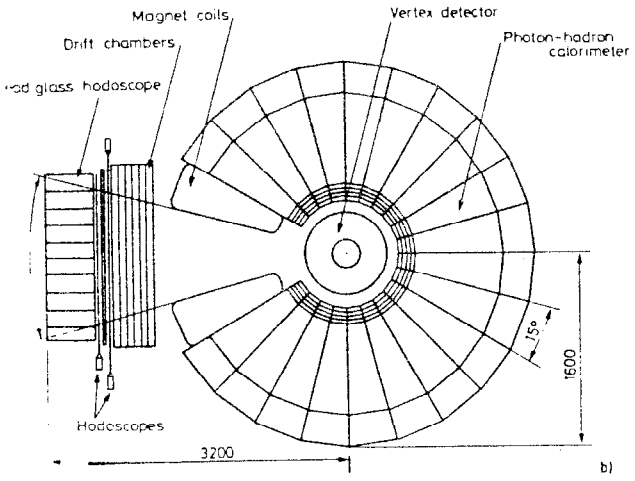


Fig. 27: The UA-2 apparatus.

collisions is apparent from casual inspection of the events. One of the most illustrative methods is the "Lego" plot, several examples of which are shown in Fig. 28. In these plots, the transverse energies of the calorimeter towers are plotted vertically above the y-ϕ or θ-ϕ plane. In many of the events, the transverse energy clearly clusters into two dense regions of y-ϕ space that are back to back in azimuth.

To be able to study these events in greater detail, clustering algorithms are being developed. The initial UA-2 cluster algorithm connects adjacent towers that contain more than 400 MeV of transverse energy, but splits into separate clusters if a 5 GeV or deeper valley exists. Using this simple algorithm, the fraction of E_t carried by the most energetic cluster and the two most energetic clusters can be studied as shown in Fig. 29a. This beautiful plot dramatically indicates the two-jet dominance of these events for $E_t > 80$ GeV. The observed E_t distribution is presented in Fig. 29b. It can be seen that at values of $E_t > 80$ GeV where the two-jet dominance becomes total, the distribution breaks away from an exponential extrapolation of the lower E_t data. Presumably the scaling behavior expected from the parton model and QCD is beginning to emerge, but more detailed analysis is needed to confirm this.

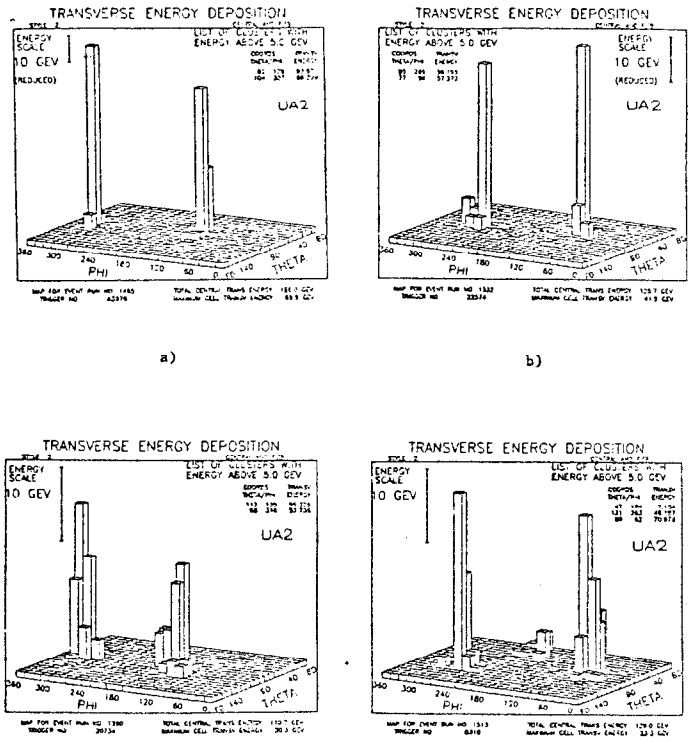


Fig. 28: "Lego" plots of observed transverse energy on the θ-ϕ plane for typical jet events observed by UA-2.

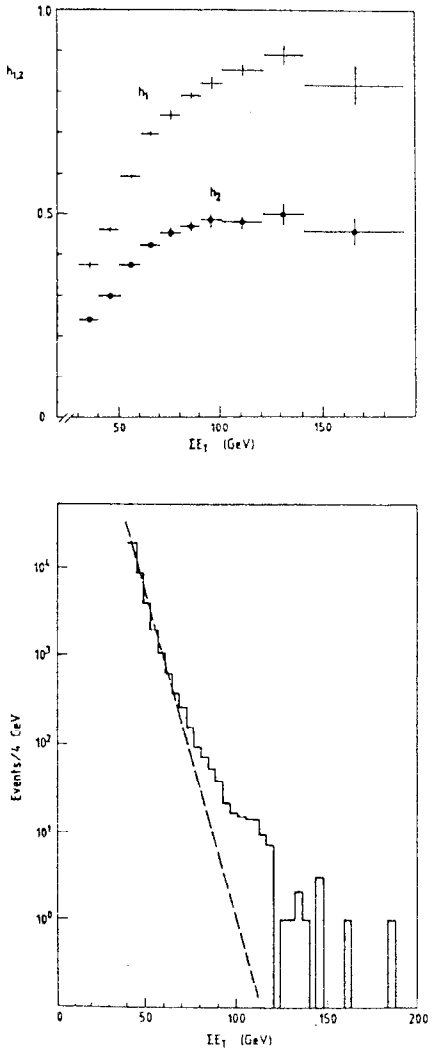


Fig. 29:

a) Fractions of E_t carried by the single cluster of largest E_t, h_2, and the two clusters of largest total E_t, h_1, vs the total E_t in events measured by UA-2.

b) Observed E_t distribution for these data.

The UA-1 collaboration (the detector is shown schematically in Fig. 30) also found convincing evidence for jets in their early runs at the $Sp\bar{p}S$ Collider.[25] The preliminary jet analyses that have appeared to date fully agree with the UA-2 results. The jet analysis divides the UA-1 calorimetry into 528 cells covering ±3 units of rapidity and 2π radians in ϕ. This is considerably larger than the UA-2 acceptance. The calorimeter cells are ordered by decreasing E_t. The cluster algorithm then associates the next cell to the closest jet if it is within a radius of one unit on the y-ϕ plane. Clustering stops for cells with E_t < 2.5 GeV, although low-E_t cells are associated with a cluster if the relative p_t is less than 1 GeV and the direction is within 45 degrees. The distribution of cell distances from clusters in the y-ϕ plane are given in Fig 31. The particles associated with a particular jet are well contained within one unit as expected from our simple jet model. The second peak in this figure corresponds to the other jet. Fig. 32 shows the charged energy flow with respect to the jet rapidity for different values of the total E_t. It can be seen that the jets become narrower as E_t increases, again in agreement with the simple jet model.

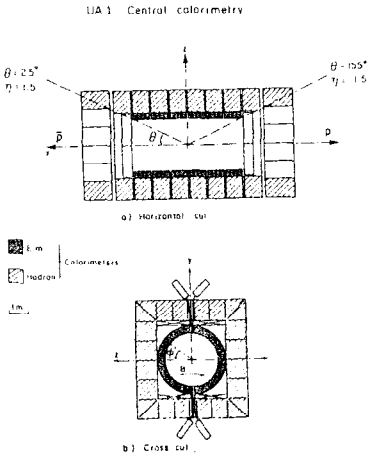


Fig. 30: UA-1 Central Calorimetry

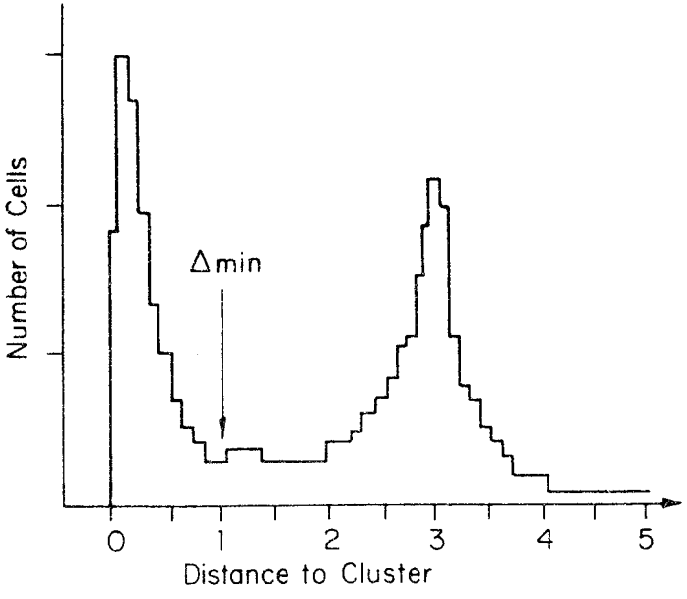


Fig. 31: Distance of UA-1 calorimeter cells having E_t>2.5 GeV from clusters in jet events from the $Sp\bar{p}S$ Collider.

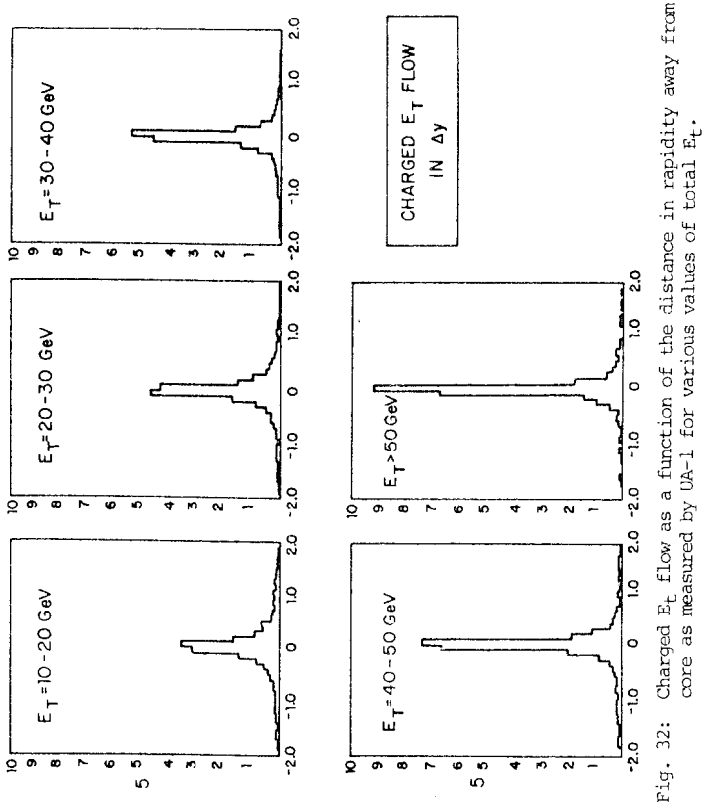


Fig. 32: Charged E_t flow as a function of the distance in rapidity away from a jet core as measured by UA-1 for various values of total E_t.

The UA-1 group has presented differential cross sections for jet events; Fig. 33 shows the single jet inclusive cross section as a function of E_t and the di-jet invariant mass distribution. Both of these quantities are in excellent agreement with Monte Carlo calculations based on QCD.

Results of many more kinds of analyses are beginning to be presented informally, but it is premature to review them now. Examples of these studies are the distributions of the rapidity differences between two jets to measure the angular distribution of the parton-parton scattering, and inclusive studies of the particles associated with jets to begin to untangle the identities of the partons giving rise to the jets.

CONCLUSIONS

There is no longer any question that jets exist in large-E_t hadronic events when $E_t \gtrsim 25$ GeV. In very high energy hadronic collisions where $E_t > 80$ GeV, the jets are truly spectacular and they dominate the cross section. The basic features of these events are in excellent agreement with expectations based on QCD and the parton model. There is much experimental activity going on now and many more definitive checks will be available soon. While the clean, spectacular jets seen

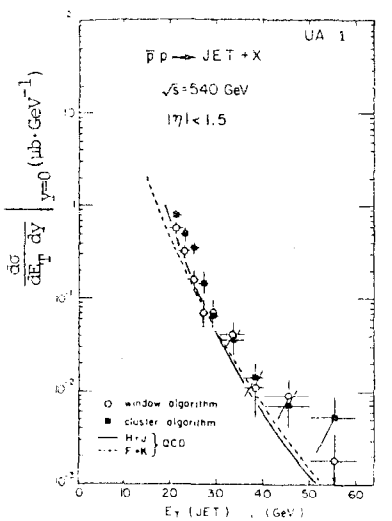
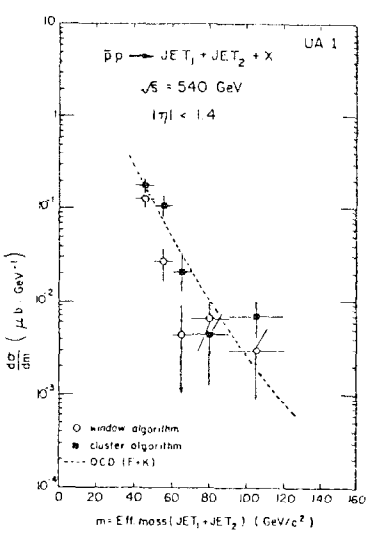


Fig. 33:

a) Inclusive cross section for single jet production vs E_t measured by UA-1.



b) Di-jet invariant mass distribution.

In both plots, the curves are from two Monte Carlo predictions based on QCD.

at the CERN $Sp\bar{p}S$ Collider are an extremely important and welcome discovery, the real experimental question remains: Can we use these jets to discover new physics and to reduce our dependence on small branching ratios?

References

* This work was supported in part by the United States Department of Energy under Contract No. DE-AC02-76ERO 3064.

† Operated by Universities Research Association Inc. under contract with the United States Department of Energy.

1. S. M. Berman, J. D. Bjorken, and J. Kogut, Phys. Rev. D 4, 3388 (1971).

2. P. Darriulat, Ann. Rev. Nucl. Part. Sci. 30, 159 (1980).

3. D. J. Gross and F. Wilczek, Phys. Rev. Lett. 30, 1343 (1973); and H. D. Politzer, Phys. Rev. Lett. 30, 1346 (1973).

4. G. Hanson, et al., Phys. Rev. Lett. 35, 1609 (1975).

5. F. W. Büsser, et al., Phys. Lett. 46B, 471 (1973).

6. M. G. Albrow, et al., Nucl. Phys. B 160, 1 (1979).

7. G. Wolf, Rapporteur talk, XXI Int. Conf. on High Energy Physics, Paris, (1982).

8. G. Fox, Lectures at the 1981 SLAC Summer School.

9. P. Söding and G. Wolf, Ann. Rev. Nucl. Part. Sci. 31, 231 (1981).

10. G. Arnison, et al., Phys. Lett. 123B, 108 (1983).

11. K. Alpgard, et al., Phys. Lett. 107B, 315 (1981).

12. M. Banner, et al., European Study Conference on Electroweak Effects at High Energies, Erice, (1983).

13. V. Cook, et al., Nucl. Phys. B 186, 219 (1981).

14. CDF Design Report, Fermilab (1981).

15. T. Åkesson, et al., Phys. Lett. 118B, 185 (1982).

16. A. L. S. Angelis, et al., Phys. Lett. 126B, 132 (1983).

17. C. Bromberg, et al., Nucl. Phys. B 171, 1 (1980).

18. M. D. Corcoran, et al., Phys. Rev. Lett. 44, 514 (1980).

19. B. Brown, et al., Phys. Rev. Lett. 49, 711 (1982).

20. M. W. Arenton, et al., Preprint ANL-HEP-PR-83-26 (1983).

21. C. DeMarzo, et al., Phys. Lett. 112B, 173 (1982) and Nucl. Phys. B 211, 375 (1983).

22. T. Åkesson, et al., Phys. Lett. 118B, 193 (1982), Phys. Lett. 123B, 133 (1983), CERN Preprint CERN-EP/83-71 (1983).

23. D. Drijard, et al., XXI Int. Conf. on High Energy Physics, Paris, (1982). See Ref. 7.

24. M. Banner, et al., Phys. Lett. 118B, 203 (1982).

25. G. Arnison, et al., Phys. Lett 123B, 115 (1983).

SLAC – PUB – 3273
December 1983
T/E

ASPECTS OF THE DYNAMICS OF HEAVY-QUARK SYSTEMS

MICHAEL E. PESKIN*

Stanford Linear Accelerator Center
Stanford University, Stanford, California 94305

Lectures presented at the 1983 SLAC Summer School

Contents:

1. Introduction
2. The Wilson Line and the Static Potential
3. Spin-Dependent Forces
4. Hadronic Transitions Between Heavy-Quark States

* Work supported by the Department of Energy, contract DE – AC03 – 76SF00515

© M. Peskin 1983

1. Introduction

The analysis of bound states composed of heavy quarks and antiquarks has provided a window into the structure of the strong interactions which has offered a view at the same time brilliantly clear and tauntingly ambiguous. These systems contain our best evidence that the quarks from which the hadrons are built are ordinary fermions which obey the Dirac equation and which couple to electromagnetism just as electrons do. The spectrum of bound states and the systematics of its quantum numbers make clear that the same basic principles that lead to the spectrum of the hydrogen atom or positronium also govern the behavior of quarks. However, the heavy-quark systems which have been studied to date, the systems of c-$\bar{c}$ and b-$\bar{b}$ bound states, seem to be bound by forces which bear no obvious relation to the gluons which we expect are the fundamental mediators of the strong interactions. The spectrum of bound states can be explained by insisting that the quark and antiquark interact through a phenomenologically determined potential. This phenomenological picture, however, seems very difficult to connect to an underlying description in terms of a color gauge theory.

The essential difficulty in understanding this connection arises from the fact that the c-$\bar{c}$ and b-$\bar{b}$ systems occupy an intermediate regime in the behavior of the gauge theory. At very small distances, comparable to those probed in deep inelastic scattering, the q-$\bar{q}$ potential is expected to become a Coulomb potential, directly reflecting one-gluon exchange. At very large distances, if the notion of quark confinement is a correct one, the potential should become simply proportional to the q-$\bar{q}$ separation, reflecting the formation of confining strings of color flux. To understand the transition region, however, a qualitative picture does not suffice; for a proper understanding, one would need to see precisely how the collective behavior of gluons modifies and alters single gluon effects. At the present time, we seem very far from such a detailed understanding. It is possible, however, to gain some insight into the nature of this intermediate regime by considering the behavior of q-$\bar{q}$ systems from a broad perspective, assembling a variety of distinct aspects of these systems which are sensitive to the properties of gauge theories at intermediate distances.

In these lectures, I will present the theory of three different facets of this behavior by the use of a unified mathematical formalism. My goal will be to clarify the interrelation of these phenomena and, more importantly, their connection to the properties of an underlying gauge theory. The plan of these lectures is as follows: In § 2, I will present some basic theoretical orientation, setting out the formalism which will be the basis of our discussion. I will also discuss the application of this formalism to the static potential; I will discuss the foundation of the static potential approximation and justify the general shape of the potential as emerging from a gauge theory. In § 3, I will discuss the theory of spin-dependent forces in heavy-quark systems, presenting a connection of these forces to gauge-theory amplitudes discovered by Eichten and Feinberg.[1] In § 4, I will discuss the theory of hadronic transitions between q-$\bar{q}$ states, following the approach of Yan.[2] This discussion will not deal with detailed phenomenological theories or extensive comparison with experiment. My intent is, rather, to make clear what gauge theories have to say about these topics. My presentation will be somewhat formal, but, as is appropriate to a summer school, the formalism will be built from the ground up and kept as comprehensible as possible. I should also make clear that none of the work to be discussed is new; these are classic topics in the theory, but ones not sufficiently widely appreciated and so most deserving of review and explication.

In the remainder of this section, I will remind you of a few of the basic features of heavy quark meson spectroscopy. The spectrum of levels of the c-$\bar{c}$ and b-$\bar{b}$ systems are generally well known, and are discussed in many reviews,[3] so I can be brief. Let me begin by simply presenting, in Fig. 1, the observed level spectrum of these heavy-quark systems, together with that of positronium. I use the notational convention, often used in q-$\bar{q}$ spectroscopy but unusual in

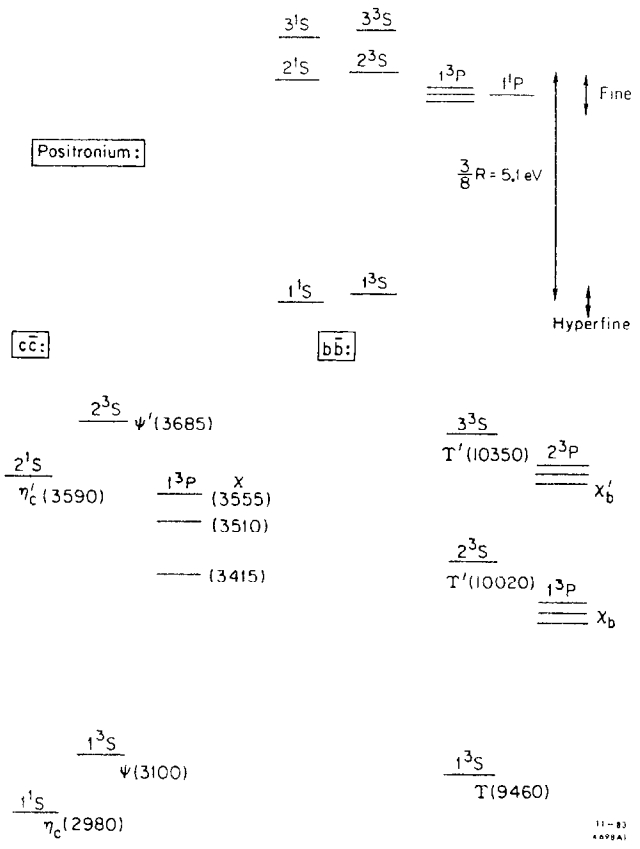


FIG. 1. The spectrum of observed levels of three anti-fermion bound-state systems, the positronium (e^+-e^-),ψ (c-$\bar{c}$), and Υ (b-$\bar{b}$) systems.

atomic systems, of labelling the lowest-lying P states as '1P'. This difference in nomenclature emphasizes the only significant qualitative difference between the heavy-quark and atomic spectra: The degeneracy of states with the same principal quantum number, a special property of the Coulomb potential, is lost in the quark systems, to which this potential does not directly apply.

The c-$\bar{c}$ and b-$\bar{b}$ level spectra shown in Fig. 1 are well known to be accurately described by a model in which the quarks are treated as nonrelativistic fermions interacting through a simple potential, if one allows the potential to be determined phenomenologically. A typical procedure is to choose a potential with a small number of parameters which may be fit, for example, to the ψ, ψ', and Υ masses and the ratio of the ψ and ψ' leptonic widths. The merits of various fitting procedures are debated in References 4-5. A number of different functional forms for the potential have been used in the literature. Some typical forms are those of Eichten *et. al.*,[4] who use a linear combination of a linear potential and a Coulomb potential, Richardson,[6] who uses the Fourier transform of a Coulomb potential with a running coupling constant

$$V(r) = \int d^3q e^{iq\cdot r}\left[\frac{\alpha_s(q^2)}{4\pi q^2}\right], \tag{1.1}$$

and Martin,[7] who uses a simple power law $V(r) \sim r^{0.1}$ for the shape of his potential. All of these potentials are quite successful; in the sense that they all give the locations of the Υ',Υ'', Υ''', and the χ_b to within about 10 MeV. This striking convergence of predictions is easy to understand by plotting these potentials against one another, as is done in Fig. 2. Also plotted in this figure are the mean radii of the various ψ and Υ states. It is clear that our restricted experimental information–most especially, the insensitivity of accessible states to the short-distance behavior of the potential–leave many possibilities open. The discovery of the top quark and the associated t-$\bar{t}$ mesons should provide an important constraint on the phenomenological potential. Until this discovery

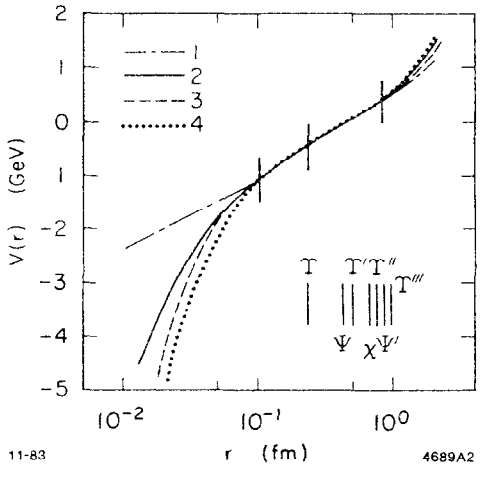


FIG. 2. A comparison of four different phenomenological q-$\bar{q}$ potentials, from Ref. 5. The potentials represented are those proposed in (1) Ref. 7, (2) Ref. 5 (a variant of that of Ref. 6), (3) Ref. 8, (4) Ref. 4.

arrives, we can learn more about heavy-quark interactions only by extending the theory which includes this potential, and applying it more widely.

2. The Wilson Line and the Static Potential

In order to argue precisely about the intricacies of heavy-quark behavior, we need a mathematical description of heavy-quark systems which is at the same time powerful and physically transparent. In this section, I would like to introduce you to such a formalism. I will explain how to represent the motion of heavy quarks directly in space-time, using the Feynman path integral approach to quantum mechanics. We will see that the static potential description of the q-$\bar{q}$ interaction emerges as an obvious first approximation to this exact representation. This observation will allow us to discuss the conditions for the validity of the static potential picture, to understand when this description is valid, and to account which quantum effects are subsumed and which omitted by this approach. I will also use this picture to explain what the gauge theories predict about the general shape of this potential.

In fermion-antifermion systems bound by electrical forces, such as positronium, it is possible to discuss the applicability of the static potential picture, and the shape of this potential, without needing to rely on any special theoretical tools. One needs only to expand systematically in powers of α. This is, of course, not completely straightforward, because a large class of Feynman diagrams–the set, shown in Fig. 3, which one would normally associate with fermion-antifermion binding all have values of order α^0. But one can show[9] that the leading terms in these diagrams have the form of the solution to a nonrelativistic Schrödinger equation. The various corrections to the static picture appear as successive powers of α are uncovered: For positronium, the fundamental scale is the reduced mass $\mu = \frac{1}{2}m$. The binding energy is then $R = \frac{1}{2}\alpha^2\mu$. That the lowest bound state is nonrelativistic follows from the fact that α is small–the Bohr radius is equal to $(\alpha\mu)^{-1}$ and the fermion velocities are of order

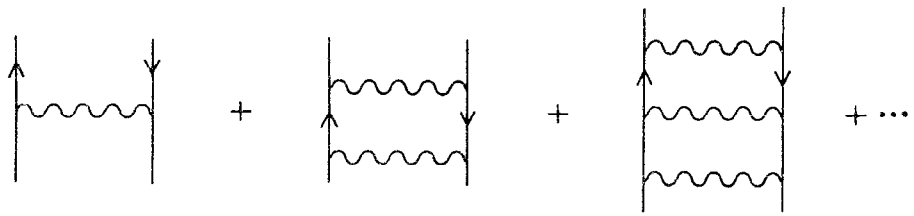


FIG. 3. Graphs whose sum produces the nonrelativistic positronium spectrum.

α. The spin-orbit splittings in the spectrum appear in order $\alpha^2 \cdot R$; the Lamb shift appears in order $\alpha^3 \log(\alpha^{-1}) \cdot R$.

In quark-antiquark systems, however, the situation is rather different. As long as the quark-antiquark binding forces remain constant in magnitude as the quark mass is increased, one will eventually reach a point at which the motion of quarks in their bound states is nonrelativistic. The phenomenological success of the potential models for the c-$\bar{\text{c}}$ system tells us that this point has been reached already for the charmed quark. However, this certainly does not imply that the strong binding forces are described by a weak-coupling approximation. All that should actually be necessary is that the bound quarks should have masses much larger than the energy scale of quark-binding in the gauge theory. This observation, though, raises a question about one's theoretical description of the heavy-quark system: We must describe the system in such a way that we can expand directly in the velocity of the quark and antiquark, without needing to make any additional approximation in describing the gauge-field dynamics.

It is clear that such an approximation scheme requires an ability to visualize the motion of the quark and antiquark in space-time, as they participate in the bound state. Such a scheme of visualization would also be interesting and informative in its own right. Let me, then, set up such a description, based on Feynman's description of quantum mechanics in terms of paths in space-time.[10]

To begin, compare the structure of the Schrödinger equation

$$i\frac{\partial}{\partial t}\psi = \left(-\frac{1}{2m}\nabla^2 + V(x)\right)\psi \tag{2.1}$$

to that of the diffusion equation:

$$-\frac{\partial}{\partial \tau}\phi = \left(-D\nabla^2 + V(x)\right)\phi\,. \tag{2.2}$$

I have added to (2.2) a term which allows the diffusing particle to be destroyed with probability $V(x)$, to make the analogy with (2.1) more precise. The process

of diffusion is apparently described by quantum mechanics, with the replacement

$$it \to \tau \,, \tag{2.3}$$

or

$$e^{-iHt} \to e^{-H\tau}, \tag{2.4}$$

and by setting $D = \frac{1}{2m}$. This relationship works also in the other direction. In principle, then, we can construct a precise representation of quantum mechanics by simulating the diffusion process and then reversing the transposition of Eq. (2.3). This program is actually quite easy to carry out in practice.

Consider first carrying out the diffusion process over a small increment of time ϵ. The probability of diffusion from x_i to x_f in time ϵ is given by

$$\phi(x_f; x_i; \epsilon) = \frac{1}{(4\pi D\epsilon)^{3/2}} \exp\left[-\frac{(x_f - x_i)^2}{4D\epsilon} - \epsilon V\left(\frac{x_i + x_f}{2}\right)\right]. \tag{2.5}$$

The probability of diffusion from x_i to x_f in a finite time τ can then be constructed by dividing the interval from 0 to τ into a large number of intervals of size ϵ and then integrating over the particle positions at these intermediate times:

$$\phi(x_f; x_i; \tau) = \int \frac{dx_1 \ldots dx_{n-1}}{(m/2\pi\epsilon)^{(n-1)\frac{3}{2}}} \prod_i \exp\left[-\epsilon\left\{\frac{m}{2}\left(\frac{x_{i+1} - x_i}{\epsilon}\right)^2 + V\left(\frac{x_{i+1} + x_i}{2}\right)\right\}\right]. \tag{2.6}$$

We may then let $\epsilon \to 0$; the points x_n become a continuous path $x(\bar{\tau})$;then the expression (2.6) can be represented as follows:

$$\phi(x_f; x_i; \tau) = \int_{\substack{\text{paths from } x_i \\ \text{to } x_f}} Dx \exp\left[-\int_0^\tau d\bar{\tau}\left[\frac{m}{2}\dot{x}^2(\bar{\tau}) + V(x(\bar{\tau}))\right]\right]. \tag{2.7}$$

Formally replacing τ by it, we find a special case of Feynman's formula for the quantum mechanical transition amplitude from x_i to x_f in time t:

$$\phi(x_f, x_i; t) = \int Dx\, e^{i\int dt L} \tag{2.8}$$

where L is the classical Lagrangian.

We will find it more useful, however, to apply Eq. (2.7) directly. To see why this is so, consider the visualization of this equation presented in Fig. 4. Consider the evolution in τ induced by a potential of the shape shown on a wave function sharply peaked about $x = 0$. The waveform diffuses into an equilibrium shape, which then decreases exponentially in magnitude under the action of the term which includes $V(x)$. Because τ is related to physical time t through (2.4), this exponential decay must be of just the form

$$\phi(x_f, \tau) = e^{-E_0\tau} \cdot \psi(x_f), \tag{2.9}$$

where E_0 is the ground-state energy in the potential $V(x)$. The equilibrium shape $\psi(x_f)$ is just the ground-state wave-function. Thus, the paths contributing to (2.7) for large τ may be thought of as particle motions in the ground state of the Schrödinger equation.

Let us now make this description relativistic. Instead of solving the Schrödinger equation, we would like to represent the solution of the Klein-Gordon equation:

$$(\partial^2 + m^2)\psi(x) = \delta^{(4)}(x - x_i)\,. \tag{2.10}$$

I have written explicitly a point source of ψ; this is implicit in our treatment of Eqs. (2.1) and (2.2). If we replace, as before, $it = x_0$, this equation becomes

$$(-\partial_0^2 - \nabla^2 + m^2)\psi = \delta^{(4)}(x - x_i)\,. \tag{2.11}$$

We may solve this equation by the trick of introducing a fictitious additional time T. Then we must solve

$$\left(\frac{\partial}{\partial T} - \frac{1}{2}\left[(\partial_0^2 + \nabla^2) - m^2\right]\right)\hat{\psi} = \delta^{(4)}(x - x_i)\delta(T)\,. \tag{2.12}$$

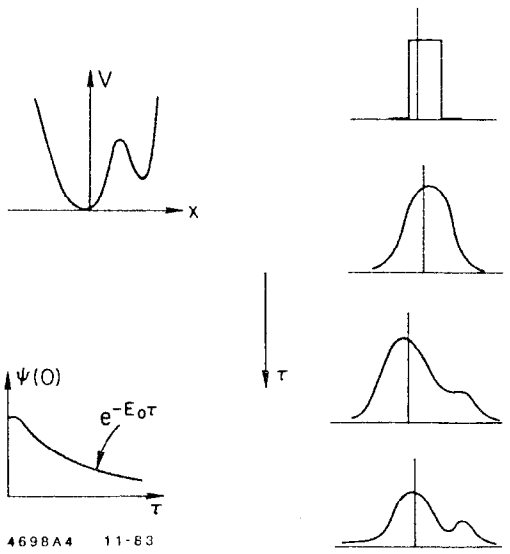


FIG. 4. Evolution on an initial waveform into the ground-state wavefunction, as the result of integrating Eq. (2.2).

But this is just a diffusion equation of the form (2.2), in 4 space dimensions, and so we can recognize immediately that the solution is

$$\hat{\psi}(x,T) = \int \mathcal{D}x \exp\left[-\int_0^T d\tau\, \frac{1}{2}(\dot{x}^2 + m^2)\right]. \tag{2.13}$$

But now note that, if we have found a $\hat{\psi}(x,T)$ which solves (2.12), we can readily construct a $\psi(x)$ which solves (2.10) by writing

$$\psi(x) = \int_0^\infty dT \quad \hat{\psi}(x,T). \tag{2.14}$$

as one can see simply by integrating Eq. (2.12) over T. This gives us a path representation of the propagator for the Klein-Gordon equation of the following form:

$$\psi(x_f; x_i) = \int_0^\infty dT \int \mathcal{D}x \exp\left[-\int_0^T d\tau\, \frac{1}{2}(\dot{x}^2 + m^2)\right]. \tag{2.15}$$

The integral $\int \mathcal{D}x$ runs over paths $x(\tau)$ which run through 4-dimensional space in a fairly arbitrary way from x_i to x_f; a typical path is shown in Fig. 5. I might note parenthetically that if this integral over $x(\tau)$ is replaced, as would be proper, by the solution to the diffusion equation, one finds

$$\psi(x_f; x_i) = \int_0^\infty dT\, \frac{1}{(2\pi T)^2} \exp\left[-\frac{(x_f - x_i)^2}{2T} - \frac{m^2}{2}T\right] \tag{2.16}$$

which is actually a standard integral representation of the free Klein-Gordon propagator.

We can extract the nonrelativistic limit of the Klein-Gordon theory directly from (2.15) in the following way: Let us choose limit points which are separated by a nonrelativistic trajectory:

$$x_i = (0,\vec{0}), \qquad x_f = (t_f,\vec{0}) \tag{2.17}$$

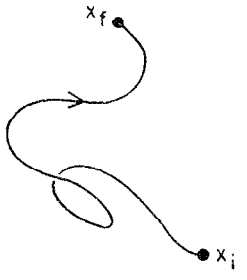


FIG. 5. A typical space-time trajectory included in the integral of Eq. (2.15).

and send $t_f \to \infty$. (To extract the propagation of a nonrelativistic antiparticle, for which the quantum numbers of ψ flow from x_i to x_f, just reverse these assignments.) In this limit, the integral over $x(\tau)$ is dominated by the path which maximizes the integrand of (2.15), or which minimizes

$$\int_0^T d\tau \frac{1}{2}\left[\dot{x}^2(\tau) + m^2\right] . \tag{2.18}$$

Setting $\delta/\delta x(\tau)$ of the above equal to 0 yields the condition

$$\ddot{x}_\mu = 0 \quad \to \quad x(\tau) = \left(t_f \cdot \frac{\tau}{T}, \vec{0}\right) . \tag{2.19}$$

If we insert (2.19) into (2.18), this exponent becomes

$$\frac{t_f^2}{2T} + m^2 \frac{T}{2} . \tag{2.20}$$

The minimum with respect to T is found at

$$T = \frac{t_f}{m} , \quad \text{or} \quad \tau = \frac{x_0}{m} . \tag{2.21}$$

Now examine the collection of paths near this joint minimum with respect to T and $x(\tau)$. We can recognize the following properties: First, in the vicinity of (2.19) and (2.21) the exponential of (2.18) becomes

$$\exp\left[-\left(\int_0^{t_f} dt \left[\frac{m}{2}\dot{x}^2\right]\right) - m\, t_f\right] \tag{2.22}$$

where now $\dot{x}$ represents the derivative of x with respect to $t = x_0$. This is just (2.7) with an extra exponential decay representing the rest energy of the heavy particle. For an antiparticle, we would find the same result, but with the dominant paths formally running backwards in time. Secondly, paths longer

than the minimal path length between x_i and x_f are suppressed by the weighting factor

$$e^{-m\Delta s} . \tag{2.23}$$

where Δs is the excess path length. This means, in particular, that paths which bend backwards in time, in the manner shown in Fig. 6, are suppressed by the factor

$$\int_0^\infty d\Delta t\, e^{-2m\Delta t} = \frac{1}{2m} . \tag{2.24}$$

By making a constant-time slice through Fig. 6, you may recognize that the back-bend represents a component of the state which contains an extra particle-antiparticle pair. The factor (2.24) is just the energy denominator associated with this higher-energy state.

To couple the Klein-Gordon equation to electromagnetism, we need only generalize (2.10) by the replacement

$$\partial_\mu \to D_\mu = (\partial_\mu - igA_\mu); \tag{2.25}$$

this prescription makes the Klein-Gordon equation properly gauge-invariant. Let us, for the moment, consider the motion of a Klein-Gordon particle in a fixed A field. We then need to solve

$$\left[-(\partial_\mu - igA_\mu)^2 + m^2\right]\psi = \delta^{(4)}(x - x_i) . \tag{2.26}$$

To solve this equation, we can again add a fictitious time:

$$\left(\frac{\partial}{\partial T} + \frac{1}{2}\left[(\partial_\mu - igA_\mu)^2 - m^2\right]\right)\hat{\psi} = \delta^{(4)}(x - x_i) . \tag{2.27}$$

The solution to (2.27) for propagation over a short time ϵ can be found by taking A_μ approximately constant. Then one can check that

$$\hat{\psi}(x_f; x_i; \epsilon) = \frac{1}{(2\pi\epsilon)^2} \exp\left[-\frac{(x_f - x_i)^2}{2\epsilon} + ig(x_f - x_i)\cdot A - \frac{\epsilon}{2} m^2\right] \tag{2.28}$$

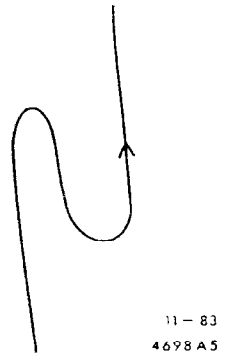


FIG. 6. A path which bends backwards in time.

by noting that

$$D_\mu(exponent) = -\frac{(x_f - x_i)_\mu}{\epsilon} \tag{2.29}$$

as before. Assembling the increments of time ϵ into a finite time t, taking the limit of continuous paths as above, and then integrating over T, we find for the solution to (2.26):

$$\psi(x_f; x_i) = \int_0^\infty dT \int \mathcal{D}x \exp\left[-\int_0^T d\tau \frac{1}{2}\left[\dot{x}^2 + m^2\right]\right] \exp\left[ig \int d\tau\, \dot{x} \cdot A(x)\right] . \tag{2.30}$$

We have shown, then, that a charged particle is described by a sum over space-time paths in which each path P is assigned the phase factor

$$W(x_f, x_i) = e^{ig \int_P dx \cdot A} . \tag{2.31}$$

This is a famous phase factor, whose relevance to the study of gauge theories has been emphasized by Schwinger,[11] Mandelstam,[12] and Wilson,[13] among others. I will discuss its beautiful properties in a moment. First, however, I should indicate how Eq. (2.31) generalizes when the Klein-Gordon equation is coupled to a non-Abelian gauge theory. In this case, the number A_μ must be replaced by a matrix in the color space

$$\mathbf{A}_\mu = A_\mu^a t^a \tag{2.32}$$

where t^a is a generator of the color gauge group. Then the various factors (2.28) which depend on $\mathbf{A}$ must be arranged and multiplied out in order. The ordered product of these phase factors may be written as follows:

$$\prod_{\substack{\text{increments} \\ \text{of path}}} {}^{\Delta} \left(e^{ig \int_\Delta d\tau\, \dot{x}(\tau) \cdot \mathbf{A}(x(\tau))}\right) = P\left(e^{ig \int_{x_i}^{x_f} dx \cdot \mathbf{A}}\right) . \tag{2.33}$$

This equation defines the path-ordering operator P. For antiparticles, since the path runs backward, the path-ordering also runs backwards in time, one finds

$$P\left(e^{ig \int_{x_f}^{x_i} dx \cdot \mathbf{A}}\right) . \tag{2.34}$$

In the same way that we saw (2.7) related to the classical action, we can recognize the exponent of the phase factor (2.31) as the classical action for the coupling of the electromagnetic field to a point particle:

$$\int L\, d^4x = \int d^4x\, j_\mu A^\mu = \int d^4x \left[\int d\tau\, g\dot{x}^\mu \delta^{(4)}(x - x(\tau))\right] A_\mu(x) . \tag{2.35}$$

Let us now discuss the properties of $W(x, y)$. We should first note that W has a very simple transformation law under gauge transformations. Under a gauge transformation in electrodynamics,

$$\psi(x) \to e^{i\alpha(x)}\psi(x) ; \quad W(x, y) \to e^{i\alpha(x)} W(x, y)\, e^{-i\alpha(y)} \tag{2.36}$$

so it is easy to build gauge-invariant quantities from W. In a non-Abelian gauge theory, W transforms as in (2.36) with the phase factor $e^{i\alpha}$ replaced by a unitary transformation in the color group. The second property of $W(x, y)$ is that it depends on the path chosen to connect x to y. It is instructive to compare the values of W evaluated over two paths P and P' which differ only by a small detour, as shown in Fig. 7. If the small square is taken to lie in the $\hat{1} - \hat{2}$ plane and to have sides of length ϵ, we can evaluate:

$$\begin{aligned} W[P'] &= W(x, z)\Big\{\Big(1 - ig\epsilon\, \mathbf{A}_2(z)\Big)\Big(1 - ig\epsilon\, \mathbf{A}_1(z + \epsilon\hat{2})\Big) \\ &\quad \cdot \Big(1 + ig\epsilon\, \mathbf{A}_2(z + \epsilon\hat{1})\Big)\Big(1 + ig\epsilon\, \mathbf{A}_1(z)\Big)\Big\} W(z, y) \\ &= W(x, z)\Big\{1 + ig\epsilon^2\Big[\partial_1 \mathbf{A}_2 - \partial_2 \mathbf{A}_1 - ig[\mathbf{A}_1, \mathbf{A}_2]\Big]\Big\} W(z, y) . \end{aligned} \tag{2.37}$$

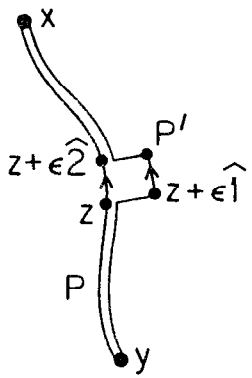


FIG. 7. Computation of the difference between two nearby Wilson lines.

Thus,

$$W[P'] - W[P] = W(x,z)(ig\Delta\sigma^{\mu\nu}\mathbf{F}_{\mu\nu})W(z,y) \tag{2.38}$$

where $\mathbf{F}_{\mu\nu}$ is the gauge field strength tensor, where $\Delta\sigma^{\mu\nu}$ is the increment of area by which P and P' differ. We can use this relation to derive a formula for the derivative of W which will be useful to us in the next section. Let $W(x,-\infty)$ represent the phase factor for a line which runs forward in the time direction from $-\infty$ and ends at x, as shown in Fig. 8. We can differentiate this quantity with respect to x by performing the motion indicated in Fig. 8 and breaking up the area between the two paths into small rectangles. This gives:

$$\epsilon^{\mu}D_{\mu}W(x,-\infty) = \int_{-\infty}^{x} d^2k\, W(x,z)(ig\,\epsilon^{\mu}\mathbf{F}_{0\mu}(z))W(z,-\infty)\ . \tag{2.39}$$

It is thus quite natural that the effect of a gauge field on a charged or colored particle should be accounted by the phase factors (2.31) or (2.33). In a quark-antiquark system, the effect of a color gauge field on the quark-antiquark state is represented by including in the path sum (2.15) for the quark and the antiquark the phase factor

$$\left[P\left(e^{i\int_{x_i}^{x_f} dx\cdot A}\right)\right]_{a_i a_f}\cdot\left[P\left(e^{ig\int_{y_f}^{y_i} dx\cdot\mathbf{A}}\right)\right]_{b_f b_i} \tag{2.40}$$

where x_i,x_f and y_i,y_f are the initial and final positions of the quark and anti-quark, respectively, and a_i,a_f and b_i, b_f are their initial and final colors. We can insist that (2.40) contains only color singlet initial and final states by bringing x_i and y_i, x_f and y_f to the same point, as indicated in Fig. 9, and then summing over colors $a_i = b_i$, $a_f = b_f$. This prescription associates to the evolving color singlet q-$\bar{\text{q}}$ state a factor

$$\text{trace}\left[P\exp\left(ig\oint_C dx\cdot\mathbf{A}\right)\right], \tag{2.41}$$

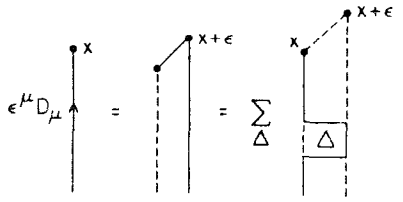


FIG. 8. Computation of the derivative of the Wilson line with respect to its endpoint.

where the integral is taken over the closed curve C indicated in Fig. 9, on which the quark moves forward and the antiquark backward in time.The factor (2.41) is often referred to as the **Wilson loop**; I will refer to an individual amplitude (2.33) as a **Wilson line.**

Now let us make the **A** field a dynamical entity also. According to Feynman's path integral prescription, we can turn the expression (2.30), valid for a fixed **A** field, into a description of mutually interacting Klein-Gordon and gauge fields by simply integrating the expression (2.30)over possible **A** field configurations, with a weight given by the classical Lagrangian for the gauge field (or, rather, because of (2.3), its continuation to imaginary time.) If we call the proper expression with a fixed **A** field $\mathcal{W}(\mathbf{A})$, then for a dynamical **A** field, we would write

$$\int \mathcal{D}\mathbf{A}\, \mathcal{W}(\mathbf{A}) \exp\left[-\int \mathcal{L}\, d^4x\right]. \tag{2.42}$$

For small values of **A**, the exponent of (2.42) is approximately a quadratic form in its components $A^a_{\mu\nu}$, so that (after fixing the gauge) we can rearrange it into the form

$$\int \mathcal{L}\, d^4x = \int d^4x\, \frac{1}{4}(\mathbf{F}_{\mu\nu})^2 \approx \frac{1}{2}\int d^4x\, A^a_\mu\, \delta_{ab}\Delta^{-1\mu\nu} A^b_\nu \tag{2.43}$$

where $\Delta^{\mu\nu}(x,y)$ is the usual gauge field propagator

$$\Delta^{\mu\nu}(x,y) = \int \frac{d^4k}{(2\pi)^4}\, e^{-ik(x-y)}\, \frac{g^{\mu\nu}}{k^2} = \frac{g^{\mu\nu}}{2\pi^2(x-y)^2}\,. \tag{2.44}$$

To understand what kind of forces the quark and antiquark experience as a result of their gauge interactions, it suffices to study the behavior of the Wilson loop (2.41) when averaged with the weight (2.42). To obtain an idea of how to treat these forces, let us evaluate the average of (2.41) in three model situations in which this average can be computed easily.

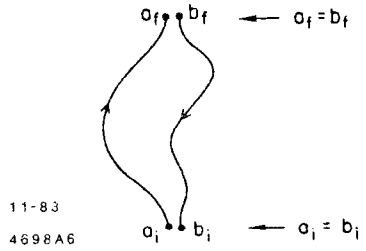


FIG. 9. Wilson lines associated with a propagating quark-antiquark pair.

The simplest case in which to examine the behavior of the Wilson loop is that of pure electrodynamics. In that case, the expectation value of the Wilson loop is given exactly by

$$\langle e^{ig\oint_c dx\cdot\mathbf{A}}\rangle = Z^{-1}\int \mathcal{D}\mathbf{A}\, e^{-\frac{1}{2}\int A\Delta^{-1}A} e^{ig\oint_c dx\cdot\mathbf{A}} \tag{2.45}$$

where Z is the indicated Gaussian integral without the factor (2.41). The integral is readily evaluated by completing the square in the exponent; then the integral over A is an identical overall factor in numerator and denominator and cancels. The result is

$$\exp\left[+\frac{1}{2}\left(ig\oint dt_1 \dot{x}^\mu(t_1)\right)\left(ig\oint dt_2 \dot{x}^\nu(t_2)\right)\ \Delta_{\mu\nu}(x(t_1)-x(t_2))\right] \tag{2.46}$$

where I have let t_1 and t_2 be the time coordinates of points on the curve C and have written:

$$dx^\mu = dt\frac{dx^\mu(t)}{dt} = dt\,\dot{x}^\mu\,. \tag{2.47}$$

Note that

$$dt\,\frac{dx^\mu}{dt} = dx^0\,\frac{dx^\mu}{dx_0} = dx^0(1,\vec{v}) \tag{2.48}$$

so that (2.46) has precisely the form of the electromagnetic interaction of charges and currents.

Now consider the behavior of the exponent of (2.46) for nearby pieces of path with zero relative velocity. There are three contributions, shown in Fig. 10. The contributions (a) and (b) are independent of the particle-antiparticle separation; these contribute only to the particle self-energies and do not affect the potential. The contribution (c) is well approximated by

$$-2\cdot\frac{g^2}{2}\int_{-\infty}^{\infty} dt_1 \int_{\infty}^{-\infty} dt_2\,\frac{1}{2\pi^2[(t_1-t_2)^2+R^2]} = g^2\cdot(\text{time of interaction})\cdot\frac{1}{4\pi R}\,. \tag{2.49}$$

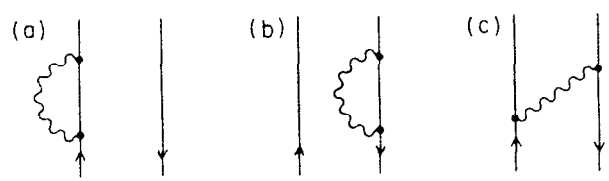


FIG. 10. Contributions from QED to the expectation value of the Wilson loop for a static q-$\bar{q}$ system.

But note also that the integral over relative times in (2.49) is highly convergent and so is insensitive to relative times much larger than the distance R between them. Thus, this formula is also approximately correct for slowly moving particles, as long as the separation between the particles varies slowly compared to R. If we call this time-varying separation $R(t)$, we can write

$$\langle e^{ig\oint dx\cdot A}\rangle \simeq \exp\left[-\int dt\left(\frac{-g^2}{4\pi R(t)}\right)\right]; \tag{2.50}$$

this result is illustrated by Fig. 11.

Now consider what happens if we give the photon a mass μ. This could be done, for example, through the Higgs mechanism, after the model of weak-interaction gauge theories. The expression (2.43) would be changed only by the replacement

$$\Delta^{\mu\nu}(x-y) \to \int \frac{d^4k}{(2\pi)^4}\, e^{-ik\cdot(x-y)}\, \frac{g^{\mu\nu}}{(k^2+\mu^2)}\,. \tag{2.51}$$

Then all of the manipulations which we carried out for the case of pure electrodynamics go through here too, and we can derive for the case of static particles an expression of precisely the form of (2.49), with the replacement

$$V(R) = -\int_{-\infty}^{\infty} dx^0\, \Delta(x^0, R) = \frac{-g^2 e^{-\mu R}}{4\pi R}\,. \tag{2.52}$$

In this case, the integral over relative times is even more convergent than before. As long as the time required to change $R(t)$ significantly is much greater than *either one* of the two distance scales R, μ^{-1}, the expression

$$\langle e^{ig\oint dx\cdot A}\rangle \simeq \exp\left[-\int dt\, V(R(t))\right] \tag{2.53}$$

gives a good approximation to the expectation value of the Wilson loop.

For my final example, let me consider again the situation of a photon field given a mass by the Higgs mechanism, but let me alter the Wilson loop slightly

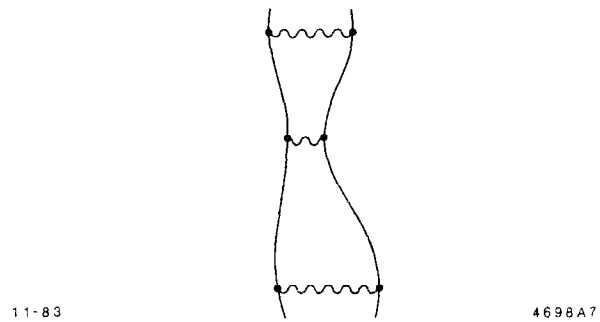


FIG. 11. Calculation of the expectation value of the Wilson loop for a slowly moving quark and antiquark, according to the approximation of Eq. (2.50).

so that it describes the interaction not of electric charges but, rather, of magnetic monopoles. This can be done straightforwardly by rewriting the integral in (2.41) by a 2-dimensional integral over a surface S which spans C:

$$\exp\Big[ig \oint_c dx \cdot A\Big] = \exp\Big[ig \int_S d\sigma^{\mu\nu} F_{\mu\nu}\Big] \tag{2.54}$$

and then replacing electric by magnetic fields in (2.54); this is done relativistically by the replacement

$$F_{\mu\nu} \to \tilde{F}_{\mu\nu} \quad \text{where} \quad \tilde{F}_{\mu\nu} = \frac{1}{2}\epsilon_{\mu\nu\lambda\sigma}F^{\lambda\sigma} \ . \tag{2.55}$$

(Actually, one must make this replacement in the gauge field Lagrangian (2.43) [14–16] by replacing

$$\begin{aligned} \int d^4x \frac{1}{4}(F_{\mu\nu})^2 = d^2x \frac{1}{4}(\tilde{F}_{\mu\nu})^2 \to \\ \int d^4x \frac{1}{4}\Big(\tilde{F}_{\mu\nu}(x) - g_m \int d^2\sigma_{\mu\nu}(y)\delta^{(4)}(x-y)\Big)^2 \ ; \end{aligned} \tag{2.56}$$

the second term added allows $\tilde{F}_{\mu\nu}$ to have sources and sinks. Multiplying out the square gives (2.54) with the replacement (2.55) (up to a factor of i), plus an extra singular term).

Now we can integrate over A by completing the square as before; for a loop which lies in a plane, the result is:

$$\langle e^{ig\oint_c dx\cdot A}\rangle = \exp\Big[+\frac{g_m^2}{2}\int d^2\sigma_x \int d^2\sigma_y \Big(\frac{\partial}{\partial \vec{x}_\perp}\cdot\frac{\partial}{\partial \vec{y}_\perp}\Delta(x-y) - \delta^{(4)}(x-y)\Big)\Big] \ ; \tag{2.57}$$

the delta function comes from the singular term identified above. This expression can be rearranged using the identity

$$\begin{aligned} \frac{\partial}{\partial \vec{x}_\perp}\cdot\frac{\partial}{\partial \vec{y}_\perp}\Delta(x-y) = -\frac{\partial^2}{\partial x_\perp^2}\Delta(x-y) = \Big(-\nabla^2 + \frac{\partial^2}{\partial x_\parallel^2}\Big)\Delta(x-y) \\ = \Big(-\frac{\partial}{\partial x_\parallel}\cdot\frac{\partial}{\partial y_\parallel} + (-\nabla^2+\mu^2) - \mu^2\Big)\Delta(x-y) \end{aligned} \tag{2.58}$$

The term including $\partial/\partial\vec{x}_\parallel \cdot \partial/\partial\vec{y}_\parallel$ can be integrated by parts to give just the result of the Higgs case above. The second term forms the equation for the massive A field and yields a delta function when acting on $\Delta(x-y)$; this cancels the singular term. The third term yields a term in the exponent of (2.57)

$$-\frac{g_m^2}{2}\int d^2\sigma_x \int d^2\sigma_y\, \mu^2 \Delta(x-y) = -\frac{g_m^2}{2}\int dt \int_0^R dx\, dy\, \frac{\mu^2 e^{-\mu|x-y|}}{4\pi|x-y|} . \quad (2.59)$$

For $R \gg \mu^{-1}$, this becomes

$$\langle e^{ig\oint_c dx\cdot A}\rangle \sim \exp\Big[-\int dR \quad K\cdot R(t)\Big] \quad (2.60)$$

where

$$K = \frac{g^2 m}{2}\Big(\frac{1}{2\pi}\int_0^\infty dy\, \frac{\mu^2}{y}\, e^{-\mu y}\Big) . \quad (2.61)$$

If the Higgs field dynamics is treated more correctly, the lower limit of integration becomes $m_{\rm Higgs}^{-1}$. This behavior corresponds to a potential $V(R)$ with the asymptotic form

$$V(R) \sim KR; \quad (2.62)$$

the particle and antiparticle represented by the Wilson loop are permanently confined. As in the previous example, the static approximation to the potential is a good one as long as R changes slowly in time on the scale either of R or of μ^{-1}.

I should note that it is not hard to understand in this case why the magnetic charges ought to be permanently confined. When the A field acquires a mass through the Higgs mechanism, the homogeneous Maxwell equations are unchanged, but the inhomogeneous equations are changed by new μ-dependent terms. Thus, we have

$$\vec{\nabla}\cdot\vec{E} = \mu^2 A^0 \quad \text{but} \quad \vec{\nabla}\cdot\vec{B} = 0. \quad (2.63)$$

The flux of $\vec{E}$ is no longer conserved. This allows the electric field to disappear into the vacuum, and it does so in a distance μ^{-1} from the charge (hence the form of (2.52)). Magnetic flux is still conserved. However, correlations of the magnetic fields must still fall off in a distance μ^{-1}. This is possible only if the magnetic field needs information only from within a distance μ^{-1} to tell it how to stay conserved. It must then form a configuration of the form of Fig. 12, in which the magnetic field forms a tube of width μ^{-1} which carries a flux corresponding to 1 unit of charge.[16–17] This mechanism has been shown to be the explanation for the permanent confinement of charge seen in the strong-coupling limit of lattice gauge theories, at least for the case of Abelian gauge groups. [18–21] Unfortunately, physical quark-antiquark systems are described, not by any of these idealized limiting cases, but rather by the $SU(3)$ color gauge theory QCD. We do not know how to compute the Wilson loop expectation value in QCD except by rather cumbersome numerical methods which are only recently beginning to show results. [22–24] However, we do have some analytical control over the limiting behavior of the potential $V(R)$. For small R, perturbative QCD is applicable, and the potential has been computed to the two-loop order. [25–27] The leading behavior for small R is just a Coulomb potential

$$\frac{-4\alpha_s(R)}{3\pi R}, \quad (2.64)$$

with $\alpha_s(R)$ the running QCD coupling constant. At large distances, our best information comes from a recent paper of Tomboulis,[28] who has proven a bound on the Wilson loop expectation value in lattice gauge theories which implies that the behavior (2.62) is true for some value of K for any finite lattice spacing. Combining these two limiting cases, we might make a sketch of the potential in QCD; it has the general form shown in Fig. 13. The principal question which remains concerning this potential is that of what sets the scale μ^{-1} which characterizes the scale over which the static gauge fields can be deformed. This quantity bears no obvious relation to the value of the constant K which appears

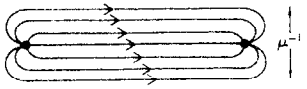


FIG. 12. Configuration of magnetic flux around a pair of magnetic sources in a superconductor.

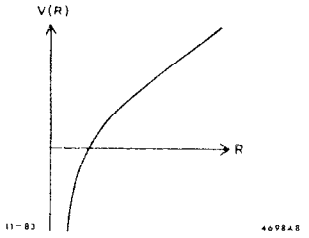


FIG. 13. Sketch of the form of V(R) in QCD.

in the potential, as Eq. (2.61) makes clear. Presumably, this scale is a mass scale of the gluon sector. But, unfortunately, the gluon dynamics is the aspect of QCD which we understand least well how to connect with phenomenology. I believe it not unreasonable to assume that the effective value of μ is of order 1 GeV; however, we should really hope that the study of heavy-quark systems can give us more precise information on this size of this quantity.

3. Spin-Dependent Forces

In the previous section, we saw how to use the Feynman path integral formalism to visualize the dynamics of nonrelativistic particles in space-time. We derived the Formula (2.22) which confirmed our intuition that such particles could be viewed as travelling on space-time trajectories which were close to being straight lines in the time direction. We saw, further, that such particles could be coupled to gauge fields by associating a phase factor (2.33) with the trajectory. These two ingredients give us a complete picture of particle-antiparticle dynamics at the leading order of a nonrelativistic expansion. In this lecture, I would like to study the simplest relativistic corrections to this picture, the spin-dependent forces in fermion-antifermion bound states. As in our study of the static potential, I will try as far as possible not to make any approximation other than the nonrelativistic limit, in order to clarify what structure for the spin-dependent forces follows directly from the gauge-theory structure of the underlying interactions. In taking this point of view, I follow the work of Eichten and Feinberg.[1] The bulk of my analysis in this section will be a derivation of a general formula for the spin-dependent forces first presented in their paper.

Before we can do any detailed analysis, we must first recall that we performed the analysis leading to equation (2.22) only for the case of the Klein-Gordon equation. We must generalize this analysis to apply to the Dirac equation. This generalization was first presented by, Feynman[29] I learned of it from the presentation of Halpern and Siegel.[30]

We need, then, to represent the solution to

$$\left[\gamma^\mu(\partial_\mu - ig\mathbf{A}_\mu) - m\right]\psi = \delta^{(4)}(x-y)\ . \tag{3.1}$$

Again, we will work with imaginary time ($it = x_0$); the appropriate Dirac matrices satisfy

$$\{\gamma^\mu, \gamma^\nu\} = 2\delta^{\mu\nu}\ . \tag{3.2}$$

It is convenient to choose the following representation of the gamma matrices:

$$\gamma^\mu = \left(\begin{array}{c|c} 0 & \sigma^\mu \\ \hline \bar{\sigma}^\mu & 0 \end{array}\right) \tag{3.3}$$

where

$$\sigma^\mu = (1, i\vec{\sigma}), \qquad \bar{\sigma}^\mu = (1, -i\vec{\sigma})\ . \tag{3.4}$$

In this basis, γ^5 is diagonal

$$\gamma^5 = \left(\begin{array}{c|c} 1 & 0 \\ \hline 0 & -1 \end{array}\right) \tag{3.5}$$

and the spin matrices $\Sigma^{\mu\nu}$ take the form

$$\Sigma^{\mu\nu} = \frac{-i}{2}\left[\gamma^\mu, \gamma^\nu\right] = \left(\begin{array}{c|c} \eta_{a\mu\nu}\sigma^a & 0 \\ \hline 0 & \bar{\eta}_{a\mu\nu}\sigma^a \end{array}\right) \tag{3.6}$$

where $\eta_{a\mu\nu}$ is a numerical tensor defined[31] by

$$\eta_{ai0} = 1, \quad \eta_{aij} = \epsilon_{aij}, \quad \eta_{a\mu\nu} = -\eta_{a\nu\mu}\ . \tag{3.7}$$

Keeping this notation in mind, we can write the solution to (3.1) in the form

$$\psi(x;y) = \left[\gamma^\mu D_\mu + m\right] G(x;y) \tag{3.8}$$

where $G(x;y)$ is the solution to

$$[\gamma^\mu D_\mu - m]\,[\gamma^\nu D_\nu + m]\,G(x;y) = \delta^{(4)}(x-y)\,. \tag{3.9}$$

Of course, it is not clear that this helps enormously: We now see that $\psi(x;y)$ can be written in the form

$$\psi(x;y) = \left(\begin{array}{c|c} m & \sigma^\mu D_\mu \\ \hline \bar\sigma^\mu D_\mu & m \end{array}\right) G(x,y)\,. \tag{3.10}$$

But what is G?

Actually, it is not hard to construct G explicitly using the set of tricks introduced in the previous section. Using the identity

$$\gamma^\mu\gamma^\nu = \frac{1}{2}\{\gamma^\mu,\gamma^\nu\} + i\left(\frac{-i}{2}[\gamma^\mu,\gamma^\nu]\right) \tag{3.11}$$

and (3.4), we can cast (3.9) into the form

$$\begin{aligned}\Big(D^2 - m^2 + i\Sigma^{\mu\nu}\Big[\partial_\mu - ig\mathbf{A}_\mu, \partial_\nu - ig\mathbf{A}_\nu\Big]\Big)\,G(x;y) \\ = -\Big(-D^2 + m^2 - \frac{g}{2}\,\Sigma^{\mu\nu}\mathbf{F}_{\mu\nu}\Big)\,G(x;y) = \delta(x-y)\,.\end{aligned} \tag{3.12}$$

This equation is of the same form as those we considered earlier, and so we may immediately write down a functional integral representation for G

$$G = \int_0^\infty dT \int \mathcal{D}x\, e^{-\int_0^T d\tau\, \frac{1}{2}\dot x^2 + m^2} P\Big(e^{i\int \dot x\cdot\mathbf{A} + \int d\tau\, \frac{g}{4}\,\Sigma^{\mu\nu}\mathbf{F}_{\mu\nu}}\Big)\,. \tag{3.13}$$

Note that, since the various components of $\Sigma^{\mu\nu}$ do not commute with one another, we must path-order these matrices just as we path-order the $\mathbf{A}_\mu$. Since the $\Sigma^{\mu\nu}$ are block-diagonal in the basis we have chosen, G also falls into the block form

$$G(x;y) = \left(\begin{array}{c|c} G_R(x;y) & 0 \\ \hline 0 & G_L(x;y) \end{array}\right)\,. \tag{3.14}$$

Within each block, we may take the nonrelativistic limit as we did above for the Klein-Gordon propagator; for G_R the result is

$$G_R = \int \mathcal{D}\vec x\, e^{-\int dt\, \frac{1}{2}\dot{\vec x}^2} \cdot P\Big(e^{i\int d\mathbf{x}\cdot\mathbf{A} + \int dt\, \frac{g}{4m}\,\eta_{a\mu\nu}\sigma^a\mathbf{F}_{\mu\nu}}\Big)\,. \tag{3.15}$$

The representation (3.15) differs from the corresponding expression (2.22) for the Klein-Gordon equation by the addition of the path-ordered factor containing the coupling of the spin to $\mathbf{F}_{\mu\nu}$. Written more explicitly, this new term has the form $(-\int dt \Delta V)$, where

$$\Delta V = -\frac{g}{2m}\vec\sigma\cdot(\vec{\mathbf{B}} - \vec{\mathbf{E}})\,. \tag{3.16}$$

The first part of this expression is obviously the magnetic-moment interaction of the fermion; note that it has just the right magnitude. The second part looks rather more peculiar. To explain its presence, I must apologize for the one awkward feature of the formalism I use in these lectures: In order to consistently work with Euclidean time ($x_0 = it$), we must also work with Euclidean $\vec{\mathbf{E}}$ fields. In particular, the $\vec{\mathbf{E}}$ fields which appear in the expression (2.42) should, like x_0, be properly considered imaginary quantities analytically continued to real values. The same goes for the $\mathbf{A}^0$ and $\vec{\mathbf{E}}$ fields in (3.13). If we introduce an external, physical $\vec{\mathbf{E}}$ field, then, we must orient it properly relative to the fluctuating $\vec{\mathbf{E}}$ by supplying a factor of i:

$$\vec{\mathbf{E}}_{\rm ext} = -i\vec{\mathbf{E}};\quad \vec{\mathbf{B}}_{\rm ext} = \vec{\mathbf{B}}\,. \tag{3.17}$$

In the same way, if we try to connect Euclidean time derivatives to physical quark position operators, we again need to supply this factor:

$$\vec{\mathbf{p}} = im\frac{d\vec x}{dx_0}\,. \tag{3.18}$$

Using (3.17), we can see that an external $\vec{\mathbf{B}}$ field causes an exponential growth or decay in the magnitude of the wave function, indicating, through comparison with the form of (2.9), that the energy of the quantum state is shifted. An external $\vec{\mathbf{E}}$ field, however, introduces only an inconsequential phase. Let me warn the reader to watch out (or not, as he prefers) for sly factors of i throughout the arguments of this section; fortunately, these factors are the only subtle feature of this formalism.

In any event, we would like to use the Formula (3.13) (or, better, its nonrelativistic reduction) to compute bound state energies in fermion-antifermion systems. Any such bound state energy shows up as a term in the functional integral which decays in amplitude as

$$\exp\,(-E_b x_0); \tag{3.19}$$

the lowest bound state (or the lowest such state with specified quantum numbers) dominates the functional integral expression as x_0 is taken large, as long as the initial conditions for the particle paths have overlap with this state. In particular, we might note that nonrelativistic fermions are approximately equal admixtures of $\gamma^5 = +1$ and $\gamma^5 = -1$ states, so that we can, if we wish, limit our attention to $\gamma^5 = +1$ components of the Green's function $\psi(x;y)$ and still retain the full information available on bound state energies. Let us, then, disregard most of (3.10) and concentrate on the upper left-hand corner of this matrix. This element has the nonrelativistic expansion:

$$\int \mathcal{D}\vec{x}\, e^{-\int dt\, \frac{1}{2}\dot{\vec{x}}^2} P\Big(e^{ig\int d\vec{x}\cdot\mathbf{A} + \int dt\, \frac{g}{2m}\vec{\sigma}\cdot(\vec{\mathbf{B}}-\vec{\mathbf{E}})}\Big). \tag{3.20}$$

We can learn whatever we might wish to know about the nonrelativistic fermion-antifermion spectrum by isolating the exponentially decaying amplitudes of the form of (3.19) contained in (3.20).

The explicitly spin-dependent term in the exponent of (3.20) contains a factor m^{-1} and is therefore of higher order in a nonrelativistic expansion. As we will see in a moment, spin-dependent effects contribute to the energy of the q-$\bar{\text{q}}$ state for the first time in order m^{-2} relative to the nonrelativistic binding energy. Since any such terms contain at least one power of the term involving $\vec{\sigma}$, the corrections to (3.23), which are by themselves of order m^{-2}, do not contribute to this order. Let us now try to account the set of leading spin-dependent terms systematically. In order to do this, it will be convenient to introduce one more piece of notation. I will use brackets to denote the expectation value of gauge field operators on the quark trajectory and path-ordered along with the Wilson line. For example,

$$\langle\vec{\mathbf{B}}(t,x_+)\rangle = \frac{1}{Z}\int \mathcal{D}x\,\mathcal{D}\mathbf{A}\, e^{-\int \mathcal{L}}\, e^{-\int \frac{1}{2}\dot{x}^2} P\Big[e^{-\int dx\cdot\mathbf{A}}\vec{\mathbf{B}}(t,x_+)\Big]. \tag{3.21}$$

In Eq. (3.21), Z denotes the value of the indicated integral without the operator $\vec{\mathbf{B}}$ and x_+ indicates the quark position; I will denote the antiquark position by x_-. This expectation value is indicated graphically in Fig. 14.

To warm up for this accounting, let us examine the various spin- dependent terms of order m^{-1}. To this order, we should bring down from the exponent one factor containing $\vec{\sigma}$; then we can ignore all other corrections to the static limit. In this approximation, the correction to the wavefunction is given by

$$\delta\psi = \langle \oint dt\Big(\frac{g}{2m}\vec{\sigma}\cdot\vec{\mathbf{B}} - \frac{g}{2m}\vec{\sigma}\cdot\vec{\mathbf{E}}\Big)\rangle\,. \tag{3.22}$$

The piece involving $\vec{\sigma}\cdot\vec{\mathbf{B}}$ gives no contribution, since

$$<\mathbf{B}^i(x_+,t)>=0 \tag{3.23}$$

by symmetry for a static $q-\bar{q}$ pair. The piece involving $\vec{\sigma}\cdot\vec{\mathbf{E}}$ can be evaluated by noting that the only component of $<\mathbf{E}^i>$ which does not vanish by symmetry

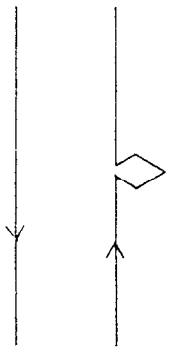


FIG. 14. Graphical representation of the expectation value shown in Eq. (1.21).

is the component in the direction of the quark-antiquark separation $\hat{R}$. This component can be evaluated by comparison with Eq. (2.39):

$$\begin{aligned} \langle \int dt\, g\mathbf{E}^i(t,x_+)\rangle &= \frac{-i}{\epsilon}\langle \int dt\, \epsilon(igF_{oi})\rangle \\ &= -i\frac{1}{Z}\frac{\partial}{\partial R^i}Z = +i\int dt\,\frac{\partial}{\partial R^i}V(R)\,. \end{aligned} \tag{3.24}$$

Exponentiated, this factor gives just a time-dependent phase and not an exponential decay; thus, it does not contribute to the bound state energy.

Now let us move on to the terms of order m^{-2}. These terms are of three types. The first arises from two insertions of $\vec{\sigma}$ terms. We might, first, bring down two factors of $\vec{\sigma}\cdot\vec{\mathbf{B}}$ on the same quark line. This gives:

$$\delta\psi = \langle \frac{1}{2}\int dt\,\frac{g}{2m}\vec{\sigma}\cdot\vec{\mathbf{B}}(t,x_+)\int dt'\frac{g}{2m}\vec{\sigma}\cdot\vec{\mathbf{B}}(t',x_+)\rangle\,. \tag{3.25}$$

But this expression is symmetric in the two $\vec{\sigma}$'s, so we may use the identity

$$\sigma^i\sigma^j + \sigma^j\sigma^i = 2\delta^{ij} \tag{3.26}$$

to see that (3.25) is not in fact spin-dependent. We can also bring down factors of $\vec{\sigma}\cdot\vec{\mathbf{B}}$ on both the quark and antiquark lines. This produces a change in the wavefunction of the form:

$$\delta\psi = \langle \int_{-\infty}^{\infty} dt \quad \frac{g}{2m}\vec{\sigma}_+\cdot\vec{\mathbf{B}}(t,x_+)\int_{-\infty}^{\infty}dt' \quad \frac{-g}{2m}\vec{\sigma}_-\cdot\vec{\mathbf{B}}(t',x_-)\rangle\,. \tag{3.27}$$

I use $\vec{\sigma}_+$ and $\vec{\sigma}_-$ to represent the spin matrices acting on the quark and antiquark lines, respectively. The expectation value indicated in the second line of (3.27)is represented graphically in Fig. 15. In the models which I presented at the end of the previous section, the correlation function of two operators $\vec{\mathbf{B}}$ is short-ranged, so that the integral over t' falls off rapidly if the separation of the two $\vec{\mathbf{B}}$

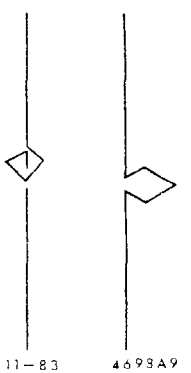


FIG. 15. Graphical representation of the expectation value appearing in Eq. (1.27).

operators is greater than R or μ^{-1}. It is then appropriate to ignore the relative motion of the quark and antiquark during the time interval $(t'-t)$ and represent this integral as some new type of static potential. Since the expectation value contains two tensor structures, we can represent it in the form:

$$\langle g^2 \int dt' \mathbf{B}^i(t,x_+)\mathbf{B}^j(t',x_-)\rangle = \left(\hat{R}^i\hat{R}^j - \frac{1}{3}\delta^{ij}\right)V_3(R) + \frac{1}{3}\delta^{ij}V_4(R)\,. \qquad (3.28)$$

Then Eq. (3.27) becomes

$$\delta\psi = -\int dt \frac{1}{4m^2}\left(\left[\hat{R}\cdot\vec{\sigma}_+\hat{R}\cdot\vec{\sigma}_- - \frac{1}{3}\vec{\sigma}_+\cdot\vec{\sigma}_-\right]V_3 + \frac{1}{3}\vec{\sigma}_+\cdot\vec{\sigma}_- V_4\right). \qquad (3.29)$$

It is appropriate to view this as the first term in the expansion of a factor $exp(-\int dt\Delta V)$; thus, Eq. (3.29) gives our first spin-dependent correction to the bound-state energy. The terms involving $\vec{\sigma}\cdot\vec{\mathbf{E}}$ do not contribute to this order: The only term which is not a pure phase is the second-order term arising from the exponentiation of (3.24).

The second type of contribution comes from bringing down one $\vec{\sigma}$ term and then expanding to first order in the quark or antiquark velocity. For definiteness, let us consider first the case in which we bring down a $\vec{\sigma}\cdot\vec{\mathbf{B}}$ term on the quark line and consider the quark velocity to be nonzero. We can represent the term of first order in the quark velocity in the manner indicated in Fig. 16, by considering it as displaced from a line aligned precisely in the time direction and expanding for small displacements as we did in Eq. (2.39). This procedure gives, for the term in $\delta\psi$ of first order in the quark velocity,

$$\begin{aligned}\delta\psi &= \int \langle dt \frac{g}{2m}\vec{\sigma}\cdot\vec{\mathbf{B}}(t,x_+)\int dt' ig\frac{d\vec{x}}{dt'}\cdot(t'-t)\cdot\vec{\mathbf{E}}(t',x_+)\rangle \\ &= \int dt \frac{1}{2m^2}\sigma^i\mathbf{p}^j\langle\int dt' g^2\mathbf{B}^i(t,x_+)t'\mathbf{E}^j(t+t',x_+)\rangle\end{aligned} \qquad (3.30)$$

In the last line, we have used Eq. (3.18) to replace the line velocity by the quark momentum operator $\vec{\mathbf{p}}$; this introduces a factor of i. The indicated expectation

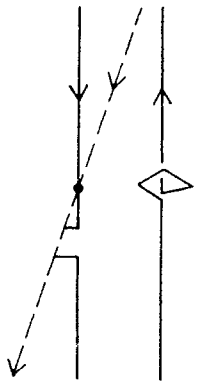


FIG. 16. Representation of the expansion of a finite- velocity Wilson line about its zero-velocity limit.

value is again highly restricted by symmetry; we may represent it in the form:

$$\langle \int dt' g^2 \mathbf{B}^i(t, x_+)\mathbf{E}^j(t', x_+)\rangle = \epsilon_{ijk}\hat{R}^k \frac{\partial}{\partial R} V_1(R) \,. \tag{3.31}$$

Then (3.30) becomes

$$\sigma\psi = -\int dt \frac{1}{2m^2}\vec{\sigma}_+ \cdot \vec{\mathbf{L}}_+ \frac{1}{R}\frac{\partial}{\partial R} V_1(R) \tag{3.32}$$

where $\vec{\mathbf{L}}_+$ denotes the angular momentum of the quark. The correction arising from a field insertion on a finite-velocity antiquark line is of almost the same form:

$$\delta\psi = +\int dt \frac{1}{2m^2}\vec{\sigma}_- \cdot \vec{\mathbf{L}}_- \frac{1}{R}\frac{\partial}{\partial R} V_1(R) \,. \tag{3.33}$$

The change in sign comes from $g \to -g$, or,equivalently, from the change in direction of the antiquark line. The corresponding terms in which $\vec{\sigma}\cdot\vec{\mathbf{E}}$ is inserted can be seen to yield only phases.

In a similar way, we can reduce the term arising from an insertion on one line and finite velocity on the other to the form:

$$\delta\psi = -\int dt \frac{1}{2m^2}(\vec{\sigma}_- \cdot \vec{\mathbf{L}}_+ - \vec{\sigma}_+ \cdot \vec{\mathbf{L}}_-)\frac{1}{R}\frac{\partial}{\partial R} V_2 \,, \tag{3.34}$$

where we have represented

$$\langle g^2 \int dt' t' \mathbf{B}^i(t, x_-)\mathbf{E}^j(t + t', x_+)\rangle \frac{\partial}{\partial R^k} V_2 \,. \tag{3.35}$$

Actually, though, V_2 is not independent of the potentials we have defined previously. Consider the effect of taking the divergence of Eq. (3.35). We can take $\partial/\partial R^k$ of this object by considering the derivative to act on the line with the $\vec{\mathbf{E}}$ insertion and using (2.39). There are two contributions, represented graphically in Fig. 17. The first contribution, in which the derivative acts on the Wilson

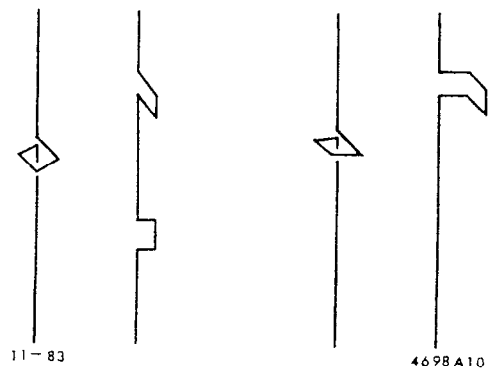


FIG. 17. Representation of the two contributions to $\nabla^2 V_2$.

line, gives zero by the antisymmetry of the ϵ_{ijk} symbol. In the second term, we can use the non-Abelian Maxwell equation

$$\vec{D} \times \vec{\mathbf{E}} = D_0 \vec{\mathbf{B}} \tag{3.36}$$

and the relation for the path-ordering operator

$$\langle D_0 \vec{\mathbf{B}}(t) \rangle = \frac{\partial}{\partial t} \langle \vec{\mathbf{B}}(t) \rangle \tag{3.37}$$

to write this term as

$$-\frac{g^2}{2} \int dt' t' \frac{\partial}{\partial t'} \langle \mathbf{B}^i(t, x_-) \mathbf{B}^j(t, t', x_+) \rangle = \frac{g^2}{2} \int dt' \langle \mathbf{B}^i(t, x_-) \mathbf{B}^j(t', x_+) \rangle \ . \tag{3.38}$$

Thus, we have the relation

$$2\nabla^2 V_2(R) = V_4(R) \ . \tag{3.39}$$

The third type of term comes from introducing the correct relation between the spin matrices $\vec{\sigma}$ appearing in (3.20) and the quark and antiquark spins. The $\vec{\sigma}$ matrices are the matrix elements of $\Sigma^{\mu\nu}$; these are connected to the spin via the relation

$$\xi^+ S^k \xi = \frac{1}{2} \epsilon_{ijk} \bar{u}(p) \Big(\frac{1}{2} \Sigma^{ij} \Big) u(p) = \xi^+ \Big(\frac{\sigma^k}{2} - \Big(\frac{d\vec{x}}{dt} \times \frac{\vec{\sigma}}{2} \Big)^k + \cdots \Big) \xi \tag{3.40}$$

where ξ is a nonrelativistic spinor and $u(p)$ is the corresponding Dirac spinor. If we correct $\vec{\sigma}$ to $\vec{S}$ in our evaluation of the order m^{-1} terms, and use (3.18), we obtain a correction of order m^{-2} which is *real* and contributes to the energy shift:

$$\mathrm{Re}\,(\delta\psi) = \int dt \, \frac{g}{m} \frac{\vec{\sigma}_+}{2} \cdot \frac{\partial}{\partial \vec{R}} V(R) \ . \tag{3.41}$$

This is precisely the classical spin-orbit contribution, familiar from first-year quantum mechanics. It is equally familiar that, since the spin has been referred to an accelerating frame of reference, this contribution to the energy must be decreased by half because of Thomas precession. A similar contribution arises from correcting the order m^{-1} term involving $\vec{\sigma}_-$.

Summing the various contributions of these three types, we find a general representation for the leading spin-dependent contributions to the q-$\bar{\text{q}}$ bound state energy. This expression, first, derived by Eichten and Feinberg,[1] is the following

$$\begin{aligned} V_{\text{spin-dep}} = & \Big(\frac{\vec{S}_+\cdot\vec{L}_+ + \vec{S}_-\cdot\vec{L}_-}{2m^2}\Big)\frac{1}{R}\frac{dV}{dR} \\ & + \Big(\frac{\vec{S}_+\cdot\vec{L}_+ + \vec{S}_-\cdot\vec{L}_-}{m^2}\Big)\frac{1}{R}\frac{dV_1}{dR} \\ & - \Big(\frac{\vec{S}_+\cdot\vec{L}_- + \vec{S}_-\cdot\vec{L}_+}{m^2}\Big)\frac{1}{R}\frac{dV_2}{dR} \\ & - \frac{2}{3m^2}\,\vec{S}_+\cdot\vec{S}_-\nabla^2 V_2(R) \\ & - \frac{1}{m^2}\,(\vec{S}_+\cdot\hat{R}\,\vec{S}_-\cdot\hat{R} - \frac{1}{3}\,\vec{S}_+\cdot\vec{S}_-)\,V_3(R)\,. \end{aligned} \tag{3.42}$$

The first three terms of (3.42) are spin-orbit interactions. The fourth is a hyperfine interaction. The fifth is a tensor force. To evaluate the matrix elements of (3.42) for two-body q-$\bar{\text{q}}$ bound states, one should set

$$\vec{L}_+ = \vec{L}_- = \vec{L}.$$

In order to use Eq. (3.42), however, we need to know the form of the various potentials V_i which appear in it. V, of course, is the same static potential used to represent the nonrelativistic bound state spectrum, but the other potentials are not otherwise accessible phenomenologically. We can get a first idea of their form by evaluating them in QED. In this case, the expectation value of two field operators in the presence of a Wilson loop is just equal to the same expectation value in free space; for example,

$$\langle \mathrm{B}^i(t,x_+)\mathrm{B}^j(t,x_-)\rangle = -\,\epsilon_{ikl}\,\epsilon_{jmn}\partial_k\partial_m\delta_{ln}\Big(\frac{1}{2\pi^2(x_+-x_-)^2}\Big)\,. \tag{3.43}$$

One can easily show, from the definitions (3.28), (3.31), (3.35), that

$$V = -\frac{e^2}{4\pi R}\,,\quad V_1 = 0\quad V_2 = \frac{e^2}{4\pi R}\,,\quad V_3 = -\frac{3e^2}{4\pi R^3}\,. \tag{3.44}$$

Inserting these results into (3.42), we find for the spin-dependent forces in QED the expression

$$\begin{aligned} V_{e-d} = & \frac{\vec{L}\cdot(\vec{S}_+ + \vec{S}_-)}{m^2}\,\frac{3}{2}\,\frac{\alpha}{R^3} + \frac{2\alpha}{3m^2}\,\vec{S}_+\cdot\vec{S}_-\,4\pi\delta(\vec{R}) \\ & + \frac{1}{m^2}\,(3\vec{S}_+\cdot\hat{R}\vec{S}_-\cdot\hat{R} - \vec{S}_+\cdot\vec{S}_-)\,\frac{\alpha}{R^3}\,. \end{aligned} \tag{3.45}$$

The corresponding formula in perturbative QCD, to leading order in perturbation theory, is obtained by replacing

$$\alpha \to \frac{4}{3}\alpha_s \tag{3.46}$$

in this equation.

However, at least for the ψ and Υ systems, we need to deal with real QCD, which does not stay entirely within the perturbative regime. The only way to proceed from here is to guess forms for the various functions V_i which have appropriate small-distance limits. These potentials should obey one general constraint which follows from the considerations at the end of the previous section. In the models we discussed there, one can readily show that gauge field correlations of

the type involved in the definitions of the V_i fall off as R^{-3} (the QED result) in the massive gauge model for $R < \mu^{-1}$, but then fall off much more rapidly, as

$$\frac{\mu^2}{R} e^{-\mu R} \tag{3.47}$$

for $R > \mu^{-1}$. I expect a similar behavior to appear in confining gauge theories, since the flux tube which binds quark and antiquark cannot carry information. Let me remark again, however, that I do not know precisely what mass scale plays the role of μ. In any event, if this is so, the first term of (3.42) gives rise to a long-ranged force, since it contains the factor

$$\frac{1}{R}\frac{dV}{dR} \to \frac{K}{R} \quad \text{as} \quad R \to \infty, \tag{3.48}$$

but the other terms decrease exponentially. Perhaps it is, then, not unreasonable to approximate these terms by their perturbative values; this is the approximation scheme chosen by Eichten and Feinberg.[1] I should, however, note two minor difficulties with this hypothesis. The first is that $\nabla^2 V_2$ should contain an exponentially decaying term of the form of (3.47), whereas in leading order of perturbation theory it is completely local, proportional to $\delta(\vec{R})$. The second is that Kogut and Parisi [32] have found a contribution to the tensor force of order m^{-4} which decays only algebraically (as R^{-5}) as $R \to \infty$; thus (3.48) is not the only long-range spin-dependent effect in the theory. A better approximation might be to evaluate the complete expression (3.42) in an explicit model of confinement such as the magnetic superconductor model of the previous section. A somewhat incomplete study of this approximation has been carried out by Banks and Spiegelglas.[33]

Despite the comment I have just made about the hyperfine interaction, it is certainly true that perturbation theory gives an extremely local interaction. It is tempting to compute this interaction more seriously in perturbative QCD and take seriously the corrections to the leading-order result. The hyperfine term in (3.42) does not contribute to the splittings of the P-wave q-$\bar{\text{q}}$ states, but it can be used to predict the splitting between the singlet and triplet S states. This calculation has been carried out by Buchmüller, Ng, and Tye,[34] who computed the one-loop radiative correction to the expression for the hyperfine interaction obtained from (3.45) and (3.46). They find

$$\Delta E(^3S - {}^1S) = \frac{32\pi}{9}\frac{\alpha_{\overline{MS}}}{m^2}|\psi(0)|^2\left[1 + \left(0.563 + 0.375\frac{(log\frac{Q^2}{m^2\tau})}{|\psi(0)|^2}\right)\frac{\alpha_{\overline{MS}}}{\pi}\right]. \tag{3.49}$$

This result is numerically quite reasonable; the $\psi - \eta_c$ mass splitting of 120 MeV would correspond, using (3.49), to a value of $\Lambda_{\overline{MS}}$ of about 300 MeV.

Let me now discuss briefly, and in very general terms, the application of Eq. (3.42) to the the splittings of the ^3P states. In this case the hyperfine term does not contribute, so we must evaluate the matrix elements of

$$\vec{L}\cdot\vec{S} \quad \text{and} \quad \hat{R}\cdot\vec{S}_+\,\hat{R}\cdot\vec{S}_- . \tag{3.50}$$

This is easily done; let me provide you with a table of the relevant diagonal matrix elements of spin operators:

	$^3P_0$	$^3P_1$	$^3P_2$
$\langle\vec{L}\cdot\vec{S}\rangle$	-2	-1	$+1$
$\langle\hat{R}\cdot\vec{S}_+\,\hat{R}\cdot\vec{S}_-\rangle$	$-\frac{1}{4}$	$\frac{1}{4}$	$\frac{1}{20}$

(3.51)

The mass splittings of the P states are most often characterized by the value of a parameter r, defined by

$$r = \frac{M(^3P_2) - M(^3P_1)}{M(^3P_1) - M(^3P_0)}. \tag{3.52}$$

Using the elements of the Table (3.51), one can see that, in the limits in which the spin-orbit and tensor terms, respectively, dominate the mass splitting, r takes

the following values:

spin-orbit dominance	$\rightarrow$	$r = 2$
tensor dominance	$\rightarrow$	$r = -0.4$
QED	$\rightarrow$	$r = 0.8$.

The third value of r is that obtained from Eq. (3.45). The experimental values of r for the c-$\bar{c}$ and b-$\bar{b}$ systems are

$c\bar{c}$	1^3P	$r = 0.48$
$b\bar{b}$	1^3P	$r \sim 1.0$
$b\bar{b}$	2^3P	$r \sim 0.9$.

It is quite reasonable that these numbers indicate the approach of the spin-dependent potentials to their perturbative form.

Clearly, there is much more that one could do to compare Eq. (3.42) to the experimental data on spin-dependent forces. One further application is given in Estia Eichten's lecture in this volume. I do not have space in the scope of this review to survey the variety of forms which have been postulated for the potentials V_i and the experimental success of these forms. But recently Rosner[35] has compiled a detailed survey of such models; I recommend his review to the interested reader.

Thus ends our formal discussion of spin-dependent forces, as they are described by gauge theories. What do we learn from this analysis? First of all, the spin-dependent interactions of heavy quarks can be analyzed systematically and represented in terms of more fundamental expectation values of the gauge fields. The classical spin-orbit interaction still appears, and this term is of long range in a confining theory. But the short-ranged part of the spin-dependent potential is a new object, a new probe of gauge field correlations in the region between confinement and perturbation theory.

4. Hadronic Transitions Between Heavy-Quark States

In this section, I would like to examine another, more dynamical aspect of the behavior of heavy quark-antiquark systems, the theory of transitions between heavy q-$\bar{q}$ states mediated by the strong interactions. Again, our analysis will be guided by its use of the Feynman path formalism, and this discussion will provide another illustration of the power of this formalism in allowing one to visualize the basic processes of the gauge theory. To begin, let me pose the problem more precisely. The c-$\bar{c}$ and b-$\bar{b}$ quark-antiquark bound states are observed to have very small widths for decay into ordinary hadrons and seem otherwise to be very weakly coupled to ordinary hadrons. Still, though, excited states of the ψ and Υ are observed to decay (albeit slowly) via:

$$\psi' \rightarrow \psi + 2\pi, \quad \psi + \eta, \quad \ldots$$

$$\Upsilon' \rightarrow \Upsilon + 2\pi, \quad \ldots \ . \tag{4.1}$$

The fact that these transitions are slow should encourage us, if we remember the Golden Rule of Perturbative QCD: That which is small is calculable (especially if it is too small to be measured). Let us explore what QCD has to say about the mechanism and rates of these transitions.

Before we enter our detailed analysis, let me pause to note that it is already remarkable that the processes (4.1) should be suppressed at all, given that they are mediated by the strong interactions acting at low momentum transfers and therefore, presumably, at full strength. Further, the observed suppression is much greater for the Υ' than for the ψ'. It was Gottfried[36] who realized that these features of the hadronic transitions are quite naturally understood within a gauge theory of the strong interactions and, indeed, display clearly the nature of the fundamental strong-interaction coupling. To see this, think about the process obtained from (4.1) by crossing, the scattering of an ordinary hadron by a heavy

q-$\bar{q}$ state. This situation is shown, in a somewhat idealized fashion, in Fig. 18. The heavy bound state is very small in its spatial extent. If we imagine taking the radius of this state to zero, the color charges of the quark and antiquark would overlap in space and precisely cancel; then this state would produce no gauge fields to interact with those of the larger light hadron. It therefore makes sense to compute the scattering amplitude as an expansion in the size of the heavy-quark system. In QED, such an expansion is well-known; it is just the multipole expansion of the charge density:

$$\int j_\mu A^\mu = QA^0(0) + \vec{d} \cdot \vec{E}(0) + ... \tag{4.2}$$

The first term is the only one independent of the size of the system. This vanishes for a particle-antiparticle system; thus, the leading contribution must come from the dipole interaction. Please note that for a hypothetical scalar gluon, the monopole term would be nonzero and the scattering amplitude would not decrease with the size of the heavy-quark system. Conversely, a gluon of spin greater than one would not couple to the dipole moment of the q-$\bar{q}$ state, but only to a higher multipole moment. Any indication we can find that the dipole interaction does dominate is evidence that the gluon is a particle of spin 1.

Still, one must realize that QCD is more subtle than its Abelian counterpart. It is, unfortunately, not quite correct in QCD simply to write down the analogue of Eq. (4.2); one must perform some more careful analysis. Let me now lead you through this analysis in several stages. First, I will discuss the idealized situation of pure perturbative QCD. After studying this system in some detail, I will outline a phenomenological generalization of this discussion, due to Kuang and Yan, [37] to the intermediate regime of distances described by the potential models. Finally, I will briefly indicate how hadronic transitions are described in the magnetic superconductor model of confinement discussed at the end of § 2.

Let us, then, attempt to derive a multipole expansion for heavy q-$\bar{q}$ bound states in QCD. My discussion here follows the work of Yan.[2] At first sight, we

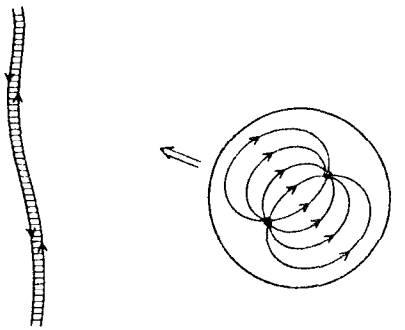


FIG. 18. Scattering of a light hadron from a heavy q-$\bar{q}$ bound state.

may produce this expansion simply by expanding the Feynman path representation of the heavy-quark bound state about the limit of zero q-$\bar{q}$ separation. The resulting expression is indicated graphically in Fig. 19. Consider first the situation in which the antiquark sits at $\vec{R} = 0$ and the quark moves freely. Using the method of Eq. (2.39), we can represent the excursions of the quark by insertions of field operators in a vertical Wilson line. In this way, we can expand:

$$e^{ig\oint dx\cdot\mathbf{A}} \simeq P\Big[e^{ig\oint dx\cdot\mathbf{A}}|_0 \cdot \Big(1 + \int dt\, ig\vec{R}_+ \cdot \vec{\mathbf{E}} + \frac{1}{2}\Big(\int dt\, ig\vec{R}_+ \cdot \vec{\mathbf{E}}\Big)^2 + \int dt\, \frac{\vec{v}_+ \times \vec{R}_+}{2} \cdot ig\vec{\mathbf{B}} + \cdots \int dt\, \frac{g}{2m}\vec{\sigma}_+ \cdot \vec{\mathbf{B}} + \cdots\Big)\Big] \tag{4.3}$$

where

$$e^{ig\oint dx\cdot\mathbf{A}}|_0 \tag{4.4}$$

represents a Wilson loop with the quark and antiquark at zero separation, and the P operator indicates that the whole expression is to be path-ordered together. The last term listed in (4.3) arises from the spin-dependent term in the exponent of (3.20) and not, strictly speaking, from the Wilson line itself. Assembling the contributions from both the quark and antiquark, we find for the expansion of the Wilson loop:

$$e^{ig\oint dx\cdot\mathbf{A}} = P\Big[e^{ig\oint dx\cdot\mathbf{A}}|_0 \cdot \exp\Big[\int dt\, ig\,\vec{R}\cdot\vec{\mathbf{E}} - \int dt\, \frac{(\vec{\mathbf{L}}_+ - \vec{\mathbf{L}}_-)}{2m}\cdot g\vec{\mathbf{B}} + \cdots\Big]\Big]. \tag{4.5}$$

The two terms listed in the exponent are the color electric and magnetic dipole interactions.

The expansion indicated in Eq. (4.5) has the general form of a series of local gauge field operators inserted into an $\vec{R} = 0$ Wilson loop:

$$P\Big[e^{ig\oint dx\cdot\mathbf{A}}|_0 \exp\Big[\int dt \sum_i C_i(\vec{R}, \vec{\mathbf{p}})\mathcal{O}_i(t)\Big]\Big]. \tag{4.6}$$

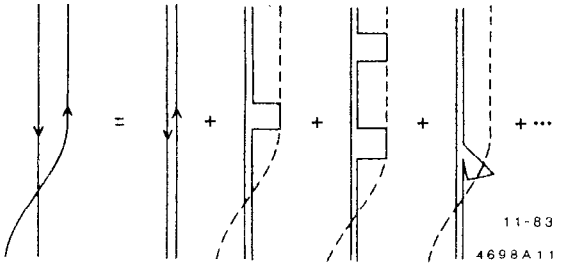


FIG. 19. Representation of the expansion of a typical quark trajectory about $\vec{R} = 0$.

It is natural to try to use this expansion to represent the emission of ordinary hadrons from the heavy q-$\bar{q}$ system by considering the gauge-field operators O_i as gluon creation operators. Then, for example, the amplitude for the q-$\bar{q}$ system to radiate a single gluon would be given by

$$< P[e^{ig\int dx\cdot \mathbf{A}} \int_{-\infty}^{\infty} dt\, g\vec{R}\cdot\vec{\mathbf{E}}_{ext}(t)] > . \tag{4.7}$$

This formula looks innocuous, and perhaps even correct, but it contains some physics which is seriously wrong. The multipole operators of Eq. (4.6) will, in general, change the color of the q-$\bar{q}$ state, and the emitted gluons will carry off color. Something that we have left out must impose quark confinement and assure that the q-$\bar{q}$ state remains a color singlet.

In principle, it might have been that we could see this color singlet restriction only by working through the physics of confinement in some detail. For this problem, however, this restriction can be found, and its effects can be studied, simply by performing QCD perturbation theory with more care. [38] We must first realize that the formal manipulations of Eq. (4.3) omit an important effect of perturbation theory–the attractive Coulomb potential between the quark and antiquark. This effect, which arises from the class of Feynman graphs shown in Fig. 20(a). produces an contribution to the amplitude for a Wilson loop with small $\vec{R}$ of the form of Eq. (3.19):

$$\exp\left[-\int dt\left(-\frac{4}{3}\frac{\alpha_s}{R}\right)\right] . \tag{4.8}$$

This Coulomb potential indicated in (4.8) is that for the attractive interaction of a quark and antiquark in a color singlet state. This contribution is nonanalytic and certainly not negligible as $\vec{R}\to 0$. Now consider the class of diagrams shown in Fig. 20(b). If the q-$\bar{q}$ system was in a color singlet state before the emission of the gluon, then afterwards it must be in a color octet state (to conserve color);

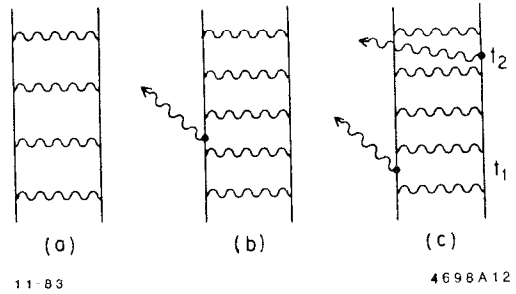


FIG. 20. Feynman graphs building up the Coulomb potential between a quark and an antiquark (a) for an undisturbed Wilson loop, (b) for a loop emitting one gluon, and (c) for a loop emitting two gluons.

the exponential factor is thus changed to the Coulomb potential appropriate to this state, which is smaller in magnitude and repulsive:

$$\exp\left[-\int dt\left(+\frac{\alpha_s}{6R}\right)\right]. \tag{4.9}$$

Eventually, this color octet state might radiate another gluon and return to a color singlet configuration (Fig. 20(c)). In this case, the exponential factor is *modified only for the length of time for which the* $q\text{-}\bar{q}$ system stayed a color octet. If the times of the two gluon emissions are labelled t_1 and t_2, respectively, this factor is given by

$$\exp\left[-\int dt\left(-\frac{4\alpha_s}{3R}\right)\right]\exp\left[-(t_2-t_1)\left(\frac{3\alpha_s}{2R}\right)\right]. \tag{4.10}$$

The higher energy of the color octet configuration provides an exponentially decaying term which restricts the size of (t_2-t_1) and thus binds together the two gluon emissions. This effect of the color Coulomb potential was first noticed by Appelquist, Dine, and Muzinich.[28]

Let us now ask how this Coulomb term—and, especially, the exponentially decaying factor displayed in Eq. (4.10)—influence the multipole expansion presented in Eq. (4.3). Clearly, it restricts the amount of time the heavy-quark system can be in a color octet state; thus it ties together two or more gluon creation operators into a cluster of emissions which is an overall color singlet. The leading term in the expansion (4.5) for the process shown in Fig. 20 is then:

$$\exp\left[-\int dt\, V_0(R)\right]\int dt_1 dt_2 ig\vec{R}\cdot\vec{\mathbf{E}}(t_2)e^{-(t_2-t_1)(H_q-E_0)}ig\vec{R}\cdot\vec{\mathbf{E}}(t_1)\,. \tag{4.11}$$

If we perform the integral over (t_2-t_1) for radiated gluons of fixed energy, including as well (by hand) the quark kinetic energy, we find a transition amplitude proportional to

$$\langle f|R^i\frac{1}{H_q-E_0}R^j|i\rangle\cdot\langle\text{hadrons}|\frac{1}{N}\,\mathrm{tr}\,\mathbf{E}^i\mathbf{E}^j|0\rangle \tag{4.12}$$

where now H_q is the complete energy of the octet $q-\bar{q}$ system. This equation represents the leading term in the multipole expansion relevant for QCD, since it is the term of lowest order which allows the heavy-quark system to begin and end in a color singlet state. More careful derivations of this formula have been given by Voloshin [39] and myself.[38]

The double-dipole Formula (4.12) will be the starting point for my discussion of the phenomenology of hadronic transitions. Before beginning this discussion, however, I would like to discuss briefly two more theoretical topics. The first is to note that, whereas the Formula (4.11) for double gluon emission does arise quite readily from the Wilson line picture, it is not quite so straightforward to derive as a sum of Feynman diagrams. One might think that it is necessary only to sum diagrams of the form of Fig. 21(a); however, these diagrams alone give a result of the form

$$g^2(R^i\partial^i\mathbf{A}^0)e^{-(3\alpha_s/2R)(t_2-t_1)}(R^j\partial^i\mathbf{A}^0) \tag{4.13}$$

which is not gauge-invariant. One must remember that the integral over (t_2-t_1), since its range is controlled by the exponential factor in Eq. (4.10), has an extent of order α_s^{-1}. This means that diagrams which are apparently of different orders in α_s can be comparable in size if they receive a large weight from this integral. This actually happens in the diagrams of Fig. 21(b) and (c). The diagrams of the form of Fig. 21(b) pick up one extra factor of α_s^{-1} and yield the result

$$(-R^i\partial^0\mathbf{A}^i)e^{-(3\alpha_s/2R)(t_2-t_1)}(R^j\partial^i\mathbf{A}^0)+(R^i\partial^i\mathbf{A}^0)e^{-(3\alpha_s/2R)(t_2-t_1)}(-R^j\partial^0\mathbf{A}^j)\,, \tag{4.14}$$

the diagrams of Fig. 21(c) yield

$$(R^i\partial^0\mathbf{A}^i)e^{-(3\alpha_s/2R)(t_2-t_1)}(R^j\partial^0\mathbf{A}^j)\,. \tag{4.15}$$

The sum of these contributions is, of course, the gauge-invariant Formula (4.11).

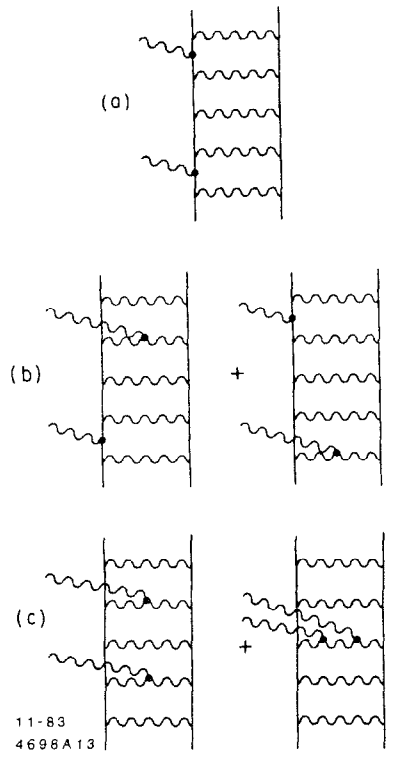


FIG. 21. Feynman diagrams contributing to the double-dipole formula for gluon emission from a heavy q-$\bar{q}$ state.

I would also like to give a first illustration of the physics of the Formula (4.12) in a context which is relatively simple, though somewhat artificial. Let me discuss the long-ranged interaction of two heavy-quark bound states, and, in particular, the question of the existence of hadronic van der Waals forces.[40] I will argue toward this point by presenting three pictures of increasing sophistication. These three viewpoints are illustrated in Fig. 22. Figure 22(a) shows the most naive picture, a dipole-dipole interaction based on the static potential $V(R)$. For a confining potential, this gives a long-ranged potential between heavy hadrons of the form

$$V_{h-h} \sim \left(\frac{\partial}{\partial R^i} \frac{\partial}{\partial R'^j} V(|\vec{R} - \vec{R}'|) \right)^2 \sim \frac{1}{|\vec{R} - \vec{R}'|^2} . \tag{4.16}$$

We can make a slightly more sophisticated picture by representing the strong-interaction fields connecting the two hadrons as gluons and using the double-dipole vertex to describe the coupling of the gluons to the heavy state. This picture, represented in Fig. 22(b), leads to a potential

$$V_{h-h} \sim \frac{1}{|\vec{R} - \vec{R}'|^7} . \tag{4.17}$$

This picture, with photons substituted for gluons, is actually the correct one for the very long range interactions of atoms; the Formula(4.17) is the color analogue of the Casimir-Polder effect[41,9] . In QCD, however, one should properly replace the gluons in the intermediate state by the various color-singlet hadron states created by the operator $tr(\mathbf{E}^i \mathbf{E}^j)$, as indicated in Fig. 22(c). The lightest such state dominates the long-range behavior. In a pure color gauge theory, this would be some glueball state; in a realistic version of QCD, it is the 2-pion state. Thus, we find at last the expression

$$V_{h-h} \sim |\langle G | \mathrm{tr}\, \mathbf{E}^i \mathbf{E}^j | \, 0 \rangle|^2 e^{-M_G |\vec{R} - \vec{R}'|} . \tag{4.18}$$

Let us now move on from these idealized considerations toward the problem of computing the rates of hadronic transitions. We would like to perform this

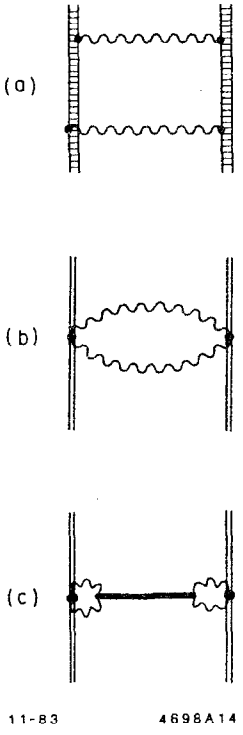


FIG. 22. Three pictures of the long-ranged interactions of two heavy-quark bound states.

computation by the direct use of the double-dipole Formula (4.12). However, perturbative QCD does not give us a precise understanding of two elements which enter into this formula–the spectrum of levels of the Hamiltonian H_8 describing a q-$\bar{\text{q}}$ pair in a relative color octet configuration, and the effective value of α_s with which the two emitted soft gluons couple. It would be valuable, then, to identify tests of this formula which are relatively independent of these two ingredients. One such test was suggested by Gottfried in his original paper.[36] Gottfried noted that the spectrum of low-lying energy levels is almost exactly the same in the ψ and Υ systems; in particular, the excitation energies of the ψ' and Υ' are almost identical:

$$m(\Upsilon') - m(\Upsilon) = 560\ MeV \quad \simeq \quad m(\psi') - m(\psi) = 585\ MeV\ . \tag{4.19}$$

Thus, the hadronic systems created in the hadronic transitions from ψ' to ψ and from Υ' to Υ are the same. It is now unreasonable that the low-lying spectrum of H_8 should also be the same in these two systems. But then, the only difference in the amplitude for the hadronic transition in these two systems comes from the dependence of the matrix element (4.12) on the size of the q-$\bar{\text{q}}$ bound states. Specifically, one should expect that these amplitudes are in the ratio

$$\frac{\mathcal{M}(\psi \to \psi + \text{hadrons})}{\mathcal{M}(\Upsilon' \to \Upsilon + \text{hadrons})} = \frac{\langle R^2 \rangle_\psi}{\langle R^2 \rangle_\Upsilon} \simeq 3 \tag{4.20}$$

so that the decay rates should be in the ratio

$$\frac{\Gamma(\psi' \to \psi + \pi^+\pi^-)}{\Gamma(\Upsilon' \to \Upsilon + \pi^+\pi^-)} \sim 10\ . \tag{4.21}$$

The experimental values of these rates are

$$\begin{aligned} \Gamma(\psi' \to \psi + \pi^+\pi^-) &= 71 \pm 14\ keV \\ \Gamma(\Upsilon' \to \Upsilon + \pi^+\pi^-) &= 6 \pm 2\ keV\ ; \end{aligned} \tag{4.22}$$

their ratio is in quite reasonable agreement with (4.21). Let me recall that, if the gluon were a spin zero object, the ratio of these rates should be 1. The results (4.22) should thus put to rest all doubts about the spin of the gluon.

A second such scaling law has been proposed by Yan[2] for hadronic transitions producing a single η. Since the η is a pseudoscalar, the matrix element for the process $\psi' \to \psi + \eta$ must have the form

$$\mathcal{M} \sim \vec{\epsilon}(\psi') \times \vec{\epsilon}(\psi) \cdot \vec{p}(\eta), \tag{4.23}$$

where the $\vec{\epsilon}$'s denote the polarization vectors of the ψ mesons and $\vec{p}(\eta)$ is the momentum of the produced η. The spin-dependence indicated in (4.23) is not present in the leading-order double-dipole formula; to find such spin-dependence, it is necessary to go to the double-magnetic-dipole and electric dipole-magnetic quadrupole terms. In either case, one finds

$$\mathcal{M} \sim \frac{1}{m^2}, \tag{4.24}$$

where m is the mass of the heavy quark. Thus, Yan expects

$$\frac{I(\psi' \to \psi + \eta)}{I(\Upsilon' \to \Upsilon + \eta)} = \left(\frac{m_b}{m_c}\right)^4 \cdot \mathcal{R} \simeq 400\,. \tag{4.25}$$

$\mathcal{R}$ is the ratio of phase space, which is a large factor (≈ 6) for this process. Unfortunately, the decay $\Upsilon' \to \Upsilon + \eta$ has not yet been observed. The scaling law (4.25) would predict

$$BR(\Upsilon' \to \Upsilon + \eta) \simeq 5 \times 10^{-4}\,. \tag{4.26}$$

In order to go beyond these scaling laws to make more detailed predictions, it is necessary to make more dynamical assumptions; in particular,one must explicitly resolve the two issues I had noted at the start of our discussion of scaling. The most complete attempt to give a detailed evaluation of the rates of hadronic transitions within this formalism has been made by Kuang and Yan[37]. These authors resolve the question of the value of α_s appropriate to Eq. (4.12) in the most straightforward way, by simply taking this coupling constant, times the amplitude for the two gluons to materialize as two pions, as a parameter and fixing it from the rate for $\psi' \to \psi + 2\pi$. The question of how to represent the spectrum of H_8 is considerably more puzzling. Kuang and Yan chose to identify the spectrum of color octet $q\text{-}\bar{q}$ states with the spectrum of $q\text{-}\bar{q}$ states in the potential corresponding to a vibrational excitation of the confining flux tube, a set of states which Giles and Tye [42] have insisted should occur in heavy quark-antiquark systems. I should note that the lowest such vibrational state has been searched for unsuccessfully in the $b\text{-}\bar{b}$ system,[43] though one should keep in mind that this search assumed a substantial coupling of this state to a single photon. In any event, Kuang and Yan have predicted a substantial number of rates for hadronic transitions in the Υ system. Let me present their predictions for the branching ratios of these transitions and compare them, where possible, to experimental results:

BR :	theory	expt.(CLEO, Ref.44)
$\Upsilon' \to \Upsilon\pi\pi$	$25 - 29\%$	$32 \pm 1\%$
$\Upsilon'' \to \Upsilon\pi\pi$	$2 - 5\%$	$7 \pm 1\%$
$\Upsilon'' \to \Upsilon'\pi\pi$	$2 - 3\%$	
$2^3P_0 \to 1^3P_0\pi\pi$	$0.05 - 0.06\%$	
$2^3P_1 \to 1^3P_1\pi\pi$	0.3%	
$2^3P_2 \to 1^3P_2\pi\pi$	0.2%	
$2^3P_2 \to 1^3P_1\pi\pi$	$0.01 - 0.02\%$	

The predictions for the rates of the $2^3P \to 1^3P$ transitions are small, but these transitions are particularly interesting in displaying additional symmetry

constraints following from the double-dipole form of the amplitude (4.12). Yan[2] has noted that there are more $2^3P \to 1^3P$ transitions than there are independent invariant amplitudes in (4.12). To see this explicitly, note that the double-dipole operator

$$R^i \frac{1}{H_8 - E_0} R^j \tag{4.27}$$

transforms under spatial rotations as a reducible tensor; it can be decomposed into spin 0, spin 1, and spin 2 components. We may associate with each of these components, taken between 2^3P and 1^3P states, a single invariant matrix element. The transition amplitude from a given 2^3P state to a given 1^3P state may be found in terms of these invariant matrix elements through some accomplished Clebsch-ology. One finds

$$\frac{d\Gamma}{d\mathcal{M}_{\pi\pi}^2}\Big((J'L'S) \to (JLS) + 2\pi\Big) = (2J+1)\sum_{k=0}^{2}\left(\begin{Bmatrix} k & L' & L \\ S & J & J' \end{Bmatrix}\right)^2 A_k \tag{4.28}$$

where the expression in brackets is the 6-j symbol. $\mathcal{M}_{\pi\pi}$ denotes the invariant mass of the two-pion system. As Eq. (4.28) indicates, this symmetry decomposition holds for each fixed value of $\mathcal{M}_{\pi\pi}$. To express the relations between various transition rates, I will use the notation:

$$d\Gamma(J' \to J) = \frac{d\Gamma}{d\mathcal{M}_{\pi\pi}{}^2}(2^3P_{J'} \to 1^3P_J). \tag{4.29}$$

Since there are 9 such transition rates and only 3 invariant amplitudes, there must be 6 symmetry relations, obtainable by eliminating the A_k from among the formulae (4.28). Yan thus finds the relations:

$$\begin{aligned}
d\Gamma(0 \to 1) &= 3d\Gamma(1 \to 0) \\
d\Gamma(0 \to 2) &= 5d\Gamma(2 \to 0) \\
3d\Gamma(1 \to 2) &= 5d\Gamma(2 \to 1) \\
d\Gamma(1 \to 1) &= d\Gamma(0 \to 0) + \frac{1}{4}d\Gamma(0 \to 1) + \frac{1}{4}d\Gamma(0 \to 2) \\
d\Gamma(1 \to 2) &= \frac{5}{12}d\Gamma(0 \to 1) + \frac{3}{4}d\Gamma(0 \to 2) \\
d\Gamma(2 \to 2) &= d\Gamma(0 \to 0) + \frac{3}{4}d\Gamma(0 \to 1) + \frac{7}{20}d\Gamma(0 \to 2)\ .
\end{aligned} \tag{4.30}$$

Yan notes, further, that the transition rates $d\Gamma(0 \to 1)$ and $d\Gamma(1 \to 0)$ should be small because of a soft-pion suppression; ignoring these quantities, (4.30) is a set of 5 relations among 7 small but finite rates.

To complete this discussion of hadronic transitions, I would like to look at the computation of such transition amplitudes from a somewhat different perspective, that of the magnetic superconductor model of confinement introduced at the end of § 2. This model contains an explicit mechanism of quark confinement, but it also replaces the gluons by a phenomenological massive gauge field. In terms of this new gauge field, the dipole operator is given by

$$g_m \vec{R} \cdot \vec{B}. \tag{4.31}$$

There is no color in this phenomenological model, so the emission of a single one of the new gauge bosons is not forbidden by symmetry. However, there is no light axial-vector boson in the hadronic spectrum (especially if it is required to be mostly glueball). Thus, for a realistic value of the mass μ of this state, the decay of ψ' to ψ plus one of these bosons should be forbidden by energetics. The simplest process allowing a hadronic transition from ψ' to ψ is one in which two gauge bosons are produced, and these two bosons recombine into two pions,

as indicated in Fig. 23. This amplitude for this process still involves a heavy-quark matrix element of the double-dipole form, so that the scaling laws and Clebsch-ology discussed above apply equally well to this model.

In this model, we might also try to understand the properties of the 2-pion state produced in the hadronic transition. To do this, of course, we must assume some form for the 2 gauge boson → 2 pion transition amplitude. However, this amplitude is restricted by the requirement from current algebra that it vanish at zero pion momentum. The simplest amplitude consistent with this requirement is

$$\delta L = \frac{1}{8}\left(a\,\partial_\mu \pi^i \partial^\mu \pi^i (F_{\lambda\sigma})^2 + b\,\partial_\mu \pi^i \partial_\nu \pi^i F^{\mu\lambda} F^{\nu}{}_{\lambda}\right). \tag{4.32}$$

If one uses this expression to evaluate the amplitude of Fig. 23, one must obtain a result containing one power of each pion's momentum. Thus, the amplitude of Fig. 23 must be of the form

$$\mathcal{M}(nS \to n'S + 2\pi) \sim (A q_1^\mu q_{2\mu} + B q_1^0 q_2^0). \tag{4.33}$$

This restriction from current algebra is of course more general than the specific model we consider here; it was first pointed out some time ago by Brown and Cahn[46] and was applied also in the analysis of Yan.[2]

As a simple way of approaching the process of Fig. 23, let me approximate the amplitude shown by considering the intermediate two-vector state to be replaced by a set of bound states; this approximation is indicated diagrammatically in Fig. 24. These bound states should have the quantum numbers of a pair of axial vectors combined symmetrically; that is, they should be scalars and tensors. The simplest case is the one in which the only intermediate state is a scalar with a large mass or a large width: In this case, the amplitude $\mathcal{M}$ has just the form of (4.33) with $B = 0$. This limit yields a decay spectrum of the form:

$$\frac{d\Gamma}{d\mathcal{M}_{\pi\pi}} \sim k \cdot (\mathcal{M}_{\pi\pi}^2 - 4m_\pi^2)^{\frac{1}{2}} \cdot (\mathcal{M}_{\pi\pi}^2 - 2m_\pi^2)^2 \tag{4.34}$$

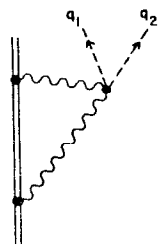


FIG. 23. The dominant process mediating hadronic transitions between heavy-quark states in the magnetic superconductor model of quark confinement.

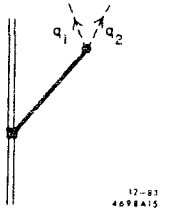


FIG. 24. An approximation to the amplitude shown in Fig. 23.

where k is the recoil 3-momentum of the final $q\text{-}\bar{q}$ state. This expression peaks for large values of $M_{\pi\pi}$. This shape for the 2-pion mass spectrum agrees strikingly with that observed in the hadronic transitions from the ψ' and Υ'. The agreement for the Υ' transition is shown in Fig. 25(a); Eq. (4.34), represented by the dashed curve, is compared there to recent results of the CLEO experiment.[46] Figure 25(b), however, indicates that this simple picture is not at all in agreement with the spectrum obtained in the transition from the Υ'' to the Υ.

To understand this discrepancy, let us write a slightly more sophisticated rendering of Fig. 24. Let me included both spin-0 and spin-2 bound states, each coupling to a double-dipole heavy-quark matrix element. These bound states are closely analogous to glueball states, and I encourage you to think of them in that way. One should represent these states with the following propagators:

$$\text{spin}-0 \quad \Delta(p) = \frac{i}{p^2 - M_G^2 + iM_G\Gamma_G} \quad ,$$

$$\begin{aligned}\text{spin}-2 \quad \Delta^{\mu\nu;\lambda\sigma} = \frac{1}{2}\Big[&\Big(g^{\mu\lambda} - \frac{p^\mu p^\lambda}{M_G^2}\Big)\Big(g^{\nu\sigma} - \frac{p^\nu p^\sigma}{M_G^2}\Big) + (\mu \leftrightarrow \nu) \\ &- \frac{2}{3}\Big(g^{\mu\nu} - \frac{p^\mu p^\nu}{M_G^2}\Big)\Big(g^{\lambda\sigma} - \frac{p^\lambda p^\sigma}{M_G^2}\Big)\Big] \cdot \Delta(p)\end{aligned} \quad . \tag{4.35}$$

The horrible spin factor in the second line arises in the following way: The polarization of the spin-2 state is characterized by the values of pair of indices $(\mu\nu)$. The propagator must contain projectors so that, first, μ and ν can take only space-like values when the meson is on shell and at rest ($p = (M_G, \vec{0})$), and, second, that the space-space components of in this frame form a traceless tensor. The latter condition can be written:

$$\delta_{ij}\,\Delta^{ij;\lambda\sigma}|_{p=(M_G,\vec{0})} = 0 \tag{4.36}$$

where i, j run over spatial indices only. These two conditions give the projector in (4.35) uniquely; the second condition produces the factor $\frac{2}{3}$ in the last line.

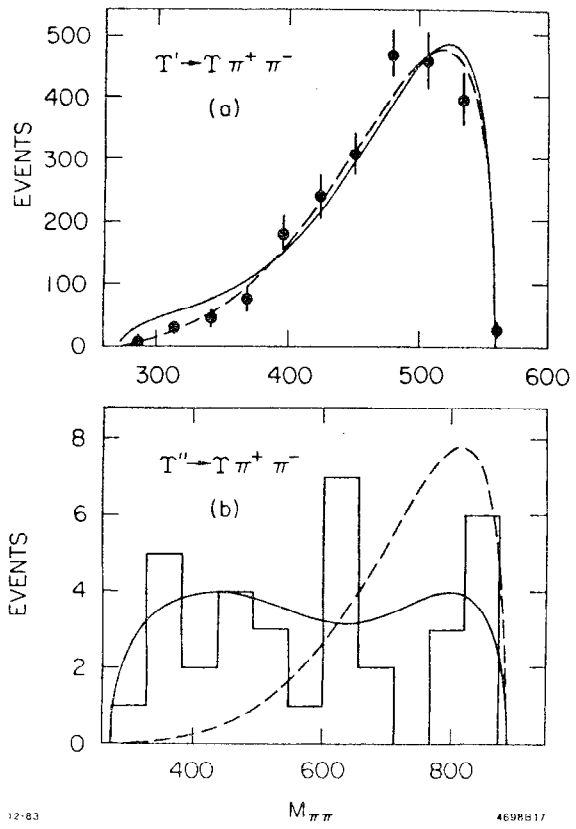


FIG. 25. Distribution of events containing hadronic transitions between Υ states according to the mass $M_{\pi\pi}$ of the 2-pion system, for (a) $\Upsilon' \to \Upsilon + 2\pi$ and (b) $\Upsilon'' \to \Upsilon + 2\pi$. The data are taken from Refs. 46 and 44, respectively. The dashed curve is the prediction of Eq. (4.34); the solid curve corresponds to Eq. (4.37) with the parameters given in the text. The overall normalization of each curve is arbitrary, and adjusted.

Using these propagators, we can write the amplitude of Fig. 24 as

$$\mathcal{M} \sim \alpha \cdot \Delta(Q)\, q_1 \cdot q_2 + (\tfrac{1}{3}\delta_{ij})\, \Delta^{ij;\lambda\sigma}(Q)\, q_{1\lambda} q_{2\sigma} \tag{4.37}$$

where $Q = q_1 + q_2$.

From Eq. (4.37), it is straightforward to generate an expression for the dipion spectrum; the formula of Yan given in Footnote 6 of Ref. 44 is useful in performing this calculation. The resulting formula has enough parameters that one has wide latitude in curve-fitting, but it is still not trivial that, using the same amplitude, one can produce pions in the low mass region for the Υ'' transition but not for the Υ'. The solid curves in Fig. 25 show a reasonable fit: In order to obtain the right behavior from the spin projectors in (4.35), it is necessary to take M_G to be very low (600 MeV). One must then insist that these states are very wide; I have set $\Gamma_G = M_G$. The remaining parameter is given by $\alpha = -2$. It is amusing that this simple model requires a set of glueball states which are at very low mass but, at the same time, are too broad to show themselves clearly as $\pi\pi$ resonances.

In this section, then, we have seen that the Feynman path formalism leads directly to multipole expansions for the interaction of heavy $q\text{-}\bar{q}$ states with external probes or with ordinary hadrons. The systematics of the rates of hadronic transitions between $q\text{-}\bar{q}$ states seems to accord well with this picture. But again, as with the topics treated earlier in these lectures, the imperfections in our knowledge of the transition region between gluons and hadrons eventually catches up with us. Can we, eventually, understand quantitatively what goes on in this intermediate regime, where perturbative QCD no longer applies but confinement is not yet an absolute constraint? I hope I have enticed you to ponder this problem and, perhaps, to find a way to solve it.

ACKNOWLEDGEMENTS

The perceptive reader should by this point appreciate the extent of my debt to all of my colleagues from Cornell, theorists and experimenters, for teaching me so much of what I know about heavy-quark systems.

REFERENCES

1) E. Eichten and F. Feinberg,Phys. Rev. Lett. 43, 1205 (1979); Phys. Rev. D23, 2724 (1981).

2) T. M. Yan, Phys. Rev. D22, 1652 (1980).

3) For example, E. D. Bloom, in Proceedings of the 1981 SLAC Summer Institute.

4) E. Eichten, K. Gottfried, T. Kinoshita, K. D. Lane, and T. M. Yan, Phys. Rev. D21, 203 (1980).

5) W. Buchmüller and S.-H. H. Tye, Phys. Rev. D24, 132 (1981).

6) J. L. Richardson, Phys. Lett. 82B, 272 (1979).

7) A. Martin, Phys. Lett. 93B, 338 (1980).

8) G. Bhanot and S. Rudaz, Phys. Lett. 78B, 119 (1978).

9) V .B. Berestetski, E. M. Lifshitz, and L. P. Pitaevski, Relativistic Quantum Theory. Pergamon Press, Oxford, 1979.

10) R. P. Feynman, Rev. Mod. Phys. 20, 267 (1948).

11) J. Schwinger, Phys. Rev. 82, 664 (1951).

12) S. Mandelstam, Ann. Phys. (N.Y.) 19, 1 (1962).

13) K. G. Wilson, Phys. Rev. D10, 2445 (1974).

14) P. A. M. Dirac, Phys. Rev. 74, 817 (1948).

15) T. Banks and E. Tomboulis, Phys. Rev. D20, 501 (1979).

16) H. B. Nielsen and P. Olesen,Nucl. Phys. B61, 45 (1973).

17) L. J. Tassie, Phys. Lett. 46B, 397 (1973).

18) T. Banks, R. Myerson, and J. Kogut, Nucl. Phys. B129, 493 (1977).

19) M. E. Peskin, Ann. Phys. (N.Y.) 113, 122 (1978).

20) M. Stone and P. R. Thomas, Phys. Rev. Lett. 41, 351 (1978).

21) A. Ukawa, P. Windey, and A. Guth, Phys. Rev. D21, 1013 (1980).

22) J. Stack, Phys. Rev. D27, 412 (1983); ITP Santa Barbara preprint NSF-ITP-83-136 (Nov., 1983).

23) C. B. Lang and C. Rebbi, Phys. Lett. 115B, 137 (1982).

24) E. Kovacs, Phys. Rev. D25, 3312 (1982).

25) W. Fischler, Nucl. Phys. B129, 157 (1977).

26) T. Appelquist, M. Dine, and I. Muzinich, Phys. Rev. D17, 2074 (1978).

27) F. Feinberg, Phys. Rev. D17, 2659 (1978).

28) E. Tomboulis, Phys. Rev. Lett. 50, 885 (1983).

29) R. P. Feynman, Phys.Rev. 84, 108 (1951).

30) M. Halpern and W. Siegel, Phys. Rev. D16, 2486 (1977).

31) G. 't Hooft, Phys. Rev. D14, 3432 (1976).

32) J. Kogut and G. Parisi, Phys. Rev. Lett. 47, 1089 (1981).

33) T. Banks and M. Spiegelglass, Nucl. Phys. B152,478 (1979).

34) W. Buchmüller, J. Ng, and S.-H. H. Tye, Phys. Rev. D24, 3003 (1981).

35) J. Rosner, U of Chicago preprint EFI-83-17-CHICAGO (1983).

36) K. Gottfried, Phys. Rev. Lett 40, 598 (1978).

37) Y.-P. Kuang and T.-M. Yan, Phys. Rev. D24, 2874 (1981) .

38) M. E. Peskin, Nucl. Phys. B156, 365 (1979) .

39) M. B. Voloshin, Nucl. Phys. B154, 365 (1979) .

40) G. Bhanot and M. E. Peskin, Nucl. Phys. B156, 391 (1979) .

41) H. B. G. Casimir and D. Polder, Phys. Rev. 73, 360(1948).

42) R. Giles and S.-H. H. Tye, Phys. Lett. 73B, 30 (1978) .

43) K. Berkelman, Phys. Repts. 98C, 145 (1983).

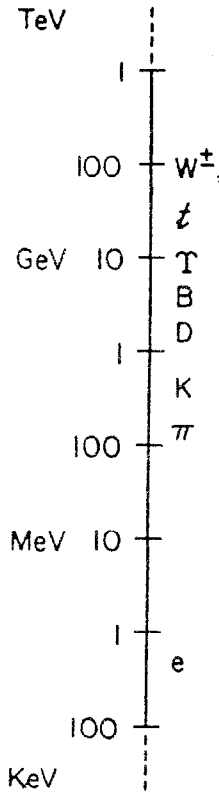
44) J. Green *et.al.*, Phys. Rev. Lett. 49, 617 (1982).

45) L. Brown and R. Cahn, Phys. Rev. Lett. 35, 1 (1975).

46) R. Giles *et. al.*, CLEO preprint C-258 (Aug., 1983), contributed to the Intl. Symp. on Lepton and Photon Interactions at High Energies, Ithaca, 1983 .

Heavy Particle Spectroscopy and Dynamics
B's to Z's

M. G. D. Gilchriese
Cornell University



Upsilon Spectroscopy

B Meson Decay

t Search

$W^{\pm}$ Discovery

Z° Discovery

Talk Presented at the 1983 SLAC Summer Institute

© M. Gilchriese 1983

Introduction

The year 1983 will be remembered (by physicists at least) as the year of the $W^{\pm}$ and Z° discoveries. These discoveries at the SPS collider cap a many decade effort to understand the electroweak interaction and begin a new era where the definition of a heavy particle has shifted to the 100 GeV mass region. The experimental investigation of the $W^{\pm}$ and Z° properties is just beginning and I have included only a "bare bones" description in this paper.

At the time this is being written there is no convincing evidence for the existence of a charge +2/3 partner to the b quark, the t quark. It is quite possible that evidence for the t quark will arise very soon (or may have by the time this is published) from a more complete analysis of the debris produced at the Collider. My description of how to find the t quark may therefore be made obsolete.

In 1983 the first reliable evidence (i.e. a mass bump) for a hadron containing a b quark was published and the first measurements of the b-hadron lifetime were reported. One can now severely restrict the couplings of the b quark to lighter quarks and determine or place limits on the parameters in the Kobayashi-Maskawa mixing matrix.

Also in 1982 and 1983 the experimental and, to a lesser extent, theoretical study of the upsilon resonances was advanced by the observation of photon transitions from the radially excited $^3S_1$ states to P-states. In particular these results serve to constrain the form of the spin dependent color force.

1. Upsilon Spectroscopy

1.1 Who Cares?

It is occasionally useful to reexamine one's motives for doing a particular brand of physics, in this case spectroscopy or more specifically upsilon spectroscopy. The evidence by now is overwhelming that quarks and antiquarks bind together to form mesons. More explicitly the upsilon states are composed of a b quark and an anti b quark bound together by the color force mediated by vector gluons. The theoretical problem is to calculate the energy levels (masses) of the upsilon states and the transition rates between states. The experimental problem is to measure with requisite precision these properties. Hopefully the final result will be a comprehensive understanding of the interquark force analogous to the Quantum Electrodynamic description of simple atoms or positronium. This has not been accomplished.

1.2 Bottomonium = Positronium

The analogy between the $b\bar{b}$ system and positronium is quite good as can be seen in Figs. 1.1 and 1.2. The various upsilon states are formed by combining the b and $\bar{b}$ quark in different spin and orbital angular momentum states. The parity and C-parity of the states follow from the formulae for neutral fermion-antifermion systems. Spectroscopic notation is used to label the states. The novice should be aware that many authors label my $2P_J$ states the $1P_J$ states

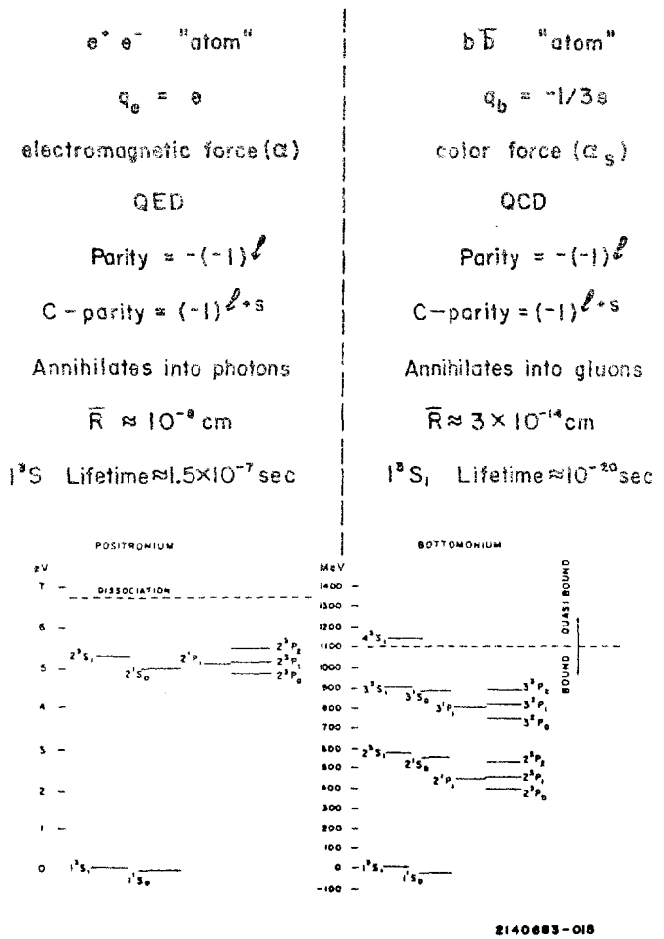


Fig. 1.1. A comparison between bottomonium and positronium.

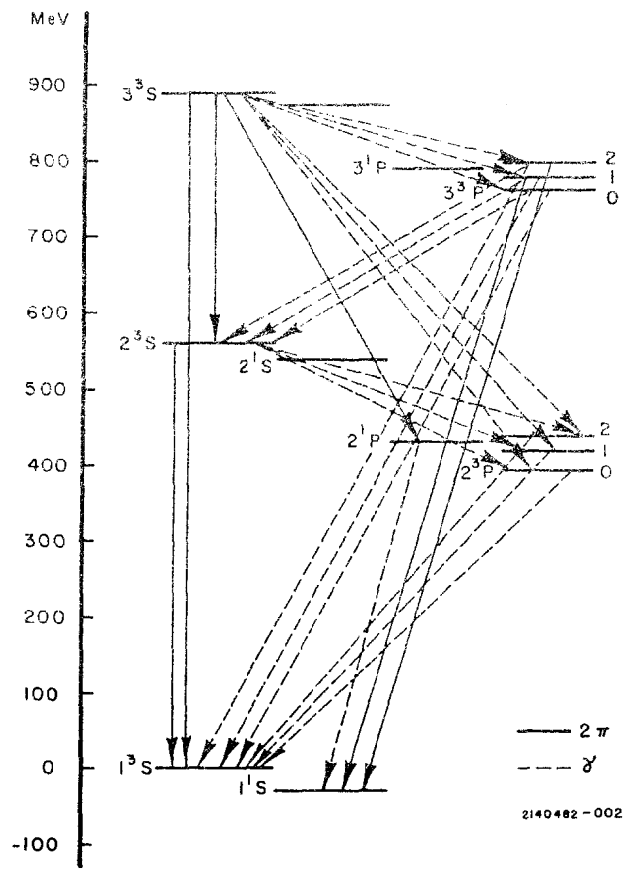


Fig. 1.2. The bottomonium system and the principal transitions.

but this is a matter of taste.

1.3 Decay Modes of the $^3S_1$ States

In Fig. 1.1 I have divided the upsilon states into two groups, bound and quasibound. The quasibound resonances decay directly into hadrons containing the b quark as shown in Fig. 1.3. This means that resonances above threshold will have large widths (MeV's) and in general become wider farther from the b-hadron threshold. At energies a GeV or so above the threshold the concept of resonant $b\bar{b}$ production disappears and we speak of continuum $b\bar{b}$ production.

The bound $^3S_1$ states can decay in more complicated ways. The decays can occur either by annihilation or by transitions to lower mass states, if allowed. Annihilation occurs when the b and $\bar{b}$ "meet" or more precisely the annihilation rate will be proportional to the square of the wavefunction of the system at zero separation. Restricting ourselves to the ground $^3S_1$ state (T) for a moment, the annihilation into three gluons is the dominant mode. The T can also annihilate into a virtual photon and hence couple to lepton or quark pairs. Finally, annihilation into a combination of photons and gluons can occur, almost exclusively into one photon and two gluons. This γ-gluon-gluon process has recently been observed by the CUSB and CLEO groups at CESR and is discussed in J. Lee-Franzini's paper in these proceedings.

There are two classes of transitions to lower mass states; photon transitions and hadronic transitions. Conceptually the photon transitions are easier to understand by close analogy to atomic or nuclear transitions. Hadronic transitions reflect the existence of

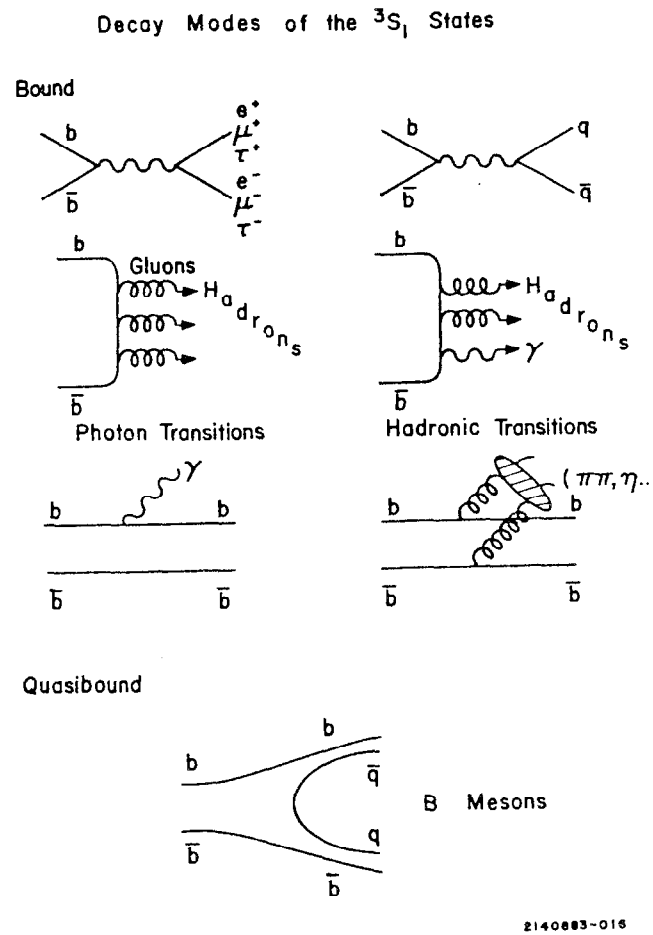


Fig. 1.3. The decay modes of the $^3S_1$ upsilon states.

the color force and in fact will be described (crudely) as arising from gluon emission from the quarks. Transitions are discussed in more detail in later sections.

1.4 Properties of the $^3S_1$ States

1.4 A. Masses

Except for the initial discovery (very important!) of the upsilons, all of the experimental information about the upsilon family has come from e^+e^- annihilation experiments, first at DORIS I in 1978, then CESR from 1979 onwards and most recently DORIS II and VEPP-4. Because of the quantum numbers of the virtual photon produced in e^+e^- annihilation essentially only the $J^{PC} = 1^{--}$ $^3S_1$ states are directly produced. ($J = 1$ D-wave states are expected to have very small leptonic couplings of order 1000 thousand times less than $^3S_1$ states through mixing with S states and a coupling proportional to the second derivative of the wave function at the origin.)

Four $^3S_1$ states in the upsilon system have been discovered so far (see Fig. 1.4). The masses of these narrow states have been recently measured to high precision using the method of resonant depolarization.[1,2,3] In all three of the storage rings, VEPP-4, DORIS and CESR, polarization of the beams is observed. The polarization can be destroyed by the application of a weak-time dependent magnetic field (order of 0.1 Gauss-meters). Resonant depolarization occurs when the applied depolarization frequency f_D satisfies

$$f_D = f_0 \left(n + \frac{\gamma(g-2)}{2}\right)$$

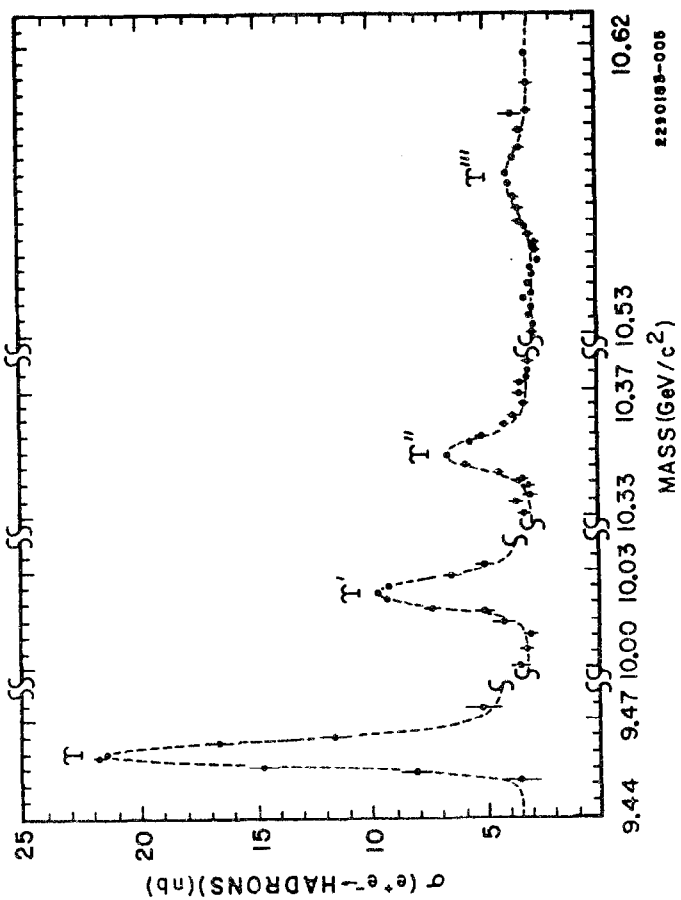


Fig. 1.4. The cross section for producing hadrons in the upsilon region. The data are from the CUSB group.

where f_0 is the very accurately known overall revolution frequency of the beam, n is an integar, γ is the Lorentz factor and g is twice the electron magnetic moment in units of the Bohr magneton. The depolarizing magnet is at a fixed position in the ring and at the frequency of f_D "kicks" the electron on successive passes such that the spin direction is rotated from the vertical direction and the polarization destroyed. This can occur in less than one minute whereas the polarization time is typically much longer.

The polarization is usually measured by a back scattered laser polarimeter. The depolarization frequency is changed and the polarization is measured (see Fig. 1.5). The dip indicates resonance depolarization. The present results are summarized in Table 1.1 below.

Table 1.1

Masses of the Bound Upsilon States in MeV/c^2

	$\Upsilon(1S)$	$\Upsilon(2S)$	$\Upsilon(3S)$
VEPP-4	9460.6±0.4±0.2	10023.8±0.5±0.2	10355±0.5±0.2
DORIS II	---	10023.1±0.4±0.5	---
CESR	9459.9±0.1±0.1	---	---

1.4 B. Leptonic Widths

The leptonic width, Γ_{ee}, of a resonance measures the strength of the coupling to leptons (e^+e^-). As we will see this can be predicted by models/theories of the interquark force and is therefore useful. The method is by now well known. Near a resonance of mass M the cross section for a particular final state (e.g. hadrons), σ_f,

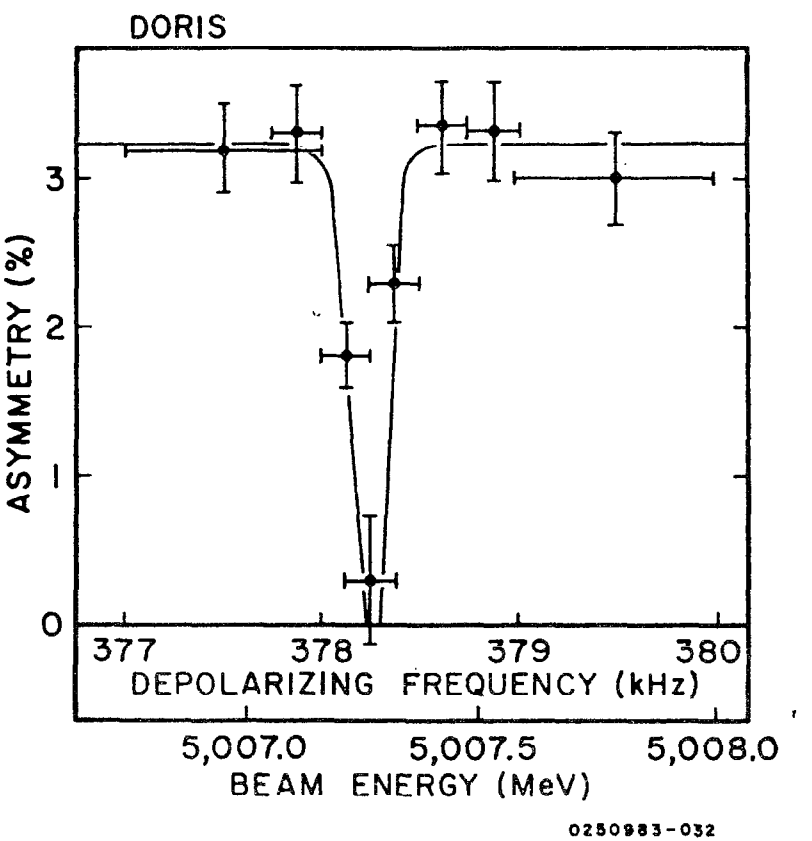


Fig. 1.5. Measured polarization vs. depolarizer frequency as measured at the DORIS II storage ring.

is given by

$$\sigma_f(W) = \frac{3\pi}{W^2} \quad \frac{\Gamma_{ee}\ \Gamma_f}{(W - M)^2 + (\Gamma_{tot}/2)^2}$$

where Γ_f is the width into the particular final state, W is the center of mass energy and Γ_{tot} is the total width of the state. Of course in a real storage ring, W is not fixed but has a distribution with a σ_{rms} of 4-10 MeV depending upon which of the three rings, DORIS, VEPP-4 or CESR, is considered. This is much larger than Γ_{tot} of the upsilons. Fortunately the area of the resonance shape is preserved up to understood radiative corrections, hence

$$\text{"Area"} = \int \sigma_f\ (W)dW = \frac{6\pi^2}{M^2} \quad \frac{\Gamma_{ee}\ \Gamma_f}{\Gamma_{tot}} \quad .$$

Typically f denotes all of the hadronic final states, Γ_{had}, so to actually extract Γ_{ee} one must know $B_{\ell\ell}$, the branching ratio into lepton pairs, such that

$$\text{"Area"} = \frac{6\pi^2}{M^2}\ \Gamma_{ee}\ (1 - 3B_{\ell\ell})$$

where lepton universality has been assumed. Values for the leptonic widths are given later in Table 1.3.

1.4 C. Leptonic Branching Ratios

The leptonic branching ratios, for example $B_{\mu\mu} = \Gamma_{\mu\mu}/\Gamma_{tot}$, are determined by measuring the production of lepton pairs in excess of the QED rate from the nonresonant continuum at each resonance. An example for muons is shown in Fig. 1.6 and values for $B_{\mu\mu}$ are given below.[4] Tau pairs and e^+e^- pairs have also been observed.[5]

Table 1.2

Leptonic Branching Ratios ($B_{\mu\mu}$) (%)

$\Upsilon(1S)$	$\Upsilon(2S)$	$\Upsilon(3S)$
2.8 ± 0.2	1.9 ± 0.6	3.3 ± 1.5

1.4 D. Total Widths

This is trivial $\Gamma_{tot} = \Gamma_{ee}/B_{\mu\mu}$.

1.5 Potential Models - The Basics

Given the properties of the $^3S_1$ states described above one can interpret them within the simple framework of potential models. What is a potential model? In simplest terms you pick some static potential V(r), plug it into the Schrödinger equation and solve. Many things are ignored in this prescription and will be discussed later. Different forms (i.e. guesses) for the potential describing the force between quarks have been tried, e.g.

$$V(r) = \frac{k}{r} + ar$$
$$= A + Br$$
$$= A \log (br) \ .$$

The parameters in these choices can be adjusted so as to yield similar mass values and hence are essentially equivalent descriptions of the effective force in the region $0.1 \leq r \leq 1.0$ fm (see Fig. 1.7).

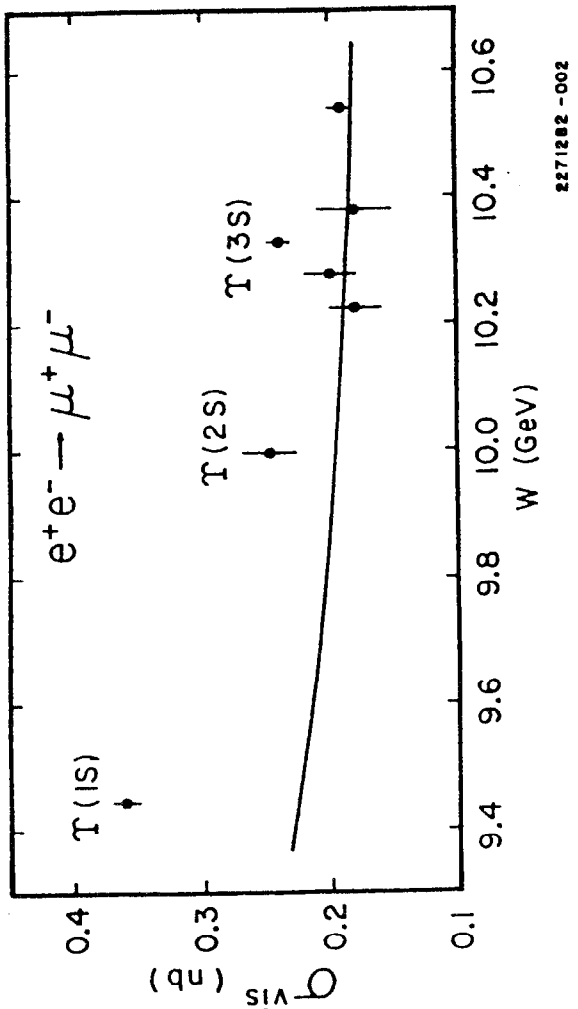


Fig. 1.6. The dimuon ($\mu^+\mu^-$) cross section vs. center of mass energy. The solid line indicates the rate expected for QED production of muon pairs. The data are from the CLEO group.

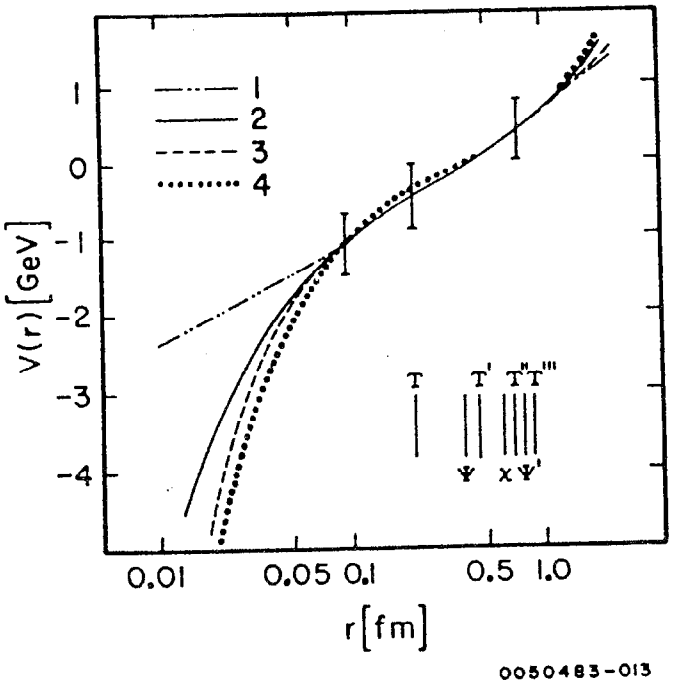


Fig. 1.7. Various quarkonium potentials showing the equivalence in the region $0.1 \leq r \leq 1.0$ fm.

The mean radii of the $c\bar{c}$ and the $b\bar{b}$ states are, of course, in this region and hence determine the potential. Potential models have been enormously useful in their predictive power but in this simple form I at least find them to be unsatisfying. They are simple representations of the complicated color force which, in principle, should be described by QCD.

There have in fact been a number of attempts to calculate or model the $q\bar{q}$ potential inspired by QCD. For an elegant introduction see M. Peskin's lectures in these proceedings. QCD suggests that at short distances the force can be described by one gluon (vector) exchange resulting in a potential $V(r) \approx \frac{4}{3} \frac{\alpha_s}{r}$ at short distances and a confining potential (no free quarks) $V(r) \approx Kr$ at large distances. Richardson first proposed a simple function for V(r) which had this limiting behavior at small and large r.[6] Other people have calculated higher order corrections to the short distance part and include them in potential. Two examples of this are the calculations of Gupta, Radford and Repko (GRR)[7] and Buchmuller, Grunberg and Tye (BGT).[8] In Fig. 1.8 is compared the measured values of $^3S_1$ masses and the P-state centers of gravity to the models of Richardson, GRR and BGT. The data and models agree at the 10-20 MeV or better level. This is particularly impressive for the Richardson potential which has only one free parameter (plus quark masses). This parameter was determined by the $c\bar{c}$ system and hence the agreement with data could be improved by using T system data.

It is clear from this comparison that QCD inspired potentials are able to predict the energy levels to an accuracy of 3% or better.

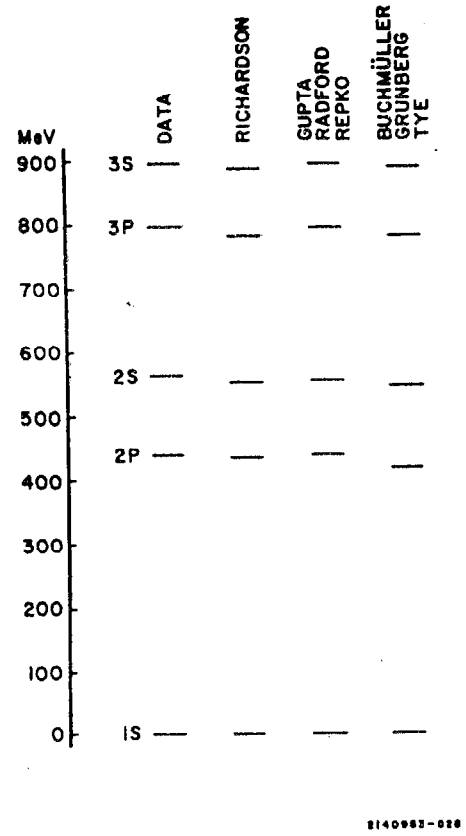


Fig. 1.8. A comparison between the measured energy levels of the upsilon states and three potential models.

This looks good but there are some problems. First the data are now much more accurate than the theory. Many of the theoretical calculations were done before the P-states were observed and should be updated. The GRR model for example contains four free parameters including M_b, which sets the ground state mass, and α_s. Changing α_s might improve the agreement. Second, these models do not include the effects of coupling to virtual B-meson states below threshold (see Fig. 1.9) which will change the energy levels. Eichten in his talk in these proceedings estimates that this could change the energy levels by 10's of MeV making the agreement between potential models which neglect such effects and data fortuitous if not actually suspicious. Either Eichten's estimates are too large or somehow by adjusting parameters one has artificially included these effects in the potential.

In summary there is considerable necessity for theoretical calculations of energy levels at an accuracy of 1 - 2 MeV. A clear challenge exists to see if this is possible,or does the concept of a static potential plus corrections break down.

Given a potential,one can determine wavefunctions and hence the *leptonic width given by the Van Royen Weiskopf formula*[9]

$$\Gamma_{ee} = \frac{16\alpha^2 e_b^2}{M^2} |\psi(0)|^2 \left(1 - \frac{16\alpha_s}{3\pi} \ldots\right) .$$

The QCD inspired potentials (GRR and BGT averaged) predict

$$\Gamma_{ee}(T(1S)) = (1.18 \pm 0.15)\text{keV}$$

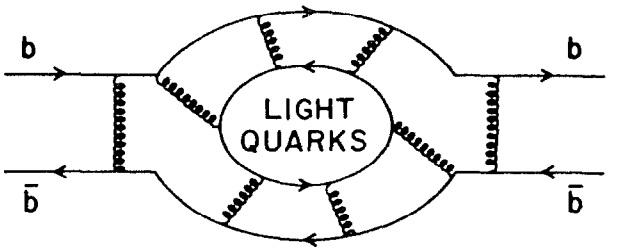


Fig. 1.9. Diagram showing the coupling to light quarks which form virtual meson states.

which is in reasonable agreement with the data[10] (see below) as are the leptonic widths of the higher mass states.

Table 1.3

Γ_{ee} (keV)

	Data	Model
T(1S)	1.22 ± 0.06	1.18
T(2S)	0.52 ± 0.03	0.53
T(3S)	0.38 ± 0.03	0.38
T(4S)	0.27 ± 0.04	0.31

1.6 The P-States - Data

Data now exist on photon transitions from the T(3S) and T(2S) to triplet P-states (^3P_J). The interest in locating these states lies in trying to unravel the relativistic spin dependent corrections to the basic nonrelativistic potential. This theoretical framework has, of course, already been extensively applied to the charmonium system.[11] The advantage of the heavier upsilon system is that the corrections should be smaller; it is more nonrelativistic than charmonium. Let's first discuss the data and then the theoretical framework.

Transitions from the T(3S) to the 3^3P_J states were first observed by the CUSB group both in the inclusive photon spectrum and in exclusive decays wherein the T(2S) or T(1S) decayed into lepton pairs.[12] The inclusive spectrum is shown in Fig. 1.10. The experimental resolution is not good enough to resolve the individual lines and a fitting procedure

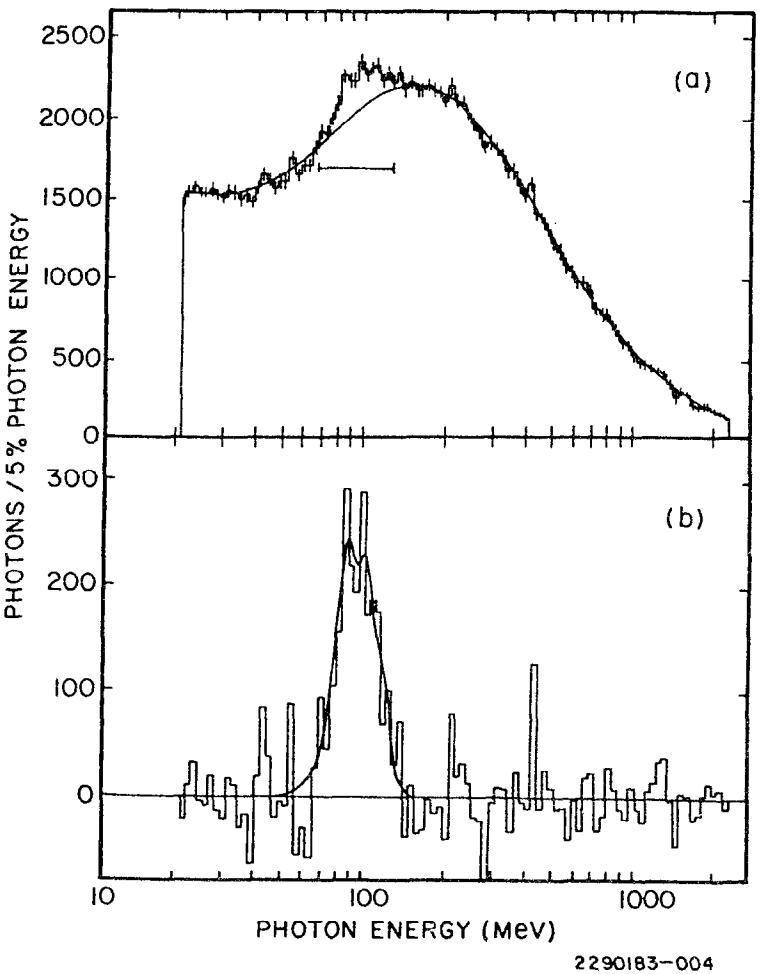


Fig. 1.10. The inclusive photon spectrum from the T(3S) measured by the CUSB group and the background subtracted spectrum.

was used to extract the photon energies. The values of the energies and branching ratios are given in Fig. 1.11. These values are from an updated analysis by the CUSB group and are slightly different than the published ones (see J. Lee-Franzini's talk in these proceedings).

Photon transitions have been observed from the T(2S) to the 2^3P_J states by the CUSB, Crystal Ball, CLEO and ARGUS groups.[13,14,15,16] This is becoming a crowded field indeed! The characteristics of these four detectors and their respective data samples as of September 1983 are given below in Table 1.4.

Table 1.4

Group	σ_E at 100 MeV (MeV)	Eff(%)	No. of (2S) Decays
CUSB	∿ 6	13	∿150K
Crystal Ball	∿ 4	22	∿ 70
CLEO	∿ 3	3-5	∿130
ARGUS	∿ 1	0.2-0.8	∿ 50

Both CLEO and ARGUS measure the photon energies by using their inner tracking chambers as pair spectrometers. This yields good resolution but poorer efficiency than the CUSB or Crystal Ball sodium iodide detectors. The inclusive photon spectra from the four groups are shown in Fig. 1.12 a,b,c,d and the results summarized below in Table 1.5. The CLEO, Crystal Ball and ARGUS numbers are preliminary, i.e., not published at the time this is being written.

Only the CUSB group has strong evidence for three lines. The Crystal Ball, ARGUS, and CLEO results are, however, statistically

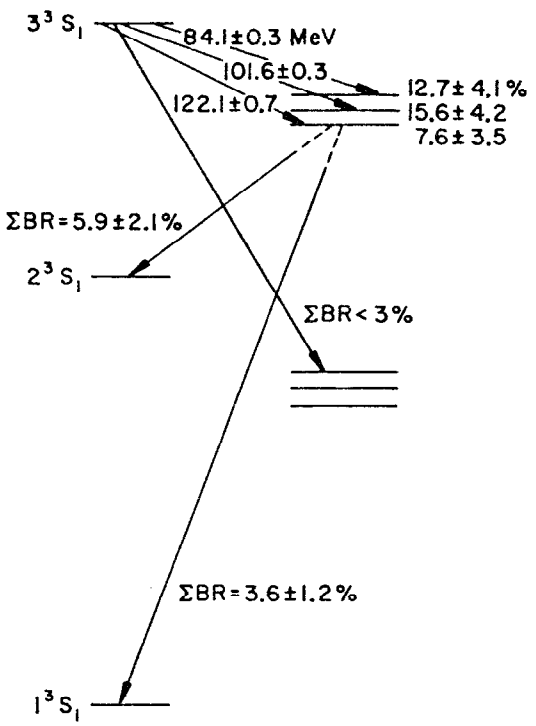


Fig. 1.11. The measurements of the CUSB group of photon transitions from the T(3S) and from the 3^3P_J states.

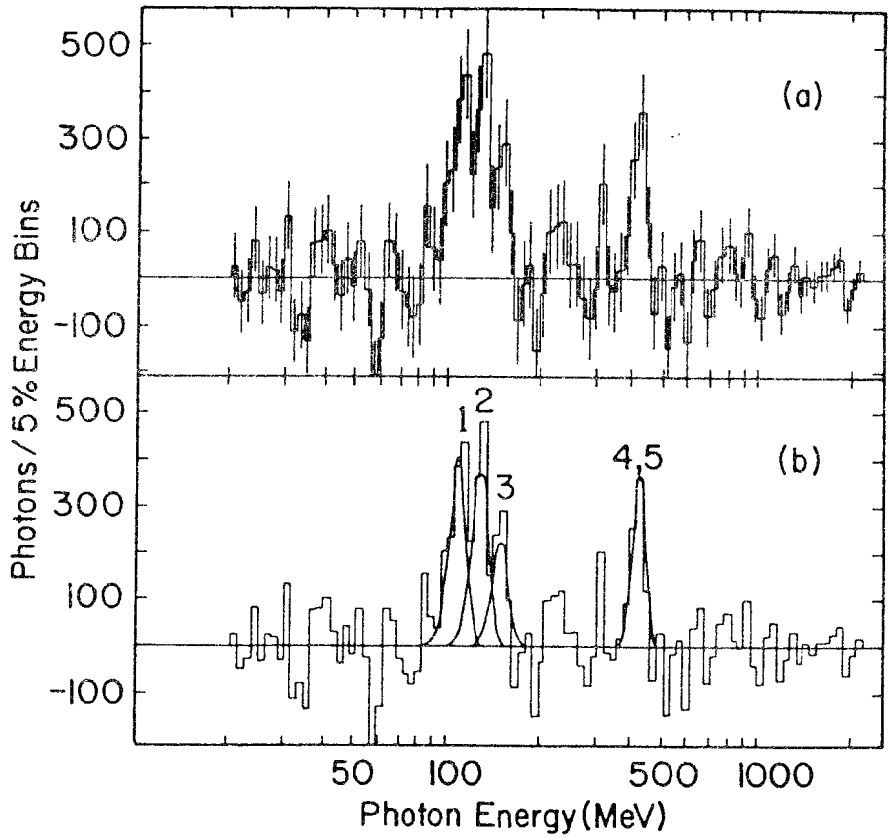


Fig. 1.12a. Inclusive photon spectrum background subtracted from T(2S) decays measured by CUSB.

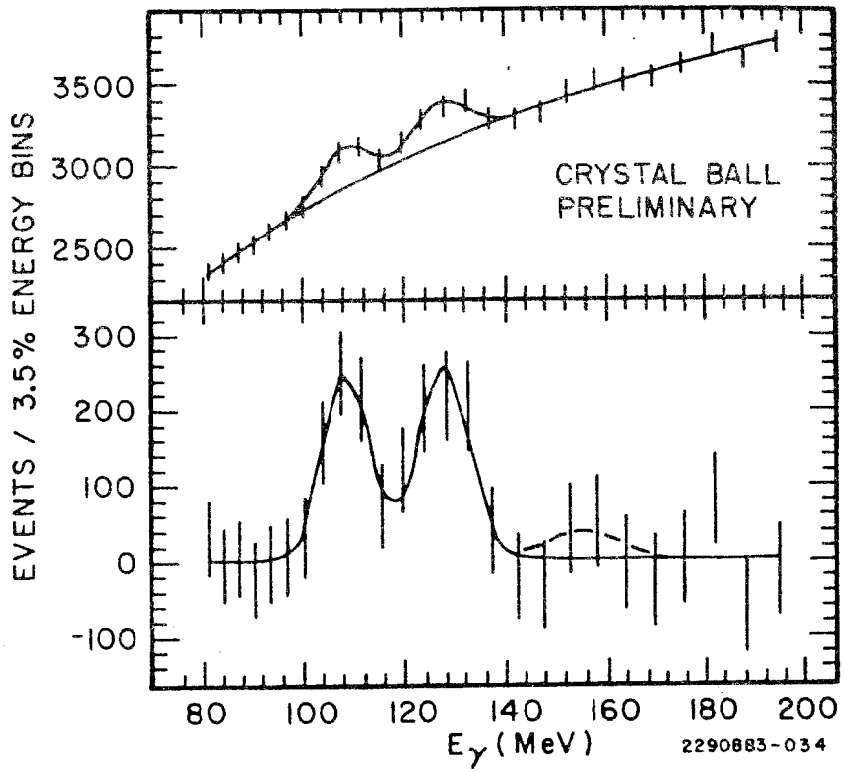


Fig. 1.12b. Inclusive photon spectrum measured by the Crystal Ball.

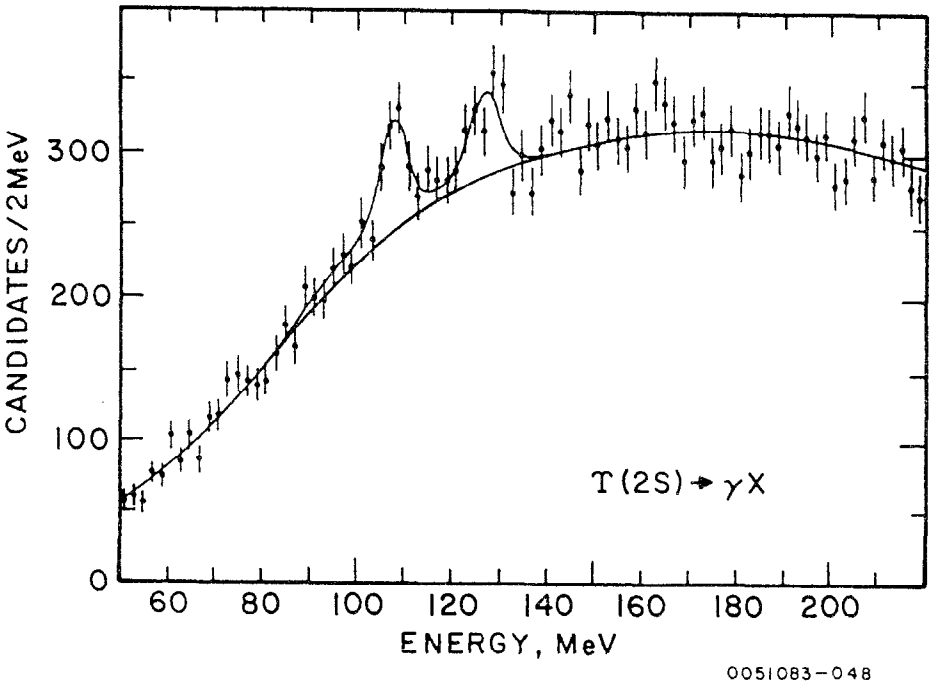


Fig. 1.12c. Inclusive photon spectrum measured by CLEO.

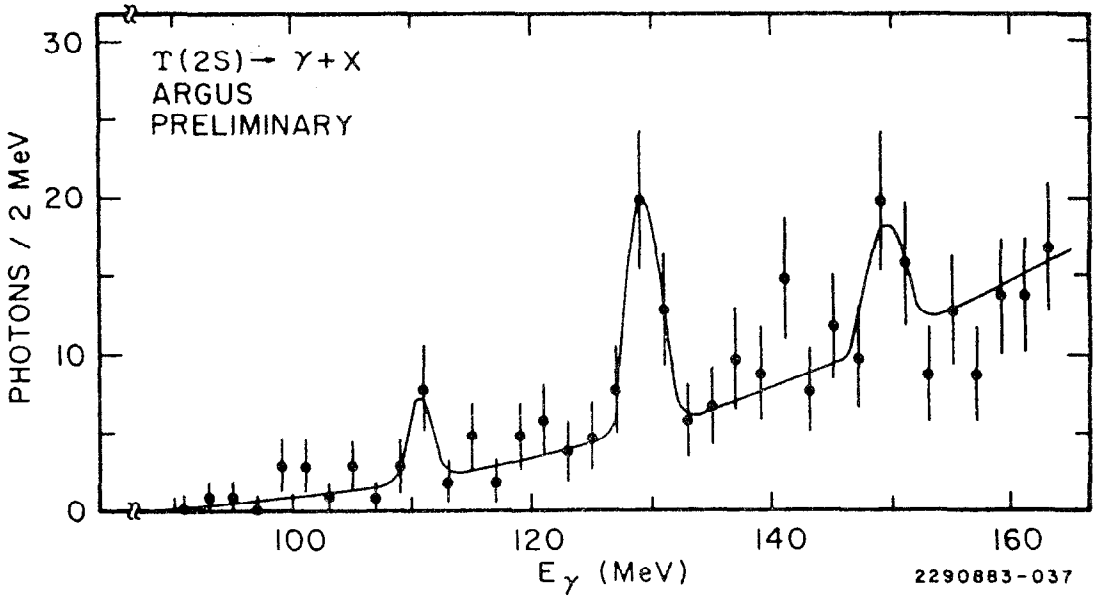


Fig. 1.12d. Inclusive photon spectrum measured by ARGUS.

compatible with the CUSB result. In the remainder of this section I will assume that CUSB is correct and use their measurement for the "third" line. The agreement between groups on the other two lines is excellent.

Table 1.5

	Group	E_γ (MeV)	BR(%)
J=2	CUSB	108.2 ± 0.3 ± 2	6.1 ± 1.4
	Crystal Ball	108.3 ± 0.9 ± 3	6.3 ± 1.3
	CLEO	109 ± 1 ± 1	10.2 ± 2.8
	ARGUS	111.4 ± 2 ± 0.6	5.6 ± 2.8
J=1	CUSB	128.1 ± 0.4 ± 3	5.9 ± 1.4
	Crystal Ball	127.5 ± 1.2 ± 1.4	6.0 ± 1.3
	CLEO	129 ± 1 ± 1	8.0 ± 2.3
	ARGUS	129.5 ± 0.6 ± 0.6	7.9 ± 2.2
J=0	CUSB	149.4 ± 0.7 ± 5	3.5 ± 1.4
	Crystal Ball	---	<4
	CLEO	---	<4
	ARGUS	148.5 ± 1.5 ± 0.8	2.7 ± 1.5

1.7 The P-States - Interpretation

I have already compared the measured center of gravity (cog.) of the P-states to various potential models in Fig. 1.8. The cog. is defined by

$$M_{cog.} = \frac{1}{9} \sum_{J=0}^{2} (2J + 1)\, M_J \ .$$

Note that I (and everyone else) assume that $M_{J=2} > M_{J=1} > M_{J=0}$ in assigning masses; none of the spins have been directly measured. The agreement between data and the potential models is reasonable. The position of the 2^3P_J cog., however, disagrees with QCD sum-rule calculations.[17]

We now turn to the fine structure. The level splitting in the upsilon system is smaller (~40 MeV) than in charmonium (~140 MeV). This is not unexpected and follows from the discussion of spin dependent forces.

The $b\bar{b}$ Hamiltonian may be written

$$H = \text{kinetic term} + V(\text{non-relativistic}) + V(\text{spin-independent relativistic corrections}) + V(\text{spin-orbit}) + V(\text{spin-spin}) + V(\text{tensor}) \ .$$

The serious student (as opposed to the casual reader) should go back and study fine structure in QED at this point; the formalism is similar.

The relativistic corrections depend upon the form assumed for the potential. Unlike in QED there is no general agreement on the form of the various parts of the spin dependent potential. An excellent introduction and review is the recent article of Rosner.[18] The paper by Eichten and Feinberg[19] presents a detailed treatment of

spin effects. They find the following expression for the spin dependent part

$$H_{spin} = \left(\frac{1}{2M_1^2}\,\vec{L}\cdot\vec{S}_1 \quad \frac{1}{2M_2^2}\,\vec{L}\cdot\vec{S}_2\right)\frac{1}{R}\,\frac{dV}{dR}$$

$$+ \frac{4\alpha_s}{3M_1M_2}\,\frac{1}{R^3}\,\vec{L}\cdot\vec{S} + \frac{8\alpha_s}{9M_1M_2}\,\vec{S}_1\cdot\vec{S}_2\,4\pi\delta(R)$$

$$+ \frac{4\alpha_s}{3M_1M_2}\,(3\vec{S}_1\cdot\hat{R}\,\vec{S}_2\cdot\hat{R} \quad \vec{S}_1\cdot\vec{S}_2)\,\frac{1}{R^3}$$

where V is the non-relativistic potential and the other notation is obvious.

The masses of the $^3P_2$, $^3P_1$, and $^3P_0$ states may then be parameterized as follows:

$$M(^3P_2) = M_{cog} + a - \frac{2}{5}b\ ,$$

$$M(^3P_1) = M_{cog} - a + 2b \quad \text{and}$$

$$M(^3P_0) = M_{cog} - 2a - 4b\ .$$

where a and b represent the contributions from spin-orbit terms and tensor forces, respectively.

A number of authors have made predictions for the fine structure in the upsilon system. They are summarized in Fig. 1.13. The predictions of Gupta, Radford and Repko, and Eichten and Feinberg are in reasonable agreement with the data.[20] The predictions of McClary and Byers[21] and Moxhay and Rosner[22] are less accurate.

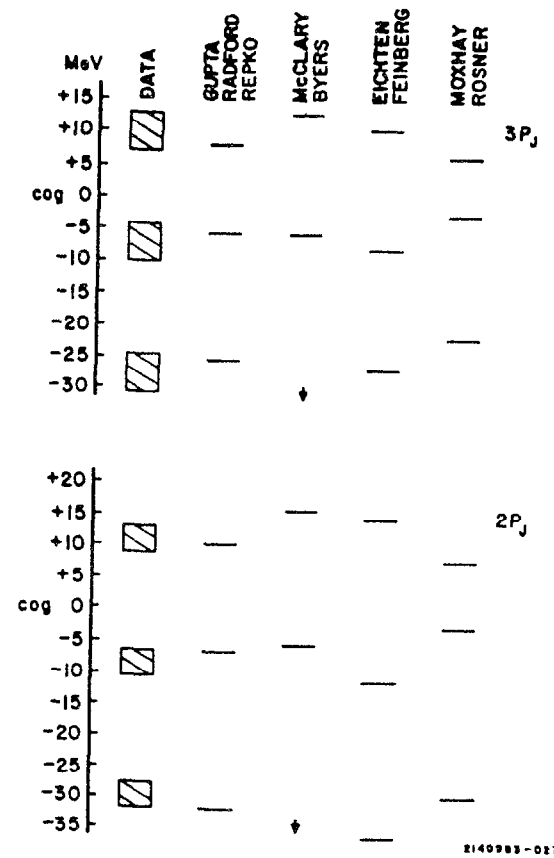


Fig. 1.13. Comparison of the measured fine structure with models.

What do we learn from this comparison? More accurate measurements are needed to further constrain the models. A global comparison of the measured fine structure in both the 3^3P_J and 2^3P_J of bottomonium and of the P-states in charmonium with models would be very useful.

1.8 Transition Rates

You will remember from undergraduate days that the transitions to the P-states are E1 transitions and the rate is

$$\Gamma_{E1_S} \alpha_s(2J + 1)\, e_q^2 \quad E_\gamma^3 |\langle f | r | i \rangle|^2$$

where e_q is the quark charge, E_γ is the photon energy and f(i) represents the final (initial) state. This formula is expected to be valid if the size of the system is small compared to the photon wavelength and in the non-relativistic case. For $E_\gamma \approx 100$ MeV, $\lambda_\gamma \approx 10$fm whereas $\langle r \rangle_T \approx 0.3$fm. In the charmonium case this simple prediction for the rate was too large by a factor of two. Recent calculations of relativistic effects have brought data and theory into agreement.[21,23] These same calculations would predict small, not yet observable deviations from the simple formula in the case of the upsilon system. The data are compared with the prediction of Ref. 21 in Table 1.6 below.

Note that the uncertainty in the total widths of the T(2S) and particularly the T(3S) are not included in the errors for the data. I have used a leptonic branching ratio of 2% in each case rather than the measured values. To claim fantastic agreement is premature but certainly the data are not ≈1/2 theory as in the charmonium case. More precise measurements are needed.

Table 1.6

Bottomonium E1 Transitions Rates

	Data	Model
$\Sigma(T(3S) \to \gamma^3P_J)$ (kev)	7.2 ± 1.4	5.9
$\Sigma(T(2S) \to \gamma^3P_J)$ (kev)	4.2 ± 0.7	4.8

1.9 Hadronic Transitions

Hadronic transitions between states of the upsilon system are of interest for two reasons. First, some states, for example the 2^1P_1, can only be discovered via a hadronic transition. Second, these transitions are manifestations of the color force in that one can view them as arising from the emission of gluons from an excited upsilon state. It is therefore of interest to measure the branching ratios of these transitions and the properties of the hadronic system.

The most successful model (multipole expansion) of hadronic transitions is that suggested by Gottfried[24] and described by Yan and Kuang,[25] and Yan.[26] Since the mass differences between upsilon states are small, perturbative QCD is not applicable. In the multipole expansion model dipion transitions, for example, can arise from double gluon emission, double color electric dipole emission as shown schematically in Fig. 1.14. Such a model predicts that

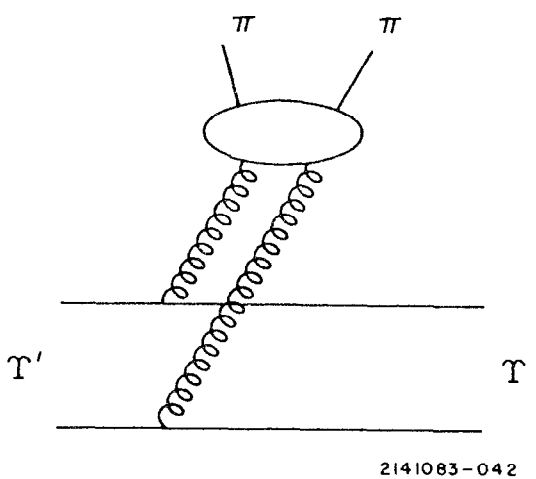


Fig. 1.14. An example of gluon emission from an excited upsilon state yielding $\pi^+\pi^-$.

$$r = \frac{\Gamma(\Psi' \to \pi^+\pi^-)}{(\Upsilon' \to \pi^+\pi^-)} \approx \left[\frac{\langle r_\Psi^2 \rangle}{\langle r_\Upsilon^2 \rangle}\right]^2 \approx 10$$

which follows from the simple formula for electric dipole emission (twice). The transition $\Upsilon(2S) \to \pi^+\pi^- \Upsilon(1S)$ has been observed by many groups working at CESR and DORIS.[27] One finds for r

$$r = \frac{71\text{kev}}{5.2\text{kev}} \approx 14$$

in reasonable agreement with the model prediction.

Dipion transitions may be the best way to locate the 2^1P_1 states and possibly the 1^1S_0 (η_B) (see Fig. 1.2 as a reminder). In charmonium the singlet S-stateswere discovered via M1 transitions from the triplet S-states. In bottomonium the corresponding rates are expected to be very small since

$$\Gamma(^3S_1 \to \gamma\, ^1S_0) \propto \left(\frac{e_q}{M_q}\right)^2 E_\gamma^{\,3} \ .$$

The hyperfine splitting in the upsilon system is expected to be ∿30 MeV as compared to ∿110 MeV in charmonium.

The branching ratio for $\Upsilon(3S) \to \pi^+\pi^- 2^1P_1$ may be ∿1% and would appear as a narrow peak in the missing mass spectrum against the $\pi^+\pi^-$ in $\Upsilon(3S)$ decays. Previous results from the most sensitive experiment (CLEO) do not reach this level; more data are needed. The 2^1P_1 is expected to decay ∿40% of the time via a photon

transition to the η_B. A detector with very good photon energy resolution and reasonable charged particle tracking would be needed to simultaneously detect both the $\pi^+\pi^-$ and the slightly Doppler shifted photon. Such a device has been proposed at CESR.[28]

A similar detector would be needed to locate $T(3S) \to \gamma 3^3P_J$, $3^3P_J \to \pi^+\pi^- \eta_B$ for J = 1,2. In principle the missing mass distribution in T(3S) decays would show two peaks (the 3^3P_J is almost at rest) but combinatorial backgrounds are very large.

1.10 The Future of Upsilon Spectroscopy

The comments immediately above lead naturally into a discussion of the next steps in the study of upsilon spectroscopy. On the experimental side we can look forward to

- improved statistics from DORIS on T(2S) decays in the next year, and
- new data from CESR in 1984 on T(3S) decays.

In the more distant future the interest will lie in precise measurements of branching ratios and spectra and in finding new states; 2^1P_1, η_B and D-states. This certainly will require substantially more data ($\sim 10^6$ decays) and new detectors optimized for soft photon and pion detection.

On the theoretical side the challenge is clear and is a subset of the more general desire to calculate the hadron spectrum. It may be that the relatively simple nature of the $b\bar{b}$ system holds the key to precisely testing our ideas about QCD and the color force.

2. B Meson Decay

B-flavored mesons are combinations of the b (or $\bar{b}$) quark with lighter, u,d,s, or c antiquarks (or quarks). Only the combinations with u and d quarks have been studied heretofore. My nomenclature (quark content) for these spin 0 mesons is:

$$B^+ = \bar{b}u \qquad B^\circ = \bar{b}d$$
$$B^- = b\bar{u} \qquad \bar{B}^\circ = b\bar{d} \ .$$

Spin 1 mesons, the B*'s, with the same quark content also must exist but have not been observed.

What do we learn from studying B meson decay?

- the spectroscopy and dynamics of heavy-light quark systems, and
- the weak interaction properties of the b quark.

The last is the more important since we would like to know if the b quark is described by the Standard Model (it is), and if so, determine the parameters of the quark mixing matrix, the Kobayashi-Maskawa (KM) matrix.

In order to study b quarks we need to make them. To date all existing data come either from CESR operating at and near the T(4S) resonance or from PETRA/PEP. At CESR one has studied the following properties of B mesons:

- inclusive distributions including multiplicity,
- masses,
- hadronic branching ratios,
- semileptonic branching ratios,

- dileptons and neutral current searches, and
- search for non-standard decay modes.

At PETRA/PEP

- lifetimes,
- semileptonic branching ratios and
- dileptons and searches for neutral currents.

In the remainder of this chapter I will discuss all of the above but first we need to describe a simple framework for how B mesons may decay.

2.1 Models of B Meson Decay

The simplest picture of B meson decay is the spectator model illustrated in Fig. 2.1. In this model the b quark is essentially treated as a free quark which undergoes weak decay. (One can also include simple Fermi motion corrections.) The weak decay of the b proceeds through a virtual W to leptons or quark-antiquark pairs with well defined branching ratios. In this model all hadrons containing the b quark would have identical lifetimes.

It is known in the charmed meson case that the D^0 and D^+ lifetimes are different by about a factor of two. This difference is believed to arise from non-spectator processes like those shown in Fig. 2.2. Annihilation into a virtual W of the b and the lighter quark can occur for the charged B mesons but not the neutral mesons. This annihilation is proportional to the b-u coupling (which is small as we shall see later) and to the $|\text{wave function at zero separation}|^2$ since the two quarks must annihilate. The final states

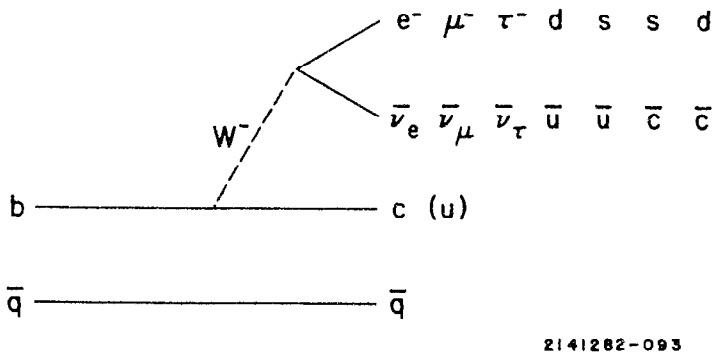


Fig. 2.1. The spectator model of B meson decay.

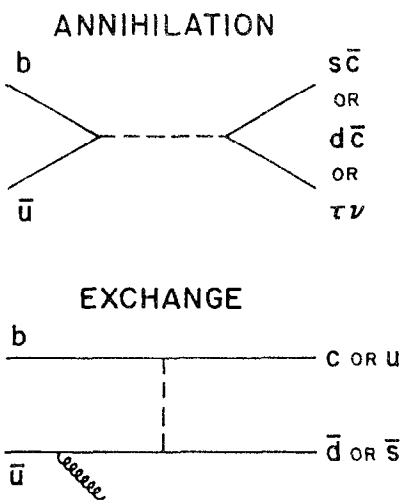


Fig. 2.2. Annihilation and exchange diagrams which can contribute to B decay.

in this case are restricted to massive particles because of helicity arguments, the same reason $\pi \to \mu\nu$ is much larger than $\pi \to e\nu$.

Exchange diagrams as shown in Fig. 2.2 can also occur. Without the gluon (or gluons) radiation this diagram would also be helicity suppressed since it again is a decay of a spin 0 object into two fermions.

Even in the purely spectator case one expects a hadronic enhancement which arises from gluon exchange between the quarks. In the very simplest terms the exchange of gluons can change the flow of color in the decay and, as the name suggests, increase the decay rate into hadronic final states.

Unlike the charm situation there is, at present, no strong evidence for the existence of non-spectator processes in B decay. The only hints come from measuring semileptonic branching ratios which I will discuss later.

2.2 Inclusive Properties of B Mesons

All of the properties that I will discuss come from data obtained at CESR by the CUSB and CLEO groups. As you know from the lecture on upsilon spectroscopy the $\Upsilon(4S)$ is a modest "B factory". Inclusive properties have been measured by sitting at the peak of the $\Upsilon(4S)$ resonance for the properties of B's and by running below the resonance in order to subtract away the continuum contribution to distributions. All of the results are believed to apply to a 60-40 mix of charged and neutral B's, respectively. (I will explain later where the 60-40 comes from.)

2.2 A Charged Particle Multiplicity

The measured mean multiplicity[29] is compared with values from ordinary e^+e^- annihilation in Fig. 2.3. A single B meson is seen to have a mean multiplicity slightly above that of e^+e^- annihilation at the same energy (mass). Perhaps this reflects the four quark nature of B decay as opposed to two quark production in the annihilation process.

2.2 B *Charged Particle Momentum Spectrum*

You might expect such spectra to be essentially uninteresting since it reflects a complicated multi-quark hadronization process. However recent attempts have been made to extract two body (i.e. $B \to D\pi^{\pm}$) branching ratios from the high momentum end of the spectrum.[30] The concept is obvious. If the B were produced at rest and decayed into $D\pi^{\pm}$, then the $\pi^{\pm}$ would be monoenergetic and you would get a bump at high x in Fig. 2.4. At the $\Upsilon(4S)$ the B is produced with enough kinetic energy to smear out the bump and one needs a model dependent fit to the distribution (which includes $D\pi\pi$, $D3\pi$, etc.modes) to extract a branching fraction. The results indicate $BR(B \to D\pi^{\pm}) \approx 1.5\%$ which is not in disagreement with explicit measurements.

2.2 C Charged and Neutral Kaon Yields

Some of the first evidence that the b quark preferred to couple to the c quark rather than the u quark came from measuring inclusive kaon yields.[31] Since we know $c \to s$ then if $b \to c$ there will be en-

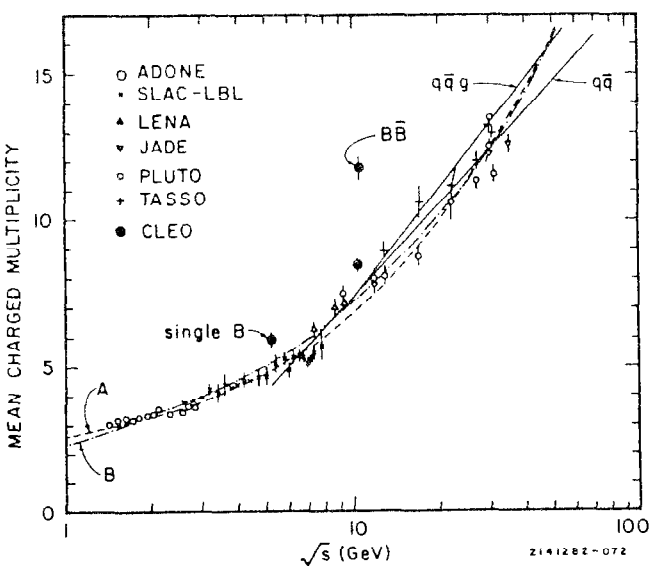


Fig. 2.3. Mean multiplicity vs. center of mass energy.

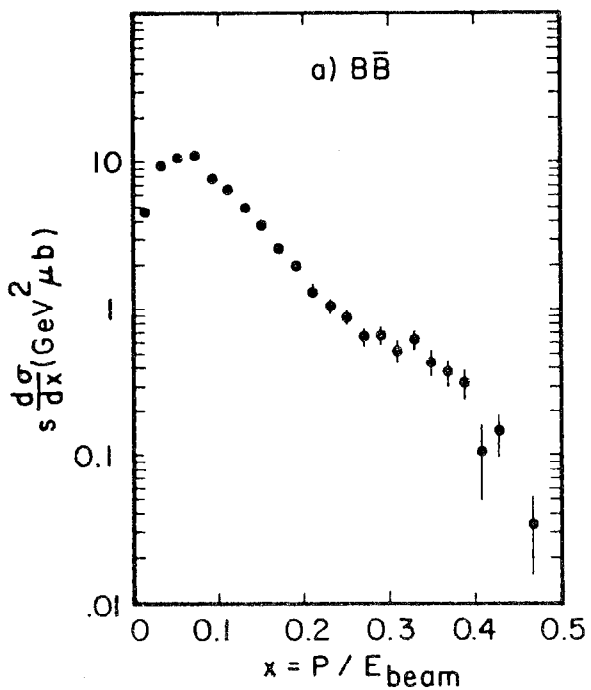


Fig. 2.4. The x spectrum of charged particles in B meson decay.

hanced production of kaons. The data are shown below in Table 2.1.

Table 2.1

	e^+e^- annihilation	$B\bar{B}$ events
No. $K^{\pm}$/event	0.9 ± 0.03	1.5 ± 0.1
No. (K° + $\bar{K}^\circ$)/event	0.9 ± 0.02	1.3 ± 0.1

Unfortunately the uncertainties of hadronization in B decay are large enough to preclude an accurate determination of the relative coupling of b → c to b → u.

2.2 D Baryon Production

Baryon production in B meson decay has been observed[32] (see Fig. 2.5). The branching ratio [BR (B → Λ + X) + BR (B → $\bar{\Lambda}$ + X)]/2 ≈ 3% and about the same for protons. This is no surprise since the B is so massive and baryons have been observed in e^+e^- annihilation at 5 GeV; the quark hadronization should be similar.

2.2 E Charmed Mesons

One way to show that b → c is by reconstructing D or D* mesons from B decay. This has been done by the CLEO group in the case of D's by looking for $D^\circ \to K^-\pi^+$ (and charge conjugate).[33] A signal can easily be seen (Fig. 2.6) in the case where the K^+ is identified in the detector.

A D° signal has also been seen without using particle identification and the D° momentum spectrum from B decay measured (see

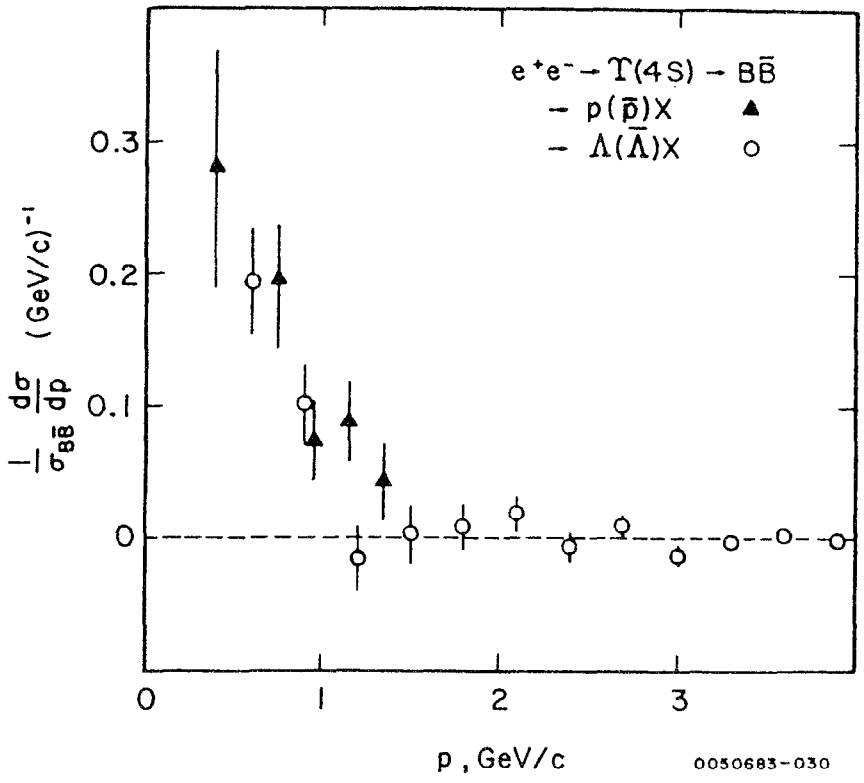


Fig. 2.5. The momentum spectrum of protons and lambdas observed in B meson decay.

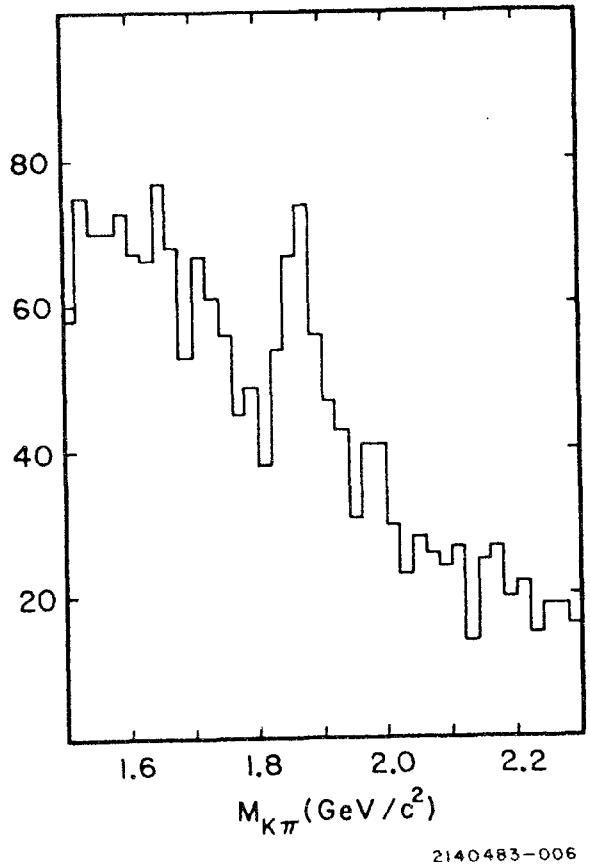


Fig. 2.6. The $K^{\pm}\pi^{\pm}$ invariant mass observed at the $\Upsilon(4S)$. Particle identification is used to tag the $K^{\pm}$.

Fig. 2.7). This spectrum is rather hard and disagrees with phase space type models (Monte Carlos) of B decay. I will return to this point later. $D^* \to D^\circ\pi^\pm$, $D^\circ \to K\pi$ signals have also been observed.

2.3 Hunting for Mass Bumps

Some years ago it was believed that the easiest way to find the B meson in the sense of seeing a peak in a mass distribution was via the mode[34] $B \to \Psi K$, $\Psi \to \mu^+\mu^-$ or e^+e^-. Inclusive dilepton yields have been measured by the CLEO group and are shown in Fig. 2.8 a. and b. There are hints of Ψ's but I prefer to quote an upper limit of $BR(B \to \Psi X) < 1.5\%$. This disagrees with some of the initial estimates in Ref. 34.

Given the copious D° and D^* production it is natural to combine one or two charged pions with the charmed mesons to look for peaks. In doing so one uses constrained fits which are essentially equivalent to using the accurately known colliding beam energy, E_{beam}, in the invariant mass formula instead of the measured B energies. The resulting mass resolution is very good as can be seen in Fig. 2.9. There is clear evidence for a modest peak which yields[35]

$$M_{B^\circ} = 5274 \pm 2 \pm 2 \text{ MeV and}$$
$$M_{B^+} = 5271 \pm 2 \pm 2 \text{ MeV}.$$

The expectation is[36] that $M_{B^\circ} - M_{B^+} \approx 4 - 5$ MeV. This follows the pattern $M_{K^\circ} - M_{K^+} = 4$ MeV and $M_{D^+} - M_{D^\circ} = 4.7$ MeV. This is clearly consistent with, but not demonstrated by, the data. Taking 4.4 MeV then at the $\Upsilon(4S)$, the relative rate of B^+B^- to $B^\circ\bar{B}^\circ$ is 60:40

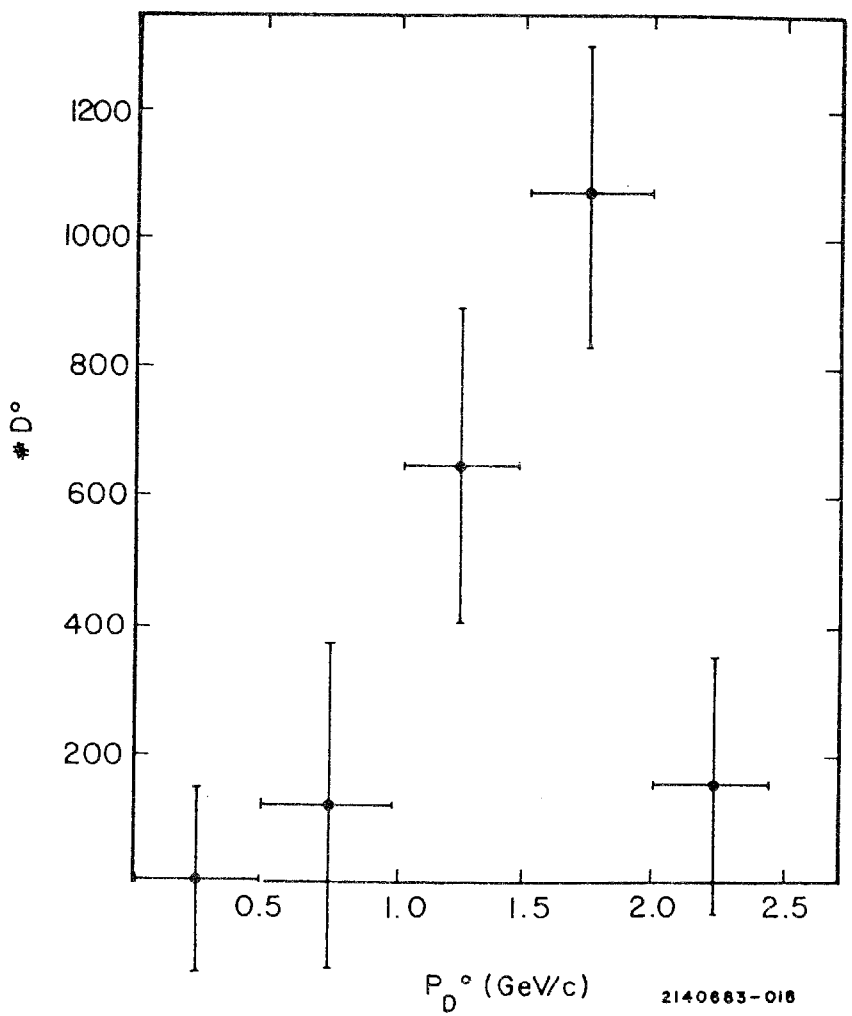


Fig. 2.7. The D° momentum spectrum in B decay.

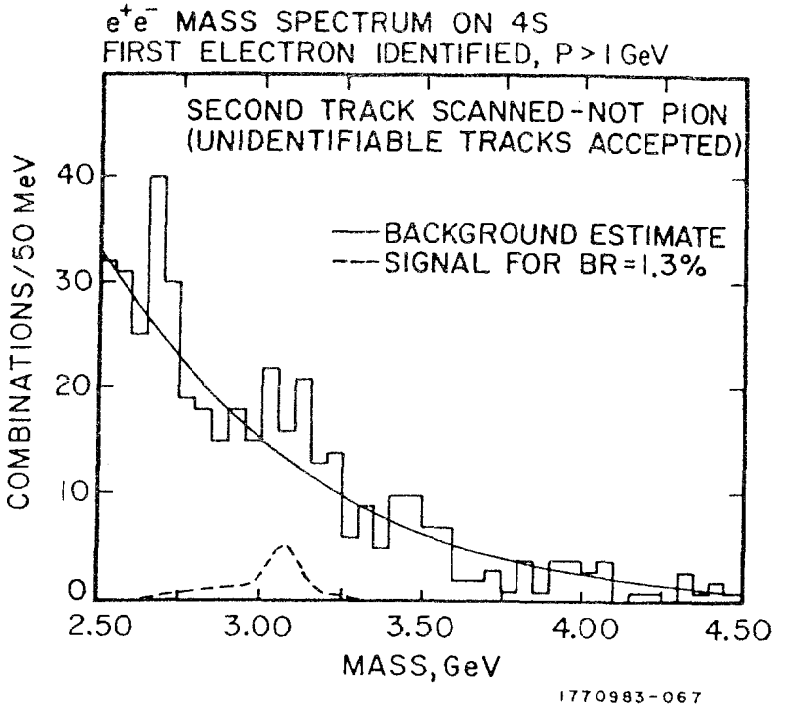


Fig. 2.8a. The dielectron invariant mass distribution.

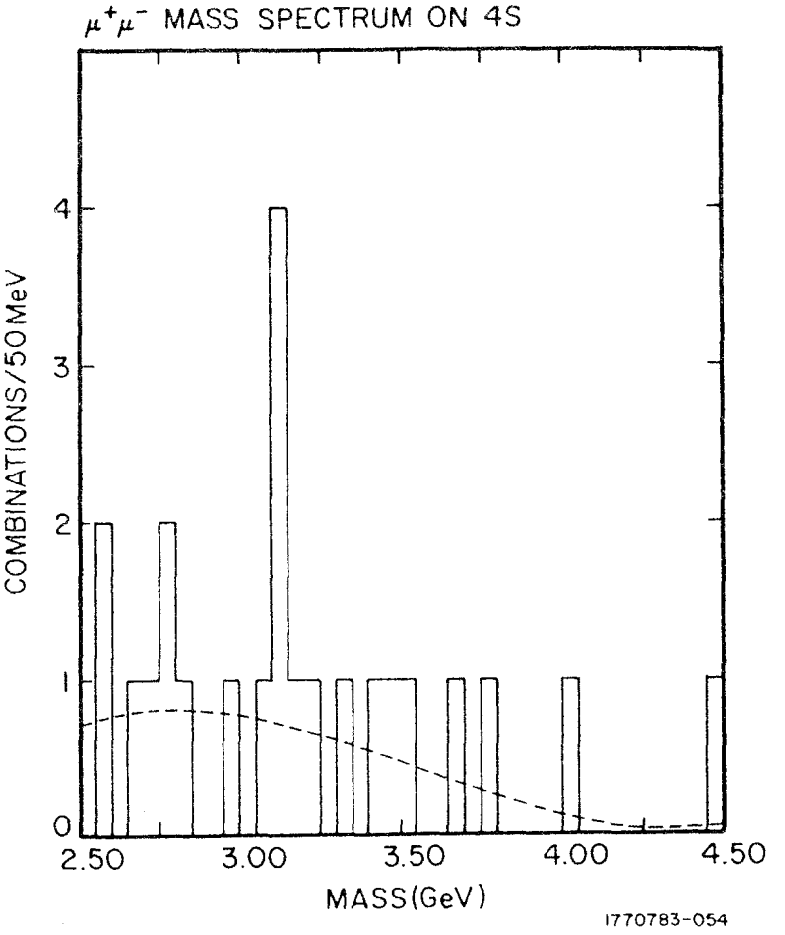


Fig. 2.8b. The dimuon invariant mass distribution.

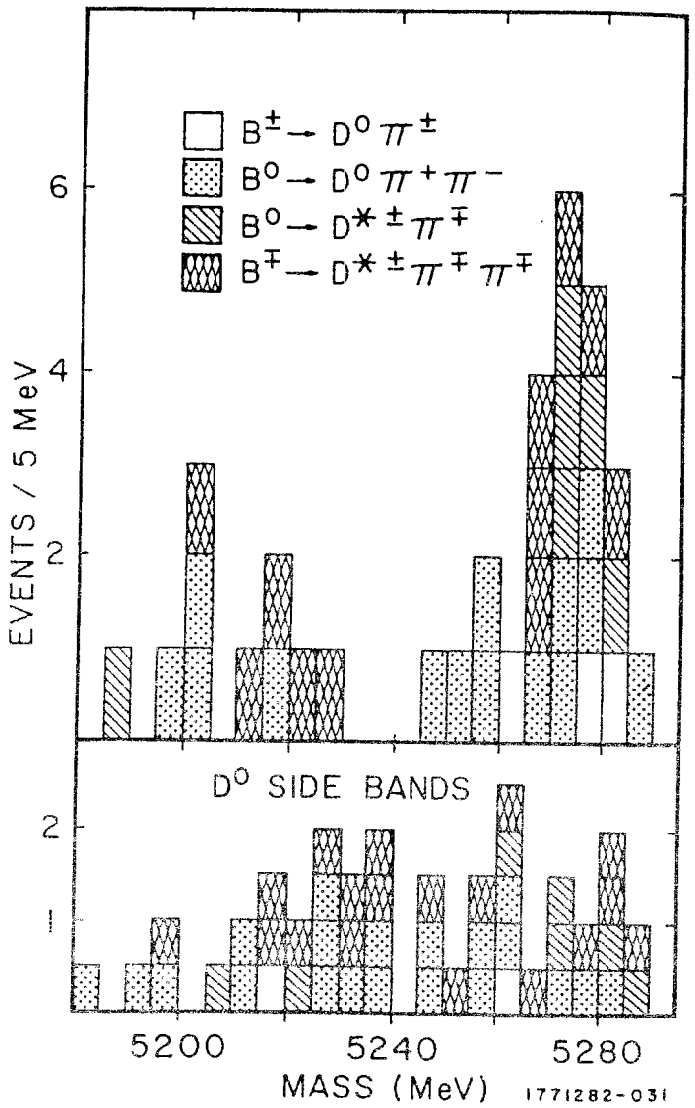


Fig. 2.9. The evidence for B mesons.

simply from phase space considerations. Given these meager statistics the branching ratios are rather poorly determined.

	BR(%)
$B^- \to D^0 \pi^-$	4.2 ± 4.2
$\overline{B}^0 \to D^0 \pi^+ \pi^-$	13 ± 9
$\overline{B}^0 \to D^{*+} \pi^-$	2.6 ± 1.9
$B^- \to D^{*+} \pi^- \pi^-$	4.8 ± 3.0

Based on the usual phase space like model of B decay usec in Monte Carlo simulations it was somewhat surprising to observe any of these modes. The reason is simple. In the "quark soup" - phase space approach the charm fragmentation is not hard and does not agree with the measured D^0 spectrum. In real decays there is some enhanced probability to have low multiplicity final states. This may have implications for studying T mesons, mesons containing the t quark, since b fragmentation is also hard. In other words $T \to B\pi$ may have a reasonable ($\sim$1%) branching ratio and could be observed in Z^0 decays if the t mass is low enough. A Monte Carlo simulation using the known b fragmentation should be done to predict the real number.

2.4 What about the B*?

The B* - B mass difference is expected to be such that[37] $BR(B^* \to \gamma B)$ is 100%. Hence the B* could be found by looking for low energy photons. This has been done at the T(4S) by the CUSB group[38] as can be seen in Fig. 2.10 which shows the expected signal for $T(4S) \to BB^*$ and $M_{B^*} - M_B = 50$ MeV. No evidence for B* production at

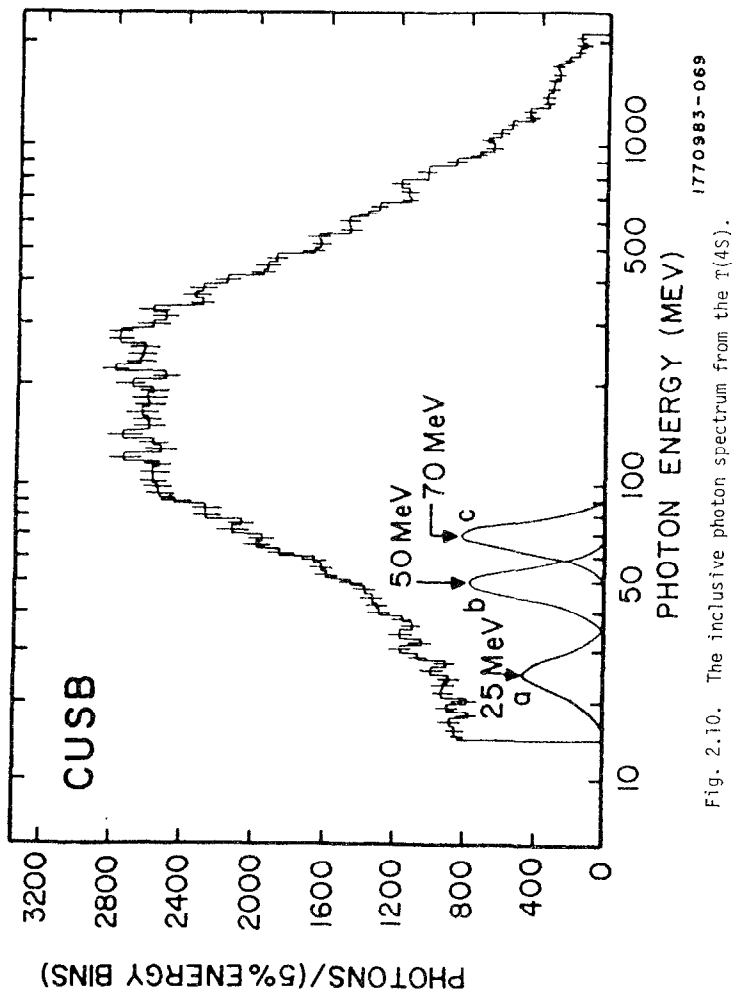
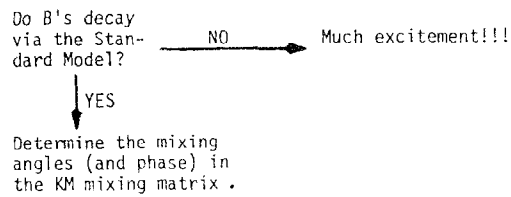


Fig. 2.10. The inclusive photon spectrum from the T(4S).

the T(4S) presently exists so the assumption is that $T(4S) \to B\bar{B}$ 100% of the time.

2.5 B Decay and the Standard Model

The implications of B decay for the Standard Model of the electroweak interaction are succinctly summarized below



The KM matrix is given below where I have used the convention of the Particle Data Group (other forms are used in the literature so beware).

$$\begin{vmatrix} V_{ud} & V_{us} & \boxed{V_{ub}} \\ V_{cd} & V_{cs} & \boxed{V_{cb}} \\ V_{td} & V_{ts} & V_{tb} \end{vmatrix} \begin{matrix} \\ \to \sin\theta_1 \sin\theta_3 \equiv S_1 S_3 \\ \to C_1 C_2 S_3 - S_2 C_3 e^{i\delta} \end{matrix}$$

A complete discussion of the KM matrix is outside the scope of these lectures and I will only concentrate on the two elements V_{ub} and V_{cb} which are relevant to B decay.

These two elements are best constrained at the moment in the following way:

- $|V_{ub}/V_{cb}|$ by the lepton spectrum measured in semileptonic B decay and
- $|V_{cb}|^2$ + (phase space factor) $|V_{ub}|^2$ by measuring the B lifetime.

One can also constrain these elements by using the fact that for example $|V_{ud}|^2 + |V_{us}|^2 + |V_{ub}|^2 = 1$.

2.6 The B Meson Lifetime

The lifetime of hadrons containing the b quark can be measured by the observation of a finite decay length either in hadroproduction, photoproduction or leptoproduction of b-hadrons in the same way that charmed meson lifetimes have been determined. To date there is no useful data from these fixed target experiments. The second way to determine a lifetime is from b-hadrons produced in e^+e^- annihilations at PEP or PETRA. This method has recently been successfully applied at PEP by the MARK II and MAC groups (see the respective talks in these proceedings).

Although the specific b-hadron species in the PEP experiments are not identified I will assume for convenience that they are B mesons. Since $B^* \to \gamma B$ very rapidly, B*'s are equivalent to B's for the lifetime measurement. In order to measure the B lifetime one must first identify B's or find an enhanced sample of B decays. This has been done by many groups using high P_T leptons produced in semileptonic B decay. Electrons or muons are identified in the detector and the thrust axis in an event is determined. P_T of the lepton is then defined with respect to the thrust axis. Since the B is massive high P_T leptons are produced. An example of a P_T spectrum is shown in Fig. 2.11. Beyond P_T of 1 - 1.5 GeV/c the spectrum comes primarily from b decay.

Given an event with an e or μ one then projects the e or μ track as shown schematically in Fig. 2.12 and determines an impact parameter. The distribution of impact parameters will be shifted for non-zero lifetime and the shift related to the lifetime. There are many complications in this method. There are backgrounds from hadrons faking leptons and from charm decay. One also must understand the errors associated with locating the collision point and with tracking algorithms. After all this the results are:

$$\tau_B = (12.0^{+4.5}_{-3.6} \pm 3.0) \times 10^{-13} \text{ sec} \quad \text{MARK II}$$
$$= (18 \pm 6 \pm 4) \times 10^{-13} \text{ sec} \quad \text{MAC}$$
$$< 14 \times 10^{-13} \text{ sec} \quad \text{JADE (95\% CL)} .$$

Clearly the result from JADE[39] is in conflict with the other two measurements and the discrepancy can only be resolved by additional measurements. For illustrative purposes I will take

$$\tau_B = 15 \times 10^{-13} \text{ sec} .$$

In the Standard Model the B decay rate is given by[40]

$$\frac{1}{\tau_B} = \Gamma_B = \frac{G_F^2 m_b^5}{192\pi^3} [a\,|V_{bu}|^2 + b\,|V_{bc}|^2]$$

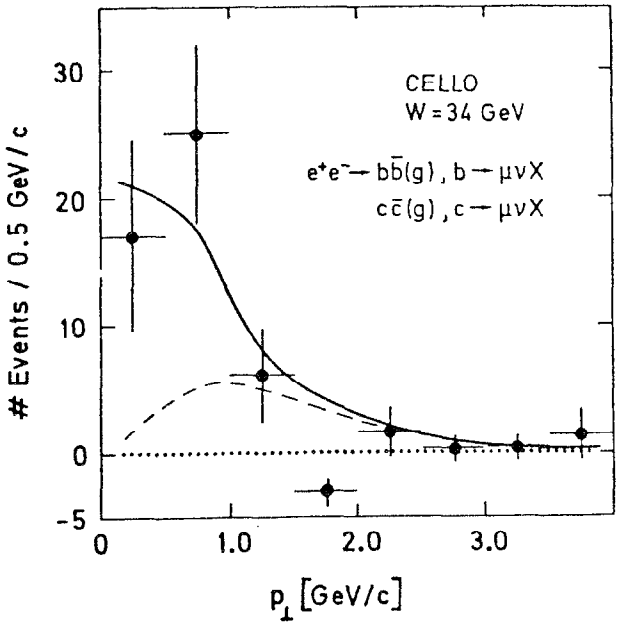


Fig. 2.11. The P_T distribution of leptons showing the contributions from charm and b decay. The data are from the CELLO Group.

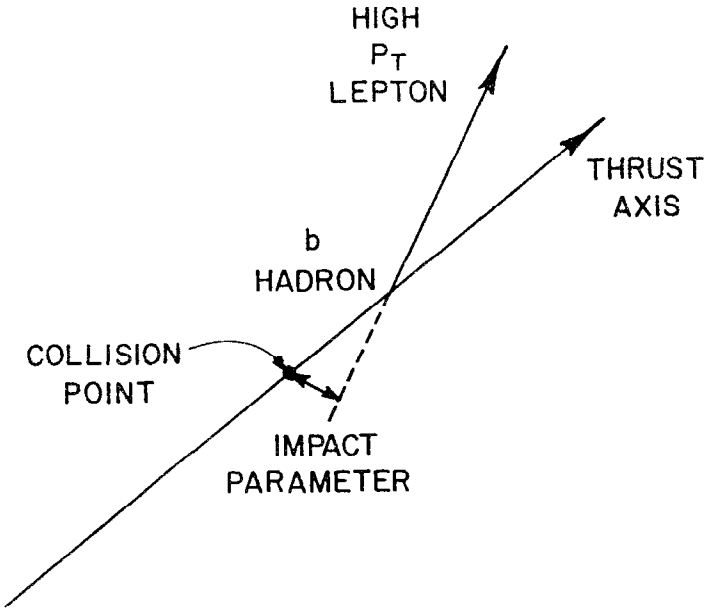


Fig. 2.12. A schematic picture of the method used to determine the b lifetime.

2141083-037

where a and b include phase space factors, hadronic enhancement factors, and can include non-spectator effects. Using

$$\frac{1}{\tau_\mu} = \Gamma_\mu = \frac{G_F^2 m_\mu^5}{192\pi^3}$$

we can write

$$\frac{1}{\tau_B} = \Gamma_B = \left(\frac{m_b}{m_\mu}\right)^5 \Gamma_\mu \left[a|V_{bu}|^2 + b|V_{bc}|^2\right] .$$

In this equation only m_μ and Γ_μ are well known. The value of m_b could range from 4.5 - 5.0 GeV/c^2 or roughly ±5% but which implies a ±25% uncertainty in the lifetime.

The ratio of a and b in the spectator approximation depends, in part, on what charmed quark mass is used in the calculation. Typical values are a = 7.7 and b = 3.3. The actual magnitude of non-spectator effects is unknown but would change the relative lifetimes of charged and neutral B's. Since the measured lifetime applies to some roughly equal mixture of charged and neutral B's the KM matrix elements cannot be determined uniquely. These effects are probably small and negligible given the present accuracy of the τ_B measurement. Ignoring non-spectator effects then (m_b = 4.75 GeV)

$$\tau_B = 1.5 \times 10^{-15} \frac{1}{\left[|V_{bu}|^2 + 0.43\ |V_{bc}|^2\right]} ,$$

or for $\tau_B = 1.5 \times 10^{-13}$ sec

$$|V_{bc}|^2 \left[1 + 2.3\frac{|V_{bu}|^2}{|V_{bc}|^2}\right] = 2.6 \times 10^{-3} .$$

We can see already that V_{bc} and V_{bu} must be small.

The next step is to determine how often $b \to c$ (V_{bc}) and $b \to u$ (V_{bu}). This is done by studying the energy spectrum of leptons emitted in semileptonic b-decay. Many measurements of BR($B \to \ell\nu X$) have been made at CESR[41] and PETRA/PEP,[42] where B represents a mixture of B^+ and B° (essentially equal). The measurements are consistent with

$$BR(B \to \ell\nu X) = 12 \pm 1 \pm 1\% .$$

One expects[40]

from quark counting	∿17%
+ hadronic enhancement	∿14 - 15%
+ non-spectator processes	∿12 - 13% .

This result gives the only hint that non-spectator processes may exist in B decay.[43]

The key to determining V_{bu}/V_{bc} is to examine the high energy tail of the lepton spectrum. Since the c quark is more massive than the u quark the lepton spectrum in $b \to c\ell\nu$ is softer than in

$b \to u\ell\nu$. What the spectrum is in the two cases is somewhat model dependent because the c or u quark hadronization is not known precisely. In the case of $b \to c$ for example one can have, in principle, $B \to D\ell\nu$, $B \to D^*\ell\nu$, $B \to D^*\pi\ell\nu$, etc. A fit to the spectrum and measurements of the multiplicity in semileptonic decay suggests that $B \to D\ell\nu$ and $B \to D^*\ell\nu$ dominate.[29]

A typical electron spectrum is shown in Fig. 2.13. There are no leptons above 2.4 GeV/c which would be populated by the $b \to u$ process. In order to extract an upper limit to $b \to u/b \to c$ one must fit spectra such as in Fig. 2.13. The fitting function F(p) consists of:

$$F(p) = F_{b\to c}(p) + F_{b\to u}(p) + F_{c\to \ell}(p) .$$

Where $F_{b\to c}$ ($F_{b\to u}$) is the appropriate spectrum for $b \to c\ell\nu$ ($b \to u\ell\nu$) and $F_{c\to\ell}$ represents the leptons from semileptonic charm decay which are predominantly at low momenta. $F_{c\to\ell}$ is taken from the measured spectrum. For $F_{b\to c}$ and $F_{b\to u}$ one can use a model such as that of[44] Altarelli et al. which essentially predicts the M_X distribution in $B \to \ell\nu$ for X = both X_c and X_u. Alternatively one can write

$$F_{b\to c}(p) = F_{B\to D}(p) + F_{B\to D^*}(p) + \ldots$$

and

$$F_{b\to u}(p) = F_{B\to\pi}(p) + F_{B\to\rho}(p) + \ldots$$

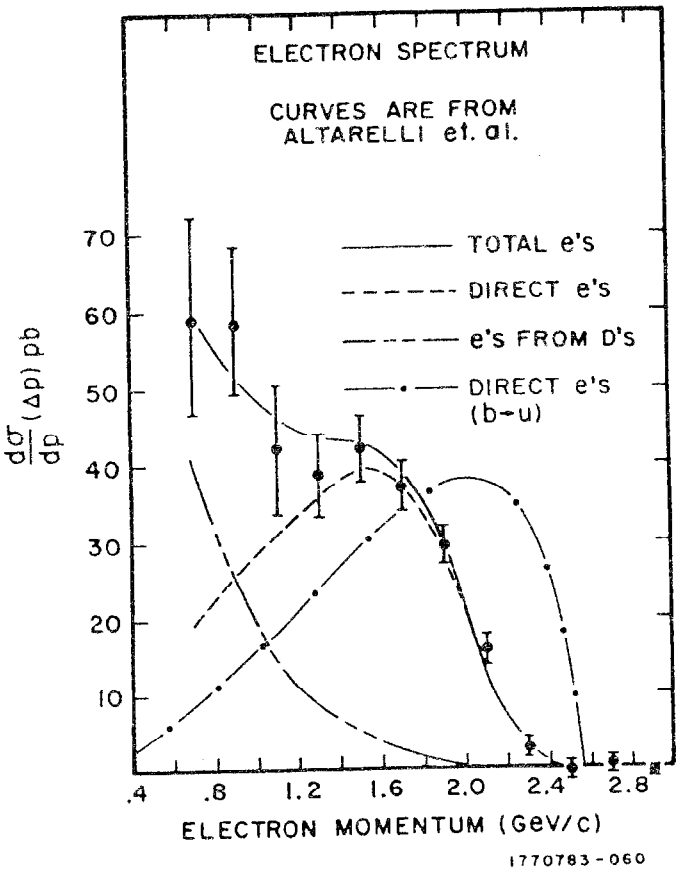


Fig. 2.13. The electron spectrum in B meson decay measured by the CLEO group.

where $F_{B\to D}$ represents $B \to D\ell\nu$, etc. All of this assumes that non-leptonic backgrounds have been subtraced (hadrons that simulate leptons).

The data from both the CLEO[4] and CUSB[4] groups, Fig. 2.13 and Fig. 2.14, respectively, are well described by the model of Altarelli et al. and yield $BR(B \to u)/BR(b \to c) < 0.055$ at 90% confidence level for both groups. One can also plot the upper limit versus the assumed hadronic mass in the $b \to u$ case as shown in Fig. 2.15 (CLEO). An upper limit of 0.05 is obtained for reasonable masses. These limits are probably reliable although the delineation of the exact spectrum awaits much higher statistics and actual observation of the $b \to u$ component.

Taking $BR(b \to u)/BR(b \to c) < 0.05$ one can obtain the corresponding limit to (V_{bu}/V_{bc}) from

$$|V_{bu}/V_{bc}| < \left[\frac{0.05}{(2.1 - 2.5)} \right] 1/2$$

where the phase space factors can differ depending upon which masses are used in the equation. Choosing 2.3 we get

$$|V_{bu}/V_{bc}| < 0.15 .$$

Remember that we found

$$|V_{bc}|^2 \left[1 + 2.3 \left|\frac{V_{bu}}{V_{bc}}\right|^2\right] \approx |V_{bc}|^2 [1 + 0.05] = 2.6 \times 10^{-3} ,$$

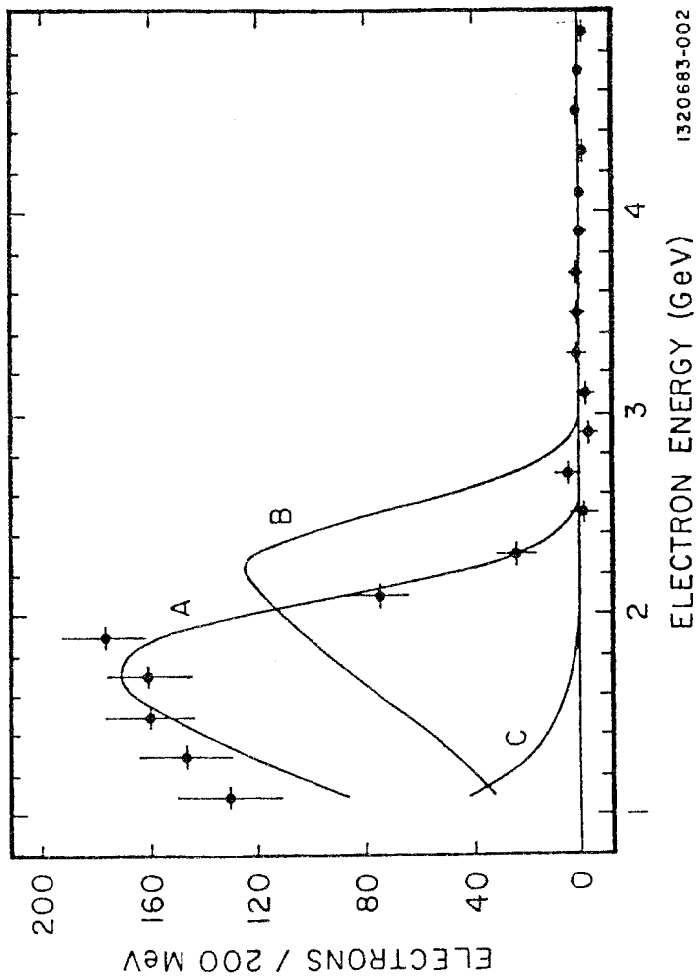


Fig. 2.14. The electron spectrum in B meson decay measured by the CUSB group. Curve A corresponds to b→c and Curve B to b→u. Curve C represents electrons from charm decay.

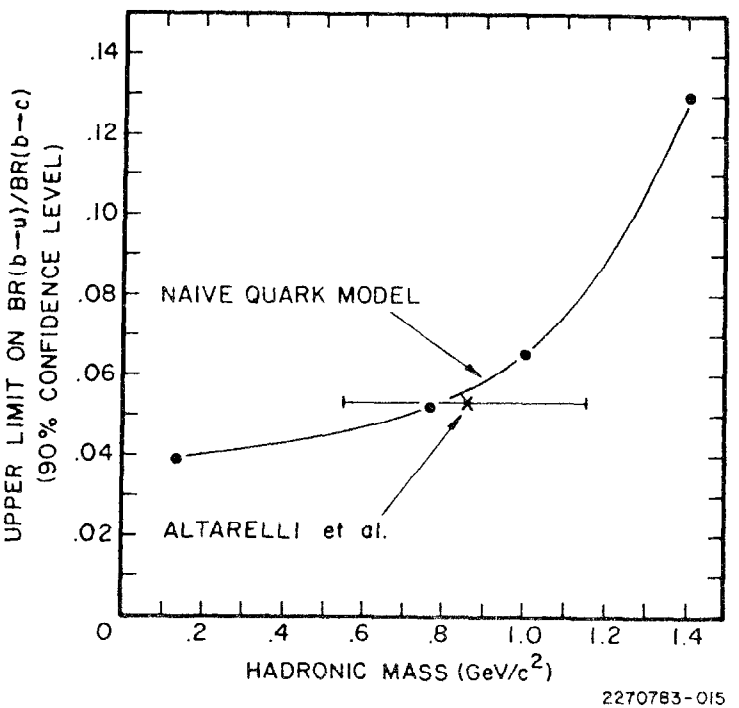


Fig. 2.15. The limit on B(b→u) vs. the hadronic mass M_X used in B→ ℓνX.

hence

$$|V_{bc}| \approx 0.05$$

and $$|V_{bu}| < 0.0075 \ .$$

Clearly the b quark is reluctant to couple to the c and especially the u quark.

2.7 The Future of B Decay Studies

With the very important exception of the B lifetime measurements most of the experimental work on this subject will take place in the next few years at CESR and DORIS II. A scan above the T(4S) is presently underway at CESR to search for the T(5S) and T(6S). Possibly one of these resonances will be fortuitously situated so as to be just below the threshold for the $b\bar{s}$ meson production. Given the history of the search for the F meson, however, considerable luck will be needed. A better bet is that evidence for the B* will be found.

The key to future studies is simple; produce more B mesons. Improvement of the crucial lifetime measurements at PEP/PETRA demand more decays and eventually superior vertex detectors with better resolution. At CESR and DORIS II the need for more B's is even more important to measure branching ratios, look for $B^0 - \bar{B}^0$ mixing, etc.. If we are fortunate the detailed study of B weak decays will provide some indication of life beyond the Standard Model.

3. Top Quarks, W's and Z's

We have seen that the properties of the b quark are consistent with the Standard Model which describes six quarks. Groups at PETRA and the SPS collider have been and will be searching for the missing quark, the t quark. An entire accelerator (TRISTAN) is being constructed with the hope that m_t is less than 35 GeV.

I will describe why we need the t quark, some indirect ways to constrain its mass and how to find it in e^+e^- and $p\bar{p}$ collisions. You should remember that if $m_t \lesssim 75$ GeV then it is produced at the SPS collider in W decay.

The importance of the discoveries of the W and Z° by the UA1 and UA2 collaborations is well known. The detection methods are so simple (after the fact) that a pedagogical treatment is quite well done by the contributions to the Topical Conference. I will make only a modest effort in this paper.

3.1 Do We Need the t Quark?

Yes! Many of the models without the t quark, unfortunately called topless models, predict unusual behaviour in b quark decay. Such exotic decays are not observed.[45] An example of particular interest is to just forget the t quark and have

$$(u,d)_L \quad (c,s)_L \quad (b)_L + \text{the usual right-handed singlets.}$$

This predicts flavor changing neutral decays ($b \to s$ or $b \to d$) at too large a rate to agree with experiment. These decays involve virtual Z° → real lepton pairs and the $\mu^+\mu^-$ or e^+e^- would be easy to see. Another kind of topless model has been ruled out by the observation of the b lifetime. In this model one has[46]

$$\begin{pmatrix} u \\ d' \end{pmatrix}_L \quad \begin{pmatrix} c \\ s' \end{pmatrix}_L \quad \begin{pmatrix} c \\ b \end{pmatrix}_R$$

and there is no mixing angle suppression of the coupling to the W resulting in very short lifetimes.

3.2 m_t, τ_B and $|V_{bu}/V_{bc}|$

Recently there have been attempts to relate these three quantities and hence determine a lower bound to m_t.[47] We saw in the last chapter on B decay that the couplings V_{bu} and V_{bc} are small. This implies that the angles θ_2 and θ_3 are also small. Now the CP violation parameter ε in the $K^\circ - \bar{K}^\circ$ system is related to θ_2, θ_3, δ and m_t according to Ref. 47 by

$$\varepsilon = -\frac{s_1^2 B G_F^2 f_K^2 m_K m_c^2}{6\sqrt{2}\,\pi^2 (m_{K_S} - m_{K_L})} c_2 s_2 s_3 s_\delta \{\eta_1 [-c_1 c_2^2 c_3 + s_2 c_2 s_3 c_\delta]$$

$$+ \eta_2 (m_t/m_c)^2 [c_1 s_2^2 c_3 + s_2 c_2 s_3 c_\delta] + \eta_3 \ln(m_t^2/m_c^2)[c_1 c_2^2 c_3 - c_1 s_2^2 c_3$$

$$- 2 s_2 c_2 s_3 c_\delta]\} e^{i\pi/4}.$$

The factors η_1, η_2 and η_3 take into account strong interaction

corrections and B is a complicated quantity which represents the matrix element of the $\Delta S=2$ operator. A somewhat more comprehensive approximate relation derived by Pakvasa and Sugawara [48] is

$$|\varepsilon| = \left|\frac{(m_t - m_c)}{m_c}\right| \quad \frac{\sin 2\theta_2 \tan\theta_3 \sin\delta}{2\sqrt{2}\cos\theta_1} \quad .$$

Roughly the smaller θ_2, θ_3 and δ then the larger m_t must be to agree with the measurement of $\varepsilon = (2.27 \times 10^{-3})e^{i\pi/4}$.

Figure 3.1 taken from Ref. 47 shows how m_t, τ_B and $BR(b \to u)/BR(b \to c)$ may be related. The problems are that the values of B and $\eta_1 - \eta_3$ are uncertain; theorists disagree. The mass of the charmed quark is also uncertain. Given this and the present errors on τ_B not much can be said about a bound on m_t. When m_t, τ_B and $BR(b \to u/BR(b \to c)$ are better determined then one should be able to check the theoretical calculations.

3.3 Finding the t Quark in e^+e^- Annihilation

Discovery of the t quark in e^+e^- experiments is trivial <u>if</u> you have a machine with enough energy. The methods are well known:

- Look for an increase in σ_{had} above threshold for T meson production or changes in event shapes.
- Find a narrow resonance - toponium.

The present and potential players in this game are:

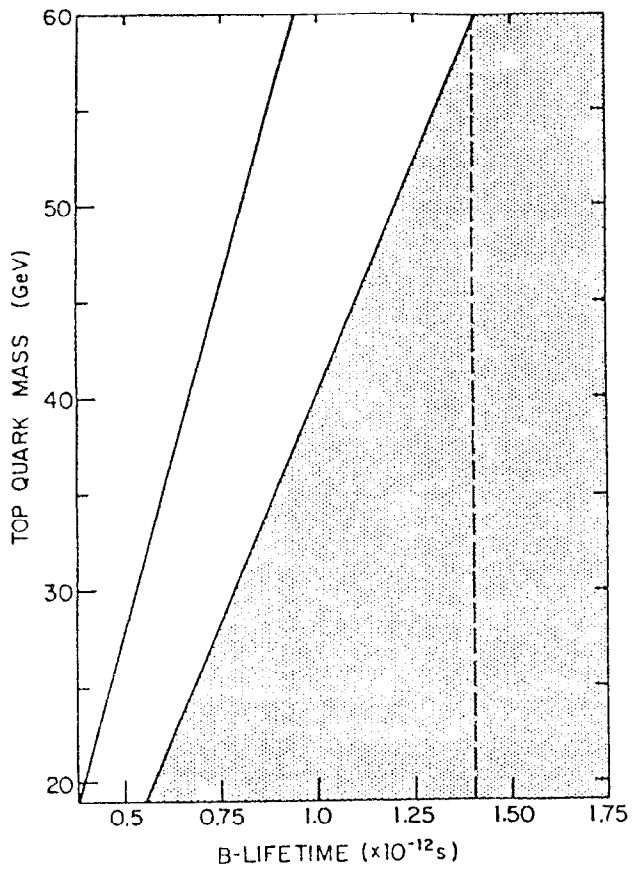


Fig. 3.1. Bounds on M_t for different values of τ_B and $BR(b \to u)/BR(b \to c) = 0.05$.

PETRA - today

TRISTAN - 1986

SLC - 1987

LEP - 1990 .

It is quite possible that the t quark will be discovered in $\bar{p}p$ collisions but detailed studies will require e^+e^- colliders, particularly for the bound state spectroscopy.

The change in the hadronic cross section seen in e^+e^- annihilation resulting from the t quark is easy to calculate. If we ignore, for the moment, contributions from the Z° tails then $R = \sigma_{had}/\sigma_{\mu\mu}$ goes from approximately $3\ ^2/_3$ + QCD corrections to 5 + QCD corrections. The Z° contribution is also calculable. The change in event shape, thrust for example, above threshold occurs because the T mesons are massive and hence yield non jet-like events.

Just below the threshold bound states, toponium, will be produced. The number of narrow states depends on the t quark mass roughly as shown in Fig. 3.2 so one expects 6 or more bound states to be observed. The toponium cross section observed in e^+e^- annihilation depends on the leptonic width, Γ_{ee}, and the natural energy spread of the colliding beams. The leptonic width can be obtained from the scaling law shown in Fig. 3.3 or from potential models. Γ_{ee} is approximately 5 KeV except when $2m_t \approx M_{Z^0}$. The beam energy spread depends on the parameters of the machine. PETRA, for example, has $\sigma_w = 2.2 \times 10^{-5}\ W^2$ where W is the center of mass energy. The consequences of this spread can be seen in

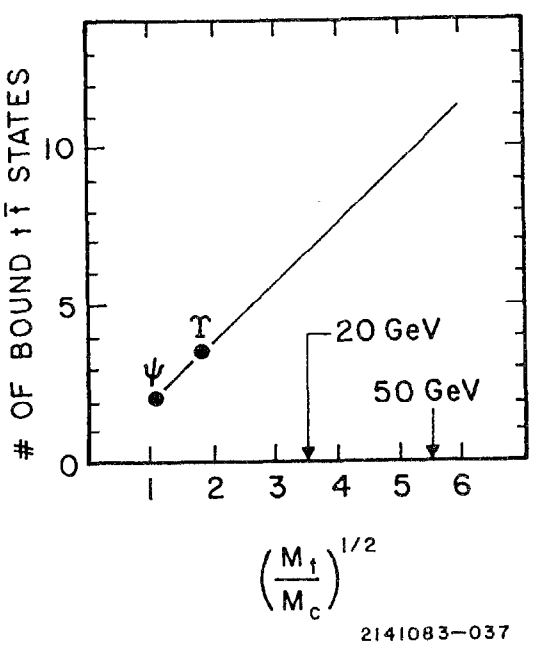


Fig. 3.2. The number of bound $t\bar{t}$ states vs. m_t.

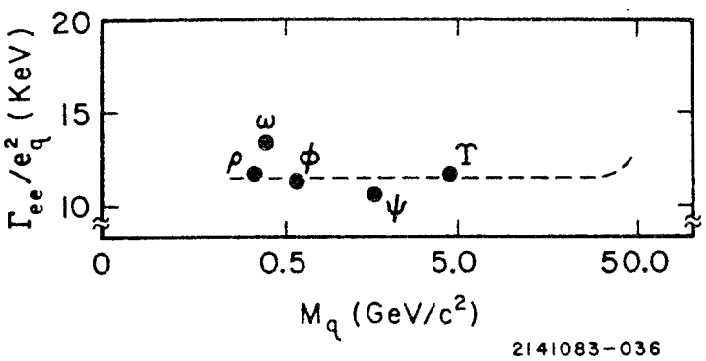


Fig. 3.3. A scaling law for leptonic widths of vector mesons.

the example of Fig. 3.4 which applies at TRISTAN. The energy spread is large enough (~50 MeV) such that the higher levels begin to merge. Initial state radiation will also cause the states to merge. To date there is no evidence for top at PETRA up to about W = 42 GeV (see E. Lohrmann's talk in these proceedings).

3.4 Producing t Quarks in Hadronic Collisions

Given the lower limit on m_t from PETRA it is useful to investigate how top might be revealed in hadronic collisions at the SPS collider or at the FNAL collider. Production of top via $W \to t + X$ is also considered in this section since the W's are produced in hadronic collisions.

3.4 A Toponium Production in Hadronic Collisions

The discovery in this way would be a repeat of the J/ψ and Υ discoveries and provide unambiguous evidence of the t quark. Present experiments at the colliders lack the resolution to resolve the individual toponium states and the different states would appear as a coalesced peak on top of a background of Drell-Yan pairs. The $t\bar{t}$ states can be produced through quark-antiquark annihilation

$$q\bar{q} \to (\gamma^*, Z^*) \to (t\bar{t})$$

or through diagrams containing gluons as shown in Fig. 3.5. The toponium production corresponds to the fraction of the cross section below open top threshold calculated from these diagrams. The cross

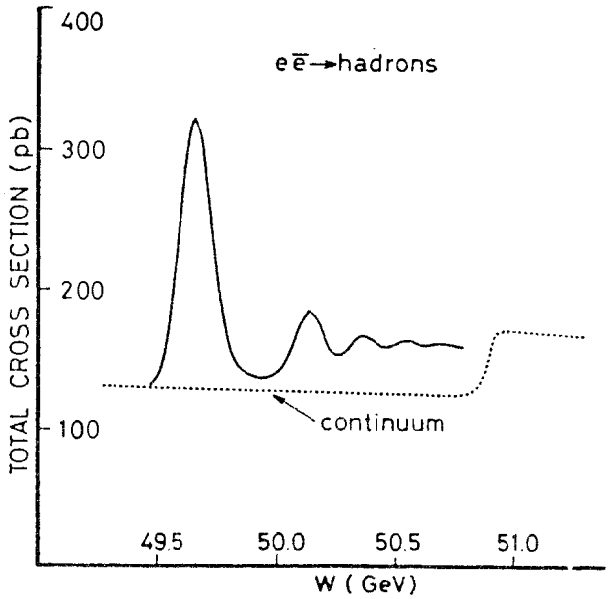


Fig. 3.4. The expected toponium cross section at TRISTAN taken from the TOPAZ Proposal.

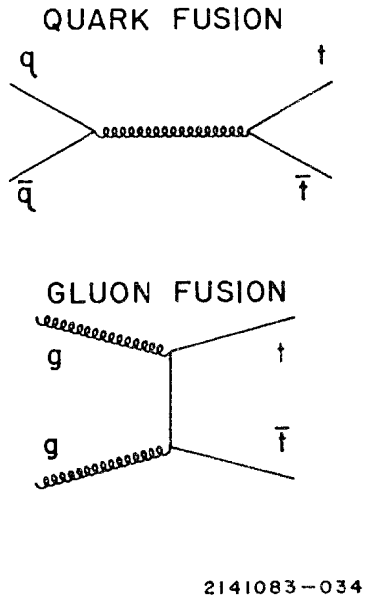


Fig. 3.5. Quark and gluon fusion diagrams for producing toponium or open top.

section can be estimated from the scaling law of Gaisser, Halzen and Paschos[49] shown in Fig. 3.6. As an example suppose $m_{t\bar{t}} = 70$ GeV then

$$\sigma \cdot B_{\mu\mu} \approx \frac{5 \times 10^{-26}}{(70)^3} \quad (50 \times 10^{-6}) \times 3 \times 0.05 \approx 1 \times 10^{-36} cm^2$$

where $B_{\mu\mu} = 5\%$, $\Gamma = 50$ KeV and $\Delta y = 3$ units of rapidity. The toponium production[50] vs. $m_{t\bar{t}}$ is shown in Fig. 3.7 for $\sqrt{s} = 540$ GeV. It $m_{t\bar{t}}$ is close to m_{Z^0}, the cross section is enhanced. Note that the integrated luminosity from the SPS collider is $\sim 100 nb^{-1}$ hence one roughly expects 0.1 events for $m_{t\bar{t}} = 70$ GeV. Much more luminosity is needed to hope to see high mass toponium.

3.4 B Open Top Production

Open t production can occur via the same diagrams as in Fig. 3.5. These processes are central (90°), non-diffractive processes and are dominated by gluon fusion and hence depend on the gluon structure functions in the proton. The gluon structure functions are not precisely known so predictions should be taken as order of magnitude estimates. For $p\bar{p}$ at $\sqrt{s} = 540$ GeV the estimates[51] are given below in Table 3.1.

Table 3.1

m_t(GeV)	σ(nb)	# Events for $100 nb^{-1}$
20	20	2000
30	5	500
40	1	100
50	0.3	30

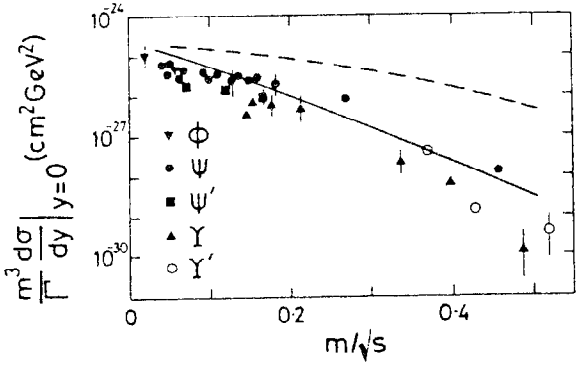


Fig. 3.6. The scaling law of Gaisser, Halzen and Paschos for vector meson production.

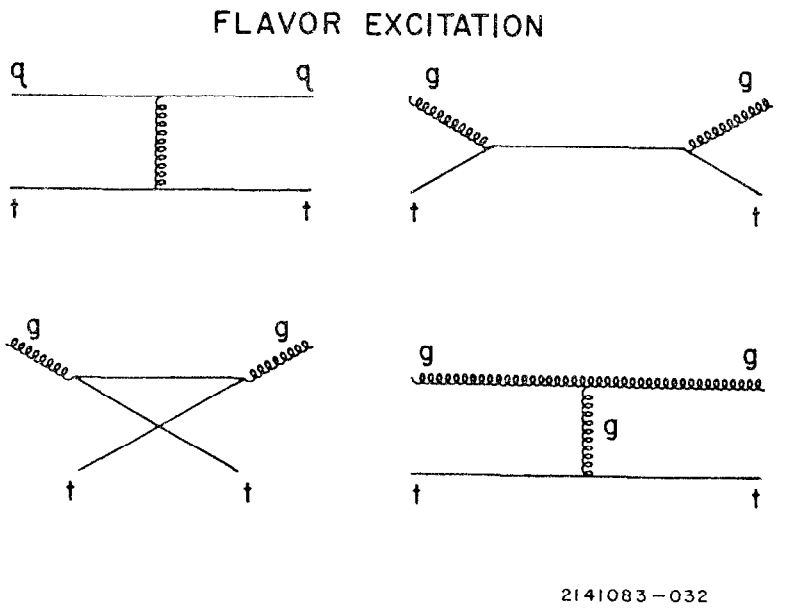


Fig. 3.7. Flavor excitation diagrams for diffractive t production.

In addition to central production there may be a significant diffractive component. Unlike gluon fusion which is strongly peaked at x = 0 because the gluon structure functions are soft, the diffractive component has a much flatter dependence. Such a component is necessary to explain Λ_c production at the ISR. These flavor excitations occurs through diagrams like those in Fig. 3.7 where the t (and $\bar{t}$) somehow come from the sea in the proton. The estimates[52] of this cross section are uncertain but are roughly as below in Table 3.2.

Table 3.2

m_t(GeV)	σ_{diff}(μb)
20	0.1 - few
50	0.001 - 0.1

Even for large masses thousands of events containing the t quark would be produced at the SPS collider. The key problem of course is to distinguish these events from a very large background. For example, b hadrons are much more copiously produced.

3.4 C Top Production in W Decay

Depending upon the actual magnitude of the t production from quark and gluon fusion, t production from the decay of the W becomes more important for $m_t \gtrsim 35$ - 50 GeV. One is also sensitive to high masses, up to $m_W - m_b \approx 75$ GeV.

Roughly one expects the branching fractions for

$$W^+ \to t\bar{b}$$
$$\to c\bar{s}$$
$$\to u\bar{d}$$
$$\to \ell\nu$$

to be equal so that a t quark is produced at a rate three times the $W \to e\nu$ rate.

As an example consider a W^+ of mass 80 GeV/c^2 produced at rest which decays into $t\bar{b}$ (see Fig. 3.8) where I take m_t = 40 GeV. This can be treated as a four stage process. In stage one the W^+ decays. In stage two hadronization occurs. We know from PEP and PETRA measurements[12] that $\langle z_b \rangle \approx 0.75$, i.e. b-hadrons carry away about 75% on average of the initial b quark energy. For t quarks I take $\langle z_t \rangle$ = 0.9. This yields energetic T and B mesons. In stage three the T meson decays semileptonically into a B meson or B meson + hadrons and $e^+\nu$. Since the T meson is massive the e^+ can come off at large P_T with respect to the t direction. In stage 4 the B mesons decay yielding hadron jets. The signature for t production then is a high P_T electron, which in many cases will appear as a high transverse energy (E_T) electron, associated with missing energy. In the case of t production by quark or gluon fusion in the central region high E_T electrons would also be a signature. The problem in this case is that $\sigma_{central} \propto \frac{1}{m_q^4}$ so b quark production is expected to be much more copious at E_T (or P_T) up to 50 GeV (see Fig. 3.9).[50] In the W case there is the extra constraint of the W mass which may help. In

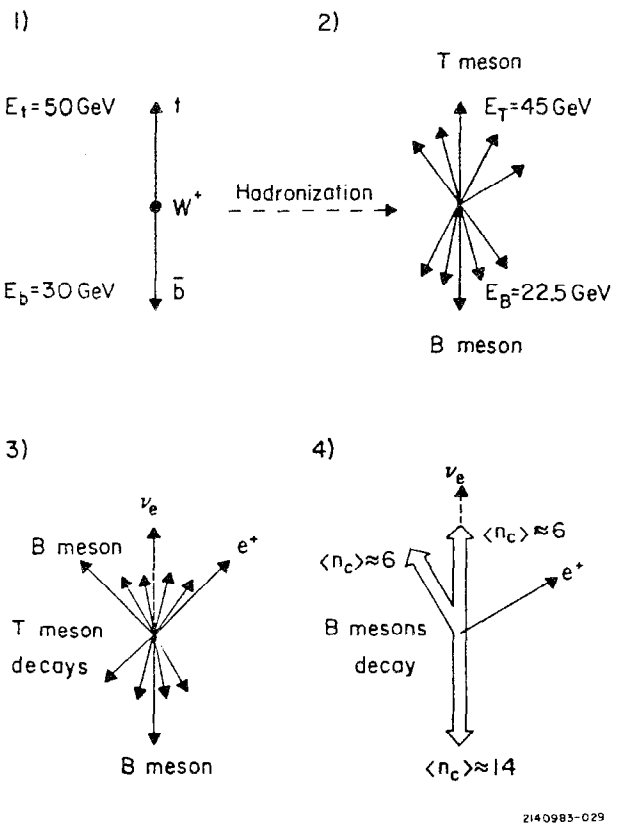


Fig. 3.8. An example of a W^+ decay at rest into $t\bar{b}$.

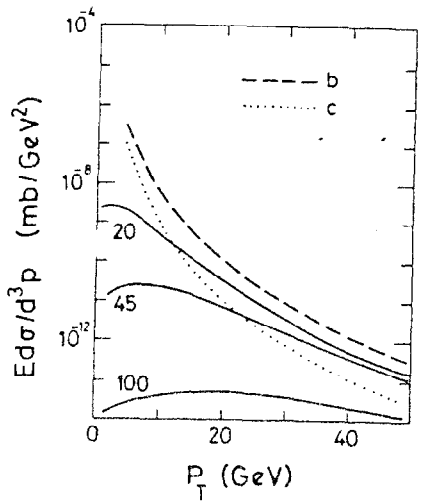


Fig. 3.9. The P_T distribution of electrons fron semileptonic charm, bottom and t decay for different values of m_t.

conclusion unlike the clean W and Z events produced in $\bar{p}p$ collisions finding the t quark is more difficult and challenging. Backgrounds are large and it may take substantially more data to observe evidence for top in some carefully selected distributions.

3.5 W's and Z's

The production of W's and Z's in $\bar{p}p$ collisions occurs through quark-antiquark annihilation as shown in Fig. 3.10. The cross sections for W and Z production may be calculated using the structure functions of the proton and Drell-Yan "experience". The results for $\sqrt{s}$ = 540 GeV are[53]

$$\sigma_W = 5\text{nb}$$
$$\sigma_{Z^\circ} = 1.5\text{nb}.$$

Leptonic decays, $W \to e\nu$ and $Z^\circ \to \mu^+\mu^-$ or e^+e^- are the distinctive features of heavy boson production. If $m_t \lesssim 75$ GeV then we expect $BR(W \to e\nu) \approx 8\%$ (it will be larger if $m_t > m_W$). For the Z° we anticipate $B(Z^\circ \to e^+e^-) \approx 3\%$. Hence in a perfect detector we would see 9 $Z^\circ \to e^+e^-$ or $\mu^+\mu^-$ events and 80 $W \to e\nu$ or $W \to \mu\nu$ events for an integrated luminosity of 100nb^{-1}. This integrated luminosity roughly corresponds to the total accumulated at the SPS.

Finding the Z° is particularly easy to explain. One simply forms the invariant mass of the e^+ and e^- (or μ^+ and μ^-) candidate tracks. The trick is to identify the tracks as leptons and you can read about the details in the Topical Conference reports. In

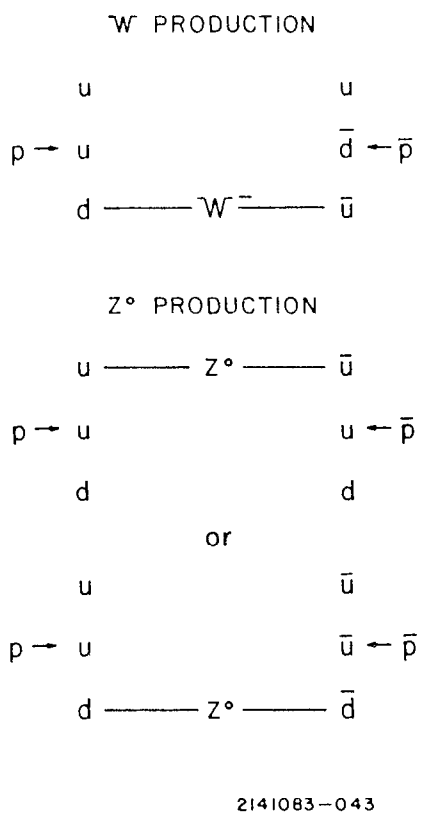


Fig. 3.10. The quark - antiquark production of W and Z bosons.

Fig. 3.11 I have reproduced the published results of UA1 collaboration.[52] Additional data and the results of the UA2 experiment make the result ever more convincing. In the Standard Model one expects[54] $M_{Z^0} = 94 \pm 2.5$ GeV in good agreement with data.

The detection of $W \to e\nu$ slightly more complicated.[55] The W's are produced approximately at rest and then decay as shown in Fig. 3.12. One therefore expects electrons with large transverse energy (E_T) in coincidence with an equal amount of missing E_T taken away by the neutrino. In Fig. 3.13 I have plotted these two variables as measured by the UA1 group.[56] The correlation is impressive. From the electron E_T distribution one can extract a mass which is in reasonable agreement with the Standard Model prediction[54] of $M_W = 83 \pm 3.0$ GeV.

The discovery of the W and Z at the "right" masses represents a beautiful confirmation of the SU(2) x U(1) electroweak theory (and makes 1000 future experimenters at LEP breathe a sigh of relief!). In the future one will obviously look for deviations from the Standard Model using the W's and Z's as tools. For example supersymmetric particles may be produced in W or Z decay and their detection at the collider presents a formidable experimental challenge. The SLC in 1987 and LEP I in 1990 will be copious sources of Z°'s in the super clean e^+e^- environment. These machines and LEP II for W^+W^- production will at least be necessary to look for rare decays modes of the W and Z and precisely measure their masses.

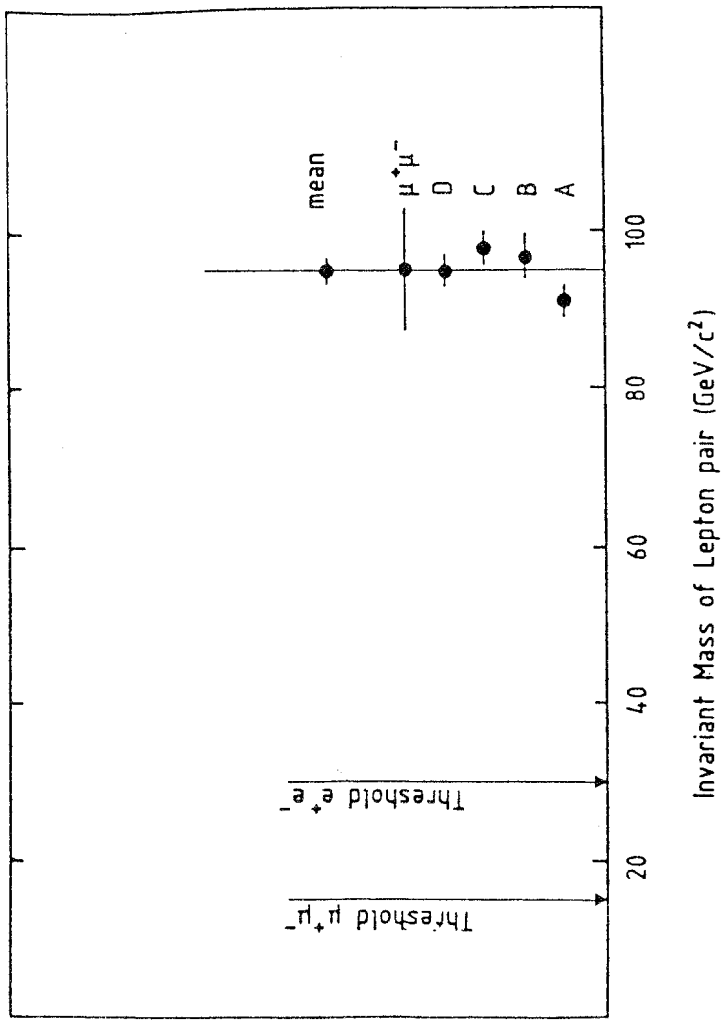


Fig. 3.11. The invariant mass of e^+e^- and $\mu^+\mu^-$ events seen by the UA1 group.

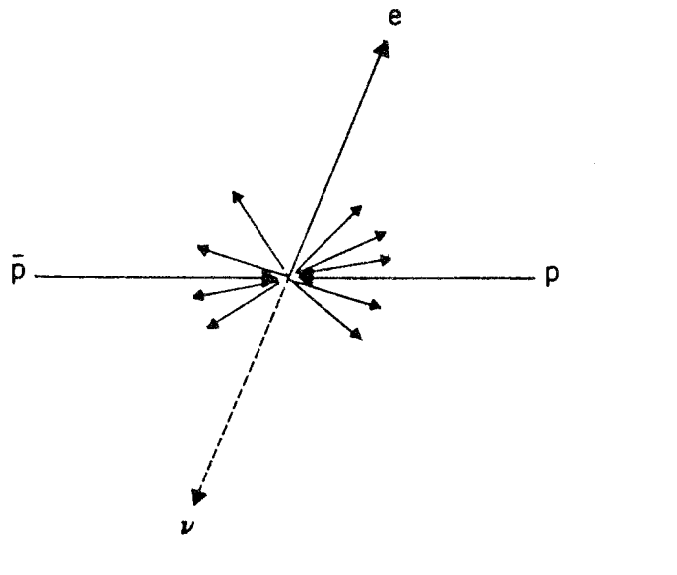


Fig. 3.12. The decay of a W into eν produced at rest in a $\bar{p}p$ collision.

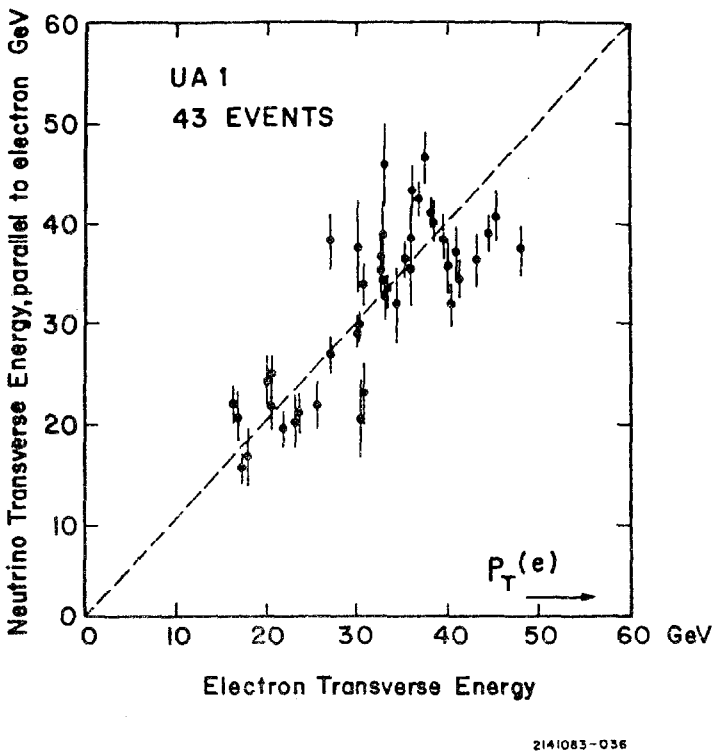


Fig. 3.13. The electron transverse energy (E_T) and missing E_T(neutrino) observed by UA1.

References and Footnotes

1. VEPP-4: A.S. Artamonov et al., Novosibirsk preprint 83-84.

2. DORIS II: D.P. Barber et al., DESY Preprint 83-067.

3. CESR: W.W. Mackay et al., submitted to the 1983 International Photon-Lepton Symposium, Cornell.

4. For a summary of older results see the Particle Data Group listings for 1982 (Phys. Lett 111B). More recent and more accurate values are given in D. Andrews et al., Phys. Rev. Lett. 50, 807 (1983) from the CLEO group and J.E. Horskotte et al., CUSB 83-09.

5. Older e^+e^- measurements are given in Particle Data Book. The τ measurements are described in R. Giles et al., Phys. Rev. Lett. 50, 877 (1983) for the T(1S); and R.S. Galik in his paper presented at the High Energy Physics Meeting at the European Physical Society, Brighton England (CLNS 83/576) for the T(2S). The values are $B_{\ell\tau}(T(1S)) = (3.6 \pm 0.4 \pm 0.5)\%$ (this replaces the value given in R. Giles et al., and $B_{\ell\tau}(T(2S)) = (1.7 \pm 1.5 \pm 0.6)\%$. The CLEO group has obtained $B_{ee}(T(1S)) = (3.0 \pm 0.8)\%$, Mark Ito private communication and internal memo CBX 82-71.

6. J.L. Richardson, Phys. Lett. 82B, 272 (1979).

7. S. Gupta, S. Radford and W. Repko, Phys. Rev. D26, 3305 (1982) and references therein.

8. W. Buchmüller and G. Grunberg and S.-H.H. Tye, Phys. Rev. Lett. 45, 103 (1980); 45 587(E) (1980). W. Buchmüller and and S.-H.H. Tye, Phys. Rev. D24, 132 (1981).

9. R. van Royen and V.F. Weisskopf, Nuoro Cimento 50A, 617 (1967). The QCD corrections given in the text have been calculated in R. Barbieri et al., Phys. Lett., 57B, 455 (1975) and W. Celmaster, Phys. Rev. D19, 1517 (1979).

10. For a recent review of the data see K. Berkelman, Cornell Preprint CLNS-83/564 and M. Tuts. Rapporteur Talk at the 1983 International Photon Lepton Symposium, Cornell. For a pedagogical introduction see E. Bloom in the Proceedings of the 1981 SLAC Summer Institute.

11. For a review of comparisons of charmonium data with models see J. Gaisser in the Moriond Workshop on New Flavors (1982).

12. K. Han et al., Phys. Rev. Lett. 49, 1612 (1982). G. Eigen et al., Phys. Rev. Lett. 49, 1616 (1982). Also see J. Lee-Franzini's talk in these proceedings.

13. CUSB: C. Klopfenstein et al., Phys. Rev. Lett. 51, 160 (1983), and J. Lee-Franzini's talk in these Proceedings.

14. Crystal Ball: Preliminary Results presented by J. Gaisser in these proceedings.

15. CLEO: private communication.

16. ARGUS: Results presented by M. Tuts at the 1983 International Photon Lepton Conference.

17. M.B. Voloshin, Moscow Institute of Theo. and Expt. Physics, Report no. JTEP-21, 1980; R. Bertlmann, CERN TH-3192(1981). See also the talk of M. Shifman in the Proceedings of the 1981 Photon-Lepton Conference, Bonn for background on QCD sum rules and related topics.

18. J. Rosner, Enrico Fermi Institute,Preprint EFI 83/17.

19. E. Eichten and F. Feinberg, Phys. Rev. D23, 2724 (1981).

20. The values obtained by Eichten and Feinberg can be brought into better agreement with the data by changing the value of α_s used in their formula, K. Gottfried, private communication.

21. R. McClary and N. Byers UCLA/82/TEP/12.

22. P. Moxhay and J. Rosner, Enrico Fermi Institute, Preprint EFI 83-15.

23. The calculations are described in detail in Ref. 21. Previous attempts are described in Ref. 11. It is slightly worrying to me that McClary and Byers do so well on charmonium E1 rates but fail miserably on bottomonium fine structure.

24. K. Gottfried, Phys. Rev. Lett. 40, 598 (1978).

25. Y.-P Kuang and T.-M. Yan, Phys. Rev. D24, 2874 (1981).

26. T.-M. Yan, Phys. Rev. D22, 1652 (1980).

27. Older values for $B(\Upsilon(2S) \to \pi^+\pi^- \Upsilon(1S))$ are given in the Particle Data Tables. Newer results were reported at the 1983 Photon-Lepton Conference:
CLEO: 19.1 ± 1.7%
CUSB: 19.4 ± 2.9
ARGUS: 17.9 ± 1.1.

28. The UPSTATE Proposal at CESR - Cal Tech, Max Planck Institute, Stanford, Louisiana State University and Princeton.

29. D. Andrews et al., Phys. Rev. Lett. 49, 357 (1982)

30. See R. Ehrlich's talk in these proceedings.

31. A. Brody et al., Phys. Rev. Lett. 48, 1070 (1982).

32. M.S. Alam et al., (CLEO) Cornell Preprint CLNS 83/570.

33. J. Green et al., (CLEO) Cornell Preprint CLNS 83/566.

34. H. Fritzsch, Phys. Letts. 86B, 164 (1979). T. DeGrand and D. Toussaint, Phys. Letts. 89B, 256 (1980). M. Wise, Phys. Lett. 89B, 229 (1980). J.H. Kühn, S. Nussinov and R. Rückl, Z. Physik C5, 117 (1980). V. Barger et al., Phys. Rev. D24, 2016 (1981).

35. S. Behrends et al., Phys. Rev. Lett. 50, 881 (1983).

36. E. Eichten, Phys. Rev. D22, 1819 (1980).

37. E. Eichten et al., Phys. Rev. D17, 3090 (1978); 21, 203 (1980).

38. Earlier results are given in R.D. Schamberger et al., Phys. Rev. D26, 720 (1982). Also see J. Lee-Franzini's talk in these proceedings for the latest results.

39. W. Bartel et al., Phys. Lett. 114B, 71 (1982).

40. J.P. Leveille in Cornell Preprint CLNS 81/505.

41. CUSB: C. Klopfenstein et al., CUSB 83-03. They obtain $B(B \to e\nu X) = (13.2 \pm 0.8 \pm 1.4)\%$.
CLEO: Earlier results are described in K. Chadwick et al., Phys. Rev. D27, 475 (1983). More recent and unpublished values are $\overline{B(B \to e\nu X)} = (11.9 \pm 0.7 \pm 0.4)\%$ and $B(B \to \mu\nu X) = (10.2 \pm 0.5 \pm 1.0)\%$. These were presented at the 1983 Photon-Lepton Conference.

42. Published values include: MARK II: M.E. Nelson et al., Phys. Rev. Lett. 50, 1542 (1983), MAC: E. Fernandez et al., Phys. Rev. Lett. 50, 2054 (1983), MARK J: B. Adera et al., Phys. Rev. Lett. 51, 443 (1983). A summary appears in the report of S. Stone at the 1983 Photon-Lepton Conference.

43. This hint also assumes that one theorist's calculations are correct.

44. G. Altarelli, et al., Nucl. Phys. B208, 365 (1982).

45. Specific exotic models of b-quark decay have been excluded; A. Chen et al., Phys. Lett., 122B, 317 (1983).

46. M. Peskin and S.-H.H. Tye in Cornell Preprint CLNS 81/485.

47. P. Ginsparg, S. Glashow and M. Wise, Phys. Rev. Lett. 50, 1415 (1983); (E) 51, 1395 (1983).

48. S. Pakvasa and H. Sugarawa, Phys. Rev. D14, 305 (1976).

49. T. Gaisser, F. Halzen and E. Paschos, Phys. Rev. D15, 2572 (1977).

50. D.M. Scott, Getting to the Top in Proton-Antiproton Collider Physics - 1981, AIP No. 85. This is a useful reference on the subject of t production.

51. Taken from Fig. 6 of Ref. 50.

52. G. Arnison et al., Phys. Letts. 126B, 398 (1983).

53. F.E. Paige and S.D. Protopopescu using the ISAJET program, BNL 29777 (1981). Also see Ref. 50.and J. Ellis et al., p. 443 in the Annual Review of Nuclear and Particle Science Vol. 32, 1982.

54. W. Marciano and Z. Parsa in the Proceedings of the DPF Summer Study on Elementary Particle Physics and Future Facilities, Snowmass (1982).

55. UA1: G. Arnison et al., Phys. Letts. 122B, 103 (1983).
UA2: G. Banner et al., Phys. Letts. 122B, 476 (1983).

56. From the talk of T. Hansl Kozanecka in this conference.

CERN TH.3747
October 1983

... AND FOR OUR NEXT SPECTROSCOPY?

John Ellis

SLAC, P.O. Box 4349, Stanford Univ.,
Stanford, CA 94309, USA

and

CERN, Geneva, Switzerland

Lectures presented at the
SLAC Institute on Particle Physics
July 18-29, 1983

© J. Ellis 1983

INTRODUCTION

These lectures offer you suggestions as to the nature of the next particle physics spectroscopy. By this I do not mean yet another quarkonium (top?) spectroscopy as discussed here by Gilchriese. Nor do I mean the spectroscopy of intermediate weak vector bosons, which has probably already been completed. Instead I discuss why theorists believe there must exist some variety of new physics which leads to qualitatively new species of particles with masses $\lesssim$ 1 TeV. What I have in mind are particles associated with the spontaneous breakdown of weak gauge symmetry: $SU(2)_L \times U(1)_Y \to U(1)_{em}$.

This is the part of the theory which is often called the Higgs sector.[1] My first job will be to convince you that there must be something there, and then I review various possibilities for it. The original models[2] had elementary Higgs scalar fields, at least one of which would be a physical particle.[3] We will briefly recall its properties and ways to search for it.[4] Then we will examine the defects of elementary Higgs fields and discuss alternative models for new physics. These include dynamical symmetry breaking, called here technicolour,[5] whose theoretical ideas, spectroscopic predictions and phenomenological problems will all be aired. Then we pass to supersymmetry (Susy)[6] which is currently my personal favourite candidate for new physics in the TeV region.

The basic ideas of Susy are reviewed, along with the necessity for breaking it, together with a discussion of possible mechanisms and their spectroscopic predictions. After a brief summary of cosmological constraints on models with broken Susy, we then pass to possible experimental searches for the anticipated Susy particles, such as squarks, sleptons, gluinos, photinos, shiggses, etc. Even if Susy is eventually untrue to us, she will have expanded our (s) linguistic (s) horizons.

1. THE NEED FOR HIGGS (OR SOMETHING LIKE IT)

Theorists want a quantum field theory to be calculable, so that they can make reliable predictions and get jobs. They can only compute reliably if the (almost[7]) inevitable infinities of quantum field theory can be tamed, i.e. if the theory is renormalizable. (One can also argue that renormalizability is essential if one is to have non-trivial physics at energy scales much less than the Planck mass.) If one calculates using perturbation theory, which is likely to be a fruitful approach for the $SU(2)_L \times U(1)_Y$ interactions whose gauge couplings are weak, then the theory is renormalizable if and only if the lowest order cross-sections have well-behaved high energy behaviour. Consider for example fermion-antifermion elastic scattering $f\bar{f} \to f\bar{f}$. The lowest order approximation to this cross-section in the Fermi 4-fermion interaction theory of Fig. 1a was

$$\sigma(s) = O(G_F^2)s \tag{1}$$

at high energies. If one then uses this to calculate the resulting contribution to $f\bar{f} \to f\bar{f}$ shown in Fig. 1b, one gets

$$\Delta\sigma \propto \left[\int ds' \sigma(s')\right]^2 \tag{2}$$

which is obviously horribly quadratically divergent and unrenormalizable. This particular disaster was avoided in gauge theories[8] by the insertion of a vector boson W exchange as in Fig. 1c, which gave

$$\sigma(s) \sim G_F^2 \left(\frac{m_W^2}{m_W^2 - s}\right)^2 s \sim \frac{\sigma(\alpha)}{s} . \tag{3}$$

This dimensional cross-section:

$$[\sigma] = L^2 \quad \therefore \quad L \sim 1/\sqrt{s} \tag{4}$$

which has no couplings with dimensions of $(\text{mass})^{-2}$ as in Eq. (1), gives only a (potentially) renormalizable logarithmic divergence when substituted into the dispersion integral (2). Unfortunately, all is not yet sweetness and light, since the cross-section for $f\bar{f} \to WW$ obtained from the graphs of Fig. 1d also blows up when the W's are massive as in the weak interactions:

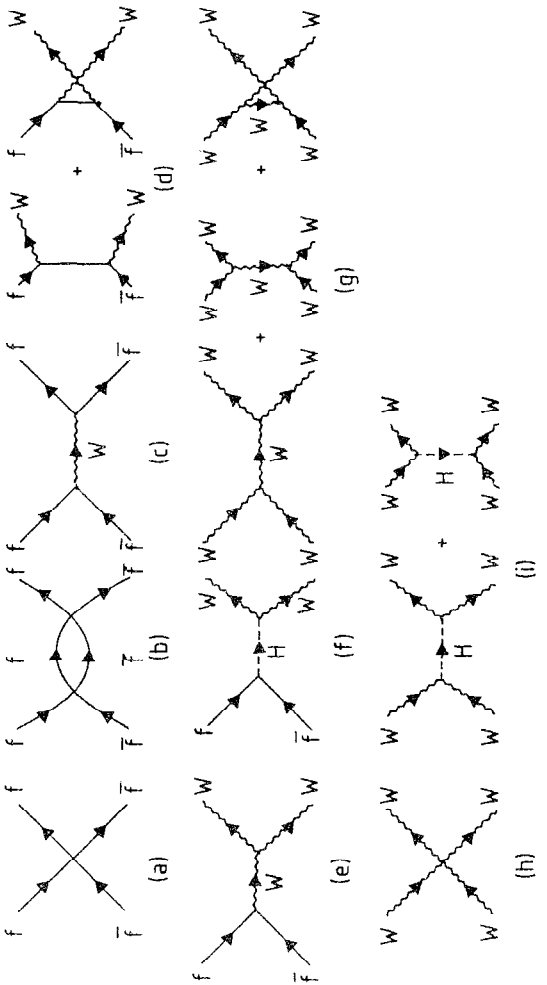


Fig. 1 Perturbative diagrams whose "good" high energy behaviour is required for renormalizability.

$$\sigma(s) \sim \frac{s}{m_W^4} . \tag{5}$$

Gauge theories[8] avoid this problem by endowing the W's with additional trilinear self-interactions, which enable Fig. 1e to be added to Fig. 1d, resulting in

$$\sigma(s) \sim \frac{O(\alpha)}{s} \tag{6}$$

again and another renormalizable contribution to our dispersion integral (2). However, the encouraging result (6) only holds if we neglect the fermion mass m_f: if we take account of it we get left with yet another potentially disastrous divergence in (2). This can only be averted[1] by adding in a scalar boson H whose exchange diagram Fig. 1f cancels out the piece $\alpha\, m_f$ left over from Figs. 1d and 1e. One can go through a similar analysis of WW → WW scattering cross-sections, deducing that the trilinear WWW vertex featured in Figs. 1e and 1g must be supplemented[8] by the quadrilinear WWWW vertex of Fig. 1h. Even this leaves us with a residual blow-up $\alpha\, m_W^4$ which can only be quenched[1] by the exchange of a scalar boson as in Fig. 1i. You might now worry about the diagrams with external scalar particles (Figs. 1j to z and beyond?), and whether this sequence of cancelling diagrams will ever terminate. In fact, it has been shown[1] that there is a unique class of field theories where all the tree-level cross-sections are dimensionally well-behaved (3,4,6): the only solutions are spontaneously broken gauge theories with elementary Higgs scalar fields.

2. PROPERTIES OF HIGGS

The form of the blow-ups ($\alpha\, m_f$, $\alpha\, m_W^4$) in the previous discussion dictates to us the generic form of the Higgs couplings:

$$g_{H\bar{f}f} \propto m_f \; ; \; g_{HWW} \propto m_W^2 . \tag{7a}$$

Since Yukawa couplings in renormalizable field theories are dimensionless, and a $HW_\mu W^\mu$ coupling has the dimension of M^1, both the couplings must contain a factor of (the only available mass = m_W)$^{-1}$. Furthermore, to get the correct power of α (6) from Figs. 1e, 1i, the Higgs couplings must be proportional to the gauge coupling g. Hence our final order of magnitude estimate of the Higgs couplings is

$$g_{H\bar{f}f} = O\left(g\frac{m_f}{m_W}\right) ; \quad g_{HWW} = O(g m_W) . \tag{7b}$$

In point of fact, the minimal Weinberg-Salam model[2] contains a single physical neutral Higgs particle H^0 and no charged Higgs bosons $H^\pm$. The H^0 couplings are completely determined[3]:

$$\left.\begin{aligned} g_{H\bar{f}f} &= \left(\sqrt{2}G_F\right)^{1/2} m_f = \frac{g}{2}\frac{m_f}{m_W} \\ g_{HWW} &= 2\left(\sqrt{2}G_F\right)^{1/2} m_W^2 = g m_W \end{aligned}\right\} \tag{7c}$$

in accord with our dimensional arguments (7a, 7b). These couplings indicate that the H^0 likes to couple to the heaviest particles available:

$$\Gamma(H^0\to\bar{b}b) : \Gamma(H^0\to\bar{c}c) : \Gamma(H^0\to\tau^+\tau^-) : \Gamma(H^0\to s\bar{s}) : \Gamma(H^0\to\mu^+\mu^-) : \Gamma(H^0\to e^+e^-)$$
$$\approx 3m_b^2 : 3m_c^2 : m_\tau^2 : 3m_s^2 : m_\mu^2 : m_e^2 . \tag{8}$$

This means, for example, that an H^0 with mass above 10 GeV (4 GeV) (1 GeV) is likely to have a $\mu^+\mu^-$ branching ratio

$$\frac{m_\mu^2}{3m_b^2}\qquad\left(\frac{m_\mu^2}{3m_c^2+m_\tau^2}\right)\qquad\left(\frac{m_\mu^2}{3m_s^2}\right) \approx 10^{-4}\quad(10^{-3})\quad\left(\tfrac{1}{7}\text{ to }\tfrac{1}{75}\right) \tag{9}$$

where the latter range includes guesses of m_s between 150 MeV and 500 MeV.

The reason for quoting several different values of the H^0 mass is that, in contrast to its well-defined couplings (7c), the mass of the H^0 is almost completely unknown. Nuclear physics, muonic atom X-ray spectra and low energy neutron-nucleus scattering together tell us[3,4,9] that

$$m_{H^0} > O(15)\,\text{MeV} . \tag{10}$$

Radiative corrections[10] and cosmological considerations[11] in the minimal $SU(2)_L \times U(1)_Y$ model suggest that

$$m_{H^0} \gtrsim O(10)\,\text{GeV} \tag{11}$$

but this should be taken with a grain of salt -- the lower mass limit (11) vanishes for a sufficiently high t quark mass (> 100 GeV). Finally, there is a "soft" upper limit on m_{H^0} -- if one wishes[12,13] to avoid a strong Higgs self-coupling, so that perturbation theory remains valid in the Higgs sector, then

$$m_{H^0} < O(1)\,\text{TeV} . \tag{12}$$

It is of course exactly this "soft" assumption of a weak Higgs self-coupling which is relaxed in technicolour models.[5] If the H^0 weighs above 200 GeV and if $m_t < m_W$, the dominant H^0 decays[13] are into W^+W^- and Z^0Z^0. For $2m_t < m_{H^0} < 2m_W$ the dominant H^0 decay mode is into $\bar{t}t$, and into the decay modes (8) for lighter H^0.

3. HUNT THE HIGGS

This must be a broad-band search, since we do not know the mass of the H^0 in the minimal model, and more complicated models contain charged Higgses $H^\pm$ as well as more neutral Higgs bosons. One favoured hunting ground is quarkonium decays.[14] In the minimal model

$$\frac{\Gamma\left({}^3S_1(\bar{q}q)\to H^0+\gamma\right)}{\Gamma\left({}^3S_1(\bar{q}q)\to\gamma^*\to e^+e^-\right)} = \frac{G_F m_q^2}{\sqrt{2}\pi\alpha}\left[1-\frac{m_{H^0}^2}{m_{^3S_1}^2}\right] \tag{13}$$

which is above 10% for $m_q > 20$ GeV, as must be the case for toponium. Thus one could expect

$$B(^3S_1(\bar{t}t) \to H^0 + \gamma) \gtrsim 1\% \qquad (14)$$

unless some unanticipated additional decay mode drowns out $^3S_1(\bar{t}t) \to 3g$ and $\bar{q}q$, $\ell^+\ell^-$. (Some unexpected additional decay modes will be mentioned in this and subsequent sections.)

In view of the $H^0 + \gamma$ decay rate (13) it is interesting to consider the interpretation of the ξ (2.22) recently discovered[15] in radiative J/ψ decays by the Mark III collaboration (see also Ref. 16). The $\xi(2.22)$ has a total width marginally consistent with zero: a Higgs decay width should be unobservably narrow. The formula (13) gives

$$B(^3S_1(\bar{c}c) \to H^0 + \gamma) \approx 2 \times 10^{-5} \quad \text{for } m_{H^0} = 2.22 \text{ GeV} \qquad (15)$$

whereas the experiment[15] observes

$$B(J/\psi \to \xi + \gamma)\, B(\xi \to K\bar{K}) \approx 8 \times 10^{-5} \qquad (16)$$

with perhaps a factor of 2 error. The experimental number (16) is somewhat higher than the prediction (15), particularly if one takes into account the unknown, and possibly small, $\xi \to K\bar{K}$ branching ratio. Furthermore, a mass of 2 GeV is way below the supposed lower limit (11) on m_{H^0}. However, as was already mentioned the limit (11) is reduced if there is a heavy t quark, and the bound (11) does not in any case apply to more complicated models with more Higgs fields. It is also possible in multiple Higgs models to enhance the branching ratio (15) by some numerical factor. A question mark remains over the likely branching ratio of $H^0 \to K\bar{K}$. As seen from (8) we expect such a H^0 to decay predominantly into strange particles, and the only quasi-two-body $s\bar{s}$ decay modes open to ξ decay if it has spin zero are

$$\xi \to K\bar{K},\ K^*\bar{K}^*,\ K\bar{Q} + \bar{K}Q. \qquad (17)$$

Thus it is not inconceivable that the $\xi \to K\bar{K}$ branching ratio may be large. A search for the other decay modes (17) allowed by the scalar Higgs hypothesis, as well as those such as $K\bar{K}^* + \bar{K}K^*$ which are disallowed for a scalar Higgs but allowed for a spin 2 particle, would be helpful in unravelling the identification of the ξ. We also await with bated breath a spin-parity analysis, which is likely to be freer of background problems in the $\xi \to K_S^0 K_S^0$ channel. We see from (9) that the ξ could have an observable branching ratio into $\mu^+\mu^-$ if it were a Higgs. This decay mode has been searched for unsuccessfully,[17] with a resulting upper limit on $B(\xi \to \mu^+\mu^-)/B(\xi \to K\bar{K})$ which is not yet determined though likely to get close to the lower end of the range (9). Things look bad, but are not necessarily fatal for the $\xi = H^0$ hypothesis. Another way to test for this possibility is to look for $\Upsilon \to \xi + \gamma$ decay: from Equation (13) we see that $B(\Upsilon \to H^0 + \gamma)$ is likely to be enhanced over $B(J/\psi \to H^0 + \gamma)$ by a factor $O(m_b^2/m_c^2)$ (modified by possible mixing factors if there is more than one Higgs doublet), whereas $B(\Upsilon \to \text{glueball or } \bar{q}q \text{ meson} + \gamma)$ is likely to be suppressed by $O(m_c^2/m_b^2)$. I would be amazed if the ξ (2.22) turned out to be a Higgs -- nevertheless it is a valuable intellectual exercise to think how one would test or exclude this ludicrous hypothesis.

Another good place to look for the H^0 is in Z^0 decays. The decay $Z^0 \to H^0 + \ell\bar{\ell} \equiv e^+e^-$, $\mu^+\mu^-$ or $\bar{\nu}\nu$ is expected[18] to have a rate:

$$\frac{1}{\Gamma(Z^0 \to \ell\bar{\ell})}\frac{d\Gamma}{dx} = \frac{\alpha}{4\sin^2\theta_W \cos^2\theta_W} \frac{\left[1 - x + \frac{x^2}{12} + \frac{2}{3}\frac{m_{H^0}^2}{m_{Z^0}^2}\right]\left(x^2 - \frac{4m_{H^0}^2}{m_{Z^0}^2}\right)^{1/2}}{\left(x - m_{H^0}^2/m_{Z^0}^2\right)^2} \qquad x \equiv \frac{2E_{H^0}}{m_{Z^0}} \qquad (18)$$

which yields a branching ratio for $Z^0 \to H^0 + (e^+e^- \text{ or } \mu^+\mu^-)$ of order

$$B \sim O(10^{-4}) \text{ for } m_{H^0} = 10 \text{ GeV} \to O(10^{-6}) \text{ for } m_{H^0} = 50 \text{ GeV} \qquad (19)$$

as seen in Fig. 2. It is worth noting that the $\ell\bar{\ell}$ pair tends to have almost as high an invariant mass as is kinematically allowed[19]:

$$m_{\ell\ell} \to m_{Z^0} - m_{H^0} \qquad (20)$$

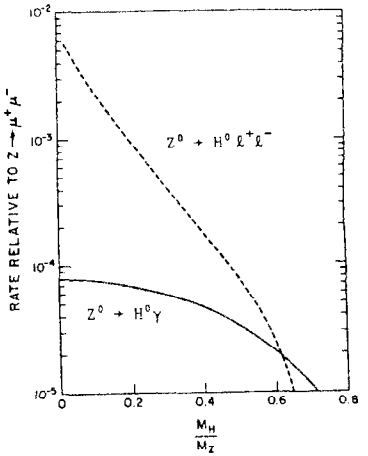


Fig. 2

Branching ratios for $Z^0 \to H^0 + \ell^+\ell^-$ [18] and $Z^0 \to H^0 + \gamma$ [21] relative to $Z^0 \to \ell^+\ell^-$, as a function of m_{H^0}.

as seen in Fig. 3. This feature makes it difficult to interpret the recently observed[20] radiative $Z^0 \to (e^+e^- \text{ or } \mu^+\mu^-) + (\gamma \text{ cluster})$ decays as $Z^0 \to (e^+e^- \text{ or } \mu^+\mu^-) + (H^0 \to \gamma\gamma \text{ or } \pi^0\pi^0)$, since the observed e^+e^- or $\mu^+\mu^-$ invariant masses are between 40 and 60 GeV. For the benefit of SLC and LEP experiments, it should be recalled that

$$B\left(Z^0 \to H^0 + \sum_{e,\mu,\tau} \bar{\nu}\nu\right) \approx 6 \times B\left(Z^0 \to H^0 + \begin{matrix} e^+e^- \\ \text{or} \\ \mu^+\mu^- \end{matrix}\right) \qquad (21)$$

so a good calorimetric experiment may be sensitive to larger branching ratios than (19). Another decay mode of the Z^0 which involves the Higgs is $Z^0 \to H^0 + \gamma$. Unfortunately its branching ratio is expected[21] to be small: $O(10^{-6})$ for $m_{H^0} \times 10$ to 50 GeV as seen in Fig. 2. Going to higher e^+e^- centre-of-mass energies, a promising reaction[3,13,22] is $e^+e^- \to Z^0 + H^0$:

$$\sigma(e^+e^- \to Z^0 + H^0) = \frac{\pi\alpha^2}{24} \frac{K}{Q} \frac{(K^2 + 3m_Z^2)}{(Q^2 - m_Z^2)^2} \frac{(1 - 4\sin^2\theta_w + 8\sin^4\theta_w)}{\sin^2\theta_w \cos^4\theta_w} . \qquad (22)$$

(K is the final state momentum of the Z^0 and H^0, Q is the centre-of-mass energy) which has values:

$$\sigma \gtrsim 0.1\,\sigma_{pt} \quad ; \quad \sigma_{pt} = \frac{4\pi\alpha^2}{3Q^2} \qquad (23)$$

for $m_{H^0} < 100$ GeV at a centre-of-mass energy Q = 200 GeV (see Fig. 4).

Reactions analogous to those discussed above might also enable one to observe Higgses at hadron-hadron colliders. For example, $W \to H^0 + (e\nu)$ can be expected to have a branching ratio similar to (18). This unfortunately means that one will probably need to produce and observe many more W's before the H^0 can be detected, unless it is extremely light. As seen from Fig. 5a, the same is probably true for $hh \to (W^\pm \text{ or } Z^0) + H^0 + X$, the analogue[22] of the reaction (22). Of course it is also possible to produce H^0 without the intermediary of a vector boson, for example by $\bar{q}q \to H^0$ collisions or by $gg \to H^0$ via quark loops.[23] Cross-sections for the latter reaction are shown in Fig. 5b: they are not very encouraging. Possible windows for

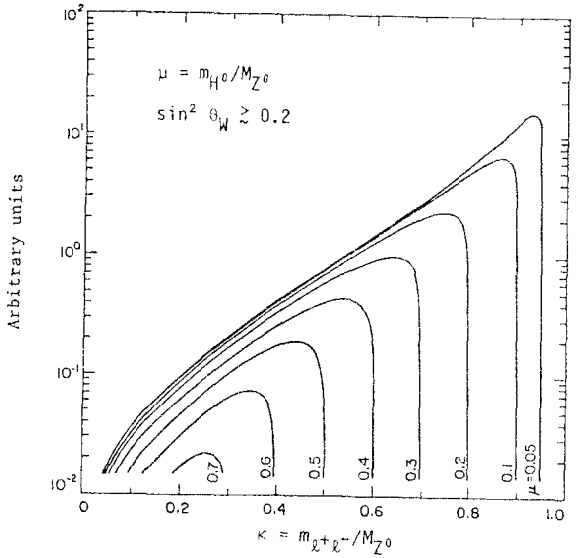


Fig. 3

Shape[19] of the $m_{\ell^+\ell^-}$ distribution in $Z^0 \to H^0 + \ell^+\ell^-$. Note that the distribution is peaked towards $m_{\ell^+\ell^-} \approx m_Z^0 - m_H^0$.

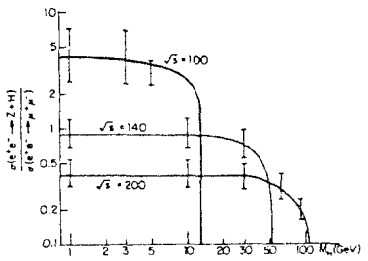


Fig. 4

Cross-section ratios for $e^+e^- \to Z^0 + H^0$ relative to $e^+e^- \to \mu^+\mu^-$, assuming $\sin^2\theta_W = 0.25^{+0.04}_{-0.03}$.[22]

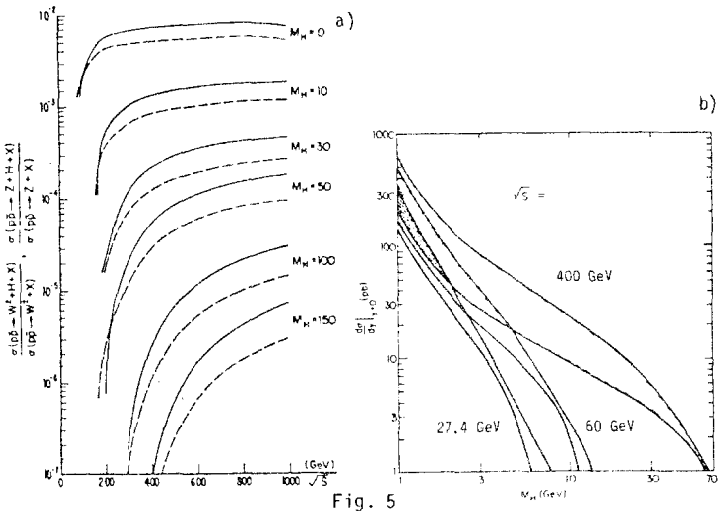


Fig. 5

Cross-sections[23] for (a) hadron + hadron $\to W^\pm + H^0 + X$ and (b) hadron + hadron $\to H^0 + X$ via gluon fusion, for possible ranges of gluon distributions.

$hh \to H^0 + X$ searches might include an H^0 weighing less than about 10 GeV, in which case its $\mu^+\mu^-$ branching ratio might not[24] be too small for it to be detectable at the Tevatron, or H^0 weighing more than 200 GeV, in which case its W^+W^- and Z^0Z^0 decays might be observable at the Desertron (sorry, SSC).

Before leaving elementary Higgses, here are a few words about looking for the charged $H^\pm$ expected in models with more than one Weinberg-Salam Higgs doublet. The obvious reaction to consider is $e^+e^- \to H^+H^-$:

$$\frac{\sigma(e^+e^- \to \gamma^* \to H^+H^-)}{\sigma(e^+e^- \to \gamma^* \to \mu^+\mu^-)} = \frac{1}{4}\beta^3 \qquad (24)$$

where β is the centre-of-mass velocity, implying a slow build-up of the cross-section above threshold. The reaction has a distinctive $\sin^2\theta$ polar angle distribution. While they are very model-dependent, one would expect H^- decay branching ratios:

$$\left.\begin{aligned} &B(H^- \to b\bar{t} : b\bar{c} : s\bar{c} : \tau^-\nu) \\ &\approx O(3m_t^2\cos^2\theta_{KM}) : O(3(m_c^2 \text{ or } m_b^2)\sin^2\theta_{KM}) : O(3m_c^2\cos^2\theta_C) : O(m_\tau^2) \\ &\approx \quad \gtrsim O(500) \quad : \quad \lesssim O(1) \quad : \quad O(3) \quad : \quad 1 . \end{aligned}\right\} \qquad (25)$$

The expressions in (25) will be modified by factors corresponding to ratios of Higgs vacuum expectation values, etc. However, we do expect the factors of 3 from colour, a preference for heavier quarks, and mixing angle factors corresponding to the familiar Cabibbo and Kobayashi-Maskawa angles. In deference to the recent MAC and Mark II results,[25] the $b\bar{c}$ missing angle has been assumed to be very small. We see from Eq. (25) that searches for leptonic decay modes are likely to be useful at PEP and PETRA, but probably not if $m_{H^\pm} > m_t$.[26] Amusing things happen if $m_{H^\pm} < m_t$: the dominant decay mode of the t quark will be

$$\Gamma(t \to b + H^+) \gg \Gamma(t \to bf\bar{f}) . \qquad (26)$$

Indeed, the $t \to b + H^+$ decay rate is so large that conventional toponium physics can be forgotten, since the t quark decays before annihilating with the $\bar{t}$ to give gluonic $H^0 + \gamma$ or $f\bar{f}$ final states:

$$\Gamma\left({}^3S_1(t\bar{t}) \to (H^+b)\bar{t} \;\hookrightarrow\; \bar{t}H^-\right) \sim O(\text{MeV}) \gg \Gamma({}^3S_1(t\bar{t}) \to \text{gluons}) . \qquad (27)$$

Seeing the $H^\pm$ may compensate for not seeing the H^0!

Searches for $H^\pm$ have been unsuccessful, resulting in the excluded ranges of mass shown in Fig. 6 for different values of the $H^\pm \to \tau\nu$ branching ratio.[2,7] Higgses with masses less than 5 GeV are excluded by the success[28] of conventional models for b decay. If the t quark is soon observed, and decays normally, this would exclude $m_{H^\pm} \lesssim m_t - m_b \approx$ $\approx$ 25 GeV(?). Unfortunately, we have even less idea about $m_{H^\pm}$ than we had about m_{H^0} in the minimal Weinberg-Salam model. However, some more precise suggestions will be provided by the technicolour and Susy theories discussed later.

4. THE TROUBLE WITH HIGGS

So far we have searched blithely for Higgs bosons without enquiring whether they were theoretically respectable. As it happens, they have skeletons in their technical closets which make them theoretical black sheep who need a supportive family of other particles to help them overcome their fundamental failings. The perturbative unitarity argument[1] of Section 1 told us that we needed at least one scalar particle H with a mass $m_H = O(m_W)$, $\lesssim O(1)$ TeV in any case (12). This is difficult to arrange, since elementary scalar boson masses are notoriously unstable. Hawking and collaborators[29] assure us that elementary scalars propagating (Fig. 7a) through the space-time foam which bubbles up at the Planck scale ($m_P = O(10^{19})$ GeV, $L_P = O(10^{-33})$ cm) due to quantum gravity effects have their masses shifted by

$$\delta m_H^2 = O(m_P^2) = O(10^{19}\text{GeV})^2 . \qquad (28)$$

Even if you are wary of accepting the reality of space-time foam, you may believe in GUTS, in which case[30] interactions between "light"

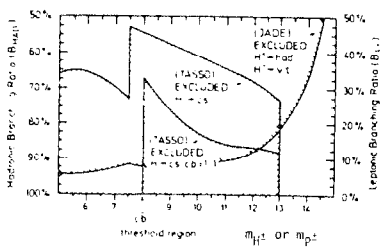


Fig. 6

Zones of $H^\pm$ (or $P^\pm$) masses and branching ratios excluded by PEP and PETRA experiments.[27]

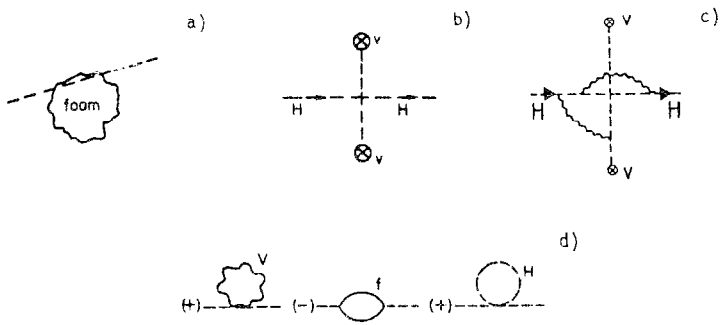


Fig. 7

Diagrams which destabilize the light Higgs boson mass: (a) propagation through space-time foam, (b) interactions with a GUT vacuum, (c) radiative corrections, (d) quadratically divergent loop diagrams.

Higgses H and "heavy" Higgses ϕ which sit in the GUT vacuum (Fig. 7b) with expectation values $O(m_X) \geq O(10^{15})$ GeV will shift the H(mass)^2 by

$$\delta m_H^2 = O(m_X^2) = O(10^{15}\,\text{GeV})^2 . \tag{29}$$

Now you may say that it is possible to cancel out these large contributions to m_H^2 and leave yourself with something which is $O(m_W^2)$. At some stage you would have to answer the questions why and how this apparently miraculous cancellation came about. Even if it had occurred, radiative corrections (Fig. 7c) to the $H^2\phi^2$ GUT diagrams (and to space-time foam?) would disturb the cancellation, yielding residual

$$\delta m_H^2 = O(\alpha^n)(m_X^2 \text{ or } m_P^2) . \tag{30}$$

In addition to these loop diagrams, there are simple quadratically divergent contributions (Fig. 7d) to the H propagator which give

$$\delta m_H^2 = O(\alpha^n)(\Lambda = O(m_X \text{ or } m_P)?)^2 . \tag{31}$$

If we say that no new physics intervenes before m_X or m_P, then we substitute such a value for Λ and reobtain the estimate (30). If we want the residual δm_H^2 to be no larger than $O(m_W^2)$ we must cancel the radiative corrections (30,31) through $O(\alpha^{12-15})$.

Currently there are two favoured strategies for removing these embarrassing contributions to m_H^2. One (dynamical symmetry breaking or technicolour[5]) is to dissolve the Higgses on a scale $\Lambda = O(1)$ TeV by making them composite, thereby avoiding the quadratic divergences (31) and making the troublesome $H^2\phi^2$ diagrams non-existent. Symmetries prevent some of the composite spin-zero fields from acquiring any masses and these are the states which give the $W^\pm$ and Z^0 masses when they are eaten. Other composite scalars P have masses

$$m_P^2 = O(\alpha^n)(\Lambda = O(1)\,\text{TeV})^2 . \tag{32}$$

The alternative strategy is based on the observation that the quadratically divergent boson and fermion diagrams have opposite signs. Therefore if we have a theory whose bosons B and fermions F have identical couplings and similar masses, then we get

$$\delta m_H^2 = O(\alpha^{\prime}) \left| m_B^2 - m_F^2 \right| \qquad (33)$$

and to keep $\delta m_H^2 = O(m_W^2)$ we need

$$\left| m_B^2 - m_F^2 \right| \leq O(1)\ \mathrm{TeV}^2 . \qquad (34)$$

A theory with identical boson and fermion couplings and similar masses has approximate supersymmetry[6] (Susy), and in such a Susy theory the large radiative corrections (30) to $H^2\phi^2$ interactions also vanish.[31]

The remaining sections of these lectures explore these technicolour and Susy alternatives.

5. THE TECHNICOLOUR ALTERNATIVE

In the minimal Weinberg-Salam model with one complex Higgs doublet (ϕ^+,ϕ^0) and its complex conjugate $(\bar{\phi}^0, -\phi^-)$ there is spontaneous symmetry breakdown with

$$\langle 0|\phi^0|0\rangle = \frac{v}{\sqrt{2}} = \langle 0|\bar{\phi}^0|0\rangle \ : \ m_W = g\frac{v}{2} . \qquad (35)$$

Three of the four spin-zero fields are massless:

$$\left(\phi^+,\ \tfrac{1}{\sqrt{2}i}(\phi^0-\bar{\phi}^0),\ \phi^-\right) \Rightarrow \left(W^+, Z^0, W^-\right) \qquad (36)$$

eaten by the $W^\pm$ and Z^0, while there is one massive physical neutral boson

$$H^0 = \frac{1}{\sqrt{2}}\left(\phi^0 + \bar{\phi}^0\right) \qquad (37)$$

whose phenomenology we discussed in Section 3. The manner in which the $W^\pm$ acquire their masses can be visualized in Fig. 8. The $\phi^\pm$ has coupling of magnitude $(gv/2)q^\mu$ to the $W^\pm$, spawning a geometric series of diagrams modifying the $W^\pm$ propagator:

$$\frac{1}{q^2} + \frac{1}{q^2}\left(\frac{gv}{2}\right)q^\mu\frac{1}{q^2}\left(\frac{gv}{2}\right)q_\mu\frac{1}{q^2} + \left(\frac{gv}{2}\right)^4\left(\frac{1}{q^2}\right)^3 + \cdots$$
$$= \frac{1}{q^2 - m_W^2} \quad : \quad m_W = g\frac{v}{2} . \qquad (38)$$

Technicolour theories replace the massless $\phi^\pm$, ϕ^0 by technipions $\pi_T^\pm, \pi_T^0$ which are bound states of new technifermions $F,\bar{F}$: the $\pi_T^\pm, \pi_T^0$ are massless because the F's aresupposed to be massless. The F and $\bar{F}$ are bound by new interactions which become strong and confine technifermions on distance scales O(1/1 TeV). The technipions π_T are coupled to the $W^\pm$ by an analogue of the conventional π decay constant f_{π_T}:

$$\langle 0|W^\mu(q)|\pi_T\rangle = igf_{\pi_T}q^\mu \qquad (39)$$

which usurps the role of gv/2 in Eq. (38). The magnitude of f_{π_T} is related to the scale Λ_T of dynamical symmetry breaking:

$$\langle 0|(\bar{F}_L F_R)|0\rangle = O(\Lambda_T^3) \ : \ m_W = gf_{\pi_T} \ : \ f_{\pi_T} = O(\Lambda_T) . \qquad (40)$$

Thus we have the Higgs-Technicolour translation dictionary shown in Table 1.

So far we have discussed every line of Table 1 except the bottom one: where do the quarks and leptons acquire their masses? In models with elementary Higgs fields this is simply done by Yukawa couplings (Fig. 9a)

$$g_{Hff} = m_f/v . \qquad (41)$$

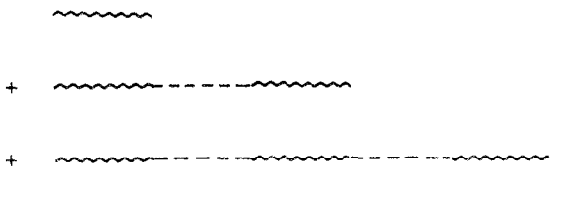
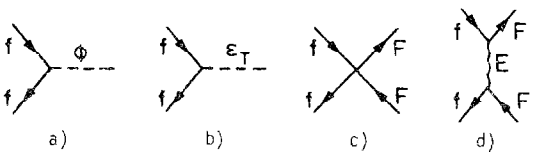


Fig. 8

Geometric series of diagrams showing how a W(~~~) coupling to a massless spin-zero boson (-----) can give the W a mass.



a) b) c) d)

Fig. 9

(a) The elementary Higgs-fermion coupling becomes (b) a composite ε_T-fermion coupling in technicolour theories, which requires (c) the introduction of a four-fermion vertex generated (d) by heavy ETC boson exchanges.

Table 1

Higgs → Technicolour Dictionary

$\langle 0\|(\bar{F}_L F_R)\|0\rangle = O(\Lambda_T^3) \neq 0$	$\langle 0\|\phi^0\|0\rangle = v/\sqrt{2} \neq 0$
Goldstones $\pi_T^{\pm,0}$	eaten Higgses $\phi^{\pm}$, $\frac{1}{i\sqrt{2}}(\phi^0 - \bar{\phi}^0)$
$x = iq_\mu g f_{\pi_T}$	$x = iq_\mu g v/2$
$m_W^2 = g^2 f_{\pi_T}^2$	$m_W^2 = g^2 v^2/4$
Technianalogue of ε(~~700 1000 1300~~ ...) meson	physical Higgs H^0
Techni η and other technihadrons	0
New strong interactions on scale of 1 TeV	0
Extended Technicolour?	fermion masses $m_f = g_{H\bar{f}f} v$

The technianalogues of Fig. 9b require the introduction of a four-fermion vertex (Fig. 9c) which is unrenormalizable, just like the vertex in Fig. 1a. Let us adopt the same trick[32] that was applied there, namely interpolating the exchange of a massive vector boson E which couples the ordinary fermion f to the technifermion F as in Fig. 9d. The E's are the so-called extended technicolour (ETC) bosons. Their exchange gives rise to fermion masses:

$$m_f = \frac{\langle 0|(\bar{F}_L F_R)|0\rangle}{m_E^2} = \frac{O(\Lambda_T^3)}{m_E^2} \quad . \tag{42}$$

Our saviour formula (42) immediately poses a new dilemma: how do we

get different masses for the different quarks and leptons? The simplest answer is postulate a number of different ETC bosons, at least one per generation, with different masses that can be estimated from (42):

$$m_E^2 = \frac{\langle 0|(\bar{F}_L F_R)|0\rangle}{m_f} . \qquad (43)$$

After fixing $\langle 0|\bar{F}_L F_R|0\rangle$ by getting the right mass (40) for the W, one can use representative fermion masses to arrive at the estimates[33] of m_E^2 in Table 2. We see that the third generation ETC boson masses may not be very far away!

Table 2

Estimated ETC Boson Masses

First generation	Second generation	Third generation
$m_{u,d} \gtrsim 10$ MeV	$m_s \simeq 200$ MeV	$m_b \simeq 5$ GeV
$m^2_{E_{u,d}} \gtrsim 1000$ TeV^2	$m^2_{E_s} \simeq 60$ TeV^2	$m^2_{E_b} \simeq 2\frac{1}{2}$ TeV^2

In the most popular class of ETC models[34] there is a single technigeneration ($U_{R,Y,B}$, $D_{R,Y,B}$, E, N) whose first seven members are responsible for the masses of charge $+^2/_3$, charge $-^1/_3$ quarks and charge -1 leptons respectively. The 8 types of technifermion F, when bound to their 8 techni-antifermions $\bar{F}$, yield 64 technipions in an SU(8) adjoint 63 and a singlet. Of these, 3 members of the 63 are strictly massless and are eaten by the $W^\pm$ and Z^0, while another, the symmetric SU(8) singlet combination

$$\eta'_T \equiv \frac{1}{2\sqrt{2}}\left(\sum_{C=R,Y,B}\left(\bar{U}_C\gamma_5 U_C + \bar{D}_C\gamma_5 D_C\right) + \bar{E}\gamma_5 E + \bar{N}\gamma_5 N\right) \qquad (44)$$

acquires a mass $O(\Lambda_T) \equiv O(1)$ TeV from an anomalous source similar to that responsible for the conventional SU(3) singlet η' mass. The remaining 60 technipions have masses which are generated by higher order effects and all smaller than 1 TeV: estimates[34] and their sources are presented in the top part of Table 3. Included in the bottom half are various technianalogues of other familiar hadrons, such as the vector ρ_T and ω_T, the tensor f_T, and the technibaryons B_T. The only parameter appearing in Table 3 is N_T, the number of technicolours which is often but not exclusively taken to be 4.

Table 3

Techniparticle Masses

Particle (Multiplicity)		Description	Mass estimate	Source
$P^{0,3}$	(2)	e.m. neutral colour singlets	$\lesssim 3$ GeV?	Interactions beyond ETC
$P^\pm$	(2)	e.m. charged colour singlets	5 to 15 GeV	SU(2) × U(1) rad. corr
P_{LQ}	(24)	colour triplet leptoquarks	150 GeV	SU(3) etc. rad. corr
$P_8^{0,3,\pm}$	(32)	colour octets	250 GeV	SU(3) etc. rad. corr
η'_T	(1)	e.m. neutral colour singlet	$(\frac{4}{N_T})$ × 970 GeV	techni-U(1) anomaly
ρ_T, ω_T	(64)	vector mesons	$\sqrt{4/N_T}$ × 900 GeV	techni-strong interactions
f_{T_1} etc.	(64) etc.	tensor mesons	$\sqrt{4/N_T}$ × 1500 GeV	"
B_T		technibaryons containing N_T technifermions	$\sqrt{N_T/4}$ × 1500 GeV	"

Technimeson masses scale $\propto 1/\sqrt{N_T}$, whereas technibaryons contain N_T technifermions in a technicolour structure $\varepsilon_{i_1 \cdots i_{N_T}} F_{i_1} \cdots F_{i_{N_T}}$, and therefore have masses scaling $\propto \sqrt{N_T}$. In addition to the particles listed, theories whose technifermions sit in a real representation of the technicolour group also contain[34] (FF) mesons, including ditechniquarks ($m_{P(QQ)_6} \sim 260$ GeV, $m_{P(QQ)_{\bar{3}}} \sim 160$ GeV), ditechnileptons (LL) and additional technileptoquarks ($m_{P_{LQ}} \sim 160$ GeV).

6. THE TROUBLE WITH TECHNICOLOUR

The basic idea[5] of dynamical symmetry breaking as a means to generate $W^\pm$ and Z^0 masses is very simple and elegant. It is the regrettable need[32] to extend technicolour so as to generate fermion masses that creates two categories of problems. One embarrassment is provided by the light colourless technipions in Table 3, particularly the charged $P^\pm$. Radiative corrections in the $SU(2)_L \times U(1)_Y$ theory give[34] them masses O(5 to 15) GeV, and ETC interactions of the type discussed earlier do not[35] add to their masses. The dominant decay modes of the $P^\pm$ are expected to resemble those of light $H^\pm$ (25): $b\bar{c}$, $\bar{c}s$, $\tau\nu$, and the unsuccessful PEP and PETRA searches of Fig. 6 therefore exclude their existence with masses up to O(15) GeV (and t decays could rule out $m_{P^\pm} \lesssim$ O(25) GeV). Yet more new interactions beyond the ETC interactions of the type discussed earlier must be postulated[32,36] in order to give masses to the uncharged and colourless neutral technipions $P^{0,3}$ (weak isosinglet and isotriplet respectively). The simplest form of such interactions is direct quark-lepton transitions of the Pati-Salam[37] type. The upper limit[38] on $K_L^0 \to \mu e$ decay gives a lower limit on the Pati-Salam vector boson masses, which in turns provides[36] an upper limit to the $P^{0,3}$ masses of about 3 GeV, and also prevents them from jacking up the $P^\pm$ masses. Such light $P^{0,3}$ are not yet excluded by experiment,[39] though they should show up soon in radiative J/ψ and Υ decays, and possibly[40] in D or B decays (see Section 7). The troubling abundance of unseen light techipions has motivated some people to consider models with fewer technifermions, namely less than a full generation,[41] but no complete and satisfactory scheme of this type has yet emerged.

Another class of techniproblems is that posed[33] by flavour-changing neutral interactions, of which the most severe are those mediated by gauge bosons accompanying the ETC bosons as seen in Fig. 10a. They give large $|\Delta S| = 2$ and $|\Delta C| = 2$ interactions of the generic form

$$\frac{(\bar{s}d)^2}{m_E^2} \quad , \quad \frac{(\bar{c}u)^2}{m_E^2} \tag{45}$$

whose magnitude may be estimated using the values of m_E guessed in Table 2. Naive estimates of the contributions of (45) to $|\Delta S| = 2$ and $|\Delta C| = 2$ processes yield[33]

$$\left.\begin{aligned} \Delta m_K &= O(10^3) \\ \Delta m_D &= O(10^2) \\ \mathrm{Im}\,\Delta m_K &= O(10^6) \end{aligned}\right\} \times (\text{experiment}). \tag{46}$$

Attempts to resolve these problems include invoking supersymmetry[42] (see Sections 8 etc.) or dynamical suppressions (perhaps the new interactions are not asymptotically free,[43] and the estimates (46) are subject to suppressions of order $(\Lambda_T/m_E)^p$) or approximate symmetries[44,45] (but difficult to suppress both $|\Delta S| = 2$ and $|\Delta C| = 2$ (46),[44] or leptons are not included in the model[45]) or models with more than one technigeneration[46] (in which case the technipions proliferate still further). None of these "outs" is completely satisfactory, but it is not yet established that no satisfactory technicolour model exists, so we move on to the next section.

7. HUNT FOR TECHNICOLOUR

We start with the lightest technipions in Table 3, namely the $P^{0,3}$. They can be produced in J/ψ or $\Upsilon \to P^{0,3} + \gamma$ decays with branching ratios similar to the neutral Higgs (13), but with a model-dependent numerical factor which is $3^{\pm 1}$ in simple models.[39] The favoured decay signals may be $P^{0,3} \to \mu^+\mu^-$ or hadrons, and upper limits in these channels are not yet low enough to exclude the $P^{0,3}$. The $P^{0,3}$ decay

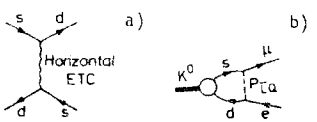


Fig. 10

(a) ETC boson exchange which can contribute to $\Delta S = 2$ processes, and (b) technileptoquark $P_{\bar{L}Q}$ exchange contribution to $K_L^0 \to \mu e$ decay.

into hadrons as pseudoscalars, and hence the ξ (2.22) cannot be identified as P^0 or P^3, though it might have an interpretation in more complicated technicolour models.[47] In some models[39,40] the $P^{0,3}$ might have large enough flavour-changing couplings and small enough masses to be produced in $D \to P^{0,3} + \pi$'s decays with a branching ratio up to 1%, though this is a very long shot. One difference between technipions and Higgs bosons is that the former are never[39,40] produced copiously in association with gauge bosons. We have already discussed past searches for the $P^{\pm}$: future searches should be modelled on these and on the $H^{\pm}$ discussion of Section 3. The $P_{\bar{L}Q}$ (and P_{LQ}) could be searched for in ep collisions at HERA[49,50] and Fig. 11 exhibits some calculated[49] cross-sections. Another way of searching indirectly for the $P_{\bar{L}Q}$ is in $K_L^0 \to \mu e$ decays: crossed channel $P_{\bar{L}Q}$ exchange (Fig. 10b) contributes[35,33] at a rate close to the experimental upper limit[38] on this decay mode if $m_{P_{\bar{L}Q}} \simeq 160$ GeV as expected (Table 3), and a significant reduction in this upper limit would be able to exclude $P_{\bar{L}Q}$ in the expected mass range. On the other hand, discovery of $K_L^0 \to \mu e$ would not confirm the existence of the $P_{\bar{L}Q}$, since there are many other mechanisms for this decay, especially in ETC theories. Searching for colour octet technipions P_8^0 is possible at the Tevatron collider or the Desertron (sorry, SSC), but may not be easy. The P_8^0 is expected to decay into gg or $\bar{t}t$, and is not expected[51] to give a large signal above the hadronic background, as cannot be seen clearly in Fig. 12. The ρ_T and possibly other techni-vector mesons can be searched for at a high energy e^+e^- collider such as the SSLC (Super-SLC) as seen in Fig. 13. It is also possible to search at the SSLC for the lightest extended technicolour boson, expected to be the E_t which may (Table 2) have a mass O(1) TeV: cross-section calculations[53] are shown in Fig. 13.

Despite the theoretical ill-health of technicolour theories, particularly in their ETC guise, they are "not dead yet" experimentally, and you are urged to look for their rich spectroscopy. High energy e^+e^- collisions appear particularly promising places to look. If you do not find a technicolour particle, you may win a consolation prize offered by subsequent sections of these lectures!

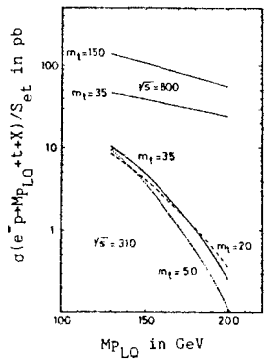


Fig. 11

Production cross-sections[49] for P_{LQ} at high energy ep colliders, to be multiplied by an unknown electron-top mixing (angle)^2 factor S_{et}.

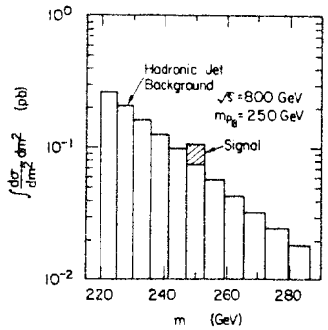


Fig. 12

Signal[51] for the production of colour octet P_8 bosons in hadron-hadron collisions.

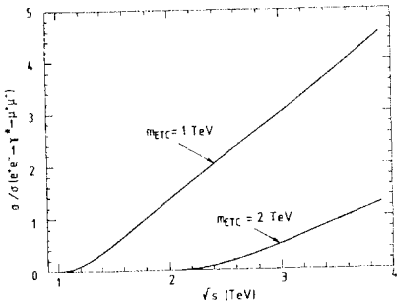


Fig. 13

Cross-section[52] for producing ETC bosons in high energy e^+e^- collisions via the reaction $e^+e^- \to \bar{q}F$ + ETC.

8. SUPERSYMMETRY

This is the second mechanism for curing the trouble with Higgs of Section 4 which cancels the nasty loop diagrams of Fig. 7c,d by invoking pairs of fermions and bosons (34). Susy[6] is a new type of symmetry relating bosons to fermions and vice versa

$$Q|F\rangle = |B\rangle \quad , \quad Q|B\rangle = |F\rangle \tag{47}$$

which is generated by spin ½ charges Q_α. These obey an anticommutation algebra:

$$\left\{ Q^i_\alpha , Q^{\dagger\dot\alpha}_j \right\} = -2(\sigma^\mu)^{\dot\alpha}_\alpha P_\mu \tag{48}$$

where P^μ is the energy-momentum operator. A new index $i = 1,\ldots,N$ has been sneaked into Eq. (48) to count the number of distinct Susy charges: $N = 1$ for a simple Susy theory and $N > 1$ for an extended Susy theory. Only $N \leq 4$ is possible in gauge theories, since each Q^i_α changes helicity by ½ a unit, and only helicities between ±1 are tolerable:

$$\lambda = +1 \;\underset{Q_1}{\rightarrow}\; +\tfrac{1}{2} \;\underset{Q_2}{\rightarrow}\; 0 \;\underset{Q_3}{\rightarrow}\; -\tfrac{1}{2} \;\underset{Q_4}{\rightarrow}\; -1 \quad . \tag{49}$$

However, $N \leq 8$ is possible in theories including gravity (supergravity theories[54]) which tolerate helicities between ±2:

$$\lambda = +2 \;\underset{Q_1}{\rightarrow}\; +\tfrac{3}{2} \;\underset{Q_2}{\rightarrow}\; +1 \;\underset{Q_3}{\rightarrow}\; +\tfrac{1}{2} \;\underset{Q_4}{\rightarrow}\; 0 \;\underset{Q_5}{\rightarrow}\; -\tfrac{1}{2} \;\underset{Q_6}{\rightarrow}\; -1 \;\underset{Q_7}{\rightarrow}\; -\tfrac{3}{2} \;\underset{Q_8}{\rightarrow}\; -2 \quad . \tag{50}$$

In what follows we will concentrate on $N = 1$ Susy, for which the relevant supermultiplets of particles related by Susy are

$$\left.\begin{array}{ll} \text{gauge:} & (1, \tfrac{1}{2}) \\ \text{chiral:} & (\tfrac{1}{2}, 0) \end{array}\right\} \quad . \tag{51}$$

In this case of simple Susy, the Susy charge Q_α carries no internal quantum numbers, and so all particles must share identical quantum numbers (colour, charge, baryon number, lepton number, ...) with their spartners. This means that no known particle can be the spartner of any other, resulting in the rich sparticle sspectroscopy shown in Table 4:

Table 4

Supersymmetric Sspectroscopy

Particle	Spin	Sparticle	Spin	Mass
quark q	½	squark $\tilde q$	0	$\geq$ O(15) GeV
lepton ℓ	½	slepton $\tilde\ell$	0	$\geq$ O(15) GeV
photon γ	1	photino $\tilde\gamma$	½	
gluon g	1	gluino $\tilde g$	½	$\geq$ O(2) GeV
$W^\pm$	1	wino $\tilde W$	½	$\geq$ O(15) GeV
Z^0	1	zino $\tilde Z$	½	
Higgs $H^\pm$	0	shiggs $\tilde H^\pm$	½	$\geq$ O(15) GeV
H^0	0	$\tilde H^0$	½	

Two Higgs doublets $H_{1,2}$ of opposite hypercharges are needed to give masses to charge $+^2/_3$ and to charge $-^1/_3$ quarks and leptons, and to cancel triangle anomalies. The lower limits on the masses of the charged sparticles come from e^+e^- annihilation, mainly unsuccessful searches for $e^+e^- \to \tilde X^+\tilde X^-$. These searches all make some assumption about the sparticle decay which could be evaded;[55] and so all the charged particle limits are somewhat model-dependent. The same is even more true for the gluino, as we shall see later. There are no direct experimental limits on the masses of the uncharged, colourless sparticles. These are expected in general to mix amongst themselves;[55,56,57] as we shall see later, and the only constraints on their properties will come from cosmology.[57,58,59] Omitted from Table 4 is one particle, the graviton of spin 2, and its spartner, the gravitino of spin $^3/_2$, which are difficult to see experimentally!

Before discussing sexperimental searches in more detail, we must first study the couplings and masses of particles in Susy.

9. SUPERSYMMETRIC COUPLINGS AND MASSES

We would expect from the algebraic connections (47) that in an exactly supersymmetric theory the boson and fermion masses would be equal:

$$m_B = m_F \quad \text{cf} \quad m_p = m_n \tag{52}$$

just as the proton and neutron would have identical masses if isospin were an exact symmetry. To see this more formally, we first look at the general form of couplings of chiral supermultiplets

$$\Phi_i \equiv (\chi_i \text{ of spin } \tfrac{1}{2},\ s_i \text{ of spin } 0). \tag{53}$$

It is conventional to work with identical helicities for all the chiral fermions ψ_i: generally they are all taken to be left-handed ψ_L. This means that instead of working with some species of right-handed fermion f_R as a fundamental building-block (e.g. q_R, e_R) we will instead use its conjugate antiparticle field which is left-handed

$$f_R \rightarrow (f^c)_L . \tag{54}$$

The full Lagrangian is of course hermitian and contains both particles and antiparticles of opposite helicities. However, the couplings of supersymmetric and gauge theories take more convenient forms when one standardizes helicities. The non-gauge couplings of chiral smultiplets ϕ_i (53) are fixed[6] by choosing a polynomial $P(\phi)$ called the superpotential which should be cubic if the theory is to be renormalizable:

$$P = a_{ij}\phi_i\phi_j + b_{ijk}\phi_i\phi_j\phi_k . \tag{55}$$

Yukawa interactions involving two fermions are obtained by extracting the fermionic components of two of the ϕ_i and keeping just the spin-zero components of the remainder. From the superpotential $P(\phi)$ (54) we extract

$$\mathcal{L}_Y \equiv (\chi_i \chi_j)\frac{\partial^2 P}{\partial\phi_i \partial\phi_j}\Big|_{\phi_k = s_k} = a_{ij}(\chi_i\chi_j) + b_{ijk}s_k(\chi_i\chi_j) . \tag{56}$$

In each of the terms of (56) the symbol $(\psi_i\psi_j)$ denotes the Lorentz scalar made out of 2 left-handed spinors: in 2-component notation

$$(\chi_i\chi_j) \equiv \epsilon^{\alpha\beta}\chi_{i\alpha}\chi_{j\beta} . \tag{57}$$

The first term on the RHS of Equation (56) is the fermion mass matrix, while the second term is a true Yukawa interaction. Multiple scalar boson interactions obtained[6] from (55) are

$$V_F \equiv \sum_i \left|\frac{\partial P}{\partial\phi_i}\right|^2_{\phi = s} = \left|a_{ij}s_j + b_{ijk}s_j s_k\right|^2 . \tag{58}$$

The square of the first term on the RHS of (58) gives us the spin-zero boson $(\text{mass})^2$ matrix:

$$(m_B^2)_{ij} = a_{ik}a^*_{kj} = (m_F m_F^*)_{ij} \tag{59}$$

which is equal to the fermion $(\text{mass})^2$ matrix as can be seen from Eq. (56). The square of the second term on the RHS of (58) gives us quartic scalar interactions, resembling those to be expected in a Higgs potential.

Next we turn to the Susy gauge interactions. Everyone remembers the fermion gauge interaction

$$g(\bar{\chi}_{L,R}\gamma^\mu T^a_{L,R}\chi_{L,R})A^a_\mu \tag{60}$$

where the left- and right-handed components of the fermions ψ may sit in different representations $T^a_{L,R}$ of the gauge group with generators a. Since N = 1 Susy has no internal quantum numbers, we also expect the

couplings

$$g\left(S^*_{L,R} \overleftrightarrow{\partial^\mu} T^a_{L,R} S_{L,R}\right) A^a_\mu \qquad (61)$$

for the scalar partners s_i of the fermions ψ_i in the chiral smultiplet ϕ_i. There are also gaugino interactions obtained[5] by substituting one of the ψ (or s) and the gauge boson A_μ by their supersymmetric partners:

$$\mathcal{L}_{\tilde{A}} \equiv \sqrt{2}\, g \left(S^*_{L,R} T^a_{L,R}\right)\left(\psi_{L,R} \tilde{A}^a_{L,R}\right) + (\text{hem. conj.}) \qquad (62)$$

where the parenthesised fermions ($\psi\tilde{A}$) have the same meaning as in Eq. (57). Equations (61, 62) enable drawing a distinction between "left-handed" and "right-handed" spin-zero fields, despite their having no intrinsic spin. For example, a left-handed selectron $\tilde{e}_L$ could couple to a neutrino ν_L (sneutrino $\tilde{\nu}_L$) via an $SU(2)_L$ gaugino $\tilde{W}_L$ (gauge boson W), whereas a right-handed selectron e_R (or left-handed conjugate selectron $\tilde{e}^c_L$) would have no $SU(2)_L$ gaugino or gauge interactions. In addition to the expected interactions (60, 61, 62) there are also additional quartic scalar interactions

$$V_D = \frac{g^2}{2} \sum_{a,s} \left| S^*_{L,R} T^a_{L,R} S_{L,R} \right|^2 \qquad (63)$$

which contribute to the full scalar potential $V = V_F + V_D$.

Let us now look at the squark and slepton mass matrices in a supersymmetric theory. The quarks and charged leptons are all Dirac fermions with both left- and right-handed helicities: $q_{L,R}$ and $\ell_{L,R}$, whereas neutrinos have only one helicity: ν_L. We normally work with the conjugate (antiparticle) fields of the right-handed components: $q_R \to q^c_L$, $\ell_R \to \ell^c_L$. The spin-zero partners of the q_L, q^c_L, ℓ_L, ℓ^c_L in chiral supermultiplets are $\tilde{q}_L$, $\tilde{q}^c_L$, $\tilde{\ell}_L$, $\tilde{\ell}^c_L$. The hermitian conjugates of the $\tilde{q}^c_L$ and $\tilde{\ell}^c_L$ we can write as $\tilde{q}_R$ and $\tilde{\ell}_R$, the spartners of the q_R and ℓ_R. The squarks and sleptons can mix in both flavour and "helicity" (L-R) space. For example, the conventional Higgs-fermion Yukawa interactions (7c) are now derived from a superpotential term

$$P(\phi) \ni g_{H\bar{q}q}\; q_L q^c_L H \qquad (64)$$

from which Eq. (58) tells us that we obtain

$$V_F \ni \left|g_{H\bar{q}q}\right|^2 \left[\left|q_L H\right|^2 + \left|\tilde{q}^c_L H\right|^2 + \left|q_L q^c_L\right|^2 \right]. \qquad (65)$$

Using a Higgs vacuum expectation value $\langle 0|H|0\rangle = v$ such that $m_q = g_{H\bar{q}q}\, v$, we obtain the following contributions to the $(\tilde{q}_L, \tilde{q}_R)$ mass matrix:

$$(\tilde{q}^*_L, \tilde{q}^*_R) \begin{pmatrix} m^2_q & \\ & m^2_q \end{pmatrix} \begin{pmatrix} \tilde{q}_L \\ \tilde{q}_R \end{pmatrix} . \qquad (66)$$

Clearly this mass matrix can be diagonalized in flavour space simultaneously with the conventional quark mass matrix, and we find as expected from (52, 59) that $m_{\tilde{q}_{L,R}} = m_q$. Since this is clearly not true experimentally, we have a disaster on our hands unless there are extra contributions to the mass matrix (66). In general there are contributions from the gauge interactions (63), but these vanish under certain circumstances, and do not in any case mitigate the disaster. To rescue the situation we must break Susy.

10. SPARTICLE MASSES IN BROKEN SUSY

To lift the unwelcome degeneracy between $\tilde{f}$ and f, we need Susy breaking $(\text{mass})^2$ terms of the general form:

$$m^2_{\tilde{q}} \left|\tilde{q}\right|^2 + m^2_{\tilde{\ell}} \left|\tilde{\ell}\right|^2 + m^2_{\tilde{\nu}} \left|\tilde{\nu}\right|^2 . \qquad (67)$$

Each of $m^2_{\tilde{q}}$ and $m^2_{\tilde{\ell}}$ can be *a priori* a general matrix in flavour and "helicity" space, but their forms are greatly restricted by phenomenological constraints arising from flavour-changing neutral interactions. To see how these arise, let us first recall how the usual Cabibbo-Kobayashi-Maskawa charged weak mixing angles arise[50] without leading

to flavour-changing neutral interactions. Higgs interactions are believed to yield quark mass matrices $m_q \bar{q}_R q_L$ which can be diagonalized by a pair of unitary transformations $U^q_{L,R}$:

$$\left.\begin{aligned} m_q \bar{q}_R q_L &= m^D_q \bar{q}^D_R q^D_L \;;\; q^D_{L,R} = U^q_{L,R}\, q_{L,R} \\ m^D_q &= U^q_R\, m_q\, U^{q\dagger}_L \;. \end{aligned}\right\} \quad (68)$$

The neutral gauge interactions remain diagonal under the unitary transformations (68):

$$\begin{aligned} \left(\bar{q}_{L,R}\gamma^\mu q_{L,R}\right) A_\mu &= \left(\bar{q}^D_{L,R}\left(U^q_{L,R}U^{\dagger q}_{L,R}\right)\gamma^\mu q^D_{L,R}\right) A_\mu \\ &= \left(\bar{q}^D_{L,R}\,\gamma^\mu\, q^D_{L,R}\right) A_\mu \;. \end{aligned} \quad (69)$$

However, the charged weak interactions are <u>de-diagonalized</u> by the unitary transformations (68) since the charge $^2/_3$ and charge $-^1/_3$ quark mass matrices are different, and require different unitary transformations $U^{u,d}_{L,R}$ for their diagonalization:

$$\left.\begin{aligned} \left(\bar{u}_L \gamma^\mu d_L\right) W_\mu &= \left(\bar{u}^D_L \left(U^u_L U^{\dagger d}_L\right)\gamma^\mu d^D_L\right) W_\mu \\ &\equiv \left(\bar{u}^D_L\, U_{CKM}\, \gamma^\mu d^D_L\right) W_\mu \end{aligned}\right\} \quad (70)$$

where the Cabibbo-Kobayashi-Maskawa matrix $U_{CKM} \neq 1$. What happens now when we try to diagonalize the squark mass matrix (66, 67)? Will we get a new Susy CKM matrix $\tilde{U}_{CKM} \neq U_{CKM}$? Imagine making a series of operations analogous to (68), (69) and (70) on the $\tilde{q}$ partners of the q. The mass matrix would be diagonalized by $\tilde{U}_{L,R}$ analogous to the $U_{L,R}$:

$$\tilde{q}^D_{L,R} \equiv \tilde{U}^q_{L,R}\, \tilde{q}_{L,R} \quad (\widetilde{68})$$

which would keep flavour-diagonal the scalars' neutral gauge interactions (61). However, the gaugino interactions (62) could get messed up:

$$\sqrt{2}\, g\, \bar{\tilde{q}}_{L,R}\left(q_{L,R}\tilde{A}_{L,R}\right) = \sqrt{2}\, g\, \bar{\tilde{q}}^D_{L,R}\left(U^q_{L,R}U^{\dagger q}_{L,R}\right)\left(q^D_{L,R}\tilde{A}_{L,R}\right). \quad (\widetilde{62})$$

The neutral gaugino interactions will no longer be flavour-diagonal unless

$$U^q_{L,R} = \tilde{U}^q_{L,R} \;\Rightarrow\; U_{CKM} = \tilde{U}_{CKM} \;. \quad (71)$$

Before you shrug your shoulders with indifference, look at Fig. 14a. This would give a catastrophically large contribution[61] to the K_1-K_2 mass matrix if we did not arrange for $\tilde{\gamma}$, $\tilde{g}$ and $\tilde{Z}$ exchanges to be flavour-diagonal and thereby decouple the $\tilde{s}$ and $\tilde{d}$ exchanges. A similar argument applies to the u and c couplings on the basis of the D_1-D_2 mass difference. We infer that the identities (71) should hold, in which case the squark $(\text{mass})^2$ matrices must be diagonalizable simultaneously with the quark mass matrix, by the same unitary transformations. This happens automatically if

$$m^2_{\tilde{q}} = \tilde{m}^2\, 1 + C_2 m^2_q + C_1 m_q \quad (72)$$

where 1 is the unit matrix in flavour space, while $\tilde{m}^2$ and C_2 may differ between $\tilde{q}_L$ and $\tilde{q}_R$ and the C_1 term mixes L and R "helicities". Spontaneously broken Susy models lead naturally to (72), which avoids potential problems[62] with the charged $\tilde{W}^\pm$ box diagram of Fig. 14b. If this is to be of comparable magnitude to the conventional GIM-Gaillard-Lee charm box[63] we need

$$\frac{m^2_{\tilde{c}} - m^2_{\tilde{u}}}{\left(m_{\tilde{q}} \text{ or } m_{\tilde{W}}\right)^2} = \frac{O\left(m^2_c - m^2_u\right)}{m^2_W} \times O(\lesssim 10) = O(10^{-3}) \quad (73)$$

which is guaranteed by the Ansatz (72).

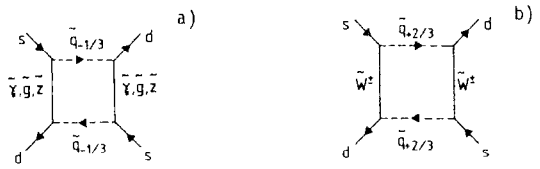


Fig. 14

Box diagrams contributing to $K^0-\bar{K}^0$ mixing in a Susy theory: (a) neutral gaugino exchange, (b) charged gaugino exchange.

Assuming (72) we can write the squark mass matrix in the flavour-diagonalized form (dropping henceforth the superfix D(68,$\widetilde{68}$) for diagonalized quantities):

$$(\bar{\tilde{q}}_L, \bar{\tilde{q}}_R)\begin{pmatrix} \tilde{m}_L^2 + C_{2_L} m_q^2 & C_1 m_q \\ C_1 m_q & \tilde{m}_R^2 + C_{2_R} m_q^2 \end{pmatrix}\begin{pmatrix} \tilde{q}_L \\ \tilde{q}_R \end{pmatrix}. \quad (74)$$

In many spontaneously broken Susy models

$$m_L^2 = L^2\tilde{m}^2\ ,\ m_R^2 = R^2\tilde{m}^2\ ,\ C_1 = A\tilde{m}\ ,\ C_{2_{L,R}} \approx 1 \quad (75)$$

where $\tilde{m}$ = O(20 to 1000)GeV, $L^2 \neq R^2$ in general and A = O(1), so that Eq. (74) becomes

$$(\bar{\tilde{q}}_L, \bar{\tilde{q}}_R)\begin{pmatrix} L^2\tilde{m}^2 + m_q^2 & A\tilde{m}m_q \\ A\tilde{m}m_q & R^2\tilde{m}^2 + m_q^2 \end{pmatrix}\begin{pmatrix} \tilde{q}_L \\ \tilde{q}_R \end{pmatrix}. \quad (76)$$

Included in the general form of the matrix (76) there should be possible terms[64] arising from the gauge interactions (63). The diagonal terms vanish if $\langle 0|H_1^0|0\rangle = \langle 0|H_2^0\rangle$, while the off-diagonal entries vanish in the limit of small H_1–H_2 mixing. These corrections can be subsumed into a redefinition of the parameters L, R and A, and are not discussed further here. The "helicity" diagonalization then requires us to rotate $\tilde{q}_L$ and $\tilde{q}_R$ through an angle θ_{LR}:

$$\tan 2\theta_{LR} = \frac{-2Am_q}{(L^2-R^2)\tilde{m}} \quad (77)$$

giving squark mass eigenstates

$$m^2_{\tilde{q}_{1,R}} = m_q^2 + \left\{ \frac{(L^2+R^2)\tilde{m}^2 \pm \sqrt{(L^2-R^2)^2\tilde{m}^4 + 4A^2m_q^2\tilde{m}^2}}{2} \right\}. \quad (78)$$

The Susy breaking mass scale $\tilde{m} \geq 20$ GeV is so large that L-R mixing (77) may be negligible except for the heavy t quark whose possibly amusing consequences[65] we will meet later.

The mass matrices[55,56,57] for the spin-½ Susy fermions of Table 4 -- gauginos and shiggses -- are also non-trivial. As mentioned above, in order to give masses to all the quarks and leptons and to cancel out fermion triangle anomalies, we need two Higgs chiral smultiplets which are weak isodoublets of equal and opposite hypercharge:

$$\begin{pmatrix} H_1^+ \\ H_1^0 \end{pmatrix}_L \quad \text{and} \quad \begin{pmatrix} H_2^0 \\ H_2^- \end{pmatrix}_L \tag{79}$$

whose fermionic components may mix through mass terms

$$\epsilon \left(\tilde{H}_1^0 \tilde{H}_2^0 - \tilde{H}_1^+ \tilde{H}_2^- \right). \tag{80}$$

These shiggses mix with the gauginos, which may have Susy breaking mass terms

$$M_3 \left(\tilde{g}^\alpha \tilde{g}^\alpha \right) + M_2 \left(\tilde{W}^a \tilde{W}^a \right) + M_1 \left(\tilde{B} \tilde{B} \right) \tag{81}$$

for the SU(3), $SU(2)_L$ and $U(L)_Y$ gauginos respectively. If the standard SU(3) × $SU(2)_L$ × $U(1)_Y$ model is eventually embedded in a (grand) unifying semi-simple non-Abelian group, these Susy breaking gaugino mass terms are in the ratios

$$M_3 : M_2 : M_1 = \alpha_3 : \alpha_2 : \tfrac{5}{3}\alpha' \tag{82}$$

where α_3, α_2 and α' are the conventional gauge coupling strengths: $g_i^2/4\pi$. In most models we expect ϵ and M_2 both to be of order m_W, though either or both might be much smaller.

We can use (80, 81, 82) to infer general forms for the charged and neutral gaugino/shiggs mass matrices. For the charged particles:

$$\left(\tilde{W}^+, \tilde{H}_1^+ \right)_L \begin{pmatrix} M_2 & g_2 v_2 \\ g_2 v_1 & -\epsilon \end{pmatrix} \begin{pmatrix} \tilde{W}^- \\ \tilde{H}_2^- \end{pmatrix}_L \tag{83}$$

where $\langle 0 | H_i | 0 \rangle \equiv v_i$ and the off-diagonal entries in the matrix (83) come from $H\tilde{H}\tilde{W}$ interactions of the form (62). It is interesting to extract from the matrix (83) a couple of limiting cases. In the limit

$$\left.\begin{array}{l} M_2 \to 0 \\ \epsilon \to 0 \end{array}\right\} \begin{array}{l} \text{mass eigenstates} : \text{masses} \\ \left(\tilde{H}_2^-, \tilde{W}^+\right)_L ; \left(\tilde{W}^-, \tilde{H}_1^+\right)_L : g_2 v_2 ; g_2 v_1 \end{array} \tag{84}$$

in which case the $\tilde{H}$-$\tilde{W}$ mixing is complete: we might call the mass eigenstates swiggses. In the limit

$$\left.\begin{array}{l} M_2 \to \infty \\ \text{arb. } \epsilon \end{array}\right\} \begin{array}{l} \text{mass eigenstates} : \text{masses} \\ \left(\tilde{W}^-, \tilde{W}^+\right)_L ; \left(\tilde{H}_2^-, \tilde{H}_1^+\right)_L : M_2 ; \max\left(\epsilon, \frac{g_2^2 v_1 v_2}{M_2}\right) \end{array} \tag{85}$$

in which case the mass eigenstates are almost pure gaugino $\tilde{W}^\pm$ and shiggs $\tilde{H}^\pm$. The neutral mass matrix has a structure analogous to the charged mass matrix (83), but is more complicated since there are 4 neutral fermions ($\tilde{W}^3$, $\tilde{B}$, $\tilde{H}_1^0$, $\tilde{H}_2^0$). Each entry in (83) is replaced by a dainty 2 × 2 submatrix:

$$\left(\tilde{W}^3, \tilde{B}, \tilde{H}_1^0, \tilde{H}_2^0 \right)_L \left(\begin{array}{cc:cc} M_2 & 0 & -\frac{g_2 v_1}{\sqrt{2}} & \frac{g_2 v_2}{\sqrt{2}} \\ 0 & \frac{5}{3}\frac{\alpha'}{\alpha_2} M_2 & \frac{g' v_1}{\sqrt{2}} & -\frac{g' v_2}{\sqrt{2}} \\ \hdashline -\frac{g_2 v_1}{\sqrt{2}} & \frac{g' v_1}{\sqrt{2}} & 0 & \epsilon \\ \frac{g_2 v_2}{\sqrt{2}} & -\frac{g' v_2}{\sqrt{2}} & \epsilon & 0 \end{array}\right) \left(\begin{array}{c} \tilde{W}^3 \\ \tilde{B} \\ \tilde{H}_1^0 \\ \tilde{H}_2^0 \end{array}\right). \tag{86}$$

The 4 Majorana mass eigenstates of the matrix (86) are in general quite complicated and not very perspicuous. However, it is easy to pick out the lightest mass eigenstate χ^0 in a couple of relevant limiting cases:

$$M_2 \to 0 : \quad \tilde{\gamma} : \quad m_{\tilde{\gamma}} \approx \frac{8}{3} \frac{g'^2}{g_2^2 + g'^2} M_2 , \tag{87}$$

$$\epsilon \to 0 : \tilde{H}^0 \equiv \frac{v_2 \tilde{H}_1^0 + v_1 \tilde{H}_2^0}{v} : m_{\tilde{H}^0} \approx \frac{2 v_1 v_2}{v^2} \epsilon . \tag{88}$$

In many models there are actually two light neutral states χ^0, $\chi^{0\prime}$ with masses $< m_{Z^0}$, as well as one charged swiggs $\chi^\pm$ with mass $< m_{W^\pm}$. Mass contours for $m_{\chi^\pm} = 20, 50, 80$ GeV (dotted lines), $m_{\chi^0} = 2, 10$ GeV (solid lines) and $m_{\chi^{0\prime}} = 2, 10$ GeV (dashed lines) are shown in Fig. 15a for the case $v_1 = v_2$ and $\epsilon > 0$.

11. COSMOLOGICAL CONSTRAINTS ON SPARTICLE MASSES

The most stringent present-day constraints on neutral sparticle sspectroscopy may come from cosmological considerations.[58,59] Cosmology is relevant and useful because the lightest supersymmetric particle (LSP) is probably stable. This can be seen immediately from the interactions of Section 9, which always involve pairs of sparticles. Thus they can only be produced in associated pairs, and each sparticle must have another sparticle among its decay products. The only way to avoid this conclusion is to have $\langle 0|\tilde{\nu}|0\rangle \neq 0$, a bizarre possibility generally discounted.[66] Since sparticles should have been abundant in the hot early Universe, we can expect the stable relic LSPs to clutter up our present-day Universe. The most conservative upper limit on their present mass density comes from the overall density of the Universe:

$$\rho < 2 \times 10^{-29} \text{ gm/cc}, \tag{89}$$

if the experimental upper limit on the Hubble deceleration parameter

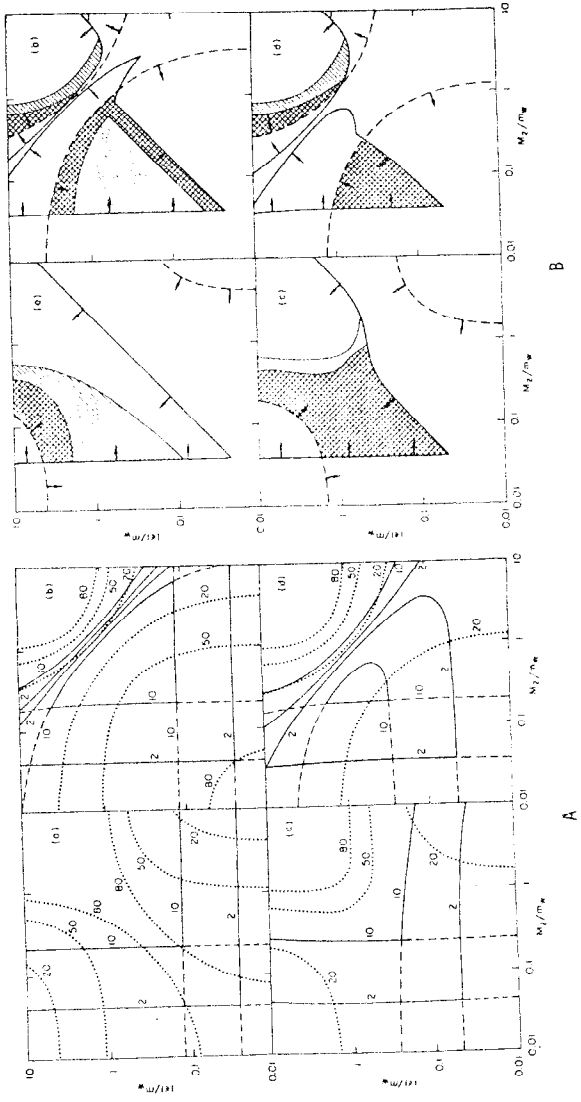


Fig. 15

(A) Charged and neutral mass eigenstates[57] for plausible ranges of $|\epsilon|/\pi_W$ and M_2/m_W, assuming (a) $v_1 = v_2$, $\epsilon > 0$; (b) $v_1 = v_2$, $\epsilon < 0$; (c) $v_1 = 4v_2$, $\epsilon > 0$; (d) $v_1 = 4v_2$, $\epsilon < 0$. Solid lines correspond to the lightest neutral eigenstate χ^0, dashed lines to the next-to-lightest neutral eigenstate $\chi^{0\prime}$, and dotted lines to the lightest charged eigenstate $\chi^\pm$.

(B) Cosmological constraints on the cosmological density of χ^0, and the requirement that $m_{\chi^\pm} > 20$ GeV (the PEP/PETRA limit) are applied to the models of Fig. 15a. The lined (cross-hatched) regions are those where one (two) Susy decay modes of the $W^\pm \to \chi^\pm + \chi^0$ (and $\chi^{0\prime}$) are kinematically allowed.

is not to be exceeded. It can be argued that the LSP might tend to condense with ordinary galaxies, in which case the limit might be strengthened by an order of magnitude corresponding to the upper limit on the missing mass in galaxies, but here we will stick to the more conservative limit (89).

The next question is: which sparticle could be the LSP? Charged sparticles ($\tilde{q}$, $\tilde{W}^{\pm}$, $\tilde{H}^{\pm}$, $\tilde{\ell}^{\pm}$) would have dissipated energy by electromagnetic interactions and condensed into ordinary matter. Any plausible abundance[67] of such heavy stable relics has been excluded[68] by searches for anomalously heavy objects in conventional matter. Therefore we rule out all charged sparticles as candidate LSPs. The same goes for a stable gluino $\tilde{g}$, which probably would have bound strongly to ordinary matter and been detected in the same experiments. The sneutrino $\tilde{\nu}$ is less easy to dismiss as a candidate LSP. There is no cosmological argument against it,[69] and one must turn to theoretical arguments. On the basis of the matrix (76) one might expect the lightest slepton to be a charged $\tilde{\tau}$ with mass

$$m^2_{\tilde{\tau}} \approx \underset{(\text{if } L>R)}{m^2_{\tilde{\nu}} - O(m^2_\tau)} \text{ or } \underset{(\text{if } L=R)}{(m_{\tilde{\nu}} - O(m_\tau))^2} \qquad (90)$$

but this argument is not water-tight (it breaks down if $R^2 >> L^2$). The case of the $\tilde{\nu}$ as the LSP is addressed in Ref. 69: here we turn to other candidates. In most models the gravitino is not the LSP, often being heavier than some $\tilde{q}$, $\tilde{\ell}$ or the photino $\tilde{\gamma}$. However, the gravitino is a potential embarrassment even if it is not the LSP, for its lifetime if it weighs $O(10^2)$ GeV is so long that its presence and decays may disrupt conventional cosmology during or after the era of nucleosynthesis.[70] To avoid this disaster, one may postulate that, some time after the Planck epoch when the Universe's temperature was $O(m_p \approx 10^{19}$ GeV), there was a period of cosmological inflation.[71] This would have had the effect of suppressing the primordial gravitino abundance, and the subsequent regeneration of gravitinos could have been acceptably inefficient so that their abundance would not have incommoded subsequent stages of the Big Bang.[72] The most likely candidates for the LSP are the neutral gaugino/shiggs fermions whose mass matrix we discussed in Section 10. Their annihilation in the early Universe at temperatures at and below their masses must have been quite efficient for the mass density of heavy LSPs

$$\rho \propto \frac{m}{\sigma} \qquad (91)$$

to have been suppressed sufficiently (89) low. This condition is generally satisfied for

$$m_{\tilde{H}^0} \gtrsim \min\left(m_{\tilde{\gamma}}, m_b \text{ or } m_t\right); \; m_{\tilde{\gamma}} \gtrsim O\left(\tfrac{1}{2}\right) \text{GeV} \qquad (92)$$

as seen in Fig. 15b. If either the $\tilde{H}^0$ of the $\tilde{\gamma}$ had been lighter than around 100 eV, it would not have been necessary to suppress their density, and they would have been as acceptable as a conventional massive neutrino. Unfortunately, the possibility of such a light LSP is disfavoured on two grounds. In the case of a light $\tilde{H}^0$ (88) one also finds a light axion-like pseudoscalar Higgs boson in most models, with a mass

$$m_a \approx \sqrt{\tilde{m} \times m_{\tilde{H}^0}} \lesssim O(1 \text{ to } 10) \text{ MeV} \qquad (93)$$

which is in a range excluded by experiment.[59] In the case of a light $\tilde{\gamma}$, one also expects in many models a light gluino[65]:

$$m_{\tilde{g}} \approx \frac{3}{8} \frac{\alpha_3}{\alpha} m_{\tilde{\gamma}} \lesssim O(5) \text{ keV} \qquad (94)$$

which is ruled out by the experimental searches discussed later. We therefore abandon the hypothesis of our LSP lighter than O(100)eV, and are left with the cosmological constraints (92).

12. SLEPTON SEARCHES

Finally we come to actual experimental searches for sparticles. The cleanest mechanism for producing the most distinctive sparticle is

$e^+e^- \to \tilde{\ell}^+\tilde{\ell}^-$. For $e^+e^- \to \tilde{\mu}^+\tilde{\mu}^-$ or $\tilde{\tau}^+\tilde{\tau}^-$ we have

$$\frac{\sigma(e^+e^- \to \gamma^* \to \tilde{\ell}^+\tilde{\ell}^-)}{\sigma(e^+e^- \to \gamma^* \to \mu^+\mu^-)} = \frac{1}{4}\beta^3 \qquad (95)$$

per flavour and per "helicity". The $e^+e^- \to \tilde{e}^+\tilde{e}^-$ cross-section may be larger than (94) thanks to $\tilde{\gamma}$ exchange.[73] Before we get too discouraged by the spin factor of $\frac{1}{4}$ in (95) and the nasty P-wave threshold suppression factor, let us not forget that in most models we expect[62] (cf. the analogue of Eq. (76) for sleptons):

$$\frac{\Delta m^2_{\tilde{\ell}}}{m^2_{\tilde{\ell}}} = O\left(\frac{\Delta m^2_{\tilde{\ell}}}{m^2_W}\right) = O\left(\frac{\Delta m^2_{\tilde{q}}}{m^2_{\tilde{q}}}\right) = O\left(\frac{\Delta m^2_{\tilde{q}}}{m^2_W}\right) = O(10^{-3}) \qquad (96)$$

This tells us that the thresholds for the different slepton flavours of the same "helicity" should be almost degenerate, and hence inseparable since the beam energy spread in e^+e^- storage rings is typically

$$\frac{\Delta E}{E} = O(10^{-3}) . \qquad (97)$$

We expect $\tilde{\ell}^\pm \to \ell^\pm + \tilde{\gamma}$ decays to dominate, giving us final states with O(50)% missing neutral energy and high acoplanarity as in Fig. 16. A more devious[74,75] way of looking for the $\tilde{e}$ is via the reaction $e^+e^- \to \tilde{e}^\pm\tilde{\gamma}e^\mp$:

$$\frac{\sigma(\tilde{e}, m_{\tilde{\gamma}}=0)}{\sigma(e^+e^- \to \gamma^* \to \mu^+\mu^-)} = \frac{\alpha}{12\pi}\ln\left(\frac{E^2_{cm}}{m^2_{\tilde{e}}}\right)\left[\frac{2}{x} + 18 - 54x + 34x^2 + 3(3-3x-4x^2)\ln x - 9x\ln^2 x\right] \qquad (98)$$

where $x = m^2_{\tilde{e}}/E^2_{cm}$. The $\tilde{e}$ is expected to decay subsequently into $e + \tilde{\gamma}$, yielding a final state containing one isolated large angle electron and another at a small angle close to the beam axis, which may pass unseen down the beam-pipe. The process (98) gives us access to $m_{\tilde{e}} \lesssim E_{cm} - m_{\tilde{\gamma}}$, and is therefore more potent than $e^+e^- \to \tilde{e}^+\tilde{e}^-$ if

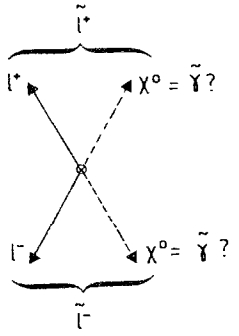


Fig. 16

Acoplanar event signature for $e^+e^- \to \tilde{\ell}^+\tilde{\ell}^-$; $\tilde{\ell}^\pm \to \ell^\pm + \tilde{\gamma}$.

$m_{\tilde{\gamma}} < m_{\tilde{e}}$ as seems plausible.

Another place to search for sleptons is in $W^{\pm}$ decay to $\tilde{\ell}^{\pm} + \tilde{\nu}$ [76,77]; the relative branching ratio

$$\frac{\Gamma(W \to \tilde{e}\tilde{\nu})}{\Gamma(W \to e\nu)} = \frac{1}{2}\left[\left(1 - \frac{m_{\tilde{\nu}}^2 + m_{\tilde{e}}^2}{m_W^2}\right)^2 - \frac{4 m_{\tilde{\nu}}^2 m_{\tilde{e}}^2}{m_W^4}\right]^{3/2} \qquad (99)$$

can be a substantial fraction of that for the known $W \to e\nu$ decay mode, as seen in Fig. 17a. Thus one can imagine looking for $\bar{p}p \to (W \to \tilde{e}\tilde{\nu}) + X$ in the present CERN collider data. The $Z^0 \to \tilde{\nu}\bar{\tilde{\nu}}$ branching ratio may also be substantial[76,78] The cross-section for $\tilde{\nu}$ pair production at $E_{cm}^2 \equiv s$ is[76]

$$\frac{d\sigma}{d\cos\theta} = \frac{\pi\alpha^2 s}{32\sin^4\theta_W}\left(1 - \frac{4m_{\tilde{\nu}}^2}{s}\right)^{3/2}\sin^2\theta \times$$

$$\times\left[\frac{1}{(m_{\tilde{W}}^2 - t)^2} + \left(\frac{(4\sin^2\theta_W - 1)^2 + 1}{8(1-\sin^2\theta_W)^2}\right)\left(\frac{1}{(m_Z^2 - s)^2 + \Gamma_Z^2 m_Z^2}\right)\right. \qquad (100)$$

$$\left. + \left(\frac{2\sin^2\theta_W - 1}{1-\sin^2\theta_W}\right)\left(\frac{1}{m_{\tilde{W}}^2 - t}\right)\left(\frac{m_Z^2 - s}{(m_Z^2 - s)^2 + \Gamma_Z^2 m_Z^2}\right)\right]$$

whose ratio $R(\tilde{\nu}\bar{\tilde{\nu}})$ relative to $e^+e^- \to \gamma^* \to \mu^+\mu^-$ is plotted in Fig. 17b. The decay modes of the $\tilde{\nu}$ may be quite complicated,[76] depending on the relative masses of the $\tilde{\nu}$ and its associated $\tilde{\ell}^{\pm}$. Observable decays of the $\tilde{\nu}$ include

$$\tilde{\nu} \to l u \bar{d}\tilde{g}\ ,\ \nu u\bar{u}\tilde{g}\ ,\ \tilde{e}u\bar{d}\tilde{g}\ ,\ldots \qquad (101)$$

while an invisible decay is $\tilde{\nu} \to \nu + \tilde{\gamma}$. Signatures for $W \to \tilde{e}\tilde{\nu}$ production and decay could include

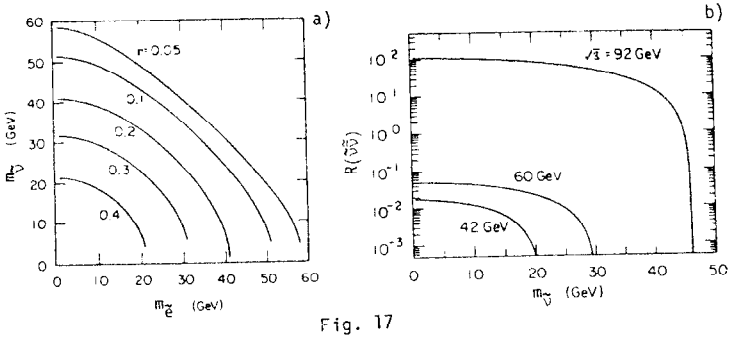


Fig. 17

Rates[76] (a) for $W \to \tilde{e}\tilde{\nu}$ relative to $W \to e\nu$, and (b) for $e^+e^- \to \tilde{\nu}\bar{\tilde{\nu}}$ relative to $e^+e^- \to \mu^+\mu^-$.

$W \to e$ + hadrons + missing transverse energy, $W \to e$ + missing transverse energy . (102)

In the case of $(e^+e^-$ or $\bar{p}p) \to Z^0 \to \tilde{\nu}\bar{\tilde{\nu}}$, one of the sneutinos might decay visibly (101), while the other decays visibly into $\nu\tilde{\gamma}$. Figure 18 shows[76] the fractions of $\tilde{\nu}\bar{\tilde{\nu}}$ events which are (visible),(visible) ≡ C-C or (invisible),(visible)≡ N-C as a function of the $\tilde{e}$ or $\tilde{\nu}$ mass, for a neutrino $\tilde{\nu}$ weighing 20 GeV. We see that the "zen" N-C events may be a substantial fraction of the total number.

A final interesting process for slepton production is deep inelastic ep scattering: $eq \to (\tilde{e}q$ or $\tilde{\nu}q')$. Cross-sections[79] for these processes are shown in Figs. 19a,b respectively: they may be quite substantial, and HERA's centre-of-mass energy of 314 GeV may give us access to $m_{\tilde{e}} + m_{\tilde{q}}$ or $m_{\tilde{\nu}} + m_{\tilde{q}} \lesssim O(200)$GeV.

13. SQUARK SEARCHES

Let us go on to look at other ways of producing squarks. Similarly to slepton pair production (95), we expect

$$\frac{\sigma(e^+e^- \to \gamma^* \to \tilde{q}\bar{\tilde{q}})}{\sigma(e^+e^- \to \gamma^* \to \mu^+\mu^-)} = \frac{3}{4} e_q^2 \beta^3 \qquad (103)$$

per flavour and "helicity" of squark. Once again, it is worth emphasizing that we expect (73,76) the first two generations of squarks to be almost degenerate in mass. The dominant decay modes of the squarks are expected to $q + \tilde{\gamma}$ or $q + \tilde{g}$:

$$\frac{\Gamma(\tilde{q} \to q + \tilde{\gamma})}{\Gamma(\tilde{q} \to q + \tilde{g})} = \frac{3}{4} \frac{\alpha}{\alpha_s} e_q^2 \qquad (104)$$

if neither decay is suppressed by phase space. The $\tilde{q} \to q + \tilde{g}$ mode would be followed by $\tilde{g}$ decay, most likely to $qq\tilde{\gamma}$ via $\tilde{q}$ exchange, though $\tilde{g} \to g + \tilde{\gamma}$ is also possible in some models.[80] We would expect about 50% of the e^+e^- E_{cm} to be in the form of missing neutrals in the

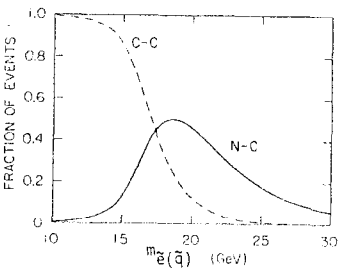


Fig. 18

Branching ratios[76] for $\tilde{\nu}\bar{\tilde{\nu}} \to$ (invisible) + (visible) final states (N-C) and (visible) + (visible) final states (C-C) as a function of $m_{\tilde{e}}$ for fixed $m_{\tilde{\nu}} = 20$ GeV.

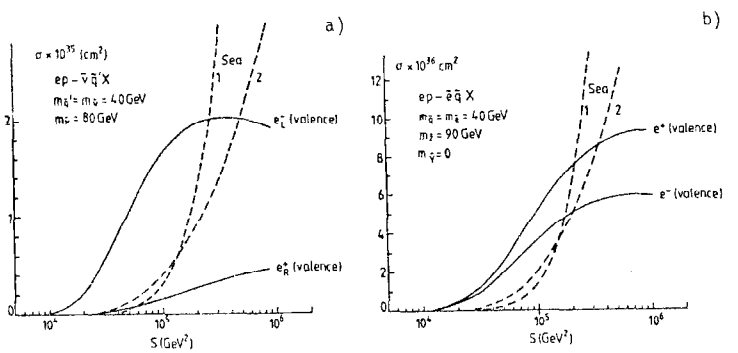


Fig. 19

Cross-sections[79] (a) for $ep \to \tilde{\nu} + \tilde{q}' + X$, (b) for $ep \to \tilde{e} + \tilde{q} + X$.

case of $\tilde{q} \to q + \tilde{\gamma}$ decay, whereas much less energy would be missing after $\tilde{q} \to q + \tilde{g}$ decay. While $q + \tilde{\gamma}$ should dominate if $m_{\tilde{g}} > m_{\tilde{q}}$, the smaller missing energies arising from $q + \tilde{g}$ decay should dominate if $m_{\tilde{g}} < m_{\tilde{q}}$. This complicates the search for $e^+e^- \to \tilde{q}\bar{\tilde{q}}$ via acoplanar 2-jet events with missing energy, as illustrated in Fig. 20.

An obvious place to look for squarks is in high energy hadron collisions: Fig. 21 shows some typical calculations of $hh \to (\tilde{q}\bar{\tilde{q}}) + X$ cross-sections. From these graphs it seems that the CERN $\bar{p}p$ collider with its present integrated luminosity of order 100 nb^{-1} might have already produced squarks weighing up to O(50)GeV. If squarks decay predominantly to $q + \tilde{\gamma}$, there could be an observable signature in 2 jet events whose final state is not coplanar with the beam axes, as seen in Fig. 20: another source of events with missing transverse energy. Unfortunately, this signature would be much less clear if $\tilde{q} \to q + \tilde{g}$ were the dominant decay mode as suggested by Eq. (104).

An amusingly curious possibility[65] is the appearance of Susy in toponium decays. It could well be that m_t and the Susy breaking mass scale $\tilde{m}$ (76) are of comparable magnitudes. In that case, Eq. (78) tells us that the splitting between the two stop mass eigenstates could be $O(m_t$ or $\tilde{m})$, and even that the lightest state $\tilde{t}_1$ could be lighter than the t quark itself!

$$\left(\frac{m_{\tilde{t}_2} - m_{\tilde{t}_1}}{m_t}\right) = O(1) \quad : \quad m_{\tilde{t}_1} < m_t \; ? \qquad (105)$$

a possibility that would be almost excluded by the observation of conventional t quark decays. In this extreme case, the branching ratio for toponium $\to \tilde{t}_1\bar{\tilde{t}}_1$ decays via gluino exchange could be very large:

$$\frac{\Gamma\left({}^3S_1(\bar{t}t) \to \bar{\tilde{t}}_1\tilde{t}_1\right)}{\Gamma\left({}^3S_1(\bar{t}t) \to \gamma^* \to e^+e^-\right)} = \frac{4}{3}\left(\frac{\alpha_s}{\alpha}\right)^2 \frac{\left(1 - m^2_{\tilde{t}_1}/m_t^2\right)^{3/2}}{\left(1 + m^2_{\tilde{g}}/m_t^2 - m^2_{\tilde{t}_1}/m_t^2\right)} . \qquad (106)$$

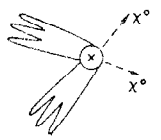


Fig. 20

Acoplanar event signature for e^+e^- (or hh) → pair of strongly interacting Susy particles decaying into hadronic showers + missing transverse energy.

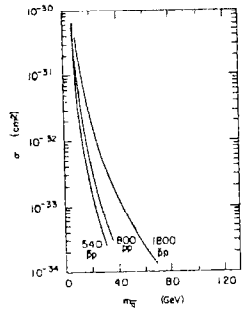


Fig. 21

Cross-sections[81] for $hh \to \tilde{q}\bar{\tilde{q}} + X$ as a function of centre-of-mass energy and $m_{\tilde{q}}$.

Moreover, if $m_t > m_{\tilde{t}} + m_{\tilde{\gamma}}$ there is an even more important decay mode where toponium just falls apart as its constituent quarks decay:

$$\frac{\Gamma(^3S_1(\bar{t}t) \to \bar{t}(t \to \tilde{t}_1 + \tilde{\gamma}) + h.c.)}{\Gamma(^3S_1(\bar{t}t) \to \gamma^* \to e^+e^-)} \approx 300 \times m_t(\mathrm{GeV}). \quad (107)$$

Thus the conventional toponium decay modes such as $H^0 + \gamma$ could be drowned out! A less baroque possibility is that $m_{\tilde{t}} > m_t$, but $m_{\tilde{g}} < m_t$, in which case the decay toponium $\to \tilde{g}\tilde{g}$ is possible if $L^2 \neq R^2$ in Eq. (76), corresponding to C and P violation in the squark mass matrix:

$$\frac{\Gamma(^3S_1(\bar{t}t) \to \tilde{g}\tilde{g})}{\Gamma(^3S_1(\bar{t}t) \to \gamma^* \to e^+e^-)} = \left(\frac{\alpha_3}{\alpha}\right)^2 \left(\frac{L^2 - R^2}{\left(2 - \frac{m_{\tilde{g}}^2}{m_{\tilde{t}}^2}\right)(L+R)^2 - \frac{\tilde{m}^2}{m_t^2}}\right). \quad (108)$$

This ratio could also be O(1) in some models -- it leads us naturally into the subject of the next section.

14. GLUINO SEARCHES

The traditional place to search for gluinos has been hadron-hadron collisions, notably in beam dump experiments.[82] The idea has been to look for the interactions of $\tilde{\gamma}$ emitted in $\tilde{g}$ decay after their pair-production: $hh \to (\tilde{g}\tilde{g}) + X$. Generally the three-body kinematics of $\tilde{g} \to q\bar{q}\tilde{\gamma}$ have been assumed: the limits are worse if two-body $g^2 \to g + \tilde{\gamma}$ decay is assumed.[81] The CHARM and E613 experiments[83] require

$$m_{\tilde{q}} \gtrsim O(2)\ \mathrm{GeV} \quad (109)$$

as seen in Fig. 22, if the squark mass is O(100)GeV. Calculations[81] for heavier gluino pair production in hadron-hadron colliders are shown in Fig. 23. ISR physicists have estimated[84] that they should be sensitive to $m_{\tilde{g}} \lesssim O(5)$GeV in searches for acoplanar jet events, while the CERN $\bar{p}p$ collider should be able to reach $m_{\tilde{g}} = O(50)$GeV. For more details about picking out such events using missing transverse energy, etc., see Ref. 84.

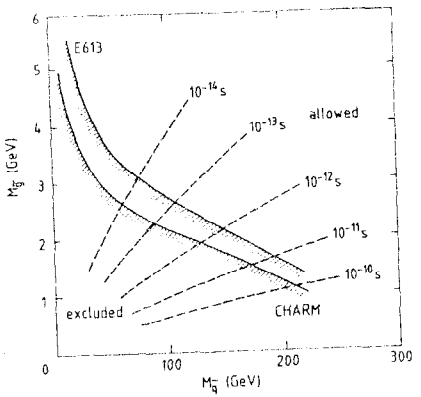


Fig. 22

Regions of $m_{\tilde{g}}$ and $m_{\tilde{q}}$ excluded by beam dump experiments,[83] assuming $\tilde{q} \to q\bar{q} + \tilde{\gamma}$ decay.

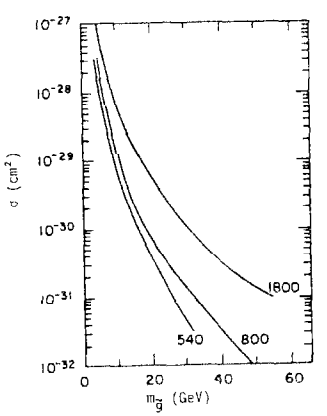


Fig. 23

Cross-sections[81] for $hh \to \tilde{g}\tilde{g} + X$ as a function of centre-of-mass energy and $m_{\tilde{g}}$.

Unfortunately, the prospects for gluino production in ep collisions: $eq \to eq(\tilde{g}\tilde{g})$ are not very good.[85] Even if $m_{\tilde{g}} = 3$ GeV, HERA can only expect $O(10^{-3})$ of its events to contain gluino pairs. Of greater potential interest to people planning hard scattering experiments are the Susy contributions to the nucleon structure functions. The standard Altarelli-Parisi equations can be modified[85,79,86] to include squarks and/or gluinos. The asymptotic momentum fractions carried by q, g, $\tilde{g}$ (if present) and $\tilde{q}$ (if present) are shown in Table 5.

Table 5

Asymptotic Momentum Fractions

	Pure QCD	QCD + $\tilde{g}$	QCD + $\tilde{g}$ + $\tilde{q}$
$q + \bar{q}$	$\frac{3N_q}{3N_q + 16}$ (0.53)	$\frac{3N_q}{3N_q + 20}$ (0.47)	$\frac{3N_q}{5N_q + 20}$ (0.36)
g	$\frac{16}{3N_q + 16}$ (0.47)	$\frac{16}{3N_q + 20}$ (0.42)	$\frac{4}{5N_q + 20}$ (0.32)
$\tilde{g}$	——	$\frac{4}{3N_q + 20}$ (0.11)	$\frac{4}{5N_q + 20}$ (0.08)
$\tilde{q} + \bar{\tilde{q}}$	——	——	$\frac{2N_q}{5N_q + 20}$ (0.24)

(The fractions in parentheses apply if the number of quarks $N_q = 6$). Asymptotically a large fraction of the proton could be supersymmetric -- but the limit is approached quite slowly if only gluinos are present, as seen in Fig. 24.

Gluinos are not produced[85] very copiously in the e^+e^- continuum:

$$\frac{\sigma(e^+e^- \to \bar{q}q(\tilde{g}\tilde{g}))}{\sigma(e^+e \to \bar{q}q)} \simeq \frac{4\alpha_s^2}{\pi} \times f\left(m_{\tilde{g}}^2/s\right) \qquad (110)$$

where the kinematic factor $f(m_{\tilde{q}}^2/s) \simeq 0.1$ to 1 for $E_{cm} = \sqrt{s} = (6 \text{ to } 20) \times m_{\tilde{g}}$. As seen in Fig. 25, a search at the SLC for gluino pairs in Z^0 decays

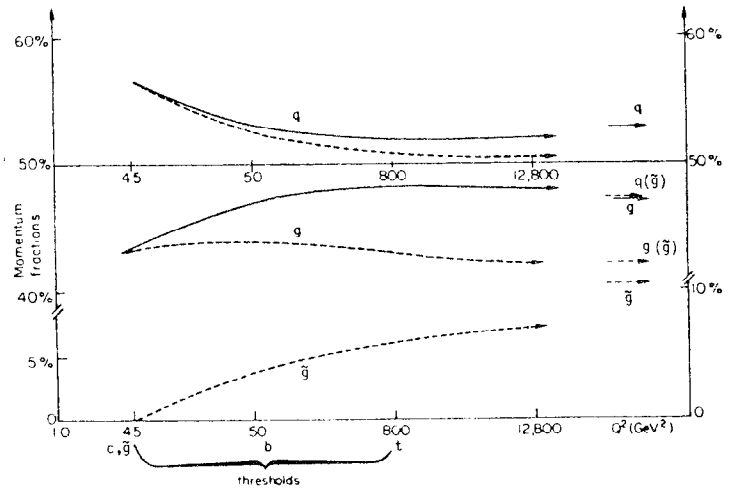


Fig. 24

Momentum fractions carried by different constituents of the proton.[85] Solid lines correspond to the absence of gluinos, dashed lines to $m_{\tilde{g}} = 1.5$ GeV.

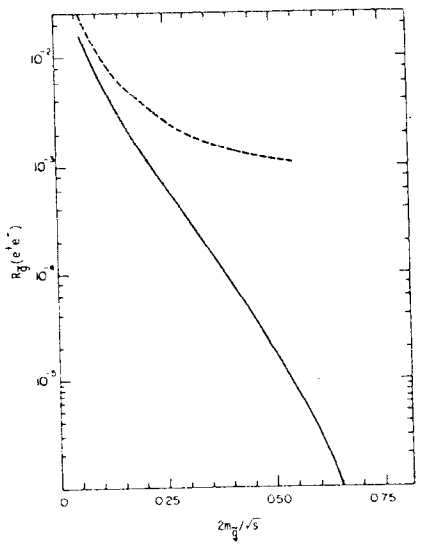


Fig. 25

Cross-section ratio $\sigma(e^+e^- \to q\bar{q}\,\tilde{g}\tilde{g})/\sigma(e^+e^- \to q\bar{q})$ as a function of $m_{\tilde{g}}/\sqrt{s}$.[85]

to the level of 10^{-4} of the total cross-section would be sensitive to $m_{\tilde{g}} \lesssim 15$ GeV. More sensitive places to look for gluinos are quarkonium decays.[85] The orthoquarkonium decay rate

$$\frac{\Gamma(^3S_1(\bar{q}q) \to gg\tilde{g}\tilde{g})}{\Gamma(^3S_1(\bar{q}q) \to ggg)} \gtrsim O(10^{-2}) \quad \text{for } m_{\tilde{g}}/m_q < 0.6 \tag{111}$$

while the P-wave quarkonium states may have even larger branching ratios into decay modes containing gluinos:

$$\frac{\Gamma(^3P_1(\bar{q}q) \to g\tilde{g}\tilde{g})}{\Gamma(^3P_1(\bar{q}q) \to g\bar{q}q)} \approx 1 \quad \text{for } m_{\tilde{g}}/m_q < 0.8. \tag{112}$$

It is worth looking for these decay modes in present Υ data, and the long awaited toponia could be a powerful probe of gluinos, even if the simpler decay (108) does not have a large branching ratio.

15. PHOTINO AND SHIGGS SEARCHES

As was already discussed in Section 11, the lightest sparticles may be the photino and/or a neutral shiggs -- which in general mix as discussed in Section 10. These are the sparticles mostly likely to be kinematically accessible to present experiments, but may also be most difficult to find. For example, $e^+e^- \to \tilde{\gamma}\tilde{\gamma}$ annihilation through selectron $\tilde{e}$ exchange leaves no detectable final state unless the $\tilde{\gamma}$ decays, which is unlikely in the theoretical framework discussed here. However, such events can be tagged[87,88] by a bremsstrahlung photon: $e^+e^- \to (\tilde{\gamma}\tilde{\gamma})\gamma$. The differential cross-section for the process follows the general rule:

$$\frac{d^2\sigma}{dx_\gamma d\cos\theta_\gamma}(e^+e^- \to X\gamma) = \frac{2\alpha}{\pi x_\gamma}\frac{1}{\sin^2\theta_\gamma}\sigma(e^+e^- \to X) \tag{113}$$

for soft γ emission: $x_\gamma \equiv 2E_\gamma/E_{cm} \to 0$. The full cross-section for

X = (massless neutral pair) is

$$\frac{d^2\sigma}{dx_\gamma d\cos\theta_\gamma} = \frac{E_{cm}^2}{x_\gamma \sin^2\theta_\gamma}\left[(1-x_\gamma)\left(1-\frac{x_\gamma}{2}\right)^2 + \frac{x_\gamma^2}{4}(1-x_\gamma)\cos^2\theta_\gamma\right]$$

$$\times\left\{\begin{array}{l} \frac{G_F^2\alpha}{6\pi^2}\left[N_\nu(g_V^2+g_A^2) + 2(g_V+g_A+1)\right] \quad g_V = \frac{1}{2} = -g_A \quad \text{for } X = \sum_{i=1}^{N_\nu} \nu_i\bar{\nu}_i \\ \frac{2}{3}\frac{\alpha^3}{m^4_{\tilde{e}_{R\,or\,L}}} \end{array}\right. \qquad (114)$$

The analogous process involving neutrinos has been proposed by Ma and Okada[89] as a good way to count their number N_ν. Using the cross-section formula (114) we find[88] a search for $e^+e^- \to \gamma$ + nothing down to the level of $\sigma = 10^{-38}$ cm^2 at $\sqrt{s}$ = 30 to 40 GeV would be sensitive to

$$m_{\tilde{\gamma}} \lesssim O(10)\,\text{GeV}\,, \quad m_{\tilde{e}_{R\,or\,L}} \lesssim O(50)\,\text{GeV} \qquad (115)$$

as seen in Fig. 26. We see that this process is sensitive indirectly to values of $m_{\tilde{e}}$ larger than can be reached directly by the reactions $e^+e^- \to \tilde{e}^+\tilde{e}^-$ or $e^+e^- \to e^\pm\tilde{e}^\mp\tilde{\gamma}$. To achieve the sensitivity of $O(10^{-38})$cm^2 one needs an electromagnetic detector with no holes (e.g. PEP21 or the MAC upgrade), so as to be able to veto QED backgrounds such as $e^+e^- \to \gamma\gamma\gamma$ or $e^+e^-\gamma$. Other reactions for $(\tilde{\gamma}\tilde{\gamma})$ pair production seem to have smaller cross-sections than (114). For example, at $\sqrt{s}$ = 30 GeV

$$\sigma(e^+e^- \to e^+e^-\tilde{\gamma}\tilde{\gamma}) \approx 0.5\times 10^{-39}\left(\frac{50\,\text{GeV}}{m_{\tilde{e}_{R\,or\,L}}}\right)^4 . \qquad (116)$$

So far the search for $e^+e^- \to \gamma$ + nothing has not pushed the lower limit on $m_{\tilde{e}}$ much beyond 20 GeV.[90] However, it has given us the best (apart possibly from Z^0 production at the CERN $\bar{p}p$ collider) particle physics limit on the number of neutrino species:

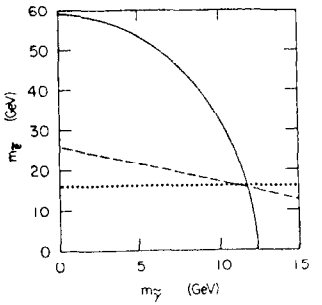


Fig. 26

Regions of $m_{\tilde{e}}$ and $m_{\tilde{\gamma}}$ which can[88] be excluded by $e^+e^- \to \tilde{e}\bar{\tilde{e}}$ searches (dotted line), $e^+e^- \to e\tilde{e}\tilde{\gamma}$ searches (dashed line) and $e^+e^- \to \tilde{\gamma}\tilde{\gamma}\gamma$ searches (solid line).

$$N_\nu \lesssim O(100) . \qquad (117)$$

The search for $\tilde{\gamma}$ may get this number down to the 3 or 4 favoured by cosmologists and GUT model-builders.

The CERN $\bar{p}p$ collider may also yield us supersymmetric decays of the $W^\pm$ into swiggses.[57] In many models the decay mode

$$W^\pm \Rightarrow (\chi^\pm \equiv \tilde{W}^\pm \text{ or } \tilde{H}^\pm) + (\chi^0 \equiv \tilde{\gamma} \text{ or } \tilde{H}^0) \qquad (118)$$

is kinematically accessible, as seen already in Fig. 15b. Since $m_{\chi^\pm} > m_{\chi^0}$ (see Section 11), the decay (118) would then be followed by

$$\chi^\pm \to \chi^0 + (\bar{q}q \text{ or } \bar{l}\nu) . \qquad (119)$$

The rates for the decay (118) and the forward backward asymmetry for the χ^- production relative to the p beam direction are shown in Fig. 27. If $m_{W^\pm} >> m_{\chi^\pm} + m_{\chi^0}$, the best experimental signature could be the one-sided "zen" event structure of Fig. 28, where the hadronic charged $\chi^\pm$ decay products (119) form a jet system on one side of the beam axis, with nothing visible on the other side. If $m_{\chi^\pm}$ is larger, the event could look more like Fig. 20, with two acoplanar jets and missing transverse energy in the final state.

It is also possible[55,91] to produce zen events in e^+e^- annihilation, through the associated production of pairs of the lightest sneutral χ^0 (mainly a $\tilde{\gamma}$?) and of the second lightest sneutral $\chi^{0\prime}$ would subsequently decay:

$$\chi^{0\prime} \to \chi^0 + (\bar{q}q \text{ or } \bar{l}l) \qquad (120)$$

with relative branching ratios which depend on the $\tilde{q}$ and $\tilde{l}$ masses. Figure 29a shows cross-sections for $e^+e^- \to \chi^0\chi^{0\prime}$ at $\sqrt{s}$ = 30 GeV in the

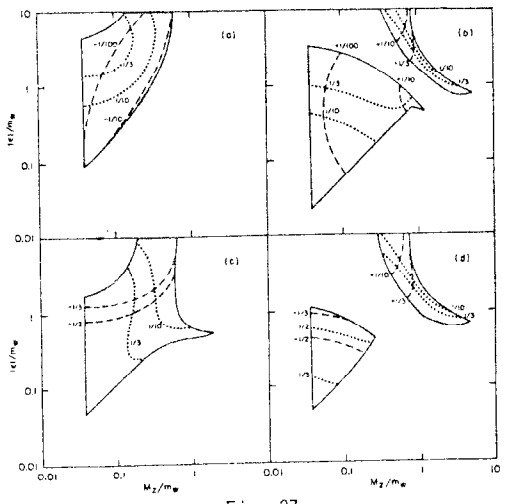


Fig. 27

Rates[57] and forward-backward asymmetries for zen events in the allowed regions of Fig. 15. Dashed lines represent forward-backward asymmetries. The labels (a) to (d) correspond to those in Fig. 15.

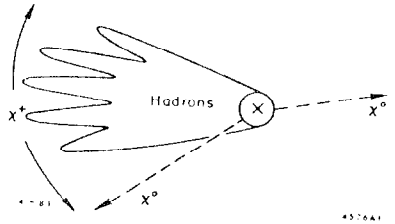
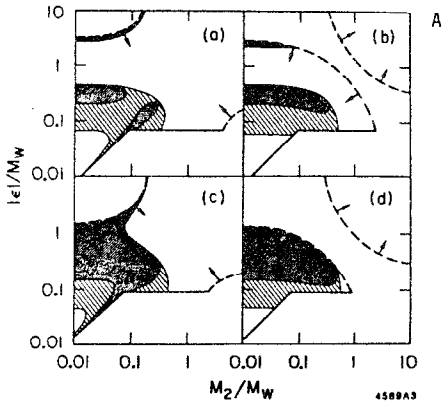


Fig. 28

Fig. 28 : One-jet "zen"[57] event signature in hh collisions.



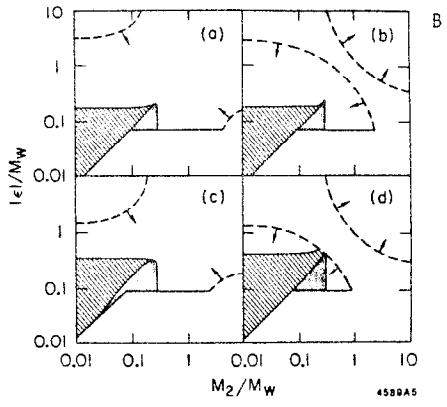


Fig. 29

(A) Cross-sections[91] for associated production events $e^+e^- \to \chi^0\chi^{0\prime}$ when $\sqrt{s}$ = 30 GeV and $m_{\tilde{e}}$ = 20 GeV, subject to PEP/PETRA bounds on $m_{\chi^\pm}$ (indicated by arrows) and the cosmological constraint on the χ^0 mass density assuming all $m_{\tilde{f}}$ = 20 GeV. This and the next cross-section are in units of $\sigma(e^+e^- \to \nu_\mu\bar{\nu}_\mu)$: in the lined regions $1/10\ \sigma(e^+e^- \to \nu_\mu\bar{\nu}_\mu) < \sigma < \sigma(e^+e^- \to \nu_\mu\bar{\nu}_\mu)$, in the dotted regions $\sigma > \sigma(e^+e^- \to \nu_\mu\bar{\nu}_\mu)$.
Cases (a) to (b) correspond to
(a) $\nu_1 = 2\nu_2$, $\varepsilon > 0$; (b) $\nu_1 = 2\nu_2$, $\varepsilon < 0$; (c) $\nu_1 = 4\nu_2$, $\varepsilon > 0$; (d) $\nu_1 = 4\nu_2$, $\varepsilon < 0$.

(B) As for Fig. 29a, but now for $\sigma(e^+e^- \to \chi^{0\prime}\chi^{0\prime})$.

same model previously used to discuss zen events in $p\bar{p}$ collisions. In some cases, even $e^+e^- \to \chi^{0\prime}\chi^{0\prime}$ is kinematically accessible at present energies, yielding the final state event signatures

$$e^+e^- \to (\bar{q}q \text{ or } l\bar{l}) + (\bar{q}q \text{ or } l\bar{l}) + \text{missing energy}. \quad (121)$$

Figure 29b shows cross-sections for $e^+e^- \to \chi^{0\prime}\chi^{0\prime}$ in our familiar model.

16. MESSAGE FROM THEORISTS

Now that experiment has confirmed[20,92] the relevance of gauge theories, one of the next most fundamental physics questions is: what is the mechanism of gauge symmetry breaking? We have seen in these lectures that something like a Higgs particle -- either elementary or composite -- is necessary. Opinions differ as to whether the underlying dynamics involve technicolour[5] or supersymmetry[6] or both or neither. In any case we can be sure that some exciting new spectroscopy awaits us somewhere in the energy range up to 1 TeV. May the force be with you in the search!

REFERENCES

1. J.S. Bell, Nuclear Phys. B30, 427 (1973);
   J.M. Cornwall, D.N. Levin and G. Tiktopoulos, Phys. Rev. Lett. 30, K68 (1973) and Phys. Rev. D10, 1145 (1974).
   C.H. Llewellyn Smith, Phys. Lett.46B, 233 (1973).

2. S. Weinberg, Phys. Rev. Lett. 19, 1264 (1967);
   A. Salam, Proc. 8th Nobel Symposium, Aspenäsgarden, 1968, ed. N. Svartholm (Almqvist and Niksells, Stockholm (1968) p. 367.

3. J. Ellis, M.K. Gaillard and D.V. Nanopoulos, Nucl. Phys. B106, 292 (1976).

4. M.K. Gaillard, Comm. Nucl. Part. Phys. 8, 31 (1978).

5. For a review, see E. Farhi and L. Susskind, Phys. Rep. 74C, 277 (1981).

6. For a review, see P. Fayet and S. Ferava, Phys. Rep. 32C, 249 (1977).

7. S. Mandelstam, Phys. Lett. 121B, 30 (1982).

8. C.N. Yang and R. Mills, Phys. Rev. 96, 191 (1954).

9. S.J. Freedman, J. Napolitano, J. Camp and M. Kroupa, ANL preprint (1983).

10. S. Coleman and E. Weinberg, Phys. Rev. D7, 788 (1973).

11. A.D. Linde, Pis'ma Zh. E.T.P. 23, 73 (1976);
    S. Weinberg, Phys. Rev. Lett. 36, 294 (1976).
    E. Witten, Nucl. Phys. B177, 477 (1981).

12. M. Veltman, Acta Phys. Polon. B8, 475 (1979);
    C.E. Vayonakis, Lett. Nuov. Cim. 17, 383 (1976) and Athens Univ. preprint (1978).

13. B.W. Lee, C. Quigg and H. Thacker, Phys. Rev. D16, 1519 (1977).

14. F. Wilczek, Phys. Rev. Lett. 39, 1304 (1977).

15. Mark III Collaboration, W. Toki, talk at this conference (1983).

16. H. Haber and G.L. Kane, SLAC-PUB-3209 (1983).

17. Mark III Collaboration, private communication (1983).

18. J.D. Bjorken, Proc. 1976 SLAC Summer Institute on Particle Physics, (SLAC-198, 1977).

19. J. Finjord, Physica Scripta 21, 525 (1980).

20. UA1 Collaboration: G. Arnison et al., Phys. Lett. 126B, 398 (1983).
    UA2 Collaboration: P. Bagnaia et al., Phys. Lett. 129B, 130 . (1983).

21. R.N. Cahn, M.S. Chanowitz and N. Fleishon, Phys. Lett. 82B, 113 (1979).

22. S.L. Glashow, D.V. Nanopoulos and A. Yildiz, Phys. Rev. D18, 1724 (1978).

23. H. Georgi, S.L. Glashow, M. Machacek and D.V. Nanopoulos, Phys. Rev. Lett. 40, 692 (1978).

24. J. Ellis, M.K. Gaillard, D.V. Nanopoulos and C.T. Sachrajda, Phys. Lett. 83B, 339 (1979).

25. MAC Collaboration: E. Fernandez et al., Phys. Rev. Lett. 51, 1022 (1983);
    Mark II Collaboration: N.S. Lockyer et al., Phys. Rev. Lett. 51, 1316 (1983).

26. G. Barbiellini et al, DESY preprint 79/27 (1979).

27. TASSO Collaboration: M. Althoff et al., Phys. Lett. 122B, 95 (1983).

28. CLEO Collaboration: A. Chen et al., Phys. Lett. 122B, 317 (1983).

29. S. Hawking, D.N. Page and C.N. Pope, Nucl. Phys. B170 (FS1) 283 (1980).

30. E. Gildener and S. Weinberg, Phys. Rev. D13, 3333 (1976);
    E. Gildener, Phys. Rev. D14, 1667 (1976).

31. J. Wess and B. Zumino, Phys. Lett. 49B, 52 (1974);
    J. Iliopoulos and B. Zumino, Nucl. Phys. B76, 310 (1974);
    S. Ferrara, J. Iliopoulos and B. Zumino, Nucl. Phys. B77, 413 (1974).

32. S. Dimopoulos and L. Susskind, Nucl. Phys. B155, 237 (1979);
    E. Eichten and K. Lane, Phys. Lett. 90B, 125 (1980).

33. S. Dimopoulos and J. Ellis, Nucl. Phys. B182, 505 (1981).

34. S. Dimopoulos, Nucl. Phys. B168, 69 (1980);
    M.F. Peskin, Nucl. Phys. B175, 199 (1980);
    J. Preskill, Nucl. Phys. B177, 21 (1981).
    S. Chadha and M.E. Peskin, Nucl. Phys. B185, 61 (1981) and B187, 541 (1981).

35. P. Binétruy, S. Chadha and P. Sikivie, Phys. Lett. 107B, 425 (1981) and Nucl. Phys. B207, 505 (1982).

36. S. Dimopoulos, S. Raby and P. Sikivie, Nucl. Phys. B182, 77 (1981).

37. J.C. Pati and A. Salam, Phys. Rev. Lett. 31, 661 (1973); Phys. Rev. D8, 1210 (1973) and Phys. Rev. D10, 275 (1979).

38. A.R. Clark et al., Phys. Rev. Lett. 26, 1667 (1970).

39. J. Ellis, M.K. Gaillard, D.V. Nanopoulos and P. Sikivie, Nucl. Phys. B182, 529 (1981).

40. J. Ellis, D.V. Nanopoulos and P. Sikivie, Phys. Lett. 101B, 387 (1981).

41. M.E. Peskin, Private communication (1983).

42. M. Dine, W. Fischler and M. Srednicki, Nucl. Phys. B189, 575 (1981);
S. Dimopoulos and S. Raby, Nucl. Phys. B192, 353 (1981);
A.J. Buras and T. Yanagida, Phys. Lett. 121B, 316 (1983).

43. R. Holdom, Phys. Rev. D24, 157 (1981).

44. J. Ellis and P. Sikivie, Phys. Lett. 104B, 141 (1981).

45. M.A.B. Bég, Phys. Lett. 124B, 403 (1983) and Rockefeller Univ. preprint RU82/B/56 (1983).

46. S. Dimopoulos, H. Georgi and S. Raby, Phys. Lett. 127B, 101 (1983).

47. H. Haber, SLAC-PUB-3193 (1983).

48. L. Arnellos, W.J. Marciano and Z. Parsa, Nucl. Phys. B196, 378 (1982).

49. S. Rudaz and J.A.M. Vermaseren, CERN preprint TH-2961 (1980).

50. S. Chadha, J. Proudfoot and D.H. Saxon, Rutherford Lab. preprint PL-83-071 (1983).

51. G. Girardi, P. Méry and P. Sorba, Nucl. Phys. B195, 410 (1982).

52. M.E. Peskin, Private communication (1983) and in K. Lane, Proc. 1982 Summer Study on Elementary Particle Physics and Future Facilities, ed. R. Donaldson, R. Gustaffon and F. Paige (APS, New York, 1983), p. 222.

53. M.E. Peskin, private communication (1983).

54. D.Z. Freedman, P. Van Nieuwenhuizen and S. Ferrara, Phys. Rev. D13, 3214 (1976);
S. Deser and B. Zumino, Phys. Lett. 61B, 335 (1976).
For a review, see P. Van Nieuwenhuizen, Phys. Rep. 68C, 189 (1981).

55. J.-M. Frère and G.L. Kane, Nucl. Phys. B223, 331 (1983).

56. J. Ellis and G.G. Ross, Phys. Lett. 117B, 397 (1982).

57. J. Ellis, J.S. Hagelin, D.V. Nanopoulos and M. Srednicki, Phys. Lett. 127B, 233 (1983).
Phenomenological Studies of the decay of $W^{\pm}$ and Z^0 into gaugino/shiggs mixtures has also been made by:
V. Barger, R.W. Robinett, W.Y. Keung and R.J.N. Phillips, Univ. of Wisconsin, Preprint MAD/PH/115 (1983);
D.A. Dicus, S. Nandi, W.W. Repko and X. Tata, Univ. of Texas, Preprint DOE-ER-03992-521 (1983);
A. Chamseddine, P. Nath and R. Arnowitt, Northeastern Univ. Preprint NUB-2588 (1983);
M. Mangano, CERN preprint TH-3717 (1983).

58. H. Goldberg, Phys. Rev. Lett. 50, 1419 (1983).

59. J. Ellis, J.S. Hagelin, D.V. Nanopoulos, K.A. Olive and M. Srednicki, SLAC-PUB-3171 (1983).

60. J. Ellis, M.K. Gaillard and D.V. Nanopoulos, Nucl. Phys. B109, 213 (1976).

61. M. Suzuki, U.C. Berkeley preprint UCB-PTH-82/8 (1982).

62. J. Ellis and D.V. Nanopoulos, Phys. Lett. 110B, 44 (1982);
R. Barbieri and R. Gatto, Phys. Lett. 110B, 44 (1982);
B.A. Campbell, Phys. Rev. D27, 1468 (1983);
T. Inami and C.S. Lim, Nucl. Phys. B207, 533 (1982);
J.F. Donoghne, H.P. Nilles and D. Wyler, Phys. Lett. 128B, 55 (1983).
A.B. Lahanas and D.V. Nanopoulos, Phys. Lett. 129B, 46 (1983).

63. M.K. Gaillard and B.W. Lee, Phys. Rev. D10, 897 (1974).

64. K. Inoue, A. Kakuto, H. Komatsu and S. Takeshita, Prog. Theor. Phys. 68, 927 (1982).

65. J. Ellis and S. Rudaz, Phys. Lett. 128B, 248 (1983).

66. See however, L.J. Hall and M. Suzuki, LBL preprint 16150 (1983).

67. S. Wolfram, Phys. Lett. 82B, 65 (1979).

68. P.F. Smith and J.R.J. Bennett, Nucl. Phys. B149, 525 (1979).

69. J.S. Hagelin, G. Kane and S. Raby, private communication (1983).

70. S. Weinberg, Phys. Rev. Lett. 48, 1303 (1982).

71. J. Ellis, A.D. Linde and D.V. Nanopoulos, Phys. Lett. 118B, 59 (1982).

72. S. Weinberg, Private communication (1983) points out that the gravitino production rate is considerably higher than estimated in Ref. 7, but is still acceptably low. See also D.V. Nanopoulos, K.A. Olive and M. Srednicki, Phys. Lett. 127B, 30 (1983).

73. G. Farrar and P. Fayet, Phys. Lett. 89B, 191 (1980).

74. M.K. Gaillard, L.J. Hall and I. Hinchliffe, Phys. Lett. 116B, 279 (1982).

75. P. Salati and C. Wallet, Phys. Lett. 122B, 397 (1983).

76. R.M. Barnett, H. Haber and K. Lackner, Phys. Lett. 126B, 64 (1983) and Phys. Rev. Lett. 51, 176 (1983).

77. R. Barbieri, N. Cabibbo, L. Maiani and S. Petrarca, Phys. Lett. 127B, 458 (1983).

78. N. Cabibbo, L. Maiani and S. Petrarca, Roma preprint (1983).

79. S. Jones and C.H. Llewellyn Smith, Nucl. Phys. B217, 145 (1983).

80. H. Haber and G. Kane, Univ. of Michigan, preprint UM TH 83-18 (1983).

81. G. Kane and J.P. Léveille, Phys. Lett. 112B, 227 (1982); P. Harrison and C.H. Llewellyn Smith, Nucl. Phys. B213, 223 (1983).

82. G. Farrar and P. Fayet, Phys. Lett. 76B, 575 (1978) and 79B, 442 (1978).

83. CHARM Collaboration, F. Bergsma et al., Phys. Lett. 121B, 429 (1983); E613, R. Ball et al., Univ. of Michigan preprint UMHE 83-13/UW EX83-234 (1983).

84. Susy Versus Experiment Workshop, ed. D.V. Nanopoulos, A. Savoy-Navarro and C. Tao, CERN preprint TH-3311/EP-82/63 (1982); I. Hinchliffe and L. Littenberg, Proc. 1982 Summer Study on Elementary Particle Physics and Future Facilities, ed. R. Donaldson, R. Gustafson and F. Paige (APS, New York, 1983), p. 242.

85. B.A. Campbell, J. Ellis and S. Rudaz, Nucl. Phys. B198, 1 (1982).

86. C. Kounnas and D.A. Ross, Nucl. Phys. B214, 317 (1983).

87. P. Fayet, Phys. Lett. 117B, 460 (1982).

88. J. Ellis and J.S. Hagelin, Phys. Lett. 122B, 303 (1983).

89. E. Ma and J. Okada, Phys. Rev. Lett. 41, 287 (1978) and Phys. Rev. D18, 4219 (1978); K.J.F. Gaemers, R. Gastmans and F.M. Renard, Phys. Rev. D19, 1605 (1979).

90. MAC Collaboration, M. Piccolo, talk at this Conference (1983).

91. J. Ellis, J.-M. Frère, J.S. Hagelin, G. Kane and S.T. Petcov, SLAC-PUB-3152 (1983).

92. UA1 Collaboration, G. Arnison et al., Phys. Lett. 122B, 95 (1983); UA2 Collaboration, M. Banner et al., Phys. Lett. 122B, 476 (1983); UA1 Collaboration, G. Arnison et al., Phys. Lett. 129B, 273 (1983).

REVIEW OF THE PHYSICS AND TECHNOLOGY OF CHARGED PARTICLE DETECTORS

A. H. Walenta

University of Siegen, West Germany

Introduction

In particle physics reactions usually are analyzed by measuring the properties of the produced energetic particles. They become accessible to the experiment by their interaction with the detection material.

Two main classes of detectors can be distinguished: The "total absorption detectors" where in one or a few interactions most of the energy is released and a shower produced. Already after the first interaction the particle has changed its properties drastically and therefore this interaction is decisive for the information obtained. The position and the type (electromagnetic, hadronic) of the interaction and the total energy can be determined. These detectors are massive in order to increase the probability of an interaction and to contain the total shower. They will be the subject of the second series of the instrumentation lectures.

The second class of detectors is as thin as possible to avoid the above mentioned "spectacular" interactions such that the trajectory and the other properties of the

© A. Walenta 1983

particle are not disturbed. Fortunately nature provides a class of particles still detectable. Charged particles still interact sufficiently, for detection. The Coulomb field interacts with the atomic electrons and exited and ionized atoms are left behind. The large number of these small energy transfers makes it possible to build detectors recording the track of these interactions following the trajectory of the particle. In a magnetic field the direction, the momentum and in principle the mass of the particle can be determined. These detectors are the subject of the first series of instrumentation lectures.

For any kind of radiation detector three steps in its function can be distinguished. It has to exhibit some mechanism of interaction, transportation of the information and its registration. In other words the detector has to be dense with respect to the radiation to be detected and transparent to some sort of reaction product which travels to the boundary of the detector where it is collected and amplified.

Only a few processes are known to fulfill all requirements which limits the number of available detector principles. One of the best (and most successful) examples are the scintillators where the material is extremely transparent to photons in the visible and at the same time has a high mass and a high absorption coefficient for any other radiation. The only drawback is the small amount of photons produced in the scintillation process such that very sensitive photon detectors have to be used limiting their application capabilities severely as tracking detectors.

The second class is characterized by the production of free charge carriers by ionization which in (most) gases and in semiconductors* travel under the influence of an electrical field (drift) some distance to an electrode where they are recorded. In the gas an amplification process by generating a limited avalanche (the principle of proportional or Geiger-counter) is possible and permits enough gain to detect even single electrons.

In order to understand these detectors and their ultimate capabilities the ionization, the drift of the free electrons, the multiplication and the signal generating process have to be investigated. The ultimate question will be what information of the passing particle is transferred to the ionization track, how much of this is preserved (or lost) in the transportation and amplification process and what information finally can be extracted and conserved in the form of electrical signals.

---

* Also a number of very pure liquids (e. g. liquid argon) permits useful conductivity for free electrons.

These questions cover the physics as well as the technology of these detectors and lead to a straightforward subdivision in chapters.

Interaction of Charged Particles with Matter - Ionization Loss

A particle with charge z and energy E passes at a distance b (impact parameter) from an atomic electron and produces a variable electrical field $\epsilon(t)$ at the position of the electron. The coupling causes a momentum transfer p' given classically by

$$p' = \int_0^\infty e\,\epsilon(t)\,dt \qquad (1)$$

and corresponds to an energy transfer

$$E' = \frac{p'^2}{2m_e} \qquad (2)$$

when the electron is considered free.

If $\phi(E',E)\,dE'dx$ is the probability for an encounter with an energy loss between E' and E' + dE' along a track segment dx, the mean number of such encounters per track length is given by

$$\left\langle \frac{dN}{dx} \right\rangle = \int_{E'_{min}}^{E'_{max}} \phi(E', E)\,dE' \qquad (3)$$

where it has to be integrated from the smallest possible energy transfer E'_{min} to the largest E'_{max}. This number is called the mean specific number of collisions and must not be confused with the specific primary ionization which considers only encounters leading to ionization. The number above contains, in addition, encounters leading to exitation. In the same way the mean specific energy loss is calculated

$$\left\langle \frac{dE}{dx} \right\rangle = \int_{E'_{min}}^{E'_{max}} E'\,\phi(E', E)\,dE' \qquad (4)$$

containing encounters leading to exitation as well as ionization.

Using (1) and (2) and the probability of an encounter with an energy loss E' determined by the probability of the corresponding impact parameter b one obtains

$$\phi(E', E)\,dE'\,dx = 2\pi NZ\,\frac{Z^2e^4}{m_ec^2\,\beta^2}\,\frac{1}{E'^2}\,dE'\,dx \qquad (5)$$

with N the number of atoms per volume, Z the atomic number $\beta = V/c$ and m_e the electron mass or in a more practical form

$$\phi(E', E)\,dE'\,dx = \frac{\tilde{A}\rho}{\beta^2}\,\frac{dE'}{E'^2}\,dx \qquad (6)$$

where $\tilde{A} = 0.1536 \frac{Z}{A}$ MeV $cm^2 g^{-1}$, A the atomic weight and ρ the density of the absorber. For the moment this simple formula with some quantum mechanical corrections will be used to calculate the mean number of primary ionizing collisions (Eq. 3) and the energy loss in thin absorbers (Eq. 4) because they are given in a closed form and the decisive parameters can be recognized. For the purpose of detector development the precision is usually sufficient.

It will be shown later that for the distribution functions and effects, depending on the statistical nature of the individual collisions, more refined calculations will be necessary.

Primary Ionization

Inserting (6) into (3) and integrating over a given track length ΔX gives

$$n_{prim/\Delta X} = \int_{E'_{min}}^{E'_{max}} \frac{\tilde{A}\rho}{\beta^2} \frac{dE'}{E'^2} = \frac{\tilde{A}\rho}{\beta^2 E'_{max}} - \frac{\tilde{A}\rho}{\beta^2 E'_{max}} \quad . \tag{7}$$

Since for thin gases $E'_{max} >> A\rho$ one obtains

$$n_{prim/\Delta X} = \frac{\tilde{A}\rho}{\beta^2} \frac{1}{E'_{min}} \quad . \tag{8}$$

Although this formula shows the correct dependence on electron density $A\rho$ and velocity dependence $1/\beta^2$ (without relativistic effects) the classical interpretation of $E'_{min} = 0$ does not make sense. At best one can argue that the number of encounters resulting in free electrons (ionization of the atoms) is obtained by interpreting E'_{min} as the ionization threshold I_o yielding the primary ionization. Similar arguments can be found for atomic exitations or purely elastic encounters and it is the equivalent of stating that quantum effects determine the number of encounters and have to be incorporated already in $\phi(E',E)$. This has been calculated by Bethe (Ref. 1) using Born's approximation. He finds that indeed formula (8) is correct if a modified value E'_{min} is used

$$E'_{min} = \frac{I_o}{r[\ln \frac{2mv^2}{I_o(1-\beta^2)} + s - \beta^2]} \tag{9}$$

which includes relativistic effects. I_o is the ionization energy of the atom and r and s are constants determined by the gas and calculated by Bethe only for hydrogen with $r = 0.285$ and $s = 3.04$. With $I_o = 15.4$ eV and $E'_{min} = 3,5$ eV $n_{prim} = 4.6$ cm^{-1} is obtained. The effective E'_{min} is much lower than the ionization threshold I_o which is not a contradiction but a result of the fact that the resonant transfer of energy is described by a mean value in a

classical picture.

A formula for other gases has been obtained by summing up contributions of individual shells (Ref. 2)

$$E'_{min} = \frac{\tilde{A}\rho}{A_1\left[A_2 + \ln\frac{\beta^2}{1-\beta^2} - \beta^2\right]} \qquad (10)$$

and values for A_1, A_2 and n_{prim} are shown in Table I for minimum ionizing particles ($\beta\gamma = 3.2$).

Table I

gas	density (mg/cm^3) ($0^\circ C$, 1atm)	I_o (eV)	A_1	A_2	n_{prim} (cm^{-1})
H_2	0.0899	15.4	Bethe's	formula	4.6
H_e	0.1785	24.6	0.244	11.64	3.5
N_e	0.9004	21.7	0.844	10.89	11.4
A_r	1.7837	15.8	1.828	11.45	25.8
X_e	5.8510	12.1	3.554	11.31	49.6
N_2	1.2506	15.5	1.941	11.43	27.1
O_2	1.4290	12.2	2.079	11.28	28.9

The experimental determination of the primary ionization is done with Geiger and proportional counters since a very high sensitivity of a single electron is required. In low pressure counters a loss of efficiency had been observed which is attributed to the events where no ionization is deposited in the sensitive volume of the detector. Since each ionizing collision is independent of the other, the probability for n collisions in an event is described by the Poisson distribution

$$P(n,\bar{n}) = \frac{\bar{n}^n}{n!} e^{-\bar{n}} \qquad (11)$$

where $\bar{n}$ is the mean value on the considered track length. The probability for no ionization is

$$P(0,\bar{n}) = 1-\varepsilon = e^{-\bar{n}x} \qquad (12)$$

and therefore $\bar{n} = n_{prim}$ can be obtained from the measurement of the inefficiency $1 - \varepsilon$ for a detector of thickness X.

The measurements recorded in the literature are all from Geiger counters (Ref. 3) and some of the results are shown in Fig. 1. Some of them are measured with well defined particle momentum and others represent a mean value for cosmic rays including effects of the relativistic rise. They are probably a few tens of percent higher than minimum ionizing. With modern electronics the efficiency of a proportional counter at atmospheric pressure could be measured for minimum-ionizing β-rays (E_β-=0.7 ... 1.5 MeV). Figure 2 shows the measured $(1-\varepsilon)$ as a function of increasing pulse height. Since the

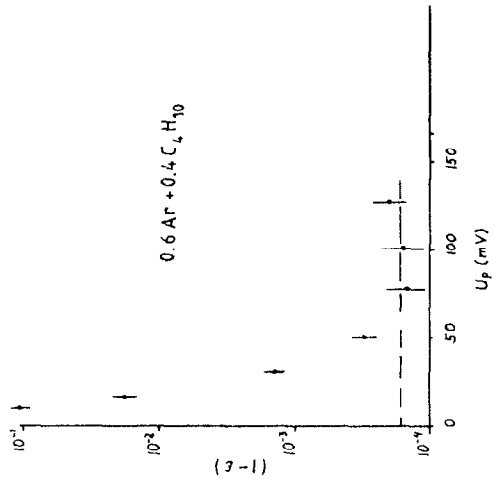


Fig. 2 Inefficiency of proportional counters as function of pulse height. Minimum ionizing particles, x=5 mm.

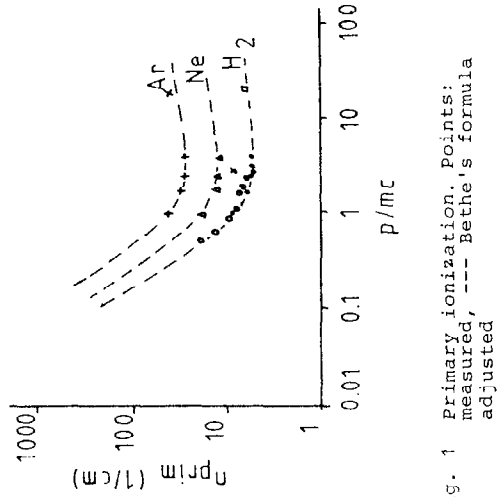


Fig. 1 Primary ionization. Points: measured, --- Bethe's formula adjusted

discriminator threshold was kept constant with increasing voltage, the sensitivity to detect single electrons would increase until saturation is reached. With x=5 mm and $1-\varepsilon = 1.6 \cdot 10^{-4}$ a value $\bar{n} = 17.5\ cm^{-1}$ is calculated. This may be a lower limit since no further tests have been made to exclude other sources of inefficiency.

The second method for measurement of the primary ionization consists of measuring the gap s between two primary ionization clusters given by

$$P(s)ds = \bar{n}\, e^{-\bar{n}s}\, ds\ . \qquad (13)$$

This method has the advantage of showing immediatly a number of possible systematic errors when the measured distribution deviates from the exponential law and only the part where it is fulfilled is used for determination of $\bar{n}$. In a drift chamber this measurement can be easily performed (Fig. 3) by recording the drift time τ of the first cluster arriving at the anode. With the assumption that the drift velocity v_{Dr} is constant (which is approximately true for a number of gases) the drift time distribution for tracks collimated on the anode wire is given by

$$P(\tau)\, d\tau = 2\bar{n} v_{Dr}\, e^{-2\bar{n} v_{Dr}\tau}\, d\tau, \qquad (14)$$

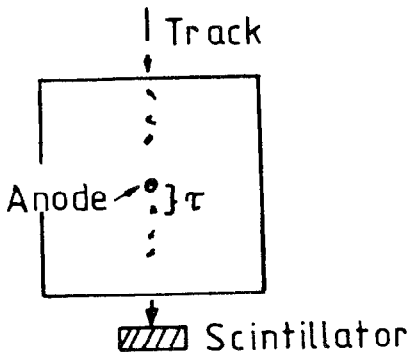


Fig. 3 Measurement of cluster spacing in drift chamber (schematically).

where the factor 2 enters because clusters from two sides can reach the anode. Figure 4 shows the result of such a measurement (Ref. 4).

The third method of measuring the primary ionization clusters is the direct counting which has been applied to photographed tracks in streamer and cloud chambers (Ref. 5) but has also been done in a specially designed drift chamber, the time expansion chamber (see below). The drift field is parallel to the track and adjusted, such that the drift velocity is low enough that the mean time difference of arrival of two subsequent clusters is large enough that the signals created in the detection region are well separated and can be counted with standard electronics. A pulse train with a few separated clusters is shown in Fig. 5.

The result of such measurements (Fig. 6) shows an excellent agreement with the expected distribution (Eq. 11). The mean number of clusters $\bar{n}$ needs some correction due to dead time losses (ca. 10 %) and ionization losses at the grid (ca. 20 %) and will then be in agreement with the other measurements.

Figure 7 shows the collected measured data. A solid line guides the eye to connect measurements obtained with Geiger counters, cloud and streamer chambers and a dashed line connecting the data from proportional

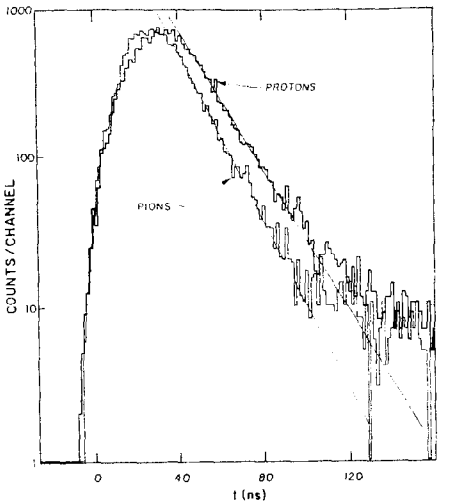


Fig. 4 Drift time spectra for arrangement of Fig. 3.

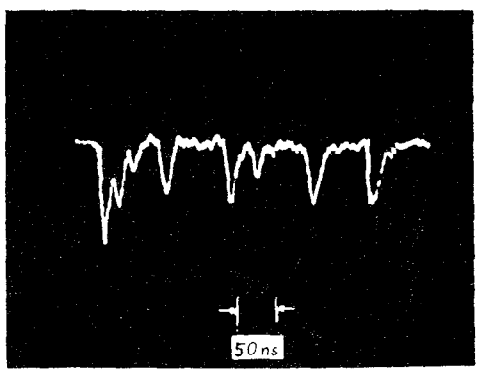


Fig. 5 Pulse train from time expansion chamber for minimum-ionizing particle showing individual clusters.

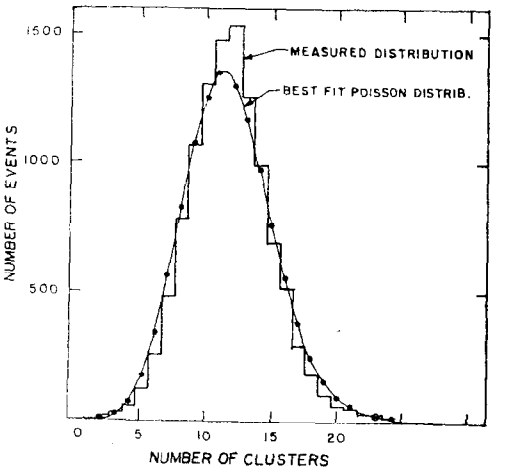


Fig. 6 Distribution of measured number of clusters. P-10 + 4 % methylal, 1 cm, minimum ionizing.

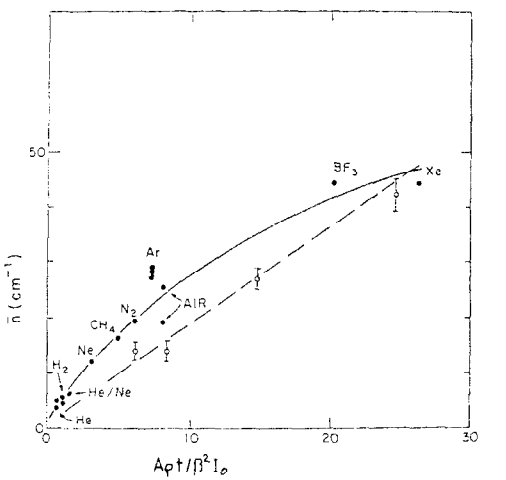


Fig. 7 Mean number of clusters.
See Eq. 9.
·Geiger counter, streamer and cloud chamber
∘drift chamber

counters. Errors in the first category have been discussed in Ref. 5 and tend to increase the measured number due to diffusion, wall effects, relativistic rise, multiple scattering, secondary ionization processes etc., while from the foregoing discussion the data of the second category may be too low. Unfortunately the discrepancy in the region of argon, the most frequently used detector gas, is almost a factor of two. For the moment the measurements and the theory do not allow more conclusive results (Ref. 6). Clearly for application in understanding the performance of proportional chambers the values obtained with the devices seem preferable.

Energy Loss

The energy loss is given by summing up the energy released in the individual clusters along the track segment. The mean value is obtained following Eq. 4

$$\left\langle \frac{dE}{dx} \right\rangle = \frac{\tilde{A}\rho}{\beta^2} \int_{E'_{min}}^{E'_{max}} \frac{dE'}{E'} \qquad (15)$$

and can be integrated immediately

$$\left\langle \frac{dE}{dx} \right\rangle = \frac{\tilde{A}\rho}{\beta^2} \ln \frac{E'_{max}}{E'_{min}} \quad . \qquad (16)$$

Here it is possible to introduce the quantum-mechanical limits E'_{max} and E'_{min} with some plausible arguments showing at the same time some of the physics involved.*
In order to transfer energy to the bound electron the perturbation has to be short compared to its typical period in orbit

$$\Delta t < \frac{1}{\langle \nu \rangle} \qquad (17)$$

where $\langle \nu \rangle$ is some characteristic frequency of the bound electron. One obtains

$$E'_{min} = \alpha \frac{\langle \nu \rangle^2 (1-\beta^2)}{\beta^2 c^2} \qquad (18)$$

with $\alpha = 2z^2e^4/m_e c^2 \beta^2$. The maximum energy transfer is limited by the condition that the impact parameter b cannot be smaller than the De Broglie wavelength of the target electron $b > \hbar/p$ and one obtains

$$E'_{max} = \alpha \frac{m_e^2 c^2 \beta^2}{\hbar^2 (1-\beta^2)} \quad . \qquad (19)$$

* A detailed treatment of this aspect is given by Ref.7.

Inserting (18) and (19) into (16) and including two corrections in the bracket $-2\beta^2-2\delta$ one obtains the formula known as Bethe-Bloch formula for the mean energy loss which has been derived by appropriate quantum mechanical treatment

$$< \frac{dE}{dx} > = \frac{\tilde{A}\rho}{\beta^2} \left(2\ln \frac{2m_e c^2}{\bar{I}^2} + 2\ln\beta\gamma - 2\beta^2 - 2\delta\right). \qquad (20)$$

The quantity $\hbar <\nu> = \bar{I}$, which was defined as some typical energy of the atom, gets a clean interpretation as $\ln\bar{I} = \Sigma f_i \ln E_i$ (Ref.1) with f_i the oscillator strength of the i-th atomic level with energy E_i. For mixtures and compounds of the atoms B^ν as $B^1_{n^1} B^2_{n^2} \ldots B^\nu_{n_\nu}$ with n_ν the number of the atoms, A_ν and Z_ν its atomic weight and atomic number respectively, the logarithmic mean is formed

$$\ln \bar{I} = \frac{\sum_\nu Z_\nu n_\nu \ln \bar{I}_\nu}{\sum_\nu Z_\nu n_\nu} \quad . \qquad (21)$$

The term $\tilde{A}\rho$ for mixtures and compounds is calculated to give the correct electron density

$$\overline{\tilde{A}\rho} = \frac{\Sigma n_\nu \frac{Z_\nu}{A_\nu} \rho_\nu}{\Sigma n_\nu} \qquad (22)$$

or if the mean density $\bar{\rho}$ is given

$$\overline{\tilde{A}\rho} = \frac{\Sigma n_\nu Z_\nu}{\Sigma n_\nu A_\nu} \bar{\rho} \quad . \qquad (23)$$

Values for $\bar{I}$ in Table II for atoms have been obtained by measurement and for the compounds and mixtures by calculation.

The correction term δ compensates for polarization effects and will be discussed below in connection with the relativistic rise.

For very thin absorbers ($\rho t < 100$ mg/cm^2) the mean energy loss (Eq. 20) is not very practical because a few collisions with large energy transfer are responsible for a long tail in the distribution which will lead to saturation in most recording equipment and therefore reliable data are difficult to obtain. Furthermore the electrons from such encounters have enough energy to leave the absorber and the mean energy deposited in the absorber will be different from the mean energy loss of the particle crossing the absorber. To avoid these problems in thin absorbers the most probable energy loss $(\Delta E)_{mp}$ is calculated (Ref.8):

$$(\Delta E)_{mp} = \frac{\tilde{A}\rho t}{\beta^2} \left\{\ln \frac{m_e c^2 \tilde{A}\rho t}{\bar{I}^2} + 0.891 + 2\ln\beta\gamma - \ln\beta^2 - \beta^2 - \delta\right\}. \qquad (24)$$

Table II

Gas	ρ (mg/cm^3) 1atm, 20°C	A (keV/cm)	ΔE_{min} (keV/cm) mostprob.	W (eV)	n_{tot} (cm^{-1})	n_{prim} (cm^{-1})	$\bar{I}$ (eV)	I_o (eV)	$\overline{\Delta E}$ (keV/cm) mean
H_2	0.0838	$1.37.10^{-2}$	0.194	36.3	5.3	5	15.6	15.3	
He	0.166	$1.27.10^{-2}$	0.156	41.3	3.8	4.5	36.0	24.56	
Ne	0.839	$6.44.10^{-2}$	0.732	36.8	19.9	12	125	21.56	
Ar	1.66	0.115	1.25	26.4	48.1	15..28	210	15.76	
Kr	3.45	0.227	2.31	24.2	96		396	14.0	
Xe	5.40	0.342	3.42	22.2	154	44	529	12.13	
CH_4	0.67	$6.4.10^{-2}$	0.873	27.3	31.2		44	13.04	1.54
C_2H_6	1.26	0.116	1.64	24.6	65.7		45.9	11.76	
C_3H_8	1.87	0.171	2.46				48		4.30
C_4H_{10}	2.52	0.227	3.38	23.0	147		45.5	10.8	
P-10		0.109	1.12				191		2.30
CO_2	1.84	0.140	1.74	32.8	53.1		118	13.73	3.20
NH_3	0.718	$6.5.10^{-2}$	0.867	30.5	28.4		50.3		

One notices that this value decreases faster than proportional with the absorber thickness ρt. The typical behavior of the most probable energy loss as well as the mean energy loss as function of $\beta\gamma = P/_{mc}$ is shown in Fig. 8 (note the double logarithmic scale). At low $\beta\gamma$ it decreases as $1/\beta^2$, goes through a minimum at $\beta\gamma = 3,5$ and increases with $\lg\beta\gamma$ which is called the relativistic rise. Occasionally this increase is compensated by the polarization of the medium until a constant value in the Fermi plateau is reached.

Values for the minimum are given in Table II for a number of detector materials. For comparison the mean energy loss also is shown and for gases this value is about a factor of two higher, indicating the limited usefulness for thin absorbers as discussed above.

Experimentally this formula has been tested directly with electrons of known energy by measuring their momentum in a spectrometer after passing through thin foils (Ref.9). For very thin foils deviations from Eq. 24 could be found which were attributed to shell effects.

For gases the energy loss cannot be measured directly. Here the ionization is measured in terms of energy and calibrated with a source releasing a known amount of energy (e.g. x-rays), the justification for this procedure being discussed below.

Figure 9 shows the minimum energy loss per cm and

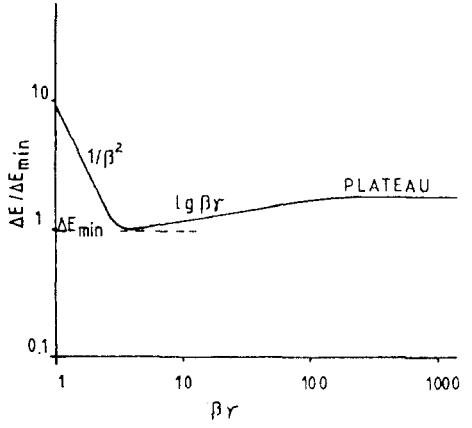


Fig. 8 Energy loss as function of $\beta\gamma$.

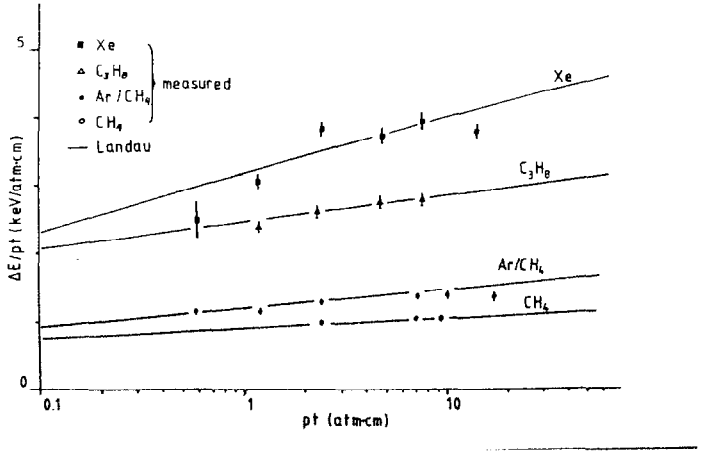


Fig. 9 Most probable energy loss in gases as function of absorber thickness. Protons $\beta\gamma$ = 3.0 (measured) Landau minimum.(——).

atm measured with protons of $\beta\gamma$ = 3.0 in a proportional counter of 23 mm thickness as function of pressure (Ref. 10). The absolute value and the predicted dependence on pressure by Eq. 24 is reproduced. Measurements have been reported (Ref. 11) where systematically lower values have been found which could indicate shell effects as in solid absorbers but at the moment considering the possible systematic errors (see for example Ref. 12) no further conclusion can be drawn.

The Relativistic Rise

Because of the importance for particle identification with track detectors, the relativistic rise of energy loss will be discussed somewhat more in detail.

Considering Eq.24 again (and Fig.8) it is noticed that the term for increasing energy loss beyond the minimum is ln γ. This effect is due to the relativistic increase of the peak electric field ϵ_{tmax} transverse to the flight path of the particle with charge q and the impact parameter b

$$\epsilon_{tmax} = q\,\gamma/b^2 . \qquad (25)$$

Since the minimum energy loss E'_{min} corresponds to a maximum impact parameter $b_{max} \propto 1/\sqrt{E'_{min}}$, the effects of

the relativistic increase of the electric peak field is the same as to increase the range $b_{max} = \sqrt{\gamma}\, b_{max.o}$ when $b_{max.o}$ is the value in the nonrelativistic case. However, the increase of b_{max} is limited by polarization effects in the medium as has been first recognized by Fermi. For sufficiently large γ a saturation is reached, the Fermi plateau. The effect of polarization is summarized in Eq. 24 for the moment in the "density correction" term δ. By simple argument it can be shown (Ref.13) that the plateau is reached at $\gamma_{sat} = \bar{I}/\hbar\omega_p$, where $\bar{I}$ is the mean ionization potential and $\omega_p = \sqrt{4\pi N_e e^2/m}$ is the plasma frequency. For noncomposite absorbers one obtains

$$\gamma_{sat} = \frac{11.5\ Z}{28.8\sqrt{\frac{Z}{A}\rho}} \qquad \rho \text{ in g/cm}^3 \tag{26}$$

$$\gamma_{sat} = 57\ \sqrt{Z/P} \quad \text{for gases (P in atm).}$$

For hydrocarbon gases $\bar{I}$ = 48 eV and Z/A = 0,6 changes very little and therefore

$$\gamma_{sat} \approx \frac{2.2}{\sqrt{\rho}} \qquad \rho \text{ in g/cm}^3 . \tag{27}$$

In Fig. 10 it can be seen that for $\gamma \gtrsim 100$ only the heavy

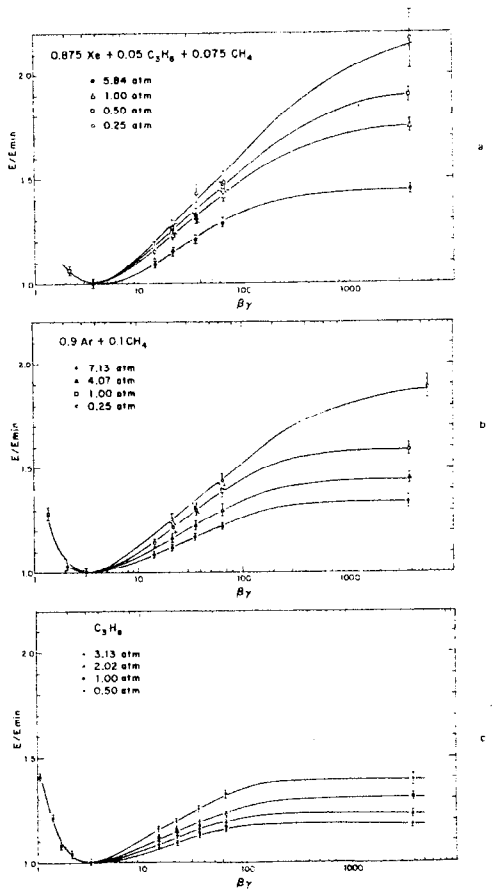


Fig. 10 Most probable energy loss. - Sternheimer adjusted. o measured.

noble gases will show a relativistic rise while up to $\gamma \approx 30$ modestly pressurized hydrocarbon gases will also show the effect (Ref. 14).

For more quantitative discussions of the relativistic rise a semiempirical formula for δ starting from absorber properties will be used (Ref. 15). More precise Monte Carlo calculations, which will be briefly outlined below, are not useful for a general discussion because input data for a number of gases are not readily available and for each parameter of interest a large number of runs have to be done but only a few of particular interest are available (a general problem of Monte Carlo calculations).

It is convenient to consider the energy loss per electron

$$\frac{(\Delta E)_{m\rho}}{\tilde{A}\ t} = \frac{1}{\beta^2}\left\{k\left(\frac{\tilde{A}\rho t}{\bar{I}^2}\right) + R(X) - \delta(X,C_\nu)\right\} \qquad (28)$$

where $X = \lg \beta\gamma$. Then it is found $R(X) = 4{,}606\ X - \ln \beta^2 - \beta^2 \approx 4{,}606X - 1$ since for the relativistic cases considered here $\beta \approx 1$. k is given by

$$k = \ln \frac{4{,}88\pi e^4 Nt}{\bar{I}^2} = \ln \frac{2{,}44 m_e c^2 A\rho t}{\bar{I}^2} \qquad (29)$$

and $\delta(X,C_\nu)$ is the density correction depending on X and a number of gas parameters C_ν (e.g. energy levels of the electrons, oscillators strength for transitions and density).

Fermi has shown that for extreme relativistic particles (plateau) one finds

$$\frac{(\Delta E)_{m\rho}}{\tilde{A}\rho t} = \ln \frac{1{,}22 \cdot 2 m_e c^2 \tilde{A}\rho t}{(\hbar\omega_p)^2} = \ln t/t_o \qquad (30)$$

with ω_p the plasma frequency of the material. Since the electron density N contained in $A\rho$ and ω_p^2 cancel $\frac{(\Delta E)_{m\rho}}{A\rho t}$ only depends on t in units of $t_o = a_{Bohr}/1{,}22 = 0{,}4342\text{Å}$.

Therefore the density correction $\delta(X)$ in Eq. 24 has to fulfill the following boundary conditions (see Fig.11)

$$\text{a)}\ \delta = 0 \text{ for } X \leq X_o \text{ and}$$
$$\text{b)}\ \delta = \ln t/t_o + k\left(\frac{A\rho t}{\bar{I}^2}\right) + R(X) \text{ for } X > X_1 . \qquad (31)$$

The condition b) can be simplified and one obtains

$$\text{c)}\ \delta = 4.606(X - X_a) \text{ for } X > X_1$$

with

$$X_a = \frac{1}{4.606}\left(\ln \frac{1^2}{(\hbar\omega_p)^2} + 1\right) .$$

The intermediate region $X < X < X_1$ has been fitted by Sternheimer by the expression

$$\delta = 4.606(X - X_a) + a(X_1 - X)^m$$

with a and m such that the slope is zero at $X = X_o$ and the

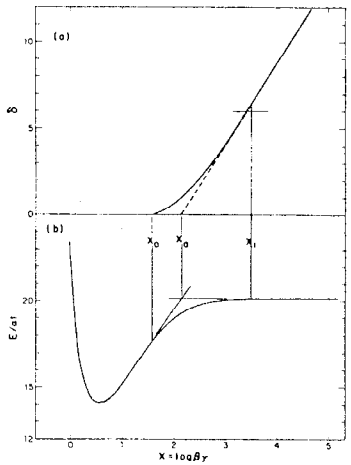


Fig. 11 Density correction. See text.

asymptotic value at $X-X_1$ is obtained. The change of gas density by a factor $\eta = \rho/\rho_{NTP}$ is equivalent to decreasing b_{max} and consequently $X_\eta = {}_{NTP} - \frac{1}{2} \lg\eta$.

The parameters X_o, X_1, X_a, m and a are listed for a number of substances. Sternheimer and Peierls have noticed a certain systematic of the parameters and shown that still acceptable results are obtained when m=3. X_a is calculated (Eq. 31), X_o, X, are functions of X_a (Fig.12) and a is determined by the boundary conditions.

This finding is another way of expressing that $\bar{I}/h\omega_p$ is a useful parameter of characterizing the density effect.

Since all substances reach the same value ($\Delta E/\tilde{A}\rho t$) in the Fermi plateau, the most important difference will be expected in the minimum of the ionization curve. From Eq. 24 one finds for the minimum with $\delta=0$ for gases and $\beta^2 \approx 1$

$$k + \ln\gamma^2_{min} = \beta^2_{min}\gamma^2_{min} . \qquad (32)$$

A good approximation (with ca. 1% for $5<k<15.5$) is given by

$$\gamma_{min} \approx 1.54k^{0.385} \qquad (33)$$

and

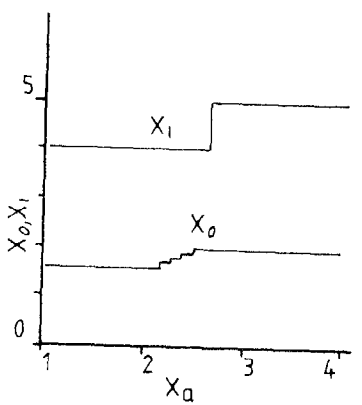


Fig. 12 Density correction. See text.

$$\frac{E_{min}}{\tilde{A}_{\rho t}} = 2.37\ k^{0.770} - 1 \,. \qquad (34)$$

For the total relativistic rise one finds

$$\frac{E_{max}}{E_{min}} = \frac{\ln t/t_o}{2.37 k^{0.770} - 1} \qquad (35)$$

with $t_o = 0.4342$ Å. In Fig.13 this relation is compared to measurements (Ref.14) with t=2.3 cm. A somewhat better fit to the data is obtained for $t_o = 0.836$ Å which reflects the general experimental finding of smaller relativistic rise than predicted by the Landau-Sternheimer calculation for a given detector thickness t.

The relativistic rise of the specific primary ionization (number of ionization clusters per track length) follows a similar dependence as the most probable energy loss. Calculations and measurements (Fig.14) confirm that the relativistic rise is somewhat smaller and saturates earlier because here the encounters with electrons of small binding energy dominate (in the calculation of n_{ion} the inner shells could be left out).

The very few measured data, however, do not allow more precise conclusions for the same reasons as has been discussed for n_{ion} above.

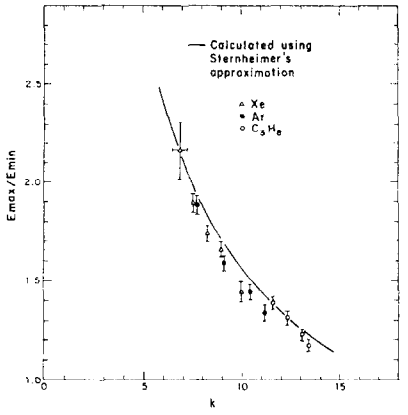


Fig. 13 Maximum relativistic rise (plateau to minimum) over parameter k (see Eq. 28)

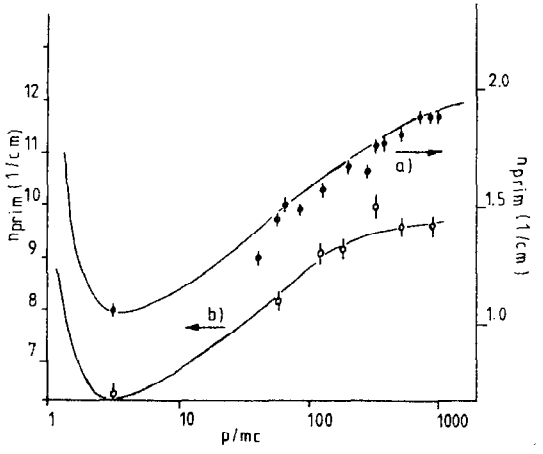


Fig. 14 Relativistic rise of primary ionization.

Fluctuation of Energy Loss

Up to now the mean energy loss and the most probable energy loss have been discussed. They are parameters of a probability density f (ΔE)d(ΔE) which gives the probability of an energy loss between ΔE and ΔE+d(ΔE). The knowledge of this distribution is important for track detectors because it influences the ultimate position resolution and because it sets a limit for using the dependence of energy loss on particle speed and charge for particle identification. It is also useful to discuss it here in more detail, because the relatively easy measurement of f (ΔE) reveals that the simple picture of energy loss developed so far needs major improvements.

The energy loss of a particle traversing an absorber of thickness t is given by the sum of the energy losses E_i' of the n individual interactions

$$\Delta E = \sum_{i}^{n} E_i' . \qquad (36)$$

This value fluctuates because the number n of inelastic encounters follows a Poisson distribution (Eq. 11) and because the individual losses E_i' are randomly different following a distribution $\phi(E', E)dE'$ (see Eq. 5).

The first successful calculation of f (ΔE) has been

performed by Landau (Ref.8) and therefore the distribution with its characteristic long tail,which is due to infrequent but frequent enough encounters with large E', is referred to as "Landau-distribution" (Fig.15).

By means of the Laplace transform he obtains the general solution for the distribution f (ΔE,t) for a given absorber thickness t

$$f(\Delta E,t) = \frac{1}{2\pi i}\int_{-i\infty+\delta}^{i\infty+\delta} e^{s\Delta E}\varphi(s,t)ds, \qquad (37)$$

where $\varphi(s,t)$ is given by

$$\varphi(s,t) = \exp\left[-t\int_0^{\infty}\phi(E')\ (1-e^{-sE'})dE'\right]. \qquad (38)$$

For $\phi(E')$ the simple Equation (5) is used and therefore the integration cannot be performed from 0 to ∞ but from E'_{min} to E'_{max}. Under the assumption that most of the energy loss is due to collisions $E' < E$ and that $sE' \ll 1$ for these events; E'_{min} is given by Eq. 18 and one obtains

$$\varphi(s,t) = e^{-\tilde{A}pts(1-C-\ln sE'_{min})} \qquad (39)$$

where C = 0.5777 ... (Eulers constant).

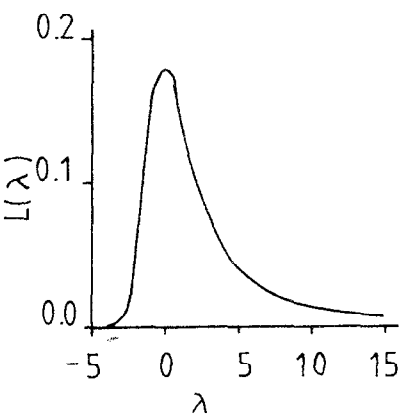


Fig. 15 Normalized Landau distribution. See text.

Then Eq. 37 can be solved

$$f(t,\Delta E) = \frac{1}{2\pi i}\frac{1}{\tilde{A}\rho t}\int_{-\infty}^{+\infty} e^{u\ln u + u\lambda}du \qquad (40)$$

with $u = \tilde{A}\rho ts$ and

$$\lambda = \frac{\Delta E - \tilde{A}\rho t(\ln\frac{\tilde{A}\rho t}{E'_{min}} - C + 1)}{\tilde{A}\rho t} . \qquad (41)$$

The energy distribution f (t,ΔE) can be factorized and is given by two parameters $\xi = A\rho t$ and λ

$$f(t,\Delta E) = \frac{1}{\xi} L(\lambda) \qquad (42)$$

with $$L(\lambda) = \frac{1}{2\pi i}\int_{-\infty}^{\infty} e^{u(\ln u + \lambda)}du$$

which originally has been calculated numerically and is shown in Fig.15.

The maximum is found at λ=-0.225* and therefore the most probable energy loss is

$$\Delta E_{mp} = \tilde{A}\rho t(\ln\frac{\tilde{A}\rho t}{E'_{min}} + 1 - C - 0.225) , \qquad (43)$$

* This value has been calculated in Ref.16 . Originally Landau used λ = -0.05.

which is equivalent to Eq. 24 except for the relativistic effects.

For solid foils and semiconductors Landau's formula was verified experimentally (Ref.17), but for thin absorbers where $\xi = A\rho t < E_K$ with E_K the binding energy of the absorber, the measured distribution becomes considerably larger (Fig.16). Blunck and Leisegang (Ref.18) have pointed out that the assumption $sE' \ll 1$ was not justified in these cases and by allowing resonant effects in $\phi(E')$ the calculation can be improved. Their results have only limited range of application and will not be reproduced here but their physics interpretation of the effect and the direction of possible solution will be discussed briefly.

In a more detailed treatment (see for example Ref.19) it can be shown that the condition $sE' \ll 1$ for $E' < E_0$, when E_0 is an energy well above the mean ionization potential $\bar{I}$, is equivalent to $2/_{A\rho t} \cdot E' \ll 1$. Choosing $\bar{I}/E_0 = 0{,}1$ one obtains a limit of validity for Landau's assumption $A\rho t/\bar{I} > 20$. For $A\rho t/\bar{I} < 20$ the simple form $\phi(E') = A\rho t/E'^2$ in connection with E'_{min} given by Eq. 18 cannot be used anymore and $\varphi(s,t)$ has to be calculated for a more realistic $\phi(E')$ containing resonant structures which makes the integral

$$\int \phi(E')\ (1-e^{-sE'})dE'$$

difficult to calculate. Blunck and Leisegang now added

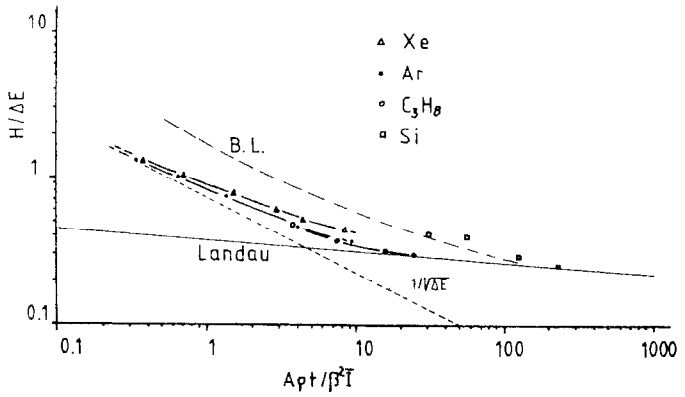


Fig. 16 Relative width (fwhm) measured and calculated Landau and B.L. for Z=18.

a resonant term

$$\phi_r(E') = \sum_i K_i \frac{\delta(E' - 1.5I_i)}{1.5I_i} \qquad (44)$$

with I_i the binding energies of the shells and with K_i such that the correct energy loss was obtained with $\phi_f(E') + \phi_r(E')$ where $\phi_f(E')$ is the form as used before.

The integral is solved by expanding

$$e^{-sE'} = \sum_{n=1}^{\infty} (-1)^n \frac{(sE)^n}{n!}$$

and then retained up to the quadratic term. Their numerical results fit quite well the data available at that time but later measurements, in particular for thinner samples, showed that the resonance effect was overestimated. Talman (Ref. 20) showed that higher orders of the expansion have to be taken into account and that the convergence is rather slow, especially for smaller Aρt. Then it is preferable to delete the contribution of the highest shells (the K-shell in Ar) and recalculate the distribution for the atom with the two missing electrons (Fig.17). A similar procedure had been used by Knop, Minten and Nellen to improve the agreement of their measurements with the calculation of Blunck and Leisegang.

With the advent of powerful computers a new approach

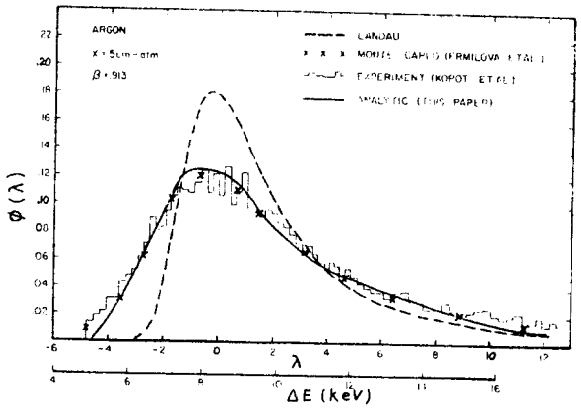


Fig. 17 Energy loss distribution. Comparison of calculations and measurements.

to the problem of fluctuation was found (Ref.21). Suppose $\phi(E')$ is known experimentally then $f(\Delta E,t)$ can be calculated by the Monte Carlo method for any thickness of the absorber. It turns out that at the same time a realistic behavior of the polarization effect for increasing γ can be built in, such that this method has proved useful for applications where particle identification is based on the measurement of the relativistic rise.

In reality it is not quite true that $\phi(E')$ is known experimentally but it can be derived from measured atomic data. The basic idea is the assumption that the spectrum of virtual photons produced by the passing charged particles (integrated over all possible impact parameters) is absorbed by the atom in the same way as real photons.

In the so called dipole approximation the energy transfer to the bound electron in the i^{th} shell is given by

$$\Delta E_i(b) = \frac{\pi e^2}{m} |\epsilon(\omega_o)|^2 \qquad (45)$$

with ω_o the resonance frequency and $\epsilon(\omega_o)$ the electrical field strength produced by the passing particle with an impact parameter b. Intergrating over all impact

parameters b and weighting the different shells with their coupling strength to the electromagnetic field characterized by the oscillator strength f_i one obtains for the specific energy loss

$$\left\langle \frac{dE}{dx} \right\rangle = N \sum_i f_i \int_{b_{min}}^{\infty} \Delta E_i(b)\, b\, db \,. \qquad (46)$$

The rigorous evaluation of f_i involves the calculation of the corresponding matrix elements for atomic transitions which has only been performed by Bethe for hydrogen-like atoms. Therefore it is already helpful if at least experimental values for f_i are available. They can be obtained from the measured photon absorption cross section $\sigma_\gamma(E')$ where E', the transfered energy, equals the photon energy.

$$f_i = \frac{mc}{2\pi^2 e^2} \int_{res} \frac{\sigma_\gamma(E')}{z}\, dE' \qquad (47)$$

where the integral is performed over the resonance region. Equations 45 and 47 inserted into (46) give the energy loss

$$\left\langle \frac{dE}{dx} \right\rangle = \int E' \phi(E', E)\, dE' \,.$$

The expression for $\phi(E', E)$ (Ref. 22) then contains three principal terms

$$\phi(E') = \frac{N}{\beta^2} \frac{\alpha}{\pi} \left[\frac{\sigma_\gamma(E')}{E'Z} \ln\left\{ \left| 1 - \beta^2 \varepsilon \right|^2 + \beta^4 \varepsilon_2^{\,2} \right\}^{1/2} \right.$$

$$\left. + \frac{\sigma_\gamma(E')}{E'Z} \ln\left(\frac{2m c^2 \beta^2}{E'} \right) + \frac{1}{E'} \int_0^E \frac{\sigma_\gamma(E)}{Z}\, dE \right] \qquad (48)$$

where the dielectric constant $\varepsilon = \varepsilon_1 + i\varepsilon_2$ has been included to describe the polarization of the medium for relativistic particles. The first term due to absorption of the transverse component with respect to the momentum transfer is recognized to be responsible for the relativistic rise and the saturation, the second and the third are due to the longitudinal components and represent the resonant and Rutherford absorption. In Fig.18 $\phi(E')$ obtained in this way is compared to the form $\phi(E') \propto 1/E'^2$ where in the latter case E'_{min} is shown to obtain the right energy loss. It is seen clearly that this simplification is not possible if the fluctuations of the energy loss are calculated because individual collisions with larger energy loss (mainly the second "bump" in the M shell and the L shell events) contribute much more than the simple model would predict.

Therefore it is not surprising that the Monte Carlo

calculations now give an excellent agreement of the spectra with the measured data (Fig.19). It is seen as well that the density effect and the Fermi plateau are in good agreement leading to the conclusion that the physics of energy loss is well understood.

Summarizing, the following picture emerges. From Eq. 38 and 39 it can be seen that the fluctuation mostly comes from encounters with $E' > A\rho t$. If in this region $\phi(E')$ has no "bumps" and is described well by Eq. 5 then Landau's distribution follows. If, however, this region shows resonant effects, the weighted contribution will be proportional to $\bar{I}$ the mean ionization potential. Therefore one can describe the fluctuation as a function of $A\rho t/\bar{I}$. For $A\rho t/\bar{I} > 20$ (see above) the Landau solution results and for smaller values the influence of the resonant effects increases. For the same reason the energy loss $\bar{I}$ is a good description of the contribution of the resonant effects as can be seen in Fig.16 where the measurements (Ref.14) show only little effect with Z over a wide range.

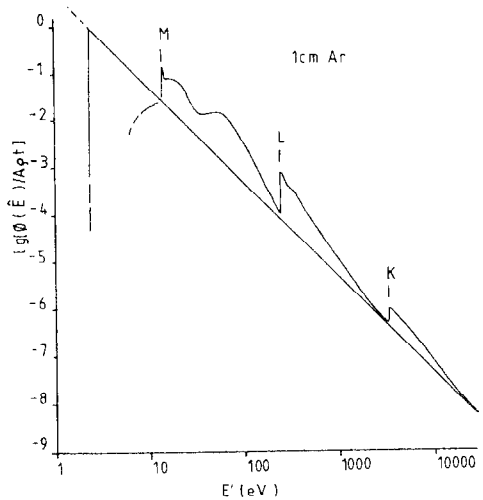


Fig. 18 $\phi(E')$ (see text).
K,L,M energies indicated.

Ionization Loss

Before we enter the discussion of applications, an essential topic for detectors has to be addressed. The

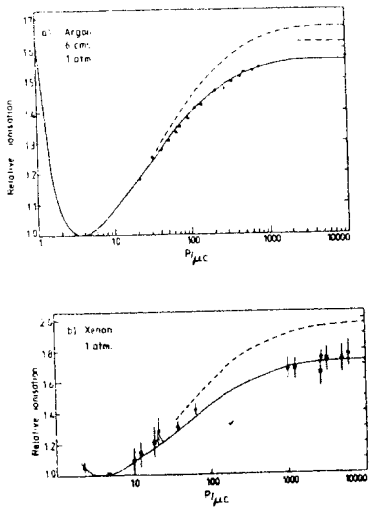


Fig. 19 Most probable energy loss. Monte Carlo calculations and measurements.

release of energy in an absorber almost entirely takes place through a few competing channels: exitation, ionization, dissociation (molecules) and bremsstrahlung. Most track detectors are sensitive to the ionization and it has been shown that between the number of produced ion pairs n_I and the energy loss ΔE the remarkable relation holds

$$\Delta E = W\, n_I \ , \qquad (49)$$

with W the mean energy spent for the production of one ion pair. Measurements have shown that the variation between gases are rather small (Table II) if one considers the fact that molecules have in addition to atomic exitations also molecular exitations and dissociation. For example, for Ar (W = 26.4 eV) almost the same value is obtained as for C_2H_6 (W = 24.6 eV). Partially the lower ionization threshold I_o = 11.76 eV in C_2H_6 compared to I_o = 15.76 in Ar may compensate for the larger number of nonionizing channels.

In solid state detectors (semiconductors) an electron lifted into the conduction band corresponds to an ionization in a gas. Since the gap width (ΔE_G = 1.1 eV in Si) is much smaller than the ionization energy I_o in gases, W = 3.7 eV is correspondingly smaller. This is a considerable advantage for track detectors where the

density of ionization is decisive.

Attempts have been made also to convert in gases more of the energy into ionization. The Penning effect has been used (Ref. 23) where in mixtures A + B exited atoms A (e.g. noble gases) ionize in collisions the atoms or molecules B with the lower ionization threshold

$$A^* + B \rightarrow A + B^+ + e^- .$$

For the moment however these mixtures are not very suited for track detectors because of poor drift or gas multiplication properties.

In liquid Xe a smaller value W_L= 15.6 eV had been observed than in the gaseous state W_g=21.5 eV which could give an indication of a transition to an electric band structure (Ref. 24).

Careful measurements of W have also shown that this quantity is almost independent of the particle energy and shows very little variation with the particle type. This is very important for spectroscopic applications. Figure 20 shows that the pulse height is, with high precision, proportional to the x-ray energy in the photopeak, i. e. in the event where no high energy fluorescent photon has escaped from the counter (Ref.25). At closer inspection this measurement reveals that photoelectrons ranging in energy from a few tens of eV to at least

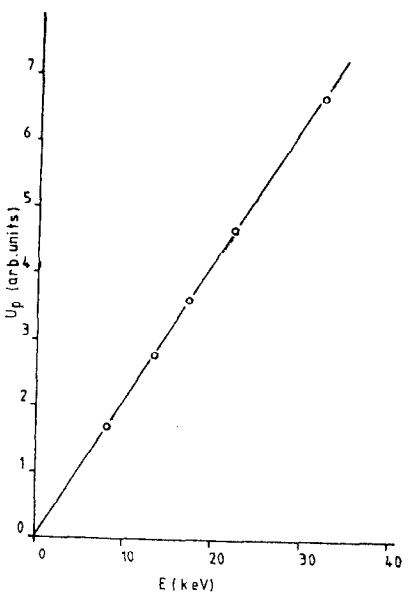


Fig. 20 Pulse height over absorbed energy of x-ray in gas scintillation counter.

20 KeV lose their energy in the same proportions to ionization, exitation and dissociation. The explanation follows from Eq. 5 giving the probability for an encounter with the energy transfer E'. First, the slope of the distribution does not depend on $1/\beta^2$ and second the cross section increases as $1/\beta^2$ for electrons losing energy and therefore a stopping particle and all its secondary electrons go through the same energy range where they are most effective (Fig.21) and where the ratio of energy spent in ionization and exitation is determined. Clearly for particles starting in this low energy region,W will undergo strong variations which has to be taken into account when quantitative values for the total ionization are calculated (Ref.26).

This particular process of distributing the lost energy over ionization, exitation and dissociation also influences the statistical variations which ultimately limits the resolution for energy measurement.

Here one has to distinguish between the fluctuation for the energy loss which is very large for minimum-ionizing particles in thin gas layers (see above), and the fluctuations of the produced ionization once deposited energy is defined (Ref.27). The latter case is experimentally realized for particles losing all their energy in the detector (α -particles, x-rays).

The total energy deposited in the detector E can be

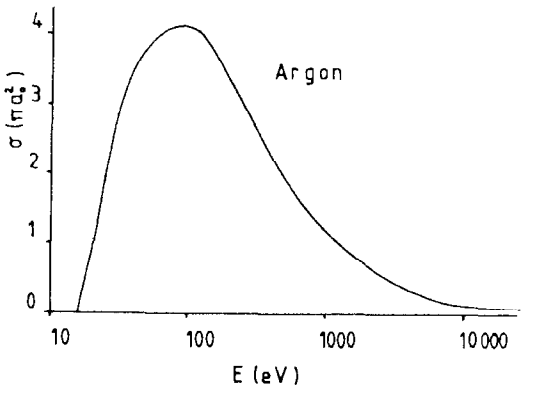


Fig. 21 Ionization cross section for electrons

represented by a number of smaller energy losses E_p in individual steps P, each generating n_p electrons. In total N steps are necessary to absorb E (Fig.22).

A few relations can be written down immediately (see Eq. 49);

$m_p^{(e)} = E_p/w$ expected number of ionization in step p and

$\bar{n} = E/w$ expected number of ionization in total .

(50)

The number of interest is the variance of n

$$\mathrm{var}(n) = (n-\bar{n})^2 = \frac{1}{L}\sum_{k=1}^{L}(n_k-n)^2 . \qquad (51)$$

The mean value is formed over many events, the quantities in the single event k obtain the corresponding subscript and one finds by definition

$$\begin{aligned} n_k-\bar{n} &= \sum_{1}^{N_k} m_{pk} - E/W \\ n_k-\bar{n} &= \sum_{1}^{N_k} m_{pk} - \frac{1}{W}\sum_{1}^{N_k} E_{pk} \\ n_k-\bar{n} &= \sum_{1}^{N_k} (m_{pk} - E_{pk}/W) = \sum_{1}^{N_k} \nu_{pk} \end{aligned} \qquad (52)$$

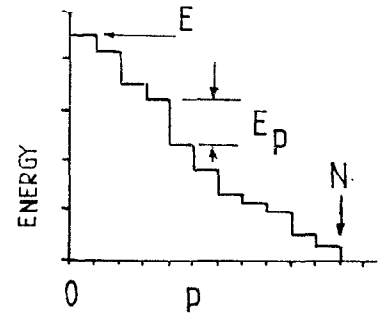


Fig. 22 Absorption process of given energy E in N steps.

if $\nu_{pk} = m_{pk} - E_{pk}/W$ for convenience.

For the variance can be written

$$\text{var}(n) = \frac{1}{L}\sum_{k=1}^{L}\Big(\sum_{p=1}^{N_k}\nu_{pk}\Big)^2$$

$$= \frac{1}{L}\Big(\sum_{k=1}^{L}\sum_{p=1}^{N_k}\nu_{pk}^2 + \sum_{k=1}^{L}\sum_{i\neq j}^{N_k}\nu_{ik}\,\nu_{jk}\Big). \qquad (53)$$

Let's first consider the second term

$$\frac{1}{L}\sum_{k=1}^{L}\sum_{i\neq j}^{N_k}\nu_i\nu_j = \frac{1}{L}\sum_{k=1}^{L}\sum_{i=1}^{N_k}\nu_{ik}\Big(\sum_{j=1}^{N_k}\nu_{jk} - \nu_{ik}\Big)$$

where the double sum has been replaced by a product of two sums and the subtraction of ν_{ik} takes care of omitting the $\nu_{ik}\nu_{jk}$ with i = j. For a given event k the mean value $\bar{\nu}_k$ can be introduced

$$\sum_{j=1}^{N_k}\nu_{jk} = N_k\,\overline{\nu_k}$$

and one obtains

$$\frac{1}{L}\sum_{k=1}^{L}\sum_{i\neq j}^{N_k}\nu_i\,\nu_j = \frac{1}{L}\sum_{k=1}^{L}N_k\,\bar{\nu}_k\,(N_k\,\bar{\nu}_k - \bar{\nu}_k)$$

$$= \frac{1}{L}\sum_{k=1}^{L}N_k\,(N_k - 1)\,\bar{\nu}_k^2 = (\bar{N}^2 - \bar{N})\bar{\nu}^2 .$$

The last line follows by forming the mean values $\bar{N}$ and $\bar{\nu}$ over a large number of events making use of the fact that N_k and $\bar{\nu}_k$ are uncorrelated and that $\bar{\nu}_k \approx \bar{\nu}$ for N_k large enough. Since $\bar{\nu} = 0$ (because of the definition of W) it is found that this term vanishes.

The remaining first term in Eq. 53 gives

$$\frac{1}{L}\sum_{k=1}^{L}\sum_{p=1}^{N_k}\nu^2{}_p = \frac{1}{L}\sum_{k=1}^{L}N_k\,\overline{\nu_k^2} = \bar{N}\,\overline{\nu^2}$$

with the same arguments as above and therefore one finds

$$\text{var}(n) = \bar{N}\,\overline{(m_p - E_p/w)^2}\,. \qquad (54)$$

Since $\bar{N} = \bar{n}/\bar{m}_p$ the result can be written

$$\text{var}(n) = \frac{\overline{(m_p - E_p/w)^2}}{\bar{m}_p}\,\bar{n}\,, \qquad (55)$$

$$\text{var}(n) = F\,\bar{n} \qquad (56)$$

with

$$F = \frac{\overline{(m_p - E_p/w)^2}}{\bar{m}_p} \qquad (57)$$

the so called Fano factor which is somewhat misleading defined by Eq. 55 in resemblance to the usual formula for a variance of a Poisson distribution var (n) = $\bar{n}$. But here it is more apropriate to think of measuring a given distance with a stick of given length by finding out how often it fits into this distance. If the stick is ideally stiff of length l_o the error will be given by $(\Delta x)^2 = \frac{1}{12} l_o^2$ and independent of the distance to be measured. Now if the stick is somewhat soft and its length undergoes random variations the variance will depend linearly on $\bar{n}$ because the error in each measurement is independent of the other which then leads to an expression of the form of Eq. 55 . However F = 1 has no particular physics meaning and even F > 1 is possible depending how "soft" the stick is.

Following Fano, an estimate of F can be obtained from Eq. 55 by summing over all atomic levels weighted with the cross sections for an energy transfer E_i. The total sum is divided into three sections with

$\sigma_i^{(e)}$: exitation, energy loss E_i ,

$\sigma_i^{(1)}$: ionization with $I_{ion} < E_i < 2\, I_{ion}$ producing one ion pair, and

$\sigma_i^{(2)}$: ionization $E > 2\, I_{ion}$ producing an electron which can ionize again.

Since the electron produced in the third category belongs to the second $m_p = 1$ and $E_p = I_{ion}$ is counted, the final formula reads

$$F = \frac{\sum_i \sigma^{(e)} (E_i/W)^2 + \sum_i \sigma_i^{(1)} (1 - E_i/W)^2 + \sum_i \sigma_i^{(2)} (1 - I_{ion}/W)^2}{\sum_i \sigma_i^{(1)} + \sum_i \sigma_i^{(2)}} \qquad (58)$$

For atomic hydrogen, Fano calculated F for two different initial energies, E_e = 100keV and E_e = 1keV, and obtained F = 0.46 and F = 0.42 respectively, which also shows that it is insensitive to the starting energy. For other materials a decreasing F with increasing Z is expected in accordance with measurements as shown in Table III.

Table III

Source	Energy	Absorber	F	Ref.
α	5.68 MeV	Ar+0.8%CH_4	0.19	28
x-ray	5.9 keV	Ar+ 10%CH_4	0.21 ± 0.1	29
x-ray	2.6 keV	Ar+ 10%CH_4	0.31 ± 0.1	29
α	5.03 MeV	Ar+ 10%CH_4	0.18 ± 0.01	30
P	1. ...4.5MeV	Si	0.16 ± 0.04	31

Particle Identification by Measurement of Ionization Loss

Equation 24 shows that the energy loss for relativistic particles first decreases rapidly as $1/\beta^2$ and then increases with $\ln \gamma$. Therefore the measurement of this quantity $< dE/dx >$ would allow particle identification (e.g. mass measurement) if the momentum is measured as well.

For a particle in the region of relativistic rise this method is of particular interest because other techniques such as time of flight are not possible or are not applicable as Čerenkov counters* if the same granularity and double track resolution is required. In the last years a few of such devices have been built and successfully operated but it has been recognized that no miracles help and hard work is necessary. The main problem is the relatively small effect (ca. 18% for π-K-separation and ca. 6% for K-p-separation) compared to the large fluctuation of energy loss in the detector as discussed above. Although most of the fluctuation in thin absorber samples is due to the shell effects, a larger detector thickness where the original Landau formula holds with a resolution of $H_L/E \approx 0.2$ (fwhm) would not be sufficient. Further increases of thickness would only improve logarithmically leading to an unrealistic length of the detector. The solution is found by means of a statistical treatment of the data (Fig. 23). The total length of the detector l is subdivided in n smaller samples with $d = l/n$. In this way n independent measurements are obtained. Forming the mean value of the 40 % smallest signals and discarding 60 % gives a better measurement for the most probable energy loss than all signals combined, which would just follow the curve in Fig. 16.

Investigations based on Monte Carlo calculations show that for the fluctuations $H^{(n)}$ (fwhm) for n samples a simple relation can be found (Ref. 14)

$$\frac{H^{(n)}}{E^{(n)}} = \frac{1}{g^{(n)}} \frac{H^{(1)}}{E^{(1)}} \qquad (59)$$

where $1/g^{(n)}$ is an improvement factor and $H^{(1)}$ and $E^{(1)}$ the width (fwhm) and most probable value of a single sample. If all distributions were Gaussians it would follow $g^{(n)} = \sqrt{n}$, but for typical Landau distributions it is found $g^{(n)} = n^{0.428}$. Figure 24 shows the resolution which can be obtained for a system with n cells and a total length of pl where p is the pressure for argon as counting gas. The lines giving constant resolution of the truncated mean (smallest 40 %) are indicated. It seems that subdividing much below 4 cm·atm does not improve the resolution. This part however corresponds to the part of the resolution curve (Fig. 16) where

* A new development of "ring imaging counters" (Ref. 32) is under way which will be competitive.

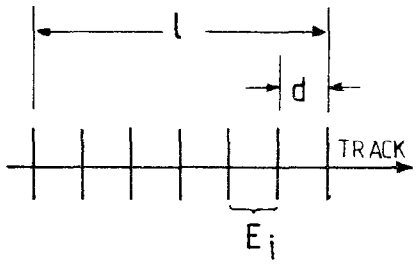


Fig. 23 Ionization sampling (schematically).

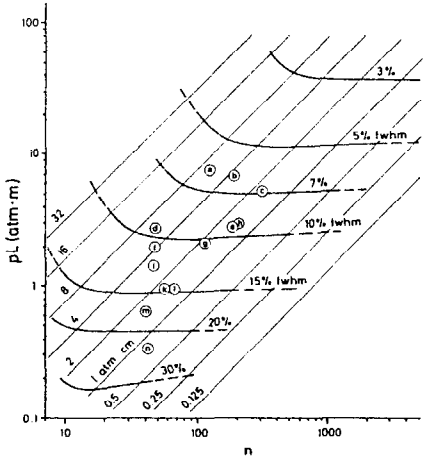


Fig. 24 Resolution obtainable by ionization sampling in Ar. Full lines: constant resolution. See Fig. 23

below $A\rho t/\bar{I} < 2$ the result becomes very sensitive to the shape of the distribution. Here the measured resolution is used which contains in addition to the energy loss spectrum the detector resolution.

As an example for the dE/dx method a detector built primarily for particle identification in e^+e^- collider jet-physics is shown in Fig. 25a. The device is called time projection chamber (TPC)* since the ionization drifts to the endcaps and produces a projected image of the tracks in this plane. The amplifying anode wires are stretched in a spiderweb geometry (Fig. 25b). These wires, 192 per wedge, are used for dE/dx-sampling while 12 per wedge are equipped with a pad readout for position measurement. The momentum of the particles is measured by the curvature due to the axial magnetic field (parallel to the drift). In order to accomodate an effective particle identification into the rather limited space inside the calorimeter the detector is operated at ca. 10 atm pressure. According to the diagram (point (b)) a resolution of 6.0 % fwhm is expected, 6.3 % fwhm has been measured after careful calibration and elimination of systematic errors.

*References and discussion of other devices are given in Ref. 53, 54, 12.

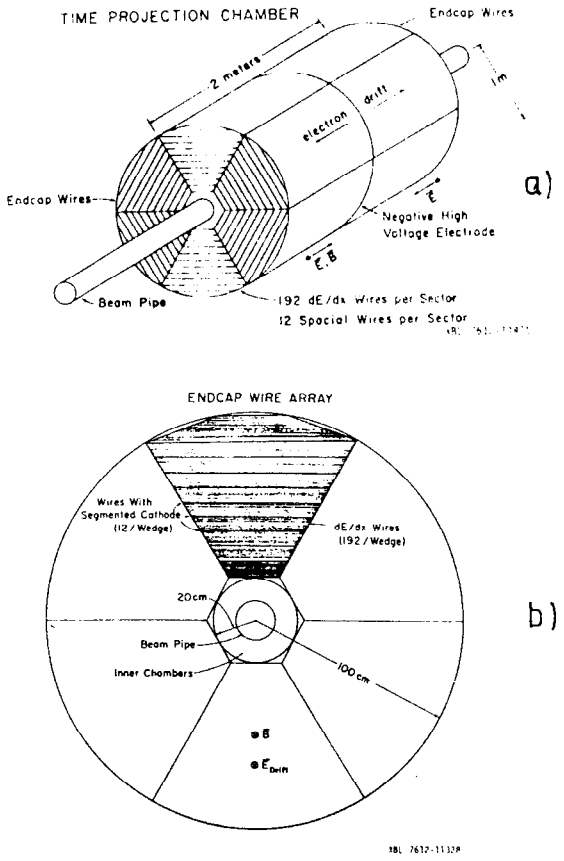


Fig. 25 TPC: a) general layout and
b) endcap .

Another method of particle identification making use of the relativistic rise measures the number of clusters produced in the primary ionization. This has been investigated in some detail with a streamer chamber and also with the time expansion chamber. The advantage would be the considerably reduced fluctuations given by Poisson statistics. A resolution of 6 % fwhm can be obtained for a measurement of $n_{prim} = 1500$ clusters which are produced in 1 m of argon at atmospheric pressure reducing the necessary absorber thickness by one order of magnitude. The sensitivity for particle identification however turns out to gain less drastically because the relativistic rise decreases. This can be easily understood if one realizes that most of the clusters are produced from ionization of the M-shell which saturates at $\beta\gamma \simeq 100$. Calculations (Ref. 22,33) predict a total relativistic rise for argon ranging from $n_{plateau}/n_{min} = 1.30$ to 1.41. Experimental values for He in a streamer chamber (Ref. 5) agree quite well while the values for the drift chamber (time expansion chamber) of $n_{plateau}/n_{min} = 1.17$ is much smaller, probably due to experimental shortcomings. Still, if these technical problems can be solved, a detector with higher resolution power should be possible.

Drift and Diffusion

Because of the much faster drift velocity and because of the easy detection by an avalanche as compared to ions only drifting, electrons are of interest in track detectors. The slow ions represent a nuisance because they only slowly clear the drift volume and may disturb the drift field by building up a space charge.

The electrons drifting under the influence of an electric field can be described separately by their random motion and by their collective motion, the drift velocity. The first is characterized by the mean energy $\varepsilon = \frac{3}{2} kT$ and gives rise to diffusion while the second is given by the drift velocity $\vec{w} = \mu\vec{E}$ with μ the mobility and $\vec{E}$ the electric field strength. The total current is given by the sum of the drift current and the diffusion current

$$\vec{\Gamma} = n\vec{w} - D\,\mathrm{grad}\, n \qquad (60)$$

with n the density and D the diffusion coefficient. Because the total number of electrons is conserved, the continuity equation holds

$$\frac{\partial n}{\partial t} + \mathrm{div}\,\vec{\Gamma} = 0. \qquad (61)$$

In detectors the development of a given initial charge distribution $n(t_o)$ as a function of time is of interest. With a homogenous electrical field $\vec{E}$ and a constant drift velocity $\vec{v}$ where only the components in z-direction differ from zero, one obtains with (60) and with (61)

$$\frac{\partial n}{\partial t} = -\frac{\partial z}{\partial t}\frac{\partial n}{\partial z} + D\,\mathrm{div}\,\mathrm{grad}\, n. \qquad (62)$$

With the product ansatz $n(x,y,z,t) = n^{(s)}(x,y,z)n^{(t)}(t)$ the equation can be solved and one obtains

$$n(x,y,z,t) = \frac{1}{8(\pi Dt)^{3/2}} \int_{\circ}^{\infty} n(x',y',z') \cdot \exp\left[-\frac{(x-x')^2+(y-y')^2+(z-w_z t-z')^2}{4\,Dt}\right] dx'\,dy'\,dz' \qquad (63)$$

where $n(x',y',z')$ for $t=0$ is the initial distribution.

If we start with a δ-function at a given time, a Gaussian distribution with $\sigma^2=2Dt$ is found (Fig. 26). A collecting electrode represents a boundary condition which would have to be incorporated into the above calculation and would give, at the position z_D of the collected charge, a somewhat distorted distribution. If the maximum of the detected current is measured at t_m the error in position will be $\Delta z = Z - w_z t_m$ when w_z is the drift velocity for the centroid of the cloud as used above. This error will be of the order of the diffusion $\Delta\sigma$ which occurs during

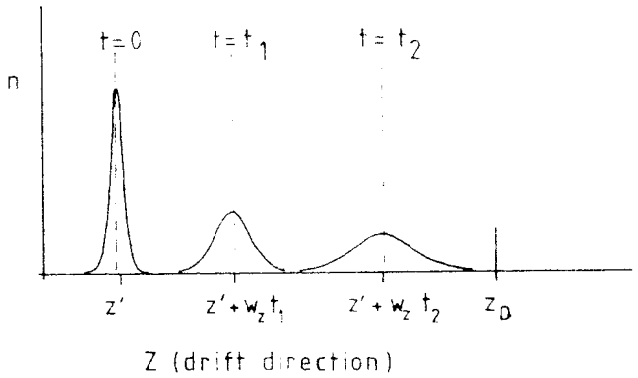


Fig. 26 Density distribution of drifting electrons. Z_D position of electrode.

accumulation of the charge $\Delta t=\sigma/w_z$. Since σ/z is small one obtains

$$\Delta z = \Delta\sigma \approx \frac{1}{2}\frac{\sigma}{t_m}\Delta t = \frac{1}{2}\frac{\sigma^2}{z} . \qquad (64)$$

This number is typically of the order of a few microns and can be neglected.

Determination of Drift Parameters

As shown above the drift velocity $\vec{w}$ and the diffusion coefficient D describe the behavior of drifting electrons sufficiently well. These quantities depend on a number of experimental parameters which will be described in the following. The behavior of the electrons is fully described if the phasespace density $nf=n(\vec{r},t)f(\vec{c},\vec{r},t)$ is known.

Then for the drift velocity one obtains when for simplicity only one component is chosen (z-direction),

$$w_z = \frac{1}{N}\int_0^\infty c_z \, nf \, d^3r \, d^3c . \qquad (65)$$

Since all velocity vectors defining a cone with an opening angle ϑ with respect to z (see Fig. 27) contribute the same c_z it can be integrated over the ring and it follows

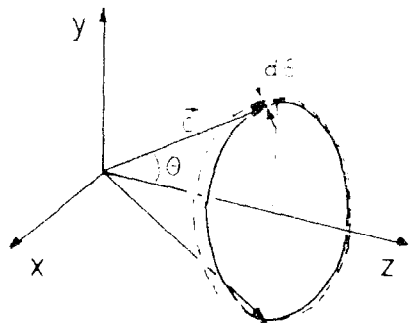


Fig. 27 Integration in velocity space. See text.

$$w_z = \frac{1}{N} \int_0^{\infty}\int_0^{\infty}\int_0^{\pi} c \cos\theta\, n f\, d^3r\, 2\pi c^2 \sin\theta\, d\theta\, dc \,. \quad (66)$$

If $f(\vec{c},\vec{r},t)$ is isotropic in $\vec{c}$ as for example the Maxwell distribution, the integration over $d\theta$ can be separated

$$w_z = \frac{2\pi}{N} \int_0^{\infty} c^3 f\, n\, d^3r dc \int_0^{\pi} \cos\theta \sin\theta\, d\theta = 0 \quad (67)$$

and the drift velocity vanishes. In order to allow for a drift velocity, $f(\vec{c})$ has to be anisotropic which usually is achieved by applying an electrical field. An expansion of f in Legendre polynomials is suitable $f = f_0 + f_1 \cos\theta + \ldots$.

Retaining the first two terms the drift velocity is

$$w_z = \frac{4\pi}{3} \int_0^{\infty} c^3 f_1\, dc \quad (68)$$

and depends only as expected on the anisotropic part of f. As we will see later the diffusion will be mostly determined by f_o.

For determination of f, the Boltzmann transport equation is used which can be considered as the continuity equation in phase space

$$\frac{\partial nf}{\partial t} + \mathrm{div}_r \vec{\gamma} + \mathrm{div}_c \vec{g} = \frac{\partial f}{\partial t}\Big|_{coll} , \quad (69)$$

where $\vec{\gamma} = \vec{c}\,nf$ is the current in configuration space, $\vec{g} = (\vec{a} + \vec{\omega}_b \times \vec{c})nf$ the current in velocity space with $\vec{a} = \frac{e}{m}\vec{E}$ and $\vec{\omega}_b = \frac{e}{m}\vec{B}$ and $\frac{\partial f}{\partial t}|_{coll}$ the change of the velocity distribution due to collisions. The solution is not straightforward and therefore usually a number of simplifications are applied. Here we follow the treatment of Uman and Warfield (Ref. 34) because their treatment includes mixture of gases which are important for detectors.

The assumptions are:

a) $\frac{\partial nf}{\partial t} = 0$, since the system is in equilibrium;

b) $\text{grad}_r nf = 0$, the spatial variation of the electrons is neglected

c) $T = 0$, the gas temperature is neglected;

d) no interaction between electrons; and

e) $f = f_o + f_1 \cos\theta$ with $\theta = \sphericalangle(\vec{c}, \vec{E})$, $\vec{B} = 0$.

This simplifies the Boltzmann equation considerably

$$\frac{eE}{m}\frac{\partial f}{\partial(c\cos\theta)} = \frac{\partial f}{\partial t}|_{coll}, \tag{70}$$

or written explicitly

$$\frac{eE}{m}\left[\cos\theta\,\frac{\partial f_o}{\partial c} + c\cos^2\theta\,\frac{\partial}{\partial c}\left(\frac{f_1}{c}\right) + \frac{f_1}{c}\right] = \frac{\partial f}{\partial t}|_{coll}. \tag{71}$$

The evaluation of the collision term is somewhat long and will not be reproduced here but it is important to note that the gas no. 1 only contributes elastic encounters

$$\frac{\Delta C_1}{C_1} = \frac{m}{M_1}(1-\cos\omega) \tag{72}$$

and gas no. 2 makes inelastic encounters

$$\frac{\Delta C_2}{C_2} = b\,\frac{m}{M_1}(1-\cos\omega) \tag{73}$$

where ω is the scattering angle and b a parameter controlling the degree of inelasticity. With the concentration N_1 and N_2 the momentum transfer cross sections σ_1 and σ_2 and $\varepsilon = \frac{1}{2}mc^2$ the two energy equations are obtained by equating terms containing cos θ separately:

$$eE\,\frac{\partial f}{\partial c}o = -mc\,f_1\,(N_1\sigma_1 + N_2\sigma_2) \text{ and} \tag{74}$$

$$eE\,f_1 = \frac{6m}{M}\,\varepsilon\,f_o(N_1\sigma_1 + bN_2\sigma_2). \tag{75}$$

These equations allow an immediate interpretation. The first represents the momentum balance the second the energy balance.

Furthermore these equations are used for the calculation of f_o and f_1:

$$f_o(c) = A \exp[-\frac{3m}{M} (\frac{m}{e})^2 (\frac{N_{tot}}{E})^2 \int_o^c c^3 \sigma^2_{tot} b_{tot} dc \text{ and}$$

$$f_1(c) = \frac{3m}{M} \frac{m}{e} \frac{N_{tot}}{E} \sigma_{tot} b_{tot} c^2 f_o$$

with

$$N_{tot} = N_1 + N_2$$

$$\sigma_{tot} b_{tot} = \frac{N_1\sigma_1 + bN_2\sigma_2}{N_{tot}}; \quad \sigma_{tot} = \frac{N_1\sigma_1 + N_2\sigma_2}{N_{tot}} \tag{76}$$

and A is defined by the requirement of normalization.

A few simple cases can be considered. Interestingly for $\sigma_{tot} b_{tot}$ = const. one obtains not a Maxwellian distribution form but

$$f_o(c) = A e^{-(\frac{c}{\alpha})^4} \tag{77}$$

which is the Druyvesteyn distribution. For $\sigma_{tot} b_{tot} \propto c^{-2}$ it follows the Maxwell distribution.

The drift velocity follows from inserting Eq. (76) into (68)

$$\vec{w} = \frac{4\pi}{3} \frac{e\vec{E}}{N} \int_o^\infty \frac{c^3}{\sigma_{tot}} \frac{\partial f_o}{\partial c} dc. \tag{78}$$

The derivation of the diffusion coefficient is less straightforward and involves the transformation of the Boltzman equation into the diffusion equation (see for example Ref. 35). With similar assumptions as for the assumption that f_o does not depend on position (which generally is not true and leads to the effect that the diffusion is not the same in all directions, see below); one obtains the usually quoted relation for the diffusion coefficient

$$D = \frac{4\pi}{3} \frac{1}{N} \int_o^\infty \frac{c^3}{\sigma_{tot}} f_o(c) dc. \tag{79}$$

It is convenient to define the mobility $\vec{\mu} = \vec{w}/E$ and then one finds

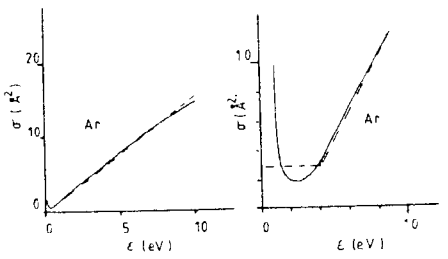
$$D/\mu = \frac{F}{e} \frac{1}{2} \overline{mc^2} = \frac{F}{e} \varepsilon \tag{80}$$

where F is a factor depending on the distribution function f_o. One finds $F = \frac{2}{3}$ for a Maxwell distribution and $F = 0.7628$ for a Druyvesteyn distribution. Usually the

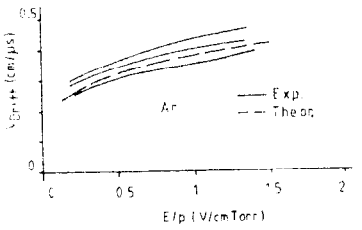
characteristic energy $\varepsilon_k = eD/\mu$ is quoted which is accessible to measurements. For calculations of ε in simple models involving mean values, $F = \frac{2}{3}$ is sufficient.

Often the approximation of a Druyvesteyn or Maxwell distribution is not sufficient. For more precise calculations of the drift parameters the knowledge of $\sigma(c)$ and $b(c)$ (or as a function of energy) is necessary. For some gases these quantities are measured and for evaluation of the integrals they are approximated (Fig. 28) giving the results shown in Fig. 29. Similar calculations have been performed by other authors (Ref. 36). The agreement with measurements is of the same quality as the different measured values between themselves reflecting the fact that the origin of the cross section and b (which can be replaced by an inelastic cross section) are frequently these measurements themselves.

A major discrepancy of these calculations and measurements, however, have been found by Wagner, Davis and Hurst (Ref. 37) showing that the diffusion measured with their apparatus in time of flight techniques (TOF) can be different by a sizeable factor from the diffusion measured perpendicular to the drift velocity. Since the latter agreed quite well with calculations as described above the conclusion was that the diffusion is not described by one diffusion constant D but more precisely by a tensor. For most applications it is sufficient (and the



a)



b)

Fig. 28 a) Momentum transfer cross section as a function of mean energy. Measurement (solid line) and approximation (dashed line).
b) Drift velocity over reduced field strength. Argon pure.

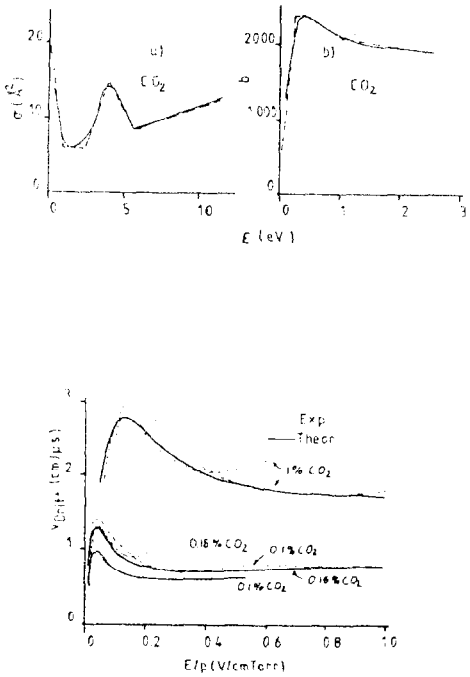


Fig. 29 Same as Fig. 28 but for Ar-CO_2 mixtures.

calculations are already difficult enough) to use only two values the "old" one D_o transverseto the direction of drift and D_L the longitudinal diffusion coefficient parallel to the direction of drift. In order to incorporate this effect into the calculation we have to go back to the Boltzmann equation and solve it without neglecting the term $\mathrm{div}_r \vec{c}nf$ which depends on the variation of $\vec{c}nf$ asafunction of position. A comprehensive treatment of this equation is given by Ref. (38). Some of the results are shown in Fig. 30. The calculation reproduces correctly even a quite complicated behavior for Ar. At low E/N the longitudinal diffusion D_L is found to be larger than the transverse diffusion D_o but at $E/N \approx 3.5 \cdot 10^{-20} Vcm^2$ the situation changes drastically and now D_L is much smaller than D_o up to high values of E/N.

A perceptual explanation can be given by a closer look at the drifting and diffusing cloud of electrons (Fig. 31). For electrons, being ahead of the center of the cloud the diffusion current will add to the drift current and for those being behind, it will subtract. This will alter the energy distribution in the leading part and increase the mean value while the mean value in the trailing part will decrease. If the drift velocity depends on the mean electron energy a compression or dilatation of the cloud depending on the sign of $W(\varepsilon)$ will be the result. Simple calculation with this mean electron model

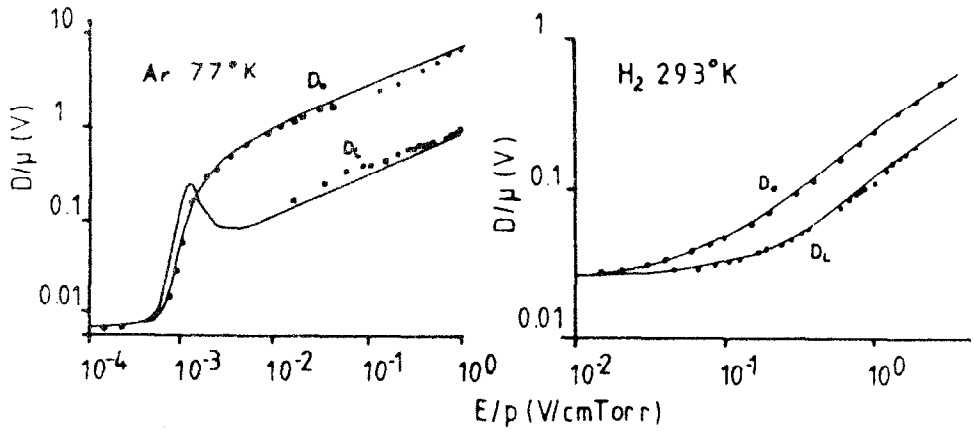


Fig. 30 D/μ as a function of reduced field strength.
• measured, - calculated. D_L parallel to drift velocity, D_o perpendicular.

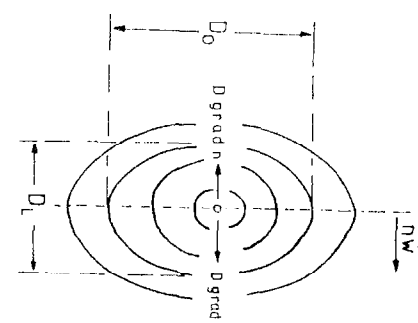


Fig. 31 Anisotropic diffusion (schematically)

(Ref. 38) gives

$$\frac{D_L}{D_o} = \frac{1}{2}\,\frac{3+1}{2+1} \qquad (81)$$

when the total cross section as function of energy can be approximated by

$$\sigma = \sigma_o \left(\frac{\varepsilon}{\varepsilon_o}\right)^{1/2} . \qquad (82)$$

A calculation based on thermodynamical calculations (Ref. 39) gives the somewhat different result

$$\frac{D_L}{D_o} = \frac{1}{1+2} \quad . \qquad (83)$$

Table IV compares the two formulas for selected values of 1.

Table IV D_L/D_o

1	Eq. 82	Eq. 83
-1	1	1
0	3/4	1/2
1	2/3	1/3
1->∞	1/2	0

The truth is expected to be in between both predictions since the limiting value $D_L/D_o = 0$ certainly is unrealistic while measurements give smaller values than calculated by Formula (82). For Ar one finds above the Ramsauer minimum 1=2.25 (Fig. 28) and values of $D_L/D_o = 0.285$ and $D_L/D_o = 0.26$ (Ref. 40) (see Fig. 32) have been found.

Position Measurement

The best track reconstruction from the ionization clusters left behind by a minimum-ionizing particle can be obtained by visualization of each individual cluster and by fitting a trajectory through the points. This is the method which was successful in recording events in bubble chambers. A similar approach is made in streamer chambers. In electronic detectors this direct visualization is not possible. Here the charge is collected on an anode wire and multiplied in the neighborhood of the wire. The position read-out performed by some means (charge division, delay line or drift time) determines the position of this collected charge. Therefore the position measurement in these detectors is performed after a mapping process controlled by the geometry of the field lines. In principle two different projections of the track are possible with respect to the anode wire. The view from the side of the anode wire (Fig. 33a) shows that the center of gravity of the distributed charge would be the

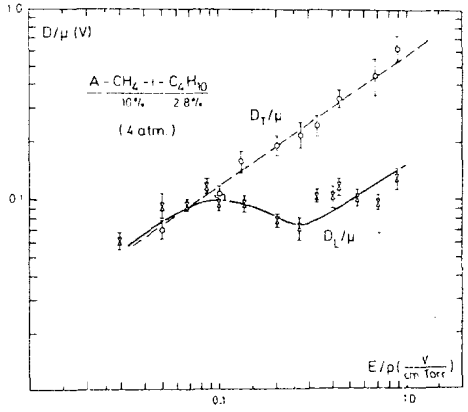


Fig. 32 Measured diffusion parallel (D_L) and perpendicular (D_T) to drift velocity

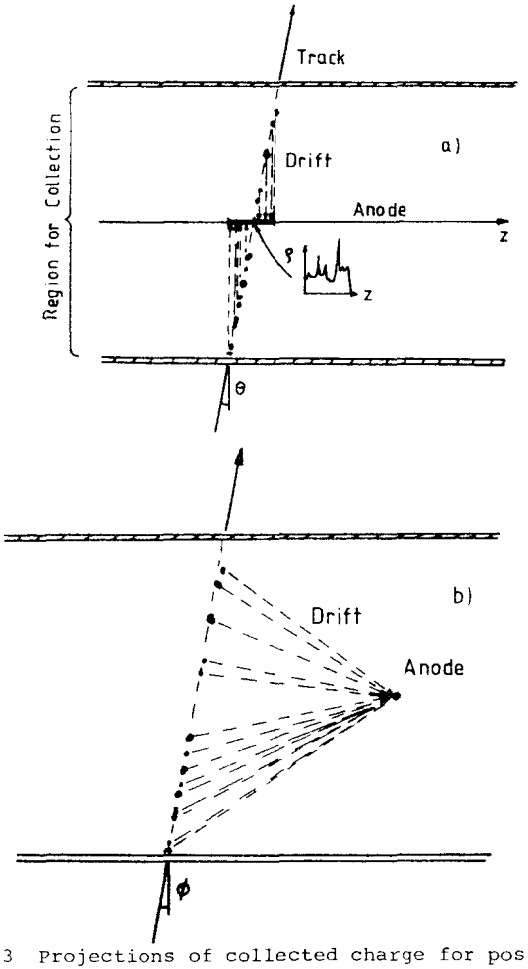


Fig. 33 Projections of collected charge for position measurement. Measured coordinate a) along anode, b) perpendicular.

first guess of the position of the particle at the height of the anode and this is indeed what is measured in the usual techniques of charge division, delay line or centroid method. The view along the anode shows a projection where the best guess of the particle trajectory is given by shortest distance from the anode. In this projection the drift time of the ionization arriving at the anode is recorded (Fig. 33b). Later arriving clusters do not contribute to the track reconstruction. The limits of position resolution in these two cases are caused by the same basic effects but the aspects are so different that they are treated separately.

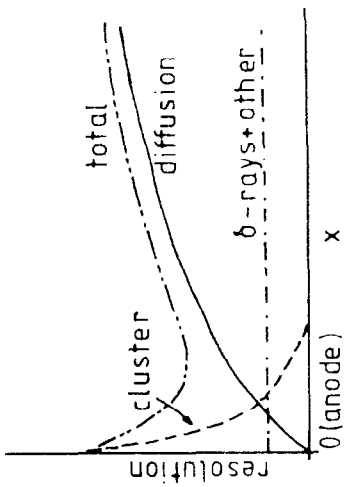
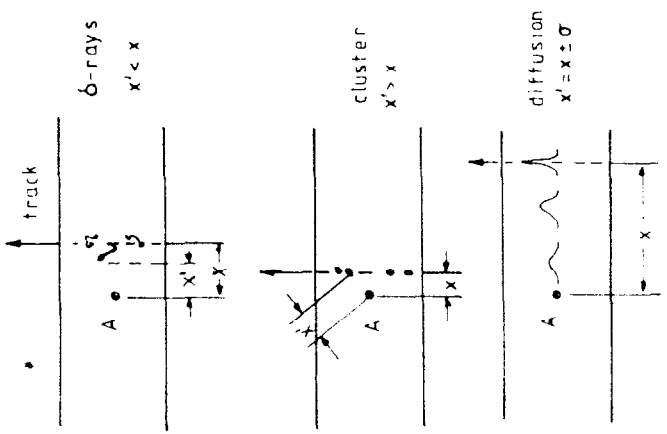


Fig. 34 Principal limitations of position resolution (schematically):
a) individual contributions,
b) dependence on drift path x .

Limits in Drift Chambers

Figure 34 shows the principal limitations of the drift time measurement. They are the range of δ-rays, the finite density of clusters distributed along the track and finally the diffusion defining the inherent precision of calculating the drift distance by measuring the drift time.

Originally those rays were called δ-rays where the energetic electrons produced by the ionization process protruded from the dense track in emulsions and bubble chambers like thin hairs. In a generalization, each electron ejected from the atom due to the interaction of



the charged particle is called δ-ray with an energy E' (Eq. 2) forming a cluster of size E'/W due to further ionization. The spatial extension of this cluster or the range of the δ-ray is a function of the energy E'. If this energy is just above ionization threshold I_{ion} one single electron is produced and its location cannot be described by the range of a charged particle but by a hot electron which will be thermalized quickly in a few tenths of a nanosecond (Ref. 41). With a diffusion constant $D \approx 1/3 \lambda_e \bar{c}$; $\lambda_e \approx 0.1$ µm and $t = 10^{-10}$ a deviation of $\sigma \approx 3$µm is estimated for a typical counting gas at atmospheric pressure. For semiconductors because of their much higher density even smaller values are expected.

For the other cases $E' >> I_{ion}$ the δ-ray behaves like a low energy particle with a reasonably well defined range. Absorption measurements with foils give a sharp decreasing probability for transmission which allows the definition of a "practical" range by extrapolating the steepest slope as shown in Fig. 35. The results of several authors agree well and are reproduced in Fig. 36. For E'>10keV an almost quadratic dependence on E' is found for E'<10keV it becomes almost linear.

For an evaluation of this effect for the position resolution on the detector, this range-energy relation has to be applied to the distribution of energy E_δ of the

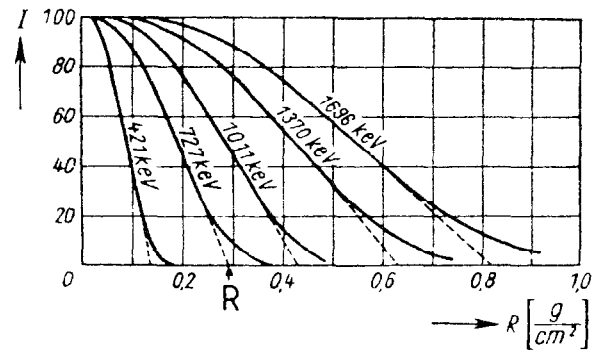


Fig. 35 Absorption of electrons in Al. The practical range R is the extrapolated value.

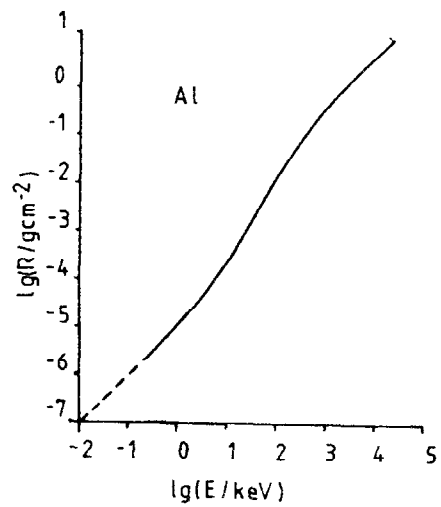


Fig. 36 Practical range for electrons of energy E. Best fit through measurements.

δ-rays. For $E' >> E_K$ where E_K is the energy of the K-shell the simple Formula (5) can be used and it can be further simplified by putting $E_\delta = E' - E_K$ since most such encounters will involve the K-shell electrons. For 1 cm Ar at 1 atm the probability of such an event is 3.2 %. The probability of such events with a range exeeding a given value is shown in Fig. 37 and one finds only a few percent with R > 100μm. This is compatible with the finding of Ref. 42 where it could be shown that the precision of a track fit through n points from n independent measurements by n wires improves as $1/\sqrt{n}$ when only a small fraction of hits with presumably large δ-ray ranges are removed (Fig. 38).

The remaining range of energies $I_{ion} < E' < E_K$ to be discussed is for high resolution detectors, the most important but the least known. Here the resonant effects will dominate and a simple calculation using Eq. (5) will give wrong results in a similar way as has been discussed for the fluctuations of energy loss where the "Landau-solution" was too small by a sizable factor. Fortunately in the case of δ-ray range the resonant effects will shorten the range. From Fig. (18) for example it can be seen that most clusters are produced by M-shell ionizations with $E_\delta \lesssim 100$eV resulting in a range of $R \lesssim 5$μm. The L-shell ionizations with a probability of the order of 10 % has important contributions up to

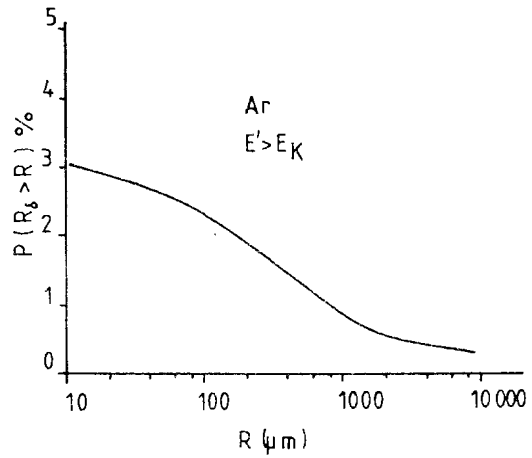


Fig. 37 Probability for a δ-ray with range $R_\delta > R$.

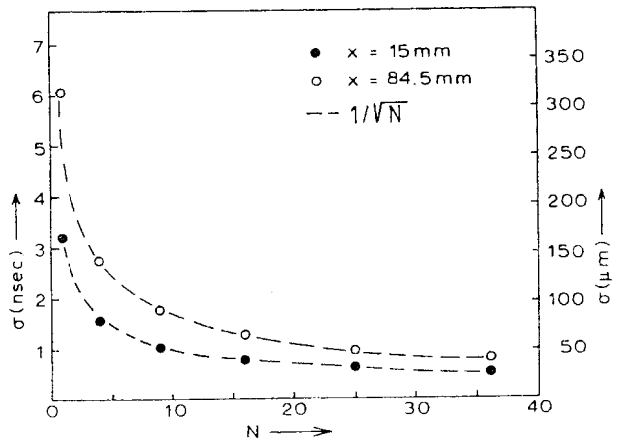


Fig. 38 Equivalent resolution of n drift wires (straight line fit). Measured and $1/\sqrt{n}$ dependence.

$E' \gtrsim 0{,}5$ keV resulting in $R \gtrsim 40$ µm and will therefore be the dominant contribution.

Since $R \sim E_\delta$ in the low energy domain the weighting of the contribution of individual shells to the mean range $\bar{R}$ can be done in the same way as the energy loss, and a dependence of $R \sim \bar{I}$ with $\bar{I}$ the mean ionization potential as defined in the Bethe-Bloch formula is expected. An indication of this effect can be seen in the measurements given in Ref.43. Here the measured resolution (Fig.39) can be extrapolated to x = 0 eliminating the effects of diffusion and cluster distribution leaving a contribution A of other errors including the range of δ-rays. The values in Table V reveal a clear effect of decreasing A with decreasing $\bar{I}$. Furthermore it is surprising that for these A values no explicit pressure dependence could be found which can be explained by realizing that the rare events with large E' start to become likely at higher pressure and then they give rather large errors which have not been suppressed in this measurement.

Table V

Gas	0.9 Ar 0.1 CH_4	0.6 Ar 0.33 C_4H_{10} 0.07 CH_4	0.3 Ar 0.67 C_4H_{10} 0.03 CH_4	C_2H_4	C_3H_8	0.75 C_2H_4 0.25 C_3H_8
A (µm)	55	55	42	35	25	20
$\bar{I}$(eV)	191	114	71	52	48	51

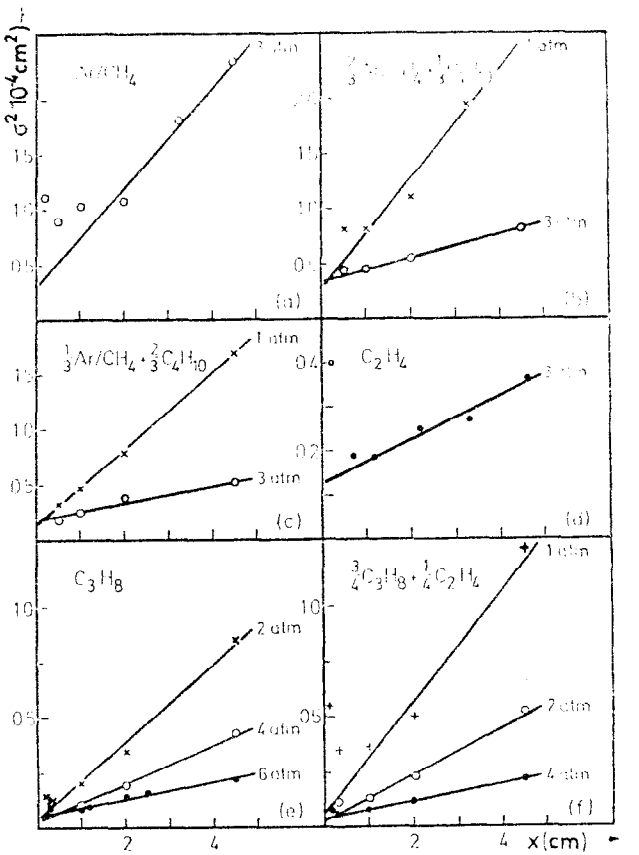


Fig. 39 Measured resolution. Extrapolated to zero diffusion.

The second effect from Fig.34 due to the random distribution of a finite number of clusters along the track contributes most for tracks passing directly over the anode. Then a typical exponentially decreasing drift time distribution is obtained as has been used above for determination of the mean number of clusters per track length $\bar{n}$ (Fig.4). Since clusters can reach the anode from both sides the mean error $\overline{\Delta x} = 1/2\bar{n}$. For tracks passing at a larger distance x from the anode wire the error becomes smaller. Assuming that the closest cluster to the anode drifts on a straight line with constant drift velocity to the anode the contribution of this cluster effect is shown in Fig.40. This explains the considerable improvement of resolution near the anode for increased pressure.

The diffusion will give a contribution which is precisely Gaussian and increasing with $\sqrt{x}$ (see Eq.3). The broadening of a drifting electron cloud can be directly observed in the time expansion chamber. Figure 41 shows the signals obtained from an ionization cluster produced by an x-ray from an Fe^{55} source (ca. 230 electrons) for a driftlength of x = 20 mm as function of the applied drift field. Calculation of the spatial width $\sigma = v_{Dr} \cdot \Delta t$ (Fig.42) shows that the width Δt of the signal is mainly determined by diffusion.

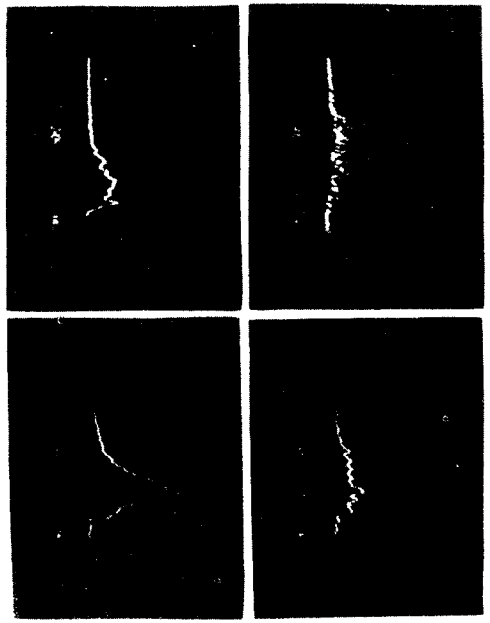


Fig. 41 Signals from time expansion chamber for pointlike ionization (^{55}Fe) for E = A) 200 V/cm B) 100 V/cm C) 50 V/cm D) 10 V/cm.P-10 + 8 % methylal.

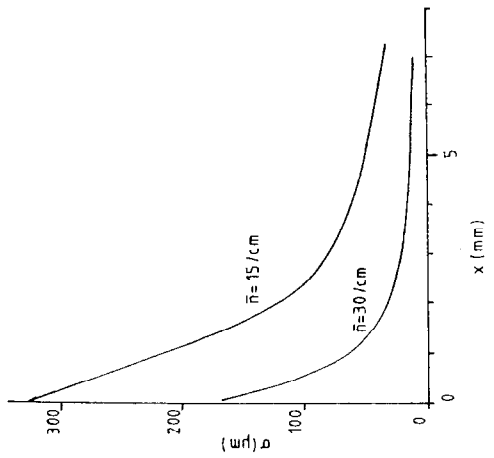


Fig. 40 Contribution of cluster effect as function of drift distance

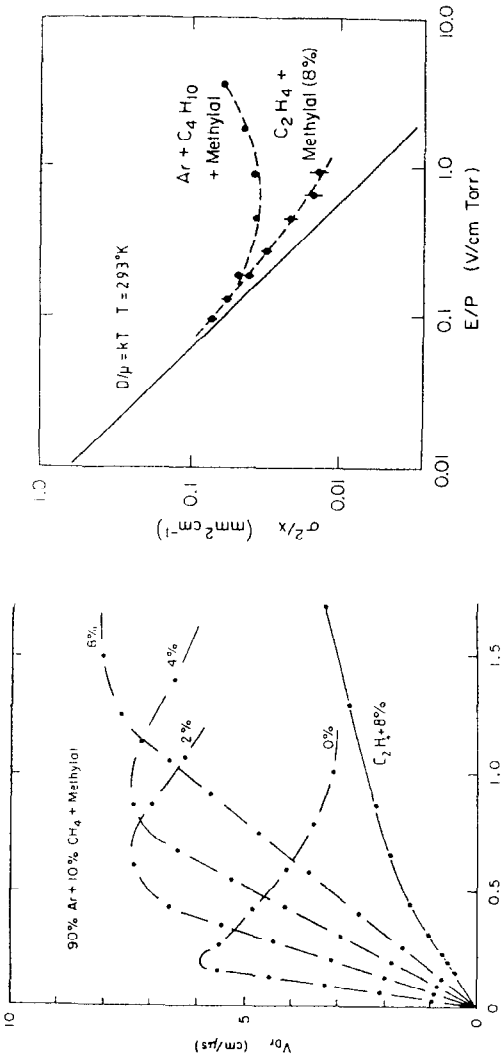


Fig. 42 a) Drift velocity for a methylal admixture (%).
b) Diffusion measured in TEC (•), from Ref. 45 (--).

In a standard drift chamber the best resolution has been found at the lowest possible threshold which agrees with the interpretation that the first arriving electron has the smallest dispersion. If a single electron has a Gaussian probability distribution $g(\tilde{x})$ to arrive with a deviation $\tilde{x} = x/\sigma_o$ from the mean drift distance expressed in units of the variance σ_o, the probability distribution for the first out of n will be

$$f_{1st}(\tilde{x}) = ng(\tilde{x})[e(\tilde{x})]^{n-1} \qquad (84)$$

where $e(\tilde{x})$ is the error function. Figure 43 shows this distribution for different values n. For $n = 1$ the Gaussian is reproduced. For larger n the distribution becomes narrower. For large n an approximation for the standard deviation can be used (Ref.44)

$$\sigma_{1st} = \frac{\pi}{2\sqrt{3 \ln n_e}} \sigma_o \qquad (85)$$

However one should be careful in applying this formula because in general for n_e the total number of collected electrons cannot be used. Only a small fraction may be within the desired precision close to an isochronous line (Fig.44) which may be of the order of 1 mm. Further-

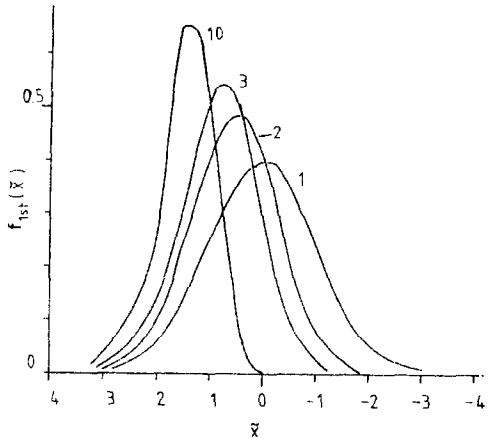


Fig. 43 Arrival time distribution for 1st of n (indicated on curves) electrons.

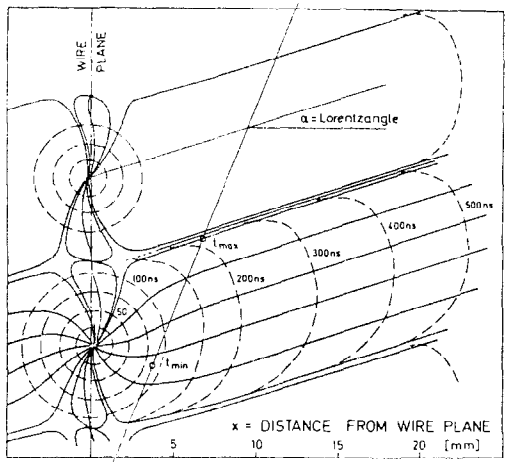


Fig. 44 Drift path (-) and isochronous lines (--) in the JADE chamber

more it has to be realized that increasing n_e does not only improve the width of the distribution but also changes its position. Since individual signals from minimum-ionizing particles have very large fluctuations the resulting shift in the mean value may offset the gain in width. A good guess of the resolution therefore would be the value of diffusion for a single electron but measured values are usually better (Ref.43) and sometimes considerably better (Ref.44) and therefore some unknown averaging mechanism may play an important role.

Despite these uncertainties the best resolution will be obtained if the center of gravity of the diffusing cloud can be measured (Ref. 45). In several laboratories tests have been made to improve the resolution using constant fraction discriminators but at best the values of the leading edge could be obtained. One reason for this negative result is the curved field lines converging on the anode wire and therefore,in connection with the random cluster distribution,fluctuations are introduced. The other reason is that the gas amplification and signal formation are not fast enough to resolve,under normal operating conditions,the diffused cloud. With good clipping of the signals of $\Delta t \approx 50$ ns,structures just barely can be resolved which correspond to a drift path of $\Delta x = 2.5$ mm at standard drift velocity. Also the information on the center of gravity of the charge distribu-

tion usually is distorted by the gas amplification process showing saturation or other space charge controlled effects.

It has been realized that the time expansion chamber in principle can solve these problems (Ref.46). It uses a low unsaturated drift velocity (v_{pr} =5 µm/ns) in drift space and a high field and high drift velocity (ca. 50 µm/ns) near the anode wire. In order to have a well defined separation,a fine grid (mesh) separates the two regions. In this way the fluctuations in drift path length near the anode wire have a reduced influence on the position measurement in the drift space. Furthermore the mesh and the small dimensions of the amplification region in connection with fast low noise preamplifiers (Ref.47) and fast shapers permit the obtaining of an anode signal of ca.15 ns width (fwhm) for a pointlike ionization. Therefore structures of ca. 75 µm in the ionization can be resolved. This arrangement is also able to reproduce the extended spatial structure in the anode signal which can be seen easily for example when the width caused by diffusion is correctly reproduced as shown above (Fig. 45).

First measurements with such a chamber have been made by digitizing the signals every ten nanoseconds with transient recorders. Figure 46 shows the position resolution when the centroid of the pulse train has been

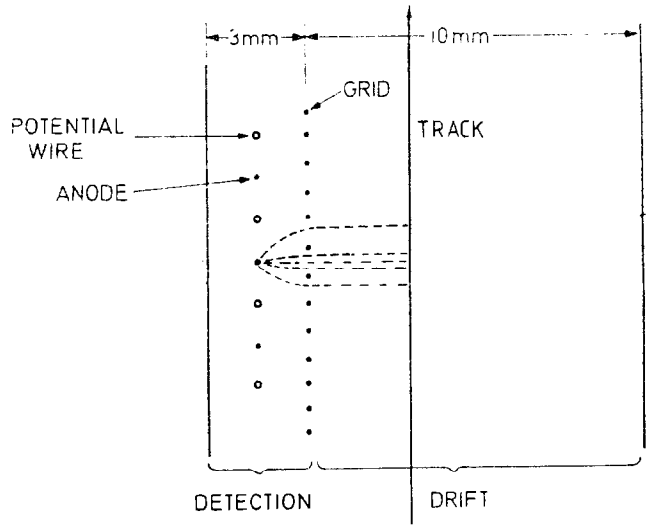


Fig. 45 Time expansion chamber (schematically) Drift path (---).

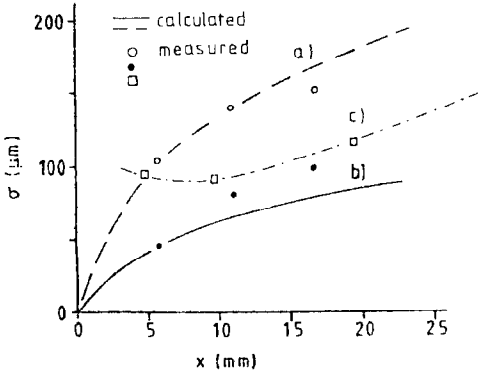


Fig. 46 Position resolution in drift chambers.
a) leading edge in TEC, b) centroid in TEC,
c) leading edge in standard chamber.

calculated (b),and for comparison when the leading edge has been used (a) to determine the drift time. The curves represent the calculated contribution of diffusion if $n_e = 14$ and $\sigma_o = 220$ μm,for gas mixture of Ar-C_2H_6 (50/50)are used and agreement is found. The comparison with directly measured leading edge discrimination (c) (Ref.43) for a gas of similar composition (2/3 Ar + 1/3 C_4H_{10}) shows here again that the latter gives a better resolution than the simple model would predict. Still the centroid method gives the better resolution particularly at small or large drift distance,and it is expected to improve with increasing pressure as 1/p while the leading edge method would follow $1/\sqrt{p}$.

Limits of Position Measurement in Detectors with Projected Tracks

As shown in Fig. 33a the charge from the track can be projected along the anode wire and a number of readout techniques are available for determining the center of gravity. In proportional or drift chambers this includes the method of charge division through the resistive anode wire or by determining the center of gravity of the induced charge on a subdivided cathode. The limitations of the methods are frequently of a technical nature but in principle it can be arranged with a careful design that the physics of the ionization, drift or amplification process limits the resolution. A fundamental treatment of the technical aspects of resolution limited by the noise of the preamplifiers is given in Ref. 48 and a survey is found in Ref. 49. In the following the basic phenomena are discussed for a silicon strip detector but can be generalized easily for gas detectors.

In silicon strip detectors an amplification of free charge carriers is difficult and therefore for a realistic position sensitive detector the simple collection of charge on a subdivided cathode is used for readout. In this case enough free charge carriers have to be produced in order to exceed the input noise of the preamplifiers reading the charge Q on each strip which requires a minimum thickness (see Fig. 47). If the track forms an angle θ large enough that the collected charge is spread over several strips, one obtains for the centroid $\hat{x}$, measured from the first strip to be counted,

$$\hat{x} = \frac{1}{Q_o} \sum_{k}^{K} k d Q_k \qquad (86)$$

where d is the strip pitch, Q_o the total accumulated charge and $1 \leq k \leq K$ with K the maximum number of strips used for calculating the centroid. It is assumed that K is as small as possible in order to avoid collecting

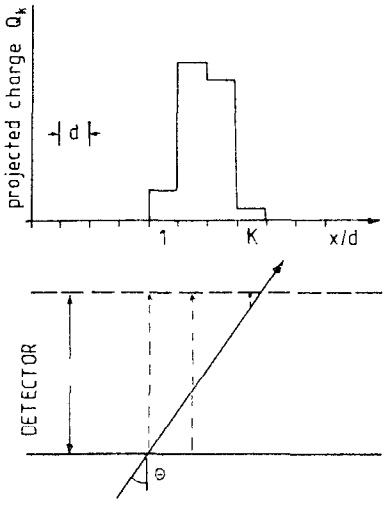


Fig. 47 Calculation of projected charge (schematically).

noise from strips which do not carry signals and therefore it will be used K = B/d with B the total width of the projected charge. The error of the centroid is determined by the noise on each strip ΔQ_k

$$(\Delta\hat{x})^2 = \left(\frac{d}{Q_o}\right)^2 \sum_1^K k^2 (\Delta Q_k)^2 \,. \qquad (87)$$

In a simple model the noise ΔQ_k has contributions from the electronics ΔQ_{kel}, and from fluctuations of ionization ΔQ_{kion} and therefore $(\Delta Q_k)^2 = (\Delta Q_{kel})^2 + (\Delta Q_{kion})^2$. For both sources the dependence on strip width is similar and can be represented by $(\Delta Q_k)^2 = [(\Delta Q_{oel})^2 + (\Delta Q_{oion})^2]/K$ with K the number of strips as defined above and ΔQ_{oel} and ΔQ_{oion} the noise if all K strips are connected together.

For K large, one has $\sum_1^K k^2 \approx \frac{1}{2} K^3$ and therefore the error for the centroid measurement is independent of K

$$(\Delta\hat{x})^2 = \frac{1}{2}\left[\frac{(\Delta Q_{oion})^2}{Q_o^2} B^2_{proj} + \frac{(\Delta Q_{oeJ})^2}{Q_o^2} B^2_{intr.}\right] . \qquad (88)$$

Because of the different sources of the noise the first part contains only the projected width of the track $B_{proj} = s \cdot tg\ \Theta$ which disappears for $\Theta = 0$ and the second

contains some sort of intrinsic width B_{intr} mostly determined by diffusion.

In proportional and drift chambers, particularly in the TPC-like detectors (Ref. 50), the ionization fluctuation dominates because s is quite large and $\Delta Q_o/Q_o$ is the Landau fluctuation extrapolated from small sample width following the $1/\sqrt{Q}$ dependence (Fig. 16). Collecting ionization from 1 cm track length in Ar one finds $\Delta\hat{x}$= 0.3 B and $\Delta\hat{x}$=0.09 B for p = 1 atm and p = 10 atm respectively. For $\theta = 10^0$ and s = 5 mm this means a contribution to position resolution of σ = 260 μm and σ = 78 μm respectively.

For silicon detectors the same calculation gives for s = 280 μm, $\Delta\hat{x} \approx 0.15 \cdot B$ and for $\theta = 10^0$ it follows $\sigma \approx 3$ μm which at the moment is not the limiting contribution but may, with improved read-out, become comparable to other contributions (Ref. 51).

The effects of diffusion and deflection of drift due to a magnetic field are in principle similar as in gaseous detectors and can be observed in the response of such a detector to ionizing radiation in the same way as the transverse diffusion usually is measured (Fig. 48, Ref.52). The charge is collected on two electrodes which are large compared to the diffusion width.

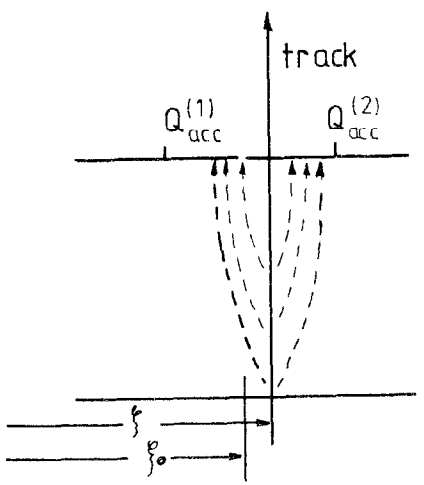


Fig. 48 Arrangement for measurement of collected charge distribution.

The accumulated charge is

$$Q_{acc}^{(1)} = Q_o \int_{-\infty}^{-\xi} f(x)dx \quad \text{and} \quad Q_{acc}^{(2)} = Q \int_{-\xi}^{\infty} f(x)dx \qquad (89)$$

for the first (1) and second (2) electrode. Figure 49 shows the measured quantity $R = Q_{acc}^{(2)} / (Q_{acc}^{(1)} + Q_{acc}^{(2)})$ as a function of $\xi - \xi_o$ with ξ_o an arbitrary offset. From this measured curve, f(x) has been reconstructed (Fig. 50). This distribution has been fitted to Eq. 63 where for the initial distribution a Gaussian is assumed with the variance $\sigma^2 = 2 D_n t_o$, in order to include all other effects formally in such a way as to prolong the drift time by the amount t_o. For the diffusion constant Eq. 80 holds and for the semiconductors of high purity (resistivity ≈ 3 kΩ cm) and an applied field of E = 4.3 kV/cm, the characteristic energy is given by $\varepsilon_K = kT_h$ with T_h the "temperature" of the drifting holes considered here.

With the literature value for the mobility $\mu = 450\ cm^2/Vs$ the fit resulted in $T_h = 390^o \pm 40^oK$ and $t_o = 0.65 \pm 0.35$ ns. The first is in agreement with expectations if the holes are in equilibrium with the lattice, and the second number translates to an intrinsic width of the track of 1.4 ± 0.7 µm which could be explained with a possible non-perpendicular incidence of the particles or with the range of δ-rays.

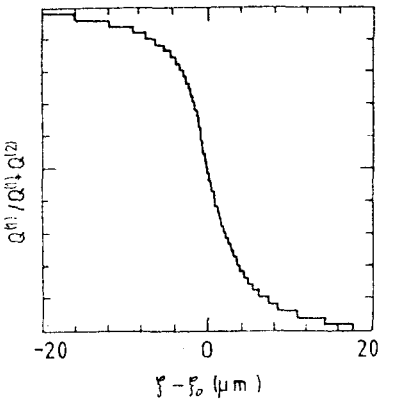


Fig. 49 Ratio of collected charges vs.distance (see Fig. 48).

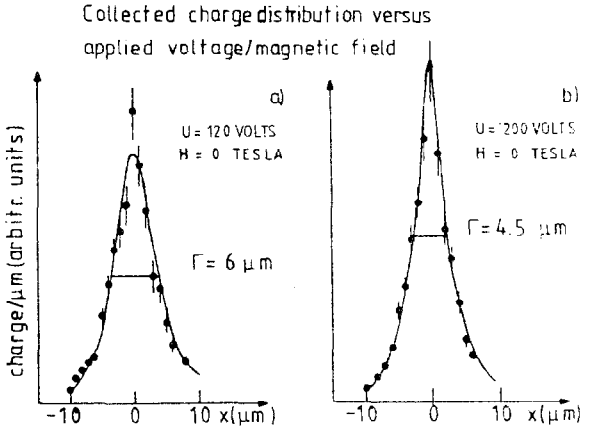


Fig. 50 Measured charge distribution, B = 0 .

Most track detectors will be used in magnetic fields in order to provide a measurement of momentum by measurement of the curvature of the particles. This magnetic field would be perpendicular to the drift direction as shown in Fig. 51 . The Lorentz force acting on the drifting holes causes them to drift under an angle θ_L with respect to the field lines. This Hall-effect is well known and used in semiconductors for a number of applications but occurs in the same way for drifting electrons in gases (see for example Ref. 51). For most detector applications a relation for the deflection angle averaging over the energy distribution of the charge carrier is sufficient :

$$\operatorname{tg} \theta_L = k \frac{e}{m} \frac{B}{E} v_{Dr} \quad (E_{red.}, B=0) \tag{90}$$

where v_{Dr} (E_{red}, B = 0) is the drift velocity at B = 0 and at the value of the reduced field $E_{red} = E \cos \theta_L$. k is a factor of the order of 1 summarizing the effect of averaging over the energy distribution. For semiconductors Eq. 90 written in a different form

$$\operatorname{tg}\theta = \mu_H B \tag{91}$$

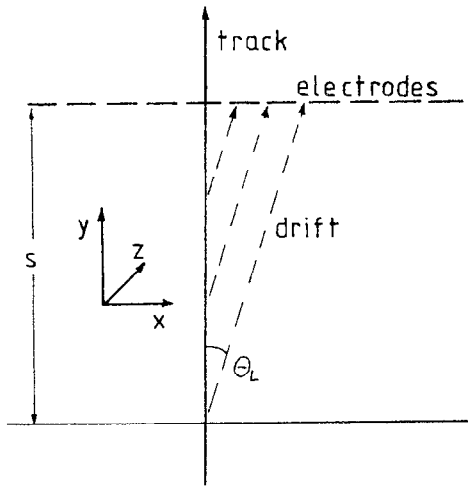


Fig. 51 Collection of charge carriers for a perpendicular magnetic field ($B_x=B_y=0$ $B_z \neq 0$).

where $\mu_H = k\mu\cos\Theta$ is smaller than μ not only because of cos Θ but also because of some small changes in k.

With the magnetic field switched on, the distribution of the collected charge takes into account the deflection through the term $y \cdot \tan \Theta_L$ where y is the coordinate in drift direction over which now has to be integrated

$$f(x) = \frac{1}{4\pi D_h} \int_0^s \frac{1}{t - t_o} \exp\left[-\frac{(x - y\,\mathrm{tg}\,\theta_L)^2}{4D_h(t + t_o)}\right] dy. \quad (92)$$

The fit to the data (Fig. 52) gave the results shown in Table VI.

Table VI

E(kV/cm)	B(T)	$\tan \Theta_L \times 10^3$	μ_H(cm^2/vs
4.28	1.68	58 ± 2.5	310 ± 30
7.14	1.68	56 ± 2.0	300 ± 25

The maximum displacement due to the Hall effect is $\Delta x = s \cdot \tan \Theta_L = 16.2$ µm which is small enough not to disturb the position measurement. For electrons, the Hall mobility of $\mu_H = 1650$ cm^2/Vs would result in a displace-

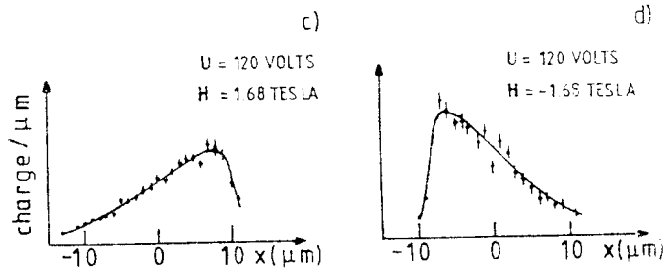


Fig. 52 Measured charge distribution $B_z \neq 0$

ment of $\Delta x = 86$ μm and seriously affect the position resolution.

Conclusion

It has been shown that track detectors for relativistic particles are devices reaching a performance which comes occasionally close to the basic limitations. However the demand for more precise and more sophisticated detectors will stimulate even more investigation of the physics phenomena behind the detectors, which in turn will stimulate the use of new technologies reaching beyond the present limits. One example is the analysis of pulse shape in drift chambers giving additional information about the ionization, another makes use of the denser ionization and good charge collection in semiconductors which now can be produced and read out in an economical way.

References

1. H.A. Bethe, Handbuch der Physik. Bd. 24 S. 273 Berlin: Springer 1933.

2. V.K. Ermilova, L.P. Kotenko, G.I. Merzon and V.A. Chechin, Sov. Phys. JETP 29 (69) 861.

3. F.L. Hereford, Phys. ReV. 74 (48) 574.

4. P. Rehak and A.H. Walenta IEEE Trans. Nucl. Sci. NS 26 No.1. (79) 160.

5. V.A. Davidenko, B.A. Dolgoshein and S.V. Somov, Sov. Phys. JETP 29 (69) 1.

6. V.A. Davidenko, B.A. Dolgoshein, S.V. Somov and V.N. Starosel'tsev, Sov. Phys. JETP 31 (70) 74.

7. J.D. Jackson, Classical Electrodynamics Wiley & Sons, New York 1962.

8. L. Landau, J. Phys. USSR 8 (44) 201.

9. E.L. Goldwasser, F.E. Mills and A.O. Hanson, Phys. ReV. 88 (52) 1137.

10. A.H. Walenta, unpublished.

11. D. West, Proc. Phys. Soc. Lond. 66 (53) 306; Y. Iga, T. Wada, Y. Yamashita and I. Yamamoto, Nucl. Instr. and Meth. 213 (83) 531.

12. A.H. Walenta, Phys. Scripta 23 (81) 353.

13. D.M. Ritson, Proc. of the Summer Institute on Particle Phys. 1980, SLAC - 239 (TIE) UC 34 d P. 177.

14. A.H. Walenta, J. Fischer, H. Okuno and C.L. Wang, Nucl. Instr. and Meth. 161 (79) 45.

15. R.M. Sternheimer and R.F. Peierls, Phys. Rev. 3 (71) 3681.

16. H.D. Maccabee and D.G. Papworth, Phys. Lett. 30A (69) 241.

17. C. Julliot and M. Cantin, Nucl. Instr. and Meth. 157 (78) 235.

18. O. Blunck and S. Leisegang, Z. f. Phys. 128 (50) 500.

19. G. Knop, A. Minten and B. Nellen, Z. f. Phys. 165 (61) 533.

20. R. Talmann, Nucl. Instr. and Meth. 159 (79) 189.

21. K.A. Ispirian, A.T. Margarian and A.M. Zverev, Nucl. Instr. and Meth. 117 (74) 125.

22. W.W.M. Allison and J.H. Cobb, Ann. Rev. Nucl. Part. Sci. 30 (80) 253.

23. H. Sipilä, IEEE Trans. Nucl. Sci. NS 26 No. 1(79) 182.

24. T. Takahashi, S. Konno, T. Hamada, M. Miyajima, S. Kubota, A. Nakamoto, A. Hitachi, E. Shibamura and T. Doke, Phys. ReV. A. Vol. 12 (75) 1771.

25. D. Gebauer, "Aufbau eines Gaszintillationsdetektors und Nachweis einer sekundären Lichverstärkung", Diplomarbeit, Siegen 1980.

26. E. Eggarter, J. Chem. Phys. 62 (75) 833.

27. U. Fano, Phys. Rev. 72 (47) 26.

28. G.D. Alkhazov, A.P. Komar and A.A.Vorob`ev, Nucl. Instr. and Meth. 48 (67) 1.

29. G.S. Hurst, S.L. Allman, M.G. Payne, K.A. Marshall and K.L. Soohoo, Nucl. Instr. and Meth. 155 (78) 203.

30. M. Kase, J. Kikuchi and T. Doke, preprint Waseda University, Tokyo, Japan.

31. T. Yamaya, R. Asano, H. Endo and K. Umeda, Nucl. Instr. and Meth. 159 (79) 181.

32. T. Ypsilantis, Physica Scripta 23 (81) 371.

33. F. Lapique and F. Piuz, Nucl. Instr. and Meth. 175 (80) 297.

34. M.A. Uman and G. Warfield, Phys. Rev. 120 (60) 1542.

35. Huxley, L.G.H. and R.W. Crompton, The Diffusion and Drift of Electrons in Gases, Wiley, New York, 1974.

36. V. Palladino and B. Sadoulet, Nucl. Instr. and Meth. 128(75) 323; G. Schultz and J. Gresser, Nucl. Instr. and Meth. 151 (78) 413; E. Mathieson and N.EL Hakeem, Nucl. Instr. and Meth. 159 (79) 489.

37. E.B. Wagner, F.J. Davis and G.S. Hurst, J. Chem. Phys. 47 (67) 3138.

38. J.H. Parker, Jr. and J.J. Lowke, Phys. Rev. 181(69) 290; J.J. Lowke and J.H. Parker, Jr., Phys. Rev.181 (69) 302.

39. R.E. Robson, Aust. J. Phys. 25 (72) 685.

40. H. Drumm, R. Eichler, B. Granz, J. Heintze, G. Heinzelmann, R.D. Heuer, J. von Krogh, P. Lennert, T. Nozaki, H. Rieseberg, A. Wagner and Warming, Nucl. Instr. and Meth. 176 (80) 333.

41. A. McDaniel, Collision Phenomena in Ionized Gases, J. Wiley & Sons, New York, 1964.

42. U. Becker, M.Steuer, J. Burger and M. White, Nucl. Instr. and Meth. 180 (81) 61; P. Duinker , J.C.Guo, D. Harting, F. Hartjes, L.O. Hertzberger, J. Hoekstra, J. Konijn, G.G.G. Massaro and A.H. Walenta, Nucl. Inst. and Meth. 201 (82) 351.

43. W. Farr, J. Heintze, K.H. Hellenbrand and A.H. Walenta, Nucl. Instr. and Meth. 154 (78) 175.

44. "Application of the Classical Theories of Electrons in Gases to Multiwire Proportional and Drift Chambers", LBL - 3012 (1974).

45. F. Sauli, Nucl. Instr. and Meth. 156 (78) 147.

46. A.H. Walenta, J. Paradiso, H. Hofer, G. Viertel and J. Fehlmann,"The Time Expansion Chamber as High Precision Drift Chamber", Proc. of the Int. Conf. on Instrumentation for Colliding Beam Physics, Stanford 1982, SLAC - 250, UC - 34d P. 34-40.

47. P. DÂngelo, A. Hrisoho, P. Jarron, P.F. Manfredi and J. Poinsignon, Nucl. Instr. and Meth. 193 (82) 533.

48. V. Radeka, IEEE Trans. Nucl. Sci. NS-21, No. 1 (74) 51.

49. M. Atac, Nucl. Instr. and Meth. 176 (80) 1 .

50. C.K. Hargrove, H. Mes, A. Bennett, D.A. Bryman, M. Hasinoff, J.A. McDonald, J.M. Poutissou, T. Numao, J. Spuller, G. Azuelos, R. Poutissou, M. Blecher, K. Gotow and A.L. Carter, Proc. of the Int. Conf. on Inst. for Coll. Beam Physics, Stanford 1982, p. 41.

51. W.P. Allis, Handbuch d. Physik, Vol. 21, Springer, Berlin, 1956, p. 384-444.

52. E. Belau, R. Klanner, G. Lutz, E. Neugebauer, H.J. Seebrumer, A. Wylie, T. Böhringer, L. Hubbeling, P. Weilhammer, J. Kemmer, U. Kötz,and M. Riebesell, preprint MPI - PAE/Exp. EL. 114, Feb. 1983.

53. D.R. Nygren, Physica Scripta, Vol. 23 (81) 584.

54. " Progress in Particle Identification by Ionisation Sampling", I. Lehraus, Invited Talk at the Wire

Chamber Conference Vienna, 1983, CERN/EF 83-3,Feb.83.

55. L.W. Cochran and D.W. Forester, Phys.Rev. 126(62)1785.

A REVIEW OF THE PHYSICS AND TECHNOLOGY OF HIGH-ENERGY CALORIMETER DEVICES

Paul M. Mockett
University of Washington
Seattle, Washington

Contents:

Introduction
Early Calorimetry
Definitions
Longitudinal Shower Profile
Transverse Shower Profile
Total Absorption Calorimeters
Resolution in Sampling Devices
Sampling Losses
Resolution Details
Gas Calorimeters
Dense Sampling Cells
Position Resolution
Hadronic Showers
Missing Energy Compensation
Calorimeter Geometries
Segmentation
Particle Identification
Hadron Calorimeter Technology
Mixed Technologies
Calibration

© Paul M. Mockett 1983

INTRODUCTION

There are a number of excellent reviews on calorimetry available in the literature [Atac 75], [Iwata 80], [Fabjan 82], [Atac 83] and [Engler 83]. In addition, the venerable book, High-Energy Particles, by B. Rossi [Rossi 52] contains most of the fundamental theory needed to understand the basic shower process. These works contain a mountain of useful information on calorimetry as well as a very extensive list of important references on the subject. The present paper has relied heavily on these works and is very much indebted to the efforts of these authors. There are also a number of well documented Monte Carlo programs that have been utilized in this study. EGS [Ford 78] is used a great deal for the study of electromagnetic shower processes. It is maintained by Ralph Nelson at SLAC. HETC and HECC [Gabriel 75] are used for hadronic processes and maintained by T. A. Gabriel at Oak Ridge. MORSE is used when the fission process and low energy neutron and photon transport are of interest [Straker 70].

It is clear that electromagnetic and hadronic calorimetry are extremely important tools for the high energy experimentalist given the demands of today's physics questions. The list of major detectors in elementary particle physics [Gidal 83] demonstrates the great importance of calorimeters in modern experiments. Nearly all of these forty detectors makes important use of calorimeters. In these detectors calorimeters are used as neutral particle spectrometers, they are used as collective triggers (jets), they are used as active targets (neutrino beams) and they are used as active beams (proton decay). They also act as a compact spectrometer and are used to identify particle types. The missing energy and missing momentum determined by calorimeters played a crucial role in the discovery of the W particle. In this discovery calorimeters were used in a new mode of neutrino identification. As the accelerator energies increase the only viable method of energy measurement available will be calorimeters. The size of calorimeters scales as lnE whereas the size of magnetic spectrometers scales a $\sqrt{E}$. A number of new and very interesting technologies for calorimetry are currently under development. Some of these will no doubt make a significant impact on the detectors of tomorrow.

The precise etymology of the word calorimeter as used in particle physics is somewhat vague. When the term is first encountered, the notions of thermodynamic equilibrium and temperature are likely to be evoked. Indeed calorimetry of of this sort is used to measure beam energies. SLAC uses a couple of calorimeters to measure the intensity of electron beams. The beam is absorbed into an insulated block of silver or copper and the subsequent temperature rise in the block is related to the total absorbed energy. This technique has little practical use for particle detectors at present. The problems are twofold. Even at the FNAL collider, the center of mass energy

domain. It is based on the rapid change in the vapor pressure of liquid helium-3 with temperature. Liquid helium is stored between capacitor plates. The change in vapor pressure with temperature produces a change in the capacitance which is sensed by an external capacitance bridge. Further study is necessary to determine the equilibrium times involved, and the time it takes to make a capacitance measurement before the potential value of such a device for high energy physics detectors might be ascertained. With present technology it might be possible to get an accuracy of 0.4 nK at 3 K. This would give a 10% energy resolution at 1 GeV. The authors [Ahlers 83] claim that a factor of 10 improvement in accuracy looks feasible. Such an improvement might make this type of calorimetry very attractive. In summary, such a device would be characterized as:

1) Compact with densities of 10 to 20 g/cc ;
2) No sampling gaps ; and
3) Resolution that decreases as 1/Energy .

The real world of calorimetry in high energy physics is not so simple as this "chemistry" calorimetry. The high energy physicist must devise ways to get some signal from the deposited energy before it becomes thermalized. To do this efficiently, uniformly and with good segmentation is the challenge to today's experimentalist.

is only 3.2 ergs. The energy carried by a single particle in a typical high energy physics experiment is a couple of orders of magnitude less. When this small amount of energy is shared with the bulk of a practical sized absorber the temperature rise is on the order of pico-kelvin. For example, it takes a lead block about 5 cm long and 3 cm in diameter to contain 80% of a 1 GeV electron shower. At 20 C the specific heat of lead is 27 joules/mole K. This gives a temperature rise in the lead of $2\ 10^{-12}$ K. This rise is about six orders of magnitude smaller than the least count obtainable with resistive thermometry. It can be concluded that calorimetry as presently used in high energy physics is not the sort of calorimetry naturally associated with the word.

The use of this type of calorimetry for individual particle measurements in high energy particle physics detectors is not necessarily impossible however. At room temperature most of the heat capacity comes from the lattice vibrations. The lattice specific heat depends upon the absolute temperature to the third power. Hence at low temperatures the heat capacity is greatly reduced. For example, the heat capacity of lead decreases by a factor of about 3000 when the temperature decreases from 20 C to 3 K. At 3 K the heat capacity of lead is about 13 millijoules/mole K. Hence the temperature rise associated with the energy deposited by the electron shower is about 4 nK. At 3 K the temperature measurement technology is also much improved. There is a simple device called a Helium-3 vapor pressure thermometer [Ahlers 83] that operates in this

EARLY CALORIMETRY

Calorimetry used today in high energy physics has its origins in early cosmic ray detectors. This early calorimetry was used to measure event energies. A standard technique for measurement of a cosmic ray event in a cloud chamber is shown in Fig. 1a. This technique relied on the photon component (pizeros) of the event to estimate the energy. Shower theory [Rossi 52] determines that the number of electrons and positrons present at the shower maximum is proportional to the shower energy. Furthermore, the position of the shower maximum increases only logarithmically with energy so that this is a good position at which to estimate the shower energy. Also the statistical fluctuations are the smallest at the shower maximum and hence the resolution is optimized by measurements at this depth in the shower. The total ionization at the shower maximum was measured for an event and the pizero energy was determined using a constant of proportionality calculated from shower theory. To obtain an estimate of the event energy, it was assumed that one third of the secondaries was a pizero and that the event inelasticity was one half. Thus a crude estimate of the event energy was determined. Large fluctuations in the inelasticity, the pizero component and the statistics of the shower curve at shower maximum produced very large uncertainties in the event energy.

About 1956 one of Murzin's coworkers [Grigorov 58] suggested an improvement on this scheme. He noted that longitudinal shower size scaled as ln(Energy) so that a finite size device could be made to contain showers over a large dynamic range. He reasoned that if shower samples were made throughout the shower a much better estimate of the shower energy could be made. Both the hadronic and electromagnetic component of the shower would be measured as well as the energy carried by the incident particle. Their device is shown schematically in Fig. 1b. This device was originally referred to as a spectrometer but eventually because of its total energy absorption characteristic it was called a calorimeter. This is misleading terminology, since the technique does not involve thermodynamic properties such as temperature or equilibrium, but the name is by now well established.

DEFINITIONS

The following are the definitions of quantities frequently appearing in shower theory. See for example [Tsai 74].

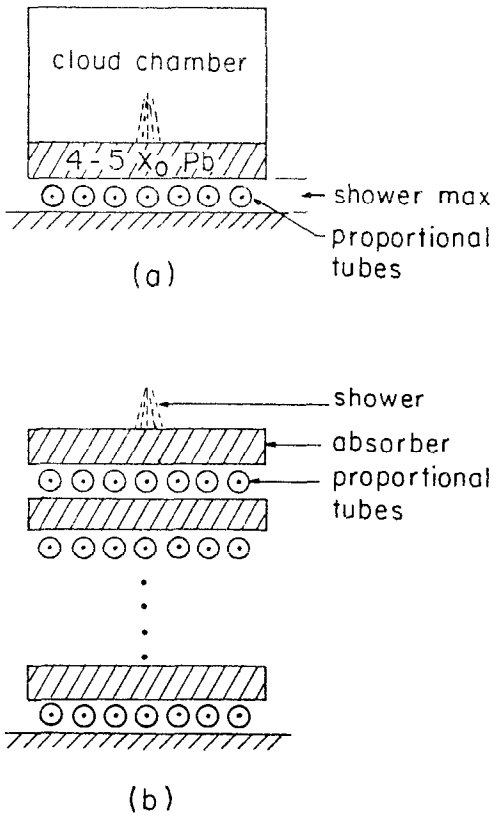


Fig. 1. (a) Early cosmic ray calorimetry - shower maximum sample.
(b) The invention of Grigorov - sampling the whole cascade.

RADIATION LENGTH, Xo in gm/cm^2

$$Xo = (A/\alpha\ r_e^2 N)\ 1/(Z^2(L_z - f) + ZL_e)$$

where

$L_z = \ln(184.15\ Z^{-1/3})$

$L_e = \ln(1194\ Z^{-2/3})$

f is a Coulomb correction

A is the atomic weight

N is Avogadro's number

α is the fine structure constant

r_e is the classical radius of the electron

Radiation lengths add reciprocally:

$1/Xo = \sum_i f_i/Xo_i$; Xo_i in gm/cm^2, f_i is the fraction by weight

Xo is often given in cm.

PAIR PRODUCTION

$$\sigma(\infty) = 7/9\ A/XoN$$

BREMSSTRAHLUNG

$$\lambda = Xo/\ln(E/k)$$

where λ is the mean free path for the radiation of photons of energy greater than k.

CRITICAL ENERGY

$$\epsilon = (dE/dX)\ Xo$$

ϵ is the ionization deposited by a minimum ionizing particle in traversing one radiation length.

The critical energy is the energy near which the predominant energy loss for electrons changes from bremsstrahlung to ionization losses.

MOLIÈRE RADIUS

$$r_M = (21\ \text{MeV}/\epsilon\ )\ Xo$$

The Molière radius is an analytic scale for the transverse dimension of an electromagnetic shower. About 95% of a shower's energy is contained within two r_M.

PHOTON MASS ABSORPTION COEFFICIENT,

$$N = No\ e^{-\mu t}\ ;\ \mu \text{ in cm}$$

$$\mu(\infty) = 7/9\ (1/Xo)\ ;\ Xo \text{ in cm}$$

ABSORPTION LENGTH

σ_i = Inelastic cross section

$= \sigma_t - \sigma_e - \sigma_q$; for high energy p, n nucleus reactions. σ_t is the total cross section, σ_e the elastic cross section and σ_q the quasi-elastic cross section.

See Figs. 2 and 3 for the characteristic photon cross sections involved in these processes [Roos 82]. Figure 4 shows the probability for energy sharing in pair production as a function of the energy fraction, η, carried by one of the particles. Figure 5 gives some typical diagrams for the electromagnetic cascade process.

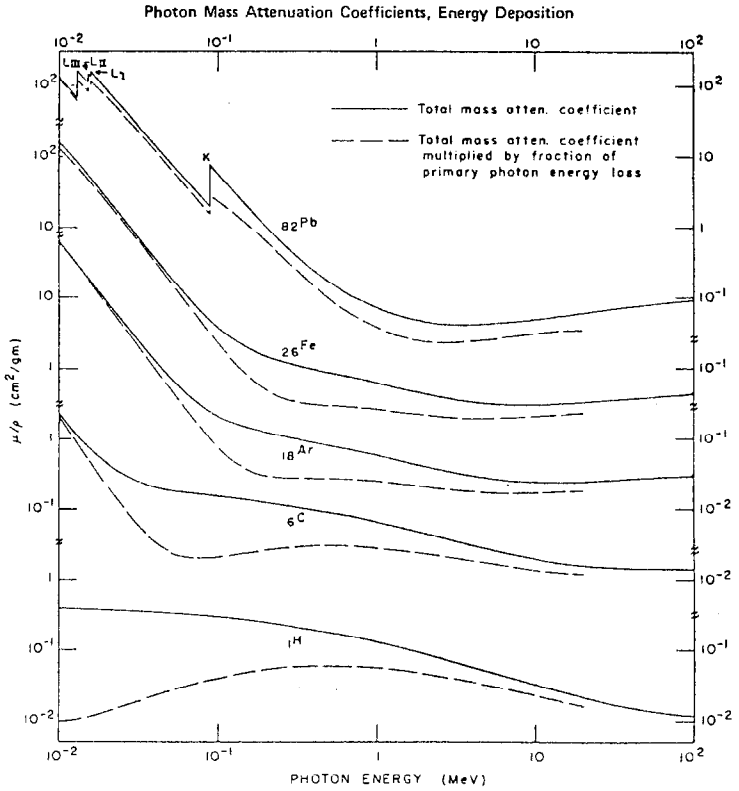
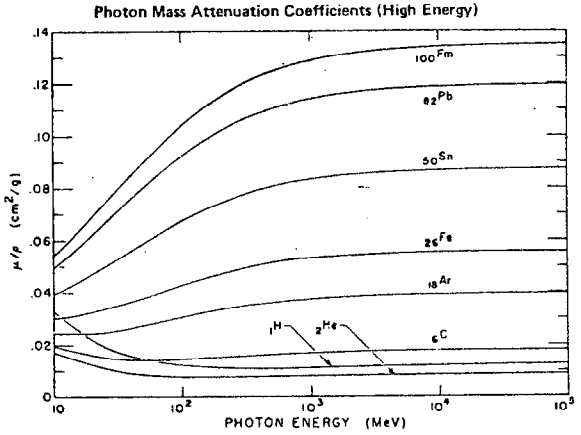
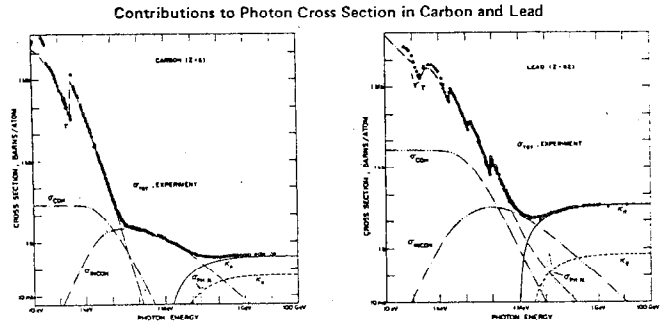


Fig. 2. Low energy photon absorption [Roos 82].



The photon mass attenuation coefficient, high energy range (note that ordinate is linear scale). See caption on previous page for details.



Photon total cross sections as a function of energy in carbon and lead, showing the contributions of different processes.

τ = Atomic photo-effect (electron ejection, photon absorption)
σ_{COH} = Coherent scattering (Rayleigh scattering — atom neither ionized nor excited)
σ_{INCOH} = Incoherent scattering (Compton scattering off an electron)
κ_n = Pair production, nuclear field
κ_e = Pair production, electron field
$\sigma_{PH.N.}$ = Photonuclear absorption (nuclear absorption, usually followed by emission of a neutron or other particle)

From Hubbell, Gimm, and Øverbø, J. Phys. Chem. Ref. Data 9, 1023 (1980). Figures courtesy J. H. Hubbell.

Fig. 3. High energy photon absorption and photon total cross sections. [Roos 82]

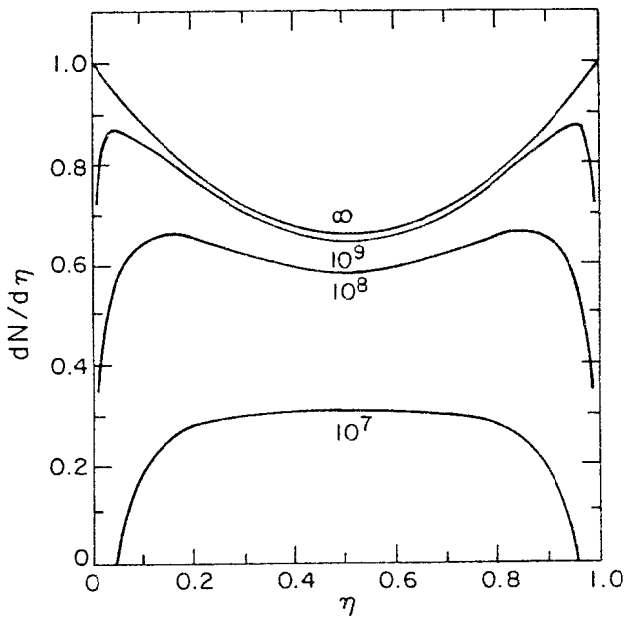


Fig. 4. Electron energy fraction in pair production - energy in eV. After [Rossi 52].

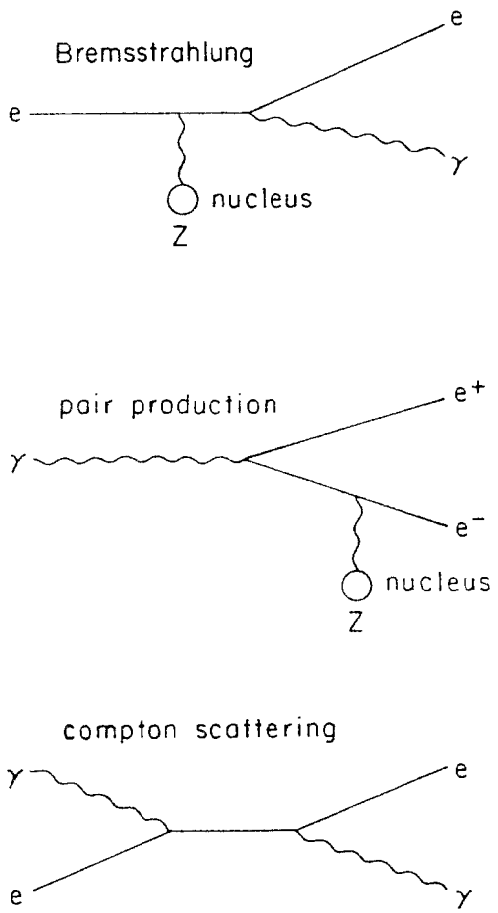


Fig. 5. Typical diagrams for the shower processes.

LONGITUDINAL SHOWER PROFILE

The qualitative features of the longitudinal distribution of the energy in a shower can be determined from a simple picture of the build up and decay of the electromagnetic cascade. Consider the simplified schematic of shower build up shown in Fig. 6. In this model there is a characteristic length, approximately the radiation length, at which a charged particle or photon interacts. In this interaction, the energy is divided equally between two daughter particles. This process continues until the energies of all the particles are less than or equal to the critical energy. When a particle reaches the critical energy then its major loss of energy is through ionization so this multiplication process stops. After traversing k lengths there are 2^k particles, each carrying about the critical energy. Hence

$$\epsilon 2^k = E, \text{ or}$$

$$k = (1/\ln 2) \ln(E/\epsilon),$$

where E is the shower energy. k gives the approximate number of radiation lengths in which the shower is contained. This is also the position of the shower maximum in this model. For real showers, the shower maximum occurs earlier because of the dissipation of energy by ionization during the shower build up and a smearing out of the build up from fluctuations in the cascade process. The experimental value of the coefficient is about 1.00 instead of the 1.44 given

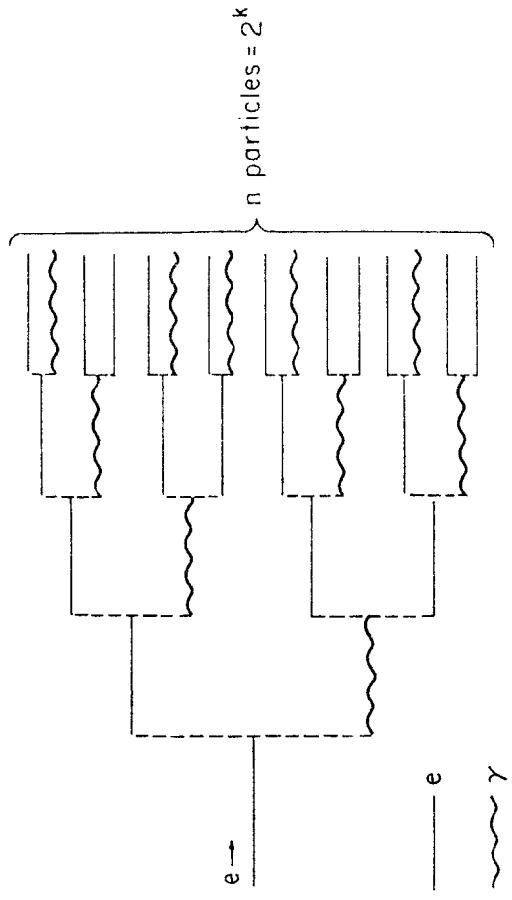


Fig. 6. Simplified shower model schematic.

by this simple model. For example, Babaev et al. find that the position of the shower maximum in a liquid argon Fe plate calorimeter is [Babaev 79]

$$t_{max} = 1.04 \ln(E/\epsilon) - 0.5$$

After reaching shower maximum the energy deposition falls off exponentially. The characteristic fall off is given by the minimum in the photon absorption cross section [Bathow 70]. Especially for high-Z materials, the photon cross section has a very pronounced minimum at about 1 to 10 MeV photon energy. The photon cross sections tabulated by the Particle Data Group [Roos 82] are shown in Fig. 3. For example, at three MeV the cross section for lead has fallen by about a factor of three from its high energy value. Although the details of the shower attenuation involve complicated mixtures of ionization, radiation and compton scattering, the characteristic attenuation appears to be very near to the minimum attenuation for photons. See Fig. 7 for shower profiles for various materials [Bathow 70]. The following table compares the measured absorption with the minimum in the photon absorption for lead, copper and aluminum.

	Pb	Cu	Al
$\lambda_{att}\,cm^{-1}$	0.46 ± 0.01	0.23 ± 0.01	0.042 ± 0.001
$\lambda_{att}\,cm^{-1}$	0.47	0.27	0.058

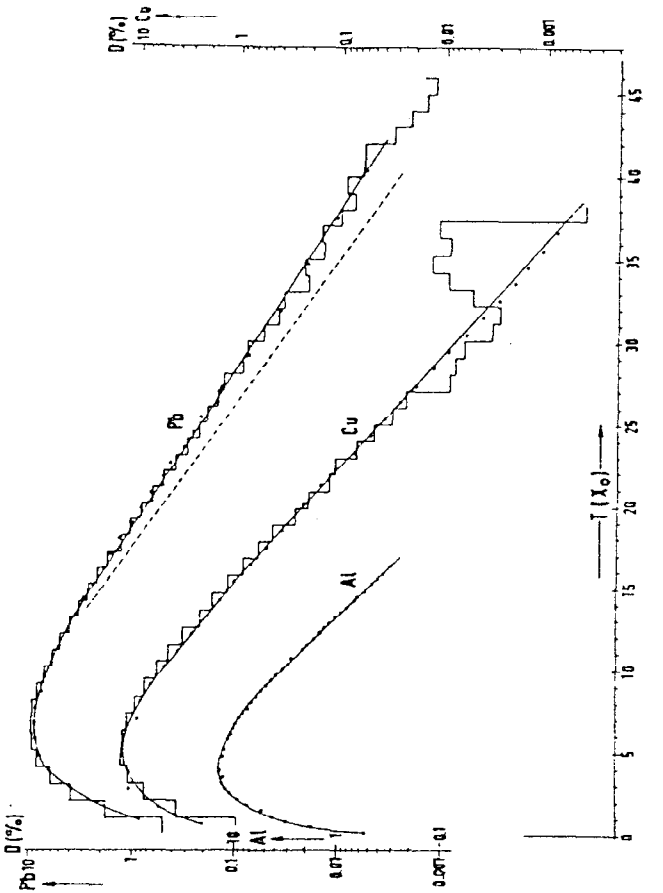


Fig. 7. Longitudinal shower profile for Al, Cu and Pb. The histogram is a Monte Carlo calculation - the dashed line an analytic calculation. The data are for 6 GeV electrons [Bathow 70].

The shower profile can be described by the function

$$N = No\ t^{a} e^{-bt}$$

where N is the number of charged particles at depth t. a and b are material and energy dependent [Longo 75]. This analytic form is also discussed by the Particle Data Group [Roos 82]. The depth of the shower maximum is given by a/b. The results of Longo are from a Monte Carlo calculation for lead glass. Although the shape appears correct, the magnitude is too large by about a factor of two. The shower profile has been measured [Müller 72] for lead for energies from 2 to 15 GeV. They also use the data to extrapolate these curves to about one TeV. These results are given in Fig. 8. It should be noted that these are the effective number of particles. The true number of particles must be obtained from the effective number by multiplying by the mean cosine of the particles at that depth.

Müller fits the number of effective particles at the shower maximum with the function

$$N = 10.71\ E^{0.935}.$$

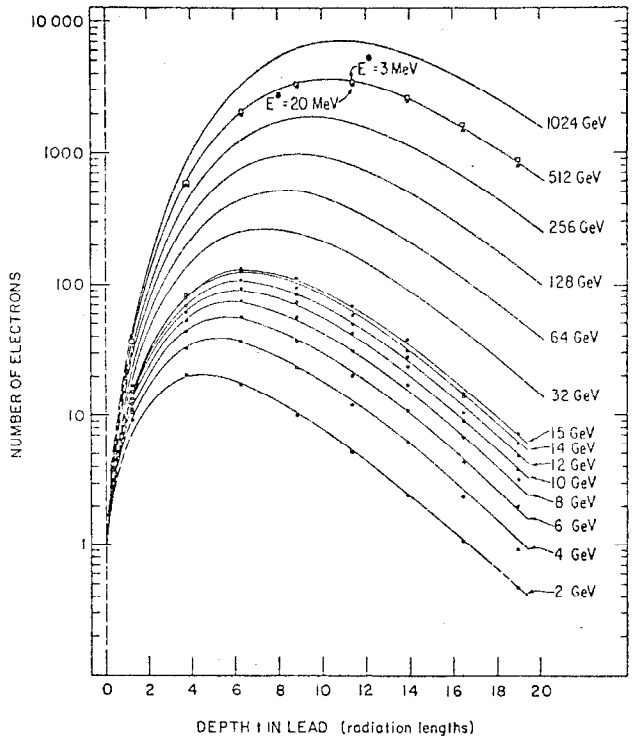


Fig. 8. Longitudinal shower profiles in Pb for a range of energies. Values for energies above 15 GeV are extrapolated from the data with the aid of Rossi's approximation B [Müller 72].

TRANSVERSE SHOWER PROFILE

The transverse dimensions of the shower scale in a quantity called the Molière radius. Since the transverse dimension of the shower is dominated by the multiple scattering of low energy particles, the shower size is not strongly dependent on the energy. Figure 9 [Bathow 70] compares lateral shower shapes at 6 GeV for different materials as a function of the radius in Molière units. Reasonable scaling in the Molière units is observed for the different absorbers.

TOTAL ABSORPTION CALORIMETERS

Total absorption calorimeters are predominately used to measure photon and electron showers, although a large tank of liquid scintillator has been used at FNAL to measure hadron showers from neutrino interactions [Benvenuti 75]. The total absorption devices which have been extensively used are made of lead glass or sodium iodide crystals. There is presently a great deal of interest in making total absorption calorimeters out of scintillating barium glass, bismuth germanate and barium fluoride.

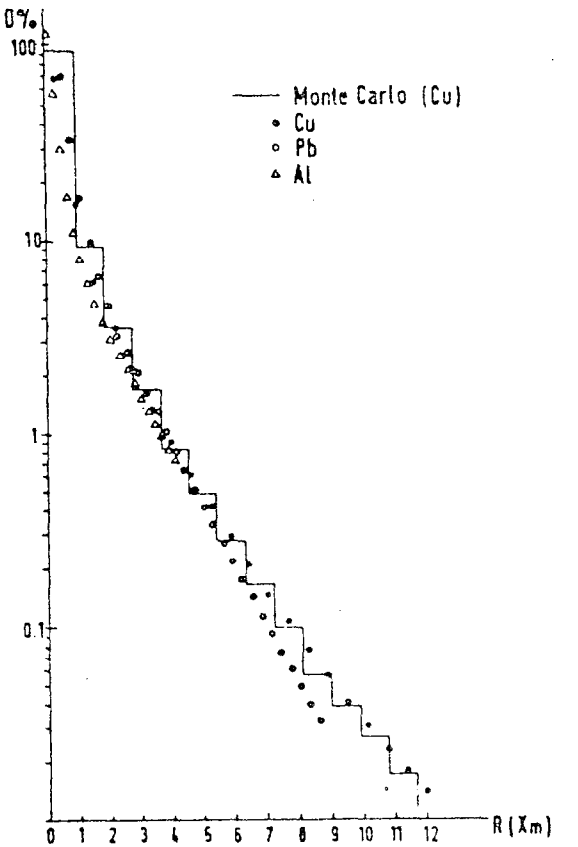


Fig. 9. Transverse shower profile for 6 GeV electrons in Al, Cu and Pg. Data show scaling in the Moliere radius [Bathow 70].

In the heavy glasses the resolution depends primarily on the photo electron statistics. Materials which give off the most light, in principle, give the best resolution. However at energies above a few GeV, fluctuations in the shower containment and variations in the longitudinal shower position and hence the fraction of the light absorbed, lead to systematic effects. These effects are typically on the order of 2% in resolution. Poor photon collection efficiency may also degrade the resolution. Perhaps the greatest source of systematic error in large systems is the calibration. A later section will discuss calibration in more detail, but basically the problem stems from getting a standard signal from each cell.

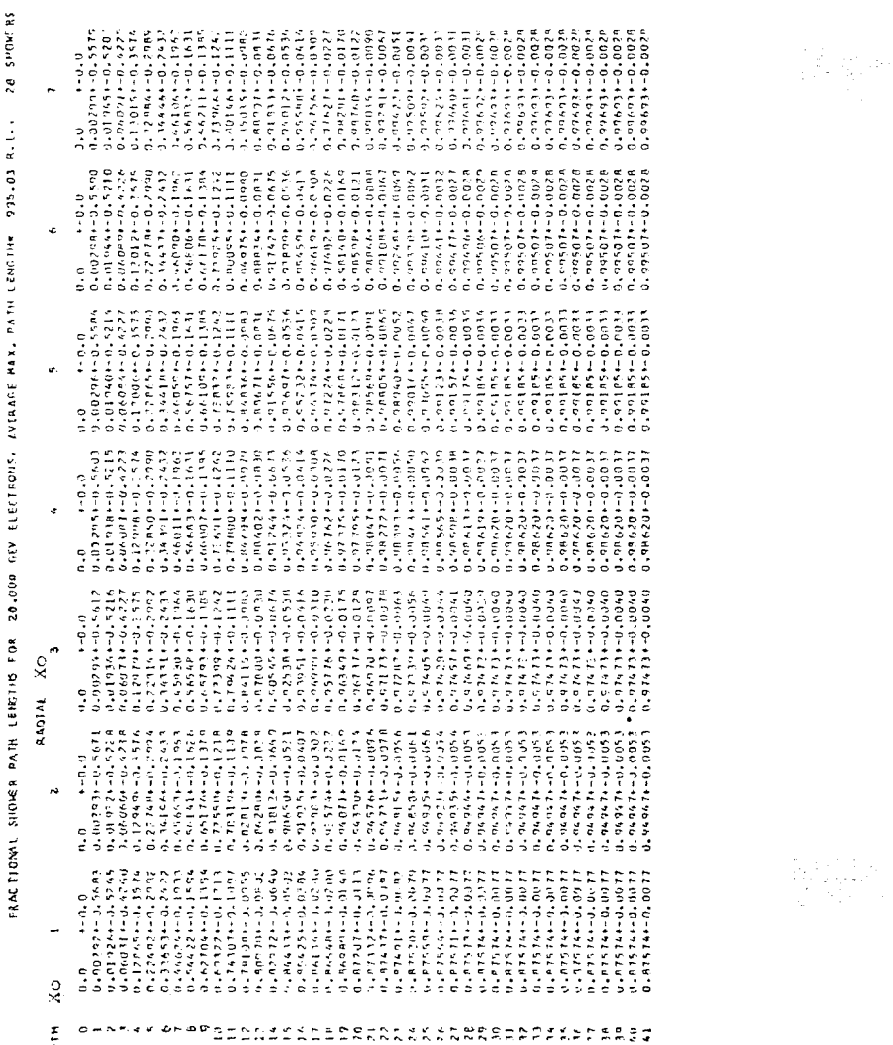
Sodium iodide (NaI-Tl), bismuth germanate (BGO) and barium fluoride (BaF_2) all produce a great deal of light. Resolutions on the order of 1% at 1 GeV are possible from the photon statistics. However it is very difficult to reduce the systematics below 1% and thus they are not substantially better in resolution than scintillating barium glass. The following table summarizes the properties of these materials.

MATERIAL	DENSITY (gm/cm^2)	Xo (cm)	PHOTONS/MEV
Liquid scintillator	0.86	45.	$3 \cdot 10^3$
Lead glass (SF5)	4.08	2.54	$6 \cdot 10$
Scintillating barium glass (SCG1)	3.5	4.35	$3 \cdot 10^2$
Sodium Iodide (NaI-Tl)	3.7	2.6	$4 \cdot 10^4$
Bismuth germanate $Bi_4Ge_3O_{12}$ (BGO)	7.1	1.1	$3 \cdot 10^3$
Barium fluoride BaF_2	4.9	2.1	$6 \cdot 10^3$

There are other features among these materials that help determine the choice for a given application. Putting cost aside, although that might be the overriding consideration, probably the radiation length is the most important. A short radiation length means a compact device. This generally means that two photons can be resolved at shorter separation distances. If the detector is constrained to fit inside a magnet coil, the compactness could make a substantial difference in cost or even control the feasibility of the design.

Shower leakage, especially at high energy, can easily destroy the very good intrinsic resolution of these materials. Table I shows the energy containment fraction and the rms fluctuation on the contained fraction for lead glass. The table was generated using EGS [Atwood 75]. The rows give the depth of the detector in radiation lengths and the columns give the detector radius in radiation lengths. The table was generated for 20 GeV electrons. For example, if the detector were only 15 radiation lengths deep (and 7 r.l. in radius) then the leakage would be 6% but the rms fluctuation would be 5%! This 5% fluctuation would be equivalent to a resolution of $22\%/\sqrt{E}$. Hence, at 20 GeV, a $2\%/\sqrt{E}$ device could become a $22\%/\sqrt{E}$ device! If this leakage energy were measured or estimated to no better than $10\%/\sqrt{E}$ then the resolution is nearly restored. The combined resolution would be $3\%/\sqrt{E}$. Mark II reports that by using the energy deposited near the back of their liquid argon calorimeter an estimate of the lost energy can be made and the resolution restored [Dorfan 83]. The correction is very simple. It utilizes the known exponential shape of the shower tail and uses the energy near the back to provide the normalization. Although total absorption devices do not usually have such information available, they usually have a short front segment followed by a long back segment. Since the leakage out the back is determined largely by where the shower begins, the ratio of the front to back energy might be sufficient to determine the lost energy.

TABLE I



FRACTIONAL SHOWER PATH LENGTHS FOR 20.000 GEV ELECTRONS, AVERAGE MAX. PATH LENGTH= 935.01 R.L.. 20 SHOWERS

RESOLUTION IN SAMPLING DEVICES

The following simple model illustrates the basic mechanism that controls the energy resolution in a sampling calorimeter. In this model it is assumed that the electrons and positrons in the shower deposit a fixed amount of energy, Eg, when crossing a gap. Let t be the thickness of the absorbing plates in radiation lengths, ϵ be the critical energy and E be the energy of the shower. If all tracks are assumed to travel perpendicular to the sampling gaps, then the number of crossings in the sampling gaps is given by

$$N = E/\epsilon t.$$

Since all of the shower is absorbed by ionization losses, this equation is derived by adding all the track lengths and dividing by t to determine how many samples are obtained.

The signal, S, and error in the signal, σ, are given by

$$S = N*Eg$$
$$\sigma = Eg*\sqrt{N}.$$

The equation for the error assumes that all the crossings are independent.

The fractional resolution in the signal and hence in the energy determination is given by

$$\sigma_E/E = \sigma/S = 1/\sqrt{N} = \sqrt{\epsilon t/E}.$$

The experimental results give a coefficient in front on the order of two. The coefficients vary from experiment to experiment and material to material but cluster around 1.8. In the next section some of the corrections to the above simple model will be discussed and their contributions to the resolution estimated.

In the case of non-perpendicular incidence of the electron or photon, the energy deposited in the sampling gap is increased by a factor of $1/\cos\theta$ while the number of gap crossings is decreased by the factor $\cos\theta$. Hence the signal remains unchanged although the resolution deteriorates by a factor $1/\sqrt{\cos\theta}$. For example, at 45° incidence, the resolution degrades by about 19%. This angular dependence for the energy response and resolution is verified by Monte Carlo calculation and by experiment [Ludlum 82].

SAMPLING LOSSES

When a minimum ionizing particle such as a muon passes through a sampling calorimeter it undergoes mainly ionization energy losses. The ratio of energy deposited in the sampling medium to the total energy deposited in the calorimeter is given by the equation (to the extent that bremsstrahlung is neglected)

$$R = (dE/dX1\ X1)/(dE/dX1\ X1 + dE/dX2\ X2)$$

where dE/dX1 is the ionization rate for the sampling material and X1 is the sampling material thickness. A similar notation is used for the absorber material and absorber plate thickness.

When an electromagnetic shower is completely absorbed in a sampling calorimeter, the initiating electron or photon energy is converted to ionization energy. The fraction of the shower energy deposited in the sampling cells would be expected to be similar to the ratio R defined above. The actual fraction of the energy deposited in the sampling cells is observed to be substantially less in calorimeter measurements and computed to be substantially less in Monte Carlo calculations. In the following section the size of the effect and the origin of the difference in energy deposition is presented.

If the sampling cell is infinitesimally thin, so that it has a negligible effect on the shower cascade, then the fraction of the energy observed would be given by the ratio R. Infinitesimally thin turns out to be much thinner than can be used in practical devices and even much thinner than can be reliably calculated with Monte Carlo programs such as EGS. For example, Crannell et al. [Crannell 69] attempted to measure the fall off in energy within a sampling gap. Thin (3 mm) sampling scintillators were used in the sampling gaps. In front of these scintillators were placed varying thicknesses of Plexiglas absorber. The resulting attenuation in the pulse height is plotted in Fig. 10. The decrease in pulse height shown by this data is not nearly sufficient to explain the calculated pulse height losses. According to this curve it would take about 5 cm of sampling gap to account for the 20 to 30 % sampling losses observed in calorimeters. For convenience we define the sampling efficiency to be the fraction of energy deposited in the sampling cell divided by the ratio R as defined above.

Some energy content of the shower is sampled when electrons produced in the absorber plates pass into the sampling cells. However some electrons are of such low energy that they penetrate little if at all into the sampling cells. This would be the case for instance with electrons produced by photons near 0.1 MeV energy. However, this component of the shower would be sampled with the ratio R if the frequency of electron production in the sampling cells was large enough to give the same relative energy deposition in the sampling cells and absorber plates as that for a

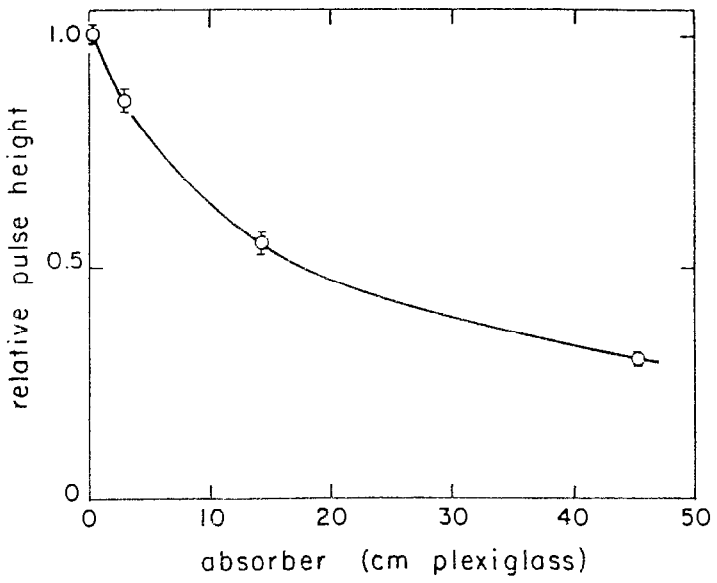


Fig. 10. Measurement of the transition effect [Crannell 69].

minimum ionizing particle. In this case, the photon cross sections could be viewed as having the same value in lead and argon per unit ionization. Consider a calorimeter made of lead absorber plates and liquid argon sampling cells. The liquid argon cross section for photons per unit ionization is less than 3% of the lead cross section near 0.1 MeV. Hence the sampling in this energy region is less than 3% efficient as defined above. This type of process contributes to the lower energy fraction deposited in the sampling cells by showers than is deposited by muons.

The sampling efficiency has been computed for uranium absorbing plates one-half radiation length thick and for various thicknesses of liquid argon. Figure 11 shows the efficiency obtained using EGS. EGS has a cut off for electron propagation at 1.5 MeV. That is, if an electron of energy less than 1.5 MeV is created, the energy is deposited at the point of creation. Photons are propagated through the calorimeter for energies greater than .1 MeV. At 1 MeV the ratio of the photon cross sections for argon and lead per unit ionization has increased to 60%. Hence the sampling efficiency is reasonably good above 1 MeV.

The fraction of the total energy deposited by particles below 1.5 MeV was found to be about 32%. This does not mean that the missing energy is purely from this energy domain of the shower. The photon cross section in argon per unit ionization remains lower than that in lead up to substantially higher values of energy and this

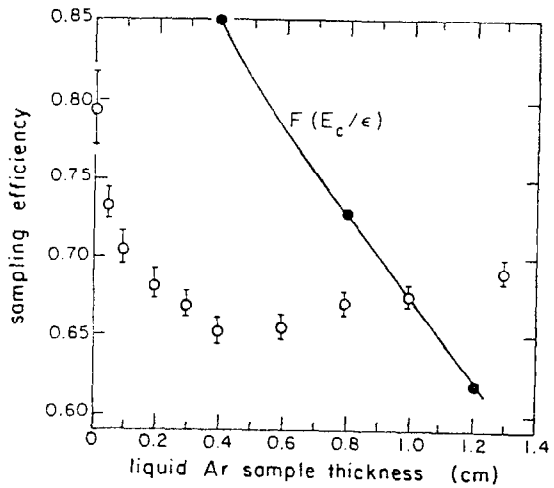


Fig. 11. Sampling efficiency as defined in the text. Closed circles are the cut-off fraction using one half the gap energy.

region of the energy spectrum also contributes to the missing energy.

This missing energy reduces the observed track length and therefore the sampling statistics. The simple model must be modified to take this loss of energy into account. The following section will discuss a number of effects that modify the constant in the resolution formula.

RESOLUTION DETAILS

Figure 12 shows the fraction of the energy carried by particles with energy above a given cut off energy [Amaldi 81]. The EGS Monte Carlo finds about the same results for uranium as the point for lead given by Nagel. About 32% of the energy in a 1 GeV shower is found to be below a cut off of 1 MeV kinetic energy. However this curve differs from the sampling efficiency discussed earlier. A cut-off value for the energy contributing to the sampled energy cannot be simply defined because the spectrum is a continuous one that extends to zero energy. Amaldi [Amaldi 81] suggests a cut off at one half the energy deposited in crossing the sampling gap. If this criteria were used to compare the cut-off curve with the sampling efficiency curve then the correspondence is very poor. The cut-off curve crosses the sampling efficiency curve at about 1 cm cell thickness and has a substantially different shape. This comparison is shown in Fig. 11.

Figure 13 shows that the resolution actually improves with the increase in the sampling thickness even though the sampling efficiency decreases. The figure gives the resolution in the sampled energy as a function of the sampling gap thickness. This is the result of an EGS Monte Carlo calculation for one half radiation length uranium plates and liquid argon sampling cells. This result is very similar to the one found by Fischer for lead absorbers, Fig. 14 [Fischer 78]. The resolution shows a rapid deterioration as the sampling gap narrows.

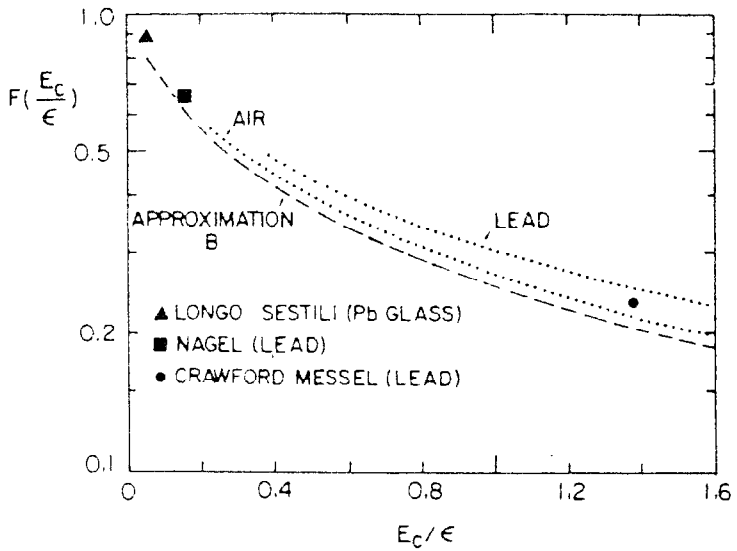


Fig. 12. Fraction of shower energy above cut-off energy [Amaldi 81].

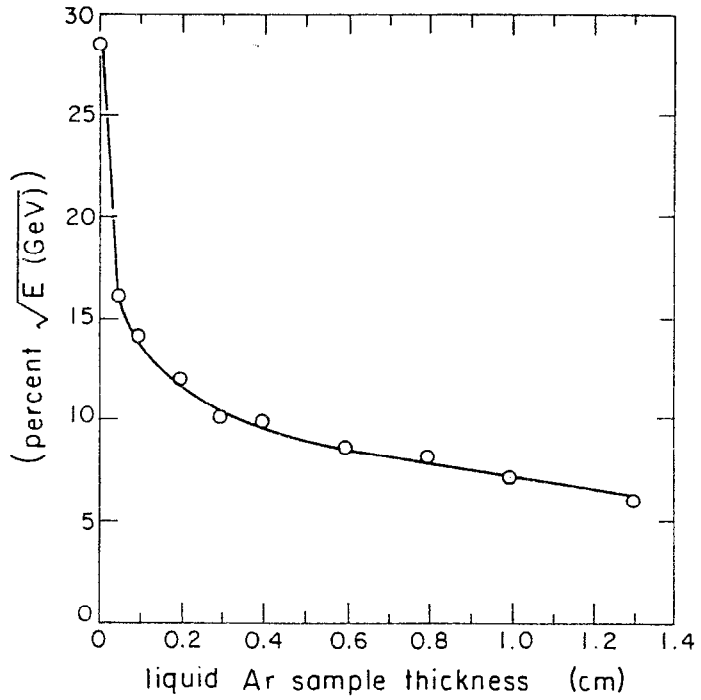


Fig. 13. Resolution as a function of liquid argon sampling thickness. Results are from the EGS Monte Carlo for one-half radiation length uranium plates.

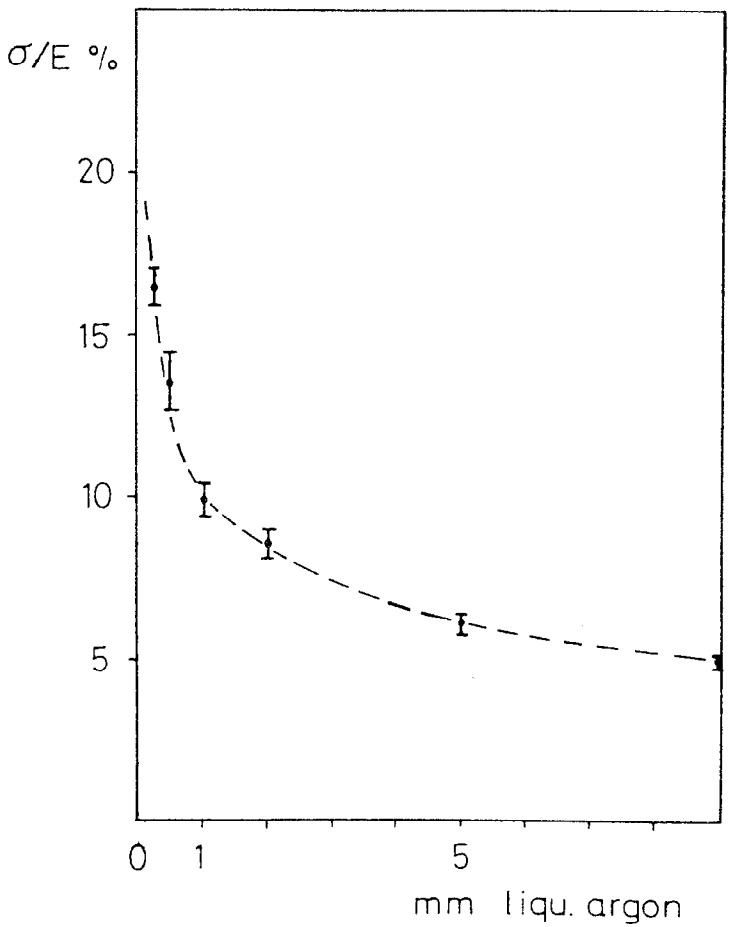


Fig. 14. Resolution as a function of liquid argon sampling thickness for one-third radiation length Pb plates [Fischer 78].

As previously pointed out [Fischer 78], this is primarily why gas calorimeters have a worse resolution than calorimeters with scintillator or liquid argon sampling cells. A gas cell is equivalent to a very thin dense cell. This effect is understood in terms of path length fluctuations [Fischer 78]. When the energy deposited in a single traversal of a sampling gap is large, then most of the energy deposited in the gap comes from relatively high energy electrons and positrons. These high energy particles tend not to have scattered much and hence they have a rather forward angular distribution. The variance on the energy deposition for these tracks is small. In contrast, narrow gaps have a substantial fraction of the energy deposited by low energy particles. These low energy particles approach a cos**2-distribution. See Fig. 15 [Fischer 78]. This large variation in track angles produces sizable variations in the deposited energy and ultimately a degraded resolution. Figure 16 shows how the resolution improves in a gas calorimeter as the maximum track length is reduced [Fischer 78].

In view of the above discussion we can understand better the coefficient appearing in the resolution formula derived from the simple model. The effective number of tracks is reduced by

(sampling efficiency)*<cos> = 0.65*0.60 = 0.39.

This give a factor of 1.6 instead of the factors which range from about 1.3 to 2.5 in different experimental arrangements. The thickness

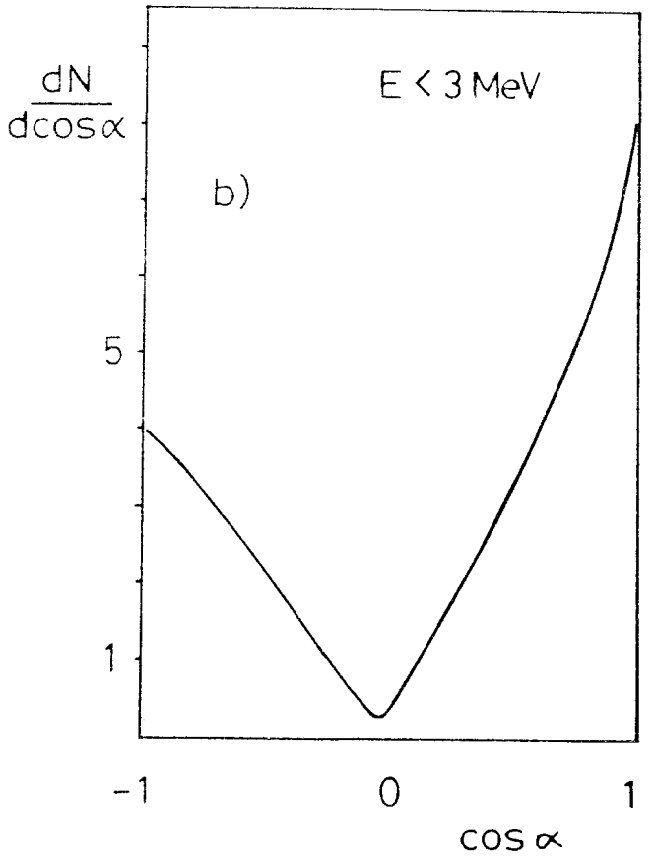


Fig. 15. Low energy electron angular distribution in Pb [Fischer 78].

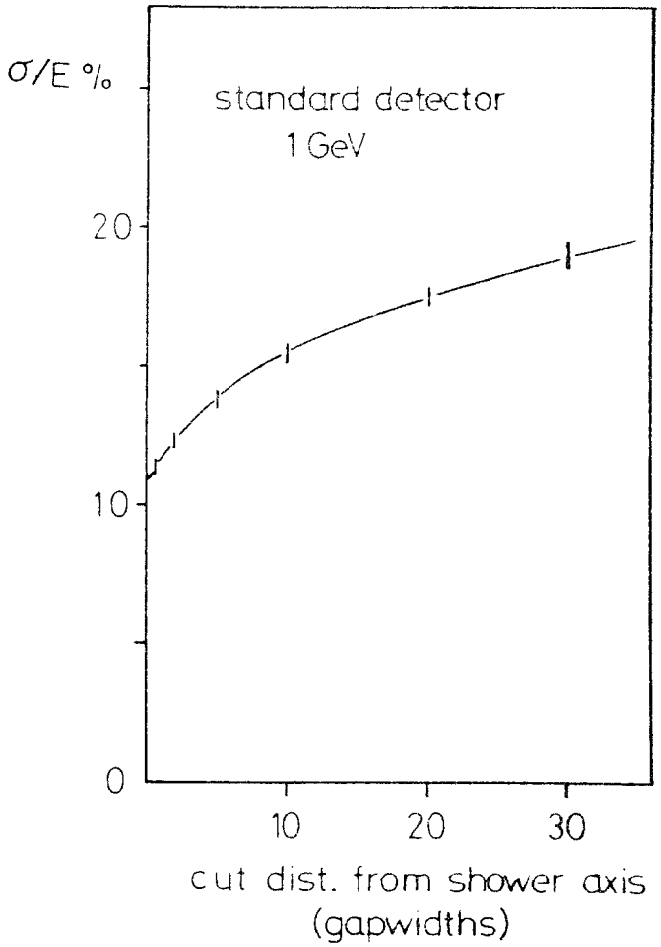


Fig. 16. Effect of track length on resolution [Fischer 78].

of the sampling layer also affects the resolution as is shown in Figs. 13 and 14. In addition several other significant effects have been neglected. First there are correlations between sampled tracks. If all the tracks were the result of pair production then the sampling statistics would be reduced by about a factor of two. The EGS program finds that 32% of the sampled energy is deposited by positrons. This means that 64% of the sampled energy comes from pair production. For this fraction of the energy the correlation between sampled electrons and positrons is very high. If a correlation coefficient of 1 is assumed, then the effective statistics are further reduced by a factor of 1.64. The resolution coefficient becomes 2 in this approximation. Furthermore, many tracks have a finite probability of crossing more than one gap. Such correlations also reduce the sampling statistics.

Second, the variance on the energy response has been neglected in the resolution calculation. The fluctuations in the energy response contribute an additional factor of (1+(sigma/Eg)**2)**1/2 to the resolution. Eg is the average gap response and sigma**2 is the variance in this response. Of course, noise in the detector system or inefficiency in collecting the sampled signal would lead to further deterioration of the resolution. Noise problems would most likely occur in a liquid argon system where the signal is very small, whereas loss of signal is common in scintillator systems where light collection efficiency may be poor.

There are also two effects which improve the resolution. The first comes from the double counting in the sampling efficiency and average cosine effects. The wide angle tracks with small cosine are the same tracks that are sampled poorly. Hence the effective cosine should be somewhat larger than the 0.6 used in obtaining the resolution coefficient. The second effect can be demonstrated with the following simplified picture.

Suppose that Eg were the energy lost in crossing a gap by a single particle. Then if half of the sampled energy were deposited by tracks contributing Eg and the other half of the sampled energy were deposited by tracks contributing only Eg/2, then the sampling statistics would be given by

$$N = Es/(2*Eg)+Es/Eg = (3/2)*Es/Eg$$

where Es is the total sampled energy. N is 50% larger than if the energy were deposited all in units of Eg. However this spread in energy introduces a variance in the sampling energy and this variance must be included in the resolution. When the effect of this variance is included, the effective statistics are improved by a factor of 4/3. There is a net improvement in the resolution no matter how many ways the sampling energy is divided up. Although the variance may be increased with additional divisions of the energy, the number of tracks increases fast enough to give a net improvement in the resolution. The shower sampling process must contain such effects because of the many low energy tracks in the shower. Since the actual experimental results span a broad range of

values, the precise contribution from these effects is hard to quantify. It is clear however that these effects do not dominate the resolution. These non-quantitative considerations clearly indicate some remaining uncertainty in the resolution coefficient. However, the variation in values of the resolution coefficient from experiment to experiment is greater still.

In very light materials such as aluminum the average particle angle decreases since the multiple scattering is less. The multiple scattering is reduced because of the low z and the higher particle energies resulting from the larger critical energy. In low z materials the sampling efficiency is higher because the photon cross sections of the absorber and the sampling medium are more nearly equal. The CHARM collaboration finds a resolution for their marble calorimeter (marble is similar to aluminum) that is given by

$$1.01\ \sqrt{\epsilon t/E}$$

[Jonker 82]. This small coefficient (good resolution) is attributed by Amaldi [Amaldi 81] to somewhat different processes than those discussed so far. He derives a different resolution formula based on the notion of an energy cut off. He suggests that this cut off is on the order of one half the energy deposited in a sampling gap by a minimum ionizing particle passing perpendicular to the gap. This formula reproduces the CHARM results very nicely but not for example [Fabjan 78]. The concept of a cut off is hard to apply as has been noted above. Clearly the corrections to the simple model will be different for a low z material than for the high z materials considered previously. For low z materials the sampling efficiency increases and the angular distribution is more forward peaked. Both these effects should lead to a smaller coefficient in the resolution formula than that for lead or iron. The CHARM calorimeter also uses 3 cm thick scintillator. Figure 13 shows that the resolution improves substantially with the thickness of the sampling medium. With the aid of this curve, a rough estimate can be made as to how much improvement in the resolution the thick scintillator makes. Since Fig. 13 is based on 0.5 Xo sampling while the CHARM calorimeter has 1 Xo sampling a comparison in resolutions at 0.3 cm and 1.5 cm is suggested. There is an improvement in the resolution by a factor of .65 between these points. This may be the dominant effect in reducing the coefficient in the resolution formula for the CHARM calorimeter.

Because of the details of the cascade process it is difficult to obtain a precise formula for the resolution expected in a given detector. However, the simple formula can be used to scale from one system to another where the situations are not too different. It also shows that it is better to use a high Z material if possible because of the dependence on the critical energy. There are of course excellent Monte Carlo programs available that can give more precise answers when they are needed.

GAS CALORIMETERS

A very attractive means of shower sampling, especially for large detectors, is to use gas as the sampling medium. Several techniques have been employed in gas calorimeters. The charge deposited in the cell has been collected using proportional planes, proportional tubes, flash tubes, Geiger cells or limited streamer tubes. Prototype devices that allow the charge to be drifted over long distances are undergoing tests [Price 82]. The basic problem in gas calorimetry is the loss of resolution because of the very thin sampling cell. As discussed earlier, large angle tracks produce large sampling fluctuations in the gaps. Figure 17 shows an EGS Monte Carlo of the particle tracks produced by a 1 GeV shower in a gas calorimeter [Hirayama 83]. The large angle tracks that move almost parallel to the sampling gaps are responsible for most of the degraded energy resolution in gas calorimeters. It should kept in mind that an electron deposits only 3 KeV when traversing a centimeter of argon gas. This is the reason that very low energy tracks can have such a big impact on the energy collected.

Although the electromagnetic energy resolution of gas calorimeters is about 70% poorer than that of scintillator or liquid argon devices for a given sampling thickness, gas calorimeters are the technology of choice for many of the large systems now under development. Recent advances in the technology of gas calorimetry

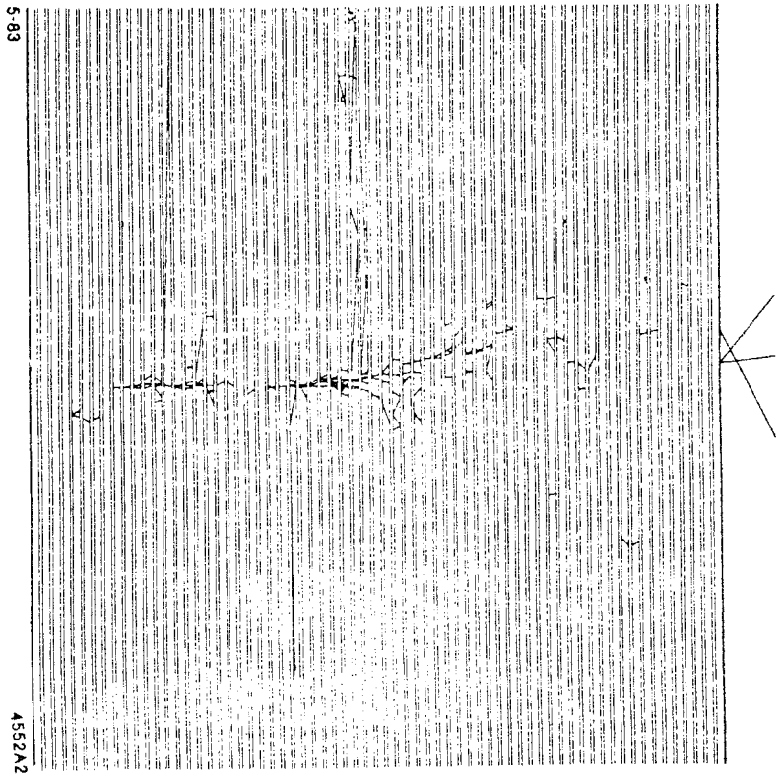


Fig. 17. EGS Monte Carlo of sampled electron tracks in a gas calorimeter from [Hirayama 83].

have made these detectors very attractive alternatives. Fischer showed that the chief limitation on good resolution was the track length fluctuations that arise because of the low density of the sampling gap. See Fig. 18 [Fischer 78]. An early attempt at reducing these fluctuations was the Geiger mode calorimeter developed for the PEP-4 facility at Berkeley [Yamauchi 82]. The basic idea was to limit the response to a gap crossing to a fixed value regardless of the ionization deposited. This was achieved by running the sense wires at a high enough voltage so that a Geiger discharge was created. The Geiger discharge was then quenched at cell intervals by the presence of nylon strings touching the sense wires. In this way a particle crossing a gap produced a unique pulse regardless of the angle of crossing or the Landau fluctuations in the ionization. However, this device suffered from saturation effects. Saturation effects occur when the probability becomes high that more than one particle crosses a gap within a single cell. The resolution is good, about $14\%/\sqrt{E}$ below 1 GeV, but stays about constant above 1 GeV. In this device, the energy must be corrected for this saturation and this is difficult when two showers are close together.

Another approach has been to utilize small tubes with proportional wires. Small tubes limit the probability of large gap angle crossings. See Fig. 16. A further attempt to give unique signals for each gap crossing has been pioneered by Atac et al. [Atac 83]. Their technique is to operate the wire gain in a region between the proportional mode and the Geiger mode. This mode is referred to as the

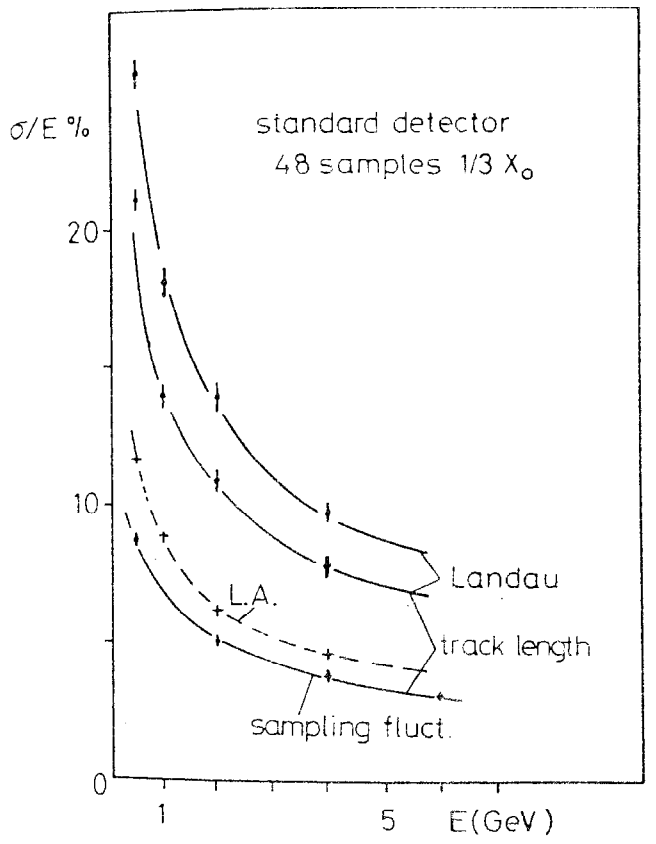


Fig. 18. EGS Monte Carlo study of the contributing factors to the energy resolution [Fisher 78].

limited streamer mode. With the appropriate gasses and voltage the ionization produces a fairly uniform and large pulse. In this way angle variations and Landau fluctuations are minimized. This technique has another very desirable feature. The very large pulses make it possible to digitize the charge without the use of an amplifier. This makes calibration much easier and lowers costs. The high gain of this mode (10**8) makes cathode pickup pads easy to use. Hence the segmentation can be made in any desired pattern.

Figure 19 shows the response of a limited streamer calorimeter to electrons of various energies and the resolution obtained [Battistoni 83]. A fall off in the response is apparent at high energy. The resolution also does not improve by $1/\sqrt{E}$. It is known from studies by the Electra Group [Battistoni 82] that the streamer statistics are not the limiting factor in the resolution. Just what does limit the resolution is not yet determined and perhaps further improvements can be made.

Table II shows a list of recent gas calorimeter devices and their resolution [Appel 83]. Also shown is their resolution scaled to one radiation length,sampling plates. The scaled resolutions cluster around 28% whereas for scintillator or liquid argon devices the equivalent resolution is about 15%. The entry from Battisoni shows that the streamer statistics allow for a factor of two improvement in the resolution. With the large amount of work going on in this area further improvements in the near future might be anticipated.

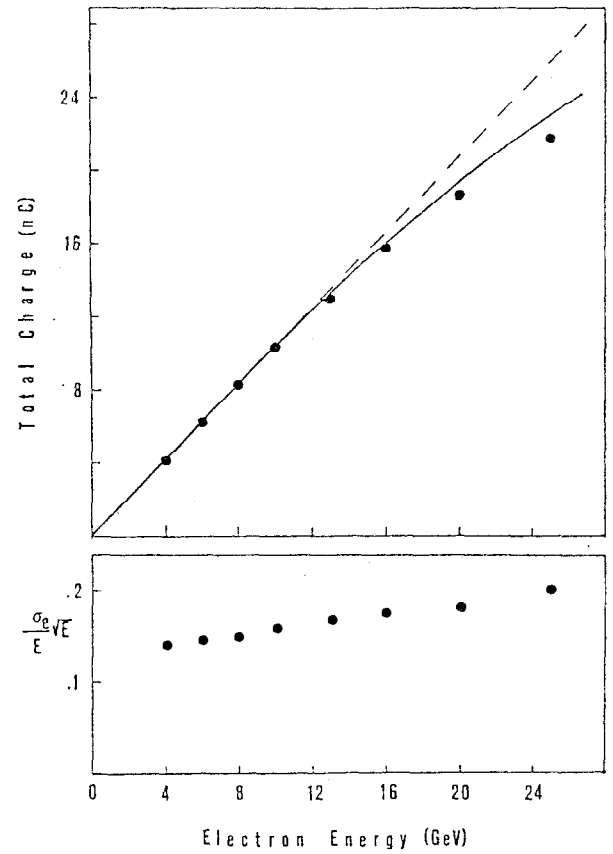


Fig. 19. Energy response and resolution in a limited streamer mode calorimeter [Battistoni 82].

TABLE II [Appel 83]

ENERGY RESOLUTION
ELECTRONS

GAS	BEST % RESOL	t	SCALED % RESOL $\times\sqrt{\frac{E}{t}}$
ATAC: MAC PROTO (S.A.)	$16.2/\sqrt{E}$	.5	23
	$19.7/\sqrt{E}$	.5	28
BATTISTONI: ELECTRA TYPE 1	$28\%/\sqrt{E}$	1	28
TYPE 2	$15\%/\sqrt{E}$	.35	25
MISHINA: CDF-EC TYPE 1	-	-	30-40
TYPE 2	$23\%/\sqrt{E}$	.5	29
LILLETHUN: HPC	$14.5\%/\sqrt{E}$	.26	28
	$*12.5\%/\sqrt{E}$	.26	24
VIDEAU: ALEPH	$16\%/\sqrt{E}$	.35	27
WENZEL: PEP4 (GEIGER)	$14\%/\sqrt{E}$	.25	28
SKUBIC: CLEO	$14.6\%/\sqrt{E}$	.2	33
BRANDENBERG: IT	$\frac{20\%}{\sqrt{E}} + 1\%$ @25 GEV	.8	28
FUESS: FLASH CH.	9.5% @5 GEV	.22	45
SCINT			
FLEGEL: CHARM	$20\%/\sqrt{E}$	1	20
PRIMARY STREAMERS (BETTER THAN STATISTICS OF PRIMARIES SHOULD BE IMPOSSIBLE)			
BATTISTONI: ELECTRA			
700 @ 4 GEV	$7.6\%/\sqrt{E}$	.35	12.7

$\sqrt{\frac{4GeV}{700}} = .076\ GeV^{\frac{1}{2}}$

DENSE SAMPLING CELLS

Although gas sampling calorimetry is being used extensively in new detector designs, sampling with scintillator or liquid argon is still a viable option. These devices offer better energy resolution and are more compact than gas sampling calorimeters. The sampling gap for a gas device might take up more than a centimeter whereas dense sampling materials require gaps of only a few millimeters. Sampling with gas can easily double the size required to contain showers. The larger gaps also lead to increased transverse dimensions as scaled by the increased Molière radius. Hence dense sampling calorimeters make possible better two photon separation.

From a performance standpoint, liquid argon is the most attractive sampling material. This technique was pioneered by Willis et al. [Willis 74]. See also [Fabjan 77]. Two large liquid argon systems have been constructed and operated for some time. The Mark II detector at SLAC [Abrams 79] and the TASSO detector at PETRA [Brandelik 82] have demonstrated excellent operating characteristics for these devices.

A liquid argon detector is a no gain device. The charge produced in the liquid argon (1 electron/50 eV) is collected on pads. Hence there are no gain variations that must be calibrated. As long as the argon is kept reasonably pure (ppm of electro-negatives) the long term stability

is essentially constant. The gain of the amplifiers that amplify the charge is easy to measure. A standard shaped pulse is induced on the pads through a precision capacitor. Calibrations can be held to 0.5% or better [Fabjan 77]. Since the charge can be collected on pads, essentially any segmentation desired can be constructed. Also liquid argon is not susceptible to radiation damage.

Liquid argon calorimeters require a cryogenic container which may present design problems and certainly adds substantially to the cost. The possibility always exists that eventually a room temperature liquid will be found that performs as well as the liquid argon. The challenge is to find something that can be purified and is not electronegative. At the present time a complicated chemical called TMS is undergoing tests as a possible substitute for liquid argon. This chemical appears to have some drawbacks but it may turn out to be successful compromise.

Another limitation to liquid argon is the low signal level that must be handled by the amplifiers. The signal to noise level may lead to difficulties in the detection of low energy photons. The Mark II detector has poor efficiency for photons below about 200 MeV whereas the gas calorimeter of the Mark III detector has essentially 100% efficiency down to at least 50 MeV!

New experimental requirements on calorimetry dictate that they have hermiticity. That is, no energy must be allowed to escape through cracks. This means that liquid argon devices meeting this condition must be built in a single cryostat so that there are no gaps such as are present in Mark II and TASSO calorimeters. Whether such giant calorimeters can be constructed remains to be seen.

Scintillator is still widely used in calorimeters. The Axial Field Spectrometer, the Argus detector and UA2 have employed scintillator in their calorimeters. The development of wave bar read out for scintillator has added a great deal of flexibility to the design options. In particular the tower structure is now possible with scintillator sampling. Wave bar read out is essentially a method for violating the Liouville theorem on photon collection. Scintillators function because of the addition of materials that absorb photons at one wave length and re-emit them at a longer wave length. The scintillator is relatively transparent to this longer wave length light and photocathodes are more efficient at these wave lengths. Figure 20 shows some emission and absorption spectra of commonly used wave shifters. Table III lists peak emission and absorption values for a number of wave shifters. By judicious choice of shifters photons can be moved through a sequence of wave lengths. At each shift the light is emitted isotropically. Some is reabsorbed and some is lost because it is outside the critical angle for internal reflection. Typical losses in intensity from these effects are on the order of 90%.

The wave bar technique utilizes this principle. In this

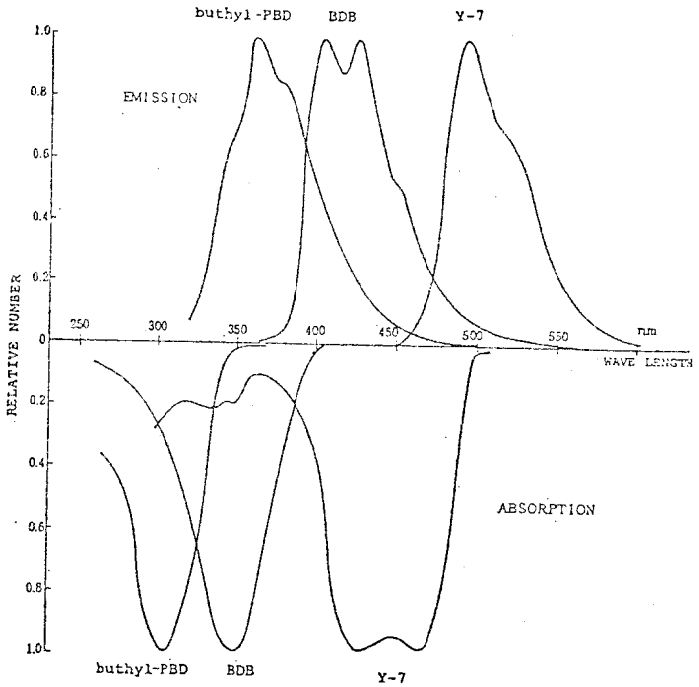


Fig. 20. Emission and absorption curves for SCSN scintillator and wave bar Y-7.

TABLE III

The wavelength, λ, of the absorption and emission peaks of different wavelength shifter and scintillator materials

Wavelength Shifter	Absorption λ [nm]	Emission λ [nm]
BBQ	380	500
Yellow 323	525	600
Perylene	410	470
K-27	430	495
Coumarin(*)	360	410
Acridine Yellow	450	520
Acridine Orange	495	530
Scintillator		
GS 2003	-	420
GS 2021	-	370

(*) Coumarin = 7 diethylamino-4-methan marin.

case a wave shifter is put in a separate bar of plastic. The bar absorbs the directed light from a piece of scintillator and re-emits it isotropically in the bar. The light that is captured is propagated to the PMT. Figure 21 shows some typical attenuations of wave bars. Figure 22 gives the schematic of a scintillator tower employing two sequential wave bars. Because of the substantial loss of light at each junction, it is easy to degrade the resolution of a device by limiting the number of collected photons. Wave bar towers also suffer from edge effects. The wave bar also scintillates, and shower particles traveling along the bar can produce substantially more light than appropriate for uniform sampling. Nevertheless these devices are relatively easy to construct and give excellent resolution. For example,the Argus calorimeter test modules gave 7% resolution at 1 GeV. Also new plastic scintillators made from Plexiglas (eg. plexipop) or polystyrene (eg. SCSN) offer low-cost material that is affordable even in very large detectors.

Plastic scintillator does suffer from radiation damage. For example UA1 had to replace a lot scintillator because of a misalignment of the beams. It also has a tendency to discolor and loose pulse height with time. Calibration is not easy and systematics in the calibration can lead to substantial degradation of the resolution (eg. UA2).

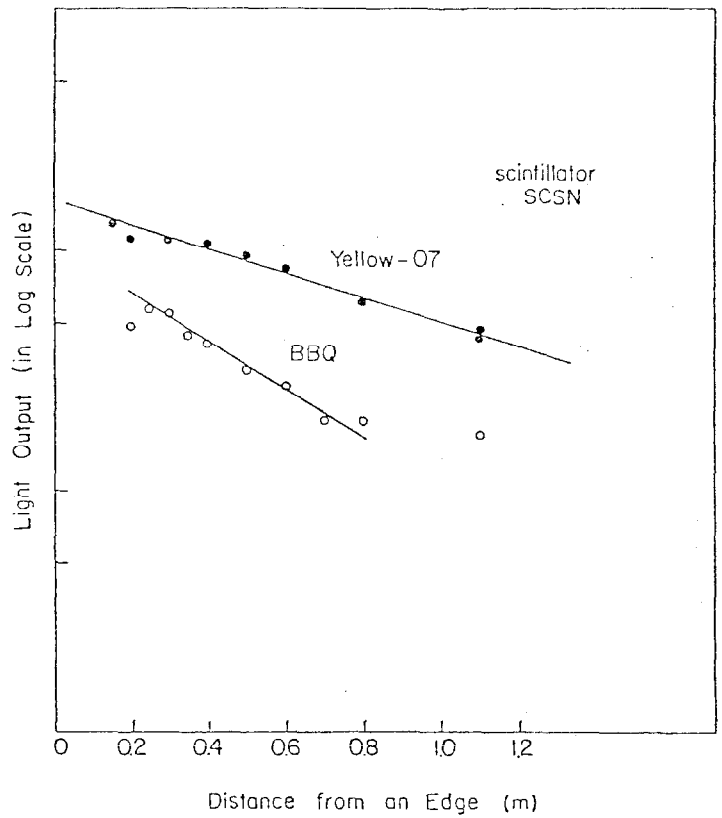


Fig. 21. Attenuation in typical wave bars.

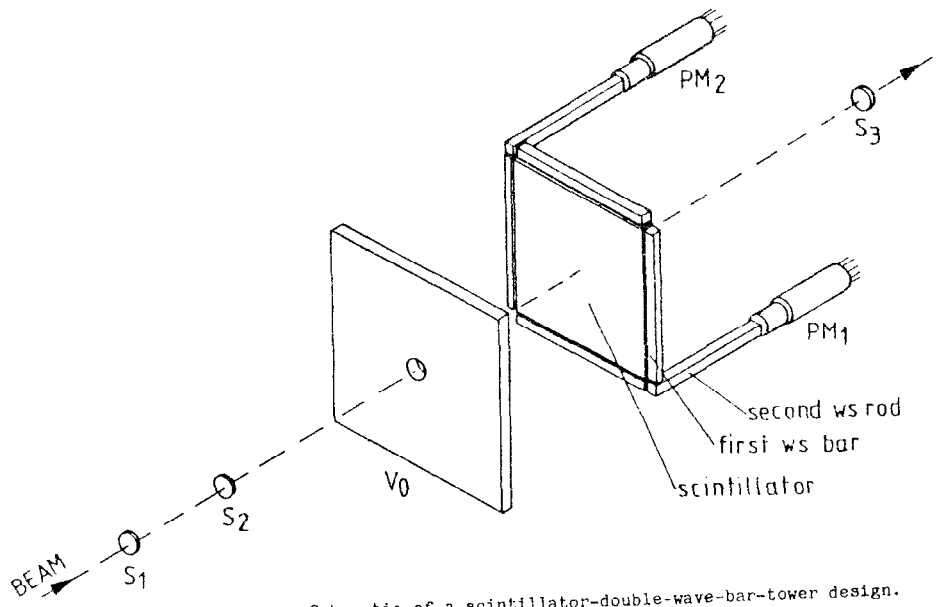


Fig. 22a. Schematic of a scintillator-double-wave-bar-tower design.

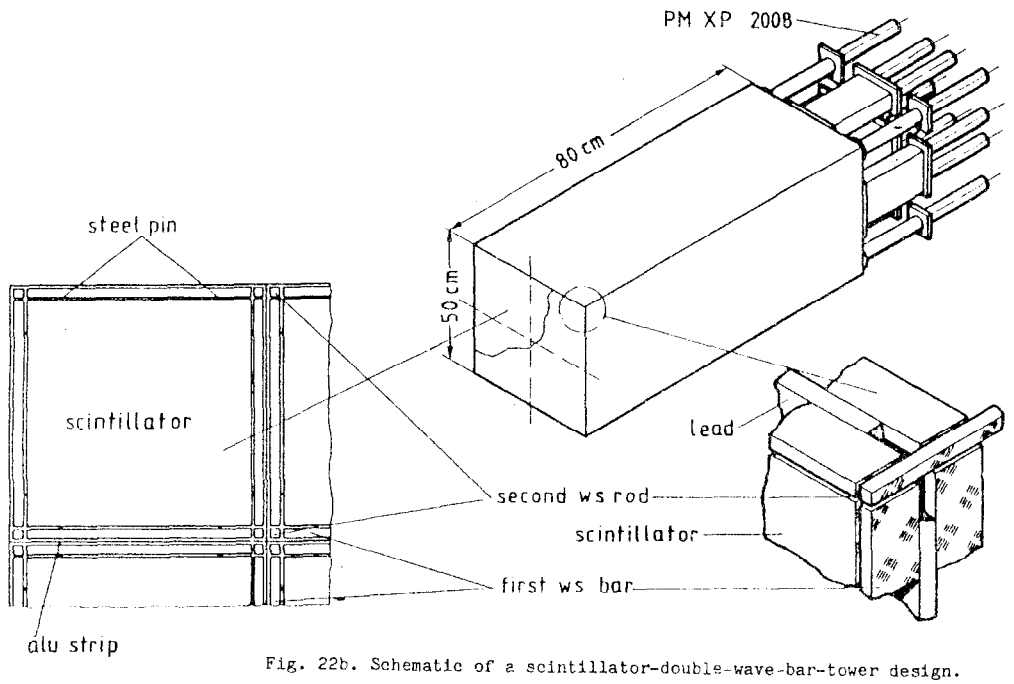


Fig. 22b. Schematic of a scintillator-double-wave-bar-tower design.

POSITION RESOLUTION

This section reviews the dependence of the photon position resolution on the calorimeter parameters. In principle, a maximum likelihood fit to the shower profile can be used to determine the position of the shower. An analytic treatment has been given by [Akopdjanov 77]. For a given cell segmentation of width d, the resolution is substantially better than $d/\sqrt{12}$ because the lateral shower profile extends into the neighboring cells and provides information on the shower position.

Unless the cell size is much smaller than the shower size, the mean energy position for the photon results in a biased estimate. This is shown in Fig. 23 from Akopdjanov et al.. Only when the shower develops along the symmetry points of the cell, namely the edge and the center, does the mean energy position give an unbiased position estimate.

The lateral shower profile has been fit with one or two exponentials [Hoffman 79], [Akopdjanov 77]. If a single exponential with attenuation length b is assumed, then the shower position with respect to a cell boundary is given by the equation

$$x = b \ln((R+1)/2R))$$

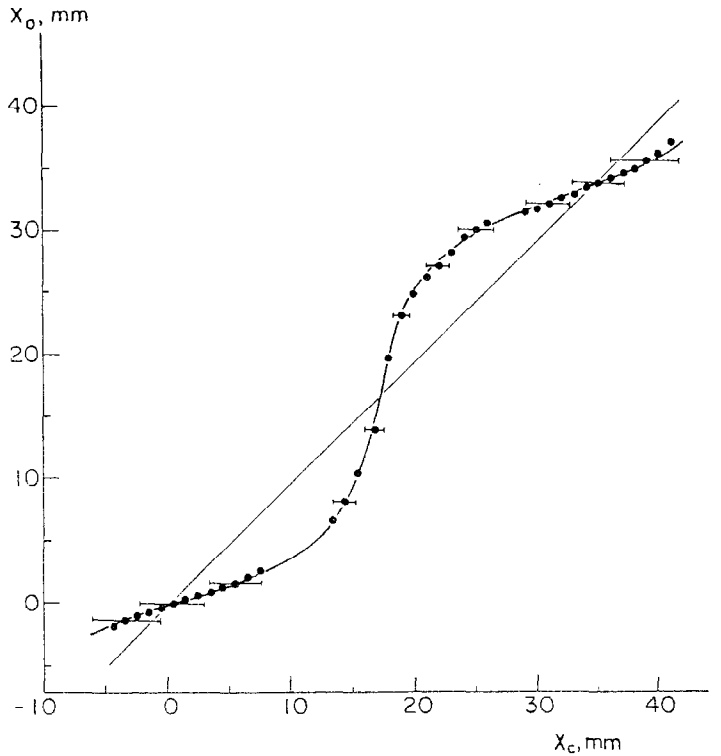


Fig. 23. Position bias from energy mean in strips or towers [Akopdjanov 77].

where R is the ratio of the energies on each side of the boundary. The denominator is taken as the larger of the two energies.

The error in x can be determined from the fluctuations in the energy on each side of the boundary. A first guess might be that the energy fluctuates the same as the energy resolution. That is, the variation on the energy across the boundary is assumed small. Then the error on x is given by

$$\sigma_x = b\eta\sqrt{R/E}\,.$$

Here η characterizes the energy resolution of the calorimeter. This formula gives an exponentially rising error as the shower moves away from the cell boundary. See Fig. 24.

The assumption of no fluctuation of the energy across the boundary leads to an underestimate of the error by about a factor of two for 10% resolution. For example the Argus detector finds a resolution of about 1.1 cm at 1 GeV, while the above formula predicts the resolution should be about one third of that. The reason is that energy fluctuations across the boundary dominate in the energy ratio. The dependence on the energy resolution is slight. The energy resolution appears in quadrature with the boundary fluctuations. Hence the energy resolution is not an important factor in the position resolution for values less than about $15\%\sqrt{E}$.

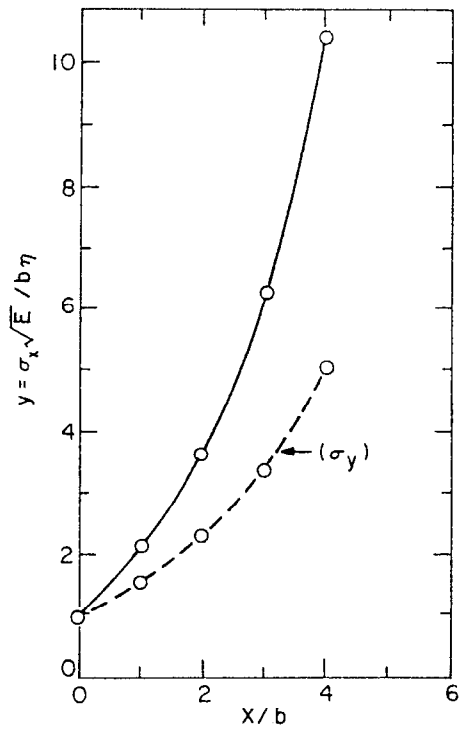


Fig. 24. Position resolution as a function of the distance from the segmentation boundary. Based on negligible energy fluctuation across the boundary.

The resolution should scale as the ratio of the cell size divided by the Molière radius. The EGS Monte Carlo predicts a shower shape shown in Fig. 25 for a Molière radius of 2.8 cm. It is not an exponential but a simple transformation

$$\zeta = \sqrt{x}$$

produces a distribution that is exponential except near to the shower axis. See Fig. 26. These results are for 0.5 Xo uranium plates and 4 mm liquid argon sampling gaps.

Figure 27 shows the average shower position, y, from a boundary, as a function of the energy ratio, R. Also shown is the average R value as a function of the shower position. Because of the skewness in the distributions, these two curves are not quite the same. In Fig. 28 the rms resolution in y is shown as a function of the position estimate for a 1 GeV shower. The resolution is found to improve as $1/\sqrt{E}$.

Figure 29 gives the position resolution for several detectors as a function of their cell size. These are for approximately 1 GeV showers. The EGS Monte Carlo point appears to be a little better than the trend of the actual detectors. It also has a shorter Molière radius and might have been expected to be a bit worse. The extent to which the Moliere radius affects fluctuations across a boundary needs to be investigated further.

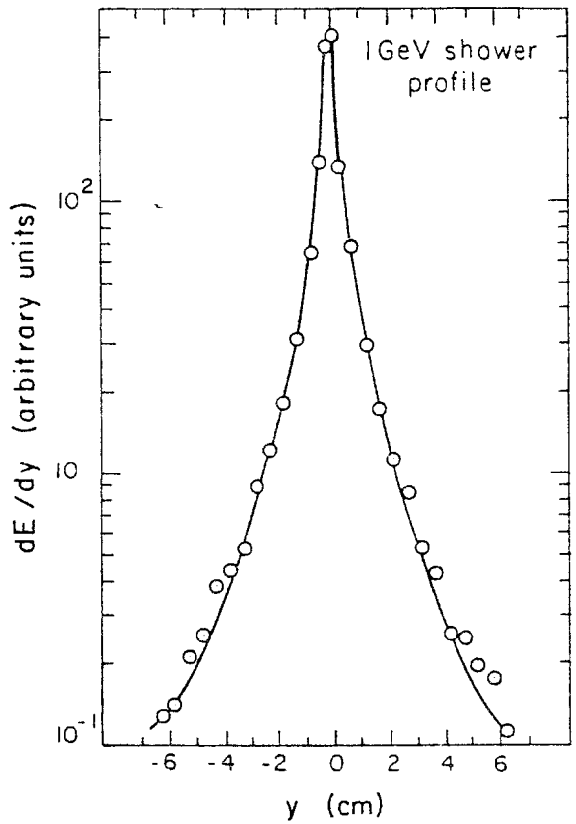


Fig. 25. Lateral shower profile from EGS Monte Carlo. One half Xo uranium plates and 4 mm liquid argon sampling gaps.

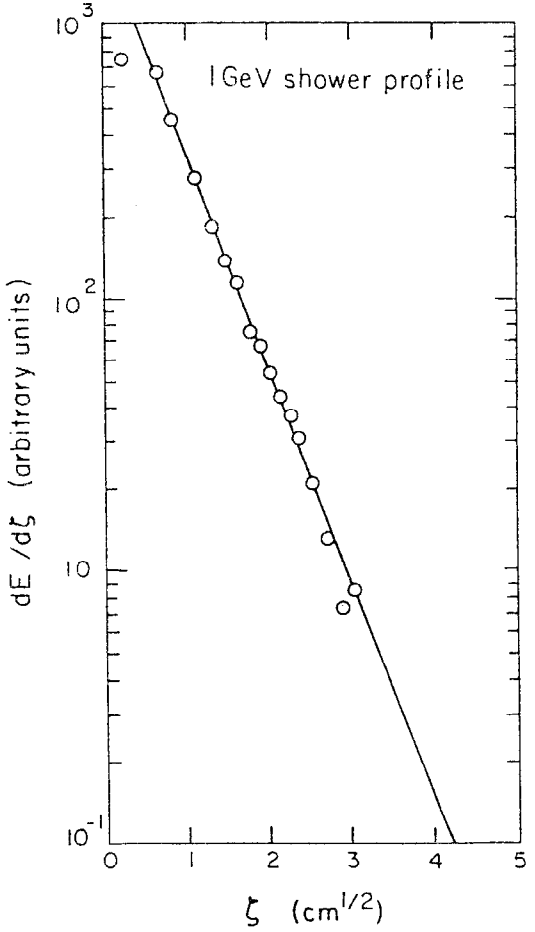


Fig. 26. Same profile as in Fig. 25 but with a new scale.

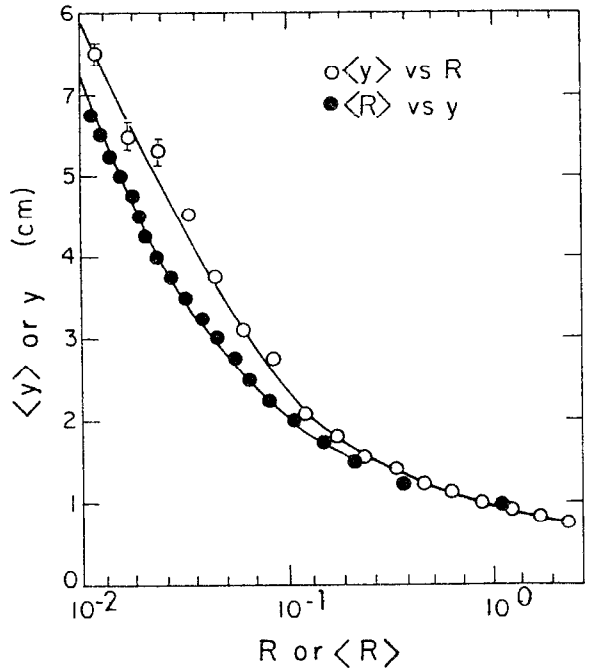


Fig. 27. Mean position as a function of the energy ratio across segmentation boundary. Also shown is the average value of the energy ratio as a function of the shower distance from the boundary.

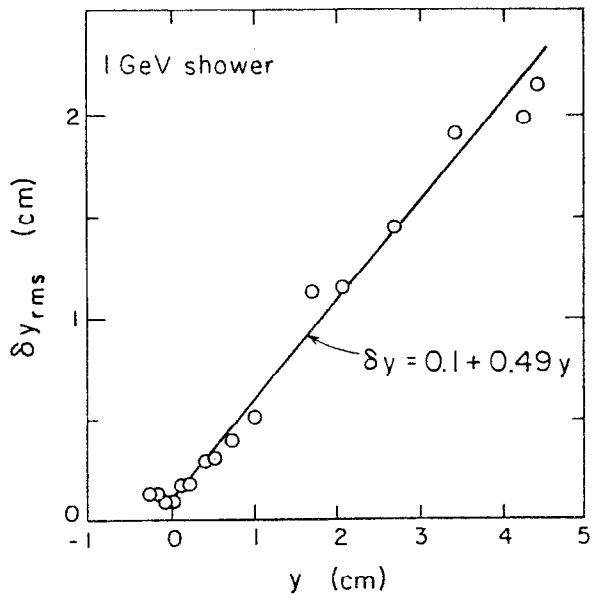


Fig. 28. Position accuracy as a function of the shower distance from the segmentation boundary. Included are the energy fluctuations across the boundary.

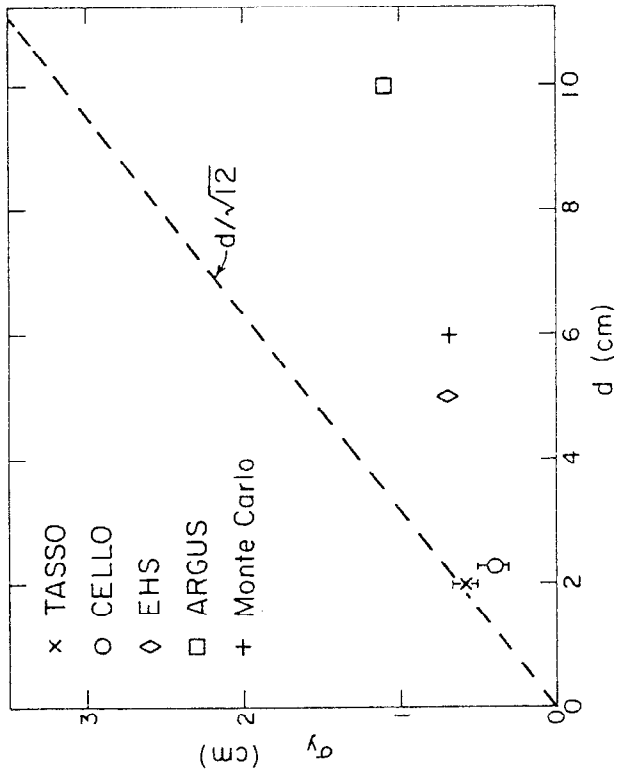


Fig. 29. Compilation of the position resolution for several segmentation values. Included (+) is the Monte Carlo result for 6 cm strips (both boundaries are used).

HADRONIC SHOWERS

Figure 30 shows a Monte Carlo generated shower for a 100 GeV negative pion in a block of iron [Grant 75]. The two most striking features are the neutrons bouncing around in the block and the uneven character of the energy deposition. The dominating scale for hadronic showers is usually the absorption length. The absorption length for aluminum is about four times longer than the radiation length while for uranium it is about thirty-three times longer than the radiation length. This results in blobs of energy from pizeros being deposited on a scale of the radiation length while the remaining energy is absorbed with a much longer scale.

Hadronic showers are much more difficult to understand because of the mixture of electromagnetic and hadronic processes. A typical two GeV pion deposits about half of its energy in the first absorption length. Shower curves in liquid scintillator are shown in Fig. 31. These results are from the HPWF neutrino detector [Benvenuti 75]. Each segment corresponds to 0.57 absorption lengths. The integrated absorption as a function of energy falls on a nearly universal curve. See Fig. 32. There are various calculations of t_{med} but the results differ by a substantial fraction of an absorption length. The results of Gabriel agree with the data fairly well. His HETC calculation gives

$$t_{med} = 1.7 + 0.2 \ln E(GeV)$$

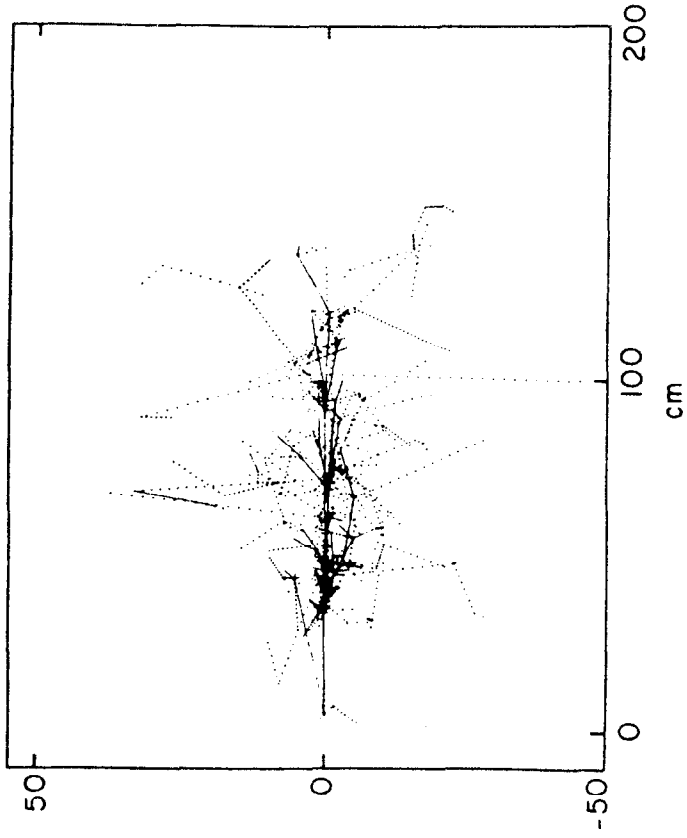


Fig. 30. A 100 GeV pion cascade in iron [Grant 75]. From [Fabjan 82].

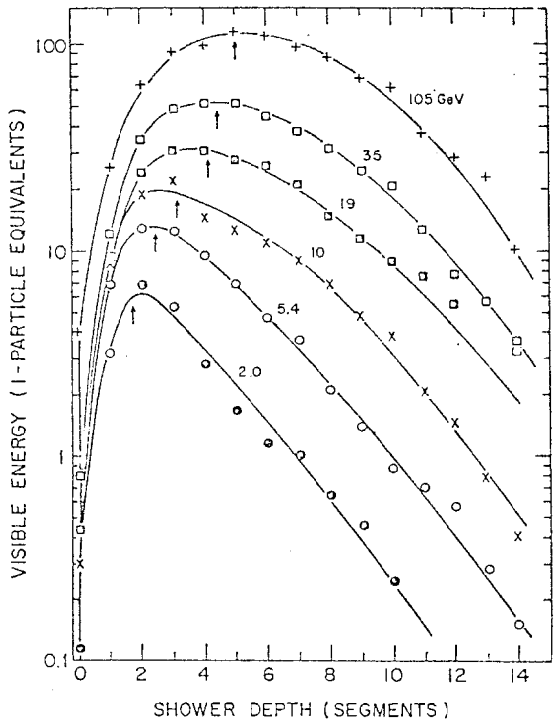


Fig. 31. Hadronic shower profiles in liquid scintillator from HPWF measurements. Presented by L. Sulak in [Atac 75].

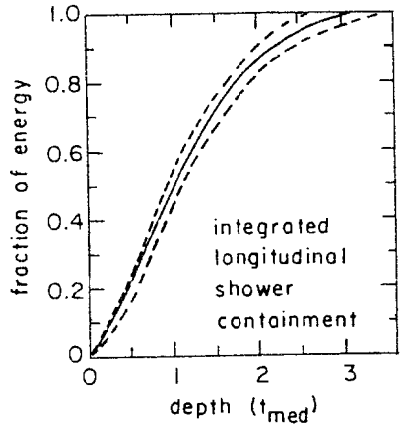


Fig. 32. Shower containment curve in terms of the 50% containment length, tmed. From HPWF in [Atac 75].

where t_{med} is in absorption lengths.

About five absorption lengths are required to fully contain a shower. The Monte Carlo calculations of Gabriel indicate that even with five absorption lengths, an appreciable fraction of the shower leaks out the back. The resolution reaches a plateau after about this depth as shown in Fig. 33 [Fabjan 77].

After the shower reaches shower maximum, the profile decreases in an approximately exponential fashion with decay constants given in Fig. 34 [Whiteside 73]. For low energy the attenuation length is approximately an absorption length.

The lateral containment can be parameterized as

$$1/E\ dE/dxdy = 0.146\ e^{-2.01 r^{0.446}}$$

where r is in cm. This result is for an iron scintillator calorimeter and 20 GeV pions. The size scales with energy roughly as the fraction of energy contained within a strip extending 5 cm on each side of the shower axis [Cook 81]. This fraction is given in percent by

$$f = 48.2 + 7.2\ \ln E(\mathrm{GeV}).$$

Approximately one absorption length in radius contains 95% of the shower energy.

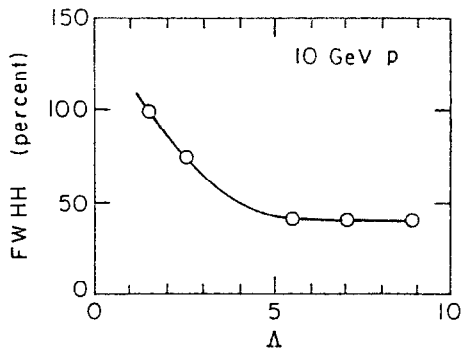


Fig. 33. Resolution as a function of calorimeter depth [Fabjan 77].

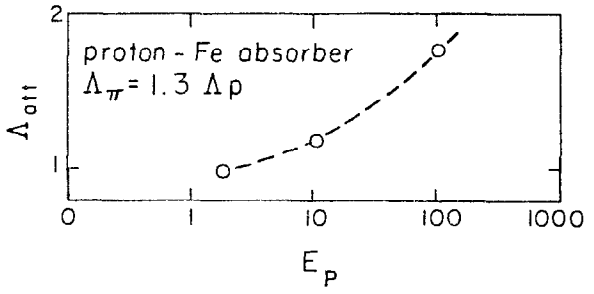


Fig. 34.Hadronic shower attenuation length (in units of the absorption length) as a function of the hadron energy [Whiteside 73].

Hadronic showers are seen to be similar to electromagnetic showers except there is a new scale, the absorption length. Also there is a slow energy dependence of the parameters unlike the situation for photon showers. To learn more about hadronic showers Monte Carlo programs must be used.

A word of caution should be made in regards to Monte Carlo programs. Although the general shower features are fit by several different codes, these codes differ in the shower structure, in particular the electromagnetic component. A comparison is made of three programs in Fig. 35 [Amaldi 81]. There is a relatively new code by Gabriel called HECC that improves the shower model for energies above about 20 GeV. Figure 36 shows a comparison of the HETC Monte Carlo result with the experimental data from a liquid scintillator iron calorimeter [Selove 75]. The agreement is exceedingly good. The calorimeter is about five absorption lengths in depth and one absorption length in radius. Table IV gives the numerical values for where the energy is dissipated for each of three energies. For the 15 GeV protons a total of 34% of the energy is lost. This comes mostly from binding energy losses (12%), out the back (11%), from nonlinear sampling (4%), out the sides (5%) and out the front (2%). Assuming that the efficiency for detecting the remaining energy is the same for electrons and pions, this loss results in an electron/pion energy response of 1.5. This difference in response is one of the major technical problems with hadron calorimetry. This may degrade the performance, particularly in a hadron jet measurement.

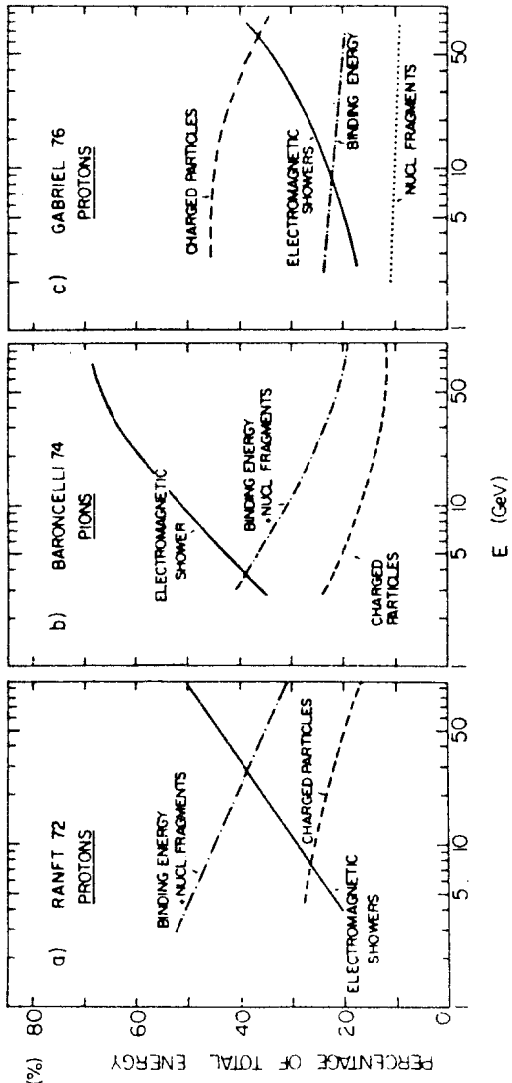
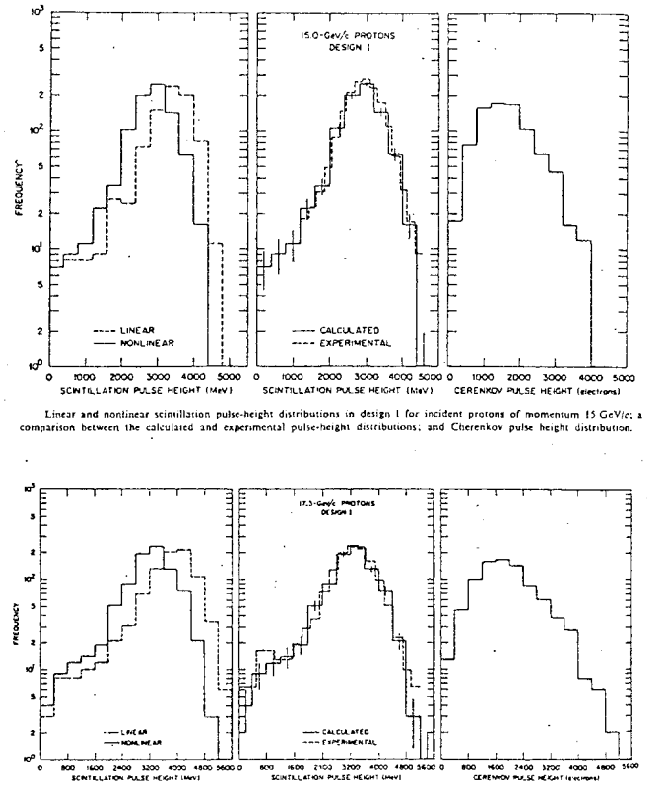


Fig. 35. Hadron shower Monte Carlo comparison [Amaldi 81].



Linear and nonlinear scintillation pulse-height distributions in design I for incident protons of momentum 15 GeV/c; a comparison between the calculated and experimental pulse-height distributions; and Cherenkov pulse height distribution.

Fig.36.HETC calculation of a liquid scintillator calorimeter response. The linear and non-linear(saturated) response is emphasized [Gabriel 75].

MINERAL-OIL-IRON IONIZATION SPECTROMETER

TABLE IV [Gabriel 75]

Energy deposition and leakage energy produced by the interaction of multi-GeV/c protons in the design 1 spectrometer

Type of energy deposition	*Energy deposition (MeV)* 7 GeV/c protons			15 GeV/c protons			17.3 GeV/c protons		
	Iron, lucite, and liquid (linear)	Liquid Linear	Liquid Nonlinear[a]	Iron, lucite, and liquid (linear)	Liquid Linear	Liquid Nonlinear[a]	Iron, lucite, and liquid (linear)	Liquid Linear	Liquid Nonlinear[a]
Primary ionization	173.	53.8	52.6	188.	59.1	57.8	199.	62.3	60.1
Secondary proton ionization	1925.	691.	556.	4010.	1458.	1181.	4466.	1623.	1308.
Secondary $\pi^{\pm}$ ionization	320.	177.	172.	1127.	382.	369.	1350.	457.	441.
Secondary $\mu^{\pm}$ ionization	8.66	3.10	2.99	16.8	5.69	5.47	21.8	8.02	7.12
Nuclear recoil and evaporated charged particles other than protons[a]	169.	69.9	9.71	361.	162.	26.5	404.	175.	25.8
Excitation energy following evaporation[a]	111.	23.7	23.7	229.	50.5	50.5	258.	57.7	57.7
Neutrons with energy <10 MeV[a]	139.	50.8	19.	320.	160.	37.2	361.	114.	42.
Electromagnetic	1128.	366.	366.	3189.	1038.	1038.	3761.	1233.	1233.
Total	4194.	1435.	1202.	9411.	3255.	2675.	10821.	3730.	3175.

Particle type	*Leakage energy (MeV)* 7 GeV/c protons Front	Side	Back	15 GeV/c protons Front	Side	Back	17.3 GeV/c protons Front	Side	Back
Protons	7.36	30.	153.	20.6	57.7	594.	27.5	58.6	701.
Neutrons	40.9	399.	222.	151.	594.	703.	194.	670.	956.
$\pi^{\pm}$	23.9	43.6	95.3	68.3	73.7	298.	78.1	96.6	392.
$\mu^{\pm}$	0.182	1.73	2.22	0	3.17	7.91	0.81	2.2	12.
γ	16.1	31.6	14.1	42.9	68.4	85.2	46.7	83.3	110.
$e^{\pm}$	6.55	4.85	3.45	17.5	19.3	27.2	11.8	13.6	36.4
Total	94.4	427.	454.	234.	817.	1720.	269.	934.	2200.
Total leakage energy (MeV)		975.			2771.			3403.	
Binding plus neutrino energy (MeV)		952.			1866.			2156.	
Electromagnetic source energy (MeV)		1212.			3444.			4068.	

[a] See description of spectrometer.
[b] ΔR = 0.01 g/cm² MeV.
[c] Assumed to deposit their energy at their point of origin.
[d] Includes rest mass energy.

This difference in response of hadrons and photons is the major cause of the relatively poor energy resolution in hadron calorimeters. The reason is that the number of pizeros produced in a hadron shower is not very large. As a consequence, the fluctuations on the number of pizeros and the different response they produce, substantially degrades the energy resolution. It is possible to obtain about $50\%/\sqrt{E}$ resolution with a conventional calorimeter but not much better. At this point the pizero fluctuations dominate the resolution.

MISSING ENERGY COMPENSATION

Because hadron showers that contain many pizeros should be short and thin whereas those that contain few pizeros should be long and fat, it is possible to improve the resolution somewhat by using the shower shape to correct the energy. This technique is not totally satisfactory nor is it appropriate in a jet environment where several showers are likely to overlap.

A technique is needed that is sensitive to the relative fraction of electromagnetic energy and hadronic energy deposited by the shower. This could be done at least hypothetically if the energy were sampled by two media; one which was sensitive to the beta equals one

electrons and another which was sensitive to both the electrons and other charged particles. For example one sampler could be lucite, which is sensitive only to fast particles, while the other sampler could be scintillator. Then the fraction of pizeros produced could be determined from the relative pulse heights in the two samplers. Another technique might be to utilize the slow scintillation pulse and the fast Cerenkov pulse in total absorbing materials such as scintillating glass or barium fluoride. By appropriate gating or wave form sampling, the magnitude of the different components could be determined and hence the fraction of electromagnetic energy in the shower.

Whether or not the precision to which the two components can be measured is sufficient to restore the resolution remains to be seen. It would also appear too expensive to build a hadron calorimeter out of scintillating glass or barium fluoride. However, the information gained in the first absorption length or so might be sufficient to reconstruct the missing energy.

Fortunately there exists a very clever technique to compensate for the missing energy. This technique, called fission amplification, was pioneered by Fabjan et al. [Fabjan 77]. This group showed that if uranium plates were used as the absorber in a sampling calorimeter, then the missing energy could be made up from energy released from fission induced by the hadronic shower. They estimated on the basis of some beam tests and the known cross sections that the number of fissions per incident GeV of energy would be 29.5. These fissions would release 236 MeV of 8 MeV gammas. In addition the fission neutrons would release an additional 327 MeV of gammas through inelastic collisions with the uranium nuclei. In this process there is a miniature chain reaction in which the primary nuclear breakup causes additional fissions and these in turn cause other fissions etc.. Fortunately the yield is less than one! More recently, Monte Carlo calculations by Gabriel show that the amount of available energy is essentially doubled for a uranium absorber [Gabriel 78]. Some fraction of this energy is sampled in the sensitive gaps and leads to compensation for the missing energy. Since the amount of fission is determined by the primary nuclear breakup which in turn is proportional to the missing energy, the compensation is just the amount needed to make up the lost energy on an event by event basis. The fission restores the resolution and brings the response for hadrons close to that for electrons or photons.

Since the fission energy is more than is needed to compensate for the binding energy losses, the exact amount of compensation will depend upon the other losses such as leakage out the back of the calorimeter. This means that the precise compensation will be a function of the calorimeter dimensions. Also since the compensation energy is in the form of low energy gammas and neutrons, the sampling medium will also effect the level of compensation. For example, scintillator is sensitive to both photons and neutrons whereas liquid argon is mainly sensitive to photons. It is possible that gas calorimeters would be inefficient for the detection of both the neutrons and photons. Thus gas sampling might show little compensation. Tests

on this particular aspect are presently under way at CERN.

Figure 37 shows the relative response of electrons and hadrons for various detectors [Willis 83]. Both the uranium-scintillator and uranium-argon devices demonstrate approximate compensation. The cause of the decrease in the ratio at low energy is not known for certain. One view is that at low energy, pions act more like muons and these are known to deposit a bigger fraction of their energy in the sampling cell than electrons do (see the previous section on missing energy in electromagnetic showers). On the other hand, shower containment gets much better at low energies and the effect could be related to less leakage.

The compensation is very fast, on the order of 100 ns, so a long gate is not necessary. However for very fast timing, the amount of compensation may be gate width dependent.

In Fig. 38 we show the hadron resolution for 4 GeV pions. This result is for 2 mm uranium plates and 2 mm thick scintillator. The limiting resolution of uranium calorimeters turns out to be about $22\%/\sqrt{E}$ although this requires impractically thin plates. More realistic numbers are about $35\%/\sqrt{E}$ for 3 mm plates. Copper or some other material may be substituted for the uranium plates for up to one in three without a significant degradation of the resolution. The cost of uranium is a some what fuzzy issue because it is not commercially available. For simple plates, 3 mm thick, a cost of about $500 per square meter has been

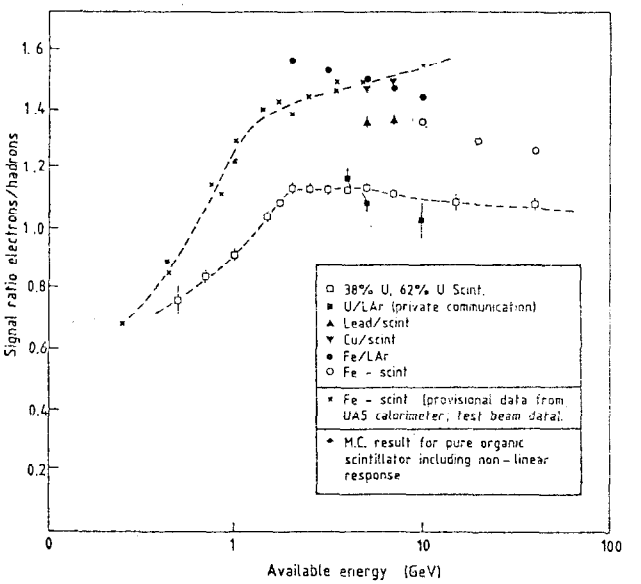


Fig.37. Electron to hadron response ratio for conventional and uranium calorimeters [Willis 83].

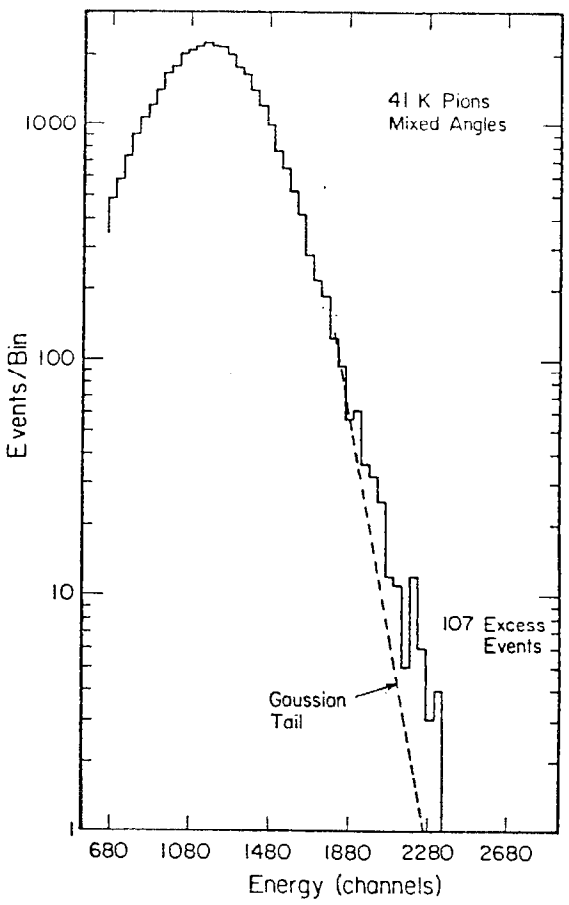


Fig. 38. Energy response to 4 GeV pions in the AFS uranium calorimeter [Willis 83].

estimated. Thinner plates cost more. Uranium can be welded, sheared or machined but this requires a special environment. The surface radioactivity is about .23 rad/hr and is primarily from low energy (about 1 MeV) betas. The radiation is not a particularly big health hazard. However it is very important to avoid breathing any uranium contaminated dust.

Since uranium is radioactive it produces noise in the sampling gaps which must be taken into account. The AFS group finds that a single tube sees 3.8 GeV equivalent noise in a 10 μs gate. This corresponds to about 60 MeV per square meter of gap per microsecond. The rms fluctuations on this noise amount to 20 MeV per square meter per microsecond. These fluctuations should scale as the square root of the area times the gate width. The noise can be shielded with plastic or G-10 sheets. Figure 39 shows the attenuation measured with a gas survey meter for various materials and thicknesses. A note of caution is due here in that shielding the uranium noise might also reduce the fission compensation.

There is a benefit to the uranium noise however. The noise can be used to calibrate each of the channels in the AFS system to about 2%. What the ultimate limits are is not clear at present. The noise provides a standard calibration pulse that uniformly illuminates the scintillator. It is difficult to produce a standard pulse in scintillator calorimeters which do not have uranium plates. Giving a standard pulse of light to the phototube is not sufficient

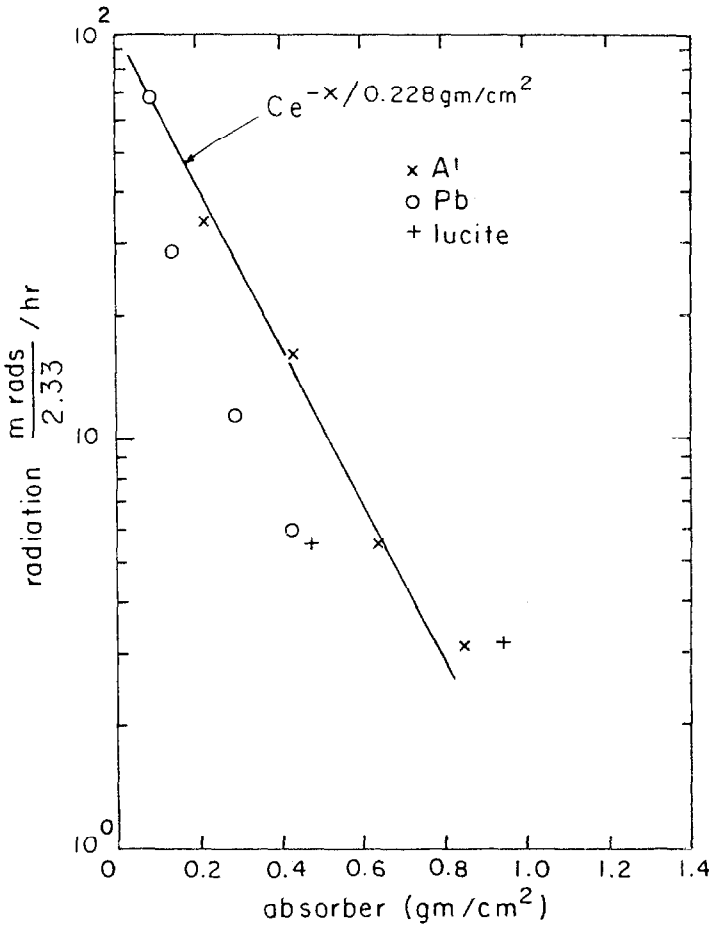


Fig. 39. Attenuation in radiation from uranium plates as a function of thickness and material.

because scintillator ages and its response decreases with time.

Although uranium absorbers are expensive, their superior performance warrants their use in modern high energy experiments. UA1 is proposing to replace their inner calorimeter modules with uranium. This would greatly reduce the problem of trying to estimate the energy of a jet of hadrons and photons and better define missing momentum. Perhaps with increased use, the fabrication techniques will improve and result in a better and cheaper product.

CALORIMETER GEOMETRIES

There are two basic options for calorimeter geometries. The segmentation can either be uniform like bricks or planks, or it can be tapered so that the it points back to the target or the point of interaction. The first type of design is indicated schematically in Fig. 40. The lines can represent either tower boundaries or strip boundaries. The figure depicts the two problems with this non-projective geometry. The first, 40(a), shows that without substantial radial segmentation, the depth at which the shower develops will not be well determined. Hence the angle measurement of the particle will be degraded. This effect is seen

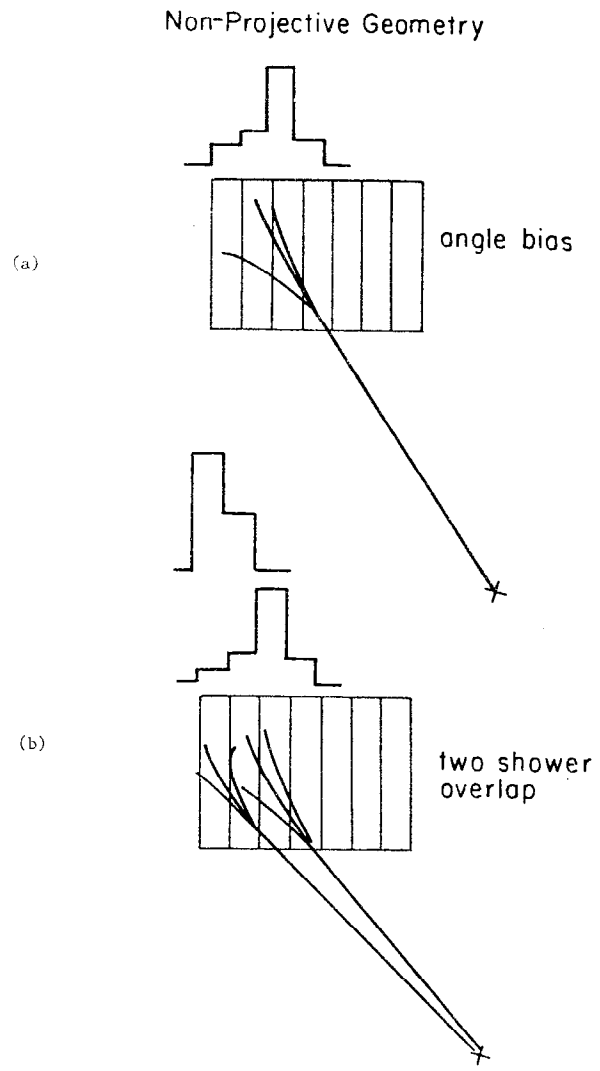


Fig. 40. Schematic illustrating non-projective geometry.

in Fig. 41. This figure gives the position errors for the AFS calorimeter. Although the towers in this calorimeter are not projective in either x or z, they are closer to being projective in x. This difference accounts in the most part for the substantially better position resolution in x than in z.

The second limitation of non-projective geometry is the degraded two particle separation. As indicated in the schematic of Fig. 40 b the showers tend to overlap in the cells and make the separation difficult.

Figure 42 indicates how projective geometry eliminates these two problems. Showers follow naturally along a cell so that spreading to other cells is kept to a minimum. Of course some materials do not lend themselves to the projective configuration. It is clear that making projectively shaped pieces of barium fluoride would cost substantially more than making rectangular pieces. On the other hand, by using pads in liquid argon calorimeters or gas calorimeters, the incremental cost in making the geometry projective is probably small.

SEGMENTATION

Another question that arises in calorimetry design is whether

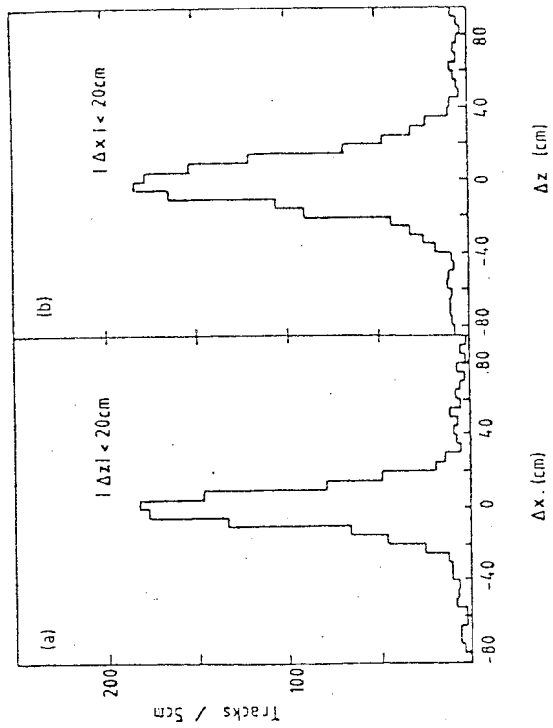


Fig. 41. Position resolution in the AFS calorimeters for the x and z (beam axis) dimensions [Willis 83].

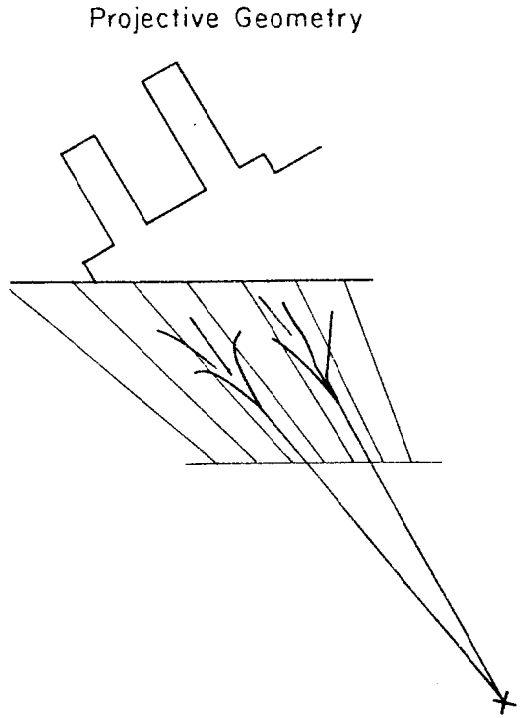


Fig. 42. Schematic illustrating the advantage of projective geometry.

to use strips, towers or a mixture of both. It is clear that if the channel count is very limited for budgetary reasons, then strips are the only solution. The number of towers needed to cover a region scales as the area whereas the number of strips scales as the square root of the area. If a reasonably high channel count is available then the question becomes more difficult.

With towers the question is whether the necessary position resolution can be obtained with the limited channel count and whether the desired two particle recognition is sufficient. This criteria is important for pizero reconstruction where two, close together gammas must be resolved. It is also important for electron pion separation where the presence of a random gamma near the pion might make the pion appear to be an electron. This problem is largely eliminated when a hadron calorimeter is present behind the electromagnetic calorimeter. The pion will deposit substantial energy in the hadron part whereas a true electron shower will be largely attenuated at that depth.

In the case of strips, they are quite adequate when the particle density is low. However when many particles occupy a small area, then ambiguities for the shower position arise. The question is then whether it is better to have good spatial resolution for some fraction of the particles, but ambiguities for others or to have poorer spatial resolution but no ambiguities.

Hauptman has explored this issue at some length in the SLC Workshop Proceedings [Hauptman 82]. He uses the geometry shown in Fig. 43. This discussion dealt with an electromagnetic calorimeter only. The channel count is given by the following equations:

$$N = 8(2\pi+3)R/s$$

$$N = 9\pi(R/t)^2$$

where L is the length, R the radius (L = 2R), s is the strip width and t the tower side. Figure 44 shows the tower or strip dimension s a function of channel count. Figure 45 shows a projected view of a jet from Z decay. The product of the energies in the three strip directions are used to untangle shower positions. The result is shown in Fig. 46 along with the actual particle positions. There appear to be any number of ghost showers. Hauptman then adds some crude towers to the system and utilizes a quadruple product. This improves the situation somewhat but there are still significant ghosts.

In Fig. 47 is shown the same event and the energy pattern using the towers. The event looks different because the previous graphs used non-rectangular coordinates. Although there are no ghosts, the particle separation appears unsatisfactory. Neither system looks very desirable. The conclusion that might be drawn from this study is that if a good coverage of 4π solid angle is the goal, then the channel count must be about 10,000 channels per radial layer. It appears hard to fix up a strip system and the tower system demands a lot of channels. Using a high channel count for a strip system does not gain much because of the

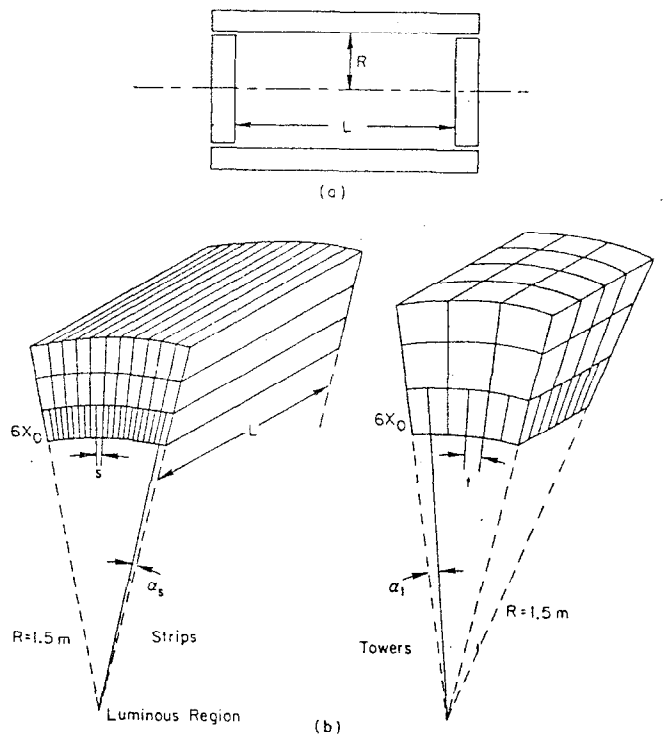


Fig. 43. (a) Relative dimensions of a barrel and end cap electromagnetic detector. (b) Strip and tower segmentation schemes. Strips also run at + and - 60 degrees with respect to the axis [Hauptman 82].

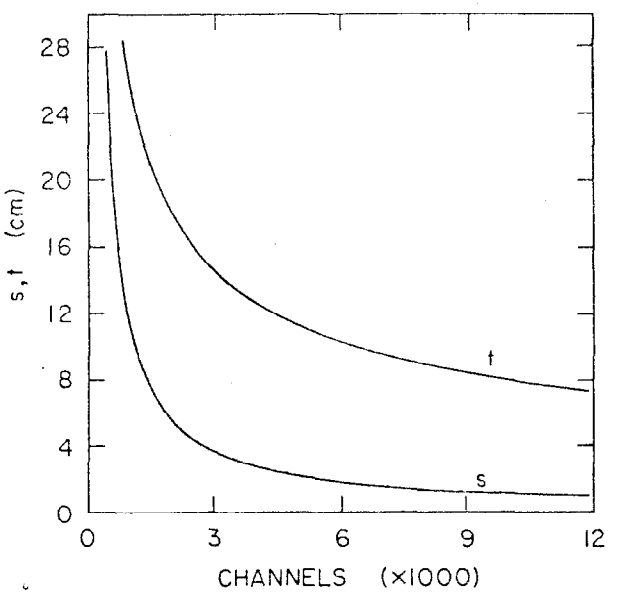


Fig. 44. Strip and tower dimensions as a function of the channel count [Hauptman 82].

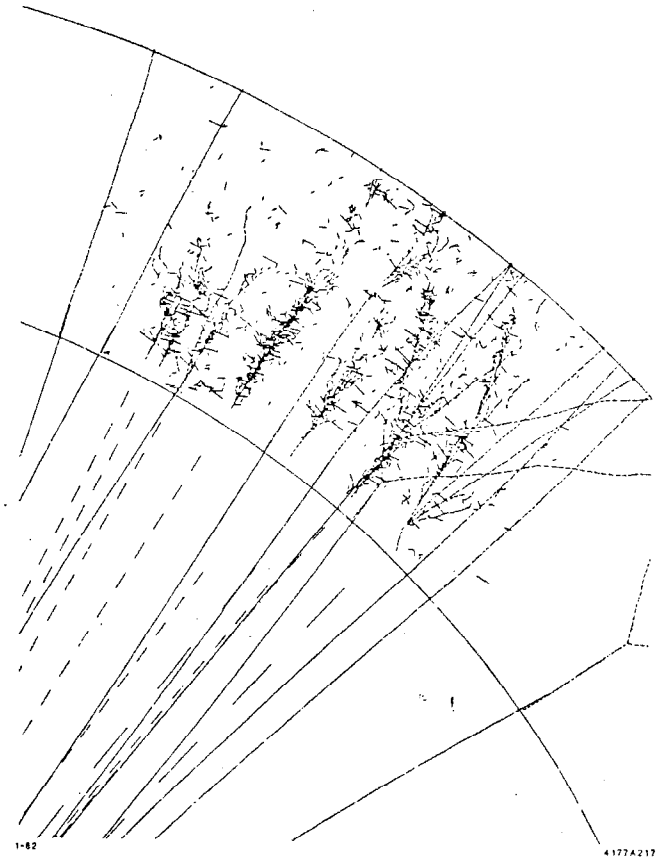


Fig. 45. Typical jet at the Z. Short dashed lines are photons and long dashed lines are neutral kaons [Hauptman 82].

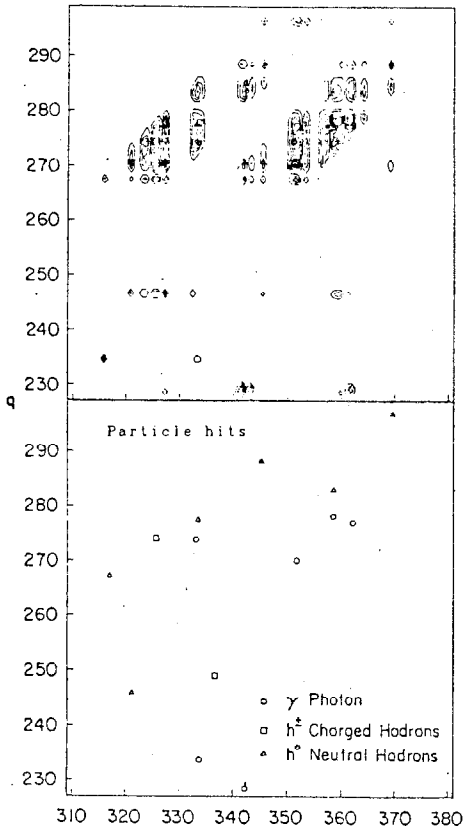


Fig. 46. Pulse height contours using the triple product of the strip pulse heights. The particle positions are also shown [Hauptman 82].

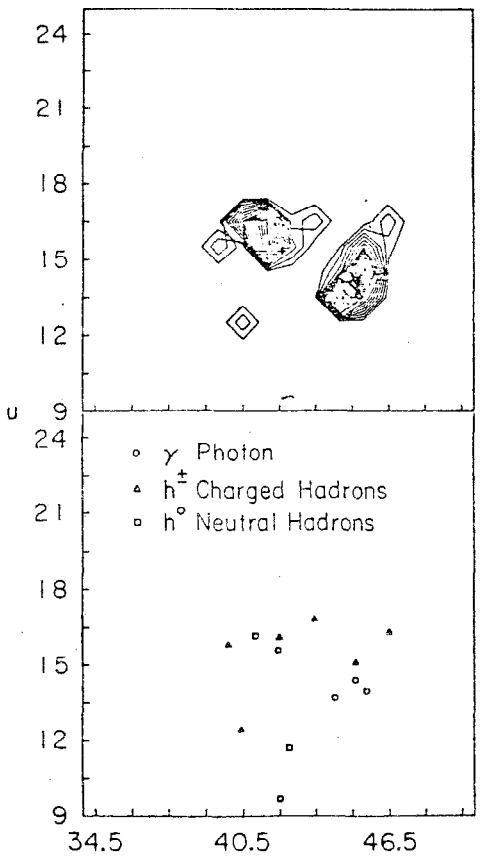


Fig. 47. Pulse height contours from towers. The particle positions are the same as in the previous figure but here the coordinate system is rectangular [Hauptman 82].

intrinsic shower sizes. There does not appear to be a clever way - as yet!

PARTICLE IDENTIFICATION

Shower counters have been in use for a long time for the separation of electrons from pions. The basic principle is that electrons produce their showers earlier than pions and electron showers build up and decay away faster than the showers from pions. The intrinsic limit to the separation is the probability that the pion charge-exchanges early in the calorimeter. Since the charge exchange cross section falls like E^{-2}, the separation gets better at high energy.

If the energy of the candidate particle is known, then the requirements that a fixed fraction of the energy be deposited in the first few radiation lengths (typically about 4) and that the total energy be within a standard deviation or so of the incident energy, produce separations on the order of 1/500 at a few GeV.

More complicated analysis can be performed when information from several radial segments is available. This analysis utilizes shower trees based on the correlations between the radial layers. However the systematics of such procedures might be difficult to determine.

The identification of muons by purely calorimetric means has not been investigated extensively. The usual technique is to track particles emerging from a thick absorber. If they point back to a track in the system before the absorber, then the particle is considered a muon candidate. Multiple layers of absorbers and trackers are sometimes employed in order to obtain the maximum rejection of pions over a broad range of momenta.

Identifying muons by purely calorimetric means involves looking for an energy deposition greater than that expected for minimum ionizing particles. A University of Seigen group has measured the shower profiles for pions and muons in a 5.4 λ calorimeter [Bleichert 82]. Figure 48 shows the energy distributions for muons and pions at 9 GeV. Cutting at about two equivalent particles gives a rejection of better than 1/500. This rejection factor must be reduced by the probability that the pion penetrates the calorimeter without interacting inelastically at all. A deeper calorimeter would improve this already quite good separation.

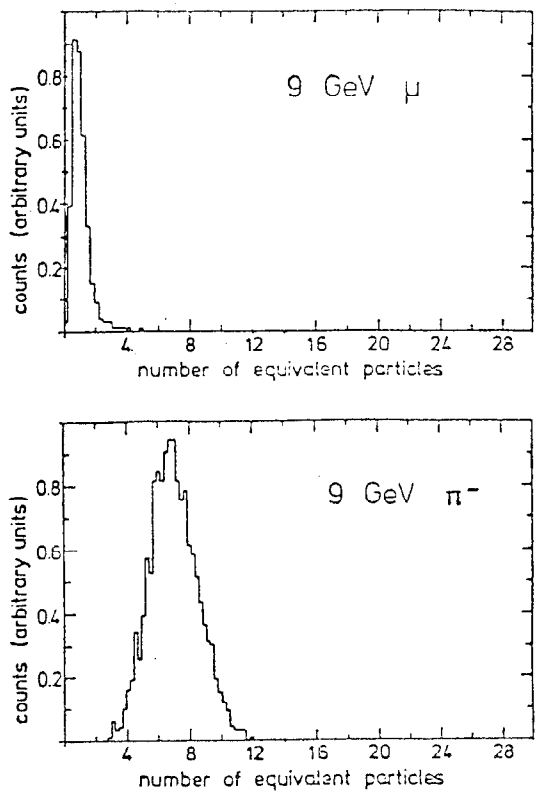


Fig. 48. The pulse height distributions for 9 GeV muons and pions in a 5.4 absorption length conventional hadron calorimeter [Bleichert 82].

HADRON CALORIMETER TECHNOLOGY

Hadron calorimeters are almost universally sampling devices.

The large mass required to contain hadronic showers excludes some of the more expensive materials such as BGO and lead glass. The best resolution from conventional hadron calorimetry has been obtained by the CHARM group. They used one radiation length marble plates and three-centimeter thick scintillator. This detector was discussed previously concerning its electromagnetic energy resolution. More typical values are in the 65 to 75% range. Table V shows a summary of the gas counter resolutions presented at the FNAL Gas Calorimetry Workshop. These calorimeters are typically much worse in resolution than the CHARM calorimeter, but not when scaled to the same sampling thickness. But the scaling used is not quite appropriate, since hadron resolution is dominated by shower fluctuations and not sampling statistics.

The uranium technique clearly improves the resolution but it requires expensive and difficult construction. In addition to the AFS detector, uranium is proposed for LEP 3 and a UA1 upgrade. The SLD group at SLAC has also proposed to use uranium for their SLC detector. In these experiments, the high initial cost can be amortized over presumably many years of operation at the frontier accelerators.

TABLE V [Appel 83]

ENERGY RESOLUTION
HADRONS

		BEST % RESOL	t (CM)	SCALED % RESOL $\times\sqrt{\frac{E}{t}}$
GAS				
ATAC: MAC PROTO		$72.8\%/\sqrt{E}$	2.7	70
		$102\%/\sqrt{E}$	5.4	70
BATTISTONI: ALEPH		$80\%/\sqrt{E}$	4.0	64
CARITHERS: CDF-EC		18.5% @ 25 GeV	5.1	65
		13.8% @ 50 GeV		69
FUESS: FLASH CH./PROP	PROP	$100\%/\sqrt{E}$	1.8	74
	FLASH	$75\%/\sqrt{E}$	.11	220
SCINT				
FLEGEL: CHARM		$47\%/\sqrt{E}$	1.5	70
CITF		$110\%/\sqrt{E}$	10.2	55
PRIMARY STREAMERS (BETTER THAN STATISTICS OF PRIMARIES SHOULD BE IMPOSSIBLE)				
BATTISTONI: ALEPH				
300 @ 25 GeV →		$29\%/\sqrt{E}$	4	58

$$\sqrt{\frac{25\ \text{GeV}}{300}} = .29\ \text{GeV}^{\frac{1}{2}}$$

Figures 49 and 50 show the shower profile for 1 and 15 GeV pions in an iron sampling calorimeter (MAC prototype). The sampling is done at one inch of iron intervals. The interesting feature to note in these profiles is that most of the energy is deposited in the first 2.5 to 3 absorption lengths. As emphasized earlier, good resolution requires about 5 absorption lengths. These extra absorption lengths are needed to prevent the fluctuations in the shower position from degrading the resolution as would happen if deep showers lost a lot of energy out the back. An interesting question is what might happen to the resolution if a very good but thin uranium calorimeter was followed with a cruder but very thick gas sampling calorimeter. Under some reasonable assumptions as to how the showers might correlate in the two devices, the resulting resolution is given by

$$\sigma_E^2 = \eta_U^2 \langle E_U \rangle + \eta_F^2 \langle E_F \rangle$$

where η_U and η_F characterize the uranium and iron calorimeter resolutions at 1 GeV, $\langle E_U \rangle$ and $\langle E_F \rangle$ the average energies contained in the two calorimeters. It is important to note that this result does not depend upon the fluctuations in the sharing of the energy but only on the average sharing. This means that if the uranium calorimeter is thick enough so that the second term is small, then the good resolution of the uranium calorimeter is preserved.

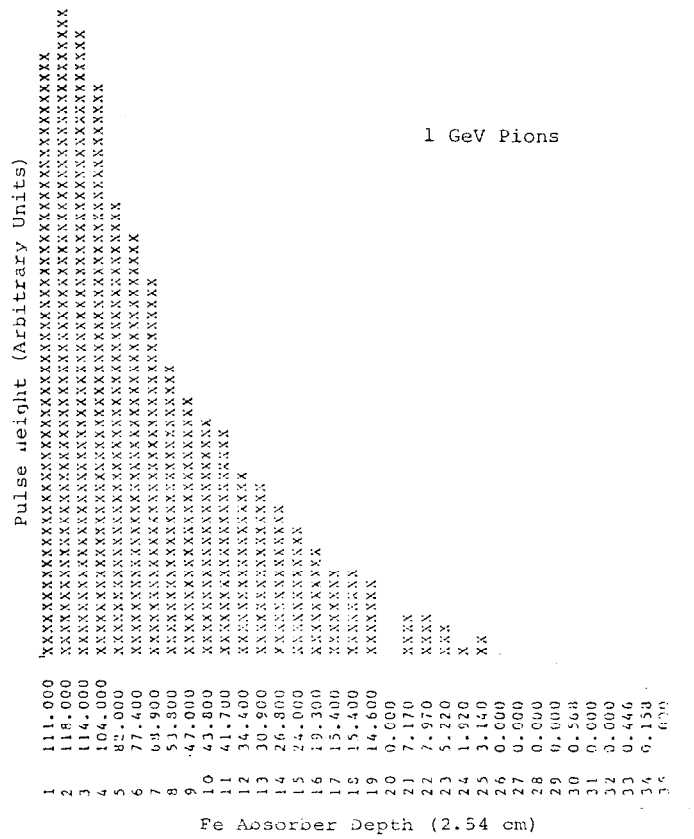


Fig. 49. Pulse height distribution as a function of depth for 1 Gev pions in the MAC prototype calorimeter. The gap in the distribution is due to a dead channel.

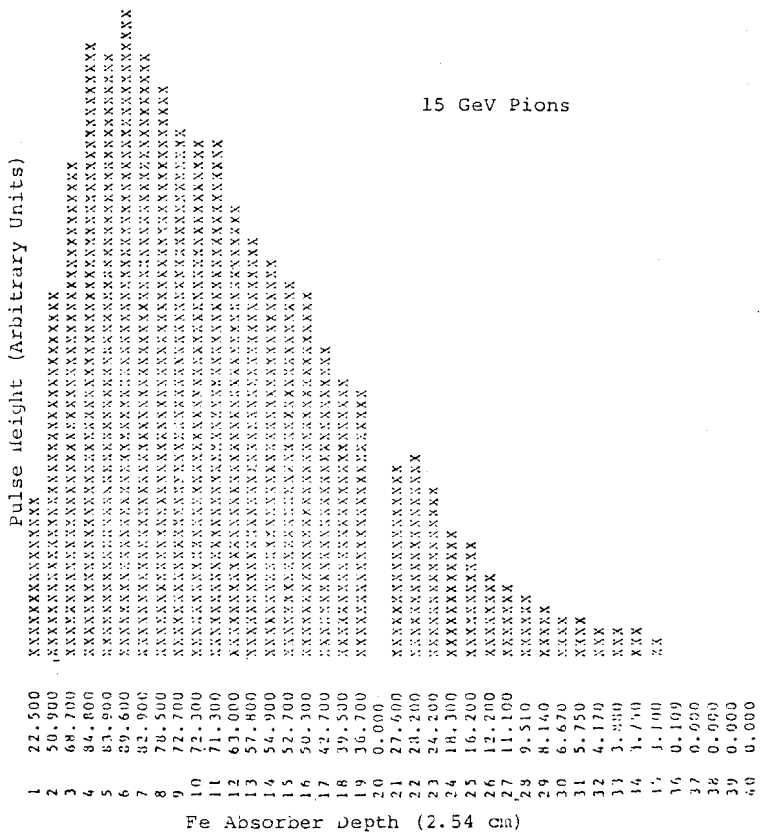


Fig. 50. The same as figure 49 for 15 GeV pions.

This condition can be fulfilled with only a thin uranium calorimeter. Figure 51 shows how the combined resolution depends upon the fraction of the energy contained on average in the uranium calorimeter for two different iron calorimeter resolutions. Points for the 1 and 15 GeV pions in a 2.5 absorption length uranium calorimeter are indicated. Since the shower size grows only logarithmically, good containment up to the highest energy expected at the Z is assured.

One important consideration is what would happen to the energy resolution if a 0.5 absorption length coil were interposed at the boundary between the calorimeters. As an aside we note that the poorest place to put the coil is after an electromagnetic calorimeter. Such devices are typically about one absorption length thick and the coil would be placed right at about shower maximum. Figure 52 shows the energy lost in a 0.5 absorption length aluminum coil [Maruyama 83]. Most of the time very little energy is lost in the coil although the distribution has a long tail. It remains to be seen whether this lost energy can be corrected for by special sampling before and after the coil. In any case, if the rms value of the energy is folded in quadrature with the previously determined resolution, then the result is not degraded appreciably. Tests are underway at SLAC to measure the resolution of such a composite device.

Such a technique is utilized for electromagnetic showers by the AFS detector. They have 5.25 Xo towers of sodium iodide crystals in front of their uranium calorimeter. The resolution

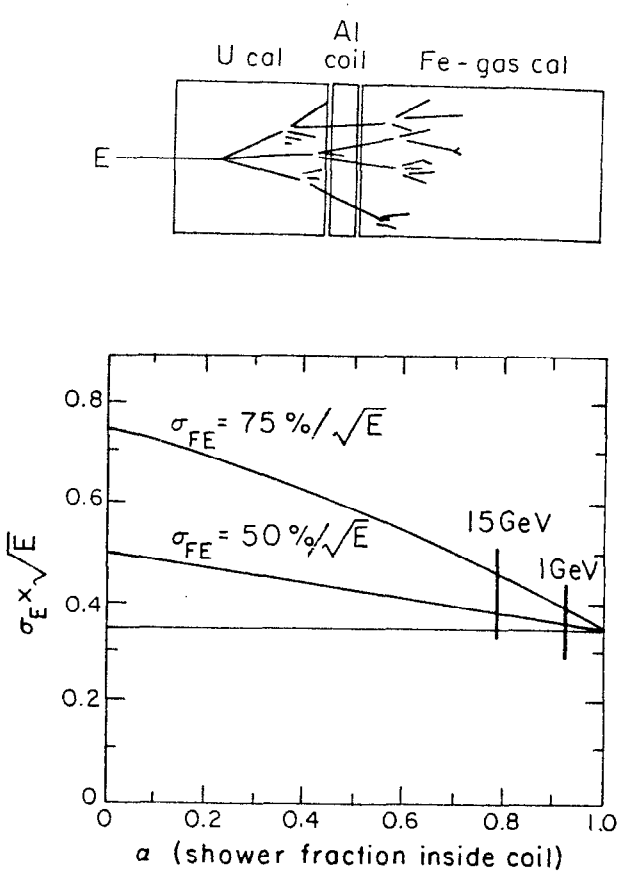


Fig. 51. Top - Schematic of a mixed technology calorimeter. Bottom - The combined resolution as a function of the average shower containment fraction for two different iron calorimeter resolutions. The uranium calorimeter has 3 mm uranium plates.

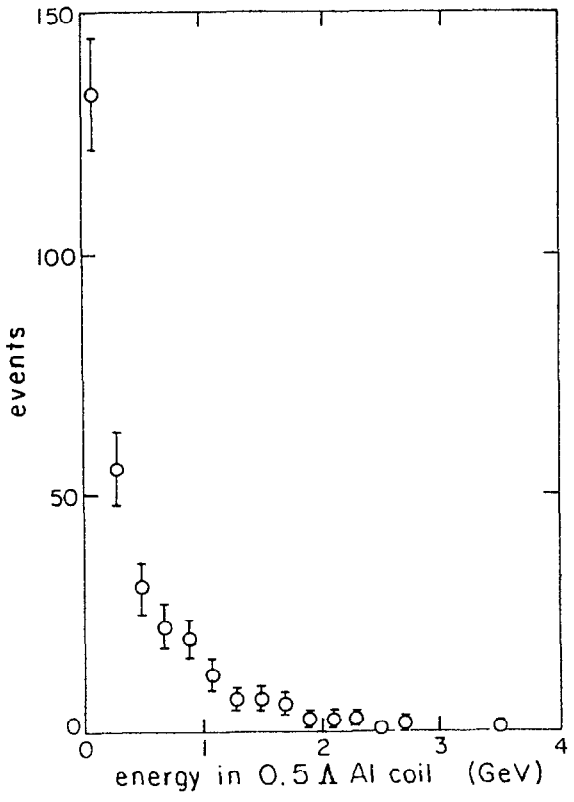


Fig. 52. HETC calculation of the energy deposited in a 0.5 absorption length coil after a 2.9 absorption length uranium calorimeter. The incident particle is a 15 GeV pion. The mean energy deposited in the coil is 0.5 GeV and the rms fluctuation is 0.6 GeV [Maruyama 83].

for the uranium part is $16\%/\sqrt{E}$ whereas the combined resolution for the sodium iodide part is $9\%/\sqrt{E}$. Although this combined resolution is not spectacular for sodium iodide, only about 50% of the shower energy is contained in the crystals. How well this technique works for hadron showers remains to be seen.

CALIBRATION

Some aspects of calibration have been discussed previously in this work. The basic principle is straight forward. Some physical processes, such as a known gamma line or muons, are used to intercalibrate each channel. A pulser or light flashing system is then used to track short term changes in this calibration. Then either beam tests or a known energy shower is used to set the energy scale. For example Bhabha scattering might be used to set the energy scale at an electron positron collider.

Some difficulties have been encountered in coupling a radioactive source to a calorimeter module in a stable fashion. For example, an americium source in scintillator was used to generate a signal for lead glass detectors. With time, the scintillator discolored and this resulted in an underestimate of the detector gain. One of the very attractive features of the uranium noise calibration, is that the radioactivity is uniformly spread through out the cell. Hence some average response of the cell is measured and the effects of local imperfections are avoided.

REFERENCES

[Abrams 79] G. S. Abrams et al.
Phys. Rev. Lett. 43 477 (1979)

[Ahlers 83] G. Ahlers et al.
UCSC Preprint

[Akopdjanov 77] G. A. Akopdjanov et al.
Nucl. Instr. & Meth. 140 441 (1977)

[Amaldi 81] U. Amaldi
Physica Scripta 23 409 (1981)

[Appel 83] J. A. Appel
Proceedings of the Gas Calorimeter Workshop, FNAL (1983)

[Atac 75] M. Atac, Editor
Proceedings of the Calorimeter Workshop, FNAL (1975)

[Atac 83] M. Atac, Editor
Proceedings of the Gas Calorimeter Workshop, FNAL (1983)

[Atwood 75] W. Atwood
Thesis, Stanford (1975)

[Babaev 79] A. Babaev et al.
Nucl. Instr. & Meth. 160 427 (1979)

[Bathow 70] G. Bathow et al.
Nucl. Phys. B20 592 (1970)

[Battistoni 82] G. Battistoni et al.
Proceedings of the Gas Calorimeter Workshop, FNAL (1983)

[Battistoni 83] G. Battistoni et al.
Proceedings of the Intern. Conf. on Instru. for Coll.
Beam Physics, SLAC 250 206 (1982)

[Benvenuti 75] A. Benvenuti et al.,
Nucl. Instr. & Meth. 125 447 (1975)

[Bleichert 82] B. M. Bleichert et al.
Si-82-13, Univ. of Siegen Preprint (1982)

[Brandelik 82] R. Bandelik et al.
Physics Letters 108B 71 (1982)

[Cook 81] V. Cook et al.
Nucl. Phys. B186 219 (1981)

[Crannell 69] C. J. Crannell et al.
Phys. Rev. 182 1435 (1969)

[Dorfan 83] J. Dorfan
Private communication

[Engler 83] J. Engler
Vienna Wire Chamber Conference (1983)

[Fabjan 77] C. W. Fabjan et al.
Nucl. Instr. & Meth. 141 61 (1977)

[Fabjan 78] C. W. Fabjan et al.
Nucl. Instr. & Meth. 158 93 (1978)

[Fabjan 82] C. W. Fabjan
CERN-ep/82-37

[Fischer 78] H. G. Fischer
Nucl. Instr. & Meth. 156 81 (1978)

[Ford 78] R. L. Ford et al.
SLAC-210 (1978)

[Gabriel 75] T. A. Gabriel et al.
Nucl. Instr. & Meth. 129 409 (1975)

[Gabriel 78] T. A. Gabriel et al.
Nucl. Instr. & Meth. 150 145 (1978)

[Gidal 83] G. Gidal et al.
LBL-191 (1983)

[Grant 75] A. Grant
Nucl. Instr. & Meth. 131 167 (1975)

[Grigorov 58] N. L. Grigorov et al.
JETP 7 348 (1958)

[Hauptman 82] J. Hauptman
Proceedings of the SLC Workshop on Experimental Use
of the SLAC Linear Collider

[Hirayama 83] H. Hirayama et al.
SLAC-PUB-3038 (1983)

[Hofmann 79] W. Hofmann et al.
Nucl. Instr. & Meth. 163 77 (1979)

[Holder 78] M. Holder et al.
Nucl. Instr. & Meth. 148 235 (1978)

[Iwata 80] S. Iwata
DPNU-13-80

[Jonker 82] M. Jonker et al.
Nucl. Instr. & Meth. 200 183 (1982)

[Longo 75] E. Longo et al.
Nucl. Instr. & Meth. 128 283 (1975)

[Ludlum 82] T. Ludlum et al.
Nucl. Instr. & Meth. 198 233 (1982)

[Maruyama 83] T. Maruyama
Private communication

[Müller 72] D. Muller
Phys. Rev. D5 2677 (1972)

[Price 82] L. E. Price
Proceedings of the Intern. Conf. on Instru. for Coll.
Beam Physics, SLAC 250 206 (1982)

[Roos 82] M. Roos et al.
Review of Particle Properties, LBL-100 (1982)

[Rossi 52] B. Rossi
High-Energy Particles, Prentice-Hall Inc. (1952)

[Selove 75] W. Selove et al.
Proceedings of the Calorimeter Workshop, FNAL (1975)

[Straker 70] E. A. Straker et al.
ORNL-4585, Oak Ridge National Laboratory (1970)

[Tsai 74] Yung-Su Tsai
Revs. Mod. Phys. 46 815 (1974)

[Whiteside 73] H. Whiteside et al.
Nucl. Instr. & Meth. 109 375 (1973)

[Willis 74] W. J. Willis et al.
Nucl. Instr. & Meth. 120 221 (1974)

[Willis 83] W. J. Willis et al.
Private communication

[Yamauchi 82] M. Yamauchi
IEEE, Nuclear Science Symposium (1982)

BARI/GT 83/10

PARTONS VS. HADRONS:
A PHYSICAL THEORY OF FRAGMENTATION

Giuliano Preparata
Dipartimento di Fisica-Universita' de Bari
and
INFN Sezione di Bari-Italy

ABSTRACT: The theory of Fire-Strings developed within a phenomenological approach to confined colored quarks [MQM,QGD] is applied to the description of the fragmentation of quarks in highly inelastic hadronic processes. A successful quantitative account of e^+e^- annihilation at high energy is presented.

© G. Preparata

INTRODUCTION

The study of the high energy interactions of subnuclear particles has long since provided strong indications that hadrons are composite objects, whose behavior is completely determined by the dynamics of much smaller systems which, following Feynman, [1] we may call "partons."

Thus the problems that detailed analyses of high energy collisions should help us solve are:

i. determine the nature of partons (spin, charge,...);

ii. infer their fundamental interactions; and

iii. describe their relation to hadrons (i.e., understand confinement).

The experimental information that has been piled up in the last decade has definitely singled out one theory, QCD, as the most plausible candidate for correctly describing the immensely varied panorama of subnuclear physics. However, as far as we have understood QCD to this day, whereas this theory provides definite answers to (i) and (ii), it fails remarkably in giving a viable approach to (iii). Such a failure is particularly unfortunate in that it precludes any realistic application of QCD to the very fascinating problem of fragmentation: that is the conversion of the partons' degrees of freedom into final state hadrons.

Nevertheless it must be admitted that QCD is indeed a very appealing theoretical framework for it realizes in 4-dimensional space-time three basic notions of subnuclear physics:

a. Hadrons are made of spin ½, pointlike constituents (the quarks);

b. The interactions among quarks are invariant under a SU(3) color group; and

c. SU(3) invariance is realized locally in space-time, i.e., through a gauge principle.

Such notions are so basic to hadrodynamics that giving up any of them would seem like going back to the "Middle Ages". The incontrovertible fact that QCD implements (a), (b) and (c) in a way that is both simple and elegant is a strong argument in favor of its being very likely the theory of strong interactions. However the calculational methods that have been so far envisaged in QCD, which rely on its perturbative expansion (perturbative QCD), do not seem adequate to make direct contact with Nature, and make it very hard to compare QCD quantitatively with the really impressive amount of experimental information available today.

It is the purpose of this talk to show that one can develop alternative methods, which not only phenomenologically incorporate the theoretical pillars (a), (b) and (c) upon which QCD is built, but also provide a solution to the point (iii) above, about which the perturbative QCD methods have so far been impotent.

Even though such a theoretical strategy does not address the problem of confinement within QCD, nor does it proceed from the QCD field equations, to the extent that it yields a simple picture of hadronic behavior which is based on (a), (b) and (c) above, and is consistent with confinement, it can give us extremely useful hints and information about the non-perturbative structure of QCD, and it may ultimately lead us to the solution of the hadrons' problem in a gauge-theoretical context.

It is with this perspective in mind that one should look at the very successful theoretical analysis of e^+e^- high energy annihilation that shall be presented in this talk.

2. THE THEORETICAL FRAMEWORK

The theoretical framework I shall consider in this talk has been proposed a long time ago, and was called the "Massive Quark Model" (MQM), [2] to stress the fact that real quarks, if they exist at all, should be much heavier than hadrons. [This was before the notion of quark confinement became generally accepted.] The MQM was later refined and sharpened into Quark-Geometro Dynamics (QGD), [3] and it has become, as I hope to convince you, a fairly powerful instrument to deal with the physics of highly inelastic collisions.

In order to convey the spirit and the scope of QGD I shall state and briefly discuss the basic ideas, the "tenets" of the "heresy", upon which it rests:

1. Hadrons are made of a small number of "almost" free quarks ($q\bar{q}$,qqq,...) confined in typically simple space-time domains, whose dimensions increase linearly with the mass of hadrons.

2. There is a basic perturbative structure in the number of quarks that can take part in a given hadronic process.

3. Hadrons emerge in the final state from the (perturbative) evolution (decay) of primitive ($q\bar{q}$,qqq,...) states.

The first tenet stems from the success of the quark model and the idea that the confining forces become strong only at large distances, where the physics is dominated by linear potentials. The second finds its deep reason in the well-known fact that hadronic interactions are not really strong. [How could we otherwise understand the Zweig rule which is operative even at the level of light quarks?] The remarkable relative slowness of the quark pair creation process is thus at the basis of the assumed perturbative structure. Finally the third tenet is just the consequence of the other two, which is particularly relevant

for the determination of the structure of hadronic final states in high energy collisions.

Starting from (1), [4] one can construct the spectra of the $q\bar{q}$- and qqq-states in terms of a "minimal" set of inputs:

m_q, the quark masses, and

R^2, the rate of increase of hadronic radii with hadronic masses.

As a result one obtains for the $q\bar{q}$-system a set of Regge trajectories described by:

$$M^2_{n\ell} \simeq \pi/R^2\ (2n+\ell), \tag{2.1}$$

where ℓ is the angular momentum and n is the radial excitation quantum number (Fig. 1). One can also derive the excited meson wave functions (w.f.'s) (Fig. 2), whose structure is given by:

$$\psi_{n\ell}(p,k) \underset{M_{n\ell}\ \text{large}}{\longrightarrow} F(p_1^2,p_2^2)\ Y^m_\ell(\Omega_{\vec{k}}) \tag{2.2}$$

where $\Omega_{\vec{k}}$ is the direction of the relative $q\bar{q}$-momentum $\vec{k}$ in the meson rest frame, and

$$F(p_1^2,p_2^2) \simeq G(p_1^2)G(p_2^2), \tag{2.3}$$

with the "quark" propagation function $G(p^2)$ having the following behaviors:

$$G(p^2)_{p^2 \simeq m_q^2} \sim \sin \frac{R^2(p^2-m_q^2)}{(p^2-m_q^2)}\ , \tag{2.4}$$

$$|\overline{p^2}| >> m_q^2 \qquad \frac{1}{p^2}\ . \tag{2.5}$$

Equation (2.4) correctly represents confinement [i.e., no singularity on the "mass-shell"], while Equation (2.5) reproduces the free field behavior at short distances [high p^2].

The quasi-degeneracy in the mass M of states with different angular momenta [See Fig. 1], allows us to construct a new set of states whose w.f.'s are [ℓ_o=M/2 R_T]:

$$\psi(p,k;\Omega_o) = \sum_{\ell=o}^{\ell_o} \sum_{m=-\ell}^{\ell} \psi_{n\ell m}(p,k)\ Y^m_\ell(\Omega_o) \Big|_{2n+\ell\ =\ \text{fixed}}\ . \tag{2.6}$$

In configuration space the structure of the state (2.6) is depicted in Fig. 3, whereupon it is evident why we can call such a state Fire-String (FS), oriented along Ω_o. A FS describes a $q\bar{q}$-system where the quarks move (approximately) in the Ω_o-direction with momenta $|\vec{p}| \simeq M/2$ [M is the mass of the Fire-String].

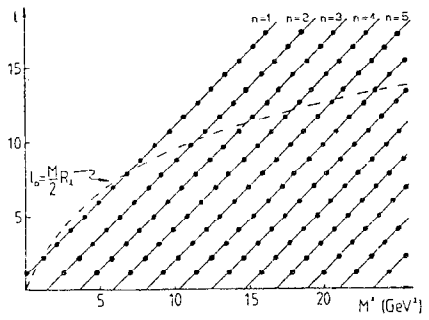


Fig.1 The Chew-Frautschi plot of the $q\bar{q}$-states according to QGD.

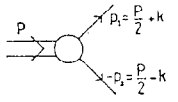


Fig.2 The Bethe-Salpeter w.f. describing a $q\bar{q}$-state of 4-momentum p.

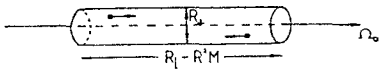


Fig. 3 The spatial structure of the state (2.6).

In a confined world, such as is envisaged in MQM-QGD, the FS-states are the closest approximation to the states of the parton model, whose phenomenological relevance has been long since appreciated. Thus the FS represents a far reaching link between two previously unrelated languages: Regge Theory and the Parton Model. In high energy hadronic behavior the FS plays the same role as the coherent states of the radiation field in the semiclassical approximation of QED. We shall see later in fact that quantum interference effects in inelastic hadronic collisions are highly suppressed so that a semiclassical picture emerges in a most natural way.

To conclude our discussion of the $q\bar{q}$-spectrum it should be stressed that its totally reasonable Regge structure allows us to think of confined hadronic states in terms of quark partons, but not of gluons. We shall see later that the dynamics of the gluon can be completely ascribed to that of quarks, thus providing some hints that the popular understanding of QCD needs some major modification.

According to the tenets (2) and (3) we can envisage the high energy interactions as consisting of the following two steps:

I. the production of a "minimal" set of FSs; and

II. the decay of each FS into stable (lowest lying) hadrons.

But let us discuss II. first.

3. THE DECAY OF THE FIRE-STRING: The basis for parton fragmentation

According to tenets (2) and (3) of the preceding section, the FS decay process consists in the break-up of the initial FS into two smaller FSs, through $q\bar{q}$ pair creation in the color field existing between the two quarks. Thus the initial decay process:

$$FS \rightarrow FS_1 + FS_2, \qquad (3.1)$$

is followed by similar processes involving FS_1 and FS_2, and so on until the produced FSs have masses of the order of hadronic low-lying states $[\pi,\rho,A_2,\ldots]$. The evolution of the FS-decay process is described in Fig. 4, where we also report the diagrams that are used to calculate the decay amplitude of the process (3.1). As discussed thoroughly in Ref. 4, the "gluon" responsible for the quark-pair creation, is not

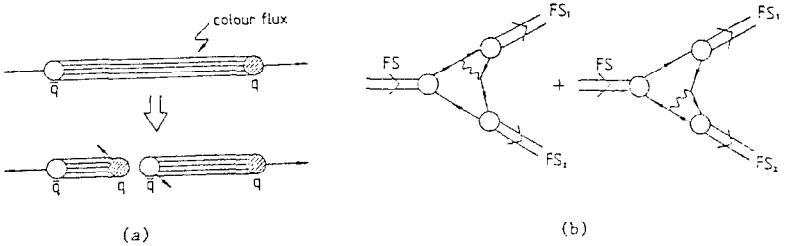


Fig.4 The evolution of the FS-decay process (a), and (b) the diagrams describing the basic FS break-up process (3.1).

a dynamical gluon but rather the longitudinal field that is envisaged in Anisotropic Chromo-Dynamics (ACD).[5] This important difference with the perturbative QCD calculation insures that the calculated amplitude is free from the nasty collinear divergences that plague perturbative QCD calculations. Calling a $(M^{\Omega},M^{\Omega}1,M^{\Omega}2;\vec{p}_T)$ the amplitude for the process (3.1), where $\vec{p}_T$ denotes the decay momentum transverse to the initial direction Ω, an important property of a is that it scales, i.e.

$$a(M^{\Omega},M_1{}^{\Omega}{}_2,M_2{}^{\Omega}{}_2;p_T) = a(x_1,x_2,\chi;\Omega,\Omega_1 m\Omega_2), \qquad (3.2)$$

where $x_1 = (M_1/M)^2$, $x_2 = (M_2/M)^2$ and $\chi = p^2/M^2$.

A few comments about our treatment of the decay process (3.1) seem appropriate:

a. The FS break-up, unlike the most popular fragmentation models, is a realistic description of a physical process, which leads from a colorless confined state to two other such states which, according to the confinement hypothesis, are the only states of the physical Hilbert space.

b. One can demonstrate the suppression of quantum interference effects, thus making it possible to calculate the FS decay process in terms of probabilities rather than quantum amplitudes (3.2). In order to get an idea of the kind of physics which is at work in FS-decay, in Fig.5 we plot the probability $P(x_1,x_2)$ for one of the two decay configurations [the "gluon" emitted by the quark line]. One thing is immediately evident, the mass distributions of the two FSs is very asymmetrical, M_1 being almost always much less than M_2, except for a small probability tail, where one can see that also χ gets large. This is the so called "3 jet-region".

c. We have so far only described the mesonic decay of the FS, but the MQM-QGD also gives us the possibility of computing the main features of baryon-antibaryon production.[6] $B\bar{B}$ production in fact arises from the process:

$$FS \to B(\vec{p})+\bar{B}(-\vec{p}) \qquad (3.3)$$

where $B(\bar{B})$ are the lowest lying baryons (antibaryons) belonging to the 56 $(\overline{56})$ representation. The diagram corresponding to (3.3) is reported in Fig.6 and it has been computed in Ref. 6. The results of this computation are described in Fig. 7, where the branching ratios for total $B\bar{B}$ production as well as for a few particular channels are plotted as a function of the FS mass M. Please note the strong suppression at high mass $(\sim 1/M^2)$, which implies that $B\bar{B}$ production will show definite correlations in rapidity. Our calculational framework is not powerful enough to determine the absolute rate of $B\bar{B}$ production, so that we must introduce it as an input to be fitted by experiment. This input parameter is the only new parameter

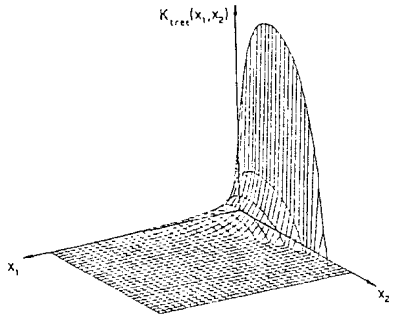


Fig.5 The x_1,x_2 distribution in the decay process of a FS.

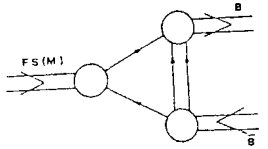


Fig. 6 The diagram describing the decay process (3.3)

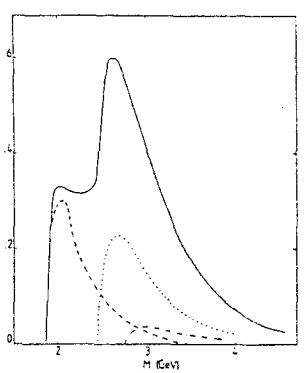


Fig.7 The unnormalized branching ratio $\Gamma_{B\bar{B}}(M)/\Gamma_{TOT}$ as a function of M_{FS} for a number of relevant channels.

entering our description of FS-decay. All other parameters (m_q, R^2) having been fixed by the structure of the spectrum.

d. Our mechanism of quark pair creation strongly suppresses heavy quark pairs. Thus, to a good approximation, only light quark pairs need be considered. Heavy flavor production thus occurs only when the initial FS contains one heavy quark. In this case the heavy meson (D,B,...) is emitted with a substantial fraction of the incoming quark momentum, in addition one predicts:

$$\frac{(c \to D^*)}{(c \to D\ )} \approx 8; \quad \frac{(c \to F^*)}{(c \to F\ )} \approx 6 \quad . \tag{3.4}$$

As we shall comment later, there is some evidence that D* is produced more abundantly than D.

4. PRODUCTION MECHANISMS OF FIRE-STRINGS

We have just seen how a FS, once it has been produced, decays depositing in the final state a multiplicity of low-lying, stable hadrons, according to a well defined and universal physical pattern. We want now to address the problem of how, according to MQM-QGD, FSs are produced in different physical processes. We shall consider two important classes of processes:

a. e^+e^- annihilation into hadrons; and

b. deep inelastic lepton-hadron scattering.

4a. e^+e^- Annihilation into Hadrons

In e^+e^- annihilation we see at work the simplest mechanism of FS production. The process to consider is:

$$e^+e^- \xrightarrow[\sqrt{s}]{} \gamma^* \xrightarrow[\sqrt{s}]{} FS(\sqrt{s}), \tag{4.1}$$

where the virtual photon γ^* of energy $\sqrt{s}$, produced by the annihilation of the electron pair couples, through the diagram in Fig. 8, to a FS of mass $\sqrt{s}$.

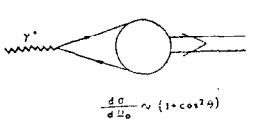


Fig. 8 The conversion of a highly virtual timelike photon into a FS.

I should like to recall that in ACD one can compute the total hadron annihilation cross section by evaluating the transition rates of a virtual photon to the $J^{PC} = 1^{--}$ excited states of the $q\bar{q}$-system, the result is the "canonical" result [7]

$$R \equiv \frac{\sigma(e^+e^- \to \text{hadrons})}{\sigma(e^+e^- \to \mu^+\mu^-)} \xrightarrow[\text{large } \sqrt{s}]{} 3 \sum_i Q_i^2, \qquad (4.2)$$

thus providing the first realistic derivation of this important confirmation of color and freedom at short distances. A further visualization of the process (4.1) is afforded by Fig. 9, where we see that the e^+e^- collision generates a FS in a direction θ, with respect to the collision axis, distributed according to the well-known law,

$$\frac{d\sigma}{d\cos\theta} \sim (1+\cos^2\theta), \qquad (4.3)$$

a manifestation of the spin ½ nature of the quarks.

Now the theoretical description of e^+e^- annihilation is complete, and in the next section I shall present and discuss its consequences.

4b. Deep Inelastic Lepton-Hadron Scattering

In order to describe this fascinating class of processes, we must first describe the quantum mechanical behavior of a hadron present in the initial state. Let us consider a proton moving at high speed in the lab; if we take a snapshot of it which is quick enough we are likely to see it dissociated (DIS) (see Fig. 10) in a low-lying baryon and a $q\bar{q}$-pair. Such a dissociation is the effect of quark pair creation in the color field holding the quarks of the proton together. [According to Tenet (2) of Section 2, higher numbers of pairs are suppressed.] This is the picture of the proton that is seen by the incoming virtual photon (or $W^{\pm}$, or Z^0) its scattering however will most of the time take place on the $q\bar{q}$-pair rather than on the virtual baryon, because to excite a baryonic FS is much more difficult, due to the peculiar alignment that the three quarks must respect in order to give rise to a physical baryonic state. Thus one basic production mechanism in deep inelastic scattering is (see Fig. 10):

$$J + N \longrightarrow B^* + FS, \qquad (4.4)$$

where the final state comprises an excited baryon [mostly a member of the SU(6) representation 56] and a FS. In order to calculate the diagram in Fig. 10, we must evaluate the proton dissociation amplitude. QGD, providing us with explicit baryonic w.f.'s, allows us to perform the calculation. [8]

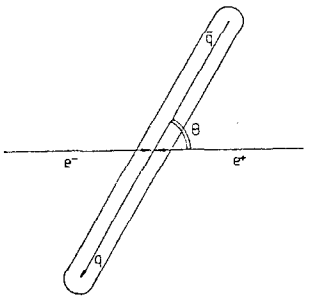


Fig.9 The production kinematics of the initial FS in e+e- annihilation.

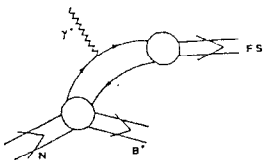


Fig. 10 The diagram corresponding to the DIS process (4.4)

But (4.4) is not the only deep inelastic scattering mechanism, even though it dominates for $x = Q^2/2M\nu \gtrsim .2$, that is, in the "valence" region. It is possible that the initial electroweak current J is itself virtually dissociated in a $q\bar{q}$-pair, in this case the physical process that takes place is (see Fig. 11)

$$J + N \longrightarrow B^* + FS_1 + FS_2 \qquad (4.5)$$

with the final state comprising 2 FSs and an excited baryon. The 2 FSs-production mechanism has also been evaluated [8] and found to dominate the deep inelastic cross-section for small values of x [$x \lesssim 0.1$], that is, in the "sea" region. One common feature of the two mechanisms (4.4) and (4.5) is the presence in the final state of a "leading" baryon, a well-known characteristic of high energy hadron-baryon scattering. The detailed evaluation of the dissociation process:

$$N \longrightarrow B^* + q\bar{q}, \qquad (4.6)$$

made possible by QGD shows that the leading baryon carries on the average about half of the initial nucleon momentum. It is then clear that the momentum carried away by such a well-defined physical system is completely lost to the inelastic collision which excites the FSs. This is a perfectly natural, and realistic answer to the famous problem of the "missing momentum", which is generally believed to imply the existence of dynamical gluons. Our analysis shows that this belief has no real compelling support, unless one wishes to consider the color field "imprisoned" inside the leading baryon as a "gluon". But then the dynamics of the gluon are the dynamics of the quarks inside the leading baryon, as envisaged in the MQM-QGD approach.

The calculational framework for deep inelastic lepton-hadron scattering is now complete, and we need only develop the computer programs to analyze the many interesting aspects of the physics of final states. Work is in progress.

5. PARTON-FRAGMENTATION IN e^+e^- ANNIHILATION [4]

The principles and the theoretical results of the MQM-QGD framework that have been sketched in the previous sections shall now be applied to an extensive analysis of the annihilation of e^+e^- into hadrons at high (> 5GeV) CM energies. The results I shall report do not pretend to cover completely this extremely interesting field of physics, but only to show the effectiveness of the framework presented in coping with the rather detailed and subtle physics which has been unravelled by the experimentation at the different e^+e^- machines over the last decade. [9]

The results to be presented were obtained by Monte Carlo methods, whose inputs [the "weights of the Monte Carlo"] were the probability amplitudes that have been calculated within our framework. The resulting Monte Carlo program, called EPOS, [10] generates hadronic

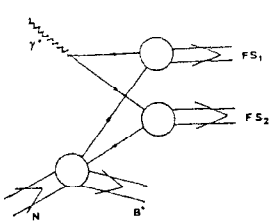


Fig. 11 The diagram corresponding to the DIS process (4.5)

final states starting with a given FS of mass M and orientation. I should like to stress that this program makes use of Monte Carlo methods in order to be able to handle a very complicated physical situation, the multiparticle nature of the hadronic final state, but it does not share the uncomfortably large amount of flexibility and tunability of the various Monte Carlo programs that are now popular. Indeed the only really tunable parameter that our calculation possesses is the relative rate between the $B\bar{B}$ and the mesonic decay of a FS of a given mass.

After these qualifications we can proceed to the analysis of e^+e^- physics. According to the discussion of Section 4a, the final states in e^+e^- annihilation are generated by the creation of a single FS with mass equal to the CM e^+e^- energy and orientation Ω_0 distributed according to (4.3).

The FS decay process outlined in Section 3 is then responsible for the hadronic structure of the annihilation event.

Let us consider first the global properties of the hadronic final states.

5a. Charged Particle Multiplicities and x-distributions

In Fig. 12 we report our calculations of the charged particle multiplicities for both stable (against strong interactions) hadrons (lower curve) and including K^0_S and Λ-decays (upper curve). Experimental data, where corrections were not applied for K^0_S and Λ-decays, are also included. Good agreement with experiments is to be noticed, along with the clear deviation of data and of our calculations from logarithmic increase of the multiplicities.

The calculated differential x-distributions for two charged particles at two different CM energies are drawn and compared with data in Fig. 13. Noteworthy is the experimentally observed deviations from scaling for both large and small x. We shall get to this point later on.

5b. Transverse Momentum Distribution

The average values $\langle p_T \rangle$ and $\langle p_T^2 \rangle$ of p_T and p_T^2 respectively [p_T is the momentum transverse to the sphericity axis] as a function of $\sqrt{s}$ are reported in Fig. 14 and compared with available data. Notice that the steep increase of $\langle p_T^2 \rangle$ with $\sqrt{s}$, which is one of the most interesting effects discovered by PETRA and PEP, is well reproduced by our calculation.

The calculated differential distributions $1/\sigma\ d\sigma/dp_T^2$ for charged particles with two different energies $\sqrt{s}$=12 and 34 GeV respectively are compared with available data in similar energy ranges in Fig. 15. The substantial rise of the high p_T-tail with energy, is well reproduced by our calculation.

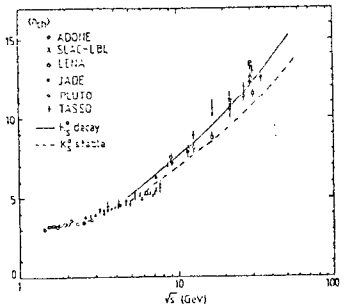


Fig. 12 The charged multiplicity as a function of CM energy

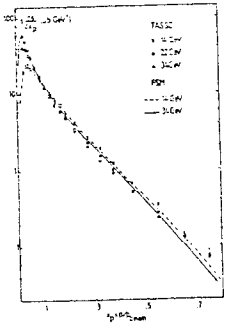


Fig. 13 x-distributions for charged particles

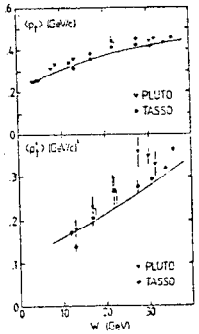


Fig. 14 $\langle p_T \rangle$ nd $\langle p_T^2 \rangle$ as a function of $\sqrt{s}$

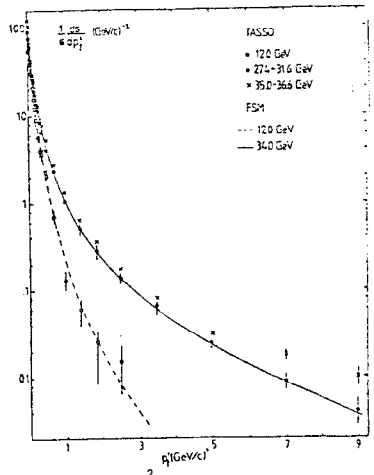


Fig. 15 $1/\sigma\ d\sigma/dp_T^2$ for charged particles

5c. Sphericity Distributions

The behavior of the average event sphericity <S> as a function of $\sqrt{s}$ is shown in Fig.16, where we plot our results together with the experimental data. The rapid decrease in energy that has been observed is again quite well reproduced by our calculation.

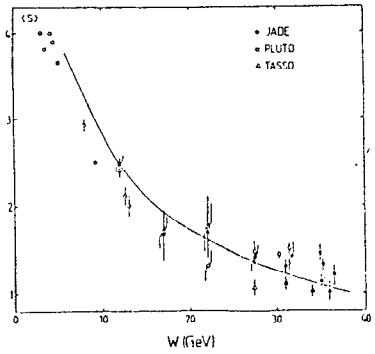


Fig. 16 <S> as a function of $\sqrt{s}$

The differential rapidity distribution at a typical PETRA-PEP energy is displayed in Fig. 17. Agreement between theory and experiment is quite good.

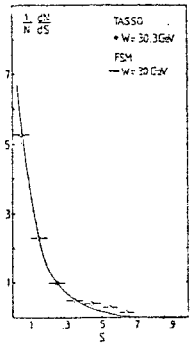


Fig. 17 Differential sphericity distribution at $\sqrt{s}$ = 30 GeV

Next we analyse the structure of hadronic final states in more detail. We begin with the different hadrons' composition.

5d. Stable Paricles' Composition of the Final States

In Table I we report our calculation for the multiplicities of different stable hadrons at three different energies and compare them with experimental data. We can clearly see that we are able to account with remarkable precision for the proportions of different hadrons in the final states.

	34 GeV		22 GeV		14 GeV	
	EXP	TH	EXP	TH	EXP	TH
$\langle n_{\pi^\pm} \rangle$	10.3±.4	10.54	9.0±.5	9.05	7.2±.6	7.47
$\langle n_{\pi^0} \rangle$	6.1±2.0	5.95		5.11		4.27
$\langle n_{K^\pm} \rangle$	2.0±.2	1.78	1.4±.2	1.49	1.2±.14	1.21
$\langle n_{K^0,\bar{K}^0} \rangle$	1.6±.1	1.73		1.45		1.17
$\langle n_{p,\bar{p}} \rangle$	.8±.1	.77	.61±.1	.61	.42±.06	.47
$\langle n_{\Lambda,\bar{\Lambda}} \rangle$	.30±.04	.35	.22±.04	.28	.13±.04	.20

TABLE I. Multiplicities of different hadrons at three different energies

The calculated x-spectra for $\pi^\pm, K^\pm, \pi^0, p\bar{p}, \Lambda\bar{\Lambda}$, and $\Xi^\pm$ at $\sqrt{s}$ = 34 GeV are displayed together with available data in Fig. 18.

Another relevant test of the effectiveness of our calculation is provided by the fragmentation of the c-quark in D*-mesons, which has recently been observed. [11] Our prediction is compared with observations in Fig. 19. One can see that the observed "hardness" of the D*-spectrum is correctly reproduced, furthermore all the normalization is in agreement with experiments.

5e. 3-Jet Events

It has been shown [9] that the increase in $\langle p_T \rangle$ with energy is associated with planar events which have a typical 3-jet structure. These events have been taken as strong evidence for the existence of dynamical gluons. According to the theory presented here, there is no such thing as a dynamical gluon, rather the unquantized color field exhibits large transverse momentum fluctuations in the form of $q\bar{q}$-pairs coupled vectorally. As an immediate consequence of this description the fragmentation of a jet does not differ substantially from that of a quark-jet, [12] and this fact, contrary to expectations, has been demonstrated by experimental data.

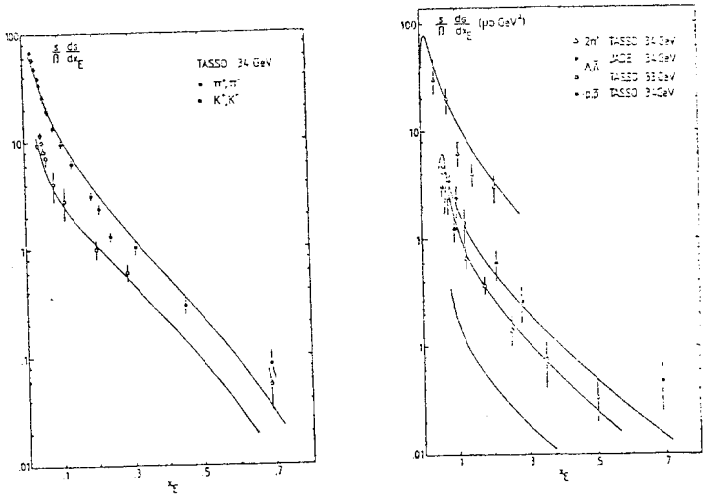


Fig. 18. x-spectra for different hadrons at $\sqrt{s}$ = 34 GeV

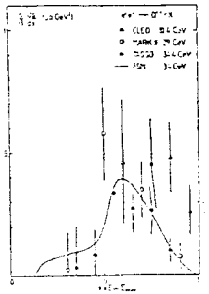


Fig. 19 The calculated D* spectrum at $\sqrt{s}$ = 34 GeV

I shall now present some of the predictions of our theory that are particularly relevant to the issue of gluonic behavior. In Fig. 20 the Ellis-Karliner [13] test on cos $\tilde{\theta}$ distribution is applied to our theoretical data and compared with experiments.

The spin 1-nature of the "gluon" is clearly observed both in data and in our calculation. Next we exhibit in Fig. 21 the calculated x distribution [$(x_1 = 2E_1/\sqrt{s})$, where E_1 is the energy of the most energetic jet] along with experimental information. Again the observed spin 1-nature of the "gluon" is well reproduced by our calculations.

Finally, as far as the observed difference of baryon-antibaryon production in 2- and 3-jet events is concerned we compute at $\sqrt{s}$ =30 GeV:

$$\langle n_{\Lambda\bar{\Lambda}} \rangle_{all} = .35 \quad \text{(Exp. .30 + .04 [14]) and} \qquad (5.1)$$

$$\langle n_{\Lambda\bar{\Lambda}} \rangle_{3jet} = .48 \quad \text{(Exp. .59 + .12 [14]).} \qquad (5.2)$$

This difference, which looks rather puzzling in the context of "traditional" QCD, has in our framework a very transparent and simple explanation. Whereas 2-jet events arise from very asymmetrical decay configurations of the FS, one FS-mass being quite modest, the other comparable to the initial FS, the 3-jet events arise from those rarer configurations which are much more symmetric. Due to the fact that $B\bar{B}$ production is only effective when the FS mass is in the mass-window $2 \div 3$ GeV, it should be clear that 3-jet events have roughly twice as large a chance of passing through the window as 2-jet events. And this is perfectly consistent with observations.

5f. $B\bar{B}$ Correlations

In Figs. 22, 23 and 24, we compare with the still scanty experimental data [15] our predictions for $B\bar{B}$ correlations in $\cos\theta_{p\bar{p}}, \Delta\Phi$ and $|y_p - y_{\bar{p}}|$. Good agreement should be noticed.

5g. Scaling Violations

A more quantitative analysis of the scaling violations, already seen in Section 5a, is compared with data in Fig. 25. Again we see that the effect is quantitatively predicted by our theory.

We end here this rapid survey of the main applications of our approach to e^+e^--physics. For a more extensive analysis the reader is referred to Ref. 4.

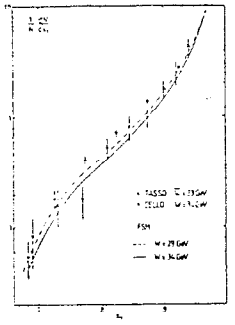


Fig. 20 The Ellis-Karliner test

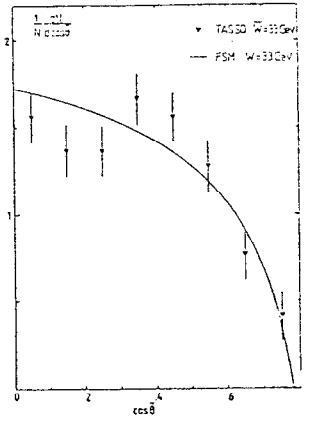


Fig. 21 The x_1-distribution for 3-jet events

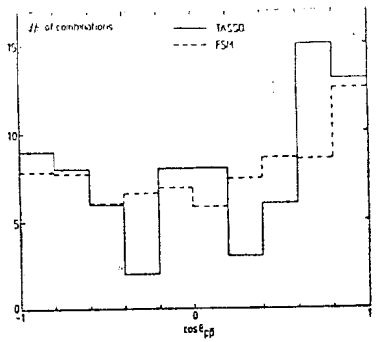


Fig. 22 $\cos\theta_{p\bar{p}}$-correlations in the experimental conditions of Ref. 15

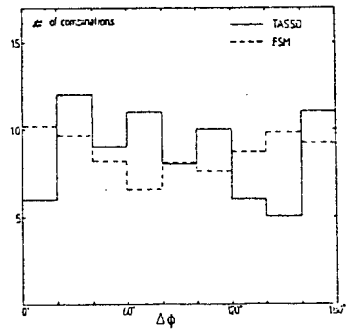


Fig. 23 Same as for Fig. 22, for $\Delta\phi$ correlations

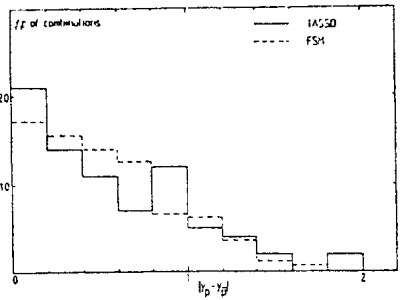


Fig. 24 Same as for Fig. 22, for $|y_p - y_{\bar{p}}|$ correlations

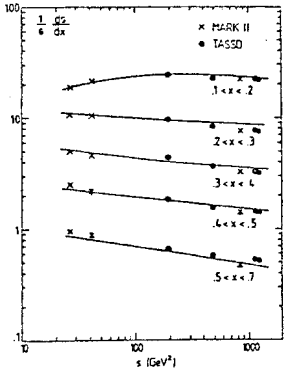


Fig. 25 Scaling violations in the charged particles' x-distribution

6. CONCLUSIONS

It is now time to conclude our discussion. It cannot be denied that the description of e^+e^- physics afforded by QGD/ACD is capable of accounting for even very fine details of the experimental observation in the range of CM energies between 10 and 40 GeV. From the quantitative point of view, our theoretical framework seems to have the basic physics well under control.

But the most important physical question is the following: what do we learn about the structure of the "true" QCD? Or put differently, in which forms do the color dynamics manifest themselves in hadronic interactions?

It is clear that some of the perturbative QCD predictions, which derive from free, short distance behavior of the quarks, [3-jet events, etc.] are reproduced by our approach, which does exhibit the same behavior. What is highly non-trivial is that we have been able to correctly account for e^+e^- annihilation by means of these thin color tubes, where quarks move almost freely, which have been called Fire-Strings. This lends strong support to the idea that confinement, absence of dynamical gluons and freedom at short distance are different manifestations of it. This then poses the crucial question of how to realize such a dynamical behavior in a gauge theory of color, and eventually in QCD. ACD [5] gives an answer which appears to differ from the generally accepted views about QCD in a fundamental way. However there are indications that ACD and QCD are in fact the same theory. [16]

If these indications will stand up to further theoretical and experimental challenges, we shall be finally in possession of a formidable theoretical weapon to bring to solution a very hard problem, the hadronic problem, which has been with us for the last 35 years.

REFERENCES

1. R. P. Feynman, Photon-Hadron Interactions, Benjamin, Reading Mass., 1972.

2. G. Preparata, Phys. Rev. D7,2973 (1973).

3. G. Preparata and N. Craigie, Nucl. Phys. B102, 478 (1976); for a review see G. Preparata, in The Why's of Subnuclear Physics, edited by A. Zichichi p. 727, Plenum Press, (1979).

4. For a more detailed recent discussion see: A. Angelini, L. Nitti, M. Pellicoro, G. Preparata and G. Valenti: "Fire-string theory of e^+e^- annihilation" (to be published in the "Rivista del Nuovo Cimento").

5. For a review of ACD, see G. Preparata, in Fundamental Interactions, Cargese 1981, ed. by Levy, Basdevant, Speiser, Weyers, Jacob and Gastmans, Plenum Publishing Corporation, 421 (1982).

6. L. Angelini, L. Nitti, M. Pellicoro, G. Preparata and G. Valenti, Phys. Let. 123B, 246 (1983).

7. P. Cea, G. Nardulli and G. Preparata, Zeit. fur Phys. C16, 135 (1983).

8. A. Giannelli, L. Nitti and G. Preparata, to be published.

9. For a broad review see P. Soding and G. Wolf, Ann. Rev. Nucl. Phys. Sci. 31, 231 (1981).

10. L. Angelini, L. Nitti, M. Pellicoro, G. Preparata and G. Valenti, EPOS, CERN Program Library (W1034), Cern Computer Newsletter 162 (1982).

11. For a very recent review of such data see J. Dorfan, Rapporteur Talk at the 1983 Cornell Conference.

12. L. Angelini, L. Nitti, M. Pellicoro, G. Preparata and G. Valenti, Phys Letters. B119, 45 (1982).

13. J. Ellis and I. Karliner, Nucl. Phys. B148, 141 (1979).

14. S. L. Wu, QCD and Hadron Jets. New Results From PEP and PETRA, DESY Report 83-007 (1983).

15. TASSO Coll., H. - J. Brandelik et al., Zeit. fur Phys. C17 (1983) 5

16. B. Preparata, Do Mass Singularities Force Yang Mills Fields To Be Anisotropic? Bari Preprint BA-GT/83-08.

MAGNETIC DIPOLE TRANSITIONS IN ONIA

Vasilis Zambetakis and Nina Byers

Department of Physics

University of California

Los Angeles, California 90024

Presented at the

Summer Institute on Particle Physics

Stanford Linear Accelerator Center

August 1983

ABSTRACT

In this talk I would like to report some results of a study of magnetic dipole transition matrix elements in the charmonium and T systems, taking into account relativistic effects to order $(v/c)^2$. Relativistic effects are small for allowed transitions. For hindered transitions, on the other hand, retardation and relativistic effects and coupled channel mixing are important. We have calculated retardation and relativistic effects, and find strong cancellation between the various contributions. Results are given for $\psi' \to \eta_c \gamma$ and for both allowed and hindered transitions in the T system. When coupled channel mixing is taken into account in the $\psi' \to \eta_c \gamma$ case, we find that theory and experiment agree within error.

© V. Zambetakis 1983

I. INTRODUCTION

There are two types of magnetic dipole transitions: allowed transitions where the initial and final nonrelativistic radial wave functions are the same, e.g. $\psi' \to \eta_c'\gamma$, $T'' \to \eta_b''\gamma$ etc., and relativistic or "hindered" transitions where the initial and final nonrelativistic wave functions are orthogonal, e.g. $\psi' \to \eta_c\gamma$, $T' \to \eta_b\gamma$ etc. Hindered transitions occur only owing to relativistic and retardation effects. In our calculation we use a theory in which relativistic effects are taken into account to order $(v/c)^2$ which seems to account for the observed electric dipole transitions and fine and hyperfine splitting of the levels in charmonium.[1] We summarize the theory of leading relativistic effects for M1 transitions first given by Sucher,[2] verify the $(v/c)^2$ correction terms of Sucher and Kang,[3] and include that due to Grotch and Sebastian.[4] Our calculation of these effects yield small corrections to allowed transition amplitudes, smaller than previously reported.[5] Consequently there may be a discrepancy between theory and experiment for the $J/\psi \to \eta_c\gamma$ rate, see Table I. For hindered transitions, relativistic effects are relatively large. They are larger than retardation effects. The various contributions have opposite signs and tend to cancel. Consequently our results here may be model dependent. We find that, for hindered transitions, the coupling of $q\bar{q}$ states to $q\bar{q}q\bar{q}$ decay channels is important. When this coupling is taken into account, the physical charmonium states, for example, become mixtures of 1S, 2S, etc., $c\bar{c}$ states, and also have some probability of being $D\bar{D}$, $D^*\bar{D}^*$ and other charmed-meson states.[6] When we take this mixing into account, we find a rate for $\psi' \to \eta_c\gamma$ in

TABLE I. Values for the overlap integral I for some allowed transitions. The contributions I_1, $I_2' = I_2 + I_{GS}$, and I_4 are explained in text; cf., Eqs. (15)-(17). We got the experimental values for the magnitude of I from the data of Ref. 8 using our Eq. (21).

	$-I_1$	$-I_2'$	$-I_4$	$-I$	$\lvert I\rvert_{exp}$
$c\bar{c}$					
$1^3S_1 \to 1^1S_0$	1.00	-0.17	0.25	1.08	0.7 ± 0.2
$2^3S_1 \to 2^1S_0$	1.00	-0.20	0.07	0.87	1.1-1.7
$b\bar{b}$					
$1^3S_1 \to 1^1S_0$	1.00	-0.07	0.11	1.04	-
$2^3S_1 \to 2^1S_0$	1.00	-0.06	0.07	1.01	-
$3^3S_1 \to 3^1S_0$	1.00	-0.07	0.03	0.96	-

rough agreement with experiment.

II. RELATIVISTIC CORRECTIONS TO M1 TRANSITION MATRIX ELEMENTS

We consider first $c\bar{c}$ and $b\bar{b}$ bound S-states which are eigenstates (neglecting S-D mixing) of the Breit-Fermi Hamiltonian

$$\begin{aligned} H_{BF} &= (p_1^2 + p_2^2)(2m)^{-1} - (p_1^4 + p_2^4)(8m^3)^{-1} + V_{NR} \\ &+ (V_v' - V_s')(\vec{\sigma}_1\cdot\hat{r} \times \vec{p}_1 - \vec{\sigma}_2\cdot\hat{r} \times \vec{p}_2)(4m^2)^{-1} \\ &- V_v' (\vec{\sigma}_1\cdot\hat{r} \times \vec{p}_2 - \vec{\sigma}_2\cdot \hat{r} \times \vec{p}_1)(2m^2)^{-1} \\ &+ (r^{-1} V_v' - V_v'')(3\vec{\sigma}_1\cdot\hat{r}\ \vec{\sigma}_2\cdot\hat{r} - \vec{\sigma}_1\cdot\vec{\sigma}_2)(12m^2)^{-1} \qquad (1) \\ &+ \vec{\sigma}_1\cdot\vec{\sigma}_2\ \nabla^2 V_v(6m^2)^{-1} + \nabla^2 V_{NR}(4m^2)^{-1} - \vec{p}_1\cdot V_s\ \vec{p}_1(2m^2)^{-1} \\ &- \vec{p}_2\ V_s\cdot\vec{p}_2(2m^2)^{-1} - \vec{p}_1\cdot (I - \vec{\nabla}\vec{\nabla}/\nabla^2)V_v\cdot\vec{p}_2(m^2)^{-1} \quad . \end{aligned}$$

with $V_{NR} = V_v + V_s$. Particle 1 is the quark and 2 the antiquark. This Hamiltonian comes from a $(v/c)^2$ expansion of the reduction to Pauli spinor form of the no-pair Dirac Hamiltonian[2]

$$H = h_1 + h_2 + \Lambda_{++}\, V\, \Lambda_{++} \qquad (2)$$

with $h = \vec{\alpha}\cdot\vec{p} + \beta m$ and

$$V = \beta_1\beta_2\, V_s + V_v - \vec{\alpha}_1\cdot(I - \frac{\vec{\nabla}\vec{\nabla}}{\nabla^2})\, V_v\cdot\vec{\alpha}_2 \quad . \qquad (3)$$

Pair creation terms omitted in (2) are included in the wave functions perturbatively.

The transition matrix element is taken to be

$$M_{\lambda fi} = (\Phi_f,\ h_\lambda\ \Phi_i) \qquad (4)$$

where Φ are eigenstates of the Breit-Fermi Hamiltonian. Here h_λ has two parts; one comes from the reduction to Pauli spinors of the usual $\vec{\alpha}\cdot\vec{A}_\lambda$ coupling, and the other comes from the perturbation to the wave functions due to pair effects. The pair terms are shown diagrammatically in Fig. 1. They are $(v/c)^4$ correction terms to matrix elements which for allowed transitions are of order $(v/c)^2$ where v is the quark velocity. Therefore we include them as first order perturbations. We separate the spin part χ and the space part ϕ of the S-state wave fuctions and write the matrix element as

$$M_{\lambda fi} = ie_q \langle\chi_f|(\vec{\sigma}_1\cdot\vec{k} \times \hat{\varepsilon}_\lambda^*/m)|\chi_i\rangle\ I \qquad (5)$$

with I a radial integral. This is possible because

$$\langle\chi_f|\vec{\sigma}_1|\chi_i\rangle = -\langle\chi_f|\vec{\sigma}_2|\chi_i\rangle \qquad (6)$$

for singlet-triplet transitions. The reduction to Pauli spinors of the $\vec{\alpha}\cdot\vec{A}$ terms to order $(v/c)^4$ yield what are called the "no-pair" contribution to the factor I. This contribution comes from the terms

$$-i\frac{\vec{\sigma}_1}{2m}\cdot(\vec{k} - \frac{\vec{p}^2\vec{k} + \vec{p}(\vec{p}\cdot\vec{k})}{2m^2}) \times \hat{\varepsilon}_\lambda^*\ e^{-i\vec{k}\cdot\vec{r}_1} + (1\leftrightarrow 2) \qquad (7)$$

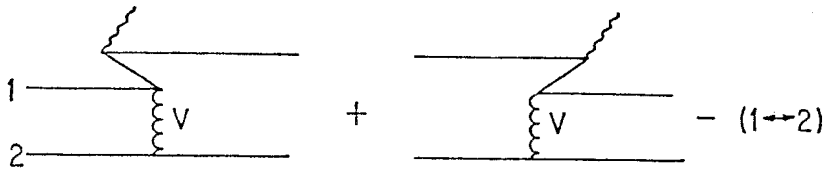


Fig. 1.: The Z-diagrams for photon emission which describe the pair creation effects which have been included as perturbations on the Breit-Fermi wave functions.

in h_λ. Here $\vec{p}_1 = -\vec{p}_2 = \vec{p}$. Including recoil, we write the final state wave function as $e^{-i\vec{k}\cdot\vec{R}}\,\phi_f(r)$ with $\vec{R} = (\vec{r}_1 + \vec{r}_2)/2$ and $\vec{r} = \vec{r}_1 - \vec{r}_2$. Then the no-pair contribution to I is

$$I^{\text{no-pair}} = \langle \phi_f \,|-j_0\,(kr/2) + 2\vec{p}^{\,2}/3m^2\,|\phi_i\rangle \quad . \tag{8}$$

The contribution of the pair effects is of particular interest because it is sensitive to the Lorentz transformation properties of the interaction potential V. Following Sucher[2] we separate the potential into even and odd parts as follows

$$V = \underbrace{\beta_1\beta_2\, V_s + V_v}_{V_{\text{even}}} + \underbrace{\vec{\alpha}_1\cdot\vec{\alpha}_2\, Y + \vec{\alpha}_1\cdot\hat{r}\;\vec{\alpha}_2\cdot\hat{r}\, Z}_{V_{\text{odd}}} \tag{9}$$

and allow the transverse gluon exchange part of V to have a more general form than in (3). We take it to be given by some f(r); viz.,

$$-\vec{\alpha}_1\cdot\left(I - \frac{\vec{\nabla}\vec{\nabla}}{\nabla^2}\right) f(r)\cdot\vec{\alpha}_2 \quad . \tag{10}$$

If one evaluates (10) in the usual way, one finds (9) with

$$Y = -(2f + Z)/3 \tag{11}$$

and

$$Z = r^{-3}\int_0^r s^3\, f'(s)ds \quad . \tag{12}$$

The four terms in (9) give to I the contribution

$$I^{pair} = \langle\phi_f|(V_s/m)j_o(kr/2) - ([rV_v' + rY' - Z]/mkr)j_1(kr/2)|\phi_f\rangle . \quad (13)$$

With $f(r) = V_v$ the transverse glue exchange piece cancels the V_v part of V_{even}, and only the V_s term in (13) survives.

Combining pair with no-pair terms, we find that the radial integral is given by

$$I = I_1 + I_2 + I_4 \quad (14)$$

where

$$I_1 = \langle\phi_f| -j_o(kr/2)|\phi_i\rangle , \quad (15)$$

$$I_2 = \langle\phi_f|2\vec{p}^2/3m^2|\phi_i\rangle \quad \text{and} \quad (16)$$

$$I_4 = \langle\phi_f|(V_s/m)j_o(kr/2)|\phi_i\rangle . \quad (17)$$

If the wave functions in (15)-(17) are taken to be eigenfunctions of a nonrelativistic Hamiltonian, these expressions agree with those of Sucher and Kang.[3] In their paper there is an additional contribution I_3 which is nonvanishing only for hindered transitions. It is the first order perturbative effect of the hyperfine interaction on the wave functions. With nonrelativistic wave functions ϕ_i and ϕ_f, it is given by

$$I_3 = -4\langle\phi_f|\nabla^2 V_v|\phi_i\rangle/6m^2(E_i - E_f) . \quad (18)$$

If instead one uses Breit-Fermi wave functions, the effect of the hyperfine interaction is included in I_1, and I_3 is redundant. The Hamiltonian we use is hermitian, so effects of the spin independent $(v/c)^2$ correction terms in the Hamiltonian do not contribute to I_1 to order $(v/c)^2$. Because $(v/c)^2$ correction terms are relatively small, results obtained with the use of Breit-Fermi wave functions are the same, to the accuracy of our calculations, as those obtained treating the hyperfine and other $(v/c)^2$ effects perturbatively. Consequently all retardation and relativistic effects to order $(v/c)^2$ except recoil corrections are included in I if we evaluate I_1 through I_4 using nonrelativistic wave functions and include I_3 for hindered transitions.

In the above analysis, recoil effects in the final state wave function were taken into account only by allowing the center of mass to recoil (Galilean invariance). Lorentz invariance gives rise to additional effects on the wave function. This induces a spin dependent difference between the constituent and center of mass coordinates; Grotch and Sebastian[4] have pointed out that this generates a contribution to M1 transitions from the convection current. Their result is that there is an additional $(v/c)^2$ correction to I given by

$$I_{GS} = \langle\phi_f|\vec{p}^2/6m^2|\phi_i\rangle . \quad (19)$$

Since this combines simply with the $(v/c)^2$ correction to the $\vec{\sigma}\cdot\vec{B}$ interaction term I_2, we quote results for I_2' where

$$I_2' = I_2 + I_{GS} = \langle\phi_f|5\vec{p}^2/6m^2|\phi_i\rangle \quad . \tag{20}$$

To exhibit the relative sizes of the various effects, we give in Tables I and II the values of I_1, I_2', I_3, and I_4 all calculated with nonrelativistic wave functions. Here I_1 simply exhibits retardation effects, I_2' is given by (20), I_3 is the hyperfine interaction effect, and I_4 gives the effect of the Z diagrams.

So far we have neglected the coupling of $q\bar{q}$ states to multiparticle channels such as $q\bar{q}q\bar{q}$. Taking coupling to closed $q\bar{q}q\bar{q}$ decay channels into account, Eichten et al.[6] showed that the physical J/ψ and ψ' states are mixtures of 1S, 2S, and other $c\bar{c}$ states, and also have some probability of being virtual $D\bar{D}$, $D^*\bar{D}$, etc., charmed-meson states. If the ψ' has some probability of being a 1S state, since the η_c is primarily a 1S state, this mixing can be important in a calculation of the $\psi' \to \eta_c\gamma$ amplitude. To estimate the effect of such mixing, we used the results of Eichten et al. for the amplitudes for the ψ' to be 1S and the η_c to be 2S $c\bar{c}$ states (see below) and found that this mixing contributes significantly to the $\psi' \to \eta_c\gamma$ amplitude.

III. RESULTS OF THE MODEL CALCULATION

We have calculated the various contributions to I using the one gluon exchange plus linear confinement model of Ref. 1. The model includes transverse gluon exchange (in Coulomb gauge) and treats

TABLE II. Calculated values for the overlap integral I for some hindered transitions. When coupled channel mixing is taken into account for the $\psi' \to \eta_c\gamma$ decay, there are additional contributions to I of the same order of magnitude as those shown here. See text. (We include the photon momenta in this Table because I_1 is proportional to k^2. The photon momenta are taken from Ref. 8 for $\psi' \to \eta_c$ and from Ref. 1 for the $b\bar{b}$ transitions.)

	k(MeV)	$-I_1$	$-I_2'$	$-I_3$	$-I_4$	$-I$
$c\bar{c}$						
$2^3S_1 \to 1^1S_0$	634	0.052	-0.136	0.127	0.073	0.116
$b\bar{b}$						
$2^3S_1 \to 1^1S_0$	639	0.019	-0.052	0.098	0.016	0.080
$3^3S_1 \to 2^1S_0$	368	0.021	-0.048	0.095	0.027	0.095
$3^3S_1 \to 1^1S_0$	948	0.010	-0.033	0.056	0.008	0.041

the linearly confining potential as a Lorentz scalar. The confining potential is given by $V_s = r/a^2+C$ with a = 0.46 fermi. The vector part of the potential is given $V_v = -\kappa\ \mathrm{erf}(\sqrt{2}\ mr)/r$ which is the Coulomb potential of a Gaussian distributed color charge whose mean square radius is given by the Compton wave length m^{-1} of the quark. The parameters of the potential and quark masses are given in Table III. The constant C in V_s is necessary in order to get the observed masses for the charmonium and upsilon states. McClary[7] found it necessary to consider C as part of V_s rather than V_v in order to fit the observed charmonium level structure taking $(v/c)^2$ corrections to the nonrelativistic Hamiltonian into account. He smeared the color charge in order to calculate relativistic corrections to E1 transition rates. The E1 rates are insensitive to this smearing, and it was simply a convenient way to get results. On the other hand, the hyperfine splitting of the levels in this model is sensitive to the short distance behavior of V_v. The model correctly accounts for the hyperfine splitting of the ground states of charmonium and is in rough agreement with the $\psi' - \eta_c'$ mass difference. Note that the diagonal matrix elements of the operator in I_3 just give the fine structure splitting of the corresponding S states. Since I_3 only contributes to hindered transition amplitudes, our results for the allowed transitions are insensitive to the smearing of the color charge. In the case of the hindered transitions, however, I_3 plays an important role. Variation of the color charge radius from a point charge to the quark Compton wave length can change the values of I_3 by as much as 30%.

The rates are related to I by (e_q = 2/3 for $c\bar{c}$ and -1/3 for $b\bar{b}$,

TABLE III. Parameter values for quark masses and V (see text).

	$c\bar{c}$	$b\bar{b}$
m (GeV)	1.84	5.17
κ	0.65	0.53
C (MeV)	-761	-745

and k is the photon momentum):

$$\Gamma\left\{^3S_1 \to {}^1S_0\right\} = e_q^2\,\alpha\,(4k^3/3m^2)\,|I|^2\,(M_i^2 + M_f^2)/2M_i^2\,. \qquad (21)$$

Rates are very sensitive to the hyperfine splitting of the levels owing to the k^3 factor in (21). The experimental value for k should be used. For allowed transitions, I is insensitive to k though I_1 has some k dependence because it contains the retardation correction. For hindered transitions, on the other hand, I_1 is proportional to k^2.

When coupled channel mixing effects are included, the physical ψ' has some probability of being a 1^3S_1 state and the η_c a 2^1S_0 state. Consequently allowed transitions occur in the $\psi' \to \eta_c\gamma$ amplitude. One should use the physical value for k to calculate the retardation effects; they are relatively large because the photon frequency is relatively large.

IV. COUPLED CHANNEL MIXING EFFECTS

To estimate the effect of coupled channel mixing, we calculate I for $\psi' \to \eta_c\gamma$ using the results of Eichten et al.[6] They give probability amplitudes that the physical J/ψ and ψ' states are 1S, 2S, etc. $c\bar{c}$ states. For the η_c, we assume weak spin dependence of coupled channel mixing in the ground states, and approximate the probability amplitudes for the physical η_c to be 1S and 2S $c\bar{c}$ states by the values given by Eichten et al. for the J/ψ. These are shown in Table IV. When we include the $1^3S_1 \to 1^1S_0$ and $2^3S_1 \to 2^1S_0$ transitions in what before was taken to be a $2^3S_1 \to 1^1S_0$ transition, the effect

TABLE IV. Modification of $c\bar{c}$ states due to decay. The probability amplitude for a physical particle (J/ψ or ψ') to be in a charmonium state is given by the number under that state. $Z_{(c\bar{c})}$ gives the norm of the physical particle in the the $c\bar{c}$ sector. This table is a portion of Table VIII in Ref. 6.

Particle	1S	2S	3S	4S	1D	2D	$Z_{(c\bar{c})}$
J/ψ	0.982	0.040	-0.010	0.003	-2×10^{-4}	-7×10^{-6}	0.966
ψ'	-0.090	0.883	0.046	-0.015	-0.031	0.006	0.791

is striking. Our value of -I is reduced from 0.116 to 0.032.

Coupled channel mixing does not affect the rate for $J/\psi \to \eta_c\gamma$ significantly; the amplitude changes by about 4%. The effect is probably larger in the $\psi' \to \eta_c'\gamma$ case. Note in Table IV that $Z_{(c\bar{c})} = 0.79$ for ψ'. We hesitate to use the same weak spin dependence approximation for η_c' as we used for the η_c because the η_c' is closer to open charm threshold. We are calculating these amplitudes directly.

It seems likely that coupled channel mixing will also be significant in hindered $b\bar{b}$ transitions. We expect this will be true in the lowest $T' \to \eta_b\gamma$ case as well as in transitions in higher states. Though open b channels are relatively farther away, their effect is expected to be significant because the relativistic and retardation effects that account for the $2^3S_1 \to 1^1S_0$ transition are also smaller in the $b\bar{b}$ system. Study of coupled channel effects in both charmonium and Υ systems is underway.

V. DISCUSSION OF RESULTS AND COMPARISON WITH EXPERIMENT

Our result for the relativistic correction to the $J/\psi \to \eta_c\gamma$ rate is smaller than previously reported results.[5] This is due to our inclusion of the constant term in the scalar potential. Had we omitted this constant we would have gotten 0.16 instead of -0.25 for I_4, and our final result for I would have been -0.63. Such a decrease in magnitude seems to be indicated by crystal ball measurements; Gaiser[8] gives values for the branching fraction and photon energy which, when combined with the width given in the 1982 Particle Data Tables and used in (21), give $|I| = 0.7 \pm 0.2$. On the other hand, no such decrease is indicated by the experimental observations in the $\psi' \to \eta_c'\gamma$ case. Gaiser's values give $|I|$ between 1.1 and 1.7 (90% c.l.). Neglecting coupled channel mixing, we find 0.86 for the magnitude of I. If we omit the contribution I_4 from C, the magnitude of I would decrease to 0.46. This would give a rate about four times smaller than the reported experimental result. From a theoretical point of view it is inconsistent to omit the constant C because, as McClary showed,[7] it must be considered part of the scalar potential if a model such as ours is to fit the charmonium spectrum. If it were part of the vector potential it would not contribute to I_4, but then the relativistic corrections to the energy level spectrum would make it impossible for the model to fit the experimental data. This discussion of our results for these allowed transitions ignores coupled channel mixing effects. Using the results of Eichten et al.,[6] we estimate that these effects decrease the $J/\psi \to \eta_c\gamma$ amplitude by about 4%. We do not have an estimate of these effects for the $\psi' \to \eta_c'\gamma$ decay.

Our results for some hindered transition matrix elements are shown in Table II. The value of $|I| = 0.116$ for the $2^3S_1 \to 1^1S_0$ $c\bar{c}$ transition is considerably larger than the experimental value of 0.047 ± 0.008 obtained from the measured rate for $\psi' \to \eta_c\gamma$.[8] Taking coupled channel mixing into account as described above, we find that the magnitude of I is decreased to 0.032 which agrees reasonably well with the experimental value considering the crudeness of our estimation.

Since the singlet S-states of $b\bar{b}$ have not been discoverd yet it is useful to give also some estimate of the branching ratios for the

M1 transitions. In this case since the rates are very sensitive to the photon momentum we give in Table V these branching ratios for an upper and lower value of k. In general the hindered transitions have a larger branching ratio than the allowed ones due to the larger values of k and they are less sensitive to the exact values of the hyperfine splittings.

Finally an interesting question is to look at the M1 transitions between the $b\bar{b}$ triplet P-states and the singlet P-states which have not been discovered yet. Whether these branching ratios are large enough to be measured is an open question and we are currently looking at this problem.

We thank J. Sucher and E. Eichten for very useful conversations. This work was supported in part by the U.S. Department of Energy under contract number DE-AT03-81ER40024-Task B.

TABLE V. Branching ratios for the M1 transitions in bottomonium calculated for an upper and a lower limit of the photon momentum k. For the total widths we used the values of Ref. 9.

	k(MeV)	BR(%)	|I|
$T \to \eta_b$	100 30	0.1 3×10^{-3}	1
$T' \to \eta_b$	639 573	0.19 0.14	0.08
$T'' \to \eta_b$	940 880	0.21 0.17	0.04
$T' \to \eta_b'$	40 15	8×10^{-3} 4×10^{-4}	1
$T'' \to \eta_b'$	363 339	7×10^{-2} 6×10^{-2}	0.1
$T'' \to \eta_b''$	31 11	4.5×10^{-3} 2×10^{-4}	1

REFERENCES

1. R. L. McClary and N. Byers, UCLA/83/TEP/12 (1983),to be published in Phys. Rev. D, Oct. 1983.
2. J. Sucher, Rep. Prog. Phys. 41, 1781 (1978).
3. J. S. Kang and J. Sucher, Phys. Rev. D 18, 2698 (1978).
4. H. Grotch and K. J. Sebastian, Phys. Rev. D25, 2944 (1982).
5. A. Martin, "Quarkonium Phenomenology,"in Proceedings XXI International Conference on High Energy Physics, Paris, 1982, Editions de Physique, Les Ulis Cedex, France (1982).
6. E. Eichten , K. Gottfried, T. Kinoshita, K. D. Lane, and T. M. Yan, Phys. Rev. D21, 203 (1980).
7. R. L. McClary, Relativistic Corrections to Radiative Transition in Quarkonium, UCLA Thesis (1982).
8. J. E. Gaiser, SLAC Rep. 255, August, 1982.
9. Lee-Franzini, Topical Conference, SLAC Summer Institute on Particle Physics (1983).

SLAC-PUB-3232
October 1983
(T/E)

RESULTS FROM THE CRYSTAL BALL AT DORIS II*

John E. Gaiser
(REPRESENTING the Crystal Ball Collaboration)[1]
Stanford Linear Accelerator Center
Stanford University, Stanford, California 94305

Abstract

Results are presented from studies of the inclusive photon spectra in hadronic decays of the Υ' and Υ and the exclusive channel $\Upsilon' \to \gamma\gamma\Upsilon \to \gamma\gamma\ell^+\ell^-$, by the Crystal Ball detector at DORIS II. We measure two signals in the $\Upsilon' \to \gamma$ + anything inclusive channel at $E(\gamma) = 108.3 \pm 0.9 \pm 3.0$ MeV and at $E(\gamma) = 127.5 \pm 1.2 \pm 4.0$ MeV. Branching ratios obtained for these signals are:

$$\mathrm{BR}[\Upsilon' \to \gamma(108) + \text{anything}] = (6.3 \pm 1.3 \pm 1.4)\%$$

$$\mathrm{BR}[\Upsilon' \to \gamma(128) + \text{anything}] = (6.0 \pm 1.3 \pm 1.4)\%$$

Presented at the 11th SLAC Summer Institute on Particle Physics
Stanford, California, July 18-29, 1983

---

* Work supported by the Department of Energy, contract DE-AC03-76SF00515.

© J. Gaiser 1983

1. Introduction

The main focus of our investigation at DORIS is a study of the $b\bar{b}$ quarkonium system with emphasis on the radiative decays of the Υ', especially transitions to the ^3P_J states. The theoretical interest in the upsilon spectrum is encouraged by the expectation that it is a less relativistic system than charmonium.[2] From an experimental point of view, it is a new and incompletely mapped family of states associated with the relatively unknown massive b-flavoured quark.[3]

Figure 1 shows the level structure for states up to the Υ' mass as expected from non-relativistic potential models.[2] Also indicated are the predicted radiative transitions between the levels. The decays $\Upsilon' \to \gamma\,^3P_J$ and the cascade decays $^3P_J \to \gamma\Upsilon$ are electric dipole (E1). The transitions involving the $^1S_0$ pseudoscalar states $\Upsilon' \to \gamma\eta_b'$ and $\Upsilon \to \gamma\eta_b$ are allowed magnetic dipole (M1) decays, while $\Upsilon' \to \gamma\eta_b$ and $\eta_b' \to \gamma\Upsilon$ are "hindered" M1. The M1 rates are expected to be small[4] (compared to the E1 rates) and no candidates for these states have been observed. Candidates for the ^3P_J states have been previously reported by the CUSB collaboration[5] in the inclusive photon channel $\Upsilon' \to \gamma\,^3P_J \to \gamma$ + hadrons. Three states were seen corresponding to photon energies of 108 ± 2, 128 ± 3, 149 ± 5 MeV, where the errors reflect the dominant systematic uncertainty. The two higher mass states were also seen in the exclusive process[5] $\Upsilon' \to \gamma\,^3P_J \to \gamma\gamma\Upsilon \to \gamma\gamma\ell^+\ell^-$. Precise identification of these states with the triplet P states of the theory awaits a measurement of their spin and parity. Finally there are hadronic transitions between Υ' and Υ. The $\Upsilon' \to \pi\pi\Upsilon \to \pi\pi\ell^+\ell^-$ decay has been observed[6] in both the $\pi^+\pi^-$ and the $\pi^o\pi^o$ channel. Neither the process $\Upsilon' \to \eta\Upsilon$ nor the isospin forbidden decay $\Upsilon' \to \pi^o\Upsilon$ have been seen.

The Crystal Ball experiment has been running at the DORIS II storage ring since the Fall 1982. We have taken data in the region of the $b\bar{b}$ resonances Υ and Υ'. The current data sets consist of 66k produced Υ' and 53k produced Υ decays, corresponding to 24.5 pb^{-1} and 7.8 pb^{-1}, respectively. The ratio of resonance to continuum hadronic decays at Υ' is about 1:1 and at Υ is about 2.5:1. We also obtained 4.8 pb^{-1} of continuum data just below the Υ', which was mainly used as a systematic check on signals observed in the Υ' resonance.

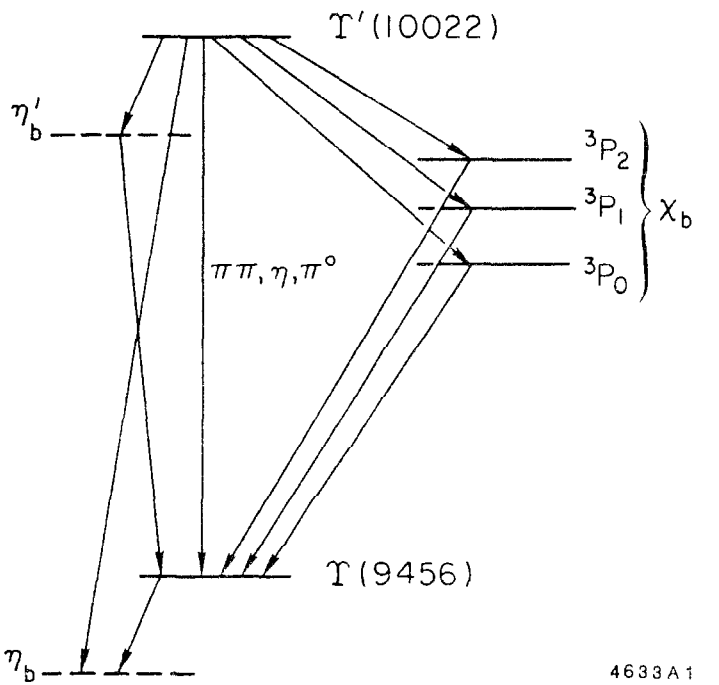


Fig. 1. The level scheme for the $b\bar{b}$ bound states below Υ'. The arrows indicate radiative transitions, except for the $\pi\pi$, η, and π^o transitions between Υ' and Υ. The $^1P_1$ spin-singlet P-wave state, which is expected to have a mass equal to the ^3P_J center of gravity, is not shown here (it is believed to be very difficult to observe[4]).

We expected the analysis of the inclusive Υ' radiative decays to be more difficult than a similar analysis at the ψ', due to a combination of factors: i) smaller branching ratios; ii) large continuum contamination; iii) higher photon multiplicities; and iv) lower photon detection efficiencies. The result is a reduction in the expected signal/noise ratio of 1/10 to 1/15 compared to ψ'.

The Crystal Ball detector is well suited to study the radiative transitions between the upsilon resonances. The components of the detector in its SPEAR configuration have been described in detail elsewhere.[7,8] Only a review of the major characteristics including the modifications for DORIS will be given here (see Fig. 2). The Crystal Ball was designed to measure electromagnetically showering particles with a high resolution over a large solid angle and consists of a segmented array of 672 NaI(Tℓ) crystals (each 16 radiation lengths deep), covering 93% of the solid angle. This coverage is increased to 98% with additional crystals forming the endcaps. No particle identification is attempted in the endcaps. For inclusive hadronic decays the energy resolution achieved for photons and electrons in the main detector is $\sigma(E)/E = (2.6 \pm 0.2)\%/E^{1/4}$ (E in GeV), with an angular resolution of 1.5-2.5° (depending slightly on energy). Charged particle tracking is provided by 3 double-layers of proportional tube chambers with charge division readout. As there is no magnetic field. The momenta of charged particles are not known while their energy is only poorly measured by the one absorption length of NaI. A minimum ionizing particle has a most probable energy loss of 205 MeV. Luminosity measurements are done by counting large angle Bhabha scattering events in the ball and independently by small angle Bhabha counters near the beam-pipe.

Several checks on the data were made to demonstrate the correct performance of the detector. In particular the $\gamma\gamma$ decay of π^0's and η's in inclusive hadronic events were studied to test the ability of the detector to measure photons (see Fig. 3). They also provided checks on the energy calibration and resolution of the crystals. Both signals have the width expected from our resolution but the fitted masses are about 2.5% below their known values[9].

In addition we checked the exclusive channel

$$\Upsilon' \to \pi^0\pi^0\Upsilon \to \gamma\gamma\gamma\gamma\ell^+\ell^-$$

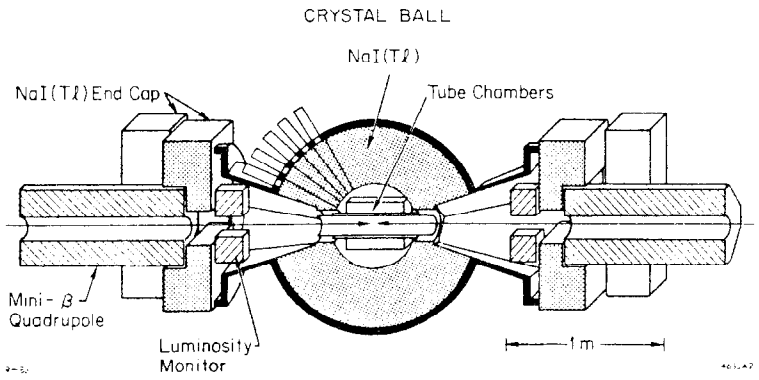


Fig. 2. The Crystal Ball detector at DORIS.

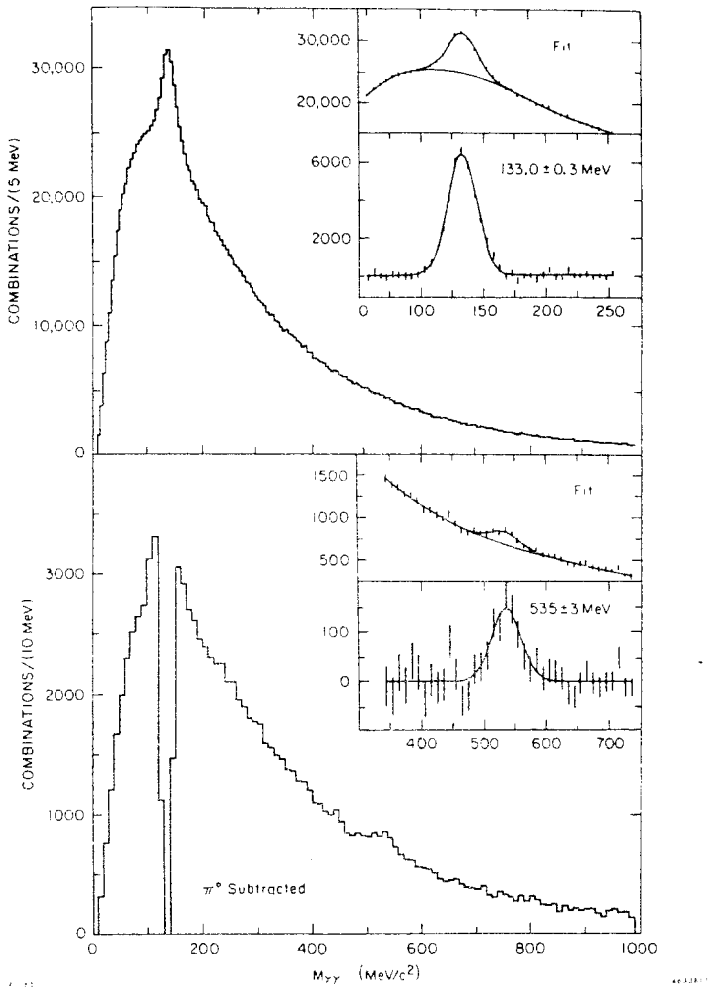


Fig. 3. The top figure shows the $\gamma\gamma$ invariant mass distribution for hadronic decays of the Υ'. The photons were required to have lateral energy deposition patterns consistent with single electromagnetic showers. The inset shows a fit to the π^o mass signal. The bottom figure shows the spectrum after removing photons which reconstruct to a π^o mass. The bottom inset shows a fit to the resulting enhanced η mass signal. Only statistical errors are shown.

(the Υ is detected through its decay into a lepton pair). In Fig. 4 we plot the mass-difference

$$\Delta M = M(\Upsilon') - M_{\rm recoil}$$

where $M_{\rm recoil}$ is the mass recoiling against the 4γ system. In this channel we would expect a signal at the Υ'-Υ mass difference (about 562 MeV).[10] Again we find that the width of the ΔM distribution agrees with what we expect from energy and angular resolution but that the mean of the distribution is about 3% below 562 MeV. Comparable shifts had been observed in similar analyses of SPEAR data in the charmonium system and indicate a systematic bias in our absolute energy scale.

2. Inclusive photon study

Of particular interest to the Crystal Ball experiment at DORIS is a search for the positive C-parity ^3P_J states lying below the Υ'. These states can be detected through the presence of monochromatic lines in the inclusive photon spectra. The method of selecting events and photons will be described below. Detailed descriptions of a similar study in the charmonium system may be found in the references.[8]

Hadronic decays were selected from the available triggers by criteria designed to remove backgrounds from beam-gas interactions, cosmic rays and QED events. The resulting sample of hadronic events contain not only contributions from the resonance decays, but also from the continuum process $e^+e^- \to$ hadrons. In this study no attempt was made to separate the two. The overall hadronic selection efficiency was found to be $\{85 \pm 10\}$% from Monte Carlo studies. The background contamination is about 2%.

The photon selection was designed to remove charged particles, photons from π^o decays and photons with showers contaminated by energy deposits of near-by particles. The following criteria were used:

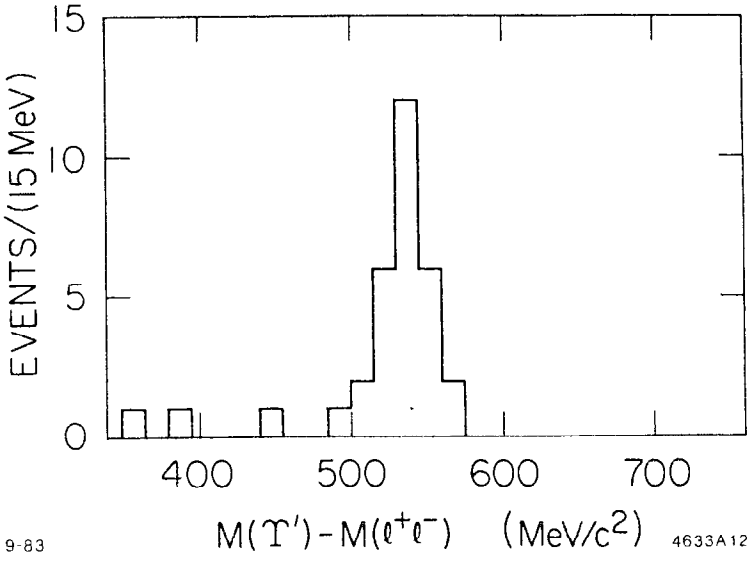


Fig. 4. For the process $\Upsilon' \to \pi^o\pi^o\ell^+\ell^- \to \gamma\gamma\gamma\gamma\ell^+\ell^-$ we plot the observed $\Delta M = M(\Upsilon') - M(\ell^+\ell^-)$ mass difference where $M(\ell^+\ell^-)$ is calculated as the mass recoiling against the 4γ system. We find that $\Delta M = (545 \pm 15)$ MeV, about 3% below the expected value of 562 MeV.[10]

1. The particle must be detected within, $|\cos\Theta_z| < 0.75$, where Θ_z is the angle between the photon and the positron beam direction. This solid angle cut ensures that the particle passes through all three proportional chambers.
2. The particle must be called neutral using information from the proportional chambers. About 7% of the charged particles were misidentified as photons, while about 15% of the photons were tagged as charged.
3. The remaining photons were searched for pairs in which both particles had lateral energy deposition patterns in the NaI consistent with a single electromagnetic shower and which reconstructed to a $\pi^o \to \gamma\gamma$ decay. The pair could not be closer than $\cos\theta_{ij} = 0.85$. These photons were removed.
4. Finally, all remaining photons were required to have lateral energy depositon patterns consistent with a single electromagnetic shower, but the criteria imposed here were more stringent than in 3.

The resulting inclusive photon spectrum for Υ' is shown in Fig. 5(a). Several clear structures are seen in the Υ' spectrum in the regions 100-150 MeV and 430 MeV. The Υ spectrum is shown in Fig. 5(b). Fits to various regions of the Υ spectrum yielded no signal with a significance of more than 2 standard deviations. We used this as a check on the validity of the structures observed in the Υ' spectrum.

In order to calculate branching ratios the photon detection efficiency was measured between 50 MeV and 500 MeV. We employed a similar technique to that used in the ψ' inclusive photon analysis.[8] The efficiency is plotted in Fig. 6 and is seen to vary from about 20% at 100 MeV to about 38% at 500 MeV. These values are lower than we measured on charmonium due to the higher multiplicity in the upsilon final states.

To investigate the structure in the Υ' spectrum, the region between 80 and 200 MeV in Fig. 5(a) was fit with two Gaussians and a quadratic background. The resolution was fixed at $\sigma(E)/E = 2.4\%/E^{1/4}$ (the value prefered by the fit) while the means and amplitudes were allowed to vary. Two clear lines are

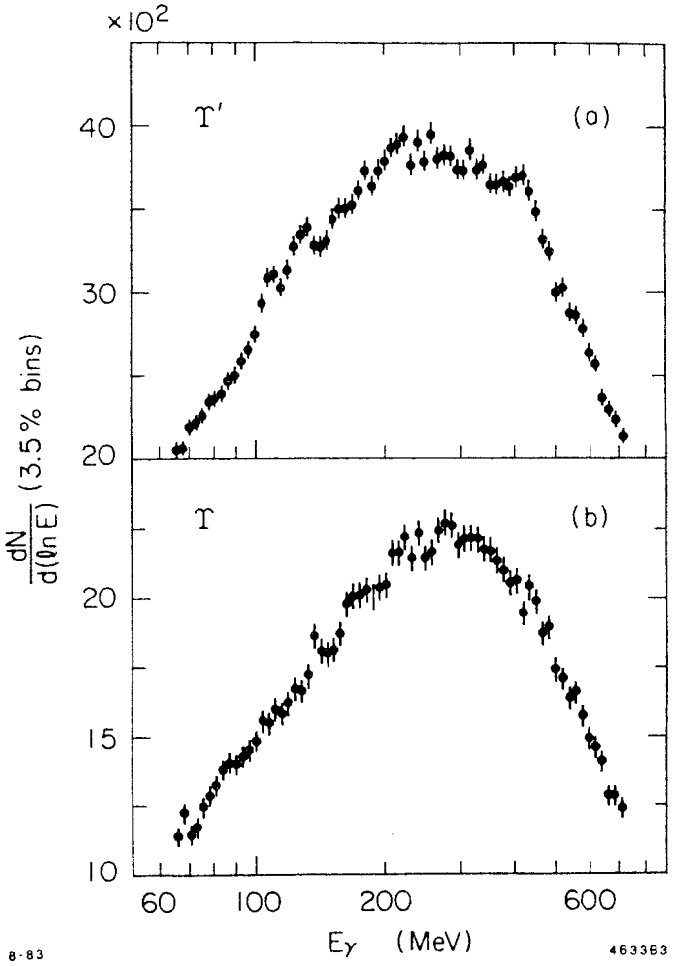


Fig. 5. Inclusive photon spectra from hadronic decays of the a) Υ' and the b) Υ resonances. The photon selection criteria are described in the text.

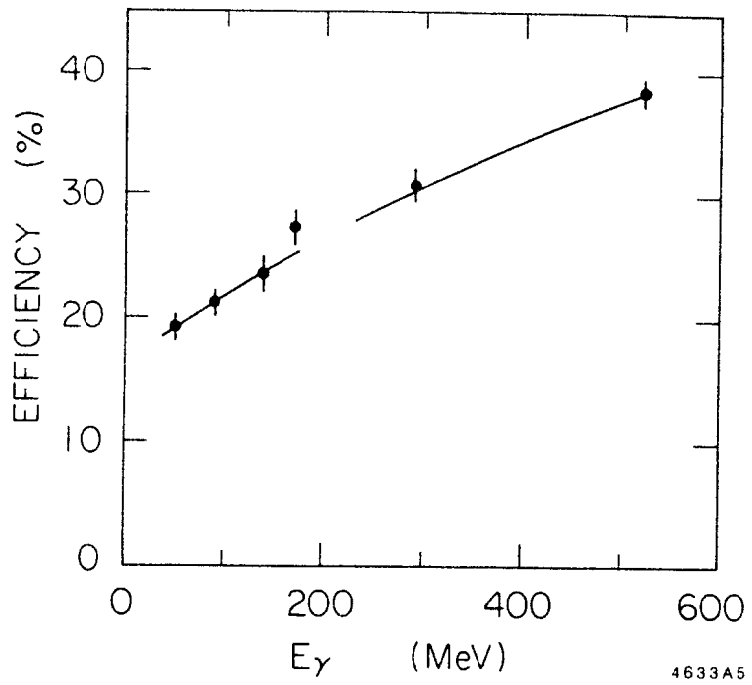


Fig. 6. Photon detection efficiency as a function of energy for the photon selection criteria used to make the spectra shown in Fig. 5. The region near 200 MeV is complicated by the contamination from minimum ionizing charged particles and so no efficiency is shown.

observed: one at about 108 MeV with a significance of 4.9σ and one at about 128 MeV with a significance of 5.0σ. The χ^2 of the fit per degrees of freedom is 7.4/19.

The results, shown in Table I, are seen to be in good agreement with the two low energy photon signals reported by the CUSB experiment,[5] both in energies and in branching ratios. In addition CUSB fitted a third line to their data at $E(\gamma) = (149.4 \pm 0.7 \pm 5.0)$ MeV. To test for the existence of this line in our data a third Gaussian folded with a Breit-Wigner line shape was included in the fit under two assumptions:

1. the natural line width of the state is negligible compared to the detector's energy resolution; and
2. the third line corresponds to a transition to a broad state with a natural line width of 10 MeV.

Table I. Results from Υ' Inclusive Photon Study.

DATUM	LINE 1	LINE 2
$E\gamma$ (MeV)		
Crystal Ball	$108.3 \pm 0.9 \pm 3.0$	$127.5 \pm 1.2 \pm 4.0$
CUSB	$108.2 \pm 0.3 \pm 2.0$	$128.1 \pm 0.4 \pm 3.0$
BR (%)		
Crystal Ball	$6.3 \pm 1.3 \pm 1.4$	$6.0 \pm 1.3 \pm 1.4$
CUSB	6.1 ± 1.4	5.9 ± 1.4

Taking into account the possible systematic uncertainty in the photon energy scale between the various experiments,[5,11] the position of the Gaussian was stepped through the region from 142 to 170 MeV. This was done to map out an upper limit for a transition in this area. Figure 7 shows an example of the fit for a third line at 155 MeV and a 10 MeV wide state. The results are given in Figure 8 along with measured branching ratios[5,11] from other experiments. Although we do not see a significant signal in the region 142-170 MeV, our upper limits are not in contradiction with these measurements.

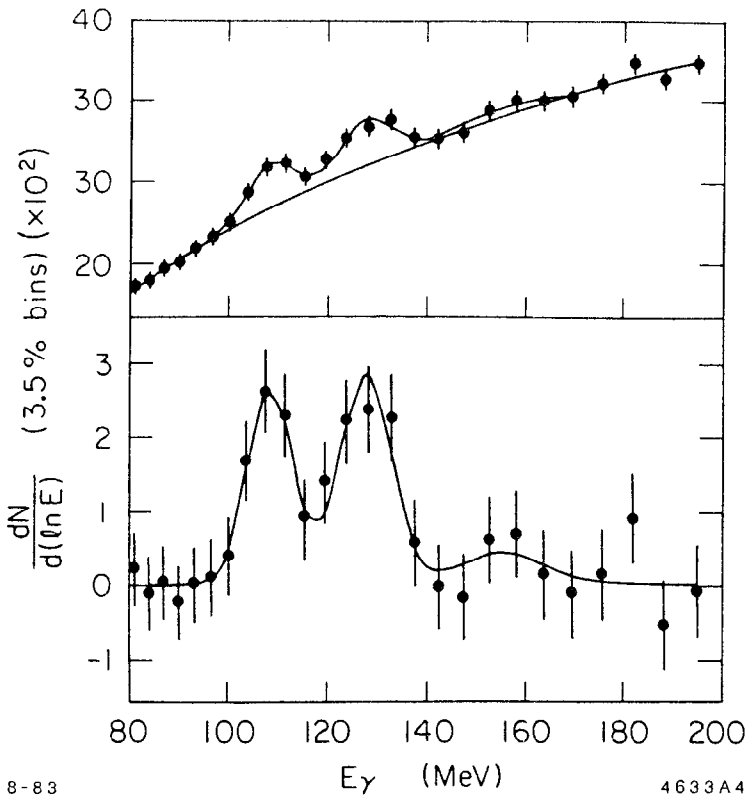


Fig. 7. An example of a fit to the Υ' spectrum in Fig. 5(a) used to map the upper limit between 142 and 170 MeV. The third line here is fixed at 155 MeV for a transition to a broad state with a natural line width of 10 MeV.

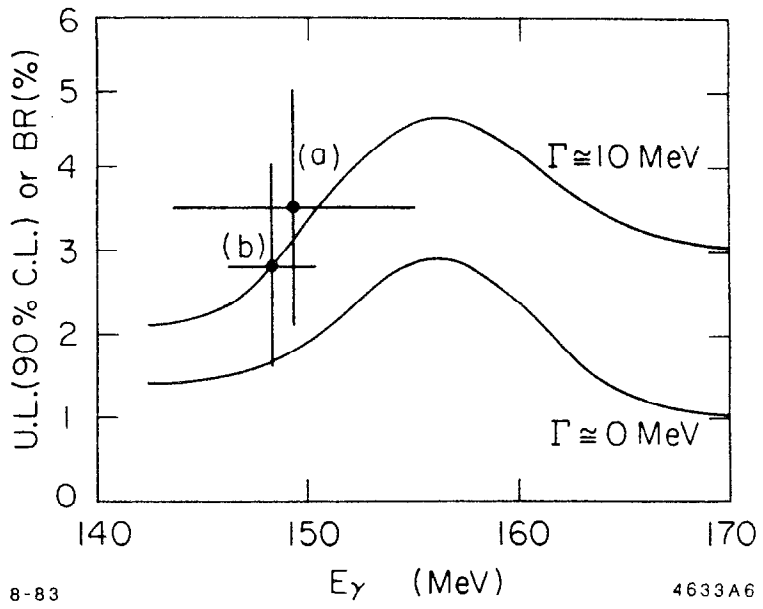


Fig. 8. The curves indicate our 90% confidence level upper limit for a radiative transition to a state with photon energy between 142 and 170 MeV, under the two indicated assumptions for the state's natural line width. The curves were obtained from fits to the Υ' inclusive photon spectrum in Fig. 5(a). A typical fit is shown in Fig. 7. The photons were assumed to have a $1+\cos^2\theta$ angular distribution in the U.L. calculation. The data points indicate measurements made by a) the CUSB experiment[5] and b) the ARGUS experiment.[11]

We now turn to an investigation of the other structure in the Υ' spectrum located near 430 MeV. A fit with a single Gaussian and a quadratic background yields a significance of 3.9 standard deviations. However the fitted width is wider than expected from our energy resolution. It is interesting to see if the 430 MeV structure is connected with the signals at 108 and 128 MeV under the cascade hypothesis $\Upsilon' \to \gamma X \to \gamma\gamma\Upsilon$ (see for example the ${}^3P_J$ states in Fig. 1). To test this hypothesis the region from 280 to 650 MeV was fitted with two Doppler-broadened Gaussians and a quadratic background. The means of the Gaussians were calculated from the 108 and 128 MeV lines and the Υ'-Υ mass difference, which was allowed to vary in the fit. The result is shown in Fig. 9. The measured mass difference from the fit is $\Delta M = M(\Upsilon') - M(\Upsilon) = (555.3 \pm 5.9)$ MeV, in excellent agreement with the known mass difference[10] of 562 ± 2 MeV, including our systematic error of $\simeq 3\%$. This is a very good indication for the validity of the cascade hypothesis. However, the relative strengths of the two contributing lines are poorly determined.

The resulting branching ratio for the single structure is

$E(\gamma)$ (MeV)	significance(s.d.)	BR (%)
427	3.9	$(3.6 \pm 0.9 \pm 0.8)$

This may be interpreted as the sum of product branching ratios

$$\mathrm{BR}(\Upsilon' \to \gamma(108) + {}^3P_2) \cdot \mathrm{BR}({}^3P_2 \to \gamma(427) + \Upsilon)$$
$$+ \mathrm{BR}(\Upsilon' \to \gamma(128) + {}^3P_1) \cdot \mathrm{BR}({}^3P_1 \to \gamma(427) + \Upsilon) \quad ,$$

assuming that the two states correspond to the ${}^3P_2$ and ${}^3P_1$ states of the $b\bar{b}$ theory. The CUSB experiment[5] measures a branching ratio of $\mathrm{BR} = (4 \pm 1)\%$ at a similar gamma energy. By simply counting the number of transition photons it is clear that the structure at 430 MeV cannot represent the primary photon line in a cascade process where the signals at 108 and 128 are the secondary lines.

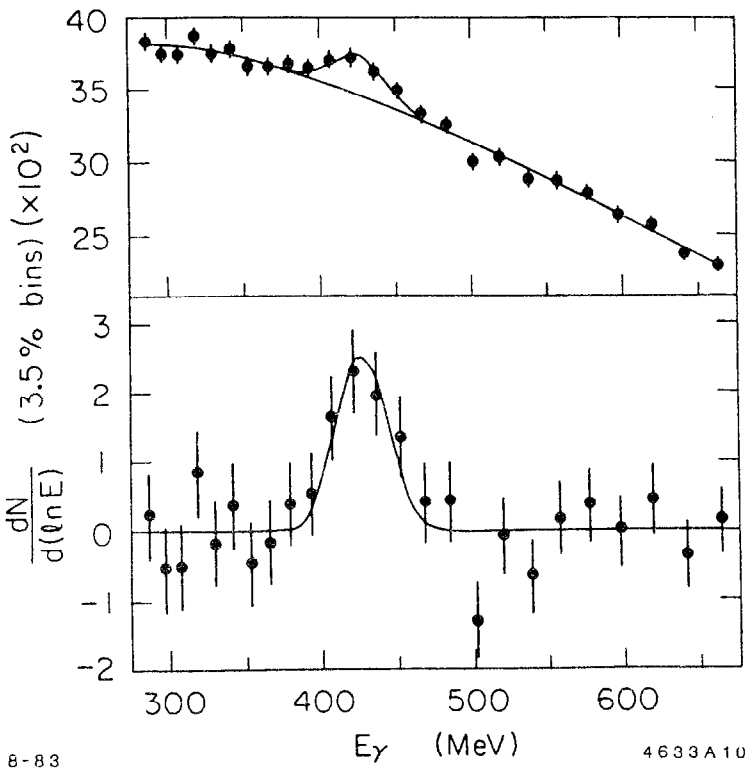


Fig. 9. The fit made to the structure near 430 MeV in the Υ' inclusive photon spectrum shown in Fig. 5(a). Two Doppler-broadened Gaussians with a quadratic background were used. The position of the signals were calculated from a cascade hypothesis assuming that the lines at 108 and 128 MeV are the primary transitions. The signals at 417 and 437 MeV are clearly not separated.

3. Exclusive Cascade Analysis

A second way to look for the ^3P_J states is to study exclusive decays in the channel

$$\Upsilon' \to \gamma\, {}^3P_J \to \gamma\Upsilon \to e^+e^-,\ \mu^+\mu^-$$

To extract candidates for these decays from the data, we imposed the following selection criteria:

1. Exactly 4 particles in the ball within a restricted angular range of $|\cos\Theta_z| < 0.90$ to ensure that detector edge effects do not degrade energy and angular resolution.
2. Two lepton candidates among the 4 particles with $\cos\theta_{ij} < -0.85$ ("back to back"). In the electron channel both electron candidates had to have an energy of $3500 < E_e < 6200$ MeV. For the muons it was required that their signature was compatible with the lateral energy deposition of a minimum ionizing particle and had an energy between 150-350 MeV.
3. The remaining two particles were considered to be the photon candidates and had to have an energy > 50 MeV and no other track closer than $\cos\theta_{ij} = 0.9$, to obtain a clean energy measurement.

The surviving events were subjected to a kinematic fit for the hypothesis $\Upsilon' \to \gamma\gamma e^+e^-$ or or $\Upsilon' \to \gamma\gamma\mu^+\mu^-$. For the electron channel this is a four constraint fit since the four momenta of all final state particles are measured. In the muon channel only the muon directions but not their energies are measured, which results in a two constraint fit. Events having a confidence level of $< 10\%$ were rejected. In Fig. 10 we plot the observed mass difference Υ'-Υ defined by

$$\Delta M = M(\Upsilon') - M_{\text{recoil}}$$

where M_{recoil} is the mass recoiling against the $\gamma\gamma$ system. Cutting on a window around 545 ± 45 MeV, which is $\pm 3\sigma$ as determined from our study of the $\Upsilon' \to \pi^0\pi^0\ell^+\ell^-$ channel, yields our final sample of 46 events (20 $\gamma\gamma e^+e^-$ and 26 $\gamma\gamma\mu^+\mu^-$).

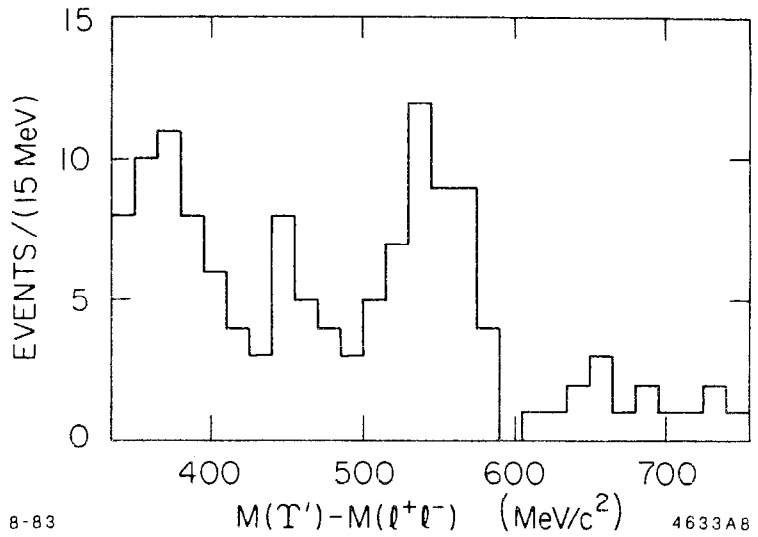


Fig. 10. A plot of the observed $M(\Upsilon')$-$M(\ell^+\ell^-)$ mass difference for events in the exclusive channel $\Upsilon' \to \gamma\gamma\ell^+\ell^-$ where $M(\ell^+\ell^-)$ is calculated as the mass recoiling against the $\gamma\gamma$ system. A cut was made at 545 ± 45 MeV to select the cascade events.

The energy distribution of the low energy photons is shown in Fig. 11. Superimposed is a fit of two Gaussians, with widths given by our detector resolution, over a flat background. The fit separates 2 lines with a confidence level of 70% and the energies are found to be $E_1 = 102 \pm 2 \pm 5$ and $E_2 = 127 \pm 2 \pm 5$ MeV. Within our errors these signals are in agreement with the transitions seen in the inclusive photon spectrum.

4. Conclusions

The Crystal Ball at DORIS has observed two monochromatic lines in the inclusive photon spectrum from decays of the Υ'; one at $E(\gamma) = (108.3 \pm 0.9 \pm 3.0)$ MeV with a branching ratio of BR $= (6.3 \pm 1.3 \pm 1.4)\%$ and one at $E(\gamma) = (127.5 \pm 1.2 \pm 4.0)$ MeV with a branching ratio of BR $= (6.0 \pm 1.3 \pm 1.4)\%$. These results are consistent with the values measured by the CUSB collaboration. We also observed a structure at $E(\gamma) \simeq 427$ MeV which has an energy and width consistent with being the second lines of the cascade process $\Upsilon' \to \gamma {}^3P_J$, ${}^3P_J \to \gamma\Upsilon$ for the two signals seen above. The summed product branching ratio for these processes is BR $= (3.6 \pm 0.9 \pm 0.8)\%$. With our present statistics we do not observe a third line between 142 to 170 MeV. We therefore set an upper limit on the branching ratio for a line in this region (see Fig. 8). We determined the mass splitting between the two observed states in the inclusive photon measurement to be

$$\Delta M = (19.2 \pm 2.0)\,\mathrm{MeV}/c^2 \quad ,$$

where we have assumed that the systematic error in our energy scale cancels in the difference. With the statistical limitations of the current data set no measure of the natural line widths of the states are possible. Presently they are consistent with our resolution. For a comparison with theory the reader is referred to the theory talk[4] in this conference.

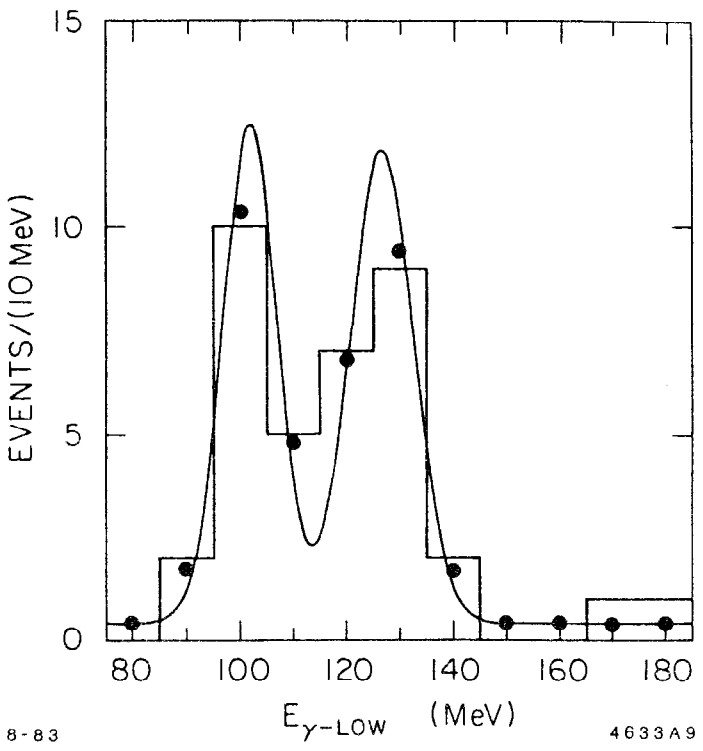


Fig. 11. The histogram shows the low energy photon distribution from the final cascade data sample ($\Upsilon' \to \gamma\gamma\ell^+\ell^-$). The curve represents a fit to the data while the dots result from integrating the fit over the data bins.

Acknowledgements

I particularly want to acknowledge the major contributions made by J. Irion to the inclusive photon analysis and the joint preparation of this report. I also would like to thank my colleagues in the Crystal Ball collaboration for many stimulating reviews of this work. In particular I am grateful to A. Schwarz, D. Gelphman, A. Litke, S. Cooper, P. Ratoff, B. Clare, and W. Lockman for detailed discussions of the exclusive and inclusive studies. Many thanks go to the Crystal Ball Collaboration and DESY-DORIS staff members for their work in collecting and preparing the calibrated data sets.

References

1. The Crystal Ball Collaboration: C. Edwards, C. Peck, F. Porter, P. Ratoff (California Institute of Technology, Pasadena, USA); I. Brock, A. Engler, B. Kraemer, D. Marlow, F. Messing, D. Prindle, B. Renger, C. Rippich (Carnegie-Mellon University, Pittsburgh, USA); Z. Jakubowski, B. Niczyporuk, G. Nowak, T. Skwarnicki (Cracow Institute of Nuclear Physics, Cracow, Poland); J. K. Bienlein, S. Cooper, B. Gomez, T. Kloiber, W. Koch, M. Schmitz, H.-J. Trost, P. Zschorsch (Deutsches Elektronen-Synchrotron DESY, Hamburg, Germany); D. Antreasyan, J. Irion, K. Strauch, D. Williams (Harvard University, Cambridge, USA); D. Besset, R. Cabenda, M. Cavalli-Sforza, R. Cowan, D. Coyne, C. Newman-Holmes (Princeton University, Princeton, USA); E. Bloom, R. Chestnut, R. Clare, J. Gaiser, G. Godfrey, S. Leffler, W. Lockman, S. Lowe, K. Wacker (Stanford Linear Accelerator Center, Stanford University, Stanford, USA); D. Gelphman, R. Hofstadter, I. Kirkbride, R. Lee, A. Litke, T. Matsui, B. Pollock, J. Tompkins (Stanford University, Department of Physics and HEPL, Stanford, USA); G. Folger, B. Lurz, U. Volland, H. Wegener (Universität Erlangen-Nürnberg, Erlangen, Germany); A. Cartacci, G. Conforto, D. de Judicibus, B. Monteleoni, P. G. Pelfer (INFN and University of Firenze, Italy); A. Fridman, F. H. Heimlich, R. Lekebusch, P. Lezoch, W. Maschmann, R. Nernst, A. Schwarz, D. Sievers, U. Strohbusch (Universität Hamburg, I. Institut für Experimentalphysik, Hamburg, Germany); A. König, J. Schotanus, R. T. Van de Walle, W. Walk (University of Nijmegen, The Netherlands); S. Kah, H. Kilian, K. Königsmann, M. Scheer, P. Schmitt (Universität Würzburg, Germany); D. Aschman (University of Cape Town, South Africa).

2. W. Buchmuller and S.-H. H. Tye, Phys. Rev. D 24, 132 (1981); E. Eichten et al., Phys. Rev. D 21, 203 (1980); K. H. Krasemann and S. Ono, Nucl. Phys. B154, 283 (1979); A. Martin, Phys. Lett. 93B, 338, (1980) and 100B, 511 (1981); C. Quigg and J. L. Rosner, Phys. Rev. D 23, 2625 (1981).

3. M. Gilchriese, "Heavy Particle Spectroscopy," Proceedings of the SLAC Summer Institute on Particle Physics, Stanford, July 18-29, 1983; R. Ehrlich, "Heavy Quark Decays," Proceedings of the SLAC Summer Institute on Particle Physics, Stanford, July 18-29, 1983; J. Lee Franzini, "CUSB Results on Υ Spectroscopy and B Physics," Proceedings of the SLAC Summer Institute on Particle Physics, Stanford, July 18-29, 1983.

4. E. Eichten, "Quarkonium from Bottom Up," Proceedings of the SLAC Summer Institute on Particle Physics, Stanford, July 18-29, 1983.

5. C. Klopfenstein et al., Phys. Rev. Lett. 51, 160 (1983).

6. B. Niczyporuk et al., Phys. Lett. 100B, 93 (1981); G. Mageras et al., Phys. Rev. Lett. 46, 113 (1983); J. J. Mueller et al., Phys. Rev. Lett. 46, 1181 (1981).

7. M. Oreglia et al., Phys. Rev. D 25 2259 (1982); M. Oreglia, Ph.D. Thesis, Stanford University, SLAC-236 (1980).

8. J. Gaiser, "Charmonium Spectroscopy from Inclusive ψ' and J/ψ Radiative Decays," SLAC-PUB-2899 (1982), to be published; J. Gaiser, Ph.D. Thesis, Stanford University, SLAC-255 (1982); F. Porter, "Recent Results from the Crystal Ball," Proceedings of the SLAC Summer Institute on Particle Physics, Stanford, July 27 - August 7, 1981, SLAC-PUB-2796.

9. Particle Data Group, Review of Particle Properties, Phys. Lett. 111B (1982).

10. A. S. Artamonov et al., J. Phys. (Paris), Colloq. 43, C3-789 (1982), report value of 9459.7 ± 0.6 MeV for Υ mass. DORIS II measurement gives 10021.6 ± 2.0 MeV for Υ' mass (reported at the Lepton Photon Conference, Cornell, 1983).

11. P. M. Tuts, "Heavy Quarkonia," Proceedings of the Lepton Photon Conference, Cornell, 1983.

HEAVY QUARK DECAYS:
RECENT RESULTS FROM CLEO

Richard D. Ehrlich
Cornell University
Ithaca, NY 14853

I. Introduction

CLEO[1], a general-purpose magnetic detector at the Cornell Electron Storage Ring (CESR), has been in operation since the fall of 1979. In the past year it has reached a new degree of maturity and productivity; with the aid of increased machine luminosity, detector performance, and "smarter" analysis, we are beginning to realize our primary mission of delineating the properties of the b-quark. The same advances that allow us to do good b-physics have, as well, provided some new results on charmed hadrons.

In Sections II through VI below, I shall discuss several selected results in b-decay which have emerged in the past year, during which time we have accumulated some 57 pb^{-1} on and near the $\Upsilon(4S)$. This luminosity, acquired between 2/82 and 11/82, corresponds to approximately 80,000 B meson decays and 150,000 continuum events.

In Section VII I will introduce CLEO's new candidate for the F ($c\bar{s}$) meson.

II. Global Properties of the $\Upsilon(4S)$

The $\Upsilon(4S)$ (See Fig. 1) is seen as an $\sim$ 1 nb enhancement in the visible hadronic cross-section at a center-of-mass energy of 10.57 GeV, above a continuum cross-section of $\sim$ 3 nb. The mean

© R. Ehrlich 1983

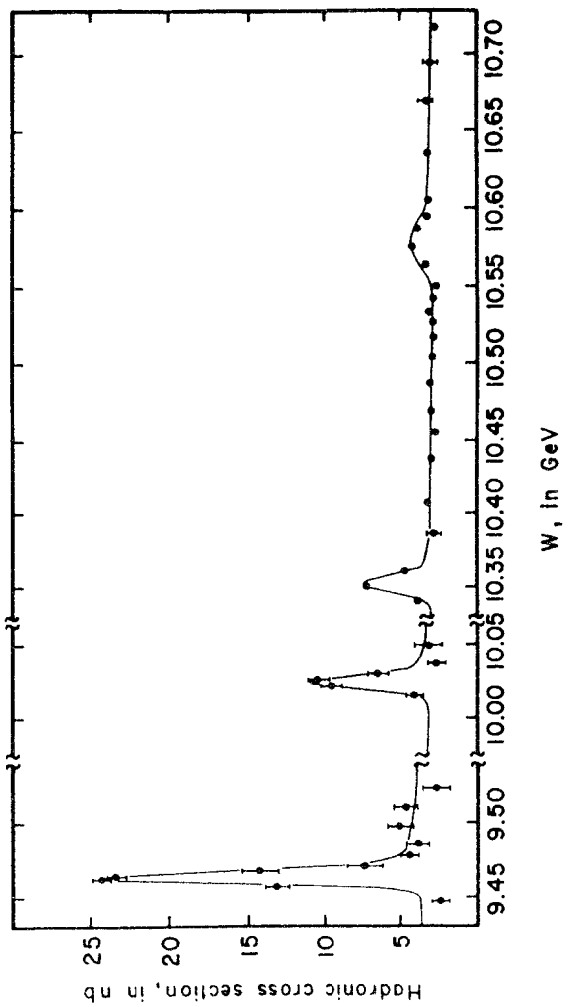


Fig. 1. Visible hadronic cross section in the Υ region.

charged multiplicity from the resonance is (11.5 ± 0.4) which is quite comparable to the PEP/PETRA multiplicity at $S^{\frac{1}{2}} = 28$ GeV. This high multiplicity, together with the modest size of the 4S enhancement and the finite detector acceptance, makes the clarification of b-decay properties a slow and arduous task.

III. B Meson Reconstruction

The most dramatic result (at least from an experimenter's view point) of the last year has been the observance of the decay of the B-meson into specific final states, and the reconstruction of the parent meson together with the determination of its mass.[2] Few (if any) members of our collaboration expected large enough branching-ratios to permit observation of the B-meson in modes other than: eg., $B \to \psi K\pi$ (this has not been seen!). Hindsight has enabled us to accept the facts, which are supported by inclusive measurements discussed in Sections IV and V.

Figure 2shows a mass spectrum of B-mesons decaying via the modes:

a) $B^- \to D^0\pi^-$, b) $B^- \to D^{*+}\pi^-\pi^-$, c) $\bar{B}^0 \to D^0\pi^+\pi^-$,

d) $\bar{B}^0 \to D^{*+}\pi^-$.

The data shown have a rather tight cut on goodness-of-fit; more events can be reconstructed at the price of a larger background.

The method employed can be outlined thus.

a) Find D^0 mesons: combine kaons identified by dE/dx or TOF with charged pion tracks in mode $D^0 \to K^-\pi^+$.

b) Find $D^{*\pm} \to D^0\pi^\pm$ mesons: use the very small Q value in

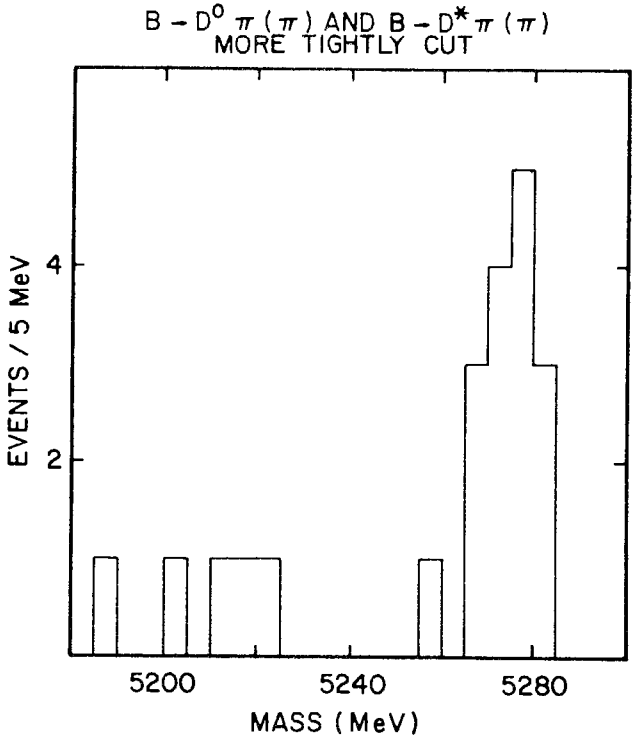


Fig. 2. Mass spectrum for fits to $B \to D\pi\pi$, $D^*\pi\pi$, tight χ^2 cut.

$D^{*\pm} \to D^0\pi^\pm$ to identify D^* without need to identify the kaon in $D \to K\pi$.

c) Combine the D or D^* with "right sign" charged pions to form candidate B mesons; eg., allow $B^- \to D^{*+}\pi^-\pi^-$ but <u>not</u> $B^- \to D^{*-}\pi^+\pi^-$.

d) Form "M_B^2" = $E^2_{BEAM} - (\Sigma \vec{P}_i)^2$; eg.,constrain the total energy of the B-meson to the beam energy.

A less important feature uses SQUAW to constrain the (D, D^*) constituents to yield the (D, D^*) mass. The resultant mass resolution is dominated by the $\sim$ 4 MeV rms. beam spread.

A somewhat dirtier but still consistent spectrum is seen in Fig. 3, where <u>no</u> particle identification is used. The hatched background comes from using K, π combinations in the D^0 sidebands. Here the mass peak is somewhat broadened by events which are reconstructed as $B \to D\pi$, but which are in fact $B \to D^*\pi$, with the soft pion (or γ in the case of D^{0*}) missing.

The results of our analysis are summarized below.

Using only the data from $D^*\pi$, $D^*\pi\pi$:

$M(B^0) = 5274.2 \pm 1.9 \pm 2.0$ MeV,

$M(B\pm) = 5270.8 \pm 2.3 \pm 2.0$ MeV,

$M(B^0) - M(B\pm) = 3.4 \pm 3.0 \pm 2.0$ MeV,

$M(4S) - 2M_B = 32.4 \pm 3.0 \pm 4.0$ MeV .

The measured branching ratios are:

$B^- \to (D^0\bar{\pi} + D^{0*}\pi^-) = 4.2 \pm 4.2\%$,

$\bar{B}^0 \to (D^0\pi^+\pi^- + D^{0*}\pi^+\pi^-) = 13 \pm 9\%$,

$\bar{B}^0 \to D^{*+}\pi^- = 2.6 \pm 1.9\%$,

$B^- \to D^{*+}\pi^-\pi^- = 4.8 \pm 3.0\%$.

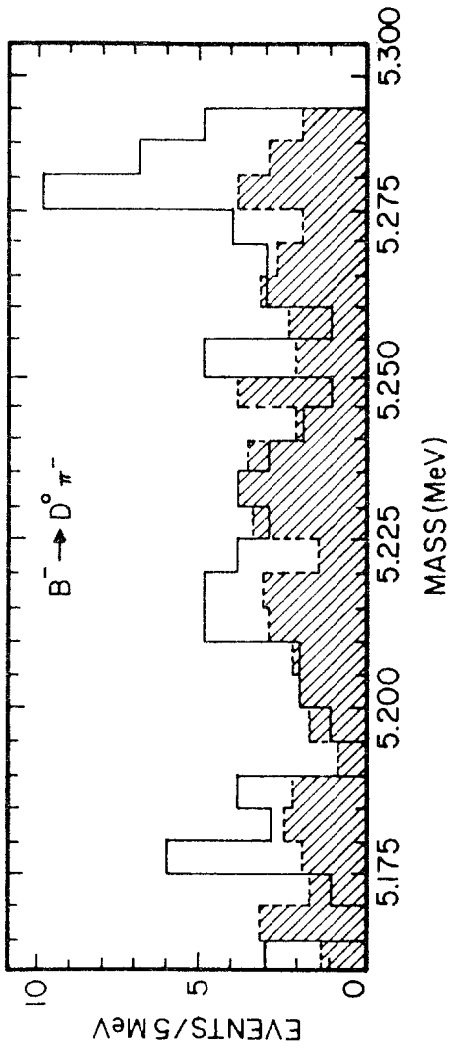


Fig. 3. Mass spectrum for fits to $B \rightarrow D\pi$—no particle ID used.

IV. The "X Bump"

An analysis by Art Snyder (unpublished) provides further evidence for the decay of B-mesons into the modes $D\pi$, $D^*\pi$ at the few percent level. Figure4 shows the single-particle inclusive spectrum (continuum subtracted) from the $\Upsilon(4S)$. The large excess at $X > .20$, although largely due to semi-leptonic decays,was not compatible with previous Monte-Carlo mocels. Figure 5 shows the X-spectra which would arise from specific D, D^* - few pion modes, using simple phase-space. It can be seen that only $D\pi$ and $D\pi\pi$ provide strength at large X ($X > .35$, say). A best fit to the high end of the X-spectrum is shown in Fig. 6.

The fit implies an average branching ratio for $B \rightarrow D\pi^{\pm} + D^*\pi^{\pm}$ of approximately 1.5%, in rough agreement with the exclusive analysis.

V. D^0 Mesons from B-Decay

Further evidence for the dominance of the decay chain $b \rightarrow c$ is provided by the recent measurement of the D^0 spectrum from B-meson decay.[3] We use the good momentum resolution of the CLEO drift chamber and a few tricks to measure $B \rightarrow D^0 + X$. The tricks are:

1) Don't use kaon identification.
2) Reduce continuum subtraction by imposing a cut on R_2 (sphericity).

With θ_K the angle (in the D rest frame) between the kaon and the D direction, requires $|\cos\theta_K| < 0.5$ for $P_D < 1.5$ GeV/c and $|\cos\theta_K| < 0.75$ for $P_D > 1.5$ GeV/c. $dN/d(\cos\theta_K)$ is flat for true

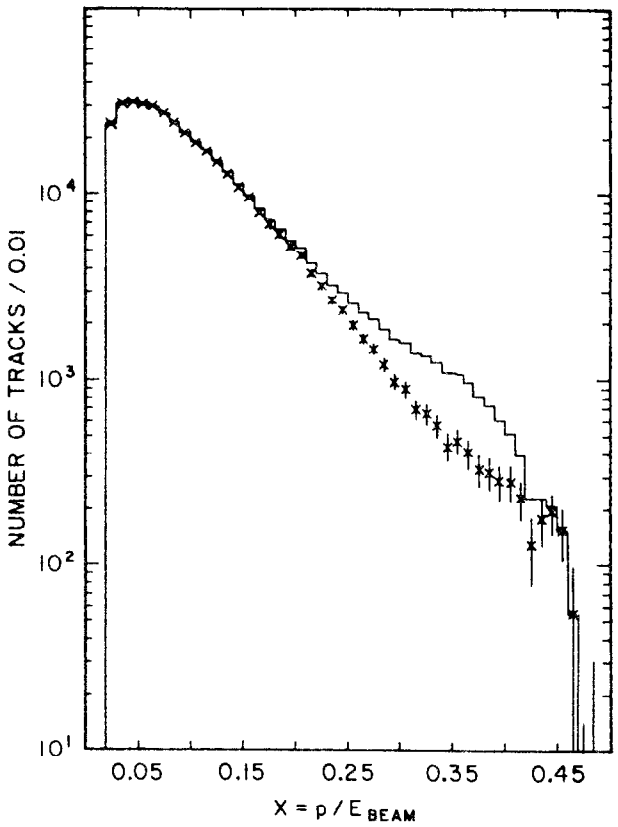


Fig. 4. The x-distribution of all tracks on the T(4S). The histogram includes leptons, while the data points have these subtracted.

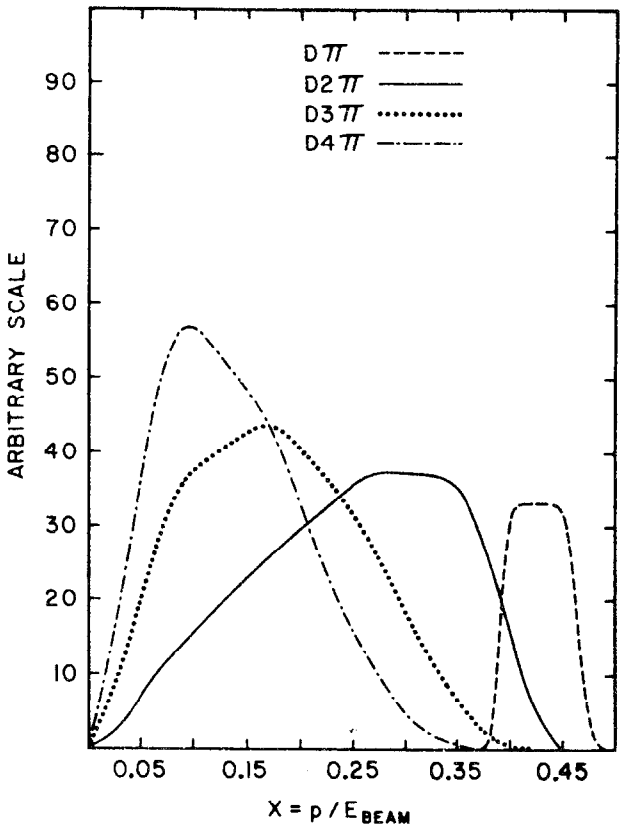


Fig. 5. Expected x-distributions for specific decay modes.

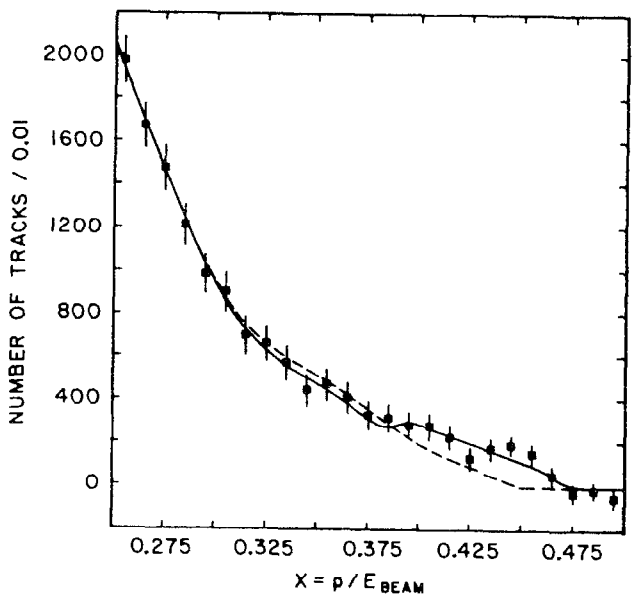


Fig. 6. Best fit to x-distribution (solid curve). The dashed curve omits $B \to D\pi$, $D^*\pi$.

D mesons and is strongly peaked for combinatorial background.

Results are shown in Figs. 7 and 8. The solid curve in Fig. 8 is the charmed-quark momentum distribution in (quark level) semi-leptonic b decay. It fits the data shockingly well, unlike the Monte-Carlo (dashed-curve) which has far too soft a D spectrum. The data imply:

a) $0.8 \pm 0.2 \pm 0.2$ D^0/B decay and

b) a hard D^0 spectrum.

The D^0 spectrum and the "X bump" suggest that in Fig. 9, fragmentation occurs separately for the color-singlet W^- fragments and for the lower charmed state, just as would happen in semi-leptonic decay.

VII. New Results on Semi-Leptonic Decay

CLEO's semi-leptonic data have also been greatly improved by the latest running. We have more data, better resolution; we have extended the electron coverage down to $P \gtrsim 0.4$ GeV/c, where secondary leptons from charm decay are manifest. The quite elaborate methods used to determine lepton efficiency, fake probability, etc. deserve more detailed discussion than I can present here,[4] I will content myself with a presentation of the results.

Figure 10 shows the electron spectrum together with a fit from Altarelli, et. al. A primary result from the lepton spectra is the improved measurement of an upper limit for the ratio $r = (b \to u)/(b \to c)$; where we find $r < 0.05$ at 90% confidence level. This implies for the ratio of the corresponding K-M matrix

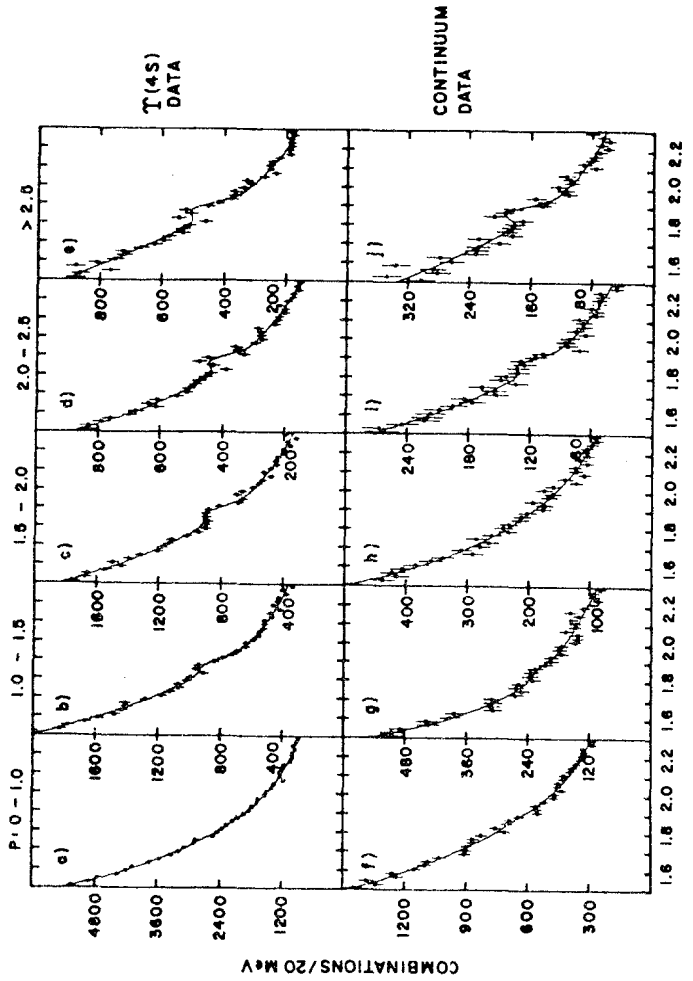


Fig. 7. Kπ mass distributions versus Kπ momentum a) on Υ(4S), b) continuum.

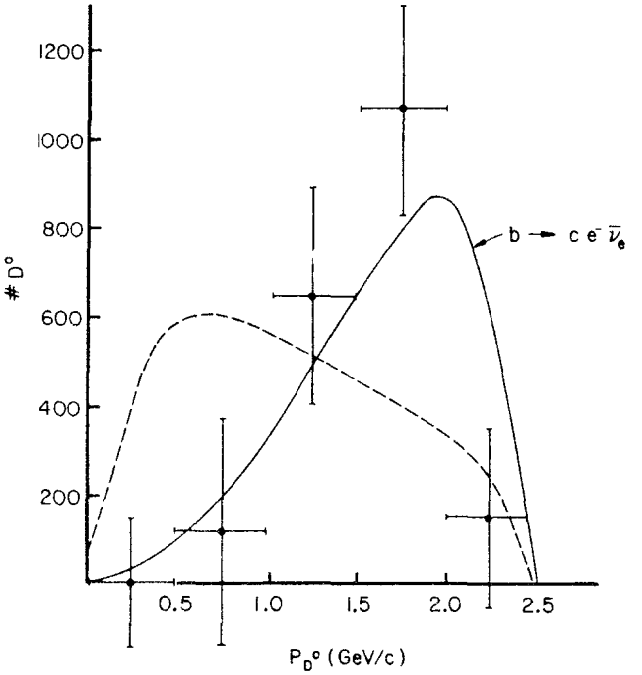


Fig. 8. Deduced D^0 momentum spectrum from B decay (data points).

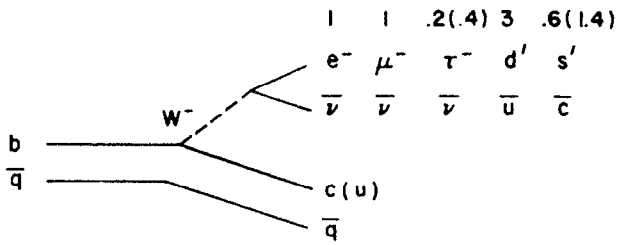


Fig. 9. Spectator model of B-meson decay.

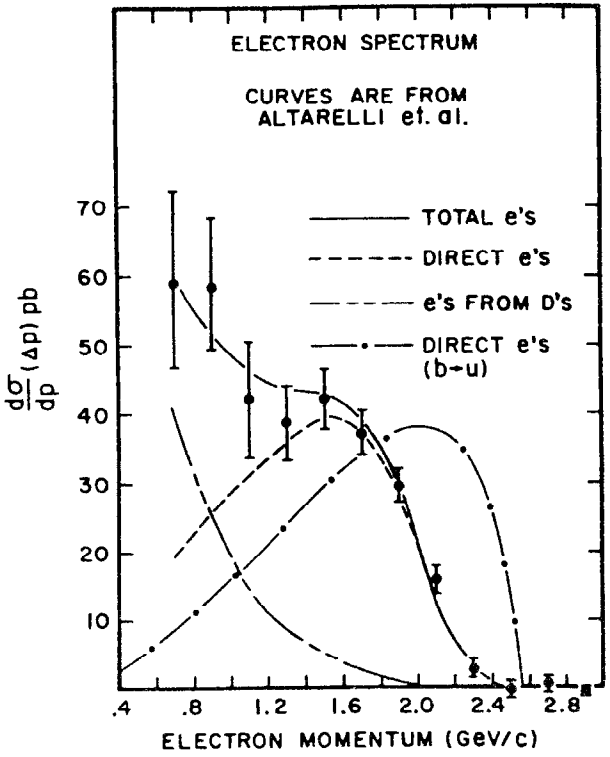


Fig. 10. Electron spectrum from B-decay. Solid curve is best fit from Ref. 5.

elements, $|V_{bu}/V_{bc}| \leq 0.15$.

VII. Is This the F Meson?[6]

Detectors with good charged-particle momentum resolution and poor neutrals detection thrive on narrow-width states with appreciable all-charged branching modes. One such state (Fig. 11) is the ϕ meson, seen here in the K^+K^- mode without the use of particle ID. The ϕ mass and width agrees with the smaller and cleaner sample which employs particle identification of at least one kaon. Figure 12a shows the result of forming mass combinations between ϕ's and charged pions, with resultant momenta > 2.5 GeV/c. The momentum cut is made to 1) emphasize leading charm, and 2) exceed the B meson kinematic limit. Figure 12b shows the same data for KK combinations just outside the ϕ band. The events within the $\sim$ 7 standard deviations peak are consistent with a (spin 0 $\rightarrow$ spin 1 + spin 0) decay. In particular, 1) the decay kaons follow a $\cos^2\theta_K$ distribution with respect to the "F" direction in the F rest frame, and 2) the pion is consistent with isotropy (see Fig. 13).

This new F-like object has a width consistent with our Monte-Carlo resolution, a mass of 1970 $\pm$ 5 $\pm$ 5 MeV, and an estimated σ. BR of 16 pb. If the total F production cross-section is $\sim$ 0.3 nb, then BR(F $\rightarrow \phi\pi$) $\sim$ 4%, not unlike $D \rightarrow K^*\pi$. Lastly, the inferred momentum spectrum (Fig. 14) is hard, very much like our measured continuum D^0 spectrum.

We think it's the F meson, although it does not appear to be the same object seen by others.[7]

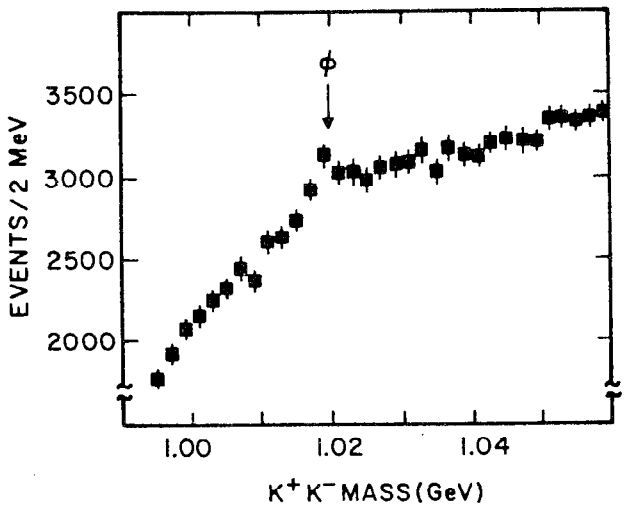


Fig. 11. Inclusive K^+K^- mass distribution—no particle ID used.

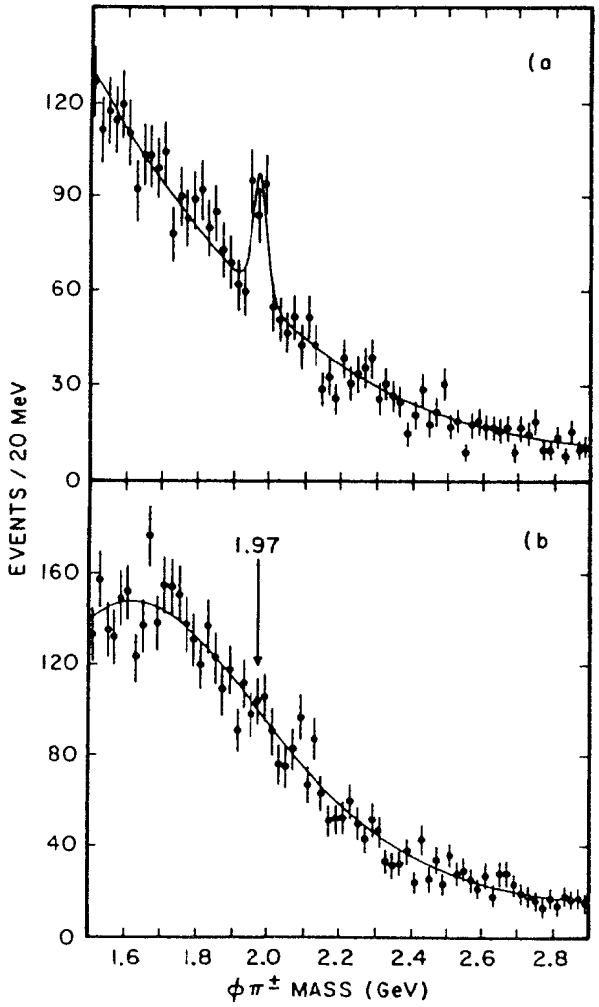


Fig. 12. $K^+K^-\pi^{\pm}$ mass distributions.
a) $|M_{KK} - M\phi| \leq 5$ MeV,
b) $|M_{KK} - M\phi| \geq 5$ MeV.

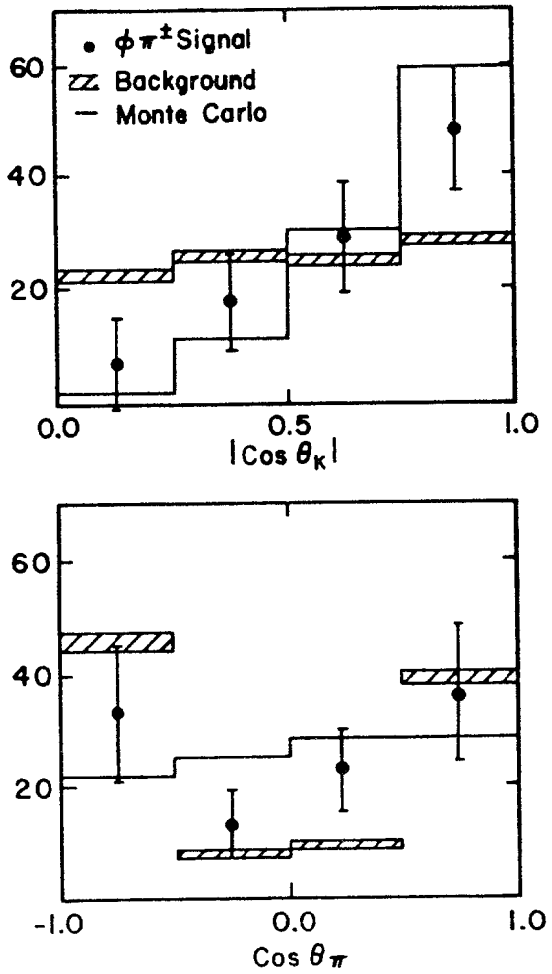


Fig. 13. F decay angular distribution.
a) Angular distribution of one kaon in F rest frame.
b) Angular distribution of pion with respect to F direction.

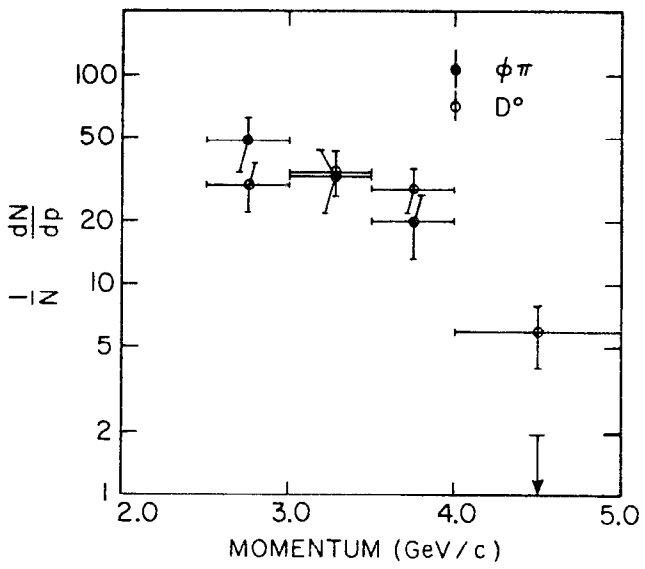


Fig. 14. $F \to \phi\pi$ momentum distribution compared to D^0.

VIII. Acknowledgements

Thanks are due my collaborators who are more responsible than I for the beautiful physics, the CESR staff for getting us the luminosity, and to the SLAC staff, especially the very patient Pat McDonough, for a fine conference.

This work was supported by the National Science Foundation.

References

1. D. Andrews et al., Nucl. Instr. Methods 211, 47 (1983).
2. S. Behrends et al., Phys. Rev. Lett. 50, 877 (1983).
3. J. Green et al., Phys. Rev. Lett. 51, 347 (1983).
4. R. Giles et al., Paper C-271 submitted to 1983 Lepton-Photon Symposium.
5. Altarelli, et al., Nucl. Phys. B208, 365 (1982).
6. A. Chen et al., Phys. Rev. Lett., 51, 634, (1983).
7. R. Ammar et al., Phys. Lett. 94B, 118 (1979); R. Brandelik, et al., Phys. Lett. 80B, 412 (1979); D. Aston, et al., Phys. Lett. 100B, 91, (1981); D. Aston, et al., Nucl. Phys. B189, 205, (1981).

RECENT CUSB RESULTS ON UPSILON SPECTROSCOPY AND B PHYSICS

Juliet Lee-Franzini

SUNY at Stony Brook, Stony Brook, N. Y. 11794

Introduction. Experimental results obtained in the past year by the CUSB collaboration[1] include: the discovery of the χ_b states; first measurements of direct photon decays from Υ's; a precision measurement of the upsilon mass; new measurements of $B_{\mu\mu}(\Upsilon)$ and $B_{\mu\mu}(\Upsilon')$; a precision measurement of the beta decay spectrum from B mesons; and upper limits on $\Gamma(\Upsilon'\to\eta+\Upsilon)$, $\Gamma(\Upsilon,\ \Upsilon' \to \gamma$ + Higgs scalars), $\Gamma(\Upsilon''\to B^*\bar{B}^*,\ B^*\bar{B}+B\bar{B}^*)$; and the production of $\Upsilon(5S)$ and $\Upsilon(6S)$. The theoretical implications of these results range from new confirmations of the scaling laws from QCD multipole expansion, the nonrelativistic potential models' descriptions of $b\bar{b}$ bound states, the flavor independence of the interquark forces, to new determinations of the QCD scale parameter Λ and stringent limits on the K-M mass mixing matrix elements. I will discuss both the experimental results and their implications, excluding those in the latter category which are covered in E. Eichten's paper.[2]

Precision Measurement of the Υ Mass. At e^+e^- colliders the mass of a resonance like the Υ is given by twice the beam energy at which the peak of the cross section is observed. The beam energy is usually determined by estimates of $\int Bdl$ of the machine guide field, obtained from measurements of field and excitation curves of the

© J. Lee-Franzini

magnets. This method results in accuracies of about 0.1 %. Thus the early results for the Υ mass were 9460 and 9434 MeV at DORIS and CESR respectively, with estimated errors of 10 to 30 MeV.

An elegant and very precise method for obtaining the energy of a stored electron beam, used first at Novosibirsk,[3] consists of measuring the difference between spin precession frequency ω_p and cyclotron frequency ω_c, due to the anomalous part of the electron magnetic moment. Precession and circulating frequencies are related by $\omega_p = \omega_c(1+\gamma(g-2)/2)$ where $\gamma = E/m_e$ is the electron Lorentz factor and $(g-2)/2 = 0.001\,159\,652\,209(13)$. ω_p is determined by applying a small periodic perturbation which produces resonant depolarization of the stored beam. Measurements at VEPP-4 resulted in a value of the Υ mass of 9459.7 ± 0.6 MeV [3] and this summer at CESR we obtained M(Υ) = 9459.95 ± 0.1 MeV.[4] Figure 1 shows the scan of the Υ peak at CESR with the energy scale determined by the resonance method described. The cross section was measured using the CUSB detector.

Search for Other States Produced in e^+e^- Annihilations. Figure 2 shows the CUSB measurements of $\sigma(e^+e^- \rightarrow \text{hadrons})$ at CESR around the known Υ's. We also made measurements of the cross sections in the intervening regions, the one between the Υ′ and the Υ″′ is shown in the bottom half of Figure 3. No obvious structures were seen. In order to quantify the negative results we use a maximum likelihood method to obtain the 90% confidence level upper limit (90% cl) for the leptonic width of a resonance whose total width is given by the machine energy spread. They range around ~32 eV in the

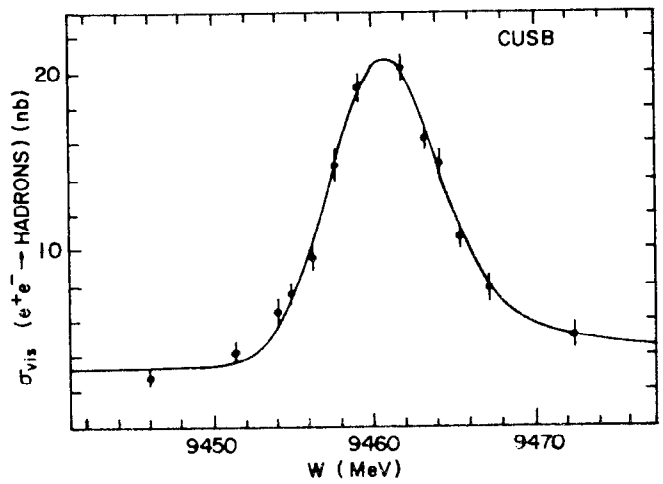


Figure 1. Scan of the Υ for the precision measurement of its mass. CUSB

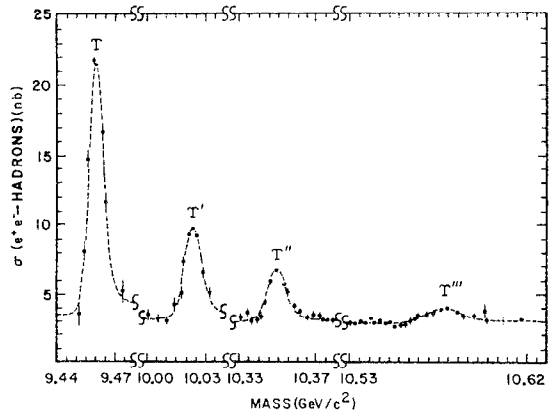


Figure 2. Cross section for e^+e^- annihilations into hadrons from CUSB.

mass interval of 9.927 to 10.008 GeV, ~24 eV in the mass interval of 10.27 to 10.33 GeV, and ~14 eV in the mass interval of 10.38 to 10.55 GeV (see top of Figure 3). These limits are an order of magnitude smaller than those expected for a bound triplet S state, therefore confirm that only three bound triplet S's exist below flavor threshold.

We had expected to see the string vibrational states, predicted by Buchmuller and Tye to lie in the mass region between 10.37 to 10.46 GeV, with leptonic widths of the order of 70 to 270 eV.[5] However, to make these predictions they had to take a phenomenological approach of identifying either the $\Psi(3.96)$ or $\psi(4.03)$ as a $(c\bar{c})$ vibrational state. Therefore our negative finding can mean either vibrational states do not exist or that the extrapolation scheme is inadequate. The latter possibility is more likely since Kuang and Yan[6] use string intermediate states for their rate computations of hadronic transitions which are in good agreement with experimental measurements.

Two triplet D-wave states are expected to lie below the b-flavor threshold, the centers of gravity (cog.) of which are predicted almost uniformly by various potential models at ~ 10.15 GeV for the $\Upsilon(1D)$ and ~ 10.43 GeV for the $\Upsilon(2D)$. Their expected leptonic widths are highly model dependent because the D-wave states can be seen in e^+e^- annihilations only through S-D mixing. In particular, the D-wave leptonic widths are given by the formula

$$\Gamma(^3D_1 \to 1^+1^-) = (200/64m_b^6)\alpha^2 e_b^2 |R_D''(0) + (2\sqrt{2}/5)m_b^2 R_S(0)|^2$$

where R are the radial wave functions and m_b, e_b are the b quark mass and electric charge respectively.[7] Moxhay and Rosner[8] find them to be

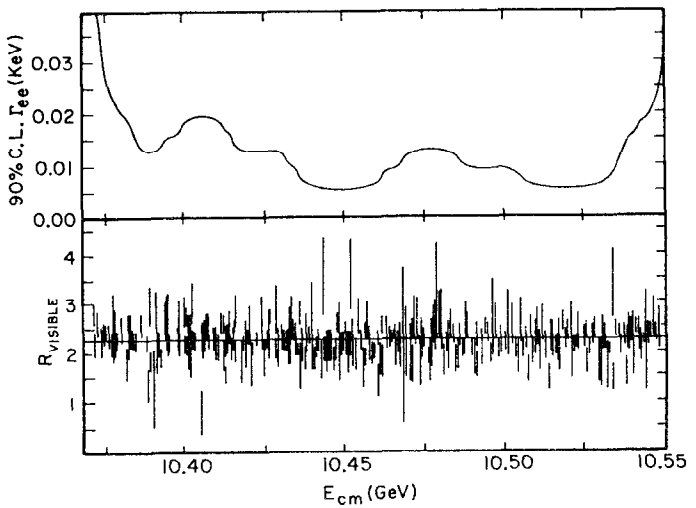


Figure 3. Search for narrow resonances, $10.37 < E_{cm} < 10.55$ GeV.

1.5 eV for the Υ(1D) and 2.7 eV for the Υ(2D), both values are below present experimental sensitivity. The present conclusion is that no unusually large S-D mixing has been observed.

Above the free b-flavor threshold the radial excitations are expected to have total widths wider than the machine energy spread, as is true of the Υ(4S). The leptonic widths are expected to be somewhat less than that of the Υ(4S) since Γ_{ee} roughly scales as 1/n where n is the principal quantum number. At the bottom of Figure 4 we show the resonance search for the Υ(5S, 6S, 7S) which most potential models predict to lie in the energy region between 10.6 to 11.3 GeV, spaced ~200 MeV apart.[9] At the top of the figure we display the 90% cl upper limit for the leptonic width assuming that the total width of the resonance is 40 MeV (~ twice that of the Υ(4S)).[10] We see from these limits of ~ 60eV (~1/4 Γ_{ee} of the Υ(4S)), that the higher Υ(nS) are not narrow like the Υ(4S) but are probably broad shallow structures overlaying the continuum.

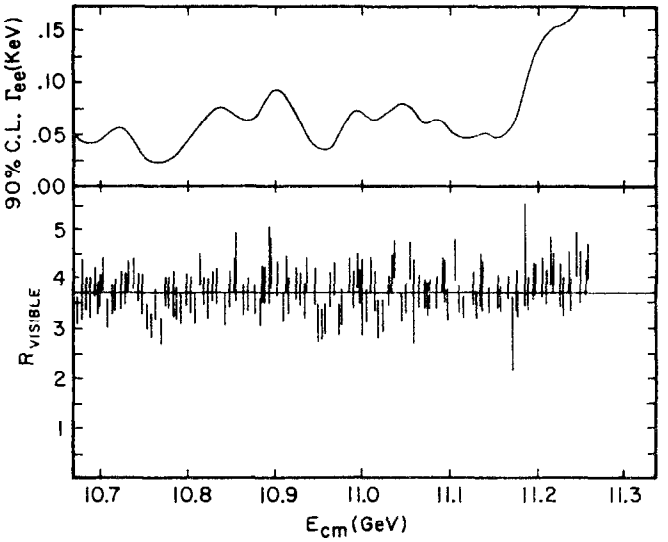


Figure 4. Search for Υ(5S) and Υ(6S).

Further Tests of the QCD Multipole Expansions. The transition $\Upsilon' \to \Upsilon\pi\pi$ is observed in the CUSB detector by seeing two charged tracks or four γ's (from two π^0's) accompanying a high energy dilepton pair resulting from the decay of the Υ. During our recent run we have increased our sample of such events by over an order of magnitude relative to the 1980 run. We now have 221 $\pi^+\pi^-ee$ events, 147 $\pi^+\pi^-\mu\mu$ events and 44 $\pi^0\pi^0ll$ events. Figure 5 shows the total energy deposited by the 4 γ's in the detector, the distribution is peaked at the $\Upsilon - \Upsilon$ mass difference with a width consistent with that computed from our known resolution. Our present branching ratio (BR)

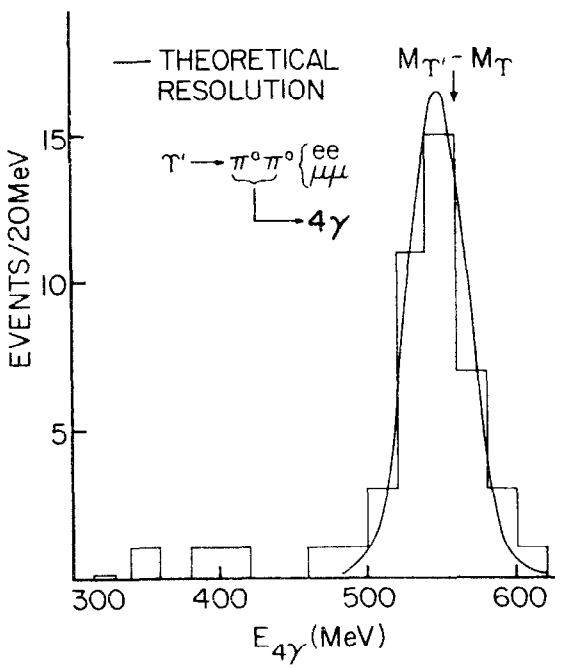


Figure 5. Spectrum of the sum of the four photon energies from $\Upsilon \rightarrow \Upsilon\pi^0\pi^0 \rightarrow \gamma\gamma\gamma\gamma\ell\ell$ events.

$BR(\Upsilon' \rightarrow \pi^+\pi^-\Upsilon) = (19.4 \pm 2.9)\%$ is fully in agreement with our previous determination of $(20 \pm 7)\%$, the error in the present case is dominated by the measurement uncertainty of $BR(\Upsilon \rightarrow \mu\mu)$, $B_{\mu\mu}$. From the observed number of $\pi^+\pi^-11$ events we expect 37 ± 10 $\pi^0\pi^0 11$ events if the $\pi\pi$ system were in an I=0 state, 0 such events for the $\pi\pi$ in an I=1 state and 148 such events for the $\pi\pi$ in an I=2 state. The observed number is 44 events, greatly favoring I=0 as is required by isospin invariance in this transition. Of course, the new partial rate for this transition in the $(b\bar{b})$ system is still 9 keV and its ratio to the corresponding one in the $(c\bar{c})$ system (110 keV) is still the best proof that these transitions are two "color-electric" dipole transitions and that the gluon has spin one.

Another scaling law obtainable from QCD multipole expansion predicts the relative rates of the $\Upsilon' \rightarrow \eta\Upsilon$ and $\psi' \rightarrow \eta\psi$ transitions to be 1 to 400.[6] Such transitions can be thought of as two M1 (or E1-M2) transitions whose matrix element scales inversely as the mass of the quark squared times the customary phase space factor. In other words $\Gamma(\Upsilon' \rightarrow \eta\Upsilon)/\Gamma(\psi' \rightarrow \eta\psi) \sim (m_c/m_b)^4 (P_\eta(\Upsilon)/P_\eta(\psi))^3 \sim 1/400$ where the P_η's are the η momenta, their ratio cubed is 1/6, while the ratio of the quark masses to the fourth power is over ten times smaller, ~1/67.

CUSB has searched for $\Upsilon' \rightarrow \eta\Upsilon$ transitions where again the Υ decays into a lepton pair and the η decays either into two photons or into $\pi^+\pi^-\pi^0$. The η is almost at rest, the minimum angle between the two γ's is 160° and their energies are 280 ± 10 MeV. For the three pion decay mode we looked for two low energy charged pions and two

photons accompanying the Υ decay dileptons. We found no candidates and obtain a 90% cl upper limit of

$BR(\Upsilon' \to \eta\Upsilon) < 0.2\%$ and $\Gamma(\Upsilon' \to \eta\Upsilon) < 0.06$ keV.

These limits when combined with those from the ψ system $BR(\psi' \to \eta\psi) = (2.8 \pm 0.6)\%$ and $\Gamma_{tot}(\psi') = (215 \pm 40)$ keV [11] yield

$\Gamma(\Upsilon' \to \eta\Upsilon)/\Gamma(\psi' \to \eta\psi)\,|_{experimental} < 1/100$.

We note that this limit is a factor 15 smaller than that expected from phase space suppression alone and goes a long way towards confirming the QCD multipole expansion picture.

While the scaling laws are derived in the QCD multipole expansion method independent of hadronization details, additional assumptions are needed for predictions of the dipion mass spectrum and angular distributions. Yan,[12] noting that the pions involved in these hadronic transitions have relatively small momenta, adopted soft pion theorems where PCAC (partially conserved axial current) and current algebra constrain the variation of soft pion emission on pion momenta. The matrix element for ππ transitions from higher triplet quarkonia states to lower ones is proportional to $(Aq_1^{\mu}q_{2\mu} + Bq_1^{o}q_2^{o})$ where q_1 and q_2 are the two pions' four momenta. Brown and Cahn[13] had noted in the study of the charmonium state transitions that the A term is dominant, and Yan had in his original formulation assumed the B term to be negligible. This assumption uniquely determines the dipion mass spectrum (to be peaked at high dipion mass) and requires the dipion to be isotropic around the colliding beam axis. With our recent data we have measured the dipion mass distribution, shown in Figure 6. Curve a (b) is the spectrum

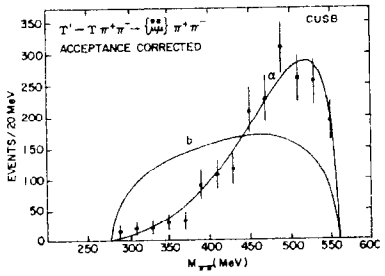
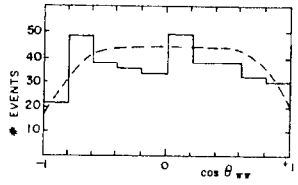


Figure 6. $M_{\pi\pi}$ spectrum from $\Upsilon' \to \Upsilon\pi^+\pi^-$ events.

resulting from the above transition amplitude with B=0 (A=0), the curves are normalized to the number of events. Our data is in excellent agreement with curve a, $\chi^2=9$ for 13 degrees of freedom. A fit to the data for the best value of B/A gives $B/A = -0.02\pm0.09$. The curve in Figure 7 is for an isotropic distribution including acceptance and normalized to the number of events. The data are clearly consistent with s-wave production of the dipion system.

This outstanding confirmation of the QCD multipole expansion plus PCAC predictions for the dipion mass and angular distributions also exists for the corresponding charmonium excited triplet S to ground triplet S state $\pi\pi$ transitions. However I would like to recall that in the decay $\Upsilon' \rightarrow \pi\pi\Upsilon$ the dipion mass spectrum is not as expected: the CUSB spectrum is perfectly consistent with phase space[14] and CLEO had obtained $(B/A)^{-1} = -.15\pm0.12$, that is, a spectrum reasonably consistent with phase space.[15] No explanation of this deviation from an otherwise highly successful theory has materialized yet.

Photonic Transitions Between Triplet S and P States. While the P wave $b\bar{b}$ bound states cannot be produced directly in e^+e^- annihilations, they can be reached from, and return to, S states via photon transitions. These photon transition rates, being proportional to both the quark charge and radius of the system squared, are expected to be an order of magnitude smaller in $b\bar{b}$ system relative to the $c\bar{c}$ system. This fact, together with the increased multiplicity of ~ 2.5 in the $b\bar{b}$ system, and the smaller production cross section for Υs, make E1 transition photon searches difficult and slow going. In the Υ system, two sets of triplet P



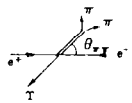


Figure 7. Distribution of $\cos\theta_{\pi\pi}$, the angle of the dipion system with respect to the beam axis. The curve is an isotropic distribution corrected for acceptance.

wave states ($2^3P_{2,1,0}$ or χ_b', and $1^3P_{2,1,0}$ or χ_b) are expected to lie below the b flavor threshold. CUSB discovered the χ_b' in 1982 and the χ_b in 1983. Their cog.'s are at 10256±5 MeV and 9901±3 MeV respectively.[16-19] The results come from studies of inclusive photon spectra taken at the Υ(3S) and Υ(2S),[16,17] and from searches for events of the type Υ(nS)→Υ([n-i]S)γγ followed by Υ([n-i]S)→ee or μμ, where i=1...n-1.[18,19]

Inclusive photon spectra The inclusive photon spectra obtained by CUSB from a 30 pb^{-1} run at the Υ' peak and a 14 pb^{-1} run at the Υ'' peak are shown in Figures 8a and 8b respectively. 150000 Υ(2S) [48000 Υ(3S)] resonance decays and 77000 [38000] continuum events contribute to the photon spectra. Not shown are photon spectra from a comparable number of Υ(1S) and continuum events taken during the Υ'' run, both of which are featureless and can be fitted with a smooth function with good χ^2, see Ref. 16. Prominent structures are apparent, both in Figure 8b at ~100 MeV and in Figure 8a at ~125 MeV, where in addition there is a statistically significant excess (833±166) at ~430 MeV. Several methods were used to obtain the background curve under the signals. The one which is totally independent of the Υ(2S) and Υ(3S) spectra consists of constructing the background spectrum from a linear combination of the Υ(1S) and continuum photon spectra, where the linear coefficients are those which yield the Υ'' and Υ' thrust distributions from continuum and Υ(1S) thrust distributions. Another method was to generate the background curve by excluding the narrow regions containing the signal and finding a polynomial fit to the rest of the spectrum. The

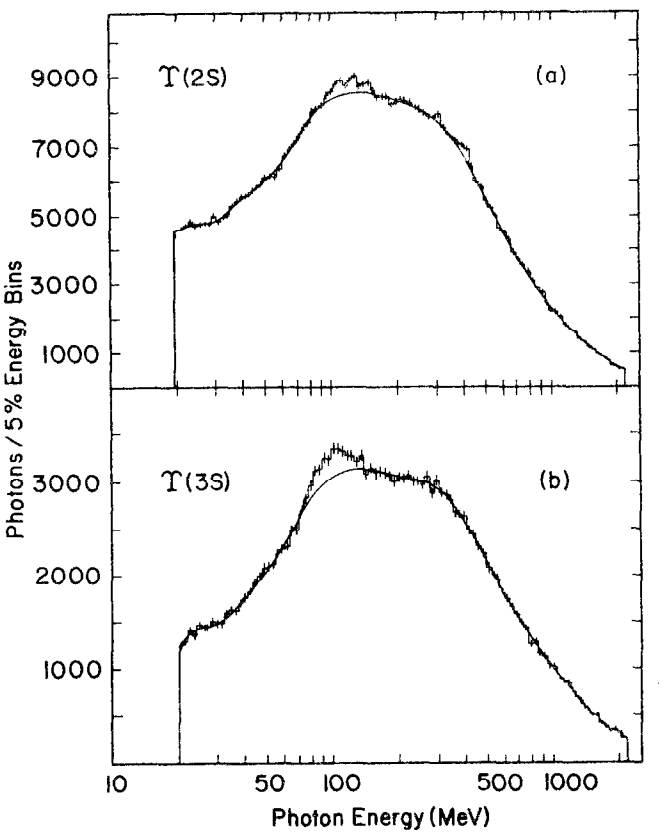


Figure 8a. (top) Inclusive photon spectrum from Υ' events.

Figure 8b. (bottom) Inclusive photon spectrum from Υ'' events. For an explanation of the solid background curves, see text.

third method, which yielded the curves shown in Figure 8, is to fit a wide band (~250 MeV) in the signal region with a cubic plus three Gaussians of arbitrary position and area but with fixed width corresponding to our resolution, and the cubic is required to match the polynomial fits to the remainder of the spectrum. All methods yield consistent results,[16] the third method yields ~3100 signal photons over 100000 background γ's at ~125 MeV and 800 signal photons over 25000 background γ's at 430 MeV for the Y(2S), and 2300 signal photons over 40000 background γ's for the Y(3S).

The subtracted spectrum from the Y(2S) run is shown in Figure 9a, below which are shown (Figure 9b) the three fitted Gaussians on the main peaks, and a fourth one at 427 MeV. χ^2 for the fit is excellent: 22.6 for 21 degrees of freedom (dof). The peak at ~430 MeV, essentially due to a monochromatic line, is observed to have an rms spread of (4.5±0.4)%, in excellent agreement with the Monte Carlo (MC) calculations of 4%, confirming our ability to correctly estimate our resolution. The resolution function of the CUSB detector and γ search code combined is determined by MC calculations by adding EGS-generated photons onto hadronic events, and the results have also been checked by reconstructing π^0's. For the spectra shown in Figure 8, the γ search code has a uniform efficiency of 0.13 between 80 and 500 MeV and the resoluton is σ_E=3.6%/$\sqrt[4]{E}$ during the Y' run when interleaved chambers (~3% r.l.) were removed and 3.9%/$\sqrt[4]{E}$ during the Y'' run. Our energy scale is obtained from continuous beam-on calibration with Cs^{137} and Co^{60} sources mounted permanently on the NaI crystals and correcting by MC calculations for energy loss in inactive materials.

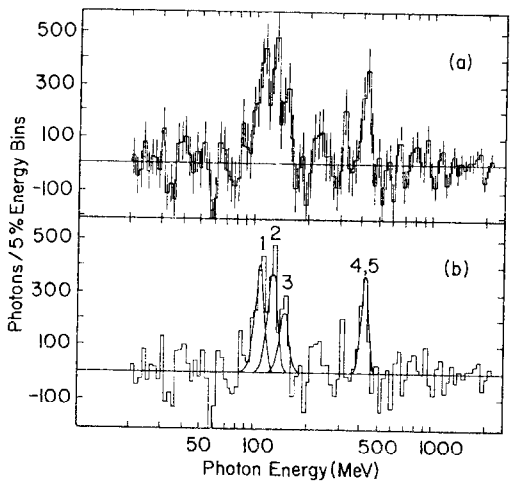


Figure 9a. Background subtracted photon spectrum for T' events.
Figure 9b. Same with fitted lines. See below for numbers.

The energy scale is checked by Bhabha events, by π^0 mass measurement during the Υ'' run and by $\Upsilon' \to \Upsilon\pi^0\pi^0$ events for the Υ' run, where all four γ's are found in the detector (see Figure 5).

The result of the fit shown in Figure 9b is that the broad enhancement is due to three photon lines smeared by resolution, centered at 108, 128 and 149 MeV respectively. If we assume that the photon signals observed correspond to $\Upsilon(2S) \to \gamma_1 X$, followed by $X \to \gamma_2 \Upsilon(1S)$, then we expect that the sum $E(\gamma_1)+E(\gamma_2)+E(\text{recoil})$ be equal to $M(\Upsilon')-M(\Upsilon)$. If X is identified with the three 1^3P_J states, it is expected and observed (see next subsection) that the product of BR's for the decays $\Upsilon(2S) \to \gamma + 1^3P_J$, $1^3P_J \to \gamma + \Upsilon(1S)$ be in the ratio of 2:5:~0 for J=2,1,0 respectively and that the above mentioned three lines correspond to the decays to the J=2,1,0 states respectively, while the 427 MeV line is due to decays of the J=2,1 states, see Figure 10 for level diagram. The energy sum rule above therefore becomes (108x2+128x5)/7 +427 +10.5 = 560 MeV to be compared with the $\Upsilon' - \Upsilon$ mass difference of 560.8 MeV. From a count of the excess number of photons in the 125 MeV region we obtain $BR(\Upsilon(2S) \to \gamma + {}^3P_J) =$ 15.5%±2.5% and for the 427 MeV signal $BR(\Upsilon(2S) \to \gamma + {}^3P) \times BR({}^3P \to \gamma + \Upsilon(1S)) = (4\pm1)\%$, confirming that the high energy photons are from subsequent decays. The cog. of the χ_b is determined to be 9901±3 MeV. The corresponding analysis for the $\Upsilon(3S)$ similarly implies that the broad enhancement is due to three photon lines smeared by resolution, although in this case the three lines centered at ~ 84, 102 and 122 MeV are more merged together, and we identify these as transitions to the $2^3P_{2,1,0}$ states respectively.

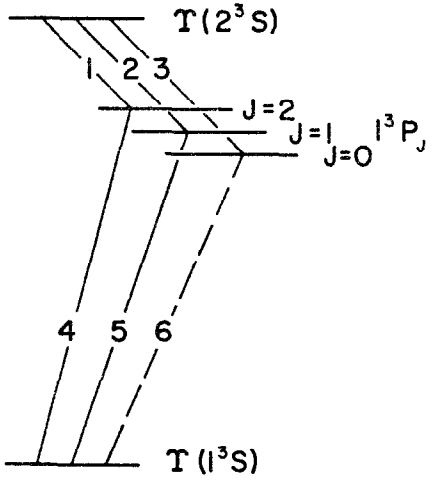


Figure 10. E1 transitions diagram.

The BR($\Upsilon(3S)\to 2^3P_J+\gamma$) is 36%±7% and the χ_b' cog. is 10256±5 MeV. The partial widths for E1 transitions are proportional to $k^3(2J+1)$, where k is the photon momentum. We have obtained the reduced widths for the S→P transition lines by dividing by the $k^3(2J+1)$ factor and normalizing to 1 for the middle line. Within the statistical uncertainties, all S→P lines' reduced widths (RW) are consistent with 1, in good agreement with the assumption of E1 transitions. Another quantity of interest, the ratios of fine splittings $r=(M(J=2)-M(J=1))/(M(J=1)-M(J=0))$ are measured by CUSB to first approximation; they are included in the Tables (I and II) which summarize our results on the χ_b states from inclusive photon and exclusive channels searches.

Exclusive channel searches CUSB has also searched for E1 transitions via the following double photon decay chains :

(a) $2^3S \to 1^3P_J + \gamma_1,\ 1^3P_J \to 1^3S + \gamma_2$;

(b) $3^3S \to 2^3P_J + \gamma_1,\ 2^3P_J \to 2^3S + \gamma_2$;

(c) $3^3S \to 2^3P_J + \gamma_1,\ 2^3P_J \to 1^3S + \gamma_2$; and

(d) $3^3S \to 1^3P_J + \gamma_1,\ 1^3P_J \to 1^3S + \gamma_2$

followed by the Υ or $\Upsilon' \to \mu\mu$ or ee. Events of this kind have a characteristic signature of two almost collinear muons or electrons of about 5 GeV, plus two photons whose energies add up to the $\Upsilon'-\Upsilon$, or $\Upsilon''-\Upsilon'$ or $\Upsilon''-\Upsilon$ mass difference. Since we cannot distinguish γ_1 from γ_2, we order the two photons by energy and label them γ_{LOW} and γ_{HIGH} for each event. In Figure 11 we show the scatter plot of the two γ's from the $\Upsilon(2S)$ run, the $\mu\mu$ [ee] $\gamma\gamma$ events are on the left [right] side of the figure. The regions (including Doppler

Table I Experimental Results for $2^3S \to 1^3P \to 1^3S$

Transition	$E_{\gamma(inc)}$(MeV)	$E_{\gamma(exc)}$(MeV)	BR(inc)(%)	RW(inc)
$2^3S_1\to 1^3P_2$	108.2±0.3±2[a]	107+2.0-2.5	6.1±1.4	1.04±0.3
$\to 1^3P_1$	128.1±0.4±3	128.0±1.5	5.9±1.4	1
$\to 1^3P_0$	149.4±0.7±5	--	3.5±1.4	1.13±0.5
$\to 1^3P_{2,1,0}$			15.5±2.5 (+5-2)	
$1^3P_2\to 1^3S_1$	427.0±1±5		20±5	
$1^3P_1\to 1^3S_1$			47±18	
Chain (a)	sum of product BR's		4.0%±1% (inc)	3.6%±0.9% (exc)
$2^3S\to 1^3P_2\to 1^3S$	product BR			1.2%±0.7% (exc)
$\to 1^3P_1$	product BR			2.4%±0.8% (exc)
$\to 1^3P_0$	product BR			<0.4% 90% cl (exc)

cog (1^3P_J) = 9901 ± 3 MeV r (1^2P_J) = 0.93 ± 0.1 ± 0.2

[a] Second set of errors indicate estimate of systematic uncertainty

Table II Experimental Results for $3^3S \to 2^3P \to (2^3S \text{ or } 1^3S)$

Transition	$E_{\gamma(inc)}$(MeV)	$E_{\gamma(exc)}$(MeV)	BR(inc)(%)	RW(inc)
$3^3S_1\to 2^3P_2$	84.2±0.3±2	84 ± 3	12.7±4.1	0.86±0.4
$\to 2^3P_1$	101.4±0.3±3	99 ± 2	15.6±4.2	1
$\to 2^3P_0$	122.1±0.7±5		7.6±3.5	0.84±0.5
$\to 2^3P_{2,1,0}$			35.9±3 (±4)	
Chain (b)	sum of product BR's		5.9%±2.1% (exc)	
Chain (c)	sum of product BR's		3.6%±1.2% (exc)	
Chain (d)	sum of product BR's		<3% 90% cl (exc)	

cog (2^3P_J) = 10256 ± 5 MeV r (2^3P_J) = 0.85 ± 0.1 ± 0.3

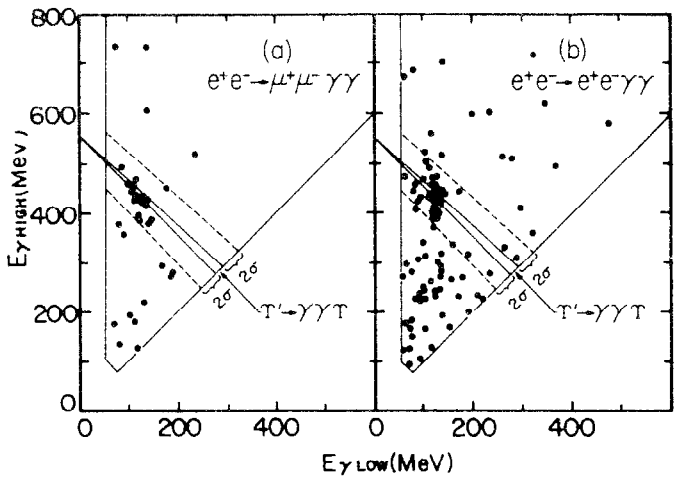


Figure 11. Scatter plots of the higher energy photon vs the lower energy photon for $e^+e^- \to \mu\mu\gamma\gamma$ (left), $e^+e^- \to ee\gamma\gamma$ events.

broadening) for the labelled transitions are indicated by solid lines, and the dashed lines show the $\pm 2\sigma$ limits of our resolution. The events cluster around (120 MeV, 430 MeV). The dimuon events are virtually background free in the signal band. Double Bremsstrahlung and $\pi^0\pi^0$ photons add background to the scatter plot but its levels are easily estimated from inspection of the total photon energy plot, see Figure 12. Product BR's for chains (a) - (c) are included in Tables I and II. Chain (d) has not been observed.[18]

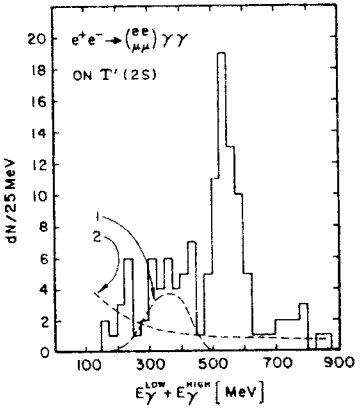


Figure 12. Spectrum of the sum of the two γ energies from all events from Fig. 11. Line 1, estimated background from $\pi^0\pi^0$ decays. Line 2, estimated background from double bremsstrahlung Bhabha scatters.

Distributions in γ_{LOW}, for example Figure 13, exhibit a two-humped behavior which can not be fit with one line, but give excellent χ^2 when fit with two lines of our known resolution. The resultant energy values are in good agreement with the inclusive photon determinations, see Tables I and II. In addition, the relative intensities of the 107 MeV line and the 128 MeV line is (0.51±0.25):1, a result which when combined with the inclusive photon measurement yields BR's for individual P states' transitions to the ground state.[17] From the lack of a clear signal in the exclusive channel search for energies E_γ=140 MeV to 185 MeV, a 90% cl upper limit for the product BR of the cascade transition via the 1^3P_0 state is 0.4%. All the product BR's are in good agreement with estimates using potential models[2] and P state hadronic widths as derived by Barbieri et al.[20]

P Wave States: Theory Versus Experiment. E. Eichten[2] in his talk at this conference gives a complete discussion of this subject. I will just summarize by saying that the measured partial rates of photon transitions are in agreement with a whole range of potential models when their predictions are rescaled with the measured photon energies.[21] The cog. of the χ_b's are also in good agreement with potential model predictions[22] but are in definite contradiction with QCD sum rule predictions for the position of the lowest P wave level to be at 9835±30 MeV[23] or 9803±10 MeV.[24]

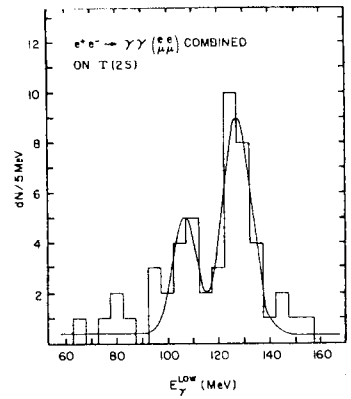


Figure 13. The lower energy photon spectrum. The curve shows the result of a two-line fit above a constant background of 0.5 events per bin.

Further Implications of the P State Measurements.

Hadronic widths of the χ_b's-- I have just mentioned how well the experimental E1 rates agree with those predicted by nonrelativistic potential models. Of considerable interest to QCD are the hadronic widths of these χ states which are predicted to within 30% accuracy to be ~190 keV, 60 keV and 750 keV for the J=2,1,0 states respectively.[8] Their explicit dependence, to first order, on α_s is as follows:

$$\Gamma(\chi_{b,J=2}\to gg) \sim (128/5)\alpha_s^2(M_p)^{-4}|R_{P'}(0)|^2$$

$$\Gamma(\chi_{b,J=1}\to q\bar{q}g_{soft}) \sim (128/3\pi)\alpha_s^3(M_p)^{-4}|R_{P'}(0)|^2\ln(M_p r_p)$$

$$\Gamma(\chi_{b,J=0}\to gg) \sim 96\alpha_s^2(M_p)^{-4}|R_{P'}(0)|^2$$

where M_p is the mass of the P state, R_p denotes its radial wave function and r_p is its radius.[20,8] We note that these widths can potentially give an independent means to measure α_s, as well as a check on these QCD computations. Experimentally, however, these widths are not directly accessible because they are so narrow. If we assume the E1 rates predicted by potential models to be correct, we can get an estimate of the hadronic widths using the CUSB measured BR's ($\chi_b\to\gamma+\Upsilon$). From $\Gamma(\chi_b\to hadrons)=\Gamma(E1)(1/BR-1)$ we have:

$$\Gamma(\chi_{b,J=2}\to hadrons) = 152\ ^{+63}_{-50}\ keV, \text{ and}$$

$$\Gamma(\chi_{b,J=1}\to hadrons) = 41\ ^{+40}_{-20}\ keV,$$

where the error is derived from measurement uncertainties only. Within the present errors these numbers are in agreement with the above quoted expectations. Clearly much more accuracy is needed both in the theoretical and experimental quantities.

P-states' Centers of Gravity and Flavor Independence-- It has been shown[21] that at least four differently derived potential models describe the triplet S bound ($b\bar{b}$) level spacing and ratios of leptonic widths equally well. This is because all succesful central potentials have the same radial dependence in the region probed by the above states, almost logarithmic, or if one were to parametrize the potential V(r)as Ar^v, v is ~ 0. Quigg and Rosner[25] have pointed out that ratios of level spacings can be directly related to the power v. Using the CUSB measured centers of gravity of the triplet bound P states of 9900 MeV for the 1^3P_1 and 10256 MeV for the 2^3P_1 and the curves of Quigg,[26] we obtain v ~-0.15 and v ~-0.22 . The corresponding analysis from the charmonium system[25] yields v ~0.15. Note that all three values are close to zero, confirming that the potential is flavor independent. The small negative value of v from the ($b\bar{b}$) system indicates that the potential has become more Coulomb like at the shorter distances.

Measurement of $\Gamma(\gamma gg)/\Gamma(ggg)$ in Υ and Υ' Decays. While the dominant decay mode for bound Y's from $b\bar{b}$ annihilation is into three gluons, a finite fraction ~α_{em}/α_s could decay into a photon and two gluons (γgg). The ratio of these two partial rates, including first order QCD corrections is[27,28]:

$$\Gamma(\Upsilon\to ggg)/\Gamma(\Upsilon\to\gamma gg) = (5/36)(1/e_b^2)(1/\alpha_{em})\alpha_s(1-2.2\alpha_s/\pi).$$

Because of cancellations , the next term in the α_s/π expansion is expected to be small, hence this ratio could be the best source for determining α_s and the QCD scale parameter $\Lambda_{\overline{MS}}$, where the two quantities are related by[29]:

$$\alpha_s(Q^2) = \frac{4\pi}{\beta_0 \ln\left[Q^2/\Lambda^2_{\overline{MS}}\right]} - \frac{4\pi\beta_1 \ln\{\ln\left[Q^2/\Lambda^2_{\overline{MS}}\right]\}}{\beta_0^3 \ln^2\left[Q^2/\Lambda^2_{\overline{MS}}\right]}$$

with $\beta_0 = 11 - (2/3)n_f$, $\beta_1 = 102 - (38/3)n_f$, $n_f = 4$, and the appropriate Q^2 to be used is $(0.157M_\Upsilon)^2$.[30]

The photon spectrum from the γgg decay is expected to peak towards the end of the kinematic spectrum. If we define $z=E_\gamma/E_{beam}$, the spectrum is given to 0th order by[31]:

$$dN/dz \sim \{2/(\pi^2-9)\}\{z(1-z)/(2-z)^2 - 2(1-z)^2\ln(1-z)/(2-z)^3 + (2-z)/z + 2(1-z)\ln(1-z)/z^2\}$$

which is essentially a straight line through the origin. Radiative corrections are expected to modify the shape of the end of the spectrum but not the integral from z_{min} to 1 of $\int(dN/dz)dz$ for reasonable z_{min}'s[32]; for example this integral is expected to be 0.75 for $z_{min}=0.5$. In contrast, the spectrum of π^0 decay photons resulting from the hadronization of the gluons of the three gluon decay mode is peaked toward very low energies ($z \sim 0.004$).

Experimentally, the high energy neutral particle spectrum includes both π^0's and γ's since the opening angle between the two decay photons from the π^0 becomes at some energy smaller than the detector's angular resolution. For the CUSB detector, the π^0's are removed statistically using the properties of the radially layered active converters in the following way. We calculate the relative conversion probability of π^0's and direct γ's in each layer of sodium iodide (for a very thin layer that ratio is two). We count for each observed energy the fraction which had converted in the first layer, second layer etc. From both pieces of information we obtain the fraction of direct photons contained in the spectrum as a function of photon energy and transform the neutral particle spectra taken at resonance peaks and on the continuum into the corresponding direct photon spectra. Since there are continuum (and continuum-like, e.g. virtual γ's) contributions in each direct photon spectrum obtained at resonance peak energies, they are removed using the measured continuum direct photon spectrum weighted by the appropriate equivalent integrated luminosities. Finally, we have to fold in our hadronic event selection efficiency which is E_γ dependent and our high energy electromagnetic shower search code acceptance (very mildly E_γ dependent) to obtain the true direct photon spectra from the Y(1S), Figure 14 and from the Y(2S), Figure 15. We note that their shapes are generally consistent with a linear dependence on z, modified by some rounding off at high z.

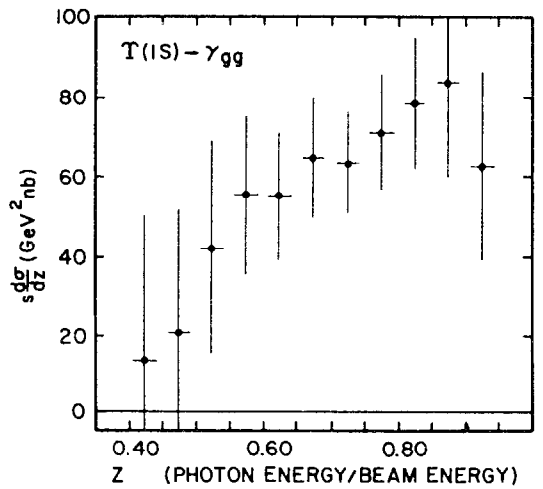


Figure 14. Acceptance corrected spectrum of direct photons from T(1S) decays.

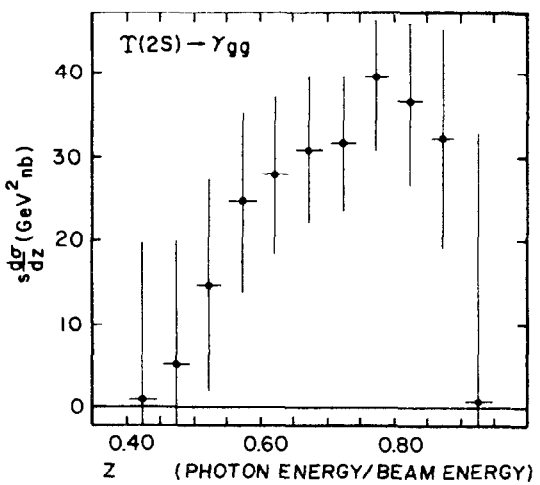


Figure 15. Acceptance corrected spectrum of direct photons from Υ(2S) decays.

We note that these spectra are devoid of fine structure, which is consistent with the results of our exotic particle search (see later) and thus assume that they are due to γgg decays. The following tables summarize the luminosity, hadronic events observed, number of neutral particles, fraction of γ's in the spectrum averaged over the spectrum and number of direct photons obtained at various beam energies (Table III) and the number of direct γ's, hadronic events, average hadron and γ efficiencies, number of γgg and ggg decays from the Υ(1S) and Υ(2S) resonance decays (Table IV). From the above numbers we obtain:

$\Gamma(\gamma gg)/\Gamma(ggg) = 0.0292 \pm 0.0030 \pm 0.0029$ for Υ(1S) decays and

$\Gamma(\gamma gg)/\Gamma(ggg) = 0.0328 \pm 0.0060 \pm 0.0066$ for Υ(2S) decays,

where the first error is statistical, the second one systematic. Using the formulae quoted at the beginning of this section we obtain:

$\alpha_s = 0.23 \pm 0.03$ and $\Lambda_{\overline{MS}} = 119$ MeV (+52-34) MeV from Υ(1S) and

$\alpha_s = 0.20 \pm 0.05$ and $\Lambda_{\overline{MS}} = 81$ MeV (+88-41) MeV from Υ(2S).

These determinations are in good agreement with those obtained from deep inelastic scattering data and are not subject to the uncertainties in hadronization details.

Measurement of $\Gamma(\mu\mu)/\Gamma(ggg)$ from Υ(1S) and Υ(2S) Decays. Using the CUSB detector we have measured $B_{\mu\mu}$ ($\Gamma_{\mu\mu}/\Gamma_{tot}$) for the Υ(1S) and Υ(2S),[33] by measuring the rate of $e^+e^- \to \mu^+\mu^-$ both on and off resonance. This rate's increase on a resonance is due to the bound $(b\bar{b})$'s annihilation into a muon pair and is proportional to that resonance's $B_{\mu\mu}$. Specifically what we measure is $B_{\mu\mu}$ =

TABLE III Observed number of direct γ's

	Luminosity (pb^{-1})	Hadronic events observed	$N(\gamma+\pi^0)$	f_γ	n_γ
Υ region	6.7	100,032	1079	0.31	334
9.452 GeV$<E_{CM}<$9.470 GeV			±33		±27
Υ' region	30.0	238,417	2507	0.30	750
10.012 GeV$<E_{CM}<$10.038 GeV			±50		±50
continuum	24.2	59,563	866	0.16	139
			±29		±27

TABLE IV Number of γgg and ggg events

	N_γ	Hadronic events	$\langle\varepsilon_h(\gamma gg)\rangle$	$\langle\varepsilon_\gamma\rangle$	$N(\gamma gg)$	$N(ggg)$
Υ(1S) decays	275	74815	0.63	0.24	1958	89240
	±28				±198	
Υ(2S) decays	482	123792	0.60	0.22	3363	147662
	±67				±658	

$\Gamma_{\mu\mu}/\Gamma_{hadrons}$ which is related through lepton universality to $B_{\mu\mu}$ $(= 3 + B_{\mu\mu}^{-1})^{-1}$.

If we define $N_{\mu\mu}(tot)$ as the total number of $\mu\mu$ events occurring at the resonance energy, $N_{\mu\mu}(res)$ as the number of $\mu\mu$ events occurring at the resonance energy through resonance production, $N_{\mu\mu}(cont)$ as the number of $\mu\mu$ events occurring at the resonance due to continuum production, $\varepsilon_{\mu\mu}(res)$ as the efficiency for detecting $\mu\mu$ events due to resonance production, and $N_h(tot)$, $N_h(res)$, $N_h(cont)$ and $\varepsilon_h(res)$ the corresponding quantities for hadronic events, then

$$\bar{B}_{\mu\mu} = [N_{\mu\mu}(res)/\varepsilon_{\mu\mu}(res)]/[N_h(res)/\varepsilon_h(res)] =$$

$$\{[N_{\mu\mu}(tot)-N_{\mu\mu}(cont)]/\varepsilon_{\mu\mu}(res)\}/\{[N_h(tot)-N_h(cont)]/\varepsilon_h(res)\}.$$

We determine $N_{\mu\mu}(cont)$ both at the Υ(4S) where $B_{\mu\mu}$ is zero and on the continuum between the Υ(4S) and Υ(3S), scaling these results by large angle Bhabhas to Υ(1S) and Υ(2S). $N_h(cont)$ is also determined from the measured rate of hadron production on the continuum between the Υ(4S) and Υ(3S) scaled by large angle Bhabhas to Υ(1S) and Υ(2S). When doing these scalings, we correct the Bhabha rate measured at the resonance energies for resonance production of e^+e^-. This correction is 3.3% for the Υ(1S) and 0.8% for the Υ(2S). We measured $\varepsilon_{\mu\mu}(res)$ by comparing the number of dimuon events seen on and below the Υ(4S) to the number calculated using the integrated luminosities determined by large angle Bhabhas and the continuum cross section. This continuum efficiency is then corrected, using the Monte Carlo of Berends and Kleiss,[34] for initial state radiation effects, which occur in continuum production but not in resonance production. We

measure

$B_{\mu\mu}(1S) = (2.7 \pm 0.3 \pm 0.3)\%$ and $B_{\mu\mu}(2S) = (1.9 \pm 0.3 \pm 0.5)\%$

where the first error is statistical and the second error is systematic, whose dominant contribution is a 3% uncertainty in the relative Bhabha normalization used to scale $N_{\mu\mu}(\text{cont})$. Using these valnes of $B_{\mu\mu}$ we can calculte $\Gamma_{ggg}/\Gamma_{\mu\mu}$ [35]:

$$\Gamma_{ggg}/\Gamma_{\mu\mu} = (1/B_{\mu\mu})\{1-0.086/\pi-B_{\mu\mu}(3+R)-B_{\gamma gg}-B_{\pi\pi}-B_{E1}\}$$

where $R=3.63$,[10] $B_{\gamma gg}$'s were given in the previous section,

$B_{\pi\pi}(1S)=B_{E1}(1S)=0$ and $B_{\pi\pi}(2S)=0.29\pm0.04$, $B_{E1}(2S)=0.155\pm0.03$,[21]

$\Gamma_{ggg}(1S)/\Gamma_{\mu\mu}(1S) = 24.8\ (+4.4-3.5)$,

$\Gamma_{ggg}(2S)/\Gamma_{\mu\mu}(2S) = 19.6\ (+4.9-3.6)$,

where the errors are statistical only

According to Brodsky, Lepage and Mackenzie,[30] the appropriate scale Q^* to use in the Y system for defining α_s is $0.157M_Y$, as we have done in the previous section when obtaining $\Lambda_{\overline{MS}}$ from $\Gamma_{ggg}/\Gamma_{\gamma gg}$. However, then

$$\Gamma_{ggg}/\Gamma_{\mu\mu} = \{10(\pi^2-9)/(81\pi e_b^2)/\alpha_{QED}^2\}\alpha_{\overline{MS}}^3(Q^*) \times\{1- 14.0\alpha_{\overline{MS}}(Q^*)/\pi + ...\}.$$

We note that the series is far from convergent, the correction term in the second bracket is almost equal to 1 and the next order term is surely large if this formula is to fit the above data. The authors suggest one should use the physical process described in the previous section to define α_D, then the correction term in the above bracket becomes $\{1- 7.4\alpha_D/\pi+...\}$ and the new Q^* is $\sim 1.3\text{x}0.157M_Y$. One notes that the second term is still of the order of 0.5, so the theoretical uncertainties are still large. We obtain from the above ratios

$\alpha_D(1S) = 0.22 \pm 0.015$, $\Lambda_{\overline{MS}} = 130$ MeV (+54-24) MeV from Y(1S) and

$\alpha_D(2S) = 0.18 \pm 0.02$, $\Lambda_{\overline{MS}} = 75$ MeV (+56-34) MeV from Y(2S).

Despite the large experimental and theoretical uncertainties, it is very rewarding to see that the QCD scale parameter extracted using two completely different processes (from this section and the last section) agree so extremely well. It certainly adds credence to $\Lambda_{\overline{MS}}$ being around 100 MeV.

Search for Axions and Higgs Particles. All current models of the electroweak interactions require the existence of at least one pseudoscalar Higgs particle.[36] They could be almost massless, as the axions postulated by Weinberg[37] and Wilczek.[38] Or, if they acquire mass through radiative corrections, be quite light ($<M_Y$), like that of Nanopolous' $M_{H^0} \sim 4.4$ GeV.[39] The Higgs particle couples to quarks proportionally to the square of the quark mass which results in the prediction[40]

$$BR(\Upsilon\to\gamma+H)/BR(\Upsilon\to\mu\mu) = G_F M_\Upsilon^2/(4\sqrt[3]{2}\alpha\pi)\text{x}[1-M_H^2/M_\Upsilon^2]$$

where G_F is the Fermi coupling constant. Models with two Higgs fields modify this result by a factor $(v_1/v_2)^2$ for charge 1/3 quarks (Y's) while the corresponding BR ratio for the ψ is multiplied by $(v_2/v_1)^2$, where v_1 and v_2 are the vacuum expectation values of the two Higgs fields.[41]

The second model applies to the Weinberg-Wilczek axion, a, which is a very light (M<1MeV), long-lived, and semiweakly interacting pseudoscalar particle, distinguished by its 'invisibility'. Since the ratio of the two vev's ($X=v_1/v_2$) is not known, one cannot predict the BR's for either Υ or $\psi\to\gamma+a$. However their product is given by:

$$BR(\Upsilon\to\gamma+a)/BR(\psi\to\gamma+a) = B_{\mu\mu}(\Upsilon)B_{\mu\mu}(\psi)G_F^2M_\Upsilon^2M_\psi^2/\{32\alpha^2\pi^2\}$$
$$= (1.6 \pm 0.3) \times 10^{-8}.$$

We searched for these decays in CUSB, where the event signature is a single neutral electromagnetic shower with $E_\gamma \sim E_{beam}$, accompanied by nothing else in the detector since the axion does not interact and if its mass is less than 10 MeV, would decay outside the detector. We found no example of such events in an equivalent sample of ~ 60000 Y decays, giving an upper limit of 1.2×10^{-4} for the BR.[42] Combining this result with the limits of Edwards et al.[43] for $\psi\to\gamma+a$ of 1.4×10^{-5}, we quote a limit of 0.6×10^{-9} for the above product of the BR's at 90% cl, an unambiguous result arguing against the existence of the axion.

We have also searched for Higgs from the decay $\Upsilon\to\gamma+H$ where the Higgs decays into hadrons. The inclusive photon spectrum from ~ 80000 Y's is shown in Figure 16. It can be fit by a smooth polynomial function (the curve in the figure). A maximum likelihood search was made for monochromatic photon signals, the 90% cl upper limit for the $BR(\Upsilon\to\gamma H)$ calculated as a function of the recoil mass is shown in Figure 17. We are at present not sensitive to the expected rate for the single Higgs model (shown as the curve in Figure 17). For models with two Higgs, the above BR is enhanced by a factor of X^2, and we can exclude a large region in the (X, M_H) plane, as is shown in Figure 18.

The B*-B Mass Difference. At the Y(4S) CLEO has recently observed exclusive decay modes of b-flavored mesons[44] and obtained a mass of 5274.2±3.9 MeV for the neutral state and 5270.8±4.3 MeV for

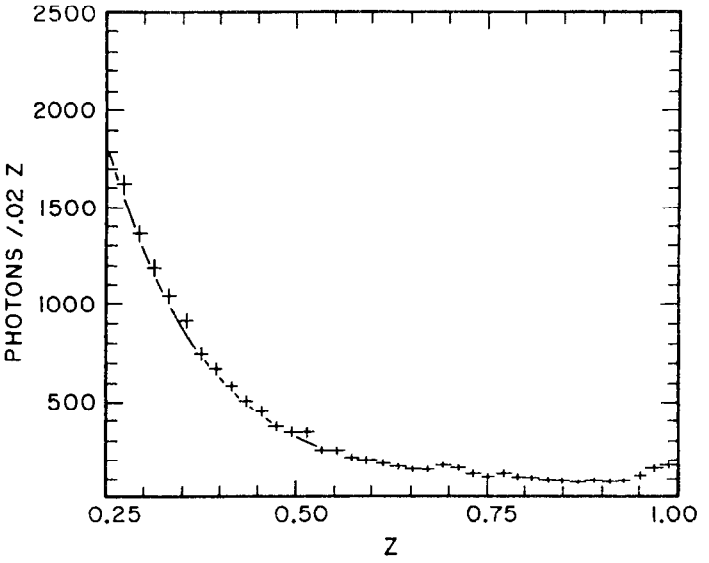


Figure 16. Inclusive high energy γ spectrum from T(1S), $z=E_\gamma/E_{beam}$.

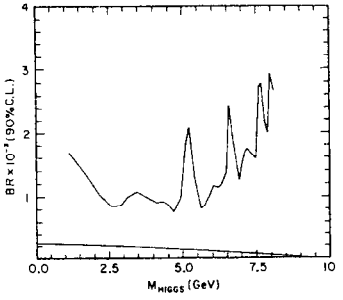


Figure 17. CUSB 90% c.l. upper limit for $BR(\Upsilon\to\gamma+H)$ vs M_{Higgs}. Curve is theoretically predicted rate for one Higgs models.

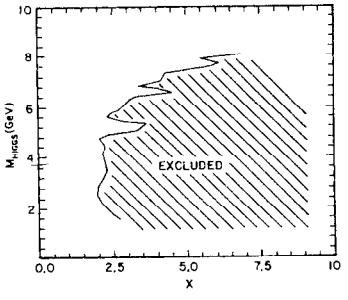


Figure 18. Contour of excluded region for (M_H, X), where $X=v_1/v_2$.

the charged state. Their particular method of identifying these b-flavored states is insensitive to the presence of additional low energy photons, therefore they can not tell whether they have reconstructed B's or B*'s whose main decay mode would be $B^* \rightarrow \gamma + B$ as long as $M(B^*)-M(B) < m_\pi$. They have established however, that the threshold for producing a pair of such b-flavored mesons is 32.4±5.0 MeV below the Y(4S). The question is then, is the Y(4S) a $B\bar{B}$, $B\bar{B}^*$ or $B^*\bar{B}^*$ factory?

The hyperfine splitting between the vector and scalar mesons is traditionally thought of as being due to a short range force resulting from a single hard gluon exchange, and thus is expected to scale inversely as the mass of the system.[45] Hence a simple estimate of the B*-B mass difference is to scale it from the D*-D mass difference inversely as the masses of the heavy quarks (b,c): $M(B^*)-M(B) \sim \{m_c/m_b\}\{M(D^*)-M(D)\} \sim 50$ MeV. CUSB had searched for such 50 MeV γ's at the Y(4S) with null result.[46] However, aside from the range of numbers one might choose for the masses of the heavy quarks, several more refined models for calculating hyperfine splitting in heavy quarkonia have been extended to light-heavy and light-light quarkonia so that the B*-B mass difference has been predicted to be even as low as 23 MeV [47] and as high as 60 MeV.[48]

We (CUSB) therefore made a renewed effort to search for low energy photons at the Y(4S) with a special algorithm optimized for finding very low energy photons. For this algorithm the acceptance and efficiency combined is $\sim \{6.2 + 2.2x([E_\gamma-25]/20)\}\%$ where E_γ is measured in MeV and the resolution is given by $\sigma(E_\gamma) = 0.9x(E_\gamma + 5)^{1/2}$ MeV. The photon spectrum from 50,000 Y(4S) decays (obtained from 170,000 hadronic events taken at the Y''' peak and subtracting 120,000 continuum events) is shown in Figure 19. The curves a, b and c are the expected contribution if there were one 25 MeV, 50 MeV and 70 MeV γ respectively per each Y(4S) decay, we clearly see no such signal. Using the maximum likehood method on the unsubtracted photon spectrum we obtained 90% cl upper limit for the branching ratio BR(Y(4S)→monochromatic γ) as a function of $\Delta M = M(B^*)-M(B) = E_\gamma$. They are ~ 10% and are shown as the horizontal boundary lines in Figure 20.

To understand the implications of these upper limits we need to know the expected partial rates for $B\bar{B}$, B^*B and B^*B^* on the Y(4S) as a function of ΔM. These partial rates also depend on whether the CLEO b-flavored particle pair production threshold is the $B\bar{B}$, $B\bar{B}^*$, or $B^*\bar{B}^*$ threshold. Since the Y(4S) is so close to these thresholds, no extra particles are produced and we can write:

$$\#\ \text{of}\ \gamma\text{'s/Y(4S)} = \{R(B\bar{B}^*)+2R(B^*\bar{B}^*)\}/\{R(B\bar{B})+R(B\bar{B}^*)+R(B^*\bar{B}^*)\}.$$

The R's are given by $\sigma(e^+e^-\rightarrow B_aB_b)/\sigma(e^+e^-\rightarrow\mu^+\mu^-) = p_{ab}^{2L+1}|M(p_{ab})|^2 S_{ab}$ where (a,b) refers to B or B*, p_{ab} is their relative momentum, $M(p_{ab})$ is a matrix element that describes the decay and S_{ab} is a statistical factor which depends on the spin of the final state. It is 1:4:7 for $B\bar{B}:B\bar{B}^*+\bar{B}B^*:B^*\bar{B}^*$.[49] Since both the B and B* have odd intrinsic parity, so does the Y(4S), L has to be odd and most likely equals 1 as we are near threshold. Therefore R_{ab} reduces to $p_{ab}^3|M(p_{ab})|^2 S_{ab}$. The momentum p_{ab} can be expressed simply in terms of the number of B*'s contained in CLEO's

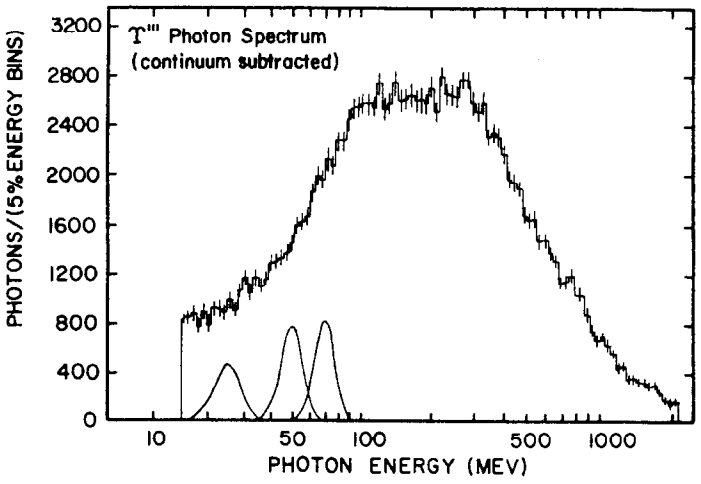


Figure 19. Inclusive γ spectrum for 48000 T(4S) events after continuum subtraction. Solid lines indicate expected γ's.

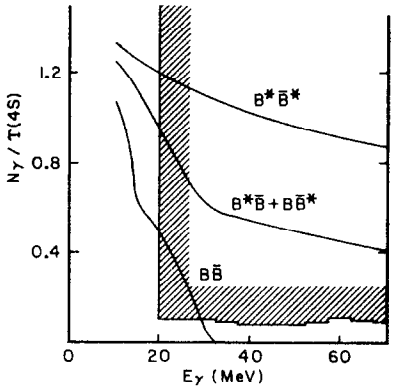


Figure 20a. Expected # of γ's per T(4S), method (i), and CUSB limits.

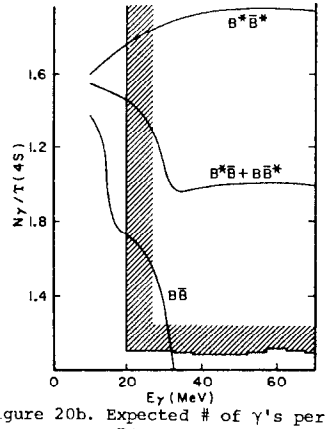


Figure 20b. Expected # of γ's per T(4S), method (ii), and CUSB limits.

reconstructed b-flavored pairs (i=0,1,2), the number of B^*'s produced per Y(4S) (j=0,1,2) and $\Delta M=E_\gamma$ in MeV: $p_{ij} \sim [5272(32.4-(i-j)E_\gamma)]^{1/2}$. We assume that the neutral and charged B mass difference can be neglected (in fact including the estimated mass difference of 2 to 4 MeV did not alter our results). The $R_{aa,ab,bb}$ can be estimated in two ways (i) by assuming $|M(p_{ab})|^2=1$, (ii) by using the Y(4S) decay amplitude from Reference 9. Method (ii), while obviously superior to method (i), is not strictly correct since we are using the Y(4S) decay amplitude alone without considering mixing with other triplet S states.

The expected number of γ's per Y(4S) as a function of E_γ and CLEO threshold is shown in Figure 20a as computed using method (i) and in Figure 20b as computed from using method (ii), superimposed on both is the experimental 90% cl upper limit. In either case we conclude that CLEO's reconstructed B meson pairs are $B\bar{B}$'s. We also conclnde that the B^*-B mass difference is > 29 MeV at 90% cl from method (i) and > 31 MeV at 90% cl from method (ii).

B Decay Leptonic Spectrum and Mixing Matrix Parameters. In the standard model, the b leptonic decay is given, ignoring the Fermi constant, by an effective coupling of the electron-neutrino current times the quark-quark current of the form $\{V_{bu}(bu)_\alpha+V_{bc}(bc)_\alpha\}$ where $(ab)_\alpha=\bar{u}_a\gamma_\alpha(1-\gamma_5)u_b$ etc. and V_{bu},V_{bc} are the relevant elements of the quark mixing matrix[50] whose relative strength can be determined from a precision measurement of the β-decay spectrum of the B meson.[51]

In the CUSB detector we can obtain a very clean electron signal for energies above 1 GeV. At 2.2 to 2.6 GeV our resolution is ~3%. Figure 21 shows the observed electron spectrum from the Y''' region where 70% of the cross section is from continuum ($q\bar{q}$) events whose contribution to the electron spectrum is shown as a solid line in the figure (background due to misidentification is included). Note the sharp fall off of the raw spectrum. The subtracted spectrum shown in Figure 22 has been compared with the model of Altarelli et al.[52] using the masses m_B=5.275 GeV and letting m_c vary. We obtain m_c=1.7 GeV as a best fit, see curve A in figure, corresponding to an average recoil mass of 1.95 GeV for the hadronic system recoiling against the electron and the neutrino. Curve B is obtained for m_q=150 MeV (which effectively accounts for QCD radiative corrections to the spectrum near the end point) which corresponds to an average mass of 820 MeV for the hadronic system formed by the decay quark and the spectator quark. Curve C is the contribution from secondary (D's from B decays) D semileptonic decays, which should be added to curve A when comparing with data.

The experimentally measured spectrum is consistent with zero contribution from b→u. On the basis of our results we obtain a 90% cl upper limit of $BR(B\to e\nu X_u)/BR(B\to e\nu X_c) < 5.5\%$. From integrating over available phase space for b→u and b→c from Ref. 52 the above limit corresponds to

$$|V_{bu}/V_{bc}|^2 < 0.026 \text{ or } |V_{bu}|/|V_{bc}| < 0.16 .$$

In the Maiani notation this imposes a bound $|\sin\beta/\sin\gamma|<0.16$ which represents a significant improvement on our knowledge of the K-M matrix even as recently summarized.[53,54] In Figure 23 we show an update of the $\sin\beta/\tan\theta$ vs $\sin\gamma$ plot of Reference 54 using our new

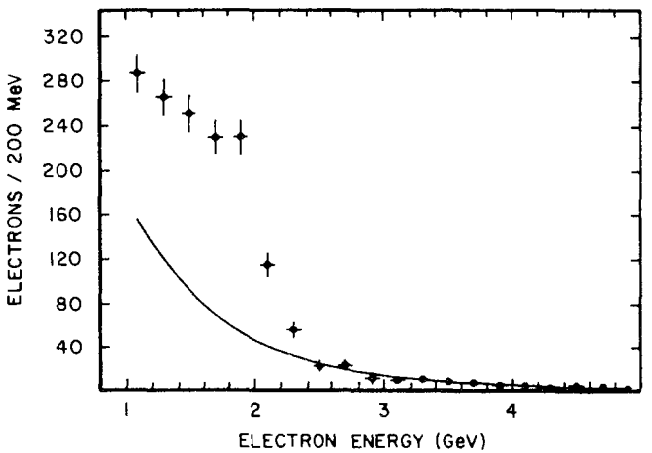


Figure 21. High energy electron spectrum from T" events (70% are continuum events). The measured continuum background is shown by the solid curve.

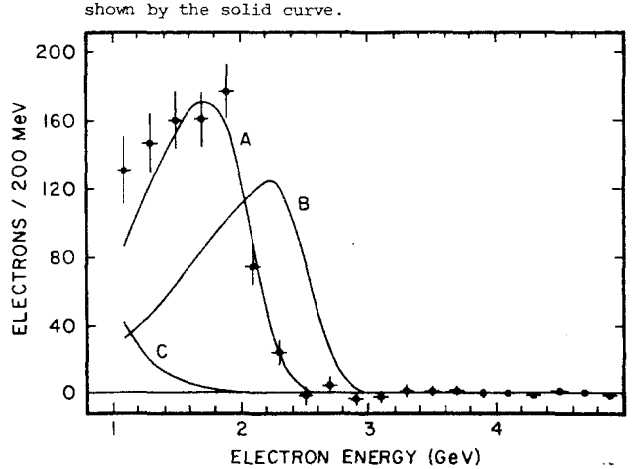
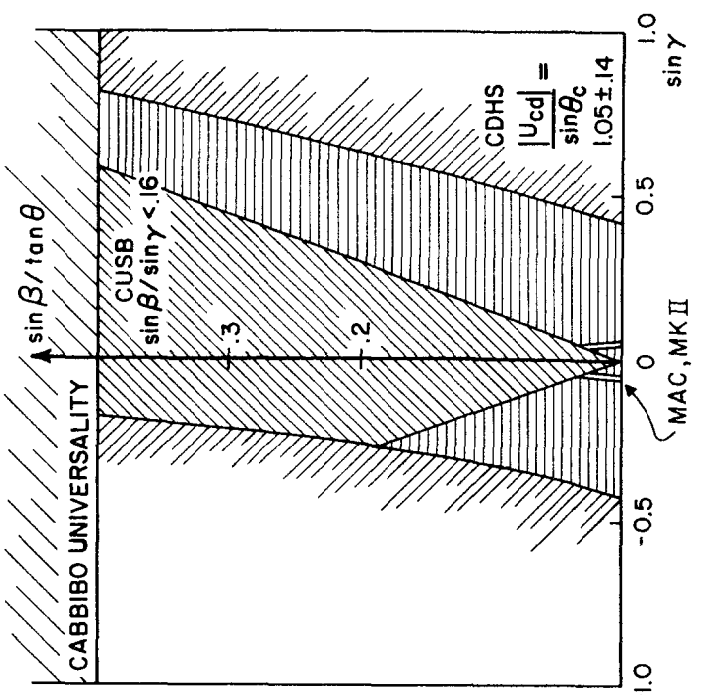


Figure 22. High energy electron spectrum from T(4S) after background subtraction. The curves are from the model of Ref. 52. A is the best fit. B is for m_q = 150 MeV (corresponding to 820 MeV for the hadronic ^{q} system formed by the decay and spectator quark). Curve C is from semileptonic D decays.

Figure 23.

Present experimental bounds on the quark mixing angles β and γ. The shaded regions of the plane are excluded. See text for explanation.



data and the recent determinations of the B lifetime by MAC[55] and MARK II.[56] Finally, from the same data we obtain an improved result for the B semileptonic BR of (13.2±0.8)%, in good agreement with spectator model calculations.[57]

Conclusions and Future Outlook. The present experimental status of upsilon spectroscopy is best summarized by the level diagram of Figure 24, where the observed levels and transitions are illustrated (solid lines). We have measured all the partial rates indicated and have made a first attempt to measure the hadronic width of the $^3P_{2,1}$ decays. We have once more confirmed the validity of the QCD multipole expansion scaling laws. We have measured the QCD scale parameter in two independent ways and found it to be around 100 MeV. We have observed no vibrational states, nor have we succeeded to unearth any light Higgs scalars so far.

We have seen the manifestation of free b flavor at the Υ'', and deduced from the lack of B*'s the B meson mass. We have observed an excess of K°'s at the Υ'',[58] indicating that b→c is favored over b→u and have excluded exotic couplings of the b quark. Finally, by a detailed study of the β decay of the B meson, we obtained the first stringent limit on the mixing matrix element squared,

$$|V_{bu}/V_{bc}|^2, \quad < 0.026 \text{ at } 90\% \text{ cl.}$$

NR potential models, which demonstrated such phenomenal success in describing the general features of the level diagram in Figure 24, cannot unambiguously predict the fine structure of the ^3P states, nor the hyperfine splittings between the triplet S and singlet S states, see Reference 2 for a complete discussion. Experimental information

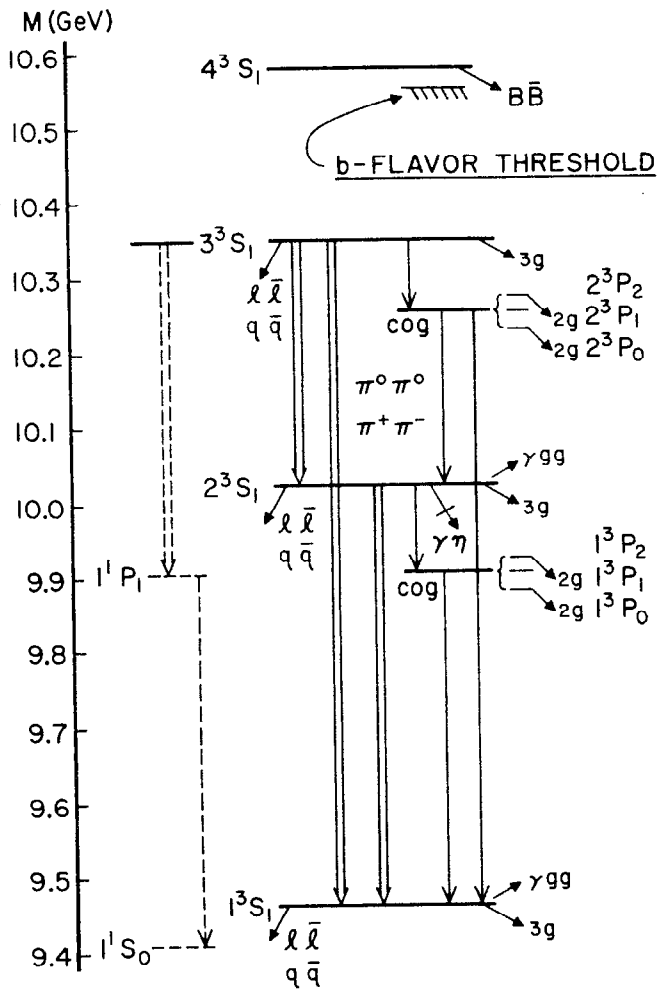


Figure 24. A level diagram of the $b\bar{b}$ bound system; double lines indicate ππ transitions and single lines indicate γ transitions. The solid lines indicate observed transitions, see text.

is necessary to establish the form of the effective spin-spin and spin-orbit interactions responsible for these effects. CUSB is now upgrading with a BGO insertion[59] for measuring the fine splitting with precision and to find the singlet S state via the promising chain depicted in dashed lines in Figure 24.

Acknowledgements. The author acknowledges all her collaborators from CUSB. In addition she thanks P. Franzini, R. D. Schamberger and P. M. Tuts for their invaluable help during the preparation of this paper. Finally, she thanks N. Byers, E. Eichten, M. Peskin and J. L. Rosner for discussions on potential models.

References

1. The CUSB Collaboration,which at any given time consists of ~22 physicists, included from 1979 to now the following persons, where a star indicates membership during July, 1983: T.Bohringer, F.Costantini, J.Dobbins, P.Franzini*, K.Han*, S.W.Herb*(now from Cornell), D.M.Kaplan, L.M.Lederman, D. Peterson, E.Rice, D.Son*, J.K.Yoh, S.Youssef*, T.Zhao*-- Columbia University. G.Finocchiaro, G.Gianinni, J.Horstkotte*, C.Klopfenstein*, J.Lee-Franzini*, L.Romero*, R.D.Schamberger*, M.Sivertz*, L.J.Spencer*, P.M.Tuts*--SUNY at Stony Brook. G.Blanar, H.Dietl*, G.Eigen*, V.Fonseca*, E.Lorenz*, F.Pauss, H.Vogel*, G.Mageras*-- Max Planck Institute. R.Imlay*, G. Levman*, W.Metcalf*, V.Sreedhar*.--Louisiana State University.

2. E. Eichten, these proceedings.

3. A. S. Artamonov et al., Phys. Lett. 118B, 225 (1982).

4. W. W. Mackay et al., to be published (1983).

5. W. Buchmuller and S.-H. H. Tye, Phys. Rev. Lett. 44, 850 (1980).

6. Y. P. Kuang and T. M. Yan, Phys. Rev. D24, 2874 (1981).

7. V. A. Navikov et al., Phys. Rep. 41C, 1 (1978).

8. P. Moxhay and J. L. Rosner, Phys. Rev. D28, 1132 (1983), and private communications.

9. E. Eichten, Phys. Rev. D22, 1819 (1980).

10. E. Rice et al., Phys. Rev. Lett. 48, 906 (1982) and new data.

11. Particle Data Group, Phys. Lett. 111B, 11 (1982).

12. T. M. Yan, Phys. Rev. D22, 1652 (1980).

13. L. S. Brown and R. N. Cahn, Phys. Rev. Lett. 35, 1 (1975).

14. G. Mageras et al., Phys. Lett. 118B, 453 (1982).

15. J. Green et al., Phys. Rev. Lett. 49, 617 (1982).

16. K. Han et al., Phys. Rev. Lett. 49, 1612 (1982).

17. C. Klopfenstein et al., Phys. Rev. Lett. 51, 160 (1983).

18. G. Eigen et al., Phys. Rev. Lett. 49, 1616 (1982).

19. F. Pauss et al., Phys. Lett., in press (1983).

20. R. Barbieri et al., Phys. Lett. 60B, 183 (1976); Ibid., 61B, 465 (1976).

21. P. Franzini and J. Lee-Franzini, Ann. Rev. of Nuc. Part. Sci. 33, 1 (1983).

22. J. L. Rosner, in Experimental Meson Spectroscopy-1983 (VIIth Int. Conf. BNL), ed. by S. U. Chung and S. J. Lindenbaum, AIP, New York, in press (1983).

23. M. Voloshin et al., ITEP Rep. ITEP-21, M. Voloshin and V. Zakharov, DESY Rep. F15-80/03, 1980 (unpublished).

24. R. A. Bertlmann, CERN Rep. TH-3192, 1981 (unpublished).

25. C. Quigg and J. L. Rosner, Phys. Rep. 56C, 167 (1979).

26. C. Quigg, private communication.

27. M. Chanowitz, Phys. Rev. D12, 918 (1975).

28. P. B. Mackenzie and G. P. Lepage, in Perturbative Quantum Chromodynamics, ed. D. W. Duke and J. F. Owens (AIP, New York, 1981).

29. A. J. Buras et al., Rev. Mod. Phys. 52, 199 (1980).

30. S. Brodsky et al., Phys. Rev. D28, 228 (1983).

31. S. Brodsky et al., Phys. Lett. 73B, 203 (1978).

32. G. P. Lepage, private communication.

33. J. E. Horstkotte et al, Bull. Am. Soc. 28, 28 (1983).

34. A. Berends and R. Kleiss, Nucl. Phys. B178, 141 (1981).

35. P. B. Mackenzie and G. P. Lepage, Phys. Rev. Lett. 47, 1244 (1981); F. J. Yndurain, Phys. Rev. Lett. 48, 897 (1982).

36. J. Ellis et al., Ann. Rev. Nucl. Part. Sci. 32, 443 (1982).

37. S. Weinberg, Phys. Rev. Lett. 40, 223 (1978).

38. F. Wilczek, Phys. Rev. Lett. 40,220 (1978).

39. D. Nanopolous et al., CERN preprint 83-TH.3651.

40. F. Wilczek, Phys. Rev. Lett. 39, 1304 (1977).

41. R. D. Peccei and H. R. Quinn, Phys. Rev. Lett. 39, 1440 (1977).

42. M. Sivertz et al., Phys. Rev. D26, 717 (1982).

43. C. Edwards et al., Phys. Rev. Lett. 48, 903 (1982).

44. S. Behrends et al., Phys. Rev. Lett. 50, 881 (1983).

45. E. Eichten et al., Phys. Rev. D21., 203 (1980); Ibid., D22, 1819 (1980).

46. R. D. Schamberger et al., Phys. Rev. D26, 720 (1982).

47. S. N. Gupta et al., Wayne State Univ. preprint 83-02.

48. A. Martin, Phys. Lett. 103B., 55 (1980).

49. E. Eichten et al., Phys. Rev. D17, 3090 (1978).

50. L. Maiani, in Proc. Int. on Lepton and Photon Interactions at High energies, Hamburg, Germany, ed F. Gutbrod, (DESY, 1977).

51. C. Klopfenstein et al., Phys. Lett. , in press (1983).

52. G. Altarelli et al., Nucl. Phys. B208, 365 (1982).

53. S. Pakvasa, Jour. de Phys. 43, Colloque C-3, 234 (1982).

54. L. Maiani, Jour. de Phys. 43, Colloque C-3, 631 (1982).

55. E. Fernandez et al., Phys. Rev. Lett. 51, 1022 (1983).

56. N. S. Lockyer et al., Preprint SLAC-PUB 3165 (1983).

57. J. P. Leveille, in Proc. of 2nd Moriond Workshop-New Flavors ed. by J. Tran Than Van and L. Montanet (editions Frontieres, Gif-sur-Yvettes, France 1982), p.191.

58. G. Gianinni et al., Nucl. Phys. B106, 1 (1982).

59. P. M. Tuts and P. Franzini, in Proc. of Int. Workshop on Bismuth Germanate, ed. C. Newman Holmes (Princeton Univ. New Jersey, 1982) p. 596.

SLAC-PUB-3262
November 1983
(T/E)

MARK III RESULTS FROM SPEAR

Walter Toki
Stanford Linear Accelerator Center
Stanford University, Stanford, California 94305

Talk presented for the MARK III Collaboration†

ABSTRACT

First results from the MARK III detector at SPEAR are presented based on 2.7 million J/ψ decays. The η_c is observed in three modes, $J/\psi \to \gamma\eta_c$, ($\eta_c \to p\bar{p}, \eta\pi^+\pi^-$, and $\phi\phi$). Using the $\phi\phi$ mode, the η_c spin-parity is determined to be 0^-. The known radiative J/ψ decays $J/\psi \to \gamma f(f \to \pi^+\pi^-)$, $\gamma\eta'(\eta' \to \gamma\rho^0, \eta\pi^+\pi^-)$, $\gamma f'(f' \to K^+K^-)$, $\gamma\theta(\theta \to K\bar{K})$, and $\gamma\iota(\iota \to \pi K\bar{K})$ are observed and their branching ratios found to be in agreement with previous measurements. In the $J/\psi \to \gamma K^+K^-$ mode a new state is observed at 2.22 GeV, and in the $J/\psi \to \gamma\gamma\rho^0$ and $\gamma\eta\pi^+\pi^-$ modes evidence for new structures near 1.4 GeV is presented.

---

* Work supported in part by the Department of Energy, contracts DE-AC03-76ER01195, DE-AM03-76SF00034 and DE-AC03-81ER40050.

† members of the MARK III Collaboration are R. M. Baltrusaitis, D. Coffman, J. Hauser, D. G. Hitlin, J. D. Richman, J. J. Russell, and R. H. Schindler, *California Institute of Technology*; K. O. Bunnell, R. E. Cassell, D. H. Coward, K. F. Einsweiler, D. P. Hutchinson, L. Moss, R. F. Mozley, A. Odian, J. R. Roehrig, W. Toki, Y. Unno, F. Villa, N. Wermes, and D. E. Wisinski, *Stanford Linear Accelerator Center*; H. L. Bledsoe, D. E. Dorfan, R. Fabrizio, F. Grancagnolo, R. P. Hamilton, C. A. Heusch, J. Perrier, H. F. Sadrozinski, T. L. Schalk, A. Seiden, and D. B. Smith, *University of California at Santa Cruz*; J. J. Becker, G. T. Blaylock, H. Cui, B. Eisenstein, G. Gladding, S. A. Plaetzer, A. L. Spadafora, J. J. Thaler, A. Wattenberg, and W. J. Wisniewski, *University of Illinois, Champaign-Urbana*; J. S. Brown, T. H. Burnett, V. Cook, C. Del Papa, A. L. Duncan, P. M. Mockett, A. Nappi, J. C. Sleeman, and H. J. Willutzki, *University of Washington, Seattle*.

Presented at the 11th SLAC Summer Institute on Particle Physics
Stanford, California, July 18-29, 1983

© W. Toki 1983

1. Introduction

The SPEAR energy range, explored now for over a decade, has an enormous amount of physics remaining to be studied in both strong and weak interactions. Since the Crystal Ball and MARK II discoveries of new J/ψ radiative decays the area has become very topical in strong interaction physics. QCD suggests that J/ψ's radiatively decay to two gluons and these gluons may form bound states or glueballs. This has generated a large amount of theoretical interest. In weak interactions, because the charged and neutral D lifetimes appear to be different, there has been considerable interest in understanding why the naive weak spectator models fail to explain this difference. Since MARK III will have a larger data sample than obtained by MARK II, there may be unexpected results, possibly as exciting as those in kaon physics. It may also prove as interesting to examine with large statistics as are decays of τ's, F's, ψ's, and Λ_c's.

MARK III is a general purpose magnetic solenoidal detector that was installed in the west pit at SPEAR in July 1981. The initial checkout was completed in the fall of 1981 and the first data run was done at the J/ψ in the spring of 1982. This was followed in the fall of 1982 by running at the ψ''. In the spring of 1983 the first half of the running was again devoted to running at the J/ψ, accumulating a total (1982+1983) of 2.7×10^6 produced J/ψ decays. During the second half a run at the ψ'' allowed the accumulation of a total (1982+1983) integrated luminosity of $\sim$ 5800 nb^{-1} or $\sim$45,000 produced $D\bar{D}$ pairs.

This report will describe the detector hardware, the performance of the detector on known J/ψ decays, and will finally discuss new results on η_c decays and radiative J/ψ decays. The results being presented are preliminary and are based on analyses completed in July 1983.

2. Apparatus

The MARK III detector has been designed to study e^+e^- reactions produced at SPEAR.[1] The detector is shown in the transverse and axial views in Figs. 1 and 2. The main design goals were to achieve large acceptance for charged and

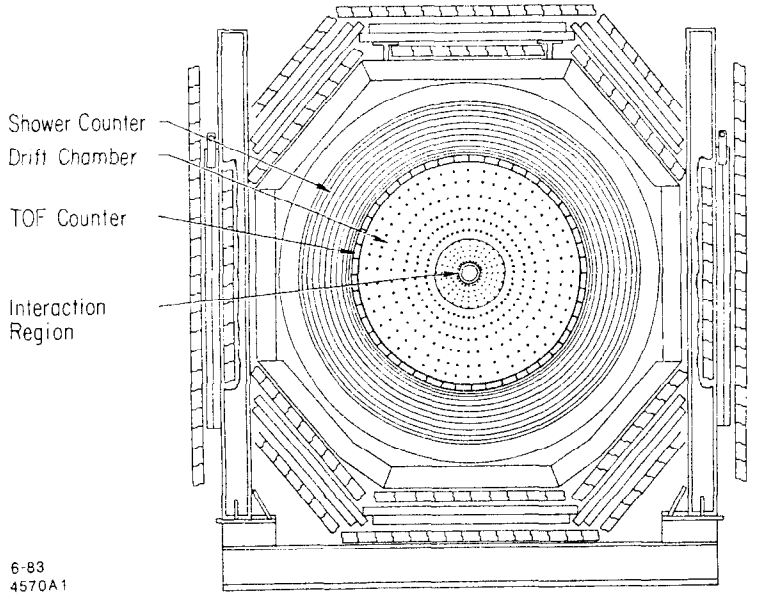


Fig. 1. Axial view of the MARK III detector.

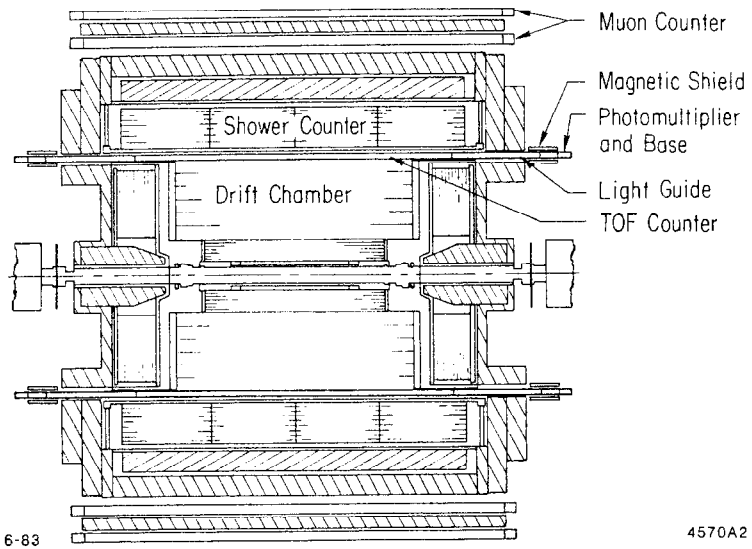


Fig. 2. Transverse view of the MARK III detector.

neutral particles, high detection efficiency for low energy gammas, good $\pi/K/p$ separation by TOF and fine charged track momentum resolution. The typical events have relatively low multiplicities and charged particle momenta of several hundred MeV.

The description of the detector will begin with the central section of the drift chamber. The beam pipe and inner detectors were designed to minimize multiple scattering. The beryllium beam pipe is 0.4% r.l. thick, the first inner drift chamber is constructed of aluminum covered foam shells and the inner face of the main drift chamber is phenolic-clad paper hexcell covered with Al foil. The main function of the inner drift chamber is to provide a pre-trigger. It has 4 layers with 32 axial sense wires per layer which are staggered by half a cell from layer to layer. The drift times in alternate sense wires in adjacent layers provide a time sum signal. This is fed into a chronotron circuit which is gated on SPEAR beam crossings to reduce the cosmic ray background and to provide a low pre-trigger rate of 3-4 kHz from the raw beam crossing rate of 1.28 mhz.

The second section of the drift chamber has 12 axial staggered sense wires in 32 cells which are read out both in time and charge. The high density of sense wires is useful for dE/dx sampling and Vee reconstruction for K_S and Λ decays. The dE/dx information was not used for the J/ψ analysis presented in this talk.

The third section of the drift chamber[2] has 4 axial and 2 stereo layers. Three of the axial layers include charge division. The basic cell design has 3 sense wires, two guard wires and five high voltage field shaping wires. This cell structure is repeated from 48 times in the 3rd layer to 128 times in the 8th layer. The drift chamber solid angle coverage is 85% of 4π and the overall momentum resolution as measured on μ-pairs in the J/ψ data is $\sigma_p/p = 1.5\% \times \sqrt{1+p^2}$, p in GeV.

The TOF system[3] has 48 scintillators which are strapped on the exterior of the drift chamber. Each scintillator is read out by two phototubes through lucite lightguides. The radial distance is 1.17 m and the solid angle coverage is 80% of 4π. The thick scintillator (5 cm) and the special design of the light guide enable high TOF resolution. The overall resolution (σ_{tof}) is 175 ps for Bhabhas ($J/\psi \to e^+e^-$), 169 ps for μ-pairs ($J/\psi \to \mu^+\mu^-$), and 189 ps for π's

from $J/\psi \rightarrow \rho\pi$ decays. The $\pi/K/p$ separation is displayed in a β vs.momentum scatter plot in Fig. 3.

The shower counter system consists of a barrel[4] and two endcaps.[5] The entire system is placed *inside* the magnet coil to improve the low energy gamma detection efficiency. The total angular coverage is 94% of 4π. The shower counter is a gas proportional tube lead sandwich system with a single anode wire in a grounded cathode cell. Each anode wire is a high resistance stainless steel wire which is read out with an ADC on each end to measure energy deposition and position along the wire. The energy resolution on electrons is $\sigma_E/E = 17\%/\sqrt{E}$, E in GeV, the ϕ angular resolution (σ) is 6 mr on Bhabhas and the position resolution (σ) per cell is 1% of the full wire length (337 cm).

Muon tubes mounted parallel to the beam axis (z-axis) on the exterior of the magnet cover 64% of 4π. They are composed of two double sets of proportional tubes separated by 12.5 cm of steel plate. The ϕ position of the track is determined by hits in two overlapping tubes and the z-position by charge division on the stainless steel anode wire. The resolution in z is 1% of the full wire length. The muon tube position resolution is limited by multiple scattering in the magnet steel.

The trigger system[6] utilizes hit patterns in layers 1, 3 and 5 to define drift chamber tracks. The number of drift chamber tracks required to trigger is selectable by computer control. The actual data taking trigger required 1 drift chamber track and 1 TOF hit, or 2 drift chamber tracks. The event rate at the J/ψ was $\sim$3 Hz and the real hadronic rate was slightly less then 1 Hz.

3. Performance Checks

The detector is studied with a variety of well known J/ψ decays. The basic analysis technique is to kinematically fit events using the four constraints of energy and momentum conservation (4-C fit). Kinematic fitting substantially improves the energy resolution for the γ's, and has been successfully applied to events with up to five γ's and four charged tracks. If the decay includes a π^0 or

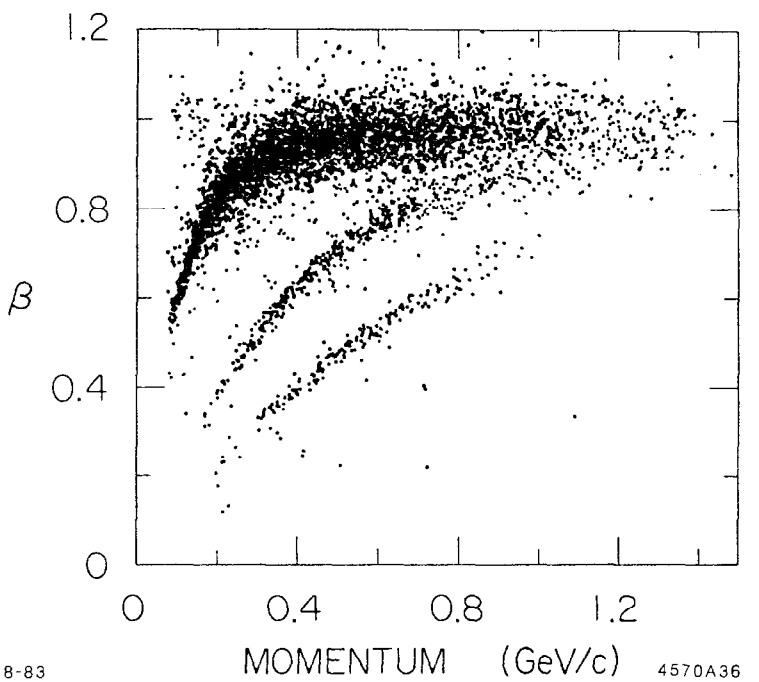


Fig. 3. Scatter plot of β versus momentum (GeV).

an η, then an additional mass constraint can be applied to the $\gamma\gamma$ system (5-C). One difficulty is the presence of spurious photons, which are due to hadronic interactions of charged particles in the shower counter. These can be removed by ignoring showers near charged tracks. TOF identification is required when topologies include kaons or protons.

The reaction $J/\psi \to \pi^+\pi^-\pi^0$ is studied with high statistics. The events are subjected to a 4-C fit to the hypothesis $J/\psi \to \gamma\gamma\pi^+\pi^-$ resulting in 22k events. A typical event is shown in Fig. 4. The Dalitz plot in Fig. 5 shows clear $\rho^0\pi^0$, $\rho^+\pi^-$, and $\rho^-\pi^+$ bands. The charged and neutral ρ mass plots are shown in Figs. 6(a), (b) and (c). The efficiency determined from a Monte Carlo simulation is 48%. The observed branching ratio, BR($J/\psi \to \pi^+\pi^-\pi^0$) $=(1.49\pm.22)\times10^{-2}$, is in agreement with Particle Data Table[7] values. The ratio of the $\rho\pi$ rates is BR($J/\psi \to \rho^0\pi^0$)/ BR($J/\psi \to \rho^\pm\pi^\mp$) $=.496\pm.04$, which is expected if the J/ψ has isospin 0.

The reaction $J/\psi \to \rho^0\pi^0$ is very useful to study the shower counter γ detection efficiency and the $\gamma\gamma$ mass resolution. The π^0 from this decay is produced essentially monochromatically at 1.45 GeV, and the γ's from these decays have an energy spectrum in the LAB frame that is flat from nearly 0 to 1.45 GeV. The energy spectrum (LAB) and $\cos\theta_\gamma$ (π^0 CMS) are plotted in Fig. 7. The angular distribution is flat as expected for spin 0 decays except at $\cos\theta_\gamma=\pm1$. Those two regions correspond to the γ's moving parallel and antiparallel to the π^0 direction. In the LAB frame the forward going γ has most of the π^0 momentum whereas the other γ has very low momentum. The energy distribution is flat to 100 MeV and falls to 50% at 50 MeV. This decay also allows a study of the $\gamma\gamma$ mass resolution. Figs. 8(a) and (b) are the reconstructed masses of the π^0 using the 4-C fitted energies and raw shower energies respectively. The mass resolution is a factor of three better with the 4-C fitted energies than with the raw shower energies.

The decay $J/\psi \to \gamma\eta'$ is studied in two decay modes, $\eta' \to \gamma\rho^0$ and $\eta' \to \eta\pi^+\pi^-(\eta \to \gamma\gamma)$. In the first mode a 4-C kinematic fit to $J/\psi \to \gamma\gamma\pi^+\pi^-$ is applied. Further cuts of mass($\gamma\gamma$)>200 MeV, to remove $\rho\pi$ background, and .425<mass($\pi^+\pi^-$)<.925 MeV, to select events with ρ^0's, are applied. The re-

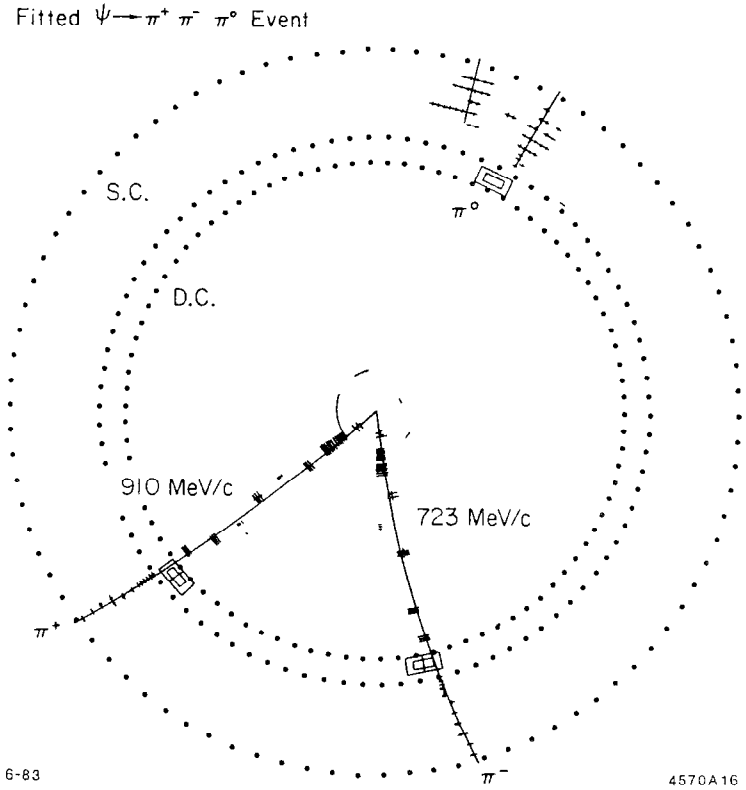


Fig. 4. $J/\psi \to \pi^+\pi^-\pi^0$ event display.

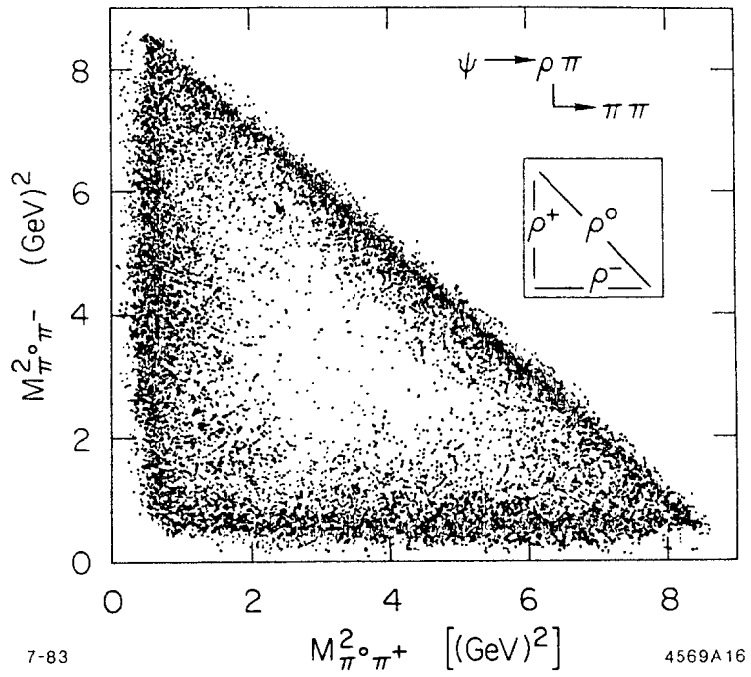


Fig. 5. Dalitz plot $mass^2_{\pi^+\pi^0}$ versus $mass^2_{\pi^-\pi^0}$ from $J/\psi \rightarrow \pi^+\pi^-\pi^0$. The schematic drawing displays the bands of the ρ decay modes.

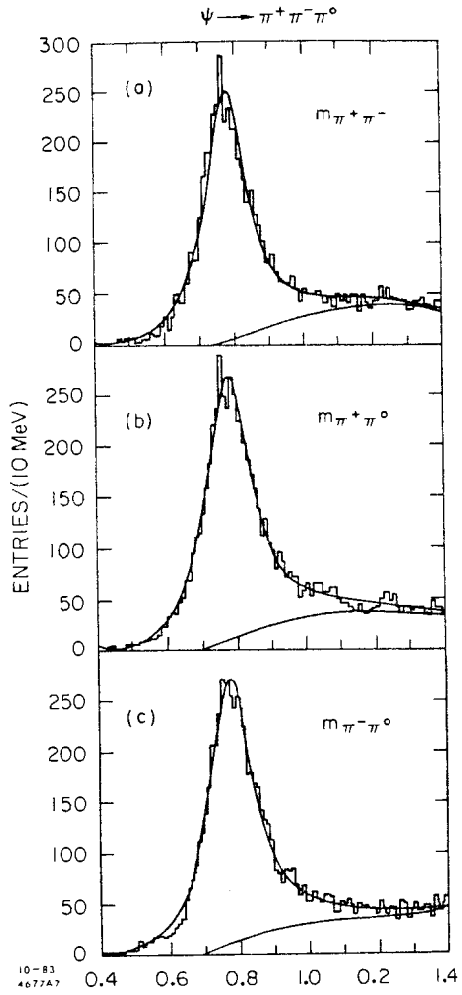


Fig. 6. (a)$Mass_{\pi^+\pi^-}$ (GeV) distribution from $J/\psi \rightarrow \pi^+\pi^-\pi^0$ drawn with a fit of a Breit-Wigner curve. (b)$Mass_{\pi^-\pi^0}$ (GeV) distribution from $J/\psi \rightarrow \pi^+\pi^-\pi^0$ drawn with a fit of a Breit-Wigner curve. (c)$Mass_{\pi^+\pi^0}$ (GeV) distribution from $J/\psi \rightarrow \pi^+\pi^-\pi^0$ drawn with a fit of a Breit-Wigner curve.

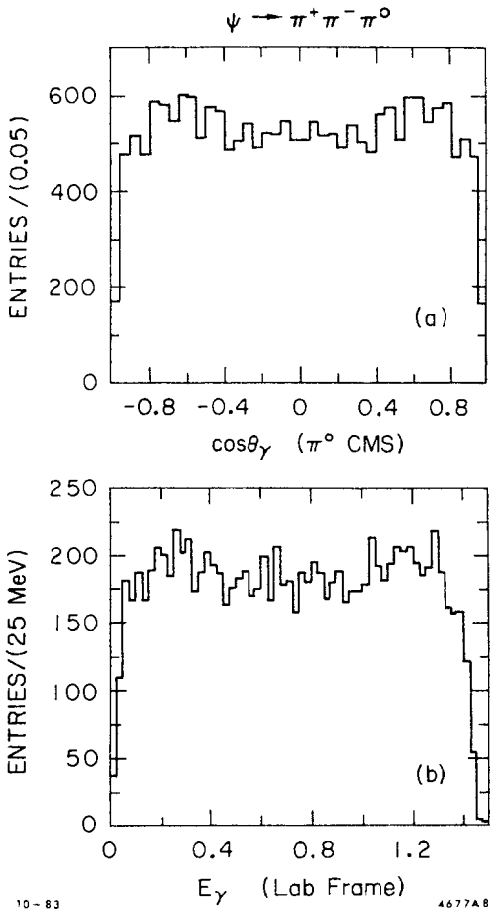


Fig. 7. (a) $\text{Cos}\theta_\gamma$ distribution in the π^0 CMS from $J/\psi \rightarrow \rho^0\pi^0$. (b)$\gamma$ energy (GeV) distribution in the LAB frame from the 1.45 GeV π^0 from $J/\psi \rightarrow \rho^0\pi^0$.

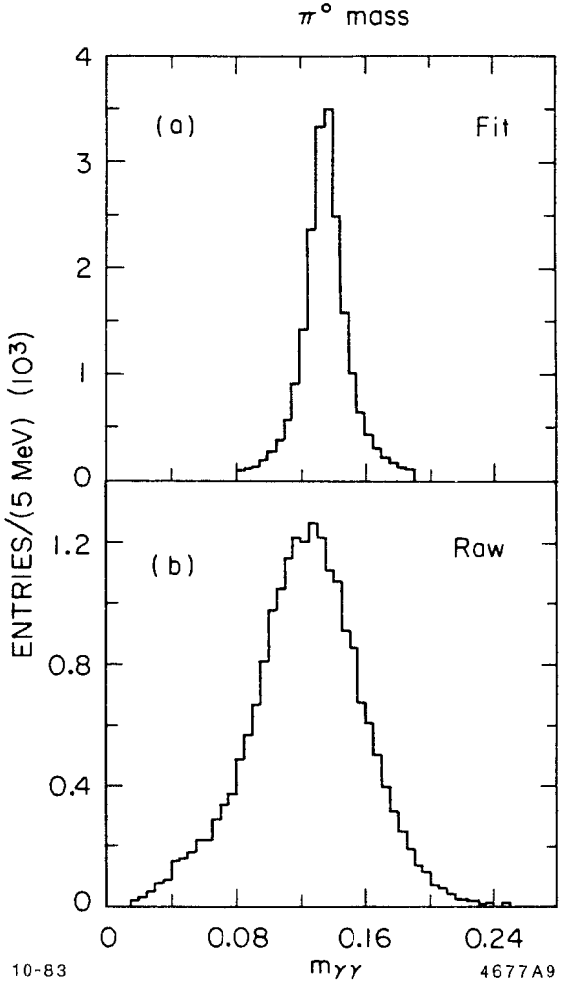


Fig. 8. (a)Reconstructed π^0 mass distribution using 4-C fitted γ energies. (b) Reconstructed π^0 mass distribution using raw shower counter energies.

sulting $\gamma\pi^+\pi^-$ mass distribution is shown in Fig. 9(a). The fitted mean is 957±.5 MeV and the mass resolution (σ) is 9±.4 MeV. In the second decay mode a kinematic 4-C fit to $J/\psi \to \gamma\gamma\gamma\pi^+\pi^-$ and a 5-C fit to $J/\psi \to \gamma\eta\pi^+\pi^-$ are applied. The resulting mass($\gamma\gamma\pi^+\pi^-$) distribution from the 5-C fits is shown in Fig. 9(b). The mean mass is 958±.3 MeV and the mass resolution (σ) is 5.7 MeV. The branching ratio is BR($J/\psi \to \gamma\eta'$) = (4.6 ± .42(statistical) ± .65(systematic)) × 10^{-3}. Both branching ratios are in reasonable agreement with the Particle Data Table[8] value of BR($J/\psi \to \gamma\eta'$) =(3.6 ± 0.5) × 10^{-3}.

These results demonstate that the MARK III detector performs very well detecting and reconstructing radiative decays. The efficiency for low energy γ detection is very high. The mass resolution (σ) achieved with constraint fitting is 8 MeV for π^0's in $\rho\pi$ decays, 9 MeV for the η' in the $\gamma\rho$ mode and 5.7 MeV in the $\eta\pi^+\pi^-$ mode. The mass scale agrees to within 1 MeV with nominal values. The measured branching ratios agree with published values, showing that the luminosity and the Monte Carlo simulation are understood.

4. η_c Results

Experimental Situation

The Crystal Ball experiment at SPEAR first observed the η_c in the inclusive γ spectrum in J/ψ and ψ' decays,[9] and obtained the following results,

$$\text{m}=2984\pm4 \text{ MeV} \quad ,$$
$$\Gamma=12.4\pm4.1 \text{ MeV} \quad ,$$
$$\text{BR}(J/\psi \to \gamma\eta_c)=(1.27\pm.36)\times 10^{-2} \quad .$$

The observed hadronic modes of the η_c have been rather sparse. In the J/ψ radiative decays, where the radiative γ energy is low (E_γ=112 MeV), the Crystal Ball[10] observed 18±6 events in the mode $\eta_c \to \eta\pi^+\pi^-$. In the ψ' radiative decays, the MARK II observed 3 events in the mode $\eta_c \to p\bar{p}$, 8 events in the mode $\eta_c \to \pi^\pm K^\mp K_S$ and by combining these modes with other hadronic modes a signal of about 25 events was obtained.[11] There has been no spin-parity determination for the η_c.

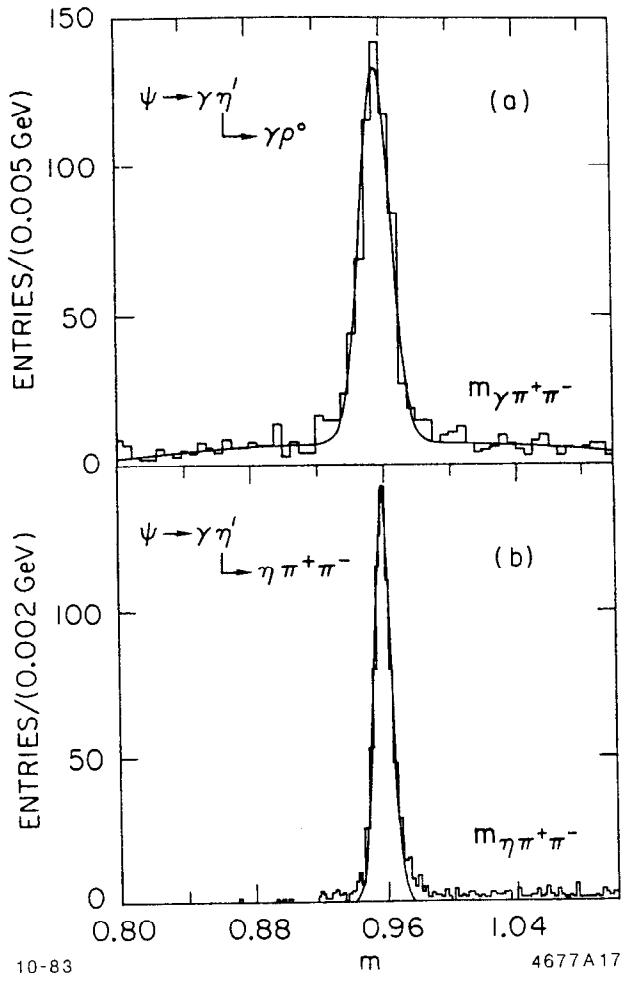


Fig. 9. (a)$Mass_{\gamma\rho^0}$ (GeV) distribution from $J/\psi \to \gamma\gamma\rho^0$. (b)$Mass_{\eta\pi^+\pi^-}$ (GeV) distribution from $J/\psi \to \gamma\eta\pi^+\pi^-$.

MARK III Results

Three η_c decay modes from J/ψ radiative decays will be presented, $J/\psi \rightarrow \gamma p\bar{p}$, $J/\psi \rightarrow \gamma\eta\pi^+\pi^-$, and $J/\psi \rightarrow \gamma\phi\phi$. Other modes will appear in future publications.

In the $p\bar{p}$ mode the analysis requires TOF identification followed by 4-C fits to the hypotheses $J/\psi \rightarrow \gamma p\bar{p}$ and $J/\psi \rightarrow \gamma\gamma p\bar{p}$. To remove spurious γ's caused by hadronic interactions of the charged tracks in the shower counter, γ's close to the p's and $\bar{p}$'s are excluded. Often the $\bar{p}$'s annihilate and produce a large amount of background. Figure 10 is a typical event of $J/\psi \rightarrow \gamma p\bar{p}$. An important background is $J/\psi \rightarrow \pi^0 p\bar{p}$. This is removed by excluding events that fit to $J/\psi \rightarrow \gamma\gamma p\bar{p}$ with $m_{\gamma\gamma} \approx m_{\pi^0}$. After these preliminary cuts the η_c signal appears just below a large feed through of $J/\psi \rightarrow p\bar{p}$. This background is removed with a collinearity cut between the p and the $\bar{p}$. The resulting mass plot is shown in Fig. 11. The branching ratio obtained is $BR(J/\psi \rightarrow \gamma\eta_c) \times BR(\eta_c \rightarrow p\bar{p}) = (2.2 \pm .6 \pm .5) \times 10^{-5}$. Using the Crystal Ball inclusive rate, $BR(J/\psi \rightarrow \gamma\eta_c)$=$(1.27 \pm .36) \times 10^{-5}$, the η_c branching ratio becomes $BR(\eta_c \rightarrow p\bar{p}) = (.18 \pm .09) \times 10^{-2}$. This is very close to the rate observed for the direct decay $J/\psi \rightarrow p\bar{p}$.[12]

The mode $\eta_c \rightarrow \eta\pi^+\pi^-$ is observed with a large signal. The events are fit to $J/\psi \rightarrow \gamma\gamma\gamma\pi^+\pi^-$ and $J/\psi \rightarrow \gamma\eta\pi^+\pi^-$. The mass$(\eta\pi^+\pi^-)$ distribution is shown in Fig. 12. The fitted mass is 2.967±.004(fit)±.01(systematic) MeV. The mass resolution (σ) is 20 MeV, which is consistent with the detector resolution as determined by Monte Carlo simulation. The measured branching ratio is $BR(J/\psi \rightarrow \gamma\eta_c) \times BR(\eta_c \rightarrow \eta\pi^+\pi^-) = [4.3 \pm .7(stat) \pm 1.3(sys)] \times 10^{-4}$.

The mode $\eta_c \rightarrow \phi\phi$ is observed via the ϕ decay to K^+K^-. Figure 13 shows a typical event. The initial data selection required 4 charged prongs with total charge zero and TOF identification for at least one K in each oppositely charged pair. After requiring that there is one ϕ, it is seen that the other recoiling K^+K^-pair also forms a ϕ as shown in Fig. 14(a). Requiring that both K^+K^- pairs are ϕ's and then looking at the quantity E_{miss} (missing energy from the two ϕ's)-P_{miss} (missing momentum from the two ϕ's) as shown in Fig. 14(b), it is

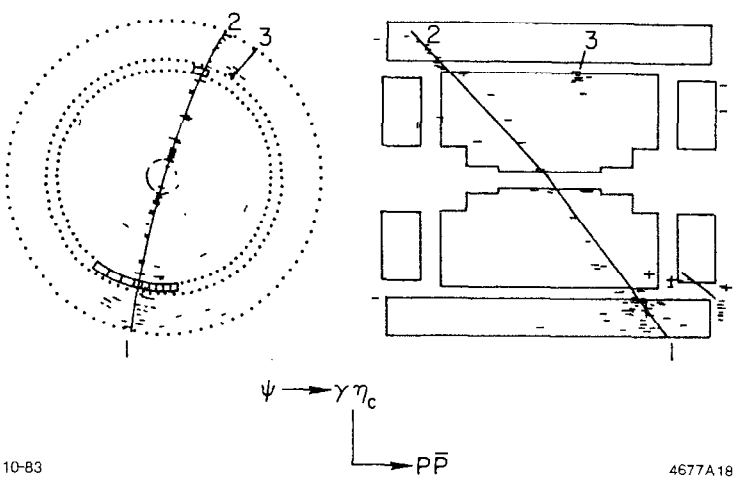


Fig. 10. $J/\psi \rightarrow \gamma p\bar{p}$ event display.

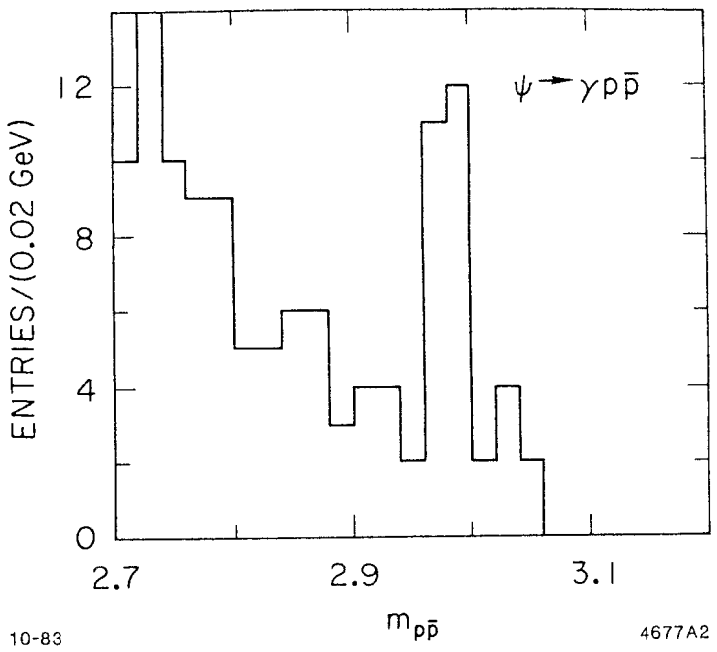


Fig. 11. $Mass_{p\bar{p}}$ (GeV) distribution after the collinearity cut from $J/\psi \rightarrow \gamma p\bar{p}$.

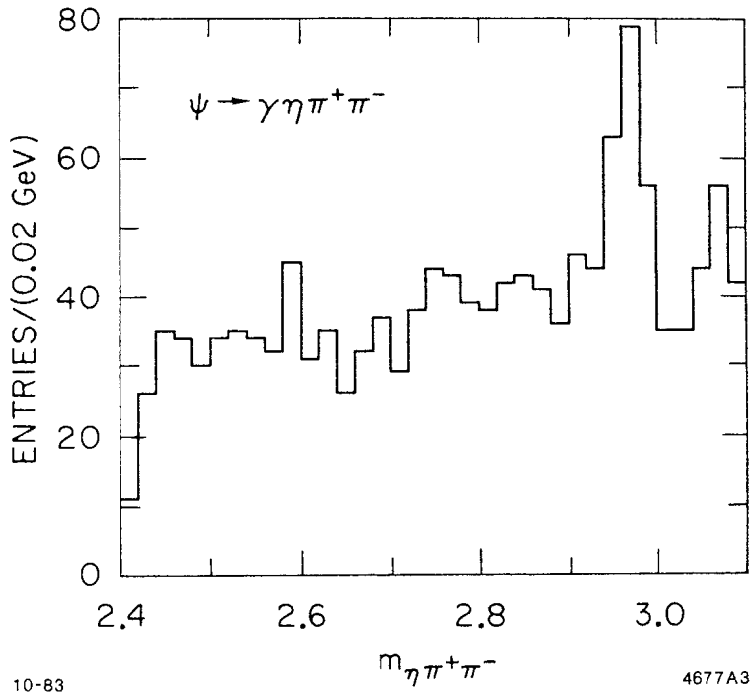


Fig. 12. $Mass_{\eta\pi^+\pi^-}$ (GeV) distribution from $J/\psi \rightarrow \gamma\eta\pi^+\pi^-$.

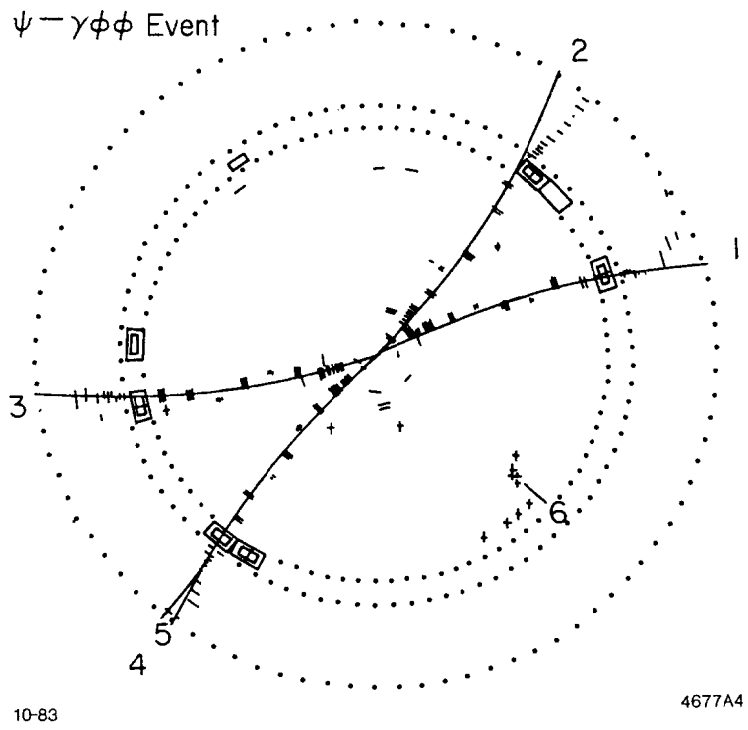


Fig. 13. $J/\psi \to \gamma\phi\phi$ event display.

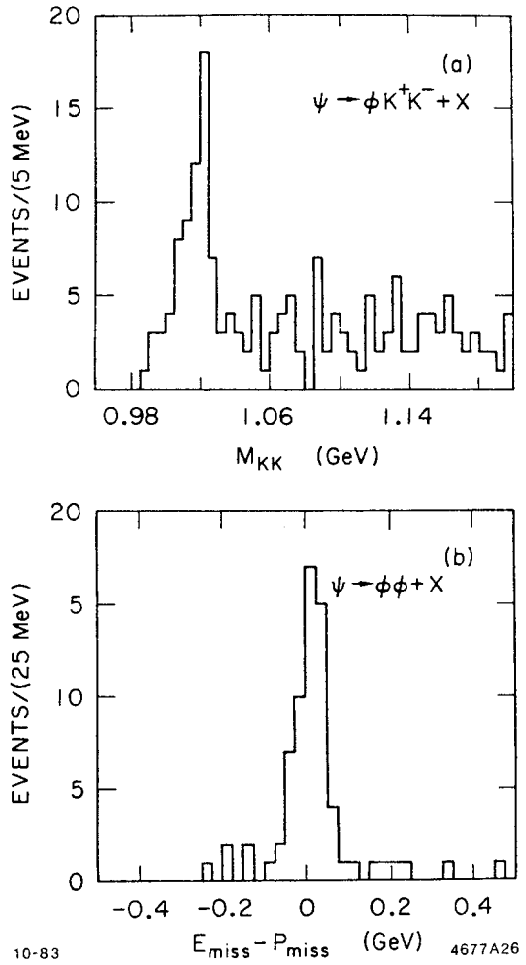


Fig. 14. (a)$Mass_{K^+K^-}$ (GeV) distribution recoiling against a ϕ. (b)E_{miss}-P_{miss} (GeV) from the $\phi\phi$.

seen that the recoiling mass against the $\phi\phi$ system could only be a γ. It should be noted that neither $J/\psi \rightarrow \pi^0\phi\phi$ nor $J/\psi \rightarrow \phi\phi$ is allowed by charge conjugation invariance. The events are 4-C fit to $J/\psi \rightarrow \gamma K^+K^-K^+K^-$ and the resulting $\phi\phi$ mass is shown in Fig. 15. A clear signal is observed at the η_c mass. The efficiency of detecting $J/\psi \rightarrow \gamma\phi\phi$ as a function of $\phi\phi$ mass is also shown in Fig. 15. The branching ratio for the η_c is $BR(J/\psi \rightarrow \gamma\eta_c) \times BR(\eta_c \rightarrow \phi\phi) = (1.24 \pm .32) \times 10^{-4}$. The fitted mass is 2.978 GeV and its width is consistent with the detector resolution. Due to kaon decays, the efficiency rapidly decreases to a few percent in the mass region near 2 Gev. Therefore it is difficult to determine if there is any structure in the region near 2 GeV.

The decay angles in the $\phi\phi$ mode allow a definitive η_c spin-parity determination.[13–14] This test is analogous to the π^0 spin-parity analysis[15] from the reaction $\pi^0 \rightarrow e^+e^-e^+e^-$. The useful decay angles (actually there are seven) are Θ_γ, the angle between the radiative γ and the e^+e^- beam direction in the LAB frame, Θ_ϕ, the angle between the η_c and one ϕ in the η_c CMS frame, Θ_{K+}, the angle between the ϕ and the K^+ in the ϕ CMS frame, and χ, the angle between the decay planes of the ϕ's in the η_c CMS frame. These decay angles are plotted in Figs. 16, 17, 18 and 19. The lines show what is expected for $J^P{=}0^-$. The angles χ and Θ_{K+} are most sensitive for likelihood tests of J^P and are independent of the initial polarization of the η_c. The event distributions are proportional to $1 + \beta \times cos(2\chi)$ and $1 + \varsigma \times P_2(\Theta_{K+})$, where β and ς depend on the J^P, and P_2 is the Legendre polynomial. The likelihood ratios for different J^P's relative to 0^-, assuming lowest l values, are summarized in Table 1.

$J^P{=}0^-$ is preferred overall as expected. This is the first spin-parity determination of the η_c. A more complete analysis will include a simultaneous fit to all the decay angles.

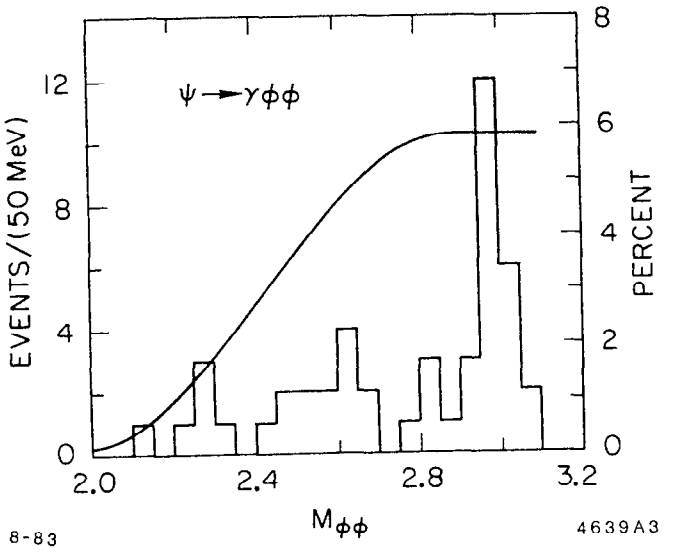


Fig. 15. $Mass_{\phi\phi}$ (GeV) distribution from $J/\psi \rightarrow \gamma\phi\phi$ with the mass acceptance overplotted.

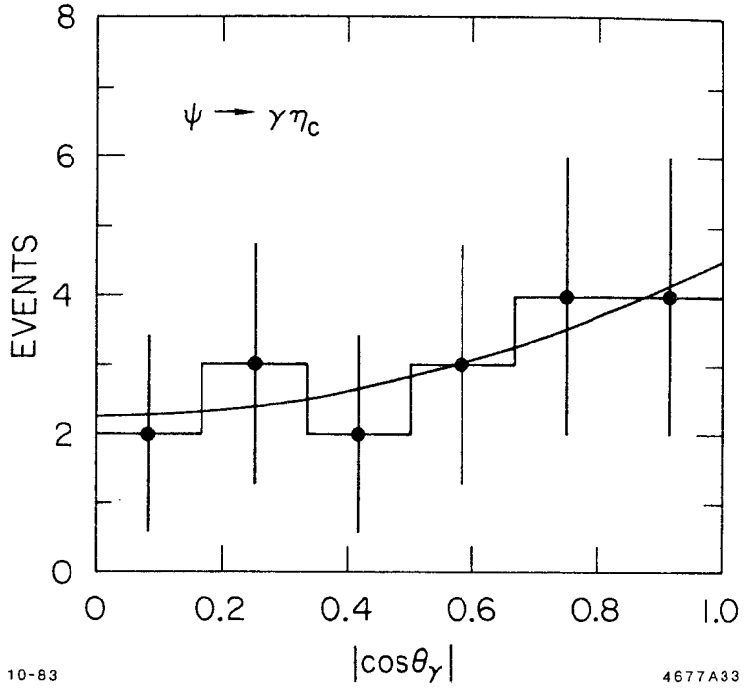


Fig. 16. Cosθ_γ in $J/\psi \rightarrow \gamma\phi\phi$ decays. The curve is the expected distribution for $J^P=0^-$.

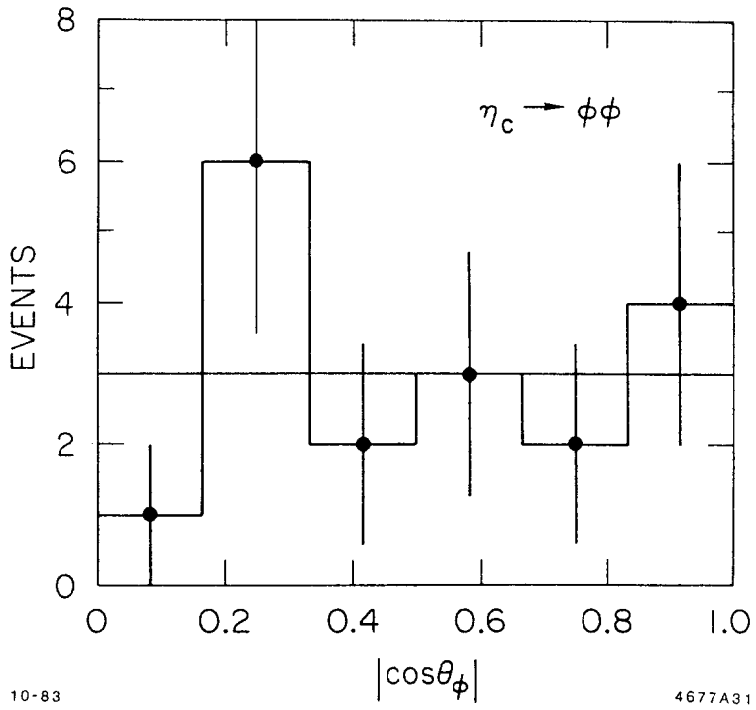


Fig. 17. Cosθ_ϕ in $J/\psi \rightarrow \gamma\phi\phi$ decays. The curve is the expected distribution for $J^P=0^-$.

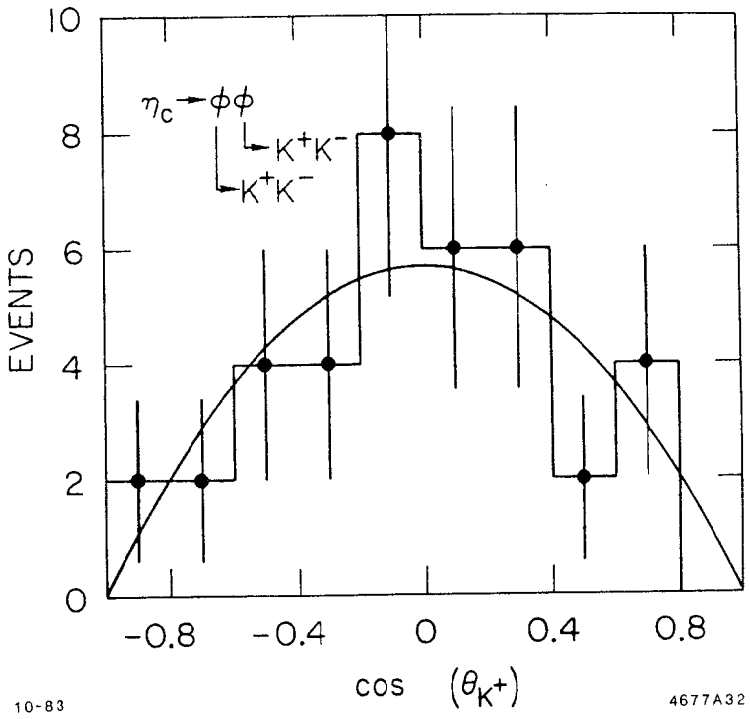


Fig. 18. $\text{Cos}\theta_{K^+}$ in $J/\psi \to \gamma\phi\phi$ decays. The curve is the expected distribution for $J^P=0^-$.

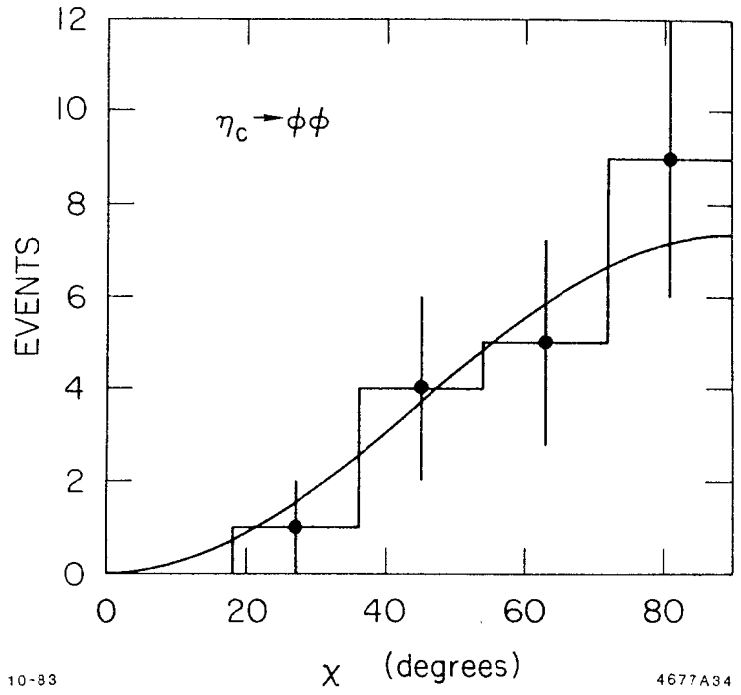


Fig. 19. χ angle in $J/\psi \to \gamma\phi\phi$ decays. The curve is the expected distribution for $J^P=0^-$.

Table 1. Likelihood Ratios for β and ς Tests

J^P	Likelihood Ratio of 0^- to J^P for β	Likelihood Ratio of 0^- to J^P for ς
odd$^\pm$	1100	47
0^+	$>10^8$	7.7
2^-	35	5.7
2^+	2400	7.7

5. J/ψ Radiative Results

Physics Interest

Recently there has been much interest in J/ψ radiative decays. Quantum chromodynamics (QCD) allows the existence of bound states of gluons or glueballs and the J/ψ radiative decays appear to be an ideal place to look for such states.[16] QCD predicts a large branching ratio for radiative decays by comparing the calculated rates between $J/\psi \rightarrow \gamma gg$ and $J/\psi \rightarrow ggg$.[17-19] The calculation predicts,

$$\Gamma(J/\psi \rightarrow \gamma + \text{hadrons})/\Gamma(J/\psi \rightarrow \text{hadrons}) \approx 10\% \quad .$$

The known measured decays total $\sim$1%. Consequently, if QCD is correct there should be a large number of J/ψ radiative decays via 2 gluons which have not yet been seen. If there are bound states of 2 gluons they should be isoscalar SU(3) singlets with even C-parity. There are many models that predict glueball masses in the 1-2 GeV region and it is possible that their widths are narrow. The mass spectrum may be very complicated due to mixing with other $q\bar{q}$ states. There may also be more complex bound states of $gq\bar{q}$,[20-21] or $q\bar{q}q\bar{q}$.[22] The thrust of this discussion is that any new states found in radiative J/ψ decays are of considerable interest.

Experimental Situation

Recently observed states in radiative decays are $\iota \rightarrow K\bar{K}\pi$[23-24] ,$\Theta \rightarrow K\bar{K}$[25] and $\eta\eta$,[26] and structures near 1700 MeV in $\eta\pi\pi$[27] and $\rho^0\rho^0$ [28] .

In the $K\bar{K}\pi$ channel the iota has been observed to have a very large branching ratio and Crystal Ball determined that the iota decays mainly via $\delta\pi$ and its spin-parity is 0^-. Various mixing models have predicted that in analogy to η', the iota should have a large $\gamma\rho^0$ decay mode.

In the $\eta\eta$ channel Crystal Ball first observed the Θ but did not clearly separate the state from the f'(1515). They did a maximum likelihood test on the spin-parity of the Θ and found that J^P=2^+ is favored over 0^+. If the Θ is a glueball there are predictions that it should be an SU(3) singlet and should decay to $\pi\pi$.

In the $\eta\pi\pi$ channel Crystal Ball found a broad structure around 1.7 GeV but set a limit on $\iota \rightarrow \eta\pi\pi$. This may be in conflict with the previous observation that the iota decays to $\delta\pi$, because the δ also decays to $\eta\pi$.

MARK III Results

MARK III has studied a large number of radiative decays. The preliminary results on the following decays will be shown: $J/\psi \rightarrow \gamma\pi^+\pi^-$, γK^+K^-, $\gamma\pi^0K_SK_S$, $\gamma\pi^\pm K^\mp K_S$, $\gamma\pi^0K^+K^-$, $\gamma\gamma\rho^0$, and $\gamma\eta\pi^+\pi^-$.

The decay mode to $\gamma\pi^+\pi^-$ is studied by applying a 4-C fit to $J/\psi \rightarrow \gamma\pi^+\pi^-$ and removing μ-pairs and radiative Bhabha ($J/\psi \rightarrow \gamma e^+e^-$) events. The resulting mass($\pi^+\pi^-$) distribution is shown in Fig. 20. The f(1270) is clearly seen and feed-through of $\rho\pi$ decays appears below 800 MeV. This feed-through occurs when one of the two γ's from the π^0 in the $\rho\pi$ decays is not detected and the reaction is incorrectly fitted to $J/\psi \rightarrow \gamma\pi^+\pi^-$. There are possible hints of structure above the f(1270) but further analysis is required to remove more background. The Dalitz plot in Fig. 21 shows the f(1270) band and the outline of the $\rho\pi$ feed-through. The f(1270) peak is fitted with a nonrelativistic Breit-

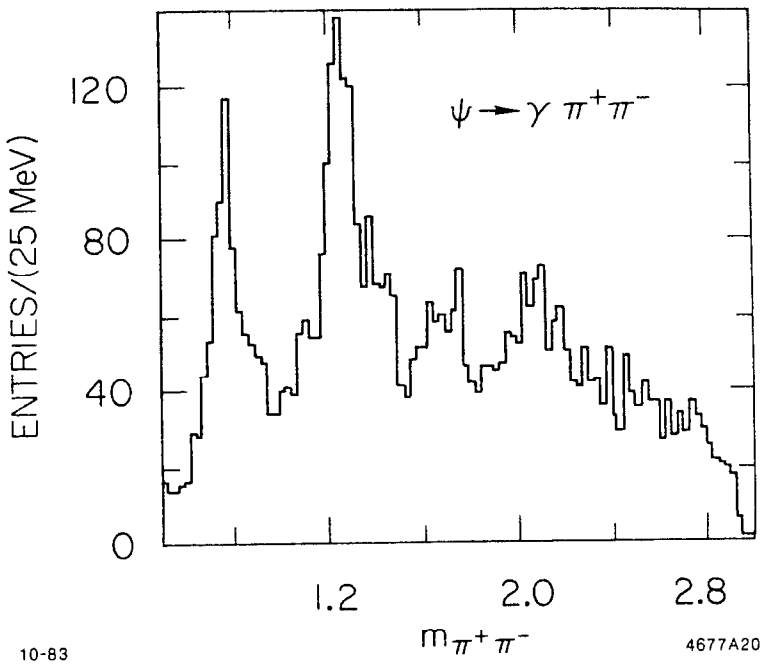


Fig. 20. $Mass_{\pi^+\pi^-}$ (GeV) distribution from $J/\psi \rightarrow \gamma\pi^+\pi^-$.

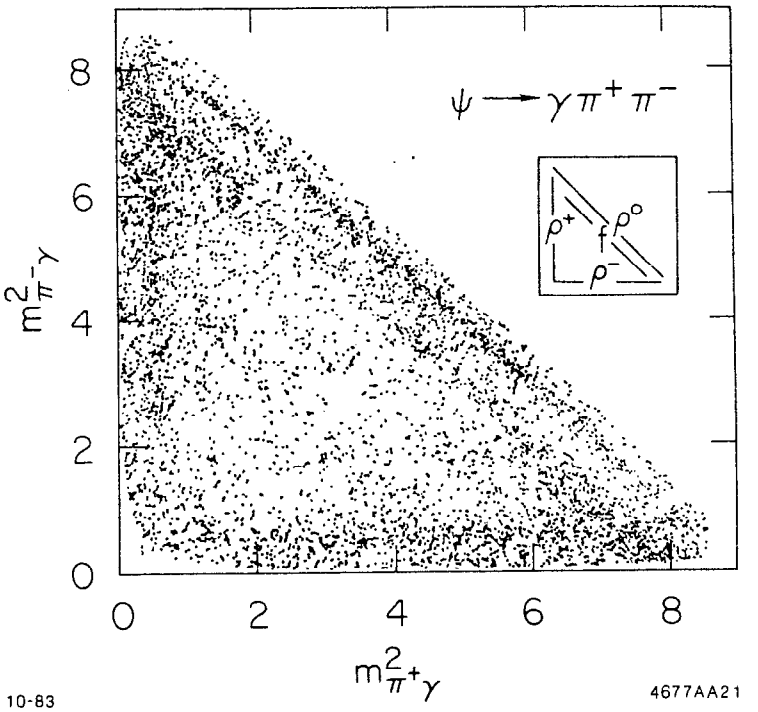


Fig. 21. Dalitz plot $mass^2_{\pi^+\gamma}$ versus $mass^2_{\pi^-\gamma}$ from $J/\psi \rightarrow \gamma\pi^+\pi^-$. The schematic drawing displays the bands of the f decays and the ρ background.

Wigner curve and the measured values are,

$$m = 1278 \pm 5 \text{ MeV} \quad \text{and}$$
$$\Gamma = 155 \pm 15 \text{ MeV} \quad .$$

These are in agreement with Particle Data Table[29] values.

The decay mode $J/\psi \rightarrow \gamma K^+K^-$ is obtained by requiring 4-C fits and TOF indentification. The mass(K^+K^-) distribution is shown in Fig. 22. The Θ and f'(1515) are clearly separated and there is evidence for a new state at 2.2 GeV which hereafter will be named the ξ. The new state has a 7 standard deviation significance. The Dalitz plot shown in Fig. 23 shows diagonal bands corresponding to the three states. The states are also observed in the mode $J/\psi \rightarrow \gamma K_S K_S$ with lower statistics. Incoherent Breit-Wigner curves are simultaneously fit to the f'(1515), the Θ, and the new state, the ξ. In the fit the masses and the widths of the θ and the ξ are allowed to vary but those of the f'(1515) are held fixed. The results are,

$$m_\Theta = 1.719 \pm 6\text{GeV} \quad ,$$
$$\Gamma_\Theta = .117 \pm 23\text{GeV} \quad ,$$
$$m_\xi = 2.22 \pm .015(stat) \pm .02(sys)\text{GeV} \quad \text{and}$$
$$\Gamma_\xi = .03 \pm .015(stat) \pm .02(sys)\text{GeV} \quad .$$

The mass plot with the fitted curves is shown in Fig. 24. The ξ width appears to be narrow in the K^+K^- mode. To accurately determine the width, the detector resolution is being examined in both the $K^+K^-$and the K_SK_S decay modes. The branching ratios are,

$$\text{BR}(J/\psi \rightarrow \gamma f') \times \text{BR}(f' \rightarrow K^+K^-) = (1.6 \pm .3(stat) \pm .35(sys)) \times 10^{-4} \ ,$$
$$\text{BR}(J/\psi \rightarrow \gamma\Theta) \times \text{BR}(\Theta \rightarrow K^+K^-) = (4.8 \pm .7(stat) \pm .9(sys)) \times 10^{-4} \text{ and}$$
$$\text{BR}(J/\psi \rightarrow \gamma\xi) \times \text{BR}(\xi \rightarrow K^+K^-) = (8.0 \pm 2.0(stat) \pm 1.6(sys)) \times 10^{-5} \ .$$

The ι is observed in three modes, $\pi^0K^+K^-$, $\pi^\pm K^\mp K_S$, and for the first time in $\pi^0K_SK_S$. The mass plots are shown in Figs. 25(a), (b) and (c). Using

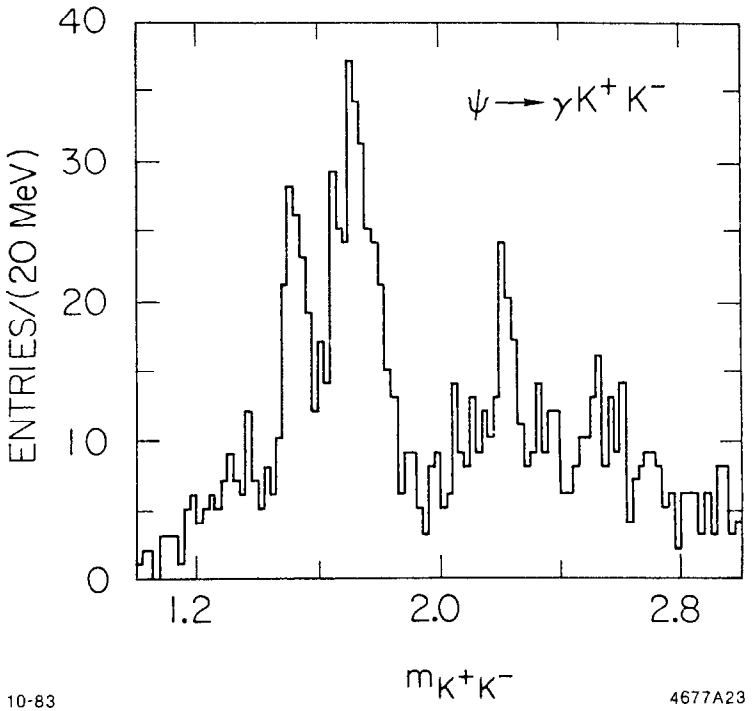


Fig. 22. $Mass_{K^+K^-}$ (GeV) distribution from $J/\psi \rightarrow \gamma K^+K^-$.

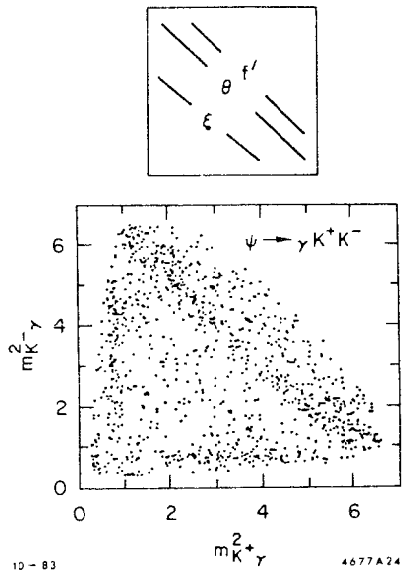


Fig. 23. Dalitz plot $mass^2_{K^+\gamma}$ versus $mass^2_{K^-\gamma}$ from $J/\psi \to \gamma K^+K^-$. The schematic drawing displays the bands of the $f'(1515)$, θ and ξ decays.

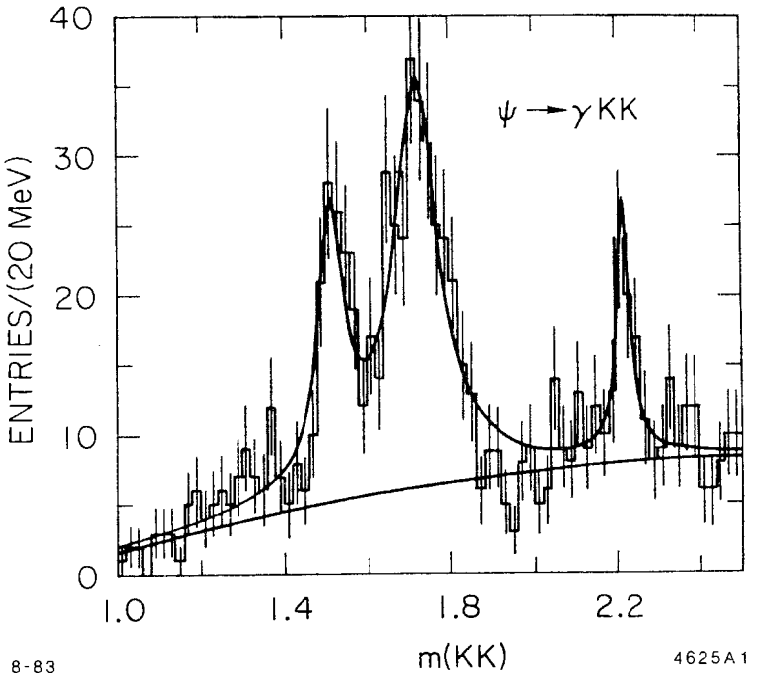


Fig. 24. $Mass_{K^+K^-}$ (GeV) distribution from $J/\psi \to \gamma K^+K^-$ drawn with a fit with three Breit-Wigner curves.

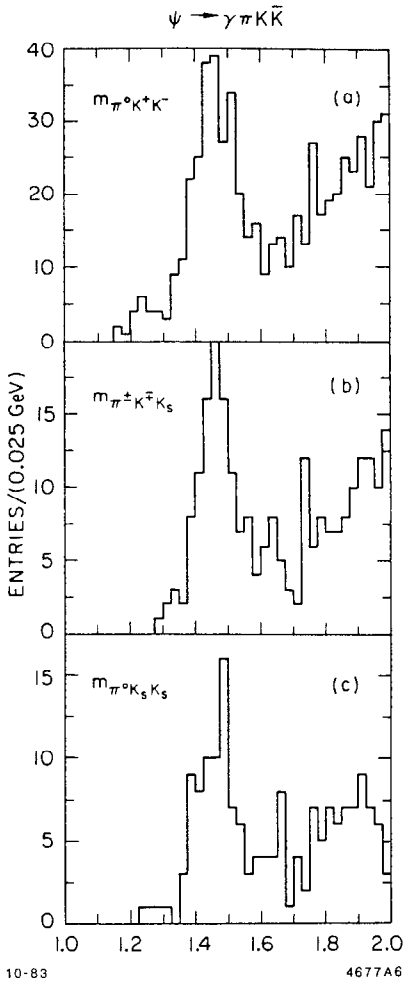


Fig. 25. (a)$Mass_{\pi^0K^+K^-}$ (GeV) distribution from $J/\psi \to \gamma\pi^0K^+K^-$. (b)$Mass_{\pi^\pm K^\mp K_S}$ (GeV) distribution from $J/\psi \to \gamma\pi^\pm K^\mp K_S$. (c)$Mass_{\pi^0K_SK_S}$ (GeV) distribution from $J/\psi \to \gamma\pi^0K_SK_S$.

the $\pi^0K^+K^-$ mode the following values are obtained from a Breit-Wigner fit to the ι,

$$m_\iota = 1.46 \pm .01 \text{ GeV} \quad ,$$
$$\Gamma_\iota = .097 \pm .025 \text{ GeV} \quad \text{and}$$
$$\text{BR}(J/\psi \to \gamma\iota) \times \text{BR}(\iota \to \pi^0K^+K^-) = [5.3 \pm .6(stat) \pm 1.9(sys)] \times 10^{-3} \quad .$$

The fit is shown in Fig. 26. The width is larger than the MARK II and Crystal Ball values because this analysis has no low mass cut on the K^+K^- mass. The branching ratios of the other modes are under study. All three branching ratios together will enable a check of the ι isospin.

The decay $J/\psi \to \gamma\gamma\rho^0$ is studied in the region above the η'. The events are 4-C fit to $J/\psi \to \gamma\gamma\pi^+\pi^-$. Figure 27 is a scatter plot of mass($\gamma_{low}\pi^+\pi^-$) versus mass($\pi^+\pi^-$). A large ρ^0 signal is observed in a band in the mass($\pi^+\pi^-$). For events with mass 1.2<mass($\gamma_{low}\pi^+\pi^-$)<1.6 GeV, the mass($\pi^+\pi^-$) is plotted in Fig. 27(b). The ρ^0 is clearly seen for events above the η'. Requiring the ρ^0 and removing $\rho\pi$ background, the resulting mass($\gamma_{low}\pi^+\pi^-$) distribution is shown in Fig. 28. The η' is off scale in the vertical scale of the plot. A wide structure above 1.4 GeV is clearly visible. Fitting two Breit-Wigner curves with one fixed at a mass of 1.275 GeV, the following values are obtained, mass=1.425 ± .014 GeV, $\Gamma = .112 \pm .067$ GeV, and BR[$J/\psi \to \gamma X(1.42)$] × BR[$X(1.42) \to \gamma\rho^0$]= $[7.4 \pm 2.2(stat) \pm 1.3(sys)] \times 10^{-5}$. The Breit-Wigner curve with a fixed mass at 1.275 GeV yields an upper limit for possible decays of f(1270)→ $\gamma\rho^0$ or η(1275)→ $\gamma\rho^0$ of 1.9×10^{-5} at 90% confidence level. Background investigations and a spin-parity analysis of this structure are currently in progress.

$J/\psi \to \gamma\eta\pi^+\pi^-$ is studied with 4-C and 5-C fits. After fitting to the 4-C hypothesis $J/\psi \to \gamma\gamma\gamma\pi^+\pi^-$, the scatter plot of mass($\gamma\gamma\pi^+\pi^-$) versus mass($\gamma\gamma$) is plotted in Fig. 29 with 3 entries per event. π^0 and η vertical bands are observed. In Figs. 30(a) and (b) the $\gamma\gamma$ mass is plotted. The π^0 and η mass peaks are clearly observed. Cutting on the η peak, .475<mass($\gamma\gamma$)<.625, the mass($\gamma\gamma\pi^+\pi^-$) is plotted in Fig. 31(a). Cutting off the η peak, .4 < mass($\gamma\gamma$) <

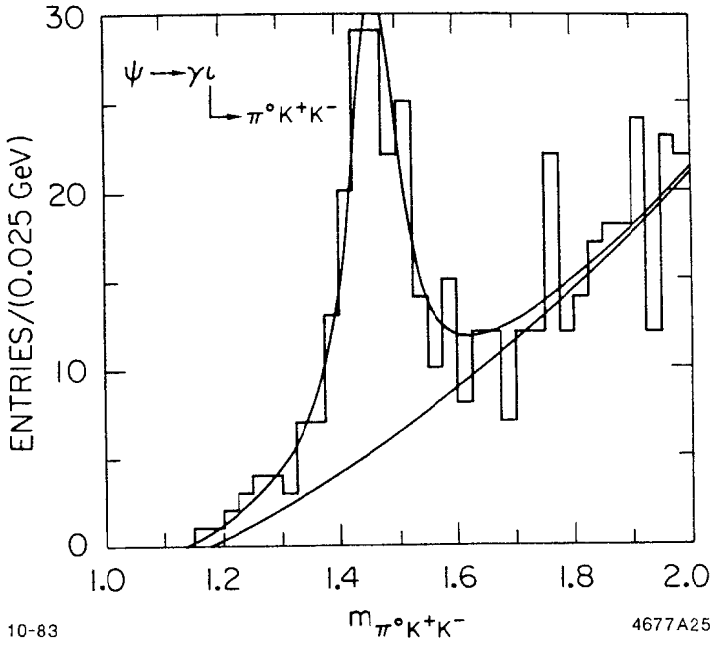


Fig. 26. $Mass_{\pi^0K^+K^-}$ (GeV) distribution fitted to a Breit-Wigner curve from $J/\psi \to \gamma\pi^0K^+K^-$

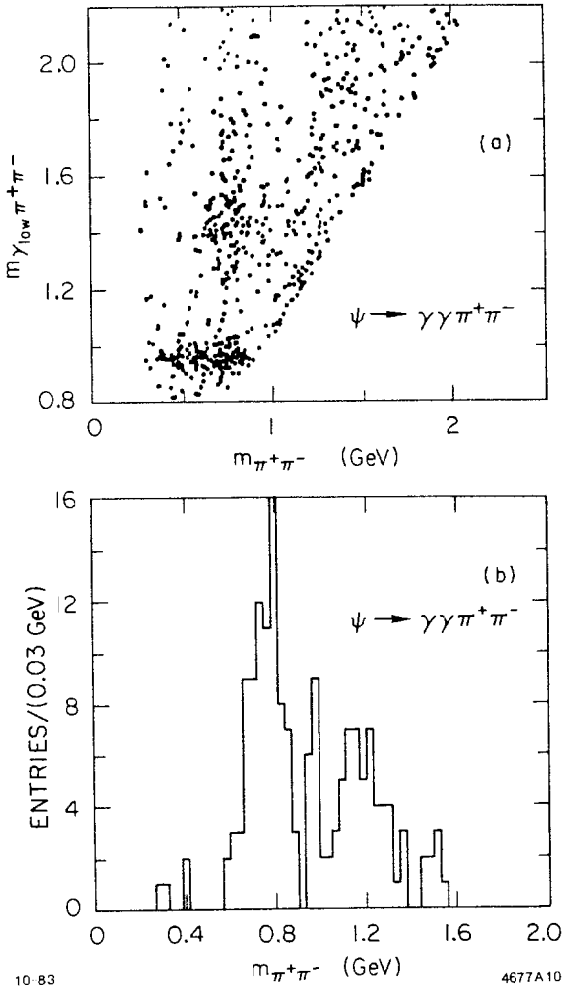


Fig. 27. (a)Scatter plot of $mass_{\gamma\pi^+\pi^-}$ versus $mass_{\pi^+\pi^-}$ from events that fit to $J/\psi \to \gamma\gamma\pi^+\pi^-$. (b)$Mass_{\pi^+\pi^-}$ projection of above plot for events satisfying $1.2 < mass_{\gamma_{low}\pi^+\pi^-} < 1.6$ GeV.

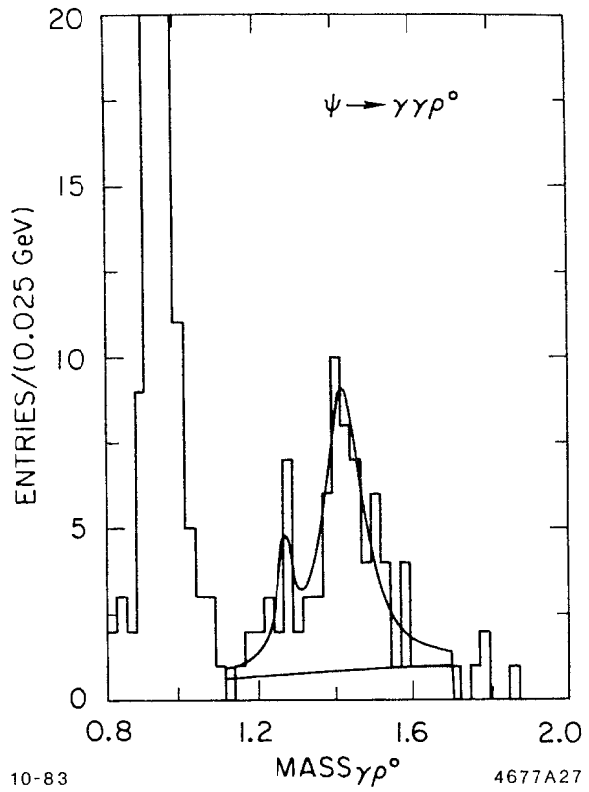


Fig. 28. Mass$_{\gamma\rho^0}$ (GeV) distribution after requiring that the $\pi^+\pi^-$ are from ρ^0 decays. The line is a fit with two Breit-Wigner curves.

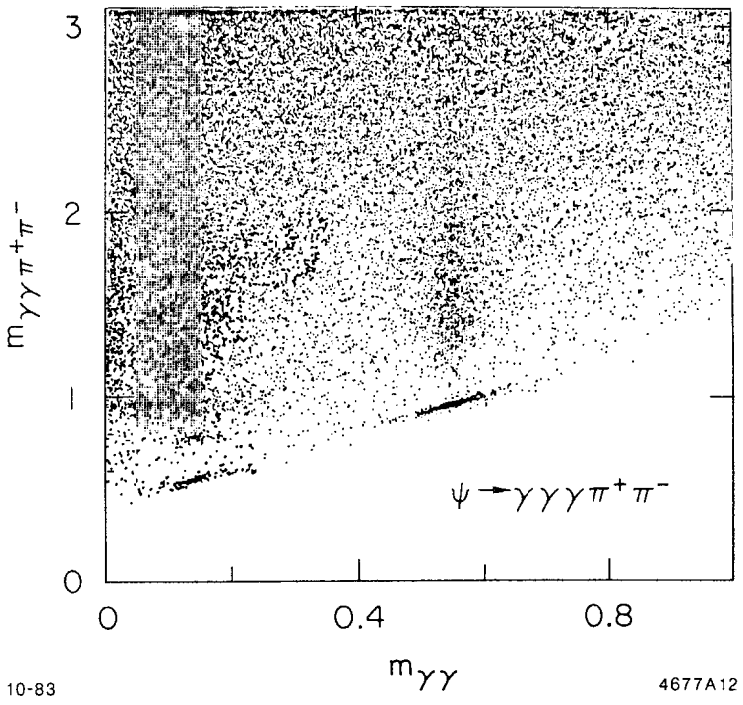


Fig. 29. *Mass*$_{\gamma\gamma}$ versus *Mass*$_{\gamma\gamma\pi^+\pi^-}$ of events that fit to $J/\psi \rightarrow \gamma\gamma\gamma\pi^+\pi^-$. There are three entries per event.

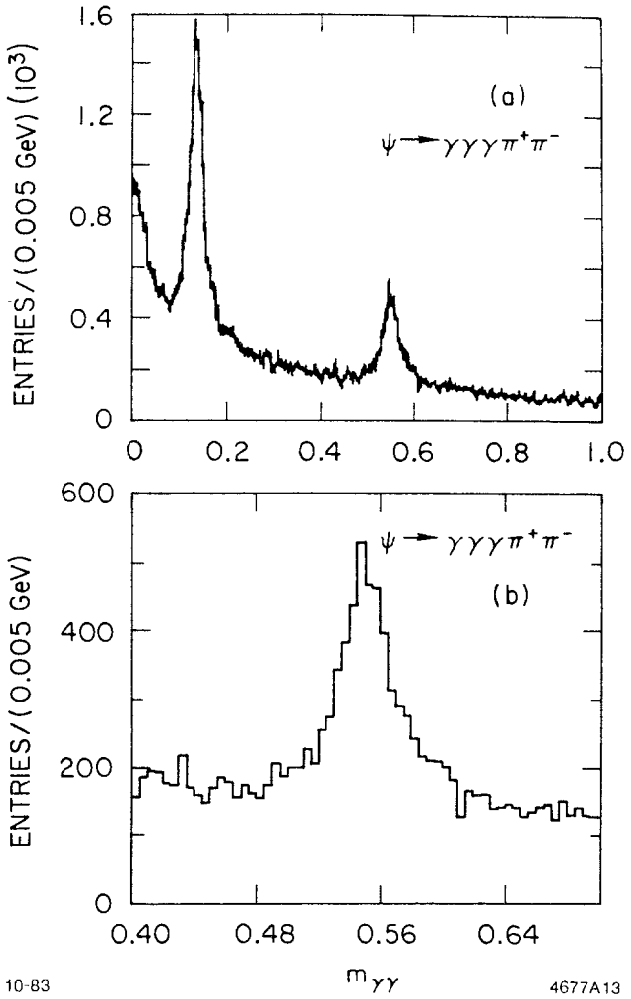


Fig. 30. (a)$Mass_{\gamma\gamma}$ (GeV) distribution from 0 to 1 GeV. (b)$Mass_{\gamma\gamma}$ (GeV) distribution from .4 to .7 GeV.

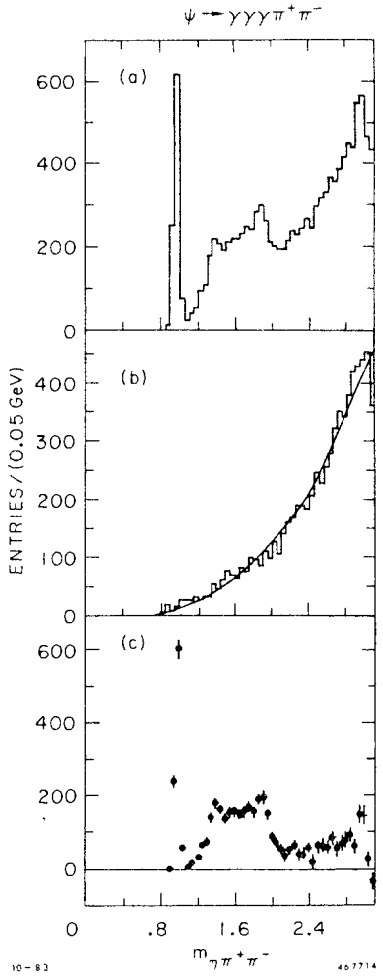


Fig. 31. (a)$Mass_{\gamma\gamma\pi^+\pi^-}$ (GeV) distribution when .475<mass($\gamma\gamma$)<.625. (b)$Mass_{\gamma\gamma\pi^+\pi^-}$ (GeV) distribution when .4<mass($\gamma\gamma$)<.475 or .625<mass($\gamma\gamma$)<.7 with a polynomial fit. (c)$Mass_{\gamma\gamma\pi^+\pi^-}$ (GeV) distribution, events in plot (a) subtracted by the polynomial fit to events in plot (b).

.475 or .625 < mass($\gamma\gamma$) < .7, the resulting mass($\gamma\gamma\pi^+\pi^-$) is plotted in Fig. 31(b). This represents the combinatorial background signal. It is fitted with a polynomial and most of this background populates the mass region above 2 GeV. To obtain the real $\eta\pi^+\pi^-$ signal, a polynomial fitted to Fig. 31(b) is subtracted from the events in Fig. 31(a). The resulting plot is shown in Fig. 31(c). The main structures are the η', a broad structure from 1 to 2 GeV and the η_c. The overall shape appears to be neither a single Breit-Wigner shaped resonance nor phase space. The approximate branching ratio of the entire structure in the 1-2 GeV region is 7×10^{-3}.

Applying a 5-C fit to the events, the Dalitz plot of mass$(\eta\pi^+)^2$ vs mass$(\eta\pi^-)^2$ is shown in Fig. 32 for those events with 1<mass($\eta\pi^+\pi^-$)<2 GeV. The plot shows a clear peak in both modes at .96 GeV^2 which corresponds to decay of the δ. Hence the decay $J/\psi \to \gamma\delta^\pm\pi^\mp$ is being observed. The mass($\eta\pi^+\pi^-$) is now studied with and without requiring the δ. Figures 33(a), (b) and (c) are mass($\eta\pi^+\pi^-$) distributions from the 5-C fit with no background subtraction. The first one is with no cuts, the second with a "δ cut", .93<mass($\eta\pi^\pm$)<1.03, and the third with an "anti δ cut", .93>mass($\eta\pi^\pm$) or mass($\eta\pi^\pm$)>1.03. The $\eta\pi^+\pi^-$ mass plot with the "δ cut", Fig. 33(b), shows no evidence for the ι at 1.44 GeV. However there appears to be a structure at 1.38 GeV. The background is not smooth and the shoulder around 1.3 GeV may be the D(1285). A conservative limit that the iota cannot be larger than the number of events at 1.44 GeV in Fig. 33(b) yields the result BR($J/\psi \to \iota$)× BR($\iota \to \delta^\pm\pi^\mp$)× BR($\delta^\pm \to \eta\pi^\pm$) < 1.1×10^{-3} at 95% confidence level. The structure, approximately 50 MeV below where the iota is expected, has been fitted separately to 1 and 2 Breit-Wigner curves with the second resonance in the fit being fixed at the D(1285) mass and width. The fits are applied to the events in Fig. 33(b). The fit to a single Breit-Wigner curve, shown in Fig. 34(a), yields the values mass=1.349±.011 GeV and Γ= .147±.036 GeV. The fit to two Breit-Wigner curves, shown in Fig. 34(b), yields the values mass=1.378±.004 GeV and Γ= .027±.018 GeV. Further reductions of backgrounds in this mode are being studied to improve the iota limit and resolve the emerging structure at 1.38 GeV.

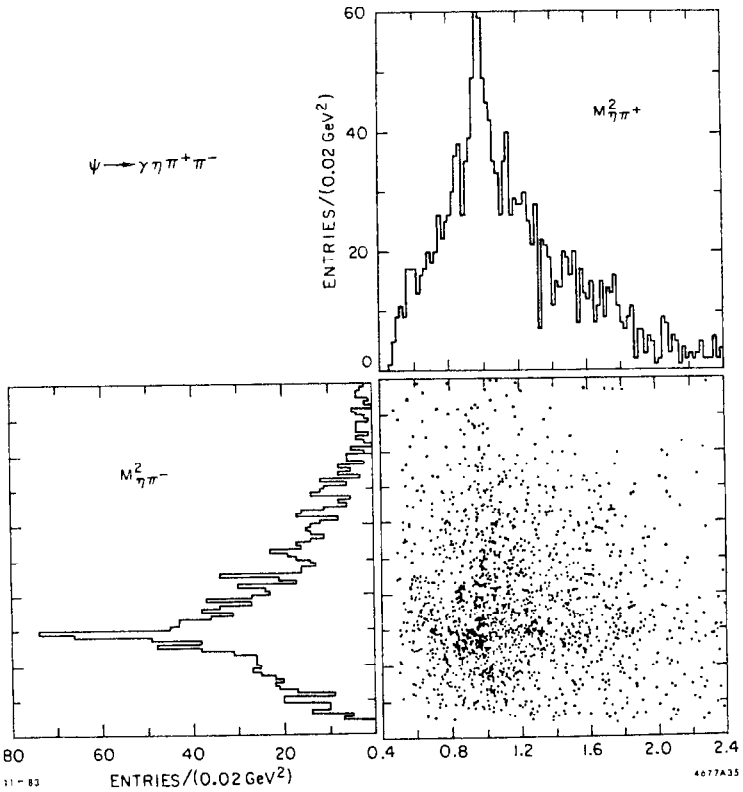


Fig. 32. Dalitz plot of mass$^2_{\eta\pi^+}$ versus mass$^2_{\eta\pi^-}$ with vertical and horizontal projections.

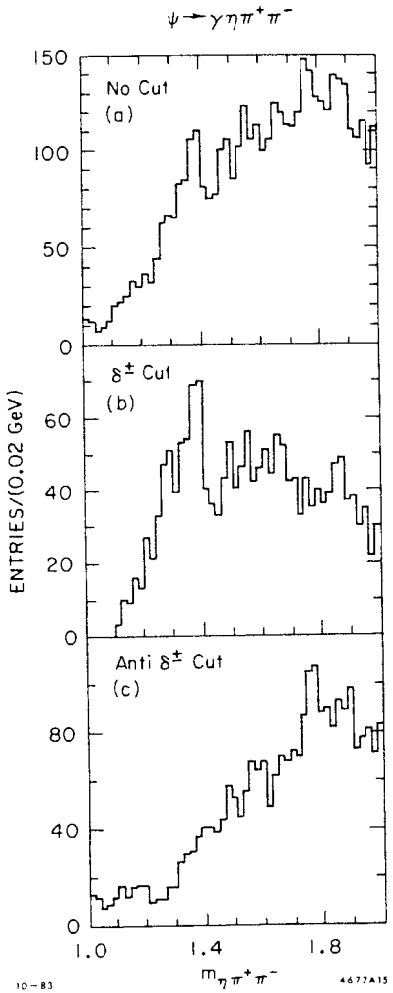


Fig. 33. (a) Mass$_{\eta\pi^+\pi^-}$ (GeV) distribution with no "δ cut" after a 5-C fit. Note that this plot has no background subtraction unlike Fig. 31(c). (b) Mass$_{\eta\pi^+\pi^-}$ (GeV) distribution with the "δ cut" after a 5-C fit. The "δ cut" requires .93<mass($\eta\pi^\pm$)<1.03. (c) Mass$_{\eta\pi^+\pi^-}$ (GeV) distribution with the "anti δ cut" after a 5-C fit. The "anti δ cut" requires .93>mass$_{\eta\pi^\pm}$ or mass$_{\eta\pi^\pm}$>1.03.

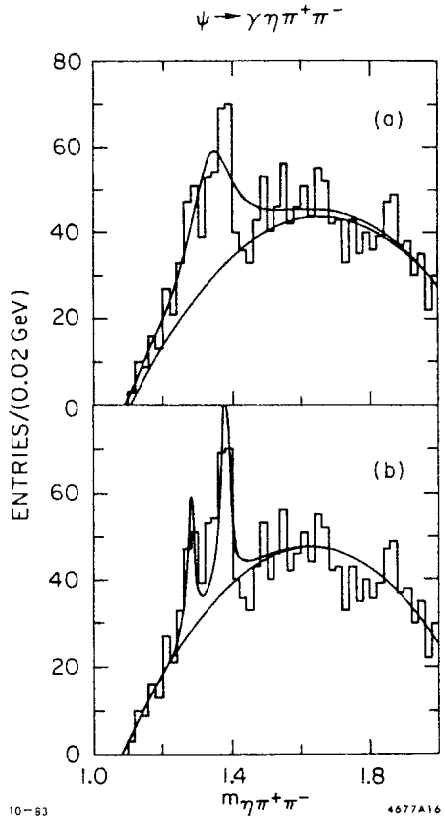


Fig. 34. (a)Figure 33(b) fitted with one Breit-Wigner curve. (b)Figure 33(b) fitted with two Breit-Wigner curves with the second fixed at the D(1285) mass.

6. Future Outlook

The preliminary results presented here are from only radiative J/ψ decays. Studies on J/ψ hadronic decays are also underway.

MARK III has accumulated $\sim$6 pb^{-1} on the ψ'' for producing neutral and charged D's. The present plans are to log another 9 pb^{-1} on the ψ'' to bring the total integrated luminosity to 15 pb^{-1}. MARK II has accumulated 2.85 pb^{-1} in total, hence MARK III should gain a factor of 5 in statistics over previous measurements. The D physics topics MARK III expects to explore are 1) measurements of the ratio of semileptonic branching ratios D^0 to $D^{\pm}$; 2) a possible direct measurement of the ratio of the Kobayashi-Maskawa matrix elements V_{cd}/V_{cs} from the ratio of $D\rightarrow \pi e\nu$ to $D\rightarrow Ke\nu$ decays and $D\rightarrow \rho e\nu$ to $D\rightarrow K^*e\nu$ decays; 3) new limits on $D^0\bar{D}^0$ mixing using D^0 and $\bar{D}^0$ tagged decays; 4) a study of the mechanism of hadronic weak decays from the relative yields of $D\rightarrow \pi\pi$, $D\rightarrow K\pi$, and $D\rightarrow KK$; and 5) measurements of the isospin of D decays. MARK III will later have the opportunity of searching for the F, and studying decays of τ's, ψ''s, and Λ_c's.

On the horizon, perhaps by the Summer of 1984, there may be an upgrade of SPEAR with the use of minibeta focusing at the interaction region. Little modification of the MARK III detector will be necessary. It is hoped that the luminosity may be increased by a factor of three. This should have a very important impact on the physics program enabling, for example, the possibility of producing 20 million J/ψ events at SPEAR in 17 weeks of running. Consequently MARK III looks forward to pursuing and producing interesting and important physics in the next few years at SLAC.

REFERENCES

1. D. Bernstein *et al.*, Stanford Linear Accelerator Center Report No. SLAC-PUB-3222 (1983).
2. J. Roehrig *et al.*, Stanford Linear Accelerator Center Report No. SLAC-PUB-3199 (1983).
3. J.S. Brown *et al.*, Stanford Linear Accelerator Center Report No. SLAC-PUB-3180 (1983).
4. W. Toki *et al.*, Stanford Linear Accelerator Center Report No. SLAC-PUB-3140 (1983).
5. H. Bledsoe *et al.*, Stanford Linear Accelerator Center Report No. SLAC-PUB-3200 (1983).
6. J.J. Thaler, V.J. Simaitis, J.J. Becker and W.J. Wisniewski, IEEE Trans. on Nucl. Sci. NS – 30, 236 (1978).
7. M. Roos *et al.*, Phys. Lett. 111*B*, 1 (1982).
8. M. Roos *et al.*, Phys. Lett. 111*B*, 1 (1982).
9. R. Partridge *et al.*, Phys. Rev. Lett. 45, 1150 (1980).
10. R. Partridge *et al.*, Phys. Rev. Lett. 45, 1150 (1980).
11. T. Himel *et al.*, Phys. Rev. Lett. 45, 1146 (1980).
12. M. Roos *et al.*, Phys. Lett. 111*B*, 1 (1982).
13. T.L. Trueman, Phys. Rev. *D*18, 3423 (1978).
14. N.P. Chang and C.A. Nelson, Phys. Rev. Lett. 40, 1617 (1978).
15. R. Plano *et al.*, Phys. Rev. Lett. 20, 3 (1959).
16. S. Brodsky *et al.*, Phys. Rev. Lett. 73*B*, 365 (1978).
17. M. Chanowitz, Phys. Rev. *D*12, 918 (1975).
18. T. Applequist *et al.*, Phys. Rev. Lett. 34, 365 (1975).
19. L. Okun and M. Voloshin, (Moscow, ITEP), ITEP-95-1976 (1976).
20. T. Barnes and F.E. Close, Phys. Lett. 116*B*, 365 (1982).
21. M. Chanowitz and S. Sharpe, Nucl. Phys. *B*222, 211 (1983).

22. R. Jaffe and K. Johnson, Phys. Lett. 60*B*, 201 (1976).

23. D. Scharre *et al.*, Phys. Lett. 97*B*, 329 (1980).

24. C. Edwards *et al.*, Phys. Rev. Lett. 49, 259 (1982).

25. M. Franklin, Ph.D. thesis, Stanford Linear Accelerator Center Report No. SLAC-254, August 1982.

26. C. Edwards *et al.*, Phys. Rev. Lett. 48, 458 (1982).

27. C. Edwards *et al.*, Phys. Rev. Lett. 51, 859 (1983).

28. D. Burke *et al.*, Phys. Rev. Lett. 49, 632 (1982).

29. M. Roos *et al.*, Phys. Lett. 111*B*, 1 (1982).

Quarkonium : From the Bottom Up

Estia Eichten
Fermi National Accelerator Laboratory
P.O.Box 500
Batavia, Ill. 60510

and
Enrico Fermi Institute
University of Chicago
Chicago, Ill. 60637

Abstract

The status of quarkonium physics is reviewed. Emphasis is placed on what can be learned from detailed studies of the $b\bar{b}$ system about both the spin dependent and spin independent relativistic corrections to the static potential. Expectations for the $t\bar{t}$ system are briefly discussed.

© E. Eichten 1983

1. Introduction

Simple nonrelativistic potential models have been extremely successful in describing the physics of heavy quark antiquark systems. A wealth of experimental data has been obtained for the $c\bar{c}$ (charmonium) system and is presently being acculumated for the $b\bar{b}$ system. All this data is in good agreement with potential model predictions. In this article I will review the present status of quarkonium physics [1] and suggest those areas of the theory in which work still needs to be done.

In Section 2 nonrelativistic potential models are reviewed and an analysis of what has been learned is presented. Section 3 contains a discussion of the much more unsettled situation with the spin dependent forces. What can be derived from Q.C.D. is discussed and the data on spin splittings presented. A model independent way to analyse the data and extract information about the strength and range of the forces is proposed. In Section 4 the spin independent relativistic corrections are discussed. Some objections are raised to the present theoretical treatments. Section 5 contains a comparison of experiment and theory for the photonic and hadronic transitions in the $b\bar{b}$ and $c\bar{c}$ systems. The possibilities for observing other $b\bar{b}$ states are discussed. Section 6 contains some remarks on expectations for the $t\bar{t}$ system. General conclusions are presented in the final Section.

2. The Explored Region - The Non Relativistic Potential

The effective potential between a heavy quark and a heavy antiquark can be defined in Q.C.D. (in the absence of light quarks) in terms of Wilson Loops. In general one can define the expectation values of any operator O in the presence of a Wilson Loop as:

$$< O > = \frac{\int dA\ P\ \{\exp[-g \int ds^{\mu} A_{\mu}^{a} t_{a}]\}\ e^{-S}\ O}{\int dA\ e^{-S}} \qquad (1)$$

where P is the path ordering operator, S the pure gauge action, and C a closed rectangular path of length R in some space direction and length T in the time direction. The Static Energy is then given by

$$\varepsilon(R) = \lim_{T\to\infty} -\frac{1}{T} \ln (< 1 >) \quad . \qquad (2)$$

A complete discussion of this formalism and the relation to the naive concept of a nonrelativistic potential appears in M. Peskin's lectures in these Proceedings.[2]

Some progress has been made recently in calculating $\varepsilon(R)$ directly by using Monte Carlo Lattice Methods.[3] There is every expectation that this approach should give an accurate numerical determination of $\varepsilon(R)$ within the next few years.

To date the only analytical calculations of the Static Energy have been in Q.C.D. perturbation theory and are therefore only valid for small R.[4] For $R \leq .1$ fm (Fermi) $\varepsilon(R)$ is given by

$$R\varepsilon(R) = -4/3\ \alpha(R) + \text{order } \alpha^{2} \qquad (3)$$

where $\alpha(R) = \frac{12\ \pi}{27\ \ln(1/(R\Lambda))}$.

In the region of R >.1 fm many phenomenological potential have been proposed. Some of the simple alternatives are:

(1) Cornell Model [5]

$$\varepsilon(R) = -\frac{\kappa}{R} + \frac{R}{a^2} \quad ,$$

(2) Richardson Model [6]

$$\varepsilon(R) = \int \frac{d^3Q}{(2\pi)^3} e^{i\vec{Q}\cdot\vec{R}} \left[-\frac{4}{3}\frac{12\pi}{27} \frac{1}{Q^2 \ln[1+Q^2/\Lambda^2]} \right] ,$$

(3) Logarithmic Model [7]

$$\varepsilon(R) = A \ln(R/R_0) ,$$

(4) Power Law Model [8]

$$\varepsilon(R) = A (R/R_0)^{\alpha} .$$

The first two models attempt to incorporate the expected behavior of Q.C.D. at short distance ($\alpha(R)/R$) and long distance ($\propto R$) while the last two are motivated purely by the data. Fitting the parameters in these potentials to the c $\bar{c}$ system all do well in predicting the gross spectrum of the b $\bar{b}$ system. This is less surprising than it might first appear when one adds an overall constant to the potentials so that they all agree at R = .4 fm and then plots the potentials fitted to the c $\bar{c}$ system on the same figure. As seen in Figure 1 , within the region .1 fm $\leq$ R $\leq$ 1.0 fm all these potentials are in remarkable numerical agreement inspite of different analytic forms. Since the $\langle R^2 \rangle^{1/2}$ for all the c $\bar{c}$ and b $\bar{b}$ states below threshold for Zweig allowed decays is in this range of

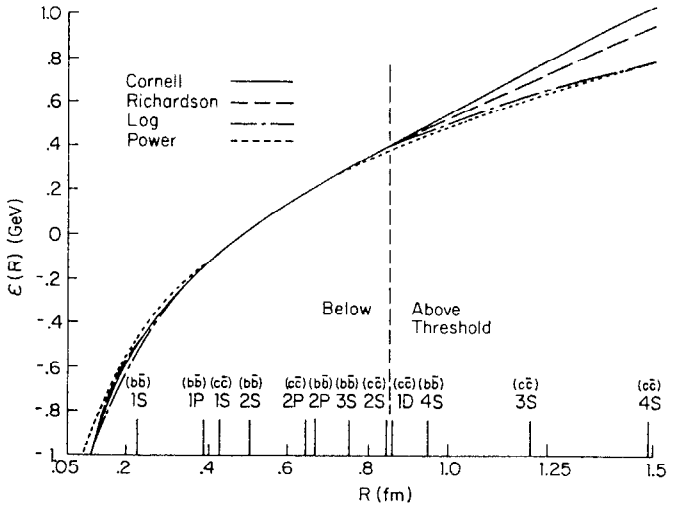


Figure 1: Phenemological Potentials for the Q $\bar{Q}$ System. The RMS radii of the observed c $\bar{c}$ and b $\bar{b}$ states are indicated by markers.

R, the agreement for the predictions of these potentials is easily understood.

Another popular approach has been to use the inverse scattering method to determine the potential from the data itself.[9] The potential so determined agrees well with those in Figure 1. Furthermore, the potential constructed from the data in the c $\bar{c}$ system agrees well with that constructed from the b $\bar{b}$ system. This supports the Q.C.D. expectation of the flavor independence of the potential.[10] This flavor independence is particularly important in view of the prediction based on the Q.C.D. Sum Rule approach that potential models would fail for the masses in the b $\bar{b}$ system because of gluon condensate dependent effects. [11] Specifically, the C.O.G. (Center of Gravity) of the 1P (b $\bar{b}$) states is in good agreement with potential model predictions [12] and disagrees with the prediction of the Q.C.D. Sum Rule approach.[11]

To summarize the present situation with regard to the nonrelativistic potential for heavy quark antiquark systems:

(1). The potential is known very accurately in the range .1 fm $\leq$ R $\leq$ 1.0 fm. All the phenomenological potentials are essentially identical (numerically) in this region. Remaining differences in this range are small compared to the relativistic corrections which have not been incorporated in these analyses. I will discuss these corrections in the next two sections.

(2). For R $\leq$ .1 fm the phenomenological potentials differ considerably, but Q.C.D. perturbation theory dictates the correct form. The toponium system (when discovered) will probe this small distance region. I will discuss this further in Section 6.

(3). The flavor independence of the potential has been tested by the agreement of potentials fitted in the c $\bar{c}$ system with the spectrum of the b $\bar{b}$ system, and model independently by the inverse scattering method.

(4). We can conclude from (1),(2), and (3) above that the nonrelativistic potential (Static Energy) is well determined and flavor independent for R $\leq$ 1 fm. However for distances greater than 1 fm the effects of open channels cannot be ignored (see Section 4). Thus a direct comparison of the spectrum with the predictions of the potential models is difficult. The Static Energy is certainly rising with R but the exact form can not be easily disentangled.

3. Spin Dependent Forces

As in the case of the potential itself, Q.C.D. dictates the form of the spin dependent forces. In particular the spin dependent potentials can be expressed in terms of expectations in the presence of a Wilson Loop.[13] Using the notation of Eq. 1:

$$V_{\substack{\text{Spin}\\ \text{Dependent}}}(R) = \left(\frac{S_1\cdot L}{2m_1^2} + \frac{S_2\cdot L}{2m_2^2}\right)\frac{1}{R}\left(\frac{d\epsilon(R)}{dR} + \frac{dV_1(R)}{dR}\right)$$
$$+ \frac{(S_1+S_2)\cdot L}{m_1\, m_2}\,\frac{1}{R}\,\frac{dV_2(R)}{dR} + \frac{2}{3m_1m_2}\,S_1\cdot S_2\,\nabla^2 V_2(R) \qquad (4)$$
$$+ \frac{1}{m_1m_2}\left[S_1\frac{R}{R}\,S_2\frac{R}{R} - \frac{1}{3}\,S_1\cdot S_2\right] . V_3(R)$$

where

$$\frac{R^k}{R}\frac{dV_1}{dR} = \epsilon^{ijk} \lim_{T\to\infty} \int_{-T/2}^{T/2} dt \int_{-T/2}^{T/2} dt' \frac{(t'-t)}{2T} g^2 \frac{\langle B^i(R,t)E^j(R,t)\rangle}{\langle 1 \rangle} \quad (5a)$$

$$\frac{R^k}{R}\frac{dV_2}{dR} = \epsilon^{ijk} \lim_{T\to\infty} \int_{-T/2}^{T/2} dt \int_{-T/2}^{T/2} dt' \frac{(t')}{2T} g^2 \frac{\langle B_i(0,t)E_j(R,t')\rangle}{\langle 1 \rangle} \quad (5b)$$

and

$$V_3(R) = \frac{3}{2}\left(\frac{R^iR^j}{R\,R} - \frac{1}{3}\delta^{ij}\right) \lim_{T\to\infty} \int_{-T/2}^{T/2} dt \int_{-T/2}^{T/2} dt' \frac{g^2}{T} \frac{\langle B_i(0,t)B_j(R,t')\rangle}{\langle 1 \rangle} . \quad (5c)$$

In the future these correlations may be calculated directly by Monte Carlo Lattice methods. However, for now, the three potentials V_1, V_2, and V_3 must be considered as unknown. It has been shown that no additional general relation exists which follows from Q.C.D. alone.[13] For the case of equal mass quark and antiquark the unknown spin dependent potentials can be written:

(1) Spin Orbit Term - V_{so}

$$\frac{(S_1 + S_2)\cdot L}{2m^2}\left\{\frac{1}{R}\frac{d\epsilon}{dR} + V_{so}\right\} \quad (6a)$$

where

$$V_{so} = \frac{1}{R}\frac{d(V_1 + V_2)}{dR}$$

(2) Tensor Term - V_t

$$\frac{1}{3m^2}\left[\, 3\, S_1\cdot\frac{R}{R}\, S_2\cdot\frac{R}{R} - S_1\cdot S_2 \,\right] V_t \quad (6b)$$

and

(3) Spin Spin Term - V_{ss}

$$\frac{2}{3m^2}\, S_1\cdot S_2\; V_{ss} \quad (6c)$$

where $V_{ss} = \nabla^2 V_2$.

Many attempts have been made to model the potentials - V_{so}, V_t, and V_{ss} based on physical assumptions about the long or short range nature of these forces, their relation to the nonrelativistic potential, or analogies with Q.E.D. .[13,14] I will not consider any of these attempts here but will propose instead a simple purely phenomenological ansatz:

$$V(R) = A\left(R/R_0\right)^{\alpha} . \quad (7)$$

Thus each unknown potential has two parameters which describe the nature of the term. A gives a measure of the strength of the interaction (R_0 = 1/GeV) and α gives a measure of the range of the interaction.

First let me deal with the spin-spin interaction. The only experimental data for the hyperfine splittings is in the $c\bar{c}$ system [15]:

$$M(\Psi') - M(\eta_c') = 111 \pm 5 \text{ MeV}$$

and

$$M(\Psi) - M(\eta_c) = 92 \pm 5 \text{ MeV} .$$

The form of the spin-spin term has been calculated in perturbation theory [16]:

$$V_{ss}(R) = 4\pi\,\delta(R)\; 4/3\; \alpha_{\overline{ms}}(m)\left\{1 + \alpha_{\overline{ms}}(m)/\pi\;\xi\right\} \quad (8)$$

where $\xi = 0.563 + 0.375\left[\langle \ln(Q^2/m^2)\rangle_{nS} / |\phi_{nS}(0)|^2\right]$.

For a value of $\Lambda_{\overline{MS}} \approx .17$ GeV the measured spin splittings in the $c\bar{c}$ system agree well with the values obtained from Eq. 8. Hence there is no evidence for any long range contribution in the spin-spin force. Using the same value of $\Lambda_{\overline{MS}}$, the predicted value for the splitting $M(T) - M(\eta_b)$ is 30 GeV.

The situation for the spin-orbit and tensor forces is more complicated and confused. I will suggest a method of analysis which can help to clarify the situation.

The masses of spin triplet P states can be expressed as

$$M(^3P_2) = M_0 + a + b - 2/5\ c\ ,$$
$$M(^3P_1) = M_0 - a - b + 2\ c\ , \qquad (9)$$
$$M(^3P_0) = M_0 - 2a - 2b - 4c\ ,$$

where

$$a = \frac{1}{2m^2}\ \frac{1}{R}\ \langle \varepsilon(R) \rangle \qquad (10)$$

which is known in terms of the nonrelativistic potential. Hence the total spin orbit term a+b has one piece (a) which is determined completely from the nonrelativistic potential and has a long range part. However the other piece

$$b = \frac{1}{2m^2}\ V_{so} \qquad (11)$$

can not be derived from the nonrelativistic potential in a model independent way and therefore needs to be modeled phenomenologically. Similarly the tensor term

$$c = \frac{1}{3m^2}\ V_t \qquad (12)$$

is not known in a model independent way.

The masses of the triplet 1P ($c\bar{c}$) states have been measured to very high accuracy by the Crystal Ball collaboration.[15] The triplet 1P and 2P ($b\bar{b}$) states have recently been measured by the CUSB collaboration .[17] The masses of the $1\,^3P_2$ and $1\,^3P_1$ ($b\bar{b}$) states have been measured to high accuracy by the CLEO [18] and Crystal Ball [19] collaborations. The present best values [20] for these masses are given in Table 1.

^3P_J (MeV)	1 P ($c\bar{c}$) Ref. [15]	1 P ($b\bar{b}$) Ref. [18]	2 P ($b\bar{b}$) Ref. [18]
J = 2	3,555.9 $\pm$ 0.6	9,913.3 $\pm$ 0.3 ($\pm$ 2)	10,266.4 $\pm$0.3 ($\pm$ 2)
J = 1	3,510.0 $\pm$ 0.6	9,893.6 $\pm$ 0.4 ($\pm$ 3)	10,249.3 $\pm$ 0.4 ($\pm$ 3)
J = 0	3,415.0 $\pm$ 1.0	9,872.6 $\pm$ 0.7 ($\pm$5)	10,228.9 $\pm$0.7 ($\pm$5)

Table 1: Masses of the Triplet P States in the $c\bar{c}$ and $b\bar{b}$ system.

Using this data we can determine the values of (a+b) and c for each of these systems. The results are shown in Table 2.

	1 P ($c\bar{c}$)	1 P ($b\bar{b}$)	2 P ($b\bar{b}$)
a + b	34.9 $\pm$ .4	11.7 $\pm$ 2.1	10.6 $\pm$ 2.1
c	10.0 $\pm$ .2	1.55 $\pm$ 1.1	2.37 $\pm$ 1.1
a	20.14	7.5	5.6

Table 2: Values of the Spin Dependent Energies in MeV.

The values of a have been determined from theory using

the nonrelativistic potential determined in Section 2.

Now knowing the experimental values of b and c, we can determine in a model independent way some properties of the unknown part of the spin-orbit force and the tensor force. The present data for the P states in the $b\bar{b}$ system has rather large errors on the splittings so any conclusions we draw must be rather tentative; however I present this analysis to show the method and with the assurance that within the year the quality of the data will be such as to allow some firm conclusions.

The key to this analysis is that (as discussed in Section 2) the nonrelativistic potential is extremely well determined in the region of R ($\leq$ 1 fm) relevant to our needs. Therefore the expectation of R in the various states of the $c\bar{c}$ and $b\bar{b}$ systems are known model independently. By the flavor independence of the spin dependent forces (true to leading order in v/c in Q.C.D.) the ratios

$$\frac{\langle R^{\alpha}\rangle_X}{\langle R^{\alpha}\rangle_Y} = \frac{\langle X|R^{\alpha}|X\rangle}{\langle Y|R^{\alpha}|Y\rangle} \qquad (13)$$

where X and Y are any two states of these systems is a known function of a single variable α. The ratio is shown in Figure 2 for Y = 1P ($c\bar{c}$) and various choices for X. Using the values of b and c from Table 2 and Eqs. (6b) and (6c) respectively we find that the experimental values for the ratios are:

X state	Spin Orbit Term - V_{so}	Tensor Term - V_t
1 P ($b\bar{b}$)	2.3 ± 1.1	$1.22 \pm .87$
2 P ($b\bar{b}$)	2.7 ± 1.2	$1.87 \pm .87$

Table 3: The Experimental Values of the Ratio $\langle R^{\alpha}\rangle_X$ / $\langle R^{\alpha}\rangle_{1P(c\bar{c})}$ for the Potentials V_{so} and V_t for Various States X.

where the charm and bottom quark masses were choosen to be 1.84 GeV and 5.17 GeV respectively. Comparing these values with the ratios in Figure 2, we can read off the effective powers α of the spin dependent potentials determined by each of these ratios.

For the Spin Orbit Term (Eqs. 6b and 11):

$$\alpha = -1.6 \begin{smallmatrix} + \\ - \end{smallmatrix} 1.0 \quad \text{for } X = 1\,P\,(b\,\bar{b}) ,$$

$$\alpha = -2.5 \begin{smallmatrix} + 1.0 \\ - 0.5 \end{smallmatrix} \quad \text{for } X = 2\,P\,(b\,\bar{b}) .$$

For the Tensor Term (Eqs.6c and 12):

$$\alpha = -.8 \begin{smallmatrix} + 2.0 \\ - 0.7 \end{smallmatrix} \quad \text{for } X = 1\,P\,(b\,\bar{b}) ,$$

$$\alpha = -1.8 \begin{smallmatrix} + \\ - \end{smallmatrix} .8 \quad \text{for } X = 2\,P\,(b\,\bar{b}) .$$

Some tentative conclusions can be drawn for the V_{so} and V_t terms:

(1). The consistence of the method requires that the range determined from the two ratios (X=1P and X= 2P) agree. Within the large experimental errors this is true.

(2). The expected behavior of a short range potential is that of Q.C.D. perturbation theory

$$V_i(R) \approx \alpha(R)/R^3 \quad \text{i.e. } -3 < \alpha_i < -2,$$

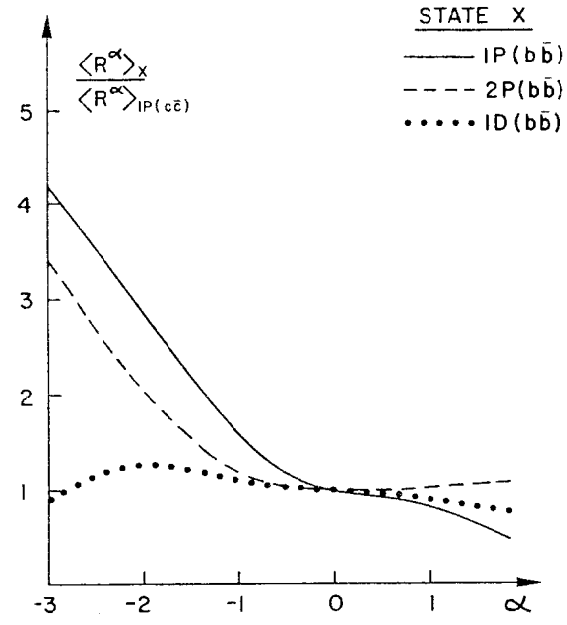


Figure 2: The Ratio of the Expectation Values of R^{α} in the State X to the Expectation Value of R^{α} in the ^{1} P $(c\ \bar{c})$ State. Expectation values are computed using the potential of Ref.. [5]

while a long range spin potential should behave like 1/R, i.e. $a_1 = -1$. Thus the spin orbit potential V_{so} ($=V_1+V_2$ of Eq. 6a) is consistent with being purely short range. This is not too surprising since we have already argued that the V_2 potential which also appears in the Spin-Spin force is consistent with perturbation theory, and the potential V_1 is zero both in perturbation theory and when instanton effects are included.[13] If better data supports the conclusion that V_{so} is short range then the whole spin orbit force would be calculable. The piece that contains a long range part (the a term) is determined directly from the nonrelativistic potential and the unknown piece (the b term) would be short range and so Q.C.D. perturbation theory should be a reliable guide.

(3). For the Tensor Term V_t (Eq.6c), the data suggests that there may be some long range component. The existence of a long range component of the tensor force has been suggested on phenomenological grounds by P. Moxhay and J. Rosner [21] and on theoretical grounds by J. Kogut and G. Parisi.[22]

(4). Finally a word of caution about the analysis in the form I have presented. This analysis would be much more accurate if it could be performed without using any data from the $c\bar{c}$ system, since the $c\bar{c}$ system is surely more relativistic and hence the corrections associated with higher order effects and the light quark effects I will discuss in the next section are substantially larger. An analysis would be possible in the $b\bar{b}$ system alone if one additional spin splitting which involves the terms b and c could be measured. The best hope is to find the Triplet 1D $(b\bar{b})$ states. Ratios could then be formed using $Y = 1D(b\bar{b})$. I will return to the feasibility of observing the $1D(b\bar{b})$ system in Section 5.

4. Spin Independent Relativistic Corrections

Many attempts to model the spin independent relativistic correction based on analogies with Q.E.D. have been made. These typically involve the reduction of the Bethe-Salpeter equation in the nonrelativistic limit with a kernel that is instantaneous and has some particular Lorentz structure. Two recent detailed treatments using somewhat different kernels have been presented. One approach (M+R) by P. Moxhay and J. Rosner [21] has a kernel with a long range potential (=R) which is a mixture of scalar and vector and has a long range tensor potential, and the other (M+B) by R. McClary and N. Byers [23] has a purely scalar long range potential. I will use these results in comparing theory with experiment in the photonic and hadronic transitions discussed in the next section. In this section, however, I would like to point out a serious shortcoming of these works and in fact all theoretical efforts to date which attempt to deal with the spin independent relativistic corrections to the potential.

There is an essential difference between Q.E.D. and Q.C.D. which first manifests itself in the leading spin independent corrections to the nonrelativistic limit. This is the effect of including light quark pair creation. Once we include light quark pairs the long range structure of the theory is drastically altered

in Q.C.D. since these terms allow the heavy quark and antiquark to be separated to infinite distance at finite energy. Each heavy quark is accompanied by the associated light quark to form a color singlet meson. That is, the interactions of light quarks allow for strong (Zweig allowed) decays of the quarkonium systems above some kinematic threshold.

The inclusion of light quarks have the following practical consequences:

(1). The strict connection between the nonrelativistic potential and the Wilson Loop (or Static Energy) is lost. However, it is still formally valid to lowest order in the nonrelativistic expansion if we can argue that an expansion in inverse powers of the light quark effective mass is also possible. Although this seems improbable at first, I will argue below that this is probably numerically consistent.

(2). If the expansion suggested in (1) is valid for the potential itself it will also hold for the leading order in the spin dependent potentials as well. But there can be no justification for ignoring these terms when one considers the leading spin independent relativistic corrections. The light quark effects are at least as large as the leading spin independent corrections arising from an analysis based on the Bethe-Salpeter approach.

Unfortunately it is difficult to calculate the effects of light quark loops directly. Dealing with Fermion loops on the lattice is plagued with technical difficulties and a Monte Carlo calculation fully incorporating Fermion loops is still some time in the future. However there is a phenomenological approach to including the effects of light quark loops. The approximate duality between using quarks and gluons as intermediate states and using the physical meson and baryon states suggests that for states near threshold for Zweig allowed decays the major effects of the light quarks will be included by including the coupling to decay channels in the manner of the Cornell Model.[5] This at least allows a rough estimate of the size of the light quark effects.

In Table 4 we compare the shift in masses due to coupling to decay channels and due to the relativistic corrections of the M+B model for various $c\bar{c}$ states below threshold. We conclude that the magnitude of these corrections are comparable. It is not possible to model the spin independent relativistic corrections without taking the light quark effects into account. The situation for the $b\bar{b}$ system is not better as is seen in Table 5.

I would also note the the magnitude of the light quark effect is considerably smaller than the energy differences between the states in the nonrelativistic limit which supports the assumption that an expansion in light quark mass as discussed in (1) above can be valid. The spin dependent shifts on the triplet $1P(c\bar{c})$ states have also been computed, [5], they are +3 MeV, -3 Mev, and -1 Mev for the $J = 2,1,0$ states respectively. This supports the claim (2) above that the effects of light quarks can also be ignored for the leading order spin dependent forces.

In conclusion, although the effects of light quarks (or coupling to decay channels) can be reasonable ignored (in leading order) for the nonrealativistic potential and the spin dependent potentials, it is

State	M+B	C-C	Virtual D $\bar{D}$
ψ'	-117	-118	.20
$^3\chi_J$(C.O.G.)	-55	-92	.12
ψ	—	-48	.04

Table 4: Mass Shifts in the c $\bar{c}$ System. The shift in mass due to the spin independent relativistic corrections of Ref. 23 are shown in Column M+B. The shift due to coupling to decay channels [5] is shown in Column C-C; while the probability for the wavefunction of the physical state to be a virtual D $\bar{D}$ state is shown in the last column. All energies are in MeV.

State	M + B	C - C
Υ''	-56	-85
Υ'	-55	-50
Υ	--	-16

Table 5: Mass Shifts in the b $\bar{b}$ System. Notation as in Table 4.

not sensible to ignore these effects at the level of the leading spin independent relativistic corrections.

5. Transitions Among the Narrow b $\bar{b}$ States

Photonic Transitions

The only remaining puzzle in the c $\bar{c}$ system for the potential models, the disagreement of the calculations for the E1 photonic transitions for the 2S to 1P states, has been resolved. The results of McClary and N. Byers [23] are given in Table 6.

$\psi' \to \gamma \chi_J$ Rate in KeV	Naive Potential Ref. 5	Coupled Channel Ref. 5	McClary + Byer Ref. 23	Experiment Ref. 15
J = 2	29	23.7	22	16.8 ± 1.1
J = 1	45	34	23	19.1 ± 1.1
J = 0	50	43.2	16	21.1 ± 1.1

Table 6: Successive Approximations to the 2S → 1P E1 Transition for the c $\bar{c}$ System.

The new ingredient in the calculation of M+B missing in the Cornell Coupled Channel Model [5] is the inclusion of the leading spin dependent and spin independent effects to the various states.

Why are these relativistic effects so large when the nominal magnitude of these corrections should be $(v/c)^2 \approx .2$. The answer provided by the calculations of M+B indicates that there is a strong cancellation in the overlap $\langle 2S|R|1P\rangle$ which determines the E1 rate. This is due to the node in the 2S radial wavefunction as can be seen in Figure 3. Because of this cancellation the amplitude is particularly sensitive to higher order correction. The sign and relative magnitudes of the effect can be determined without any detailed calculations. The spin dependent terms will be strongly attractive for small R for the 1P J=0 state, neutral for the 1P J = 1 state , and repulsive for the 1P J =2 state; while the spin independent corrections (associated with kinetic energy corrections) will be attractive for all three 1P states. Hence the net effect is to provide a strongly attractive term at short distance for the 1P J=0 state, a mildly attractive term for the 1P J=1 state, and an essentially neutral term for the 1P J=2 state. An attractive short range force will enhance the wavefunction of the state at short distance. Referring again to Figure 3 we see that enhancing the wavefunction of a 1P state at small R will increase the cancellation. This explains qualitatively the large effect seen in Table 6 for the J=0 1P state.

In general we may expect greater sensitivity to higher order correction whenever we have such cancellations. We should expect this in the $b\bar{b}$ system as well.

The spectrum of states below threshold for Zweig allowed decays in the $b\bar{b}$ system and the expected E1 and M1 transitions is shown in Figure 4. Transitions which would be expected to be sensitive to the

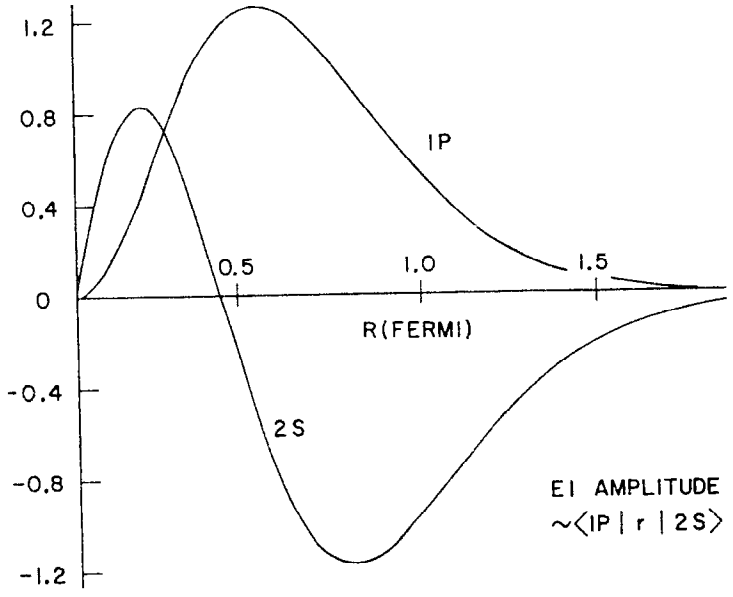


Figure 3: The Radial Wavefunctions for the $2\,^3S_1$ $(c\bar{c})$ and $1\,^3P_J$ States. The potential is given in Ref. [5].

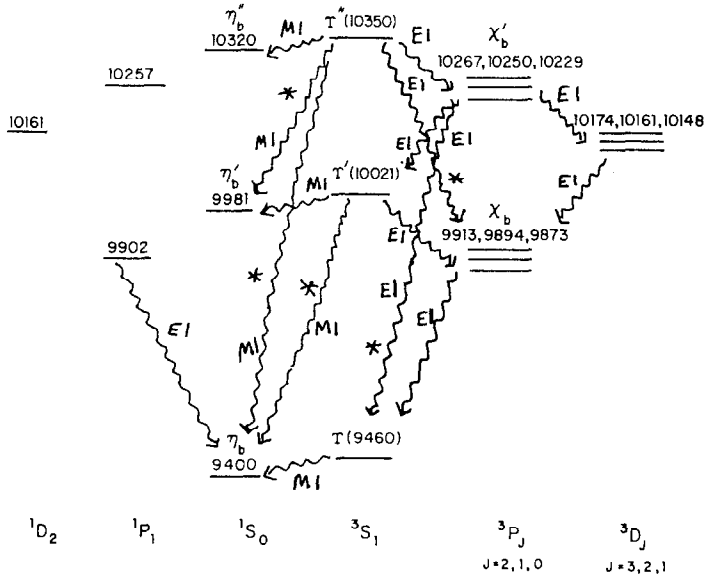


Figure 4: E1 and M1 Transitions in the b $\bar{b}$ System. Numbers above each set of states are the observed masses (in MeV) arranged in descending order of J. For states not yet observed the predicted masses (Ref. [13]) are indicated. Transitions which are particularly sensitive to relativistic corrections are indicated by a star.

treatment of higher order corrections are indicated with a star. The detailed comparison of the theoretical rates [21] and experiment is shown in Tables 7a and 7b.

Hadronic Transitions

The theory for hadronic transitions was discussed by M. Peskin in his lectures.[2] The basic idea is to make a multipole expansion for gluon radiation similar to the usual multipole expansion for photons. The expected hadronic transitions for the b $\bar{b}$ system are shown in Figure 5.

One difficulty is how to model the gluon to light hadron transitions. Kuang and Yan [24] have used a vibrating string model for the total rates for the transitions $n\,^3S_1 \to m\,^3S_1 + 2\,\pi$ and $n\,^3S_1 \to m\,^1S_0 + \eta$, while using free gluons projected onto into the right J^{PC} for all other transitions. Their results and a comparison with the present experimental rates are given in Table 8. For the shape of the spectrum in the $n\,^3S_1 \to m\,^3S_1 + 2\,\pi$ transition Kuang and Yan used soft pion theorems. The resulting shapes are in good agreement with the data for the $T'' \to T' + 2\,\pi$ and $T' \to T + 2\,\pi$ transitions, but give a poor fit to the spectrum shape in the case of the $T'' \to T + 2\,\pi$ transition in which the two pion system has the greatest energy (890 Mev). Whether the poor fit is just a result of a large extrapolation in two pion energy from the region of the soft pion theorems or a more basic problem with the hadronization model of Kuang and Yan is not known.

Transition	Theory	Experiment
$3S \to 2P_J$ J=2,1,0	11,12,6	13,16,3
$3S \to 1P_J$ J=2,1,0	.6,.1,.1	seen
$2S \to 1P_J$ J=2,1,0	7,6,3	6,6,3
$2P_J \to 2S$ J=2,1,0	10,18,2	seen
$2P_J \to 1S$ J=2,1,0	9,15,1	seen
$1P_J \to 1S$ J=2,1,0	19,60,4	26,44,-
$2P_2 \to 1D_J$ J=3,2,1	1.4,3,~0	-
$2P_1 \to 1D_J$ J=3,2,1	0,2.5,2.2	-
$2P_0 \to 1D_J$ J=3,2,1	0,0,.8	-
$1^1P_1 \to {}^1S_0$	40	-

Table 7a: E1 Transitions in the $b\bar{b}$ System. The experimental branching ratios are taken from Ref.. [20] The theoretical rates are from Ref.. [21] Sensitivity to higher order relativistic effects is indicated in Figure 4. All branching ratios are in percent. Where not otherwise indicated the transition is between spin triplet states.

Transition	Theory
$3^3S_1 \to 3^1S_0$	10^{-3}
$\to 2^1S_0$	10^{-4}
$\to 1^1S_0$	10^{-5}
$2^3S_1 \to 2^1S_0$	2.0×10^{-3}
$\to 1^1S_0$	10^{-2}
$1^3S_1 \to 1^1S_0$	2.0×10^{-2}

Table 7b: M1 Transitions in the $b\bar{b}$ System. Theoretical branching ratios are from Ref..[25] The hindered M1 transitions are highly sensitive to the treatment of relativistic corrections. All entries are in percent.

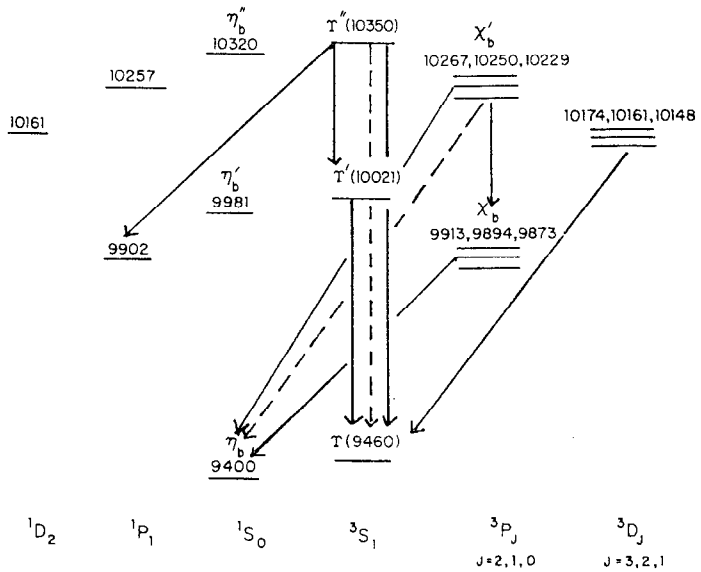


Figure 5: Some Hadronic Transitions in the b $\bar{b}$ System. A solid line denotes a 2 π transition and a dashed line an η transition. The notation for the states is described in Figure 4.

Transition	Theory	Experiment
$3^3S_1 \rightarrow 2^3S_1 + 2\pi$	2	5
$\rightarrow 1^3S_1 + 2\pi$	5	7
$2^3S_1 \rightarrow 1^3S_1 + 2\pi$	29	25
$2^3P_J \rightarrow 1^3P_{J'} + 2\pi$	.2,.3,.06	-
$2^3P_1 \rightarrow 1^1S_0 + 2\pi$	2	-
$3^3S_1 \rightarrow 1^3S_1 + \eta$	.03	-
$2^3S_1 \rightarrow 1^3S_1 + \eta$	.04	-
$3^3S_1 \rightarrow 1^1P_1 + 2\pi$	.1	-

Table 8: Some Hadronic Transitions in the b $\bar{b}$ System. Experimental results are taken from Ref. [20] Theoretical estimates based on the results of Ref. [24] All branching ratios are in percents.

Observing Additional States in the $b\bar{b}$ System

We can use the predicted transition rates to determine which of the many additional states below threshold in the $b\bar{b}$ system can possibly be observed experimentally.

(1) The best available ways to observe the $^3D_1$ states are by the transitions

$$^3S_1 \to \gamma_1 + {}^3P_J \to \gamma_1 + \gamma_2 + {}^3D_J.$$

(a) For J=2 and J′=3, γ_1 = 83 MeV and γ_2 = 93 MeV
with a product branching ratio = .1%.

(b) For J=2 and J′=2, γ_2 = 106 Mev
with a product branching ratio = .25%.

(c) For J=1 and J′=2, γ_1 = 100 MeV and γ_2 = 76 Mev
with a product branching ratio = .5%.

(d) For J=1 and J′=1, γ_2 = 89 MeV
with a product branching ratio = .4%.

(2) The best way to see the $^1P_1$ state is through the hadronic transition $T'' \to {}^1P_1 + 2\pi$ which has a branching ratio of .4 - .8 %. This rate is however highly dependent on the model of gluon hadronization.[24]

(3) If the $^1P_1$ state is observed via (2) the state $^1S_0$ (η_b) can also be observed since the branching ratio for

$^1P_1 \to {}^1S_0 + \gamma$ with γ = 502 MeV is approximately 30%.

(4) Unfortunately the M1 transition rates are uniformly tiny, making observing the singlet S states impossible by these transitions. For example, the M1 transition $T \to \eta_b + \gamma$ with γ = 50 MeV has a branching ratio of approximately .06%.[25] However the transition

$$3^3S_1 \to \gamma + 2^3P_1 \to \gamma + 1^1S_0 + 2\pi$$

has a combined branching ratio of .3%. Hence the η_b may be observable by this mode.

6. Up from Bottom

The last remaining heavy quark system in the three generation model is the top system. We know from PETRA measurements [26] that the mass of the top quark must be greater that 19.3 GeV. If its mass is less than approximately 60 GeV it will be observed in W decays at $Sp\bar{p}S$ in the near future. What can we learn from toponium if the mass of the top quark lies in this range?

(1). There will be a rich spectrum of states below threshold. If we use a semiclassical argument [27] the number of S states are approximately $2(m_t/m_c)$. For m_t = 30 GeV there would be 8 S states below threshold and the maximum orbital angular momentum of a state below threshold would be 7; thus the total number of states below threshold would be approximately 45.

(2). We can probe the potential into smaller distances. As shown in Figure 6 the $\langle R^2 \rangle^{.5}$ for the 1S state is 0.09 fm for m_t =20 GeV and .05 fm for m_t =60 GeV. Thus we can test the perturbative Q.C.D. region of the potential. The difference between the 2S - 1S splitting in the Log and Q.C.D. inspired Richardson potential is shown in Table 9.

M(2S) - M(1S)	Top Quark Mass (Gev)				
	20	30	40	50	60
Log Potential	560	560	560	560	560
"Q.C.D."	587	610	630	645	660

Table 9: Dependence of 2S - 1S Splitting on the Top Quark Mass for Various Potentials. The Log potential is given in Ref. 7 and the "Q.C.D." potential in Ref. 6. All splittings are in Mev.

(3). The decays of the $t\bar{t}$ spin one ground state must include the full electroweak structure of the gauge interactions.[28] In particular we must include: (a) Virtual Electroweak term - photon and Z exchange in the s channel and W exchange in the t channel; (b) weak t quark decays ; (c) the three gluon annihilation term ; and (d) the two gluon plus photon term. The various decay rates are shown in Figure 7. Note that the three gluon annihilation no longer dominates these decays.

(4). If non-standard models such as Technicolor or Supersymmetry are correct the ground state $t\bar{t}$ system could decay predominantly into new particles. For example, $1^3S_1 \rightarrow P^+ + b + t$ or $1^3S_1 \rightarrow \tilde{g} + \tilde{g}$.

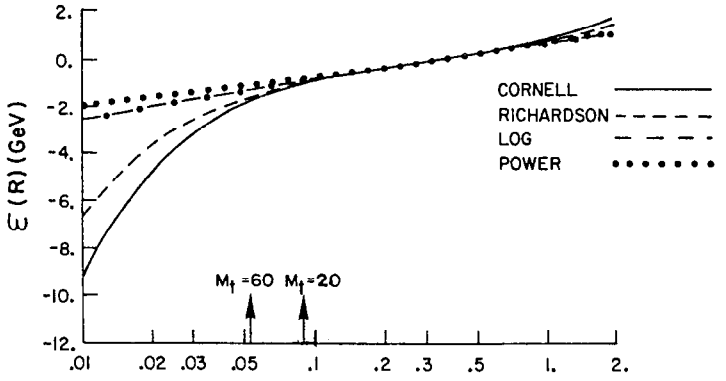


Figure 6: The Various $Q\bar{Q}$ Potentials of Figure 1 with their Short Distance Behavior Displayed. The horizontal axis is the distance R in Fermi on a log scale. The markers indicate the radius of the 1^3S_1 $(t\bar{t})$ state for m_t = 20 GeV and m_t = 60 GeV.

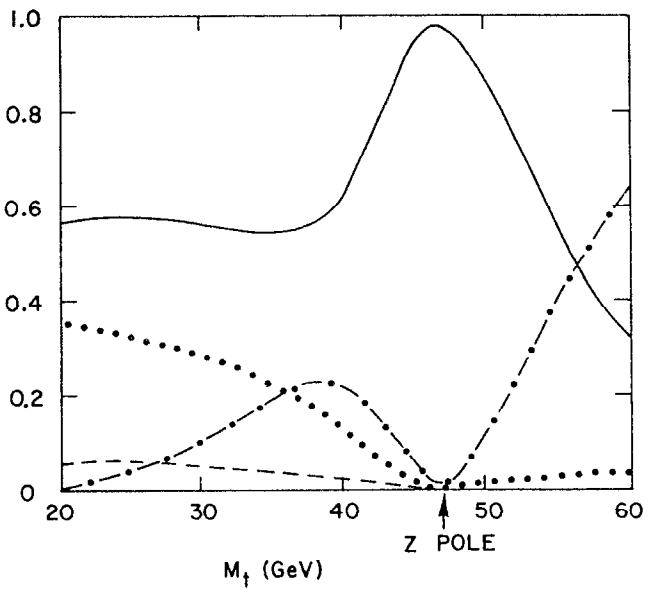


Figure 7: The Decay Branching Ratios for the $1\ ^3S_1$ ($t\bar{t}$) State as a Function of Top Quark Mass. The solid curve is the contribution of the virtual electroweak decays; the dotted curve the three gloun decays; the dot-dashed curve the $W^{\pm}$ weak t decays; and the dashed curve the two gluon -photon decays.

(5). Even if no unexpected decays dominate, accessing the rest of the spectrum with L = 0 through photonic or hadronic transitions from excited $^3S_1$ states will become extremely difficult for $m_t > m(Z_o)/2$. The expected branching ratios for direct decays ,photonic transitions and hadronic transitions are shown in Figure 8. The direct decays are as in (3) above. While for m_t in the range 20 - 60 Gev the photonic transitions satisfy the approximate scaling law $\propto (m_b/m_t)^{2/3}$ from the corresponding state in the $b\bar{b}$ system. The hadronic transition rates scale according to Ref. . [24]

7. Summary

In conclusion let me summarize the major results of our analysis of the status of Quarkonium Physics:

(1). The form of the nonrelativistic potential is established phenomenologically in the range $0.1 \leq R \leq 1.0$ fm. The next step is to derive this form from Q.C.D. For $R \leq 0.1$ fm the potential can be calculated in Q.C.D. perturbation theory; we need to confirm this form experimentally in the $t\bar{t}$ system.

(2). Leading order spin dependent relativistic corrections are in reasonable shape. The forms (range and strengths) of $V_{so}(R)$, $V_t(R)$, and $V_{ss}(R)$ will soon be known for experiment. The time will then be ripe for renewed model building for the spin dependent forces. Eventually these potentials will be calculated by lattice methods.

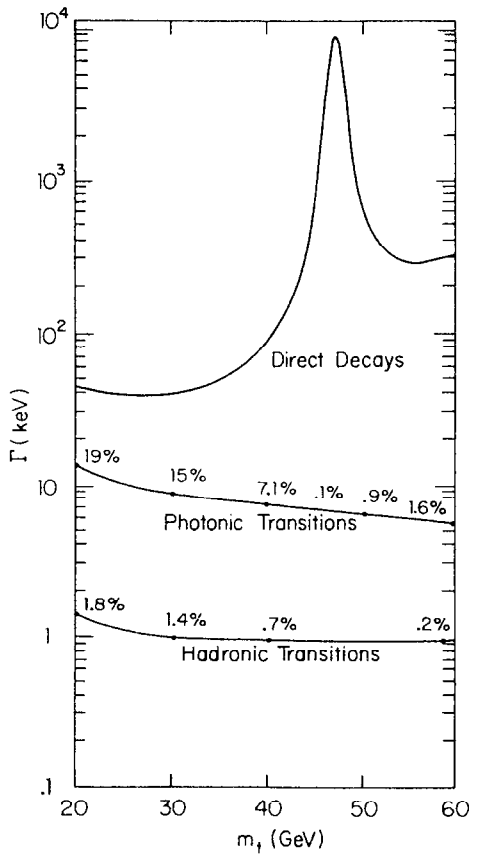


Figure 8: The Partial Widths of the Decays of the $3\ ^3S_1$ ($t\bar{t}$) State.

(3). Spin independent relativistic corrections pose a very complicated problem. One can not ignore the effects of light quark loops (or equivalently coupling to decay channels).

(4). The theory of photonic transitions is in good agreement with the data. Care must be exercised when calculating rates to watch for E1 transitions which involve significant cancellation in the overlap integrals and for hindered M1 transitions, because these rates are more likely to be sensitive to higher order relativistic terms.

(5). The multipole expansion works well for hadronic transitions. It gives the correct scaling rules and overall rates. The hadronization of the gluons is not yet under theoretical control.

The $b\bar{b}$ system provides a rich spectrum of states in which to study the detailed structure of heavy quark systems. We are just beginning to learn this system. The $t\bar{t}$ system will provide an even richer spectrum and if $m_t \leq m(Z_0)$ we can look forward to one final system in which to study standard Quarkonium Physics.

References

1. For other reviews on the current status of Quarkonium Physics see: K. Gottfried, Rapporteur's talk given at International European Conference on High Energy Physics, Brighton, England, July, 1983; Cornell Preprint CLNS-83/579 (1983); and J. Rosner,"Progress in the Description Of Heavy Quark Systems", Enrico Fermi Institute Preprint EFI-83-17 (1983). I will not discuss the status of perturbative Q.C.D. applied to heavy quark systems. For a review of the situation in this field see: P. LePage,"Perturbative Q.C.D.",Summary talk presented at the International Symposium on Lepton and Photon Interactions at High Energies, Cornell University, Aug. 4-9 1983.

2. M. Peskin, Lectures presented at the 1983 SLAC Summer Institute. Published in the Proceedings of the 1983 Summer Institute On Particle Physics, Edited by P. McDonough ,Stanford, CA.

3. For a review of the status of Lattice Monte Carlo methods for Q.C.D. see: J. Kuti,"Lattice Gauge Theories", Summary Talk at the International Symposium of Lepton and Photon Interaction at High Energies, Cornell University, Aug. 4-9, 1983.

4. This potential has been calculated through two loops by: F.L. Feinberg, Phys. Rev. Lett. 39, 316 (1977); T. Appelquist , M. Dine, and I. Muzinich, Phys. Lett. 69B, 231 (1977); and W. Fischler, Nucl. Phys. B129, 157 (1977).

5. E. Eichten et. al.,Phys. Rev. D17, 3090 (1979); D21,203 (1980).

6. J. Richardson, Phys. Lett. 82B, 272 (1979). For an extension of this model see: W. Buchmuller and S. H. H. Tye, Phys. Rev., D24, 132 (1981).

7. C. Quigg and J. Rosner, Phys. Lett.71B, 153 (1977).

8. A. Martin, Phys. Lett. 93B, 338, (1980).

9. C. Quigg, H. B. Thacker, and J. Rosner, Phys. Rev. D18, 274 (1978); D18, 287 (1978); D21, 234 (1980).

10. C. Quigg and J. Rosner, Phys. Rev. D23, 2625 (1981).

11. M. A. Shifman, Proceedings of the 1981 Symposium on Lepton and Photon Interactions at High Energies, p.242 Ed. W. Pfeil, Bonn, (1981). Also see M. B. Voloshin ,preprint ITEP-21 (1980).

12. See References 5 and 6 above.

13. E. Eichten and F. Feinberg, Phys. Rev. Lett. 43, 1205 (1979); Phys. Rev. D23, 2724 (1981).

14. W. Buchmuller, Phys. Letts. 112B, 479 (1982). Also see References 21 and 23.

15. J. Gaiser,"Charmonium Spectroscopy From the Radiative Decays of the J/ψ and ψ` ", Ph. D. Thesis, Stanford University; SLAC-PUB 255 (1982).

16. W. Buchmuller, Y. J. Ng, and S. H. H. Tye, Phys. Rev., D24, 3003 (1981).

17. K. Han et.al., Phys. Rev. Lett. 49, 1612 (1982); G. Eigen et.al., Phys. Rev. Lett., 49, 1616 (1982); and C. Klopfenstein et.al., Phys. Rev. Lett., 51, 60 (1983).

18. M. S. Alam et. al., Cornell Preprint Print 83-0869 (1983).

19. J. Gaiser, "Results From The Crystal Ball at Doris II", Presented at the 11th SLAC Summer Institute on Particle Physics, Stanford, CA., July 18-29 (1983); SLAC-PUB-3223.

20. P. M. Tuts, "Heavy Quarkonia", Summary talk presented at the International Symposium on the Lepton and Photon interactions at High Energies, Cornell University, Aug 4-9 (1983).

21. P. Moxhay and J. Rosner, Phys. Rev. D28, 1132 (1983).

22. J. Kogut and G. Parisi, Phys. Rev. Lett. 47, 1089 (1981).

23. R. McClary and N. Byers, Phys. Rev. D28, 1692 (1983).

24. Y.P. Kuang and T. M. Yan, Phys. Rev. D24, 2874 (1981).

25. V. Zambetakis and N. Byers, "Magnetic Dipole Transitions in Onia", U.C.L.A. preprint UCLA/83/11 (1983).

26. B. Adeva et.al., Phys. Rev. Lett. 50, 799 (1983).

27. C. Quigg and J. Rosner, Phys. Letts. 72B, 462 (1978).

28. For details on decays including the Electroweak couplings see: J. H. Kuhn and K. H. Streng, Nucl. Phys. B198, 71 (1982).

FIRST RESULTS FROM THE CDHS*) ν OSCILLATION EXPERIMENT AT CERN

Jörg Wotschack, CERN

ABSTRACT

First results on the CDHS low energy ν oscillation experiment at the CERN PS are reported. The experiment looks for the disappearance of ν_μ measuring simultaneously the ν flux at 130 and 885 m distance from the target. No significant deviation from the expected flux ratio has been found. The experiment excludes therefore oscillations of the type $\nu_\mu \rightarrow$ anything in the range $0.26 < \Delta m < 90$ eV^2 for maximal mixing. The best limit on the mixing angle $\sin^2 2\theta$ is 0.05 for $\Delta m^2 \simeq 2.5$ eV^2.

*) CERN-Dortmund-Heidelberg-Saclay-Warsaw collaboration

© J. Wotschack 1983

1. INTRODUCTION

For the oscillation experiment the CDHS neutrino detector, designed to cope with high energy neutrinos from the CERN Super Proton Synchrotron (SPS), has been used in a very non-standard way: neutrinos were provided by the Proton Synchrotron (PS) instead of the SPS; their energies were only a few GeV; no attempt was made to measure the hadronic energy; and the muon momenta were determined from range rather than from the track curvature in the magnetic field. The iron modules were not magnetized and the driftchambers were switched off. In addition, two detectors have been used instead of one.

2. FORMALISM

The concept that weak interaction eigenstate neutrinos ν_e, ν_μ, ..., might be superpositions of massive neutrinos ν_m, where $m = 1, 2, \ldots$, goes back to an idea of B. Pontecorvo in the late fifties [1]. Assuming there were only two neutrinos, the observable ν_μ and ν_e and the mass eigenstates ν_m are correlated simply by the mixing angle θ as

$$\begin{pmatrix} \nu_e \\ \nu_\mu \end{pmatrix} = \begin{pmatrix} \cos\theta & \sin\theta \\ -\sin\theta & \cos\theta \end{pmatrix} \begin{pmatrix} \nu_1 \\ \nu_2 \end{pmatrix}.$$

If now $m_{\nu_1} \neq m_{\nu_2}$ then ν_1 and ν_2 will develop differently with time and an initially pure ν_μ beam will appear as a mixture of ν_μ and ν_e at some distance from its origin. The probability that a ν_μ transforms into a ν_e depends on the mixing angle θ, the mass difference squared $\Delta m^2 = |m_{\nu_1}{}^2 - m_{\nu_2}{}^2|$ in eV^2, the distance of flight L(m) and the neutrino energy E(MeV) as

$$P_{\nu_\mu \to \nu_e} = \sin^2 2\theta \cdot \sin^2(1.27 \cdot \Delta m^2 \cdot \frac{L}{E}). \qquad (1)$$

Here $\sin^2 2\theta$ determines the amplitude of the oscillation and the second term containing Δm^2 and L/E the oscillation length. The sensitivity of the experiment on the range of mass differences squared is, to a large extent, given by the ratio of distances of flight and neutrino energy, L/E. Large values of L/E allow the small Δm^2 regions to be explored. Big mass differences squared would result in rapid oscillations: for large values of L/E the second term of Equation 1 would average to ½ and the sensitivity of the experiment is only determined by the value of the mixing angle θ.

3. PRESENT BEST LIMITS

Since the oscillation probability depends on both the mixing angle θ and Δm^2, results are usually presented in a two-dimensional plot in Δm^2 and $\sin^2 2\theta$.

No experiment so far has convincing evidence for the existence of oscillations. The present best limits for the different oscillation channels are shown in Figure 1. By far the smallest Δm^2 values, down to $\Delta m^2 = 0.017$ for $\sin^2 2\theta = 1$, [2] have been explored by a reactor experiment measuring the $\bar{\nu}_e$ flux at some distance from the reactor core. Since these experiments look for the disappearance of $\bar{\nu}_e$, i.e. $\bar{\nu}_e \to$ anything, they set at the same time a limit on $(\bar{\nu})_\mu \leftrightarrow \bar{\nu}_e$ oscillations.

Using ν_μ as initial neutrino state, the present limits are much less restrictive. Here the best limits have been obtained for the transition $\nu_\mu \to \nu_e$ by the BNL-Columbia 15' FNAL bubble chamber experiment [3] looking for an abnormal ν_e admixture in the ν_μ beam. No excess of ν_e has been found leading to the limits as shown in Fig. 1. From the same negative result, conclusions on the oscillation $\nu_\mu \to \nu_\tau$ can be drawn if one uses the 16% branching ratio $\tau \to e\nu\bar{\nu}$. Of course the limits are poorer than for the ν_e case giving $\Delta m^2 \simeq 2.5\ eV^2$ for maximal mixing. The same limit has also been reached by an emulsion experiment at FNAL [4] looking directly for τ decays. Among about 700 charged current interactions no τ has been observed.

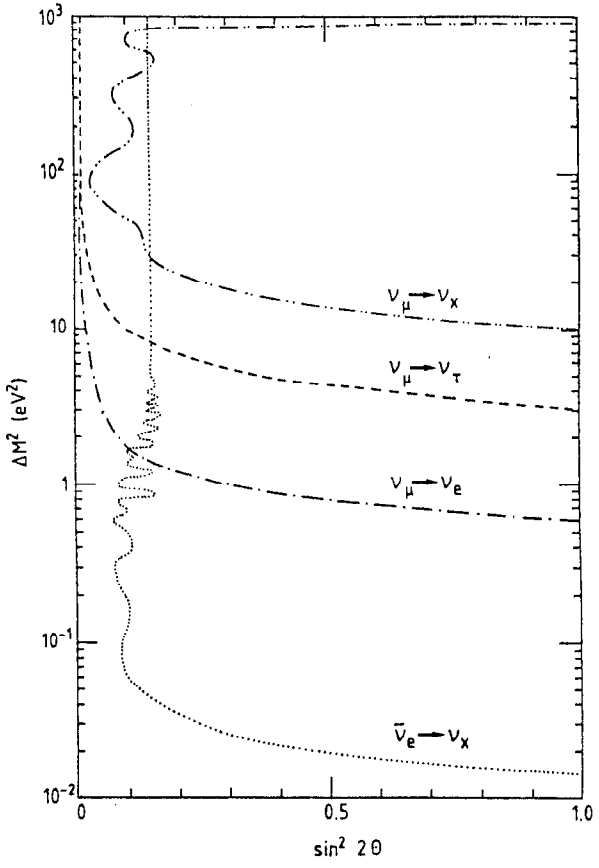


Figure 1: Present best limits on the mixing angle parameter $\sin^2 2\theta$ and the mass difference squared, Δm^2, for different oscillation channels. Results on $\bar{\nu}_e \rightarrow \nu_x$ are from the Gösgen reactor experiment [2], on $\nu_\mu \rightarrow \nu_e$ from a FNAL 15' bubble chamber for experiment [3], on $\nu_\mu \rightarrow \nu_\tau$ also from [3] and from a FNAL emulsion experiment [4]. The only limit on $\nu_\mu \rightarrow \nu_x$ comes from the CCFR experiment at FNAL. [5]

In contrast to these experiments which look for the appearance of new neutrino flavours, the CDHS oscillation search looks for a change in the primary ν_μ flux. This method - although statistically much more demanding - has the clear advantage of not being restricted to $\nu_\mu \rightarrow \nu_e$ and $\nu_\mu \rightarrow \nu_\tau$ oscillations. It also allows oscillations into thus far unknown types of neutrinos to be detected. The only existing result on such an inclusive search comes from the CCFR high energy ν_μ disappearance experiment, [5] which however is only sensitive to mass differences squared in the range 20 - 900 eV^2.

4. EXPERIMENTAL SET-UP

Oscillations of ν_μ into other types of neutrinos lead to a change of the ν_μ flux with distance from the neutrino origin. The idea is therefore to measure the ν_μ flux at two positions using ν_μ charged current events as signature. In order to become independent of an absolute flux determination the measurement was done simultaneously. The same acceptance and systematics are assured by using two detectors as identical as possible.

Neutrinos are produced in a bare target beam with a ν flux approximately proportional to L^{-2} where L is the distance from the target.

The general layout of the experiment on the CERN site is shown in Fig. 2. A new low energy neutrino facility has been constructed at the PS with a beam line pointing towards the existing CDHS west area detector which sits at 885 m from the new target. The second detector is implanted at 130 m distance from the target.

Protons of 19.2 GeV are provided from the PS every 1.2 sec in 20 bunches each 5-10 nsec wide and separated by 105 nsec. The target is a 60 cm long rod of Beryllium 8 mm in diameter. It is followed by a 52 m tunnel to allow the kaons and pions produced in the target to decay. The muons, produced at the same

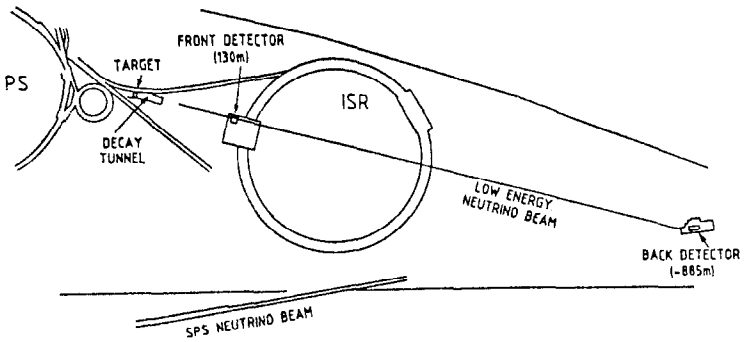


Figure 2: Layout of the CERN neutrino oscillation facility at the PS. Indicated are the positions of the two CDHS detectors at 130 and 885 m from the target.

time, and the remaining hadrons are absorbed in 4 m of iron and 70 m of molasse behind the decay tunnel.

There is no focussing behind the target. The neutrino beam has, therefore, a divergence much larger than the solid angle subtended by the two detectors. The neutrino flux is almost constant over the detector surface, independent of the neutrino energy, for energies larger than 1 GeV. The neutrino spectrum peaks at about 1 GeV and decreases proportionally to e^{-E_ν} at higher energies.

The layout of the two detectors is shown in Fig. 3. Both detectors are inclined by 22° with respect to the beam axis. They are composed of modules constructed of circular iron plates, 3.85 m in diameter, interleaved with plastic scintillator hodoscopes. Three distinct types of modules are used. Their main differences are in the sampling width in beam direction and the horizontal and vertical granularity of the hodoscopes. Type I modules have 2.5 cm iron sampling but five consecutive scintillators are viewed by the same photomultiplier leading to an effective sampling of 12.5 cm of iron. The horizontal and vertical granularity is 15×15 cm^2. Type II modules are sampled every 5 cm of iron. The vertical resolution is 45 cm and no information on horizontal position is available. The same structure is used in the type III modules only here the sampling width is 15 cm. The back detector is formed of 10, 5, and 6 modules of the three types respectively, while the front detector consists of two modules of each type, see Fig. 3.

The trigger is based on the projected range of iron traversed by the most penetrating particle of the event. Trigger planes were constructed by adding all of the signals of single planes in the type I modules and of groups of three consecutive planes in the type II modules. The modules of type III were not used in the trigger. The thickness in iron per trigger plane is 12.5 cm and 15 cm correspondingly. An event is registered if three out of four adjacent trigger planes have a signal larger than 1/5 of

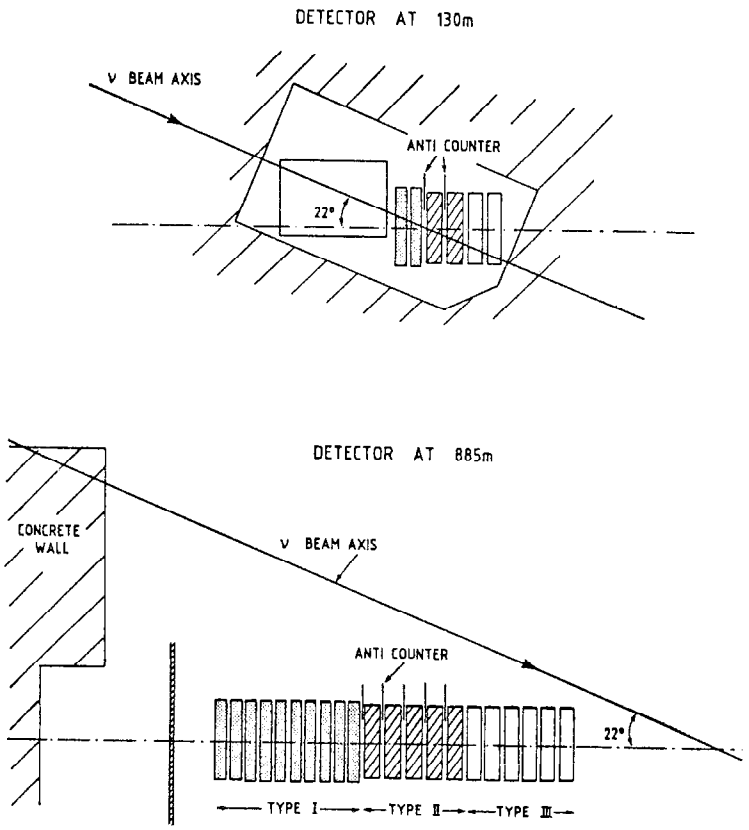


Figure 3: Layout of the two detectors of the CDHS neutrino oscillation experiment. The front detector is sitting in a 6 m deep hole, completely surrounded by concrete. This is simulated at the back detector by erecting an 8 m thick concrete wall in front of the detector.

that released by a minimum-ionizing particle. With this condition full trigger efficiency is achieved for events with projected ranges longer than 40 cm. The two detectors are linked and controlled and readout by a single computer ensuring identical life- and down-times.

An offline reconstruction program assigned to each event the geometrical vertex position and determined the event range in iron, projected onto the detector axis. The last plane of an event was either defined by the point where the most penetrating particle came to rest or left the detector. Also the vertical angle and - for the type I modules - the horizontal angle of the track of the most penetrating particle (usually a muon) has been determined.

5. DATA AND BACKGROUNDS

Data were taken during six weeks in February and March 1983. The useful number of protons on target was 7×10^{18} with bursts of typically 10^{13} protons every 1.2 sec. Events were taken in a 3μs gate around the 2.1 μs long neutrino spill. The corresponding data rates in the front and back detector were 1/5 and 1/70 beam correlated events per burst and 1/250 and 1/60 cosmic ray events. The deadtime due to these rates were (9±1)% and (2±0.2)%. In order to determine the background from cosmic ray events and to monitor the detector performance,data were also taken in a second gate, outside the spill and 600 μs long.

There were two main sources of background to the experiment: cosmic ray events and muons from neutrino interactions in the material surrounding the detectors. The cosmic ray background can be neglected in the front detector but is, however, as big as the signal in the back detector. The majority of cosmic ray events was easily eliminated by requiring that the event vertex was inside the detector and that the vertical angle of the muon track with the detector axis was less than 45^{o}. A remaining background

of 0.5% in the front detector and about 9% in the back detector has been subtracted statistically using the rates measured in the out of spill gate.

The neutrino induced muons entering the detector from the outside are beam correlated and their relative importance is much larger in the front detector than in the back. To ensure the same background muon environment in both detectors an 8 m thick concrete wall had been piled up in front of the back detector simulating the concrete surrounding the front detector, see Fig. 3. Once created, these muons were then rejected by using the first planes of the detectors as anticounters. Muons entering the detector through the sides were rejected in the type I modules by requiring that the vertex was not more than 1.6 m away from the detector axis. In the type II modules, events were rejected if they started in the top or bottom layers of scintillators or if there was a signal in the anti-counter installed in front of each module on the side facing the beam.

In addition to these cuts, events were only retained if their vertex was inside the fiducial volume which was chosen so that differences between the two detector set-ups were minimal. For each type of module, only events originating in the volume from the second plane of the first module to the first plane of the last module were accepted. The corresponding fiducial volumes are nine modules of type I and four modules of type II in the back detector and one module of each type in the front detector.

After all cuts, approximately 22,000 and 3,300 events were left in the front and back detector respectively, with a contamination of 50 and 300 cosmic ray events.

6. RESULTS

In the analysis the following principles were applied. Events were classified according to their range in iron. This minimizes any dependence on pulseheight calibration in the two detectors. A minimal projected range of four and ten planes in the modules of type I and II, respectively, ensured full trigger efficiency and, at the same time, reduced the contribution of neutral current events to the event sample to less than 5%. The average neutrino energy of the accepted events was about 3 GeV in both detectors. Events starting in modules of type I and II were analysed separately. Only relative rates in the two detectors were used.

Small differences in the neutrino spectrum and in the detector geometry were corrected for, with the help of Monte Carlo generated events. This simulation included hadron production and neutrino interaction cross sections. It also included effects such as secondary proton interactions and hadron absorption in the target, as well as hadron production in the decay region and in the beam dump. Neutrino interactions in the material surrounding the detectors, neutral current interactions, and minor differences in the functioning of the two detectors were also taken into account. The typical correction to the geometrical scaling (the ratio of the distances squared divided by the number of fiducial modules) is 5%.

Table 1

Detector Type Loc. *)	$\frac{\text{Distance}^2}{\text{fid. vol.}}$	Number of events		
		Data	MC	Data/MC
I F	$129.1^2/1$	10180	8863	
I B	$880^2/9$	2005	1685	
I B/F	0.1937	0.1970±0.0048	0.1901±0.0014	1.036±0.030
II F	$130.7^2/1$	13120	12252	
II B	$887^2/4$	1156	1019	
II B/F	0.0868	0.0881±0.0027	0.0832±0.007	1.059±0.040

*) F = Front, B = Back

Table I gives the final event numbers and their ratios for the two types of modules. The errors are statistical only. Also given are the expected back/front ratios of the neutrino flux assuming L^{-2} scaling and the result of the Monte Carlo calculation for the case of no oscillations.

The systematic uncertainties of the experiment were estimated by varying the parameters of the analysis over the expected range of uncertainty and studying the effect on the ratio of events in the two detectors. The most serious contributions came from the dead-time correction, the differences in event reconstruction efficiency and the performance of the two detectors, and the number of events entering the fiducial volume from outside, but not identified as such. Each of these uncertainties was found to be 1%. The second serious group of uncertainties came from our imperfect knowledge of the hadron production energy and transverse momentum spectra, the hadron absorption in the target, the hadronic spectra from secondary proton interactions, the effect of proton interactions downstream of the target and possible trigger inefficiencies. Each of them was estimated to be at most 0.5%. Finally uncertainties in neutrino cross-sections and the cosmic ray event subtraction were found to contribute less than 0.5%. By adding all of these contributions in quadrature, the overall systematic uncertainty in the ratio of the event rates in the two detectors was estimated to be 2.5%.

From the integrated rates in Table 1, taking into account the systematic uncertainty, limits on Δm^2 and $\sin^2 2\theta$ can be obtained as shown in Fig. 4. Small Δm^2 oscillations would result in a suppressed flux of neutrinos in the back detector giving a back/front smaller than unity. For $\Delta m^2 \gtrsim 10\ eV^2$, however, the back/front ratio can become unity or even larger and an analysis using integrated event numbers is not sensitive.

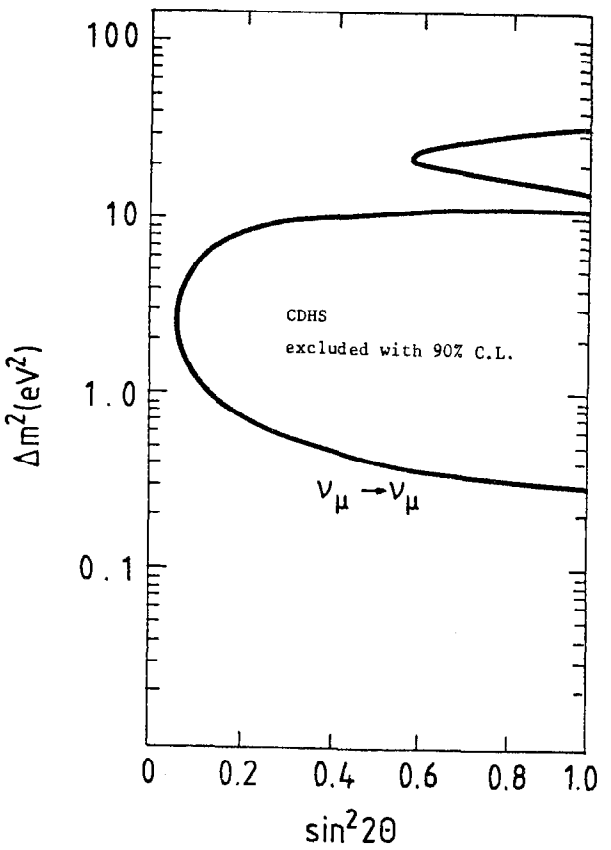


Figure 4: Limit on neutrino oscillations $\nu_\mu \rightarrow$ anything in terms of Δm^2 and $\sin^2 2\theta$ as obtained by comparing integrated event rates in the two detectors. The region on the right side of the curve is excluded (90% C.L.).

More information than from the integrated rates can be obtained by looking at the ratio of events as a function of their projected range in iron. Figures 5a and 5b show the back/front ratios for data and Monte Carlo events in the two types of modules, respectively. The ratio of data and MC is given in Fig. 6 together with the expected variation of this ratio as a function of range for different assumptions of Δm^2 and $\sin^2 2\theta$. In the case of no oscillations this ratio should be unity independent of range. The data show no significant signs of an oscillation. From the event rates in the two detectors as a function of range, including the 2.5% systematic error, limits on ν_μ oscillations can be set in terms of $\sin^2 2\theta$ and Δm^2, as shown in Fig. 7. The area to the right of the curve is excluded at the 90% confidence level. For maximal mixing Δm^2 values between 0.26 and 90 eV^2 are excluded. The most restrictive limit on the neutrino mixing angle parameter $\sin^2 2\theta$ is 0.05 at $\Delta m^2 = 2.5\ eV^2$. A comparison with the best limits obtained in earlier experiments, see Fig. 1, shows that the best Δm^2 limit for $\nu_\mu \rightarrow \nu_e$ oscillations has been improved by a factor of two. The improvement in the transition $\nu_\mu \rightarrow \nu_\tau$ is about a factor ten and for the oscillation $\nu_\mu \rightarrow$ anything the limit on Δm^2 has been ameliorated by a factor of $\sim$60.

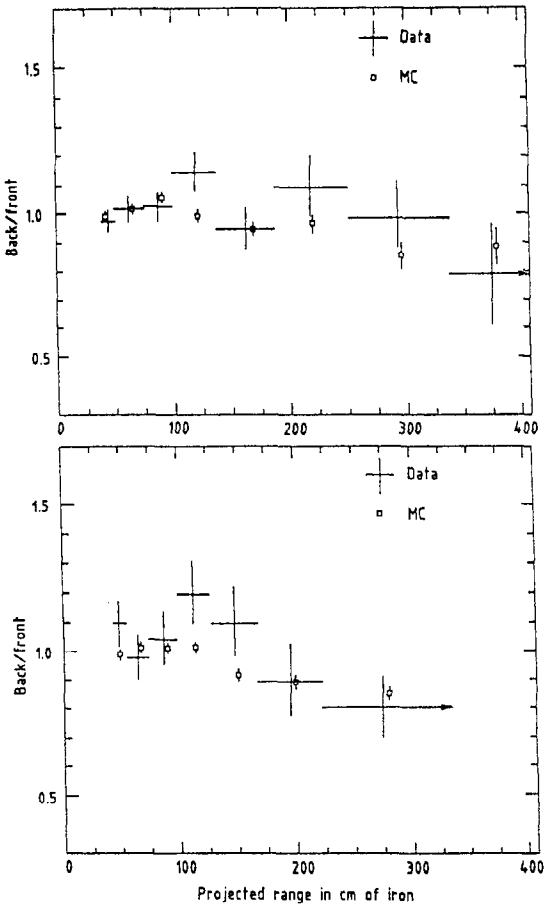


Figure 5: Ratio of event rates in the back and front detector as as function of the projected range of the events in iron. Data ratios and the corresponding Monte Carlo ratios are shown in 5a) for events starting in modules of type I and in 5b) for events starting in type II modules.

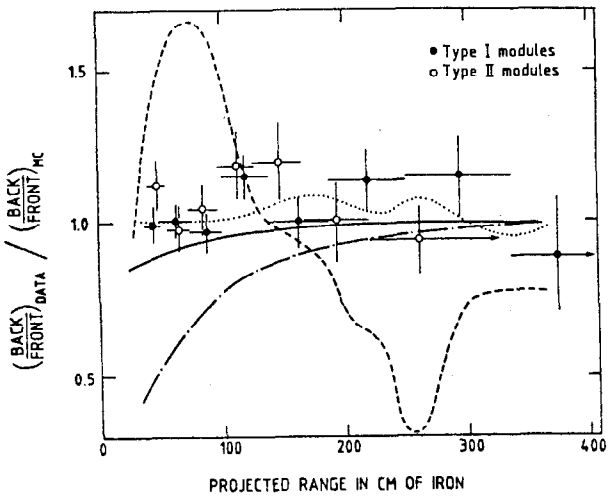


Figure 6: Ratio of Monte Carlo corrected event rates in the back and front detector as a function of projected range in iron. Events starting in the two types of modules are given separately. Also shown are curves indicating the expected behaviour of these ratios in the case of oscillations for different choices of Δm^2 and $\sin^2 2\theta$. ——— $\Delta m^2 = 1$ eV^2 and $\sin^2 2\theta = 0.2$; -·-·- $\Delta m^2 = 1$ eV^2 and $\sin^2 2\theta = 1$; ····· $\Delta m^2 = 32$ eV^2 and $\sin^2 2\theta = 0.2$; ----- $\Delta m^2 = 32$ eV^2 and $\sin^2 2\theta = 1$.

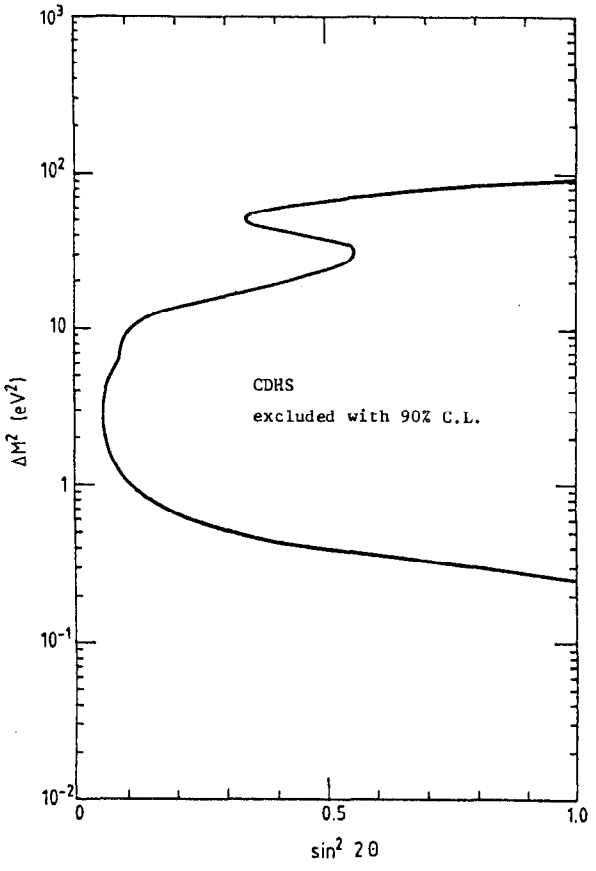


Figure 7: Final limits set by the experiment on ν_μ + anything obtained from a fit to the ratio of event rates as a function of projected range in iron. The area to the right side of the curve is excluded with 90% C.L.

REFERENCES

1) B. Pontecorvo, Sov. Phys. JETP 6 (1958) 429; 7 (1958) 172; 26 (1968) 984.

2) J.L. Vuilleumier et al., Phys. Lett. 114B (1982) 298.

3) N.J. Baker et al., Phys. Rev. Lett. 47 (1981) 1576.

4) N. Ushida et al., Phys. Rev. Lett. 47 (1981) 1694.

5) C. Haber et al., Fermilab preprint, FERMILAB-CONF-83/57-EXP (1983).

RESULTS FROM THE CCFR NEUTRINO OSCILLATION EXPERIMENT

Presented by M. Oreglia,

Representing the CCFR collaboration:

D. Garfinkle, F. S. Merritt, M. Oreglia, P. Reutens
Enrico Fermi Institute, University of Chicago,
Chicago, Illinois 60637

and

P. S. Auchincloss, R. Blair, C. Haber, M. Ruiz[a]
F. Sciulli, M. H. Shaevitz, W. H. Smith, R. Zhu[b]
Columbia University, New York, New York 10027

and

R. Coleman, H. E. Fisk, B. Jin[b], D. Levinthal[c]
W. Marsh, P. A. Rapidis, H. White, D. Yovanovitch
Fermi National Acclerator Laboratory,
Batavia, Illinois 60510

and

A. Bodek, F. Borcherding, N. Giokaris,
K. Lang, I. E. Stockdale
University of Rochester, Rochester, New York 14627

Abstract

A search for inclusive ν_μ oscillations has been performed in the Fermilab narrow band neutrino beam using two detectors running simultaneously at different distances from the neutrino source. The data show no signal and rule out oscillations of ν_μ into any other single type of neutrino for $20 < \Delta m^2 < 900$ eV^2 and $\sin^2(2\theta) > 0.03$-0.10.

© M. Oreglia 1983

INTRODUCTION

We report here results from the preliminary analysis of experiment E701 at Fermilab, a search for muon neutrino oscillations. The consequences of a neutrino mass and a unitary mixing matrix, and the experimental attempts to measure the neutrino properties, have been described in a recent review article.[1] For three lepton generations the neutrino mass eigenstates are

$$\nu_\alpha = \Sigma\, U_{\alpha j}\nu_j \ , \ \alpha = e,\mu,\tau\ldots \ , \ j = 1,2,3\ldots \quad , \tag{1}$$

where U contains three mixing angles and one CP violating phase as with the Kobayashi-Maskawa mixing of quarks. The CP violation would create a difference in the oscillation rates for $\nu_\mu \to \nu_e$ and $\bar{\nu}_\mu \to \bar{\nu}_e$.

Evolution of a pure mass eigenstate proceeds as e^{-iEt}. If the neutrinos possess energies much larger than their masses, the probability amplitude for observing muon neutrinos at a distance L from a pure ν_μ source is

$$\begin{aligned} A(\nu_\mu \to \nu_\mu) = 1 &- A_{12}\left\{1-\cos(2\pi L/L_{12})\right\} \\ &- A_{13}\left\{1-\cos(2\pi L/L_{13})\right\} \\ &- A_{23}\left\{1-\cos(2\pi L/L_{23})\right\} \end{aligned} \tag{2}$$

In the preceding equation the A_{ij} are functions of the four mixing parameters, and the oscillation lengths are defined as

$$L_{ij} = \frac{4\pi E}{m^2_{\nu_i} - m^2_{\nu_j}} = \frac{4\pi E}{\Delta m^2_{ij}} \quad . \tag{3}$$

If one of the oscillation channels (c) dominates, the A_{ij} ($i,j \neq c$) are small, so the intensity corresponding to Equation 2 reduces to the single harmonic form

$$P(\nu_\mu \to \nu_\mu) = 1 - \sin^2 2\theta\, \sin^2(1.27\, \Delta m^2\, L/E) \quad , \tag{4}$$

where Δm^2 is in eV^2, L in km and E in GeV; the behavior of this function is shown in Figure 1. If an oscillation measurement is performed by placing detectors at two values of E/L, then there is a high-Δm^2 limit to the sensitivity of the experiment. This limit corresponds to the point at which both detectors are many oscillation periods from the source. The high-Δm^2 limit is absent if one detector is at the neutrino source or if the intensity of the source is well understood. The effect of an oscillation is maximal when $1.27*\Delta m^2*L/E$ is near $\pi/2$; therefore, E/L serves as a figure of merit for the measurement of Δm^2. The FNAL neutrino beam area (E/L = 50) is sensitive to Δm^2 in the 10-1000 eV^2 range, the CERN PS (E/L = 3) to 1-100 eV^2, reactors (E/L = 1) to 0.1-5 eV^2, and so forth. In general, we have no reason to expect that the mixing angles are large. If the Cabbibo angle is to be considered as indicative of

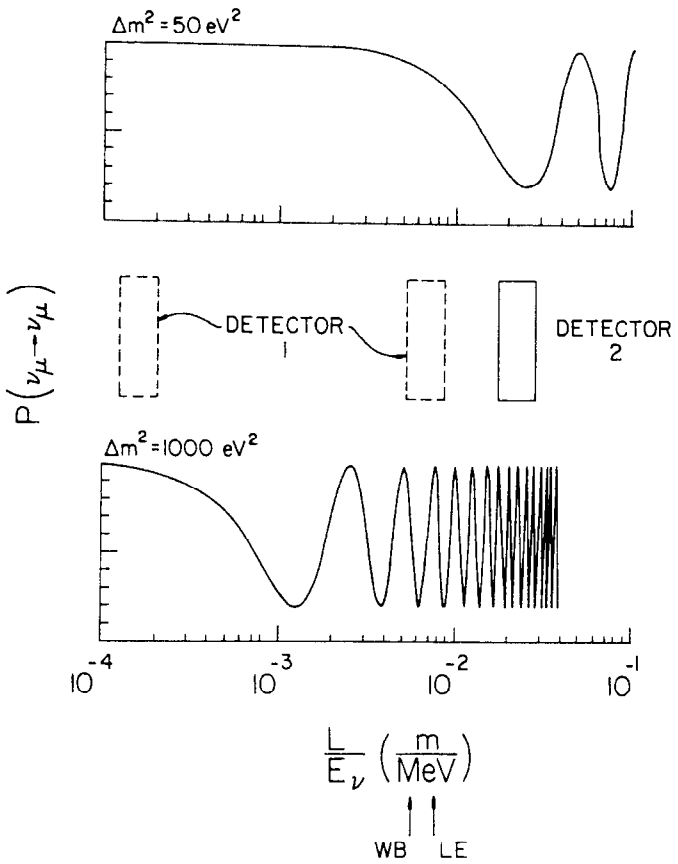


Fig. 1. Intensity of ν_μ, from a pure source, as a function of L/E. For one oscillation channel with $\sin^2 2\theta = 0.8$, the upper plot has $\Delta m^2 = 50$ eV^2 and the lower plot 1000 eV^2. For a two-detector experiment, the variable position of the upstream detector indicates how an experiment is limited for Δm^2 large. Detector positions for this experiment are shown at the bottom.

possible mixing in the neutrino sector, then an experiment should be sensitive to θ on the order of 13° ($\sin^2 2\theta = 0.2$) or smaller.

Oscillations can be detected from an initially pure beam of ν_μ either by exclusively searching for ν_e and ν_τ downstream of the source, or inclusively by measuring a change in the ν_μ flux as a function of distance from the source. Upper limits on the channels $\nu_\mu \rightarrow \nu_\tau$ [2] and $\nu_\mu \rightarrow \nu_e$ [3] have been set by exclusive experiments for Δm^2 larger than 1-3 eV^2 and θ larger than 2° to 3°; the 90% confidence level limits as a function of Δm^2 and $\sin^2 2\theta$ are shown in Figure 2. It should be pointed out that new results [4] from a beta decay experiment indicate an electron neutrino mass of greater than 20 eV. Furthermore, astrophysical measurements suggest an excess of dark matter in the universe [5]; neutrinos having masses in this range are a possible source of the dark matter.

Exclusive measurements are not sensitive to the oscillation channels $\nu_\mu \rightarrow \nu_x$, where x refers to any new generation having a charged lepton too massive to be produced in present neutrino beams. Similarly, the exclusive searches are insensitive to the oscillations $\nu_\mu \rightarrow \bar{\nu}_{\mu\text{LEFT}}$ in which the left-handed antineutrino is

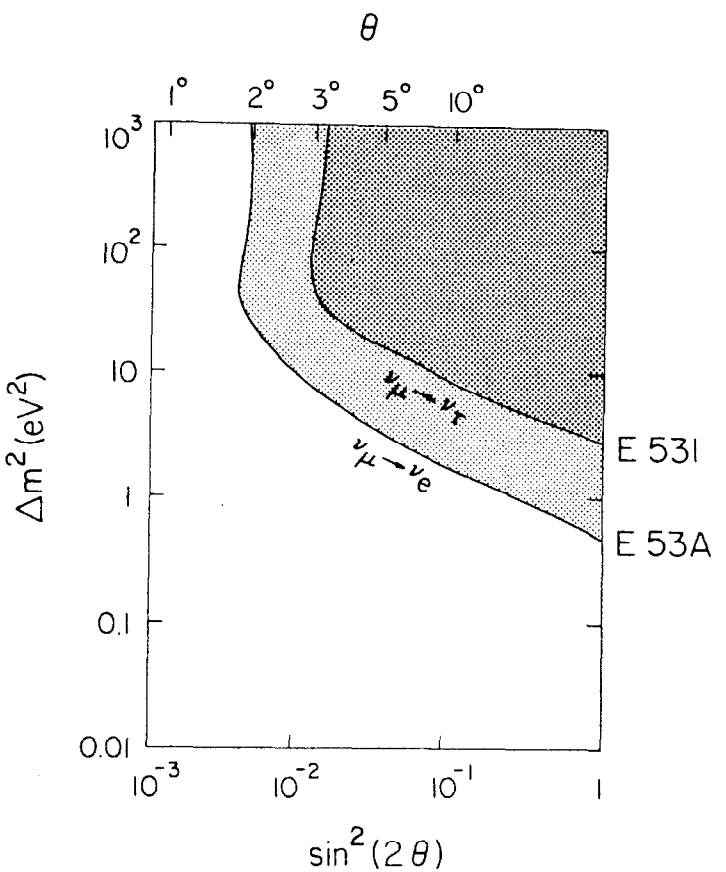


Fig. 2. Existing limits on exclusive ν_μ oscillation channels. The regions to the right of the boundary are excluded at the 90% confidence level. The ν_τ channel is from [2] and the ν_e channel from [3].

sterile by virture of its null V-A coupling. Inclusive measurements are sensitive to all oscillation channels.

We report here the preliminary results from the first ν_μ inclusive oscillation experiment using two detectors. This experiment is sensitive to the disappearence in flux of ν_μ charged-current events, with $m^2(\nu_\mu)-m^2(\nu_x)$ in the range 10-1000 eV^2, and with a sensitivity in the mixing amplitude corresponding to $\theta > 6°$. The positions of the ν_μ source and the two muon neutrino detectors in this inclusive experiment are shown in Figure 3. Muon neutrinos having energies between 40 and 230 GeV were produced at the FNAL narrow-band beam line. Systematic errors are reduced by using the two-detector ratio of the ν_μ charged-current event rate as a function of neutrino energy; in particular, a knowledge of the absolute neutrino flux was not necessary. To give an impression of the sensitivity of the experiment, Figure 4 illustrates the difference in the ν_μ flux at the detectors for a hypothetical Δm^2 of 380 eV^2 and a ν_μ-ν_x mixing amplitude of 20%.

NEUTRINO LINE AND DETECTORS

At the FNAL neutrino line as depicted in Figure 3, pions and kaons are produced by 400 GeV protons impinging

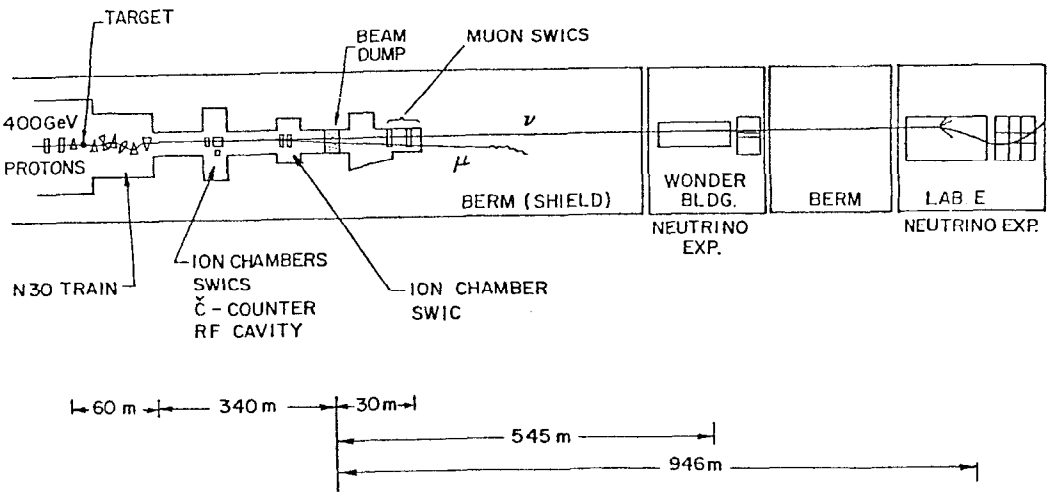


Fig. 3. Layout of the FNAL narrow-band beam neutrino area. The "N30 train", a.k.a. "dichromatic train", selects secondary hadrons of a given momentum and charge. Mesons decay in a 352 m material-free path.

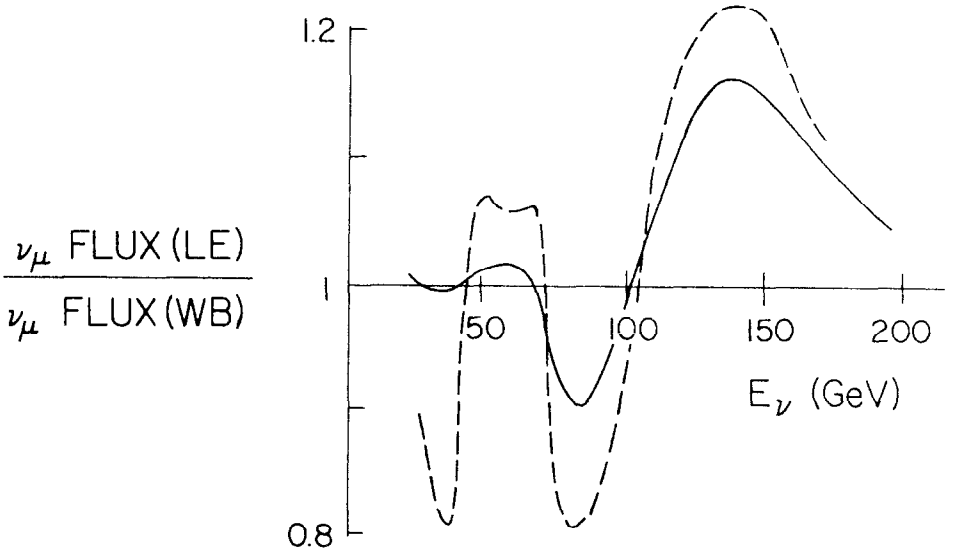


Fig. 4. Difference in number of ν_μ seen at LE vs. WB for a hypothetical oscillation with $\sin^2 2\theta = 0.2$ and $\Delta m^2 = 380$ eV^2. The broken curve depicts a point ν_μ source, while the solid curve includes the effects from the extended decay region and energy spread of the beam.

on a BeO target. These hadrons are momentum and charge selected by a series of dipole and quadrupole magnets (the dichromatic train), with a resulting RMS momentum spread of 11%. Following the train is a 352m evacuated pipe in which the mesons decay into ν_μ primarily via the two-body mode; the decay spectrum is shown in Figure 5. For a train setting of 165 GeV, 4% of the pions and 25% of the kaons decay in the 352m decay pipe. Beam monitors are located in the decay pipe at two stations located 137m and 292m from the upstream end of the pipe. Only three types of the monitors indicated in Figure 3 are relevant to the oscillation analysis; these are the segmented wire ionization chambers (SWIC) for measuring the hadron beam profile, the split-plate ionization chambers, used for steering the hadron beam, and the beam current transformer which is used to determine the detector live times. The SWICs are especially important for measuring the divergence of the hadron beam; this divergence affects the relative solid angle that the two detectors view. Also useful for measuring the divergence are a scanning scintillator and a segmented-strip ion chamber, the latter used in conjuction with a moveable narrow-aperture collimator at the entrance to the decay pipe.

Protons were delivered to the target in one-second

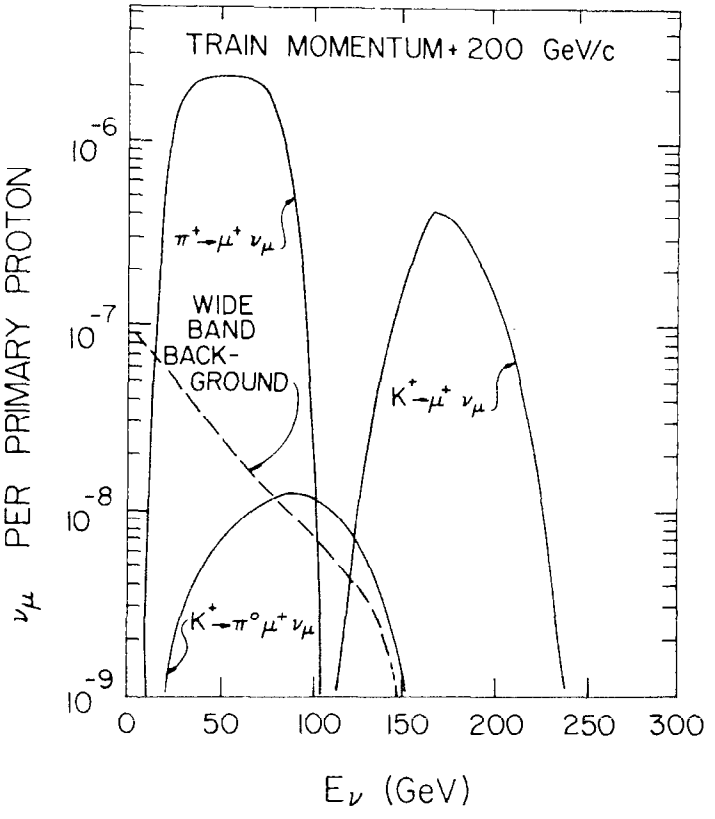


Fig. 5. Flux of ν_μ generated in the narrow-band beam.

duration spills which occurred every 11 to 15 seconds. Each spill consisted of six one-millisecond pulses (pings) during which a total of about 1.5×10^{13} protons were delivered to the target. This resulted in an average of about 1.5 neutrino interactions per detector per spill.

The two neutrino detectors are located after the muon shielding (earth and steel) at distances of 715m and 1116m from the decay pipe center. The downstream detector (Laboratory E, or LE) is the pre-existing apparatus of the CCFR collaboration and has been described in detail.[6] Briefly, it consists of a 444 metric ton steel calorimeter having 56 scintillator counters, one after every 10cm of steel. The $(3m)^2 \times 2.5cm$ counters contain liquid scintillator which is viewed by four photomultiplier tubes via wavelength-shifter bars. Spark chambers measuring $(3m)^2$ and using magnetostrictive readout are positioned after every 20cm of steel. This target calorimeter has achieved a hadron energy resolution $\sigma(E)=0.9\sqrt{E}$. Following the target is a muon spectrometer consisting of spark chambers and three steel toroid magnets having a total transverse momentum kick of 2.4 GeV/c. These toroids measure 1.8m in radius by 1.6m long, and have an inner hole (for the coil) with a radius of 12.7cm. The spectrometer measures muon momentum with a resolution $\sigma(p)=0.11p$ in the range 7 to 400 GeV/c. Figure 6 illustrates the layout of the detector.

The upstream detector (Wonder Building, or WB) was constructed to be similar to the LE apparatus, but scaled in transverse dimensions to occupy roughly the same solid angle from the neutrino source as LE. The WB target contains 108 tons of steel, with 56 $(1.5m)^2 \times 2.5cm$ acrylic scintillator counters, one after every 10cm of steel. These counters are viewed by two phototubes via wave-shifter bars, and they provide calorimetry with a hadron energy resolution equal to that in Lab E. Spark chambers are positioned after every 30cm of steel in the WB target, which is followed by a single steel toroid, 2.4m long, having a 1.2 GeV/c momentum kick. This results in a muon momentum resolution $\sigma(p)=0.15p$ which is somewhat poorer than that achieved at LE due to the reduced transverse momentum kick. This detector is also shown in Figure 6. The detectors provide a resolution of about 15% on the neutrino energy after combining the resolutions from the hadron calorimetry and the muon momentum determination. A comparison of the detector properties is given in Table 1.

The trigger conditions and fiducial volumes were

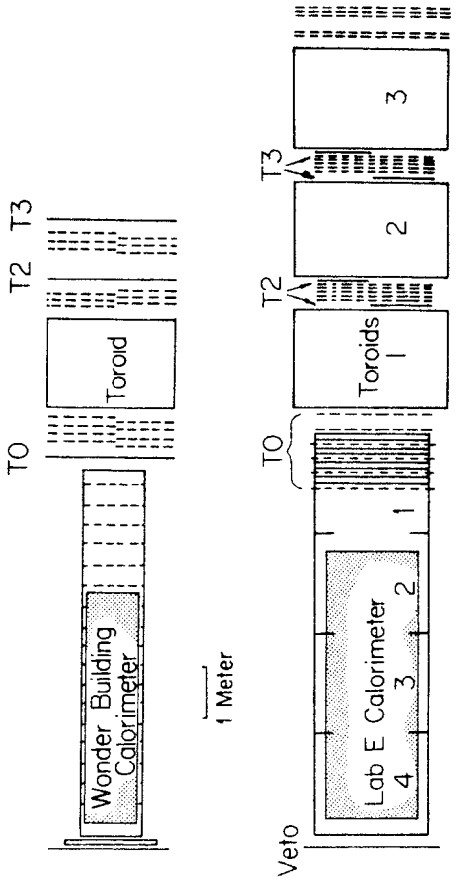


Fig. 6. Layout of the two ν_μ detectors. Broken lines indicate some of the spark chambers. The fiducial volumes are shaded. For WB a top view is given; for LE a side view.

TABLE 1

	LE	WB	UNITS
TARGET CALORIMETER			
Mean distance to decay pipe	1116	715	m
Steel, absolute:			
length	5.7	5.7	m
breadth	3 x 3	1.5 x 1.5	m
mass	444	108	metric ton
Steel, fiducial:			
length	3.8	3.8	m
breadth	2 x 2	1.3 x 1.3	m
mass	116	48	metric ton
Steel per counter	10.2	10.2	cm
Steel per chamber	20.3	30.5	cm
Hadron energy $\sigma(E)/E$	$0.9/\sqrt{E}$	$0.9/\sqrt{E}$	GeV
MAGNET SYSTEM			
Toriod:			
length	4.8	2.4	m
outer radius	1.8	1.5	m
inner radius	12.7	12.7	cm
field	17.5	17.5	kG
p_t kick	2.4	1.2	GeV/c
$\sigma(x)$, spark chambers	0.9	0.9	mm
$\sigma(p_\mu)/p_\mu$	0.11	0.15	

chosen to make the two detectors look identical and to select charged-current neutrino interactions which could be fully analyzed. Triggers from muons escaping the shielding beam were rejected by veto scintillators preceding the detectors; these scintillators were followed by at least 7.5cm of steel to prevent vetoing from backwards-going charged particles originating in the target. In addition to the veto requirement, a valid trigger required at least one minimum-ionizing signal in one of the target counters in coincidence with hits in the trigger scintillators T0 and T2, which were located in front of and behind the first toroid, respectively. For the LE detector, T0 consists of a majority logic condition on the first eight target counters. A second trigger requires only that a total energy of at least 5 GeV be measured in the target and that minimum-ionizing signals occur in at least 12 of the target counters. This corresponds to a muon penetrating at least 1.2m of steel.

In order to fully contain the hadron showers, the event vertex is required to be a safe distance from the edge of the target. In particular, the vertex of the event had to be at least two counters into the target calorimeter and 17 before the end. The transverse position of the vertex had to be within a 1.27m × 1.27m square at the WB, or 1.98m × 1.98m at LE; these dimensions are in the ratio 1:1.56, which is the ratio of the distances of the detector target centers from the decay pipe center. These conditions result in fiducial volumes of 48 tons and 116 tons for WB and LE, respectively.

EVENT KINEMATICS

For neutrinos originating from a point source of pion and kaon two-body decays there is a simple relation between the neutrino energy and the radius of the neutrino interaction vertex in the detector:

$$E_\nu = \begin{Bmatrix} \frac{0.43}{0.95} & , \pi \\ & , K \end{Bmatrix} \frac{P(\text{train})}{1 + \gamma^2\theta^2} \quad , \gamma \equiv \frac{P}{M}\Big|_{\pi,K} \tag{5}$$

where the parameter 0.43 is for pion decay, 0.93 is for kaons, θ is the angle between the ν_μ and the hadron beam, and P(train) is the momentum setting of the dichromatic train. The Lorentz angle $\theta = \gamma^{-1}$, which is the 90° decay in the hadron CMS, provides a measure of the solid angle covered by the detectors for ν_μ^π and ν_μ^K at various train momenta. At all the train settings between 100 GeV/c and 250 GeV/c, the ν_μ^π are essentially contained by both detectors. The ν_μ^K, however, have a γ^{-1} which corresponds to a LE radius of 5.5m at the 100 GeV/c train setting, or

2.2m for the maximum setting of 250 GeV/c; this is to be compared with the LE fiducial volume of maximum radius 1m. Therefore, a large percentage of the ν_μ^K are not detected for all the train momentum settings.

In order to obtain similar resolution for neutrino energy bins at the two detectors, our analysis makes use of energy bins as determined from the interaction radius of the event rather than bins of visible energy (i.e., $E_{had}+E_\mu$). This scheme, however, requires that ν_μ^π be differentiated from ν_μ^K on the basis of the visible energy and the vertex radius. Figure 7 shows the ν_μ^π/ν_μ^K separation achieved by the two detectors at different train settings. The ν_μ^π/ν_μ^K separation is sharp for all the train settings.

It is important to identify the neutrino beam centerline on a spill by spill basis in light of the binning. This is accomplished by using the split-plate ion chamber information to reject events if the split-plate measured centerline deviates from the nominal neutrino beam centerline at LE by more than ±2.5cm. The nominal centerline is determined to better than ±1cm from the distribution of high energy ν_μ^π vertices.

For a given train setting, the events are separated

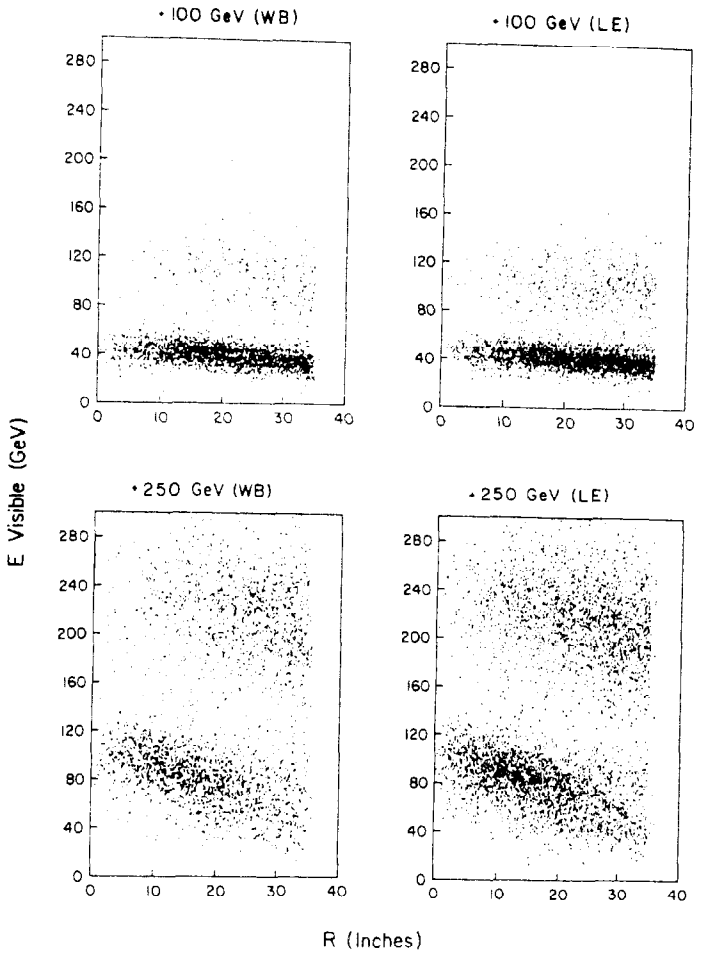


Fig. 7a. Measured ν_μ energy vs. interaction radius at the WB and LE detectors for π^+ and K^+ momenta of 100 and 250 GeV/c. WB radius is multiplied by 1.56. Upper bands are from kaon decays and lower bands from pions.

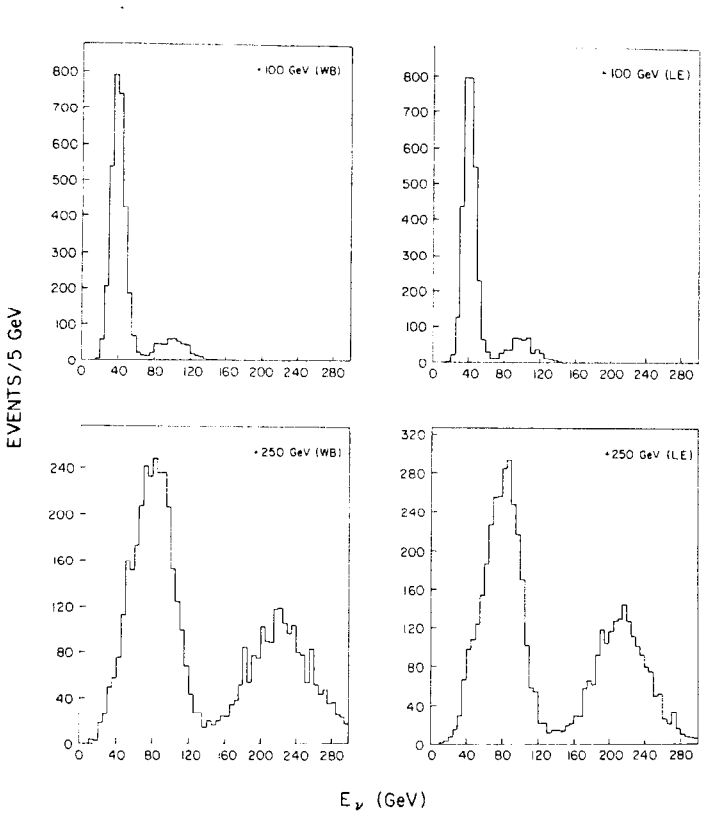


Fig. 7b. Projections of Fig. 7a onto energy axis.

into three bins. The ν_μ^K events constitute one of the bins; ν_μ^π with LE vertices between 0 and 51cm, and with vertices between 51cm and 99cm radii comprise the other two bins. Because of the radius-energy correlation, these bins are effectively energy bins. Events at the WB are projected (in a manner to be described) to LE in order to determine the appropriate bin. The energies of these fifteen bins that result from running at train settings of 100, 140, 165, 200, and 250 GeV/c are illustrated in Figure 8.

A point source of neutrinos at the decay pipe center would give rise to equal WB and LE fluxes in all bins, in the absence of oscillations. Two effects which alter this are the longitudinal extent of the decay pipe and the angular divergence of the hadron beam. The former effect is small (1%) and easily corrected for. On the other hand, the divergence effect is significant for the ν_μ^π at the higher energy train settings. Here γ^{-1} is on the order of 0.5 mrad, which is comparable to the beam divergence of 0.2 mrad. Correcting for this effect with a Monte Carlo simulation of the beam introduces a systematic error arising from the uncertainty in modeling the beam. We test the beam Monte Carlo program by attempting to match the hadron beam profiles available from the SWICs in the decay pipe with the Monte Carlo

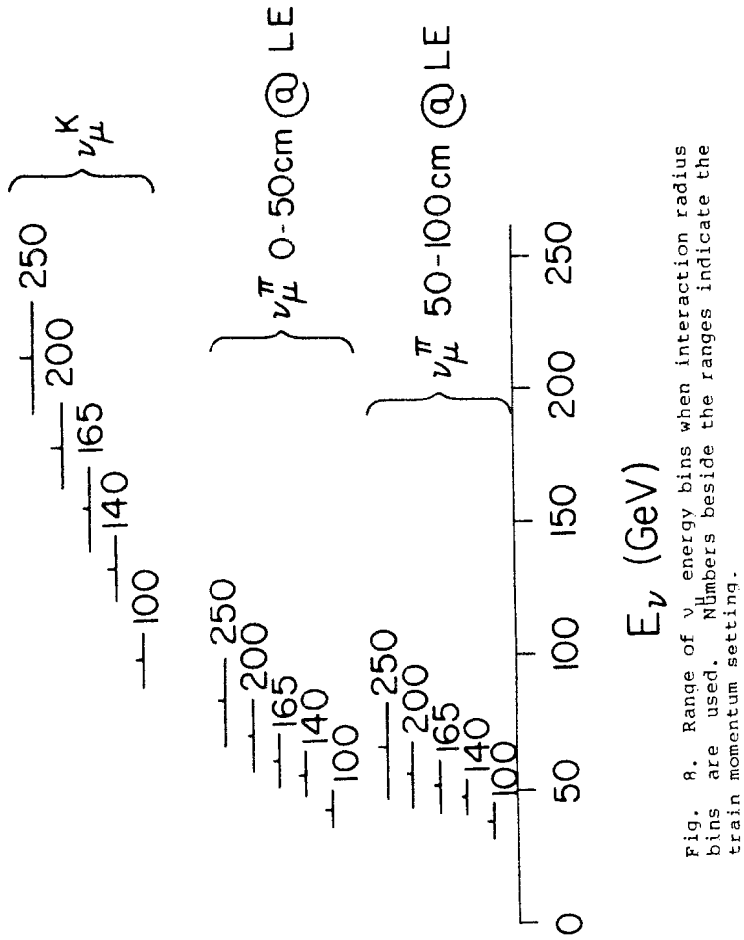


Fig. 8. Range of ν_μ energy bins when interaction radius bins are used. Numbers beside the ranges indicate the train momentum setting.

prediction. The SWIC measurement is done with the train set up for negatively charged hadrons in order to remove the proton contribution to the SWIC profile. The results of this comparison are shown in Figure 9. Agreement between SWIC data and beam Monte Carlo predictions is good, but not perfect; we estimate the uncertainty on the beam divergence to be 0.05 mrad. Currently we are attempting to correlate profiles from muon-SWICs at the end of the decay pipe with Monte Carlo generated muon profiles. We are also studying the intensity profiles obtained with a segmented-strip ion chamber during runs employing a narrow-aperture collimator between the train and the decay pipe. The collimator was scanned over the hadron beam aperture.

Another distortion of the event ratios arises from ν_μ generated before the dichromatic train. This wide-band background (shown in Figure 5) acts as a far-upstream source. It has been measured by taking data at all the train settings with the collimator slits closed, and these data are then incorporated into the beam Monte Carlo program. The overall correction to the event ratios is about 1% for ν_μ^π and 0.5% for ν_μ^K.

Figure 10 shows the full Monte Carlo prediction, including the above effect, for the LE/WB event ratios in

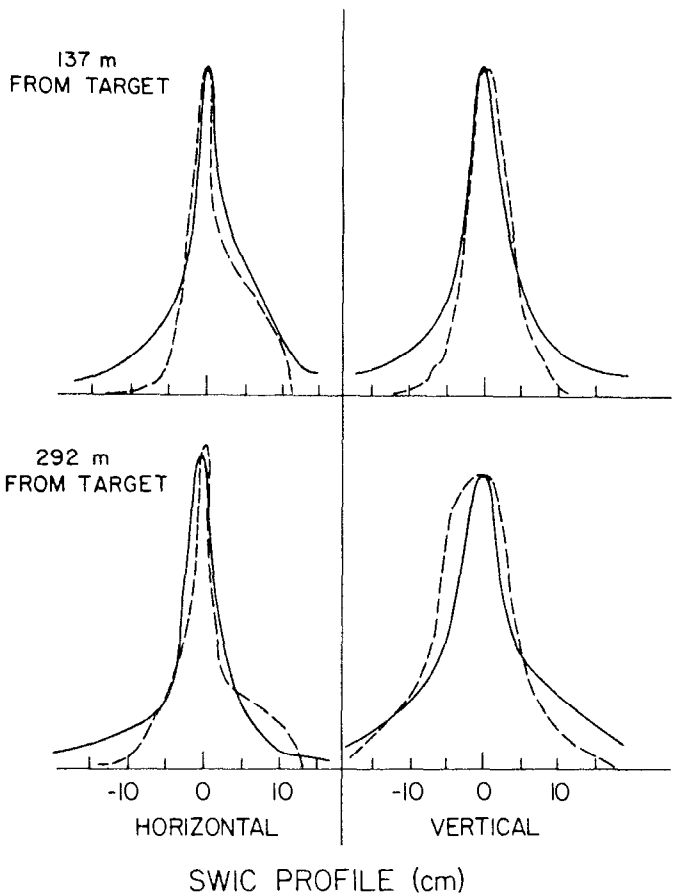


Fig. 9. Profiles of the hadron beam for a train setting of 165 GeV/c negatively-charged particles. Solid curves are SWIC measurements; broken curves are Monte Carlo generated profiles. Upper plots are for the upstream monitor station; lower plots are for the downstream station.

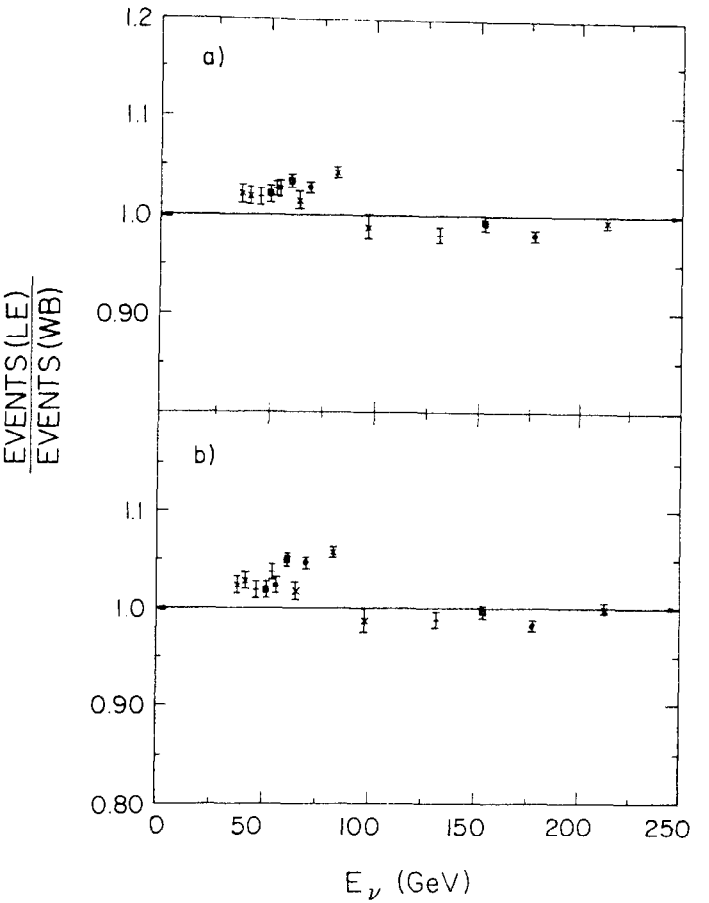


Fig. 10. Monte Carlo predictions for ν_μ events measured at LE vs. at WB, in the absense of oscillations. The points represent the radius bins for the 5 train momenta. a) shows the effect for our best determination of the beam, while b) shows the effect when we assume a hadron beam divergence 0.05 mrad larger.

the absence of oscillations; this ratio would be unity for a point source of ν_μ. The Monte Carlo prediction is plotted both for a beam with our best estimate of the angular divergence, and for a divergence 0.05 mrad larger. The larger divergence alters the flux ratios by up to 2%.

OSCILLATION ANALYSIS

The general philosophy of the analysis for ν_μ oscillations is to apply cuts to the data which result in an identical acceptance in both detectors for charged-current interactions. To the degree that this is not possible, corrections based on predictions by the beam Monte Carlo program are necessary. First, cuts are applied at the detector where an event was observed, in order to ensure that the event can be fully reconstructed. The muon emerging from the target calorimeter must have an angle with respect to the beam centerline of less than 200 mrad. A straight line extrapolation of this muon through the first toroid magnet (which focusses muons) must intersect the active area of T2; this trigger counter is shown in Figure 6. The extrapolated muon path must not spend more than 20% of its total toroid travel in the central hole. Finally, the reconstructed muon momentum must exceed 7.5 GeV/c.

If an event passes the above cuts it is then translated to the other detector to see if it would pass the cuts had it occurred there. The translated depth into the target calorimeter (from the upstream end) is not changed. The transverse position is determined by translating the vertex along a line that intersects the original vertex and the decay pipe center. The angle and orientation of the emergent muon are not altered. This procedure is depicted in Figure 11. After translating the event, the cuts are applied once again; this ensures that the geometrical acceptance for each bin is similar for the two detectors.

Data were considered for analysis only if both of the detectors were "up" and ready to take data, a period representing about 3.4×10^{18} protons on target. The dichromatic train settings for this data were 100, 140, 165, 200, and 250 GeV/c, all for positively charged pions and kaons. After applying the cuts described previously, the data sample consists of about 25,000 ν_μ^π and 11,000 ν_μ^K events at each detector.

In addition to the Monte Carlo corrections for beam divergence and decay pipe length, three corrections are made to the data. First, the ratio $N_{events}^{LE}/N_{events}^{WB}$ is corrected for the LE/WB ratios of detector livetime

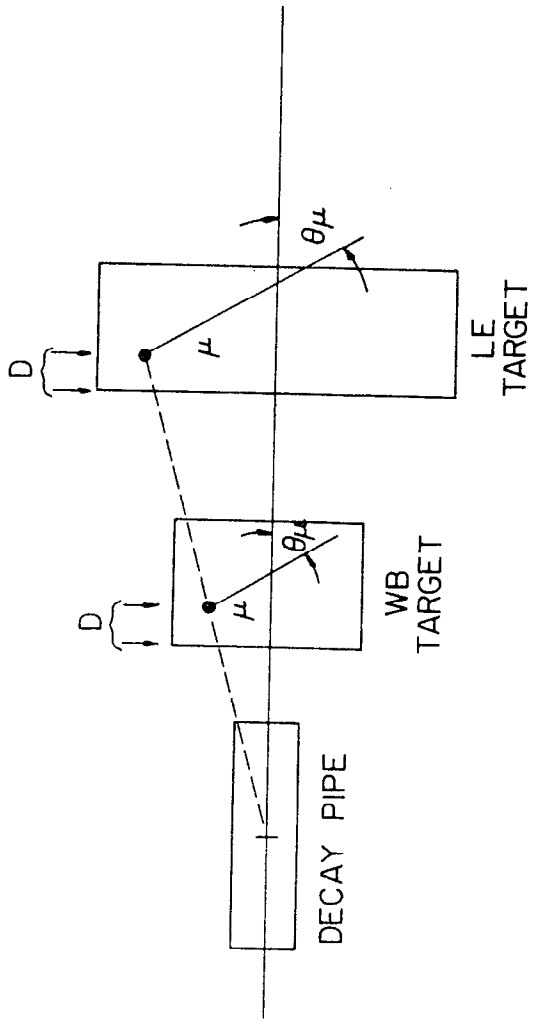


Fig. 11. Schematic of the projection procedure. "D" is the interaction point as measured from the upstream end of the calorimeter. Distances are not to scale.

and veto deadtime, which represents a 2% to 14% correction with an uncertainty of 0.3% on the event ratio. The reconstruction efficiency differs somewhat for the two detectors; by visually scanning failures in the reconstruction of events this has been measured to be (98.7±0.3)% for LE and (97.5±0.6)% for WB. Finally, the two fiducial volumes are slightly different, leading to a correction of 1.036±0.005 for LE over WB. A systematic error of 1% results from these corrections.

The fully corrected data are shown in Figure 12. There is a total systematic error of about 1.5% at each energy bin when the beam divergence correction is taken into account. These data are consistent with no oscillations. A fit to unity gives $\chi^2/DF=16.1/13$, which represents a confidence level of 22%. The best fit to a single-harmonic oscillation is shown on the Figure. The fit gives $\chi^2/DF=15.2/13$ and a confidence level of 30%, with $\Delta m^2 = 160\ eV^2$ and $\sin^2 2\theta = 0.06$.

A 90% confidence level upper limit on single-harmonic oscillations as a function of Δm^2 and $\sin^2 2\theta$ is shown in Figure 13 and has been calculated in the following manner. A systematic relative scale error of 1.5% on the LE/WB event ratios is included for each dichromatic train setting; this uncertainty is referred to as σ_s, and f_s is

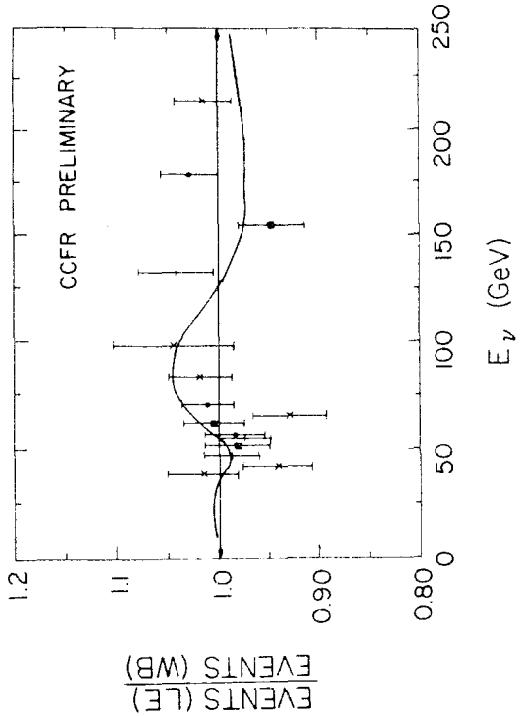


Fig. 12. Measured ν_μ events at LE vs. at WB. Errors shown include both systematic and statistical uncertainties. Solid curve is the best fit to a single-harmonic oscillation (discussed in text).

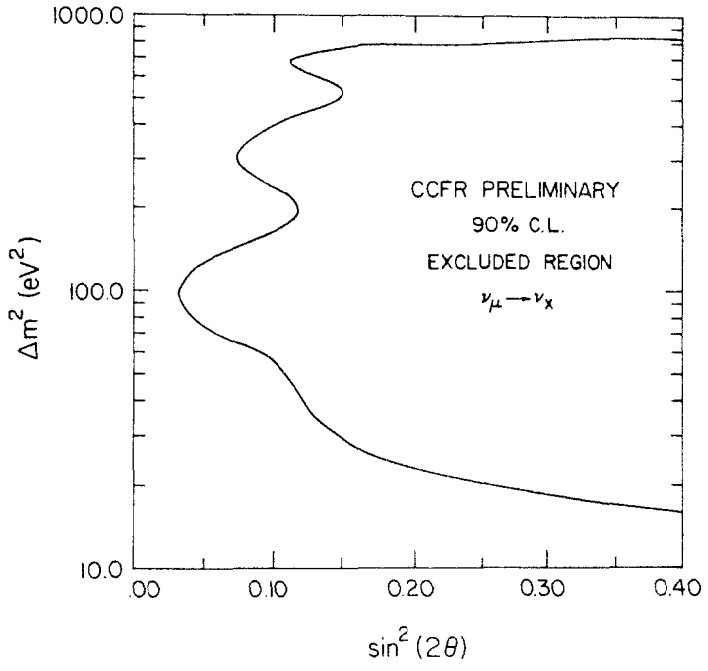


Fig. 13. Upper limit for single-harmonic oscillations as determined from Fig. 12. The region to the right of the boundary is excluded at the 90% C.L.

the necessary normalization to the ratios at different train settings. The parameter σ_s contains all the systematic effects, except for the beam divergence uncertainty. The latter is incorporated into the χ^2 procedure by computing χ^2 for any given oscillation hypothesis using two sets of Monte Carlo predicted event ratios P_i; one set is for a beam divergence 0.05 mrad larger than our best determination, and the other set for 0.05 mrad smaller. The set giving the less stringent upper limit is then used to compute χ^2 for determination of the 90% C.L. Defining σ_i as the statistical and Monte Carlo program uncertainty for the 15 bins i, and R_i as the event ratios, the f_s and χ^2 are determined by minimizing χ^2 as follows:

$$\chi^2 = \sum_i f_s \left[\frac{R_i - P_i}{\sigma_i}\right]^2 + \sum_{\substack{\text{train} \\ \text{set s}}} \left[\frac{f_s - 1}{\sigma_s}\right]^2 \qquad (6)$$

$$\frac{\partial \chi^2}{\partial f_s} = 0 \ .$$

Then, for each value of Δm^2, Figure 13 shows the $\sin^2 2\theta$ value required to achieve 22.3 (the 90% C.L. for 15 DF) in χ^2 between the data and the single harmonic prediction.

At present we are continuing to study the systematic errors and the hadron beam divergence in order to set a somewhat better oscillation limit than that presented here. Our limit can be compared to one obtained by a very similar CERN experiment [7] described at this conference. It is apparent from Figure 14 that the measurements constrain inclusive ν_μ oscillations to have $\sin^2 2\theta$ less than about 0.1 for Δm^2 in the range 1 to 900 eV^2.

The consequences of the oscillation measurements can be considered in light of the recent ν_e mass measurement of 33 eV. It has been pointed out by Steigman [8] that massive neutrinos may account for an apparent excess of dark matter in the universe. Within the Standard Model, the sum of the masses of the neutrino species must not exceed about 25-100 eV, with at least one species having a mass of about 20 eV or larger. Our experiment is sensitive to masses in this range, thus the results imply that, if the models described by Steigman are correct, either the oscillation intensity ($\sin^2 2\theta$) is small, or the neutrino mass differences are restricted to rather select ranges.

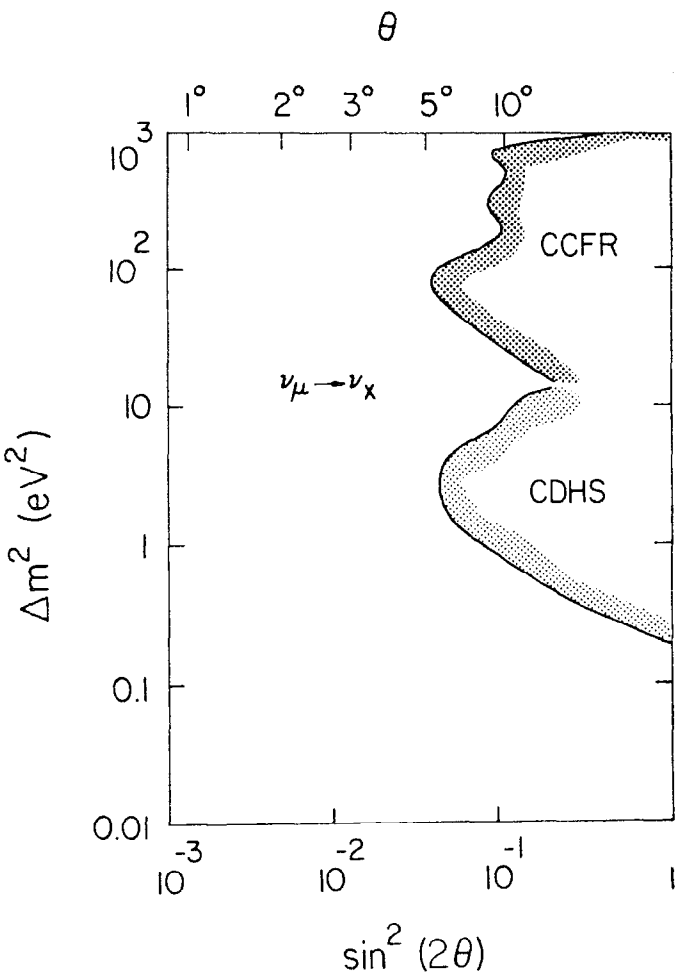


Fig. 14. Upper limits from this experiment and from a recent CDHS experiment [2]. Regions to the right are excluded at the 90% C. L.

REFERENCES

(a) Present address: Department of Physics, University of Florida, Gainesville, FL 32601

(b) Present address: Institute for High Energy Physics, Beijing, Peoples' Republic of China

(c) Present address: Department of Physics, Florida State University, Tallahassee, FL 32306

1. See, for example, the review by P.H. Frampton and P. Vogel, Phys. Rep. 82, 339 (1982).

2. N. Ushida et al., Phys. Rev. Lett. 47, 1694 (1981).

3. C. Baltay, Proc. of ν-82 Int. Conf. on Neutrino Physics and Astrophysics, Balatonfüred, Hungary, 14-19 June 1982; J. Blietschau et al., Nucl. Phys. B133, 205 (1978).

4. V.A. Lubimov et al., presented at EPS 1983 meeting, Brighton, U.K.

5. R. Cowsik and J. McClelland, Phys. Rev. Lett. 29, 669 (1972).

6. H.E. Fisk and F. Sciulli, Ann. Rev. Nucl. Part. Sci. 32, 499, (1982).

7. J. Wotschack, at this conference.

8. G. Steigman, in Proc. 10th SLAC Summer Inst. on Part. Phys., ed. A. Mosher, August 1982 (SLAC Report 259).

RECENT RESULTS FROM THE IMB DETECTOR

Irvine-Michigan-Brookhaven Collaboration

R.M. Bionta,[2] G. Blewitt,[4] C.B. Bratton,[5] B.G. Cortez,[2,a] S. Errede,[2] G.W. Foster,[2,a] W. Gajewski,[1] M. Goldhaber,[3] T.J. Haines,[1] T.W. Jones,[2,7] D. Kielczewski,[1,b] W.R. Kropp,[1] J.G. Learned,[6] E. Lehmann,[4] J.M. LoSecco,[4] H.S. Park,[2] F. Reines,[1] J. Schultz,[1] E. Shumard,[2] D. Sinclair,[2] H.W. Sobel,[1] J.L. Stone,[2] L.R. Sulak,[2] R. Svoboda,[6] J.C. van der Velde,[2] and C. Wuest[1]

(1) The University of California at Irvine
Irvine, California 92717
(2) The University of Michigan
Ann Arbor, Michigan 48109
(3) Brookhaven National Laboratory
Upton, New York 11973
(4) California Institute of Technology
Pasadena, California 91125
(5) Cleveland State University
Cleveland, Ohio 44115
(6) The University of Hawaii
Honolulu, Hawaii 96822
(7) University College
London, U.K.

ABSTRACT

Results are presented from the first 130 days of observation with the IMB detector. A total of 109 observed interactions in a 3300 metric ton fiducial volume are consistent with atmospheric neutrinos. Lower limits are set at the 90% C.L. for the lifetime/branching ratio for $p \to e^+\pi^\circ$ and $p \to \mu^+\pi^\circ$ at 1.0×10^{32} years, $p \to \mu^+K^\circ$ at 2.6×10^{31} years, and $n \to \nu K^\circ$ at 0.8×10^{31} years. For $n \to \bar{n}$ in oxygen, the lifetime is greater than 1.6×10^{31} years.

Presented by L.R. Sulak
SLAC Topical Conference on Particle Physics
Stanford, CA
July 1983

© L. Sulak 1983

The Irvine-Michigan-Brookhaven proton decay detector[1] is located 2000 feet underground in the Morton-Thiokol salt mine in Painesville, Ohio. It is a large rectangular volume of water, 22.8 × 17.8 × 16.9 m, viewed by 2048 photomultiplier tubes (PM's) covering all six faces. The fiducial volume of 3300 metric tons or 2.0×10^{33} nucleons begins 2.0 m in from the tube planes, which, in turn, begin nominally 0.5 m in from the walls.

Above the threshold β of 0.75, charged particles in the water give off Cherenkov light. A stopping track lights up a ring of PM's, each at about the one photoelectron level. By utilizing the relative timing of the lit PM's and their geometric pattern, the vertex position of single tracks can be reconstructed to an accuracy of ~ 1 m. For multi-track nucleon decay events with opening angles greater than 90° (so that the Cherenkov cones do not overlap), the vertex can be reconstructed to within 40 cm.

Three independent analysis chains find events with their vertex in the fiducial volume. These events could be atmospheric neutrino interactions, possible proton decay candidates, or other new physics. The details of one of these analysis chains are presented here; the results are consistent with those of the other chains.

Whenever 12 tubes anywhere in the detector fire within 50 nsec of each other, the detector is triggered. Since the energy calibration yields 4 MeV/photoelectron, this corresponds to a threshold of 50 MeV. There are 2.3×10^{5}/triggers per day, predominantly straight through cosmic ray muons. We initially require 30-300 lit PM's, which reduces the data by a factor of three. This range includes most nucleon decay modes. Under the hypothesis that the lit tubes were illuminated by a single point source of light, the second step locates that point. By requiring that this point lies within the fiducial volume, we eliminate a factor of 100 of the entering tracks while saving 80% of neutrino interactions originating in the fiducial volume. Over 90% of multitrack events, e.g., most nucleon decay modes, are saved.

The remaining triggers are primarily short stopping muons or tracks that clip the corners. The light illuminating a PM is then required to emanate at the Cherenkov angle of 41° from a hypothesized track. If the likelihood is high that the vertex is at the surface of the detector, the event is rejected as an entering track. About 3 events per day remain with a best fit in or near the fiducial volume and with $\geq$ 40 PM's. Physicists scanning with a color graphics system help the fitter to optimize the vertex. This reduces the number of contained events to ~ 1 event per day. The combined efficiency to keep the predominantly low energy, single track ν events (averaged over ν types and energies) is 75%.

The number of observed neutrino-induced events, 109 in 130 days, is consistent with that predicted using either of two neutrino flux calculations[2] and the above detection efficiency. We use the neutrino events observed by the Gargamelle collaboration

in a freon-filled bubble chamber[3] to simulate what is expected in the detector. The Gargamelle events are weighted to mimic the expected atmospheric neutrino energy spectrum, and electron neutrino events are generated by changing the observed μ to an electron of the same momentum. The characteristics of the 109 events are consistent with those expected from ν interactions. The energy distribution[1] agrees well, and the event vertices[1] are distributed uniformly in the detector and are reasonably isotropic in direction.

A muon decay electron is identified by a coincidence of 5 or more PM's in a 60 ns window up to 7.5 μsec after the main event. Using a sample of entering stopping tracks, we have measured the efficiency to be 66±5% for μ^+ decay detection. We expect ~ 30% of the neutrino events to have an identified μ decay, compared to 30±8% observed.

To look for $e^+\pi^\circ$, we search for events with two tracks, each with more than 40 tubes and an opening angle greater than 100°. Three events remain.[1] Each has either too much energy to be a proton decay, or too small an opening angle, or a visible μ decay. In oxygen, our intranuclear cascade program indicates that 40% of the π°'s are lost outside of our cuts on energy and opening angle. This gives a limit of

$$\tau/B(p \to e^+\pi^\circ) > (1/2.3) \times (130/365) \times 2\times10^{33} \times (10/18) \times 0.9 \times 0.68$$
$$= 1.0\times10^{32} \text{ years},$$

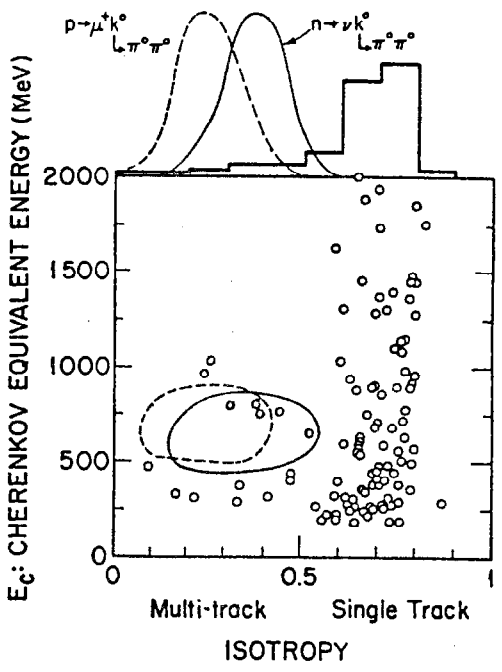
where 0.68 represents the probability for π°'s to survive nuclear interactions averaged over all protons in water and 0.9 is the efficiency for reconstructing events with a back-to-back, equal-energy-sharing, 1 GeV energy deposition. We similarly have no events for $p \to \mu^+\pi^\circ$, leading to

$$\tau/B\ (p \to \mu^+\pi^\circ) > 1.0 \times 10^{32} \text{ years}.$$

One way to search for $p \to \mu^+K^\circ$ is based on the decay $K^\circ_S \to \pi^\circ\pi^\circ$, which gives off 4 γ's and produces a nearly isotropic source of Cherenkov light. The rings from the four tracks overlap, so it is difficult to separate the showers. Instead, we construct a measure of the isotropy of the event. We calculate the magnitude of the vector sum of the unit vectors from the vertex to each lit PM and divide by the total number of lit PM's. If this quantity $\underline{I}$ (the isotropy) is near 0, the event is isotropic; for an event with a single short track, $\underline{I} \sim 0.7$, the cosine of the Cherenkov angle. To minimize the smearing due to scattering of the light in the tank, only PM's within ±15 ns of their expected firing times are used to calculate $\underline{I}$.

The second requirement is that $550 < E_C < 850$ MeV, where E_C is the visible Cherenkov light yield of a massless, nonshowering particle of total energy, E_T. For an electron, photon, or π°, $E_C = E_T$. For a muon, $E_C \approx E_T - 250$ MeV due to the muon rest mass and the energy deposited below Cherenkov threshold. We do not require the presence of a μ decay. Figure 1 is a scatterplot of E_C vs $\underline{I}$ for the 109 events. The dashed region is the area in which

Scatterplot of Cherenkov energy vs isotropy for the 109 contained events. The region inside the dashed curve contains 90% of simulated $p \to \mu^+ K^\circ$, $K^\circ \to \pi^\circ\pi^\circ$ events; the region inside the solid curve is for $n \to \nu K^\circ$, $K^\circ \to \pi^\circ\pi^\circ$. Histograms of the isotropy of the contained events and simulated proton decay events are also shown.



90% of the events for this decay mode are expected. Three events fall inside the region. The first has 600 MeV in one track, which is not possible for this decay mode. The second event has no evidence of a μ in the backward direction. The third event is a possible candidate, although it could also be neutrino-induced. Setting a conservative limit by not subtracting the neutrino background estimate of one event yields

$$\tau/B > (1/3.9) \times (132/365) \times 2\times10^{33} \times (10/18) \times 0.16 \times 0.9 \times 0.95$$

or 1.4×10^{31} years at 90% C.L., where 0.16 is the branching ratio $K^\circ \to \pi^\circ\pi^\circ$ (ignoring all K_L° interactions) and 0.9 ± 0.1 is the detection efficiency. The correction for nuclear absorption of K°'s (and not $\overline{K^\circ}$'s) is 0.95.

We estimate that 10% of the K_L°'s will interact to give a signal within the same region of the E_C and $\underline{I}$ plot. Including the K_L°'s effectively increases the branching ratio from 0.16 to 0.21, resulting in $\tau/B > 1.8\times10^{31}$ years at 90% C.L.

A second method to search for $p \to \mu^+ K^\circ$ uses the decay $K_S^\circ \to \pi^+\pi^-$ and the subsequent $\pi^+ \to \mu^+$ decay. This mode gives two muon decays. Since the mean number of PM's hit is 45 for $p \to \mu^+ K^\circ$, $K_S^\circ \to \pi^+\pi^-$, we require at least 20 PM's to fire. The detection efficiency for this mode is 0.83 ± 0.1. The probability for the π^+ to stop and decay into a μ^+ is calculated to be 80%. The overall detection efficiency is $0.80\times0.83\times(0.66)^2\times0.94 = 0.27$,

where the 0.94 corrects for the overlap probability of the two muon decays. We observe two events with two μ decays. One event has only one clean track with 500 MeV total energy. One of the muon decays probably comes from a π^+ produced below Cherenkov threshold by a ν interaction. Since a simulation of 250 $p \to \mu^+K^\circ$, $K^\circ \to \pi^+\pi^-$ events yields no event with a single track of energy this high, it is not a viable candidate. Based on the one remaining possible candidate, the 90% C.L. limit for this decay mode is

$$\tau/B > (1/3.9) \times (132/365) \times 2\times10^{33} \times (10/18) \times 0.27 \times 0.35 \times 0.95$$

or 1.0×10^{31}, years using the branching ratio of 0.35 for $K^\circ \to \pi^+\pi^-$. Including the 30% of K°_L interactions that yield a π^+ or μ^+ increases the effective branching ratio to 50%, yielding $\tau/B > 1.3\times10^{31}$ years.

Combining the limits on $p \to \mu^+K^\circ$ into the two independent modes (by calculating the combined detection efficiency) we arrive at the 90% C.L. limit of

$$\tau/B(p \to \mu K^\circ) > 2.6\times10^{31} \text{ years.}$$

We can apply the first method used for $p \to \mu K^\circ$ to obtain a limit on $n \to \nu K^\circ$, $K^\circ \to \pi^\circ\pi^\circ$. The region of energy versus isotropy space for 90% of the events is shown by the solid curve in Figure 1. The event that was a possible $p \to \mu^+K^\circ$ candidate is no longer one for $n \to \nu K^\circ$ because it has a muon decay. The second event that appears in the dashed region fails as a νK° candidate for the same reason it failed as a μK° event. The third event which failed as a candidate for μ^+K° is a candidate for νK°. There are two additional candidates to consider, although they could be neutrino-induced. Again adopting a conservative view and not subtracting background, we obtain at 90% C.L.

$$\tau/B > (1/6.9) \times (132/365) \times 8/18 \times 2\times10^{33} \times 0.21 \times 0.9 \times 0.95$$

$$\tau/B(n \to \nu K^\circ) > 0.8\times10^{31} \text{ years,}$$

where the branching ratio, detection efficiency, and nucleon absorption factors are the last three numbers, respectively.

We also search for $\Delta B = 2$ processes. If a neutron turns into an antineutron, it immediately annihilates in the nucleus and gives off 2 GeV in the form of pions. Many of these pions will stop and decay into μ^+'s. Two μ decays in an event producing an isotropic deposition of light are a clean signal for $n \to \bar{n}$. The expected mean number of hit tubes and their standard deviations obtained from the simulation of $n\bar{n}$ events (taking into account nuclear effects in water) are the following:

No Nuclear or H_2O Effects	200±47
H_2O Effects Only	185±55
Nuclear and H_2O Effects	150±55

Note the significant decrease in the light output due to pion interactions in the oxygen nucleus. With nuclear and H_2O effects included, 25% and 7% of the events will have 2 or 3 muon decays, respectively. This stopping rate leads to an overall efficiency of 14%

of observing two or more stopping signatures from an $n\bar{n}$ annihilation. The annihilation events pass through the complete analysis chain with an efficiency of 90%. A further efficiency factor of 94% accounts for those decays occurring too close in time.

Since none of the 109 events has two decay signatures and, at the same time, satisfies the requirements on the number of tubes and isotropy, the lifetime limit is

$$\tau(n + \bar{n}) > (1/2.3) \times (132/365) \times 2\times10^{33} \times (8/18) \times 0.14 \times 0.9 \times 0.94$$
$$= 1.7\times10^{31} \text{ years.}$$

REFERENCES AND FOOTNOTES

This work supported in part by the U.S. Department of Energy.

a. Also at Harvard University.

b. Permanent Address: Warsaw University, Poland.

1. R. Bionta, et al., PRL Vol. 51, No. 1 (1983); R. Bionta, et al., Proceedings of the 1982 Moriond Conf., Tran Than Van, ed., (1982).

2. T. Gaisser, et al., Proc. of the Fourth Workshop on Grand Unification, Philadelphia, 1983 (G. Segre, ed.); J.L. Osborne and E.C.M. Young in "Cosmic Rays at Ground Level" (A. Wolfendale, ed.) 1973.

3. H. Deden, et al., Nuclear Physics B85, 269 (1975).

4. G. Battistoni, Phys. Lett. 118B, p. 461 (1982).

SEARCH FOR RIGHT-HANDED CURRENTS IN MUON DECAY*

D.P. Stoker

Lawrence Berkeley Laboratory and Department of Physics

University of California, Berkeley, California 94720.

ABSTRACT

Limits are reported on right-handed currents, based on precise measurement of the e^+ spectrum end point in μ^+ decay. Highly polarized muons from the TRIUMF "surface" beam were stopped in metal foils within a 1.1 T spin-holding longitudinal field or a 70 G spin-precessing field. For the spin-held data, the V-A rate vanishes in the beam direction at the end point. Measurement of this rate sets the 90% confidence limits $\xi P_\mu \delta/\rho > 0.9959$ and $M(W_R) > 380$ GeV, where W_R is the possible right-handed gauge boson. The μSR signal amplitude of the spin-precessed data independently sets the limits $\xi P_\mu \delta/\rho > 0.9918$ and $M(W_R) > 320$ GeV. Limits on non-(V-A) currents, familons, and composite leptons are also presented.

---

* Berkeley-LBL / Northwestern† / TRIUMF# collaboration:
J. Carr, G.Gidal, B. Gobbi†, A. Jodidio, C.J. Oram#, K.A. Shinsky,[a]
H.M. Steiner, D.P. Stoker, M. Strovink, and R.D. Tripp.

a Deceased

© D.P. Stoker 1983

INTRODUCTION

The Glashow-Weinberg-Salam electroweak model, based on the gauge group $SU(2)_L \times U(1)$, is at present consistent with the available experimental data. The main surviving alternative to the standard model is the left-right symmetric model with gauge group $SU(2)_L \times SU(2)_R \times U(1)$.[1]

The appeal of the left-right symmetric model is partly aesthetic. In the standard model the left-handedness of the interaction is a consequence of the choice of gauge group: left-handed fermions are assigned to doublets under $SU(2)_L$ and interact with the left-handed gauge bosons $W_L^{\pm}$. Extension of the gauge group to $SU(2)_L \times SU(2)_R \times U(1)$ restores left-right symmetry at the Lagrangian level with the addition of right-handed gauge bosons $W_R^{\pm}$ and the assignment of right-handed fermions to doublets under $SU(2)_R$.

The dominance of left-handed charged currents at present energies could then arise from a W_L - W_R mass splitting which is tiny on the grand-unification scale. If the mass scale $M(W_R)$ where parity is spontaneously broken is increased to infinity the left-right symmetric model reduces to the standard model, and therefore can never be ruled out by experiments which support the standard model.

In these left-right symmetric theories the physical bosons W_1 and W_2, with mass-squared ratio $\alpha = M^2(W_1)/M^2(W_2)$, are linear combinations of the gauge bosons:

$$W_1 = W_L \cos\zeta - W_R \sin\zeta$$
$$W_2 = W_L \sin\zeta + W_R \cos\zeta .$$

The effects of W_L - W_R mixing and W_1 exchange relative to W_2 exchange become independent of momentum transfer for $q^2 \ll M^2(W_1)$. Analyses[2,3] which neglect the kinematic effect of finite ν_R mass obtain the strongest limits on α and ζ from muon and nucleon β decay.[4-9]

Unlike the standard model in which there are only massless ν_L, the left-right symmetric model admits both ν_L and ν_R of finite mass. The ν_R mass may depend critically on whether neutrinos are Dirac or Majorana particles. In the Dirac case, ν_L and ν_R necessarily have the same mass since they are different helicity states of the same particle. In the Majorana case, as suggested by Gell-Mann, Ramond and Slansky,[10] the smallness of the ν_L mass may be related to the maximality of parity violation. Mohapatra and Senjanovic[11] find $m(\nu_L) \propto 1/M(W_R)$, and propose models in which $m(\nu_{\ell L}) = m_\ell^2/M(W_R)$ and $m(\nu_{\ell R}) = M(W_R)$. In these models W_R decouples from low energy leptonic processes such as μ decay, and semileptonic processes except where the right-handed current is all hadronic.

The present experiment[12] is insensitive to right-handed currents if the ν_R masses are greater than 10 MeV. The effective low-energy interaction Hamiltonian for charged current processes with light neutrinos is:

$$H_{int} = [g^2/2M^2(W_1)][J_L J_L^\dagger + \alpha J_R J_R^\dagger + \zeta(J_L J_R^\dagger + J_R J_L^\dagger)] .$$

The already existing experimental bounds on α and ζ are displayed as contours in Fig. 1. Only the μ decay asymmetry, which the present experiment also measures, gives a closed contour. Additional

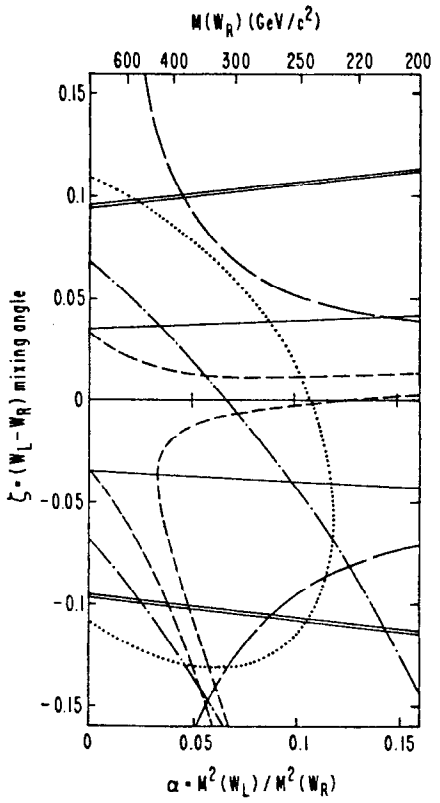


FIG. 1. Experimental 90% confidence limits on the $W_{L,R}$ mass-squared ratio α and mixing angle ζ. The allowed regions are those which include $\alpha=\zeta=0$. Muon decay contours are derived from the polarization parameter ξP_μ (dotted, Ref. 4), and the Michel parameter ρ (solid, Ref. 5). Nuclear β decay contours are obtained from the Gamow-Teller β polarization (dot-dashed, Ref. 6); the comparison of Gamow-Teller and Fermi β polarizations (long-dashed, Ref. 7); and the ^{19}Ne asymmetry A(0) and ft ratio, assuming CVC (short-dashed, Ref. 8). Limits from the y distributions in νN and $\bar{\nu}N$ scattering (double-lines, Ref. 9) are valid irrespective of the ν_R mass.

constraints are placed by model-dependent calculations of the $K_L - K_S$ mass difference. Beall et al[13] found $M(W_R) > 1600$ GeV, while the later more complete calculations by DeForcrand,[14] Mohapatra et al.,[15] and Denis[16] give lower limits in the range 200 - 400 GeV.

In this experiment we observe the decay of polarized μ^+ stopped in essentially non-depolarizing pure metal foils. The decays of interest are those which emit e^+ near the momentum spectrum end point $x = p_e/p_e(\max) = 1$. Neglecting radiative corrections and assuming massless neutrinos the μ^+ differential decay rate is:

$$d^2\Gamma/x^2dxd\cos\theta \propto (3-2x) + (4\rho/3-1)(4x-3) + 12(m_e x/m_\mu)(1-x)\eta - [(2x-1) + (4\delta/3-1)(4x-3)]\xi P_\mu \cos\theta \qquad (1)$$

where $\pi-\theta$ is the angle between $\hat{p}_e$ and the direction of the μ^+ polarization P_μ, and ρ,η,δ, and ξ are the muon decay parameters.[17] The (V-A) values of the decay parameters are shown in Table 1 together with the world average experimental values. For pure (V+A) the 'asymmetry parameter' $\xi=-1$, while the other decay parameters retain their (V-A) values. Thus measurement of the decay asymmetry is a sensitive test for admixtures of right-handed currents. The (V-A) forward-backward μ^+ decay asymmetry is shown in Fig. 2.

The decay rate relative to that for unpolarized muons is

$$R(x,\theta) = 1 - \frac{1-2\bar{x}-\tilde{\delta}+4\bar{x}\tilde{\delta}}{1+2\bar{x}-\tilde{\rho}+4\bar{x}\tilde{\rho}}\,\xi P_\mu \cos\theta \qquad (2)$$

where $\bar{x}=1-x$, $\tilde{\delta}=1-4\delta/3$, $\tilde{\rho}=1-4\rho/3$. [Radiative corrections[17] and finite electron mass effects absent from (1) and (2) are included in the actual analysis.]

TABLE 1.

The (V-A) values of the muon decay parameters and their world average experimental values.

Muon Decay Parameter	(V-A) Value	World Average Value
ρ	3/4	0.7517±0.0026
η	0	-0.12 ±0.21
δ	3/4	0.7551±0.0085
ξ	1	0.972 ±0.014

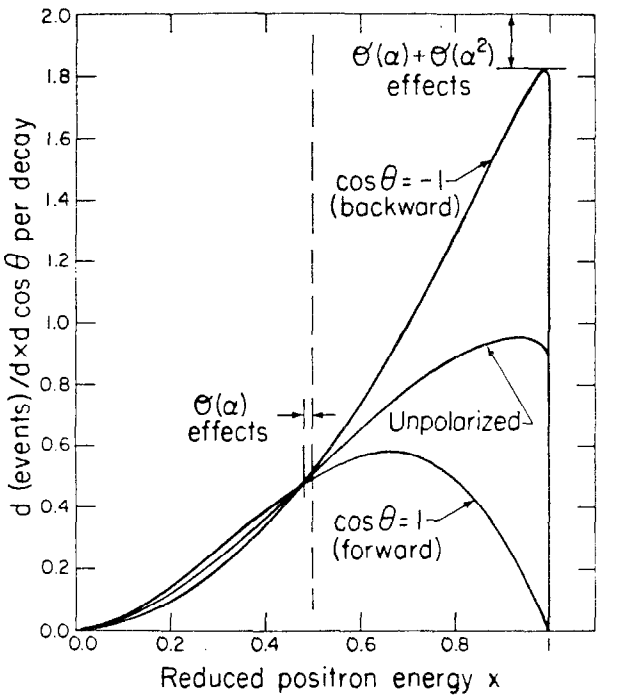


FIG. 2. The (V-A) forward-backward asymmetry in μ^+ decay. The angle between the μ^+ spin direction and the e^+ momentum is $\pi-\theta$.

The experiment was run in two modes, each of which allows determination of the decay asymmetry. In the first mode, with greater statistical power, we observe e^+ emitted near $x=1$ and also near $\theta=0$ from stopped μ^+ with their spins held in a 1.1 T longitudinal field. At the end point $R(1,0)=1-\xi P_\mu \delta/\rho$ and in the (V-A) limit, $R(x\to1,\theta\to0)=6-4x-P_\mu\cos\theta$. For a μ^+ beam derived from π^+ decay at rest, θ becomes the angle between the e^+ and μ^+ momenta. In the (V-A) limit with massless neutrinos, angular momentum conservation requires $P_\mu=1$. In left-right symmetric theories $P_\mu=1-2(\alpha+\zeta)^2$, and the end point decay rate $R(1,0)=2(2\alpha^2+2\alpha\zeta+\zeta^2)$ constrains both α and ζ.

The second mode is a muon spin-rotation (μSR) experiment in which the muon spins are precessed by a 70 G transverse field substituted for the 1.1 T longitudinal field. The decay asymmetry may then be determined from the amplitude of the resulting μSR signal.

EXPERIMENTAL APPARATUS

This experiment is made possible by the nearly complete polarization of a μ^+ beam derived from π^+ decay at rest near the surface of the production target.[18] Muons from π^+ decay deeper inside the production target have lower momentum and are less polarized due to Coulomb scattering. Tuning the beam line to the surface muon edge (Fig. 3) therefore momentum selects the most highly polarized muons. The M13 beam[19] at TRIUMF produces 15,000 29.5MeV/c μ^+/sec within a 1% momentum bite and a 12×10mm spot from 100μA of 500 MeV protons incident on a 2mm thick carbon target. The 2% contamination of prompt

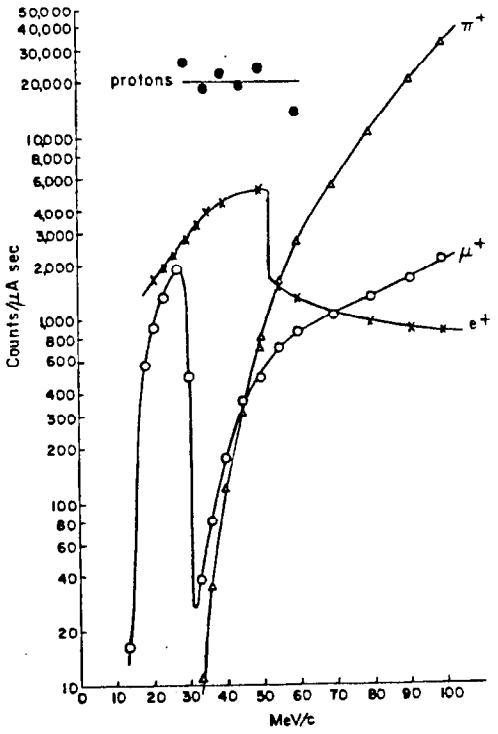


FIG. 3. Particle fluxes in the M13 beam at TRIUMF (taken from Ref. 19). The μ^+ with momenta corresponding to the sharp (surface muon) edge at 29.5 MeV/c are those produced by π^+ decay near the surface of the production target. Those with smaller momenta are from π^+ decay deeper in the production target, and are less polarized. Muons with momenta above the edge are from π^+ decay in flight near the production target.

("cloud") μ^+ from π^+ decay in flight near the production target is less polarized and is rejected by requiring the μ^+ to be produced well within the 43 nsec interval between proton bursts. A smaller π^+ flux is similarly rejected. Beam e^+, which constitute about 50% of the total flux, pass through the μ stopping target and do not satisfy the trigger requirements.

The apparatus is shown in Fig. 4. After traversing 50 mg/cm^2, beam μ^+ are stopped by target foils of ≥99.9% pure Al (155 mg/cm^2), Cu (233 mg/cm^2), Ag (275 mg/cm^2), and Au (233 mg/cm^2). The high free-electron concentration in these metals screens the stopped μ^+ from prolonged spin-spin coupling to particular electrons, which otherwise would lead to its depolarization. A 1.1 T longitudinal field (B_L) is also applied to preserve the stopped μ^+ spin direction. During alternate hourly runs the longitudinal field is nulled to within ±3 gauss and a 70 gauss transverse field (B_T) is substituted. This precesses the μ^+ spin about a vertical axis so that its time-averaged polarization is zero.

The incoming μ^+ direction is determined using proportional chambers P1 and P2, and the outgoing e^+ direction is determined by proportional chamber P3 and drift-chambers D1 and D2. All chambers use a 92% methane - 8% methylal gas mixture. Downstream of the target the decay e^+ is focused by a 0.5 T-m solenoidal field lens. The septum between the target and solenoid bore essentially decouples the focal length from the choice of target field orientation.

The decay e^+ is momentum-analysed by an NMR-monitored cylindrical dipole magnet having a central field of 0.32 T. Low mass drift-chambers are located near its conjugate foci and the intervening

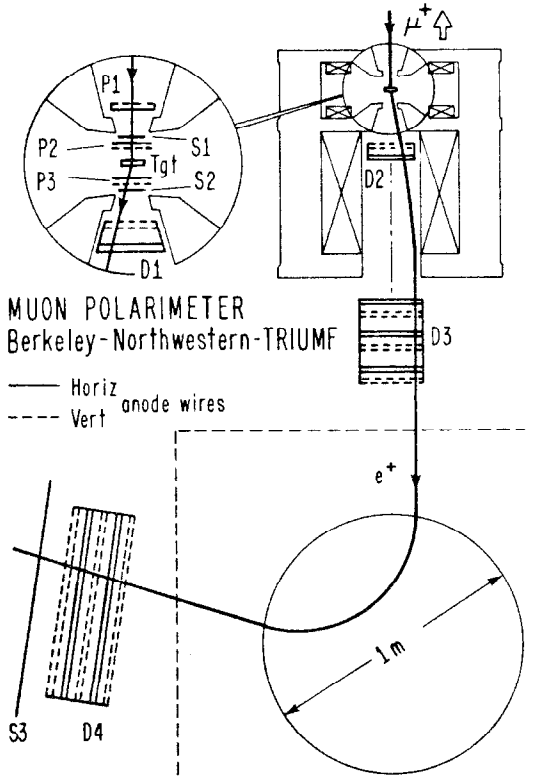


FIG. 4. Plan view of the muon polarimeter. P1-P3 are proportional wire chambers, D1-D4 are drift-chambers, and S1-S3 are scintillators. The trigger is T1·T2, where T1 is P1·S1·P2·$\overline{V1}$·$\overline{P3}$·$\overline{S2}$ at the μ^+ stopping time, T2 is P3·S2·S3·$\overline{P1}$·$\overline{S1}$·$\overline{V1}$·$\overline{P2}$·$\overline{V2}$ at the μ^+ decay time, and V1 and V2 are veto scintillators surrounding S1 and S2, respectively (not shown).

volume is evacuated. The dispersion $\Delta p/p\Delta s$ was measured to be 1.07%/cm by passing e^+ beams of different momenta, determined using the NMR-monitored beam line dipoles, through the spectrometer. The combined system of field lens and positron spectrometer has an acceptance of 250 msr and a momentum bite of ±20%; in the analysis described below, these are restricted to 160 msr and ±8%.

The trigger requires the signature of a beam particle stopping in the foil target, in delayed (0.2 - 10 μs) coincidence with that of a decay positron passing through the spectrometer. Events with an extra beam particle arriving between the μ-stop and decay are tagged and rejected later. The data reported here are based on 3.5×10^6 triggers from the initial run. An additional 10^7 triggers were collected later in 1982.

Incoming μ^+ tracks were reconstructed using P1 and P2. Nearly straight e^+ track segments were found separately in the horizontal and vertical projections of three groups of wire chamber planes: P3,D1,D2; D3; and D4 (Fig. 4). All possible combinations of hits were considered, and tracks in all six segments were found in 99% of the triggers. Of these, 95% had multiplicities corresponding to a single track; the remainder were rejected. Projections of the track segments were required to agree at the target, in the bore of the solenoid, and in position and vertical slope in the spectrometer. The first of these requirements rejects most of the remaining small fraction of events where the e^+ is emitted from a μ^+ other than the current μ-stop. Track segment residuals were used to dynamically fine-tune the drift-chamber space-time calibration, producing residuals of ≤250 μm in the spectrometer chambers D3 and D4.

The hits found in P1 through D2 were then fitted to curved trajectories based on the first-order optics of cylindrically symmetric fields. The μ^+ and e^+ polar angles θ_μ and θ_e with respect to the beam axis were thereby determined with resolutions of 20 and 10 mrad respectively. Monte Carlo simulation based on higher-order field optics confirms the accuracy of this procedure to within an uncertainty of ±0.0005 in $\cos\theta_\mu$ and $\cos\theta_e$. For the B_L data the transverse component of the μ^+ spin precesses about the beam axis too rapidly to be followed. Thus for $\cos\theta=-\hat{P}_\mu\cdot\hat{p}_e$ in Eq. (2) we substitute $\cos\theta_\mu\cos\theta_e$, which is equivalent in an average over many events.

The e^+ momentum was obtained, to first order, from the measured dispersion and the sum of the horizontal coordinates at the conjugate foci of the 98° horizontally focusing spectrometer magnet. Empirical corrections to second order, based primarily on the end point position for the B_T data, were made for deviation from the median plane and impact parameter with respect to the magnet axis. The sharp edge at x=1 in Fig. 5 curve(a) exhibits a gaussian resolution which is less than 0.2% rms, with a rounded shoulder due to non-uniform energy loss in the 180 mg/cm^2 of material upstream.

We have dropped events with $x<0.92$ or $\cos\theta<0.975$ ($\cos\theta<0.965$ for the μSR analysis), which have low statistical power for determining the decay asymmetry. After conservative fiducial cuts the final distributions in Fig. 5 retain 7.5% of the raw triggers. We have checked that any reasonable variation of the cuts would negligibly affect the the result.

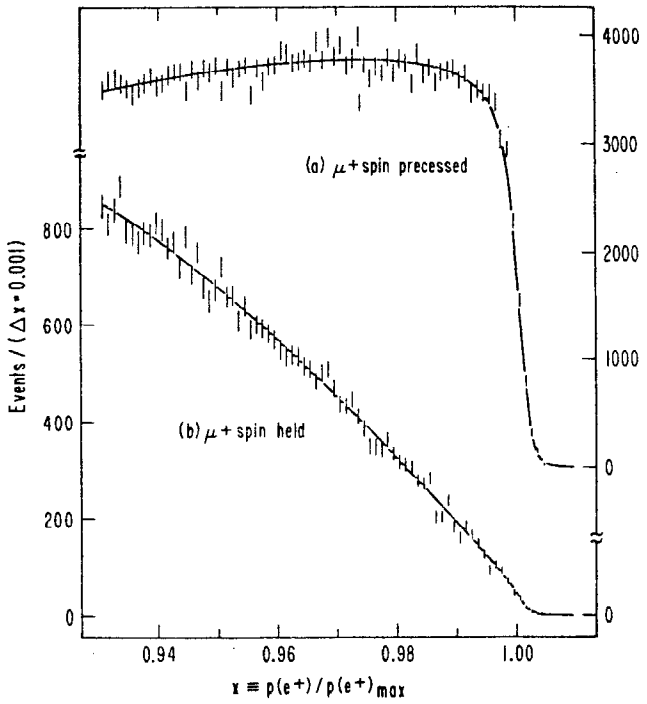


FIG. 5. Distributions (uncorrected for acceptance) in reduced positron momentum with the μ^+ spin (a) precessed and (b) held. The indicated errors are statistical. The edge in (a) corresponds to a resolution with a gaussian part <0.2% rms. The fits are described in the text.

DATA ANALYSIS

A. SPIN-HELD DATA

Fitting proceeds in two stages. The B_T data in Fig. 5(a) are fitted to the radiatively corrected spectrum expected for unpolarized μ^+ decay, smeared by a sum of gaussian resolution functions and by the expected e^+ energy-loss straggling. The fit simultaneously calibrates the edge position x=1 and determines the momentum resolution and the (quadratic) dependence of the acceptance upon x. The B_L spectrum in Fig. 5(b) can be represented as the shape expected from pure (V-A) and $P_\mu \cdot \cos\theta = 1$, with a small admixture of the unpolarized spectrum in Fig. 5(a). This unpolarized fraction is essentially equal to $1-(\xi P_\mu \delta/\rho)\langle\cos\theta\rangle$. To fit this fraction, we use the B_T fit to fix the x resolution, x acceptance, and edge position x=1, but allow the acceptance for B_L data relative to that for B_T data to vary linearly with x. This allows for the (<2%) difference in angular acceptance caused by the different field configuration near the target. Using data with partly polarized cloud μ^+, we have checked that the x=1 calibration is consistent for B_L and B_T fields. In the resulting curve in Fig. 5(b), the slight kink near x=1 reflects the unpolarized fraction, which arises mostly from the measured value $\langle\cos\theta\rangle = 0.9862$ for these data.

The result reported here is based on this same fitting procedure carried out for data in each of five bins in cosθ. The subdivision checks that the results of these fits are consistent with a linear

dependence on $\langle\cos\theta\rangle$. The value of $\xi P_\mu \delta/\rho$ is determined by making a fixed slope extrapolation to $\cos\theta=1$ (see Fig. 6). Separate fits for each of the four stopping target materials (see Fig. 7) give values of $\xi P_\mu \delta/\rho$ which are statistically consistent ($\chi^2=2.1$), with a combined statistical error of ± 0.0015. Within statistical errors the result is also independent of the time of muon decay.

Multiple Coulomb scattering in the production and stopping targets causes a misalignment of the μ^+ spin and momentum, resulting in the measured values of $\cos\theta_\mu$ being systematically too large. An estimated correction of $+0.0012\pm0.0005$ is made to $\xi P_\mu \delta/\rho$. Table 2 summarises the major sources of systematic error. All other sources contribute $<10^{-4}$. In principle the systematic errors should be uncorrelated; in quadrature they add to ± 0.0018. The resulting value is $\xi P_\mu \delta/\rho = 0.9989\pm0.0015\pm0.0018$. We have made no correction for unknown sources of μ^+ depolarization either along the beam or in the stopping target. Since such effects can only decrease the apparent result, we therefore quote the limit:

$$\xi P_\mu \delta/\rho > 0.9959 \qquad (90\% \text{ confidence}) .$$

The corresponding limits on the mass and mixing parameters α and ζ are represented by the small bold contour in Fig. 8. In particular, for infinite W_R mass $|\zeta|<0.045$; for any mixing angle $M(W_R)>380$ GeV; and for zero mixing angle $M(W_R)>450$ GeV.

We also note that for a (V+A) amplitude admixture, $(V-A)+\varepsilon(V+A)$, assuming no left-right mixing $\xi P_\mu \delta/\rho = 1-4\varepsilon^2$. Our result implies $|\varepsilon|< 0.032$ with 90% confidence.

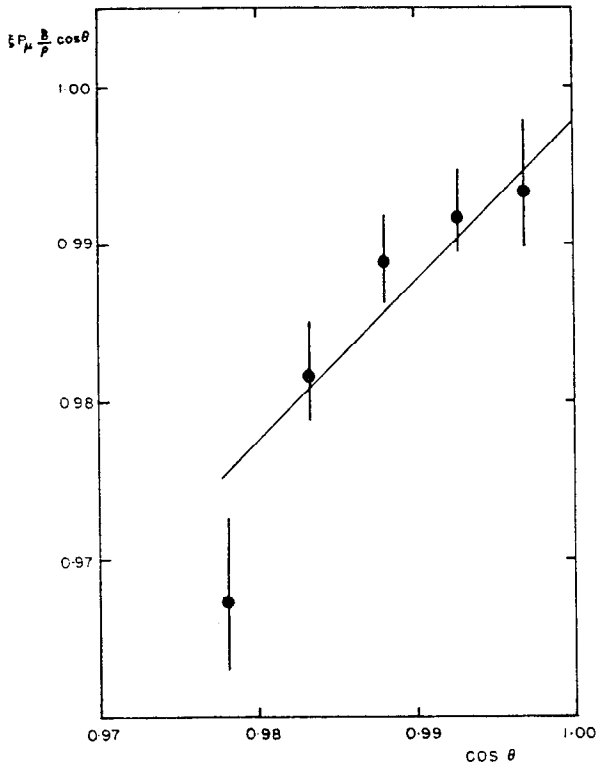


FIG. 6. The fitted values of $(\xi P_\mu \delta/\rho)\langle\cos\theta\rangle$ for data in each of five bins in $\cos\theta$. The errors are statistical. A fixed slope extrapolation to $\cos\theta=1$ is made to determine $\xi P_\mu \delta/\rho$.

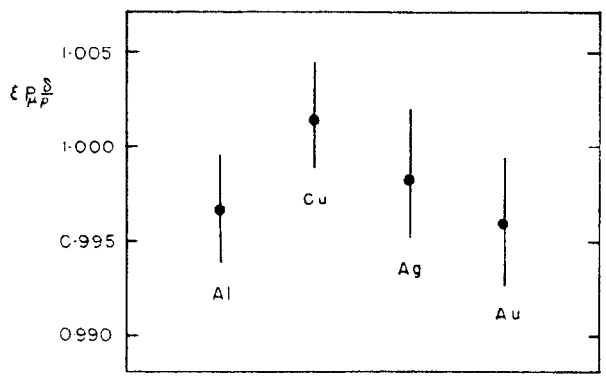


FIG. 7. The fitted values of $\xi P_\mu \delta/\rho$ for each of the four stopping target materials.

TABLE 2.

Major sources of systematic error and their estimated contributions.

Source of systematic error	Error
Coulomb scattering in targets	±0.0005
Correction of θ_μ and θ_e for bending in B_L field at target	±0.0010
Smearing of θ_μ and θ_e due to detector resolution and scattering	±0.0006
Possible shift in θ_e due to random hits and inefficiencies in D1 and D2	±0.0005
Method of averaging $\langle\cos\theta\rangle$	±0.0004
Difference in x=1 edge calibration between B_T and B_L data	±0.0008
Normalization of B_L relative to B_T data	±0.0007

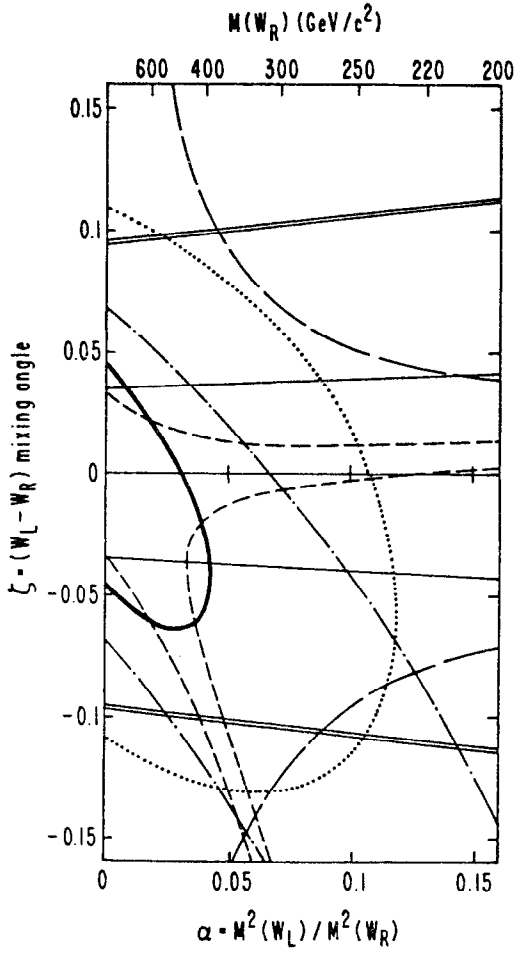


FIG. 8. The small bold contour representing the present result is shown together with the contours of Fig. 1.

B. μSR DATA

The B_T data may be used for an independent measurement of the decay asymmetry. Figures 9 and 10 show the B_L and B_T data time spectra for all target materials combined.

A maximum likelihood fit using Poisson statistics is made simultaneously to 125,000 B_T events and 59,000 B_L events in 115 time bins. For the B_L data, the expected number of events in each time bin is given by:

$$N_L(t) = N_L^o \exp(-t/\tau_\mu) + C_L .$$

The B_T data are fitted in four x bins, each 0.02 wide, to the radiatively corrected differential decay rate, assuming (V-A) values for the muon decay parameters η, ρ, and δ. The expected number of events in each time bin is then given by:

$$N_T(t) = N_T^o \left[\int_x A(x)dx + R(t)\langle\cos\theta\rangle_t \xi P_\mu \int_x B(x)dx \right] \exp(-t/\tau_\mu) + C_T$$

where A(x) and B(x) are the angle independent and angle dependent parts of the differential decay rate respectively; $\langle\cos\theta\rangle_t$ is the value of $-\hat{P}_\mu(t).\hat{p}_e$ appropriate to the particular time bin; and

$$R(t) = \exp\left[-2\sigma^2\tau_c^2[\exp(-t/\tau_c)-1+t/\tau_c]\right]$$

is an effective relaxation function[20] parametrizing the effects of slightly different muon spin-precession rates due to small variations in the magnetic field strength over the target foil and from run to run.

The $\langle\cos\theta\rangle_t$ are determined from the observed μ^+ and e^+ track

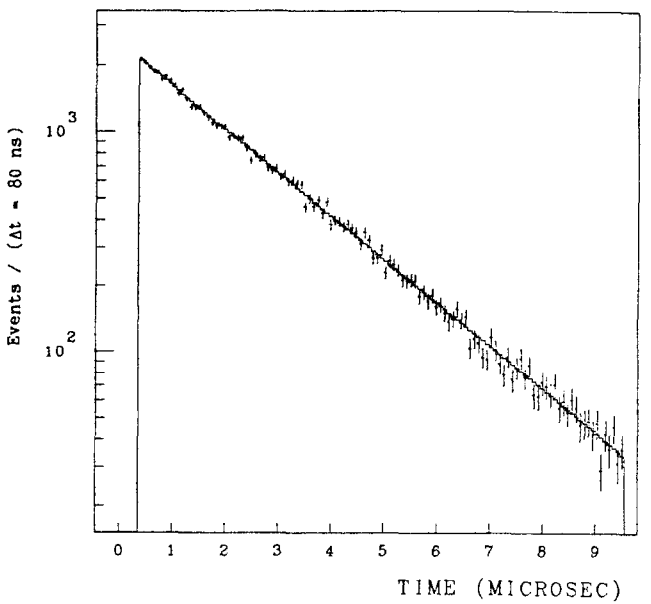


FIG. 9. The time spectrum of the spin-held B_L data with the fit described in the text. The fitted muon life-time, determined simultaneously from the B_L and B_T data, is τ_μ=2.204±0.010±0.044 μs, which is consistent with the accepted value of 2.197 μs. The fitted background is 0.07±1.1.

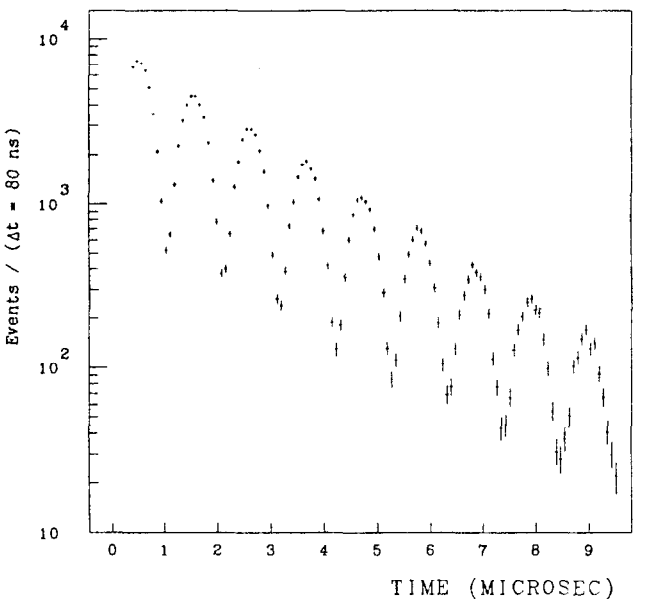


FIG. 10. The time spectrum of the spin-precessed B_T data for all target materials combined. The decay asymmetry is determined from the amplitude of the μSR signal. The small decrease in the signal amplitude with time is due to slightly different muon spin-precession rates resulting from small variations in the magnetic field strength over the stopping target and from run to run.

directions at the stopping target in a large part of the B_T data time spectrum for which the decaying muons are, on average, unpolarized. Since the decay of unpolarized muons is isotropic, the observed angular distribution of the e^+ in these events is determined only by the acceptance of the apparatus. Similarly, the observed angular distribution of the incoming μ^+ is determined only by the acceptance of the apparatus and the beam phase-space. Allowing the muon spin-precession rate to be a free parameter in the fit then permits an unbiased determination of $\langle\cos\theta\rangle_t=-\hat{P}_\mu(t).\hat{p}_e$ for each time bin by calculating the average cosθ for every precessed μ^+ spin direction combined with every outgoing e^+ direction. The resulting fit is shown superimposed on the B_T data in Fig. 11 with the muon life-time deperdence removed.

We make corrections for μ^+ multiple Coulomb scattering (+0.0012±0.0005); the effect of an incompletely nulled longitudinal field in the stopping target region (+0.0003±0.0003); and for a small background due to incomplete rejection of additional μ^+ arriving after the μ-stop (-0.0005±0.0005). The resulting value $\xi P_\mu \delta/\rho=0.9970\pm0.0037\pm0.0015$ is consistent with the value obtained from the spin-held data. The smaller systematic error for the μSR data is mainly due to less uncertainty in determining the μ^+ and e^+ momenta directions in the absence of the 1.1 T longitudinal field.

The 90% confidence limit $\xi P_\mu \delta/\rho>0.9918$ for these data implies that for infinite W_R mass $|\zeta|<0.064$; for any mixing angle $M(W_R)>320$ GeV; and for zero mixing angle $M(W_R)>380$ GeV.

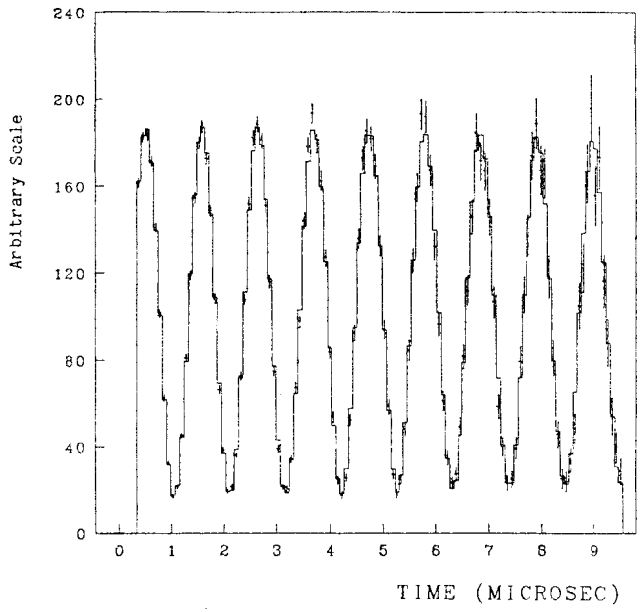


FIG. 11. The time spectrum of the spin-precessed data, after removal of the muon life-time dependence, shown together with the maximum likelihood fit. The ordinate scale is arbitrary.

LIMITS ON SCALAR AND TENSOR CURRENTS

The most general four-fermi interaction for muon decay may be written in flavor retention form as

$$L_{int} = -(G_F/\sqrt{2})\sum_i[(\bar{e}\Gamma_i\nu_e)[\bar{\nu}_\mu\Gamma_i(G_i+G_i'\gamma_5)\mu] + \text{hermitian conjugate}$$

where $\Gamma_i = 1, \gamma_\lambda, \sigma_{\lambda\kappa}, \gamma_\lambda\gamma_5, i\gamma_5$.

Time reversal invariance requires the G_i and G_i' to be real. Fierz transforming to the charge retention form then leads to the following relations between $\xi\delta/\rho$ and the G_i and G_i' for the special cases of flavor retention scalar or tensor admixtures to (V-A):

1. (V-A) + tensor: $\xi\delta/\rho = 1-(G_T+G_T')^2/8$
2. (V-A) + scalar + pseudoscalar: $\xi\delta/\rho = 1-[(G_S-G_P')^2+(G_S'-G_P)^2]/16$

Hence from our result $\xi\delta/\rho \geq \xi P_\mu \delta/\rho > 0.9959$ we obtain the 90% confidence limits:

$$(G_T+G_T')^2 < 0.033$$

$$(G_S-G_P')^2+(G_S'-G_P)^2 < 0.066$$

Mursula et al.[21] have set limits based on all previous available data subject to various sets of assumptions, all somewhat different from those used to determine our limits.

LIMITS ON FAMILONS

Recently, Wilczek[22] has suggested replacing the Peccei-Quinn U(1) quasisymmetry with a group of genuine flavor symmetries. Spontaneous breakdown of family symmetries would involve characteristic massless axion-like Nambu-Goldstone bosons $f_{\ell\ell'}$ (familons) coupling to the divergences of currents which change flavor quantum numbers.

The decay $\mu \to e+f$ could then occur via

$$\Delta L = (1/F_{\mu e})\bar{\mu}\gamma_\rho e\partial_\rho f_{\mu e}$$

with a branching ratio $\Gamma(\mu\to ef)/\Gamma(\mu\to e\nu\bar{\nu}) = 2.5\times10^{14}\text{GeV}^2/F_{\mu e}^2$ where $F_{\mu e}$ is the energy scale at which the flavor symmetry is spontaneously broken. It was further suggested on cosmological grounds that 10^9 GeV $< F_{\mu e} < 10^{14}$ GeV implying

$$2.5\times10^{-10} < \Gamma(\mu\to ef)/\Gamma(\mu\to e\nu\bar{\nu}) < 2.5\times10^{-4} .$$

Since $\mu\to ef$ is isotropic and $M(f)=0$, the clearest evidence for this decay in our experiment would be the observation of a spike at the end point of the momentum spectrum for polarized μ^+ decay opposite to the muon spin direction, where the V-A rate vanishes.

Fitting the spin-held data with various assumed $\mu\to ef$ branching ratios yields the limit

$$\Gamma(\mu\to ef)/\Gamma(\mu\to e\nu\bar{\nu}) < 6\times10^{-6}$$

and

$$F_{\mu e} > 4.2\times10^{10} \text{ GeV}.$$

LIMITS ON COMPOSITE LEPTONS

The possibility that leptons and quarks are composite at some mass scale Λ has received considerable attention in recent years. Among the strongest experimental limits on Λ currently quoted[23,24] are those from Bhabba scattering (>750 GeV), muon (g-2) (>860 GeV), and a more model-dependent estimate from ν-hadron scattering (>2.5 TeV).

The effects of compositeness may be analysed in terms of new effective contact interactions. Following the analyses of Peskin,[25] and Lane and Barany[26] the most general SU(2)×U(1) invariant contact interaction contributing to $\mu^+e\nu\bar{\nu}$ is

$$\begin{aligned} L_{cont} = (g^2/\Lambda^2)[&\eta_1(\bar{\nu}_{\mu L}\gamma^\kappa\mu_L)(\bar{e}_L\gamma_\kappa\nu_{eL}) + \eta_2(\bar{\nu}_{\mu R}\gamma^\kappa\mu_R)(\bar{e}_R\gamma_\kappa\nu_{eR}) \\ &+ \eta_3(\bar{\nu}_{\mu L}\gamma^\kappa\nu_{eL})(\bar{e}_R\gamma_\kappa\mu_R) + \eta_4(\bar{e}_L\gamma^\kappa\mu_L)(\bar{\nu}_{\mu R}\gamma_\kappa\nu_{eR}) \\ &+ \eta_5(\bar{\nu}_{\mu L}\mu_R)(\bar{e}_L\nu_{eR}) + \eta_6(\bar{\nu}_{\mu L}\nu_{eR})(\bar{e}_L\mu_R) \\ &+ \eta_7(\bar{\nu}_{\mu R}\mu_L)(\bar{e}_R\nu_{eL}) + \eta_8(\bar{\nu}_{\mu R}\nu_{eL})(\bar{e}_R\mu_L)] \end{aligned} \qquad (3)$$

where g is a coupling of hadronic strength; the η_i are of order unity and are normalized so that $|\eta_L|=1$ in the diagonal coupling

$$(g^2/2\Lambda^2)[\eta_L(\bar{e}_L\gamma^\kappa e_L)(\bar{e}_L\gamma_\kappa e_L) + \ldots\ ].$$

The first and second terms in (3) are purely left-handed and right-handed respectively, and hence are indistinguishable from the usual (V-A) and (V+A) interactions.

There are three special cases of interest:

1. If only left-handed (right-handed) leptons are composite then only the purely left-handed (right-handed) term survives, i.e. only η_1 (η_2) ≠ 0.

2. If both left-handed and right-handed leptons are composite but contain quite different sets of constituents then the purely left-handed and right-handed terms dominate, i.e. η_1,η_2>>other η_i.

3. If there is no ν_R, or $M(\nu_R)$ is very large, only $\eta_1,\eta_3\neq 0$.

Assuming an effective interaction Lagrangian

$$L_{eff} = L_{V-A} + L_{cont}$$

we obtain [cf (2)] the end point decay rate

$$R(1,0) = 2(620\text{GeV}/\Lambda)^4(g^2/4\pi)^2(\eta_2^2+\eta_3^2+\eta_5^2/4).$$

Our limit $R(1,0)=1-\xi P_\mu\delta/\rho<0.0041$ then implies

$$\Lambda^2 > (2920\text{GeV})^2(g^2/4\pi)\sqrt{(\eta_2^2+\eta_3^2+\eta_5^2/4)}$$

with 90% confidence. (If the not unreasonable assumptions $g^2/4\pi\sim 2.1$ and $\eta_i>0.2$ are made, the limit $\Lambda>2300$ GeV would be obtained.)

For the special cases discussed earlier the limit becomes

1. Only left-handed leptons composite: no limit.
2. Left and right-handed leptons have different sets of constituents: $\Lambda^2>(2920\text{GeV})^2(g^2/4\pi)\eta_2$.
3. No ν_R, or $M(\nu_R)$ very large: $\Lambda^2>(2920\text{GeV})^2(g^2/4\pi)\eta_3$.

PROSPECTS

The results presented here are based on the data collected during the first run of the experiment. Analysis of about three times as much data from the second run should be completed in late 1983.

A third and final run of the experiment is scheduled for early 1984. The run will be partially devoted to measuring the muon decay parameter δ to a proposed $\sigma(\delta)=0.003$. The μSR mode will be used to measure the decay asymmetry over the reduced momentum range $x=0.4$ - 1.0.

Any theory with two-component neutrinos has $\delta=3/4$. This is also the case in the left-right symmetric model $SU(2)_L \times SU(2)_R \times U(1)$. However, theories with heavy neutrinos such as the fermion-mirror fermion mixing models,[27] which arise from the 'big' gauge groups SO(n) with n>10 or SU(n) with n>5, predict values of δ different from 3/4. Hence a measurement of δ can be used, together with measurements of other quantities, to constrain the parameters of these theories.

In addition, measurement of the decay asymmetry over a much wider range of x will allow sensitivity to right-handed currents if $M(\nu_R) < 50$ MeV.

This research was supported in part by the U. S. Department of Energy through Contracts No. DE-AC-76SF00098 and AC02-ER02289.

REFERENCES

1. J.C. Pati and A. Salam, Phys. Rev. Lett. 31, 661 (1973) and Phys. Rev. D10, 275 (1974);
R.N. Mohapatra and J.C. Pati, Phys. Rev. D11, 566 and 2588 (1975)
2. M.A.B. Beg et al., Phys. Rev. Lett. 38, 1252 (1977).
3. B.R. Holstein and S.B. Treiman, Phys. Rev. D16, 2369 (1977).
4. The primary input to the world average is V.V. Akhmanov et al., Yad. Fiz. 6, 316 (1967).
5. The primary input to the world average is J. Peoples, Nevis Cyclotron Report No. 147 (1966).
6. J. Van Klinken, Nucl. Phys. 75, 145 (1966).
7. J. Van Klinken et al., Phys. Rev. Lett. 50, 94 (1983).
8. D. Schreiber and F.T. Calaprice, private communication; D. Schreiber, Ph.D. Thesis, Princeton University, 1983 (unpublished). We calculated the contour plotted in Fig. 1 using $A(0)=0.0363\pm0.0008$; ft ratio=1.797±0.002. See also F.T. Calaprice et al., Phys. Rev. Lett. 35, 1566 (1975).
9. H. Abramowicz et al., Z. Phys. C12, 225 (1982)
10. M. Gell-Mann, P. Ramond and R. Slansky, unpublished.
11. R.N. Mohapatra and G. Senjanovic, Phys. Rev. Lett. 44, 912 (1980) and Phys. Rev. D23, 165 (1981).
12. J. Carr et al., Phys. Rev. Lett. 51, 627 (1983).
13. G. Beall, M. Bander and A. Soni, Phys. Rev. Lett. 48, 848 (1982).
14. P. DeForcrand, Ph.D. Thesis, Univ. of Calif., Berkeley (1982), LBL-14692.
15. R.N. Mohapatra et al., Phys. Rev. D28, 546 (1983).

16. M. Denis, Phys. Rev. D28, 1219 (1983).

17. F. Scheck, Phys. Lett. C44, 187 (1978); A.M. Sachs and A. Sirlin, in Muon Physics, Vol. II, V. Hughes and C.S. Wu, eds. (Academic Press, N.Y., 1975), p. 50.

18. A.E. Pifer et al., Nucl. Inst. Meth. 135, 39 (1976).

19. C.J. Oram et al., Nucl. Inst. Meth. 179, 95 (1981).

20. A. Abragam, The Principles of Nuclear Magnetism [Oxford Uni. Press (Clarendon), London and N.Y., 1970]

21. K. Mursula et al., Nucl. Phys. B219, 321 (1983).

22. F. Wilczek, Phys. Rev. Lett. 49, 1549 (1982).

23. M. Abolins et al., Proc. 1982 DPF Summer Study Elem. Part. Phys. and Future Facilities, p.274 (Snowmass, 1982).

24. E.J. Eichten et al., Phys. Rev. Lett. 50, 811 (1983).

25. M.E. Peskin, private communication.

26. K.D. Lane and E. Barany, private communication.

27. J. Maalampi et al., Nucl. Phys. B207, 233 (1982).

Review of e^+e^--Physics with PETRA

E.Lohrmann *

II. Institut für Experimentalphysik, Universität Hamburg,

* Report based on a Talk given at the Topical Conference on Particle Physics at SLAC - 27-29 July 1983.

© E. Lohrmann 1983

I. PARTICLE SEARCHES

Extensive searches for new particles have been undertaken in the past by the CELLO, JADE, MARK J, PLUTO and TASSO Collaborations. Their work is summarized in Review articles by A.Böhm,[1] J.Bürger[2] and S.Yamada.[3]

I shall not repeat these reviews here, but rather present an update by mentioning the most recent contributions.

1.1 Toponium

In its improvement program the PETRA e^+e^--storage ring has now (September 1983) been equipped with 112 RF cavities, and 9.6 MW of RF power have been installed. This allows a search for the top quark at the highest energies, which have so far been available in e^+e^--storage rings.

Production of $t\bar{t}$ bound states (toponium) occurs below the threshold for open top-quark production, and a scan for those states has been made. To this end the storage ring energy was moved upwards in steps of 30 MeV cms energy, and the experiments CELLO, JADE, MARK-J and TASSO measured the total hadronic cross section in a search for a toponium resonance. The size of the effect is given by

$$\int \sigma \cdot dE_{CM} = \frac{6\pi^2}{M^2} B_h \cdot \Gamma_{ee} \qquad (1)$$

where σ is the cross section for the production and subsequent hadronic decay of toponium, M is the toponium mass, B_h is the branching ratio of the toponium to decay into hadrons, Γ_{ee} is the toponium e^+e^--decay width and E_{CM} is the CM energy.

Equation (1) describes the area under the Breit-Wigner resonance curve of toponium. In the PETRA measurements the beam energy spread is about 24 MeV at a beam energy of 20 GeV, leading to a cms energy spread of about 34 MeV, and this is much larger than the natural width of toponium. One expects then to see a roughly Gaussian shape with $\sigma \sim 34$ MeV for the toponium signal, with the area still given by Eq. (1). In addition one has to take radiative corrections into account, which modify the shape of the signal appreciably.

Using $B_h \sim 0.8$ and $\Gamma_{ee} = 5$ keV, as expected for a quark of charge 2/3, the toponium signal should be easily visible under the conditions of the scan (see Fig. 1).

No signal has been observed up to a cms energy of 43.2 GeV. From the biggest fluctuations observed, all four experiments have obtained upper limits (95% c.l.) of about 2 keV [3] for $\Gamma_{ee} \cdot B_h$, which is well below the 4 keV expected for toponium.

The MARK-J experiment[4] has also put a limit on a possible step in the total hadronic cross section

$$\Delta R < 0.07 \qquad \text{for } 40 \text{ GeV} < E_{cm} < 43 \text{ GeV}$$

to be compared with the (asymptotic) step size of $\Delta R = 4/3$ after passing the threshold for open top quark production.

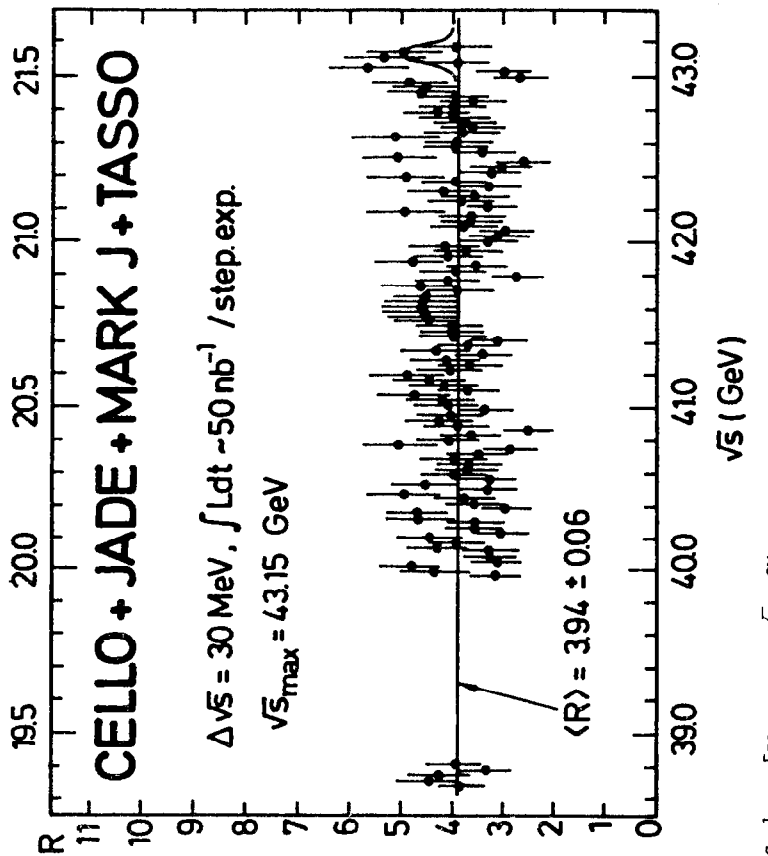


Fig. 1 - Energy scan, $\sqrt{s}$ = CM energy, $R = \sigma_{tot}(e^+e^- \rightarrow \text{hadrons})/\sigma_0$ (from Ref. 3).

1.2 Search for a b'-Quark

The MARK-J group and TASSO[5] have excluded the existence of a heavy b'-quark with charge $|Q| = 1/3$ for a mass M

$$M < 16 \text{ GeV}/c^2 .$$

The MARK-J group draws this conclusion from the dependence of the inclusive muon yield on the thrust T of the jets,[4] and from the limit $\Delta R < 0.07$ mentioned above. Depending on assumptions on the threshold behavior, the mass limit may actually be higher.

1.3 Magnetic Monopole

A search for the production of magnetic monopoles was made with the help of Kapton foils placed inside the PETRA vacuum chamber. Monopoles would be detected in these foils by their high ionization rate. After exposure the foils are developed in 15% NaCl solution for 4 hours and any tracks would appear as holes in the plastic.

The charge g of a magnetic monopole is given by Dirac's equation

$$e \cdot g = n \cdot \frac{\hbar c}{2}$$

with n being an integer, n = 1, 2, 3, ...

The search was specifically made for monopoles with large magnetic charge $n > 1$. Figure 2 shows the region of values n and monopole mass m excluded by the experiment.[7] It supplements earlier measurements made at SLAC.[6] Assuming a production process by monopole-antimonopole pair production $e^+e^- \rightarrow M\bar{M}$, an upper limit (95% c.l.)

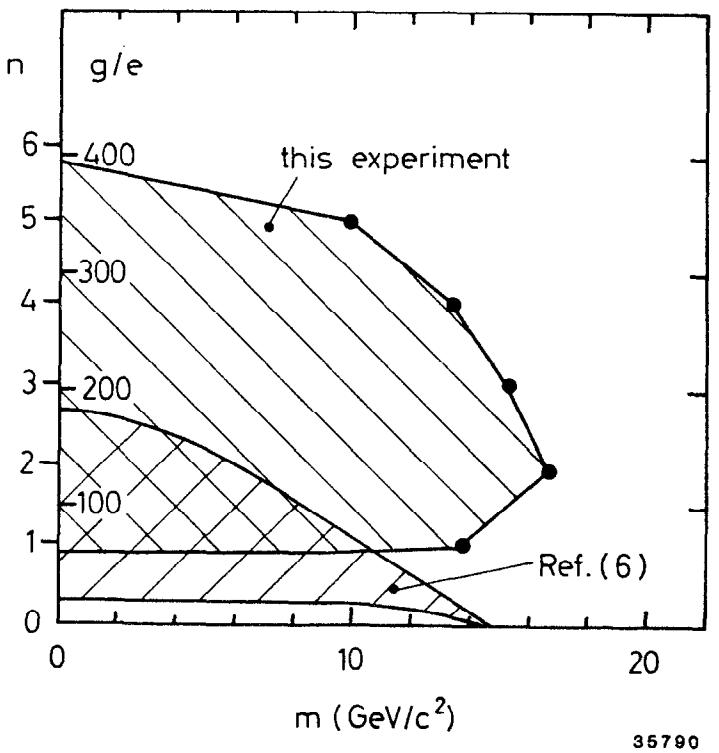


Fig. 2 - Monopole mass m, for which search is sensitive from Ref. 7); also shown is the result of Ref. 6.

on the cross section is

$$\sigma(e^+e^- \to M\bar{M}) \;<\; 4 \cdot 10^{-38}\ cm^2 \ .$$

The corresponding R-value is

$$R_{M\bar{M}} = \sigma(M\bar{M}) \,/\, \sigma(\mu^+\mu^-) \;<\; 0.6 \cdot 10^{-3} \ .$$

1.4 Excited Leptons

Table 1.1 - Mass Limits for Excited Leptons

	Excluded Mass
$e^* \to e\gamma$	$M < 61$ GeV
$\mu^* \to \mu\gamma$	$M < 17.9$ GeV

The mass limits in Table 1.1 are taken from the earlier review article by A.Böhm [1] and from new measurements by JADE. [8] They are derived from a study of $e^+e^- \to \gamma\gamma$ for e^* (Fig. 3) and from a study of radiative corrections to $e^+e^- \to \mu^+\mu^-$ for the μ^*. The $e^*e\gamma$ ($\mu^*\mu\gamma$) coupling is given by λe, the mass limits in Table 1.1 are derived for $\lambda = 1$.

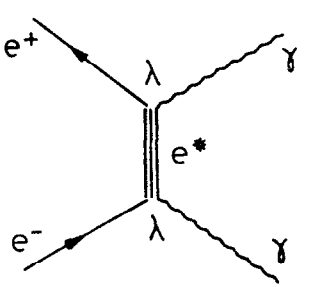


Fig. 3 - Hypothetical contribution to the QED reaction $e^+e^- \to \gamma\gamma$ by the exchange of an excited electron.

1.5 Sequential Lepton

A new lepton in the sequence e, μ, τ, ... would be detected by its decay into a muon or an electron and two neutrinos, the muon or electron appearing at large transverse momenta. A new limit has been set by the MARK-J[5] experiment and by JADE,[8] excluding masses M:

$$M < 20.6 \text{ GeV} \quad \text{(JADE)}.^{8)}$$

1.6 Heavy Neutral Electron

A heavy neutral electron E^0 would be coupled to the W-boson by the standard weak interaction, allowing V + A or V - A, see Fig. 4a.

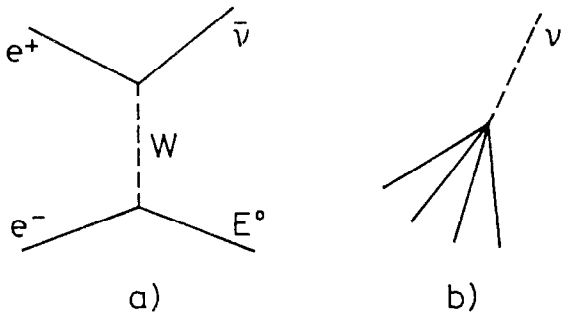


Fig. 4 - Production (a) and signature (b) of heavy neutral lepton E^0.

The E^0 is produced via

$$e^+e^- \rightarrow E^0 \bar{\nu}$$

with the E^0 decaying via

$$E^0 \rightarrow e^-l^+ \nu_l, \; e^- \bar{d} u \; ; \; e^- \bar{s} c \; .$$

The JADE Collaboration[8] has searched for the E^0 by the signature shown in Fig. 4b, where one has a single jet from $e^- \bar{d} u$ going to one side. They can exclude an E^0 with a mass M

$$M < 23 \text{ GeV} \; .$$

1.7 Supersymmetric Particles

According to supersymmetry models,[9] there is a pair of scalar particles corresponding to each spin 1/2 fermion and there is a supersymmetric fermion corresponding to each elementary scalar particle, see Table 1.2. A review on mass limits for e_s, μ_s, τ_s achieved in earlier work has been given by A.Böhm.[1] The JADE Collaboration[8] has made a new search for e_s, μ_s, q_s and γ_s, where they consider the case of both stable and of unstable e_s and μ_s.

Production of a stable e_s or μ_s would look like $e^+e^- \rightarrow \mu^+\mu^-$, with a particle momentum of $P_s = \sqrt{E^2_{beam} - M^2}$; production of an unstable e_s or μ_s would lead to an e^+e^- or $\mu^+\mu^-$ pair with missing energy and momentum in the final state. The expected number of events of each type can be calculated from QED and a signal of the expected size can be excluded experimentally.

The search for q_s proceeds along similar lines. If the q_s is unstable, the unseen momentum carried away by the q_s would lead to two acoplanar quark-jets in the final state. From studying the measured acoplanarity distribution of jets, the JADE Collaboration has derived mass limits[8] on the q_s but they had to choose specific assumptions on the decay of the q_s and on fragmentation.

The CELLO [10] Collaboration has made a search for a massive unstable γ_s. New data come from JADE.[8]

Table 1.3 lists the mass values excluded by these searches.

Table 1.2 - Supersymmetric Particles

Particle	Supersym. partner (only one shown)	Decay
e electron	e_s	$e_s \to e\,\gamma_s$
μ muon	μ_s	$\mu_s \to \mu\gamma_s$
τ tau	τ_s	$\tau_s \to \tau\gamma_s$
q quark	q_s	$q_s \to g_s q,\ \gamma_s q$
γ photon	γ_s	$\gamma_s \to \gamma G_s^*$
g gluon	g_s	

* G_s = supersymmetric partner to the graviton; there may be other decays.

Table 1.3 - Excluded Mass Values for Supersymmetry-Particles*

Particle	Mass excluded (GeV)	Remarks
e_s	$M < 16.6$	stable e_s
	$M < 17.8$	unstable e_s ($m_{\gamma_s}=0$)
μ_s	$M < 16.6$	stable μ_s
	$M < 18$	unstable μ_s (MARK-J)
τ_s	$M < 16.5$	MARK J
q_s	$2.5 < M < 13.5$	stable q_s
	$7.4 < M < 16$	unstable q_s, specific assumptions
γ_s	$M < 17$	if unstable, specific assumptions

*) See also Review of Particle Searches by A.Böhm.[1)]
Table 1.3 contains the most recent limits obtained by JADE, unless otherwise stated.

1.8 Charged Higgs /Technipion $H^{\pm}$

This scalar particle is coupled preferentially to heavy particles, so the dominant decay modes should be

$$H^+ \to \tau^+\nu_\tau, \to c\bar{s}, \to c\bar{b} \ .$$

Searches have been made by the CELLO, JADE, MARK J, MARK II, MAC and TASSO experiments.[11] In particular, the TASSO[12] experiment has excluded the case of predominant decay into heavy quarks. This excludes the following mass values for the H :

$$5 \text{ GeV} < M < 13 \text{ GeV} \ .$$

2. ELECTROWEAK AND WEAK INTERACTIONS

2.1 Cross Sections According to the Standard Model

Consider the differential cross section for the process: $e^+e^- \to f\bar{f}$ (f = fermion), described in lowest order by the Feynman diagrams of Fig. 5(a).

$$f \equiv e^-, \mu^-, \tau^-, q \ .$$

$$d\sigma/d\Omega = \frac{\alpha^2}{4s} \ (R \ (1 + \cos^2\theta) + C \cos\theta \tag{2}$$

$$R = Q_f^2 - 2 \ v_e v_f \ Q_f \ \mathrm{Re}(X) + (v_e^2 + a_e^2) \cdot (v_f^2 + a_f^2)|X|^2 \tag{3}$$

$$C = -4 \ a_e \ a_f \ Q_f \ \mathrm{Re}(X) + 8 v_e \cdot v_f \ a_e a_f |X|^2 \ . \tag{4}$$

(If f = quark, one must include a factor of 3 for color.)

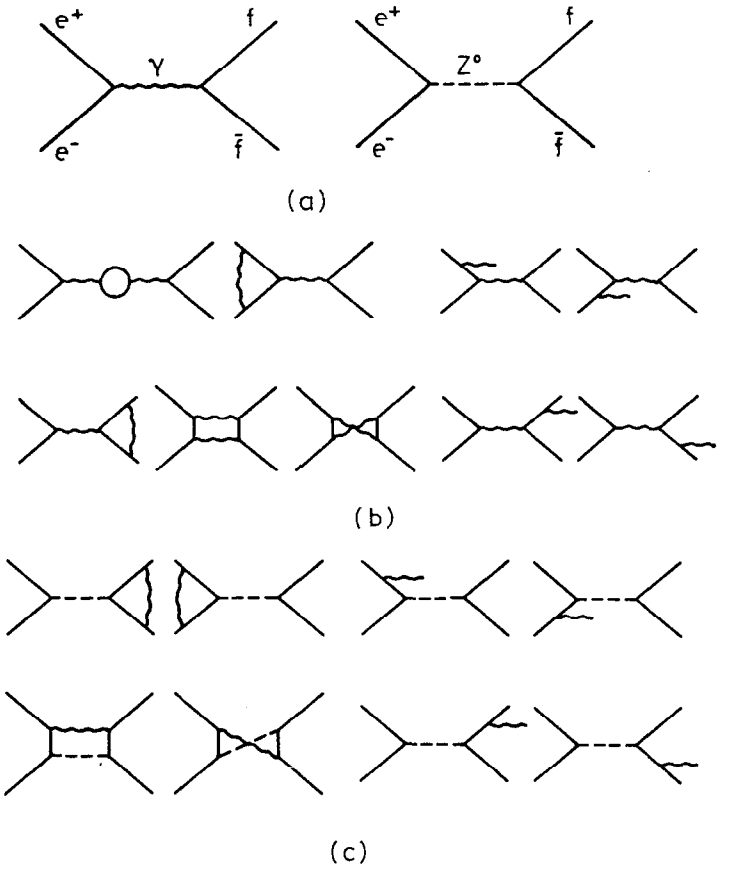


Fig. 5 - Feynman Diagrams for $e^+e^- \to f\bar{f}$(a) first order (b) purely QED radiative corrections, (c) radiative corrections including the Z^0 (additional weak radiative corrections not shown). (b) was included, (c) was not included in comparison of experiment and theory.

2.2 Lepton Asymmetry

New values for the muon asymmetry $A_{\mu\mu}$ have been given by JADE ($-11.0 \pm 1.8\%$), PLUTO ($-12.4 \pm 3.1\%$), MARK-J ($-11.7 \pm 1.7\%$) and TASSO ($-9.1 \pm 2.3\%$).[14] These values include QED radiative corrections from diagrams containing only photons and electrons (Fig. 5b) and amounting to about +1.6% (slightly experiment dependent). The new weighted average at the average PETRA CMS energy of 34.5 GeV, including CELLO ($-6.4 \pm 6.4\%$) is

$$A_{\mu\mu} = (-10.9 \pm 1.0)\%$$

with an additional systematic error which I estimate to be 0.5%. This value can be compared with the prediction of the standard model Eq. (3,4,5), which for a Z^0 mass of 92 GeV and 34.5 GeV CM energy is

$$A_{\mu\mu}^{th} = (-9.3 \pm 0.3)\%$$

still in reasonable agreement with experiment.

Actually, for a comparison with the theoretical value of -9.3% the experimental value has in addition to be corrected for radiative effects from the diagrams containing a Z^0. The diagrams of Fig. 5c make an (experiment dependent) correction[15,16] which for TASSO (PLUTO) is 0.7% (+ 1.0%). Applying it would bring the TASSO (PLUTO) asymmetry to $-9.8 \pm 2.3\%$ ($-13.4 \pm 3.1\%$). However, there are additional purely weak contributions to the radiative corrections (not shown in Fig. 5), whose size is not

with

$$X = \frac{G_F}{2\pi\alpha\sqrt{2}} \cdot \frac{M_z^2}{s - M_z^2 + iM_z\Gamma_z} ,$$

Q_f = fermion charge, v_f, a_f are the weak vector and axial vector coupling constants, G_F (Fermi coupling constant) = $1.02 \cdot 10^{-10}/M_p^2$, and M_z = Z^0 mass. For the case of quarks one has to include QCD corrections, which are omitted here for simplicity, for the formulae, see Eq.(6) and Ref.(13).

The forward-backward asymmetry is given by

$$A_{ff} = \frac{F - B}{F + B} = \frac{3}{8}\frac{C}{R} \qquad (5)$$

where F = forward means the number of fermions going in the forward hemisphere as defined by the direction of the e^-, B = the same for backwards.

Table 2.1 gives the values of the coupling constants according to the standard model.

Table 2.1 - Coupling Constants According to the Standard Model

f	Q_f	a_f	v_f	v_f for $\sin^2\theta_W$=0.23
ν	0	1/2	1/2	1/2
e^-,μ^-,τ^-	-1	-1/2	$-1/2 + 2\sin^2\theta_W$	-0.04
u,c	2/3	1/2	$1/2-(4/3)\sin^2\theta_W$	0.19
d,s,b	-1/3	-1/2	$-1/2+(2/3)\sin^2\theta_W$	-0.35

where θ_W = Weinberg angle.

yet clear. I have therefore preferred to omit the contributions from the diagrams in Fig. 5c.

The asymmetry for the tau lepton is[17]

$$A_{\tau\tau} = (-7.9 \pm 2.2)\%$$

again in agreement with the theoretical prediction.

The values of the muon and tau asymmetry $A_{\mu\mu}$ and $A_{\tau\tau}$ depend essentially on the three coupling constants a_e, a_μ, a_τ. In order to determine them separately from experiment, one needs a third experimental input, which one can take from measurements of neutrino-electron scattering. They yield[18]

$$a_e = -0.51 \pm 0.05 .$$

Using this value, one obtains then

$$a_\mu = -0.57 \pm 0.08$$

$$a_\tau = -0.42 \pm 0.11$$

to be compared with the standard-model value of -1/2. The combination of neutrino- and e^+e^--data allows in addition a resolution of the sign ambiguity of a_e and of the a_e/v_e ambiguity in the neutrino data,[19] which has been used for the determination of a_e above.

These data provide a check of the standard model at four momentum transfers of $Q^2 = 1200\ \mathrm{GeV}^2$, and they are also an important check for e-μ-τ universality.

2.3 Heavy Quark Forward-Backward Asymmetry

Measuring this asymmetry provides an important check on the charges and the weak coupling of the heavy quarks. Experimentally one has to determine the flavor and the sign of the charge of the original quark, which is hidden in the jets.

Two methods have been used:

i) $e^+e^- \rightarrow c\bar{c} \rightarrow D^{*+} D^{*-}$

It has been possible to identify the D* experimentally.[20] Since the D*'s have a hard momentum spectrum (average momentum ≈ 60% of the beam energy), one believes that the D^{*+} follows the direction of the c-quark.

ii) $e^+e^- \rightarrow c\bar{c}$, $c \rightarrow s W^+$, $W^+ \rightarrow l^+ \nu_l$

$\rightarrow b\bar{b}$, $b \rightarrow c W^-$, $W^- \rightarrow l^- \bar{\nu}_l$

In this method one uses the semileptonic ($l = e^\pm$ or $\mu^\pm$) D- and B-decays to tag the c- and b quarks. The method has its difficulties, because one can only achieve a partial separation of leptons coming from c- and b-decay, and because of a background of misidentified leptons.

Figure 6 gives as an example the inclusive muon transverse momentum spectrum as obtained by MARK-J. The figure also shows the muon spectra expected from semileptonic c- and b-decays separately and one sees how they add up to give the measured curve. By choosing appropriate cuts in transverse momentum, momentum, and maybe other variables of the jets, one tries to get data samples enriched in c- or b-decay events, and then uses them to compute the asymmetry. This still requires a critical subtraction of background.

Table 2.2 gives a summary of results. The values are in accord with the standard model!

2.3 Vector Coupling Constant

At PETRA energies the weak vector coupling constants v_f appear essentially in the expression for the total cross sections. Table 2.1 shows, that one has small numerical values of v_f in the standard model. Accordingly the effects of weak interactions are at the limit of observability. Still this can serve to set upper limits on the v_f-coupling constants and therefore limits on $\sin^2\theta_W$.

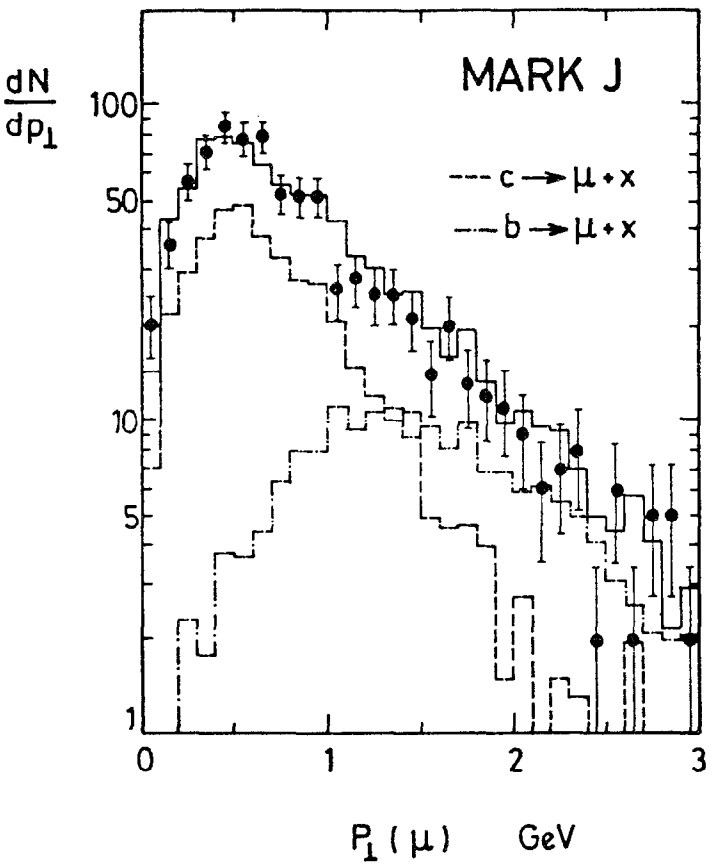


Fig. 6 - Distribution of inclusive muon transverse momentum relative to the jet axis, also shown are predicted contributions from semileptonic c- and b-decays. The solid histogram is the prediction with u,d,s,c and b quarks including decay and punchthrough.(Ref. 4).

Table 2.2 - Forward-Backward Asymmetry of Heavy Quarks [21]

	$A_{c\bar{c}}$	$A_{b\bar{b}}$	Method
TASSO	-0.13 ± 0.10		$D^*\bar{D}^*$
TASSO		-0.38 ± 0.28	μ incl.
JADE	-0.27 ± 0.14		$D^*\bar{D}^*$
JADE		-0.26 ± 0.09	μ incl.
MARK-J	-0.17 ± 0.09	-0.15 ± 0.22	μ incl.
average	-0.17 ± 0.06	-0.25 ± 0.08	
standard model prediction	-0.14	-0.25	

From a new accurate measurement of the total hadronic cross-section (see Section 3.1) the JADE Collaboration obtains

$$\sin^2\theta_W = 0.23 \pm 0.05 .$$

From an overall fit to the leptonic reactions $e^+e^- \to e^+e^-$ and $e^+e^- \to \mu^+\mu^-$ the TASSO Collaboration gets[14]

$$\sin^2\theta_W = 0.26 \pm 0.07 .$$

These values agree with the world average of 0.23. The errors are larger than those achieved by neutrino experiments or by experiments with polarized e- or μ-beams. Still the results are interesting, because the measurement has been done at the very large value of $Q^2 \approx 1200\ \text{GeV}^2$.

2.4 Branching Ratios for τ- and Heavy Quark Decay

The CELLO Collaboration has communicated new measurements of branching ratios of tau decay. The results are[22]

$$BR(\tau \to \rho\nu) = (22.8 \pm 2.5 \pm 2.1)\%$$
$$\to \pi\nu) = (9.9 \pm 1.7 \pm 1.3)\%$$
$$\to e\nu\nu) = (18.3 \pm 2.4 \pm 1.9)\%$$
$$\to \mu\nu\nu) = (17.6 \pm 2.6 \pm 2.1)\% .$$

The branching ratios for the semileptonic decays of c- and b-quarks can be obtained from the inclusive electron or muon momentum spectra. First one has to separate the contributions from c-decay, b-decay and background in the spectra, as explained in Section 2.2.

If one then assumes, that the numbers of hadrons containing a $(\bar{c})$- or $(\bar{b})$-quark are respectively 2 x (4/11) or 2 x (1/11) per event, one obtains the semileptonic branching ratios of Table 2.3. Upper limits of 0.7% have been found for the branching ratio of $b \to \mu^+\mu^- X$ by the JADE and MARK J Collaboration.[24] This limit excludes certain models[25] having 5 quark flavors instead of 6.

3. STRONG INTERACTIONS

3.1 Measurement of α_s

The JADE Collaboration has made a new accurate measurement of the total hadronic cross section (see Fig. 7) and improved earlier[26] measurements by TASSO ($R = 4.01 \pm 0.03 \pm 0.2$) and MARK-J ($R = 3.84 \pm 0.05 \pm 0.22$). (See also MAC ($R = 3.89 \pm 0.02 \pm 0.11$)).

The average R- value of JADE[26] is

$$\langle R \rangle = \frac{\sigma_T(e^+e^- \to \text{hadrons})}{\sigma_0(e^+e^- \to \mu^+\mu^-)} = 3.97 \pm 0.05 \pm 0.10$$

where $\sigma_0 = \frac{4\pi}{3}\alpha^2/s$ and $s = E_{CM}^2$.

Table 2.3 - Semileptonic Branching Ratios of Hadrons Containing c- and b-quarks[23]

Experiment	c μ X (%)	b e X (%)	b μ X (%)
CELLO	$12.3 \pm 2.9 \pm 3.9$	$14.1 \pm 5.8 \pm 3.0$	$8.8 \pm 3.4 \pm 3.5$
MARK J	$11.5 \pm 1.0 \pm 1.7$	-	$10.5 \pm 1.5 \pm 1.3$
TASSO	-	$13.6 \pm 4.9 \pm 4.0$	$15.0 \pm 3.5 \pm 3.5$
Average	$11.6 \pm 1.0 \pm 1.7$	$13.9 \pm 3.8 \pm 2.5$	$10.8 \pm 1.3 \pm 1.1$

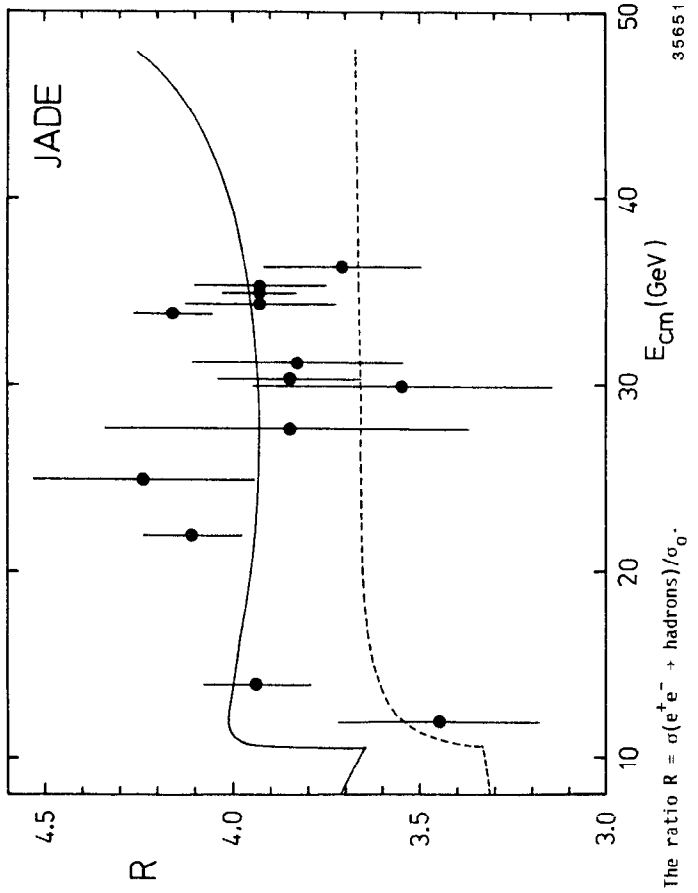


Fig. 7 - The ratio $R = \sigma(e^+e^- \rightarrow \text{hadrons})/\sigma_0$. Dashed curve: quark parton model; full curve: fit to Eq. 6, plus weak interaction corrections.

The theoretical expression for R, including QCD, but without weak interaction corrections, is ($\overline{\text{MS}}$ scheme, 5 flavors)

$$R = 3 \cdot (1 + \frac{\alpha_s}{\pi} + C_2(\frac{\alpha_s}{\pi})^2) \cdot \sum_q Q_q^2 \quad , \text{ and} \qquad (6)$$

$$C_2 = 1.99 - 0.12\ N_f = 1.39)$$

(with a factor 3 for color included; for the full formula including weak interaction corrections, see Ref.26).

From a simultaneous fit to the strong coupling constant α_s and to $\sin^2\theta_W$ they obtain

$$\alpha_s = 0.20 \pm 0.08 \quad \text{and}$$
$$\sin^2\theta_W = 0.23 \pm 0.05 \quad \text{(see Section 2.3).}$$

This method of finding α_s is on a sound theoretical basis, but the experimental errors are large, because R depends on α_s roughly as

$$R \approx 3\Sigma\, Q_f^2\ (\ 1 + \frac{\alpha_s}{\pi}),$$

α_s being contained in the correction term.

In contrast the relative frequency of three-jet events arising from gluon bremsstrahlung (see Fig. 8b) should depend on α_s directly and therefore allow a potentially more acurate determination of α_s.

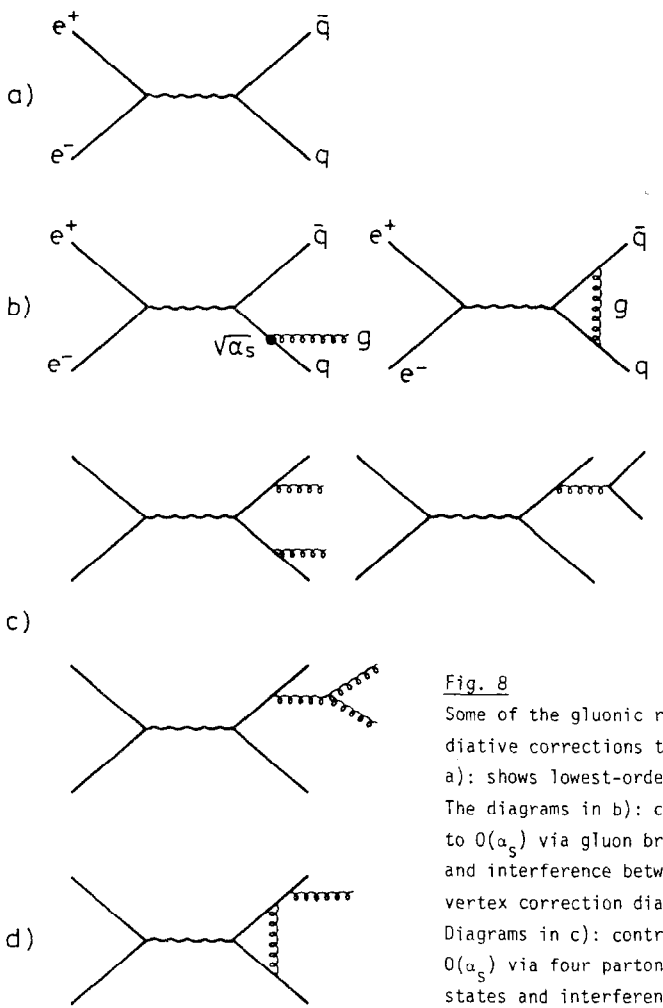


Fig. 8
Some of the gluonic radiative corrections to $O(\alpha_s)$. a): shows lowest-order diagrams. The diagrams in b): contribute to $O(\alpha_s)$ via gluon bremsstrahlung and interference between a) and vertex correction diagram in b). Diagrams in c): contribute to $O(\alpha_s)$ via four parton final states and interference terms (not all diagrams are drawn).

However, there are now other difficulties. First, there are the higher order corrections Fig. 8c - 8d). Although the various theoretical results on the next higher order $O(\alpha_s)^2$ now roughly agree and we understand how one has to choose the cuts on the experimental data in the correct way,[27] there may still be small but important differences.[28]

The corrections are not large enough to raise wories on the validity of the perturbation series, but still large enough to matter. Indeed, all PETRA groups now have results derived from comparison with QCD calculations in $O(\alpha_s)^2$.

We now come to the second difficulty. The QCD calculations in perturbation theory are valid on the level of the partons, the quarks and gluons. The observation however is in terms of jets of hadrons. In order to go from jets to partons, one needs phenomenological models on the hadronization process of the partons. Two extreme models are shown in Fig. 9, the independent fragmentation model à la Feynman Field (IP) and the string model à la Lund (LD).

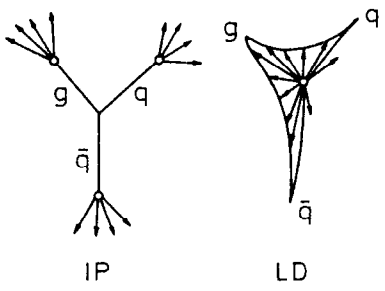


Fig. 9 - Hadronization via the independent parton model (IP) (each parton fragments into hadrons) and the string model (LD): hadronization along color flux lines stretched between gluon and quarks.

The PETRA groups have invested a great amount of work to fit the two models to the data and to compare to second order QCD calculations. The result is shown in Fig. 10.

The CELLO Collaboration has used the asymmetry of the energy-energy correlation.[29] This method is unfortunately - contrary to earlier hopes - also sensitive to fragmentations. In addition, it appears to be sensitive to the way energy conservation is introduced into the fragmentation models. The independent parton model (IP) and the string model (LD) give different results. This sensitivity to fragmentation had already been pointed out by earlier work of CELLO.[30]

The JADE Collaboration used cluster analysis to reconstruct the original partons, and used the distribution of x_{max} (x-value of most energetic parton) and $x_{\perp}$ (transverse x of other parton). They find - within errors - no dependence on the fragmentation model.[31]

MARK-J used the asymmetry of the energy-energy correlation.[32]

TASSO fitted a number of event shape parameters to the data in both models, and got good agreement between the data and the model predictions for the listed values of α_s.[33] Like CELLO, they see an appreciable dependence on the fragmentation model.

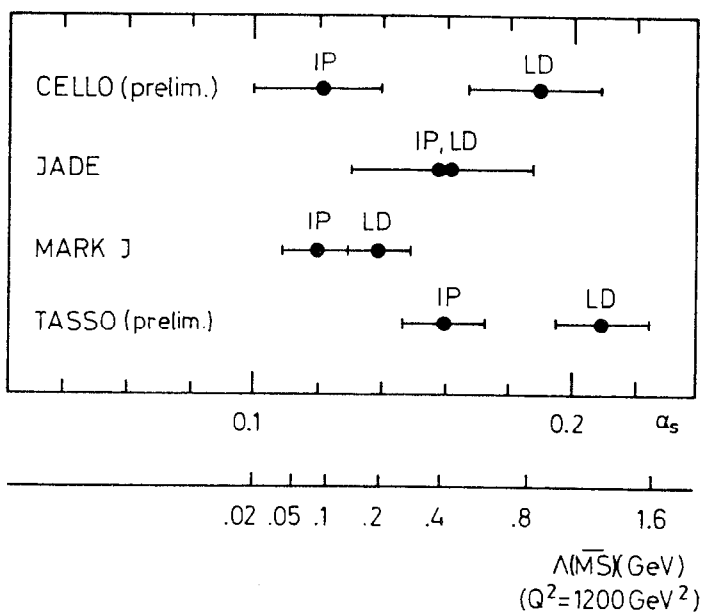


Fig. 10 - Measurement of α_s in second order by PETRA groups.
IP = independent parton model,
LD = string model used for fragmentation.

The groups differ in the way they apply second order corrections. MARK-J has used the work of ERT;[34] the other three groups have used FKSS.[35] This could also be a source of disagreement.

In summary the Lund model gives larger values of α_s than the IP-model, but there is disagreement on the size of this effect. It also appears that the value of α_s obtained in the analysis is sensitive to the way the second order corrections are applied. Since the IP and LD models constitute two extremes among fragmentation models, I believe that the true value of α_s may lie between $\alpha_s = 0.12$ and $\alpha_s = 0.22$. Whereas one could imagine worse measuremets of α_s, it is not accurate enough to yield a useful value*) for $\Lambda_{\overline{MS}}$. Obviously one needs more information to make progress, such as, e.g., the energy dependence of jet measures, as first tried by the PLUTO Collaboration[36]; and maybe a new look at second order corrections.

3.2 General Properties of the Hadronic Final State

i) The PLUTO Collaboration has presented interesting studies on the transverse momentum of jets and on energy moments à la Konishi, Ukawa and Veneziano.[37]

---

*) In second order, and in the $\overline{MS}$ renormalization scheme

$$\alpha_{s,\overline{MS}}^{(2)} = \frac{12\pi}{(33-2N_f)\ln(s/\Lambda^2) + \frac{6\cdot(153-19N_f)}{(33-2N_f)}\cdot \ln\ln(s/\Lambda^2)}$$

where N_f = number of flavors = 5, s = (cm energy)^2.

ii) The JADE Collaboration[38] has presented new measurements of the mean number of charged particles in a jet $\langle n_s \rangle$ as a function of cm energy (Fig. 11).

iii) They have also presented new accurate multiplicity distributions at several cm energies, which show impressive evidence for KNO scaling (Fig. 12). It should be noted that the shape of the "universal" KNO scaling function is in general different for e^+e^- than for hadron interactions.

iv) The CELLO Collaboration has presented new evidence for scaling violation of the fragmentation function.[39] It agrees with earlier measurements of TASSO,[39] MARK II,[39] and JADE.[38]

3.3 Particle Composition

The particle composition of the hadronic final state has now been measured over the whole momentum range. The CELLO, JADE and TASSO experiments have made contributions. The results for a CM energy of 34 GeV are shown in Table 3.1.

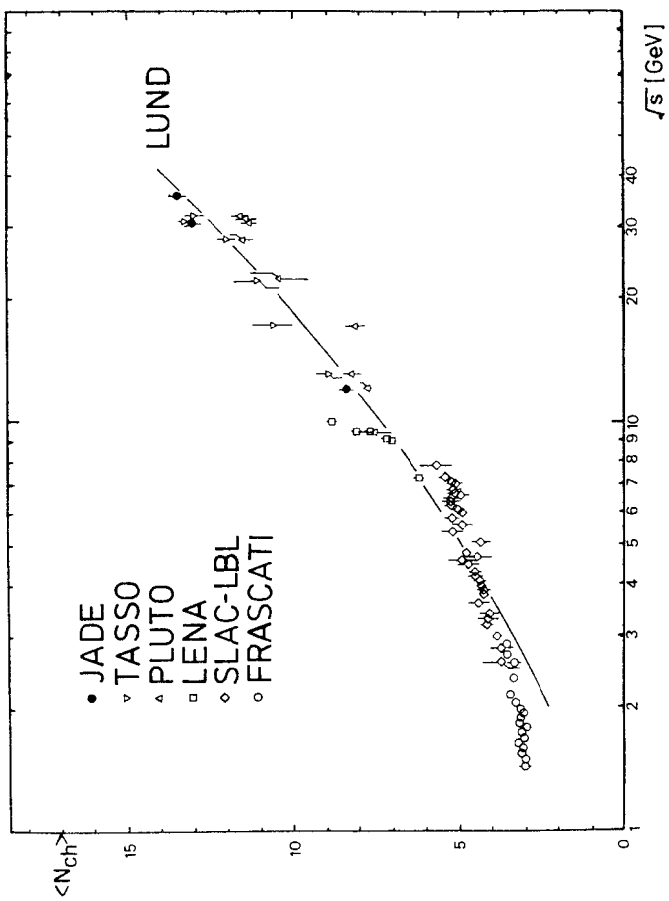


Fig. 11 - Mean multiplicity of charged particles in e^+e^- annihilation as a function of the cm energy. Decay products of K_s are included (from Ref.38).

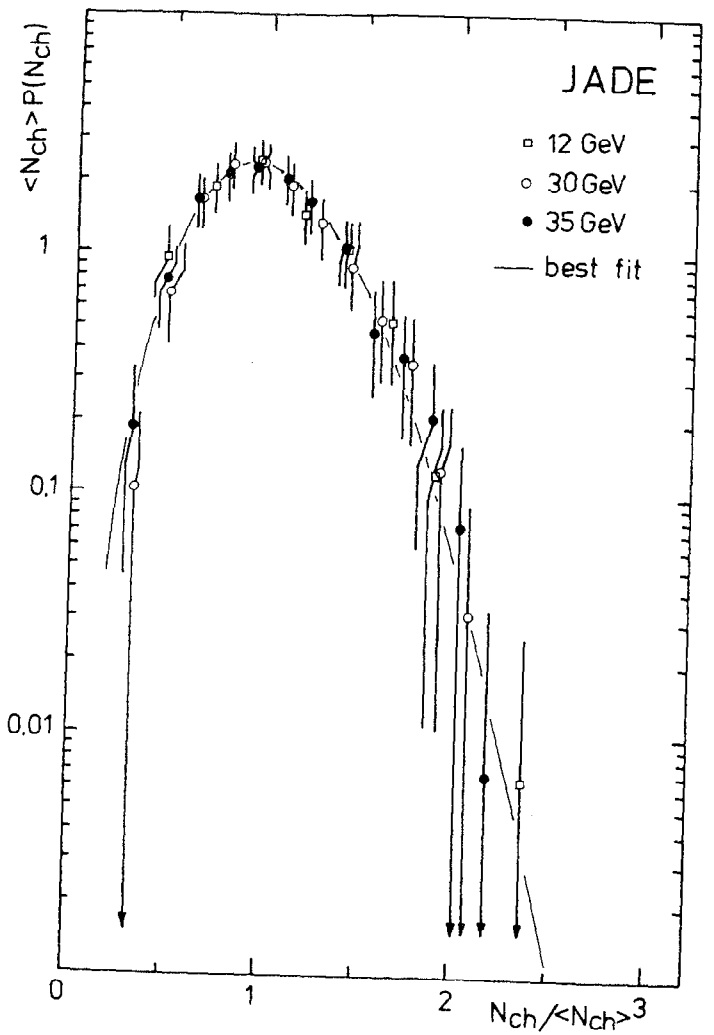


Fig. 12 - Distribution of charged multiplicity at various CM energies (Ref.38). The data follow KNO SCALING: Also shown is the fit to the KNO function used by PLUTO (Phys.Lett.81B(1979)410).

Table 3.1 - Mean Number of Particles Produced at 34 GeV cm Energy

Particle i	$\langle n_i \rangle$	Reference
$\pi^+ + \pi^-$	10.3 ± 0.4	TASSO[40]
π^0	6.1 ± 2.0	TASSO[41]
	5.2	CELLO [42]*)
η	$.72 \pm .10 \pm .18$	JADE[43]
ρ^0	$.73 \pm 0.06$	TASSO[44]
	$.82 \pm .12 \pm .10$	JADE[45]
$K^+ + K^-$	2.0 ± 0.2	TASSO [40]
$K^0 + \bar{K}^0$	1.6 ± 0.1	TASSO[46]
	1.45 ± 0.17	JADE[45]
$K^{*+} + K^{*-}$	$.83 \pm .18 \pm .13$ (prelim.)	JADE[45]
$D^{*+} + D^{*-}$	$.31 \pm .07 \pm .11$	TASSO[20]
$p + \bar{p}$	0.8 ± 0.1	TASSO[40]
$\Lambda + \bar{\Lambda}$	0.28 ± 0.04	TASSO[47]
$\Xi^- + \bar{\Xi}^-$	$0.026 \pm 0.008 \pm 0.009$	TASSO[48]

*) From a comparison of $\pi^+\pi^-$ and π^0 data Fig. 13, π^0's are assumed to be $(\pi^+ + \pi^-)/2$.

In addition to the published results of TASSO there are a number of important new contributions. Figure 13 shows a new measurement[42] of the π^0 momentum spectrum, made by CELLO with their lead-liquid argon shower counter. It is compared with the TASSO π^+, π^-. The π^0 mesons are seen to agree with the average of π^+ and π^-.

Figure 14 shows evidence for the η mesons, obtained by JADE with their lead glass shower counter. Figure 14a shows the π^0 signal in the $\gamma\gamma$ invariant mass distribution and a shoulder at the η mass. A lower limit of 200 MeV for the photon energy was applied. If one omits those photons, which are part of a $\gamma\gamma$ mass combination in the π^0 mass band, and whose energy is above 300 MeV, one obtains Fig. 14b, where the η signal is seen more clearly, because the combinatorial background has been reduced. Fig. 14c shows the background subtracted $\gamma\gamma$ mass distribution in the η region with a clear signal. Figure 15 shows the $K^{*\pm}$ signal of JADE in the $K^0_S\pi^\pm$ mass distribution.

Figure 16 shows the evidence for the production and decay of the Ξ^- / ($\bar{\Xi}^-$) hyperon, obtained by the TASSO Collaboration. Figure 16a shows a clear peak at the Ξ^- mass in the combined $\Lambda\pi^-$ and $\bar{\Lambda}\pi^+$ mass distributions. As a check the "wrong" combinations $\Lambda\pi^+$ and $\bar{\Lambda}\pi^-$ are plotted in Fig. 16b, and no signal is seen there.

Consequently, we have now a rather complete overview of the particle composition of the hadronic final state.

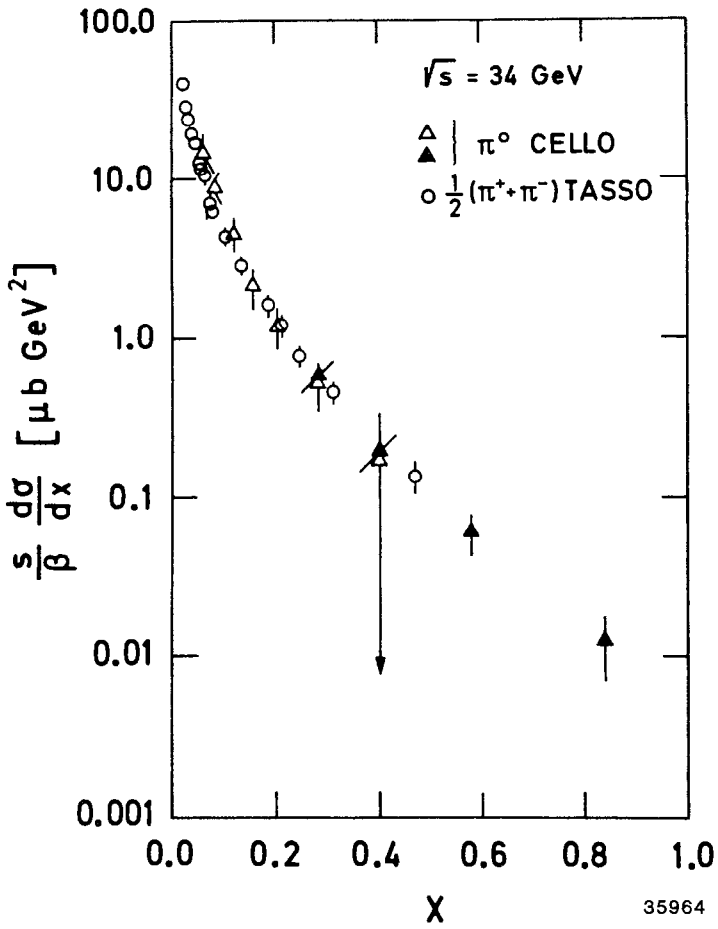


Fig. 13 - Inclusive cross section for π^0 production at 34 GeV CMS energy (Ref. 42) $x = 2E(\pi^0) / E_{CM}$.

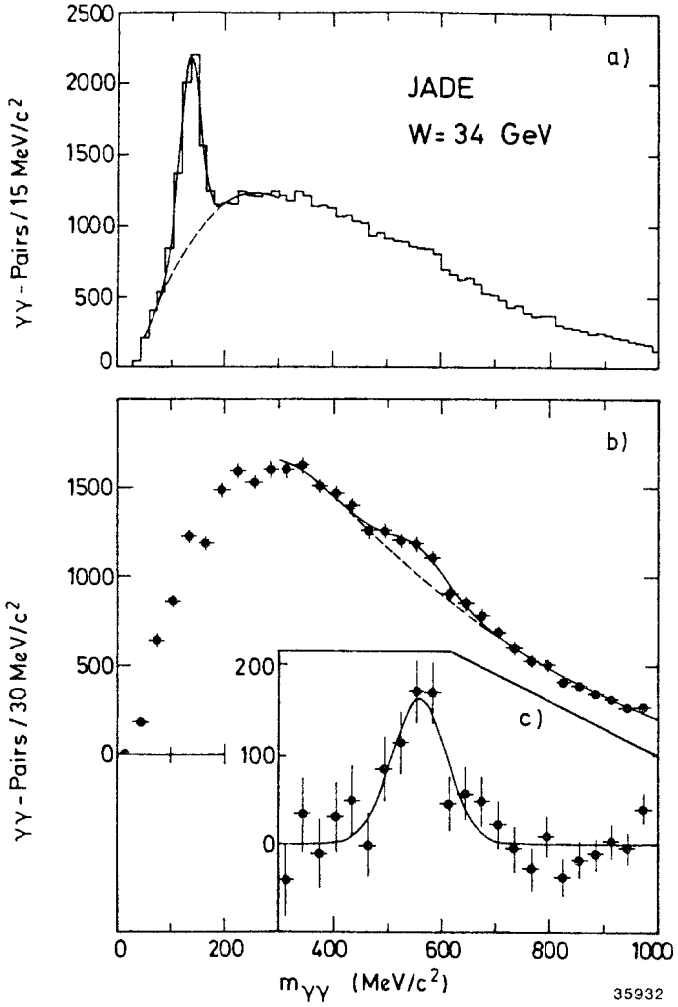


Fig. 14 - Inclusive η production at 34 GeV CMS energy
a) γγ-mass distribution, b) with cuts (see text);
c) background subtracted signal (Ref.43).

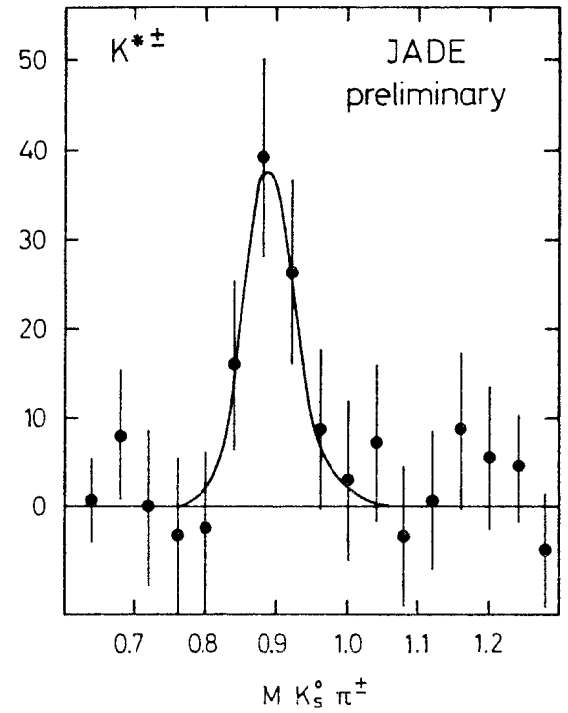


Fig. 15 - K^0_S-$\pi^\pm$ mass distribution, after background subtraction (Ref. 45).

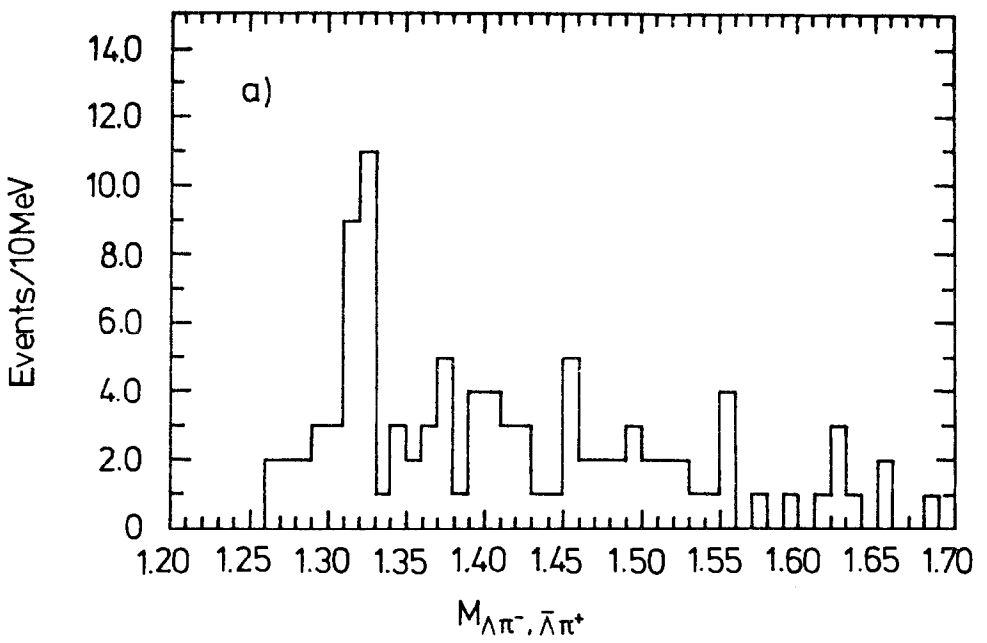


Fig. 16a - Evidence for Ξ^- ($\bar{\Xi}^-$) production in the $\Lambda\pi^-$, $\bar{\Lambda}\pi^+$ mass distribution.

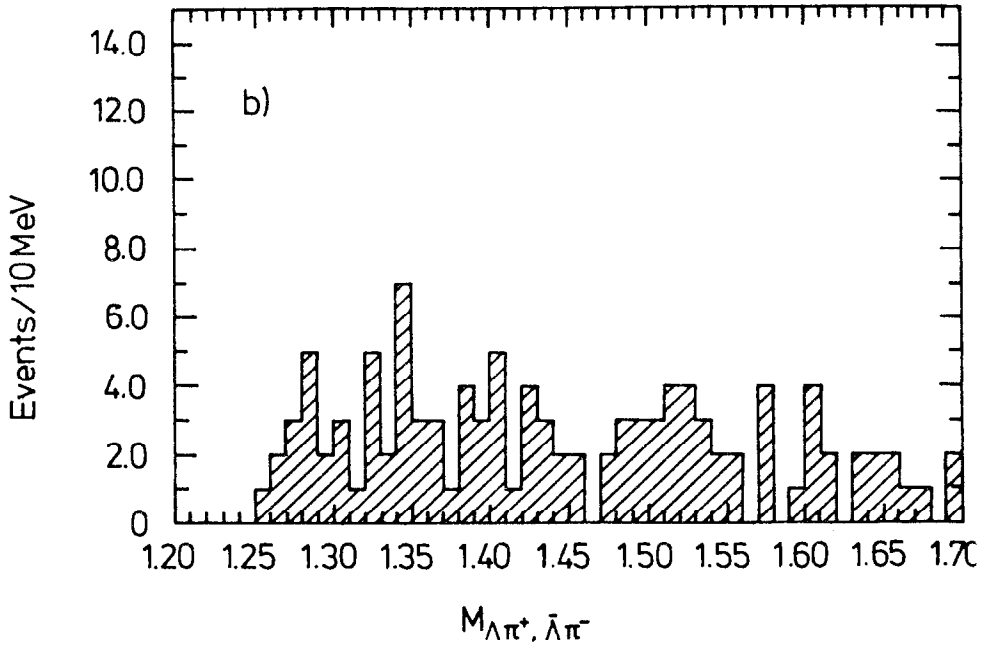


Fig. 16 b - Check with $\bar{\Lambda}\pi^-$, $\Lambda\pi^+$ mass distribution TASSO, Ref. 48.

A few simple remarks are the following:

i) The question of how many "particles" are produced on average requires a careful definition. Certainly the total number of hadrons produced on average in a e^+e^- collision is not the sum of the numbers in Table 3.1, because some of those particles may be decay products of other hadrons. For example, the listed number of $\pi^+ + \pi^-$ includes those pions which come from the decay of K^0_S, Λ, D, D*, ρ^{0+-} etc. Assuming equal numbers of ρ^+, ρ^- and ρ^0 produced, and similar equalities for the other resonances, one finds from Table 3.1 that at least 70% of the pions come from the decay of heavier hadrons. Likewise one finds that about 20% of the protons come from Λ decay.

ii) Consider the number of kaons produced in the first step of the annihilation reaction $e^+e^- \to q\bar{q}$. The $q\bar{q}$ pair will be $c\bar{c}$ in the fraction 4/11 of the cases, it will be $s\bar{s}$ in the fraction 1/11 of the cases, and the same fraction holds for $b\bar{b}$. Neglecting baryon production, and assuming that each c, s or b quark will ultimately give rise to a kaon, one expects on average 2 x (4/11 + 1/11 + 1/11) = 1.09 kaons/event, arising from the first direct $q\bar{q}$ pair. The total number of kaons found however is 3.5. This means, that only about 30% of the kaons come from the original $s\bar{s}$, $c\bar{c}$, $b\bar{b}$ - quark pairs, and about 70% of the kaons are produced in the subsequent hadronization step.

iii) Assuming equal numbers of $p\bar{p}$ and $n\bar{n}$, and noting that every baryon will finally end up as p or n, one sees that on average 0.8 baryon pairs are produced per event.

iv) Observation of the Ξ^- puts new important constraints on fragmentation models because we now know the fraction of strange particles among the hadrons and we know some fractions of baryon species with strangeness 0, -1 and -2, and these numbers have to be accommodated with a small number of input parameters for the models.

3.4 Properties of Jets

i) Properties of gluon jets: The JADE Collaboration[49] has updated earlier work, in which they look at the transverse momentum of particles relative to the jet axis in three-jet events. They find that particles in the least energetic of the three jets have a larger mean transverse momentum than those in the two other jets, if normalized to the same jet energy (Fig. 17). Since the least energetic jet has a larger probability to be the gluon jet than the other two jets, this indicates that the particles in gluon jets have a larger mean transverse momentum than those in quark jets.

In addition the particle composition may be different in gluon jets. There are indications, that gluon jets may contain more η's (JADE) and more Λ's (TASSO) than quark jets, but they are at present at the statistical level of 2 - 3 standard deviations.

ii) Comparison of string (Lund) model and independent parton (Feynman-Field) model of fragmentation: The JADE Collaboration[49] has updated earlier work in which they have looked at the energy flow of three-jet events in the event plane. Figure 18 shows, that the pattern better fits the string model than the independent parton model. Figure 19 shows that the low energy particles in a jet define a different jet axis from the one of the high energy particles. Assuming one has assigned the low energy particles correctly to the jets, this observation would again favor the string model.

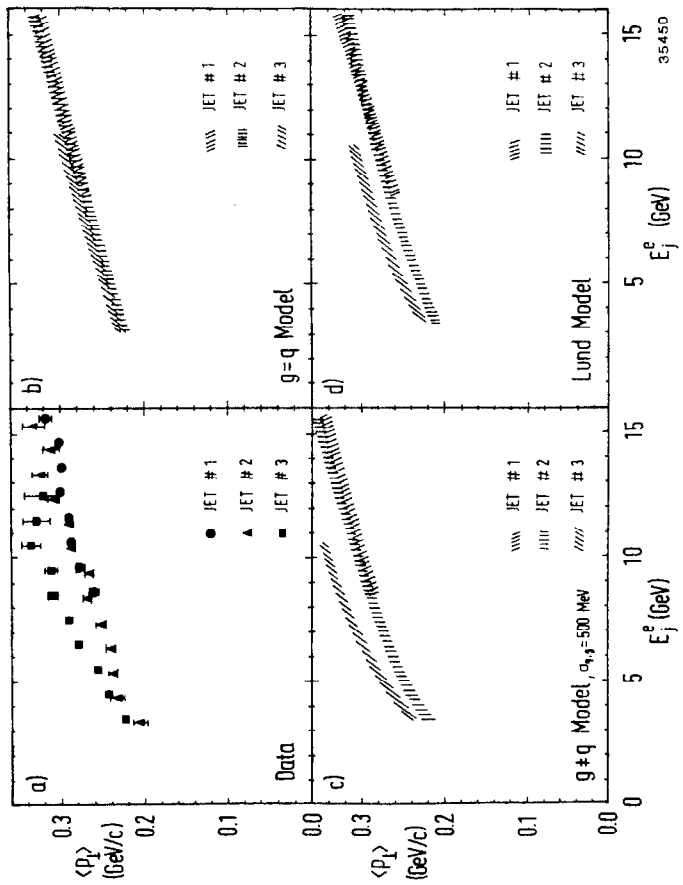


Fig. 17 - Average transverse momentum of charged and neutral particles within a jet relative to the jet axis as a function of jet energy E_j for a) experimental data b,c,d) different models (Ref.49).

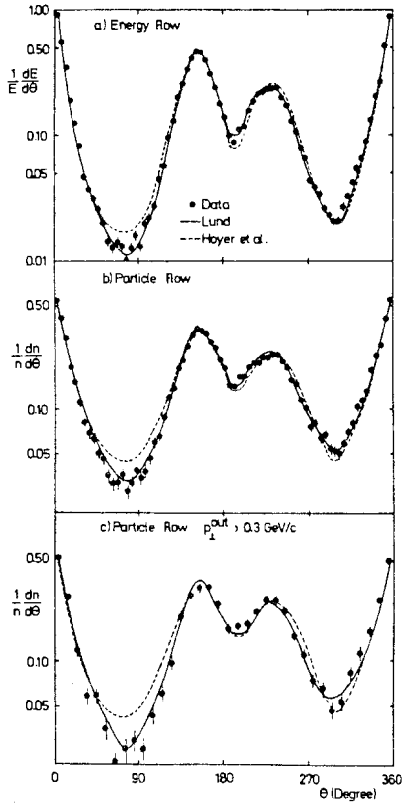


Fig. 18 - a) Normalized energy flow in the event plane of three-jet events together with predictions of the independent parton model (Hoyer et al.) and the string model (Lund); b) Normalized charged and neutral particle flow; c) normalized charged and neutral particle flow for particles with $p_{\perp o}$(out) > 0.3 GeV (Ref.49).

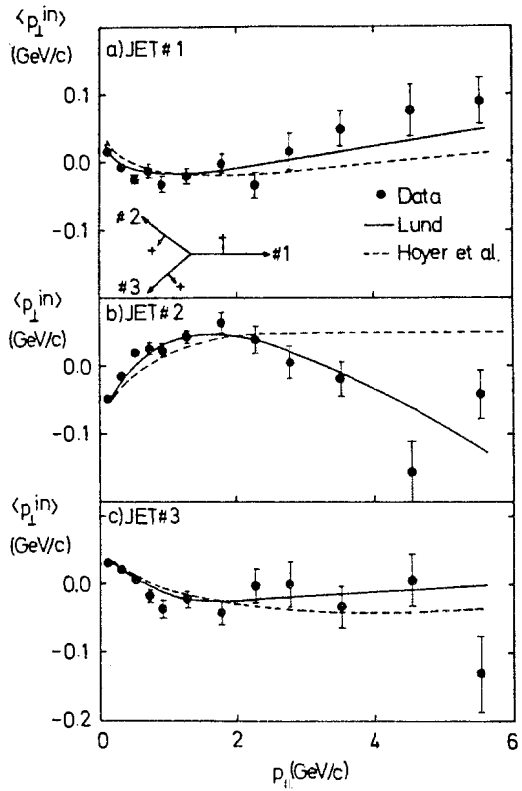


Fig. 19 - Average transverse momentum in the event plane of three-jet events with respect to their jet axis $\langle p_\perp^{in} \rangle$ as a function of the momentum component parallel to the jet axis for charged and neutral particles of jets 1, 2, and 3. The sign convention is sketched as well (Ref.49).

3.5 Baryon Number Compensation

The TASSO Collaboration has investigated events with two identified protons and/or antiprotons.[50] The protons (antiprotons) were required to have relatively large momenta ($p > 1$ GeV/c), and they were identified by time-of-flight and by Čerenkov counters. Table 3.2 shows the resulting number of events after a background subtraction of misidentified protons (antiprotons). The two particles in the combinations pp or $p\bar{p}$ or $\bar{p}\bar{p}$ may originate in the same jet or in opposite jets. Events of the type pp or $\bar{p}\bar{p}$ must have two or more baryon-antibaryon pairs produced, whereas events of the type $p\bar{p}$ have predominantly a single baryon-antibaryon pair. It is evident from the table, that for the $p\bar{p}$ combination the two particles have a strong tendency to originate from the same jet, pointing towards a local compensation of baryon number in the hadronization process.

Table 3.2 - Proton- (Anti-) Proton Correlations

Pairing	Number of events with the two particles in the	
	same jet	opposite jet
pp or $\bar{p}\bar{p}$	-0.2 ± 2.1	2.7 ± 3.1
$p\bar{p}$	15.0 ± 4.6	3.0 ± 3.0

3.6 Fragmentation Function of Heavy Quarks

There are two methods to obtain information on the momentum distribution of the c- and b-quarks.

i) The first method identifies these heavy quarks by the semi-leptonic decays of the respective hadrons (assumed to be mostly D- or B-mesons). The inclusive momentum spectra of electrons and/or muons are fitted to the theoretical decay spectrum of D- or B-mesons, folded with different assumed distributions for the D- or B-momenta, see Section 2.2 for experimental details.

This method is somewhat indirect and requires delicate background subtractions. Moreover, it measures by definition the momentum distribution of the lightest meson species of a given flavor, which may be the decay product of heavier resonant states. As an example look at Table 3.1, which indicates, that a large fraction of c-quark production may be in the form of the D*-resonance.

ii) The second method identifies the D- or B-mesons directly. This is good in principle, but severely limited by statistics and/or failure to resolve the D- or B-mass peaks. So far it has worked only for the case of the D* .

The results are given in Table 3.3 in terms of the average value of z, where

$$z = p / E_b$$

and p = momentum of the D- or B-meson, and E_b = beam energy.

Table 3.3 - Average Values of z for Mesons Containing a c- or b-quark

Experiment	$\langle z_c \rangle$	$\langle z_b \rangle$	$\langle z_{D^*} \rangle$	Method
MARK-J[23),51)]	$.46 \pm .02 \pm .05$	$.75 \pm .03 \pm .06$		(i)
TASSO[50)]			$.57 \pm .04$	(ii)

4. TWO PHOTON PHYSICS

4.1 Two Photon Decay Widths of Mesons

The Feynman diagram Fig. 20 shows the principle of the method.

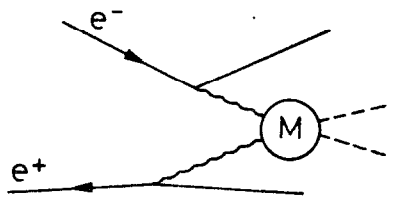


Fig. 20

One observes the cross section for the reaction

$$e^+e^- \to e^+e^- \; \gamma\gamma, \quad \gamma\gamma \to M$$

where γ is an almost real photon, and M is a meson which is identified by its decay. This cross section can be connected to the width $\Gamma_{\gamma\gamma}$ of the decay of the meson M into two photons. The approximate relation for the total production cross section of the meson M is[52)]:

$$\sigma(e^+e^- \to e^+e^-M) \cong 2\left(\frac{\alpha}{\pi} \ln \frac{E}{m_e}\right)^2 \int_0^{4E^2} \frac{ds}{s} f\left(\frac{\sqrt{s}}{2E}\right) \sigma(\gamma\gamma \to M(s)) .$$

With $\sigma(\gamma\gamma \to M) = 8\pi^2 (2J+1) \cdot \frac{\Gamma(M \to \gamma\gamma)}{M_r} \delta(s - M_r^2)$ we have

$$\sigma(e^+e^- \to e^+e^-M) \cong 2\left(\frac{\alpha}{\pi} \ln \frac{E}{m_e}\right)^2 \cdot 8\pi^2 (2J+1) \cdot \frac{\Gamma_{\gamma\gamma}}{M_r^3} \cdot f\left(\frac{M_r}{2E}\right), \quad (7)$$

where E = beam energy, M_r and J are the mass and the spin of the meson, and $f(x) = (2+x^2)^2 \ln\left(\frac{1}{x}\right) - (1-x^2)(3+x^2)$. Results are shown in Table 4.1.

Table 4.1 - Two-Photon Decay Widths[53]

Experiment	$\Gamma(f \to \gamma\gamma)$ keV	Remarks
MARK II	$3.6 \pm 0.3 \pm 0.5$	$f \to \pi^+\pi^-$
CELLO	$2.5 \pm 0.1 \pm 0.5$	$f \to \pi^+\pi^-$
XALL BALL	$2.9 \pm {}^{0.6}_{0.4} \pm 0.6$	$f \to \pi^0\pi^0$
JADE	$2.3 \pm 0.2 \pm 0.5$ (preliminary)	$f \to \pi^0\pi^0$
TASSO	$3.2 \pm 0.2 \pm 0.6$	$f \to \pi^+\pi^-$
PLUTO	$2.3 \pm 0.5 \pm 0.35$	$f \to \pi^+\pi^-$
	$\Gamma(A_2 \to \gamma\gamma)$ keV	
CELLO	$0.81 \pm 0.19 \pm {}^{0.42}_{0.11}$	
JADE	$0.84 \pm .07 \pm .15$ (preliminary)	
XALL BALL	$0.77 \pm 0.18 \pm 0.27$	
	$\Gamma(f' \to \gamma\gamma)$ keV	
TASSO	$0.11 \pm 0.02 \pm 0.04$	
	$\Gamma(\eta' \to \gamma\gamma)$ keV	
PLUTO	$3.7 \pm 0.2 \pm 0.6$	preliminary
JADE	$5.0 \pm 0.5 \pm 0.9$	
CELLO	$6.2 \pm 1.1 \pm 0.8$	
TASSO	$4.1 \pm 0.4 \pm 1.5$	preliminary
MARK II	$5.8 \pm 1.1 \pm 1.2$	

Remarks:

(i) There has been a difficulty on the fits of the f-mass distribution, with the fitted mass value coming out too low. From recent CELLO work this now seems better understood.

(ii) Flavor SU_3 gives a relation between the widths of the 2^{++} mesons f, A_2 and f'. The data are in agreement with a mixing angle of about 30°, close to ideal mixing.

(iii) The η' width $\Gamma(\eta' \to \gamma\gamma)$ agrees with the value ~ 5 keV expected from the standard quark model.

4.2 Production of Hadron Pairs

The reaction of interest is

$$\gamma + \gamma \to h\,\bar{h}$$

where the two photons are almost real and $h\,\bar{h}$ is a hadron-anti-hadron pair. For large values of the $h\,\bar{h}$ invariant mass, this process can in principle be calculated with perturbative QCD (see Fig. 21). There are now first experimental and theoretical results, and they are interesting but not too much should be expected in the way of accuracy at the present time.

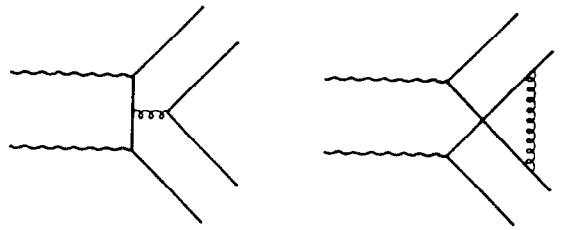


Fig. 21 - Some Feynman Diagrams for computing the process $\gamma\gamma \to h\,\bar{h}$, h being a meson.

The TASSO and CELLO Collaborations[54] have measured the reaction $\gamma\gamma \to \rho^0\rho^0$. The results are shown in Fig. 22. Considering the difficulty of the measurement, there is reasonable agreement. The JADE Collaboration[54] has tried to measure $\gamma\gamma \to \rho^+\rho^-$. This cross section is small, and they have only obtained upper limits which are also shown in Fig. 22. The JADE measurement puts severe constraints on models which have tried to explain the relatively large cross section for $\gamma\gamma \to \rho^0\rho^0$ at low energies by resonance formation.

The TASSO Collaboration[55] has measured the reaction $\gamma\gamma \to p\,\bar{p}$. Figure 23 shows their result. The cross section is smaller, by an order of magnitude, than the value obtained from a naive calculation using a pointlike proton, and it seems to agree within a factor of 2 - 3 with a QCD calculation by Damgaard.[56]

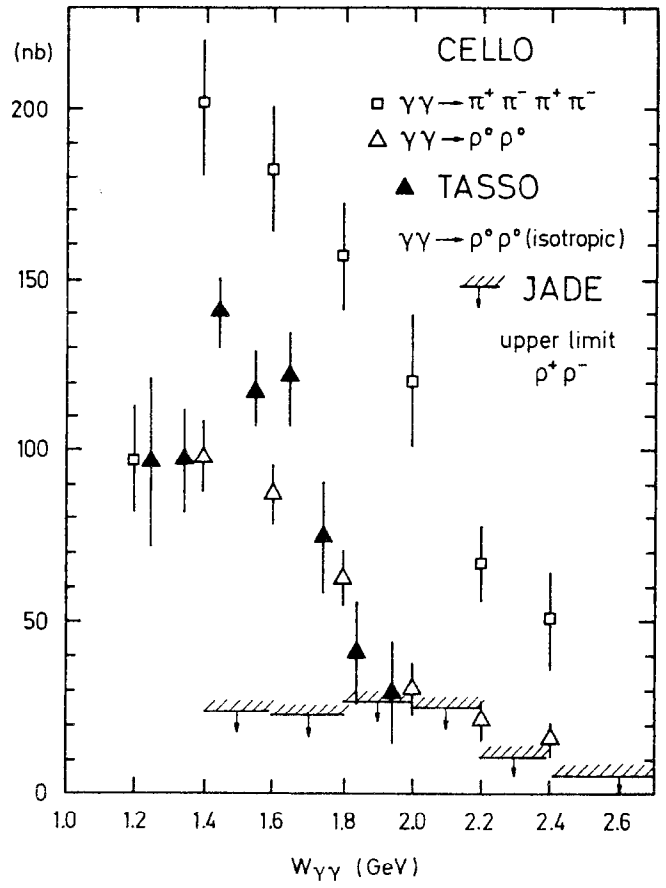


Fig. 22 - Cross section for the reaction $\gamma\gamma \to \rho^0\rho^0$ and $\gamma\gamma \to \rho^+\rho^-$ as function of the $\gamma\gamma$ CM energy $W_{\gamma\gamma}$.

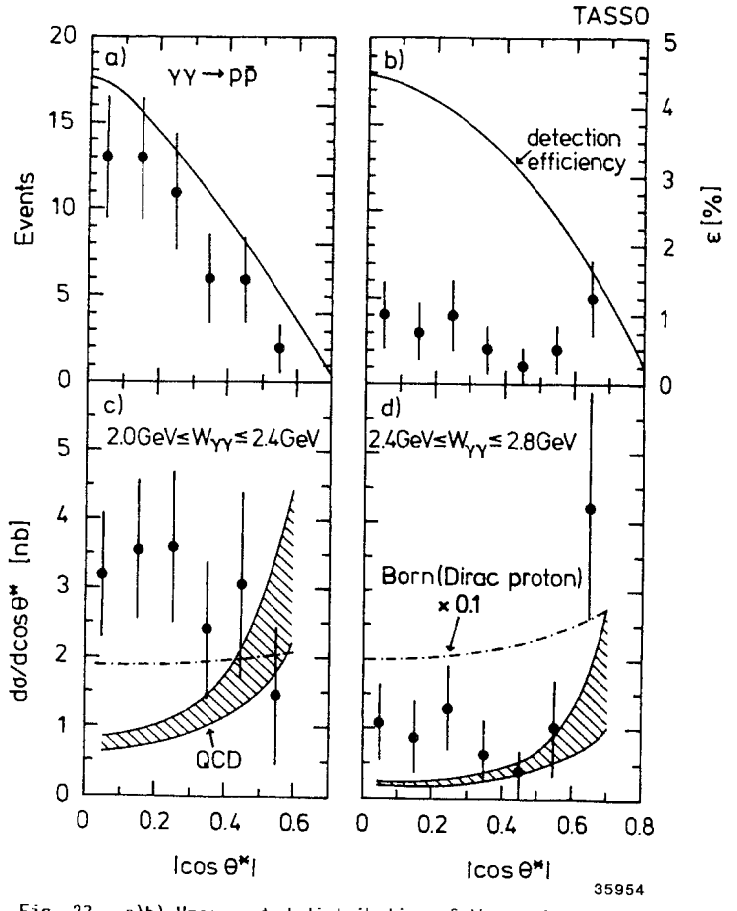


Fig. 23 - a)b) Uncorrected distribution of the proton scattering angle in the $\gamma\gamma$ CM system, and detection efficiency; c)d) differential cross section of $\gamma\gamma \to p\bar{p}$. The data are compared with the Born approximation for Dirac protons and with Ref. 56.

The PLUTO Collaboration has measured the reaction

$$\gamma\gamma \to h^+h^-$$

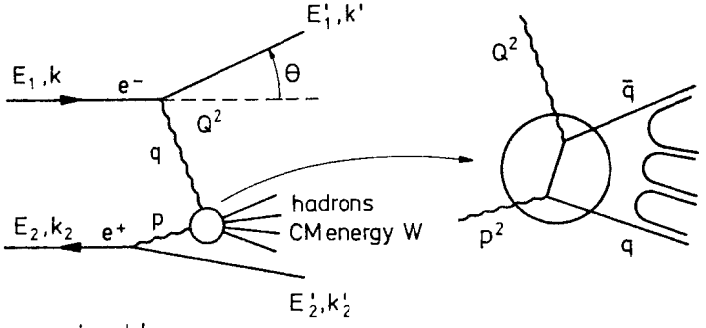
with $h^{\pm}$ being mostly $\pi^{\pm}$. Their result for a h^+h^- invariant mass $W > 2$ GeV/c^2 is[57]:

$$\frac{(e^+e^- \to e^+e^- h^+h^-)}{(e^+e^- \to e^+e^- \mu^+\mu^-)} = 0.061 \pm 0.019 \pm 0.015$$

to be compared with the value 0.020 ± 0.01 expected from a QCD calculation.[58]

4.3 Photon Structure Function

Consider the process $e^+e^- \to e^+e^-\ \gamma\gamma \to e^+e^-$ + hadrons described in its simplest version by the Feynman diagram Fig. 24a.



$\underline{p} = \underline{k}_2 - \underline{k}'_2$

$\underline{q} = \underline{k} - \underline{k}'$

$E_\gamma = E_2 - E'_2$

a) b)

Fig. 24

If one of the photons has a large absolute value Q^2 of the four momentum transfer squared, and if the cm energy W of the hadrons is large, then one expects that the quark parton model as shown in the diagram in Fig. 24b will give the main contribution to the cross section. The cross section then becomes calculable by the quark parton model or by QCD if gluon effects are included.

If one of the two photons has a small value q^2 of the four momentum transfer squared ($|q^2| < M^2$), and the other one has a large value Q^2, the process can - if one likes - be viewed as the deep inelastic scattering of an electron with momentum transfer Q^2 off an almost real "target" photon, and the cross section formulae can be cast into a form similar to those for deep inelastic scattering. With the symbols as explained in Fig. 24a, one has for the inelastic scattering of an electron off an (almost) real photon of energy E_γ [59]:

$$\frac{d^2\sigma(e\gamma \to e\ \text{hadrons})}{dxdy} = \frac{16\pi\cdot\alpha^2}{Q^4}\cdot E_1\cdot E_\gamma \cdot [(1-y)F_2(x,Q^2)+xy^2F_1(x,Q^2)]; \quad (8)$$

with

$$Q^2 = -(\underline{k} - \underline{k}')^2 \simeq E_1E_1' \sin^2\theta/2$$

$$x = Q^2/(2\underline{p}\cdot \underline{q}) \approx Q^2/(Q^2 + W^2)$$

$$W^2 = (\underline{p} + \underline{q})^2$$

$$y = (\underline{p}\cdot\underline{q}) / (\underline{k}\cdot\underline{p}) = 1-(E_1' / E_1)\cdot\cos^2\theta/2$$

E_1, E_1', E_2, E_2' are electron and positron energies before and after the collision, and $\underline{k}$, $\underline{k}'$, $\underline{k}_2$, $\underline{k}_2'$ are the corresponding four vectors.

Under most experimental conditions, xy^2 is small, so that one can neglect the term with $F_1(x,Q^2)$. The structure function $F_2(x,Q^2)$ can be computed in the quark parton model according to Fig. 24b and one gets [58]

$$F_2^{QPM}(x,Q^2) \simeq \frac{3\alpha}{\pi}\cdot\Sigma Q_q^4\cdot x\cdot[(x^2+(1-x)^2)\cdot\ln\frac{W^2}{m_q^2} + 8x(1-x)-1] \quad (9)$$

a factor 3 for color is included.

Equation (9) contains the (unkown) masses of the quarks. As one includes the effect of gluons, one gets the following expression for the photon structure function in QCD:

$$F_2^{QCD}(x, Q^2) \simeq \frac{3\alpha}{\pi}\Sigma Q_f^4 \ln\frac{Q^2}{\Lambda^2}\cdot h(x) \quad (10)$$

where the sum is over the charges Q_f of the quarks considered, there is a factor 3 in the formula for color, $h(x)$ is a calculable function [60] and Λ is the QCD constant. One has therefore - in principle - a process which allows a check of QCD and a determination of Λ.

In practice, there are the following difficulties:

i) It is experimentally difficult to measure W, the total hadronic energy, because this requires very good solid angle coverage and calorimetry. The deficiencies of the detector have to be corrected by more or less critical Monte Carlo calculations. Since W enters into the expression for x, there is a difficulty in knowing x.

ii) There are still difficulties in computing the QCD part, especially at finite values of Q^2.

iii) There is an ambiguity in how to include the heavy quarks. It has been customary to describe the u, d, s - quarks by QCD (Eq. 10), and the c, b - quarks by Eq.9.

There is a hadronic-vector-meson-dominance-like part of the photon, which is not described by the QCD mechanism, and which can be approximated by an addition to the QCD structure function, namely[61]:

$$F_2^{VDM}(x,Q^2) \cong \alpha \cdot 0.2 \cdot (1-x) . \qquad (11)$$

The data have to be fit to a sum of Eq.11 and Eq.9 and/or Eq.10.

In spite of these difficulties measurements of deep inelastic electron-photon scattering may finally offer a very good check of QCD. First encouraging measurements have been made by the CELLO, JADE and PLUTO Collaborations. As a first check on the experimental procedure one measures[62] the cross section for $e^+e^- \to e^+e^-\mu^+\mu^-$, $e^+e^-e^+e^-$ which is very similar on the parton level and which can be calculated in QED (see Fig. 25). Measurements of the photon structure function are shown in Fig. 26 and Fig. 27. They are in agreement with a value of Λ between 100 MeV and 300 MeV, as are measurements by CELLO.[66]

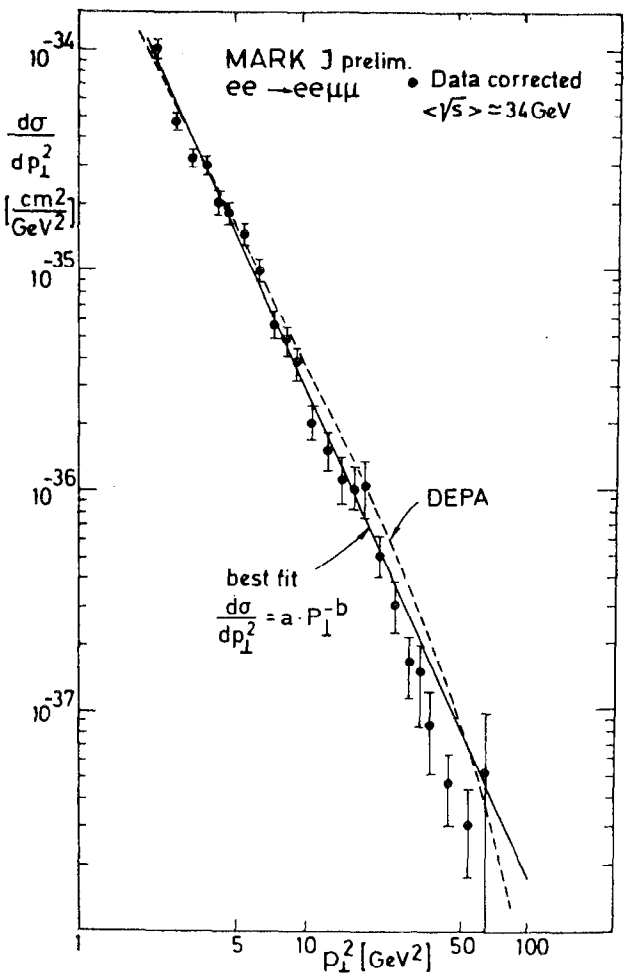


Fig. 25 - Cross section $d\sigma/dp_\perp^2$ for two photon muon pairs from MARK-J. The data are compared to a DEPA[63] calculation and fitted to a power law (from Ref. 62).

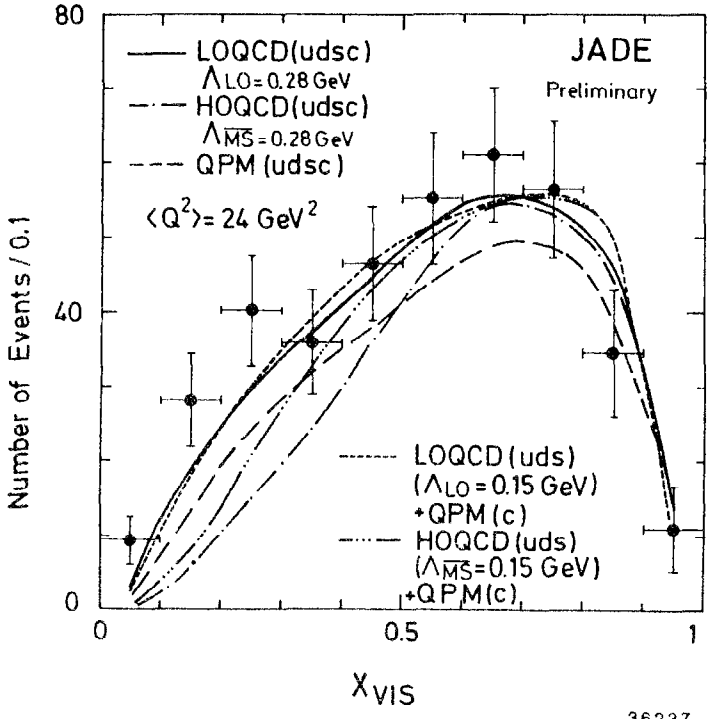


Fig. 26 a)b)

Photon structure function as a function of X_{VIS}, the value of x computed from the visible hadron energy W_{VIS}, at two different values of average Q^2 from JADE.[64] Comparison with various theoretical models LOQCD (leading order QCD Ref. 60), HOQCD (higher order QCD Ref.65), and QPM = Quark parton model Eq.9.

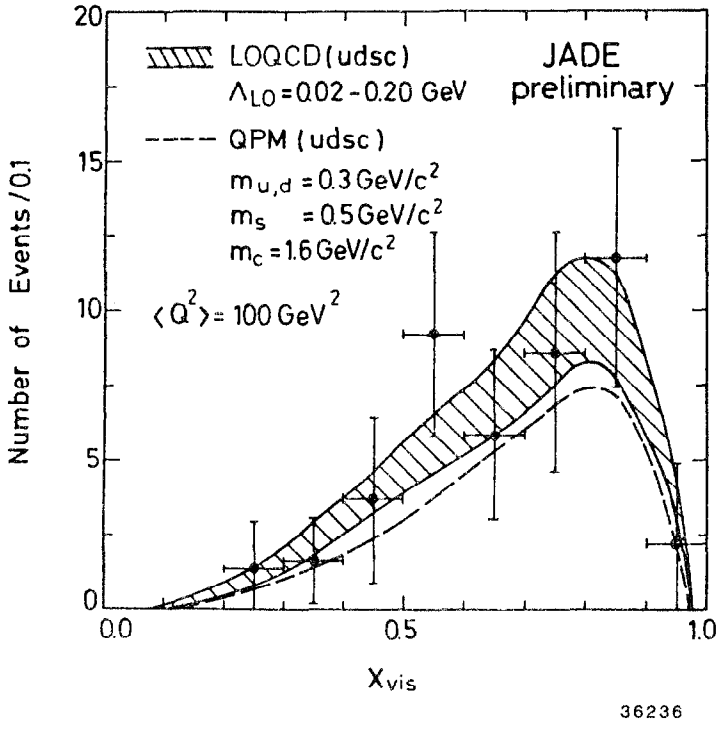


Fig. 26 b -

Photon structure function as a function of X_{VIS}, the value of x computed from the visible hadron energy W_{VIS}, at two different values of average Q^2 from JADE.[64] Comparison with various theoretical models LOQCD (leading order QCD Ref. 60), HOQCD (higher order QCD Ref.65), and QPM = Quark parton model Eq.9.

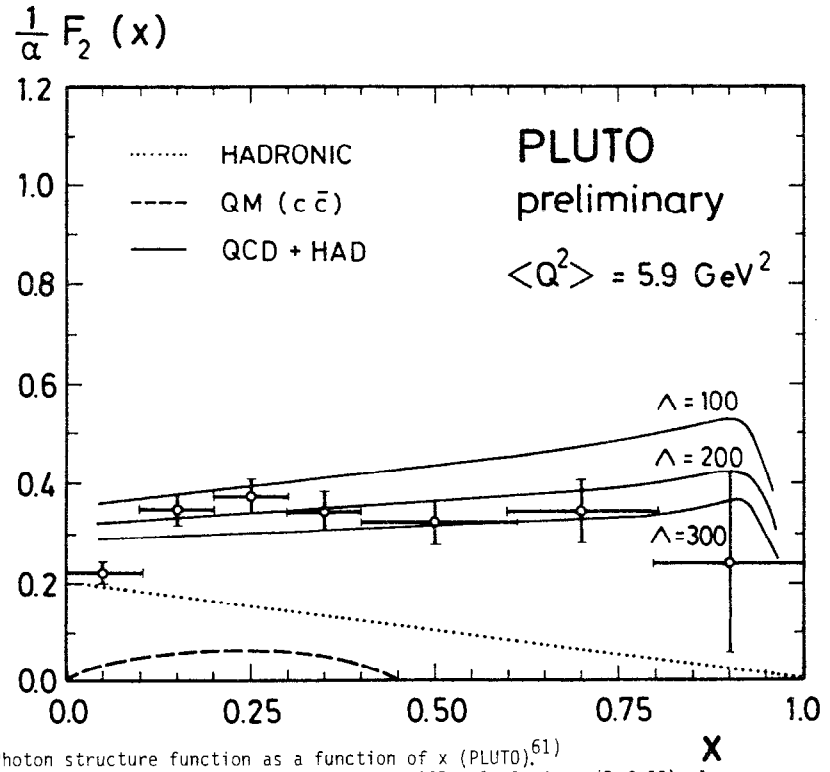


Fig. 27 - Photon structure function as a function of x (PLUTO).[61]
The data are compared with leading order QCD calculations (Ref.60) plus hadronic part (Eq.11).

Acknowledgements

I like to thank Dr. R.Felst, Dr. G.Wolf, Dr. U.Timm, Prof. G.Flügge, Prof. A.Böhm and Dr. W.Wagner for their help in preparing this talk and for discussions and criticism. I also thank Dr. B.Naroska for useful comments. Finally I thank the organizers of the SLAC Summer Study for a most stimulating and inspiring meeting.

REFERENCES

1) A.Böhm, DESY Report 82-027 .

2) J.Bürger, 1981 Int.Symp. on Lepton and Photon Int. at High Energies, Bonn, Germany.

3) S.Yamada, DESY report 83-056 and Review talk at the 1983 Cornell Conference on Lepton and Photon Int. at High Energies.

4) MARK-J, B.Adeva et al., Contribution to the 1983 Cornell Conference.

5) TASSO Collaboration, Contribution to the 1983 Cornell Conference.

6) K.Kinoshita, P.B.Price and D.Fryberger, Phys.Rev.Lett. 48 (1982) 77.

7) P.Musset, M.Price and E.Lohrmann, Phys.Lett. 128B (1983) 333.

8) JADE Collaboration, contribution to the 1983 Cornell Conference, (see also Ref. 3).

9) Yu.A.Gel'fand and E.P.Likhtman, JETP Letters 13 (1971) 323; J.Wess and B.Zumino, Nucl.Phys. B70 (1974) 39; and P.Fayet and S.Ferrara, Phys.Rep. 3C (1977) 249.

10) CELLO Collaboration, H.-J.Behrend et al., Phys.Lett. 123B (1983) 127.

11) JADE Collaboration, W.Bartel et al., Phys.Lett. 114B (1982) 211; CELLO Collaboration, H.-J.Behrend et al., DESY 82-021; MARK-J Collaboration, A.Adeva et al., LNS Tech.Rep. 125 (1982); MARK-II Collaboration, C.A.Blocker et al., SLAC-PUB-2923 (1982); and MAC Collaboration, Proc. Int. Conference on High Energy Physics, Paris 1982.

12) TASSO Collaboration, M.Althoff et al., Phys.Lett. 122B (1983) 95.

13) J.Ellis and M.K.Gaillard, CERN Rep. 76-18 (1976); J.Jersak, E.Laermann and P.M.Zerwas, Phys.Lett. 98B (1981) 363; and Th.Appelquist and H.P.Politzer, Phys.Rev. D12 (1975) 1404.

14) JADE Collaboration, Contribution to 1983 Cornell Conference; MARK-J. Collaboration, Contribution to 1983 Cornell Conference; PLUTO-Collaboration, Ch.Berger et al., DESY 83-084; and TASSO Collaboration, M.Althoff et al., DESY 83-089.

15) F.A.Berends, R.Kleiss and S.Jadach, Nucl.Phys. B 202 (1982) 63.

16) M.Böhm and W.Hollik, DESY 83-060.

17) Review by A.Böhm, DESY 82-084.

18) W.Krenz, Aachen Preprint PITHA 82-26.

19) MARK-J. Collaboration, D.P.Barber et al., Aachen preprint PITHA 80-8, J.J.Sakurai, Proc. 17 Recontre de Moriond 1982.

20) J.M.Yelton et al., Phys.Rev.Lett. 49 (1982) 430; CLEO Collaboration, C.Bebek et al., Phys.Rev.Lett. 49 (1982) 610 ; and TASSO Collaboration, M.Althoff et al., Phys.Lett. 126B (1983) 493.

21) Contributuions to the 1983 Cornell Conference, see Review talk by B.Naroska.

22) CELLO Collaboration, H.-J.Behrend et al., Contribution to the 1983 Cornell Conference.

23) MARK-J. Collaboration, B.Adeva et al., Phys.Rev.Lett. 51 (1983) 443; CELLO Collaboration, H.-J.Behrend et al., Z.Phys. C 19 (1983) 291; TASSO Collaboration, contribution to the 1983 Cornell Conference.

24) JADE Collaboration, W.Bartel et al., DESY 83-049; and
MARK-J Collaboration, B.Adeva et al., Phys.Rev.Lett.50
(1983) 799.

25) H.Georgi and S.Glashow, Nucl.Phys. B 167 (1980) 173;
V.Barger, W.Y.Keung and R.J.N.Phillips, Phys.Rev. D 24
(1981) 1328; and
G.L.Kane and M.E.Peskin, Nucl.Phys. B 195 (1982) 29.

26) JADE Collaboration, W.Bartel et al., Phys.Lett. 129B (1983) 145;
TASSO Collaboration, R.Brandelik et al., Phys.Lett. 113B
(1982) 499;
MARK-J. Collaboration, Review talk by A.Böhm, DESY 82-084; and
MAC Collaboration, Contribution to the 1983 Cornell Conf.

27) G.Kramer, DESY 83-068 and DESY 82-029;
T.Gottschalk, Phys.Lett. 109B (1982) 331.

28) G.Wolf, Talk at the Theory Workshop "Hadron and Jet Structure"
DESY, 27th September 1983.

29) CELLO Collaboration, H.-J.Behrend et al., Contribution to
the 1983 EPS Conference in Brighton.

30) CELLO Collaboration, H.-J.Behrend et al., Nucl.Phys. B218
(1983) 269.

31) JADE Collaboration, W.BArtel et al., Phys.Lett. 119B (1982) 239.

32) MARK-J Collaboration, B.Adeva et al., Phys.Rev.Lett. 50
(1983) 2051.

33) TASSO Collaboration, Contribution to the 1983 Cornell Conference.

34) R.K.Ellis, D.A.Ross and A.E.Terrano, Phys.Rev.Lett.45
(1980) 1226;and Nucl.Phys. B 178 (1981) 421; and

34) continued - J.Vermaseren et al., Nucl.Phys. B 187 (1981) 301.

35) K.Fabricius, G.Kramer, G.Schierholz and I.Schmitt,
Z.Phys. C11 (1982) 315 -(see also Ref. 27).

36) PLUTO Collaboration, Ch.Berger et al., Z.Phys. C12 (1982) 1297.

37) PLUTO Collaboration, Ch.Berger et al., DESY 83-040 ; and
K.Konishi, A.Ukawa and G.Veneziano, Nucl.Phys. B157 (1979) 45.

38) JADE Collaboration, W.Bartel et al., DESY 83-042.

39) CELLO Collaboration, H.-J.Behrend et al., Contribution to
the 1983 Cornell Conference;
TASSO Collaboration, R.Brandelik et al., Phys.Lett. 114B
(1982) 65;
MARK-II Collaboration, J.F.Patrick et al., Phys.Rev.Lett. 49
(1982) 1232.

40) TASSO Collaboration, M.Althoff et al., Z.Phys. C 17 (1983) 5.

41) TASSO Collaboration, R.Brandelik et al., Phys.Lett. 108B
(1982) 71.

42) CELLO Collaboration, H.-J.Behrend et al., DESY 83-066.

43) JADE Collaboration, W.BArtel et al., DESY 83-063.

44) TASSO Collaboration, R.Brandelik et al., Phys.Lett. 117 B
(1982) 135.

45) JADE Collaboration, W.Bartel et al., Contribution to the
1983 EPS Conference in Brighton.

46) TASSO Collaboration, R.Brandelik et al., Phys.Lett. 94B
(1980) 91.

47) TASSO Collaboration, R.Brandelik et al., Phys.Lett. 105B
(1981) 75.

48) TASSO Collaboration, M.Althoff et al., DESY 83-071.

49) JADE Collaboration, W.Bartel et al., Phys.Lett. 123B (1983) 460; and DESY 83-080.

50) TASSO Collaboration, M.Althoff et al., Contribution to the 1983 EPS Conference in Brighton.

51) MARK-J Collaboration, B.Adeva et al., DESY 83-029 (see Ref.23).

52) H.Terazawa, Rev.Mod.Phys. 45 (1973) 615.

53) f: MARK-II Collaboration, A.Roussarie et al., Phys.Lett. 105 B (1981) 304,
CELLO Collaboration, H.-J.Behrend et al., Contribution to the 1983 EPS Conference in Brighton;
XALL BALL Collaboration, C.Edwards et al., Phys.Lett. 110B (1982) 82;
JADE Collaboration, W.Bartel et al., Contribution to the 1983 EPS Conference in Brighton;
TASSO Collaboration, R.Brandelik et al., Z.Phys. C 10 (1981) 117;
PLUTO Collaboration, Ch.Berger et al., Phys.Lett. 94B (1980) 254.
A_2: CELLO Collaboration. H.-J.Behrend et al., Phys.Lett. 114B (1982) 378, and Erratum Phys.Lett. 125B (1983) 518;
JADE: see f;
XALL BALL: see f.
f': TASSO Collaboration, M.Althoff et al., Phys.Lett. 121B (1983) 216.
η': PLUTO Collaboration, Contribution to the 1983 EPS Conference in Brighton;
JADE Collaboration, W.Bartel et al., Phys.Lett. 113B(1982)190;

53) η' continued:
CELLO: see A_2;
TASSO: Contribution to the 1983 EPS Conference in Brighton;
MARK-II Collaboration, G.Abrams et al., Phys.Rev.Lett. 43 (1979) 477; and
P.Jenni et al., Phys.Rev. D 27 (1983) 1031.

54) TASSO Collaboration, M.Althoff et al., Z.Phys. C16 (1982) 13;
CELLO Collaboration, H.-J.Behrend et al., DESY 83-081; and
JADE Collaboration, W.Bartel et al., Contribution to the 1983 EPS Brighton Conference.

55) TASSO Collaboration, M.Althoff et al., DESY 83-064.

56) P.H.Damgaard, Nucl.Phys. B211 (1983) 435.

57) PLUTO Collaboration, Contribution to the 1983 EPS Conference in Brighton.

58) S.J.Brodsky and G.P.Lepage, Phys.Rev. D 24 (1981) 1808.

59) C.Peterson, T.F.Walsh and P.M.Zerwas, Nucl.Phys. B 174 (1980) 424.

60) E.Witten, Nucl.Phys. B 120 (1977) 189;
W.R.Frazer and J.F.Gunion, Phys.REv. D 20 (1979) 147;
C.H.Llewellyn Smith, Phys.Lett. 79B (1978) 83; and
R.Dewitt et al., Phys.Rev. D 19 (1979) 166.

61) PLUTO Collaboration, Review talk by W.Wagner at the Int. Workshop on Photon-Photon Collisions Aachen, April 1983 (PITHA 83/17).

62) Review by M.Pohl, DESY 83-047.

63) Double equivalent photon approximation A. Coureau CAL 82/19 (1982).

64) JADE Collaboration, W. Bartel et al., Contribution to the
1983 EPS Conference in Brighton; see also DESY 82-064.

65) W.A. Bardeen and A. J. Buras, Phys. Rev. D 20 (1979) 166;
D. W. Duke and J. F. Owens, Phys. Rev. D 22 (1980) 2280; and
T. Vematsu and T. F. Walsh, Fermilab-PUB-81/55-THY.

66) CELLO Collaboration, H. J. Behrend et al., DESY 83-018; and
Phys. Lett. 126 B (1983) 391.

SLAC-PUB-3260
November 1983
(E)

RECENT RESULTS FROM DELCO*

W. B. Atwood, P. H. Baillon, B. C. Barish, G. R. Bonneaud,
H. DeStaebler, G. J. Donaldson, R. Dubois, M. M. Duro, E. Elsen, S. G. Gao,
Y. Z. Huang, G. M. Irwin, R. P. Johnson, H. Kichimi, J. Kirkby, D. E. Klem,
D. E. Koop, J. Ludwig, G. B. Mills, A. Ogawa, T. Pal, D. Perret-Gallix,
R. Pitthan, D. L. Pollard, C. Y. Prescott, L. Z. Rivkin, L. S. Rochester,
W. Ruckstuhl, M. Sakuda, S. S. Sherman, E. J. Siskind, R. Stroynowski,
S. Q. Wang, S. G. Wojcicki, H. Yamamoto, W. G. Yen and C. C. Young

Presented by Charles C. Young

California Institute of Technology, Pasadena, California 91125
Stanford Linear Accelerator Center and Physics Department
Stanford University, Stanford, California 94305

Presented at the 11th SLAC Summer Institute on Particle Physics
Stanford, California, July 18–29, 1983

* Work supported by the Department of Energy, contract numbers DE-AC03-76SF00515 (SLAC) and DE-AC03-81-ER40050 (CIT), and The National Science Foundation.

© C. Young 1983

1. Introduction

DELCO is a magnetic spectrometer with Čerenkov, Time-of-Flight (TOF) and shower counters for particle identification. It is located in IR8 of the PEP storage ring. Data have been obtained at a center of mass energy, $\sqrt{s}$, of 29 GeV. We report on:

1) the fraction of P, K, π in hadronic events,

2) the observation of direct electron signals, and

3) the measurement of D^* fragmentation function and its total cross-section.

2. Detector

DELCO is a magnetic detector with drift chambers for tracking, and Čerenkov, Time-of-Flight, and shower counters for particle identification. See Figures 1 and 2. The magnetic field is generated by two coils. A total bending strength of .18 T-m imparts 50 MeV/c transverse momentum to charged particles. There are 16 layers in the two drift chambers around the beam pipe, and each layer has a position resolution of 160 μm. There are six more layers of drift chambers at $r \simeq 1.5$ m. This results in a momentum resolution $\sigma_p/p = \sqrt{.06^2 + (.02p)^2}$, where p is the momentum in GeV/c. The inverse momentum distribution of Bhabha tracks is shown in Figure 3.

The 36-cell Čerenkov counter is situated between the two sets of drift chambers. It is operated at atmospheric pressure, and was filled with isobutane (nitrogen) for 80% (20%) of the data. Čerenkov light is focused by ellipsoidal mirrors onto RCA 8854 Quantacon photomultiplier tubes. The use of ellipsoidal mirrors results in isochronous signals for particles coming from the origin. Timing resolution of 300 psec (450 psec) was achieved for isobutane (nitrogen) radiator. Other stray particles can be discriminated against on the basis of timing. The single-photoelectron capability of the photomultiplier and the relatively high light yield of 26(5) photoelectrons made the Čerenkov counter efficient. Figure 4 shows the measured light yield of 10.6 K Bhabha tracks. Two tracks registered no pulse height, corresponding to an inefficiency of .02%. For momentum below 200 MeV/c, there is an inefficiency due to track curvature.

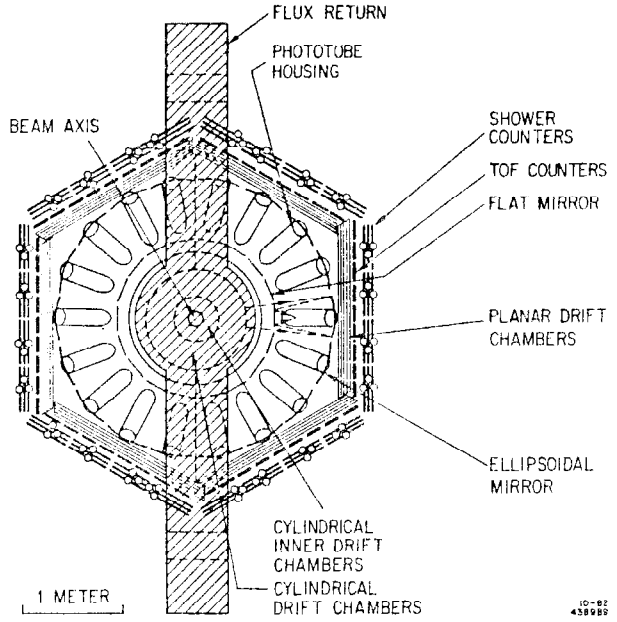


Figure 1 Plan view of DELCO detector.

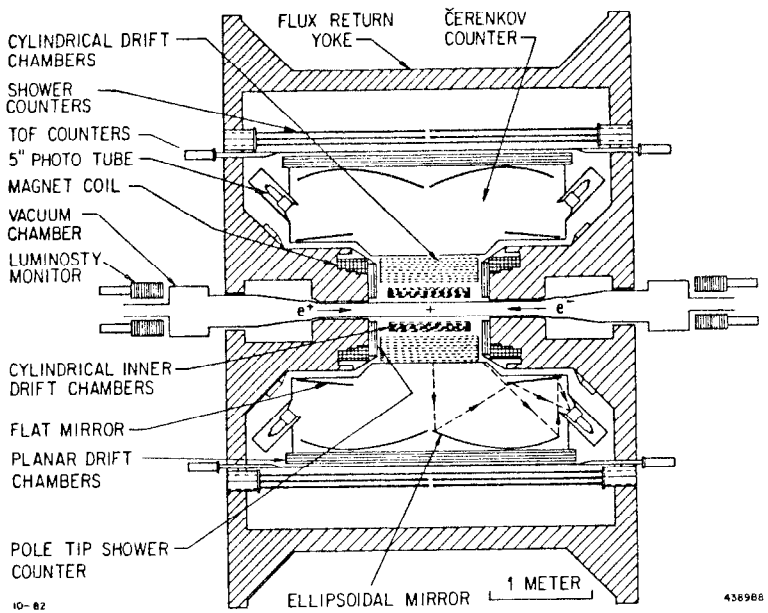


Figure 2 End view of DELCO detector.

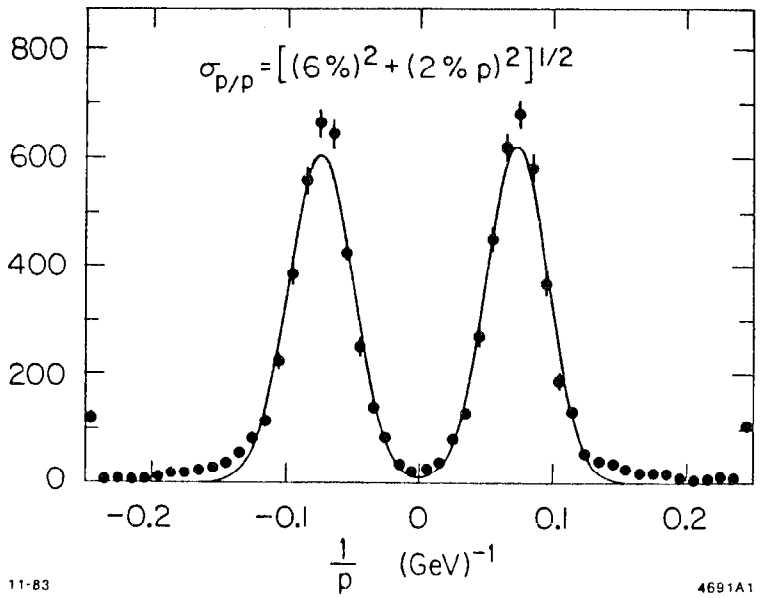


Figure 3 1/p of Bhabha tracks.

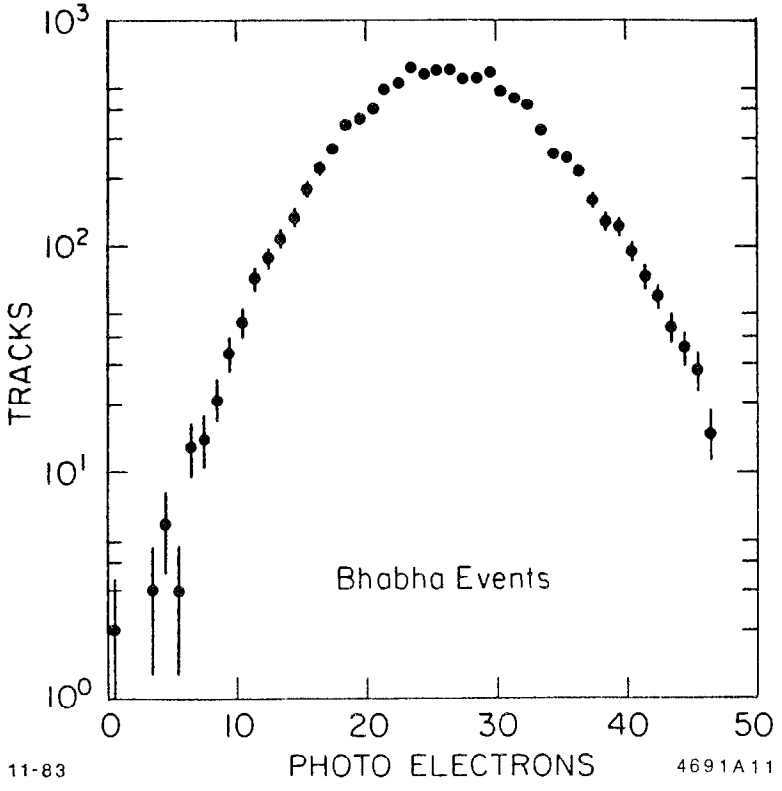


Figure 4 Čerenkov pulse height distribution in Bhabha events. Response has been normalized to 100 cm path length.

There are 52 TOF counters outside the outer drift chambers. Each counter is viewed at both ends, and a timing resolution of 300 psec is achieved in low multiplicity events. The resolution in hadronic events is 350 psec.

There are 48 shower counters outside the TOF counters. They are made of lead-scintillator sandwiches, and are read out at three different depths: two, four and six radiation lengths (X_0).

There are 36 shower counters mounted on the two pole-tips, covering the angular range $.79 < |\cos\vartheta| < .98$. These are 5-$X_0$ lead-scintillator sandwiches, and the light is read out using wave-shifter bars.

The luminosity counters cover the region 25 mrad $< \vartheta <$ 68 mrad. These 16-X_0 counters are divided into six azimuthal pairs. Their construction and read-out are similar to the pole-tip shower counters.

The open geometry of the detector ensures that there is little material (.05 X_0) before the Čerenkov counter. This minimizes photon conversion and therefore the background in the Čerenkov counter. Table 1 summarizes the material before the Čerenkov counter.

Table 1

Summary of Material Before Čerenkov Counter

	Material	Thickness cm	Thickness X_0	Total Thickness X_0
Beam Pipe	Al	0.2	2.2 %	2.2 %
Drift Chamber			1.8 %	4.0 %
Čerenkov Entrance Window	Al	0.07	0.8 %	4.8 %
Čerenkov Gas	Isobutane	85	0.5 %	5.3 %

A summary of the detector's acceptance and performance is given in Table 2.

Table 2

Summary of the Acceptance and Performance of the DELCO Detector	
Magnet	Open-geometry (aperture $\|\cos\vartheta\| < 0.78$) Pole-tip diameter 101 cm, separation 125 cm $B_0 = 3.3$ kG, $\int Bdl = 1.8$ kG m
Tracking	Central (cylindrical) drift chambers: 94 cm maximum wire length, 12–49 cm radius Low mass (2.3 % X_0) Depth (z) measurement by narrow angle stereo 16 points on tracks with $\|\cos\vartheta\| < 0.69$ Outer (planar) drift chambers: 285 cm wire length, 160 cm (radius) Depth measurement by wide angle stereo 6 points on tracks with $\|\cos\vartheta\| < 0.65$ Multiple hit digital electronics (4 nsec bin width) $\sigma_p/p = \sqrt{(2\%\ p)^2 + (6\%)^2}$
Čerenkov Counter	1 atm isobutane threshold counter ($\gamma_t = 10.1$) 36 cells each with (pTP-coated) 5" RCA 8854 Quantacon Radiator length 55–110 cm $\langle pe\rangle = 26, \langle N_0\rangle = 80$ cm^{-1} $\sigma_t = 300$ psec Acceptance $\|\cos\vartheta\| < 0.62$
Shower Counters	Barrel ($\|\cos\vartheta\| < 0.62$): 48 Pb–scintillator counters, 6 X_0 Pole-tip ($0.79 < \|\cos\vartheta\| < 0.98$): 36 Pb–scintillator BBQ counters, 5 X_0
Time-of-Flight	52 counters 324 cm length, 180 cm (radius) $\sigma_t = 350$ psec Acceptance $\|\cos\vartheta\| < 0.67$
Luminosity Monitor	12 Pb–scintillator BBQ counters, 16 X_0 Acceptance 25–68 mrad relative to beam axis

3. Data

Data were collected in 1982 and 1983 at $\sqrt{s} = 29$ GeV. A total luminosity of 116 pb^{-1}, corresponding to $\simeq$ 53K hadrons, was recorded.

Approximately 80 % of the data was taken with isobutane as the Čerenkov radiator; while for the remaining 20 %, the Čerenkov counter was filled with nitrogen. Pion threshold is 2.6 GeV/c (5.6 GeV/c) in isobutane (nitrogen). Thus in the isobutane data, electrons below 2.5 GeV/c can be identified by the presence of a Čerenkov signal and K above 2.5 GeV/c by the absence of a Čerenkov pulse. The nitrogen data extended the electron identification to 5.6 GeV/c. This is summarized in Table 3.

Table 3

Data Summary		
Čerenkov Radiator	Isobutane	Nitrogen
$\int \mathcal{L}dt$ (pb^{-1})	94	22
Hadronic Events Detected	43 K	10 K
π Threshold (GeV/c)	2.6	5.6
K Threshold (GeV/c)	9.2	20
Average Number of Photoelectrons	26	5

4. Particle Fractions

10 K hadronic events ($\int \mathcal{L}\,dt = 22$ pb^{-1}) with isobutane as the Čerenkov radiator have been analyzed to obtain the fraction of π, K and P.

Below 2 GeV/c, particles were identified using the TOF system. Even though the resolution is not sufficient to identify individual tracks, a statistical separation is possible. The measured mass-square (M^2) distribution of each momentum bin is fitted to the sum of three Gaussians to obtain the number of π, K and P. Such a fit is shown in Figure 5. These numbers are then corrected for decay, interaction and range-out, these corrections being done independently for $\pi^{\pm}$, $K^{\pm}$, P and $\bar{P}$. The corrected numbers are then normalized to get the particle fractions.

Above π threshold, the Čerenkov counter separates π from K and P; however, there is no separation between K and P.

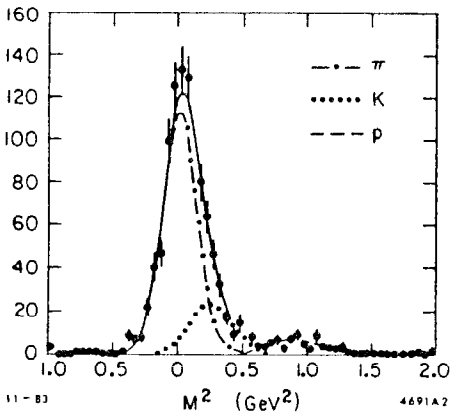


Figure 5 M^2 distribution for $0.3 < p < 0.4$ GeV/c. The solid line is the result of a fit to the sum of three Gaussians. The individual Gaussians are also shown.

The particle fractions in hadronic events are shown in Figure 6 as a function of momentum. Data from TASSO[1] at $\sqrt{s} = 34$ GeV are also shown for comparison.

3. Direct Electron

3.1 Introduction

We will use the term "direct electrons" to refer to those electrons which are the primary decay products of a heavy quark (c or b).

Direct electrons have a distinct signature. Their momentum (p) and transverse momentum (p_t) relative to the jet direction are characterized by the mass of the parent quark, while the electrons from γ-conversion, K-decay, et cetera, are usually much less energetic.

The branching ratio (BR) of a heavy quark to any individual hadronic decay mode is expected to be small because of the large number of available channels. However, the semileptonic BR is expected to be $\simeq$ 10%. Therefore, direct electrons are distinct and efficient tags of heavy quark flavors.

Previous measurements[2,3] of direct lepton production were generally restricted to $p > 1.5$ GeV/c (Figure 7); however, more than 1/2 of the electrons from c-quarks are expected to be below 2 GeV/c. DELCO's low-mass detector and Čerenkov counter extend this measurement to $p = 200$ MeV/c.

3.2 Electron Identification

Electrons are identified using Čerenkov and shower counters. Track curvature at low momenta leads to inefficiencies in the Čerenkov counter, while the upper momentum limit is determined by π threshold. Therefore electrons in the momentum range 200 (500) MeV/c to 2.5 (5.5) GeV/c can be identified when the radiator is isobutane (nitrogen). Electrons are required to have a minimum pulse height of 16 (1.8) photoelectrons. The signal is further required to be in-time within 1 nsec (1.5 nsec).

The shower counter response is required to be within two standard deviations of that expected from an electron. These two requirements were satisfied by 85 % of all electrons. The efficiency was determined using electrons from two-γ events.

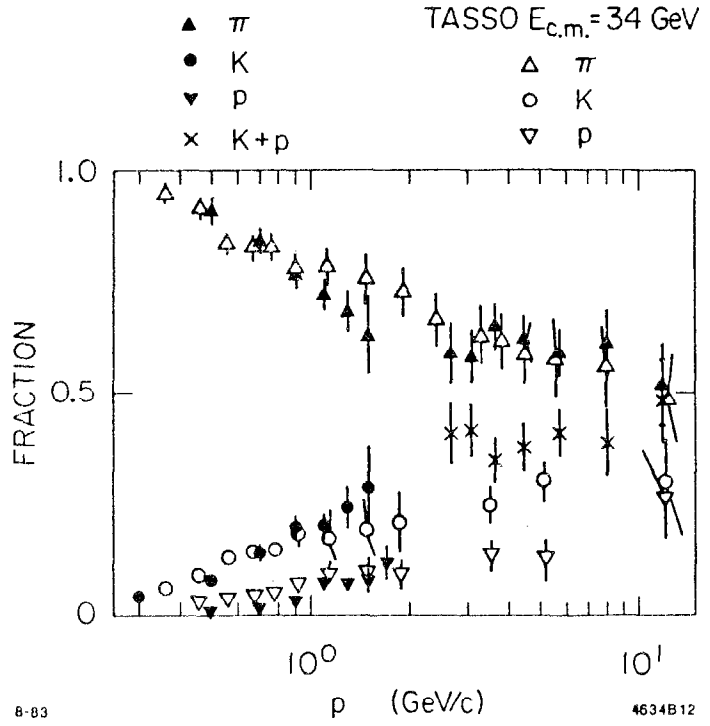


Figure 6 π, K and P fractions in hadronic events versus momentum. Data from TASSO at $\sqrt{s} = 34$ GeV are also shown.

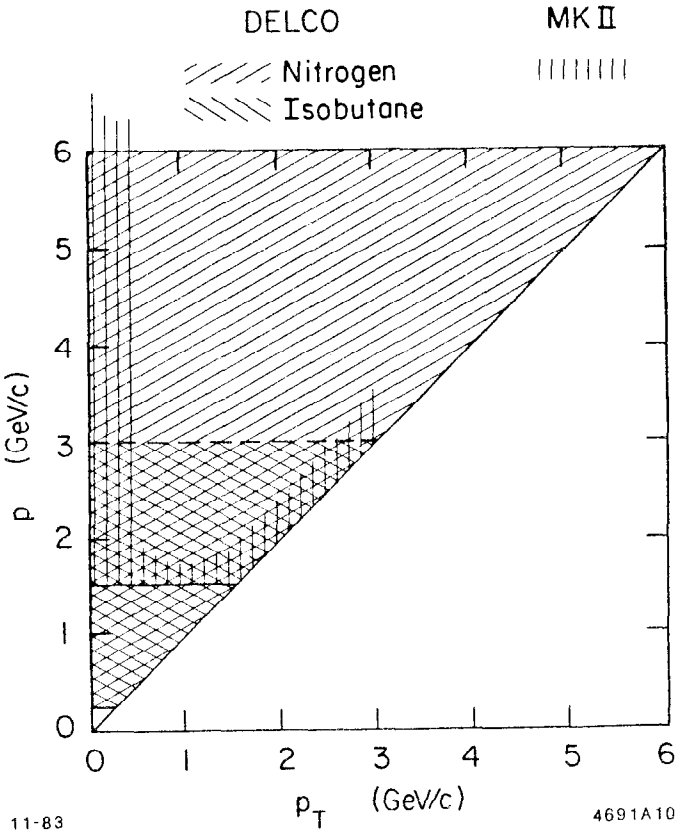


Figure 7 The momentum range covered in e^+e^- direct lepton production experiments. Other published results cover a range similar to MARK II.

3.3 Background Subtraction

There are two dominant backgrounds to the electron signal:

1. real electrons from γ–conversions and Dalitz decays, and
2. non-electron tracks whose counter response mimicked that of an electron, e.g., π traversing a Čerenkov cell which is fired by an undetected γ–conversion.

Much of the background is identified and removed event-by-event. The residual background is then subtracted statistically based on Monte Carlo predictions. This subtraction represents a 25% correction.

The number of γ–conversions is minimized by having little material (5% X_0) before the Čerenkov counter. A γ–reconstruction program was used to identify and reject photons and Dalitz decays. The surviving events were hand-scanned for asymmetric conversions, where the momentum of one electron is too low to be reconstructed efficiently. The hand-scan is sensitive to tracks with momenta above 20 MeV/c. The residual γ background is subtracted statistically using the predictions of the Monte Carlo.

The non-electron background is primarily due to a hadron traversing a Čerenkov cell which was fired by a γ–conversion that occurred too late to be tracked in the inner drift chambers. However, uncorrelated track stubs in the outer drift chamber tag these late conversions. The residual background was calculated and subtracted. The Monte Carlo predictions were checked by "track-flipping". A track is reflected about the origin and the event re-analyzed to see if the new track would now be identified as an electron. Figure 8 compares the backgrounds calculated by these two methods for the same integrated luminosity.

There are other sources of background. Momentum mismeasurement of π above threshold, δ–ray and K–decay, were considered. They constitute a small background and have been subtracted.

3.4 Results

The differential cross-section $(d\sigma/dp)$for isobutane and nitrogen data are shown separately in Figure 9. Their agreement at low momenta (up to π threshold in isobutane) is good. The combined results are plotted in Figure 10, and compared with published results from MARK II.[2] There is an overall normalization uncertainty of 30%.

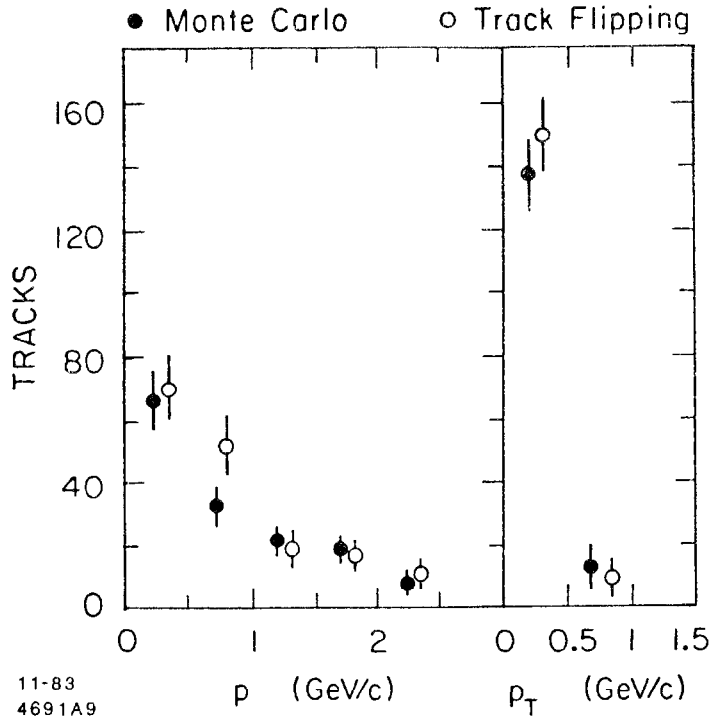


Figure 8 Comparison of background calculations from Monte Carlo and track-flipping techniques. The two calculations are for the same integrated luminosity.

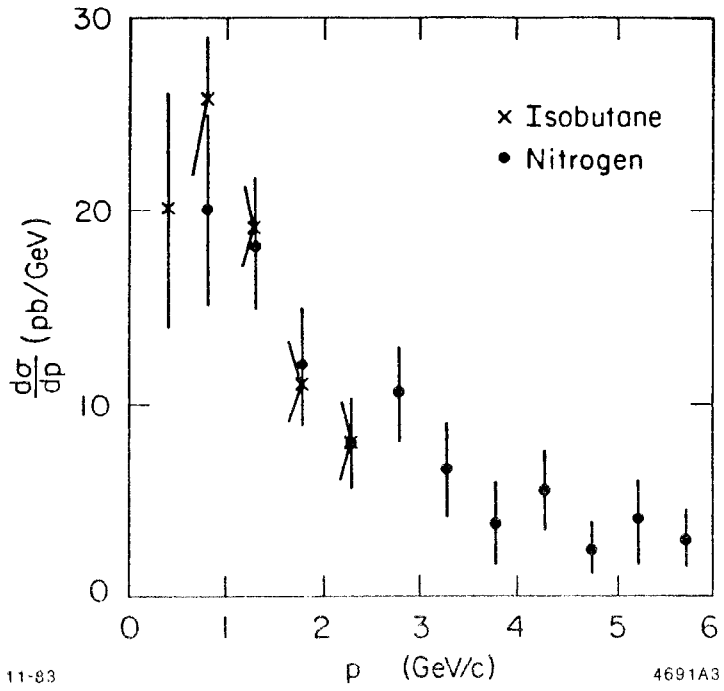


Figure 9 Differential cross-section of direct electrons. Isobutane and nitrogen data are shown separately.

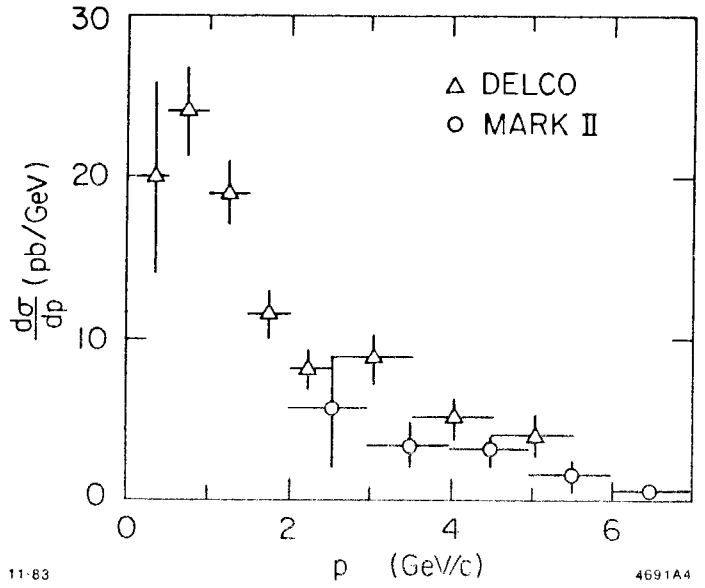


Figure 10 Comparison of $d\sigma/dp$ with MARK II results. There is an overall normalization uncertainty of 30% which is not included in the error bars.

Comparison with the prediction of the Lund Monte Carlo,[4] using the Peterson fragmentation function[5] for heavy quarks, is shown in Figure 11. However, the differential cross section is insensitive to the fragmentation function, and cannot be used to determine fragmentation parameters.

This distribution has been integrated to obtain the total cross-section, and the results are in Table 4. The cross section to produce a hadron with one or more direct electrons is σ_{1e}, and $R_{1e} = \sigma_{1e}/\sigma_{\mu\mu}$. The Lund Monte Carlo predicts $R_{1e} = 0.41$, integrated over all momenta.

Table 4

Total Cross Section to Produce Direct Electrons (The first uncertainty is statistical and the second is systematic.)		
Momentum Range	σ_{1e}	R_{1e}
$.2 < p < 2.5\,\mathrm{GeV/c}$	$36 \pm 2 \pm 10\,\mathrm{pb}$	$.35 \pm .0 \pm .07$
$.2 < p < 5.5\,\mathrm{GeV/c}$	$52 \pm 3 \pm 16\,\mathrm{pb}$	$.51 \pm .03 \pm .10$

3.3 Two-Electron Events

There are several conventional sources of two-electron events. They can be divided into four classes by their charge combinations and the jets that they belong to. Some conventionally expected sources are illustrated in Table 5.

Table 5

Some Conventional Sources of Two-Electron Events		
	Same Jet	Opposite Jet
Same Charge		$b \to c \to s\nu e^+$ $\bar{b} \to \bar{c}\,\nu e^+$
Opposite Charge	$b \to c\nu e^-$ $\hookrightarrow s\nu e^+$	$c \to s\nu e^+$ $\bar{c} \to \bar{s}\,\nu e^-$

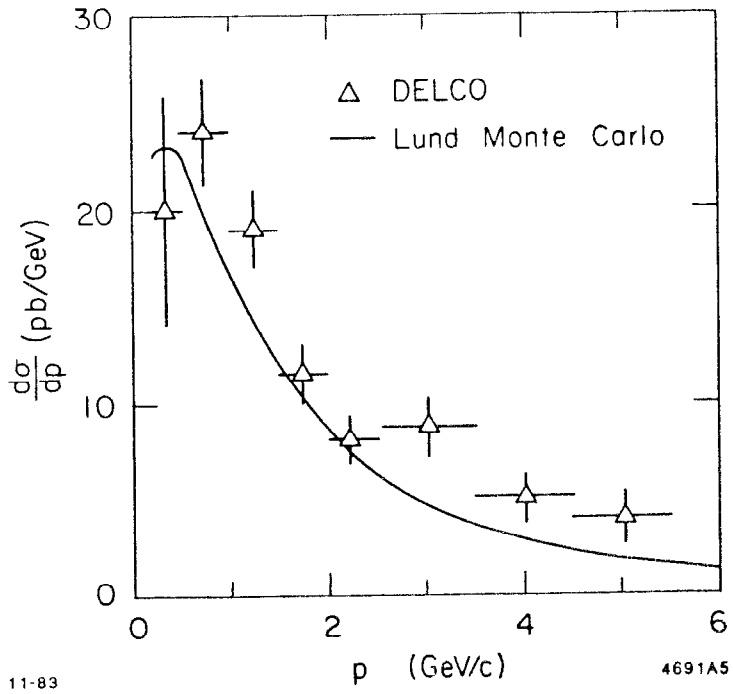


Figure 11 Comparison of $d\sigma/dp$ with predictions of the Lund Monte Carlo.

The background can be divided into two groups:

1. both electrons are background tracks;
2. one electron is a genuine direct electron, while the other track is background.

These background rates can be computed from the known genuine and background single electron rates obtained in the previous analysis. Ten background events are expected, and 26 events are found in 116 pb^{-1}.

This corresponds to a cross-section ratio $R_{2e} = (2.1 \pm .8 \pm 1.)\ 10^{-2}$, where the first uncertainty is statistical and the second one is systematic. In a model where $BR(b \to e) = 12\,\%$, $BR(c \to e) = 8\,\%$, $BR(b \to \tau \to e) = 1\,\%$, and neither B nor D mix, the cross-section ratio is predicted to be 3.8×10^{-2}.

The momentum distributions of the data and Monte Carlo are compared in Figure 12. The correlation matrix of the observed data is compared with the predicted signal plus background in Table 6. The comparisons show that the 'standard' model, as outlined above, is consistent with data. However, the preliminary nature of the data and its limited statistics preclude a detailed comparison.

Table 6

Comparison of Number of Two-Electron Events with Monte Carlo Predictions
(Background contributions are included in both sets of numbers.)

		Same Jet	Opposite Jet
Same Charge	(Data)	1	3
	(MC)	2	7
Opposite Charge	(Data)	9	12
	(MC)	4	13

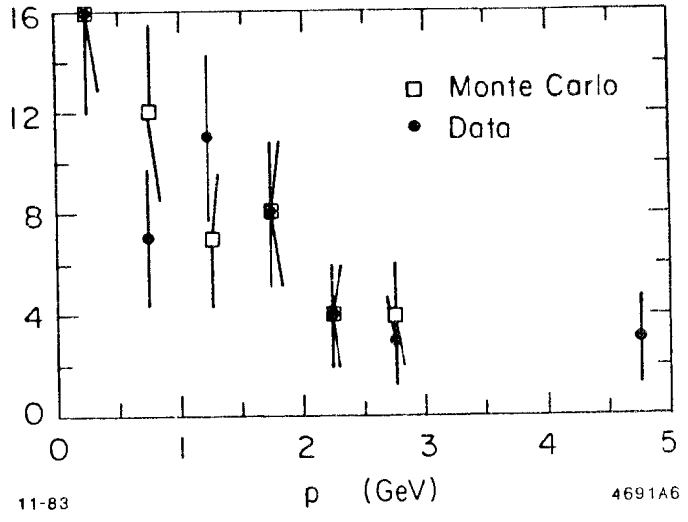


Figure 12 Comparison of Monte-Carlo and measured momentum distributions of two-electron events. Both distributions include background contributions.

4. D^* Production

4.1 Introduction

D^*'s have been detected[6,7] through the decay chain

$$D^{*+} \to D^0 + \pi^+$$
$$\hookrightarrow\ K^- + \pi^+ \quad .$$

The conjugate decay for D^{*-} is implied. The small Q value of the primary decay (6 MeV) leads to good resolution in the mass difference $\Delta M = M(D^*) - M(D^0)$. We have looked for D^*'s using several decays of the D^0, and will report on the total cross-section and fragmentation function.

4.2 Analysis

A particle above π threshold is identified by the Čerenkov counter as a π or K by the presence or absence of a signal. It is then paired with all oppositely charged particles to make $(K^{\mp}\pi^{\pm})$ combinations. Those combinations with an invariant mass in the range 1.66 to 2.20 GeV are taken to be D^0 candidates. The energy of the D^0 is then calculated using the measured momenta and its known mass. The D^0 candidate is then paired with all appropriately charged π's, i.e., $(K^{\mp}\pi^{\pm})\pi^{\pm}$. The mass difference distribution (Figure 13) shows a distinct peak at the expected value.

The background due to random combinations is estimated using "wrong-sign" pions. Assuming no $D^0 - \overline{D^0}$ mixing, the pion from the initial D^* decay and the kaon should have opposite charge. D^0's were paired with wrong-sign pions and the resulting mass difference is also shown in Figure 13. This distribution shows no enhancement in the signal region, but is consistent with the right-sign data in the high mass region.

The background estimate was further checked by "track-flipping". The Čerenkov-identified track (K or π) is reflected about the origin, and the entire analysis repeated. Both the right-sign and wrong-sign pions should produce background events. There were 33 (28) events with the right (wrong) sign.

Several decay modes of the D^0 were examined:

1. $D^0 \to K^- + \pi^+$,
2. $D^0 \to K^- + \pi^+ + X$,
3. $D^0 \to K^- + \pi^+ + \pi^- + \pi^+$.

TOF identification of kaons was also used in the analysis of the first decay mode. Figure 14 is the mass difference distribution of TOF identified events.

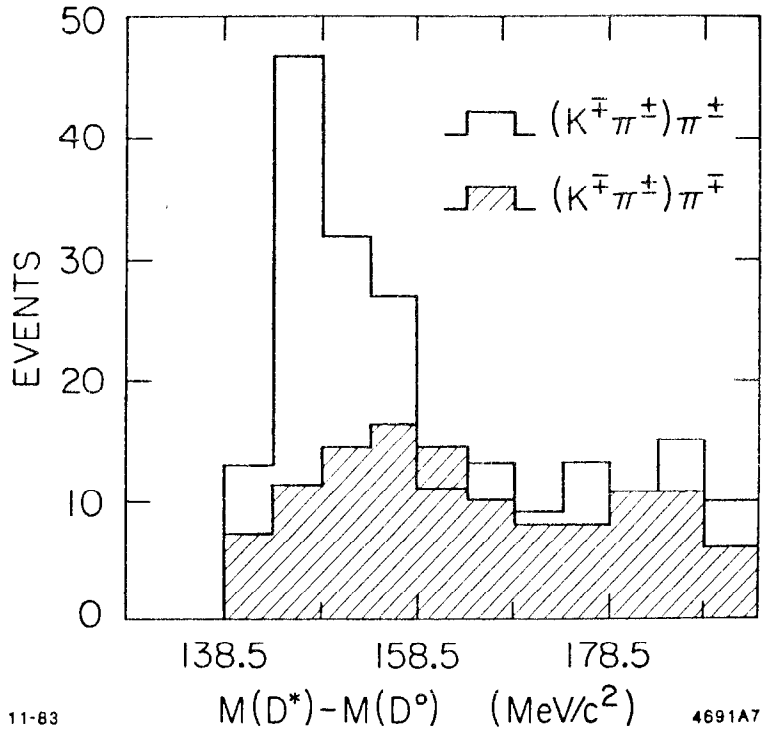


Figure 13 Mass difference $[M(D^*) - M(D^0)]$ distribution in $D^{*+} \to D^0\pi^+ \to K^-\pi^+\pi^+$ where the K is Čerenkov-identified. The background, as measured by wrong-sign π, is indicated in the shaded region.

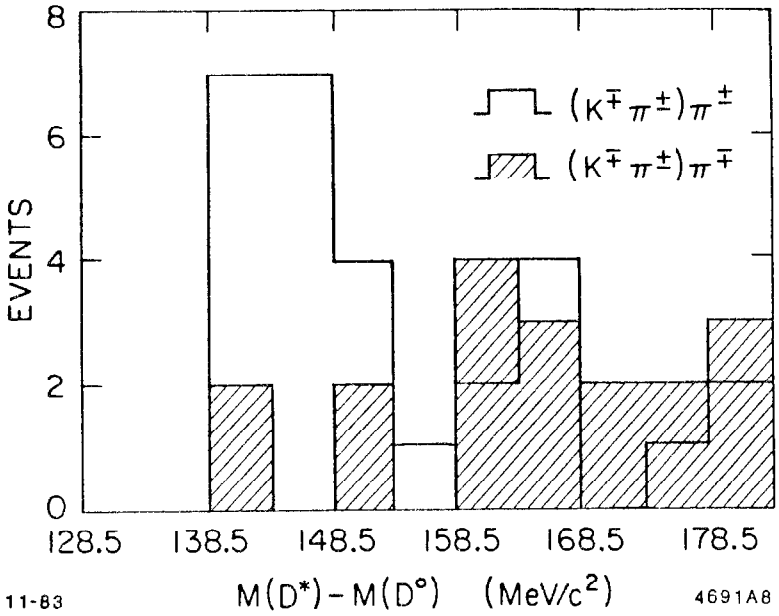


Figure 14 Mass difference $[M(D^*) - M(D^0)]$ distribution in $D^{*+} \rightarrow D^0\pi^+ \rightarrow K^-\pi^+\pi^+$ where the K is TOF-identified. The background, as measured by wrong-sign π, is indicated in the shaded region.

4.3 RESULTS

After correcting for detection efficiencies (Figure 15) and branching ratios[8] (Table 7), the total cross-section is obtained for each of the 3 decay modes used. The results are summarized in Table 8. The data span the entire kinematically allowed momentum range, and a measurement of the total cross-section is possible without an extrapolation.

Table 7

Branching Ratios Used in Calculating Total Cross-Sections

Decay Mode	BR
$D^{*+} \rightarrow D^0 + \pi^+$	0.44
$D^0 \rightarrow K^-\pi^+$	0.03
$D^0 \rightarrow K^-\pi^+X$	0.072
$D^0 \rightarrow K^-(3\pi)^+$	0.085

Table 8

Total Cross-Section to Produce $D^{*\pm}$ at $\sqrt{s} = 29$ GeV
(The first uncertainty is statistical and the second is systematic.)

D^0 Decay Mode	$\sigma(D^{*\pm})$ (nb)
$K\pi$	$.152 \pm .026$
$K\pi X$	$.151 \pm .029$
$K3\pi$	$.151 \pm .025$
Average	$.151 \pm .020 \pm .040$

The average value of $0.151 \pm .020 \pm .040$ nb is compared with published results in Table 9.

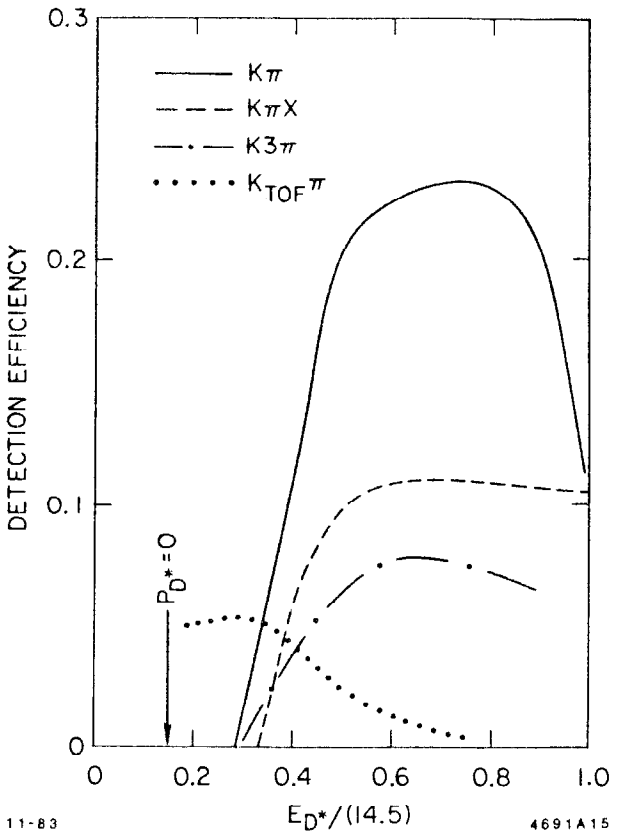


Figure 15 D^* detection efficiency as a function of E_{D^*}/E_{beam} for three D° decay modes.

Table 9

Comparison of D^* Total Cross-Section with MARK II and TASSO Measurements	
Experiment	$\sigma(D^{*\pm})$ (nb)
This Experiment	$0.151 \pm .020 \pm .040$
MARK II[6]	0.25 ± 0.13
TASSO[7]	$0.20 \pm 0.05 \pm 0.07$

The differential cross-section, $d\sigma/dx$ where $x = E_{D^*}/E_{beam}$, is compared with MARK II and TASSO data in Figure 16. The lowest x point uses TOF-identified K's, and has a normalization uncertainty of 30% relative to the other data points. When this distribution is fitted to the function[5]

$$f(x) = 1/x(1 - 1/x - \epsilon/(1-x))^{-2}$$

one obtains $\epsilon = 0.79$. See Figure 17.

It should be emphasized that the quark fragmentation function is a function of $z = E_{D^*}/E_{quark}$ and not x. The effects of initial state photon radiation and gluon bremsstrahlung are to soften the observed momentum distribution. These effects were simulated and the contribution of b quarks was taken into account by assuming $\epsilon_q \alpha\, 1/M_q$. The predictions for three different values of ϵ are shown in Figure 18. The data do not show a strong preference for a particular value of ϵ.

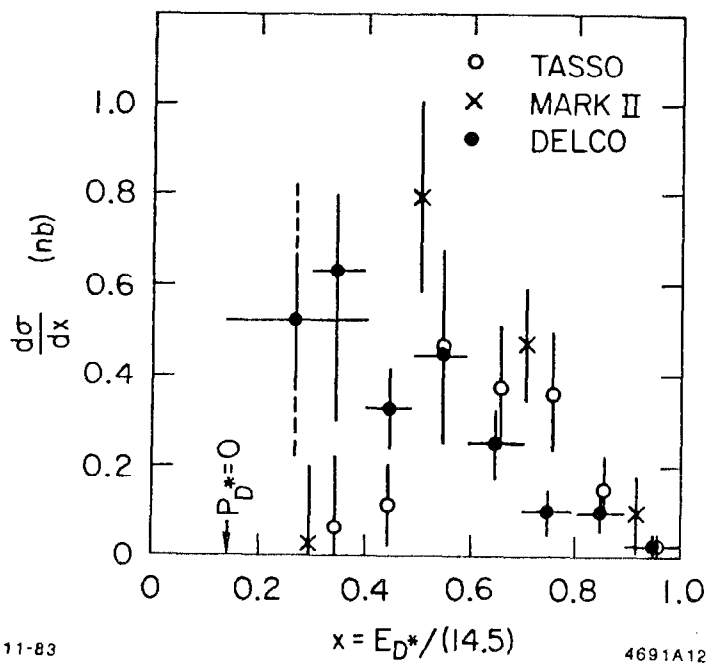


Figure 16 Comparison of $d\sigma/dx$, where $x = E_{D^*}/E_{beam}$, with MARK II and TASSO results. Except for the data at $x = 0.25$, the errors do not include relative normalization uncertainties. The DELCO data at $x = 0.25$ use TOF-identified K's and have a normalization uncertainty of 30% relative to the other DELCO data points. This is shown by the dashed lines.

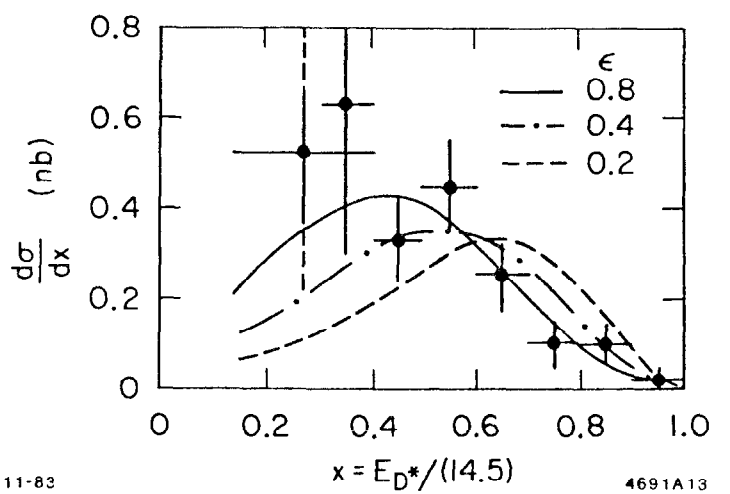


Figure 17 Comparison of $d\sigma/dx$ with the function $f(x) = 1/x[1 - 1/x - \epsilon/(1-x)]^{-2}$ for three values of ϵ. The best fit is obtained with $\epsilon = 0.79$.

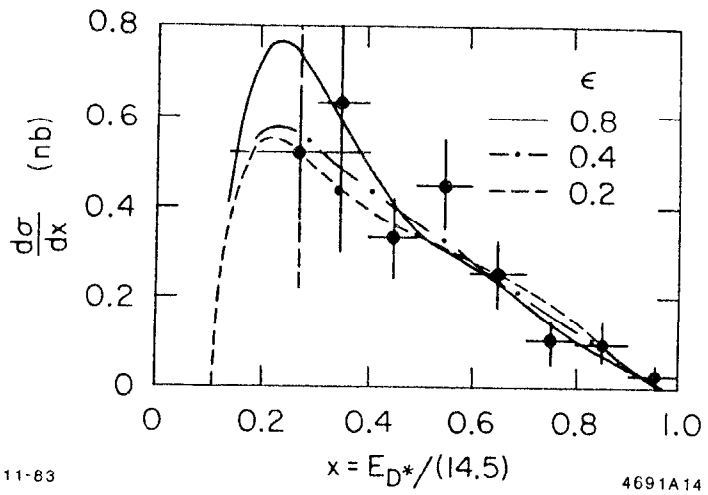


Figure 18 Comparison of $d\sigma/dx$ with predictions using a fragmentation function of the form

$$f(z) = 1/z[1 - 1/z - \epsilon/(1-z)]^{-2} \quad .$$

The effects of initial state radiation and gluon Bremsstrahlung, as well as the contributions of b-quark are included. Three values of ϵ for the c-quark are shown.

References

1. M. Althoff *et al.*, Z. Phys. C17, 5 (1983).
2. Previous measurements of direct electron production in e^+e^- collisions: M. E. Nelson *et al.*, Phys. Rev. Lett. 50, 1542 (1983); H. J. Behrends *et al.*, Z. Phys. C19, 291 (1983).
3. Previous measurements of direct muon production in e^+e^- collisions: E. Fernandez *et al.*, Phys. Rev. Lett. 50, 2054 (1983); W. Bartel *et al.*, Phys. Lett. 99B, 277 (1981); B. Adeva *et al.*, Phys. Rev. Lett. 51, 443 (1983).
4. T. Sjostrand, Comput. Phys. Commun. 28, 229 (1983).
5. C. Peterson *et al.*, Phys. Rev. D27, 105 (1983).
6. J. M. Yelton *et al.*, Phys. Rev. Lett. 49, 430 (1983).
7. M. Althoff *et al.*, Phys. Lett. 126B, 493 (1983).
8. Particle Data Group, LBL-91 (1983). Note that some analyses have assumed $BR(D^{*+} \to D^\circ + \pi^+) = 0.66$ instead of 0.44.

RECENT RESULTS FROM THE PEP4-TPC ON QUARK FRAGMENTATION

Werner Hofmann

Representing the PEP-4 TPC Collaboration [1]

November 1983

---

[1] Members of the TPC Collaboration are:

H. Aihara(6), M. Alston-Garnjost(1), D.H. Badke(4),
J.A. Bakken(4), A. Barbaro-Galtieri(1), A.V. Barnes(1),
B.A. Barnett(4), B.J. Blumenfeld(4), A.D. Bross(1),
C.D. Buchanan(2), W.C. Carithers(1), O. Chamberlain(1),
C. Chen(1), J. Chiba(6), C-Y. Chien(4), A.R. Clark(1),
O.I. Dahl(1), C.T. Day(1), P. Delpierre(1), K.A. Derby(1),
P.H. Eberhard(1), D.L. Fancher(1), H. Fujii(6), T. Fujii(6),
B. Gabioud(1), J.W. Gary(1), W. Gorn(3), W. Gu(1),
N.J. Hadley(1), J.M. Hauptman(2), B. Heck(1), H.J. Hilke(1),
W. Hofmann(1), J.E. Huth(1), J. Hylen(4), H. Iwasaki(1),
T. Kamae(6), R.W. Kenney(1), L.T. Kerth(1), R.I. Koda(2),
R.R. Kofler(5), K.K. Kwong(3), J.G. Layter(3),
C.S. Lindsey(3), S.C. Loken(1), G.W. London(1), X-Q. Lu(4),
G.R. Lynch(1), L. Madansky(4), R.J. Madaras(1), R. Majka(7),
J. Mallet(1), P.S. Martin(1), K. Maruyama(6), J.N. Marx(1),
J.A.J. Matthews(4), S.O. Melnikoff(3), W. Moses(1),
P. Nemethy(1), D.R. Nygren(1), P.J. Oddone(1), D.A. Park(2),
A. Pevsner(4), M. Pripstein(1), P.R. Robrish(1),
M.T. Ronan(1), R.R. Ross(1), F.R. Rouse(1),
R.R. Sauerwein(1), G. Shapiro(1), M.D. Shapiro(1),
B.C. Shen(3), W.E. Slater(2), M.L. Stevenson(1),
D.H. Stork(2), H.K. Ticho(2), N. Toge(6), M. Urban(1),
R.F. van Daalen Wetters(2), C.J. VanDalen(3), R. van Tyen(1),
H. Videau(1), M.R. Wayne(2), W.A. Wenzel(1), M. Yamauchi(6),
M.E. Zeller(7), W-M. Zhang(4)

(1) Lawrence Berkeley Laboratory, Berkeley, CA 94720
(2) University of California, Los Angeles, CA 90024
(3) University of California, Riverside, CA 92521
(4) Johns Hopkins University, Baltimore, MD 21218
(5) University of Massachusetts, Amherst, MA 01003
(6) University of Tokyo, Tokyo, JAPAN
(7) Yale University, New Haven, CT 06520

Presented at the
SLAC Summer Institute on Particle Physics
Stanford, CA
August 16-27, 1982

© W. Hofmann 1983

1) Introduction

The PEP4-TPC detector [2] is the most recent addition to the detector arsenal at the PEP electron-positron storage ring. First completely assembled in October 1981, the TPC went into the PEP beam line early in 1982 and started regular data taking in May 1982; most of the results presented here are based on high-luminosity runs in the 1982-1983 cycle.

Among the detectors at PEP and PETRA, the TPC detector has the following unique features:

1. The truly 3-dimensional tracking of charged particles in the TPC; for each point on a track, the x,y,z-coordinates are measured simultaneously. In the reconstruction of complex hadronic events this offers a major advantage over conventional detectors where tracks in space are reconstructed from 2-dimensional projections.

2. Particle identification based on ionization energy loss over almost the entire momentum range and solid angle.

3. Together with the PEP-9 forward detector system, the facility offers a nearly complete coverage down to polar angles of 30 mrad for charged and neutral particle detection.

Accordingly, the physics goals for the PEP-4/PEP-9 experiment concentrate on two areas: the fragmentation properties of quarks and gluons produced in e+e- annihilation, and the investigation of hadron production in 2-photon collisions. In this paper, only the first of these topics will be addressed.

Despite the many successes of QCD in the description of deep inelastic reactions, the basic fragmentation process of quarks and gluons is not very well understood. This lack of knowledge has been shown to jeopardize precise tests of QCD, such as the accurate determination of the strong coupling constant. [3] With its ability to disentangle complex hadronic events and to identify most of the final state particles, the TPC allows new and more sensitive tests of fragmentation models.

This paper is organized as follows: following the introduction is a brief description of the detector and the particle identification by ionization energy loss. Next, the inclusive production of stable hadrons and of resonances is discussed, and limits on the inclusive production of fractional, charged particles are given. The next chapter deals with a new analysis of long-range correlations in e+e- annihilation. A brief summary and outlook concludes the paper.

cesented in this paper are prelimary, and
pn for final publication.

P-4 Detector

Detector (Fig. 1) is a solenoid detector. Its
sh have been described previously, [4] include
and outer drift chambers, hexagonal and
romagnetic calorimeters and muon detection
the analyses presented here, only the
om the TPC and the hexagonal calorimeters was
r charged track, up to 15 space points are
i TPC with a typical accuracy of 190 microns in
ıg plane) and 350 microns in z (the beam
ıe momentum resolution at low momentum, dp/p =
by multiple scattering; for high momentum
esolution is typically 3.5%*p, for the present
gonal calorimeter detects photons over 45 % of
e, with a typical energy resolution of 15 % at

e Identification by dE/dx

ıe amount of ionization depends only on
charge, particles can be identified by
measuring momentum and ionization energy loss

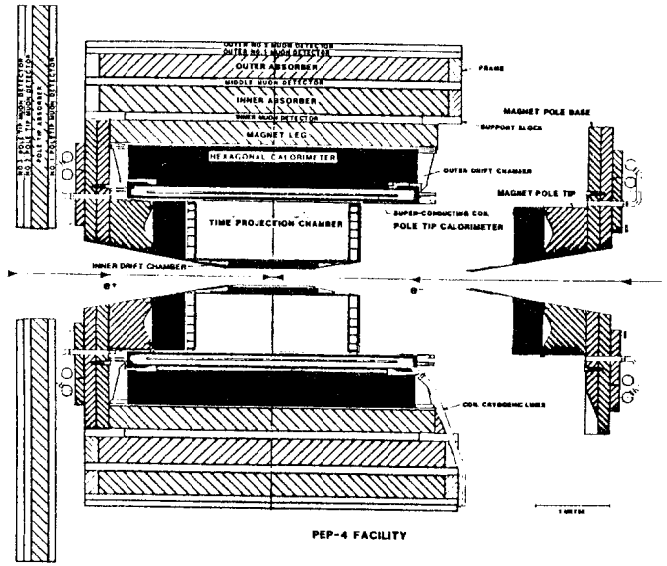


Figure 1

Cross section of the PEP-4 TPC detector, showing the different detector subsystems.

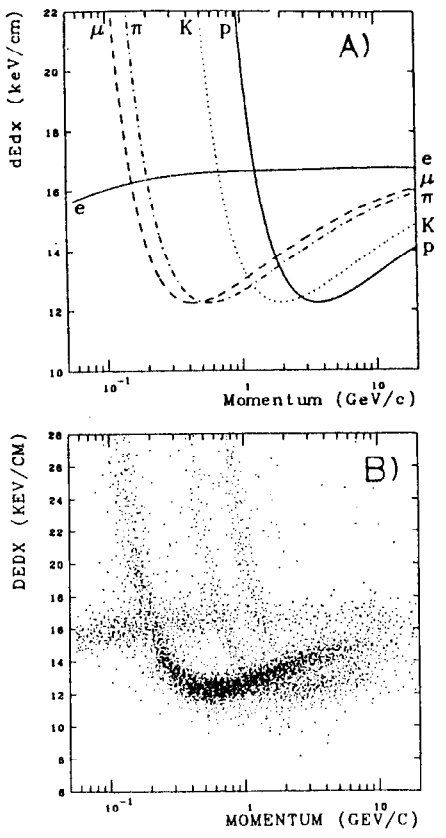


Figure 2 a) & b)

a) Average ionization energy loss as a function of momentum, for different particle types. b) Distribution of ionization energy loss vs. momentum for tracks in hadronic events. Only tracks with at least 80 dE/dx samples are included.

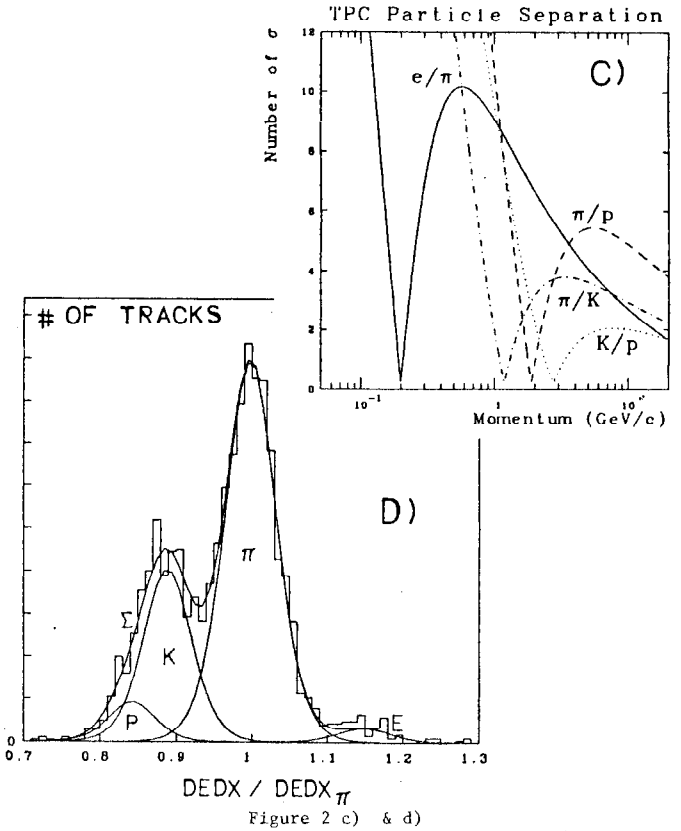


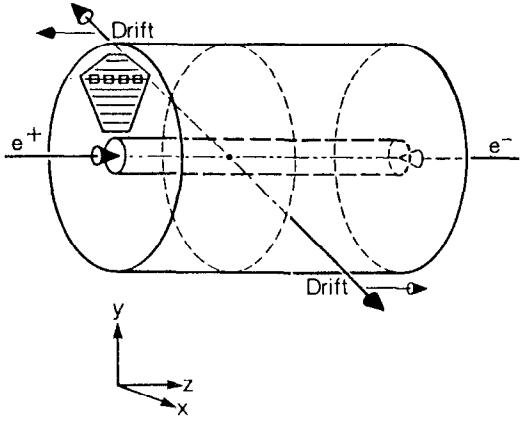
Figure 2 c) & d)

c) Calculated separation between particle types (in standard deviations), as a function of momentum, for tracks with at least 80 dE/dx samples. d) Ratio of measured dE/dx to the expected dE/dx for pions, for momenta between 3.5 and 6 GeV/c. The lines represent the contributions from protons, kaons, pions and electrons.

The fact that the TPC is the first storage ring detector using dE/dx for particle identification over the full momentum range warrants a more detailed description of the system.

The ionization electrons from tracks passing through the TPC drift axially under the influence of an electric field to endcap sectors, where they are detected in multiwire proportional chambers (Fig. 3). Each of the up to 183 dE/dx samples is obtained from the pulse height of the corresponding wire, corrected for the track length seen by the wire, the wire gain, the electronic gain and the electron capture along the drift distance. The calibration of the gain is obtained in situ in three positions along each wire using remotely controlled Fe^{55} sources. A gain map taken before the detector was assembled allows interpolation between these three points. The pulse heights are also corrected for variations in the gain due to changes in gas density and purity and are continously monitored using minimum ionizing pions.

The ionization energy loss has a broad spectrum with a long,high-energy (Landau) tail; many samples, therefore, are needed to define an effective dE/dx. In practice we define dE/dx for each track to be the mean of the smallest 65% of the individual samples. To ensure an accurate particle identification, each track was required to have at least 80 dE/dx samples.



XBL 8310-754

Figure 3

Schematic view of the TPC. Track ionization formed in the sensitive volume drifts to arrays of proportional wires (only one set of wires shown). Position in the bending plane (x,y) is found from signals induced on cathode pads beneath the wires.

Figure 2b shows the distribution of dE/dx versus momentum for events where e+e- annihilates into hadrons. In the low-momentum region below 1 GeV/c, the pion, kaon and proton bands are well separated. Above 1 GeV/c the dE/dx resolution of 3.7% (for tracks with at least 80 dE/dx samples) is comparable to the differences in dE/dx for the various particle types, and the bands overlap. At 3.5 GeV/c, for example, the separation in dE/dx is 3.5 standard deviations for pions and protons, and 1.4 standard deviations for kaons and protons (Fig. 2c,d). Most of the particles in the horizontal electron band in Fig. 2b result from photon conversions in the 0.2 radiation lengths of material before the TPC.

4) Data Sample and Event Selection

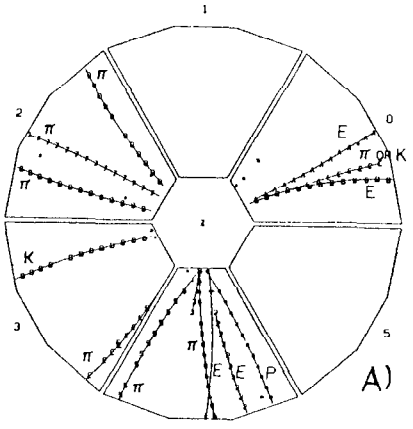
The experimental data discussed in this paper correspond to an integrated luminosity of approximately 29 pb^{-1} at a center of mass energy of 29 GeV.

For the selection of annihilation events and the subsequent anaylysis, "good" charged tracks were defined requiring that the extrapolated orbit passes the nominal interaction point within +- 10 cm in the beam direction and within 6 cm in the plane perpendicular to the beam; only tracks at polar angles between 30 degrees and 150 degrees and with a well- measured momentum were accepted.

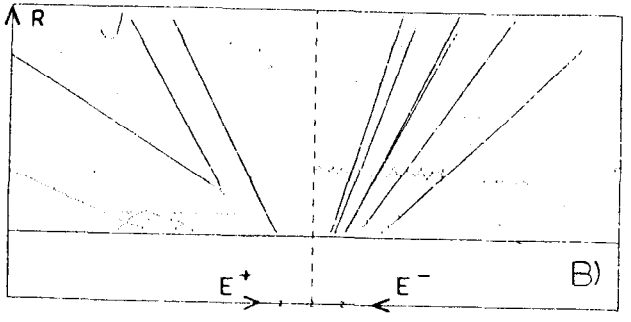
An event candidate had to have at least 5 good, charged tracks, not including electrons from photon conversions which were eliminated based on their dE/dx in the TPC or by geometrical reconstruction. In order to remove two-photon and beam-gas events, the total energy E_{ch} of the charged particles (including electrons) had to exceed one half the beam momentum, and the sum of the momentum components along the beam direction had to be less than 40% of E_{ch}. Three-prong tau decays were removed by requiring at least one jet in the event having either more than 3 non-electron tracks, or an invariant mass above 2 GeV.

Two examples of typical multihadron events, as observed in the TPC detector, are shown in Fig. 4 .

From the number of hadronic events corrected for effects of initial state radiation, and the integrated luminosity determined from Bhabha events in the calorimeters, we obtain a value for R, the ratio of the measured total hadronic cross section to the muon pair cross section, of 3.7 +/- 0.4. This value is in good agreement with the results of measurements made by other detectors at similar energies at PEP and PETRA.[5]



Typical hadronic events in the TPC detector: a) View along the beam line; shown are the pad-hits and the corresponding track fits. As indicated in the figure, except for one all particles are unambigiously identified by their ionization energy loss.



b) View of wire-data in the r-z plane. All 6 wegdes of the TPC folded on top of each other.

Figure 4

5) Inclusive Hadron Production

As a first step, the understanding of the fragmentation process of quarks and gluons into hadrons requires the knowledge of the production cross sections of pions, kaons and protons in e+e- annihilation at high energy.

Figure 5 shows the inclusive cross sections for charged hadron production. In the low-momentum region the raw numbers of pions, kaons and protons were obtained by counting tracks in the bands corresponding to the various particle types in Fig. 2b ; at high momentum a maximum likelihood fit to the dE/dx distribution was used (Fig. 2d). As an input to this fit, the position of the average dE/dx as a function of velocity was determined from independent measurements of cosmic muons and conversion electrons to better than 0.3 %. The cross sections shown in Fig. 5 are corrected for detector acceptance and for the effects of the event selection and of initial state radiation. The errors shown are dominated by systematic uncertainties.

In order to simplify the comparison with other experiments, and to eliminate uncertainties related to the (at present) rather limited accuracy of the luminosity measurements, we present the results on inclusive cross sections normalized to the total annihilation cross section into hadrons, i.e. in terms of fragmentation functions.

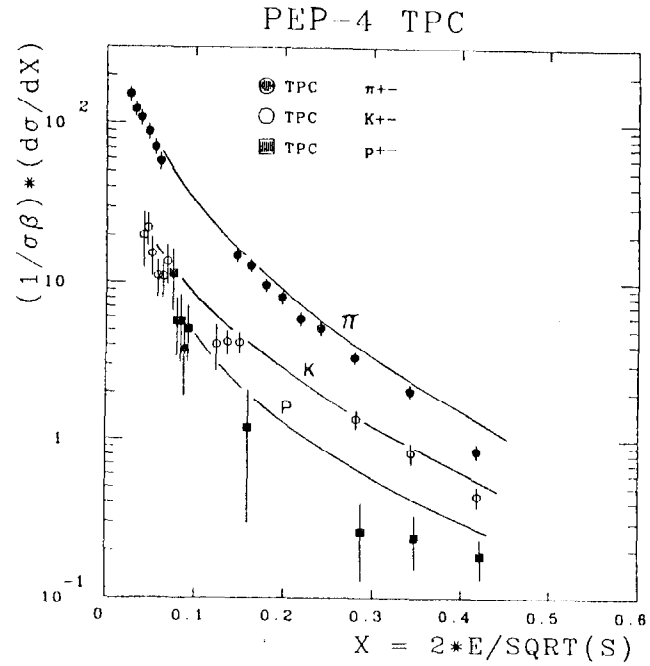


Figure 5

Normalized differential cross section $(1/\sigma\beta)/(d\sigma/dx)$ for charged pion, kaon and proton production in e+e- annihilation at 29 GeV cms energy. X is defined as the hadron energy scaled by the beam energy. The solid lines represent predictions from the LUND fragmentation model for s/u = 0.3.

Included in Fig. 5 are predictions from the LUND-model for quark and gluon fragmentation. [6] The model calculations use the standard parameters, including a production ratio of s and u quarks in color strings of 0.3. The agreement with our measurements is quite good; using the kaon inclusive cross section, s/u can be constrained to 0.3 +- 0.1.

Figure 6 shows the fraction of pions, kaons and protons among charged hadrons, in comparison with earlier data from TASSO.[7] Our measurements confirm the rise of the kaon and proton fractions with increasing momentum, although even at the highest momentum baryon production is still strongly suppressed relative to pions and kaons. Note that most of this rise is explained by phase-space effects and as a result of resonance decays, which tend to soften the pion spectra more than the spectra of heavy hadrons. [8] The observed spectra are e.g. consistent with a constant baryon/meson ratio for the primarily produced hadrons , if a vector/scalar ratio of 1 is assumed.

The particle ratios and fragmentation functions given in Figs. 5 & 6 include decay products of particles with lifetimes below $5 * 10^{-10}$ sec.

The photon detection in the hexagonal calorimeter allows the reconstruction of neutral pions. The π^0 spectrum can then be compared with the charged pion spectrum. Figure 7a

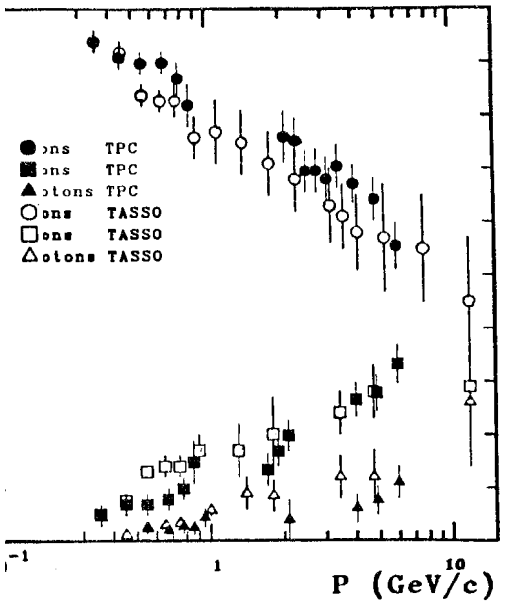
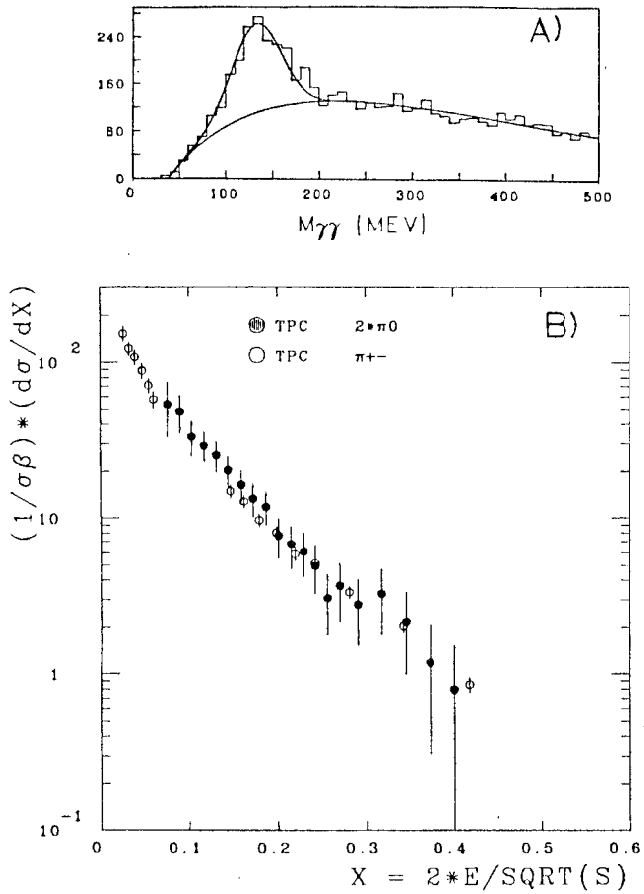


Figure 6

adrc fractions vs momentum for pions, kaons and forhe TPC and TASSO[7] experiments. For the TPC errbars shown are dominated by systematic effects.



a) Distribution for the 2-photon invariant mass from the hexagonal calorimeter. b) Normalized cross section for inclusive π^0-production at 29 GeV cms energy, compared to the inclusive cross section for charged pions.

Figure 7

shows the distribution of 2-photon invariant masses, for photon energies above 500 MeV. A clear peak is seen at the π^0 mass, with a width of 26 MeV rms. The background under the π^0 peak was estimated from Monte-Carlo simulations, and from events with a fake photon generated by flipping one photon into the opposite jet and combining it with real photons.

The resulting π^0 cross sections agree well with previous measurements.[9] This is compared with the inclusive charged pion cross section in Fig. 7b . Within the errors, the two agree as expected from isospin symmetry.

6) Particle Fractions in 3-Jet Events

The fragmentation functions and particle ratios presented in the previous chapter are averages over all types of jets generated in e+e- annihilation, i.e. all quark flavors and gluon jets. The next question is to what extent the properties of quark jets depend on the flavor of the parent quark (we shall return to that question in Section 9) and especially if gluon jets differ from quark jets.

We have extracted a sample of 3-jet events using a clustering method.[10] The lowest momentum jet ('jet 3') in these events has a probability of 55 % of being a gluon jet, as compared to 30 % for the medium-momentum jet ('jet 2'). For these events, the pion fractions were determined for fast particles ($p > 2$ GeV/c). These fast particles can be unambigiously assigned to a jet and should be sensitive to the type of parton generating the jet. Because of the limited statistics, kaons and protons could not be separated for that sample.

The resulting pion fractions, 73+-4 %, 68+-4% and 69+-7% for jets 1, 2 and 3, respectively, are consistent with being the same for all three jets. However, the numerical values cannot be compared directly, since the fractions are measured at different scaled momenta (z) in the jets. In Fig. 8 the pion fractions are displayed as a function of the mean z of the particles contributing to the data point, along with the inclusive pion fraction in hadronic events. For the 3-jet events, z is the momentum of a particle scaled to the jet momentum (which is derived from the angles between the reconstructed jet axes); for the inclusive ratios, the particle momenta are scaled to the beam momentum. Assuming that the particle fractions in quark jets approximately scale in z, the pion fraction in the lowest-momentum ('gluon') jet is slightly higher than in the high momentum jets. A drastic enhancement of heavy hadron production in gluon jets can be excluded (Note that we are only sensitive to the sum of kaon + proton production; an increase in the baryon rate, as seen in Upsilon decays,[11] is still possible provided the kaon rate is reduced correspondingly).

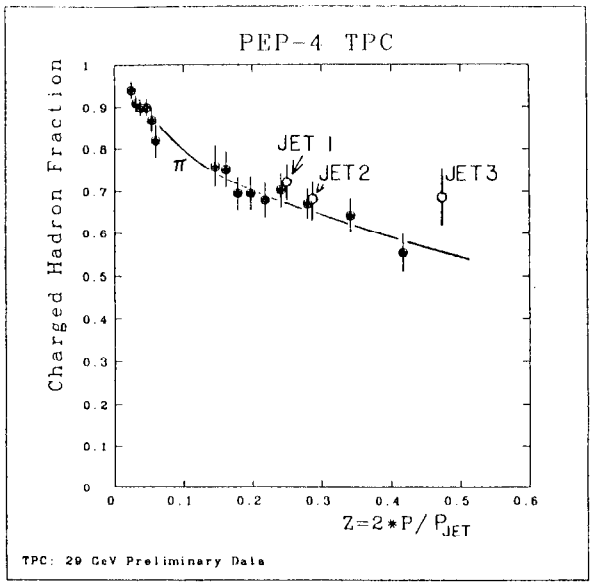


Figure 8

Fraction of pions among particles with p ⟩ 2 GeV/c in jets 1, 2 and 3 in 3-jet events. The fractions are plotted at the average z of hadrons with p ⟩ 2 GeV/c in the corresponding jet. For comparison, the inclusive pion fraction as a function of z (= particle momentum / beam momentum) is included.

At first, this result may seem surprising, since the (flavor-blind) giuon is expected to generate more leading strange mesons than for instance a u-quark. A more detailed study however, shows that this 'advantage' is offset by strange particle production in the s, c, and b jets produced in e+e- annihilation. Standard fragmentation models like the LUND model reproduce our result.

7) Search for Fractional Charged Objects

Results from quark searches in matter have cast some doubts on the dogma of perfect quark confinement. On the other hand fractional charge searches at accelerators (largely concentrated on production of charge 1/3 and 2/3 particles) have set rather stringent limits. Recently, however, models have been proposed [12] in which color triplets are confined, yet some states with higher order representations of SU(3)color are unconfined; one could, for example, have free charge 4/3 diquarks.

Using the dE/dx information, the TPC detector is well suited to look for stable particles with unusual signatures, e.g., fractionally charged particles.

A first search in hadron events of 22 pb^{-1} integrated luminosity yielded 50 candidate tracks with high momentum and unusally high energy loss. The main background source for that sample consists of unresolved pairs of nearby tracks,

which fake a single track with twice the expected ionization.

The fine spatial segmentation of the TPC allowed us to develop a series of cuts to reduce this background, based on the widths of the pad and wire hits.[13] These cuts reject all candidates, while retaining good efficiency for protons with similar dE/dx.

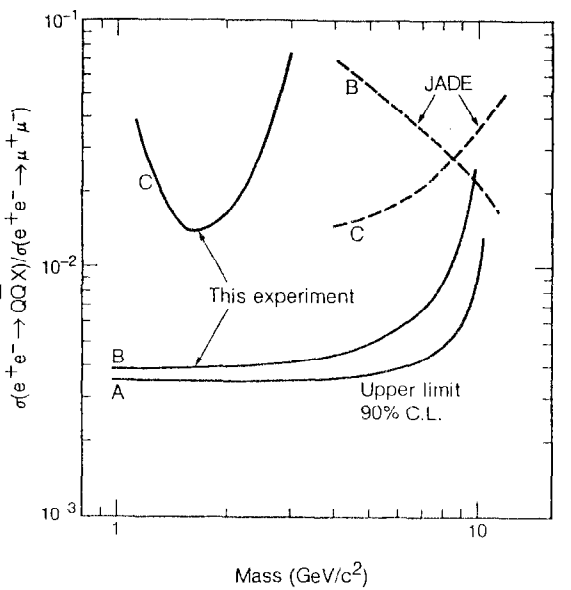
Figure 9 shows the limits on inclusive production of stable charge 4/3 particles in hadronic events,[13] along with results of a similar search by JADE. [14] The limits depend on the assumptions for the inclusive production spectra and on the mass of the object; they are typically of the order $5 * 10^{-3}$ for flat momentum distributions.

Preliminary limits of similar order have been obtained for inclusive production of charge 2/3 objects.

8) Inclusive Resonance Production in e+e- Annihilation

The investigation of resonance production in e+e- annihilation yields additional information on quark fragmentation beyond what can be learned from the study of stable hadrons:

1. Since most of the stable particles are decay products, the spectra of direct hadrons are more relevant for an understanding of the fragmentation process.



XBL 8310-752

Figure 9

Limits on the inclusive production cross section for charge 4/3 objects, scaled to the muon-pair cross section, as a function of the mass of the object. The curves represent different momentum distributions: a) dN/dp = p**2/E, b) dN/dp = constant, c) dN/dp = (p**2/E)*exp(-3.5*E). The dotted lines show limits from a similar search performed by JADE.[14]

2. Phenomenological models [15] 'predict' the mass spectrum of hadrons produced in e+e- annihilation.

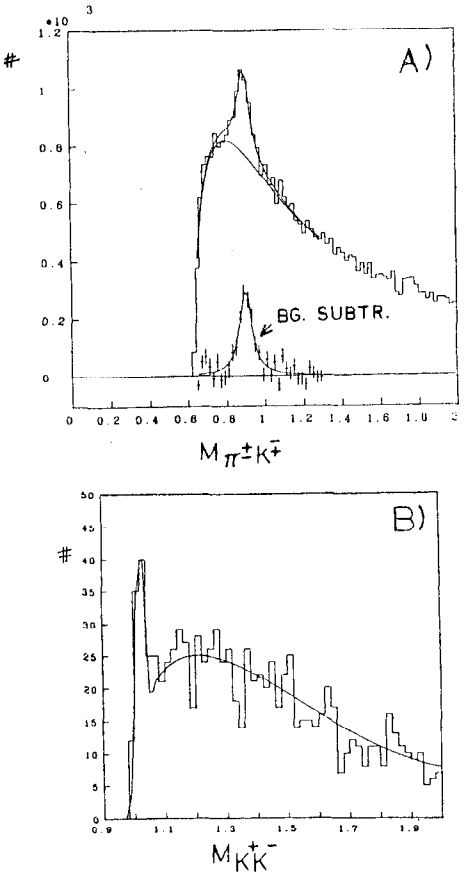
3. The fraction of vector mesons, as well as other parameters are inputs in most of the 'standard' fragmentation models like [6]

We will report here on inclusive k^{*0} and ϕ production.

To search for resonances, dE/dx-identified hadrons were used. In momentum regions where hadrons cannot be identified unambigiously , the probability for a particle to be of a particular kind was calculated from the difference of its measured dE/dx and the known average dE/dx for that kind at the given momentum. These probabilities were weighted with the measured particle fractions (Fig. 6). A minimum (weighted) probability for the best assignment was required for particles used in the mass combinations. No further cuts were applied except for a standard track selection.

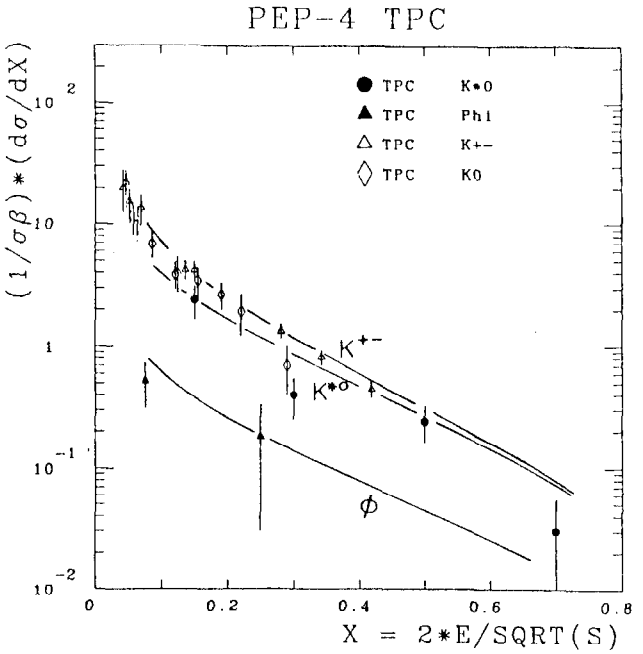
Figure 10a and 10b show the invariant mass distributions for unlike-sign k-pi and k-k combinations, respectivly, together with fits of a resonance shape and a background taken from like-sign combinations. Clear K^{*0} and ϕ signals are visible.

The inclusive k^{*0} and ϕ cross sections (normalized to the total cross section) are shown in Fig. 11 along with the spectra of kaons; also included is a prediction by the



a) Mass spectrum of unlike-sign k-pi combinations. b) Mass spectrum of k+k- combinations. The full lines are fits using a Breit-Wigner resonance shape and a background shape derived from like-sign combinations. The particles are identified by dE/dx.

Figure 10



TPC: 29 GEV PRELIMINARY DATA

Inclusive cross section for k*0 and ϕ production in e+e- annihilation at 29 GeV, normalized to the total hadronic cross section. Also shown is the spectrum of kaons, and predictions from the LUND model using s/u = 0.3 and v/s = 1.

Figure 11

LUND model [6] using a vector/scalar ratio of 1 and s/u = 0.3.

At high momentum, k^{*o} and normal kaons are produced at similar rates, in agreement with the model calculation. Production ratios of 3:1, as expected from the spin weights, are clearly excluded. It is furthermore interesting to note that the model gives a reasonable description of ϕ production, indicating that the mechanism of OZI suppression, which is built in implicitly, is appropriate.

9) Long-Range Correlations in e+e- Annihilation

From the previous discussion it seems obvious that in order to gain deeper insight into the mechanisms of parton fragmentation, the study of inclusive particle production has to be supplemented by other techniques.

The recent observation of strong, long-range correlations (LRC) in proton-antiproton interactions, and the increase of the strength of the correlations with the cms energy, [16] which proves that LRCs are not a non-asymptotic phenomenon, has revived the interest in LRCs in electron-positron annihilation.

The term "long-range correlations" refers to the observation that the properties of the two jets in an event--the "beam" and the "target" jet in p-p and in pbar-p interactions, and the "quark" and the "anti quark" jet in

e+e- annihilations -- are correlated, and that these correlations have a large range in rapidity, in contrast to the well- known , short-range correlations (SRC), whose strength decreases exponentially with increasing separation in rapidity.

In the following, we shall adopt the usual (historical) notation and refer to the two jets as to the "forward" (F) and "backward" (B) jets; "forward-backward" (FB) correlation will be used as a synonym for LRC. The forward jet is defined as the ensemble of particles having rapidities $y > 0$ in the overall cms, with y referring to the sphericity axis of the event. Correspondingly, particles with $y < 0$ form the backward jet.

In general, FB-correlations can have different origins:

1. The reaction investigated represents an average over many different processes. This is the case in hadron-hadron interactions, where particles are produced in inelastic collisions with different impact parameters. Similarly, the production of different quark flavors in high energy e+e- annihilation should result in LRCs if there are differences in the jets produced by different quark species.

2. True dynamical long range correlations. If color confinement bears some analogy to a phase transition, one expects LRCs, which could be interpreted as coherent fluctuations of the "string tension" in a color flux tube . [17] On the other hand, such LRCs are inconsistent with one of the postulates of the quark-parton-model (QPM), namely that the fragmentation of a parton is independent of its production (except for SRC)effects, of course.

3. Correlations of purely kinematical origin due to phase-space restrictions. These correlations should be negligible provided that the cms energy is very large compared to the masses and transverse momenta of the hadrons involved.

Experimentally, a FB correlation coefficient , C , can be defined as follows (we use the FB multiplicity correlation as an example):

$$C = (NF*NB) - (NF)*(NB).$$

NF and NB denote the hadron multiplicities in the forward and backward jets, respectively. The standard way to present FB correlations is to study the dependence of (NF) on NB. Any FB correlation is characterized by a non-zero slope S:

$$S = d(NF)/dNB .$$

S and C are related via

$$S = C/(SF*SB)$$

where SF and SB represent the rms width of the NF and NB distributions.

Assuming that in e+e- annihilation the production of different quark flavors is the only potential source for LRCs, it is easy to show that C is always 0 or positive; and that C**1/2 is a measure for the rms variation of the mean hadron multiplicity over the different jet flavors.[18]

A measurement of C or S therefore provides a new tool in the investigation of parton fragmentation [18]: a result $C < 0$ would indicate that basic assumptions of the parton model are violated; on the other hand, $C >= 0$, supplemented with the assumption of independent fragmentation, measures differences in the fragmentation properties of the various quark flavors. Of course, as we shall see, the study of LRCs is not restricted to multiplicity correlations. Identical arguments hold for LRCs between the mean transverse momentum of particles in jets, the inclusive fragmentation functions, etc.[18]

The main experimental problem in the study of LRCs is given by the fact that any non-ideal detector tends to induce artificial correlations between jets, e.g., due to the requirement of a minimum number of particles seen in the detector in order to accept an event. This is demonstrated in Fig. 12 , where (NB) is shown as a function of NB for normal hadronic events. The negative correlation at low multiplicities is purely artificial. In addition, part of the (small) positive correlation at high multiplicities is due to the correlated detector acceptances for two back to back jets.

In the present analysis, great care has been taken to avoid such biases. For example, each event was divided into two jets, each of which had to pass separate acceptance cuts; only events with two 'good' jets were used. Each jet was required to be contained well within the fiducial area of the detector, and to have a minimum momentum, number of particles etc. Events clearly inconsistent with a 2-jet structure were rejected; the contamination in the event sample due to tau-tau and 2-photon eventswas below 1.1 %. Such a selection should avoid any problems of the type evident from Fig. 12 ; various checks have been performed using both data and Monte-Carlo models to ensure that this is actually the case.

To reduce the influence of short-range effects on the FB-correlation, a rapidity gap of one unit was introduced between the forward and the backward regions. Only particles with $|y| > 0.5$ were taken into into account.

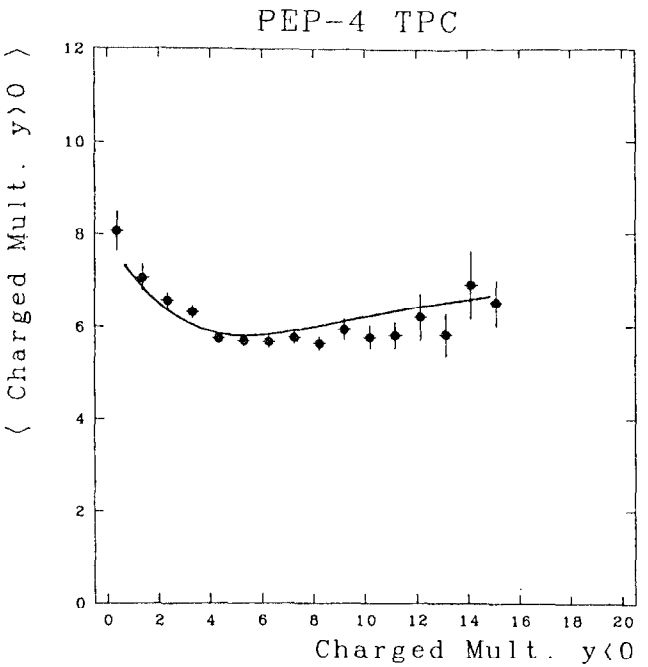


Figure 12

Mean multiplicity in the "backward" jet as a function of the multiplicity in the "forward" jet, for hadronic events with at least 6 charged tracks.

Figure 13 shows the FB correlation S for some typical properties of jets, like the multiplicity of charged hadrons, the jet mass, the mean scaled momentum of hadrons in a jet, their mean rapidity, mean pseudorapidity and mean transverse momentum. As expected in the basic quark-parton-model, all correlations were either consistent with 0 or positive . Assuming that true dynamical LRCs are absent ,[19] these values of S demonstrate the universality of transverse momentum scales in jets, and the non-universality of longitudinal fragmentation functions for different quark species.

Summary

Based on particle identification by ionization energy loss new measurements of inclusive pion, kaon and proton production in e+e- annihilation at 29 GeV are reported. The inclusive production of particles with unusual ionization, like charge-2/3 or charge-4/3, is excluded at a level of less than 10^{-2} .

For the first time at PEP and PETRA energies, inclusive production of k^{*0} and ϕ has been studied. All inclusive spectra and particle ratios agree reasonably well with predictions from the LUND model using s/u = 0.3 and v/s = 1.

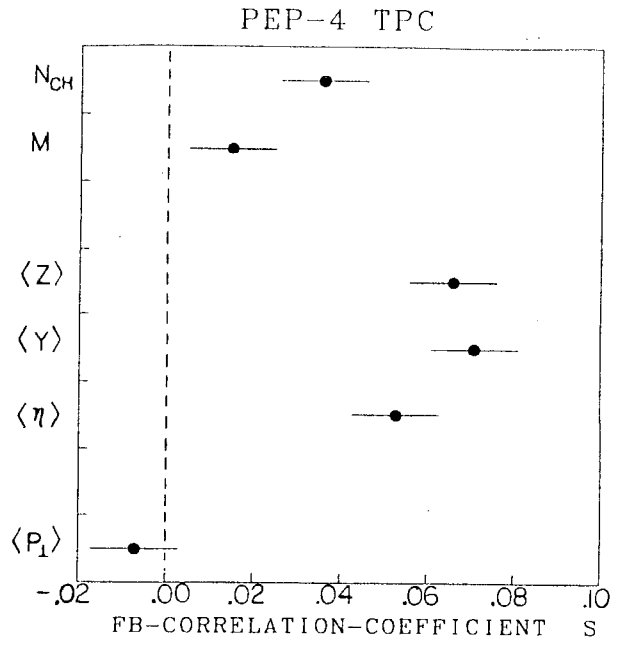


Figure 13

Forward-backward correlation coefficient S (see text) for the hadron multiplicity Nch in jets, jet masses M, mean scaled momentum ⟨z⟩, mean rapidity ⟨y⟩, mean pseudorapidity ⟨η⟩ and mean transverse momentum ⟨$p_\perp$⟩. The systematic error due to remaining detector effects is estimated to +- 0.01 (not included in the error bars).

Long range correlations of particles in jets have been exploited to investigate differences in the fragmentation of the various quark species.

Due to the limited space, many interesting topics like the entire area of 2-photon physics had to be omitted in this presentation. Nevertheless it is obvious that the special capabilities of the TPC open new and interesting possibilities even in a field as crowded as the physics of e+e- annihilation at PEP and PETRA energies.

Acknowledgements

This work was supported in part by the United States Department of Energy under contracts DE-AC03-76SF00098, DE-AM03-76SF00034, by the National Science Foundation, and by the Joint Japan - United States Collaboration in High Energy Physics.

References

1. (See title page.)

2. Proposal for a PEP facility based on the time projection chamber; John Hopkins University, Lawrence Berkeley Lab., University of California at Los Angeles, University of California at Riverside, Yale University (1976).

3. CELLO Collab., H.J. Behrend et al., DESY 82-061 (1982); and H.J. Behrend, Proc. of the 21st Int. Conf. on High Energy Physics, Paris (1982).

4. TPC Collab., H. Aihara et al., IEEE Trans.Nucl.Sci. NS-30 (1983) 63; NS-30 (1983) 67; NS-30 (1983) 76; NS-30 (1983) 117; NS-30 (1983) 153.

5. JADE Collab., W. Bartel et al., Phys.Lett. 129 (1983) 145
TASSO Collab., R. Brandelik et al., Phys.Lett. 113B (1982) 499
MARK J Collab., B. Adeva et al., Phys.Rev.Lett. 50 (1983) 499
MAC Collab., M. Piccolo, these proc.

6. B. Andersson, G. Gustavson, C. Peterson, Z. Phys. C1 (1978) 105;
B. Andersson, G. Gustavson, Z. Phys. C3 (1980) 223;
B. Andersson, G. Gustavson, T. Sjoestrand, Z. Phys. C6 (1980) 235;
T. Sjoestrand, Computer Phys. Com. 27 (1982) 243.

7. TASSO Collab., M. Althoff et al., Z.Phys. C17 (1983) 5.

8. B. Andersson, G. Gustavson, C. Peterson, Nucl.Phys. B135 (1978) 273.

9. CELLO Collab., H.J. Behrend et al., Z.Phys. C14 (1982) 189;
TASSO Collab., R. Brandelik et al., Phys.Lett. B108 (1982) 71.

10. A. Baecker, Z.Phys. C12 (1982) 161.

11. DASP-II Collab., H. Albrecht et al.; Phys.Lett. 102B (1981) 291;
CLEO Collab., P. Avery et al., Paper submitted to 1983 Int. Symp. on Lepton and Photon Interactions, Cornell.

12. R. Slansky, T. Goldman, G. Shaw, Phys.Rev.Lett. 47 (1981) 887;
A. DeRujula, R. Giles, R. Jaffe, Phys.Rev. D17 (1978) 285.

13. TPC Collab., H. Aihara et al., submitted to Phys.Rev.Lett.

14. JADE Collab., W. Bartel et al., Z.Phys. C6 (1980) 295 .

15. R.D. Field, S. Wolfram, Nucl.Phys. B213 (1983) 65 ;
T.D. Gottschalk, Nucl.Phys. B124 (1983) 201;
CALT-68-1052 (1983);
M.G. Bowler, Z.Phys. C11 (1981) 169.

16. UA5 Collab., K. Alpgard et al., CERN-EP/83-20 (1983).

17. J.H. Kuehn, H. Schneider, Z.Phys. C8 (1981) 115.

18. P. Hoyer, SLAC-PUB-3166 (1983).

19. Note that in the LUND model, partons fragment independently in the sense used in this article; the string fragmentation scheme doesn't introduce significant LRCs (relative to the LRCs due to the differences in heavy and light quark fragmentation).

ANL-HEP-CP-83-50

Results from HRS at PEP

J. M. Weiss

Argonne National Laboratory
Argonne, Ill. 60439

Presented at the SLAC Topical Conference,
SLAC Summer Institute, Stanford, Ca. July 27-29, 1983.

Introduction

The High Resolution Spectrometer (HRS)[1] has been collecting data at PEP since the end of 1981 and has now accumulated 120 pb^{-1} of integrated luminosity. I report here the results of our analysis in the following areas:

- QED and Electroweak Tests:
- Scalar Electron Search:
- Inclusive Hadron Production:
- D^0, D^+ and D^* Production:
- Studies of Quark Fragmentation:

Only the 20 pb^{-1} of integrated luminosity obtained during our first year of running has been completely analyzed and this provides the data sample for most of the above topics. For others I report a preliminary analysis of a total sample of 80 pb^{-1}.

© J. Weiss 1983

The Detector

The HRS detector, shown in Figure 1, is a new general purpose e^+e^- detector operating at PEP which very much emphasizes high-quality charged particle tracking. It combines the elements of a 1.6 T. magnetic field, 2.0 m. tracking radius and 200μ spatial resolution with very low multiple scattering ($0.02x_0$ material) to achieve a momentum resolution of $\sigma_p/p = 0.1 \cdot p\%$ for all tracks with $p \geq 5$ GeV/c over 65% of the solid angle. For 90% of the total solid angle the momentum resolution for these tracks is better than $0.5 \cdot p\%$ which remains quite a respectable value by the standards of previous e^+e^- detectors even in their central regions.

The detector also incorporates electromagnetic shower calorimeters located inside the coil for γ and electron detection. These are $11x_0$ lead-scintillator sandwich modules which cover the "barrel" region ($60\% \cdot 4\pi$) and the "end-cap" region ($27\% \cdot 4\pi$) with resolutions $\sigma(E)/E = 0.16/\sqrt{E}$ and $0.20/\sqrt{E}$, respectively. A single layer of proportional wire chambers with charge division provide spatial resolutions of $\Delta x, \Delta y \approx 2$ cm. and $\Delta\theta \approx 10$ mr.

Hadron identification is provided by time-of-flight measurements using the scintillator after $3x_0$ of the shower counters and also by 11 toroidal photo-ionization Čerenkov detectors shown in Figure 1. A time-of-flight resolution of $\sigma_t = 360$ psec. is achieved for minimum-ionizing particles, enabling 1σ K/π separation to 1 GeV/c momentum and p/K separation to 1.9 GeV/c. The Čerenkov counters are highly segmented (704 cells) and will permit $\pi/(Kp)$ separation in the range 1.5-6.0 GeV/c and $p/(K\pi)$ separation for momenta greater than 6.0

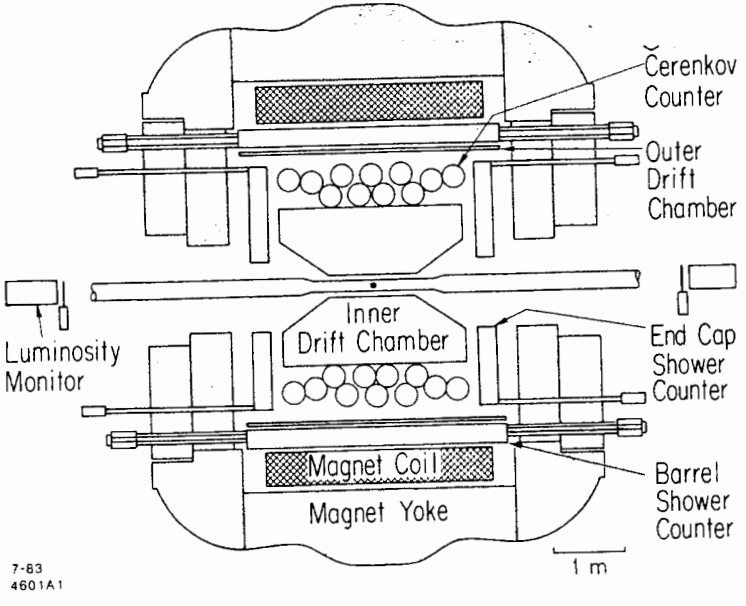


Fig. 1

The HRS Detector

GeV/c over 60% of the solid angle. Installed and running for most of the second year's operation, analysis of the Čerenkov counters signals is still underway and no results reported here use the information that they will soon provide.

The observed momentum distribution for Bhabha-scattered electrons, plotted in Figure 2, shows a resolution of $\sigma_p/p=1.0\times10^{-3}\cdot p$ (GeV/c) which is dominated by measurement error, after unfolding radiative effects. These measurement errors, in turn, permit calculation of the expected momentum resolution for all momenta which is shown in Figure 3. Low momentum tracks are measured with resolutions σ_p/p of ≈0.3% and ≈0.6% for the first and second years'running, respectively. The elements which provide this high resolution also make possible a high tracking efficiency which does not begin to fall off until polar angles below ≈26° are reached, giving the detector a particularly large, high resolution acceptance for charged particle resonant states.

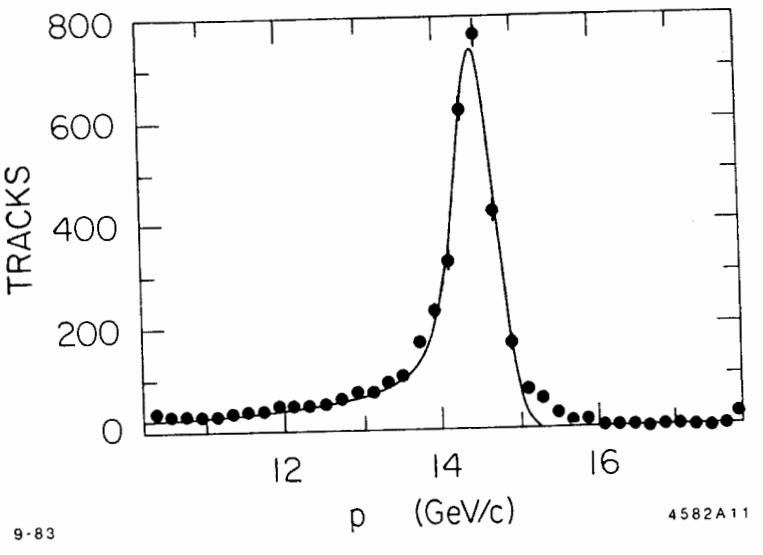


Fig. 2

Momentum Distribution of Bhabha-scattered Electrons

QED Tests at 29 GeV

I present results[2] here on the processes:

$$e^+e^- \rightarrow e^+e^- \qquad (1)$$

and

$$e^+e^- \rightarrow \mu^+\mu^- \qquad (2).$$

Event selection proceeded from the 19.6 pb^{-1} sample of the first year's running by requiring 2 charged prongs, each with $p\geq7.25$ GeV/c, with a colinearity angle between them less than 25°. A good vertex was required ($r<0.01$m, $|z|<0.09$m) for all tracks and time difference cuts were applied to the two tracks for cosmic rejection. Muons and

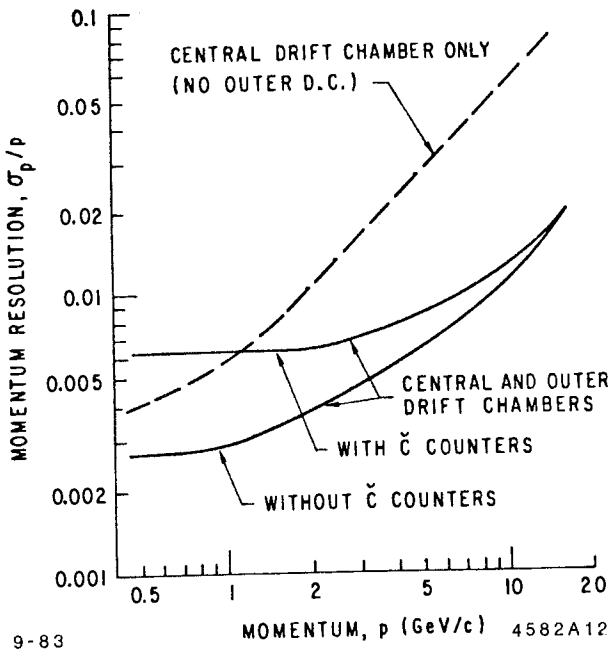


Fig. 3

Calculated Momentum Resolution For All Tracks

electrons are distinguished in the HRS entirely by the electromagnetic shower calorimeter energy deposit. Tracks with energy deposited in the barrel calorimeter of <1.0 GeV are taken as $\mu^{\pm}$ candidates and those with barrel energy ≥0.4·p are taken as $e^{\pm}$. This selection resulted in 8915 Bhabha-scattering events in the barrel region, 811 μ pair events in the barrel region and 168 μ pair events in the end-cap region.

The response of the calorimeters to minimum-ionizing particles and to Bhabha-scattered electrons is shown in Figure 4. The minimum-ionizing tracks leave an average of 0.2 GeV of energy deposited in each system. Folding all 40 barrel modules, Figure 5 shows the azimuthal (ϕ) dependence in the modules where fiducial cuts were then imposed to eliminate 1° cracks at the edges. After making all the listed cuts, Figure 6 shows how well μ-e separation is accomplished without a muon detection system by plotting the <u>total</u> shower energy of the 2 charged tracks. There is clearly negligible feedthrough of electrons into the muon sample.

The results are then compared in detail with a Monte Carlo calculation based on the α^3 QED model including electroweak effects of Berends, Kleiss and Jadach.[3] Figure 7(a) compares the measured acolinearity distribution for $e^+e^-\rightarrow e^+e^-$ with the predicted distribution and Figure 7(b) does the same for the acoplanarity distribution showing good agreement with theory. The observed angular distribution for $e^+e^-\rightarrow e^+e^-$ is then shown in Figure 8. The normalization here is arbitrary since these wide angle Bhabha events are used to determine the actual accumulated integrated luminosity of the experiment. Nonetheless the shape of the angular distribution can be compared with the α^3 QED

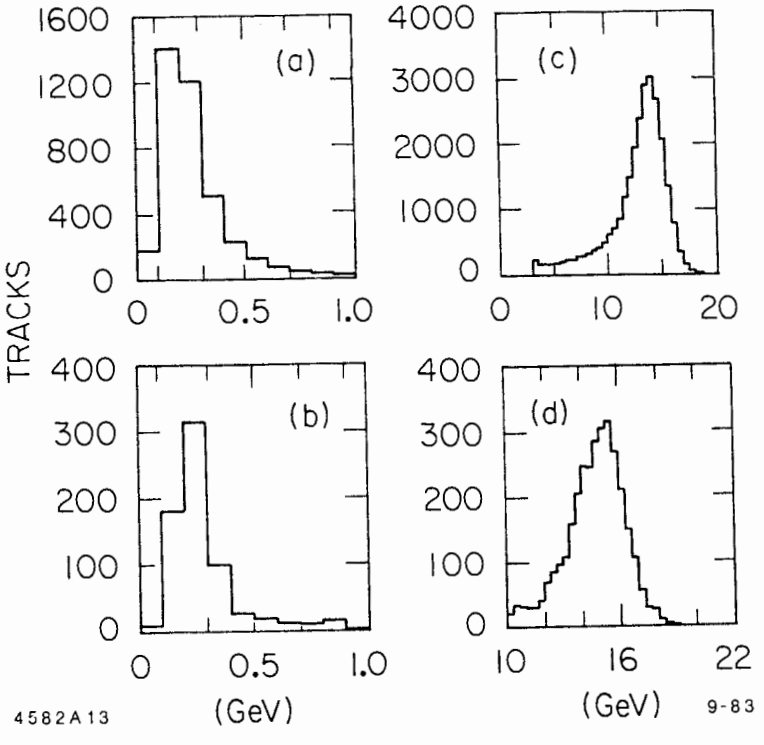


Fig. 4

Energy Deposit of Minimum-ionizing (a),(b) and Bhabha-scattered Electrons (c),(d) in Barrel and End Cap, respectively

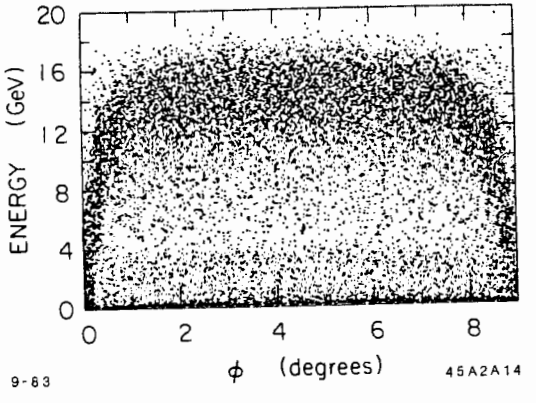


Fig. 5

Azimuthal Dependence of Hits in Barrel Module

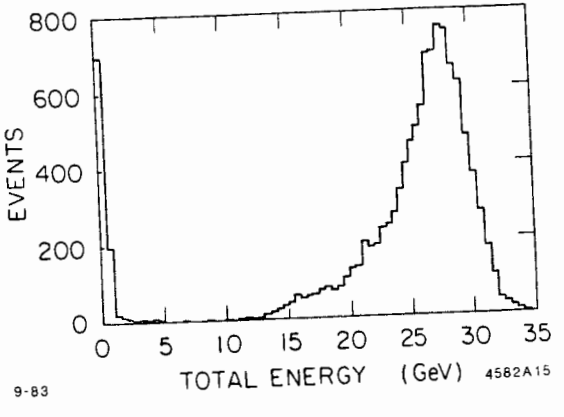


Fig. 6

Total Shower energy for 2 Track Events

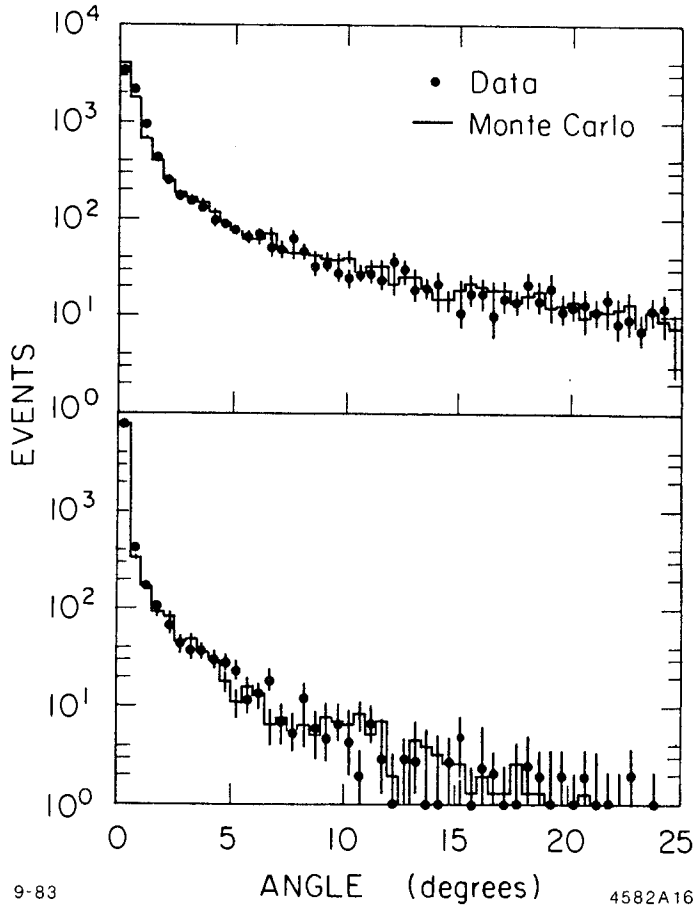


Fig. 7

(a) Acolinearity and (b) Acoplanarity for $e^+e^- \to e^+e^-$

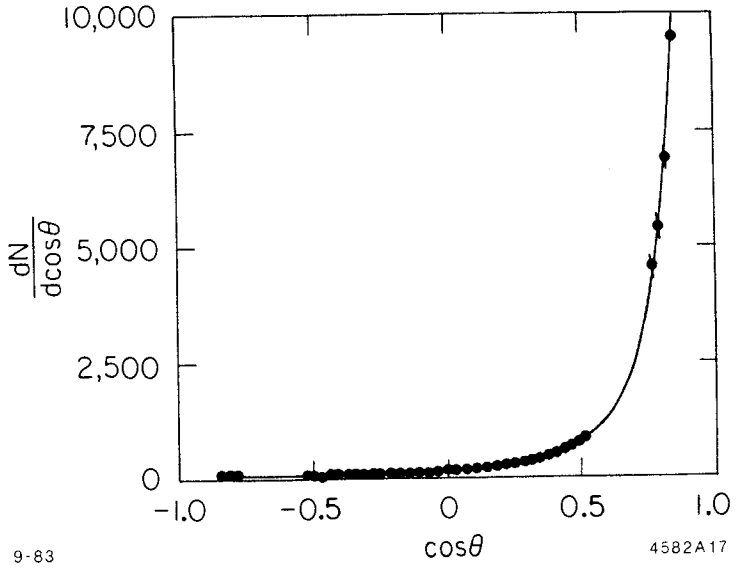


Fig. 8

Angular distribution for $e^+e^- \to e^+e^-$

predictions where δ_{meas} in Figure 9 is the ratio of observation to prediction. Deviations from the theory may be characterized in terms of cutoff parameters Λ_+. which can be related to modifications of the photon propagator or a finite size of the electron. Our values for the cutoff parameters are compared with other experiments in Table I.

The collinearity distribution for $e^+e^-\to\mu^+\mu^-$ is shown in Figure 10 and, once again, very good agreement is obtained with the Monte Carlo prediction. Using the luminosity from the Bhabhas, we measure for our acceptance $\sigma(e^+e^-\to\mu^+\mu^-) = 0.0353 \pm 0.0015$ nb. while the QED prediction for our solid angle from Berends, Kleiss and Jadach is 0.0352 ± 0.0008 nb. The comparison of these two numbers places limits on the cutoff parameters related to the size of the muon of $\Lambda_+,\Lambda_- > 172$ GeV (95% confidence level).

Measurement of the muon angular distribution in Figure 11 allows extraction of the electroweak parameters g_v^2 and g_a^2. With g_v^2 constrained to the value of 0.00 ± 0.18 obtained from a global fit to all the Bhabha scattering and μ pair data, the μ pair data alone is fit to obtain a value for the axial coupling constant of $g_a^2 = 0.33\pm0.17$. The corresponding asymmetry in the μ^+ angular distribution is $A_{\mu\mu} = -0.084 \pm 0.043$ and these results are compared with the results of other experiments in Figure 12 and in Table II. Agreement is quite good although the world average remains dominated by the high-statistics experiments of MAC,[4] TASSO[5] and Mark J.[6]

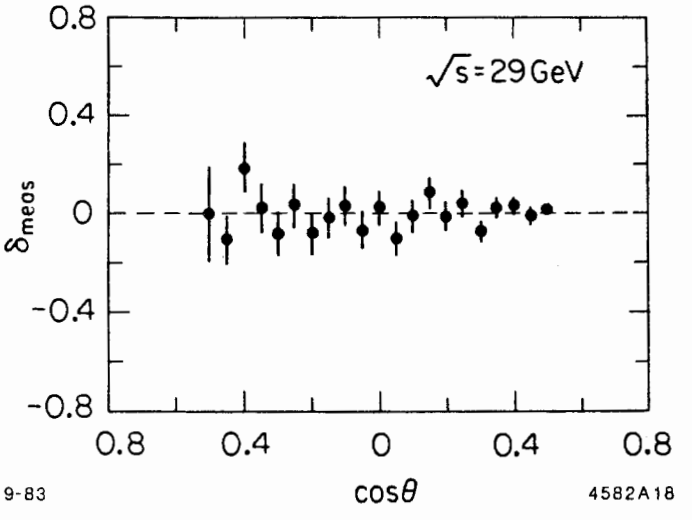


Fig. 9

Ratio of Measurement to Prediction for Bhabha Angular Distribution

Table I.

QED Cutoff Parameters

Experiment	Λ_+ (Gev)	Λ_- (Gev)
HRS	121	118
CELLO	83	155
JADE	112	106
MARK-J	128	161
PLUTO	80	234
TASSO	140	296

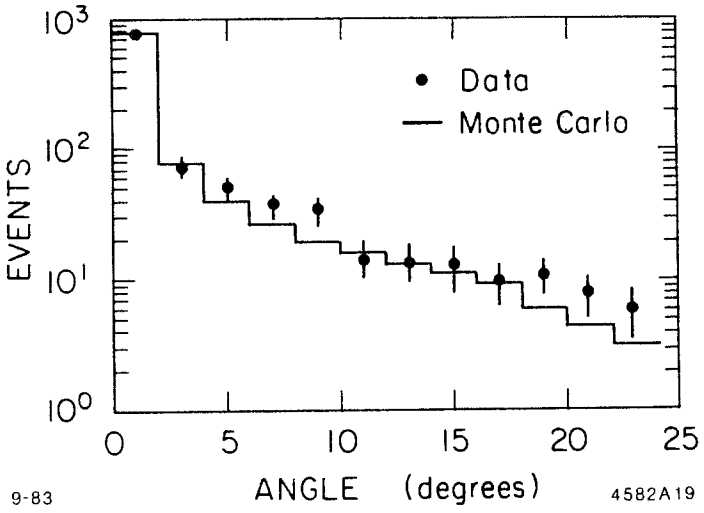


Fig. 10

Colinearity Distribution for $e^+e^- \to \mu^+\mu^-$

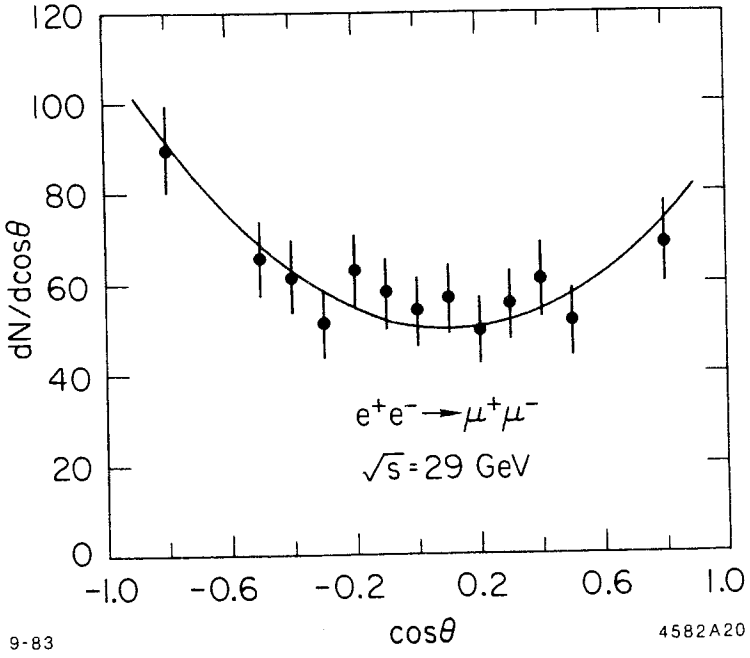


Fig. 11

Angular Distribution for $e^+e^- \to \mu^+\mu^-$

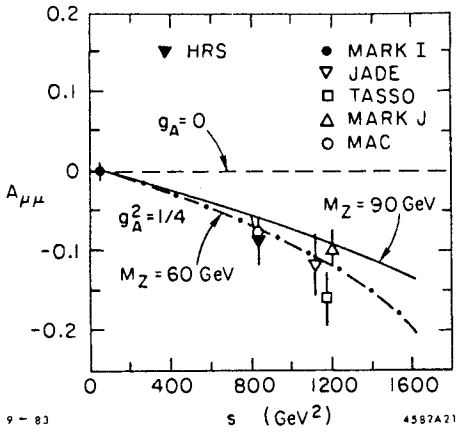


Fig. 12

Comparison of Muon Asymmetry from Different Experiments

Table II.

Weak Interaction Parameters

Experiment	g_a^2	g_v^2	$\sin^2\theta_W$	C
MRS	0.33±0.17	0.00±0.18	0.17±0.20	0.038
TASSO	0.35±0.09	-0.04±0.06	0.27±0.07	0.018
JADE	0.39±0.11	0.05±0.08	0.25±0.15	0.039
MARKJ	0.28±0.08	0.01±0.08	0.26±0.09	0.021
CELLO	0.17±0.17	-	0.21±0.12	-
PLUTO	-	-	0.23±0.17	0.060
MAC	0.31±0.08	-	0.24±0.10	-
MARKII	0.24±0.16	0.05±0.10	-	-

Scalar Electron Search

Among the predictions of supersymmetric models much discussed at this conference,[7] are the existence of scalar partners to the electron which could be produced in e^+e^- annihilation via the diagrams shown in Figure 13. Neglecting the contributions of the Z^0 and its supersymmetric partner, the Zino, these diagrams can be calculated, assuming here a very light or massless photino. Since the scalar electron is expected to decay rapidly into an ordinary electron and the neutrino-like photino, the event signature would be a highly coplanar electron pair with substantial missing energy, (on average approximately half).

Event selection[8] proceeded in way similar to the QED analysis described above: two prongs, both now required to be showering particles with E(Barrel)$>0.3\cdot$p, each with p $\geq$ 1.0 GeV/c and $|\cos\theta| \leq 0.55$ to confine tracks to the barrel region. Similar vertex and cosmic time-difference cuts were made. Then the sum of the magnitudes of the reconstructed momenta $|\vec{p}|$ was required to be between $0.2E_{cm}$ and $0.95E_{cm}$. The lower limit was to eliminate beam-gas and two-photon backgrounds while the upper limit was to cut out what was the principle background for the search: radiative Bhabha scattering. The real handle against Bhabha-scattered electron events with radiation was the acoplanarity which we required to be larger than 25°. In addition we required no observed hard ($E_\gamma \geq 0.4$ GeV) photons observed in the event. With these cuts, 6 events survived out of the 1.4×10^7 triggers accumulated in the 19.6 pb^{-1} data sample. The α^3 QED Monte Carlo calculation predicts 4.8 radiative Bhabha events are expected, as well as a negligible 0.02 τ events.

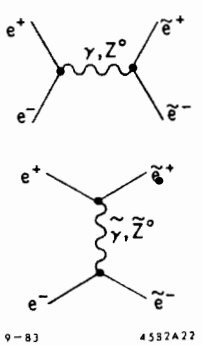


Fig. 13

Diagrams for Scalar Electron Production in e^+e^- Annihilation

Of the 6 surviving events, 4 were found by further examination to be entirely consistent with $e^+e^-\rightarrow e^+e^-\gamma$ with a calculated γ ray direction pointing directly at either the end or edge of a barrel counter which had recorded a substandard pulse height. The 5th event did not satisfy this interpretation but was quite consistent with a double radiative Bhabha process (α^4). Assuming colinear photons, as expected from the kinematics, the expected photons aim toward the very ends of 2 barrel modules which have in fact recorded substandard energy deposits. The remaining event had no struck barrel modules at all and is shown in Figure 14. It can also be interpreted as a double radiative event with photons directed toward the gap region between the barrel and end-cap calorimeters, but because it cannot be classified definitively, this event forms the basis for our upper limit on scalar electron production. Using the predicted cross section and our calculated acceptance, this upper limit is plotted in Figure 15 as a function of scalar electron mass. Masses between 1.8 GeV/c^2 and 14.3 GeV/c^2 can be ruled out at the 95% confidence level by this experiment for this simplest version of supersymmetric models.

Inclusive Hadron Production

The following section presents a preliminary analysis[9] using time-of-flight techniques of the charge particle fractions in hadronic events at E_{cm} = 29 GeV. Hadronic event selection required at least 5 reconstructed tracks be observed with good vertex ($|z| \leq 0.1$m and $r \leq 0.02$m), scaler momentum sum $|\vec{p}| \geq 8.7$ GeV/c ($0.3 \cdot E_{cm}$) and total calorimeter energy deposit greater than 1.45 GeV ($0.05 \cdot E_{cm}$). The data

H R S RUN=2327

EVENT= 8897 ECODE = 0
DCHITS = 49
NPRNG = 2 TRIG.= F1 F2 F3 S6 A1 D1 D2
SH SUM= 7.1 + 0.0

TRACK MOMENTUM THETA
1 −3.1 85.9
2 2.9 116.1

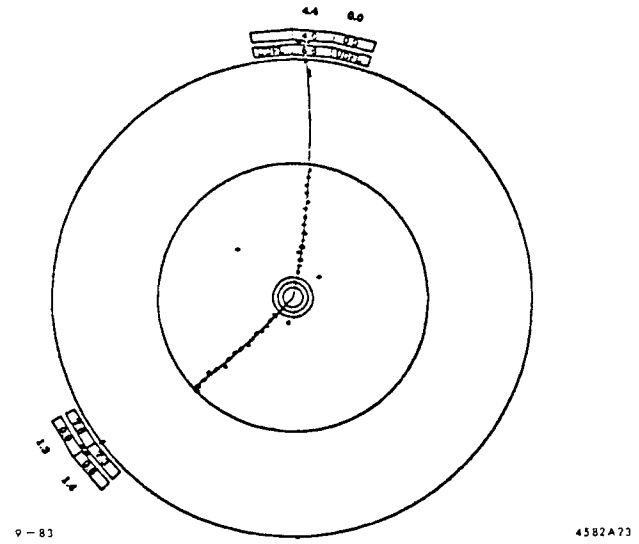


Fig. 14

Remaining Scalar Electron Event "Candidate", also consistent with double radiative Bhabha

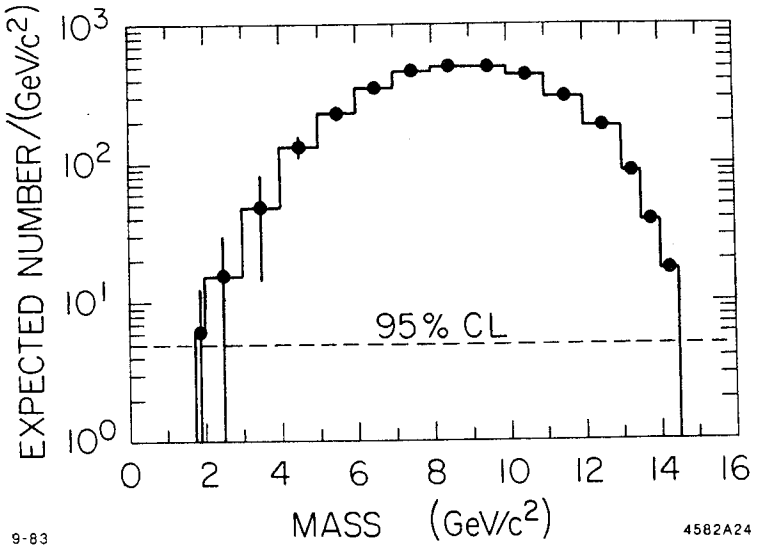


Fig. 15

Upper limit on Scalar Electron Cross Section versus Mass

sample used was once again the 19.6 pb^{-1} from our first year's running and this selection resulted in 8200 hadronic events with 88200 tracks.

A further selection of tracks for time-of-flight applicability was made in the preliminary analysis of these events: Tracks to be used were required to have struck a barrel module and the struck barrel modules were required to have had 1 and only 1 track intersect the module. Furthermore it was also required that there was no photon (additional PWC cluster) in the module struck by the charged particle and that the 3 methods of determining its z position (TDC, DC track, PWC) were consistent. Barrel fiducial cuts were also applied resulting in a surviving sample of 10100 tracks with very clean time-of-flight measurements.

Charged particle identification for this analysis was then done on a statistical basis by comparing the reconstructed mass-squared distributions for various momentum bins with the calculated resolution curves expected for various mixtures of produced pions, kaons and protons. Knowledge of the shape of the expected resolution for a given particle and pathlength is well understood from studying the shapes of well isolated minimum-ionizing particles such as those in μ pair events. Examples of m^2 distributions and the fits to them to determine the a priori produced particle rates are shown in Figures 16(a),(b) and (c) for typical low, moderate and high momentum bins, respectively. These plots show clearly, that even without classical separation criteria being met, the presence of the heavy particles, even at the highest momenta covered by the analysis, results in statistically significant effects in the m^2 distributions which are fit by well-understood resolution functions.

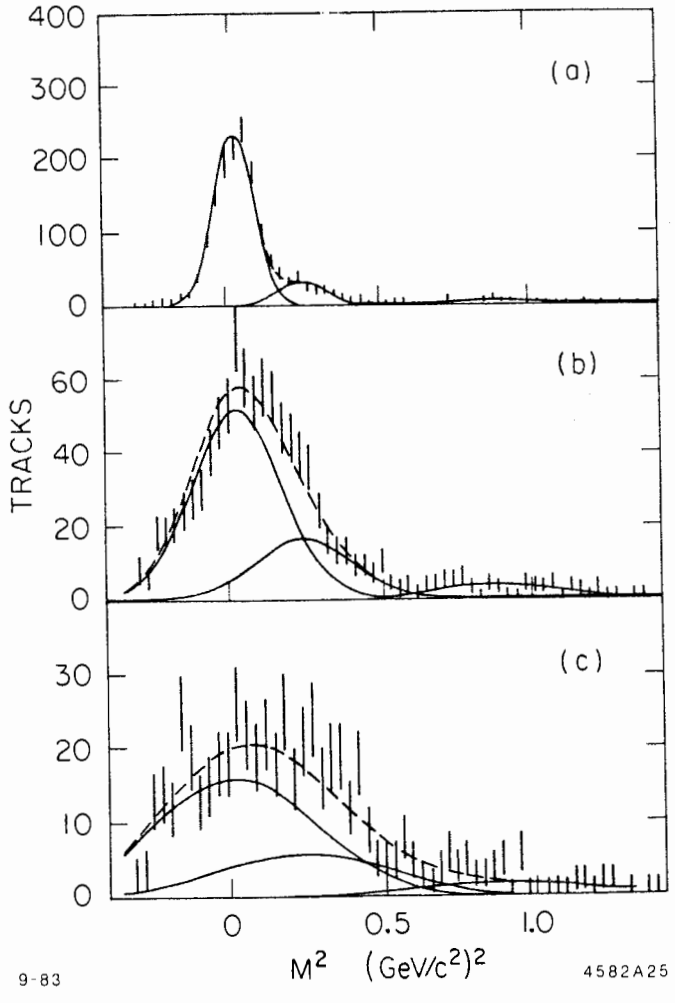


Fig. 16

M^2 Distribution from TOF for (a) $0.7 \leq p \leq 0.9$ (b) $1.1 \leq p \leq 1.3$ and (c) $1.5 \leq p \leq 1.7$

Detailed acceptance calculations which include all the effects of the track selection have not yet been done, but preliminary charged hadron fractions are plotted in Figure 17 and are compared there to results from the TASSO[10] collaboration at E_{cm} = 34 GeV. In terms of cross section $d\sigma/dp$, these results are compared in Figure 18. Figure 19 shows a comparison of our proton cross sections with those of Mark II,[11] TASSO[10] and JADE.[12]

D and D* Production

The search for different modes of charmed meson production has been performed with two different data samples. The first results were obtained from our completely analyzed data sample of 19.6 pb^{-1} and further preliminary results have been obtained from a special analysis of new data from the second year's running. When added to the 19.6 pb^{-1}, the second sample reaches a total integrated luminosity of ≈80 pb^{-1}. These samples correspond to 18% and 67%, respectively, of the data we have collected to date.

Hadron event selection for the 19.6 pb^{-1} sample proceeded as described in the previous section. No particle identification, however, has been applied in any of the resonance reconstruction presented here. Trying all tracks as both kaons and pions, the effective $K^-\pi^+$ mass distribution reconstructed in the HRS is shown in Figure 20(a) for $z_D \geq 0.4$ and 0.5, respectively, where $z_D \equiv 2E_D/E_{cm}$. A clear D° signal is directly observed in this data at $m_{K\pi}$ = 1.861 ± 0.005 GeV/c^2 containing 114±25 events for $z_D \geq 0.4$. The observed width of σ=0.017 GeV/c^2 is consistent with our calculated mass resolution for this state.

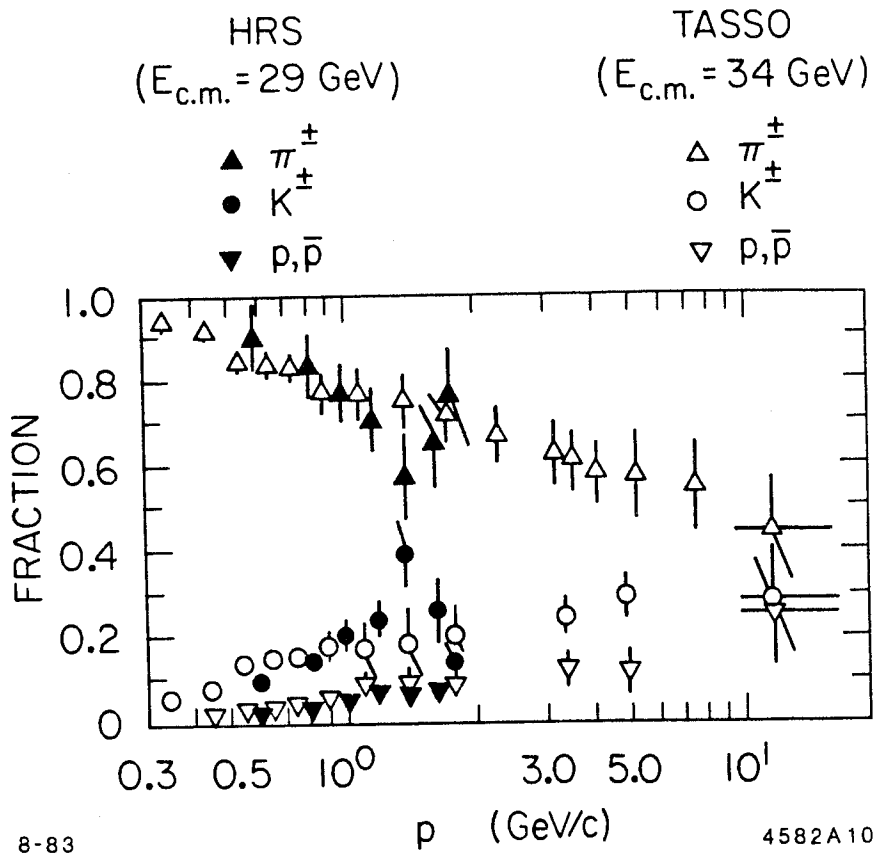


Fig. 17

Charged Hadron Fractions

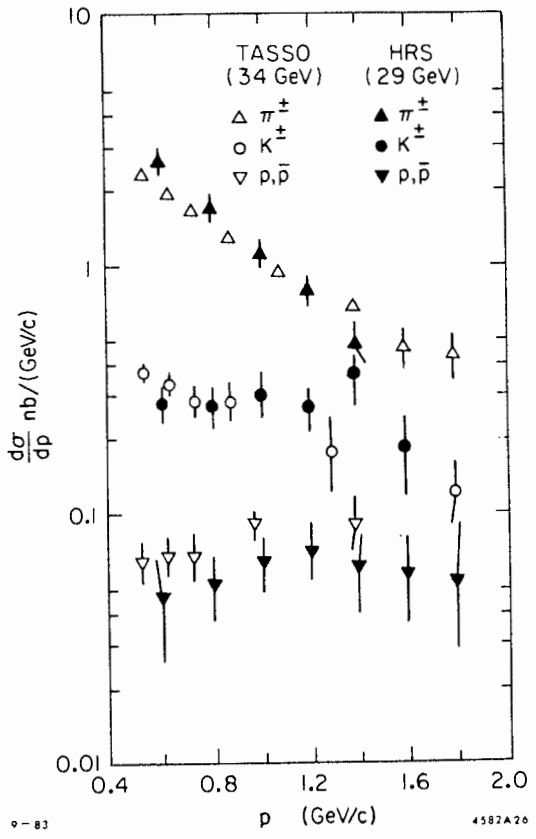


Fig. 18

Charged Hadron Cross Sections dσ/dp

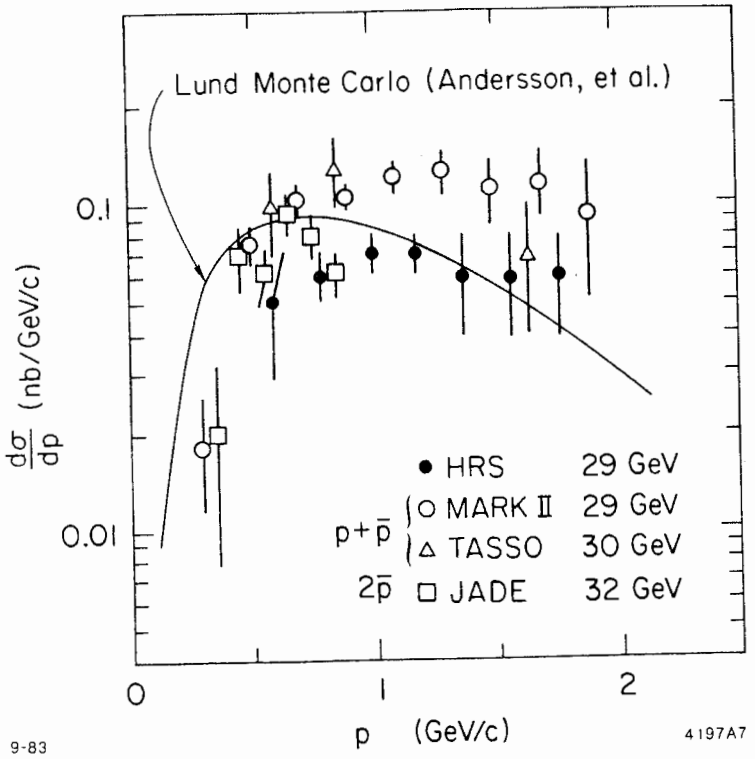


Fig. 19

Proton Cross Sections

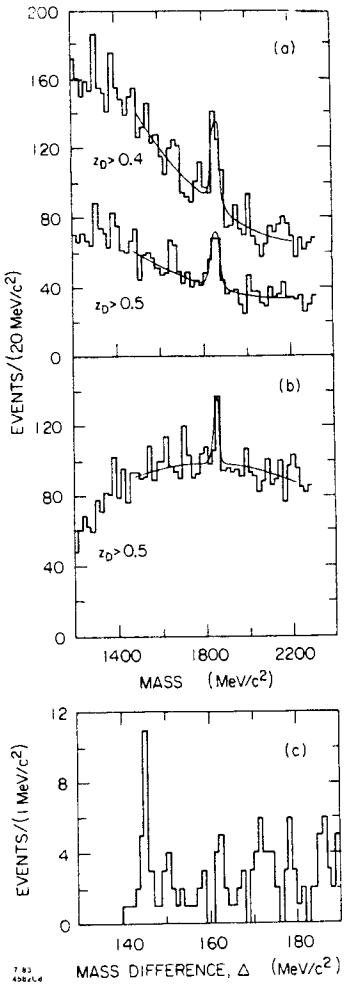


Fig. 20

(a) $K^-\pi^+$, b) $K^-\pi^+\pi^+$ effective mass distributions and (c) $D^0\pi^+$ - D^0 mass difference

A similar effective mass distribution for $K^-\pi^+\pi^+$ combinations is shown in Figure 20(b) for $z_D \geq 0.5$. It shows good evidence also for the D^+ with 52±16 events observed at $m_{K\pi\pi} = 1.867 \pm 0.004$ GeV/c². Both measured mass values for the D^0 and the D^+ are in good agreement with the particle data book values. The observed D^+ width (0.011 GeV/c²) is once again in good agreement with our calculation.

We have also measured D^* production using the now standard technique[13-15] of exploiting the low Q available in

$$D^{*+} \rightarrow D^0\pi^+ \quad (3)$$
$$\hookrightarrow K^-\pi^+$$

to obtain good resolution in the $D^0\pi$-D^0 mass difference. Figure 20(c) shows that for the HRS this technique allows us to see a clear D^* signal without making any z_{D^*} requirement at all. Here 16±4.5 events are observed with mass difference $\Delta = 0.1458 \pm 0.0015$ GeV/c².

Measuring D^0, D^+ and D^* in the same apparatus allows us to compare rates without problems of normalization between experiments. In the case of the previously observed $D^* \rightarrow D^0$ transition, some reported cross sections[13] have been extremely large with $R(D^*+\bar{D}^*)$ as high as 6.0 units. The latter value would exceed the total expected charm cross section of $R(c+\bar{c})=3.53$ units. We measure the ratio of produced D^0/D^* in the same interval of $z_D \geq 0.4$. This ratio is independent of the $D^0 \rightarrow K^-\pi^+$ branching fraction[16] with its large systematic uncertainty and only weakly dependent upon the acceptance calculation but it still depends on the $D^{*+} \rightarrow D^0\pi^+$ branching fraction[17] which also has a large uncertainty. We obtain the value 1.7±0.7 where 0.7 would be expected based on the D^{*+}

branching fraction[17] if all D°'s came from the D*-D° transition. Thus with large errors, our results imply that there is probably some direct D° production in addition to that from D*. A similar ratio D°/D⁺ is measured in the z_D interval $z_D \geq 0.5$ to be 2.3 ± 1.2.

All three processes that we measure are related, of course, and together they place further constraints on D/D* ratio and, therefore, the production mechanism for D and D* production at PEP/PETRA energies. We show this in Figure 21 by plotting simultaneously the D⁺/D° and D**/D° rates where by rates we mean the observed rates in the particular mode being detected. That is, in Figure 21 we have extracted the branching ratios with their significant systematic errors from the measurements and attached those instead to the the "theoretical" curve also plotted in Figure 21. The theoretical curve simply connects the expectation for 100% D* production at one extreme with 100% direct D production and the assumption of pure isospin conservation, $\sigma(D^+)=\sigma(D^\circ)$, at the other extreme. Here direct means D production which does not come from process (3). The 1 σ and 2 σ contours of our measurement in Figure 21 also indicate that some admixture of direct and indirect D production is favored over the hypothesis of all observed D's coming indirectly from D* production. The preferred admixture, once again, would seem to be approximately equal amounts of direct and indirect D production.

The fact that the measured point in Figure 21 appears to be below the "theoretical" line could, in principle, have significance in terms of the possible production mechanism(s) for D mesons. For example, the production of D mesons which are products of B meson decays would be a

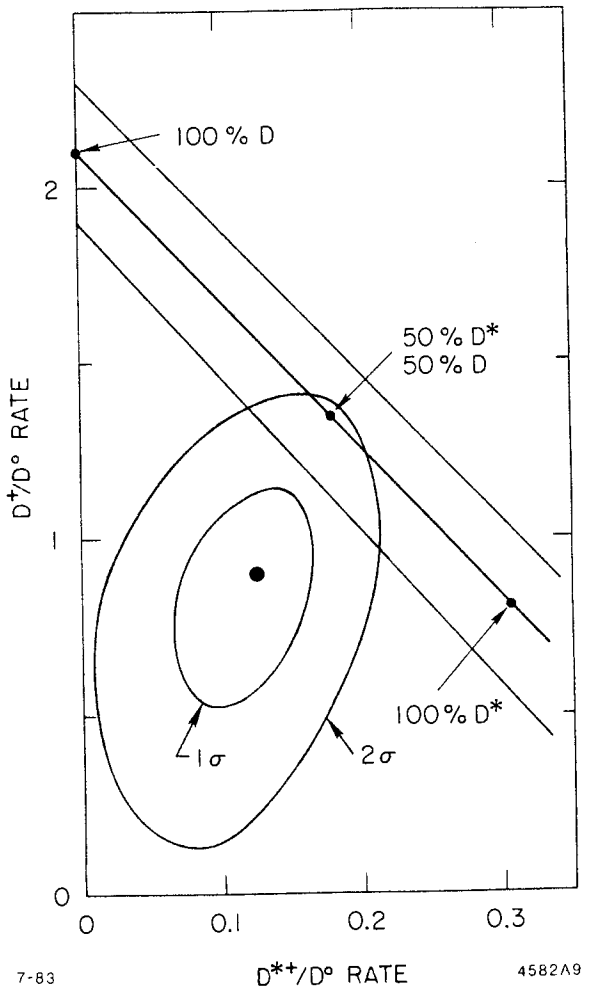


Fig. 21

D⁺/D° Rate versus D**/D° Rate

potential natural isospin violating mechanism which could favor D^0 production over D^+ and give this effect. This is suggested by the diagrams shown in Figure 22 for B^0 and B^- decay which can give extra D^0 production if, instead of the spectator quarks, quarks from the W decay are used to make the outgoing D.

Figure 23 shows the D^0 data broken into z_D bins where we have performed a simultaneous fit to a smoothly falling background which is a function of both $m_{K\pi}$ and z_D to extract D^0 cross sections as a function of z_D. Due to the low background, extracting D^* cross sections as a function of z is a much easier task and the results for both particles are presented in Figure 24(a) as $D(z) \equiv 1/\sigma \cdot d\sigma/dz$. The D^0 and D^+ fragmentation functions, defined in this way, are in very good agreement with each other and can be simultaneously characterized by $\epsilon = 0.36 \pm 0.12$ where ϵ is the parameter in the form suggested by Peterson et.al.[18] for heavy quark fragmentation functions. A comparison of $s \cdot d\sigma/dz$ for D^{*+} production with other experiments at PEP and PETRA energies is shown in Figure 24(b). There are clear normalization differences between experiments for D^* production and also some disagreement among experiments about the shape at low z.

We have used a variety of forms consistent with our observed z-dependance to extrapolate the observed cross sections to all z to obtain measurements of the total cross sections for D^0, D^+ and D^* production. After full corrections including initial state radiation, we express these as ratios to the μ pair cross section:

$$R(D^0+\bar{D}^0) = 3.25 \pm 1.2$$

$$R(D^++D^-) = 1.35 \pm 0.6$$

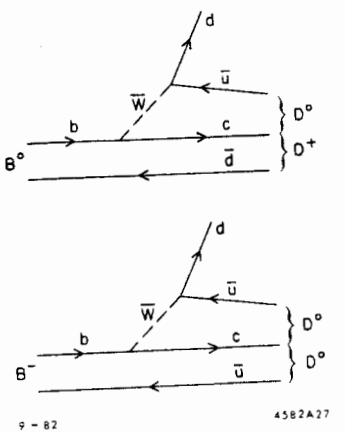


Fig. 22

Spectator Diagrams for B^0, B^- Decay

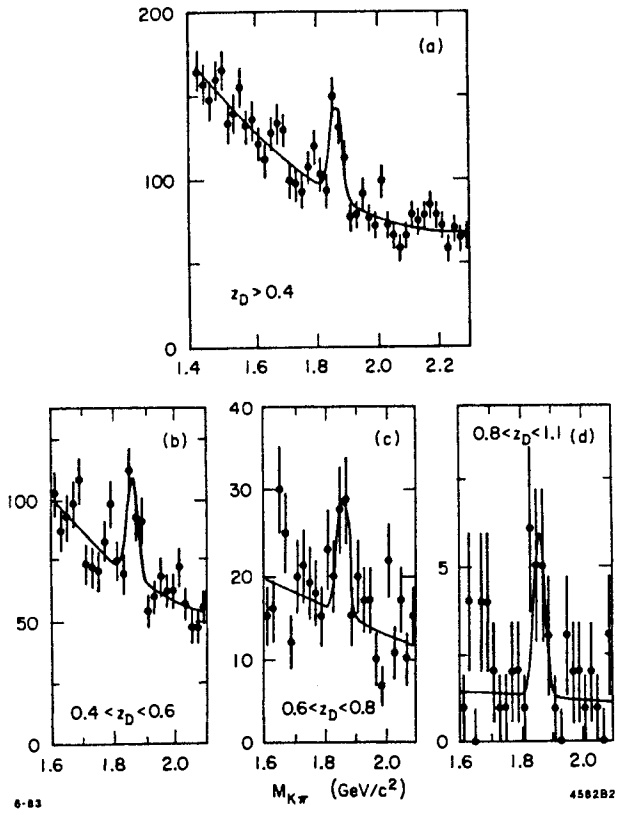


Fig. 23

$K^-\pi^+$ Mass Distribution as a function of z_D

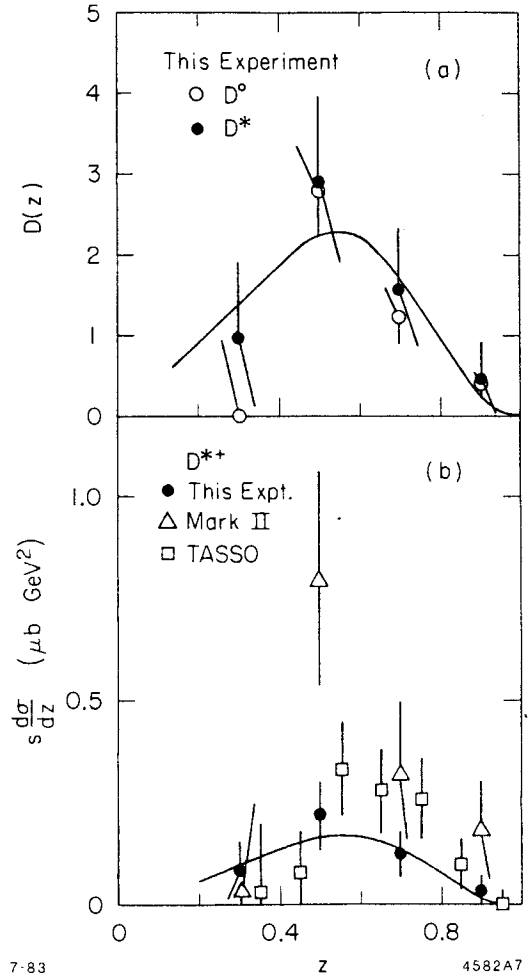


Fig. 24

(a). D°, D* Fragmentation Functions and (b) Comparison of s·dσ/dz between Experiments

and, assuming from isospin $\sigma(D^{*0})=\sigma(D^{*+})$,

$$R(D^*+\bar{D}^*) = 1.9 \pm 0.7.$$

Of these, $R(D^*+\bar{D}^*)$ can be compared with previous measurements. Our measurement is in good agreement with the value of 2.50±.64±.88 obtained by TASSO[14] but is substantially lower then Mark II's published value[13] of 3.1±1.55 for D^{*+} production alone. All experiments are consistent, however, within the large systematic errors.

Summing the above R-values for D^0 and D^+ production and dividing by $2\cdot\sigma_{\mu\mu}$, I plot our measurement of the quantity R_D in Figure 25 along with the only previous measurements which were obtained at SPEAR energies. I also show here the prediction for R_c as a function of energy (dashed line). Within the error bar, our measurement is consistent with expectation for total charm production although one must allow also for some F and charmed baryon production as well.

Events from the second year's running, added to make the 80 pb^{-1} sample, have been obtained via an online "express" selection of hadronic events. This made the additional requirements of ≥3 trigger processor tracks and, more importantly, calorimetric energy deposit ≥ 4.8 GeV ($0.17\cdot E_{cm}$). With the improved statistics provided by the preliminary analysis of this data, Figure 26 shows the D^* signal is easily observable as a cluster in a 2 dimensional plot of $m_{K\pi\pi}$ versus mass difference Δ with $z_D \geq 0.2$. The projections of this plot on the two axes are shown in Figures 27(a) and (b). Figure 27(a) shows very clear D^* peak with most of the events falling in a single 1 MeV/c^2 bin in the mass difference Δ. A total of 66 ± 14 events are observed. With such

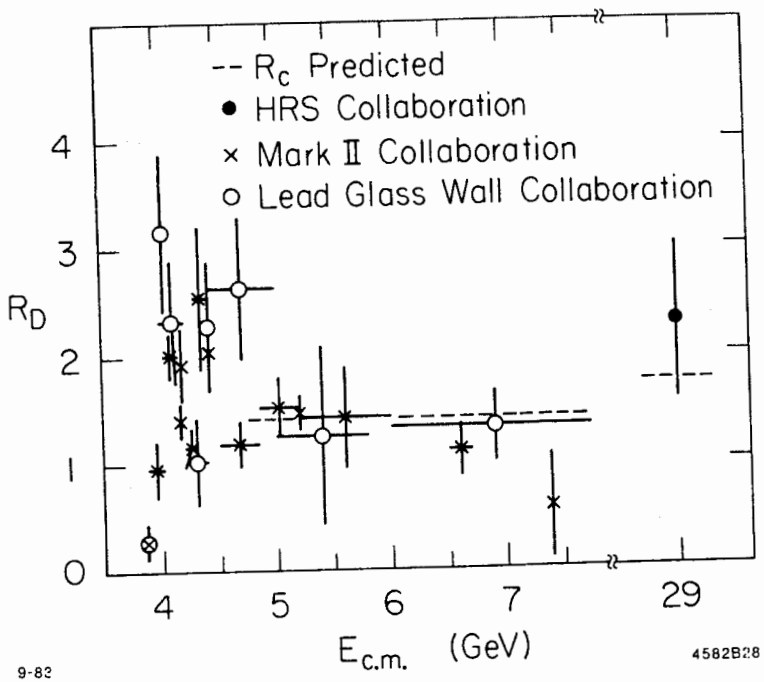


Fig. 25

$R_D \equiv (\sigma_{D^0}+\sigma_{D^+})/2\sigma_{\mu\mu}$ from Different Experiments

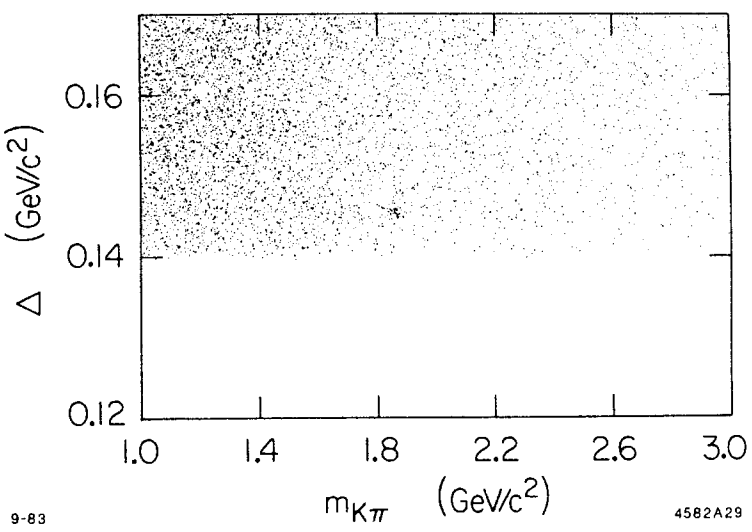


Fig. 26

$m_{K\pi\pi} - m_{K\pi}$ Mass Difference versus $m_{K\pi}$ Mass

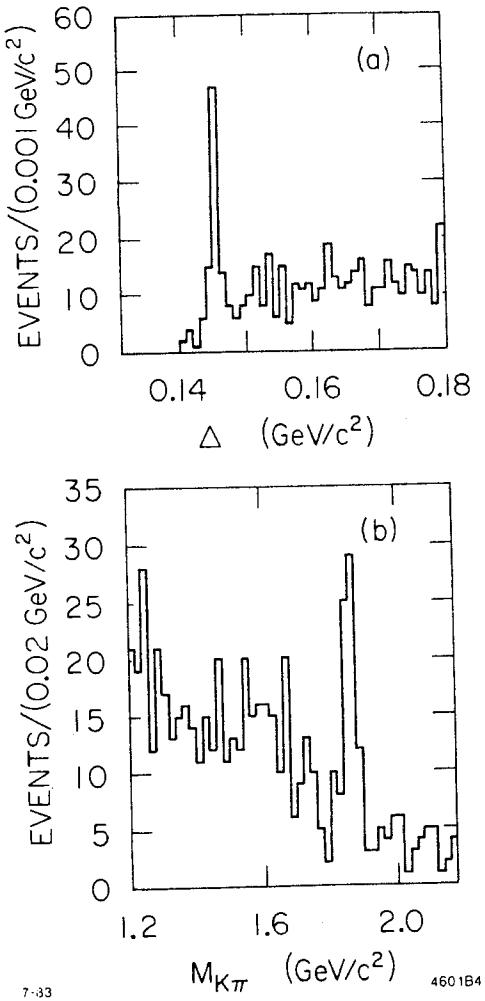


Fig. 27

(a) Mass Difference $m_{K\pi\pi} - m_{K\pi}$ for D^0 Band in $m_{K\pi}$ and (b) Mass $m_{K\pi}$ for $D^{*}-D^0$ Band in Mass Difference

data the z-dependance can almost be read off the 2 dimensional plot of z_{D^*} versus Δ shown in Figure 28. Figure 29 shows the Δ plot for several bins of z_{D^*}. A clear signal is observed in the lowest z-bin of 0.2 to 0.4 which has not been observed previously. These data allow the cleanest high-statistics' determination of the D* fragmentation function to date. This is shown in Figure 30 and can be characterized by the ε parameter in an empirical fit of $\epsilon = 0.29 \pm 0.10$. The preliminary cross section measured from the 80 pb^{-1} data sample is $R(D^{*+}\bar{D}^{*}) = 2.0 \pm 0.7$ and this is completely consistent with the value which was obtained from our completely analyzed 19.6 pb^{-1} sample, given previously.[19]

We have used this data to measure the D* angular distribution which is plotted in Figure 31. An asymmetry is observed of $A = -0.25 \pm 0.18$ in these data for $z_{D^*} \geq 0.4$ where the standard model predicts an asymmetry of ≈-0.09 for a pure c-quark sample. Before doing this analysis, careful systematic studies of possible asymmetries in the detection efficiency, done previously for the μ pair asymmetry measurement, have been extended to the hadronic event sample. Upper limits for such systematic effects are incorporated in the quoted error for the D* asymmetry.

Study of Quark Fragmentation at 29 GeV

We have begun a systematic study of quark fragmentation at 29 GeV with two points of view in mind:

1. that quark fragmentation should be better understood before focussing on explicit effects of different QCD models, and
2. a comparison of e^+e^- results with those of hadronic interactions may reveal new insights about both.

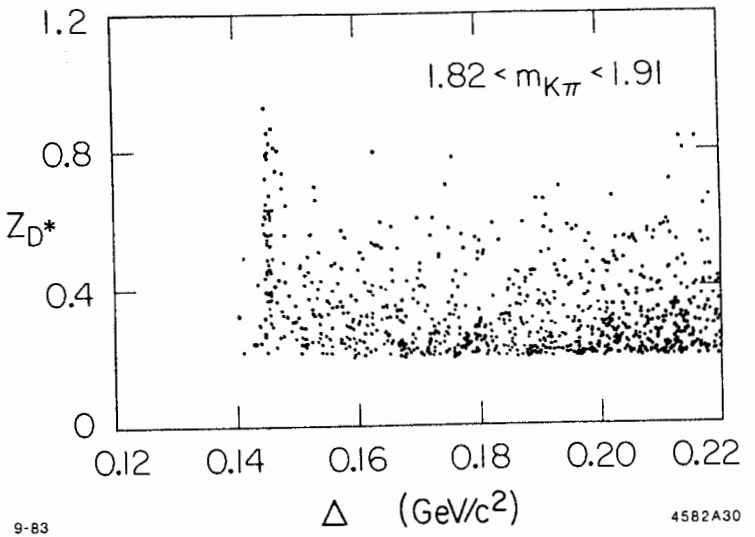


Fig. 28

Mass Difference Δ versus z_{D^*}

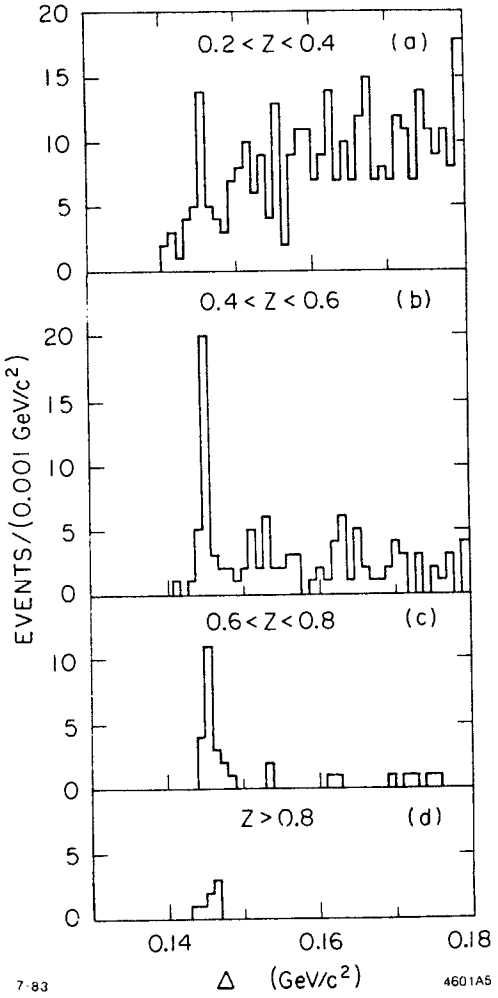


Fig. 29

Mass Difference for several bins of z_{D^*}

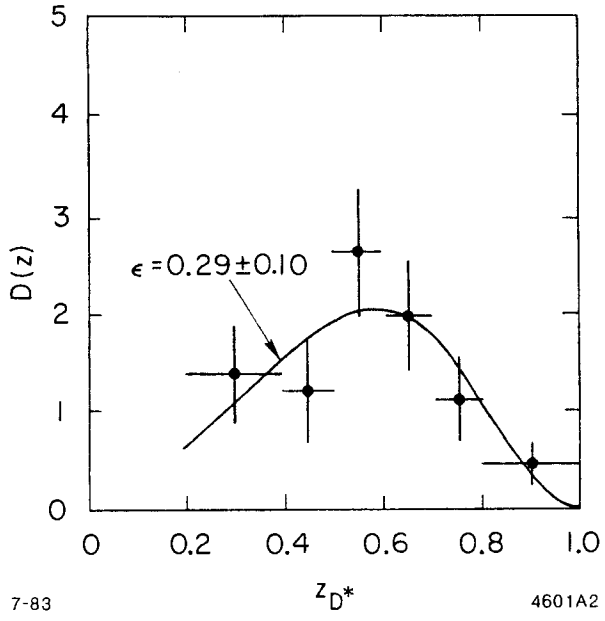


Fig. 30

D* Fragmentation Function measured from 80 pb^{-1} Data

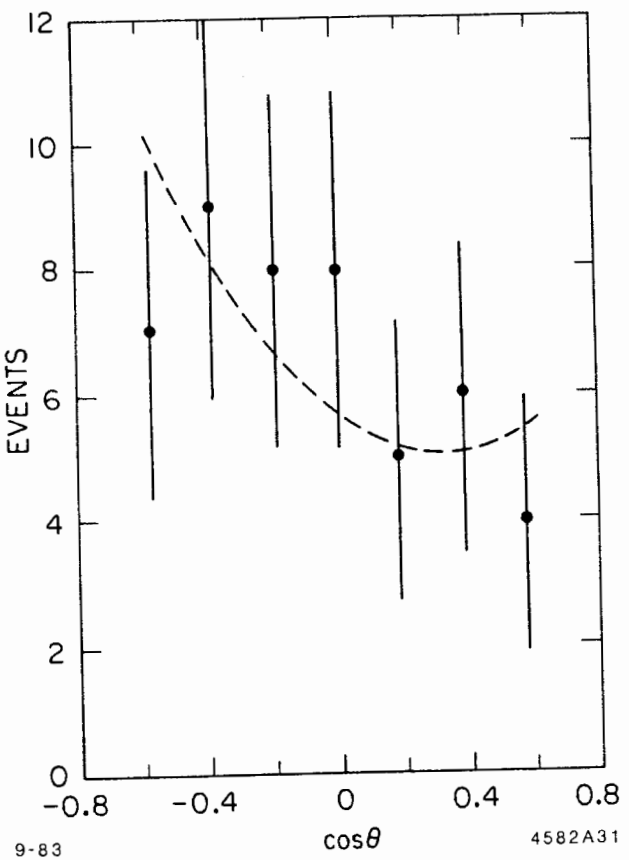


Fig. 31

D** Angular Distribution (z_D*≥0.4)

I report here preliminary results from the HRS on: (i) jet parameters and 2-jet selection, (ii) multiplicity, (iii) independent fragmentation tests, (iv) single particle distributions and (v) two particle correlations.

Hadronic event selection was as before: $\Sigma|\vec{p}| \geq 0.3 \cdot E_{cm}$, E(calorim)$\geq 0.05 \cdot E_{cm}$ and ≥5 tracks with good vertex. In addition, we have made a 2-jet requirement on the events used for this study. This was done by requiring the sphericity S ≤ 0.25 and aplanarity A ≤ 0.1 for these events. In addition, the thrust axis was required to be ≥45° for fiducial containment and we also required $\Sigma|\vec{p}|$ ≥2 GeV/c for the momenta in each jet separately. Figure 32 shows a plot of sphericity versus aplanarity for hadronic events where the cuts described above are indicated. These resulted in a sample of 4183 2-jet events.

Comparison of our global jet parameters gives quite satisfactory agreement with many previously published results and I only show one example (in Figure 33) of our average sphericity. A preliminary measurement of the multiplicity distribution is plotted in Figure 34 scaled by the average value. We measure $\langle N_{ch} \rangle = 12.0 \pm 0.2$ and compare the distribution here to the KNO scaling behavior observed in $\bar{p}p$ and pp interactions. Clear differences between hadronic and e^+e^- interactions are indicated here.

The idea of independent fragmentation of the 2 jets in these events can be tested by studying the correlation between the mean multiplicity measured for each jet. This is shown for our data in Figure 35, where we have arbitrally defined "forward" and "backward" jets relative to the thrust axis for the event. Figure 35 shows that the mean multiplicity

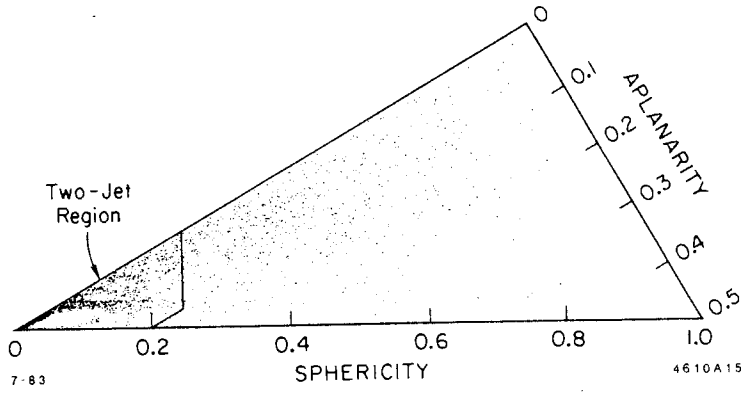


Fig. 32

Sphericity versus Aplanarity for hadronic events

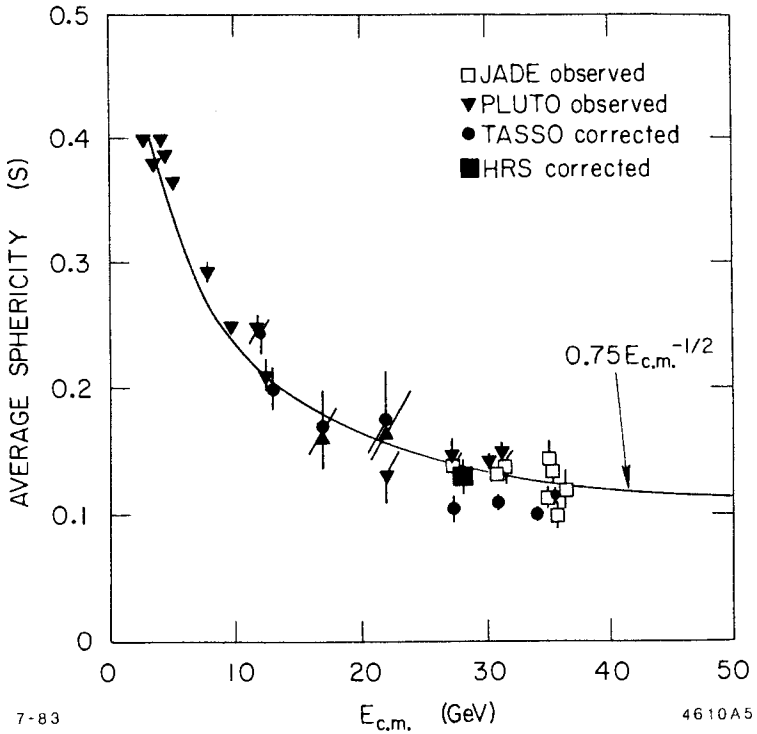


Fig. 33

Average Sphericity versus Energy

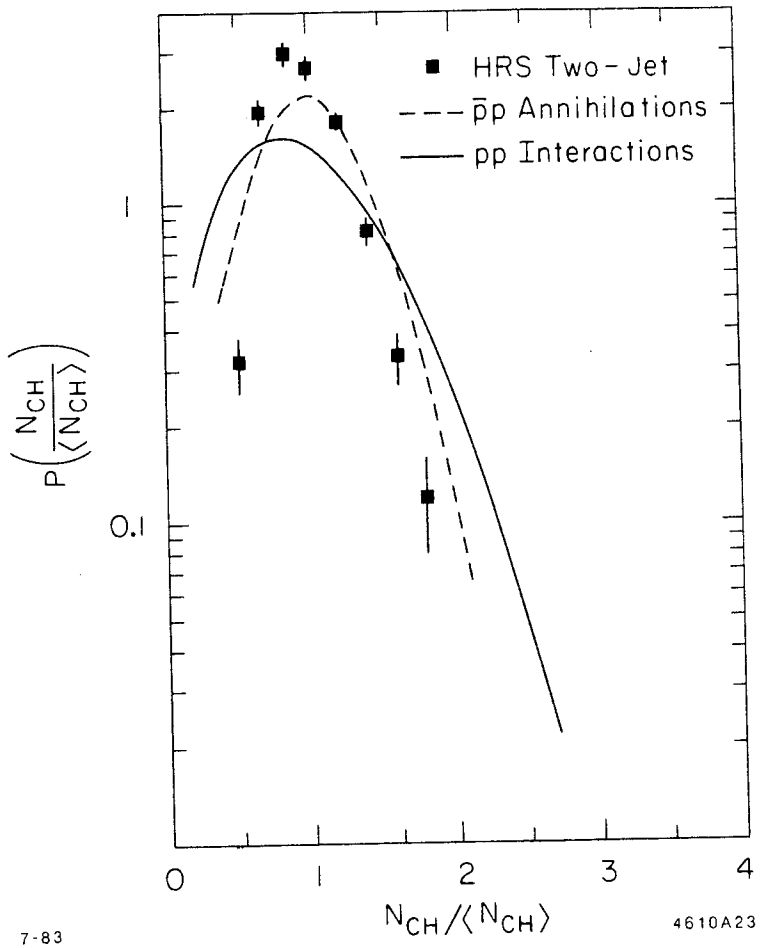


Fig. 34

KNO Scaling Multiplicity Distributions

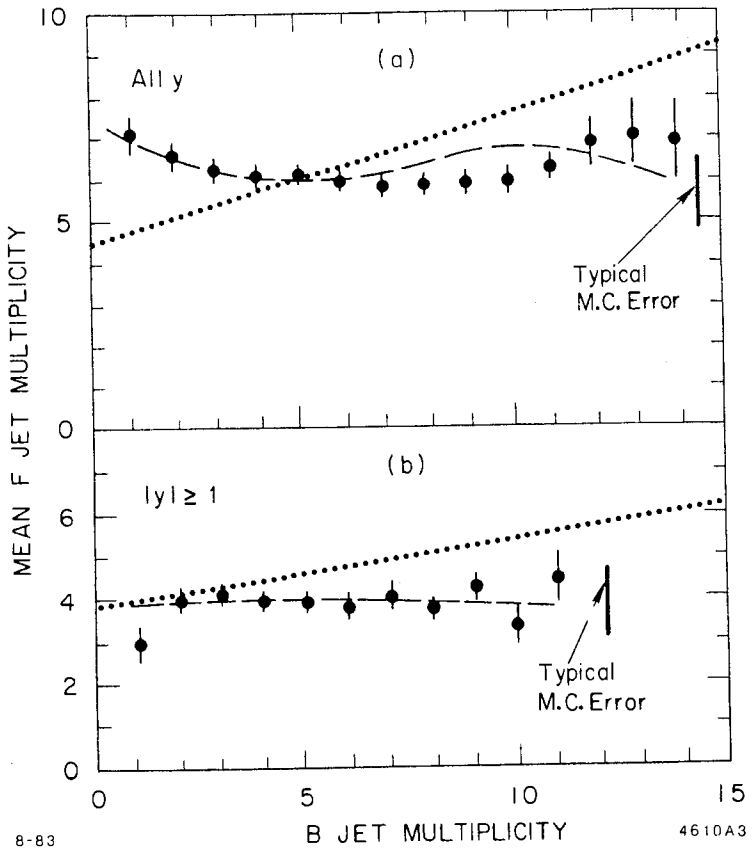


Fig. 35

Charged Particle Multiplicity Correlations

of the two jets is found to be quite independent of each other, especially when one has extracted the poorly measured $|y| \leq 1$ region. Comparison with 540 GeV $p\bar{p}$ results (solid line) shows quite different behavior is observed in the central region of hadronic interactions. This is probably explained by the fact that the hadronic case is effectively summing over the $q\bar{q}$ center-of-mass energy, which introduces the observed strong correlation. Our results in Figure 35 are quite consistent with the predictions of the Monte Carlo (dashed line) that we have used to correct the data. This Monte Carlo is based on the Lund model[20] using Feynman-Field fragmentation functions.

Figure 36 shows the rapidity distribution of single particles within the jets. We then define 2-body correlation functions

$$R = \frac{\rho_2(y_1,y_2)}{f\rho_1(y_1)\rho_1(y_2)} - 1 \qquad (4)$$

where the particle densities are defined

$$\rho_2(y_1,y_2) = 1/\sigma \cdot d^2\sigma/dy_1dy_2$$

$$\rho_1(y) = 1/\sigma \cdot d\sigma/dy$$

and

$$f = \langle N(N-1)\rangle/\langle N\rangle^2.$$

Figure 37 shows plots of the measured 2-body correlation as a function of y_2 for different values of test region rapidity y_1, as we scan y_1 from low to high values. For test rapidities in the central region ($0 \leq y_1 \leq 0.75$) we observe short-range correlations very similar to those observed in hadronic interactions with a correlation length of approximately one unit of rapidity. The 2-body correlations that we observe are, for all test regions, quite consistent with the Monte Carlo predictions.

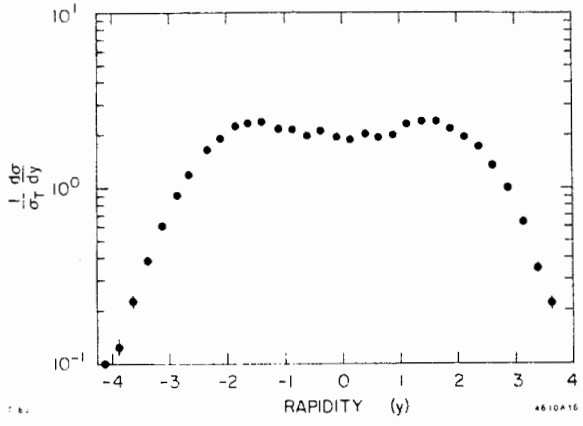


Fig. 36

36. Single Particle Rapidity Distribution

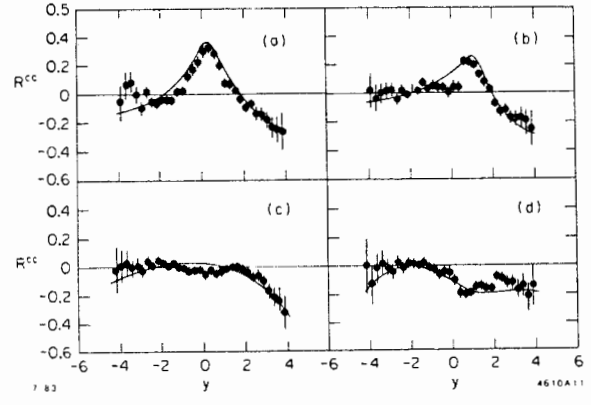


Fig. 37

37. Measurements of the 2-Particle Correlation Function of y_2 for (a) $0 < y_1 < .75$, (b) $.75 < y_1 < 1.5$, (c) $1.5 < y_1 < 2.5$ and (d) $2.5 < y_1 < 5.0$

A charge correlation function can be defined as

$$\phi(y_1,y_2) \propto [\rho^{+-}(y_1,y_2) + \rho^{-+}(y_1,y_2)] - [\rho^{++}(y_1,y_2) + \rho^{--}(y_1,y_2)] \quad (5)$$

with appropriate normalization. Taking a test region $2.5 \leq y_1 \leq 5.5$ which is as high a rapidity as possible in order to search for long-range charge correlations, our results are shown in Figure 38. We do in fact observe here long-range charge correlations beyond the strong short-range peak corresponding to local charge compensation within the jet. The magnitude of the long-range term is shown to be well reproduced by the Monte Carlo which we have been using.

A final interesting comparison between our e^+e^- results and those of hadronic interactions comes from looking at the rapidity gap distribution between two particles in the events. For a flat, uniformly-populated, single particle rapidity distribution and a Poisson multiplicity distribution, one would predict a pure exponential distribution of rapidity gaps with a mean gap length of λ equal to the observed average particle rapidity density, $\Delta y_\pi / \langle N \rangle$. Our results show in Figure 39 very good consistency with this simple prediction (solid line) using the average density λ that we measure from the single particle rapidity data of Figure 36 of 0.48 ± 0.05. This is in contrast to hadronic interactions which have reported non-exponential behavior here which has, in the past, been interpreted as the effects of low-mass clusters. No evidence for such clusters is observed in our data. This suggests rather that the hadronic effects, once again, are coming from the effects of summing over a wide range of center-of-mass energies and impact parameters.

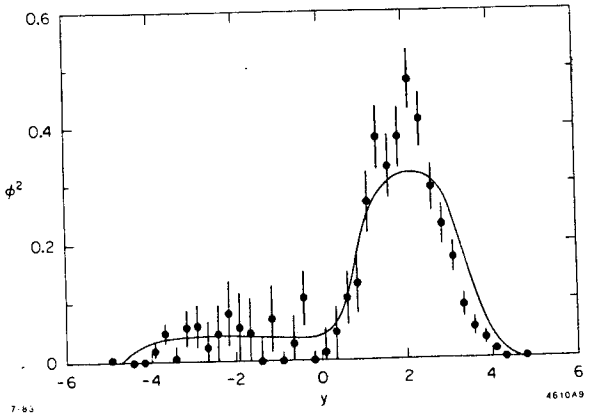


Fig. 38

38. Long Range Charge Correlations

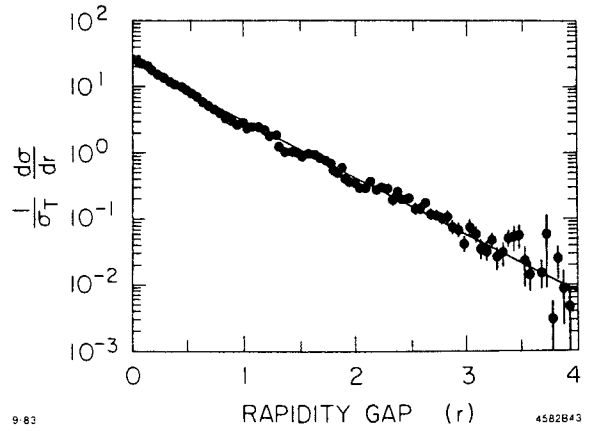


Fig. 39

39. Rapidity Gap Distribution

In summary, we observe that: (i) quarks fragment independently, (ii) jets remember the charge of the primary quark, (iii) short-range rapidity correlations very similar to those in hadron interactions are seen in e^+e^- and, finally, (iv) clusters do not seem to be seen in the e^+e^- data. This work marks the beginning of a systematic study of these and other related issues.

I would like to acknowledge my colleagues for discussions and for their hard work. Also discussions with F.Gilman and M.Jacob were very helpful. This work was supported by the U.S. Department of Energy.

References

1. C. Akerlof, G. Baranko, P. Baringer, I. Beltrami, D. Bender, D. Blockus, B. Brabson, J. Chapman, Y. Cho, S.T. Chui, B. Cork, R. DeBonte, M. Derrick, S. Ems, D. Errede, E. Fernandez, G.E. Forden, R. Fries, K.K. Gan, G. Gieraltowski, S.W. Gray, J.-P. Guillaud, N. Harnew, L. Hyman, K. Jaeger, L. Keller, P. Kesten, R. Klem, D. Koltick, P. Kooijman, S. Kooijman, F. Loeffler, J.S. Loos, F. LoPinto, U. Mallik, R. McIlwain, D.I. Meyer, D.H. Miller, B. Musgrave, H. Neal, C.R. Ng, D. Nitz, H. Ogren, P.P. Ong, L.E. Price, L.K. Rangan, D. Rubin, D. Rust, J. Schlereth, P. Schreiner, A.A. Seidl, E.I. Shibata, R. Singer, P. Smith, R. Stevens, R. Thun, T. Trinko, M. Valdata-Nappi, J. Va'vra, L.T. Wang, C. Ward, J.M. Weiss, M. Willutzky, R.J. Wilson and D.E. Wood, Argonne National Laboratory, Argonne, Illinois 60439, Indiana University, Bloomington, Indiana 47405, Lawrence Berkeley Laboratory, Berkeley, California 94720, University of Michigan, Ann Arbor, Michigan 48109, Purdue University, W. Lafayette, Indiana 47907 and Stanford Linear Accelerator Center, Stanford, California 94305.
2. See also D. Rubin, Thesis, University of Michigan, 1983.
3. F.A. Berends, R. Kleiss and S. Jadach, Nucl. Phys., B202, (1982).
4. E.Fernandez et.al., SLAC-PUB-3032, Jan. 1983.
5. R. Brandelik et.al., Phys. Lett. 117B, 369 (1982).
6. D.P. Barber et.al., MIT-LNS 124 (1982).
7. See contribution of J. Ellis to these proceedings.
8. See also R.J. Wilson, Thesis, Purdue University, 1983.
9. See also P.P. Ong, Thesis, Purdue University, 1983.

10. M. Althoff et.al., Z. Phys. 17, 5 (1983).

11. G. Goldhaber and J.M. Weiss, Proceedings of the APS/DPF Conference, Santa Cruz, 163 (1981).

12. W. Bartel et.al., Phys. Lett. 104B, 325 (1981).

13. J.M. Yelton et.al., Phys. Rev. Lett. 49, 430 (1982).

14. M. Althoff et. al., Phys. Lett. 126B, 493 (1983).

15. C. Bebek et. al., Phys. Rev. Lett. 49, 610 (1982).

16. R. Schindler et. al., Phys. Rev. D24, 78 (1981).

17. M.W. Coles et. al., Phys. Rev. D26, 2190 (1982).

18. C. Peterson et. al., Phys. Rev D27, 105 (1983).

19. We note that, in spite of the improved statistics, the error is relatively unchanged since it is dominated by the large uncertainties in the branching ratios.

20. J. Andersson, G. Gustafson and T. Sjoestrand, Phys. Lett. 94B, 211 (1980).

RECENT RESULTS FROM MAC

by M. Piccolo
for the MAC Collaboration *

ABSTRACT

MAC is currently taking data at PEP at a c.m. energy of 29 GeV. Topics presented in this talk include the accurate determination of the values of R, a high statistics study of the muon pair asymmetry, inclusive leptons measurements, the first measure of the b lifetime, limits on the production of the selectron for masses up to 22-25 GeV, and the photon structure function.

---

* Members of the MAC Collaboration are: E. Fernandez, W.T. Ford, A.L. Read Jr., J.G. Smith (University of Colorado); R. De Sangro, A. Marini, I. Peruzzi, M. Piccolo, F. Ronga (Laboratori Nazionali di Frascati dell'INFN, Italy); H.T. Blume, H.B. Wald, R. Weinstein (University of Houston); H.R. Band, M.W. Gettner, G.P. Goderre, B. Gottschalk, R.B. Hurst, O.A. Meyer, J.H. Moromisato, W.D. Shambroom, E. von Goeler (Northeastern University); W.W. Ash, G.B. Chadwick, S.H. Clearwater, R.W. Coombes, A.S. Kaye, K.H. Lau, R.E. Leedy, H.L. Lynch, R.L. Messner, S.J. Michalowski, K. Rich, D.M. Ritson, L.J. Rosenberg, D.E. Wiser, R.W. Zdarko (Stanford University and SLAC); D.E. Groom, H.Y. Lee, E.C. Loh (University of Utah); M.C. Delfino, B.K. Heltsley, J.R. Johnson, T.L. Lavine, T. Maruyama, R. Prepost (University of Wisconsin).

© M. Piccolo 1983

1. INTRODUCTION

MAC is a large solid-angle device with charged particle tracking, lepton identification capability and total energy measurement, and has been described elsewhere.[1]

Briefly, it consists of a cylindrical drift chamber with 10 layers of wires, immersed in a magnetic field of 5.7 kGauss produced by a solenoidal coil, and surrounded by an electromagnetic calorimeter, a set of 144 scintillation counters, a hadronic calorimeter and muon chambers (Fig. 1). For the analysis described in this talk, here is a summary of the most relevant parameters.

The central drift chamber (CD in the following) has a spatial resolution per point of 200 μm, and a momentum resolution $\sigma(p\perp)/p\perp = 0.065\ p\perp$ ($p\perp$ in GeV/c); the inner radius is 12 cm. The electromagnetic calorimeter (S.C.) consists of a lead-proportional wire chamber (PWC) sandwich in the central section and an iron-PWC sandwich in the end caps. Each lead sheet is 2.5 mm thick, the total thickness is of $\sim$ 15 r.l. The energy resolution measured with Bhabha events (at 14.5 GeV) is $dE/E = 0.05$, which corresponds to about 20% at 1 GeV. The segmentation for the readout is 192 sectors in azimuth and 3 layers in depth; the z coordinate is measured by current division.

The hadron calorimeter consists of 91 cm of steel absorber interspaced with PWC for a total of about 5 absorption lengths. The steel plates are magnetized by toroidal coils to about 18 kGauss, providing a momentum measurement with $dp/p = 0.30$, practically independent of p. The calorimeters cover $\sim$ 98% of the total solid angle and are surrounded by 4 layers of drift tubes for tracking muons.

The data whose analysis I will describe here were collected at PEP, the SLAC e^+e^- storage ring, from November 1981 to June 1983. The total integrated luminosity is 143 pb^{-1}, all taken at a c.m. energy of 29 GeV. Almost 2/3 of all data were obtained after February 1983 when, thanks to the efforts of the machine group, a very valuable increase in the machine luminosity was achieved.

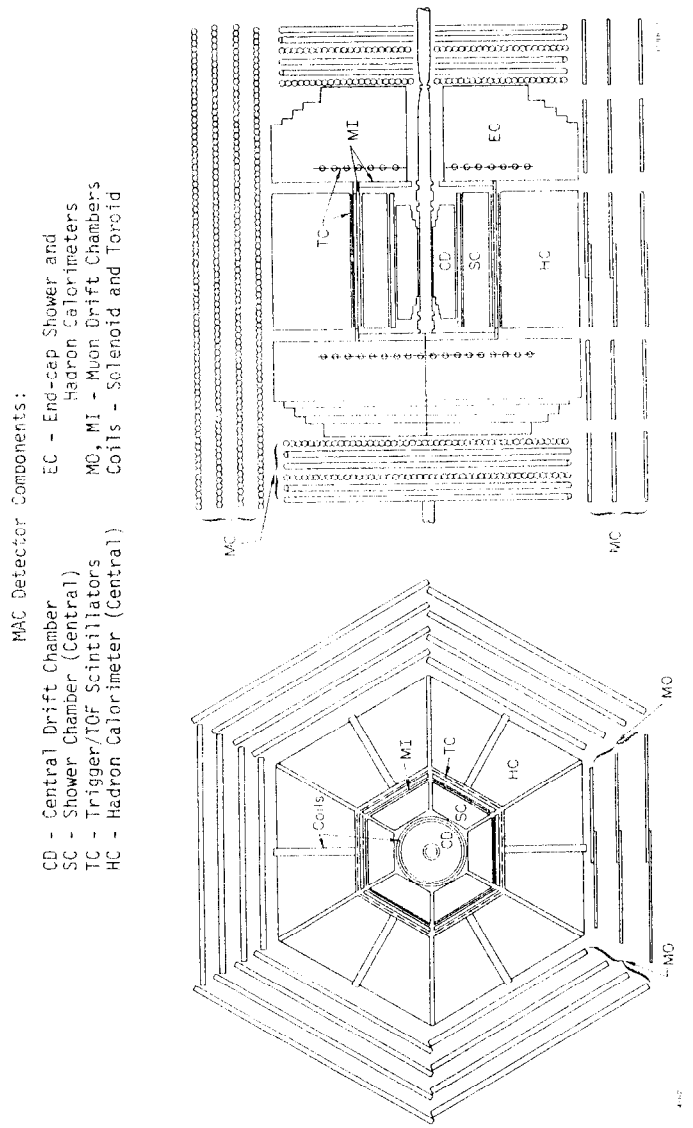


Fig. 1. MAC detector layout. The components are: CD central drift chamber, SC shower chamber, TC scintillators, HC central hadron calorimeter, EC end-cap calorimeter, MI, MO inner and outer muon drift chambers. Also indicated are the beam pipe, and the solenoid and toroidal coils.

2. THE MEASUREMENT OF R

Due to the increased statistics and the improved understanding of the systematics, we have measured R, the ratio of the total hadronic cross section to the muon pair production, to a precision of 3%.

We have performed two independent measurements of R, one using only a "fiducial" volume in the central part of the apparatus where the backgrounds are minimal, and another one which makes full use of the large solid-angle coverage to decrease the model dependence of the efficiency calculation.

The first analysis was performed on a sample of 18,356 events, for a total integrated luminosity of 81 pb^{-1}; in the second analysis 22,778 events were studied, corresponding to 49 pb^{-1}. The results from the two methods are in good agreement and our best estimate for the value of R is:

$$R = 3.89 \pm 0.02 \pm 0.11 \quad .$$

The error is dominated by the systematic uncertainties with the main contributions coming from the luminosity measurement (1.7%) and from the evaluation of the radiative corrections (1.5% and 1.1% for the two analyses respectively).

3. MUON PAIR ASYMMETRY

In the Standard Model the interference between the electromagnetic and weak interactions gives rise to an asymmetry in the angular distribution of the muon pairs.[2] This effect is sensitive to the axial-vector part of the weak neutral current, to order αG we have[3] :

$$d\sigma/dcos\theta = \frac{\pi\alpha^2}{2s}[(1+a_1)(1+cos^2\theta) + 2a_2 cos\theta], \qquad (Eq.\ 1)$$

$$a_1 = g_V^e\, g_V^\mu \;\frac{1}{\pi\alpha}\;\frac{G}{\sqrt{2}}\;\frac{-s}{1-s/M_{Z^\circ}^2}, \text{ and} \qquad (Eq.\ 2)$$

$$a_2 = g_A^e\, g_A^\mu \;\frac{1}{\pi\alpha}\;\frac{G}{\sqrt{2}}\;\frac{-s}{1-s/M_{Z^\circ}^2} \qquad (Eq.\ 3)$$

where θ is the angle between the incoming e^+ and the outgoing μ^+, and M_{Z° is the mass of the Z°. The asymmetry is given by:

$$A_{\mu\mu} = \frac{N^+ - N^-}{N^+ + N^-} = \frac{3}{4}a_2(1-a_1) \quad . \qquad (Eq.\ 4)$$

A forward-backward asymmetry is also expected from pure QED[4] : we have calculated the radiative corrections to Eq. (1) with the Monte Carlo (M.C.) program of Berends and Kleiss[5] to the order α^3. These terms produce a charge asymmetry of + 0.028 which has to be subtracted from the data in order to calculate the weak effect.

We have analyzed a sample of 10,258 events for a total integrated luminosity of 143 pb^{-1}; the background contamination from Bhabha ($< 0.3\%$) and tau pairs (0.8%) is evaluated to be 80 events. The differential cross section after radiative corrections is shown in Fig. 2.

In the assumption that $a_1 \ll 1$, we find the best fit value of a_2 from a maximum-likelihood calculation. The result is:

$$A_{\mu\mu} = -0.058 \pm 0.010 \pm 0.003 \quad ,$$

the systematic error is mainly due to possible Bhabha background.

The prediction of the Standard Model with $g_A^e g_A^\mu = 0.25$ and $M_{Z^\circ} = 90$ GeV is $A_{\mu\mu} = -0.060$ (including radiative corrections to the Z° exchange diagram).[6] The product of the axial-vector coupling constants from the fit is

$$g_A^e g_A^\mu = 0.24 \pm 0.04 \quad .$$

The ratio of the absolute cross section measured in MAC and the pure QED value ($a_1 = a_2 = 0$) is

$$\frac{\sigma_{meas}}{\sigma_{QED}} = 0.976 \pm 0.014 \pm 0.034 \quad ,$$

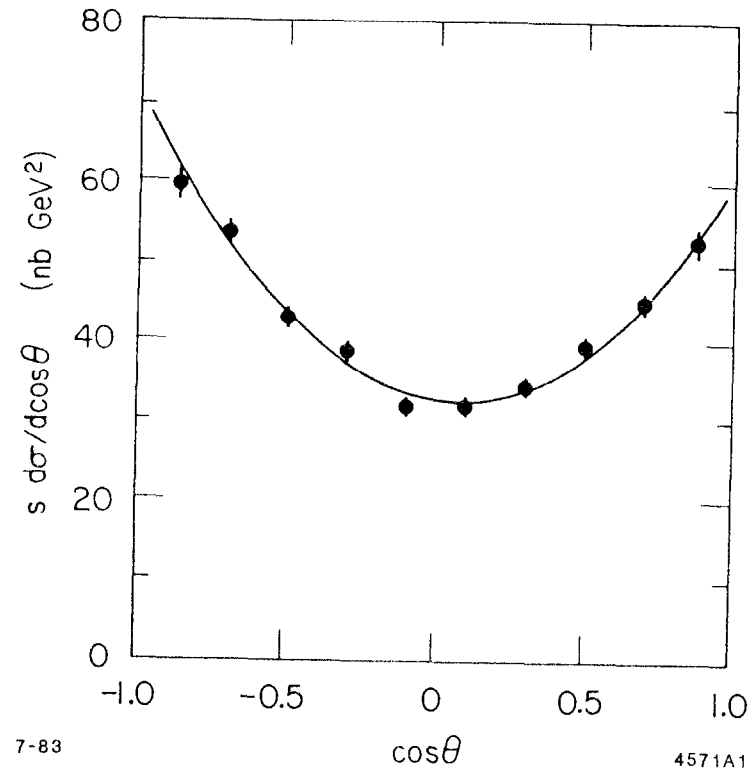


Fig. 2. Differential cross section of $\mu^+\mu^-$ pair production, after radiative corrections. The curve is the result of the fit.

from which we find

$$g_v^e g_v^\mu = 0.07 \pm 0.11 \quad ,$$

the error is dominated by systematic uncertainties in the normalization.

4. HEAVY QUARK FLAVOR TAGGING

Semileptonic decays of D and B mesons provide a simple signature for $c\bar{c}$ and $b\bar{b}$ events. From the study of multihadronic events containing a lepton, several properties of the primary quarks can be inferred.

Since the b quark is much heavier than the c quark, leptons from the B decay tend to have a higher $p_\perp$ with respect to the thrust axis of the event, the direction of which is close to that of the B meson.

Experimentally, in order to obtain a sufficiently clean sample of muons and electrons, we have to impose a cut of 2 GeV/c in momentum; semileptonic branching fractions and fragmentation functions of the c and b quarks are then coupled and cannot be measured separately.

4.1 Inclusive Muons

In MAC a muon is seen as a particle penetrating through the hadron calorimeter and tracked in the external chambers. In order to reduce hadronic punch-through we use only tracks with $p > 2.0$ GeV/c.

We have performed several studies based on muons[7] ; the criteria used to identify a muon vary with the purpose of the analysis. The identification efficiency depends, of course, on the set of cuts applied: it can be as high as 80% if a contamination of 50% background can be tolerated, or as low as 50% if a "clean" sample is needed, as in the case of the b lifetime measurement.

We have already published an analysis[8] on a partial sample of hadronic events ($\sim$ 25,000 for a total integrated luminosity of 54 pb^{-1}) where a sample of 476 muons

was used to study the fragmentation function $D_b(z)$, with

$$z = \frac{E_B + p_{//B}}{E_b + p_{//b}}. \qquad (Eq.\ 5)$$

The $p\perp$ distribution is shown in Fig. 3. From a simultaneous fit to the p and $p\perp$ distributions we extracted the fragmentation function to be peaked at high value, with an average $<z> = 0.8 \pm 0.1$ (Fig. 4).

If one parametrizes $D(z)$ according to Peterson et al.[9] as

$$D(z) = \frac{1}{z(1 - 1/z - \frac{\epsilon}{1-z})^2} \quad , \qquad (Eq.\ 6)$$

the fit to our data gives $\epsilon = 0.008^{+0.037}_{-0.008}$.

We have now an updated analysis based on our complete sample of data ($\sim$ 69,000 events, 143 pb^{-1}), in which a sample of $\sim$ 1,500 muons are identified, with a background evaluated to be 42%. We assume for the c quark fragmentation Eq. (6) with $\epsilon = 0.4$,[10] and fit the data to find the semimuonic branching fractions:

$$BR\,(b \rightarrow \mu X) = (12.3 \pm 1.8^{+1.7}_{-1.3} \pm 0.8)\%$$

$$BR\,(c \rightarrow \mu X) = (9 \pm 3)\% \quad .$$

The additional 0.8 error in $BR\,(b \rightarrow \mu X)$ takes into account the fact that its value changes from 11.3 to 12.9 as ϵ varies within its 68% confidence level range.

4.2 Inclusive Electrons

Electrons are identified as a track in the CD followed by consistent energy deposition in the shower chamber and no track in the hadron calorimeter. The selection criteria have been derived from the study of electrons in the detector (Bhabha and $ee\gamma$ events). In this analysis we consider only tracks with at least 1.8 GeV/c of momentum and in the central part of the detector ($|cos\theta| < 0.7$). We then require that the energy deposition in a narrow region around the track be consistent

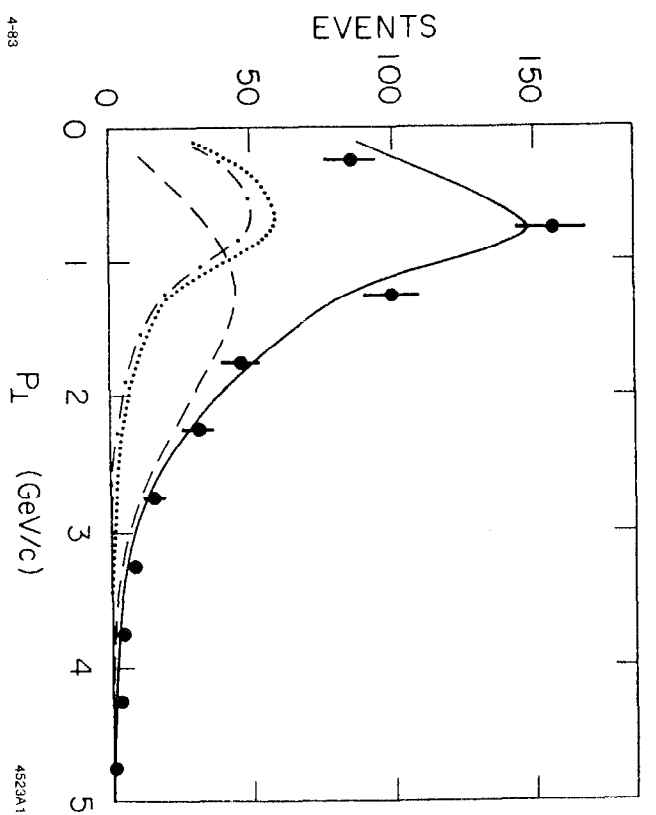


Fig. 3. $p\perp$ distribution of muons with $b\bar{b}$ (dashed curve) $c\bar{c}$ (dot-dashed), background (dotted), and total (solid curve) predictions.

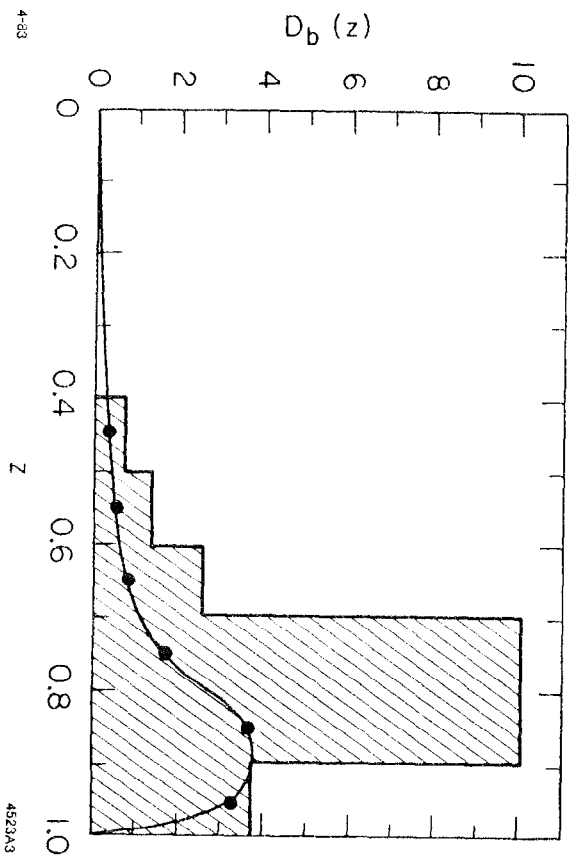


Fig. 4. One standard deviation envelope of all b quark fragmentation functions with acceptable fits to the data. The curve represents function (2) for $\epsilon_b = 0.008$.

with the longitudinal development of an electromagnetic shower. More in detail, the set of cuts imposed are the following:

$$\frac{E_I}{p} \geq 0.1, \frac{E_{II}}{p} \geq 0.3, \frac{E_I + E_{II} + E_{III}}{p} \leq 1.8, \frac{E_{hc}}{p} \leq 0.12$$

where $E_I, E_{II}, E_{III}, E_{hc}$ are the energy left in each layer of the shower chamber and in the hadron calorimeter, respectively, p is the momentum measured in the CD. The identification efficiency is $\sim 60\%$, with a slight p dependence. In a sample of $\sim 60{,}000$ multihadron events we observe 1540 electron candidates. The background comes essentially from three sources:

1. Early showering hadrons; the contamination has been calculated by M.C.[11] to be 1:230. We have performed a check using the 3-prong from τ decay, and found good agreement between data and Monte Carlo.
2. Overlap of a charged track with a shower from a hard photon; this effect has been also calculated by M.C.[12] Its effect is large in the low $p_\perp$ region and decreases rapidly with $p_\perp$.
3. Electrons from other sources; not all electrons come from the semileptonic decay of particles containing the c or the b quarks. There are cases in which a photon converts in the pipe but only one electron is tracked and appears to come from the primary vertex; there are electrons from the decay of the ψ or vector mesons, etc. The momentum distribution of these electrons is soft and the contribution in the high momentum range is negligible compared to 1) and 2).

From a fit to the $p_\perp$ distribution, assuming the same c and b fragmentation functions as for the muon analysis, we find the following values for the semielectronic branching ratios:

$$BR\,(b \to eX) = (11.3 \pm 1.9 \pm 3.0)\%$$

$$BR\,(c \to eX) = (8 \pm 3)\% \quad .$$

These results must be considered preliminary, they are however, in good agreement with previously reported data from other experiments.[13]

5. MEASUREMENT OF b LIFETIME

High $p_\perp$ leptons are a good tag for $b\bar{b}$ events, as shown in Fig. 3; for $p_\perp > 1.5$ GeV/c both the background and the contribution of the decay of charmed particles decrease rapidly. The lifetime of particles containing the b quark can then be inferred from the study of the distribution of the impact parameter of high $p_\perp$ leptons.

For this analysis[14] we have used a sample of $\sim$ 50,000 multihadronic events. Muon candidates were defined as requiring that a track in the external drift chambers be matched in polar angle and momentum measurement to a track reconstructed in the CD,and to a segment reconstructed from the energy deposited in the calorimeters, with pulse heights compatible with those of minimum ionizing particles. For $p_\perp > 1.5$ GeV/c the misidentification probability is 1:500, which corresponds to a background of (14 ± 7) % divided roughly into 6% from pion and kaon decays and 8% from punch-throughs.

Electron candidates were found in a slightly smaller sample of events, corresponding to 98 pb^{-1}, and were defined as in the analysis of inclusive electrons described above. With a cut at $p_\perp = 1.5$ GeV/c the background is (25 ± 8) %, almost entirely due to early interacting hadrons.

The sample of leptons so obtained consists of 155 muons and 113 electrons; for each of these tracks the impact parameter δ, as projected in a plane perpendicular to the beam axis, was measured. The flight path ℓ of the parent meson and the decay angle ψ were defined, in the same plane, as shown in Fig. 5. The quantity δ is defined with a sign: it is assumed to be positive if a particle emitted along the thrust axis, toward the intersection with the lepton track, would decay into the lepton in the forward direction.

Apart from the effect of the finite resolution, a true decay can produce a negative δ in two cases: if the lepton is emitted backward, or if its direction is in between the parent and the thrust axis. This dilutes the effect of a non-zero lifetime, Monte Carlo calculations show that the loss of sensitivity of the method is negligible for

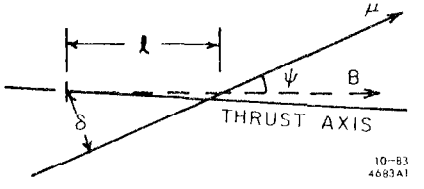


Fig. 5. Definition of the impact parameter δ. The dashed line is the (unknown) direction of the B mesons.

B mesons, while for the background the cancellation is nearly complete.

The lifetime can be related to the average value of the δ distribution:

$$< \delta >=< \beta\gamma \quad sin \quad \theta \quad sin \quad \psi > c\tau = \alpha c\tau \qquad (Eq.\ 7)$$

where θ is the polar angle of the lepton track.

The factor α can be calculated by Monte Carlo, the result is not practically affected by the hypothesis introduced for the production and decay of B mesons. The result is in fact quite insensitive to the B momentum: the decay angle ψ shrinks at the increase of the B momentum while the path length ℓ grows for the relativistic boost, and the two effects almost entirely compensate.

The error with which δ is measured depends on the accuracy in the extrapolation of the lepton track and on the effective size of the beam interaction area. The center of this area is known quite precisely and its position is monitored on a run-by-run basis from the study of the Bhabha events. We find that the effective rms beam size is $\sim$ 0.4 mm horizontally, and $\sim$ 0.1 mm vertically. The error in the extrapolation of the lepton direction is obtained from the error matrix in the fit to the track. The distribution of the global error in δ is shown in Fig. 6; tracks for which this error is bigger than 1 mm are rejected. The distribution of δ, weighted by the inverse of the squared error, is shown in Fig. 7 for muons and electrons separately. In both cases the average value is significantly different from zero:

$$< \delta_\mu >= (158 \pm 81)\mu m \quad < \delta_e >= (174 \pm 75)\mu m \quad .$$

If we define f_b, f_c, f_{bg} as the fractions of $b\bar{b}$, $c\bar{c}$ and background events in the sample, and δ_c and δ_{bg} as the average values of δ expected for $c\bar{c}$ and background, we have:

$$< \delta >= f_b\ \alpha c\ \tau_b + f_c\delta_c + f_{bg} \quad \delta_{bg} \quad . \qquad (Eq.\ 8)$$

The values of δ_c and δ_{bg} were obtained from Monte Carlo using the Lund Production Model[15] and the literature values of the charmed particles' lifetimes.[16] The heavy

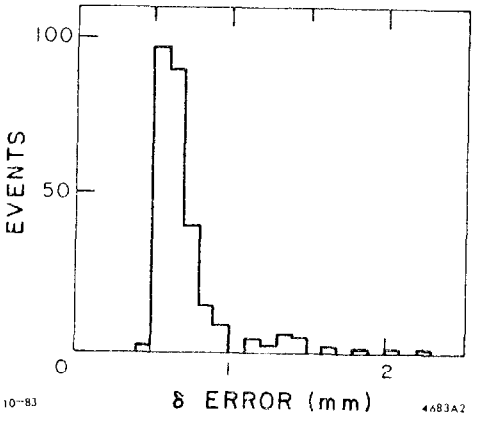


Fig. 6. Distribution of the global error in the measurement of δ.

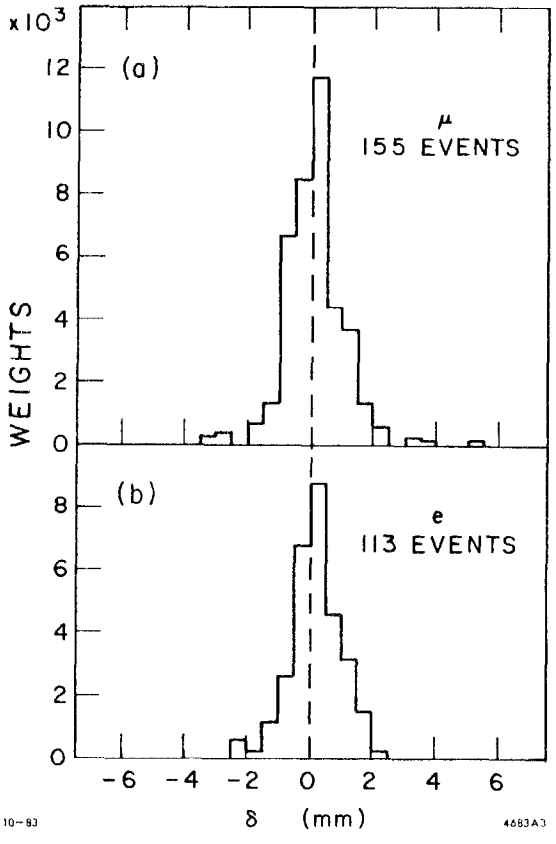


Fig. 7. Distribution of δ: (a) muon sample, (b) electron sample.

quarks' fragmentation function and semileptonic branching ratios were also taken to agree with the measured ones[17] : variations of these parameters do not affect sensibly the results, and are taken into account in the systematic errors used in the calculation of the b lifetime. (See Table I.) The results of the two independent samples are in good agreement. We finally introduce an additional uncertainty of 30 μm in σ to account for possible systematic bias, and we obtain the average:

$$\tau_b = (1.8 \pm 0.6 \pm 0.4)10^{-12} sec \quad .$$

We have performed several checks to study possible bias in the distribution of δ. A control sample was obtained using all tracks with $p > 2$ GeV/c and $p_\perp > 1.5$GeV/c in our multihadronic events. For these we expect $\delta = 20\mu$m if we use the Monte Carlo zero lifetime for the B particles, or $\delta = 30\mu$m if we use our measured τ_b. The distribution that we obtain with $\sim$ 18,000 tracks is shown in Fig. 8, the average value is:

$$< \delta >= (34 \pm 8)\mu m.$$

As a further test, we have used this impact parameter method to measure the τ lifetime, which has previously been measured using the vertex distribution of the 3-prong τ decay. We select 1-3 prong configurations of $\tau^+\tau^-$ events, and study the δ distribution of the one prong: we obtain from 2099 tracks, $< \delta >= 53 \pm 19\mu m$ which corresponds to

$$\tau_\tau = (3.9 \pm 1.4).10^{-13} sec$$

in very good agreement with the previously measured values.[18]

The b meson lifetime has been related by several authors to the quark mixing angles[19] ; for example Gaillard and Maiani[20] express τ_b as

$$\tau_b = \tau_b^\circ \frac{1}{(2.75 sin^2\gamma + 7.69 sin^2\beta - 5.75 sin^2\beta sin^2\gamma) + 0(sin^4\gamma, sin^4\beta)} \quad . (Eq.9)$$

TABLE I

Summary of parameters used to compute τ_b.

	μ sample	e sample
No. of events	155	113
f_b	0.72 ± 0.08	0.63 ± 0.07
f_c	0.14 ± 0.04	0.12 ± 0.05
f_{bg}	0.14 ± 0.07	0.25 ± 0.08
δ_c (μm)	24 ± 11	19 ± 11
δ_{bg} (μm)	26 ± 8	24 ± 6
α	0.43 ± 0.03	0.46 ± 0.03
$\langle \delta \rangle$ (μm)	158 ± 81	174 ± 75
τ_b (10^{-12} sec)	1.62 ± 0.87	2.00 ± 0.84

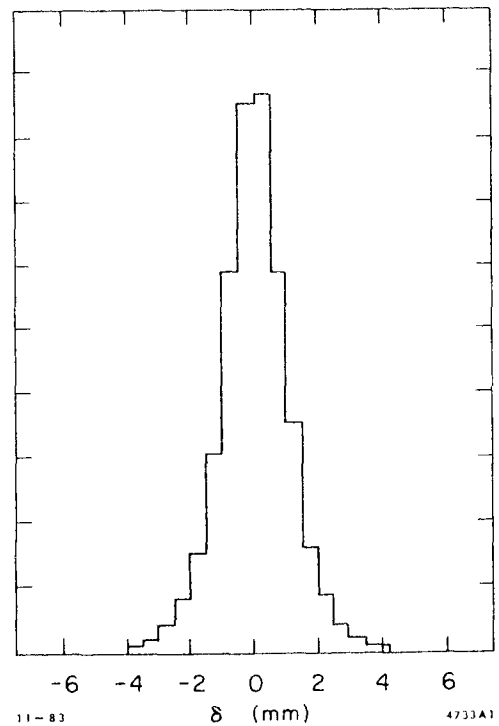


Fig. 8. Distribution of δ for the control sample.

Where

$$\tau_b^\circ \sim \tau_\mu \left(\frac{m}{m_b}\right)^5 \quad \frac{1}{\Theta} \sim 10^{-15} sec \qquad (Eq.\ 10)$$

is the lifetime expected for hadrons containing a b quark in absence of suppression due to small mixing between the second and the third generation. β and γ are the angles in the K.M. matrix.

Together with the limit on $\Gamma(b \to e\,\bar{\nu}\,X_u)/(\Gamma(b \to e\,\bar{\nu}\,X_c)$ reported by the CUSB group at this Conference,[21] our result implies:

$$|sin\gamma| = 0.043 \pm 0.01 \text{ and}$$

$$sin\beta < 0.009 \text{ (95\% confidence level)} \quad .$$

6. SEARCH FOR SUPERSYMMETRIC PARTICLES

While the recent discoveries of the $W^\pm$ and Z° have proved the validity of the Standard Model, there is a lot of theoretical effort in order to provide schemes which go "beyond" this model.

One of the most attractive of these theories is Supersymmetry,[22] which provides a simple way to cancel the quadratically divergent diagrams contributing to the Higgs mass. SUSY introduces a symmetry between bosons and fermions, assigning to the same multiplet particles whose spin differs by 1/2 unit, so that fermions can be transformed into bosons, and vice versa.

In such a scheme, each known particle must have a supersymmetric partner: there must be a "photino" with spin 1/2, a "selectron" with spin 0, "sleptons," "squarks," and so on. Since up to now no boson-fermion mass degenerate pair has been observed, this supersymmetry must be broken; the mass values of the new particles, depend on how this breaking occurs.

Several breaking schemes have been proposed, some of them interesting from the experimental point of view, as they indicate SUSY particles to be light enough, to be within reach of present experiments. In the model proposed by Fayet,[23] for example, the masses of the SUSY partners of the fermions are bound to be less than 1/2 of the mass of the W.

Squarks and sleptons can be produced in e^+e^- annihilation: the pair production of scalar leptons or quarks via the processes

$$e^+e^- \to \tilde{e}\,\bar{\tilde{e}},\ \tilde{\mu}\,\bar{\tilde{\mu}},\ \tilde{q}\,\bar{\tilde{q}} \quad ,$$

would result in the presence of pairs ee, $\mu\mu$, or $q\bar{q}$ with missing energy and momentum, in excess of QED. Searches of this kind have already excluded sleptons for masses up to 15-16 GeV.[24] The measurement of R at PETRA also excludes 2/3 squarks up to 18.5 GeV/c.

Several processes[25] have been suggested in order to extend the sensitivity of the search up to masses higher than the beam energy. The processes considered are:

$$e^+e^- \to \tilde{\gamma}\tilde{\gamma}\gamma \qquad \text{Process (1)}$$

and

$$e^+e^- \to e\tilde{\gamma}\tilde{e} \quad \hookrightarrow \tilde{\gamma}e \quad . \qquad \text{Process (2)}$$

6.1 SINGLE PHOTON SEARCH

The cross section of Process (1) can be sensitive, at PEP energy, to selectron masses up to 60 GeV/c:

$$\frac{d\sigma}{dx\,dy} = \frac{4}{3}\frac{3}{M_{\tilde{e}}^4}\frac{S}{X(1-y^2)}\left[(1-X)\left(1-\frac{x^2}{2}\right)+\frac{x^2}{4}(1-x)y^2\right]\left(1-\frac{4m_{\tilde{\gamma}}^2}{s(1-x)}\right)^{3/2} \qquad (Eq.\ 11)$$

where

$$x = \frac{E_\gamma}{E_{beam}} \quad , \quad y = \cos\theta_\gamma \quad . \qquad (Eq.\ 12)$$

The experimental signature for this kind of event is one photon and nothing else detected in the apparatus; background processes are:

$$e^+e^- \rightarrow e^+e^-\gamma \qquad \text{Process (3)}$$

where both electrons escape detection because they are at small angles or

$$e^+e^- \rightarrow \gamma\gamma\gamma \qquad \text{Process (4)}$$

where only one photon is detected.

Both background processes can be substantially reduced requiring transverse energy balancing: if a γ is emitted at an angle θ with an energy E_γ, Processes (3) and (4) can be tagged because they will produce detectable particles at angles $\theta' \geq E_\gamma \sin\theta/(2E_b)$.

MAC has recently successfully tested a new trigger sensitive to Process (1) with efficiency 97% for γ energy above 2.5 GeV. This efficiency has been measured as a function of the γ energy using the $e^+e^-\gamma$ events in which two particles are detected in the end caps and another trigger is fired (Fig. 9).

A search for single photon events has been performed using a sample corresponding to an integrated luminosity of $\sim 39 pb^{-1}$. The selection criteria were the following: total energy deposited less than 20 GeV in the central S.C., less than 1 GeV in the hadron calorimeter, less than 0.5 GeV in the end caps; no end-cap scintillators fired and, of course, a clean CD (< 15 hits, total); and subsequent eye scanning in order to reject cosmic rays, identify hot channels in the S.C., etc.

Possible candidates were required to have $|\cos\theta| \leq 0.8$ and to verticize in the origin. The transverse energy distribution of the candidates is shown in Fig. 10, together with the Monte Carlo simulation of Process (3), with a veto angle of 10°.

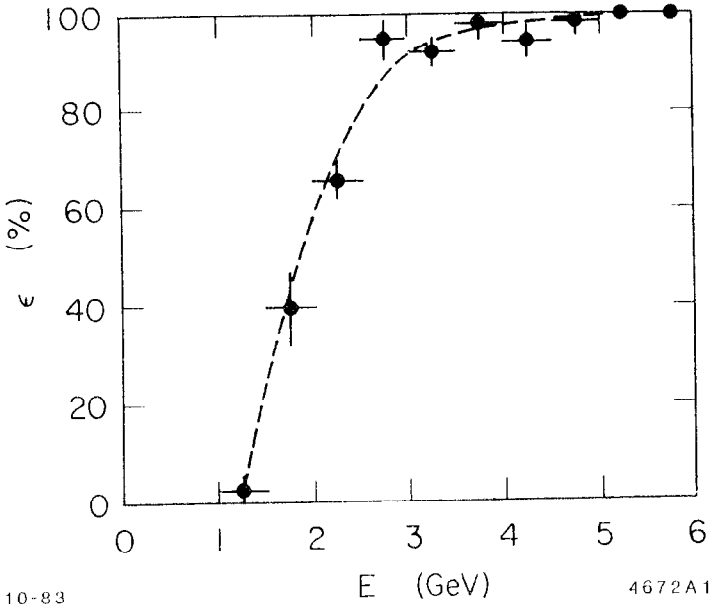


Fig. 9. Single photon trigger efficiency as a function of E_γ.

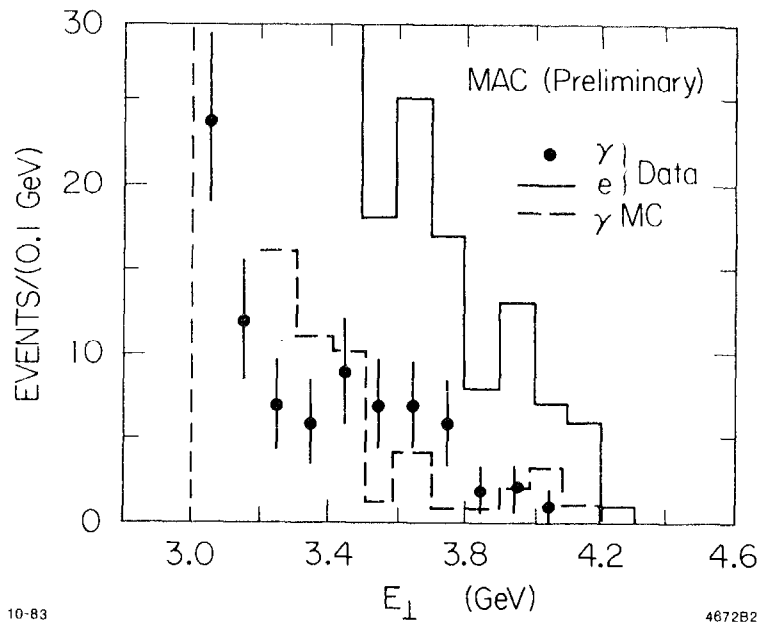


Fig. 10. $E_\perp$ distribution of single photon event candidates.

The absence of candidates for $E_\perp > 4.3$ GeV allows us to set a lower limit for the mass of the selectron at 25 GeV, with 90% confidence level.

6.2 Single Electron Search

Process (2) produces two electrons and two photinos in the final state, but only the one from the decay of the selectron can be detected in the apparatus, the other being emitted at too small an angle. If the photinos are stable or more in general can be considered neutrino-like as behavior in the apparatus, the signature for these events is given by events with only one electron detected.

A search for these kinds of events has been performed in the sample of data collected with the updated trigger. Candidates were required to have only one track in the CD with $|\cos\theta| \leq 0.8$, followed by an energy deposition of at least 2.5 GeV in the shower chamber. A limit of 1.0 GeV was imposed on the energy deposited in the end caps. All events satisfying these criteria and where the electron had more than 6 GeV energy were hand-scanned. The number of candidates was then restricted to 8 with the additional requirement that no end-cap scintillator had fired. No event with $E_{el} > 8.0$ GeV was found.

From the cross sections calculated in Ref. 25, one would expect about 7 events for $M_{Se} = 20$ GeV, and 3.4 events for $M_{Se} = 22$ GeV in our sample data.

This summer a new veto system is being installed in MAC extending the veto capability to 5° over the full azimuth and partial coverage of the region between 2° and 5°. Next year MAC will then be able to search for selectron masses up to 40 GeV.

7. PHOTON STRUCTURE FUNCTION

We have also studied the production of multihadrons arising from photon-photon collision under the so-called single-tag condition where one of the scattered beam electrons is detected. Combined with the central drift chambers, the end-cap electromagnetic shower chambers can efficiently tag energetic electrons down to 18°.

The scattered electron is identified as a track with $162° > \theta > 18°$, associated with an electromagnetic shower energy in excess of 6 GeV.

To further remove other backgrounds from one-photon multihadron production and other two-photon processes, we impose in addition the following requirements:

- charged multiplicity (including the electron) > 4,
- the imbalance defined as $(|E_N - E_S|)/(E_N + E_S) > 0.3$, and
- thrust < 0.98.

Fiducial cuts were applied to the end-cap regions to remove inefficient areas. This resulted in a loss of about 1/3 of the solid angle in the polar region $18° \div 25°$. The candidates were visually scanned to remove remaining Bhabha scattering events; 400 events were left after all these cuts. The remaining background from all sources has been estimated to be about 20% by Monte Carlo studies.

Since the mechanism of multihadron production is expected to be dominated by quark pair production which then fragments to hadrons, we have compared our results with the simple quark pair production model. After background subtraction and taking into account the detection efficiency, the number of observed events is in agreement with model calculations. The systematic error in the measurement and calculation is at the level of 30%.

Since the process resembles the deep-inelastic scattering of the electron off the real photon target, this measurement also constitutes a measurement of the structure function of the photon as a function of Q^2, the four-momentum-transfer squared of the electron.

The Q^2 of the scattered electron is given by:

$$Q^2 = 4E_b E' sin(\theta/2)^2 \qquad (Eq.\ 13)$$

where E_b is the beam energy, E' is the energy of the scattered electron and θ is the scattering angle of the electron. The distribution of the scaling variable $x = Q^2/(Q^2 + W^2)$, where W^2 is the invariant mass of the hadronic system, is shown in Fig. 11. In this spectrum the measured values of Q^2 and W were used. The distribution has not been corrected for background and acceptance effects. However, it is in reasonable agreement with the simple quark parton model calculation. Since the photon structure functions are directly compared with theoretical prediction, we are in the process of converting the visible x distribution to the real structure function F_2.

ACKNOWLEDGEMENTS

The results that I have presented here were obtained thanks to the work and dedication of all members of the MAC collaboration. Many of these results however, could not have been possible without the big increase in luminosity and the smooth running of PEP.

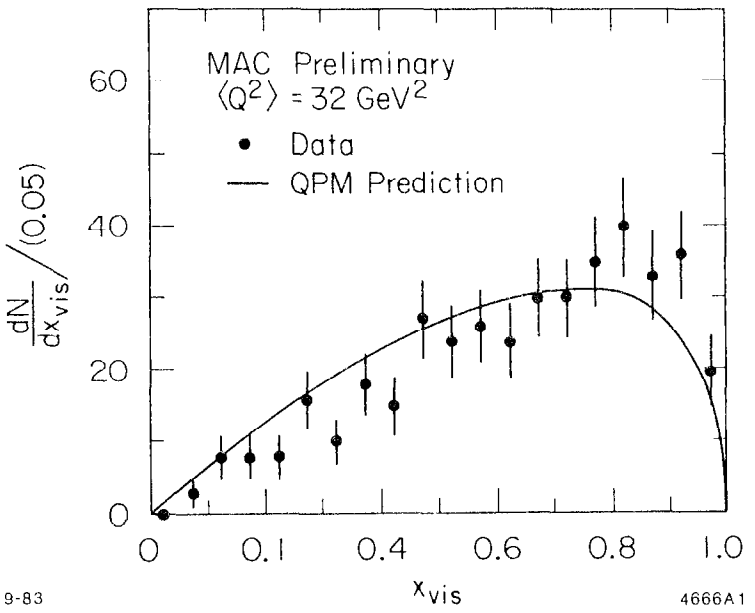


Fig. 11. Distribution of $X_{vis} = Q^2/(Q^2 + W^2)$.

REFERENCES

1. W. T. Ford et al., in **Proc. of the Intern. Conf. on Instrumentation for Colliding Beams,** SLAC-PUB-250, Ed. by W. Ash, (1982); also R. Weinstein in AIP Proc. No. 98 (1982).
2. S. Weinberg, Phys. Rev. Letters **19**, 1264 (1967) and Phys. Rev. **D5**, 1412 (1982); A. Salam and J.C. Ward, Phys. Letters **13**, 168 (1964); S.L. Glashow, Nuclear Phys. **22**, 579 (1961).
3. R. Budny, Phys. Letters **45B**, 340 (1973).
4. M. Greco et al., Nuclear Physics **B171**, 118 (1980), (E: **B197**, 543 (1982)).
5. F.A. Berends and R. Kleiss, Nuclear Phys. **B177**, 237 (1981).
6. F.A. Berends, R. Kleiss and S. Jadach, Nuclear Phys. **B202**, 63 (1982).
7. E. Fernandez et al., Phys. Rev. Letters **50**, 1238 (1983); E. Fernandez et al., SLAC-PUB-3144, Submitted to Phys. Rev. D.; W.T. Ford et al., Phys. Rev. Letters **51**, 257 (1983).
8. E. Fernandez et al., Phys. Rev. Letters **50**, 2054 (1983).
9. C. Peterson et al., Phys. Rev. **D27**, 105(1983).
10. For summaries of c fragmentation function results, see D. Schlatter, SLAC-PUB-2982 (1978) and K. Kleinknecht and B. Renk, University of Dortmund Report No. UNIDO-82/274 (1982).
11. Electromagnetic showers are simulated by EGS, described in R.L. Ford and W.R. Nelson, SLAC-PUB-210 (1978); hadronic cascades are simulated by HETC, described in T.V. Armstrong in **Computer Techniques in Radiation Transport and Dosimetry,** Ed. by W.R. Nelson and R.P. Feynman (Plenum Press, N.Y. 1980).
12. The simulation of multihadronic events is from Ali et al., DESY Report in DESY T80/d, (1980).
13. K. Chadwick et al., Phys. Rev. **D27,** 475 (1983); J. Lee Franzini talk given at this Conf.; M.E. Nelson et al., Phys. Rev. Letters **50**, 1549 (1983).
14. E. Fernandez et al., SLAC-PUB-3154, and COLO-HEP-64 (1982) submitted to Phys. Rev. Letters.
15. T. Sjostrand, Compt. Phys. Comm. **27**, 247 (1982); LUND University,

Report LU-TP-82-7 (1982).
16. For a review see for example, G. Kalmis in **Proc. of the 21st. Intern. Conf. on High Energy Physics,** Paris (1982).
17. For the c quark branching ratios see: R. Brandelik et al., Phys. Letters **B70**, 387 (1977); J. M. Feller et al., Phys. Rev. Letters **40**, 1677 (1978); W. Bacino et al., Phys. Rev. Letters **43**, 1073 (1979); R. Schindler et al., Phys. Rev. **D24**, 78 (1981). For the b quark we have used the value quoted in Ref. 8.
18. For a high-precision measurement see N. Lockyer, these proceedings.
19. See, for example, M. Kobayashi and K. Maskawa, Prog. Theor. Physics **49**, 452 (1973); L. Maiani **8th Intern. Symp. on Lepton and Photon Inter. at High Energies**, Hamburg (1977).
20. M.K. Gaillard and L. Maiani, **Proc. of the 1979 Cargese Summer Institute on Quarks and Leptons** (Plenum Press, 1979) p. 433.
21. J. Lee-Franzini, these proceedings.
22. For a recent review see for instance: B. Zumino, U.C. Berkeley Report No. UCB PTH 83/2 (1983), and references therein.
23. P. Fayet, Phys. Letters **B117**, 460 (1982).
24. See E. Lohrmann, these proceedings.
25. M. K. Gaillard et al., Phys. Letters **B116**, 279 (1982).

SLAC-PUB-3245
October 1983
(T/E)

LATEST RESULTS FROM THE MARK II AT PEP*

NIGEL LOCKYER
Stanford Linear Accelerator Center
Stanford University, Stanford, California 94305

ABSTRACT

We present single photon annihilation results from the MARK II detector at PEP based on $\sim$ 100 pb^{-1} of integrated luminosity taken at a center of mass energy $\sqrt{s}$ = 29 GeV. A study of inclusive leptons for momenta $\geq$ 2 GeV/c yield the average semileptonic branching ratios of bottom (b) and charm (c) quarks and information about the b fragmentation function. A measurement of the bottom hadron lifetime is presented based on a study of the prompt lepton impact parameters. In addition we report on a precise measurement of the tau lifetime and an updated D° lifetime. We also present a search for supersymmetric electrons, weak neutral current couplings from leptons and bottom particles and evidence for K*'s at PEP.

* Work supported by the Department of Energy, contract DE-AC03-76SF00515.

Presented at the 11th SLAC Summer Institute on Particle Physics
Stanford, California, July 18-29, 1983

© N. Lockyer 1983

1. Introduction

The MARK II group,[1] has investigated several interesting physics topics in e^+e^- annihilation during the last year. Many of the results to be discussed here were made possible by the excellent luminosity and reliable operating conditions of the PEP storage ring since January 1983. At that time a new "mini-beta" scheme (positioning of the final focusing quadrupoles ~ 7 m from the intersection point) enabled a very successful configuration which produced low backgrounds (trigger rate ~ 2 Hz) and a high average luminosity of ~ 1 pb^{-1}/day.[2] By June, we had logged ~ 150 pb^{-1} and processed about two-thirds of that. Another important factor in our physics program was the continued successful operation of a high spatial resolution cylindrical drift chamber, called the MARK II vertex[3] detector, located between the beryllium beam pipe and the main drift chamber. An isometric view of the MARK II detector is shown in Fig. 1 and a closeup of the vertex detector is shown in Fig. 2.

The vertex detector is 120 cm in length, has seven axial layers of drift cells and an average spatial resolution in hadronic events of 110 μ/layer. Tracks are extrapolated to the intersection point with an accuracy of $\sigma_T(\mu) = \sqrt{110^2 + [95/p\,(\mathrm{GeV/c})]^2}$ in the plane perpendicular to the beams, the second term arising from multiple scattering in the 0.6% radiation length (X_0) thick beam pipe. The vertex detector is important for lifetime measurements, reducing the cosmic trigger rate, increasing charged particle tracking acceptance and improving our momentum resolution. When used with the main tracking chamber we obtained a momentum resolution of $\Delta p/p = \sqrt{(0.02)^2 + (0.0095p)^2}$ (p in GeV/c) for tracks constrained to the beam intersection point.

The MARK II solenoid developed a short between the inner and outer coils in January (1982) and we have been operating since then at half field, 0.24T by powering only the outer coil. Fortunately the improved track resolution provided by the vertex detector has nearly cancelled the decrease to the momentum resolution from the lower magnetic field.

The following discussion will be limited to the most recent results from single photon annihilation. For information on recent work not covered here, see Ref. 4.

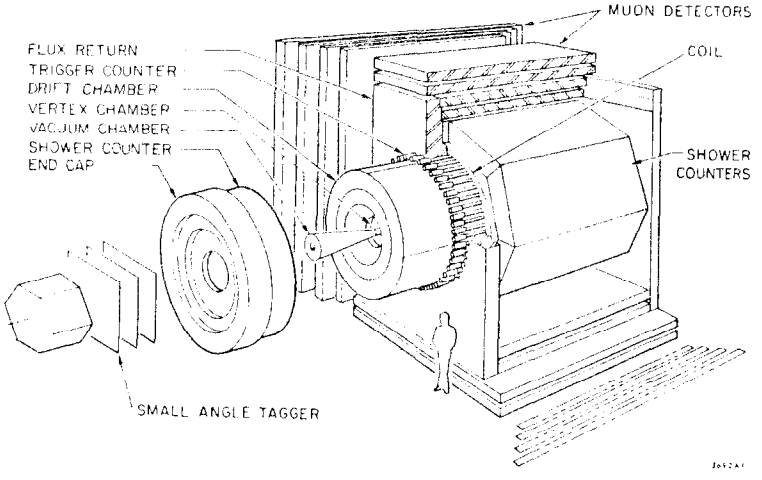


Fig. 1. Isometric view of the MARK II detector.

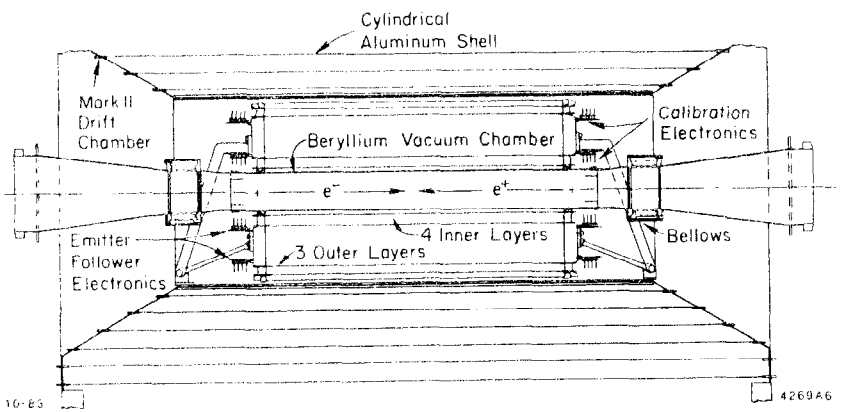


Fig. 2. Cross-section of the vertex detector as installed in the MARK II detector.

2. Inclusive Leptons

The study of prompt leptons in hadronic events produced in high energy e^+e^- annihilation gives information on (c) charm or (b) bottom quarks. In particular the production rates of these leptons depend on the weak semileptonic branching ratios. The momentum spectra of the leptons derive from the parent hadron momentum spectra and this provides information on the quark fragmentation functions. The c and b quarks are expected to pass a larger fraction of their momentum to the hadron containing the heavy quark, contrary to the case with the lighter quarks.[5] Experimental evidence seems to support this point of view for both b and c quarks.[1,6–7] The first experimental information on b quark fragmentation was reported by the MARK II group based on a study of inclusive electrons.[8] Here we report on electrons and muons with a slightly more refined analysis than Ref. 8.

We take advantage in this analysis of the higher mass of the b quark relative to the c quark. This leads to a harder p_T, transverse momentum with respect to the event thrust axis, spectrum of leptons from b decay relative to c decay.[9] After accounting for background we perform a maximum likelihood fit to the lepton populations in p, p_T space. The signal is assumed to come from 3 sources: (i) bottom decays in $b\bar{b}$ events (b primary); (ii) charm decays in $b\bar{b}$ events (c secondary); and (iii) charm decays in $c\bar{c}$ events (c primary). We use a Feynman-Field hadronization model[10] with gluon radiation as incorporated by Ali, et al.,[11] to represent the above processes. The lepton spectra used in the Monte Carlo agree with those of DELCO[12] (charm) and CLEO/CUSB[13] (bottom) experiments.

We have parametrized the b quark fragmentation function D_b^H into hadron H by

$$D_b^H(z) = \frac{A}{z\left[1 - \frac{1}{z} - \frac{\epsilon_b}{(1-z)}\right]^2} \tag{1}$$

where z is E_{hadron}/E_b, A is a normalization factor, and ϵ_b is a parameter. It has been shown that Eq. (1), with $\epsilon_c \simeq .25$ represents the measured charmed meson momentum spectra.[14,15] We have fit for 3 quantities; B_ℓ(b) and B_ℓ(c), the average semileptonic branching ratios in b and c quark decay, and ϵ_b, in Eq. (1). Because of the lepton tag, the average semileptonic branching ratios are averages over all weakly decaying particles, weighted by their relative populations. Furthermore we assume

the production of charm and bottom quark pairs follows from the square of the quark charges when determining B_ℓ(b) and B_ℓ(c). We assume the B_ℓ(c) from contributions (ii) and (iii) is the same and that bottom always decays into charm.

The branching ratios and ϵ parameter values obtained from the fit are given in Table I. The B_ℓ(b) agree well with those obtained at CESR and B_ℓ(c) agree with other PEP/PETRA experiments.[16] The $\langle z \rangle_b \sim .75$-$.80$ is indicating a hard b fragmentation in good agreement with other results. The form of the fragmentation function used is shown in Fig. 3.

From this analysis it is interesting to estimate the composition of the signal in terms of the relative fractions of b's, c's, $b \to c \to \ell$, and background. This is shown graphically in Figs. 4 and 5. The ability to select an enriched sample of $b\bar{b}$ events with a p_T cut of greater than one is evident. This will be discussed in more detail in the b lifetime section.

The background to the prompt electrons comes primarily from pions showering in the lead-liquid argon (LA) electromagnetic calorimeter and the overlap associated with photons or other particles within a jet. The algorithm for finding electrons in a strip geometry calorimeter and the technique for determining the misidentification probability is described in detail in Ref. 17. We identify electrons over 65% of 4π with an efficiency

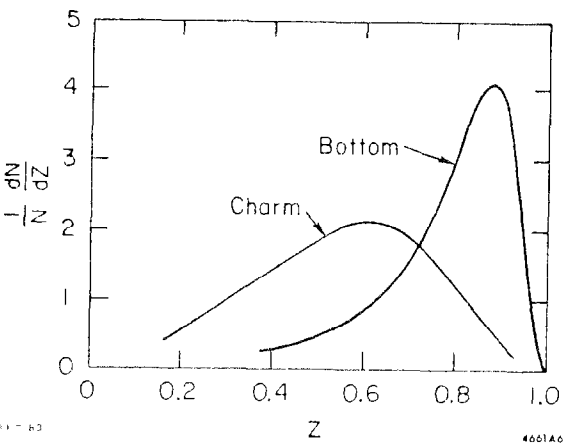


Fig. 3. Comparison of charm and bottom fragmentation functions. Solid curves are results of our fits. From left to right $\epsilon_c = 0.25$, and $\epsilon_b = 0.015$.

Table I
Branching ratios and fragmentation results

	Electron Results	Muon Results
$B(b)$	$13.5 \pm 2.6 \pm 2.0$	$12.6 \pm 5.2 \pm 3.0$
$B(c)$	$6.6 \pm 1.4 \pm 2.8$	$8.3 \pm 1.3 \pm 1.8$
ϵ_b	$0.015 \begin{smallmatrix} + 0.022 \\ - 0.011 \end{smallmatrix} \begin{smallmatrix} + 0.023 \\ - 0.011 \end{smallmatrix}$	$0.042 \begin{smallmatrix} + 0.218 \\ - 0.041 \end{smallmatrix} \begin{smallmatrix} + 0.120 \\ - 0.035 \end{smallmatrix}$
$\langle z \rangle_b$	$0.79 \pm 0.06 \pm 0.06$	$0.73 \pm 0.15 \pm 0.10$

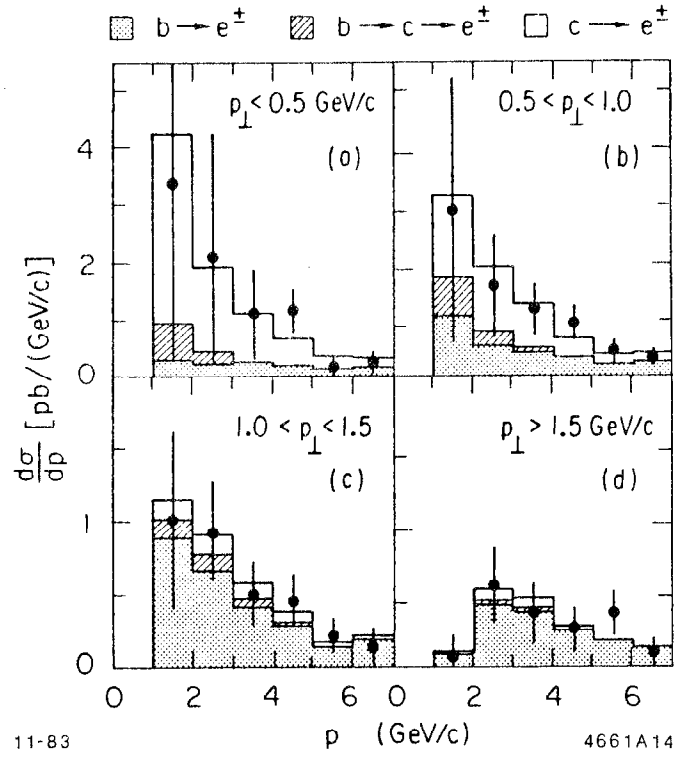


Fig. 4. Prompt-electron momentum spectra in four regions of transverse momentum $p_\perp$ (GeV/c): (a) $p_\perp < 0.5$, (b) $0.5 < p_\perp < 1.0$, (c) $1.0 < p_\perp < 1.5$, and (d) $p_\perp > 1.5$. Two sets of error bars are shown for each data point. The smaller ones are statistical only. The larger ones are the statistical and systematic errors added in quadrature. The highest momentum bin includes all momenta ≥ 6 GeV/c. The histograms show the results of the fit. The three contributions shown are (i) b primary (solid), (ii) c secondary (diagonally hatched), and (iii) c primary (unshaded).

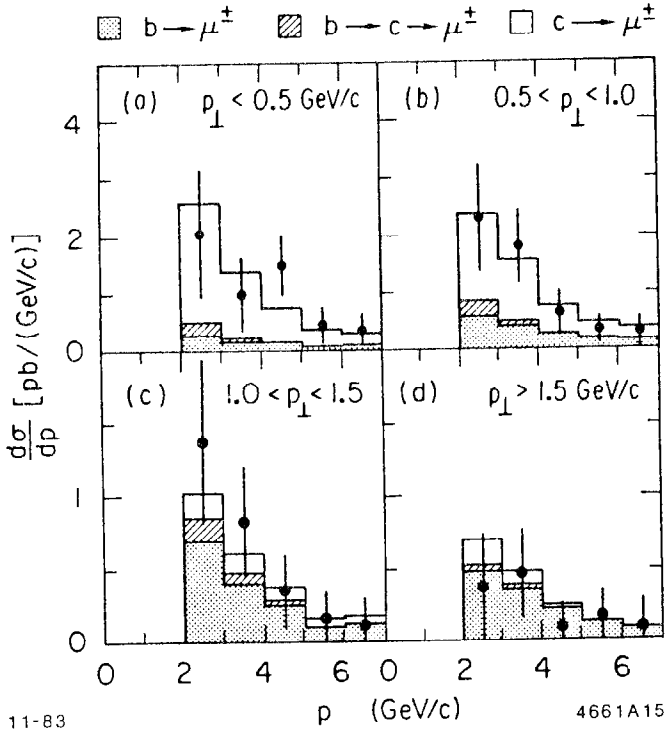


Fig. 5. Prompt-muon momentum spectra in four regions of transverse momentum $p_\perp$ (GeV/c): (a) $p_\perp < 0.5$, (b) $0.5 < p_\perp < 1.0$, (c) $1.0 < p_\perp < 1.5$, and (d) $p_\perp > 1.5$. Two sets of error bars are shown for each data point. The smaller ones are statistical only. The larger ones are the statistical and systematic errors added in quadrature. The highest momentum bin includes all momenta ≥ 6 GeV/c. The histograms show the results of the fit. The three contributions shown are (i) b primary (solid), (ii) c secondary (diagonally hatched), and (iii) c primary (unshaded).

which varies from 78% at 1 GeV/c to 93% at the highest momenta. The misidentification probability varies from 3% at low p and p_T to 0.5% at $p_T > 1.0$ GeV/c. This reflects the difficulty of finding electrons within a tight jet of particles. Conversions and Dalitz pairs are small in number because of the beryllium beam pipe. We remove $\sim 70\%$ of the pairs with a geometrical pair finder.

The background to the prompt muon signal comes from two major sources, pion punch through and π and K decay. There is a few percent probability that a π of $p \sim 2$ GeV/c or more can pass through the four layers of iron absorber without interacting. When combined with the large number of pions per hadronic event this is a significant background to direct muons. The average misidentification probability for punch through is about 0.4%. This varies only slightly with p_T and increases with p, as you expect. We estimate this background using all charged tracks in our hadronic sample. If a given track points at the muon system (we cover 45% of 4π) and has enough momentum to pass through all four layers, it is a candidate track. This track is considered a punch through if it does not reach the fourth layer. We of course take into account range straggling, multiple scattering and electronic inefficiency. We measure the punch through in the first three levels and extrapolate to the fourth level. Therefore we call a muon a charged track which extrapolates into the muon system, and has a hit in each of the four layers within 2σ of the track. Sigma reflects the uncertainty in the track extrapolation from the drift chambers through the calorimeter and the associated multiple Coulomb scattering effects. The effects of π's and K's decaying in flight are determined from Monte Carlo simulation and we find the misidentification probability averages about 0.5%.

Another way of studying these backgrounds is to use samples of pure pions, such as one gets from K^0_S, τ, and D^0 decay. Here the statistics are poor, though we have checked they give results consistent with the method described. A more complete description can be found in Ref. 17.

3. Bottom Hadron Lifetime

The b quark lifetime measures the mixing between the second and third quark generations when viewed in the context of the six quark standard model. The preferred decay of the b quark is to its weak isospin doublet partner, the top quark, but this is obviously not allowed by energy conservation since $m_t > m_b$. The 3×3 quark mixing matrix U_{ij} of Kobayashi and Maskawa (K-M)[18] mixes the weak interaction eigenstates $(d's'b')$ and the mass eigenstates (dsb) using three Cabibbo-like angles θ_i and a phase δ. The unitary K-M matrix can be written

$$U = \begin{pmatrix} U_{ud} & U_{us} & U_{ub} \\ U_{cd} & U_{cs} & U_{cb} \\ U_{td} & U_{ts} & U_{tb} \end{pmatrix} = \begin{pmatrix} c_1 & s_1c_3 & s_1s_3 \\ -s_1c_2 & c_1c_2c_3 - s_2s_3e^{i\delta} & c_1c_2s_3 + s_2c_3e^{i\delta} \\ -s_1s_2 & c_1s_2c_3 + c_2s_3e^{i\delta} & c_1s_2s_3 - c_2c_3e^{i\delta} \end{pmatrix} \quad (2)$$

where $(d's'b') = (dsb)U^T$, U^T is the transposed matrix of U, $c_1 = \cos\theta_1$ and $s_1 = \sin\theta_1$ etc. The U_{ij}'s therefore modify the coupling of the quarks q_iq_j to the intermediate vector boson $W^{\pm}$. The b lifetime can be expressed in terms of simple W emission from the quark line as shown in the spectator diagram for b decay in Fig. 6. The lifetime of the b quark depends on the magnitude of the matrix elements U_{bc} and U_{bu}. We know from the single lepton energy spectrum as measured by CLEO/CUSB[13] at CESR that the $Br(b \to u)/Br(b \to c) < 5.5\%$. This implies the b lifetime predominately measures the matrix element U_{bc}. This has implications to the top quark mass and CP violation.[19,20]

We study the bottom and charm lifetimes by measuring the projected impact parameter of prompt leptons produced in their decays.[21] Bottom is separated from charm kinematically, since leptons with large p_T come principally from the heavier bottom quark. A measurement of the impact parameter distribution for each group, and the knowledge of the relative ratios of bottom and charm populations in each group enable us to disentangle the lifetimes.

The selection of hadronic events is simple and independent of the lifetime of the primary quarks. We search for lepton candidates in those events where the charged energy exceeds .25 $E_{c.m.}$, the center-of-mass energy of 29 GeV. Each event has at least five charged particles, each of which passes within 5 mm of the collision point in the plane perpendicular to the beams and within 7 cm of the collision point along the beam direction. The leptons are identified as described in the previous section.

We ensure the lepton candidate trajectory is well measured in several ways. Each track has a minimum of 13 out of a possible 27 hits in the drift chambers. This is a sufficient number of hits in the drift chambers to allow left-right ambiguities to be

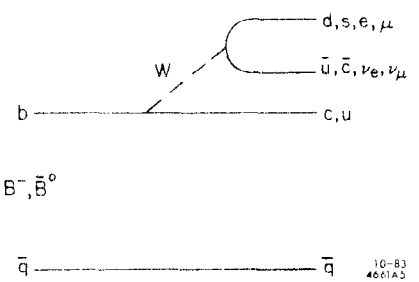


Fig. 6. Spectator diagram for bottom decay.

determined correctly. Using hits from both the inner and outer band of cells in the vertex chamber optimizes the projected resolution after extrapolation to the origin. This is a level arm effect and is described by the equation

$$\sigma^2 = \frac{(r_1^2\sigma_2^2 + r_2^2\sigma_1^2)}{(r_2 - r_1)^2} \tag{3}$$

where the track has transverse errors σ_1 and σ_2 at radii r_1 and r_2. This does not include multiple scattering (see introduction). Each track has at least two hits in the inner band and one hit in the outer band. Furthermore we ensure a good track fit in both the vertex detector and main drift chamber by requiring the χ^2/dof of the track fit to be less than 4.

The direction of the charm or bottom hadron is approximated by the thrust direction. The thrust direction is determined using all charged tracks, including the lepton, which pass loose track quality cuts. The thrust axis for each event has a $|\cos\theta| < 0.7$, measured with respect to the beam direction. This helps contain events within the detector fiducial volume and therefore aids in the accuracy with which we determine the b quark direction.

Leptons with $p_T > 1$ GeV/c and $p > 2$ GeV/c comprise the bottom-enriched sample; those with $p_T < 1$ GeV/c and $p > 3$ GeV/c are the charm sample. The slightly higher cutoff for charm helps reduce the background from the low p, p_T region where the misidentification probability is high. In the b region, $20 \pm 7\%$ of the lepton candidates are nonprompt, which we call background sources; in the c region $34 \pm 9\%$ of the lepton candidates are classified as background. After accounting for background, $80 \pm 8\%$ of the prompt leptons in the b region are from bottom decays and $20 \pm 8\%$ are from charm decays. In the c region, $32 \pm 8\%$ of the prompt leptons are from bottom decays and $68 \pm 8\%$ are from charm decays. The errors quoted are systematic.[17] The errors reflect uncertainties in the lepton decay spectra, the fragmentation functions and the ratio $Br(b \to \ell x)/Br(c \to \ell x)$. The b region is rich in the ratio of bottom decays relative to charm, about 4 to 1, while the c region is only 2 to 1 in the ratio of charm to bottom decays. The b region is less contaminated with background than the c region principally because the electron backgrounds are smaller at high p_T.

The impact parameter δ is the distance of closest approach between the lepton trajectory and the e^+e^- collision point, projected in the plane perpendicular to the

beams. We identify the primary vertex with the average beam position. A positive sign is given to δ if the intersection of the lepton trajectory with the parent hadron trajectory corresponds to a positive decay length, and we assign it a negative δ otherwise. We assume the bottom or charm parent hadron travels from the primary vertex along the thrust direction and decays into a forward going lepton. Negative δ's may arise from mismeasured beam positions or from a parent hadron which decays into a backward going lepton.

The beam position is determined run-by-run by finding the position which minimizes the distance of closest approach for tracks coming from Bhabha and hadronic events. In a typical two hour storage ring fill, we measure the average beam position to within 20μ vertically and 50μ horizontally. The rms beam size is $65 \pm 15\mu$ vertically and $480 \pm 10\mu$ horizontally. The beam position is usually stable during a fill, but in cases of steering, beam position monitors allow us to ignore these runs. In Fig. 7 we show the distance of closest approach divided by the error for both horizontal and vertical tracks from Bhabhas separately. It is a fit to this distribution that yielded the above beam sizes as well as demonstrating that the errors on the measurement are Gaussian and understood, since the widths are very close to unity, with little in the tails. The error on the impact parameter for leptons is dominated by the beam size and ranges from 120μ to 490μ depending on the azimuthal angle of the lepton. The impact parameter error distribution for the leptons is shown in Fig. 8. The shape of the distribution reflects the shape of the beam, small in the vertical and large in the horizontal. We accept only those lepton candidates with $\sigma_\delta < 350\mu$, which leaves 307 leptons for the remaining analysis.

The measured lepton impact parameter distributions are shown in Fig. 9(a) for the b region and Fig. 9(b) for the c region. Only tracks with $|\delta| < 1$ mm are considered when computing the averages and in making the fits to the data. We do this to help reduce the effects of the tails on the final answer. The mean of the b enriched plot is $106 \pm 29\mu$ and of the c enriched plot is $63 \pm 18\mu$. The dominant background for electrons and muons is misidentified hadrons. We have measured the impact parameter distribution for nonleptons in the b region and c region, weighting the sample in p, p_T space according to the misidentification probability. Only one hadron track per event enters the histogram and this track passes all quality cuts normally applied to the

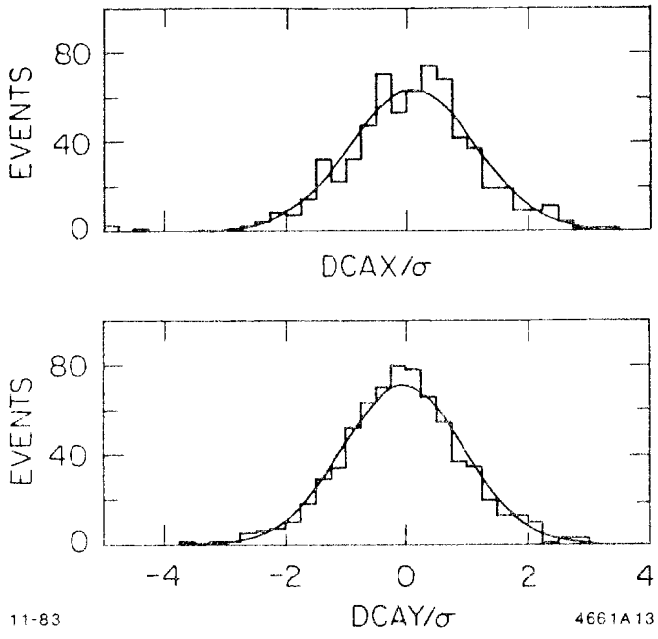


Fig. 7. The top graph is the distance of closest approach of horizontal Bhabha tracks DCAX with respect to the beam position divided by the individual errors on each measurement. A fit to a Gaussian yields a vertical beam size of 65 μm. The lower graph uses vertical Bhabhas and the fit yields a horizontal beam size of 480 μm.

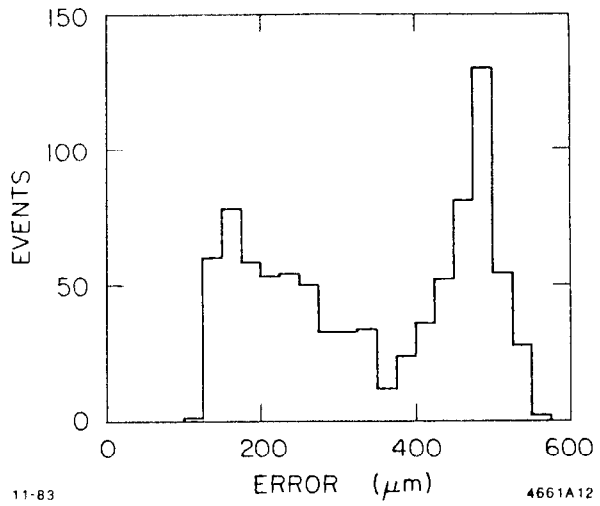


Fig. 8. Distribution of impact parameter errors for leptons in the bottom enriched and charm enriched regions. Events with an error $\leq$ 350 micron are accepted.

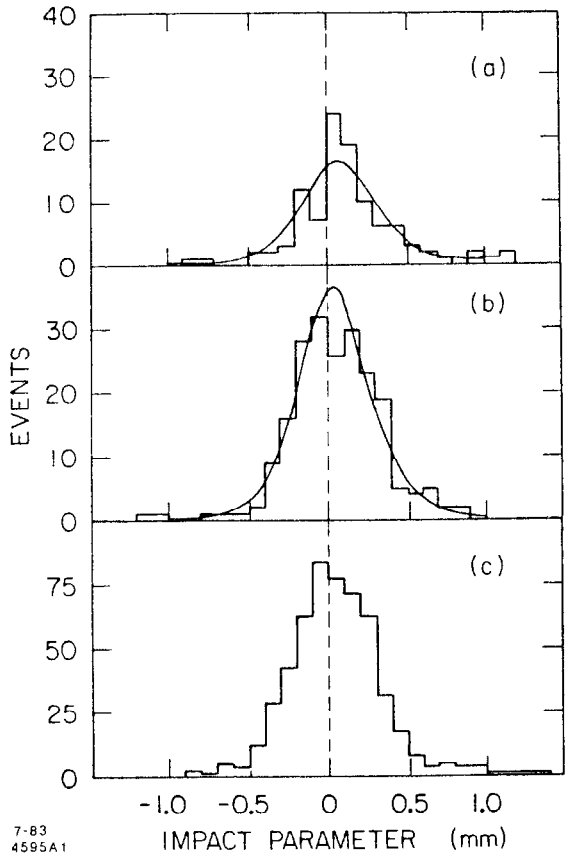


Fig. 9. Impact parameter distributions for (a) leptons in the b region; (b) leptons in the c region; (c) hadrons in the b region. The solid curves are the result of the fit described in the text.

leptons. The background from conversions are negligible because very little material (0.6% of a radiation length) preceeds the tracking chambers. Conversions after the inner band of the cells in the vertex chamber are eliminated by the minimum hit requirement in this band and remaining conversions are removed with a 70% efficient geometrical pair finder. The impact parameter distribution for the pion and kaon decay background is similar to that for nonleptons. Further, since the thrust axis does not in general follow the direction of the decaying pion or kaon, the sign of the impact parameter may be positive or negative thereby reducing the concern that this background leads to a positive definite impact parameter distribution. The impact parameter distribution for the hadrons in the b region is shown in Fig. 9(c) and for hadrons in the c region in Fig. 10. The average impact parameter of hadrons in the b region is $36 \pm 12\mu$ and in the c region it is $12 \pm 7\mu$.

Lifetimes are extracted from the two lepton impact parameter distributions, b region and c region, by fitting simultaneously for a bottom and charm lifetime using a maximum likelihood technique, after accounting for the background. We consider the impact parameter distribution in the b or c (i = 1,2) region to be composed of three distributions; a normalized shape for the background $dn/d\delta_{hi}$ weighted by the fraction of background f_{hi}, and a shape for the bottom and charm decay's impact parameters weighted in proportion to their respective populations, $(1-f_{hi})f_{bi}$ for b's and $(1-f_{hi})(1-f_{bi})$ for c's. The normalized impact parameter distributions $dn/d\delta_i$ can then be written

$$\frac{dn}{d\delta_i} = f_{hi}\,\frac{dn}{d\delta_{hi}} + (1-f_{hi})\left[f_{bi}\,\frac{dn}{d\delta_{bi}} + (1-f_{bi})\,\frac{dn}{d\delta_{ci}}\right] \quad . \tag{4}$$

The normalized impact parameter distributions $dn/d\delta_{bi}$ for b decay and $dn/d\delta_{ci}$ for c decay are computed by convoluting the 'true' impact parameter distribution with our experimental resolution, a Gaussian centered on zero of width σ_δ, on an event by event basis. We calculate the 'true' impact parameter for b and c decay in both the b and c regions using Monte Carlo techniques which include the experimental lepton spectra[13] and kinematic selection criteria but no detector resolution effects. There are four such distributions, one of which is shown in Fig. 11, the other three are similar. They are peaked at low impact parameter, have exponentially decreasing tails, and scale with the lifetime of the parent hadron. Roughly 6% of the bottom decays are

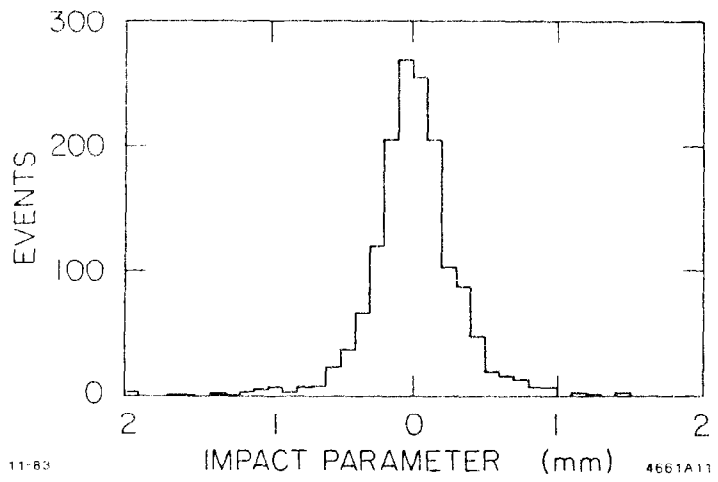


Fig. 10. Impact parameter distributions for hadrons in the c region.

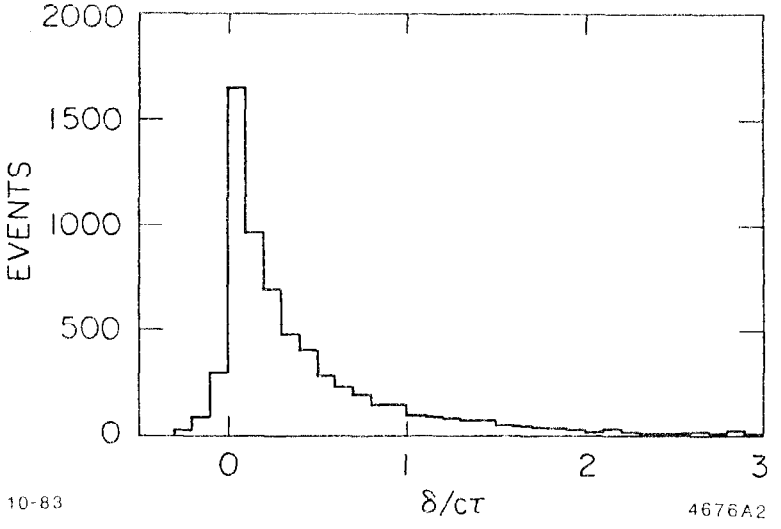


Fig. 11. Monte Carlo produced distribution of impact parameters divided by $c\tau$ for leptons produced in bottom decays. The above represents events in the b region.

backwards and this is accounted for by the small negative impact parameters in the b distributions. The average impact parameter from b decays is about $135\mu/10^{-12}$ sec in the b region and $70\mu/10^{-12}$ sec in the c region; for charm decays it is about $120\mu/10^{-12}$ sec in the b region and $95\mu/10^{-12}$ sec in the c region. The b region with its high $\langle p_T \rangle$, preferentially selects large angles with respect to the thrust axis and therefore larger impact parameters than does the low $\langle p_T \rangle$ of the charm sample.

The result of the fit is summarized in Fig. 12 which shows equal likelihood contours in the $\tau_c - \tau_b$ plane. The plot shows substantial correlation between the two lifetimes. From our own data we find $\tau_b = \left(10.3^{+\,5.2}_{-\,4.2}\right) \times 10^{-13}$ sec and $\tau_c = \left(8.3^{+\,5.1}_{-\,4.8}\right) \times 10^{-13}$ sec. We can obtain a more precise value of τ_b by using world data on charm lifetimes. We estimate the appropriate average to be $\tau_c = (6.0 \pm 1.5) \times 10^{-13}$ sec, where we have taken into account the large D^* production at PEP, and the measured lifetimes and branching ratios of the charmed particles. The quoted error includes the uncertainties in both individual lifetimes and relative production rates of the various charmed particles. After refitting with this estimate, which agrees within errors with our own τ_c measurement, we find $\tau_b = \left(12.0^{+\,4.5}_{-\,3.6}\right) \times 10^{-13}$ sec.

We have checked that with input lifetimes found above for bottom and charm; a Monte Carlo simulation of the background yields $37 \pm 24\mu$ in the b region and $14 \pm 12\mu$ in the c region, in good agreement with the measured values. Furthermore we determined the bottom hadron lifetime from the electron and muon samples separately, and found they agree within errors. The background distributions themselves offer a good general check that geometric alignment, mistracked tracks, or incorrect beam positions are not the source of the shift observed by the leptons. Since the backgrounds were handled identically to the leptons the only difference in the two samples is the number of tracks which come from bottom hadrons. Simply, high p_T leptons tag bottom hadrons more efficiently than just high p_T hadrons. The measurement technique has been checked with Monte Carlo simulated data, and we found that fitted lifetimes agreed with input lifetimes to within the statistical errors.

The systematic error derives principally from the uncertainties in the background fractions, bottom-hadron fractions, fragmentation functions and fitting procedures. The above lead to a 25% uncertainty in the bottom hadron lifetime.

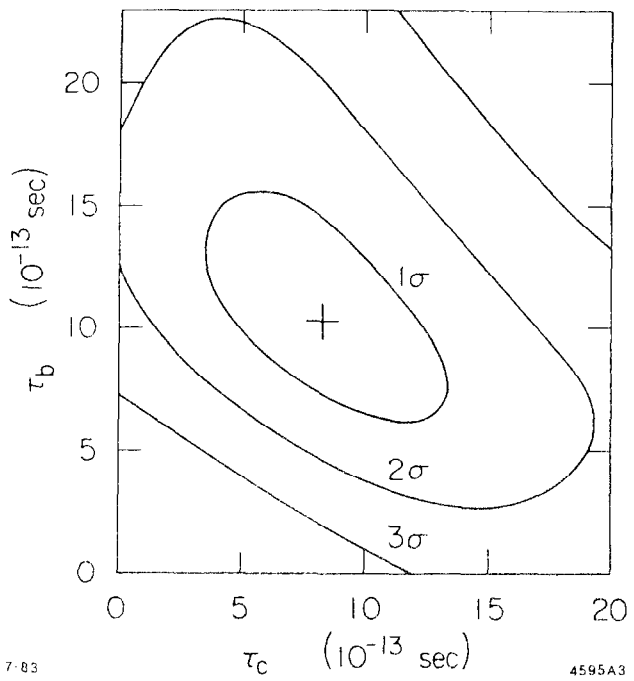


Fig. 12. Equal likelihood contours in the $\tau_c - \tau_b$ plane, corresponding to one, two, and three standard deviations from the best fit values.

In summary, we have measured the average lifetimes of bottom hadrons and found $\tau_b = \left(12.0 \pm {}^{4.5}_{3.6} \pm 3.0\right) \times 10^{-13}$ sec. This lifetime represents an average over bottom hadron species, weighted by the product of their respective production cross sections and semileptonic branching ratios. This measurement of τ_b is consistent with the value presented at this conference by M. Piccolo of the MAC Collaboration.

The bottom hadron lifetime has relevance to the top quark mass and CP violation[19,20] because it significantly constrains the magnitude of the K-M mixing matrix parameters. The bottom hadron lifetime has been related to the K-M matrix elements by Gaillard and Maiani:[22]

$$\tau_b = \frac{\tau_b^\circ}{(2.75|U_{bc}|^2 + 7.7|U_{bu}|^2)} \quad . \tag{5}$$

Here $\tau_b^\circ = \tau_\mu (m_\mu/m_b)^5$, where τ_μ is the muon lifetime and m_μ/m_b is the ratio of the muon and b quark masses. As stated earlier, the limit on the ratio $Br(b \to u)/Br(b \to c) < 5.5\%$ [13] implies that $|U_{bu}|^2 < 0.02|U_{bc}|^2$, so we consider U_{bu} negligible in Eq. (5). Using $m_b = 5$ GeV/c^2 we find $|U_{bc}| = 0.053 \pm {}^{.010}_{.009}$, statistical errors only. This can be compared to the sine of the Cabibbo angle, $U_{su} = 0.22$, about four times larger.

The calculation of the CP violating amplitudes in the $K^\circ - \bar{K}^\circ$ system involve products of the K-M angles $\sin\theta_2 \cos\theta_2 \sin\theta_3 \sin\delta$ or $s_2 c_2 s_3 s_\delta$. Using the above information, the b lifetime and the $Br(b \to u)/Br(b \to c)$, one can place a lower bound on $s_2 c_2 s_3 s_\delta$ and therefore ϵ'/ϵ.[23,24] Here ϵ' is a measure of direct CP violation in the decay $K_L \to 2\pi$, and ϵ is the dominant contribution which arises from the CP impurity of the K_L. A different approach uses the experimental value of ϵ as a constraint and proceeds to calculate a lower bound on the top quark mass as a function of the b lifetime.[20] All of this hinges on the existence of the top quark and, at present, considerable theoretical uncertainties.

Finally, it is clear that a statistically more significant b lifetime measurement is needed. We hope to obtain greater precision in the lifetime by reducing the uncertainty in the position of the primary vertex by using tracks within the event. In addition, we are attempting to measure the lifetime by a path length technique.

4. Precise Measurement of the Tau Lifetime

The tau lepton is expected to couple to the charged weak current with the universal Fermi strength in the standard model. This universality assumption for the third lepton generation is tested by a measurement of the tau lifetime. Since the lifetime can be calculated to better than 10% within the context of the standard model,[25] a measurement of equivalent precision is desirable.[26–28] We present here a new measurement of the tau lifetime based on an integrated luminosity of 41 pb^{-1} which has been made using our high precision vertex detector.[3]

The tau lifetime is determined by measuring the distribution of displacements between the e^+e^- collision point, which we identify with the beam position, and the vertex of the three prong decay mode of the tau. We can calculate the lifetime from this distribution since the tau is produced with the beam energy and thus the relativistic gamma factor is known.

The selection of $1+3$ and $3+3$ event topologies of the tau can be made with very little background at the PEP $E_{c.m.}$ of 29 GeV. The tau direction is assumed to lie along the direction of the 3 prong system. The average beam position is determined run-by-run, using the same method as described earlier for the bottom hadron lifetime analysis. The projected decay length is given by

$$\ell_p = \frac{x_v\sigma_{yy}t_x + y_v\sigma_{xx}t_y - \sigma_{xy}(x_vt_y + y_vt_x)}{\sigma_{yy}t_x^2 + \sigma_{xx}t_y^2 - 2\sigma_{xy}t_xt_y} \qquad (6)$$

where (x_v, y_v) is the decay vertex position relative to the beam position, σ_{ij} is the sum of the beam and vertex error matrices, and t_i are the projected τ direction cosines. The decay length is then $\ell = \ell_p/\sin\theta$, where θ is the angle between the tau and beam directions. Figure 13 shows the decay length distribution for 156 decays where the resolution on each decay length has been required to be less than 1700μ. The resolution on the decay length depends on the 3 prong opening angles, track momenta, and orientation of each decay and varies between 500μ and 1800μ for most decays and averages $\sim 1100\mu$.

We use a maximum likelihood fitting procedure to extract the lifetime from the decay length distribution. The fitting function is a convolution of an exponential decay length distribution and a Gaussian resolution function of width σ_ℓ, calculated event by event. The Gaussian is centered on zero. The result of the fit, which yields a mean

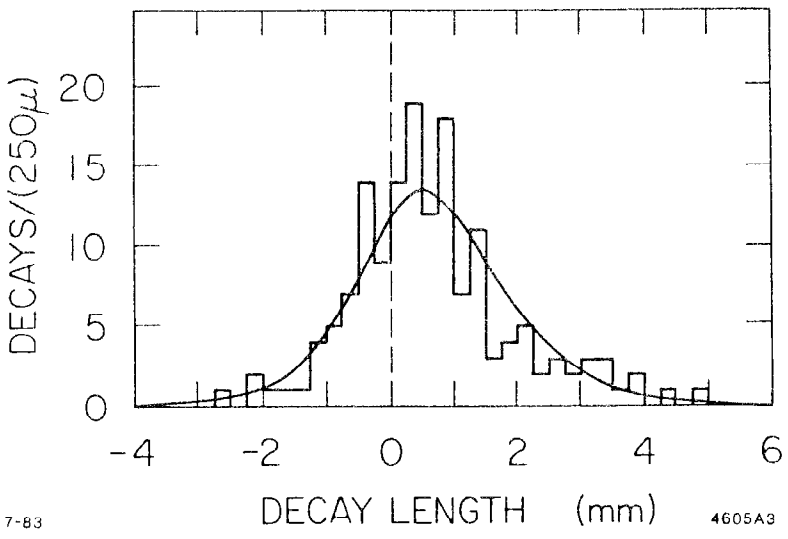


Fig. 13. Measured τ decay lengths. The solid curve is the best fit to the data.

decay length of $705 \pm 87\mu$ (statistical), is shown superimposed on the data in Fig. 13, and describes the data well. We find $\tau_\tau = (3.20 \pm 0.41) \times 10^{-13}$ sec after correcting for the small amount of background ($+30\mu$) and the effects of initial state radiation. This is to be compared with the expected value $\tau_\tau = \tau_\mu (m_\mu/m_\tau)^5 B_e = 2.8 \pm 0.2 \times 10^{-13}$ sec where $\tau_\mu(m_\mu)$ is the muon lifetime (mass) and B_e is the tau branching ratio into $e\nu\bar{\nu}$.[29]

A sample of tracks which simulate the momentum and topology of tau decays was constructed in order to check for bias in the fitting technique and measurement. We selected a sample of 3 prongs from hadronic events and excluded tracks coming from K_S^0 decay and the highest momentum track in a jet to suppress tracks not coming from the e^+e^- collision point. The decay length distribution for this control sample is shown in Fig. 14(a). The fitted mean decay length is $72 \pm 38\mu$. From Monte Carlo studies we find this procedure gives decay lengths in the range 50μ to 150μ depending on the D^+/D^0 ratio and the bottom lifetime. The width of the resolution function is important in our fitting procedure. In Fig. 14(b) we show the decay length divided by its error for the control sample. A unit-width Gaussian describes the data well and we determined the width of the resolution function is correct to 5%.

We have studied several sources of systematic error. One measurement bias comes from mismeasurement of the track angles, or simple multiple scattering of the tracks from tau decay. Tracks that scatter or are mismeasured to larger angles extrapolate back to give longer decay displacements from the collision point. Larger opening angles give smaller vertex errors and hence these longer lived events carry proportionately more weight in the fit. In previous determinations of the tau decay length,[26–28] corrections of $\sim 250\mu$ were made to compensate for this effect. This measurement has reduced this effect to $\sim 25\mu$ by having reduced multiple scattering and improved track resolution. The uncertainties in the resolution function, background corrections, and other uncertainties in the analysis lead to a systematic error of 80μ.

In summary, we have measured the tau lifetime to be $\tau_\tau = (3.20 \pm 0.41 \pm 0.35) \times 10^{-13}$ sec, where the first error is statistical and the second is systematic. This analysis was based on 41 pb^{-1} and further improvements in the lifetime must await a better understanding of the systematic errors involved. We will certainly continue this work in order to provide an even better test of $e - \mu - \tau$ universality.

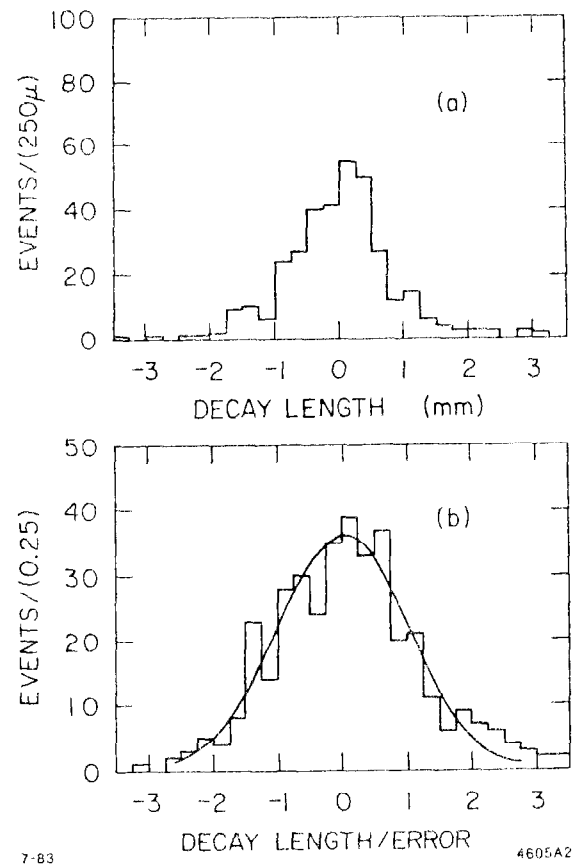


Fig. 14. (a) Measured decay lengths for "pseudo-τ" decays; (b) decay length divided by its calculated error for pseudo-τ decays. The solid curve is a unit-width Gaussian function, normalized to the data between $-2.5 \leq \ell/\sigma \leq 2.5$.

5. D° Lifetime

The measurement of charm lifetimes has been an area of considerable experimental activity over the last few years. Of particular interest is the ratio of $\tau_{D^+}/\tau_{D^\circ}$, which gives information about the relative strengths of the spectator and nonspectator amplitudes. Since there is no nonspectator diagram for the D^+, it is expected to have a longer lifetime than the other charm particles (if nonspectator diagrams are important). The MARK II at present can contribute information on the lifetime of the D° meson only. Here we report preliminary results based on a small clean sample of D°'s. The detection method and analysis procedure used to identify the D° meson is independent of the D° lifetime.

The sample of D° mesons used is obtained by observing the decay

$$D^{*+} \rightarrow D^\circ \pi^+ \\ \rightarrow K^- \pi^+ \quad .$$

It has been shown previously[30] that this decay can be isolated with very little background at high values of z, where z is twice the energy of the D^{*+} divided by $E_{c.m.}$. For this analysis, all particles were tried as pions or kaons, and all oppositely charged kaon pion pairs with invariant mass of 1.72 GeV/c^2 $< M_{K\pi} <$ 2.00 GeV/c^2 were taken as D° candidates. With their momenta constrained to the D° mass, each D° candidate was then combined with the additional pions in the event and those combinations with a small mass difference ($M_{D\pi} - M_D$) were called D^{*+} candidates. Further cuts were then applied to ensure that the production point of the D° was well measured by the vertex chamber. In addition, a well constructed D° decay vertex was ensured by accepting only those decay vertices with a χ^2/dof < 5. This cut discriminates against events where tracks from the D° have scattered or been mismeasured. The mass difference after all cuts is shown in Fig. 15. D^{*+} events were defined to be those with a $z_{D^*} > 0.6$ and a mass difference of $143 < (M_{D\pi} - M_D) < 149$ MeV/c^2. A total of 20 well measured events are seen in the D^{*+} region, and no other combinations are shown. We estimate a background of about $1\frac{1}{2}$ events. It is estimated that at most 5% of the D^{*+}'s with $z > 0.6$ originate from bottom meson decays.

The decay length for each observed D° decay was calculated as the distance between the D° vertex and the e^+e^- collision point, taken to be the average beam position

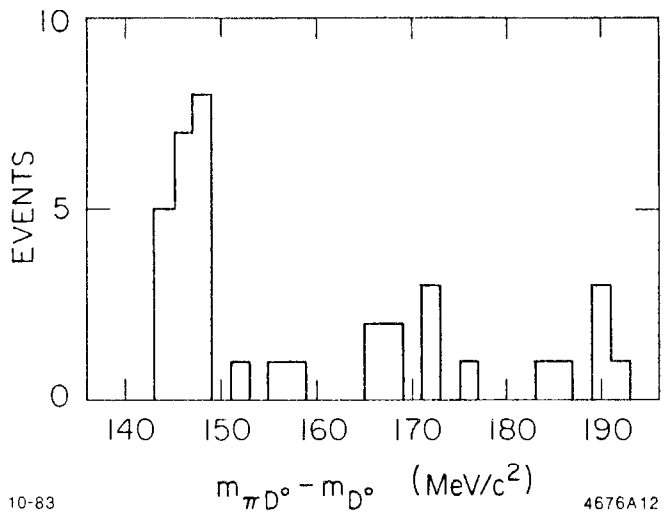


Fig. 15. The mass difference ($m_{\pi D^\circ} - m_{D^\circ}$) for D^{*+} candidates with $z > 0.6$ (preliminary data).

for a run. The measurement took place in the plane perpendicular to the beam direction and then corrected for the polar angle using the D^0 direction. The properties of the beam and the fitting procedure have been described in the sections on the tau lifetime and b lifetime. The 20 individual measurements of the lifetime shown in Fig. 16. The most probable mean decay time for the D^0 was found using a maximum likelihood fit to an exponential decay distribution, convoluted with Gaussian errors, the individual errors being retained. The result of the fit gives $\tau_{D^0} = \left(4.0^{+\ 1.4}_{-\ 1.1}\right) \times 10^{-13}$ sec, where the error is statistical.

To check for biases in the vertexing and fitting procedure we used Monte Carlo simulated data for D^0 production and decay. For several mean input lifetimes, the analysis method yielded these lifetimes within the statistical errors. As a further check, we constructed a sample of "pseudo D^0's" from tracks in hadronic events having similar topology and kinematics to that of the D^0 events. Tracks giving an invariant mass consistent with a K^0_S were removed. The mean lifetime of the fake D^0's was found to be slightly positive. This was expected since some candidate tracks came from heavy quark decays. From the above and other considerations we estimate the systematic error to be 1.0×10^{-13} sec.

In summary, we have measured the D^0 lifetime to be $\tau_{D^0} = \left(4.0^{+\ 1.4}_{-\ 1.1} \pm 1.0\right) \times 10^{-13}$ sec where the first error is statistical, the second systematic. The analysis was based on $\sim$ 100 pb^{-1} yielding 20 well measured events with small background. This measurement is consistent with all other measurements of the D^0 lifetime using different techniques.

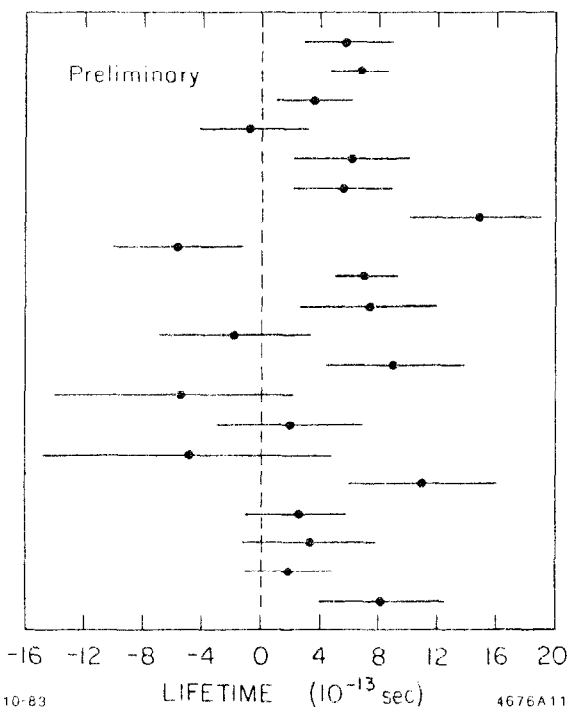


Fig. 16. The individual measurements of the lifetime for the 20 D^0 candidates.

6. A Search for Supersymmetric Electrons

Supersymmetric theories[31] associate fermions and bosons in multiplets such that all known particles have supersymmetric partners whose spins differ from ordinary particles by $\pm 1/2$. Each supersymmetric particle has the same electromagnetic and weak couplings as its partner, although its mass may be different because of symmetry breaking. It is possible that all superpartners have large masses compared to M_W, in which case evidence supporting the theory will have to wait for some time. Supersymmetry has been popular since it helps solve the hierarchy problem of the standard gauge theories.[32] At present, there is no experimental evidence supporting the existence of any superpartners.

We have made a search for the selectron, $\tilde{e}$, the supersymmetric partner of the electron. It can be singly produced in association with photinos, $\tilde{\gamma}$ (spin -1/2, neutral partner of the photon), through the reaction $e^+e^- \rightarrow e^{\pm} + \tilde{e}^{\mp} + \tilde{\gamma}$. The Feynman graphs for this production are shown in Fig. 17. The produced selectron is assumed to decay rapidly into a photino and electron. The photinos are assumed to be massless and noninteracting. This gives a distinct experimental signature; one hard electron detected with large transverse momentum relative to the beam axis.[33] This procedure allows us to extend the mass range of the search to 75% of the $E_{c.m.}$. This is of course in contrast to previous pair production searches which are limited to masses no greater than 50% of the $E_{c.m.}$.[34–36]

Several properties of the detector not mentioned earlier are important for this search. Charged particles can be detected to within 10° of the beam axis using the inner band of wires in the vertex detector. The small angle tagging (SAT) system consists of four semicircular modules, with two on either side of the main detector. This calorimeter covers the forward and backward cones between 2° and 4° from the beam axis, and is 15 radiation lengths (X_0) thick. The endcaps have an acceptance of $0.75 < |\cos\theta| < 0.92$, and are approximately $5X_0$ thick but have a substantial break in their azimuthal coverage due to their support stand.

The following criteria were applied to all events which passed the trigger requirement; one charged track depositing at least 1 GeV in the LA calorimeter. First, in order to measure the energy of the charged track reliably, we required the particle to have $|\cos\theta| < 0.70$ and to miss the azimuthal gaps between the modules by at least 2.7°. The detected track was called an electron if it deposited at least 6 GeV in the LA module. This also helped eliminate background from two-photon production of low energy electrons. To eliminate cosmic ray showers, tracks were required to originate from the beam luminous region and the event was required to have less than 50 hits in the drift chambers. Events containing photons were ignored unless they were within 10° of the track, which would be consistent with an electron radiating in the detector material before the LA system. In addition we confined all unseen particles to within 2° of the cone about the beam axis by requiring no evidence for low angle tracks in the vertex detector or energy deposit above 3 GeV in the SAT shower counters. After the above cuts we were left with 763 events to analyse. One further cut was applied to these events after a study of the background sources.

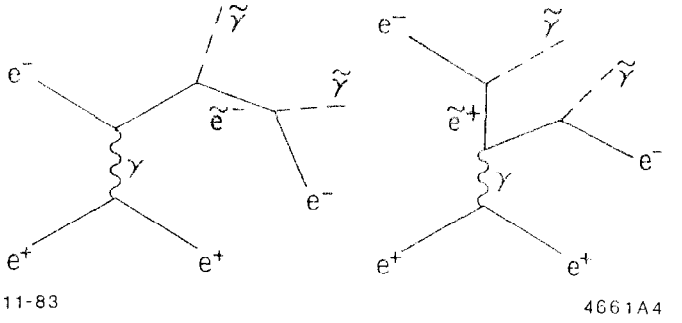


Fig. 17. Diagrams for production of a single supersymmetric electron in e^+e^- annihilation.

The major sources of background in this search are QED processes, in particular $e^+e^- \to e^+ + e^- + \gamma$ ($ee\gamma$) where one electron is detected, one goes down the beam axis at a small angle and the gamma falls into a dead or inefficient region of the calorimeter. The three body kinematics of these events, together with the confinement of the unseen electron to within 2° of the beam axis allows the gamma direction to be determined. The accuracy of predicting the gamma direction was checked by using events in which the gamma is detected. Figure 18 shows a plot of χ_{cos}, the normalized error distribution in the cosine of the gamma polar angle, ($\cos\theta_\gamma$), with a Gaussian fit superimposed. The fit, which did not include the tails, fits the data well and supports the three body hypothesis. The tails are assumed to arise from higher order QED processes and non-Gaussian tails in the experimental resolution. The distribution of deviations in the azimuthal angle was found to have a FWHM of 0.02 radians. In addition, we have studied the angular distribution of the detected photons in the $ee\gamma$ events. From this we calculate that 266 events with an undetected photon fall into the dead region of our calorimetric acceptance ($\cos\theta$ between 0.715 and 0.750, between the LA system and the endcap). This number and the resolution determined from Fig. 18 suggest a cut of $|\cos\theta_\gamma| < 0.54$ would reduce the $ee\gamma$ background to less than one event. After this cut the efficiency for high mass selectrons remains $\sim 40\%$ since their angular distribution is quite uniform. The additional backgrounds coming from higher order QED processes such as $ee\gamma\gamma$, tau production and two photon processes were found to be small.

The effect of all cuts used in this analysis defines an acceptance shown in Fig. 19 for a single (negatively) charged prong. The data points shown are consistent with the known background estimates. The search yielded no final candidate events for an integrated luminosity of 123 pb^{-1}. This yields a 95% confidence level upper limit on the cross section within the acceptance of Fig. 19 of 2.4×10^{-2} pb.

Finally, we set an upper limit on the cross section for selectron production as a function of the selectron mass. The cross section of Ref. 33 was integrated over the acceptance and is shown in Fig. 20. The upper limit on the cross section gives a 95% confidence level lower limit on the mass of the selectron of

$$M_{\tilde{e}} > 22.2 \text{ GeV/c}^2 \quad .$$

Here we assume the photino does not interact in the detector and that the parameters

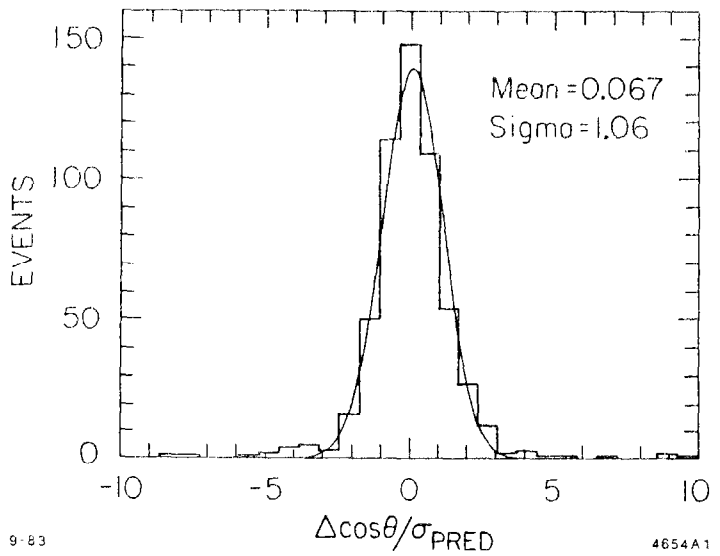


Fig. 18. Distribution of $(\cos\theta_{\text{predicted}} - \cos\theta_{\text{observed}})/\sigma_{\cos\theta}$ for events with one seen electron and one seen photon. The solid curve is the best fit to the data as described in the text.

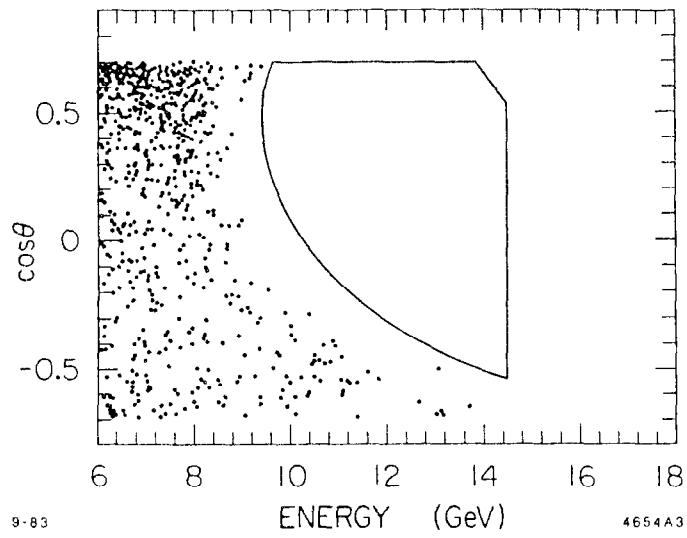


Fig. 19. MARK II acceptance for single negative prongs. Also shown is a scatter plot of single-prong events. Positive-charge prongs have $\cos\theta$ replaced by $-\cos\theta$.

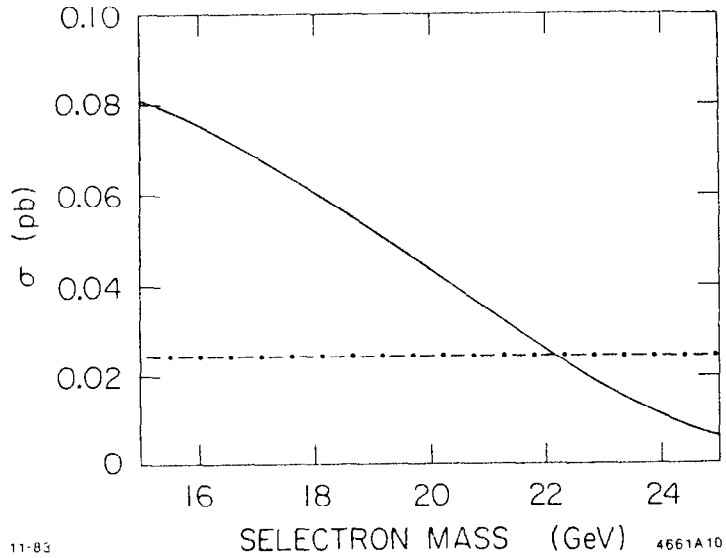


Fig. 20. Cross-section for singly produced selectrons as a function of selectron mass. The dot-dashed line is the 95% C.L. limit on single selectron production.

of right-handed and left-handed electrons are degenerate. If one partner is infinitely heavy, the mass limit for the lighter selection becomes 19.4 GeV/c^2. Both limits exceed previously published limits on the selectron mass.[34–36]

6. Weak Neutral Current Couplings of Leptons

The standard model[37] of Weinberg-Salam-Glashow unified the weak and electromagnetic interactions. In this model the differential cross sections for lepton pair production were sensitive to the interference between the weak neutral current and the electromagnetic current. The weak neutral current, mediated by the Z°, was characterized by two dimensionless coupling constants g_a (axial vector) and g_v (vector). The model predicts $g_a = -1/2$ and relates g_v to the weak mixing angle, $g_v = 2\sin^2\theta_W - 1/2$. We report a high statistics measurement of the differential cross sections for the reactions:

$$e^+e^- \to e^+e^- \qquad \text{(Reaction 1)}$$

$$e^+e^- \to \mu^+\mu^- \qquad \text{(Reaction 2)}$$

$$e^+e^- \to \tau^+\tau^- \qquad \text{(Reaction 3)}$$

based on a data sample corresponding to an integrated luminosity of 100 pb^{-1}.

The unpolarized relativistic cross section for Reactions (2) and (3), including Z° exchange, is

$$\frac{4s}{\alpha^2}\frac{d\sigma}{d\Omega} = (1+\cos^2\theta)\left(1 + \frac{G_F g_v^e g_v^\ell}{\pi\alpha\sqrt{2}}\,\frac{sM_z^2}{s-M_z^2}\right) + \left(\frac{2G_F g_a^e g_a^\ell}{\pi\alpha\sqrt{2}}\,\frac{sM_z^2}{s-M_z^2}\right)\cdot\cos\theta \qquad (7)$$

where G_F is the Fermi coupling constant, and θ is the angle between the outgoing positive lepton ℓ and the positron beam direction $\hat{z}$. Terms proportional to G_F arise from the interference between the weak and electromagnetic amplitudes. The axial vector component produces a forward-backward asymmetry in Reactions (2) and (3), and the vector component shifts their cross section relative to (1); both g_a and g_v modify the shape of the cross section in Reaction (1). The expression for Bhabha scattering is more complicated due to t-channel exchange diagrams.

The selection criteria for Reactions (1) and (2) yield 5312 μ pairs and 81309 Bhabha events. The more complicated decay topology of the tau gives 3714 events after all selection criteria are applied. Total background corrections of 0.03% ($e^+e^- \to \tau^+\tau^-$) and 2.9%±0.9% ($e^+e^- \to e^+e^-\mu^+\mu^-$, $\tau^+\tau^-$, hadrons) are applied to Reactions (1) and (2) respectively. Reaction (3) is corrected for contaminations of 1.6% from $e^+e^- \to \mu^+\mu^-(\gamma)$, 1.4% from hadronic backgrounds, and 3.1% from two-photon processes. The event acceptances at $\cos\theta = 0$ are 77%, 80% and 60% for Reactions (1), (2) and (3) respectively, and fall to 73%, 77% and 52% at $|\cos\theta| = 0.6$. The acceptance corrected, background subtracted, differential cross sections are shown in Figs. 21, 22 and 23 and are compared to $\mathcal{O}(\alpha^3)$ QED prediction.

From uncertainties in the background estimates, errors in detector simulation and uncertainty in the decay modes of the tau, we find a 1.6% normalization error on the ratio $\sigma_{\mu\mu}/\sigma_{ee}$ and a 2.8% error on the ratio $\sigma_{\tau\tau}/\sigma_{ee}$.

We use a maximum likelihood technique to fit Reactions (1)-(3) to the $\mathcal{O}(\alpha^3)$ QED cross section plus the weak contributions[38] using the corrected $\cos\theta$ distributions. Setting $g_v^2 = 0$, we find $g_a^e g_a^\mu = .32 \pm .07 \pm .02$ and $g_a^e g_a^\tau = .10 \pm .09 \pm .02$, where the first error is statistical and the second systematic. The fits yield acceptance, background, and QED corrected forward-backward electroweak asymmetries, extrapolated to full $\cos\theta$ interval, of $A_\mu^{weak} = -7.1\% \pm 1.7\%$ and $A_\tau^{weak} = -4.2\% \pm 2.0\%$ where the standard model predicts $A^{weak} = -5.7\%$, radiatively corrected.[39] The fitted cross sections are superimposed on the data in Figs. 22 and 23. The $\mu - \tau$ universality of the axial-vector current is tested and we find $g_a^\tau/g_a^\mu = 0.6 \pm 0.3$. If we assume $e-\mu-\tau$ universality $g_a^2 = .27 \pm .06 \pm .02$ from Reactions (2) and (3). From a simultaneous fit to all three reactions we find $g_a^2 = .23 \pm .05 \pm .02$ and $g_v^2 = .03 \pm .03 \pm .03$, where systematic errors have been explicitly included in the fit and the fitted cross section is superimposed on the data in Fig. 23. Table II[40] summarizes e^+e^- data on g_v^2 and g_a^2 and gives a world average.

These results are in good agreement with the standard model. The probability that QED alone would have led to the results presented here is 6×10^{-7}. The weak couplings were computed in the limit $M_Z \to \infty$. For a $M_Z \sim 93$ GeV/c^2,[41] and including radiative corrections, g_a^2 is only decreased by 2.5%.

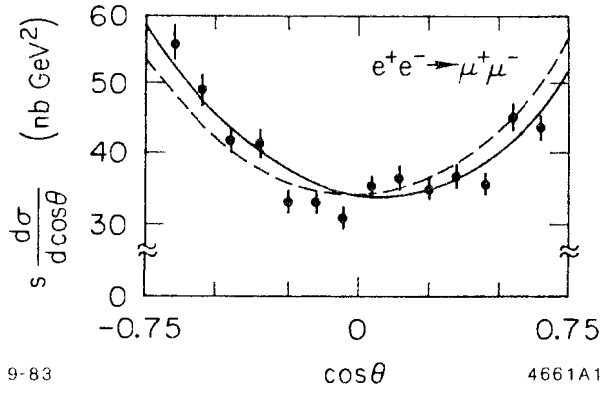


Fig. 21. The differential cross sections for Reaction (2), normalized to the QED prediction are shown. The dashed line corresponds to the $O(\alpha^3)$ QED cross section and the solid line to the fitted cross section.

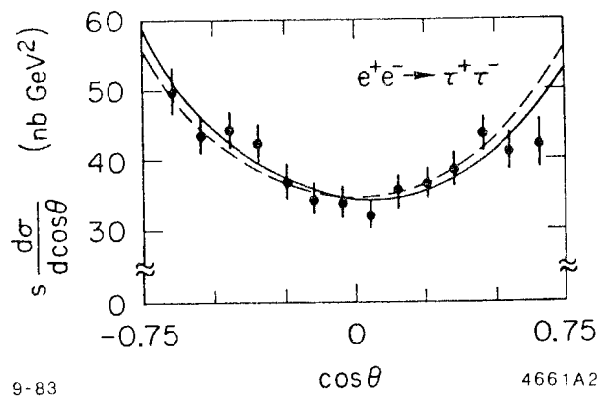


Fig. 22. The differential cross sections for Reaction (3), normalized to the QED prediction are shown. The dashed line corresponds to the $O(\alpha^3)$ QED cross section and the solid line to the fitted cross section.

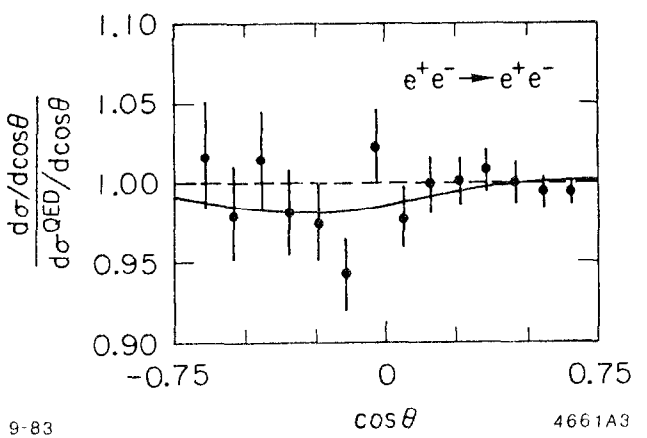


Fig. 23. This is the ratio of the differential cross section for Reaction (1) to the $O(\alpha^3)$ QED prediction. The experimental cross section is normalized to the electroweak cross section taken from a simultaneous fit to all three reactions. The dashed line corresponds to the $O(\alpha^3)$ QED cross section and the solid line to the fitted cross section.

Table II

Expt.	g_v^2	g_a^2
CELLO	$-.03 \pm .08$	$.30 \pm .12$
JADE	$.01 \pm .08$	$.30 \pm .05 \pm .03$
MAC	$.03 \pm .16$	$.24 \pm .04 \pm .01$
MARK II	$.03 \pm .03 \pm .03$	$.23 \pm .05 \pm .02$
MARK J	$.01 \pm .05 \pm .06$	$.31 \pm .04 \pm .03$
TASSO	$-.04 \pm .06$	$.24 \pm .06 \pm .01$
WORLD AVG.	$.005 \pm .03$	$.26 \pm .02$

If we assume $(g_a^e)^2 = 1/4$ from the standard model, take $g_v^2 = 0.0016$ ($\sin^2\theta_W = 0.23$) from neutrino scattering experiments, and set $M_Z = 93$ GeV/c^2, then we find the ratio of the measured to the expected cross section normalized to Bhabha events is $1.002 \pm .013 \pm .016$ in Reaction (2), and $0.996 \pm .016 \pm .028$ in Reaction (3) and extract the vector couplings $g_v^e g_v^\mu = .00 \pm .05 \pm .06$ and $g_v^e g_v^\tau = .01 \pm .06 \pm .09$. The coupling of the tau are summarized in Table III[42] and compared to world data.

Table III

Expt.	$g_v^e g_v^\tau$	$g_a^e g_a^\tau$
CELLO	$---$	$.28 \pm .14$
JADE	$---$	$.22 \pm .08$
MAC	$---$	$.06 \pm .13$
MARK II	$.01 \pm .06 \pm .09$	$.19 \pm .09 \pm .02$
MARK J	$---$	$.22 \pm .11$
TASSO	$< .55$	$.16 \pm .13$
WORLD AVG.		$.19 \pm .04$

A thorough description of this electroweak analysis can be found in Ref. 43.

7. Weak Neutral Current Couplings of the b Quark

We present a preliminary study of the angular distributions of events tagged with an energetic lepton in order to find evidence for the weak neutral current in the process

$$e^+e^- \to b\bar{b} \quad .$$

A very simple form of the angular distribution for the above process is given by

$$\frac{d\sigma}{d\cos\theta} = \frac{\pi\alpha^2 Q_b^2}{2s}\left[(1+\cos^2\theta) - \frac{4g_a^e g_a^b \chi}{\alpha Q_b}\cos\theta\right] \qquad (8)$$

where χ is a constant related to the Fermi coupling G_F, the square of the center-of-mass energy s and M_Z. Here Q_b is the charge of the bottom quark, $-1/3$, g_a^b is the axial vector coupling of the b quark and θ is the polar angle between the quark and the incoming electron.

We study the b quark couplings because bottom events are relatively easy to tag using leptons and we expect a large forward-backward asymmetry at $\sqrt{s} = 29$ GeV of

$$A_b = -0.19$$

with a full solid angle detector. However the reality of the measurement is there exists no clean sample of bottom events and the low tagging efficiency reduces the statistics compared to $e^+e^- \to \mu^+\mu^-$ by over an order of magnitude.

The technique is quite straightforward. A b-enriched, c-enriched and background sample of events are assembled using the lepton tagging technique described in Section 2. The sign of the quark comes from the sign of the lepton. Therefore

$$b \to e^- \quad \bar{b} \to e^+ \qquad \text{and} \qquad c \to e^+ \quad \bar{c} \to e^- \quad .$$

However, the b-enriched sample contains $c\bar{c}$ events, leptons from the cascade decay $b \to c \to \ell$, and nonprompt sources of leptons. These effects and others either cancel or dilute the signal we are trying to measure.

We use a maximum likelihood technique to fit for g_a^b where we fix charm relative to bottom and take into account the fractions of each type of background and the corresponding asymmetries of these backgrounds. The angular distributions for the three regions, b-enriched, c-enriched and background are shown in Figs. 24(a)-(c). The solid curves are the best fit solutions and the dashed curves are for the symmetrical case. From the fit, we find $g_a^b = -0.75^{+0.35}_{-0.30} \pm 0.20$ which can be compared to the Weinberg-Salam-Glashow value of $g_a^b = -1/2$. The above results are consistent with zero at a confidence level of only 2%.

8. K* Production

We have searched for evidence of the reaction $K^{*\pm} \to K_S^0\pi^\pm$ based on a data sample of hadronic events corresponding to an integrated luminosity of ~ 100 pb^{-1}. A preliminary analysis shows a clear signal for $E_{K^*} > 3.5$ GeV. This is shown in Fig. 25. We form the ratio of cross sections for K^* and K° and find

$$\frac{\sigma_{K^*}}{\sigma_{K^\circ}} = 0.84 \pm .17 \pm .25$$

for $E_{K^*,K} > 3.5$ GeV. This indicates a large vector fraction in the fragmentation process. Naively, we expect three vector particles for every one pseudo scalar, and hence a ratio of 0.75. Our results are consistent with data presented by the TPC (W. Hofmann) collaboration at this conference.

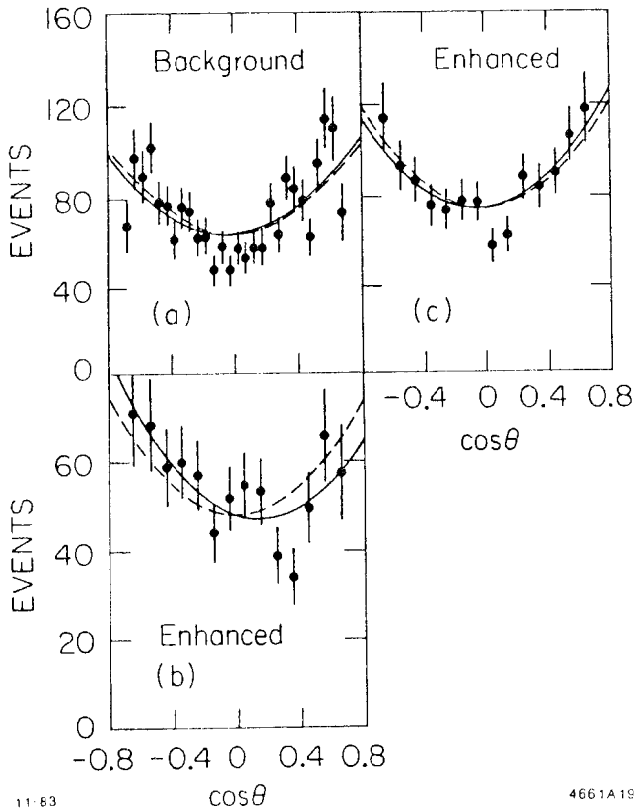


Fig. 24. Thrust angular distributions in the three regions. Dashed line is a symmetrical curve and solid curve is best fit to the data.

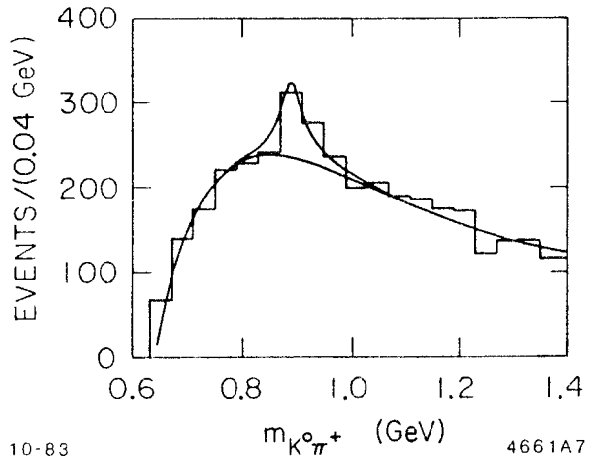


Fig. 25. $K_S\pi$ invariant mass distribution for $E_{K^+} > 3.5$ GeV. Curves show area fit to the background and K^*.

References

1. Members of the MARK II SLAC-LBL-Harvard Collaboration are: G. S. Abrams, D. Amidei, A. R. Baden, C. A. Blocker, A. M. Boyarski, M. Breidenbach, P. Burchat, D. L. Burke, J. M. Dorfan, G. J. Feldman, G. Gidal, L. Gladney, M. S. Gold, G. Goldhaber, L. Golding, G. Hanson, D. Herrup, R. J. Hollebeek, W. R. Innes, J. A. Jaros, M. Jonker, I. Juricic, J. A. Kadyk, A. J. Lankford, R. R. Larsen, B. LeClaire, M. Levi, N. S. Lockyer, V. Lüth, C. Matteuzzi, M. E. Nelson, R. A. Ong, M. L. Perl, B. Richter, M. C. Ross, P. C. Rowson, T. Schaad, H. Schellman, D. Schlatter, R. F. Schwitters, P. D. Sheldon, J. Strait, G. H. Trilling, C. de la Vaissiere, J. M. Yelton and C. Zaiser.
2. R. Helm *et al.*, SLAC-PUB-3070 (1983).
3. J. A. Jaros, in *Proceedings of the International Conference on Instrumentation for Colliding Beam Physics*, SLAC-Report 250, edited by W. Ash, Stanford, California (1982).
4. J. Dorfan, SLAC-PUB-2813 (1981).
5. J. D. Bjorken, Phys. Rev. D17, 171 (1978); M. Suzuki, Phys. Lett. 71B, 139 (1977).
6. N. Abramowicz *et al.*, Z. Phys. C15, 19 (1982).
7. W. B. Atwood, SLAC-PUB-2980, 1982.
8. M. E. Nelson *et al.*, Phys. Rev. Lett. 50, 1542 (1983).
9. M. J. Puhala *et al.*, Phys. Rev. D25, 695 (1982).
10. R. D. Field and R. P. Feynman, Nucl. Phys. B136, 1 (1978).
11. A. Ali *et al.*, Phys. Lett. 39B, 155 (1980).
12. W. Bacino *et al.*, Phys. Rev. Lett. 43, 1073 (1979).
13. E. Thorndike, talk presented at XVIII Rencontre de Moriond (CLEO), March (1983); P. M. Tuts, talk presented at XVIII Rencontre de Moriond (CUSB), March (1983).
14. C. Peterson *et al.*, Phys. Rev. D27, 105 (1983).
15. D. Schlatter, SLAC-PUB-2982, 1982.
16. See talks at this Conference by R. Ehrlich (CLEO), J. Lee-Franzini (CUSB), C. Young (DELCO), M. Piccolo (MAC), E. Lohrmann (PETRA Review).
17. M. E. Nelson, Ph.D. Thesis, LBL-16724 (1983).
18. M. Kobayashi and T. Maskawa, Prog. Theor. Phys. 49, 652 (1973). For a recent review of quark mixing angles see Ling-Lie Chau, Phys. Rep. 95, (1983).
19. P. Ginsparg and M. Wise, HUTP-83/A027 (1983); E. Paschos, B. Stech and U. Turke, CERN-TH-3601 (1983).
20. P. Ginsparg, S. Glashow and M. Wise, Phys. Rev. Lett. 50, 1415 (1983).
21. E. Fernandez *et al.*, Phys. Rev. Lett. 51, 1022 (1983); N. S. Lockyer *et al.*, Phys. Rev. Lett. 51, 1316 (1983).
22. M. Gaillard and L. Maiani, in *Proceedings of the 1979 Cargese Summer Institute on Quarks and Leptons*, ed. by M. Levy *et al.*, Plenum Press, New York, 1979, p. 433.
23. F. J. Gilman and J. S. Hagelin, Phys. Lett. 126B, 111 (1983); and SLAC-PUB-3226 (1983).
24. B. Winstein *et al.*, Fermilab proposal 617.
25. See for example M. Wirbel, Phys. Lett. 121B, 252 (1983).
26. G. J. Feldman *et al.*, Phys. Rev. Lett. 48, 66 (1982).
27. W. T. Ford *et al.*, Phys. Rev. Lett. 49, 106 01982).
28. H. J. Behrend *et al.*, Nucl. Phys. B211, 369 (1983).
29. C. A. Blocker *et al.*, Phys. Lett. 109B, 119 (1982). The uncertainty in τ_τ comes primarily from the error in B_e.
30. J. M. Yelton *et al.*, Phys. Rev. Lett. 49, 430 (1982).
31. P. Fayet and S. Ferrara, Phys. Rep. 32C, 249 (1977).
32. E. Witten, Nucl. Phys. B202, 253 (1982).
33. M. K. Gaillard, I. Hinchliffe and L. Hall, Phys. Lett. 116B, 279 (1982); Phys. Lett. Errata, to be published.
34. H. J. Behrend *et al.*, Phys. Lett. 114B, 287 (1982).

35. R. Brandelik *et al.*, Phys. Lett. 117B, 365 (1982).

36. D. Cords, *Proceedings of the 20th International Conference on HEP*, Wisconsin, 1980, p. 590.

37. S. Glashow, Nucl. Phys. 22, 579 (1961); S. Weinberg, Phys. Rev. Lett. 19, 1264 (1967); A. Salam, in "Elementary Particle Theory," Proceedings of the 8th Nobel Symposium, ed. by N. Svartholm (Almquvist and Wiksells, Stockholm, 1968), p. 367.

38. R. Budny, Phys. Lett. 45B, 340 (1973); Phys. Lett. 55B, 227 (1975).

39. F. A. Berends, R. Kleiss and S. Jadach, Nucl. Phys. B202, 63 (1982).

40. H. J. Behrend *et al.*, Z. Phys. C16, 301 (1983). W. Bartel *et al.*, Phys. Lett. 108B, 140 (1982). Phys. Lett. 99B, 281 (1981). E. Fernandez *et al.*, Phys. Rev. Lett. 50, 1238 (1983). B. Adeva *et al.*, Phys. Rev. Lett. 48, 1701 (1982). R. Brandelik *et al.*, Phys. Lett. 117B, 365 (1982). B. Naroska, invited talk presented at the International Symposium on Lepton and Photon Interactions at High Energies, Ithaca, New York (1983).

41. G. Arnison *et al.*, Phys. Lett. 126B, 398 (1983). P. Bagnaia *et al.*, Phys. Lett. 129B, 130 (1983).

42. H. J. Behrend *et al.*, Phys. Lett. 114B, 282 (1982). B. Naroska, invited talk presented at the International Symposium on Lepton and Photon Interactions at High Energies, Ithaca, New York (1983).

43. M. Levi *et al.*, Phys. Rev. Lett. 51, 1941 (1983).

JETS IN HIGH TRANSVERSE ENERGY EVENTS PRODUCED IN pp COLLISIONS AT THE CERN ISR

D. Lissauer
CERN and Tel-Aviv University

ABSTRACT

Recent results on jet production from the Axial Field Spectrometer Collaboration at the ISR will be presented. Events with large transverse energy into a calorimeter with a full azimuthal coverage and $|y| < 0.9$ have been investigated at $\sqrt{s}$ = 30, 45 and 63 GeV. A clear emergence of jets is observed at $\sqrt{s}$ = 63 and 45 GeV in the region of 30 GeV transverse energy. The properties of the jets produced in the high E_T events have been investigated and found to be similar to those produced in e^+e^- annihilation. The charge correlation of positive and negative particles show differences consistent with expectations from valence quark scattering.

INTRODUCTION

Recent experiments at $\sqrt{s}$ = 63 and 540 GeV have observed important contributions from jet production at sufficiently large transverse energy, E_T [1-6], deposited in calorimeters which are large compared to the jet size. Such events are interpreted in terms of hard scattering of the hadron constituents, and provide a relatively unbiased way of studying deep inelastic hadron scattering [7]. At lower $\sqrt{s}$, similar experiments [8] did not find a dominant jet production, even at the highest accessible E_T. This can be explained in terms of contamination of jets by beam fragmentation [9] and significant smearing of the hard scattering by gluon bremsstrahlung [10].

© D. Lissauer 1983

In this paper I will report on the results obtained by the AFS collaboration [11] which is investigating jet production at the CERN ISR. A brief overview of the experimental set up will be given in Section I. Section II will give results on energy dependence of jet production. The emergence of jets in high E_T events will be discussed in Section III. Jet properties will be discussed in Section IV.

I. EXPERIMENTAL SET UP:

The data on which I will report here were taken with the CERN Axial Field Spectrometer (AFS). Figure 1 shows a view of the spectrometer components used and details of a calorimeter stack. Each calorimeter wall is formed of 32 stacks, each stack consisting of 6 towers creating a matrix of 12 x 16 towers, each with a 20 x 21.6 cm^2 face in a plane 118 cm from the beam intersection. The towers have 4-fold wavelength-shifter read-out: right and left, at each of two depths (the first 6 radiation lengths, and the second $\sim$ 3.6 absorption lengths). An energy resolution of 16% and 37% at 1 GeV is obtained in test beams for electromagnetic and hadronic showers, respectively. This hadronic resolution is consistent with that found at the ISR using low-multiplicity minimum-bias events by comparing the energy deposited in the calorimeter to that measured in the drift chamber of the AFS. Inter-tower calibration is maintained to $\pm$ 1.5% by frequent monitoring of the uranium activity. The estimated uncertainty in the absolute energy scale for isolated showers is $\leq$ 4%. This error is dominated by the calorimeter response for low momentum (< 1 GeV) hadrons. The uncertainty in the E_T measurement is dominated by other factors and will be discussed later. The calorimeter has 2π azimuthal coverage and an 8.8 sr solid angle. The rapidity coverage in the centre-of-mass varies with azimuth from $|y| < 0.6$ to $|y| < 1.2$ because of the beam-beam crossing angle and the box-like construction of the calorimeter.

With the non-projective geometry of the calorimeter, isolated electromagnetic showers are localized to $\sim$ 1 cm, and hadronic showers to between 3 to 10 cm on the calorimeter face (for energies $\geq$ 0.5 GeV) depending on the incident angle. For more details on the calorimeter see Ref [12].

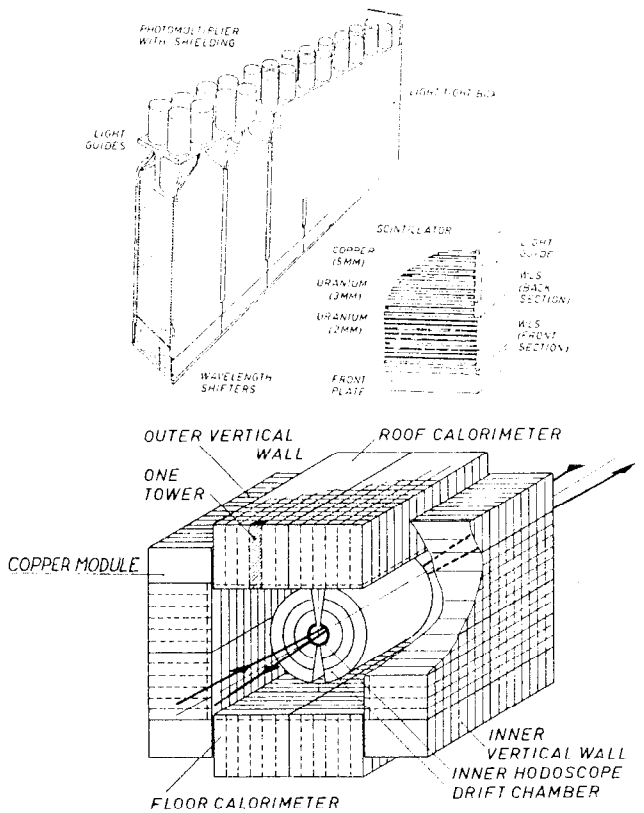


Fig. 1: Experimental set-up and details of the calorimeter stacks.

The central detector is a 42-layer cylindrical drift chamber segmented in 82 four-degree sectors. The coordinate in the transverse plane is provided by drift time, and the coordinate along the beam direction is provided by charge division. The resulting momentum error is 2% for 1 GeV/c particle.

The data which I will be discussing here were taken using two different E_T trigger configurations at the different $\sqrt{s}$ available at the ISR. The E_T trigger was formed by addition of the phototube dynode signals, weighted to transform pulse height in the laboratory to transverse energy in the CMS. The calorimeter signal was placed in coincidence with a minimum multiplicity signal of ≥ 2 hits, in the 44 element scintillation counters (IH) surrounding the beam. Upstream and downstream counters (BB), covering $2° < \theta < 6°$ in polar angle, are used to monitor the luminosity.

For the inclusive jet production cross-section discussed in Section II, only the roof stacks were used in the trigger. Data at $\sqrt{s}$ = 45 and $\sqrt{s}$ = 63 were obtained with an integrated luminosity of 1.23×10^{35} cm^{-2} and 3.6×10^{35} cm^{-2}, respectively. For the jet dominance data and jet properties analysis discussed in Sections III and IV the trigger was an overall E_T trigger, where the towers of all four walls were used in the sum. Data in this configuration were taken with various trigger thresholds at $\sqrt{s}$ = 30, 45 and 63 GeV with integrated luminosities of 9.9×10^{34}, 6.8×10^{35}, and 3.0×10^{36} cm^{-2}, respectively.

II. INCLUSIVE JET CROSS-SECTION

For this analysis only the roof calorimeter was used (historically because it was the first available). The data obtained were analysed using a pattern recognition program to reconstruct individual showers. Here one is utilizing the advantage of the high granularity of the AFS calorimeter. The transverse energy E_T is then calculated by using the energy of the individual showers.

In Figure 2 the spectra for the two center-of-mass energies are shown. The spectra are uncorrected for resolution, effects of energy leakage, and different calorimeter response to hadronic and electromagnetic showers. The errors shown are statistical only. The correction for the spectra are

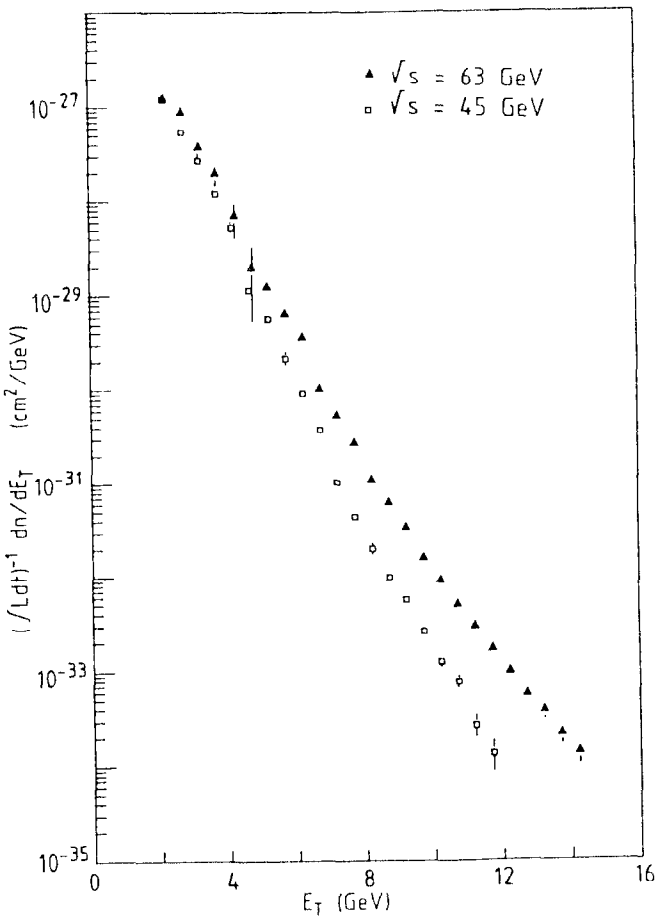


Fig. 2: The uncorrected transverse energy spectrum into a single calorimeter wall (roof). Error bars are statistical only.

model dependent and will depend on particle composition and momenta spectra because of differences in electromagnetic to hadronic shower response and the different leakage.

In order to investigate the structure of the events a thrust like quantity was defined

$$T = \sum \hat{E}' \cdot \vec{E}_i \; / \; \sum |\vec{E}_i|,$$

where sums were carried out over all clusters; E' is the unit vector representing the energy flow into the roof calorimeter and $\vec{E}_i$ are the individual cluster energy vectors; T is not explicitly maximized by variation of the E' direction and can take on values between 0.7 and 1.0. A pencil-like jet has T ≃ 1, and highly isotropic events have <T> ≃ 0.86. The minimum value of T, T = 0.7, corresponds to an event with maximally separated showers within the calorimeter wall.

Figure 3 shows the thrust distribution for a few E_T bins for both values of $\sqrt{s}$. The shape of the thrust distributions at the two energies are clearly changing with increasing E_T. They clearly deviate from what is expected for isotropic events by building up a high-thrust component. At $\sqrt{s}$ = 45 GeV, this component does not dominate to the same degree as it does at $\sqrt{s}$ = 63 GeV.

In order to obtain a jet cross-section, the fraction of events consistent with a hard-scattering constituent model is extracted from the shapes of the thrust distributions. Events with and without a hard-scattering constituent are generated using ISAJET [13], passed through a full simulation of the calorimeter response [14], and processed through the normal analysis chain.

In the fit one assumes that the thrust distributions have two components. The first component (jet) is described by hard-scattering constituents. The second component (non-jet) has a more isotropic event shape with a thrust distribution essentially the same as that observed for the events in the low E_T bins. The results show an increasing fraction of jet events with E_T. For a given E_T bin, events at $\sqrt{s}$ = 63 GeV have a higher fraction of jet events in the bin.

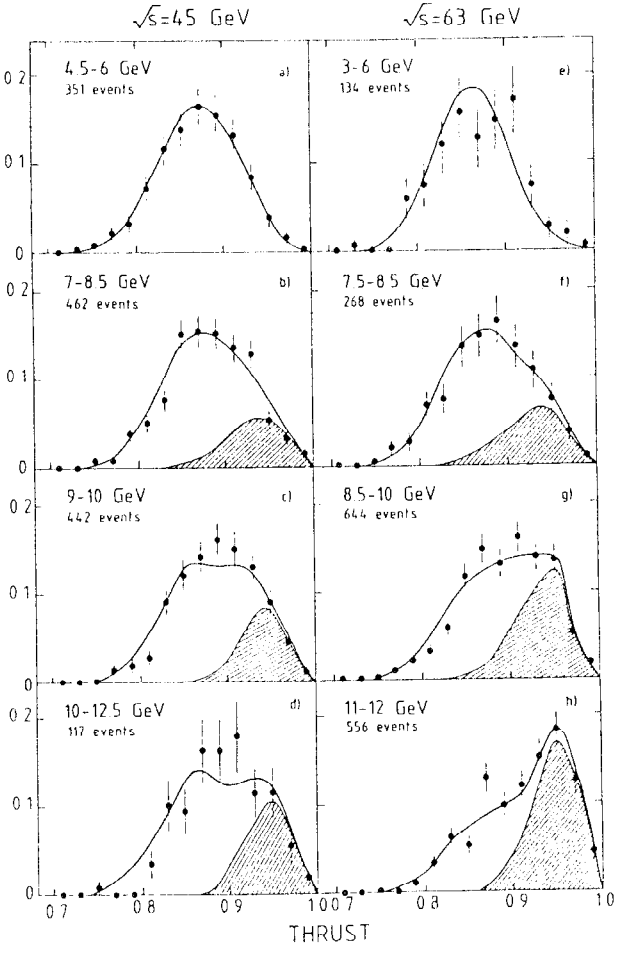


Fig. 3: Fraction of events per 0.02 units of thrust for different E_T bins at $\sqrt{s}$ = 65 GeV and $\sqrt{s}$ = 48 GeV. The shaded region represents contributions from jet component. Solid curves are results of the total fit.

Using the ISAJET Monte Carlo events and the detector simulation, one is able to relate the initial jet p_T to the E_T detected in the calorimeter. This together with the fit results enables one to transform the observed E_T spectrum into the p_T spectrum of the scattered constituent. The resulting inclusive jet production cross-section at y = 0 is shown in Fig.4. The inner errors reflect the statistical error of the fit and correction procedure. The outer errors include systematic uncertainties. An exponential fit, $\exp(-bp_T)$, gives a value for $b = 1.35 \pm 0.14\ GeV^{-1}$ at $\sqrt{s}$ = 45 GeV, and $1.02 \pm 0.09\ GeV^{-1}$ at $\sqrt{s}$ = 63 GeV. The dotted lines in Fig. 4 are the ISAJET predictions for the jet cross-section. The agreement in both shape and absolute normalization is good.

To parametrize the cross-section as a function of energy, one can fit the ISR data to a function of the form $A(1-x_T)^m \cdot p_T^{-n}$ (where $x_T = 2\,p_T/\sqrt{s}$). The results of the fit give values of $A = (1.6 \pm 1.0) \times 10^{-26}$, $m = 10.6 \pm 1.0$, and $n = 5.3 \pm 0.2$, where only the statistical errors are included. Since one expects that at low-x_T the pp and $p\bar{p}$ jet cross-sections will be essentially the same, one can compare the results with the $p\bar{p}$ data at $\sqrt{s}$ = 540 GeV presented in this conference, and indeed they are in very good agreement with the extrapolation of the above function. (See Fig. 5).

III. JET DOMINANCE AT HIGH E_T

The data obtained with total E_T trigger were analysed and E_T spectra for all three $\sqrt{s}$ energies are shown in Fig. 6. The spectra is uncorrected for resolution, energy leakage, and the different responses to hadronic and electromagnetic showers. To estimate the apparatus effect on the E_T distributions, events were generated using the observed single particle p_T distributions and the charged particle multiplicity distributions as measured in the drift chamber. The events were generated in the different E_T regions and simulated the apparatus response on these events. The correction to the spectra estimated to be a factor of eight at E_T = 40 GeV and less than a factor of four for $E_T < 25$ GeV. The spectra are consistent with an exponential fall off at large E_T.

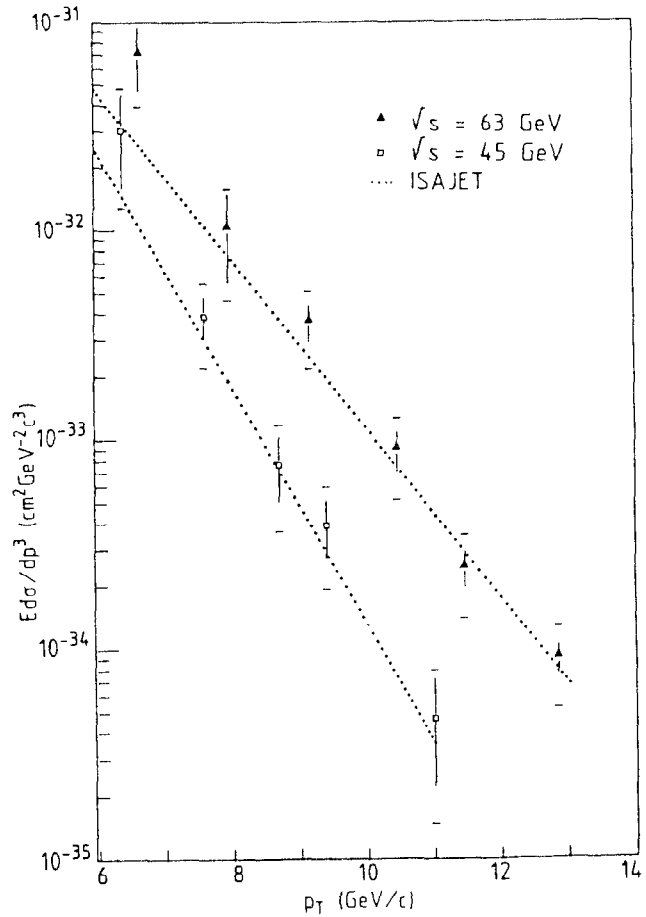


Fig. 4: Invariant jet cross-section at y = 0 versus p_T. The dotted lines are theoretical predictions (ISAJET).

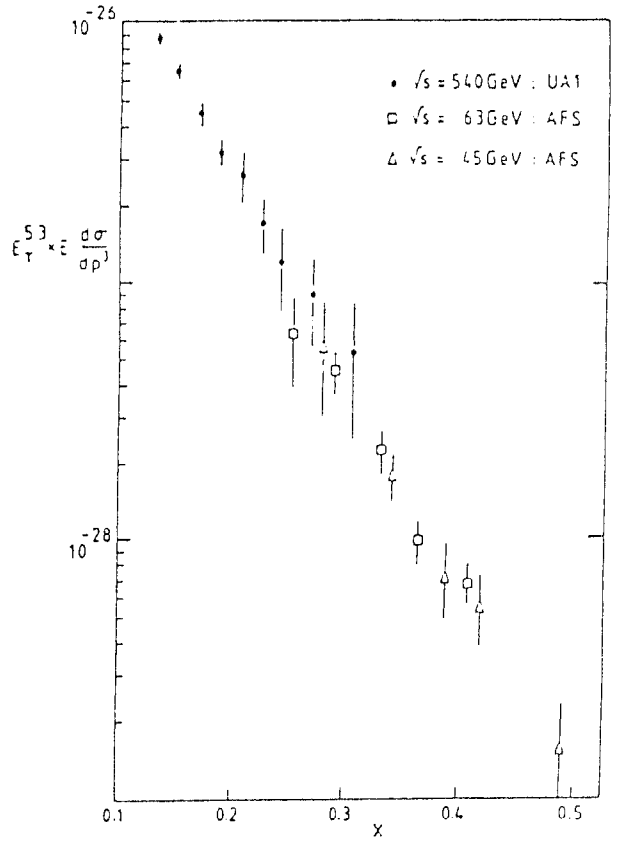


Fig. 5: The invariant jet cross-section multiplied by $E_T^{5.3}$ including data from UA1 experiment.

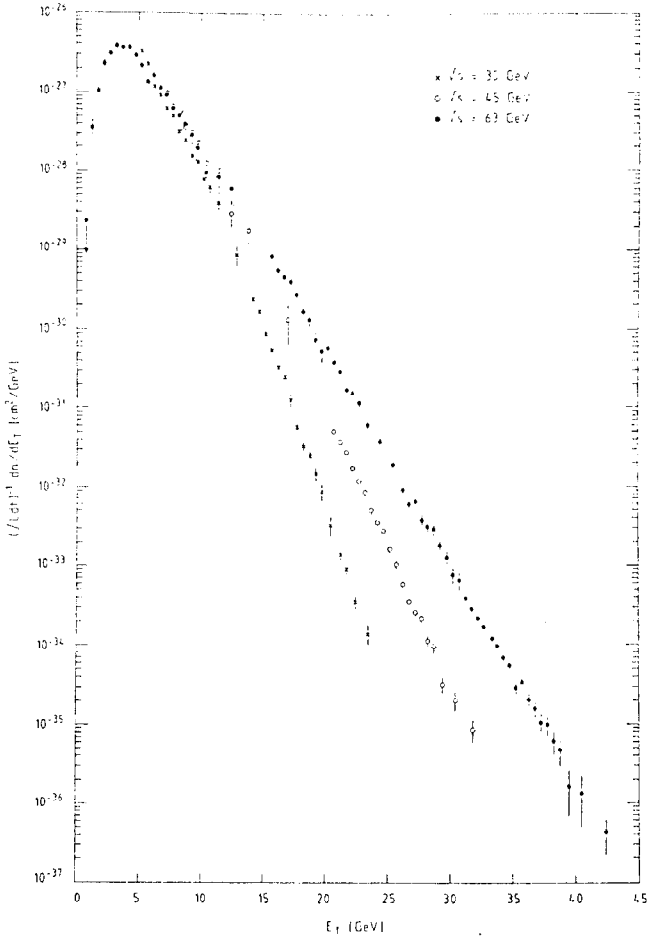


Fig. 6: The uncorrected transverse energy spectrum is to the full calorimeter at $\sqrt{s}$ = 30, 45 and 63 GeV; errors are statistical only.

In order to investigate the event shape, the circularity (C) was calculated. For each event the momentum tensor made up of the contribution of the transverse momentum of each cluster in the calorimeter is diagonalized. The quantity C is formed from the eigenvalues A and B (A > B):

$$C = 1 - [(A - B)/(A + B)] = \min \sum p_T^2 \; / \; 1/2 \sum p^2.$$

C is related to the planarity (P) by C = 1 - P. Circularity is the two-dimensional equivalent of sphericity.

The C-distributions are shown in Fig. 7 for the three c.m. energies in bins of E_T. For $\sqrt{s}$ = 30 GeV the distributions do not show a substantial change with E_T. For $\sqrt{s}$ = 45 GeV the C-distributions are quite similar except for the bin 25 < E_T < 30 GeV where the fraction of events at low circularity increases significantly.

At $\sqrt{s}$ = 63 GeV, the C-distributions are similar to those at lower $\sqrt{s}$ in comparable E_T bins. For E_T larger than 25 GeV the fraction of low circularity events increases very strongly with increasing E_T. For the highest bin 35 < 4_T < 40 GeV, most of the events are at low circularity, as would be expected if the contribution to the E_T is dominated by two jets. The peak at low circularity is evidence for an increasing dominance of simple two-body hard scattering over more complicated processes.

Fig. 8a shows the average value of C versus E_T for all three c.m. energies. The mean value of C is rather constant ($\sim$ 0.55 independent of energy) until E_T of 25 GeV where it decreases strongly. Fig. 8b displays the fraction of events with C < 0.2 versus E_T for the three c.m. energies, showing that this fraction starts increasing rapidly at $E_T \sim$ 25 GeV. Fig. 8c shows the fraction of events with more than 60% of the total E_T in two non-overlapping regions of $\Delta\phi$ = 60° and Δy = 1, versus E_T. This distribution also rises rapidly at $E_T \sim$ 25 GeV.

It is important to note that the character of the event seems to change over a relatively short range in E_T. The $\sqrt{s}$ dependence does not

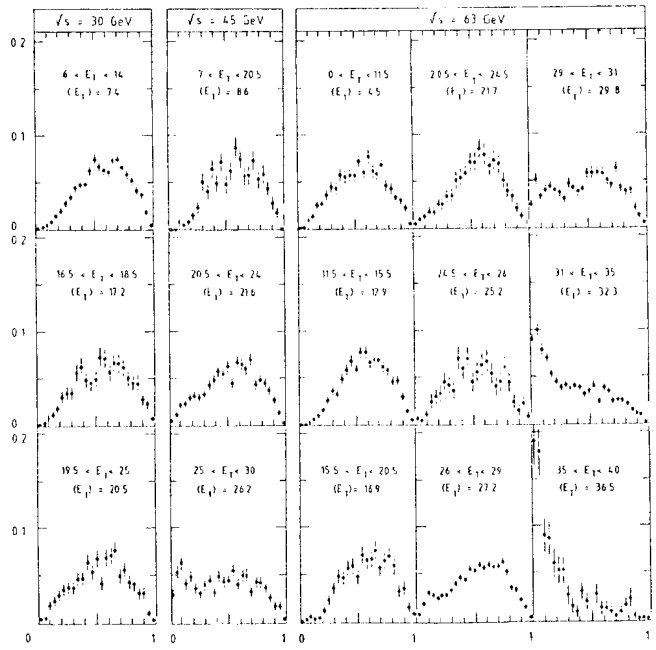


Fig. 7: Circularity distributions for bins in E_T and $\sqrt{s}$.

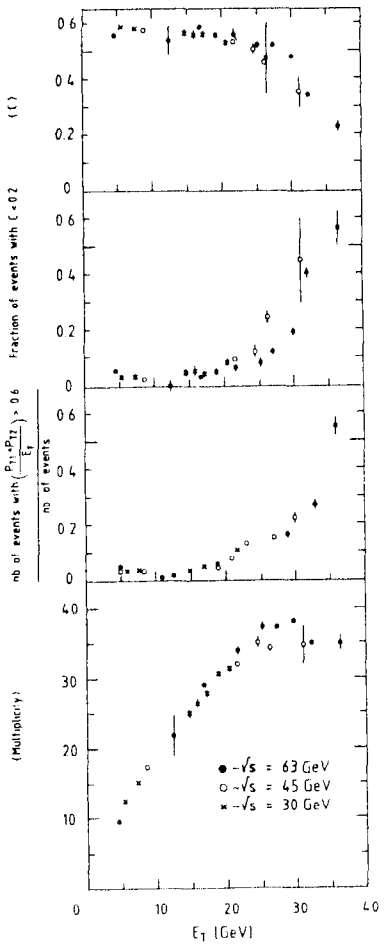


Fig. 8: a) Average circularity versus E_T;
b) Fraction of events with C < 0.2 versus E_T;
c) Fraction of events with more than 60% of their E_T in two non-overlapping regions of $\Delta\phi = 60^\circ$ and $\Delta y = 1$; and
d) Total multiplicity into the calorimeter versus E_T.

seem to be strong for a given E_T bin. At lower $\sqrt{s}$ one does not reach the E_T region where jets seem to dominate because of kinematical consideration.

To exhibit the difference between events at the circularity regions, the plot at E_T = 30 GeV of the single particle distribution for events with C < 0.15 and for events with C > 0.45 is shown in Fig. 9, one order of magnitude excess of high p_T particles for events with C < 0.15 over the events at high circularity.

In Fig. 10 we show some typical events with high E_T. The first three events show a clear two-jet structure where the energy clusters are observed to be back to back in ϕ. The fourth event shown exhibits a three-jet structure. In the next section we will investigate in more detail the properties of the jets observed at high p_T.

IV. JET PROPERTIES

The clarity of jet dominant events at high E_T enables us to look in more detail at the characteristics of jets produced in hadron interactions. At ISR energies low circularity events with E_T > 33 GeV/c contain typically two jets of about 15 GeV each. This corresponds to a constituent with x value of $\sim$ 0.5, a region where one expects valence quarks to start dominating over the gluon distribution, which dominate at lower x values. Thus while at collider energy the jets observed are expected to be mainly gluon jets, in these p_T ranges at the ISR they are expected to have a sizeable if not dominant valence quark contribution.

The fragmentation of jets is usually described by the variable $x_p = 2p/\sqrt{s}$. In this case one has to define $\sqrt{s}$ as the centre-of-mass energy of the colliding constituents. To compare the x_p distribution in an unambiguous way, one has to be able to define $\sqrt{s}$, on an event-by-event basis. In hadron scattering one then has to distinguish between the particles belonging to the scattered constituents and those not associated directly with them. This is important to both the calculation of $\hat{s}$ and for deciding which particle to include in the jet fragmentation. A way of calculating the x_p distribution is to assume that at 90° one is

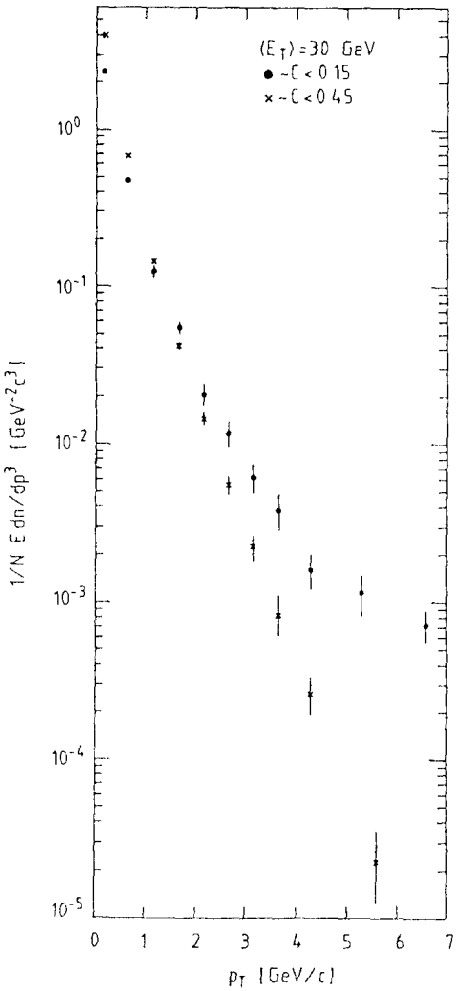


Fig. 9: The inclusive particle distributions at E_T = 30 GeV for events with C > 0.15 and for events with C > 0.45.

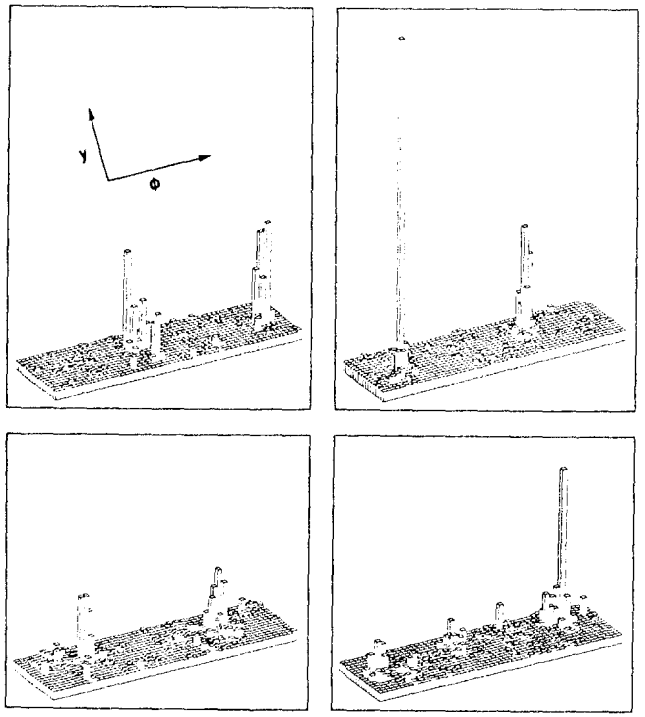


Fig.10: Examples of events with transverse energy in excess of 35 GeV.

completely dominated by the jet fragments and that other contributions are negligible. To measure the x_p distribution, one a) selects events with the two jets centrally in the calorimeter; b) calculates W, the invariant mass of all clusters in the calorimeter, as an estimate of $\sqrt{s}$; c) calculates x_p and normalizes the distribution to the number of jets. The result is compared with $d\sigma/dx_p$ measured by TASSO [15] normalized to two times the hadronic cross-section. The result shows the data to have the same shape but to lie below the e^+e^- results. The relation between the invariant mass of all particles in the event and $\sqrt{s}$ on the parton level is unclear; using all the energy at 90° will overestimate $\sqrt{s}$ and will tend to shift the distribution. Alternatively one can use a high-p_T Monte Carlo program [16] to better estimate the true $\sqrt{s}$ for each event by removing some contributions due to particles not belonging to the jets. In the Monte Carlo one finds the relation between $\sqrt{s}$ and the invariant mass M of all particles with $p_T > 1$ GeV/c in the detector. A cut at 1 GeV/c is made to remove, from both the data and Monte Carlo, contributions from soft particles. The true $\sqrt{s}$ is about 20% higher than calculated using this cut according to the Monte Carlo. In the data the invariant mass M is calculated for all particles with more than 1 GeV/c transverse momenta in the calorimeter to estimate W'. Figure 11 shows the x_p distributions calculated with W'. It is in good agreement, in both slope and normalization, with the e^+e^- data.

To measure the width of the jets, it is necessary to know the direction of the scattered constituents. Unlike e^+e^- jets, the constituent jets in hadron interactions are not generally collinear in the centre-of-mass of both beams; the colliding partons have different x-values and a contribution from initial transverse momentum k_T. The jet axis will be found by the calorimeter, and the individual particle momenta will be measured by the central detector.

To find the jet axis a cluster algorithm that was developed in Ref [17] was used. The algorithm uses as a distance-measure the transverse momentum between the particles. The algorithm is provided with a cut-off parameter q_T^{cut} defining the largest allowed distance between two particles to be joined together. The procedure of the algorithm is as follows:

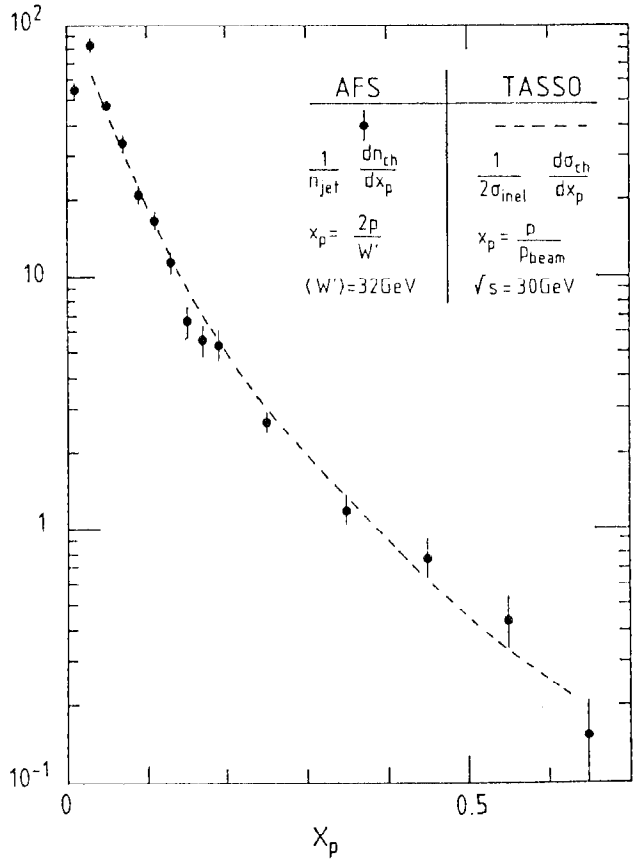


Fig. 11: x_p distribution using the invariant mass of particles with $p_T > 1.0$ GeV/c and information from high-p_T Monte-Carlo (16) to estimate $\sqrt{s}$.

1) A pre-clustering is made by taking the highest momentum particle and joining it to all particles with a q_T < 250 MeV/c away from it. Of the remaining particles, the largest momentum particle is found, and all remaining particles with a q_T < 250 MeV/c are joined to it. This procedure is repeated until all clusters with q_T relative to another cluster of less than 250 MeV/c are merged.

2) Using these pre-clusters, one finds the two closest clusters and, if their internal distance is less than q_T^{cut}, joins them. The procedure is repeated until one is left with a number of clusters, all with distances between any two clusters greater than q_T^{cut}. After each merging, the cluster algorithm checks whether all the particles are assigned to the closest cluster, and if not, it allows reassignment.

Figure 12 shows the result of using the cluster algorithm with different values on q_T^{cut}, on data, and on a high-p_T Monte Carlo [16] with detector simulation [14]. From the result, it can be seen that the fraction of events with more than two jets is strongly dependent on the cut-off value. In addition, it should be noted that for a given cut-off value the fraction of events with more than two jets is quite larger in the data than in the Monte Carlo. We will measure the $\langle q_T \rangle$ in the data which satisfy the two-jet assumption when using the cluster algorithm only on particles with p_T > 1.0 GeV/c, and with the cut-off parameter set to 4 GeV/c. In this case, the algorithm finds two jets in the majority of events. From the Monte Carlo, the mean angle between the initial parton direction and found jet direction is four degrees. In Figure 13 we plot $\langle q_T \rangle$ against z, where z is defined as the momentum component along the jet axis divided by $\sqrt{s}/2$. Superimposed on the figure are predictions from the Monte Carlo. The solid line is obtained in the Monte Carlo with a jet width $\langle Q_T \rangle$ = 0.4, where Q_T is an internal parameter in the Monte Carlo setting the width of the jet fragmentation; and the dashed line is when the jet width is measured to $\langle Q_T \rangle$ = 0.65 GeV/c. Both lines include detector simulation. It is clear from the figure that the data favour $\langle Q_T \rangle$ = 0.65 GeV/c.

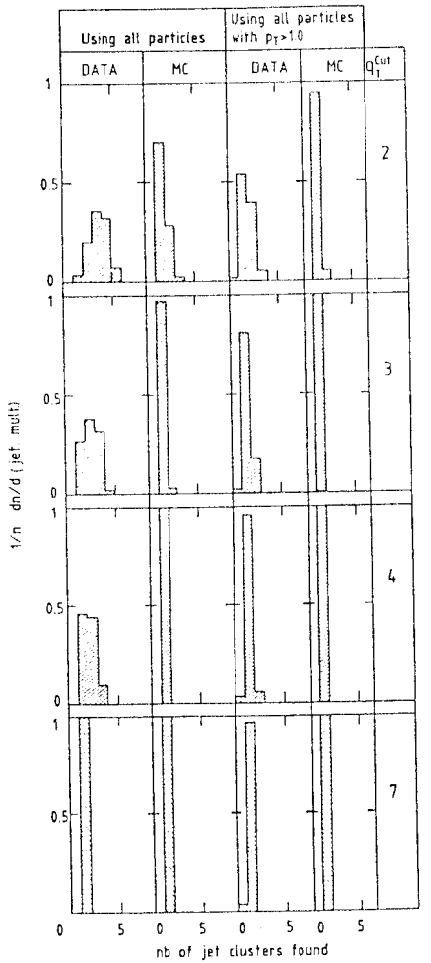


Fig.12: Performance of the cluster algorithm (17) for different values of the cut-off parameter.

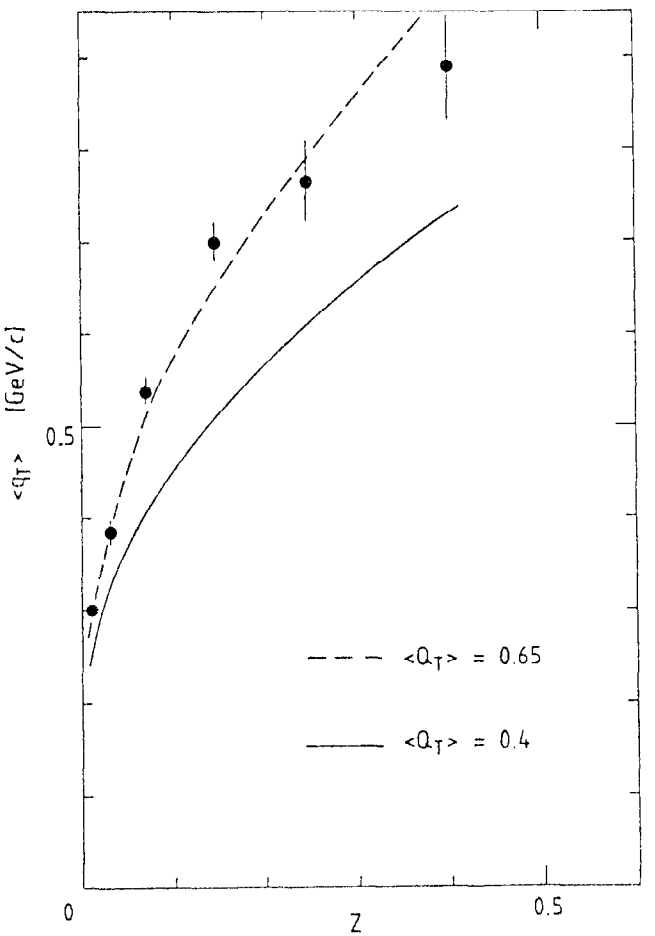


Fig. 13: Mean transverse momentum with respect to the jet axis as a function of Z. The solid line shows the Monte Carlo for $\langle Q_T \rangle$ = 0.4 GeV/c and the dashed line for $\langle Q_T \rangle$ = 0.65 GeV/c.

It should be noted that also in e^+e^-, if all events are analysed under a two-jet assumption, the $\langle q_T \rangle$ versus z observed is very similar to the one in Fig. 13 [15]. Thus one interpretation is that the two-jet Monte Carlo broadens the jet width instead of estimating the contribution from hard gluons producing a third jet.

The next thing we examine is the charge compensation within a jet and the charge correlation with the other jet [18]. We use the function:

$$\Phi(y,y') = [d^2\sigma/dydy')_{\text{opposite charge}} - (d^2\sigma/dydy')_{\text{same charge}}]/d\sigma dy'$$

where y and y' are the rapidity along the jet axis of the individual particles. In Fig. 14 we show the variation of Φ with y' fixed and various y'. From the figure it is seen that the behaviour is rather different for a positive particle in a bin centred at y'. The difference in the long-range correlation can be seen by comparing Figs. 14e and 14h, where for negative y we get positive correlation with the negative trigger and anticorrelation for the positive trigger. The difference is easily understood as a consequence of having two valence u-quarks and only one valence d-quark. Thus no matter what the "trigger" at y' is, it is more probable to have a positive recoil jet. Figs 14c and 14g show that for a negative "trigger" at y' near the central region the charge correlation is positive throughout the y range, while for a positive "trigger" it is positive only in the central region, and for highly |y| it becomes negative, again reflecting the higher probability of the leading charge to be positive.

CONCLUSIONS

The AFS collaboration at the ISR have investigated systematically the production of jets at the ISR energy range of $\sqrt{s}$ = 30 to 63 GeV. The inclusive jet production cross-section at $\sqrt{s}$ = 45 and 63 GeV were measured and found in good agreement with a QCD motivated model. The cross-section at these two energies show a scaling behaviour confirmed by the measurements at collider energies.

From the full 2π-calorimeter triggered data clear jet dominance emerges at $E_T \geq 30$ GeV. The transition region between the more circularly symmetric events and jet dominated events is fairly small (25 to 35 GeV). No strong energy dependence of this transition region is observed

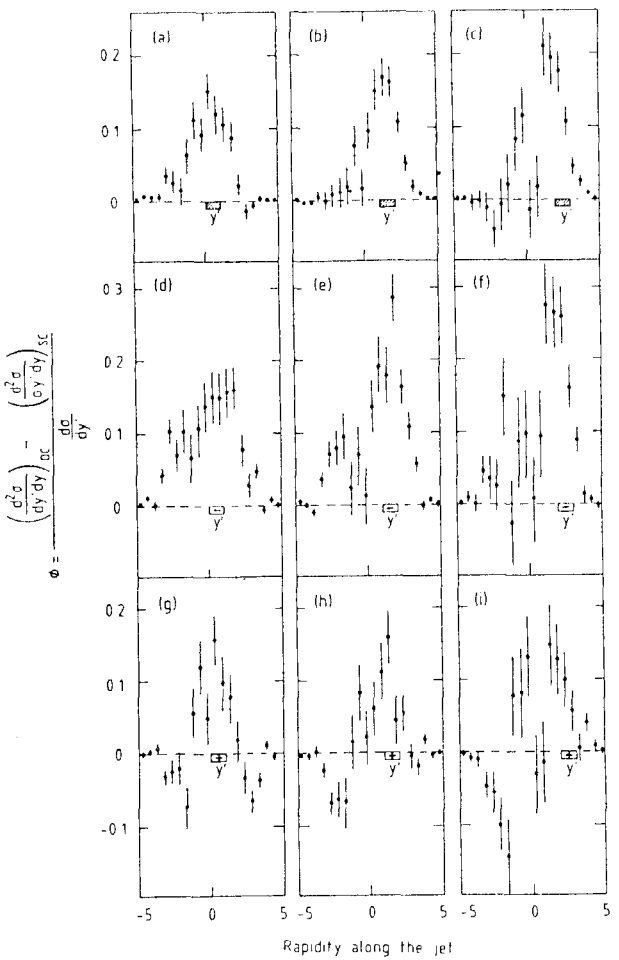


Fig. 14: Charge compensation as a function of rapidity along the jet axis: (a) to (c) all charges, (d) to (f) for negative "trigger", (g) to (i) for positive "trigger".

at the ISR. In the collider data where $\sqrt{s}$ has increased by nearly an order of magnitude, one sees jet dominance at $E_T \approx 50$ GeV.

The properties of jets produced at ISR were compared to those in e^+e^- and found to be very similar. The charge correlation shows clear evidence of valence quark participation in the hard collision. This is in agreement with the expectation that for jets with $p_T > 15$ GeV, the participating constituents are dominantly coming from $x > 0.5$, where valence quarks are expected to dominate over gluons. At lower relative p_T gluon jets are expected to dominate: thus the ISR is in the unique position of being able to study jets dominated by valence quarks.

REFERENCES

[1] T. Akesson et al., Phys. Lett. 118B (1982) 185;
T. Akesson et al., Phys. Lett. 118B (1982) 193.

[2] T. Akesson et al., Phys. Lett. 121B (1983) 133.

[3] T. Akesson et al., Phys. Lett. 128B (1983) 354.

[4] A.L.S. Angelis et al., Phys. Lett. 126B (1983) 132.

[5] M. Banner et al., Phys. Lett. 118B (1982) 203;
P. Bagnaia et al., preprint CERN-EP/83-94 (1983) submitted to Z. Phys. C.

[6] G. Arnison et al., Phys. Lett. 123B (1983) 115;
G. Arnison et al., preprint CERN-EP/83-118 (1983), submitted to Phys. Lett.

[7] J.D. Bjorken, Phys. Rev. D9 (1973) 4098;
W. Ochs and L. Stodolsky, Phys. Lett. 69B (1977) 225;
J.H. Cobb et al., Phys. Rev. Lett. 40 (1978) 1420;
W. Ochs, Phys. Scripta 19 (1979) 127.

[8] See, for example, C. Bromberg et al., Phys. Rev. Lett. 38 (1977) 1447;
M. Corcoran et al., Phys. Rev. D21 (1980) 641;
C. de Marzo et al., Phys. Lett. 112B (1982) 173;
B. Brown et al., Phys. Rev. Lett. 49 (1982) 711.

[9] T. Akesson and H-U. Bengtsson, "The Transverse Energy Distribution and Hard Constituent Scattering," to be published in Physics Letters.

[10] G.C. Fox and R.L. Kelly, LBL-13985/CALT-68-90 (1982).

[11] The data reported here is from the Axial Field Spectrometer Collaboration which is composed of (Brookhaven[1], Cambridge[3], CERN[4], Copenhagen[5], Lund[6], Pennsylvania[7], Pittsburg[8], Queen Mary college[9], RAL[10], Tel-Aviv[11]) with the following physicists involved:
T. Akesson[4], M.G. Albrow[10], S. Almehed[6], R. Batley[4], O. Benary[11], H. Bøggild[5], O. Botner[5], H. Breuker[4], H. Brody[7], V. Burkert[4], R. Carosi[4], A.A. Carter[9], J.R. Carter[3], P. Cecil[3], S.U. Chung[1], W.E. Cleland[8], D. Cockerill[10], S. Dagan[11], E. Dahl-Jensen[5], I. Dahl-Jensen[5], P. Dam[4], G. Damgaard[5], S. Eidelman[4], W.M. Evans[10], C.W. Fabjan[4], P. Frandsen[4], S. Frankel[7], W. Frati[7], M. Gibson[10], U. Goerlach[4], H. Gordon[1], A. Hallgren[4], K.H. Hansen[5], B. Heck[4], V. Hedberg[6], J. Hiddleston[10], H.J. Hilke[4], J. Hooper[5], G. Jarlskog[6], P. Jeffreys[4,10], T. Jensen[4], A. Kalinovsky[4], G. Kesseler[4], T. Killian[1], R. Kroeger[8], K. Kulka[6], J. v.d. Lans[4], J. Lindsay[4], D. Lissauer[11], B. Lörstad[6], T. Ludlam[1], A. Markou[4], N.A. McCubbin[10], U. Mjörnmark[6], R. Møller[5], W. Molzon[7], B.S. Nielsen[4], A. Nilsson[6], L.H. Olsen[4], Y. Oren[11], L. Rosselet[4], E. Rosso[4], A. Rudge[4], R. Schindler[4], I. Stumer[1], M. Sullivan[8], G. Thorstenson[6], E. Vella[7], J. Williamson[10], W.J. Willis[4], M. Winik[1], W. Witzeling[4], C. Woody[1], W.A. Zajc[7].

[12] H. Gordon et al., Nucl. Instrum. Methods 196 (1982) 303;
O. Botner et al., Nucl. Instrum. Methods 196 (1982) 314;
O. Botner et al., IEEE Trans. Nucl. Science, Vol. NS-28 No. 1 (1981).

[13] F.E. Paige and S.D. Protopropescu, ISAJET: A Monte Carlo Generator for pp and $p\bar{p}$ Interactions, BNL 19777 (1980).

[14] O. Benary et al., BNL Internal Report OG-613 (1981) and CERN Internal Report R807/313;
R. Bock et al., CERN EP/80-206 (1980).

[15] R. Brandelik et al., (TASSO Collaboration), Phys. Lett. 94B (1980) 437.

[16] H.U. Bengtsson, The Lund Monte Carlo for High-p_T Physics, LUTP 82-15.

[17] T. Sjöstrand, The Lund Monte Carlo for e^+e^- jet physics, LUTP 82-7 (1982), and references therein.

[18] R. Brandelik et al., (TASSO Collaboration), Phys. Lett. 100B (1981) 357.

A STUDY OF JET PRODUCTION AND JET PROPERTIES BY THE UA1 EXPERIMENT AT THE CERN $p\bar{p}$ COLLIDER

UA1 Collaboration, CERN, Geneva, Switzerland
Aachen–Annecy (LAPP)–Birmingham–CERN–Helsinki–
London (Queen Mary College)–Paris (Coll. de France)–Riverside–Rome–
Rutherford Appleton Lab.–Saclay (CEN)–Vienna Collaboration

Presented by Alan Honma
Queen Mary College, London, England

ABSTRACT

Results from a study of jet-type events produced in $p\bar{p}$ collisions at $\sqrt{s} = 540$ GeV are presented. At large total transverse energy, jet event dominance is clearly observed. The inclusive jet cross-section has been measured up to E_T (jet) = 100 GeV. Jet fragmentation into charged particles shows no striking difference between jets produced in $p\bar{p}$ collisions and jets produced in e^+e^- collisions. The angular distribution of jets in the parton–parton centre of mass is consistent with QCD predictions (favouring vector gluon exchange over scalar gluon models). A measurement of the proton structure function is also obtained. The proton structure function is measured at $q^2 = 1200$ GeV^2 and is found to be in qualitative agreement with QCD extrapolation from low-q^2 data.

© A. Honma 1983

1. JET PHYSICS IN $p\bar{p}$ COLLISIONS

A standard picture of jet production in $p\bar{p}$ collisions is shown in Fig. 1a, where a parton (hard constituent) from each of the incoming particles undergoes a hard collision. The outgoing partons then fragment into jets.

Note that a parton can be a quark or a gluon, and hence the hard collision includes gluon–gluon, gluon–quark (or antiquark), and quark–quark, as well as higher-order processes (see Fig. 1b). From QCD one expects the gluon–gluon and gluon–quark (antiquark) scattering subprocesses to dominate (in the present q^2 range)—hence the production of mostly gluon jets. In contrast, jets from e^+e^- collisions are expected to be produced primarily from the production of quark–antiquark pairs—hence domination by quark jets (see Fig. 1c).

In this standard picture of jets from $p\bar{p}$ collisions, three major processes are involved. First, there is the structure function, which tells us something about the distribution of partons within the proton. Second , there is the angular distribution, which is indicative of the nature of the hard scattering. Third , there is the fragmentation function, which reflects the hadronization processes of the partons. We report on results obtained from studies of all of these three major elements of jet events seen in $p\bar{p}$ collisions.[1-3]

2. THE UA1 DETECTOR

The UA1 detector has been described in detail elsewhere,[4] so only the aspects specifically concerned with this study will be presented. The central part of the detector consists of a large cylindrical tracking chamber centred on the collision point, surrounded by a shell of electromagnetic (e.m.) calorimeters and then by the hadronic calorimeter, which also serves as the return yoke for the 0.7 T dipole magnetic field. There are also tracking chambers and calorimeters in the more forward regions but these were not used in this study. The central detector (CD) and central calorimetry has almost complete geometrical coverage down to 5° to the beam axis. In the variables commonly used for such descriptions, this translates to -3.0 to 3.0 in pseudorapidity ($\eta = -\ln[\tan\theta/2]$, where θ is the polar angle from the beam axis), and nearly 2π coverage in azimuth about the beam axis (ϕ). A schematic of the calorimeter is shown in Fig. 2.

The central tracking chamber consists of a 5.8 m long and 2.3 m diameter cylindrical drift chamber. This chamber provides three-dimensional coordinate information, enabling efficient track reconstruction. This, combined with the 0.7 T magnetic field, results in accurate momentum measurement for nearly all charged tracks.

The central calorimetry consists of lead/scintillator sandwich e.m. shower calorimeters surrounded by iron/scintillator sandwich hadronic calorimeters. These calorimeters are highly segmented in order to obtain position information of the energy deposition. Details of the geometry are given in Table 1.

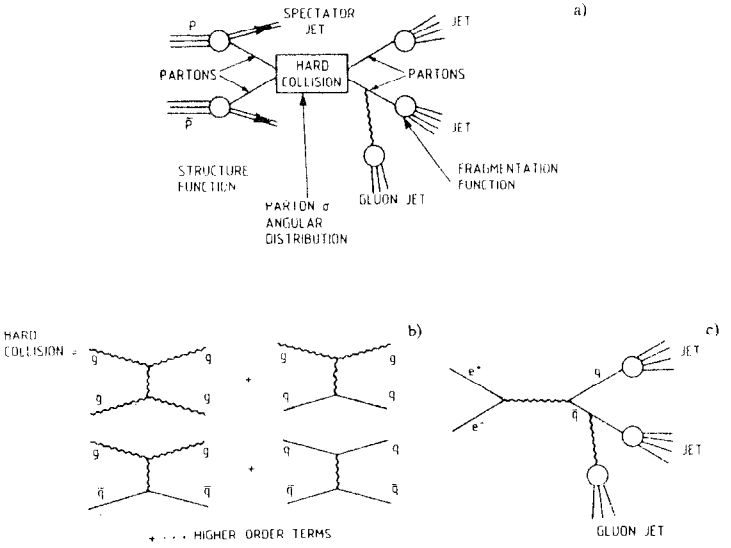


Fig. 1 a) Schematic of jet production in $p\bar{p}$ collisions;
b) The parton-parton hard scattering. Lowest-order processes;
c) Schematic of jet production in e^+e^- collisions.

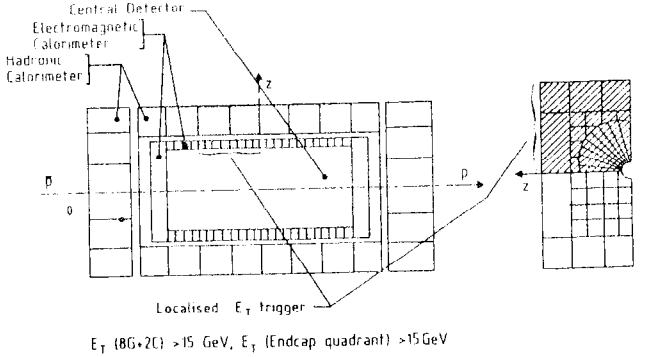


Fig. 2 Schematic of the central part of the UA1 detector. Shaded and hatched regions of calorimeter are the elements summed to obtain the E_T of a cluster for the trigger.

Table 1

UA1 central calorimeters

Calorimeter	Type	Thickness at normal incidence	Rapidity range	Number of cells	Cell size $\Delta\eta \times \Delta\phi$ (approx.)	Comments
Gondolas	Electromag.	26.4 X_0/1.1 λ	$\|\eta\| < 1.5$	48	$0.11 \times 180°$	Azimuth from light attenuation
C's	Hadronic	5.0 λ	$\|\eta\| < 1.5$	232	$0.30 \times 15°$	
Bouchons	Electromag.	27.0 X_0/1.2 λ	$1.5 \leq \|\eta\| < 3$	64	$1.5 \times 11°$	Rapidity from position detector
I's	Hadronic	7.1 λ	$1.5 \leq \|\eta\| < 3$	128	$0.40 \times 15°$	

(x_0 are radiation lengths, λ absorption lengths.)

3. TRIGGER AND DATA SAMPLE

Making use of the knowledge gained from the previous (1981) collider run [5], a localized transverse energy hardware trigger was implemented to select jet-like events for the 1982 run. This trigger required that the transverse energy (E_T) measured within a calorimeter "block" be greater than 15 GeV. A "block" was defined in the central region as two hadron calorimeter units plus the e.m. calorimeter elements in front of them. A "block" in the end-cap region was defined as the hadronic and e.m. elements comprising one quadrant of an end-cap (see Fig. 2 for the schematic of this trigger). With this trigger, a data sample of $\int L\, dt = 14\ nb^{-1}$ was obtained in the 1982 collider run, which constitutes the sample used for the jet studies reported in this paper. In the 1983 run, approximately 118 nb^{-1} of data were collected. Only the inclusive jet cross-section will include results from the 1983 data sample.

4. THE UA1 JET-FINDING ALGORITHM

The UA1 calorimetry is segmented into 462 electromagnetic and hadronic cells, as shown in Table 1. To each cell is associated a transverse-energy vector indicating the spatial position and the magnitude of an energy deposition. The procedure [5] is then to order all cells by decreasing E_T. Starting with the largest E_T cell, one associates the next largest cell to the first if the distance in (η,ϕ) space is less than some Δ_{min}, where Δ_{min} was chosen to be 1 (Fig. 3 shows a clear association of cells up to a distance of 1 in η–ϕ space). Then a cluster axis is defined by adding the cells vectorially. This procedure is continued on subsequent cells (always in order of decreasing E_T), associating cells and redefining the cluster until no more cells of $E_T > 2.5$ GeV remain. Cells with $E_T < 2.5$ GeV are associated with the cluster if the transverse momentum of the cell relative to the cluster is less than 1.0 GeV and if the spatial angle between the cell and the cluster axis is less than 45°.

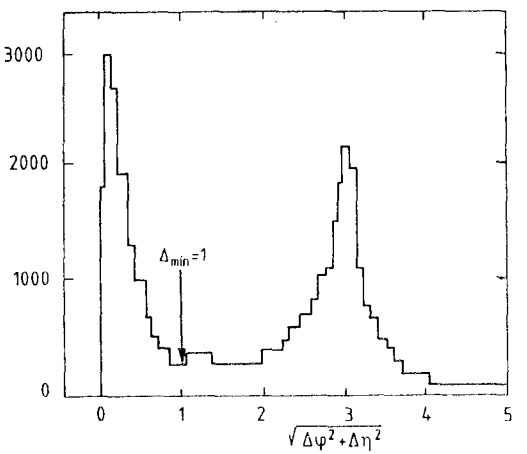


Fig. 3 Distribution of calorimeter cells as a function of distance in η,ϕ space from the jet axis as defined by the UA1 jet-finding algorithm.

The vectorial sum of cells associated with the cluster give the energy and spatial direction (axis) of the newly defined "jet". This procedure is repeated on all remaining cells in the event until all such jets are found. This definition of "jet" applies to all the results presented in this paper.

5. THE EMERGENCE OF JETS

The analysis of the data from the first collider run (1981) led to the observation that at very high sum of transverse energy (Σ E_T), jet-like events clearly emerged from the more isotropic event topologies seen thus far. In fact, in both the UA1 and UA2 experiments, jets were shown to dominate for $\Sigma E_T > 100$ GeV when restricting the E_T sum to a small rapidity range of $|\eta| < 1.5$.[5,6] In Fig. 4, the jet-like nature of such events is clearly visible by eye, as seen in this picture of the raw track digitizings. Such events are fairly typical of those with the very highest ΣE_T values. A common method of showing the transverse energy distribution in an event is the so-called "Lego" plot, where one displays the E_T measured in bins of η-ϕ space in a two-dimensional histogram. Figure 5 shows the Lego plots for six events which are typical of events with very high E_T (in this case $\Sigma E_T > 140$ GeV). In these plots one can easily see the jet-like clusters by the appearance of "towers" that they form in E_T. Events with two-jet, three-jet, and even more complicated structures are observed.

The study of the jet-like nature of high-Σ $E_T$events enabled the refinement of the jet-finding algorithm and provided the justification of a localised E_T (cluster) trigger for use in the 1982 run. The large increase in integrated luminosity in 1982 (14 nb^{-1} versus 22 μb^{-1} in 1981) resulted in a high statistics jet sample.

6. E_T, p_T, AND CHARGED MULTIPLICITY FLOW IN JETS

Information about the structure of jets and about the evolution of that structure with increasing jet energy can be obtained by examining the average flow of E_T, charged transverse momentum (p_T) and charged multiplicity (N_{ch}) about the jet axis. The method used to obtain these distributions involved calculating the three quantities (E_T, p_T, N_{ch}) in bins of ($\Delta\eta$, $\Delta\phi$) about the jet axis for all events with E_T (jet) greater than 20 GeV.

The result for mean transverse energy flow using the above method is shown in the form of a Lego-type plot in Fig. 6. In this figure we see the clear, narrow structure of the jet. Outside the jet there is a large flat region in both η and ϕ space, then at $\pm 180°$ away in $\Delta\phi$ one sees a ridge due to the presence of the recoil jet which is not a single peak since it is smeared out over a large region in η.

If we now take only the "towards" ($|\Delta\phi| < 90°$) hemisphere and integrate over $\Delta\phi$, we obtain the average flow of E_T, p_T, and N_{ch} about the jet axis in pseudorapidity space (this is chosen because the natural granularity of the detectors is best in η). These distributions are shown in Fig. 7, where the left, middle and right plots represent different regions of E_T of the jet

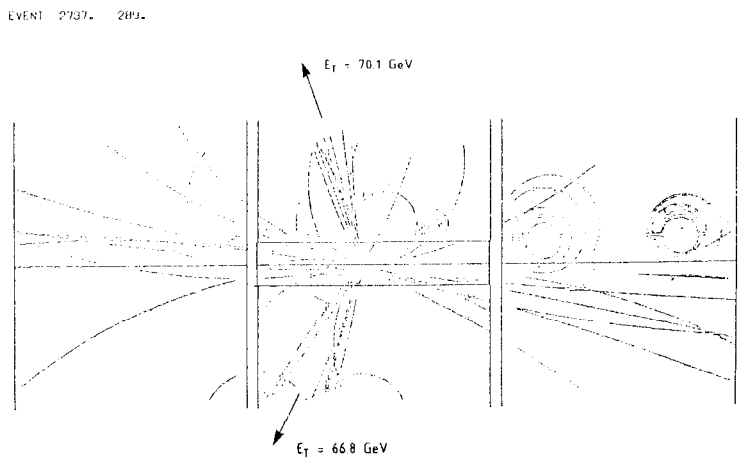


Fig. 4 A two-jet event as seen in the raw digitizings of tracks in the central drift chamber.

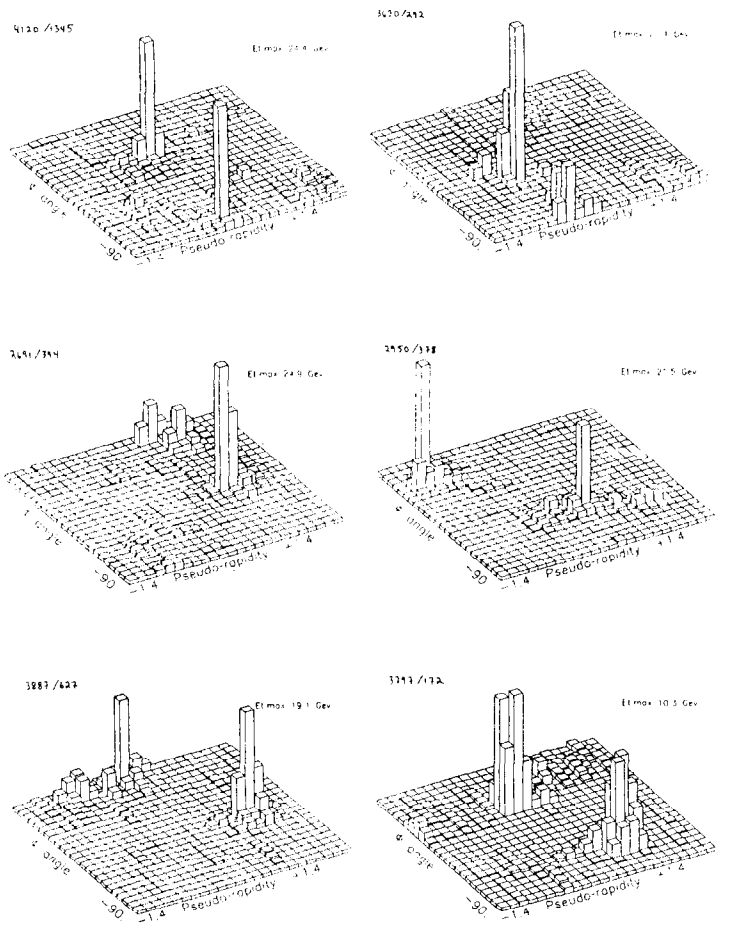


Fig. 5 The "Lego" plots of six events with $\Sigma E_T > 140$ GeV.

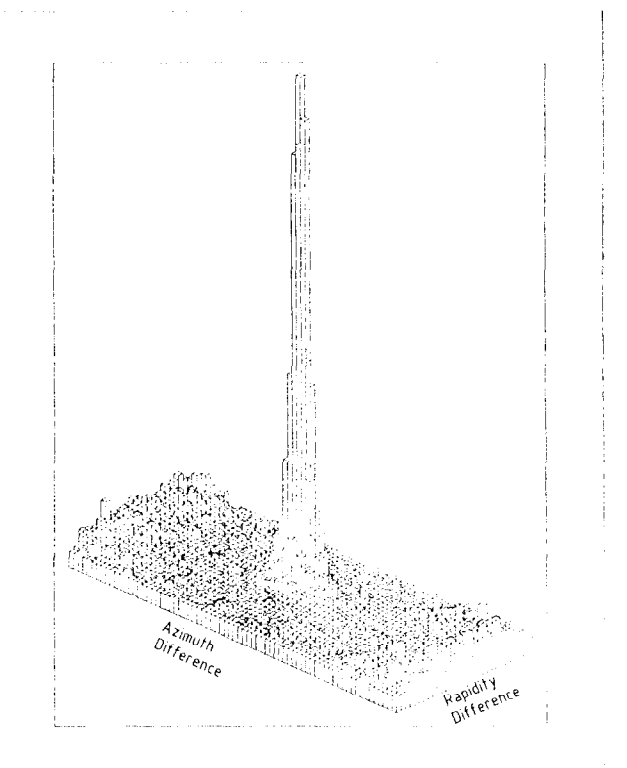


Fig. 6 Transverse energy flow about the jet axis. The rapidity difference varies from -3 to $+3$ and the azimuth difference varies from $-180°$ to $+180°$.

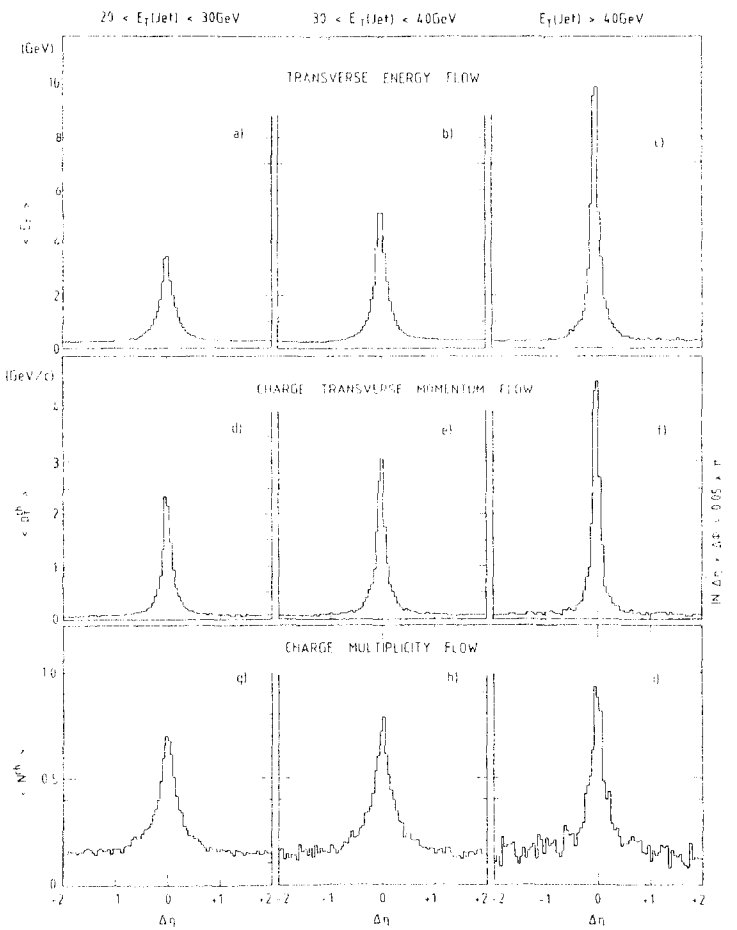


Fig. 7 (a–c) Transverse energy flow as a function of $\Delta\eta$, i.e. the pseudorapidity distance from the jet axis, for three slices of jet E_T;
(d–f) Charged transverse momentum flow as a function of $\Delta\eta$;
(g–i) Charged multiplicity flow as a function of $\Delta\eta$.

(20–30, 30–40, > 40 GeV, respectively). Let us now consider the core of the jet, $|\Delta\eta| < 0.2$. The average transverse energy of the core is seen to grow narrower and to increase strongly with increasing jet energy. We can see that any effects due to calorimeter granularity do not play a large role since the same effect is seen in the average charged transverse momentum, which is obtained completely independently (E_T is determined from calorimetry alone, p_T from the CD alone). If we now look at the charged multiplicity flow, we see that there is also an increase in multiplicity in the core of the jet, but which is not nearly as large as the increase in E_T. This implies that the leading particles of the jet are taking more and more energy per particle rather than having more particles taking the same amount of energy per particle. If we now consider the "background" to the jet, i.e. the region far outside the core ($|\Delta\eta| > 0.5$), we see that the E_T, p_T and N_{ch} do not change to any large extent with increasing E_T of the jet.

Two different Monte Carlo programs with different hadronization models have been compared with the data in order to better understand how much of the various distributions is due to the jet and how much is due to the rest of the event (i.e. spectator fragments and/or gluon radiation). The first Monte Carlo program is based on a naïve parton–parton, hard-scattering model with scattered and spectator partons fragmented according to cylindrical phase space (CPS).[1] This CPS program does not include QCD radiative effects. The second program is the ISAJET Monte Carlo, which incorporates QCD radiated gluons in the final state.[7]

Both programs reproduce the general shape of the jet when looking at transverse energy and charged multiplicity flows, although both programs have problems reproducing the "background" region (far from the jet axis). This could be attributed to the lack of complete multi-jet production (initial- and final-state gluon radiation) in the two Monte Carlo programs.

Figure 8 shows the charged multiplicity flow about the jet axis. Here we see that the CPS model reproduces the data well, but ISAJET drops to a much lower plateau level away from the jet. This is because ISAJET is tuned to give a minimum-bias level of multiplicity outside of the jet. The minimum-bias level for N_{ch} is also shown, and it is obvious that the "background" level of multiplicity outside the jet is not the same as minimum bias. In fact, the level is more than twice that of minimum bias.

The average charged multiplicity in a jet can be estimated by using the CPS model to obtain a background subtraction. The results of this are shown in Table 2 for different bins of E_T (jet). These results can then be compared with those obtained from PETRA and PEP for e^+e^- produced jets if the approximation is made that $\sqrt{s} = 2E_T$ (jet). In this comparison it is

Table 2

Charged-track multiplicities in single jets

E_T (jet)	20–30 GeV	30–40 GeV	> 40 GeV
$\langle E_T \rangle$ in bin	24.3 GeV	33.5 GeV	47.4 GeV
$\langle N_{ch} \rangle$	6.7 ± 0.7	7.5 ± 0.7	7.7 ± 0.8

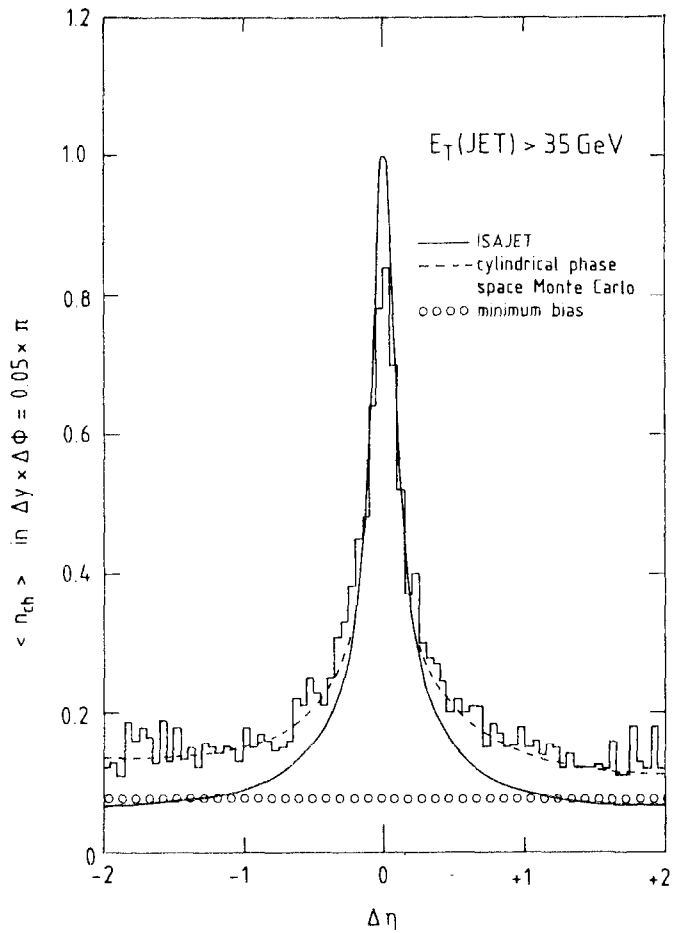


Fig. 8 Charged multiplicity flow for jets with $E_T > 35$ GeV as a function of $\Delta\eta$. Dashed and solid curves are full Monte Carlo simulations based on different theoretical expectations of jet structure.

found that the jets produced in $p\bar{p}$ collisions have multiplicities slightly lower than but comparable to that expected for e^+e^- jets extrapolated to the relevant $\sqrt{s}$ region (six to eight charged tracks per $p\bar{p}$ jet, compared to seven to nine charged tracks per e^+e^- jet).

7. INCLUSIVE JET CROSS-SECTION

Measurements of the inclusive jet yield were obtained from the 1981, 1982, and 1983 collider-run data samples. More restrictive cuts were applied to the original jet sample in order to obtain a precise measurement of the inclusive jet cross-section. This involved using the best acceptance regions in η–ϕ space. The over-all systematic uncertainty in the cross-section is estimated to be 65%, primarily due to the uncertainty in the absolute energy scale. Since the inclusive cross-section is a steeply falling spectrum, a slight error in the energy scale will result in a large error in the absolute cross-section.

The result for the inclusive cross-section is shown in Fig. 9. Also shown is a banded region corresponding to QCD predictions, the band representing an estimate of the theoretical uncertainty.[8] Note that the energy scale in the QCD predictions refers to the transverse momenta of the scattered partons, whereas for the data the scale is based on the sum of jet-fragment momenta. Nevertheless, the agreement between experiment and theory is excellent over many orders of magnitude.

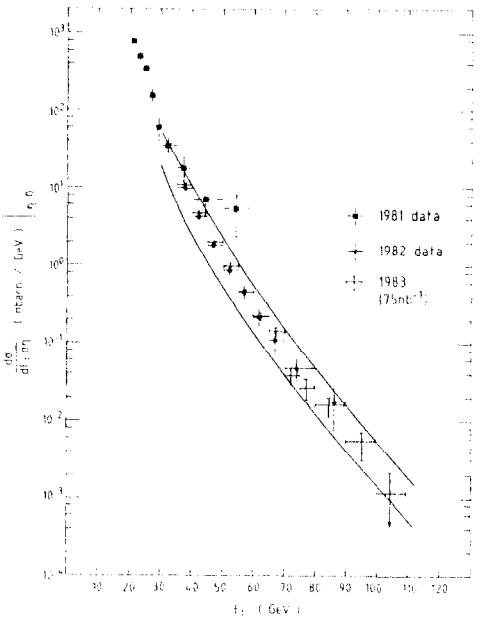
Studies of two-jet mass distributions have been made. The distribution includes events with more than 200 GeV for the invariant jet–jet mass. A preliminary study of the potentially interesting (W,Z) 50–150 GeV mass region reveals no obvious structures.

From the sample of inclusive jet events it was possible to examine the rate of multi-jet production. In Fig. 10 we show the fraction of events with one, two, and three jets as a function of the E_T of the trigger jet. Note that the two-jet topology dominates over the full range in E_T at a level of 80–85%. The fraction of one-jet events becomes negligible at higher E_T (their existence at low E_T is mainly due to the loss of one jet from two-jet events as a result of E_T cut threshold effects). The fraction of three-jet events grows to about 15% and levels off. The presence of the third jet is a strong indication of that which is expected from gluon bremsstrahlung and is similar to what is seen in e^+e^- produced events. A further study of the possibility of more than two jets per event has been done using the p_{out} variable (momentum perpendicular to the plane containing the trigger jet axis and the beam axis). The results are consistent with the hypothesis of gluon radiation effects as calculated in QCD and not consistent with a simple two-jet production model.[1]

8. JET FRAGMENTATION

The jet fragmentation study is conducted in a purely inclusive way using the charged particles as measured by the CD in order to obtain the details of the internal jet structure. The method [2] is to take the sample of jets with $E_T > 30$ GeV as obtained from the UA1

Fig. 9
Inclusive jet cross-section as a function of E_T for the 1981, 1982, and 1983 data samples. The hatched band corresponds to the region of QCD predictions.



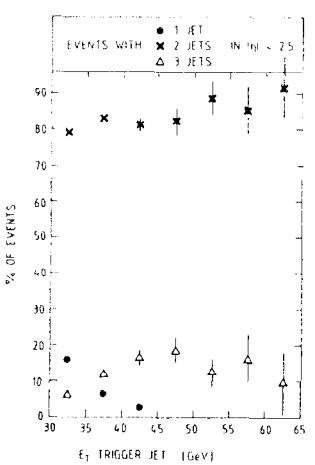


Fig. 10
Fraction of events with 1, 2, and 3 jets of $E_T >$ 15 GeV as a function of the E_T of the highest E_T jet.

jet-finding algorithm, and find all charged particles in a cone of 35° half-angle about the jet axis. The choice of 35° is based on measured charged-particle distributions about the jet axis. For each charged particle in the cone, the following quantity can be calculated:

$$z = p_L^{\dagger}(\text{jet axis})/|p(\text{jet})|\,, \qquad \text{where } 0 \leq z \leq 1\,.$$

The fragmentation function is defined as follows:

$$D(z) = (1/N_{\text{jets}})(dN_{\text{ch}}/dz)\,.$$

Figure 11a shows the plot for D(z) for $z > 0.02$. This distribution falls rapidly with z at low z-values. At high z-values its form is approximately exponential. Also shown in this plot are results for D(z) obtained by the TASSO Collaboration for jets with energies of 17 GeV produced in e^+e^- collisions.[9] Although at substantially different jet energies (30 versus 17 GeV), this comparison is considered to be meaningful since the scaling violations in e^+e^- are small. The absence of large differences in the two distributions gives a strong indication that the fragmentation of $p\bar{p}$ jets (expected to be gluon dominated) is to a first approximation quite similar to the fragmentation of e^+e^- jets (expected to be quark dominated), at least for $z > 0.02$.

In Fig. 11b the behaviour of D(z) as a function of E_T (jet) is displayed. No large scaling violations are observed, although there is a tendency for D(z) to shrink at higher E_T.

One can also study the distribution of transverse momentum with respect to the charged jet axis for the charged particles in a jet. These results are shown in Fig. 12a, where the curve is a fit to the data using a power law formula. The formula was found to fit well to the charged p_T spectrum of minimum bias events. The observed mean internal p_T of the jet is measured to be 600 MeV/c for $z > 0.1$. The internal p_T distribution was also checked for scaling behaviour (Fig. 12b). The result is that there is only slight energy dependence of the internal p_T. From this absence of change in the internal p_T of jets, combined with the earlier result that the charged-particle multiplicity is only slowly increasing for increasing jet energy, it is clear that the jet must become more and more collimated. In the extreme case of very high energy jets, a very pencil-like jet structure would be expected.

9. ANGULAR DISTRIBUTION AND STRUCTURE FUNCTION

From the sample of two-jet events, it is possible to measure the angular distribution of the parton hard-scattering process and extract the structure function of the proton based on the assumption that the parton parameters are obtained from the measurements of the jets. The two-jet cross-section can then be written as:

$$d^3\sigma/dx_1dx_2d\cos\theta = \sum_{ij}[f_i(x_1)/x_1]\,[f_j(x_2)/x_2]\,(d\sigma_{ij}/d\cos\theta)\,,$$

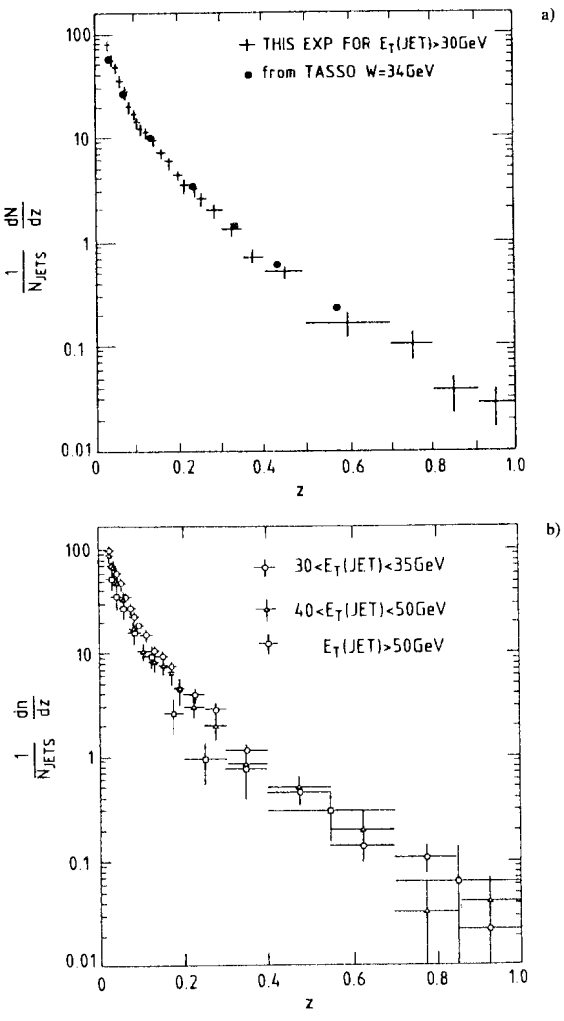


Fig. 11 a) Charged-particle fragmentation function for E_T (jet) > 30 GeV, compared with similar results from the TASSO experiment at PETRA at $\sqrt{s}$ = 34 GeV; b) Charged particle fragmentation function for three different regions of E_T (jet).

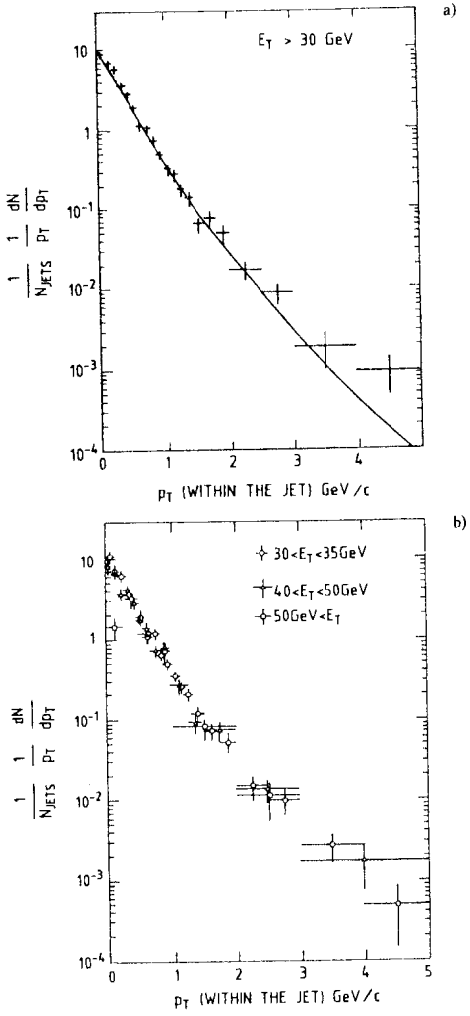


Fig. 12 a) Charged-particle p_T distribution within a jet (with respect to the charged jet axis) for E_T (jet) > 30 GeV. The curve is a fit using the power law formula $(p_T + p_T^0)^{-n}$; b) The same distribution for three different regions of E_T(jet).

where θ is the scattering angle in the jet–jet centre of mass, i and j are the type of parton (quark flavour, gluon), and the f(x)/x are the structure functions for the proton and antiproton. The differential cross-section term is for scattering subprocesses involving partons of type i and j. These scattering subprocesses have been calculated to leading order in QCD,[10] and in fact are found to be very similar for all subprocesses that are expected to dominate (dominant subprocesses are gg, gq, $g\bar{q}$, $q\bar{q}$ scattering, as was shown in Fig. 1b). In the approximation that these subprocesses have the same form, the two-jet cross-section can be fully factorized as:

$$d^3\sigma/dx_1dx_2d\cos\theta = [F(x_1)/x_1][F(x_2)/x_2](d\sigma/d\cos\theta).$$

Furthermore, the quark and gluon components of the structure function can be obtained from knowledge of the couplings and as a result of factorization, and are found to be

$$F(x) = g(x) + 4/9\, q(x).$$

Then from the knowledge of the data distribution as a function of x_1, x_2, and $\cos\theta$, we can obtain the angular distribution $d\sigma/d\cos\theta$ and the structure function F(x). The quantities x_1, x_2, and $\cos\theta$ are easily calculated from the measured rapidity of the jets and from their measured momentum. The distribution of events in x_1–x_2 space is shown in Fig. 13. Most events are concentrated at low x_1 or x_2 near the boundary imposed by the geometrical cuts.

In order to check the hypothesis of factorization, we first need to show that the distribution of events in $\cos\theta$ is independent of the region in x_1–x_2 space. This is shown clearly in Fig. 14, where the curves are based on QCD predictions normalized to the data. It is now possible to use the full data sample to derive the angular distribution. This is accomplished by combining the distributions from different x_1–x_2 regions and using their range of overlap to normalize the results properly. The result -- the combined angular distribution -- is shown in Fig. 15. The data are compared with the theoretical predictions for different dominant scattering subprocesses from QCD (based on vector gluon exchange [10]). Also shown is the region expected for the angular distribution based on an Abelian scalar gluon theory.[11] Here we see that the data favour the vector gluon exchange hypothesis and reject the scalar gluons.

The density of events in the x_1–x_2 scatter plot reflects the product of the structure functions $F(x_1)$ and $F(x_2)$. The hypothesis of factorization of the structure function part of the cross-section formula can be tested by means of comparisons of the density distributions in different x_1–x_2 regions. This has been checked, and the results are consistent with factorization. We then obtain the proton structure function F(x), uncorrected for algorithm efficiency and energy resolution, as shown in Fig. 16. The dotted curve is the measurement for F(x) at low q^2 (q^2 = 2 to 200 GeV^2) by the CERN–Dortmund–Heidelberg–Saclay (CDHS) Collaboration from ν-Fe data.[12] The solid curves give the CDHS result extrapolated to the q^2 range appropriate to the UA1 data (500–2000 GeV^2). This extrapolation is based on the expected scaling violations calculated in QCD. The good agreement between the data and the extrapolation from the lower q^2 region indicates the existence of QCD scaling deviations over a large range in q^2.

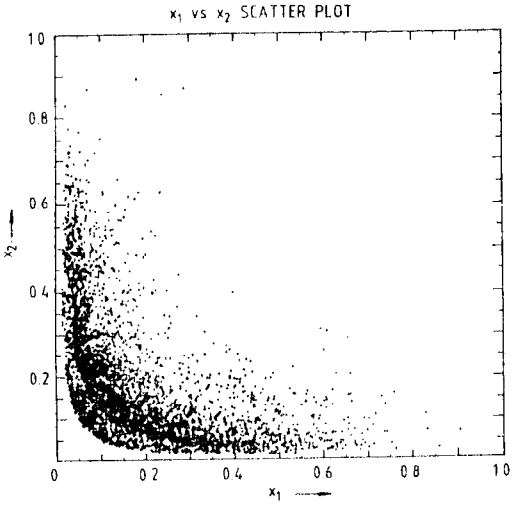


Fig. 13 Distribution of jet–jet events in x_1–x_2 space.

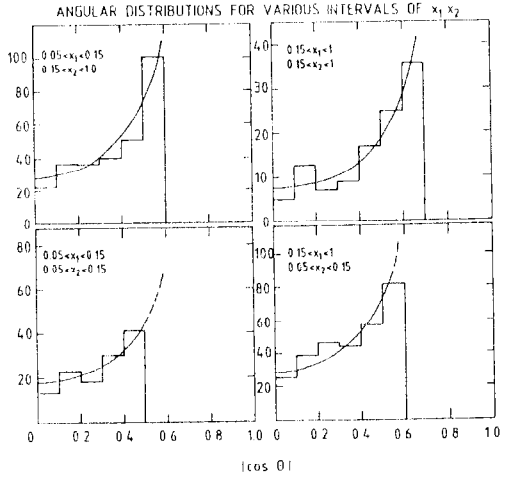
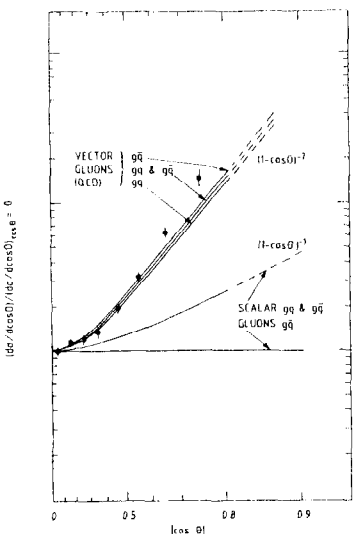


Fig. 14 Jet–jet angular distributions for four different regions in x_1–x_2.

Fig. 15
Jet–jet angular distribution. The curves show predictions based on vector gluon exchange (QCD). The region between the two lower solid curves is for Abelian scalar gluon theory.



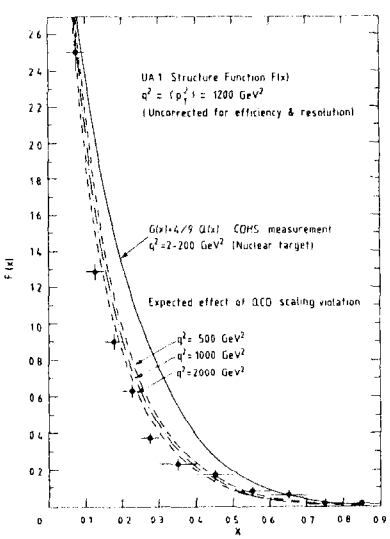


Fig. 16
Proton structure function as a function of x.

10. CONCLUSIONS AND FUTURE JET PHYSICS IN UA1

Perhaps the most striking feature revealed by the study of jets in $p\bar{p}$ collisions is the fact that hadron–hadron interactions are becoming easier to understand: as we go to large localised transverse energies, the jet-like nature of events becomes quite evident and it is possible to develop a clear picture of the hard parton collision processes. With the large data sample of jet events available, we have been able to probe the structure of the proton, to confirm the vector nature of the hard-scattering processes, and to learn about how the partons fragment. We have also been able to make some direct comparisons with QCD predictions and have so far found quite good agreement.

The UA1 Collaboration is continuing a program of jet physics analysis. Some of the topics now under study include results on gluon bremsstrahlung in jet events, structure in multi-jet invariant mass ($W,Z \rightarrow$ jets), search for evidence of the top quark in jets and studies of single-jet events (e.g. search for W decay into heavy leptons or supersymmetric particles, etc). Thus we are quite optimistic about the future of jet physics in $p\bar{p}$ collisions and hope to have many new results to present at the SLAC conference next summer.

Acknowledgements:

I would like to thank the SLAC Summer Institute for their invitation and for organizing an enjoyable conference. I am indebted to my colleagues in the UA1 Collaboration for their effort that made possible the results presented in this paper.

REFERENCES

[1] (Most of the results presented in this paper have been published in the first three references.)
G. Arnison et al. (UA1 Collaboration), preprint CERN–EP/83-118 (1983), submitted to Physics Letters B.

[2] G. Arnison et al. (UA1 Collaboration), preprint CERN–EP/83-119 (1983), submitted to Physics Letters B.

[3] G. Arnison et al. (UA1 Collaboration), Angular distributions and structure functions from two-jet events at the CERN Proton–Antiproton Collider, in preparation.

[4] UA1 proposal: A 4π solid-angle detector for the SPS used as a proton–antiproton collider at a centre-of-mass energy of 540 GeV, CERN/SPSC 78-06 (1978).
M. Barranco Luque et al., Nucl. Instrum. Methods **176** (1980) 175.
M. Calvetti et al., Nucl. Instrum. Methods **176** (1980) 255.
K. Eggert et al., Nucl. Instrum. Methods **176** (1980) 217 and 233.
A. Astbury, Phys. Scr. **23** (1981) 397.
UA1 Collaboration, The UA1 detector (presented by J. Timmer), *in* Antiproton–Proton Physics, Proc. 18th Rencontre de Moriond, La Plagne, 1983 (in press).
[5] G. Arnison et al. (UA1 Collaboration), Phys. Lett. **123B** (1983) 115.
[6] M. Banner et al. (UA2 Collaboration), Phys. Lett. **118B** (1982) 203.
[7] F.E. Paige and S.D. Protopopescu, ISAJET, BNL 31987 (1982).
[8] Z. Kunszt and E. Pietarinen, CERN preprint TH 3584 (1983).
[9] TASSO Collaboration, private communication.
[10] B. Combridge et al., Phys. Lett. **70B** (1977) 234.
[11] D. Drijard et al., Phys. Lett. **121B** (1983) 433.
[12] H. Abramowicz et al., Z. Phys. C **12** (1982) 289.

SEARCH FOR W AND Z^0 AT THE CERN $p\bar{p}$ COLLIDER

UA1 Collaboration, CERN, Geneva, Switzerland
Aachen–Annecy (LAPP)–Birmingham–CERN–Helsinki–
London (Queen Mary College)–Paris (Coll. de France)–Riverside–Rome–
Rutherford Appleton Lab.–Saclay (CEN)–Vienna Collaboration

Presented by T. Hansl-Kozanecka

ABSTRACT

We report on two searches made at the CERN Proton–Antiproton Collider: one for high-mass $\mu^+\mu^-$ and e^+e^- pairs, the other for isolated large-transverse-energy electrons. Six high-mass lepton–antilepton pairs and 52 electron–neutrino pairs have been observed with negligible background. The characteristics of those events fit well the hypothesis that they are produced by the processes $p\bar{p} \to Z^0X$, with $Z^0 \to e^+e^-$ or $\mu^+\mu^-$, and $p\bar{p} \to W^\pm X$, with $W^\pm \to e^\pm \nu$. Here $W^\pm$ and Z^0 are the Intermediate Vector Bosons postulated by the unified theory of weak and electromagnetic interactions.

SLAC Summer Institute on Particle Physics,
Stanford, Calif., USA, 27–29 July 1983

© T. Hansl-Kozanecka 1983

1. INTRODUCTION

The primary goal of the experimental program at the CERN $p\bar{p}$ collider [1] has been to search for the massive Intermediate Vector Bosons (IVBs), which are postulated to mediate the electroweak interaction.

Properties of the IVBs are precisely specified within the theoretical framework of the unified theory of weak and electromagnetic interactions.[2]The predicted masses are

$$m_{W^{\pm}} = 82 \pm 2.4\ \mathrm{GeV/c^2}\ , \tag{1}$$

$$m_{Z^0} = 94 \pm 2.5\ \mathrm{GeV/c^2} \tag{2}$$

for the presently preferred [3] experimental value of the Weinberg angle $\sin^2\theta_W = 0.23 \pm 0.01$.

The cross-section for production is also reasonably well anticipated [4]:

$$\sigma(p\bar{p} \to W^{\pm}X) \simeq 0.4 \times k \times 10^{-33}\ \mathrm{cm^2}\ , \quad W^{\pm} \to e^{\pm}\nu \tag{3}$$

$$\sigma(p\bar{p} \to Z^0X) \simeq 0.05 \times k \times 10^{-33}\ \mathrm{cm^2}\ , \quad Z^0 \to e^+e^- \text{ or } \mu^+\mu^- \tag{4}$$

where k is an enhancement factor of ~ 1.5. It arises from QCD diagrams with gluon emission that contribute, in addition, to the simple Drell-Yan cross-section.

Here we report the preliminary results of a search for single electrons of high transverse momentum, which are expected to originate from Reaction (3), and the search for high-energy lepton pairs, characteristic of Reaction (4). The analysis is based on a sample of proton-antiproton collisions at $\sqrt{s} = 540$ GeV, corresponding to an integrated luminosity of 136 $\mathrm{nb^{-1}}$. A total of 52 $W^{\pm} \to e^{\pm}\nu$ [5,6] events have been recorded, together with 4 e^+e^- pairs and 2 $\mu^+\mu^-$ pairs [7] at high invariant mass.

2. THE DETECTOR

The UA1 detector has been described in detail elsewhere [8]. We limit our discussion to those components that are relevant to the identification of electrons, neutrinos, and muons.

2.1 The track detector

The momenta of charged tracks are determined by magnetic analysis in the central detector (CD), a cylindrical wide-gap drift chamber system, 5.8 m in length and 2.3 m in diameter, which surrounds the beam crossing region. The central dipole magnet generates a uniform field of 0.7 T over the full drift volume. This system yields a high-quality, three-dimensional picture of each $p\bar{p}$ interaction. The precision of the momentum determination is typically $\Delta p/p = 0.5\% \times p$ (p in GeV/c) for a 1 m long track. The ionization of tracks is measured to an accuracy of 10%, which allows the identification of unresolved e^+e^- pairs.

2.2 Calorimetry

The detailed CD information of charged tracks is complemented by the energy determination of interacting charged and neutral particles in the surrounding calorimeters (Fig. 1).

The central section of electromagnetic and hadronic calorimetry has been used to identify electrons over a pseudorapidity interval $|\eta| < 3$ with full azimuthal coverage. Additional calorimetry, both electromagnetic and hadronic, extends to the forward regions of the experiment, down to 0.2°.

The electromagnetic (e.m.) calorimeters consist of two different parts:

i) The central region ($\eta < 1.5$) is covered by 48 semicylindrical modules (gondolas) of alternate layers of lead and scintillator. Each module extends over $\sim 170°$ in azimuth and 22.5 cm along the beam direction. They are 27 radiation lengths deep, thus ensuring the full absorption of e.m. showers. The segmentation in depth into four compartments (1:2:3:2) is adapted to the optimal detection of the e.m. shower shape. Light is collected at the four corners of each compartment via wavelength shifter plates. The light attenuation is exploited to localize the centroid of the energy deposition: the azimuthal angle is measured to an accuracy $\Delta\phi\ (rad) = 0.3/\sqrt{E\ (GeV)}$ and the position along the beam direction to an accuracy $\Delta x(cm) = 6.3/\sqrt{E\ (GeV)}$. The energy resolution is $\Delta E/E = 0.15\sqrt{E\ (GeV)}$.

ii) The end-cap e.m. shower counters (bouchons, $1.5 < \eta < 3$) consist of 64 petals. The segmentation in depth is similar to the one of the gondola modules. A position detector at a depth of 11 radiation lengths (two planes of orthogonal proportional tubes) locates the centre of gravity of energetic e.m. showers to ±2 mm in space.

Energy calibrations are performed periodically with a strong, collimated, Co^{60} source and detailed scans over the whole detector surface. The source is absolutely calibrated in a test beam with two spare gondolas and electrons of well-known energy. Short-term stability of the photomultiplier and electronics chain is monitored using a laser and fibre optics system, the laser itself being monitored by comparing it with an Am^{241} radioactive source.

The analysis of all the tiny systematics that affect the absolute calibration is still under way. Therefore we will quote a systematic error of 3% on the over-all energy scale which reflects the uncertainty in the absolute calibration of our e.m. calorimeter, the uncertainty in the subtraction of uncorrelated low-momentum hadrons hitting the same calorimeter element, and the small inhomogeneities in the relative calibration of various cells of the calorimeter.

The e.m. calorimeter is surrounded by the hadron calorimeter (iron/scintillator sandwich), which is subdivided in depth into two compartments, each having 40 cm ($\eta < 1.5$) or 60 cm ($1.5 < \eta < 3$) iron (Fig. 1). The resolution is $\Delta E/E = 0.8/\sqrt{E\ (GeV)}$. In the search for electrons, the hadron calorimeter plays the role of a veto counter only; in the search for muons it confirms the passage of a single minimum-ionizing particle.

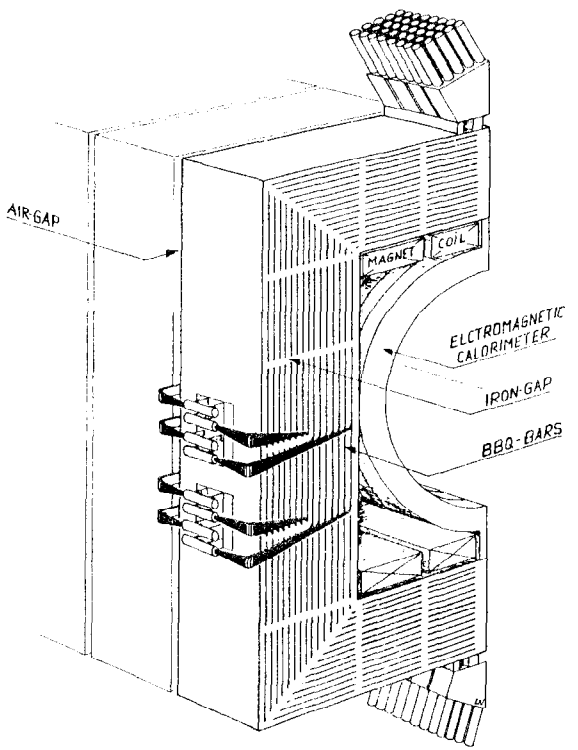


Fig. 1 The central calorimeter cell.

2.3 Muon detector

The outer shell of the UA1 detector is formed by fifty muon chambers, nearly 4×6 m^2 in size. Each chamber consists of two orthogonal layers of drift tubes with two planes per projection (Fig. 2a). An average spatial resolution of 300 μm per measured point has been achieved. A second chamber with four planes is placed 60 cm from the first one. This long lever-arm was chosen in order to reach an angular resolution of a few milliradians, comparable to the multiple scattering angle, typically 3 mrad for a muon at 40 GeV/c. In addition it allows a fast trigger, on muons pointing to the vertex, which is based only on the tubes hit.

2.4 Lepton identification

2.4.1 Electron identification

i) In order for an e.m. energy cluster to be accepted as an electron, there has to be a CD track that points to it. By this we mean that the impact point of the extrapolated CD track agrees with the centroid of the localized e.m. energy deposition.

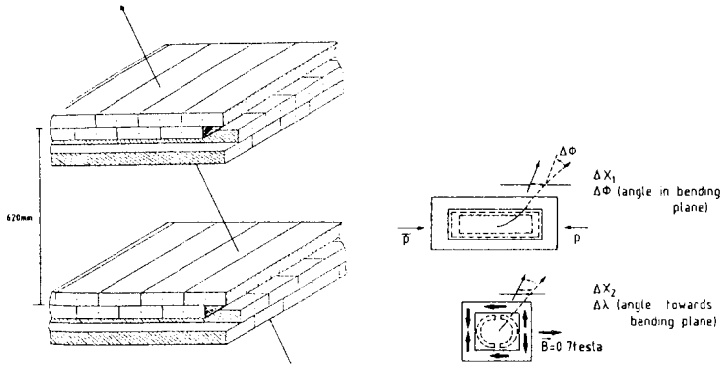
ii) Isolated electrons are identified by their characteristic transition curve, and in particular by the lack of penetration in the hadron calorimeter. Extensive studies of the response of the e.m. calorimeter in a test beam have shown that 98% of the electrons deposit less than 1% of their energy in the hadron calorimeter behind the e.m. cell. The fraction of hadrons (pions) delivering an energy deposition E_c below a given threshold in the hadron calorimeter is a rapidly falling function of energy (Fig. 3), amounting to about 0.7% for $p \approx 40$ GeV/c.

2.4.2 Neutrino identification

The emission of neutrinos is signalled by an apparent visible energy imbalance of the event (missing energy). To achieve such a measurement, the calorimeters have been made completely hermetic down to angles of 0.2° with respect to the direction of the beams. An energy flow vector $\vec{\Delta E}$ is defined, adding vectorially the observed energy depositions over the whole solid angle (including muons). Neglecting particle masses, and with an ideal calorimeter response and solid-angle coverage, momentum conservation requires $\vec{\Delta E} = 0$. For minimum bias and jet-enriched events for which neutrino emission ordinarily does not occur, the transverse components ΔE_y and ΔE_zexhibit small residuals centred on zero, with an r.m.s. deviation well described by the law $\Delta E_{y,z} = 0.4 \sqrt{E_T}$ (Fig. 4), where all units are in GeV and the quantity under the square root is the scalar sum of all transverse energy contributions recorded in the event. The distributions have Gaussian shape and no prominent tails (Fig. 5). The longitudinal component ΔE_x is of little use, since it is strongly affected by energy flow escaping undetected through the beam pipes.

2.4.3 Muon identification

Muons traverse the calorimeters ($\gtrsim 7$ absorption lengths) and the added absorbers ($\gtrsim 3$ absorption lengths) without deviations beyond those of multiple scattering, and without significant energy deposition in excess of ionization losses in the four e.m. and the two hadron calorimeter segments. To be accepted as a muon candidate from amongst tracks found in the muon chambers, the extrapolated CD track must agree in position and angle with the one



a) schematic view of the tube arrangement b) principle of muon identification

Fig. 2 Muon chambers

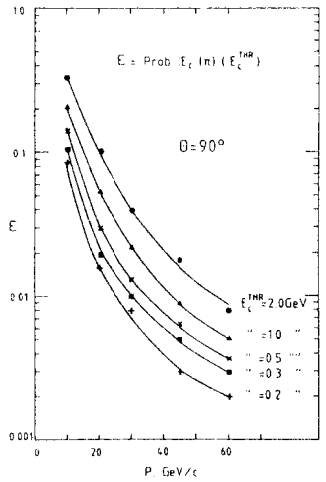


Fig. 3 Probability ε of a pion to deposit energy below the threshold value E_c^{thr} in the hadron calorimeter following immediately the e.m. calorimeter.

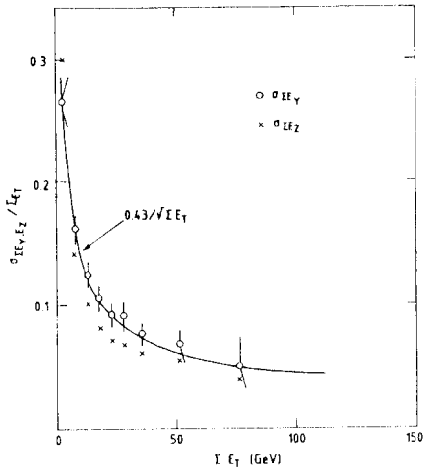


Fig. 4 Energy resolution for the transverse energy components E_y (vertical) and E_z (horizontal) as a function of the total transverse energy E_T.

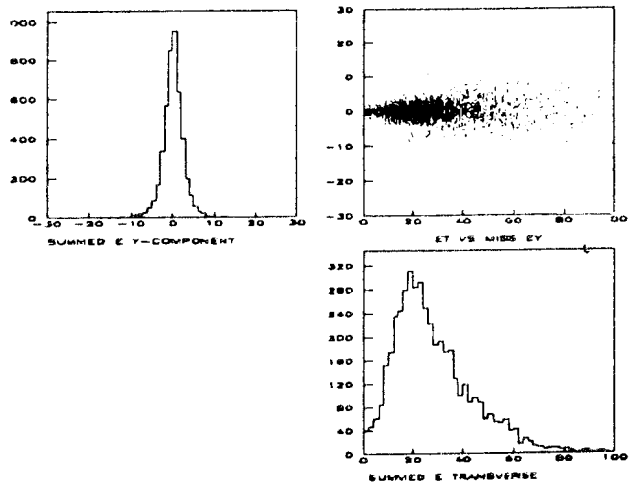


Fig. 5 The missing transverse energy component in the y direction (ΔE_y) as a function of the total transverse energy E_T for minimum-bias-trigger events.

measured in the muon chamber (Fig. 2b). This is a very sensitive test, as the large distance of the chambers from the vertex (~ 6 m) leads to a long lever-arm for the extrapolation.

The muon momentum, as measured in the CD, may be confirmed by two independent methods.

i) Muons traverse the magnetized iron of the magnet yoke. A momentum determination is performed using the position of the interaction vertex, and the track direction at the vertex as measured by the CD, and comparing it with the position and direction of the track in the muon chamber. Excellent agreement is found with the momentum measurements in the CD for vertical cosmic-ray muons in the momentum range 10 to 50 GeV/c (relative precision $\Delta p/p \sim 0.25$).

ii) Finally, the muon momentum may be determined, relying on over-all transverse momentum conservation. For example, for $Z^0 \rightarrow \mu^+\mu^-$ events, where no neutrino is emitted, the recoil of the hadronic debris must be equal to the transverse momentum of the $(\mu^+\mu^-)$ pair. The directions of the two muons then suffice to calculate the momenta. Uncertainties of the muon momenta are then dominated by the errors of the calorimetry.

3. TRIGGER AND INITIAL EVENT SELECTION

The present work is based on a four-month period of data-taking during the autumn of 1982 and the spring of 1983. The integrated luminosity after subtraction of dead-time and other instrumental inefficiencies was 136 nb^{-1}, corresponding to about 8×10^9 collisions between protons and antiprotons at $\sqrt{s} = 540$ GeV. The instantaneous luminosity varied from 3×10^{28} to 1.5×10^{29} $cm^{-2} s^{-1}$.

3.1 Event trigger

Four types of triggers were operated simultaneously:

i) An "electron trigger", with at least 15 GeV of transverse energy deposited in two adjacent elements of the e.m. calorimeters in the pseudorapidity region $|\eta| < 3$.

ii) A "muon trigger", with at least one penetrating track detected in the muon chambers, $|\eta| \leq 1.3$, and pointing in both projections to the interaction vertex within a cone of aperture ± 150 mrad.

iii) A "jet trigger", namely at least 25 GeV of transverse energy in a localized calorimeter cluster in the central region ($|\eta| < 3$).

iv) A global "E_T trigger", with > 50 GeV of total transverse energy from all calorimeters, with $|\eta| < 1.4$.

Only the first two trigger conditions are relevant for this report.

3.2 Initial event selection

Events were further selected by the so-called "express line", consisting of a set of four 168E computers [9] operated independently in real time during the data-taking. A subsample of 120,000 events with either $E_T \geq 15$ GeV in two adjacent e.m. calorimeter segments, or a dimuon candidate (flagged by the trigger), are selected and written on a dedicated magnetic tape. These events have been fully processed off-line and further subdivided into four main classes:

i) muon pair selection to find $Z^0 \rightarrow \mu^+\mu^-$ events;

ii) two or more e.m. clusters with $E_T > 25$ GeV for $Z^0 \rightarrow e^+e^-$ candidates;

iii) single e.m. clusters with $E_T > 15$ GeV and at least one high-p_T track in order to extract $W^+ \rightarrow e^+\nu$ events; and

iv) events with a CD track of transverse momentum (within one standard deviation) $p_T > 25$ GeV/c, in order to evaluate some of the background contributions.

We will now discuss the different categories in detail.

4. SEARCH FOR DILEPTON PAIRS

4.1 Events with two muon candidates

Events from the dimuon trigger flag have been submitted to the additional requirement that there be

i) at least one muon track reconstructed off-line in the muon chambers, and

ii) one track of reasonable projected length ($\geq$ 40 cm) with $p_T \geq 7$ GeV/c in the CD.

Ninety-two events survive these selection criteria. Careful scanning of these events has led to a total of seven clean dimuon candidates (most of the remaining events are due to cosmic rays): five of them display a $(\mu^+\mu^-)$ invariant mass between 10 and 16 GeV, just above trigger threshold; and two have a mass consistent with 95 GeV/c^2, [10] see Fig. 6.

The parameters of the two dimuon events at high mass (one of which is displayed in Fig. 7) are listed in Tables 1 and 2. Although very loose cuts were applied in the selection, the muons fulfill the stringent criteria for the muon identification. The coordinates and the angles measured at the exit of the iron absorber are in complete agreement with the extrapolated CD tracks (Fig. 8). The events exhibit clean isolated tracks, even though isolation is not required in the muon selection. Energy losses in the calorimeters traversed by the muon tracks are well within expectations (Fig. 9). Furthermore, the different methods of determining the muon momentum give consistent results (Table 2).

4.2 Events with two electron depositions

In order to select electron pairs, the following successive cuts [11] have been applied to the data (the effect on the invariant electron-electron mass is shown in Fig. 10:

i) there are at least two clusters of two adjacent e.m. cells, with $E_T > 25$ GeV for each cluster;

ii) "electron signature" for *one* cluster, i.e.

a) a fast track ($p_T > 15$ GeV/c) is pointing to the cluster ($\Delta\phi < 3\sigma$);

b) small (or no) hadron deposition in the hadron calorimeters immediately behind the e.m. cells ($E_{had} < 0.600$ GeV);

iii) the cluster must be isolated, i.e. the total transverse momentum of all other tracks pointing to this cluster is less than 2.5 GeV/c; and

iv) the electron signature [(ii), (iii)] is required also for the second cluster.

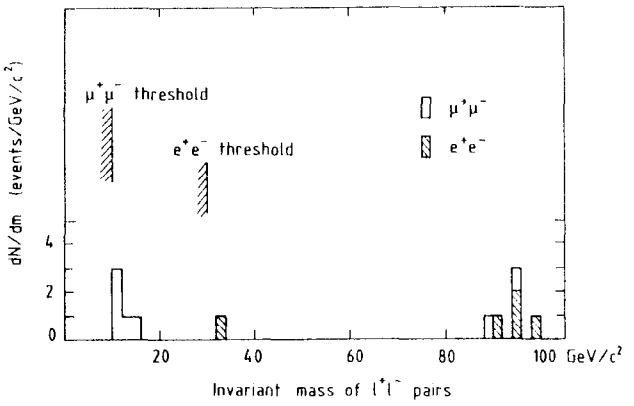


Fig. 6 Invariant mass distribution of the lepton pairs.

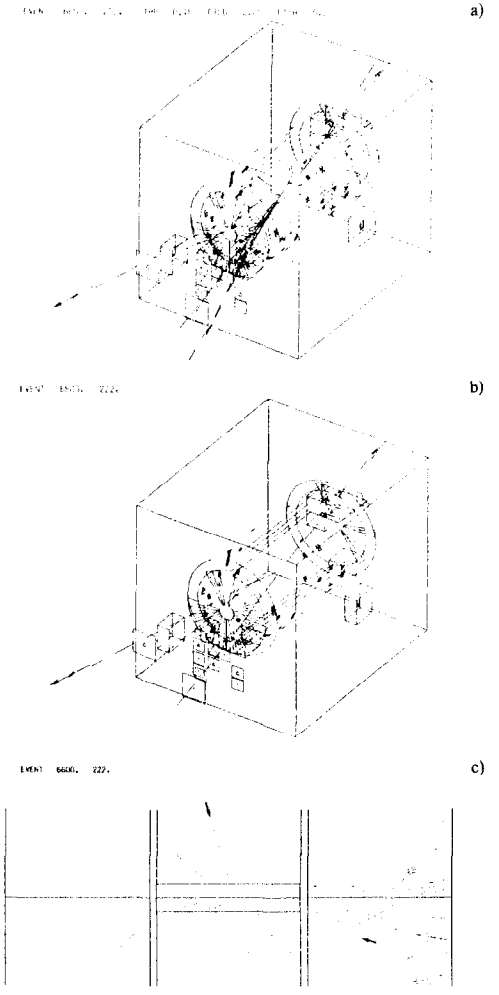


Fig. 7 Display of a high-invariant-mass muon pair event:
a) all tracks and calorimeter cells;
b) with $p_T > 1$ GeV/c for tracks and $E_T > 0.5$ GeV for calorimeter cells;
c) raw CD digitizings.

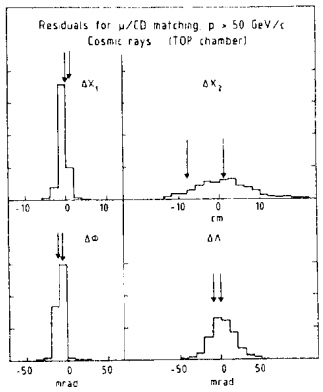


Fig. 8 Residuals for the muon/CD track matching. Distributions come from cosmic-ray muons with p > 50 GeV/c; arrows show the residuals for the muons of the Z^0 events.

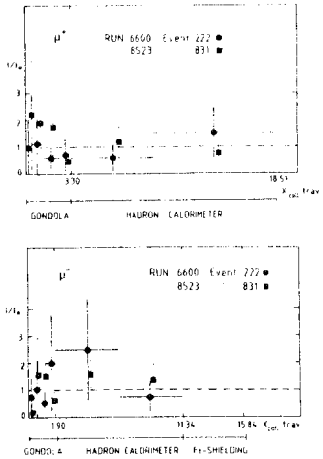


Fig. 9 Normalized energy depositions of the four muons of the Z^0 events.

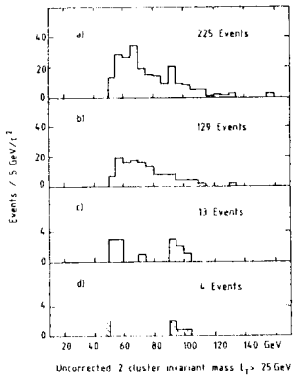


Fig. 10 Uncorrected two-cluster invariant mass ($E_T > 25$ GeV per cluster):
a) all clusters;
b) one cluster with a fast track and
c) this cluster being "electron-like" (see text);
d) both clusters "electron-like".

Table I

Mass and energy properties of lepton-pair events

Run, event	Lepton-pair properties			General event properties			
	Mass a) (GeV/c²)	p_T (GeV/c)	x_F b)	E_{tot} (GeV)	$\sum \lvert E_T \rvert$ (GeV)	Missing E_T (GeV)	Charged tracks
A 7433 1001	91 ± 3	2.9 ± 0.9	0.02 ± 0.01	274	82	2.1 ± 3.6	27
B 7434 746	96 ± 3	7.9 ± 1.2	0.39 ± 0.01	494	149	9.3 ± 5.0	67
C 6059 1010	98 ± 3	8.0 ± 1.5	0.17 ± 0.01	412	143	3.3 ± 4.8	38
D 7339 1279	95 ± 3	8.4 ± 1.4	0.17 ± 0.01	493	157	0.8 ± 5.0	54
E (μμ) 6600 222	95 ± 8	24 ± 5	0.14 ± 0.02	278 c)	128 c)	3.4 ± 5.9 c)	28
F (μμ) 8523 831	88.4 + 33.3 - 18.9	2.2 ± 2.4	0.15 ± 0.01	349 c)	102 c)	0 ± 2.4 c)	24

a) These errors have been scaled up arbitrarily to 3 GeV to represent the present level of uncertainty in the over-all calibration of the e.m. calorimeter.
b) x_F is defined as the longitudinal momentum of the dilepton divided by beam energy.
c) Includes the muon energies.

Table 2

Properties of the muons of the high-mass dimuon events

Q	Track parameters				Muon identification				
					Normalized ionization I/I_0			CD matching c)	
	p_T (GeV/c)	θ (°)	ν	ϕ (°)	e.m. calorimeter	hadron calorimeter	$\Delta\phi$ abs	Position (cm)	Angle (mrad)
	Run 6680, Event 222								
+	58.8 + 8 a) − 6								
−	60.3 ± 10.8 b)	176	1.19	-25.6	0.8 ± 0.5	1.2 ± 0.5	140.5	Δx_1 = -1.3 ± 1.9 Δx_2 = 11.6 ± 10.2	$\Delta\phi$ = -2 ± 6 $\Delta\lambda$ = 11 ± 14
	59.2 + 6.1 c) − 5.2								
−	65.6 + 30 a) − 15								
+	45.1 ± 6.2 b)	80	-0.28	119.1	1.2 ± 0.9	0.6 ± 0.8	111.1	Δx_1 = -0.1 ± 8.0 Δx_2 = -8.0 ± 8.5	$\Delta\phi$ = -6 ± 3 $\Delta\lambda$ = -9 ± 14
	46.1 + 6.1 c) − 5.2								
	Run 6823, Event 851								
+	51.6 + 27 a) − 11.8	123	-0.86	66.6	1.56 ± 1.07	0.75 ± 0.57	11	Δx_1 = 1.7 ± 1.9 Δx_2 = 1.3 ± 5.8	$\Delta\phi$ = -10 ± 4 $\Delta\lambda$ = 0 ± 10
−	56.3 + 15.3 b) − 10.1								
−	50.7 + 56 d) − 17.4								
+	42.6 + 58.6 b) − 8.9	85	-0.12	-110.5	1.14 ± 0.81	1.12 ± 0.57	11	Δx_1 = -1.4 ± 1.5	$\Delta\phi$ = 1 ± 5

a) Determined in CD and muon chamber (statistical errors only).
b) Determined from transverse momentum balance.
c) Weighted average of (a) and (b).
d) Determined in CD (statistical and systematic errors).
e) Difference between the extrapolated CD track and the muon chamber track.

Four e^+e^- events survive the cuts; two of them are shown in Figs. 11 and 12. The main parameters are listed in Tables 1 and 3. In Figs. 13a and 13b the momenta measured in the CD are compared with the energy deposition in the e.m. calorimeters. All tracks but one have consistent energy and momentum measurements.[12] The matching in position is shown in Fig. 14.

4.3 Background estimates

Most "trivial" backgrounds are not expected to exhibit a clustering at high masses. Also, most backgrounds would have an equal probability for ($e\mu$) pairs and same-sign dilepton pairs. Such pairs are not observed, indicating that tbe background is small. We have nevertheless considered several sources of background.

i) Two ordinary *large-transverse-momentum jets*, which both fragment into isolated high-momentum tracks, may simulate muons or electrons. This background was estimated using the measured jet cross-section and jet charged-fragmentation function ($P \approx 10^{-3}$ for each jet separately).[14,15] Requiring, in addition, the e.m. signature, or a hadron to be misidentified as a muon, yields a background of 2×10^{-3} events for the electron and the muon sample separately.

ii) Heavy-flavour jets with subsequent decay into leptons. In a sample corresponding to 11 nb^{-1} of integrated luminosity, we have observed two events with a single isolated muon of $p_T > 15$ GeV/c accompanied by one recoil jet. If these events originate from associated heavy-flavour production, we can estimate the probability that the other heavy-flavour jet fragments with a leading lepton and no other identified debris. Using the predicted fragmentation function [16] and a semileptonic branching ratio of 10%, we obtain a background of $(1.5 \pm 1.0) \times 10^{-3}$ events from this source.

iii) *Drell–Yan continuum*

The cross-section for the Drell–Yan process $p\bar{p} \to \gamma \to e^+e^-$ or $\mu^+\mu^-$ [17] is approximately 10^{-5} nb/GeV for a dilepton mass of 80 GeV. This yields a background of $\sim 2.5 \times 10^{-2}$ events for masses greater than 80 GeV. We have lowered the energy threshold for the (e^+e^-) pair search to $E_T > 15$ GeV per cluster. One additional (e^+e^-) pair was found with a mass just above 30 GeV (Fig. 6), in good agreement with the expectation from the Drell–Yan cross-section ($dM/dy \approx 6 \times 10^{-3}$ nb for $m \geq 30$ GeV/c^2).

iv) Cross-sections for other backgrounds such as W^+W^- pair production [18] or onium decay from a new quark [19] appear to be much too small to account for an effect in the mass range of 95 GeV/c^2.

In conclusion, none of the effects listed above can produce either the number or the features of the observed events.

4.4 Dilepton events as Z^0 decays

The dominant feature of the events consists of the two very prominent high transverse momenta of the two electrons or muons (Fig. 15). All events appear to balance the visible total transverse energy components (Table 1). Thus there is no evidence for the emission of energetic neutrinos.

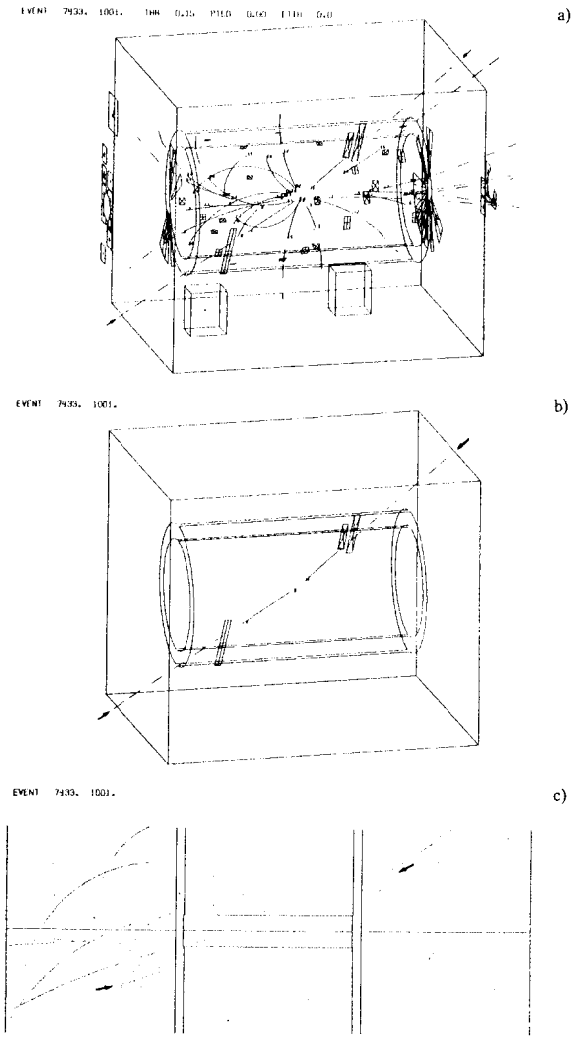


Fig. 11 Display of a high-invariant-mass electron pair event (cf. Fig. 6): low-multiplicity event.

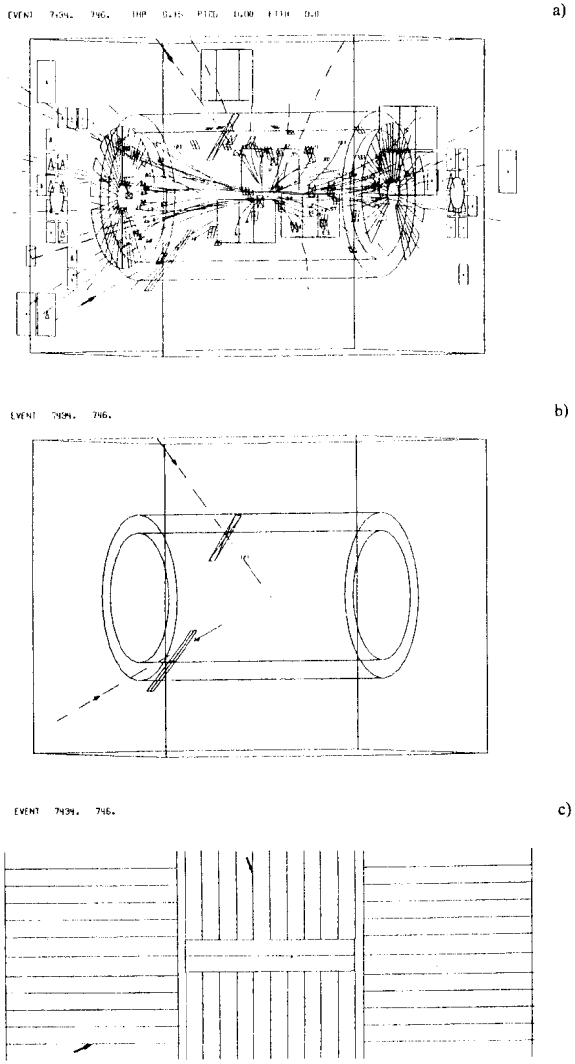


Fig.12 Same as Fig. 10, but for a high-multiplicity event.

Table 3

Properties of the individual electrons of the pair events

Run, event	Drift chamber measurement						Shower counter measurement					
	p (GeV)	Δp a) (GeV)	Q	dE/dx b)	y c)	φ (deg)	E_{tot} e) (GeV)	Electromagnetic samples (GeV)				Had. energy
								S_1	S_2	S_3	S_4	H
A 7433 1001	33	+9 −6	+	1.8 ± 0.3	1.01	144	44	14	27	3	0.0	0.0
	63	+23 −13	−	1.7 ± 0.2	-1.19	-31	48	6	37	4	0.2	0.0
B 7434 746	27	+19 −8	+	1.6 ± 0.3	-0.36	131	42	2	18	20	1.3	0.1
	93	+66 −28	−	1.8 ± 0.2	-1.45	-60	102	42	56	4	0.2	0.0
C 6059 1010	32	+11 −6	+	1.3 ± 0.2	0.64	67	61	1	37	22	0.6	0.0
	9	+1 −1	−	1.4 ± 0.1	0.24	-121	48	1	23	23	1.3	0.0
D 7339 1279	∞ d)	∞ d)	d)	d)	-0.19	169	51	1	13	34	2.4	0.0
	50	+50 −17	−	1.5 ± 0.2	-0.79	-9	55	8	38	9	0.0	0.1

a) $\pm\sigma$ including systematic errors.
b) Ionization loss normalized to minimum ionizing pion.
c) The rapidity y is defined as positive in the direction of outgoing $\bar{p}$.
d) Unmeasured owing to large dip angle.
e) Before pile-up, angular, and ageing corrections.

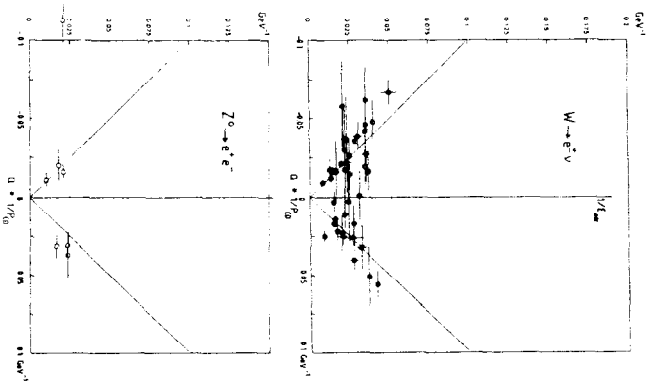


Fig. 13 a)
Comparison of the inverse of the track momentum (multiplied by its charge) with the inverse of the e.m. energy for the electrons from $W \to e\nu$ and $Z^0 \to e^+e^-$ candidates.

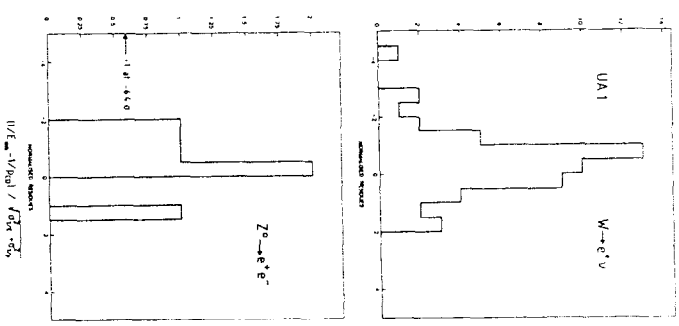


Fig. 13 b)
Difference between the inverse e.m. energy and the inverse momentum normalized to the expected error. The slight shift to negative values is expected for radiative effects.

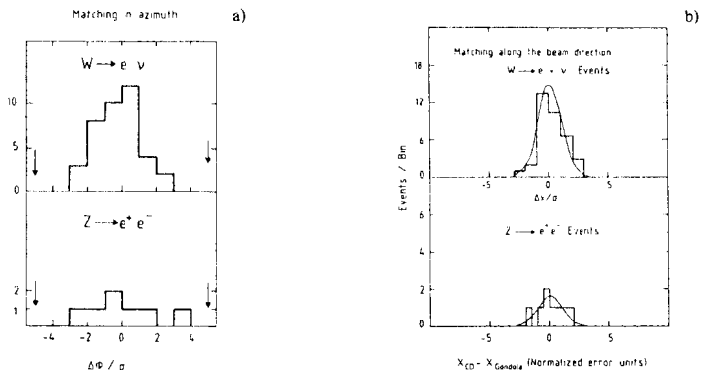


Fig. 14 Geometrical matching in position between the CD track and the centroid of the e.m. deposition (for $W \to e\nu$ and $Z^0 \to e^+e^-$ candidates):
a) in azimuth (the cut applied is indicated by arrows);
b) along the beam (no cut applied). The low-momentum track of event C is the only one that shows a large deviation ($\sim 4\sigma$), see Ref. 12.

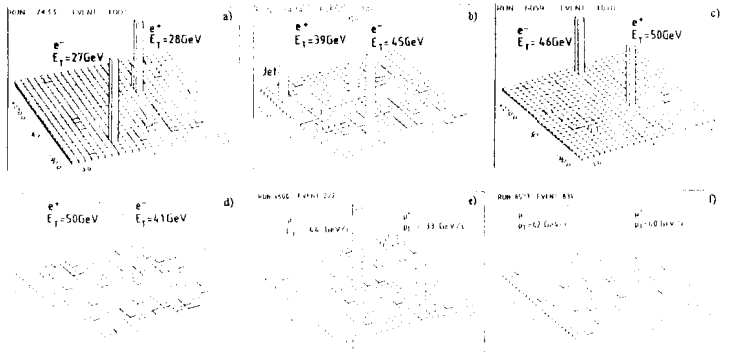


Fig. 15 Transverse energy deposition and transverse momentum for the four electron and two muon Z^0 events as a function of rapidity and azimuth.

The second striking feature of the events is their common value of the invariant mass (Fig. 6). For the (e^+e^-) pairs, the values agree within a few percent, as expected from experimental resolution. The Z^0 mass value and the width are deduced from the electron events only, since the error for the muon events is much larger. The straight average gives $m_{Z^0} = 95.1 \pm 1.6$ (stat.) GeV/c^2; the r.m.s. width is 2.8 GeV/c^2, consistent with the expected Z^0 width and our experimental resolution. Under the hypothesis of Breit-Wigner distribution, we find

$$m_{Z^0} = 95.6 \pm 1.4\,(\text{stat.}) \pm 3\,(\text{syst.})\ \text{GeV}/c^2\ ,$$

and an upper limit can be placed on the full width

$$\Gamma_{Z^0} < 8.5\ \text{GeV}/c^2 \qquad (90\%\ \text{CL})\ ,$$

corresponding to a maximum of 31 (90% CL) different neutrino types in the universe.[20]

The transverse momentum distribution of the Z^0 candidates is shown in Fig. 16, compared with QCD calculations. The high-p_T muon event shows a visible jet structure, which perfectly balances the transverse momentum of the $(\mu^+\mu^-)$ pair.

Thus all the observations are in agreement with the hypothesis that the events are due to the production and decay of the neutral IVB Z^0. The number of observed events agrees with the expected number (6 events for each of the decay channels, e^+e^- or $\mu^+\mu^-$) once detection efficiencies are taken into account ($\sim 85\%$ for e^+e^-, $\sim 30\%$ for the two-muon trigger [10]).

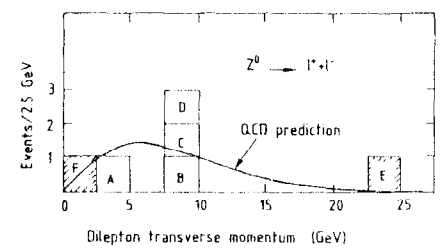


Fig. 16 Transverse momentum of the Z^0.

5. SEARCH FOR ELECTRON-NEUTRINO PAIRS

5.1 Events with single high-p_T electrons

We start again from the initial event sample selected by the "express line". Requiring at least one e.m. cluster with $E_T > 15$ GeV reduced the sample to 1.2×10^5 events that were fully reconstructed. Three conditions are imposed in succession to ensure that the calorimeter cluster corresponds to an electron:

i) A track of high transverse momentum ($p_T > 7$ GeV/c) has to point towards the e.m. cluster (1.8×10^4 events).

ii) The track must be isolated; here, isolation means that the track must be the dominant source ($> 90\%$) of energy within a cone around the track (1.5×10^3 events).

iii) Next the shower profile is required to be consistent with that of an electron, i.e. the energy deposition in the hadronic calorimeters aimed at by the track must not exceed 600 MeV and the ratio of the energy deposition in the fourth and third sampling of the e.m. calorimeter may not exceed 25%.

This reduces the sample to 346 events, which are classified according to their jet content (E_T(jet) > 10 GeV) [14]: 291 events with a jet opposite to the "electron" track within 30° in azimuth; and 55 events with either no jet activity or a jet not back-to-back with the track (5 events). These two classes show striking differences: whilst events with jet activity have

essentially no missing energy, [5] the ones with no jets cluster at high values of missing transverse energy (Fig. 17), suggesting the presence of an energetic neutrino. At most, the three events with lowest missing energy are compatible with no neutrino emission. They are excluded by the cut $E_T^{miss} > 15$ GeV.

The electron signature of the track, in the 52 events with $E_T^{miss} > 15$ GeV, is further confirmed by making a comparison between CD and calorimeter measurements. Cuts on geometrical matching between the charged track and the calorimeter cluster are well satisfied (see Fig. 14). The shower profiles of the electron candidates fall well within expectations: there are no tails extending even close to the imposed cuts (Fig. 18). The momentum measured by magnetic analysis in the CD agrees, within errors, with the energy deposited in the electromagnetic calorimeter (see Fig. 13) for both charge signs and up to the highest observed energies.

Figures 19 and 20 show two events. The diagrams of transverse momenta in the CD and transverse energies in the calorimeter cells (Fig. 19d and 20d) reveal no hadronic energy in the cells following the e.m. cluster, no jet structure, and very little over-all activity. This is typical for the selected events. Removing the electron candidate leaves an event that is very similar to normal $p\bar{p}$ interactions (minimum bias event) in the multiplicity, transverse momentum, and rapidity distributions of the charged tracks and in the over-all transverse energy deposition in the calorimeters.

5.2 Background evaluation

We have chosen two experimental approaches to estimate a possible background contamination.

i) In our 136 nb^{-1} sample we have searched for isolated high-p_T charged hadrons satisfying the same isolation criteria as those for our electron candidates. This time, however, we impose no cuts on the shower profile in the e.m. calorimeter, but require $E_{had} > 600$ MeV to ensure hadronic signature. After imposing no jet activity, we are left with eight events with $E_T > 15$ GeV. Once the measured pion rejection table is folded in (Fig. 3), the resulting background amounts to at most 0.2 events. It should be pointed out that some of the observed isolated high-p_T hadrons could be due to $W \to \tau\nu$ decay, followed by $\tau^{\pm} \to \pi^{\pm}\pi^0\nu$, with a leading π^0. The quoted background therefore represents an upper limit.

ii) An independent study has been carried out, using the measured high-p_T π^0 spectrum in the forward region ($1.5 < |\eta| < 3.0$) to estimate the inclusive hadron spectrum. Assuming $\pi^0 = \frac{1}{2}(\pi^+ + \pi^-)$, this method yields a background of 0.3 events.

A further test against pile-up is given by the matching, in the x-direction, between the charged track of the CD and the centroid of the energy depositions in the gondolas, which is very good for all events (Fig. 10b).

iii) High-p_T π^0, η^0, or γ internally (Dalitz) or externally converted to an e^+e^- pair with one leg missed. The number of isolated e.m. conversions (π^0, η, γ, etc.) per unit of rapidity has been directly measured as a function of E_T in the bouchons, using the position detectors over the interval 10-40 GeV. From this spectrum, the Bethe-Heitler formula for pair creation, and the Kroll-Wada formula for Dalitz pairs, [21] the expected number of events

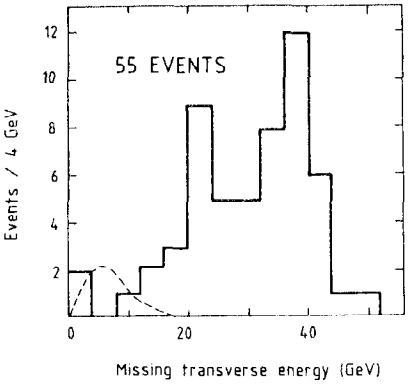


Fig. 17 Missing transverse energy for the events with isolated electrons ($E_T > 15$ GeV), and no jet back-to-back. The resolution function for no missing energy is indicated by the curve, normalized to the three lowest missing-energy events.

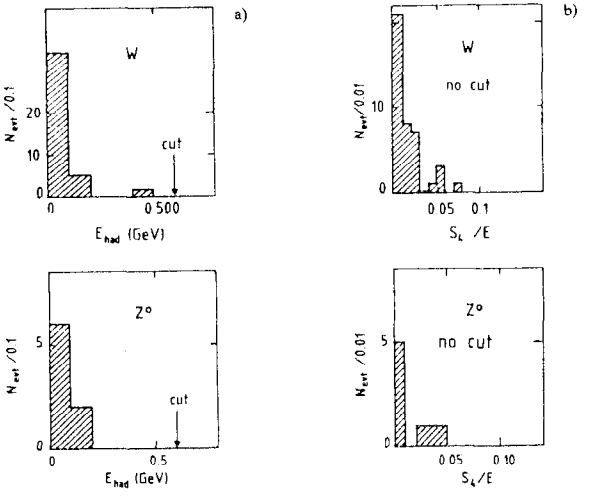


Fig. 18 Longitudinal profile of the e.m. shower:
a) energy deposited in the hadron calorimeter following immediately the e.m. calorimeter;
b) fraction of energy deposited in the last (fourth) e.m. calorimeter.

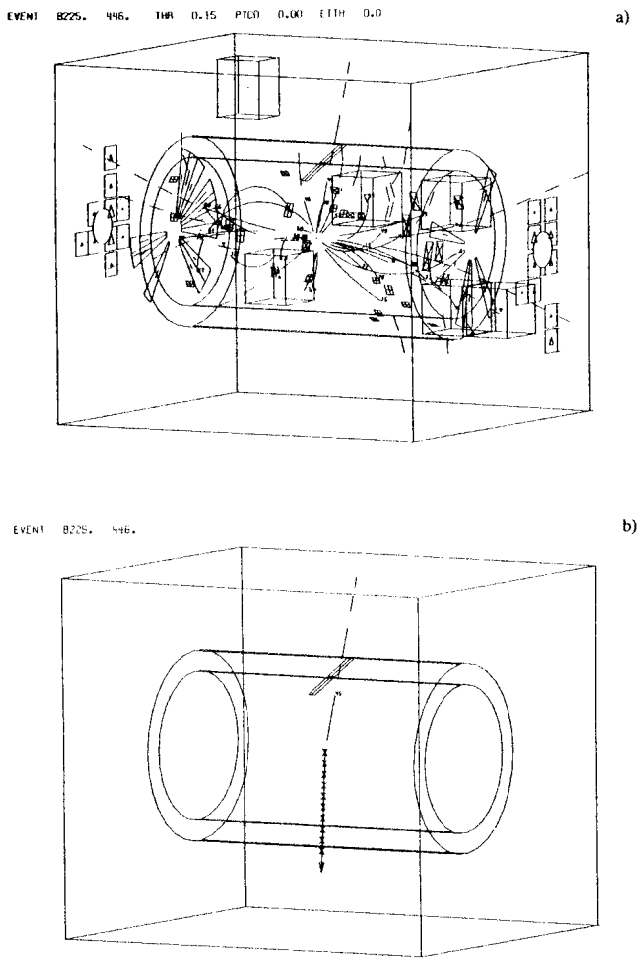


Fig. 19 Display of a $W \rightarrow e\nu$ event:
a) All calorimeter cells with $E > 0.15$ GeV and all tracks.
b) $E_T > 0.5$ GeV for calorimeter cells and $p_T > 1$ GeV/c for tracks. The high-momentum electron hits one *central* e.m. segment. The arrow marked by crosses (corresponding to 3 GeV energy intervals) shows the missing energy ($\not{\nu}$).

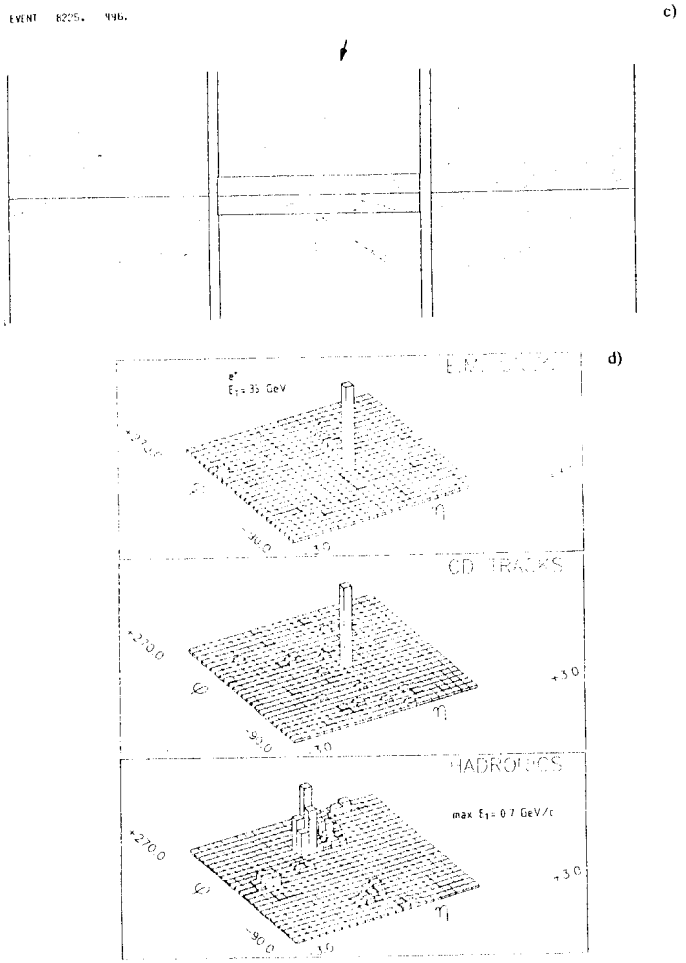


Fig. 19 (cont.) Display of a $W \rightarrow e\nu$ event:
c) Raw CD digitizings.
d) Transverse energy deposition in the e.m. calorimeters, transverse momentum distribution in the CD, and transverse energy distribution in the hadron calorimeter (notice the changed scale for the latter).

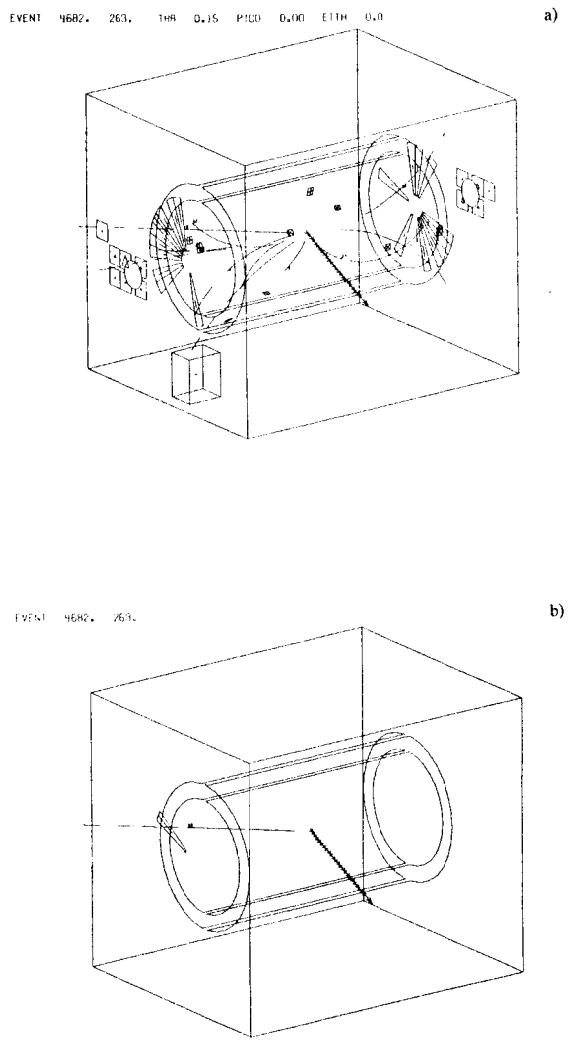


Fig. 20(a) and (b). The same as Fig. 19(a) and (b), but for a *forward* high-momentum electron.

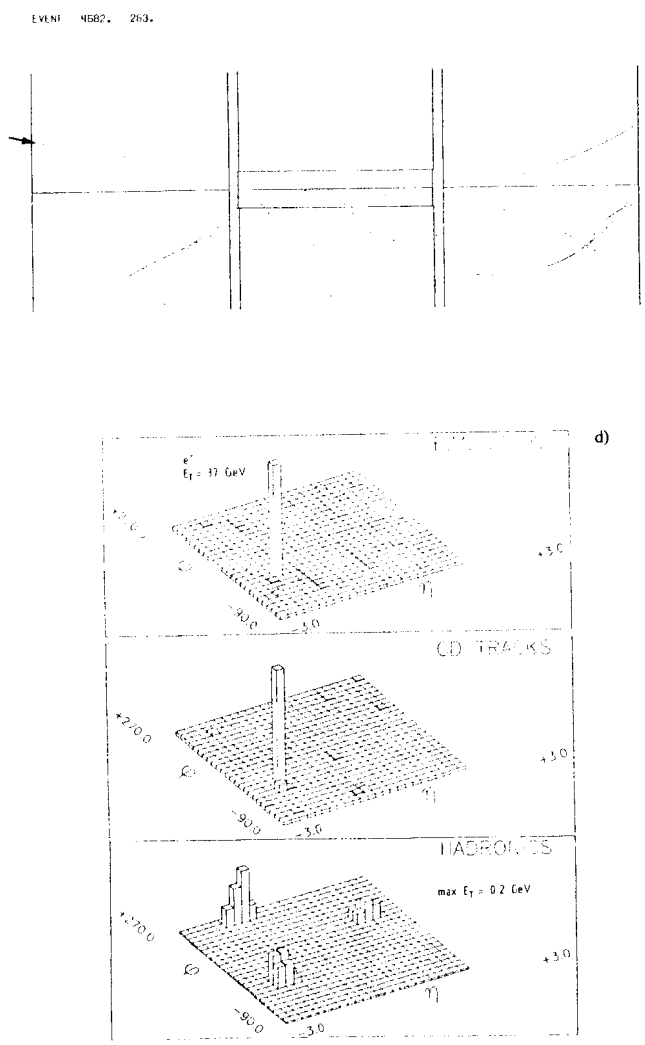


Fig. 20(c) and (d). The same as Fig. 19(c) and (d), but for a *forward* high-momentum electron.

with a "single" $e^{\pm}$ with $p_T > 20$ GeV/c is 1.4 p_0 (in GeV/c), largely independent of the composition of the e.m. component; p_0 is the effective momentum below which the low-energy leg of the pair becomes undetectable. Very conservatively, we can take $p_0 = 200$ MeV/c (curvature radius 1.2 m) and conclude that this background is negligible.

In summary, we have been unable to find a background process capable of simulating the observed high-energy electrons. Thus we are led to the conclusion that they are electrons.

5.3 The electron–neutrino pairs as $W \to e\nu$ decays

For the following we restrict our analysis to the 52 events with missing energy in excess of 15 GeV. We further require that the electron direction points more than 15° away from the vertical plane, where quickly varying light-collection efficiency makes the calorimeter energy measurement less accurate. We are thus left with a sample of 43 events with $p_T^e > 15$ GeV, $p_T^\nu > 15$ GeV, $\phi_e < 75°$, and no jet above 10 GeV transverse energy collinear with the electron.

These events show a missing transverse energy of the same magnitude as the electron transverse energy (Fig. 21a), with the vector momenta of the electron and the neutrino almost exactly balanced back-to-back. The component of the missing transverse energy perpendicular to the electron direction is small and shows no correlation with the electron transverse momentum (Fig. 21b). This strongly indicates the two-body decay of a massive object nearly at rest. The transverse momentum spectra of both leptons exhibit the "Jacobian peak" expected at approximately half the mass of this object (Fig. 22).

The high-p_T end of these spectra, however, is affected by the transverse momentum with which the parent particle was produced. The p_T distribution of all electron-neutrino pairs is presented in Fig. 23a, in good agreement with QCD calculations.[22] Five of our candidates contain a clearly identified jet. This is indeed expected, if, in addition to the lowest-order diagram for Drell–Yan W production, higher-order QCD diagrams involving gluons are considered. In these five events, we observe that the transverse momentum of the lepton pair is approximately balanced by the p_T of the recoiling jet (Fig. 23b).

5.3.1 Mass of the W

A lower bound to the mass, practically insensitive to the transverse momentum distribution of the W, can be obtained from the transverse mass, $m_t^2 = 2(E_T^e E_T^\nu - \vec{p}_T^{\,e} \vec{p}_T^{\,\nu})$ (Fig. 24a). The low-mass tail of this distribution may be contaminated by $W \to \tau\nu_\tau$ decays. To obtain a clean and well-measured set of data, we retain, for the mass determination, only those events with transverse electron and neutrino momenta greater than 30 GeV (27 events, Fig. 24b). A maximum-likelihood fit was performed leaving the mass m_W and the width Γ_W as free parameters, and taking into account the electron and neutrino transverse energy resolution, and the longitudinal and transverse momentum of the $(e\nu)$ pair (see subsection 5.3.2). The fit yields [6]

$$m_W = 80.9 \pm 1.5\,(\text{stat.}) \pm 3\,(\text{syst.})\ \text{GeV/c}^2$$

$$\Gamma_W < 7\ \text{GeV/c}^2 \qquad (95\%\ \text{CL})\ ,$$

in excellent agreement with the Weinberg–Salam model and with previous measurements [5].

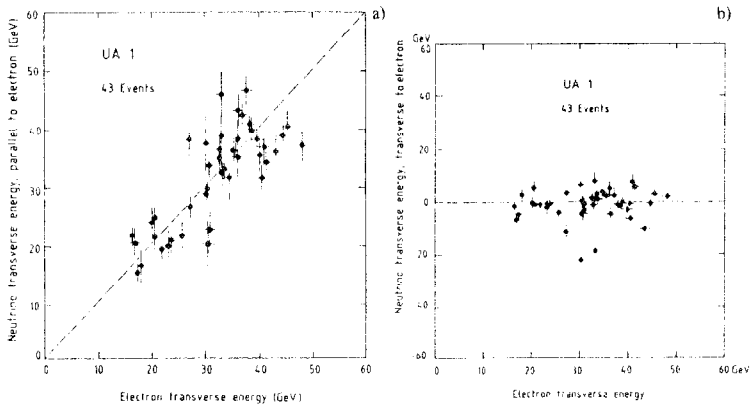


Fig. 21 Correlation between the electron and neutrino transverse energies:
a) The neutrino component along the electron direction is plotted against the electron transverse energy.
b) The neutrino component perpendicular to the electron direction is plotted against the electron transverse energy.

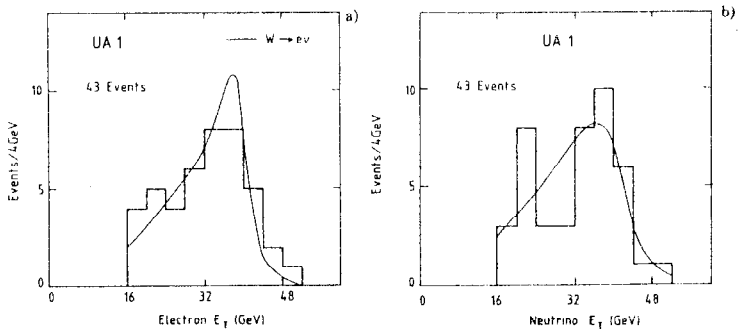


Fig. 22 Lepton transverse-energy distribution for $W \to e\nu$ events, for a) the electron, b) the neutrino. The curves show the result of a fit of the transverse mass distribution (Fig. 24b) to the hypothesis $W \to e\nu$.

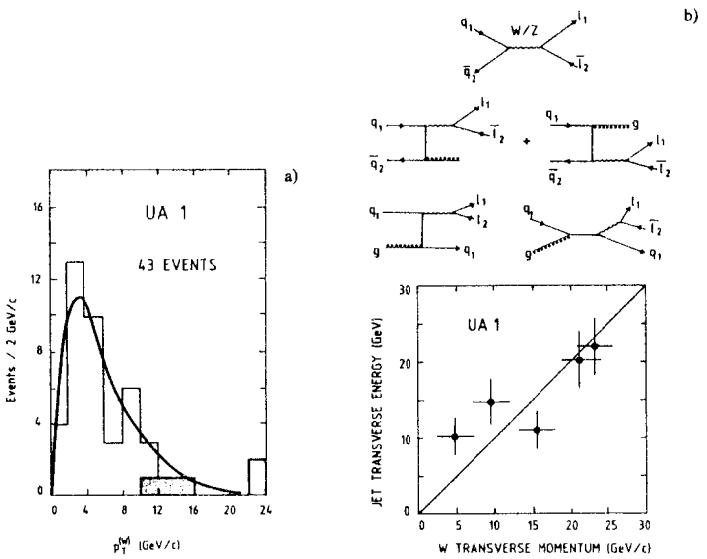


Fig. 23 a) The transverse-momentum distribution of the W. The highest $p_T^{(W)}$ events have a visible jet (hatched areas). The data are compared with the theoretical prediction of Aurenche et al. (see Ref. 22).

b) Transverse momentum of the W plotted against the jet transverse energy for those ($e\nu$) events containing a jet of $E_T > 10$ GeV not collinear with the electron.

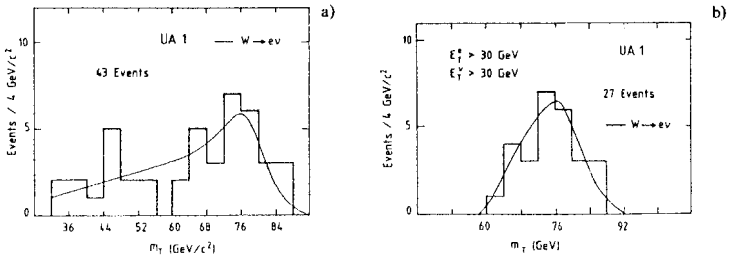


Fig. 24 The distribution of the transverse mass derived from the measured electron and missing-energy, transverse-energy vectors.

a) ($e\nu$) pairs with $E_T^e, E_T^\nu > 15$ GeV;

b) ($e\nu$) pairs with $E_T^e, E_T^\nu > 30$ GeV. The curve shows the result of a fit to the $W \to e\nu$ hypothesis.

5.3.2 Longitudinal momentum

Once the mass value is established, we can determine the centre-of-mass distribution of the decay products and the longitudinal momentum of the W. Using the W mass as the constraint enables us to extract the fractional longitudinal momenta x_q and $x_{\bar{q}}$ of the quarks involved in the collision,

$$m_W^2 = x_q x_{\bar{q}} \times s \ ,$$

$$x_W = x_q - x_{\bar{q}} \ ,$$

where x_W denotes the fractional longitudinal momentum of the W.

An ambiguity arises in the kinematics because we do not measure the longitudinal component of the neutrino momentum, and therefore do not know whether the electron was emitted forward or backward in the W rest frame. This results in two solutions for θ^*, the c.m.s. angle of the electron, and for x_W and x_q, $x_{\bar{q}}$.

However, for a substantial fraction of the events, this ambiguity can be removed in two stages. First, constraining the longitudinal momentum of the W not to exceed the beam energy will remove the ambiguity in about one-third of all cases, as one of the two solutions is unphysical ($x_W > 1$). Next, the measured longitudinal components of the total energy in each event set upper limits separately on x_q and $x_{\bar{q}}$, again making one of the two solutions unphysical. The remaining events, for which the ambiguity still persists, correspond to W's produced almost at rest, with the electron being emitted around 90° in the W rest frame.

In Fig. 25 we present the resulting x_W distribution. In three-quarters of all cases (shaded) the solution is unique. When the ambiguity persists, the lowest of the two x_W values has been plotted. Contributions of the u and d quarks can also be separated, using the charge of the produced W events, since $(u\bar{d}) \to W^+$ and $(\bar{u}d) \to W^-$. The distributions agree with the expected x distributions [4] for quarks (Fig. 26).

5.3.3 Charge asymmetry

Because of the V−A structure of charged-current weak interactions, the W is expected to be produced with longitudinal polarization. This results in a decay asymmetry: electrons from W^- decay are emitted preferentially along the incident quark (proton) direction and positrons along the initial antiquark (antiproton) direction.

To test this prediction, we now restrict ourselves to those cases where the charge of the electron is unambiguously determined. Figure 27 shows for these 29 events (20 negative, 9 positive) the distribution of charge times rapidity (defined as positive along the outgoing antiproton direction) of the charged lepton. Already in this simple form, the data display a clear asymmetry. Actually the lepton angular distribution depends on the lepton transverse momentum: it is maximum at low p_T and vanishes for $p_T \approx 35$ GeV. The predicted behaviour is clearly supported by the data (Fig. 28).

In the centre-of-mass frame, the angular distribution predicted by the V−A theory takes the very simple form

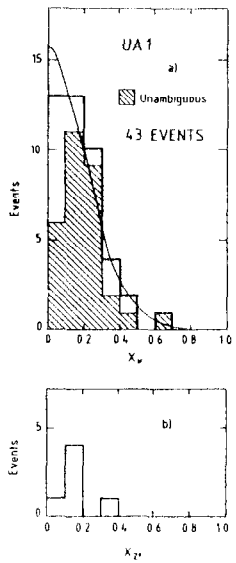


Fig. 25
The fractional beam energy carried by the W or the Z. There are in general two kinematic *solutions* for x_W that can be decided in 70% of the cases (see text). The curves indicate the prediction obtained by assuming the W has been produced by $q\bar{q}$ fusion of valence quarks, where the quark x-distributions are $(1-x)^n$ with n = 3 or 4 for u or d quarks, respectively.

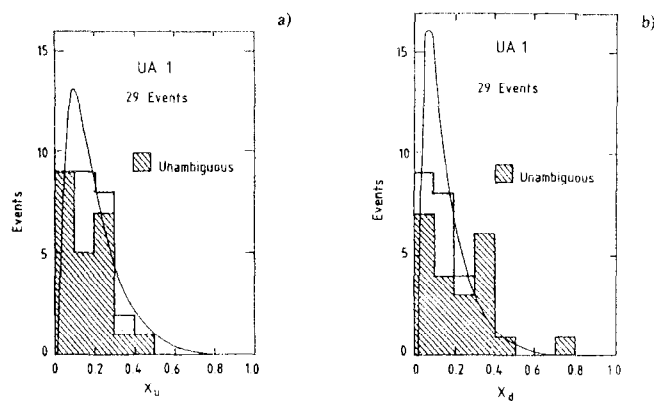


Fig. 26 a) Fractional beam energy carried by the u ($\bar{u}$) quark producing the W.
b) The same as (a) for the d ($\bar{d}$) quarks.
The curves indicate the prediction assuming $q\bar{q}$ fusion.

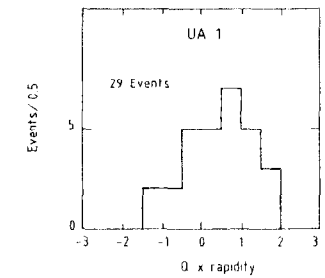


Fig. 27 Distribution of the electron rapidity multiplied by the electron charge. Only events with unambiguous charge assignment are displayed (rapidity is positive in the outgoing antiproton direction).

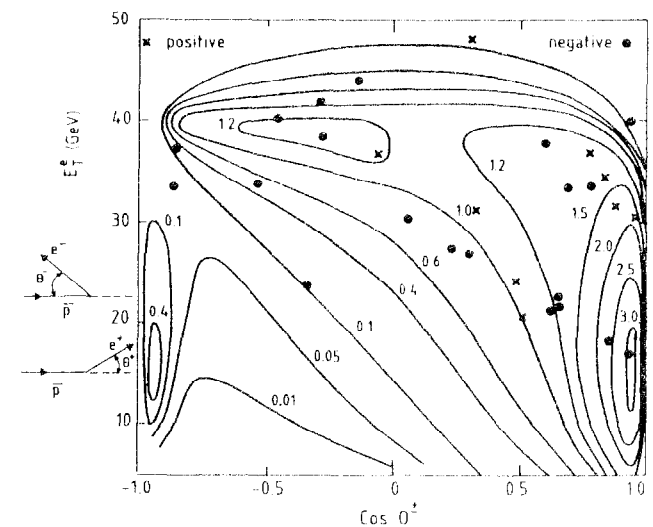


Fig. 28 Three-dimensional representation of the W^+ population as a function of electron angle and transverse momentum. The lines represent (theoretically predicted) levels of equal population, with an arbitrary normalization (Halzen et al., Ref. 22). The circles represent the observed W^- events, the crosses the observed W^+ events.

$$dN^{e^+}/d\cos\theta^* = (1 + \cos\theta^*)^2 \ ,$$

where in the rest frame of the W, θ^* is the angle between the e^+ (or e^-) and the outgoing antiproton (or proton) direction.

Only events with no reconstruction ambiguity can be used to study this distribution. The data, corrected for the inefficiency in solving the x_W ambiguity, are shown in Fig. 29. They confirm the V−A structure of the interaction producing the W, and the maximum parity violation in the decay. The fact that experimentally $\langle\cos\theta^*\rangle = 0.4 \pm 0.1$, supports the $J = 1$ assignment for the W.[6]

In summary, the observed events exhibit the signature, the transverse and longitudinal production characteristics, the decay angular distribution, and the mass expected for the charged intermediate vector bosons $W^{\pm}$.

Once detection efficiency (65% for $p_T^e > 20$ GeV/c) and the uncertainty in the integrated luminosity (15%) are taken into account, we find a cross-section of [6]

$$(\sigma \cdot B)_W = 0.53 \pm 0.08(\text{stat.}) \pm 0.09(\text{syst.})\ \text{nb} \ ,$$

in very good agreement with the expected value.[4]

6. COMPARISON WITH THE STANDARD MODEL

We finally compare our result with the prediction of the SU(2) × U(1) Standard Model. In Fig. 30a we have plotted m_{Z^0} versus m_W. The elliptical shape of the errors reflects the uncertainty in the energy scale. The parameters $\sin^2\theta_W$ and ρ are related to M_Z and M_W

$$M_W = \mu/\sin\theta \ , \qquad \mu = 38.5\ \text{GeV/c}^2$$
$$M_Z = M_W/\sqrt{\rho}\cos\theta \ ,$$

where higher-order corrections ($\sim +3\%$) have been taken into account in the constant μ.[23] The two-parameter fit to our mass values (Fig. 30b) gives

$$\sin^2\theta_W = 0.226 \pm 0.008(\text{stat.}) \pm 0.014(\text{syst.}) \ ,$$
$$\rho = 0.926 \pm 0.038(\text{stat.}) \pm 0.016(\text{syst.})$$

in very good agreement with the Weinberg angle from low-energy data, corrected up to the W mass [2] and with the expectation $\rho = 1$ in the minimal SU(2) × U(1) model and for one Higgs doublet only.

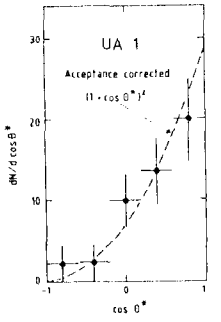
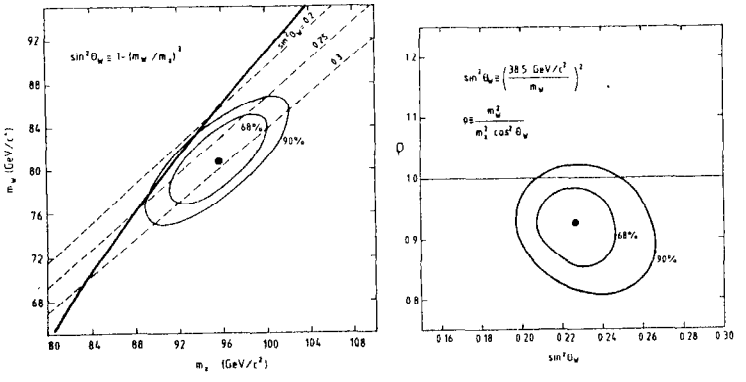


Fig. 29 Angular distribution of the electrons in the W centre of mass, corrected for acceptance.



a) b)

Fig. 30 a) m_{Z^0} plotted against m_W. The elliptical error curves reflect the uncertainty in the energy scale. The heavy curve shows the Standard Model prediction for $\rho = 1$ as a function of the Z^0 and W masses.
b) Confidence levels on the determination of $\sin^2\theta_W$ and ρ (systematic errors included).

Acknowledgements

These results have been made possible owing to the superlative performance of the whole CERN accelerator complex.

My thanks go to Carlo Rubbia for this opportunity to give an early report of exciting results. I wish to thank all my colleagues whose patience, enthusiasm and open collaboration has led the experiment to success.

REFERENCES AND FOOTNOTES

[1] C. Rubbia, P. McIntyre and D. Cline, Proc. Int. Neutrino Conference, Aachen, 1976 (Vieweg, Braunschweig, 1977), p. 683.
The staff of the CERN proton–antiproton project, Phys. Lett. **107B** (1981) 306.

[2] S. Weinberg, Phys. Rev. Lett. **19** (1967) 1264.
A. Salam, Proc. 8th Nobel Symposium, Aspenäsgården, 1968 (Almqvist and Wiksell, Stockholm, 1968), p. 367.
S.L. Glashow, Nucl. Phys. **22** (1961) 579.
For latest parameters, see W.J. Marciano and Z. Parsa, Proc. AIP Division of Particles and Fields Summer Study on Elementary Particle Physics and Future Facilities, Snowmass, Colorado, 1982 (AIP, New York, 1983), p. 155.
M.A. Beg and A. Sirlin, Phys. Rep. **88** (1982) 1.

[3] J.E. Kim et al., Rev. Mod. Phys. **53** (1981) 211.
I. Liede and M. Roos, Nucl. Phys. **B167** (1980) 397.

[4] F.E. Paige, "Physics with hadron colliders," *in* Antiproton–Proton Physics, Proc. 18th Rencontre de Moriond, La Plagne, 1983, and references quoted therein (in press).
F.E. Paige and S.D. Protopopescu, ISAJET program, BNL 29777 (1981).

[5] G. Arnison et al. (UA1 Collaboration), Phys. Lett. **122B** (1983) 103.
See also the corresponding result by the UA2 Collaboration: G. Banner et al., Phys. Lett. **122B** (1983) 476.

[6] G. Arnison et al. (UA1 Collaboration), Phys. Lett. **129B** (1983) 273.

[7] G. Arnison et al. (UA1 Collaboration), Phys. Lett. **126B** (1983) 398.
(Since this publication, the calibration work has been completed and the Z^0 mass value has slightly changed.)
See also the corresponding result by the UA2 Collaboration: P. Bagnaia et al., Phys. Lett. **129B** (1983) 130, and J.P. Repellin, "Results of the UA2 experiment on jets and high transverse momentum electrons," Talk given at this conference.

[8] "UA1 proposal: A 4π solid-angle detector for the SPS used as a proton–antiproton collider at a centre-of-mass energy of 540 GeV," CERN/SPSC 78–06 (1978).
M. Barranco Luque et al., Nucl. Instrum. Methods **176** (1980) 175.
M. Calvetti et al., Nucl. Instrum. Methods **176** (1980) 255.
K. Eggert et al., Nucl. Instrum. Methods **176** (1980) 217 and 233.
A. Astbury, Phys. Scr. **23** (1981) 397.
M.J. Corden et al., Phys. Scr. **25** (1982) 5.
M.J. Corden et al., Phys. Scr. **25** (1982) 11.
B. Aubert et al., Nucl. Instrum. Methods **176** (1980) 195.
M. Calvetti et al., IEEE Trans. Nucl. Sci. **NS–30** (1983) 71.
M. Calvetti et al., "The UA1 central detector," Proc. Int. Conf. on Instrumentation for Colliding Beam Physics, SLAC, Stanford, 1982 (SLAC-250, Stanford, 1982), p. 16.
"The UA1 Collaboration, The UA1 data-acquisition system," ibid., p. 151.

[9] J.T. Carroll, S. Cittolin, M. Demoulin, A. Fucci, B. Martin, A. Norton, J.-P. Porte, P. Ross and K.M. Storr, "Data acquisition using the 168E," Paper presented at the Three-Day In-Depth Review on the Impact of Specialized Processors in Elementary Particle Physics, Padua, 1983, in press.

[10] Shortly after this talk, two further high-mass dimuon events were found in the event sample accepted by the (1μ) trigger. The acceptance of the (1μ) trigger for Z^0 events is $\sim$ 70%, to be compared with the acceptance of the (2μ) trigger of $\sim$ 30%.

[11] For a detailed description of the Z^0 and W selection criteria and background evaluation, see: "UA1 Collaboration, Search for the weak intermediate bosons at the CERN $p\bar{p}$ Collider" (presented by W. Kozanecki), Proc. 6th Warsaw Symposium on Elementary Particle Physics, Kazimierz (Poland), 1983 (in press).

[12] The low-momentum track of event C could be interpreted as being due to a hard bremsstrahlung process, either internal or in the corrugated vacuum chamber. We have estimated the probability, integrated over all photon emission angles, that one electron radiates at least 80% of its energy, and have found it to be 3%, [7,13] assuming that the average thickness is traversed by all tracks.
The track of event C, however, is the only one that shows a larger deviation of the impact of the electron track on the e.m. calorimeter from the centroid of the energy deposition (Fig. 13a), corresponding to an angle difference between the electron track and the γ of $a \approx 11° \pm 4°$. If this large angle difference is significant, then external bremsstrahlung is ruled out and the internal bremsstrahlung interpretation becomes unlikely [Prob($a > 10°, E_\gamma/E_e + E_\gamma > 0.8$) $\approx 2 \times 10^{-3}$].

[13] F.A. Berends et al., Nucl. Phys. **B202** (1982) 63.

[14] For the definition of a jet in the UA1 analysis, see G. Arnison et al. (UA1 Collaboration),"Hadronic jet production at the $p\bar{p}$ Collider,"submitted to Phys. Letters, and (presented by A. Honma), UA1 Collaboration,"A study of jet production and jet properties by the UA1 experiment at the CERN $p\bar{p}$ Collider," Talk given at this conference.

[15] G. Arnison et al. (UA1 Collaboration),"Jet fragmentation into charged particles at the CERN $p\bar{p}$ Collider,"submitted to Physics Letters.

[16] C. Peterson et al., Phys. Rev. **D27** (1983) 105.

[17] S.D. Drell and T.M. Yan, Phys. Rev. Lett. **25** (1970) 316.

[18] See, for example, R. Kinnunen, Proc. Proton-Antiproton Collider Physics Workshop, Madison, 1981 (Univ. Wisconsin, Madison, 1982), p. 236.

[19] T.K. Gaisser, F. Halzen and E.A. Paschos, Phys. Rev. D **15** (1977) 2572.
R. Baier and R. Rückl, Phys. Rev. Lett. **102B** (1981) 364.

[20] For the dependence of the Z^0 width on the number of neutrinos, see, for example, J. Ellis, M.K. Gaillard, G. Girardi and P. Sorba, Ann. Rev. Nucl. Part. Sci. **32** (1982) 443.

[21] H.M. Kroll and W. Wada, Phys. Rev. **98** (1955) 1355.

[22] M. Chaichian, M. Hayashi and K. Yamagishi, Phys. Rev. D **25** (1982) 130.
F. Halzen, A.D. Martin and D.M. Scott, Phys. Rev. D **25** (1982) 754.
P. Aurenche and J. Lindfors, Nucl. Phys. **B185** (1981) 301 and 274.
P. Chiappetta and M. Greco, Nucl. Phys. **B199** (1982) 77.
P. Aurenche and R. Kinnunen,"QCD predictions for weak vector boson production in $p\bar{p}$ collisions," LAPP-TH-78 (1983), and references quoted therein.

[23] For a recent review, see M. Consoli, S.L. Presti and L. Maiani, Univ. Catania preprint, PP/738-14/1/1983.

EUROPEAN ORGANIZATION FOR NUCLEAR RESEARCH

LATEST RESULTS FROM THE UA2 EXPERIMENT AT THE CERN $\bar{p}p$ COLLIDER : HADRON JETS, $W \rightarrow e\nu$, $Z^0 \rightarrow e^+e^-$

The UA2 collaboration
(Bern, CERN, Copenhagen, Orsay, Pavia, Saclay)

presented by

J-P. Repellin
LAL, Orsay, France

Invited talk given at the SLAC Summer Institute, July 29 1983.

Geneva, September 22, 1983

Abstract:

We describe the production and the properties of high transverse momentum hadron jets in the UA2 experiment at the CERN $\bar{p}p$ Collider. The cross sections for inclusive jet production and for two-jet masses of up to 270 GeV/c^2 are presented.

We report preliminary results of searches for high p_T single electrons and for high p_T electron pairs in the UA2 experiment at the CERN $\bar{p}p$ Collider. Thirty five single electrons associated with events with large missing transverse momentum are measured, and are compatible with $\bar{p}p \rightarrow W^+X$ and $W \rightarrow e\nu$. Eight observed high p_T electron pairs, with invariant masses around 90 GeV/c^2, are interpreted as resulting from $\bar{p}p \rightarrow Z^0+X$ with $Z^0 \rightarrow e^+e^-(\gamma)$.

© J. Repellin 1983

1. INTRODUCTION

The main purpose for the conversion of the CERN SPS accelerator into a $\bar{p}p$ collider was to search for the very massive Intermediate Vector Bosons (IVB) W^+,W^- and Z^0, and to study hadronic interactions at high energies, i.e. to investigate the production of high transverse momentum jets at an energy ($\sqrt{s}$ = 540 GeV) ten times higher than at ISR. Following the successful operation of the $\bar{p}p$ Collider, the UA2 experiment has collected a total data sample corresponding to an integrated luminosity of 131 nb^{-1}. The data analysis revealed 35 candidates for $W^{\pm} \rightarrow e^{\pm} + \nu(\bar{\nu})$, eight candidates for $Z^0 \rightarrow e^+ + e^-$ ($+ \gamma$) and a large sample of events containing at least two clear jets with invariant masses up to half of the total available centre of mass energy.

This talk is structured as follows:

- Introduction
- Detector and Data Taking
- Hadron Jets at Large Transverse Energy
  - Two-jet Dominance
  - Jet Fragmentation
  - Two-jet Production Properties
  - Study of Additional Clusters in the Two-jet Events
  - Inclusive Jet and Two-jet Production Cross Sections
  - Conclusion
- W,Z^0 Data Analysis
  - First Data Reduction
  - Electron Identification
- W Analysis
  - Final Sample
  - Mass Determination
  - Charge Asymmetry in Forward Directions
- Z^0 Analysis
  - Final Sample
  - Mass Determination
  - Comparison With Models

2. DETECTOR AND DATA TAKING

The experimental apparatus [1] is shown in Fig. 1.

-At the centre of the apparatus a system of cylindrical chambers (vertex detector) measures charged particle trajectories in a region without magnetic field. The vertex detector consists of : a) four multi-wire proportional chambers having cathode strips with pulse height read-out at ±45° to the wires; and b) two drift chambers with measurement of the charge division on a total of 12 wires per track. These chambers are used to obtain tracking information and to evaluate the most likely ionisation (in units of equivalent minimum ionising particles, m.i.p.) associated with each track. The tracking efficiency has been measured to be 97% for transverse reconstruction and about 85% for space reconstruction. The two track resolution is about 25 mrad in the plane transverse to the beam and 40 mrad in the plane parallel to the beam. From the reconstructed charged particle tracks the position of the event vertex is determined with a precision of ±1 mm in all directions.

-The vertex detector is surrounded by an electromagnetic and hadronic calorimeter [1] (central calorimeter), which covers the full azimuth and a polar angle interval $40° < \theta < 140°$, (corresponding to pseudorapidity interval $-1 < \eta < 1$). The calorimeter is segmented into 240 cells , each covering 15° in ϕ and 10° in θ and built in a tower structure pointing to the centre of the interaction region. The cells are segmented longitudinally into a 17 radiation lengths thick electromagnetic compartment (lead-scintillator) followed by two hadronic compartments (iron-scintillator) of ≈ 2 absorption lengths each. The light from each compartment is channelled to two photomultipliers (PMs) by means of BBQ-doped light guides on opposite sides of the cell.

In the angular region covered by the central calorimeter a cylindrical tungsten converter, 1.5 radiation lengths thick, followed by a cylindrical proportional chamber, is located just after the vertex detector. This chamber, named C5 (see Fig. 1), has cathode strips at ±45° to the wires. We measure the pulse height on the cathode strips and the charge division on the wires. This device localises electromagnetic showers initiated in the tungsten with a precision of 3 mm. The resolving power for neighbour showers is about 20 mm.

For the first 15 nb^{-1} of integrated luminosity, collected during Autumn of 1982, the azimuthal coverage of the central calorimeter was only 300°. The remaining interval (±30° around the horizontal plane) was covered by the wedge detector, to measure charged particle production [2]. This detector,

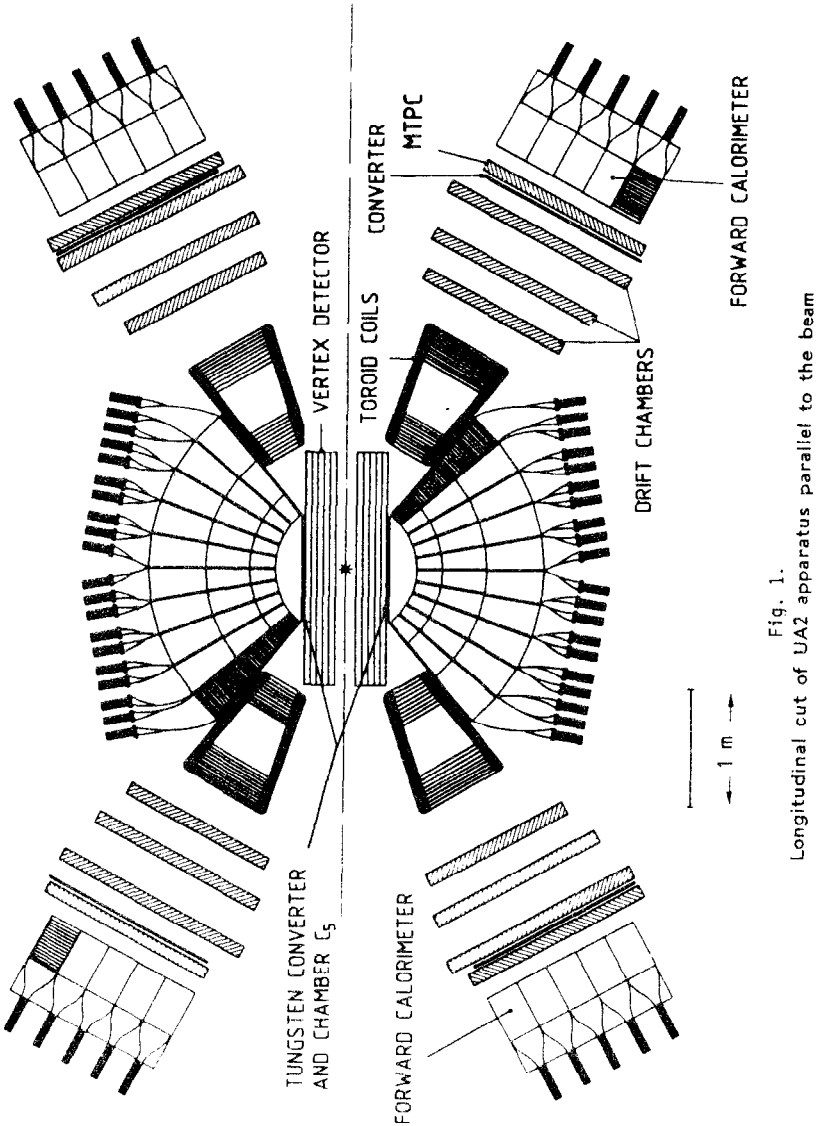


Fig. 1.
Longitudinal cut of UA2 apparatus parallel to the beam

Fig. 2, was a single-arm spectrometer in the horizontal plane covering 28° in ϕ and 68° in θ (± 0.7 units in rapidity) symmetrically around $\theta = 90°$ with respect to the colliding beams. The magnet occupies the space of four central calorimeter modules that have been removed for that purpose. The calorimeter is used as a return yoke. The field integral is about 1.1 Tm. The charged particle trajectories are measured before the magnet with the vertex detector , and after in a set of 12 large drift chamber planes. The momentum accuracy is $\sigma_p/p = 0.01 \times p$ (p in GeV/c). These chambers are followed by a scintillator-iron-scintillator sandwich and by a 14 radiation lengths thick lead-glass wall.

The two forward regions ($20° < \theta < 37.5°$ and $142.5° < \theta < 160°$) are each equipped with twelve toroidal magnet sectors having a mean field integral of 0.38 Tm. Each sector is instrumented with :

a) Three drift chambers [1] located after the magnetic field region. Each chamber consists of three planes, with wires at $-7°, 0°, +7°$ with respect to the magnetic field direction. The momentum of charged particles is measured with an accuracy $\sigma_p/p \leq 0.02 \times p$ (p in GeV/c).

b) A 1.4 radiation lengths thick lead-iron converter, followed by a chamber [1] consisting of two pairs of layers of 20 mm diameter proportional tubes (MTPC), staggered by a tube radius and equipped with pulse height measurement. There is a 77° angle between the tubes of the two pairs of layers, with the tubes of the first one being parallel to the magnetic field direction. This device localises electromagnetic showers with a precision of $\lesssim 8$ mm.

c) An electromagnetic calorimeter consisting of lead-scintillator counters assembled in ten independent cells, each covering 15° in ϕ and 3.5° in θ. Each cell is subdivided into two independent longitudinal sections, 24 and 6 radiation lengths thick, the latter providing rejection against hadrons. The light from each section is collected by two BBQ-doped light guides on opposite sides of the cell.

Each cell of the central and forward calorimeters has been calibrated in a 10 GeV beam from the CERN PS, using incident electrons and muons. The stability of the calibration has since been monitored using a light flasher system, a Co^{60} source and a measurement of the average energy flow into each module for unbiased $\bar{p}p$ collisions [1]. The systematic uncertainty in the energy calibration of the electromagnetic calorimeters for the data discussed here amounts to an average value of $\pm 1.5\%$. The cell-to-cell calibration uncertainty has a distribution with a r.m.s. of 3%. The systematic uncertainty in the energy calibration of the hadronic calorimeter is less than $\pm 4\%$.

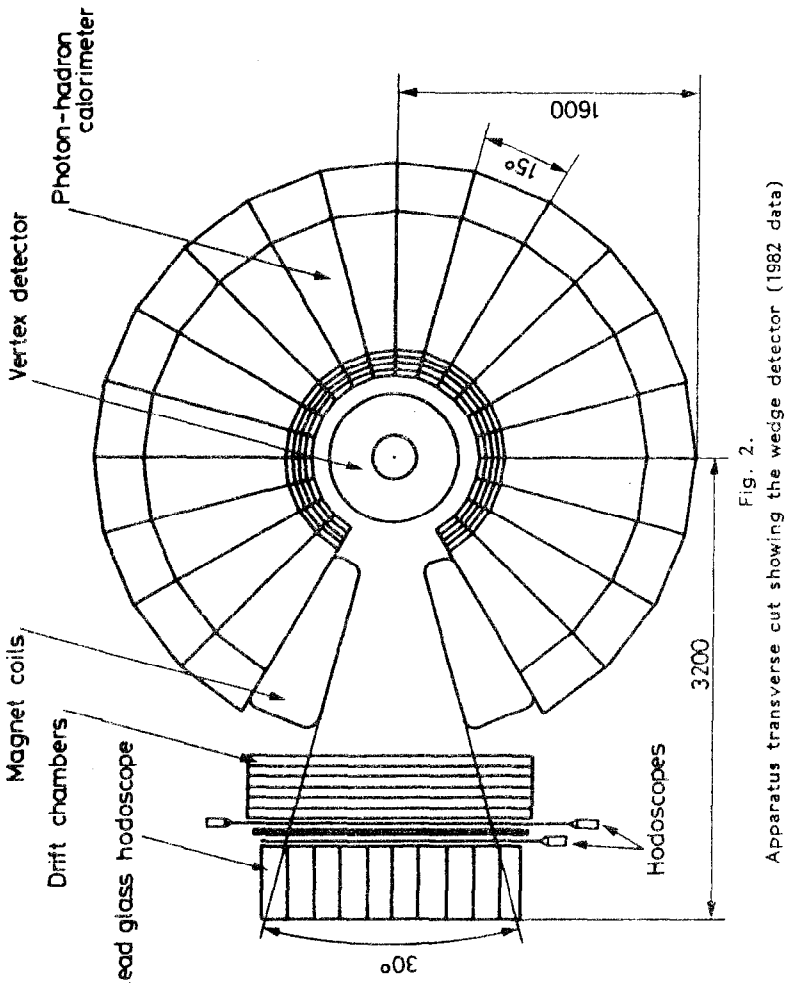


Fig. 2. Apparatus transverse cut showing the wedge detector (1982 data)

The response of both calorimeters to electrons, single hadrons and multi-hadrons (produced in a target located in front of the calorimeter) has been measured at the CERN PS and SPS machines using beams from 1 to 70 GeV/c. In particular we have studied the longitudinal and transverse shower development and the effect of particles impinging near the cell boundaries. The energy resolution for electrons is measured to be $\sigma_E/E=0.14/\sqrt{E}$ (E in GeV). In the case of hadrons, σ_E/E varies from 32% at 1 GeV to 11% at 70 GeV, approximately proportional to $E^{-1/4}$. The resolution for multihadron systems of more than 20 GeV is similar to that of single hadrons.

To implement a trigger sensitive to electrons of high transverse momentum, the PM gains in all calorimeters were adjusted so that their signals were proportional to the transverse energy. Because of the cell dimensions, electromagnetic showers initiated by electrons may be shared among adjacent cells, and therefore trigger thresholds were applied to linear sums of signals from matrices of 2×2 cells. In the central calorimeter, all possible 2×2 matrices were considered ; in the forward calorimeters, only those matrices made up of cells belonging to the same sector were considered. A W-trigger signal was generated whenever the transverse energy deposition in one such matrix exceeded a threshold corresponding to a transverse energy deposition of 8 GeV. A Z^0-trigger signal was generated whenever the transverse energy deposition in at least two such matrices, separated in azimuth by more than 60°, exceeded a threshold corresponding to a transverse energy deposition of 3.5 GeV.

For the jet study a trigger sensitive to events with large transverse energy (electromagnetic + hadronic) ΣE_T in the central calorimeter was implemented. The signals of all the photomultipliers of the central calorimeter were linearly added and their sum was required to exceed a given threshold.

3. HADRON JETS AT LARGE TRANSVERSE ENERGY

The study of hadron-hadron interactions at high energies, i.e. $\bar{p}p$ collisions at $\sqrt{s}$ = 540 GeV, gives us the opportunity to test predictions of the strong interaction theory, the Quantum Chromo-Dynamics (QCD), at short distances. As proposed more than ten years ago for such reactions, the now generally accepted picture, sketched in figure 3 , is the hard scattering of hadron constituents (partons) resulting in two hadron jets with roughly the same momenta as the scattered partons [3]. In order to get a

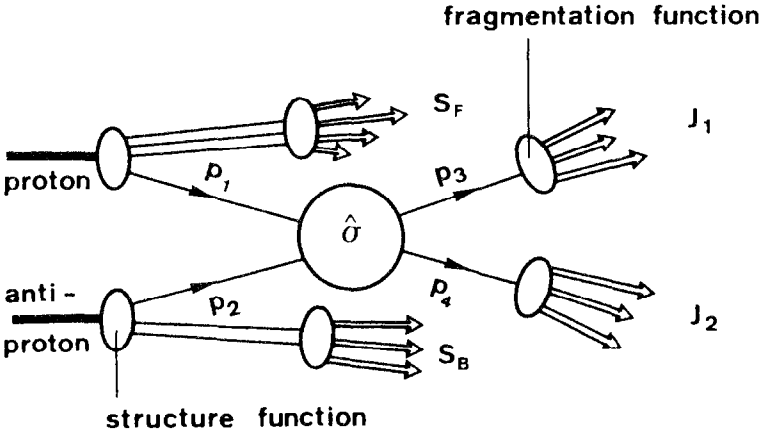


Fig. 3.
Schematic $\bar{p}p \rightarrow jet^{+}jet^{+}X$ production mechanism in the parton picture.

quantitative description of the data, it is necessary, as will be seen, to include gluon bremsstrahlung effects in the parton scattering process.

We report here results mainly obtained from data accumulated in 1982, using a trigger sensitive to events with large transverse energy (ΣE_T) in the central calorimeter. The total transverse energy had to exceed a threshold of 25 GeV for an integrated luminosity $L = 1.8\ nb^{-1}$ and of 35 GeV for $L = 13.3\ nb^{-1}$.

To suppress background from non $\bar{p}p$ collisions the trigger requires a coincidence with two signals obtained from scintillator arrays covering an angular range $0.47 < \Theta < 2.84°$ on both sides of the collision region [4].

The events collected with the large transverse energy trigger include a small background contamination from sources other than $\bar{p}p$ collisions.

The background events exhibit a characteristic pattern in the detector different from that of large ΣE_T $\bar{p}p$ events. They are rejected from the data sample by two selection criteria:

1. if they are associated with an early signal in the small angle scintillator arrays; and
2. if they have an abnormally large total transverse energy fraction in the hadronic compartments (more than 60 % in the second one or more than 95 % in both together).

These requirements reduce the background contamination in the data sample to < 5 % independent of ΣE_T. The loss of good events introduced by the cuts is negligible.

The present data not only confirm the dominance of two-jet configurations in events having large transverse energy measured in the central region, as found previously in the UA2 experiment [5], but also allow for a first study of their most outstanding properties.

3.1. TWO-JET DOMINANCE

In order to investigate the pattern of energy distribution in the events we adopt, as in our previous analysis [5], a straight-forward clustering algorithm taking advantage of the fine granularity of the calorimeter segmentation. We join into a cluster all cells which have a common side and have a cell energy $E_{cell} > E_{cell}^{min} = 400$ MeV. Clusters having two or more local maxima separated by a valley deeper than 5 GeV are then split. In each event we rank the clusters in order of decreasing transverse energies and denote them by $E_T^1 > E_T^2 > E_T^3 \ldots$

The mean values of the fractions $h_1 = E_T^1/\Sigma E_T$ and $h_2 = (E_T^1 + E_T^2)/\Sigma E_T$ are shown in Fig. 4 as a function of ΣE_T. Their behaviour illustrates the emergence of a dominant two-jet structure at large values of ΣE_T. A large fraction of the total transverse energy of large ΣE_T events is shared on average by two clusters only. An ideal event containing only two jets of equal transverse energies would have $h_1 = 0.5$ and $h_2 = 1$.

The azimuthal separation $\Delta\Phi_{12}$ between the two clusters having the largest transverse energies per event (E_T^1 and E_T^2) is shown in Fig. 5 for events with $\Sigma E_T > 60$ GeV and $E_T^1, E_T^2 > 20$ GeV. The distribution of $\Delta\Phi_{12}$ is observed to peak near 180° showing that the two clusters are approximately back-to-back in the transverse plane.

Direct evidence for two-jet dominance is also obtained from an inspection of the transverse energy distribution in the Φ-Θ plane. As an example Fig. 6 shows the configuration of an event with a large value of ΣE_T, 213 GeV. The transverse energy is concentrated within two small regions (Fig. 6a) which are separated in azimuth by $\Delta\Phi_{12} = 180°$ and towards which several collimated tracks are observed to point (Fig. 6b).

3.2. JET FRAGMENTATION

The event configuration in Fig. 6b is a general feature of the present data and suggests the existence of hadron jets originating from the fragmentation of scattered partons.

3.2.1. Charged Particle Multiplicity

The vertex detector ($20° < \Theta < 160°$ and full azimuth) measures the charged particle multiplicity in jets. To get the highest track reconstruction efficiency (96 ± 2) %, we restrict the analysis to the transverse plane. Events considered contain two clusters in the central calorimeter, each with a transverse energy in excess of 15 GeV and an azimuthal separation $\Delta\Phi_{12} > 150°$. Distributions of the azimuthal separation $\Delta\Phi$ between each track and the centroid of the highest transverse energy cluster are shown in Fig. 7 for two intervals of m_{jj}, the invariant mass associated with the two highest energy clusters. Clear peaks are seen at $\Delta\Phi \approx 0$ and $\Delta\Phi \approx \pi$, as expected for two-jet events. The distribution is more peaked for the larger m_{jj} slice, showing that higher energy jets are more collimated.

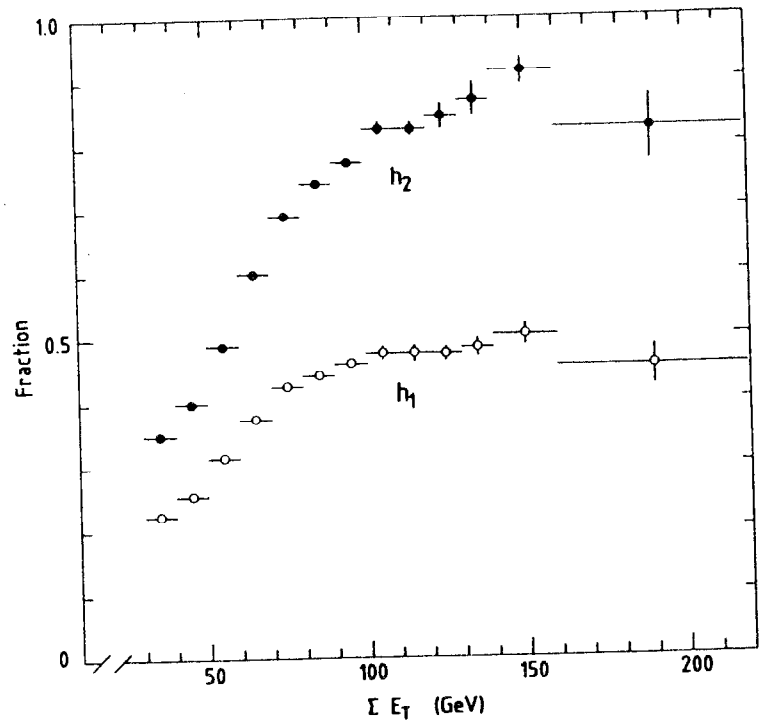


Fig. 4.
The fractions h_1 and h_2 of the total transverse energy ΣE_T, contained in the cluster, or the two clusters, respectively, having the largest E_T, are displayed versus ΣE_T.

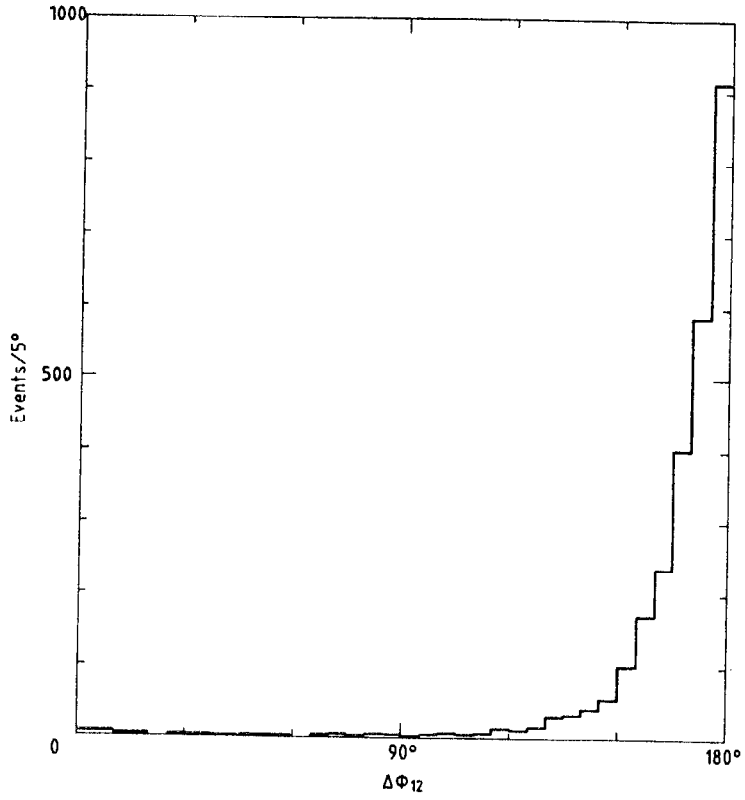


Fig. 5.
Azimuthal separation $\Delta\Phi_{12}$ between the two largest clusters having E_T > 20 GeV for events with ΣE_T > 60 GeV.

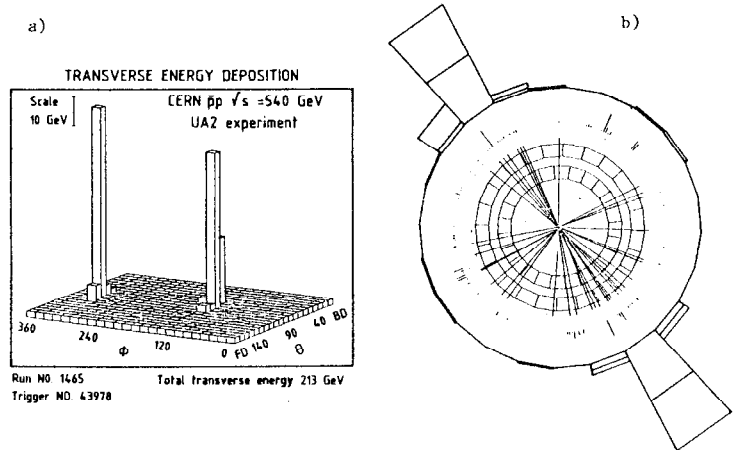


Fig. 6 .
Configuration of an event with large ΣE_T (213 GeV).
a) Cell transverse energy distribution as a function of polar angle Θ and azimuth Φ.
b) Transverse display of the calorimeter and vertex detector.

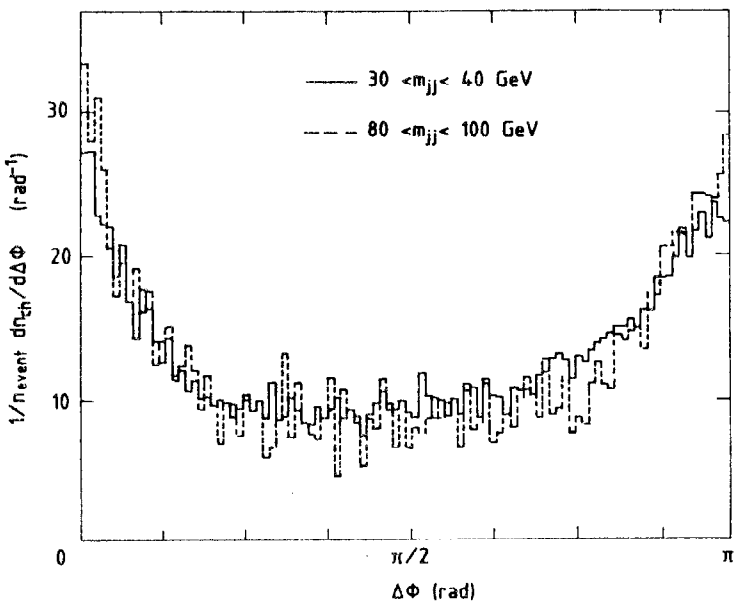


Fig. 7.
Azimuthal separation $\Delta\Phi$ between the energy cluster centroid of jet 1 and all charged, transverse, vertex tracks.

As shown in Fig. 7 the track density $\rho(\Delta\Phi) = dN/d(\Delta\Phi)$ is approximately constant over a large $\Delta\Phi$ range around $\Delta\Phi = \pi/2$, where it takes a value ρ_0. On the average ρ_0 is measured to be ~ 2 times as large as in minimum bias events. Particles not associated with the jets are assumed to contribute a uniform distribution to $\rho(\Delta\Phi)$, $\lambda\rho_0$ with $0 < \lambda < 1$. The contribution of jet fragments at $\Delta\Phi = \pi/2$ to the track density is $\rho^{jet}(\pi/2) = (1-\lambda)\rho_0$. If λ were known, we would be able to measure the average jet charged particle multiplicity as

$$n_{ch}^{jet} = (1/2)_0\int^{\pi}\{\rho(\Delta\Phi)-\lambda\rho_0\}d(\Delta\Phi) \qquad \text{Eq. (1).}$$

Lacking the knowledge of λ, we use two different approaches [6] :

1. Evaluation of a lower bound of n_{ch}^{jet} by setting $\lambda = 1$ in Eq. (1). The values obtained are displayed in Fig. 8a and include only the leading jet fragments. They are compared with e^+e^- data, for which the same method has been applied [7].
2. Evaluation of n_{ch}^{jet} from Eq. (1) for two different estimates of λ, one for quarks and one for gluons, using a reasonable fragmentation model [8]. The results are shown in Fig. 8b and compared with e^+e^- [9] and pp [10] data.

Both approaches indicate a larger charged particle multiplicity in the present sample of jets than in jets observed in e^+e^- collisions at lower energies. These results are consistent with expectations based on QCD calculations which predict that at relatively low $x_T = 2E_T/\sqrt{s}$, gluon jets, having higher multiplicities than quark jets [8,11], tend to dominate [12] in $\bar{p}p$ collisions.

3.2.2. Energy Flow

The evaluation of the energy flow with respect to the jet axis shows the following : large angle jet fragments carry only a small fraction of the jet energy. Therefore their identification is non-essential. Two-jet events with each jet having a transverse energy in excess of 15 GeV and at least one of them (called A) well contained in the central calorimeter are selected. The distribution of the azimuthal transverse energy density, $dE_T/d(\Delta\Phi)$, integrated over a rapidity interval of $\pm$ 0.7 around cluster A is shown in fig. 9 for several intervals of the transverse energy E_T of cluster A. (The quantity $\Delta\Phi$ is measured with respect to the centroid of cluster A.) The peak near $\Delta\Phi = 0$ increases with E_T and the density around $\Delta\Phi = \pi/2$ is about 2.5 times larger than in minimum bias events.

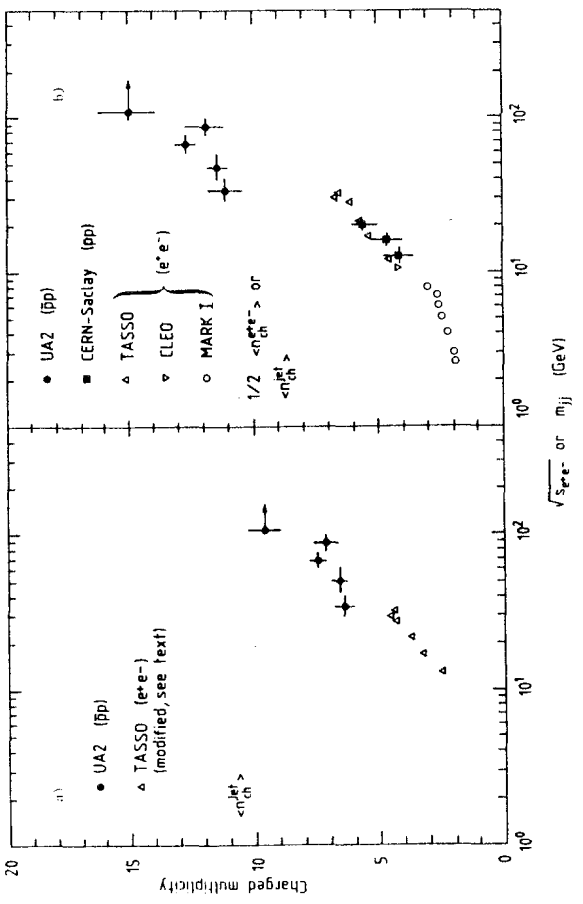


Fig. 8.
Mean charged particle multiplicities n_{ch}^{jet} as a function of $s_{e^+e^-}$ for e^+e^- and of the invariant two-jet mass m_{jj} for $\bar{p}p$.
a) Lower bound on n_{ch}^{jet}. b) Corrected values of n_{ch}^{jet} for $\bar{p}p$ data.

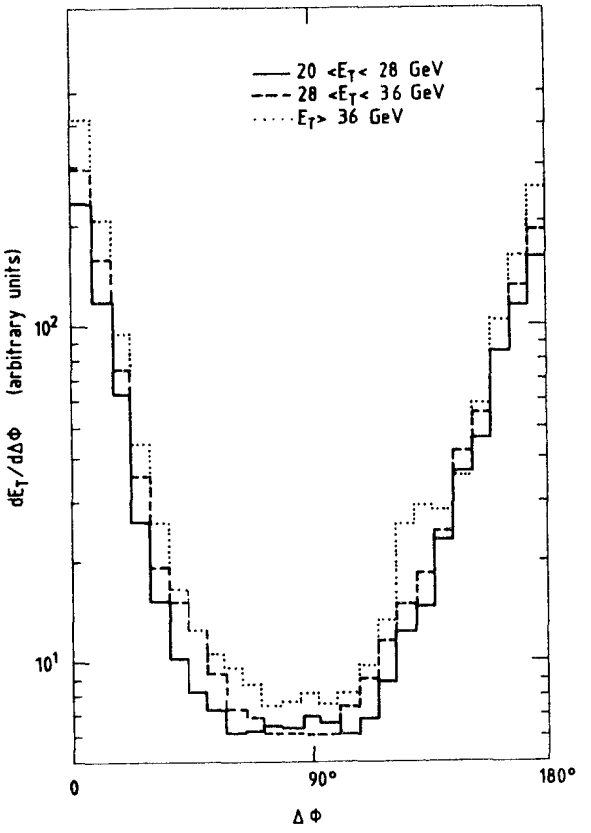


Fig. 9.
Distribution of the azimuthal transverse energy density $dE_T/d(\Delta\Phi)$, where $\Delta\Phi$ is measured with respect to the centroid of the highest E_T cluster. The results are shown separately for three ranges of E_T.

3.3. TWO-JET PRODUCTION PROPERTIES

3.3.1. Transverse Momentum

In order to get information about the jet production mechanism, we study the transverse momentum (P_T^{jj}) distribution of the two-jet system. The measurement of $P_T^{jj} = P_T^{j1} + P_T^{j2}$, i.e. the sum of two large and opposite vectors, is sensitive to instrumental effects. This fact calls for a detailed Monte Carlo calculation with the aim to extract the initial P_T^{jj} distribution from the observed data. The azimuthal distribution of P_T^{jj} is assumed to be uniform and its modulus to have a Gaussian distribution :

$$dN/d(P_T^{jj})^2 \propto \exp(-\alpha(P_T^{jj})^2)$$

with

$$\langle P_T^{jj} \rangle = \sqrt{(\pi/4\alpha)}.$$

The P_T^{jj} distribution is measured in a sample of two-jet events identified as having two clusters, each with a transverse energy in excess of 20 GeV and together more than 50 GeV.

The components P_ξ^{jj} and P_η^{jj} of P_T^{jj}, measured along two axes, ξ and η, chosen as the bisectors of the two transverse jet momenta (Fig. 10a), are studied separately because they are associated with different sources of systematic uncertainties. Their distributions and the corresponding Monte Carlo results using $\langle P_T^{jj} \rangle = 5$ GeV/c are shown in Fig. 10b,c.

Under the above hypotheses (P_T^{jj} uniform in ϕ, $dN/d(P_T^{jj})^2$ Gaussian distributed) confirmed by the data, we extract the following mean value of P_T^{jj} :

$$\langle P_T^{jj} \rangle = (5 \pm 2) \text{ GeV/c}.$$

No significant dependence of $\langle P_T^{jj} \rangle$ upon the invariant mass m_{jj} of the two-jet system is observed.

3.3.2. Longitudinal Momentum and Angular Distribution

According to the parton picture, the longitudinal momentum P_L^{jj} of a two-jet system is, on the contrary to the measured limited transverse momentum, expected to take large values since the colliding partons may carry very different initial longitudinal momenta.

The measured scattering angles $\Theta_{1,2}$ of the jet axes with respect to the beam are related to the rapidity y_{jj} of the two jets and to their CMS scattering angle Θ^*. For a sample of two-jet events with $P_T^{jj} < 15$ GeV/c, $m_{jj} > 56$ GeV/c^2 and $|\cos\Theta^*| < 0.3$, the $\tanh(y_{jj})$-distribution displayed in

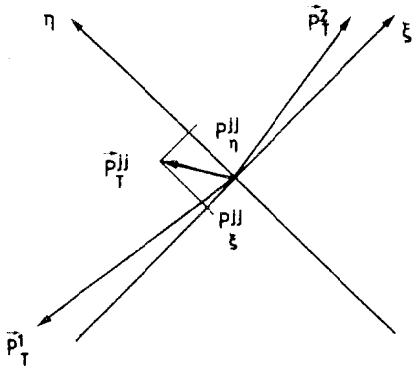


Fig. 10a.
Definition of the (ξ,η) coordinate system in the transverse plane.

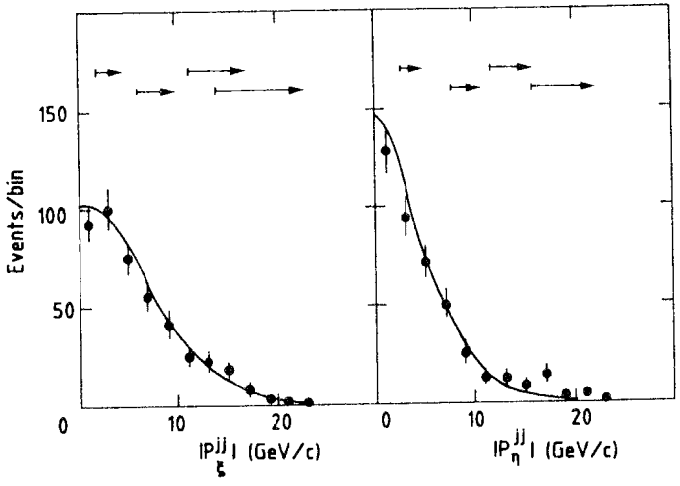


Fig. 10b,c.
The distributions of P_ξ^{jj} and P_η^{jj} (black circles) for a sample of two jet events are compared with the results of a Monte Carlo calculation using $\langle P_T^{jj} \rangle = 5$ GeV/c. Horizontal arrows indicate measurement distortions of instrumental origin.

Fig. 11 is compatible with the result of a Monte Carlo calculation assuming a uniform y_{jj}-distribution.

The measured $\cos\Theta^*$-distribution for events having $|\tanh(y_{jj})| < 0.28$ (Fig. 12) shows a clear deviation from isotropy. The data are consistent with any of the QCD subprocesses ($gg \to gg$, $qq \to qq$, $gq \to gq$ etc.) [13] which are expected to have similar $\cos\Theta^*$-dependences within the calorimeter. However the data do not allow disentangling their independent contributions.

3.4. STUDY OF ADDITIONAL CLUSTERS IN THE TWO-JET EVENTS

We now study the energy density distribution in the angular region not covered by the aperture of the two leading jets. This region is expected to be populated partly by the debris of the spectator partons or initial state gluon bremsstrahlung, and partly by final state gluon bremsstrahlung. With this fact in mind we try to investigate the three-jet production for configurations in which two of the jet momenta are correlated.

A sample of two-jet events is selected, each jet having $E_T > 20$ GeV, in which a third cluster with $E_T^3 > 4$ GeV is observed. While 29 % of the initial two-jet sample satisfy this condition only 4.5 % of minimum bias events contain such a hard cluster. The two main jets are labelled 1 and 2 according to the relation $E_T^1 > E_T^2$, and the angle ω_{13} (ω_{23}) is calculated between the momentum associated with the third cluster and that of jet 1 (2). The distributions in $\cos\omega_{13}$ and $\cos\omega_{23}$ (Fig. 13) show a clear correlation between the third cluster and jet 2 [6]. Imposing a higher E_T^3 threshold enhances this correlation at the price of reducing the event sample.

In order to evaluate the three-jet production rate the acceptance must be determined and the contribution of uncorrelated third clusters must be subtracted. For this purpose a Monte Carlo simulation is written, which takes the detector response into account.

We define $P(z,\cos\omega)$ as the probability that the event contains a third jet, correlated to jet 2, with a fraction z of the parent parton momentum and emitted at an angle ω to it. In the region $0.2 < z < 0.5$, $0.25 < \cos\omega < 0.75$, one finds

$$P(z,\cos\omega) = 0.22 \pm 0.06.$$

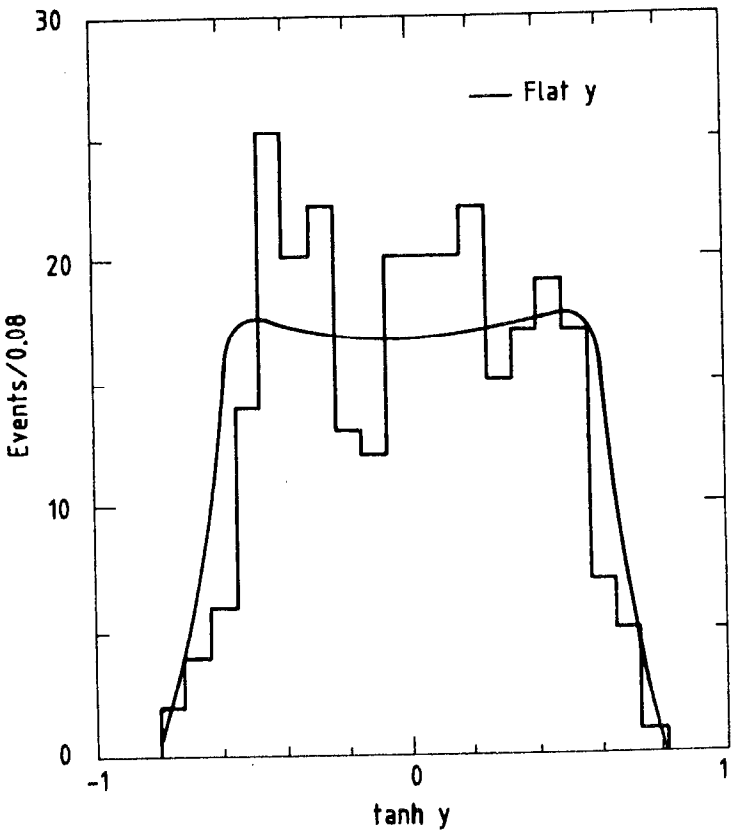


Fig. 11.
Uncorrected distribution of $\tanh(y_{jj})$. The curve shows the result of a Monte Carlo calculation with a uniform y distribution.

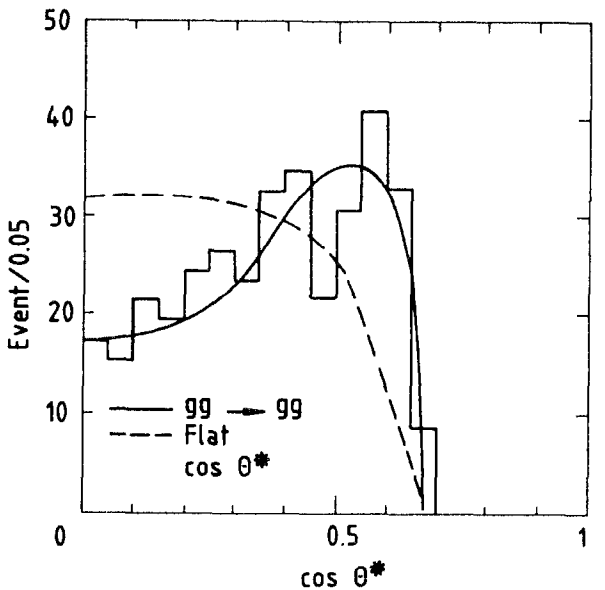


Fig. 12.

Uncorrected CMS scattering angle distribution. The dashed curve is the result of a Monte Carlo calculation for a uniform distribution of $\cos\theta^*$ whereas the solid curve shows the prediction for gg → gg scattering (arbitrary normalization).

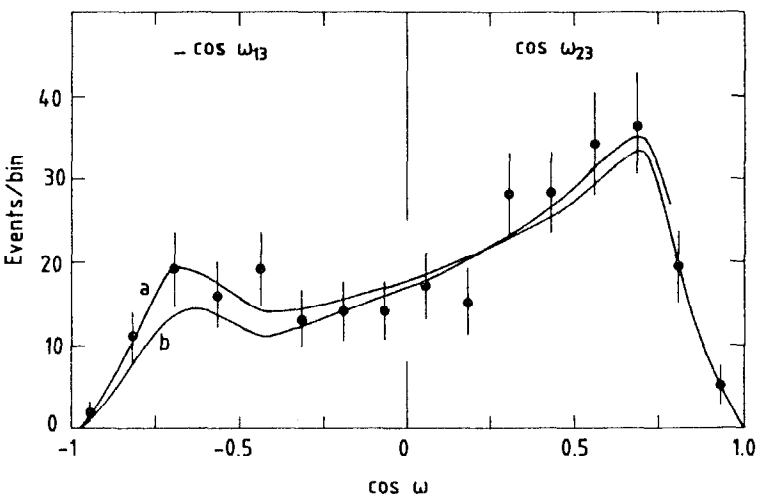


Fig. 13.

Angular correlation in three-jet events. Here $\cos\omega$ is defined as $\cos\omega = \cos\omega_{23}$ if $\cos\omega_{23} > 0$, and $\cos\omega = -\cos\omega_{13}$ if $\cos\omega_{13} > 0$. Best fits to the data (black circles) are presented for two underlying event configurations (see [6]).

The region in $(z,\cos\omega)$ is chosen to ensure a good acceptance. The quoted error is mostly systematic and includes the uncertainty attached to our knowledge of the contribution of uncorrelated clusters.

The number of events in the data sample is not sufficient to allow a measurement of a possible dependence of P on the three-jet invariant mass.

3.5. INCLUSIVE JET AND TWO-JET PRODUCTION CROSS SECTIONS

The measurement of the inclusive production cross sections

$$\bar{p}p \rightarrow \text{jet} + \text{anything},$$

$$\bar{p}p \rightarrow \text{jet}_1 + \text{jet}_2 + \text{anything}$$

can be compared directly with QCD predictions. To the extent that the jets are correctly identified, such comparisons do not require any assumption about the fragmentation mechanism. The leading and next to leading order QCD diagrams describing parton scatterings are expected to provide a good approximation to the production cross section for large transverse momentum jets.

From the data accumulated with the low (high) hardware trigger threshold on ΣE_T, events are selected containing at least one cluster with $E_T > 30$ GeV (45 GeV) and events containing at least two clusters with $E_T > 15$ GeV (20 GeV). In addition the clusters are required to have pseudorapidities in the interval $-0.85 < \eta < 0.85$ and to have $40° < \Phi < 320°$. In order to partly account for final state gluon radiation, the jet momenta are defined in the following way: the momenta of all clusters having $E_T > 3$ GeV and separated by an angle ω from the selected cluster momentum with $\cos\omega > 0.2$ are added to the measured momentum.

3.5.1. Inclusive Jet Production

The evaluation of the inclusive jet production cross section and of the two-jet invariant mass distribution from these events requires the knowledge of the integrated luminosity and the detector acceptance.

The integrated luminosity is obtained by counting the total number of minimum bias events that occured during data taking, and by using the cross section for the minimum bias counters [4]. It amounts to $L = 15.1\ \text{nb}^{-1}$.

The cross section for inclusive jet production $d^2\sigma/dE_T d\eta$ at $\eta = 0$ is shown in fig. 14 as a function of the jet transverse energy E_T. The quoted errors include the statistical errors and the energy dependent

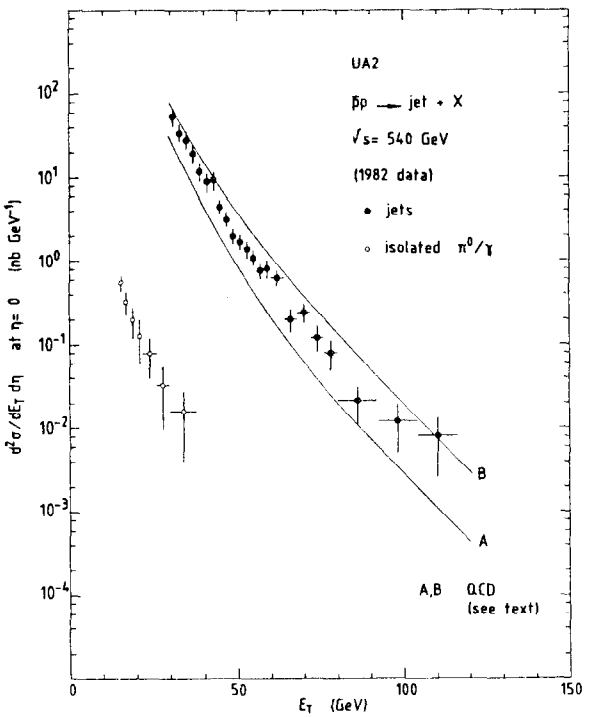


Fig. 14.
Inclusive jet cross section. The additional systematic uncertainty is ± 40 %. Curves A and B are predictions from QCD calculations [14] using different parametrizations for the structure functions. The open points correspond to to single isolated neutral particles (see text).

systematic uncertainty of the acceptance function. A systematic normalization uncertainty of ± 25 % in the cross section scale (total integrated luminosity, acceptance calculation) as well as a ± 6 % uncertainty in the E_T scale (calorimeter calibration, the response to hadrons etc.) have to be added. The resulting overall systematic uncertainty in the inclusive jet cross section is about ± 40 %.

From a fit to the data with the form $d^2\sigma/dE_T d\eta \propto AE_T^{-n}$ we obtain $A = (4.7 \pm 0.3)\cdot 10^{12}$ nb GeV^{-1}, $n = 7.2 \pm 0.2$ with a χ^2 of 15 for 21 degrees of freedom.

The experimental results are at a level comparable with QCD studies [12,14,15] as also shown in Fig. 14 (see also [5,16]). To get an idea about the relevant subprocesses we display the contribution of the dominant processes to the inclusive jet cross section in Fig. 15.

3.5.2. Isolated Neutral Particles

The cross section for the production of large, transverse momentum, single neutral particles ($\gamma, \pi^0, \eta, \ldots$), identified by means of the pre-shower counter (C5) in front of the electromagnetic calorimeter, is also shown in Fig. 14 (1982 data, open circles). The events contributing to the cross section are selected according to a procedure quite similar to that used to search for high transverse momentum electrons [17], but requiring no track facing a highly electromagnetic cluster (energy of the hadron compartments less than 10 % of cluster energy). By studying the distribution of the number of photons converted, we find that the data are consistent with being all from π^0, but the ratio γ/π could be as large as 35 % (90 % confidence level). As an example for a single γ (π^0) candidate, Fig. 16 shows an event found in the 1983 data.

3.5.3. Two-jet Mass Distribution

Figure 17a shows the distribution of the invariant two-jet mass (m_{jj}) for events containing two jets, each having $E_T > 20$ GeV and lying within $-0.85 < \eta < 0.85$ (see also [5,16]). The errors shown are statistical only. There are additional uncertainties arising from the same sources as already discussed for the inclusive jet cross section. The normalization uncertainty is ± 40 % which includes the uncertainty on the mass scale of ± 6 %. The rms mass resolution in the region of 80 GeV/c² is ~ ± 8 GeV/c². On the basis of the observed $W \rightarrow e\nu$ events in the central calorimeter [17], we expect in this mass region about 15 (150) events from the 1982 (1983) data,

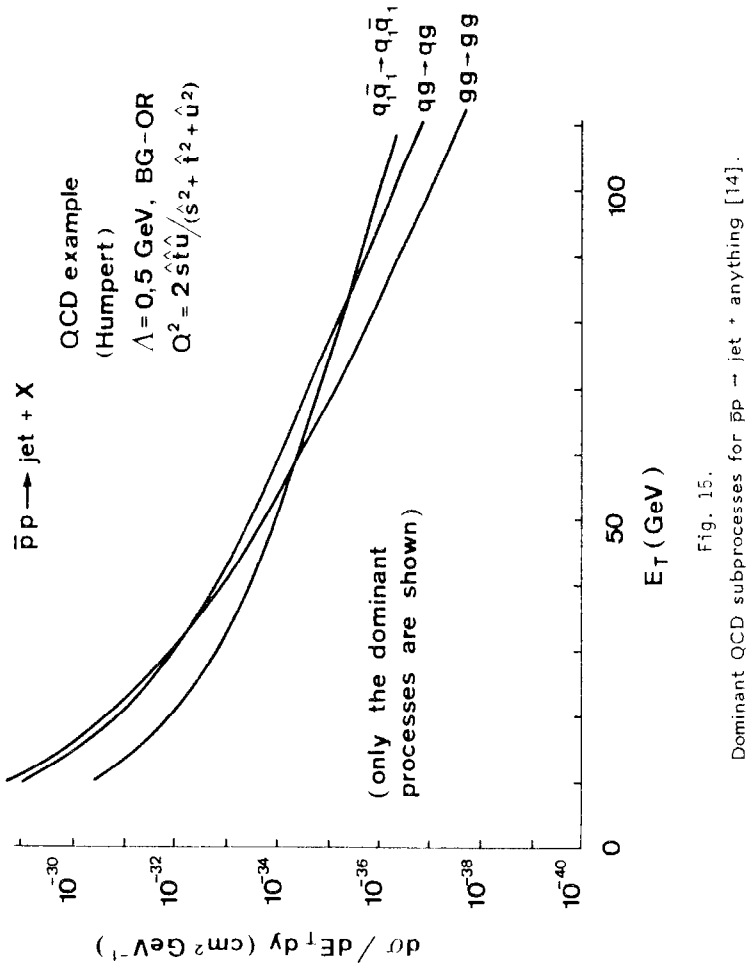


Fig. 15.
Dominant QCD subprocesses for $\bar{p}p \rightarrow$ jet + anything [14].

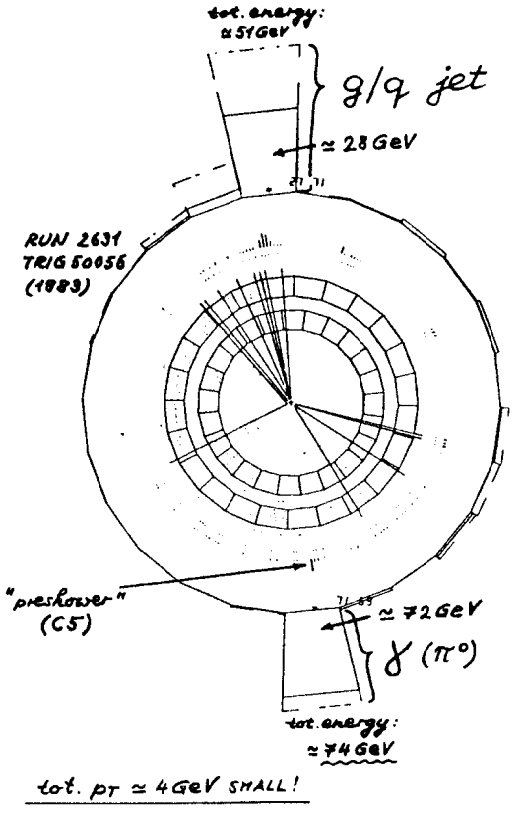


Fig. 16.
Single γ (π^0) recoiling against gluon/quark jet.

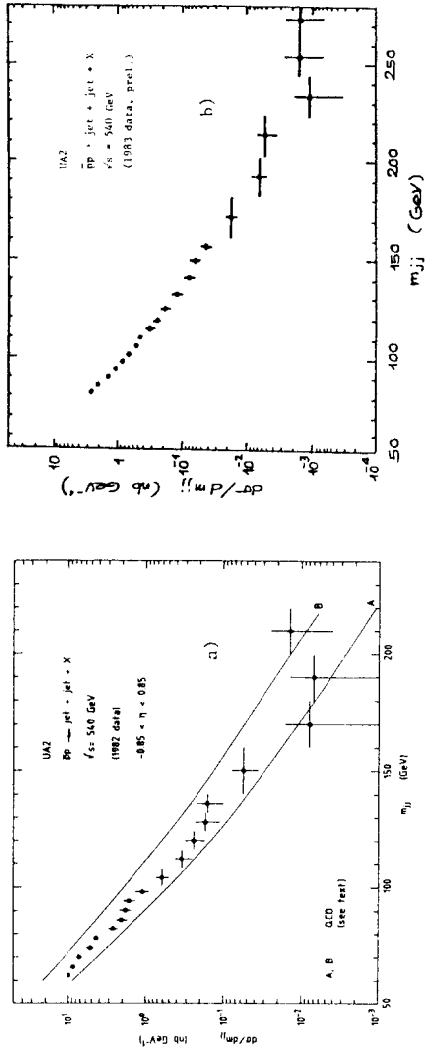


Fig. 17.
Two-jet production cross section in the pseudorapidity range
$-0.85 < \eta < 0.85$. The additional systematic uncertainty is ± 40 %.
a) 1982 data (curves as for Fig. 14), and
b) 1983 data (preliminary).

originating from the production of the intermediate vector bosons ($W^{\pm}$, Z^0) and their subsequent decay into two jets. However, no evidence for significant structure is seen: with the present statistics, the signal is expected to be hidden by the large background of continuum two-jet production. In the mass range $60 < m_{jj} < 220$ GeV/c^2, the data fit a form $d\sigma/dm_{jj} \propto Ae^{-bm_{jj}}$ with $A = 586 \pm 85$ GeV$^{-1}c^2$, $b = (6.6 \pm 0.2)\cdot 10^{-2}$ GeV$^{-1}c^2$ and with a χ^2 of 17 for 17 degrees of freedom.

Analyzing the data collected in 1983, we find a preliminary two-jet mass distribution as given in Fig. 17b. The accessible mass region extends now to 270 GeV/c^2, a value, which corresponds to half of the available CMS energy.

3.6. CONCLUSION

Events in $\bar{p}p$ collisions at $\sqrt{s}$ = 540 GeV with large transverse energy show a dominant two-jet structure. Detailed studies of the fragmentation properties of these jets led to first results. The inclusive jet production cross section and the two-jet invariant mass distribution are determined and found to be compatible with QCD calculations. In the jet-jet mass plot, no significant structure is seen.

4. W,Z^0 DATA ANALYSIS

4.1. FIRST DATA REDUCTION

The full data samples consist of approximately 7×10^5 W-triggers and 7×10^5 Z^0-triggers, which correspond to an integrated luminosity $L=\int\mathcal{L}dt=131$ nb^{-1}. To speed up the W and Z^0 analysis a first data reduction is made by requiring:

a) for the $W^{\pm}$, the presence of an energy cluster with a transverse electromagnetic energy greater than 15 GeV; and

b) for the Z^0, a total electromagnetic transverse energy exceeding 30 GeV and the presence of a pair of energy clusters (electromagnetic and hadronic) having an invariant mass in excess of 50 GeV/c^2.

In the central calorimeter, clusters are obtained by joining all electromagnetic cells which share a side and contain at least 0.5 GeV. A contribution from the cells having at least one side in common with a cluster is also added. The forward calorimeter clusters consist of at most two adjacent cells having the same azimuth. (Here the cell is far from the interaction point and much larger than the lateral extension of an electromagnetic shower, and the dead region between cells at different azimuths is too large to allow clustering across it.)

In both cases the cluster energy E_{cl} is defined as $E_{cl} = E_{em} + E_{had}$ where E_{em} is the summed energy deposited in the electromagnetic compartment of the cluster cells and E_{had} is the corresponding sum for the hadronic compartments.

The invariant mass of the cluster pair in the Z^0-sample is initially calculated under the assumption that the event vertex is at the centre of the apparatus. The cluster centroids are used to define the particle momenta.

The remaining W-sample contains about 83000 events and the remaining Z^0-sample 7427 events. At this stage the event samples are dominated by two-jet events.

All the events are then fully reconstructed and the invariant mass M of the cluster pair for Z^0-trigger is calculated again, this time taking into account the exact position of the reconstructed event vertex. The difference between the new value and the previous one does not exceed 2 GeV/c^2.

4.2. ELECTRON IDENTIFICATION

In the surviving events, a search is made for configurations consistent with the presence of at least one electron among the collision products. An electron is identified from the observation of :

a) a track measured in the wire chambers;

b) a large signal detected in the preshower counters (the C5 chamber in the central detector or the MTPCs in the two forward regions);

c) an energy deposition in the calorimeters, with small lateral size and with limited penetration into the hadronic compartments; and

d) the quality matching in space among the three above properties.

The first step to identify an electron is to require that the energy cluster has a small lateral size in the electromagnetic compartment of the calorimeter and a limited energy leakage in the hadronic compartment. For clusters in the central calorimeter, cluster sizes R_θ, R_ϕ are calculated from the cluster centroid and the energy weighted values of θ and ϕ at each cell centre. The condition $\max(R_\theta, R_\phi) < 0.5$ cell size is required. In the forward calorimeters we require that the sum of the energies deposited in the cells adjacent to the cluster cells does not exceed 3 GeV. The condition that the showers have only a small energy leakage in the hadronic

compartments of the calorimeters is applied by requiring that the ratio $H=E_{had}/E_{cl}$ does not exceed a value H_0, equal to 0.02 for the forward calorimeters, and $0.023 + 0.034 \times \ln(E_{cl})$ where E_{cl} is in GeV, for the central one.

The cuts applied at this stage are very loose and are satisfied by more than 95% of isolated electrons between 10 and 80 GeV, as verified experimentally using test beam data. The W-sample is then reduced to 10169 events (8192 central events and 1977 forward events). The Z^0-sample, where both electron candidates satisfy these cuts, contains 24 events, whose invariant mass distribution is shown in Fig. 18. There are 12 events with both clusters in the central region, 8 events with one cluster in the central region and the other in the forward regions, and 4 events with both clusters in the forward regions.

In the following step we define a series of additional criteria for electron identification. We use measurements of the response of various parts of the detector to isolated electrons [1] from which we evaluate approximate cut efficiencies η. The cuts are described in Table I for both the central and forward regions. The efficiencies resulting from the simultaneous application of all selection criteria are at least as large as the products of the individual efficiencies η, namely 67% for the central region and 83% for the forward regions.

5. W ANALYSIS

5.1. FINAL SAMPLE

Applying the last electron cuts (cuts 2 to 6 of Table I), there remain 134 events (104 in the central region and 30 in the forward regions).

To eliminate the remaining background from two-jet events, we cut on the total transverse momentum of the particles observed in the event (excluding the electron candidate). To each calorimeter cell i one associates a vector p_i with magnitude equal to the energy deposited in the cell and with direction along the line joining the vertex to the cell centre. The total visible transverse momentum of the event (electron excluded) , p_T^{vis} , is then projected onto the direction of the electron to define the component of the visible transverse momentum of the remaining event parallel to the electron direction :

$$p_T{}''^{vis} = (p_T^{vis} \cdot p_T^{el}) / p_T^{el} \ .$$

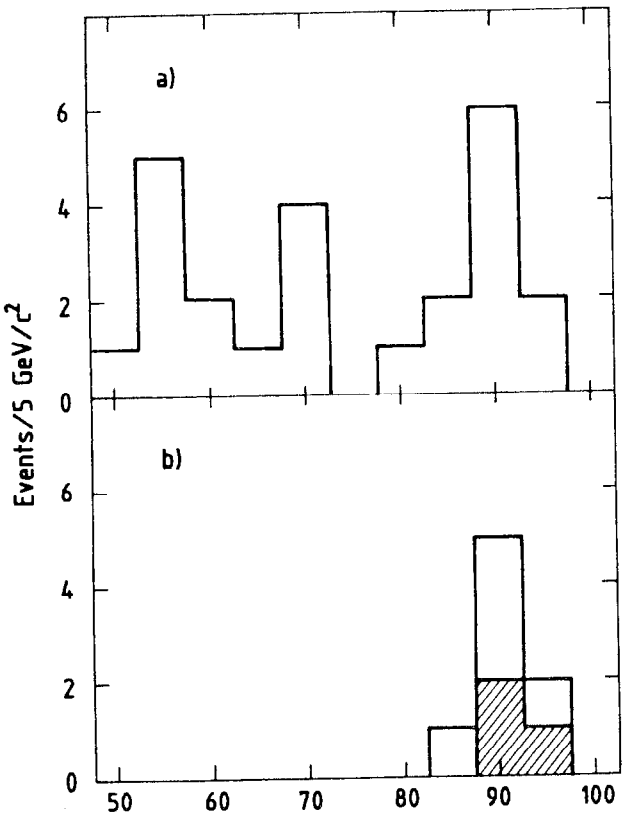


Fig 18. Invariant mass in GeV/c²

TABLE I : ELECTRON IDENTIFICATION CRITERIA

REQUIREMENTS	CENTRAL REGION		FORWARD REGIONS	
	Description	η(%)	Description	η(%)
1. Presence of a calorimeter cluster (preselection)	Electromagnetic cluster size $R_{\theta,\phi} < 0.5$. Hadronic leakage : $H < .023 + .034 \ln E_{cl}$.	98	Cluster size ⩽ 2 cells. Energy in adjacent cells $E_{adj} < 3$ GeV. Hadronic leakage $H < 0.02$.	98
2. Presence of a track	Reconstructed in the vertex detector in both transverse and longitudinal projections.	85	Reconstructed a) in the vertex detector in transverse projection with $N \geqslant 1$ signal in the two inner chambers, b) in the forward drift chambers. Azimuth difference between a) and b) $\Delta\phi(a,b)$ less than 40 mrad.	92
3. Track/cluster match	Track impact to cluster centroid distance $\Delta < 1$ cell size. Compare the energy distribution observed in the 3 × 3 cells centered on the impact cell to that expected for an electron incident along the track. Light sharing between phototubes of impact cell and hadronic leakage are taken into account. Require that the probability P, that the energy distribution for an electron is farther from the mean than that observed, is larger than 0.01.	95	Shower position calculated from light sharing between impact cell phototubes must be consistent with the track impact point to within Δx ⩽ 70 mm.	98
4. Presence of a preshower counter signal	Measured in C5 as a coincidence in space of charge clusters measured on the anode wires and the inner and outer cathode strips. Its charge q_s must exceed 4 mip.	(*) >90	Measured in MTPC in both coordinate planes. Its charge Q(MTPC) must exceed 6 mip.	95
5. Track/preshower position match	Within d ⩽ 7 mm measured on the C5 surface.	94	Within Δx, Δy < 50 mm in each direction.	100
6. Momentum measurement			Momentum p measured in spectrometer and energy E measured in calorimeter must satisfy $\|p^{-1}-E^{-1}\| / \sigma\,(p^{-1}-E^{-1}) < 3$.	99

(*) This does not include a 5% inefficiency due to a $\Delta\phi = 18^\circ$ azimuthal region in which C5 was not operational because of electrical breakdown.

If the W is produced with a relatively small p_T, the electron is balanced in transverse momentum by an undetected neutrino and $p_T{}^{"vis}$ is small. In the case of a two-jet event contained in the apparatus $p_T{}^{"vis}$ will compensate the $p_T{}^{el}$ of the misidentified electron, one has: $p_T{}^{"vis} = -p_T{}^{el}$.

The same relation is true for $Z^0 \to e^+e^-$ events, where both electrons are detected. Figures 19a and 19b show the scatter plot of the events, $p_T{}^{"vis}$ versus $p_T{}^{el}$, for the central and forward regions. One sees clearly three regions :

- $p_T{}^{"vis} \simeq 0$ W-events region;
- $p_T{}^{"vis} \simeq -p_T{}^{el}$ and $p_T{}^{el} > 25$ GeV/c Z^0 region ; and
- $p_T{}^{"vis} \gtrsim -p_T{}^{el}$ and $p_T{}^{el} < 25$ GeV/c two-jet background.

The two-jet events are eliminated by requiring $p_T{}^{"vis} \gtrsim -0.2 \times p_T{}^{el}$. The rejection of this last cut has been determined from a sample with less restrictive electron cuts and has been found to be a factor of 8, roughly independent of $p_T{}^{el}$. After the $p_T{}^{"vis}$ cut there remain 35 events (26 in the central region and 9 in the forward regions).

The two-jet background inside the final W-sample is estimated from the events having $p_T{}^{"vis} < -0.2 \times p_T{}^{el}$ and the measured rejection given by this cut (Z^0 events have been removed for this evaluation). The background is estimated to be 7±1 events, rapidly falling with $p_T{}^{el}$ (5.2 events in the range 15-20 GeV/c, 1.5 events in the range 20-25 GeV/c and .3 events above 25 GeV/c).

5.2. MASS DETERMINATION

Figure 20 shows the $p_T{}^{el}$ distribution of the 35 events left. These events result from four contributions:

a) $W \to e\,\nu$: 22 ± 1.6 events.

b) Two-jet background: 7 ± 1 events.

c) $W \to \tau\,\nu$, $\tau \to e\,\nu\,\bar{\nu}$: 2.4±0.6 events.

d) $Z^0 \to e^+e^-$ with an undetected electron: 3.6 ± 1.3 events.

The contribution c) is computed assuming the same branching ratio for $W \to e\,\nu$ and for $W \to \tau\,\nu$ and the known value (16%) [18] of the branching ratio $\tau \to e\,\nu\,\bar{\nu}$. The contribution d) is evaluated from the observed number of Z^0s and the relative acceptances for $Z^0 \to e^+e^-$ with two detected electrons and for $Z^0 \to e^+e^-$ with one detected electron. The mass of the W is determined from the $p_T{}^{el}$ distribution of fig. 19 by a maximum likelihood method, using only the 22 events in the central region with $p_T{}^{el}$

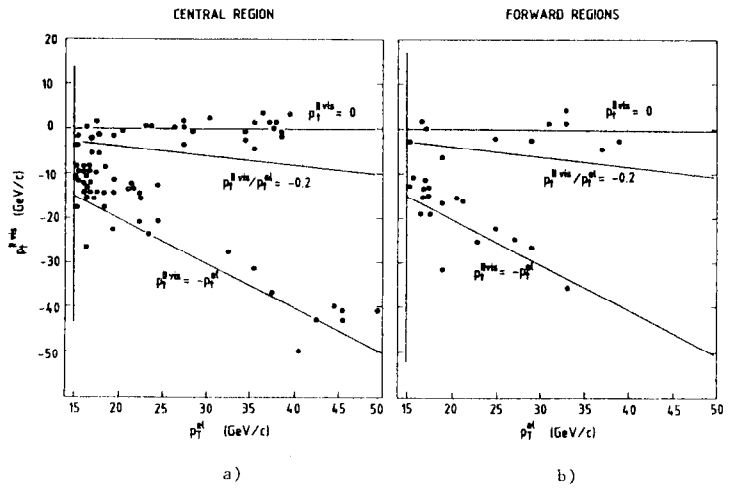


Figure 19a and 19b . $p_T^{"vis}$ / p_T^{el} plots.

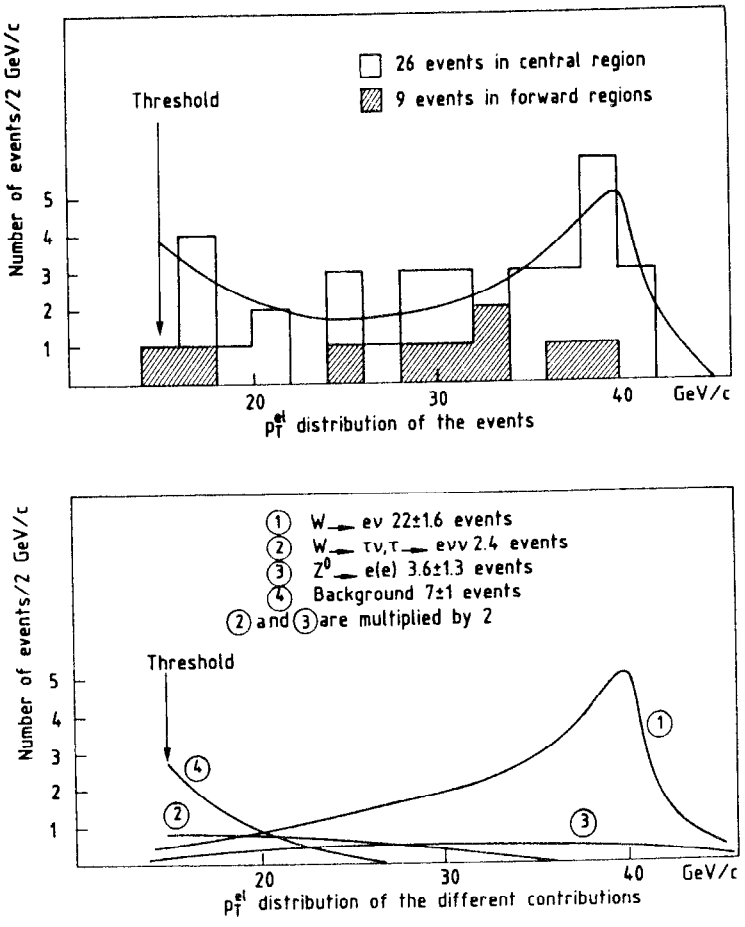


Fig. 20. p_T^{el} distributions.

above 20 GeV/c and all the events in the forward regions. The W longitudinal momentum distribution is calculated using the proton (antiproton) structure functions of Gluck et al. [19]. The shape of W transverse momentum distribution is taken from Halzen et al. [20] but its mean transverse momentum $\langle p_T^W \rangle$ has been varied between 4 and 8 GeV/c. Taking into account the contribution from background sources the evaluated mass is:

$$M_W = 81.0 \pm 2.5 \pm 1.3 \text{ GeV/c}^2$$

where the first error takes into account the statistics and the error variation with $\langle p_T^W \rangle$. The second error is the systematic one resulting from energy calibration uncertainties of the electromagnetic calorimeters. This mass value should be regarded as preliminary.

5.3. CHARGE ASYMMETRY IN FORWARD DIRECTIONS

The weak coupling (V-A) of the W to the qq and ev system gives rise to a charge asymmetry in the forward directions as shown in Fig. 21. The asymmetry α is defined by :

$$\alpha = [(Ne^+(f)-Ne^-(f)) + (Ne^-(b)-Ne^+(b)]/N_{tot}$$

where $Ne^{\pm}(b)$ is the number of $e^{\pm}$ for $20^\circ<\theta<37.5^\circ$, $Ne^{\pm}(f)$ is the number of $e^{\pm}$ for $142.5^\circ<\theta<160^\circ$ and N_{tot} is the total number of events. For $p_T^{el} > 15$ GeV/c α is expected to be 0.68 (assuming no error in charge determination). The observed asymmetry is $\alpha_{exp} = 0.78 \pm 0.21$, which is more than three standard deviations away from zero and in agreement with V-A prediction. (Note: V+A will give the same asymmetry.)

One observes that for the 9 forward events, 8 are observed at $\theta>142.5^\circ$ and one at $\theta<37.5^\circ$. The probability of detecting less than two events in one forward region is P ≈ 4%. No instrumental reason for this asymmetry has yet been found.

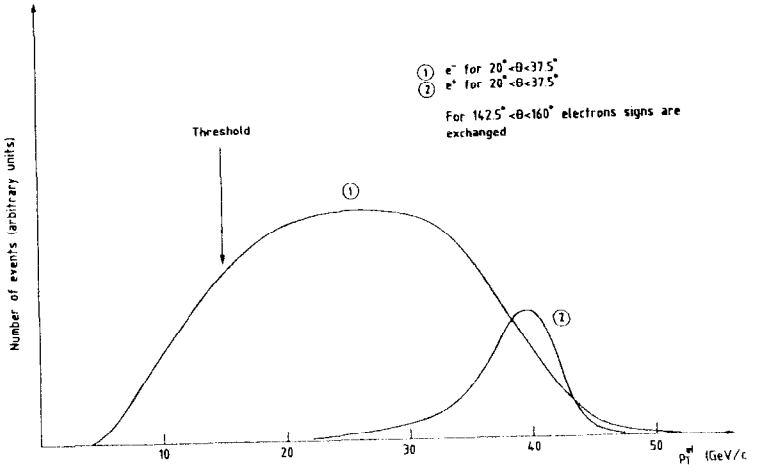


Fig. 21. Charge asymmetry in forward regions.

6. Z^0 ANALYSIS

6.1. FINAL SAMPLE

Figure 18 shows the mass histogram of the events satisfying the electron preselection cut for both electrons (cut 1 of Table I). We have studied the effect of applying the electron cuts (cuts 2 to 6 of Table I) to our initial Z^0-sample. We find that the rejection power of any one of these cuts enters as the square if applied to both clusters simultaneously. Furthermore the

shape of the mass distribution shows no dependence, within statistics, on the combination of cuts used. These two observations provide a simple method to estimate the background contribution from two-jet events to any mass region in a sample of events surviving a given combination of cuts.

Figure 18b shows the mass distribution for the events of Fig. 18a with at least one cluster satisfying all the electron identification criteria. There are eight events in this plot all of which cluster around a mass value of 90 GeV/c^2. A list of relevant parameters for these events (named A to H) is given in [1]. For clusters passing cut 3 of Table I the cluster energy has been corrected to account for the calorimeter response as a function of the electron incidence and impact point. The corrected energy value, together with the measured track direction, has been used to calculate the invariant mass plotted in Figs. 18a and 18b.

An upper limit on the background contribution to the eight events in Fig. 18b can be inferred from Fig. 18a under the assumption that background events have the same distribution in both samples. By comparing the event populations above and below 80 GeV/c^2 we find an upper limit of 0.32 background events to the signal in Fig. 18b. However this estimate implies the presence of up to 2.3 low mass events ($M < 80$ GeV/c^2) in Fig. 18b. In fact we observe no event. This estimate substantially overestimates the background.

A better estimate implies a more realistic evaluation of the expected number of low mass background events in Fig. 18b. This can be done starting from a much richer event sample, simply by releasing cut 1 (hadronic leakage and cluster size) on one of the two clusters and evaluating the rejection power of cuts 2 to 6 (applied to reduce the sample of Fig. 18a to that of Fig. 18b) on the other cluster. We have checked that the absence of significant correlation between the fragmentations of the two jets in background events makes this procedure legitimate. In this way we estimate a background contribution of 0.03 events to the signal of Fig. 18b.

If we apply the full electron identification criteria to both clusters, only three events (A to C, shown cross-hatched in Fig. 18b) survive, with an estimated background of 2×10^{-4} events above a mass of 80 GeV/c^2. For two of them (A and C) one of the electrons is in the forward directions, the other electrons are in the central region. Events A and B are interpreted as resulting from the decay $Z^0 \rightarrow e^+e^-$. Event C consists of two electrons and a well separated high energy photon (or unresolved photons such as from the $\gamma\gamma$ decay of a π^0 or a η meson). The invariant mass value plotted in Fig. 18b is calculated for the three particles. We have estimated [21] that $Z^0 \rightarrow e^+e^-\gamma$ decays with a photon at least as hard as the observed one, and with e^+e^- opening angles equal to, or smaller than the measured one, occur approximately once every 200 $Z^0 \rightarrow e^+e^-$ decays.

Figure 22a shows the longitudinal view of event A in the plane containing the central electron. Figures 22b and 23a show the cell energy distribution in θ and ϕ for events A and C. The transverse view of event C, indicating the presence of the additional photon at an angle of $\approx 30^0$ to the electron, is shown in Fig. 23b.

We next discuss the five other events (D to H), in which one of the two electron candidates fails at least one of the strict selection criteria described in Table I.

- The forward electron candidate of event D is associated with a track measured in the vertex detector as pointing to the coil of the magnet at a place where its thickness is ≈ 0.5 radiation lengths. Three tracks, measured in the forward drift chambers, point to the energy cluster. One of them passes cut 2 but fails cut 6. Several MTPC clusters satisfy cut 4 but cuts 3 and 5 are never simultaneously satisfied. This configuration is consistent with the hypothesis of an electron initiating an electromagnetic shower in the magnet coil. The mass value of this event has been calculated under this hypothesis. Event D belongs to the data sample collected in 1982 and has been previously published [22].

- The central electron candidate of event E passes all strict cuts except 4 and 5. Its associated C5 cluster has a charge of only 2.4 m.i.p. and is 9±2 mm away from the track impact. The occurence of such a configuration in the present sample is compatible with the cut efficiencies listed in Table I and event E is consistent with an electron pair hypothesis. We note however that the forward electron is accompanied by another particle having a measured momentum of 2.3 GeV/c and hitting the same calorimeter cell. The mass value of event E has been corrected accordingly. In minimum bias events the probability that a particle with a measured momentum >2.3 GeV/c hits a given calorimeter cell of the same θ is only 0.2%.

- One of the central electron candidates of event F passes all strict cuts except cut 3. The measured ratio of the signals from the two light guides of the impact cell is 0.71±0.02 instead of 0.88±0.02 as predicted from the track impact. Nothing suspicious has been found in the behaviour of the calorimeter cell from the monitoring of the stability of its calibration using light flasher and Co^{60} source measurements. We have also checked that the ratio between the light transmitted by the two light guides has the expected distribution in minimum bias events. Event F could be compatible

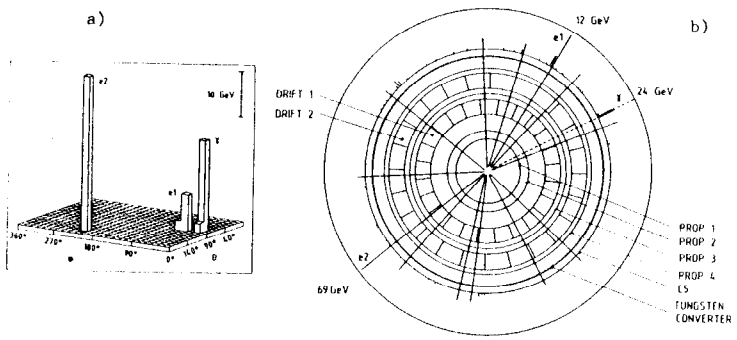


Fig. 22. Event A: Longitudinal view and cell energy distribution.

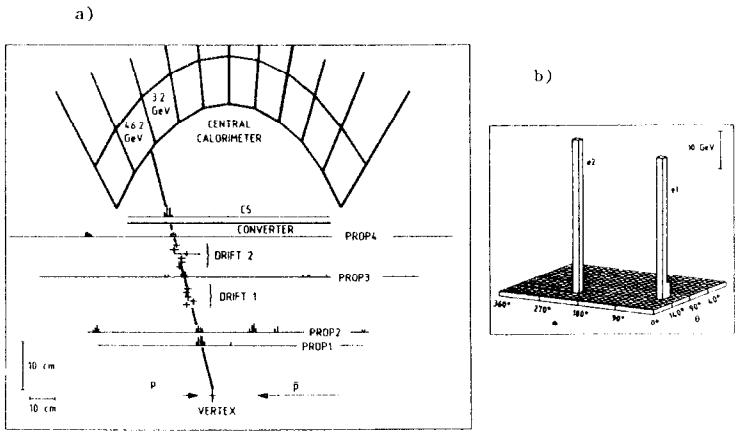


Fig. 23. Event C: Cell energy distribution and transverse view.

with an electron pair hypothesis if a neutral particle (for example a hard bremsstrahlung photon) had entered the calorimeter cell very near its edge (≈ 70 mrad away from the electron) causing many shower particles to cross the associated light guide. However the absence of a C5 cluster facing this region would imply that the photon did not convert in the 1.5 radiation lengths thick converter.

- The electron candidates of events G and H which do not pass the strict cuts are both observed in the central region. The latter fails cut 4 because the electron track traverses the small region ($\Delta\phi \approx 18°$) where C5 was not operational for part of the run period. We ignore this fact in the present discussion. Both fail cut 3 for the following reason: additional energy (≈ 3 GeV) is observed in neighbour cells, inconsistent with lateral and longitudinal leakages of a shower initiated by an electron of the measured energy. In both cases this additional energy has an important component in the hadronic compartments: it is therefore difficult to ascribe it to radiative effects. We observe no track pointing to these cells, and no C5 cluster facing them. In the case of minimum bias events superimposed at random on identified large transverse momentum electrons we find the probability of observing similar configurations is about 0.1%. We have also checked, using the light flasher system, that cross-talk between neighbour cells is negligible.

The presence of additional energy in these events has been ignored when calculating the invariant mass (Fig.18).

From the above discussion we retain the following points:

a) Eight events (A to H) are observed with at least one electron passing the strict electron criteria. Their masses cluster in the 90 GeV/c^2 region where the expected background is only 0.03 events.

b) Five of these events (A to E) are either identified as, or are perfectly compatible with, e^+e^- or $e^+e^-\gamma$ configurations.

c) The three other events (F to H) have both clusters in the central region. In each of these events one cluster fails cut 3. Although we retain the interpretation that this cluster is in each case associated with an electron, its configuration is inconsistent with our present knowledge of the detailed response of the central calorimeter to high energy electrons. However, we shall repeat the measurements of relevance in a high energy electron beam before drawing any definite conclusion on the significance of these inconsistencies.

The presence in Fig. 18 b of a signal free of background contamination, and the difficulties encountered in interpreting events F to H in terms of electron pairs, have led us to consider the hypothesis that the sample of

Fig. 18b could be contaminated by a background peaking in the (W, Z^0) mass region, but not made of genuine electron pairs. W and Z^0 decay modes other than $e^{\pm}\nu$ and e^+e^- (for example into two hadron jets) could provide such a mechanism. However we find it difficult to retain such a hypothesis because the sample of Fig. 18a contains only two extra events, compatible with the background expectation of 0.7 events, in the mass region above 80 GeV/c^2.

The most likely interpretation of the eight events in Fig. 18b is that they all result from the decays $Z^0 \rightarrow e^+e^-$ or $Z^0 \rightarrow e^+e^-\gamma$.

6.2. MASS DETERMINATION

We use only the sample of four events (A,B,C and E) where the energy of the electrons is correctly measured, to evaluate the Z^0 mass and width.

From these events we measure the mass of the Z^0 boson to be:

$$M_Z = 91.9 \pm 1.3 \pm 1.4 \text{ GeV/c}^2$$

where the first error accounts for measurements errors and the second for the uncertainty on the overall energy scale.

The rms of this distribution is 2.6 GeV/c^2 and is consistent with the expected Z^0 width [23] and with our experimental resolution of ≈ 3% (including systematic uncertainties).

6.3. COMPARISON WITH MODELS

The standard SU(2)×U(1) electroweak model makes definite predictions on the Z^0 mass. Taking into account radiative corrections to O(α) one finds [23]:

$$M_Z = 77\ \rho^{-1/2}\ (\sin 2\theta_W)^{-1} \text{ GeV/c}^2$$

where θ_W is the renormalized weak mixing angle defined by modified minimal subtraction, and ρ is a parameter which is unity in the minimal model.

Assuming $\rho = 1$ we find:

$$\sin^2\theta_W = 0.227 \pm 0.009\ .$$

However, we can also use the preliminary value of the W mass found in this experiment, and the formula [23]:

$$M_W = 38.5\ (\sin\theta_W)^{-1} \text{ GeV/c}^2.$$

We find $\sin^2\theta_W = 0.226 \pm 0.014$, and using also the formula giving the Z^0 mass and our experimental value we obtain :

$$\rho = 1.004 \pm 0.052$$

in agreement with the prediction of the minimal SU(2)×U(1) model, with the recent results of the UA1 experiment [24], and with the results of low energy neutrino experiments [25].

References

[1] The UA2 collaboration: P. Bagnaia et al, Phys. Lett. 129B(1983),130. References concerning the apparatus can be found therein.

[2] M. Banner et al, Phys. Lett. 115B(1982),59.
M. Banner et al, Phys. Lett. 122B(1983),322.

[3] R.P. Feynman, Photon Hadron Interactions, Benjamin, New York, 1972;
S.M. Berman and M. Jacob, Phys. Rev. Lett. 25 (1970), 1683;
S.M. Berman, J.D. Bjorken and J.B. Kogut,
Phys. Rev. D4 (1971), 3388.

[4] The cross section seen by the "minimum bias" trigger counters amounts to 43.9 ± 3.5 mb as measured by :
The UA4 collaboration, R. Battiston et al., Phys. Lett. 117B (1982), 126 and contribution to the XVIII Rencontre de Moriond on Proton-Antiproton Collider Physics, La Plagne, March 19-25, 1983 (to be published).

[5] The UA2 Collaboration, M. Banner et al., Phys. Lett. 118B (1982), 203.

[6] The UA2 Collaboration, P. Bagnaia et al., CERN-EP/83-94 accepted for publication in Zeitschrift fuer Physik C.

[7] The TASSO Collaboration, R. Brandelik et al.,
Phys. Lett. 86B (1979), 243 and 89B (1980), 418 and
private communication from M. Holder and G. Wolf.

[8] B.R. Webber, Contribution to the XVIII Rencontre de Moriond on Proton-Antiproton Collider Physics, La Plagne, March 19-25, 1983 and CERN TH-3569 (1983).

[9] Compiled in : G. Wolf, High energy e^+e^- interaction, DESY 81-086 (1981);
R. Plunkett, PhD Thesis Cornell University (1983).

[10] A.G. Clark et al., Nucl. Phys. B160 (1979), 397.

[11] G. Sterman and S. Weinberg, Phys. Rev. Lett. 39 (1977), 1436 ;
K. Shizuya and S.-H. H. Tye, Phys. Rev. Lett. 41 (1978), 787;
M. B. Einhorn and B. G. Weeks, Nucl. Phys. B146 (1978), 445.

[12] R. Horgan and M. Jacob, Nucl. Phys. B179 (1981), 441.

[13] B. L. Combridge, J. Kirpfganz and J. Ranft, Phys. Lett. 70B (1977), 234.

[14] B. Humpert, private communication.
The curves shown in Figs. 14 and 17 with Λ = 0.5 GeV and parametrizations for the structure functions according to (curve A) the counting rule parametrization of J. Owens and E. Reya, Phys. Rev. D17 (1978), 3003 or (curve B) R. Bayer et al., Zeitschr. f. Physik C, 2 (1979), 265;
B. Humpert, in preparation.

[15] W. Furmanski and H. Kowalski, CERN-EP/83-21 (1983);
N. G. Antoniou et al., LPTHE Orsay 83/4, and Phys. Lett. B (in press);

Z. Kunszt and E. Pietarinen, Ref. TH-3584 CERN (1983).
[16] The UA1 Collaboration, G. Arnison et al., Phys. Lett. 123B (1983),115.
[17] The UA2 Collaboration, M. Banner et al., Phys. Lett. 122B (1983), 476.
[18] Review of Particles Properties, Phys. Lett. 111B(1982).
[19] M. Gluck, E. Hoffmann and E. Reya, Z. Phys. C13(1982),119.
[20] F. Halzen A.D. Martin and D.M. Scott, Phys. Rev. D25(1982),754.
[21] We thank R. Petronzio for assistance in making this calculation (to first order in α).
[22] The UA2 collaboration, presented by P. Darriulat at the Third Topical Workshop on $\bar{p}p$ Collider Physics, Rome, 12-14 January 1983, CERN 83-04(10 may 1983), C. Bacci and G. Salvini editors, p235-236.
[23] For a review see M.A. Beg and A. Sirlin, Phys. Rep. 88(1982),1 and references quoted therein (in particular section 4, ref. 27 to 39).
[24] G. Arnison et al, Phys. Lett. 126B(1983),398.
[25] For a review see M. Davier: 21st International Conference on High Energy Physics, Journal de Physique, Colloque C3, supplement au n°12 Tome 43 p.401.

COLLIDER PHYSICS - PRESENT AND PROSPECTS

M. Jacob

CERN
1211 Geneva 23, Switzerland

1. - INTRODUCTION

At present it is deemed appropriate to define "collider physics" as the physics of hadron-hadron interactions in an energy range where the centre-of-mass energy which is typically available at the constituent level is of the order of 100 GeV, the energy scale set by the electroweak theory. Since a constituent quark carries on the average 1/6 of the momentum of the hadron it is associated with, this corresponds to hadron-hadron collisions at energies of the order of 0.5 TeV or more. This domain of research has been brilliantly opened by the successful development of the $p\bar{p}$ programme at CERN. [1] The CERN SPS is now used, part of the time, as a proton-antiproton accelerator and colliding ring, operating at an energy of 270 GeV per beam, hence 540 GeV in the $p\bar{p}$ centre-of-mass. The most important recent results have been presented at this conference. [2] The first interactions were observed in 1981 [3] and, by 1983, the W and the Z gauge bosons have been discovered, [4)-5)] with the anticipated masses. One has thus already reached the goal which motivated the corresponding efforts and developments.

This success compensates for the fact that no unexpected phenomena have been met with so far, a deceived hope when opening up such a new energy domain to experimentation. Surprises may, however, still come! On the other hand, the important new feature, which actually helped a great deal with the discovery of the W and the Z, is the clarity of the event structure, interesting short range processes being very clearly seen over an otherwise quiet background which, only a few years ago, could be feared to be overwhelming. It is this event clarity which now acts as a very strong encouragement to study hadron-hadron interactions at much higher energies. [6] It now seems that one should not encounter too difficult problems observing hitherto unknown short range phenomena relevant to constituent collisions in the TeV range. Some associated large transverse momentum effects could clearly stand against background in multi TeV collisions. On a shorter time scale, it is this event clarity which acts as a strong encouragement to increase

© M. Jacob, 1983

the luminosity in order to see processes with still smaller cross-sections. Background problems no longer appear to be as important as mere rate problems. We shall come back to this at length in the following.

Despite the fact that the results obtained as of now appear to be of a disappointing conformity to the standard model, they are extremely important and a strong encouragement to continue with higher luminosities and higher energies.

Expectations for the first round of experiments have indeed been met to the very full. As it could be discussed several years ago, the key goals set for collider physics were [7] :

(i) to find the intermediate bosons; prospects were high provided that the luminosity would not be too far below 10^{29} $cm^{-2}s^{-1}$; on the other hand prospects of finding new quarkonia, with masses in excess of 40 GeV were considered low, because of rates;

(ii) to study jet phenomena, with spectacular effects associated with relatively large cross-sections, thus reaching p_T values in excess of 100 GeV/c;

(iii) to excite new quark flavours (if any) on the grounds that, for $p_T >> m_q$, all heavy quarks would appear on the same footing;

(iv) to see whether or not the logarithmic extrapolation of ISR results would apply as expected to the global features of hadronic interactions; hints from cosmic ray research indicated that it should be the case, [8] peculiar configurations such as Centauros having been reported at much higher energies only;

(v) to find exciting and unexpected phenomena.

Anticipations were, to a large extent, based upon the fact that, at such an energy, the colliding particles would each behave as a broad band beam of quarks and gluons, acting to a good approximation incoherently of one another. This looked very reasonable but background and luminosity constraints were, however, considered to be serious. At present, one may say that expectations associated with points (i), (ii) and (iv) have been met to the very full, and one may hope for some progress soon with respect to point (iii). A very important question in assessing prospects is that of the luminosity, insofar as most interesting cross-sections are small.

One may therefore attempt to summarize the present situation in a dual way. On the one hand we have the graph of Figure 1, which shows the integrated

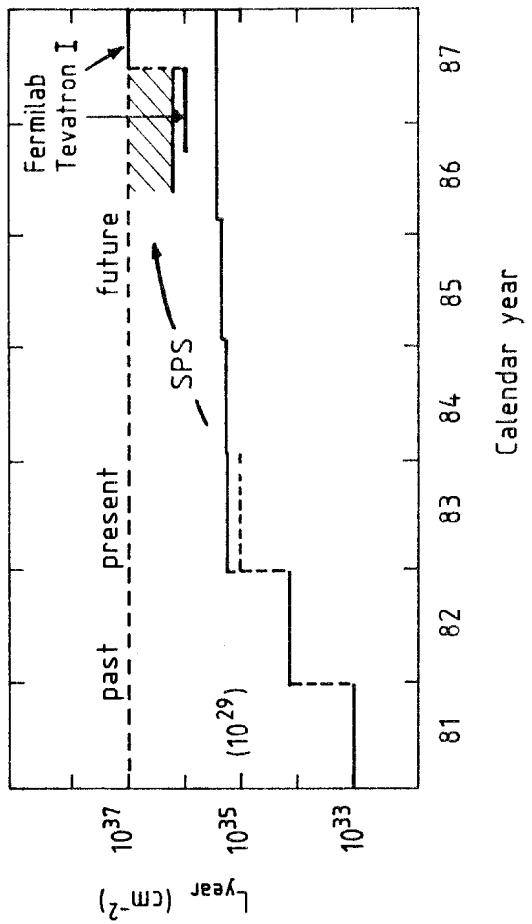


Fig. 1 - The luminosity available over a year (standard run) according to a typical schedule for the $p\bar{p}$ collider at CERN. The past ('81-'83) is shown as a solid line. The future is considered according to two limiting cases. The mere extrapolation of the present situation is shown with small improvements (lower curve) and the reasonable prospects of a strong improvement programme (upper band). Also shown (after '86) are the expected corresponding values for Tevatron I.

luminosity available per year over the recent past ('81 and '82) and now ('83). The very successful run of '83 gave an integrated luminosity of the order of 1.4×10^{35} cm^{-2}. If one merely extrapolates the present situation, one cannot anticipate any very large gain. However, if a serious effort is made, as it will be the case, one could reach by '86-'87 an integrated luminosity of say 2×10^{36} to (optimistically) 10^{37} per year. The transition from the present régime to such a (hoped for) future régime is not fully defined yet. The hoped-for luminosity level is comparable to the expected value for Tevatron I, which could reach 10^{36} (integrated over a year) in '86-'87 and 10^{37} in '87-'88, and this with a centre-of-mass energy three times larger.[9)]

Such luminosity levels will act as guide lines for our discussion of the anticipated physics. They are of course much below those which would be accessible with a dedicated pp collider such as CBA (this is by three to four orders of magnitude). While ingenuity (and some money) buys the energy when transforming a proton accelerator into a $p\bar{p}$ collider, the luminosity (presently limited by the antiproton source and later by the bunched nature of the beams) remains limited.

We may now, on the other hand, attempt to summarize the physics situation, saying that:

(i) short-range phenomena show up clearly over a very quiet background; the standard model based upon the $SU(2) \times U(1) \times SU(3)_c$ gauge group has brilliantly passed all the new tests; hard scattering and hadron structure are, so far as anticipated;

(ii) the logarithmic extrapolation of the dominant features of hadron interactions ("1ns physics") appears to be satisfactory; and

(iii) no unexpected features have been found but finding the expected ones already stands as an achievement in view of their spectacular character.

The clarity of the event structure is, as previously stressed, the important new feature. This is illustrated by a few of the now famous lego plots which show the angular distribution of the transverse energy for particular configurations. They are put together in Figure 2. Figure 2a corresponds to $W \to e\nu$ production. The transverse energy of the large p_T electron (in the Jacobian peak) is not compensated, as expected for a two-body mode involving a neutrino. It stands in a remarkable way over an otherwise very quiet background. Figure 2b corresponds to

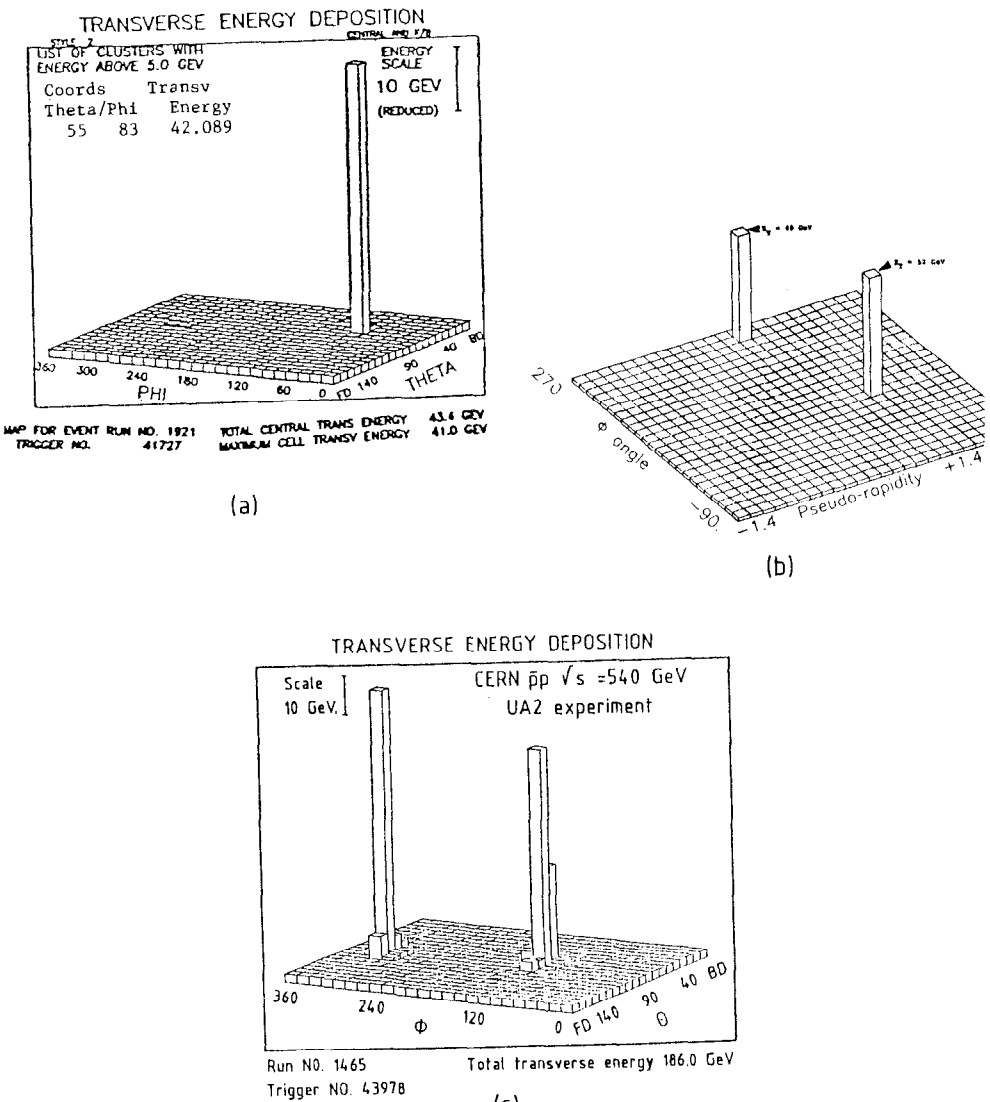


Fig. 2 - The clarity of the event structure illustrated with lego plots representing the angular distribution of the transverse energy in the central region:
2a : $W \to e\nu$ (a UA2 event),
2b : $Z^o \to e^+e^-$ (a UA1 event),
2c : a two-jet system as routinely observed by UA1 and UA2.

$Z \to e^+e^-$ production. The transverse energy peaks correspond to the two large p_T electrons balancing to a good approximation their transverse momenta. Figure 2c corresponds to a two-jet event, as now routinely observed by the UA1 and UA2 collaborations. The transverse energy associated with the two jets of hadrons is in both cases strongly collimated. The two jets balance to a good approximation their transverse momenta , while dwarfing anything else in the process.

Looking at such events one is strongly encouraged to move to higher energies in order to probe hadronic structure to still shorter distances (higher transverse momenta). The background associated with the wake of 50 or so particles, also produced albeit as low p_T in such reactions, can easily be disposed of.

The peculiar events reported in cosmic ray research [8] have also been a strong encouragement for machine experimentation at very high energy. Insofar as a few observed events indicate a large cross-section they should appear clearly, even at low luminosity. The most spectacular ones are the Centauro events with a very large number of energetic charged fragments and practically no accompanying neutrals. As shown by Figure 3, nothing as such appears .[10] It should be said, however, that the energy measured for Centauros puts them in the TeV region in the centre-of-mass, hence above the energy covered by the CERN collider and also that, if Centauros exist, they may well not correspond to the result of proton-proton collisions .[11] At present one may say that such peculiar events notwithstanding, all large cross-section features are in reasonable agreement with expectation based on cosmic ray results .[12]

This review is organized as follows. In Section 2 we briefly survey the key features of the present situation, trying to avoid too much overlap with the thorough reviews of the particularly important topics presented separately at this Conference .[2] We consider in turn large cross-section processes, electroweak processes and jet phenomena. In each case we mention the type of progress which one already expects from the analysis of the recent run ('83) or from forthcoming ones, stressing at the same time cases where strong limitations due to rate are felt. In Section 3 we turn to processes for which a sizeable increase in luminosity (and maybe in energy) appears as needed. We discuss in particular some features of the present search for the top quark. Finally, Section 4 is an attempt to look at collider physics in a broader perspective, combining a list of physics questions with a list of hadron colliders presently approved or contemplated for the near future.

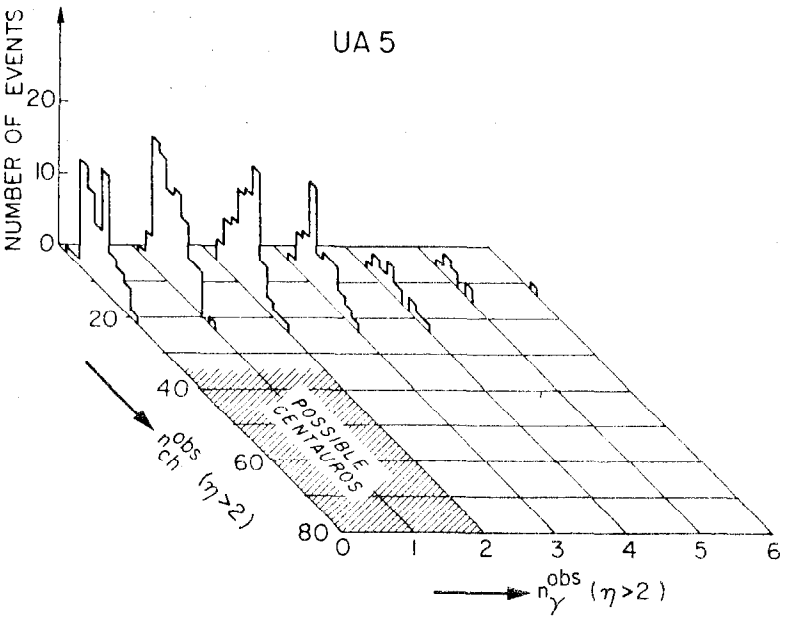


Fig. 3 - A negative search for Centauro events; number of neutral particles as a function of the number of charged particles. Results from UA5.

Our definition of collider physics in terms of the energy scale set by the electroweak theory, namely 100 GeV, should be considered as the present one. The brilliant successes already achieved are such that collider energy in the TeV range is very seriously considered. This may be "collider physics" in the nineties.[6] Excluded from our definition is also collider physics in the seventies which corresponds to research at the CERN-ISR.[13)-14)] As is well known, it led to many interesting physics results and it also led to the development of detector designs which have made research at the SPS collider so efficient and successful almost from its very start. Ten years of research at the ISR deserve a fair credit for the present successes of collider physics.

2. - *THE PRESENT SITUATION AND SHORT-TERM EXPECTATIONS*

We consider in turn large cross-section effects, the production of the weak bosons, and jet phenomena. In each case we do not attempt to be complete but to merely present some general features, stressing progress anticipated from the continuation of the present data taking and analysis.

2.a. - The global features of hadronic interactions

Priority had of course been given to the weak bosons, and questions related to global features of hadronic interactions have not been studied in great detail yet, despite the very large amount of collected data. Some general properties have, however, been already ascertained. We illustrate this with a few examples.

Figure 4 shows the behaviour of the rapidity density in the central region as a function of centre-of-mass energy. Shown is actually $1/\sigma(d\sigma/d\eta)$ where η is the pseudorapidity,[15)] as measured by experiment UA5.[16)] This experiment uses a streamer chamber which was previously installed at the ISR as experiment R703. On Figure 4, one thus finds an ISR and a collider point obtained with the same detector and other ISR points. The densities thus measured exclude single diffractive events and are thus larger (by 10%, say) than mean densities defined for all inelastic events. One sees an important rise (by almost a factor two) as one goes from ISR energy to collider energy. It corresponds, however, to a mere logarithmic extrapolation of the ISR data. On a logarithmic plot a linear rise fitted to the ISR points agrees with the present measurement at collider energy.[16)] This is an example of the mere continuation of "lns physics".

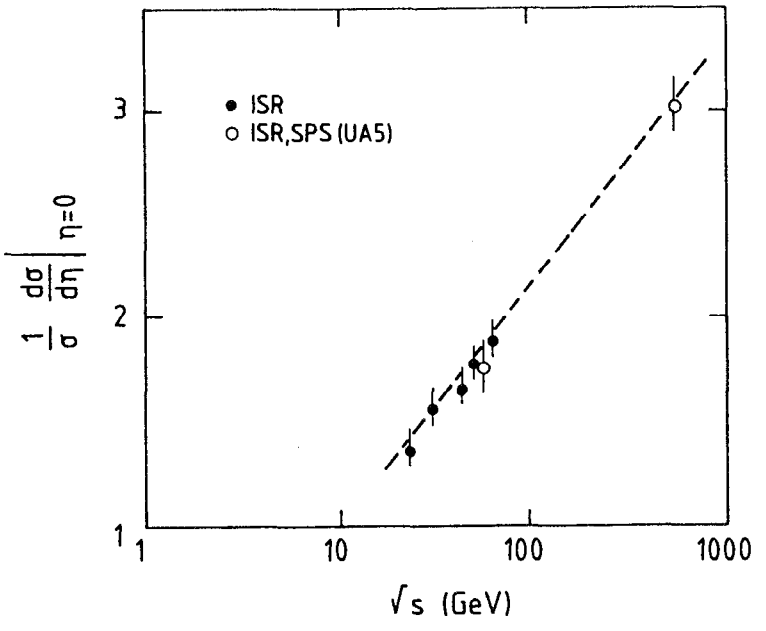


Fig. 4 - The central pseudorapidity density as a function of energy. ISR and collider (UA5) results.

The value measured by UA5 (Fig. 4) is compatible (in view of different trigger biases) with the higher value reported by UA1.[17] Such an important rise of the density of the central plateau was expected from cosmic ray results and in particular from the emulsion chamber data,[8] which could claim its discovery.

The rapidity density averages over different types of configurations, low multiplicity ones as large multiplicity ones. Such different configurations can probably be associated with different values of the impact parameter.[18] As is already well known at lower energy, one has thus important long range correlations when expressed in terms of particle densities. A large (low) multiplicity observed forward in the centre-of-mass system implies a large (low) mean multiplicity backward. This is different from the situation in e^+e^- collisions where the two jets fragment practically independently of each other. It is typical of the superposition of events of different types which is the situation met in hadronic collisions. The new collider results allow one to ascertain such a property in a much clearer way than before.[15] Figure 5 shows the mean multiplicity backward (forward) as a function of the measured forward (backward) multiplicity. The linear rise $\langle N_F \rangle = A + B\, N_B$ can now be followed up to $N_B \approx 30$. The fitted value of B is of the order of 0.5 when one would expect $B = 1$ excluding, important short range clustering effects.[15] Experiment UA5 made a detailed study of such correlations and came to the conclusion that the observed values correspond to correlation effects very similar to those observed at the ISR.[19] A large multiplicity backward signals a large multiplicity event and therefore implies a large multiplicity forward, this being tempered by short range effects which clearly reduce the value of B, since they imply sizeable fluctuations.

Figure 6 shows the rise of the total cross-section. In this case a global study of the total cross-section and of the parameter ρ, the ratio of the real to the imaginary part of the forward elastic amplitude leads to a $\ln^2 s$ fit and extrapolation of the ISR results.[20] The expected rise, a conclusion further strengthened by an analysis including ISR $p\bar{p}$ results,[21] is very much compatible with the measured values, as obtained by experiments UA4[22] and UA1.[23] Errors are still large but one may expect a much-increased precision in the near future. In this energy range, the rise of the total cross-section is expected to be associated with a rise of ρ. The value of ρ, close to 0 at ISR energy, should reach 0.15 to 0.20 at collider energy. This increase of the value of ρ may explain why the marked

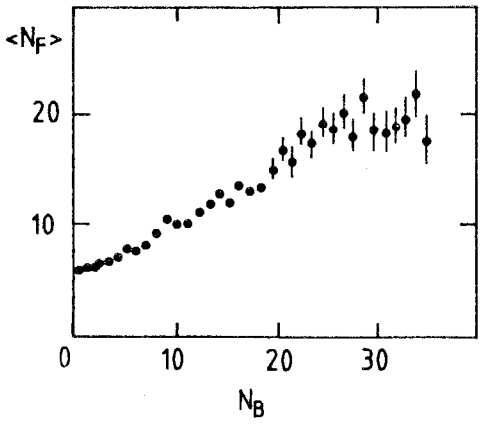


Fig. 5 - The mean multiplicity forward as a function of the measured multiplicity backward. Results from UA1.

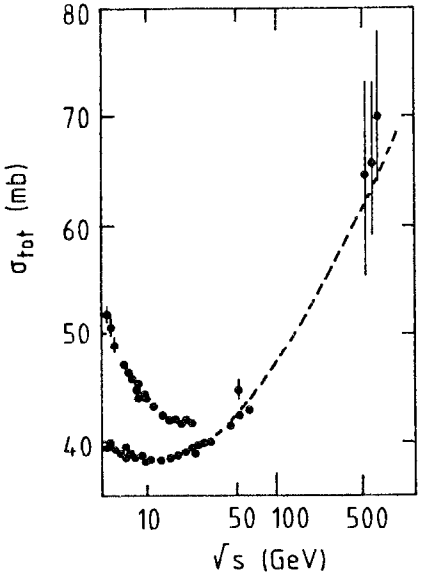


Fig. 6 - The total cross-section for pp and $p\bar{p}$ scattering as a function of energy (UA1 and UA4).

dip seen in $p\bar{p}$ elastic scattering at lower energy [20] should eventually transform itself into a mere shoulder as the forward peak shrinks when going to collider energy. This is indeed what occurs, as reported by UA4.[24] It is an interesting question [25] which calls for a measurement of $p\bar{p}$ elastic scattering at the ISR past the dip (in pp scattering) region. Let us hope it can be made.

The forward (diffractive) peak is narrower at the collider than at ISR energies.[26] The slope parameter B increases from typically 13.9 (ISR) to 17.2 (collider) at low $|t|$ ($|t| < 0.1$) [27] and from 10.7 (ISR) to 13.3 (collider) at larger $|t|$ ($|t| \simeq 0.2$).[28] The cross-section area (the proton/antiproton size) thus increases much from ISR to collider energies, this being clear from σ_{tot} (Fig. 6) and from the slope measurements. The shape remains, however, remarkably constant. This is illustrated by Figure 7 which shows the ratio σ_{el}/σ_{tot} for pp and $p\bar{p}$ scattering, respectively, as functions of the incident (equivalent laboratory) momenta The collider value may be slightly higher than the ISR value but remains (within errors) the same. A $p\bar{p}$ collision is thus far from reaching a black disc limit. The constancy of the proton/antiproton shape (geometrical scaling) is a challenging property.

Such a data sampling illustrates the continuation of "lns physics". Whether considering $\sigma_{tot}, \sigma_{el}$, B, $1/\sigma(d\sigma/d\eta)$,..., simple logarithmic extrapolations of ISR data could predict the newly measured value.[7] One may say that "lns physics" was a proper nickname. Nevertheless, success in predicting does not mean understanding! We still do not know why all these parameters vary so little since they vary at all, at a level which could be deemed satisfactory.

I now turn to a property which was reported in cosmic ray research.[8) 12] It has now been verified at the collider and at the ISR and it may give some interesting clues on reaction mechanisms. The emulsion chamber results [8] have shown a positive correlation between the central particle density and the mean value of transverse momentum. This is shown in Figure 8a. A group of points (at low η_γ and low $\langle p_T \rangle$) have been circled. They agree with simulations based on the mere extrapolation of Fermilab events analyzed with the same emulsion technique. The others correspond to a reported new type of configuration . An increase of $\langle p_T \rangle$ with η_γ [the emulsion detectors are sensitive to the electromagnetic (π^0) energy only] goes against naive conclusions based on energy conservation and is therefore

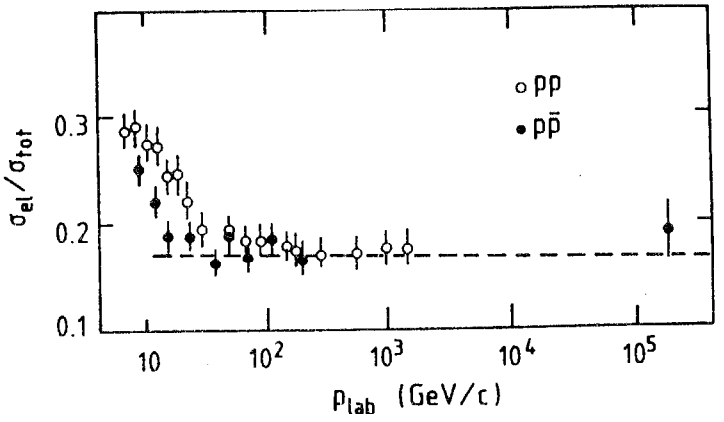


Fig. 7 - σ_{el}/σ_{tot} for pp and $p\bar{p}$ scattering as a function of the incident (equivalent laboratory) momentum.

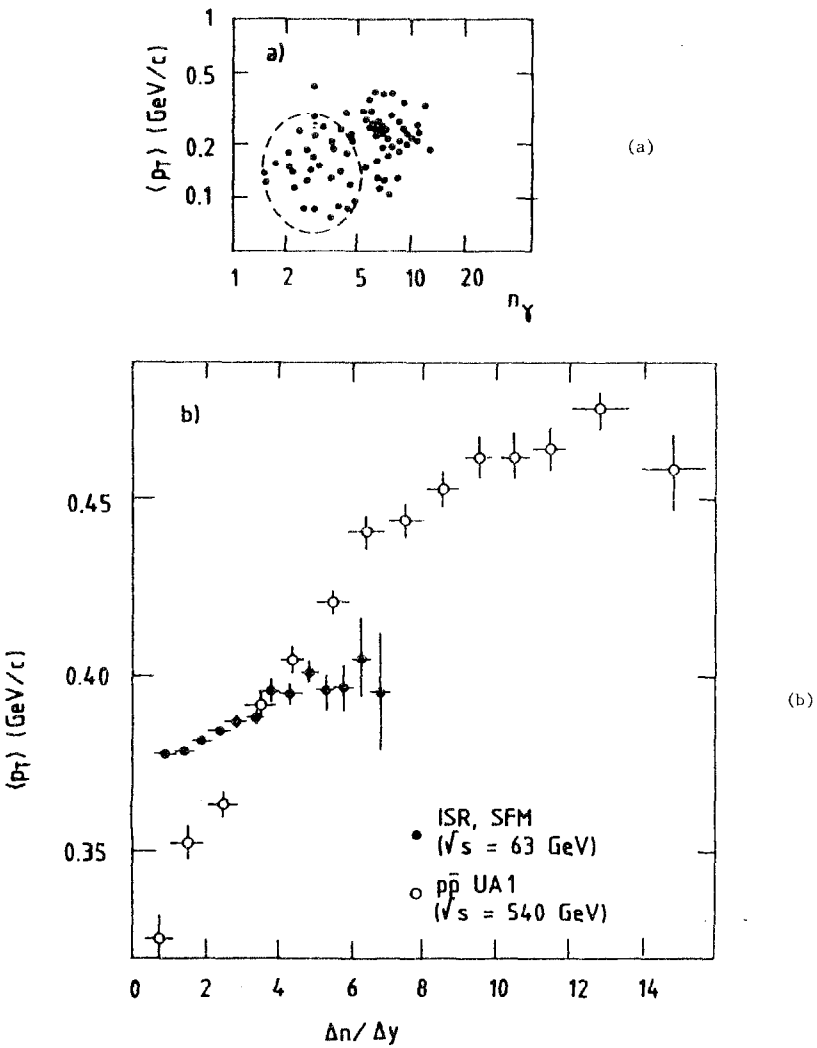


Fig. 8 - The relation between $\langle p_T \rangle$ and the central particle density:
8a : the scatter plot determined by cosmic ray results (emulsion chamber results);
8b : results from UA1 (collider) and R420 (ISR).

very interesting. Such two types of events have been dubbed mirin and açu respectively [8] (small and big in Amazonian Indian vernacular). While such a dichotomy might be considered too strong, a checking for a rise of $\langle p_T \rangle$ with central rapidity density was a very interesting question at collider energy.[7] Figure 8b shows the UA1 results [29] together with recent ISR results.[30] One clearly sees a rise of $\langle p_T \rangle$ with the central rapidity density dn/dy. It is less pronounced but definitely present at the ISR.

The emergence of açu type configurations has been associated with the fact that, at collider energy, many (plentiful) low x partons have already large enough centre-of-mass energy to give several mini-jets (of a few GeV) fragmenting independently of one another. This corresponds to an increase in entropy from typical lower energy configurations and readily gives larger values of both particle density and $\langle p_T \rangle$.[7),31] The effect clearly seen at the collider should also be present though far less strongly at the ISR. Such statements seem to be in good agreement with the recent results. Two further consequences are firstly the emergence of clear four-jet events - this will be discussed later - and, secondly a correlated increase of the K/π ratio, due to the independent fragmentation of several mini-jets. The latter one remains to be checked.

I choose to stress this point since it seems to provide evidence for a new type of reaction mechanism which becomes obvious at collider energy only. This may explain the energy dependence of several parameters. The question of hard scattering among low x partons indeed offers very interesting theoretical challenges. Such processes are now known under the name of semi-hard processes.[32] This is a domain which is likely to develop.

This rapid survey of some of the global features of hadronic interactions is far from exhausting present information.[33] It was merely meant to illustrate some of the recent results since they are not separately covered by specialized talks. It also gives a hint of the large amount of information still to come when the collected data are analyzed.

2.b. - The weak bosons

This is at present the most important question. However, since it is very well covered by other talks, I only touch on it in order to stress the big question of rates and to discuss some features which should be eventually studied in detail with increased statistics.

At collider energy, with centre-of-mass energy of the order of M_W or M_Z easily available at the quark level, the production cross-section is essentially determined by the Fermi constant $G_F \approx 4\times10^{-33}$ cm^2. One, however, cannot use the full cross-section since non-leptonic modes were (rightfully) expected to be hiden by the large hadronic jet background.[7] Looking for the $e\nu$ decay of the W and the e^+e^- decay of the Z one is left with much smaller cross-sections. They can tentatively be set at [34]

$$\sigma(W^\pm \to e^\pm\nu) \approx 5\times10^{-34} \text{ cm}^2$$
$$\sigma(Z^0 \to e^+e^-) \approx 5\times10^{-35} \text{ cm}^2 . \qquad (2.1)$$

The integrated luminosity in '82 was of the order of 2.5×10^{34} cm^{-2}. The W was discovered as one could hope for in view of the expected production rate. It was frustrating but understandable that no Z^0 was seen. The integrated luminosity in '83 was of the order of 1.4×10^{35} cm^{-2}. Several Z^0 were seen as many new W's (about fifty) were collected in each of the two experiments.

The weak bosons have thus been met at the rendezvous set up for them by Carlo Rubbia.[1] While there is still an experimental uncertainty in rate by typically a factor 2, the production cross-sections are as expected, namely at the $\frac{1}{2}$nb level for the W in its leptonic mode.[7]

At present the luminosity (averaged over a day) is of the order of 10^{28} cm^{-2}, with as a result an integrated luminosity over the typical yearly run in excess of 10^{35} cm^{-2}. One may hope in the near future for a luminosity (averaged over a day) of 10^{29} and therefore an integrated luminosity of 10^{36} in '84. Reaching a luminosity of 10^{30} (a present goal) could give an integrated luminosity of 10^{37} over a typical run. These are the values to be used together with the production cross-sections (2.1) when discussing present prospects.

There is now no doubt that the W and the Z have been discovered. An important question in W production and leptonic decay is the asymmetry associated with the weak process. It can easily be seen to result from a simple helicity argument.[35] The electrons are expected to follow preferentially the proton direction while the positrons follow the antiproton direction. Figure 9 shows the expected angular distributions. The forward electrons correspond, however, to relatively low p_T values when the clear W candidates are most easily recognized in the Jacobian peak ($p_T \approx M_W/2$) and hence in the central region, where the asymmetry is small. As now reported,[2] the asymmetry is as expected. This is the crucial test of the weak nature of the process. The effect is far less pronounced for the Z since the value of $\sin^2\theta_W$ is such that the electron coupling is almost purely axial. In any case testing it for the W required the statistics now available, with about 50 events in each experiment.

Figure 10 shows the x distribution for W^+ produced in $p\bar{p}$ and pp collisions. They are both shown in order to display the asymmetry expected in $p\bar{p}$ collisions. The wide nature of the x distribution had also been long emphasized. With the present event sample such a distribution can be tested. This provides a test of the Drell-Yan approach used at predicting yield or as a test of QCD used in its leading log approximation. Measuring the transverse momentum distribution k_T of the W is also very important. This tests higher order corrections in the prediction of the yield, as obtained in perturbative QCD.[36] One expects a peak at relatively low k_T (a few GeV) and a tail associated with the observation of a recoiling jet. As reported at this conference,[2] these distributions are now becoming available and seem to agree with expectations. It is clear that a few times as many events would be most worthwhile. This would require several years of running if the luminosity could not be increased by a sizeable factor. Increasing the luminosity by an order of magnitude would be a very important improvement at analyzing W production. It is a must in order to get some information about the Z.

The observation of the W and Z leptonic modes with the predicted rates shows that nothing very peculiar occurs in a dominant way, thus quenching the corresponding branching ratios. It is important to try to depart from the purely leptonic sector and in particular to observe the W and the Z in their two-jet modes. As is well known and clear from the next subsection, the hadronic

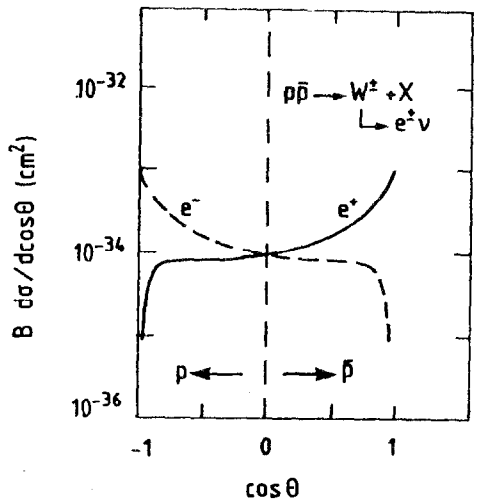


Fig. 9 - Angular distribution for $e^-(e^+)$ produced through $p\bar{p} \to W^{\mp}X$ ($W^{\mp} \to e^{\mp}\nu$) reactions.

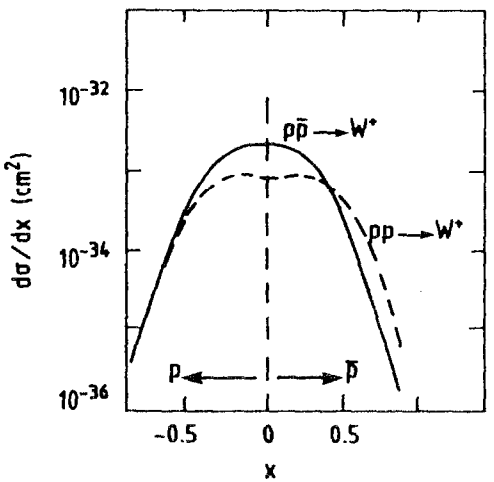


Fig. 10 - Feynman x distributions for W^+ produced in $p\bar{p}$ and pp collisions.

background is high. Nevertheless, improvements in jet energy resolution could allow one to observe the corresponding relatively small (0.1, say) enhancement before too long. The W and Z mass range (for a two-jet system) is also a place to look for new particles for the very same reasons as those itemized in relation with e^+e^- colliders.[37] We shall come back to this in Section 3.

It may sound peculiar that both experiments find a Z decay with a large momentum γ ray. An event for which the probability should be at the per cent level seems to appear one fifth of the time.[2] One, of course, cannot conclude at this stage. It may be a statistical fluctuation. It may hint at something new (an unexpected structure effect). It is very important to collect a few times as many Z^0's for this reason alone.

2.c. - Jet studies

Jet production in hadron collisions has been discussed for a long time already, in particular in connection with particle production at large p_T.[38] One had, however, to wait for collider energy to see jets appearing in a spectacular way (Fig. 2c). The production of jets had long been expected to result from hard scattering among partons [39] and it was indeed discussed in detail at SLAC many years ago.[40] This is actually the mere generalization to hadron-hadron collisions [41] of the deep inelastic behaviour so brillantly studied at this laboratory in lepton-hadron scattering.

At present jet studies offer a very interesting testing ground for perturbative QCD and for hadron structure. Predictions of perturbative QCD can be considered as being of different kinds and one may distinguish [42] :

(i) qualitative predictions. They are those associated with the parton model, for which QCD provides a rationale, and with explicit departures from the simple parton model with, for instance, radiation of hard gluons.

(ii) semi-quantitative predictions. They are predictions which should be considered as valid at the order of magnitude level. They are, for instance, those which one can make at present using the leading log approximation in hard hadron collisions. Since very big effects (involving several orders of magnitude) can often be anticipated, such approximative predictions are interesting.

(iii) quantitative predictions. They are those which can in principle lead to a determination of α_s through the analysis of scaling violations in deep inelastic scattering or through the study of the energy dependence of the cross-section for e^+e^- annihilations into hadrons.

Predictions of type (i) speak for themselves (Fig. 2c).

Predictions of type (iii) are at present limited in their applications by experimental precision.

We shall here focus on predictions of type (ii) which have scored a good success with the recent collider results. The colliding hadrons can be considered as broad band beams of quarks and gluons. These beam properties are already reasonably well known and hard processes in which they directly matter can be predicted (up to a factor 3 say, both ways). This is what is meant by a prediction at the order of magnitude level.

A hard collision between two hadrons is depicted as shown in Figure 11a. Two partons, with respective momentum fractions x_1 and x_2, scatter with a large transverse momentum p_T. The hadron structure is thus probed with a resolution power $Q^2 \sim p_T^2$ and relevant parton densities are determined accordingly, taking proper account of scaling violations. They are here calculated in the leading log approximation.

The parton-parton centre-of-mass energy squared is $\hat{s} = x_1 x_2 s = \tau s$ and the important quantity for determining a hard process, the parton-parton cross-section of which is calculated perturbatively, is the parton-parton luminosity with the proper matching τ available once two hadrons collide. The most useful quantity [7] is actually $\tau(dL/d\tau)$ and Figure 11b gives it as a function of $\sqrt{\tau}$ for $u\bar{u}$ and gg collisions in a $p\bar{p}$ reaction.

One sees that the differential luminosity falls steeply with $\sqrt{\tau}$ as one runs out of partons with high enough fractional momenta. By the same token one expects large increases in yield when for fixed $\hat{s}$ (or p_T^2) one increases s and thus decreases τ. One thus runs up the differential luminosity curves. For jets produced at wide angle one finds that $\sqrt{\tau} \sim 2P_T/\sqrt{s}$. At fixed high p_T yields increase therefore with energy.

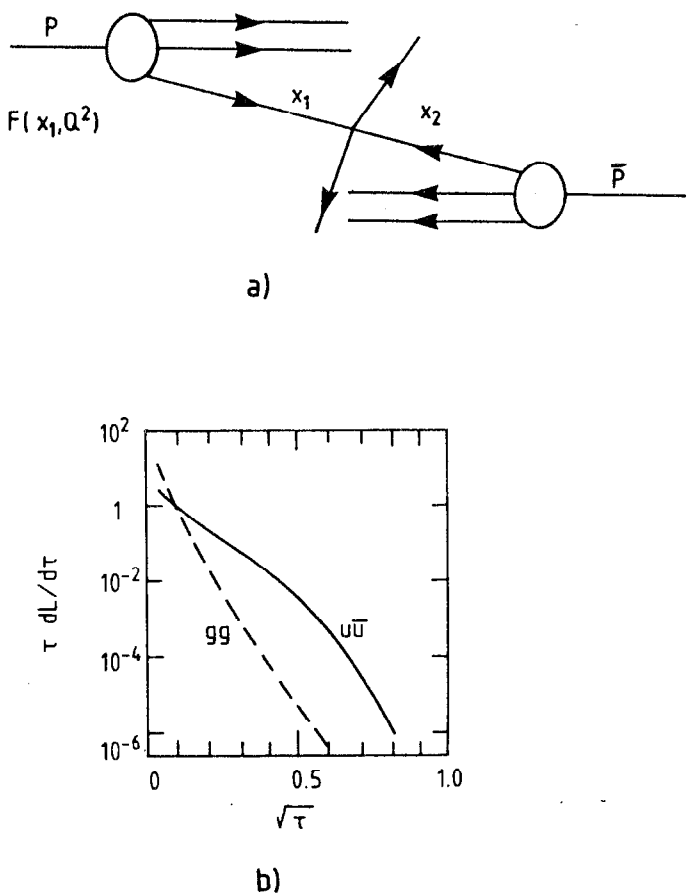


Fig. 11 - 11a : a hard collision between two partons;
11b : the differential luminosity for $u\bar{u}$ and gg collisions in $p\bar{p}$ collisions at collider energy. Scaling violations are included.

From known (quark) and assumed (gluon) structure one could calculate jet yields expected from hard scattering. Figure 12 shows the expected production cross-sections at 90° as a function of the jet momentum p_T at ISR (63 GeV) and collider (540 GeV) energies.[43] One sees in particular the very large increase in yield expected where an experimental overlap is possible (10-20 GeV). One deals with several orders of magnitude! The p_T dependence is very sensitive to the hadron structure. It is determined more by the variation of the differential luminosity (Fig. 11b) than by the intrinsic p_T^{-4} dependence associated with point-like scattering. Indeed the decrease of the jet yield at collider energy, when fitted to an inverse power p_T^{-N} gives $N \approx 9$ as opposed to 4 which applies at fixed $x_T = 2p_T/\sqrt{s}$, only. Also shown are the data of UA1 [44] and UA2 [45] corresponding to different runs and extending further and further in p_T with increasing integrated luminosity. The data point fall reasonably close to the predicted rate. For reasons given above, one should perhaps not attach too strong a weight to an exact fit in view of the approximations made. There is general agreement [46] but such predictions are to be considered as valid within a factor 3, say. More relevant is the fact that the shape is correctly reproduced and this over more than six orders of magnitude. The jet yield measured at the ISR (R807) is also shown.[47] The experimental values meet reasonably well the predicted ones.[7] As previously stressed it is very important that all large predicted ratios ($\sigma(\sqrt{s} = 540, p_T = 20$ GeV)/$\sigma(\sqrt{s} = 540, p_T = 100$ GeV), $\sigma(\sqrt{s} = 540, p_T = 15$ GeV)/$\sigma(\sqrt{s} = 63, p_T = 15$ GeV)...) are in good agreement with the new experimental values.

The global jet yield presented in Figure 12 corresponds to a mixture of quark jets and gluon jets and the mixture is expected to vary with p_T as softer gluons leave their dominant role to harder quarks. Figure 13 gives the u quark and gluon jet yields expected at 540 GeV, together with the global jet yield (Fig. 12). Gluons clearly dominate, up to 40 GeV, say, but quark jets take eventually the leading rôle. Also shown on Figure 13 is the increase in jet yield expected for $p_T = 100$ GeV, when going to $\sqrt{s} = 620$ GeV (which should soon be achieved on the SPS), to Tevatron I ($\sqrt{s} = 2$ TeV) and to $\sqrt{s} = 20$ TeV. One is again dealing with several orders of magnitude. There is now little doubt that these new big factors are correct. Differentiating between quark and gluon jets remains a very challenging problem and one may hope that with the new collider data some progress will be made soon.

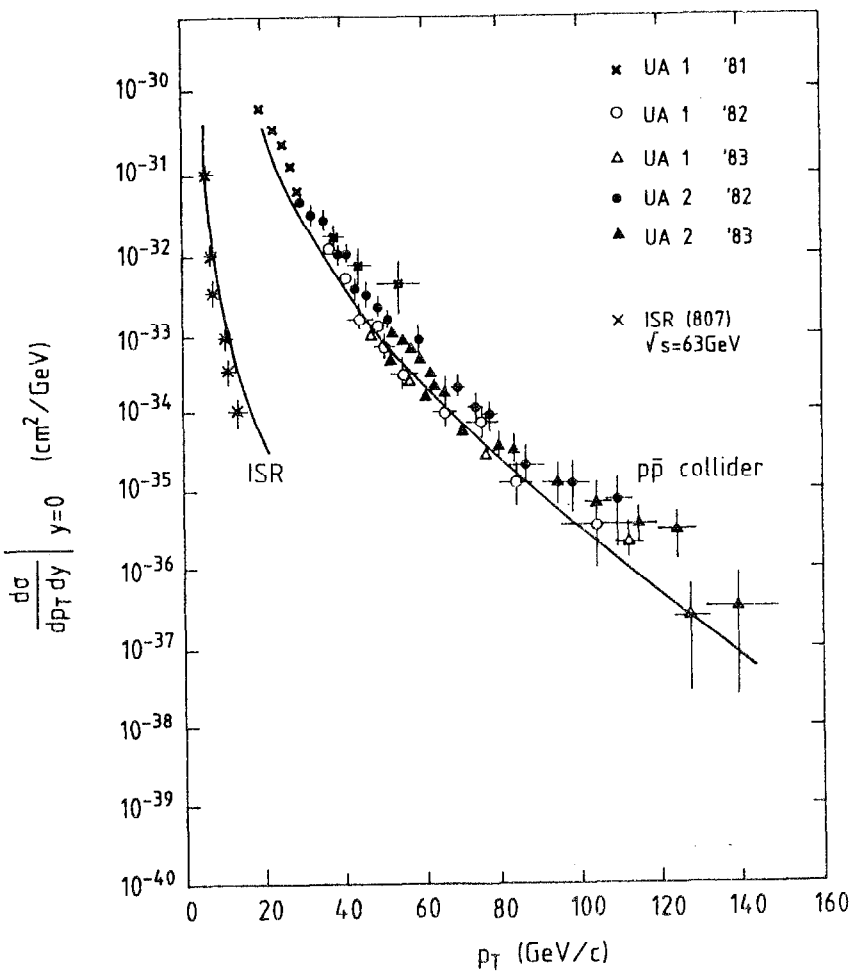


Fig. 12 - Jet yields at 90° at ISR and collider energy. QCD predictions [H.J. of Ref. 7)] with UA1 and UA2 data in '81, '82 and '83, and with R807, ISR.

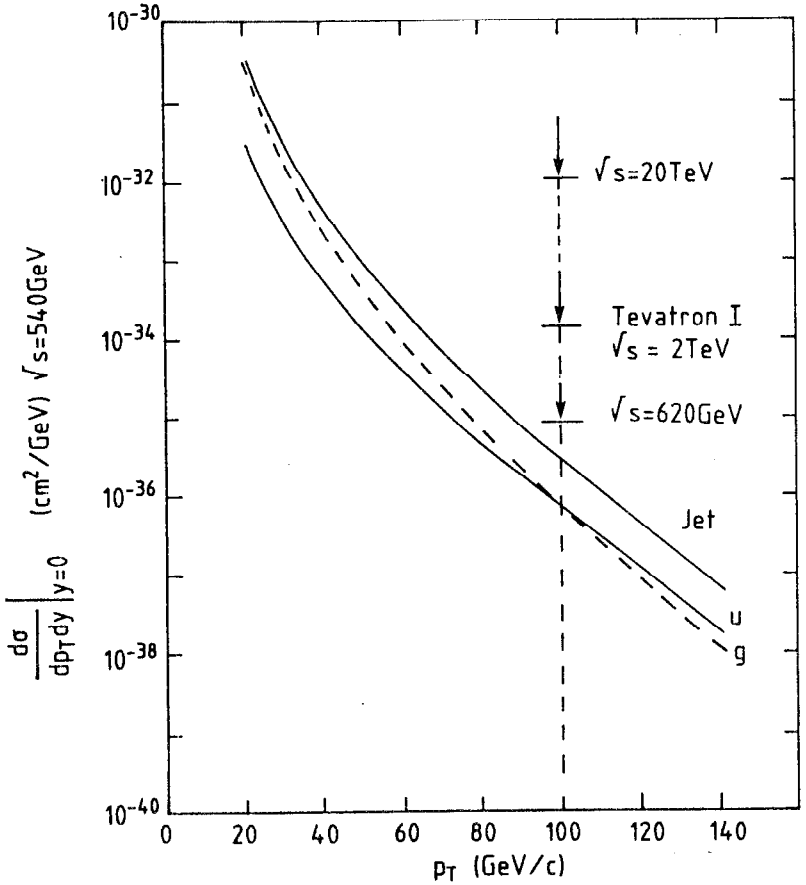


Fig. 13 - Expected u quark and gluon jet yields at collider energy as functions of p_T, together with the global jet yield. At p_T = 100 GeV/c, jet yields expected at $\sqrt{s}$ = 620 GeV, 2 TeV and 20 TeV are also shown.

This is a difficult question in e^+e^- annihilation [48] and it is likely to be difficult at the collider. While cross-sections for inclusive jet yields at wide angle, such as those shown in Figures 12 and 13, appeared as interesting parameters, the clarity of the jet structure (Fig. 2c) is such that there is hardly any problem in determining the actual angular distribution for parton-parton scattering from the observed two-jet events. Such distributions have been shown.[2] They have been observed by UA1 and UA2. One clearly sees the forward-backward peaking proper to generalized Bhabha scattering for the dominant $gg \to gg$, $gu \to gu$, $u\bar{u} \to u\bar{u}$ processes. This is a very important check of the hard scattering approach. The measured distributions cannot, however, yet distinguish between gluon and quark scattering.

One may attempt to push the analysis further with increased statistics. Figure 14 gives some angular distributions which could be helpful to that effect. Shown are the $\cos\theta^*$ dependence (θ^* is the reconstructed scattering angle in the parton-parton centre-of-mass system) for gluon, and u quark jets, with a $45^\circ < \theta < 135^\circ$ cut imposed in the $p\bar{p}$ centre-of-mass system. This is done for different p_T values 20, 50 and 80 GeV/c, respectively. One sees a change in the distributions as p_T increases and quark jets (the $\bar{u}$ distribution is symmetric to the u distribution) become dominant. Such features may eventually be checked to support a change in dominant jet species with p_T, as presently expected.

Assessing prospects in jet studies we may try to first summarize the present situation saying that :

(i) jets exist as expected and dominate events selected according to a large global transverse energy E_t (E_t > 60 GeV, say, with $\Delta y = \pm 1$);
(ii) the p_T dependence is good and the rates meet expectations (Fig. 12);
(iii) the k_T dependence (k_T is the transverse momentum of the two-jet system) also corresponds to expectations, being limited in most cases to relatively low values (a few GeV); and
(iv) the angular distributions at the parton level behave as expected (generalized Bhabha scattering).

Another important feature now verified beyond doubt is the large ratio between jet yields and single particle yields at the same p_T. This results from a well known trigger bias effect.[49] Figure 15 shows the global jet yield

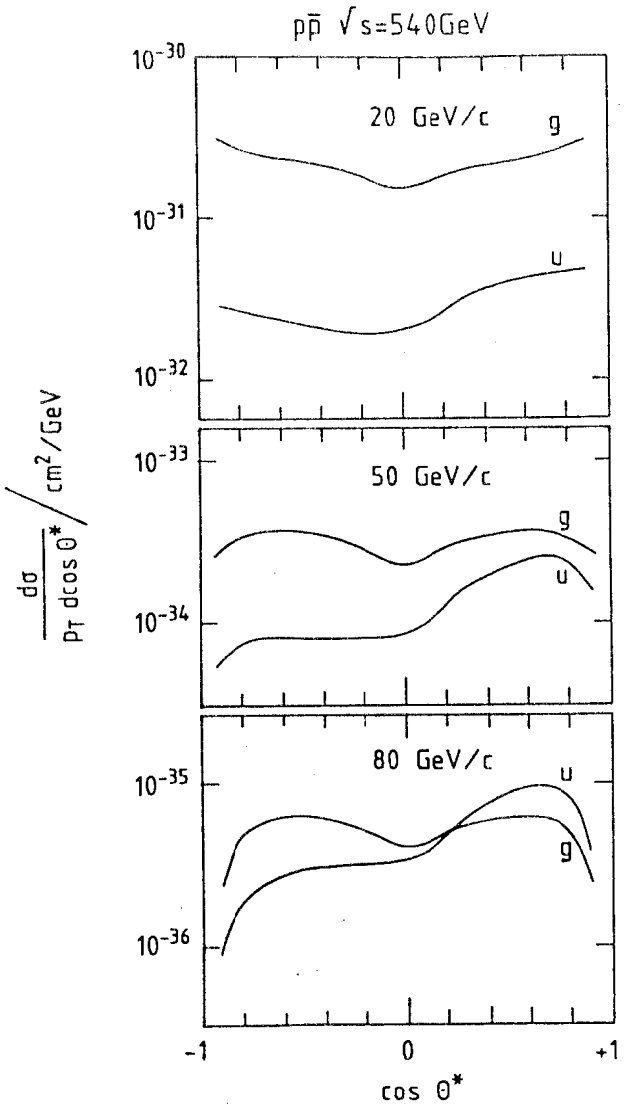


Fig. 14 - Parton-parton centre-of-mass distributions for gluon and quark jets detected within $45^o < \theta < 135^o$ for different p_T values 20 GeV/c, 50 GeV/c, and 80 GeV/c.

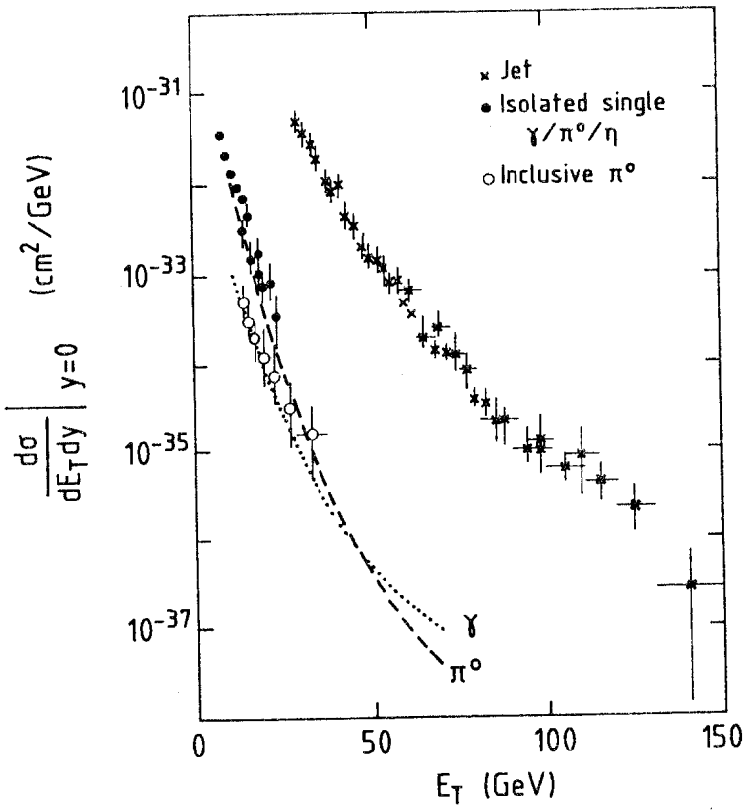


Fig. 15 - Global jet yield and single particle yield (isolated neutrals and inclusive π^o). Results from UA2 and predictions from H.J. in Ref. 7).

observed by UA2 [50] together with the differential cross-sections measured for isolated neutrals (γ, π^o, η) and inclusive π^o. The ratio, of the order of 10^3, is as large as expected.[43] It is important to note that this ratio is very sensitive to scaling violations (this corresponds to an order of magnitude). One also sees that one expects the γ/π^o ratio to increase beyond 1 by $p_T \sim 50$ GeV/c.[43),51]

The large value of the jet/π ratio is an important check of general ideas about jet fragmentation. The large (as compared with α) value of the γ/π ratio is also a very important effect. It has been first found at the ISR.[52] It still remains to be checked at collider energy. Results from UA1 on the π^o/jet ratio [53] are in agreement with the UA2 data shown on Figure 15. The jet/π ratio has been recently measured at the ISR [54] and is also found to be of the order of 10^3. One should remark that this large value at ISR energy is due to the relative softness of the pion distribution in a fragmenting parton tested for a large value of $x_T = 2p_T/\sqrt{s}$. At collider energy it should a priori be smaller ($\sim 10^2$) because x_T is rather small but, since p_T is large, scaling violations have to be taken into account and they bring back the ratio to 10^3.

In connection with that one should also mention that E260 [55] obtained a correct result with its analysis of its Fermilab data, despite all the doubts later raised by the results of NA5.[56] Trigger bias effects and global jet yields are just as expected.

For the near future one sees, of course, more information coming up on jet fragmentation, and in particular on multiplicities, transverse momenta and fragmentation distributions. Contributions to this conference [2] provide a very good survey of the work presently going on. Of particular importance is the question of jet branching. The analysis of three-jet events may help to distinguish between the quark jet case (e^+e^- annihilation) and the gluon/quark jet case (collider). Measuring the probability for hard gluon emission may provide interesting clues. This is a case where the perturbative factor of 9/4 for gluon radiation from a gluon and a quark respectively, should apply.

The radiation of a hard jet by one of the jets will break the coplanarity structure typical of dominant two-jet events (Fig. 11a). As a result, the P_{out} distribution of a jet on the opposite side to a large p_T jet, used as a trigger, should present an extending tail, more and more pronounced as p_T increases. Such distributions for three ranges of p_T values (30-50 GeV; 50-70 GeV; and 70-120 GeV) are shown in Figure 16.[57] A clear three-jet system is here a priori required imposing $p_{T1} > p_T$ (the trigger value set), $p_{T2} > 15$ GeV/c, $p_{T3} > 15$ GeV/c and $\Delta_{ij} = \sqrt{(\Delta\eta_{ij})^2+(\Delta\phi_{ij})^2} > 1$ where ϕ and η are the pseudorapidity and the azimuthal angle of each jet, respectively.

Checking such distributions provides a test of perturbative QCD used for a two-parton → three-parton process with clearly separated jets.

At present, distributions for the invariant two-jet mass M_{JJ} are being measured. They provide tests of QCD which complement those associated with inclusive yields (Fig. 12). The quality of these data will improve and with increasing resolution one may hope to see structures (though not very prominent ones) associated with the dominant two-jet decays of the weak bosons and perhaps other things! A very important question is that of heavy quark jets. This is discussed in Section 3. We conclude this section with a few remarks about multi-jet events which have only been seen and not yet studied.

In Section 2.a, we already discussed the question of multiple parton scattering. At collider energy we have large numbers of relatively low x partons which can in principle independently scatter at wide angle, thus giving multi-jet events. One should see in particular four-jet events with two two-jet systems separately compensating their large transverse momenta. Figure 17 shows a very good candidate for such a process. This event has been observed by UA1. Such "show-case" events are not expected to be very frequent. They should occur at the 10^{-2} to 10^{-3} level when compared to dominant two-jet events at the same E_t.[58] This relative probability should also decrease with E_t, with two-jet events eventually dominating anything else at large E_t. This can easily be understood.[59),31] Once two partons collide at a wide angle with a cross-section σ_1, the cross-section for two other partons also colliding at wide angle, σ_2, is proportional to σ_1 but also to $\alpha_s^2(E_t^2)$ (relative perturbative probability) and inversely proportional to R^2, the hadron radius. One therefore has $\sigma^2/\sigma^1 \sim \alpha_s^2(E_t^2)/R^2E_t^2$ since the dimensional quantity R^2 has to be compensated for by the only free dynamical variable. The presence of the factor R^2 in the denominator is simply due to the fact that we have to consider the scattering of two

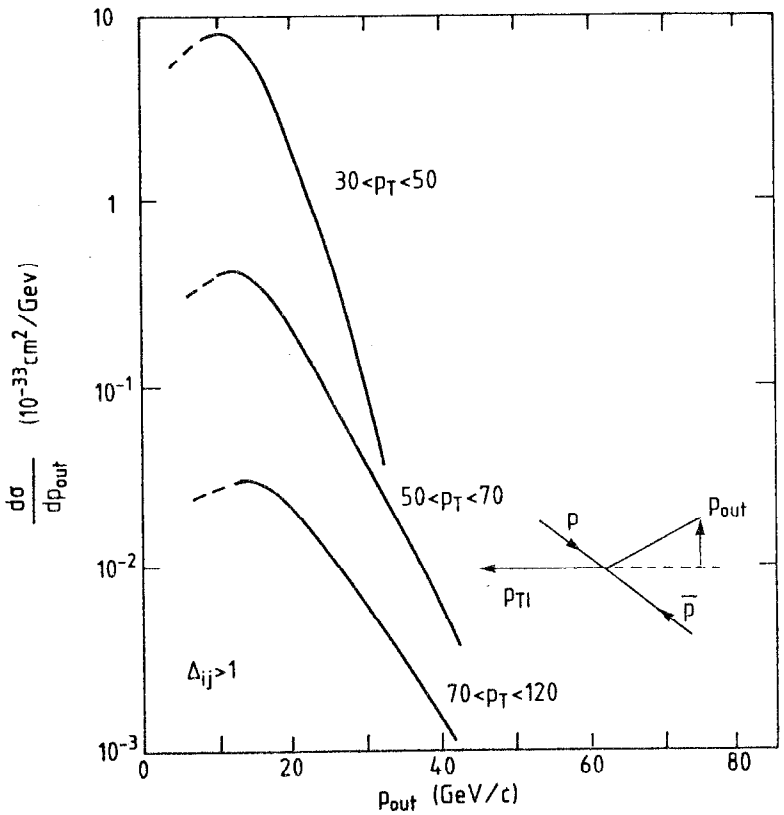


Fig. 16 - Distribution in p_{out} providing evidence for jet radiation for different jet transverse momenta. Predictions from Ref. 37).

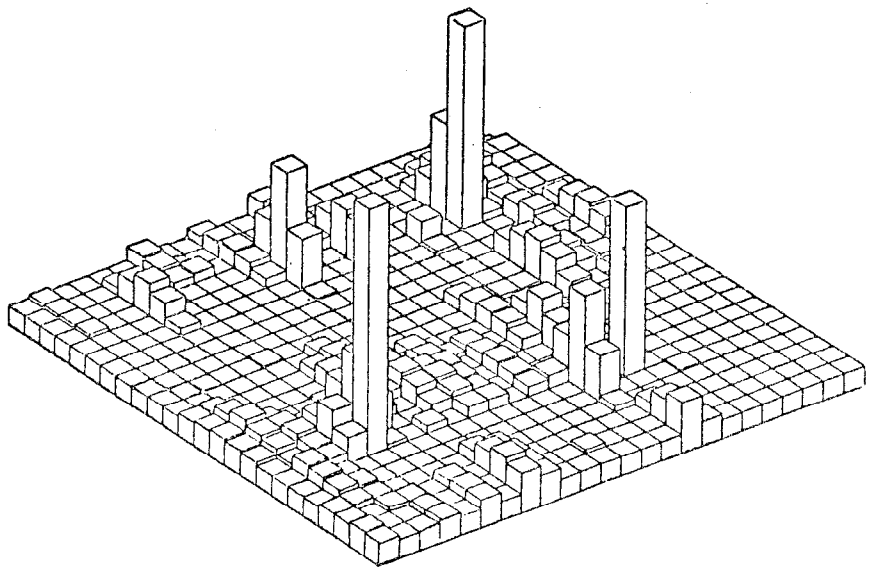


Fig. 17 - A "show case" four-jet event (double hard parton scattering). Results from UA1.

parton fluxes (each proportional to R^{-2}) and integrate over the hadron overlap region (factor R^2).

The observation of such events is interesting insofar as it provides information on hadron structure. One may emphatically say that if parton-parton scattering (Fig. 2c) is the Rutherford experiment of this decade, Figure 17 goes further showing evidence for several point-like scattering centres within the colliding hadrons.

Four-jet events obviously originate from several mechanisms. Nevertheless the two by two momentum matching of Figure 17 speaks for itself. In practice different mechanisms could be sorted out according to different E_t dependences and p_T ratios.

Multi-jet events are also related to semi-hard processes.[32] Experimental information should be very useful. Much can already be expected from the analysis of the present run.

3. - GOING FURTHER IN LUMINOSITY AND FURTHER PROSPECTS

The success of perturbative QCD with jet yields (Fig. 12) is a strong encouragement at considering further predictions and in particular those associated with heavy quark jets which are expected to result from gluon-gluon collisions and other processes. Figure 18 gives the expected yields [43),60)] for different quark species as functions of p_T. Heavy quark production is assumed to result from gg and $q\bar{q}$ scattering only, while strange quark production also results from the presence of an SU(3) symmetric sea (two limiting behaviours). As long as $p_T >> m_q$ all heavy quarks are on the same footing and one expects them to appear though at a level of 10^{-2} when compared with the global jet yield. Very heavy quark jets may give peculiar structures but, in view of the overwhelming background due to gluon and light quark jets, some specific signature may be needed. All heavy quark jets should have semileptonic decays with branching ratios at the level of 0.1 and thus contribute to the prompt lepton yield at large p_T. Conversely, looking for large p_T leptons may provide a reasonable signature for heavy quark jet production. The fragmentation of heavy quark jets into leptons has been

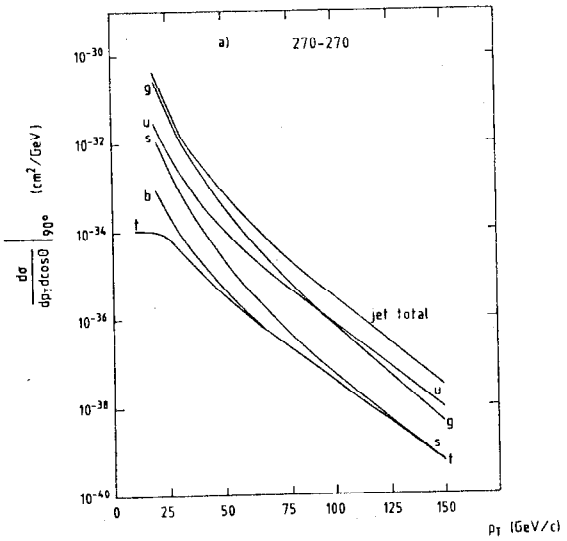


Fig. 18 - Heavy quark yields at large p_T. The t quark mass is taken as 30 GeV. Predictions from H.J. in Ref. 7).

already much discussed.[60)-61)] Figure 19 shows the expected yields [7)] in comparison with other yields (global jet yield, single π^o yields, lepton from weak bosons...) which now have all been verified.

The lepton yield from W and Z formation and decay shows the present stage of investigation, at the level of 10 to 50 events. One clearly sees that a good measurement of the prompt lepton yield from heavy quarks calls for an increase in luminosity. At low p_T ($p_T < 20$ GeV/c) there are important background problems. At large p_T ($p_T > 20$ GeV/c) the low rate is the problem. Yet the relatively large value of the e/π ratio, increasing with p_T, does justify a search. One is used to values at the level of 10^{-4} (Fermilab) or 10^{-3} (ISR). The presence of heavy quark jets at the level of 10^{-2} is a further and important test of the QCD approach (Section 2c).

This low rate predicament also affects a priori interesting modes for W and Z decays. If one considers for instance the $b\bar{t}$ mode of the W^-, it is up by a factor three [provided that the t quark is not too heavy ($m_t \lesssim 30$ GeV, say)] when compared to the $e\bar{\nu}$ mode, but down by a factor 10 if one requires to see a lepton, and down by an extra factor 30 or so if one requires a lepton at relatively high p_T ($20 < p_T < 30$ GeV/c, say). Again, a gain by a factor 10 in luminosity would help very much.

One may illustrate this point with two topical questions. The search for the top quark and the search for SUSY particles.[62)]

There are many ways to look for the t quark.[63)] We shall consider only two here which have both to do with t quark jet at high p_T. Let us assume for the sake of the argument that the top quark mass is anything between 20 GeV and 40 GeV. The fragmentation of the t jet should be peculiar because of the large Q value. The jet should be rather widely open with a large reconstructed invariant mass. One may search for such jets but the background is overwhelming (Fig. 18). It thus looks worth while to take a beating in rate, requiring a large p_T lepton, in order to limit the background. If a large p_T lepton is observed it is likely to come from a b quark.[64)] This is due to the fact that a b quark can transfer a maximum energy (M/2) to its lepton daughter, whereas a c or a t quark cannot. This is well known from the e and $\bar{\nu}$ spectrum in μ

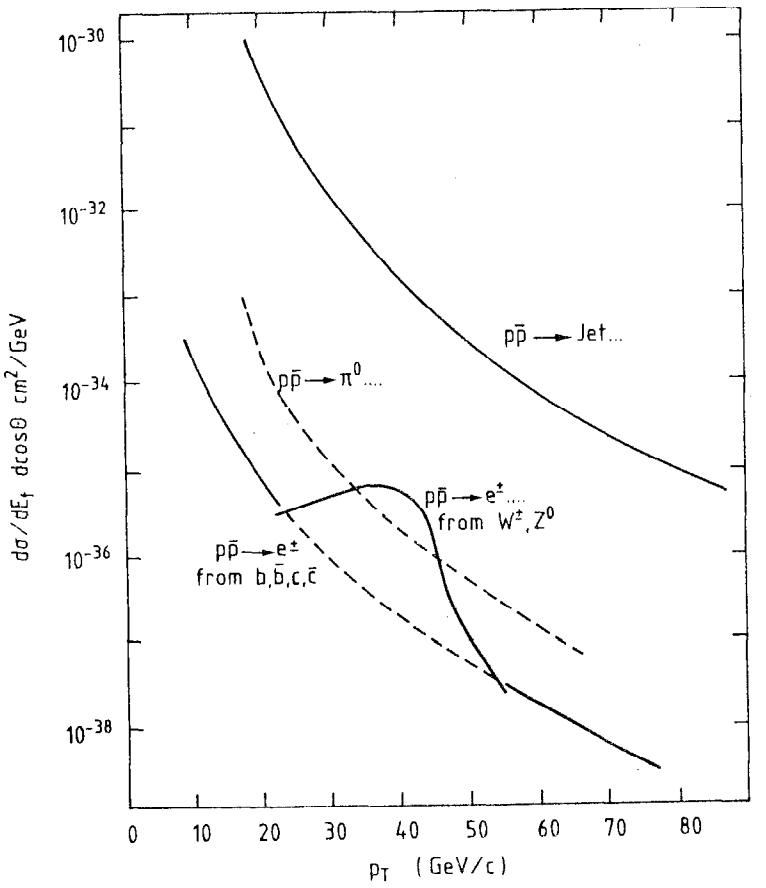


Fig. 19 – A comparative display of the global jet yield, the π^o jet yield and the large p_T prompt lepton yield whether associated with heavy quark hadronic production and semileptonic decays or with weak boson production and decay. The W and Z contributions have been smeared to take into account radiative corrections and resolution, at least in an approximate way.

decay. Let us assume that we thus get an enriched sample in b quark. Such a b quark may also come from a $b\bar{b}$ pair produced in a strong process (dominant) or also from Z decay. In the two latter cases the recoiling jet should be normal (background).

Figure 20 gives the anticipated lepton yield with signal ($b\bar{t}$,$b\bar{t}$) and background ($b\bar{b}$,$c\bar{c}$), for a t quark of 30 GeV, say.[65] The interesting point is that one finds a "bottleneck" where the signal over background ratio is maximized (>0.1). This should be an interesting place to look. Rates may, however, still be too small with present luminosity.

One may then try looking in a different way for a lepton originating from t decay with, in this case, an accompanying jet at an angle, in view of the large Q value. Figure 21 gives in that case the angular distribution expected for the accompanying b jet, for different jet momenta, when the trigger lepton is detected at 90°. The lepton-jet configuration should look typical enough, but the rates are very small.[65] Yet here one benefits from the fact that most of the t quark jets are from hard processes rather than from W and Z fragmentation. This is again a plea for an increase in luminosity. Indeed, from such curves one may say that, with 10 times the present luminosity, there is a good chance that a top quark with a mass in the 20-40 GeV should be discovered. A search is highly worthwhile with the present data sample, since none of these predictions should be considered correct at more than the order of magnitude level. It, however, looks difficult.

The same plea for a higher luminosity applies to the search of SUSY particles.[62),66] Here one interesting signal to look for corresponds to the fragmentation of the W into two supersymmetric particles $W^- \to f^o f^-$ where f^o would be the lowest mass stable one (photino, say). In such a case, the decay of the f^- into $f^o\, q\bar{q}$ could give a peculiar fan-like jet (Zen-type) [66] because of a large Q value. It should not be balanced in p_T because of the former f^o escaping detection. The signal is then a peculiar jet in an event selected according to a relatively large amount of missing transverse energy and no lepton seen. Background and rate problems are both important. Again a factor 10 in luminosity should help a great deal.

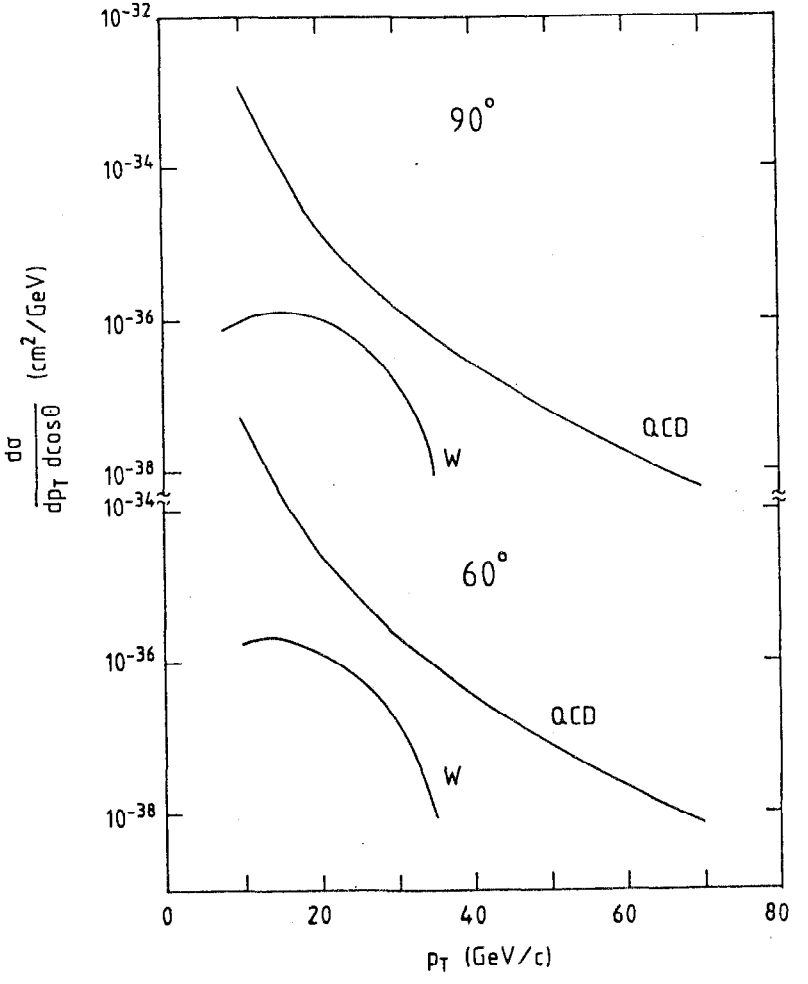


Fig. 20 - Signal (lower curve) and background (upper curve) for prompt leptons coming from heavy quark decay at two different lepton production angles (90° and 60°). The signal corresponds to $W \to b\bar{t}(t\bar{b})$ production. The background corresponds to $c\bar{c}$, $b\bar{b}$ and $t\bar{t}$ production through strong processes. The minority role of production through Z is neglected here. The top mass is set at 30 GeV.

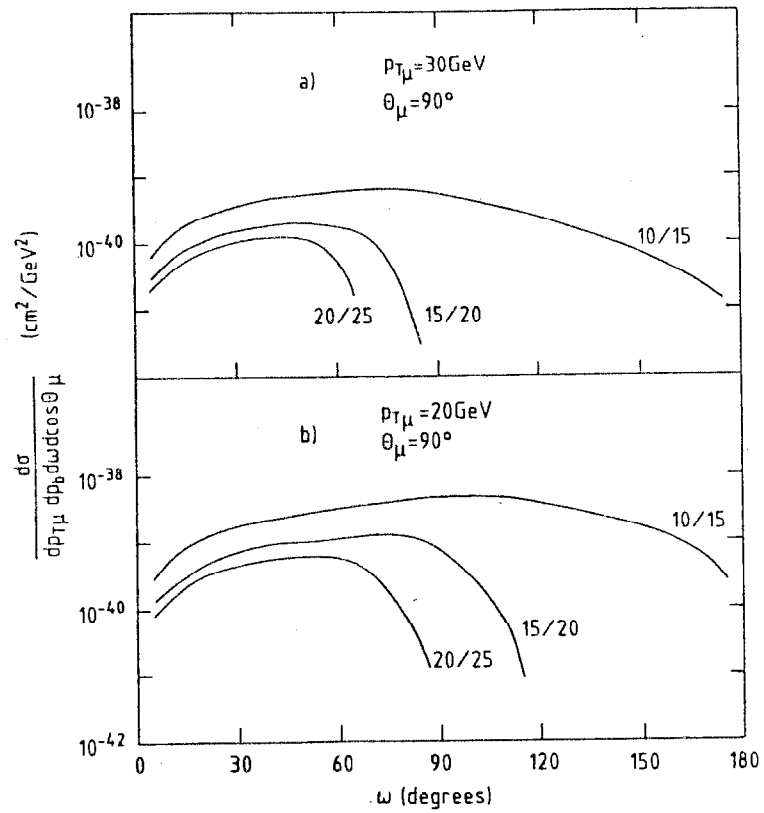


Fig. 21 - Angular distribution of the associated b jet with respect to the direction (here 90°) of the prompt lepton at large p_T, used as a trigger for $t \to e(\nu)$ b decay for different ranges of the b quark jet momentum.
21a : transverse lepton momentum of 30 GeV/c;
21b : transverse lepton momentum of 20 GeV/c.

Going further we may consider what may appear today as a fantasy and take an integrated luminosity at the 10^{38} level. In such a case the cross-section for W pair production would be within reach, as shown in Figure 22 if one could look for events with a leptonic and a non-leptonic decay. This might be elusive until the higher energy of Tevatron I brings up the rate at an acceptable value. On the way to W pair, one has, however, the $W\gamma$ cross-section with a high p_T photon (Fig. 22). This could be seen with an extra factor 10 in luminosity only. While it may seem not as interesting as W pair production, which checks the gauge coupling, it would provide a measurement of the W magnetic moment (an interesting point in connection with the observed $Z^o \to e^+e^-\gamma$ decay events).[68] If the electromagnetic coupling of the W is minimal, a spectacular dip structure should be seen in the angular distribution.[69] At the level of W pairs one also has Higgs production in association with Z, but only if the Higgs mass is of the order of 20 GeV or less. A very massive Higgs (200 GeV) could, on the other hand, be seen in the W^+W^- system.[67]

While the results already obtained at the collider can be rightfully considered as spectacular, one already feels a very strong limitation due to rates. It should be remarked that this limitation comes in some cases from the fact that the beautiful jet signal of today (Fig. 2c) is already a very embarrassing background when searching for other features. One has to lose on rate (looking for a large p_T lepton, a photon say) in order to limit the background. This should be meditated when considering the potential of colliders for exploring very short range structures at much higher energies.[70] One should be clever at selecting signals and dispose of high enough a luminosity to allow for special triggers.

4. - COLLIDER PHYSICS IN A GENERAL PERSPECTIVE

The analysis of the present data and the continuation of the collider runs at CERN over the coming years (Fig. 1) should allow for many further tests of the standard model which is based on the $SU(2)\times U(1)\times SU(3)$ gauge group. It is the basis for our present understanding of physics in the energy range probed so far, with centre-of-mass energy extending up to the 0.5 TeV level (>0.1 TeV at the constituent level). Surprises may appear. The top quark, if its mass is less than 50 GeV say, should be discovered. New phenomena may be discovered with increased statistics and precision. The analysis of prompt photon production may

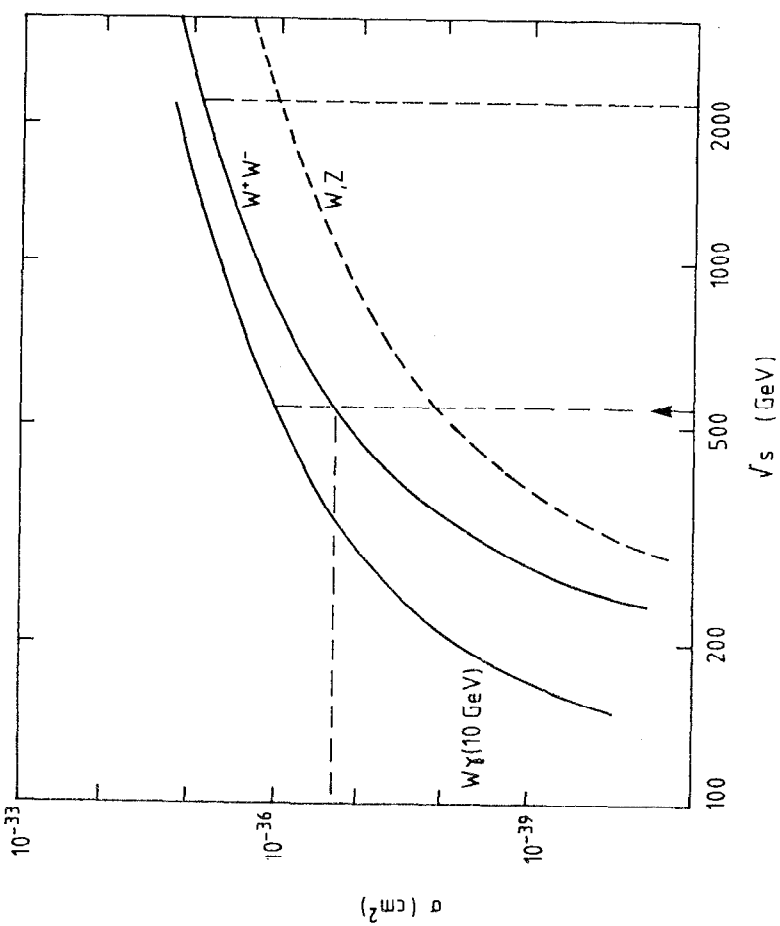


Fig. 22 - Expected rates for γW, W^+W^- and WZ production as a function of collider energy. Scaling violations are taken into account in the leading log approximation.

give interesting results.[7] Starting in '86-'87, Tevatron I will allow one to continue at much higher energies and provide a very strong competition to the extension of the CERN present programme (Fig. 1). This is an interesting challenge.

There are many open questions which may, however, require probing at still shorter distances and hence with much higher energies.

The list is now standard. It involves the question of symmetry breaking and therefore the role of scalars (the Higgs sector), the question of new fermions and new gauge bosons, the question of a possible substructure for quarks and leptons and of course the question of supersymmetric partners of present particles. But perhaps for the latter case, approaching these questions experimentally may require centre-of-mass energy at the constituent level in excess of 1 TeV and therefore collider energies in the range of 10 TeV or more. One would then use pp ($p\bar{p}$) collisions as an intense source of gluon-gluon interactions at very high energies. This is of course the reason for the present enthusiasm for a very high energy collider in the several tens of TeV ranges such as the SSC.

Without looking rather far, that is, well into the nineties, we have also, at the end of the eighties, the very exciting prospects offered by LEP (in its phase I then) and by SLC. These projects were to a large extent motivated by their providing a factory for Z^0 production. Now that the Z^0 has been discovered at the predicted mass, things are all the more interesting! While the present $p\bar{p}$ programme provides 10 (say) Z^0 per year in their e^+e^- mode, and could eventually provide 100 (Fig. 1), the expected luminosities of LEP and SLC are such that an experiment could collect 10^6 Z^0 events in a single run. We thus have a clear two-tier approach, $p\bar{p}$ colliders providing a first (and so far very successful) exploration and reaching very high energies, though with diminishing rates, while e^+e^- colliders will provide very high statistics for electroweak processes and this with the clarity associated with perfectly well defined initial conditions.

Focusing here on hadron machines and coming back to Figure 1, we have for the near future:

(i) the extension of the CERN programme with a centre-of-mass energy eventually increased from 540 to 620 GeV and a luminosity (averaged over a day) increasing to several times 10^{29}, maybe 10^{30};

(ii) the start of Tevatron I in '86-'87 with a centre-of-mass energy in the 1600-2000 GeV range and a design luminosity of the order of 10^{30}; and

(iii) the UNK machine, which in the nineties should work in a collider mode with centre-of-mass energy in the 2200-6000 GeV range and a high luminosity (10^{31}).

The presently proposed machines, CBA, a pp collider of very high luminosity (10^{33}) and 800 GeV of centre-of-mass energy, and the Fermilab dedicated collider, with a luminosity of 10^{31} in its $p\bar{p}$ mode and a centre-of-mass energy of 4000 GeV, have not recently found the type of support which their proponents requested. It seems that interest has shifted very quickly to much higher energies, where new grounds could be broken and entirely new physics could be probed. The clarity of the event structure met at present collider energy is certainly a key point in building the enthusiasm which now prevails. However, the impressive jet yield of today (and certainly of tomorrow) may soon appear as a background with which one has to fight when trying to see new signals associated with hitherto unknown phenomena [70]. The SSC, presently defined as a 40 TeV pp machine is now attracting a lot of interest as the new big project to be contemplated for the U.S. At CERN the possibility of installing superconducting magnets (10 Tesla is possible) in the LEP tunnel played a role reaching a consensus when choosing the large radius of the LEP machine. The success of the present $p\bar{p}$ programme has of course increased the number of supporters for such a scheme.

Very high energy pp ($p\bar{p}$) colliders in the ten or more TeV region have rapidly become most interesting contenders for the big new step in energy which presently appears as extremely promising in view of all the positive points scored by the standard model. The standard model has had indeed an amazing success. The questions which it raises are all the more fascinating. How far will one go? Figure 23 [71] shows the apparatus used by Hertz for his discovery of electromagnetic radiation almost a century ago. This was a brilliant success for predictions based on the unification of electricity and magnetism in the framework of Maxwell's theory. We have seen, presented several times, [2] the very powerful equipment used

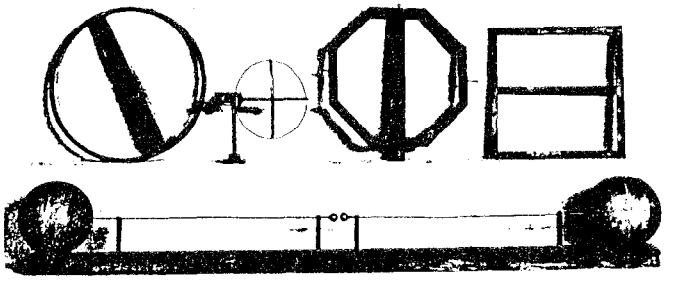


Fig. 23 - The apparatus with which Hertz discovered electromagnetic radiation almost a century ago, as displayed at the Science Museum in Munich.

a century later for the discovery of the W and Z radiations as predicted in the framework of the electroweak theory of Glashow, Weinberg and Salam. What shall our descendants consider a century from now?

ACKNOWLEDGEMENTS

I would like to thank many colleagues from UA1, UA2, UA4 and UA5 for frequent and stimulating discussions. The material presented in this talk which is new corresponds to a collaboration with R. Horgan.

I would like to express my thanks to F. Gilman and D. Leith for their organizing this very stimulating and pleasant meeting at SLAC.

REFERENCES

1) C. Rubbia, P. McIntyre and D. Cline, Proceedings International Neutrino Conference, Aachen 1976 (Vieweg, Braunschweig, 1977);
C. Rubbia, Proceedings EPS International Conference on High Energy Physics, Geneva 1979 (CERN, 1980);
The staff of the CERN $p\bar{p}$ project, Phys.Letters 107B (1981) 306;
For a review of stochastic cooling which played a key role in the development of the programme, see:
D. Möhl, G. Petrucci, L. Thorndahl and S. Van der Meer, Physics Reports 58 (1982) No 2, and
F.T. Cole and F.E. Mills, Ann.Rev.Nucl.Part.Sci. 31 (1981) 295.

2) One should consult the reports at this Conference by A. Honma (Jets; UA1); T. Hansl-Kozanecka (W,Z; UA1); J.P. Repellin (W,Z,jets; UA2), and D. Lissauer (Jets; R807,ISR).

3) Reports from UA1 and UA5 at the Topical Conference on Forward Collider Physics, Madison, WI (1981), AIP Conference Proceedings No 85, V. Barger, D. Cline and F. Halzen Eds. (1982).

4) G. Arnison et al., Phys.Letters 122B (1983) 103, UA1;
M. Banner et al., Phys.Letters 122B (1983) 476, UA2.

5) G. Arnison et al., Phys.Letters 126B (1983) 391, UA1;
P. Bagnaia et al., CERN-EP/83-112 (1983), UA2.

6) L. Lederman, Third Topical Workshop on $p\bar{p}$ Collider Physics, Rome 1981, G. Salvini Ed. (CERN, 1983);
C. Rubbia, Ibid;
Woodshole Panel Recommendations (1983);
ECFA Statement, as reported in CERN Courrier 7 (1983).

7) R. Horgan and M. Jacob, Proceedings of the CERN School, Malente 1980, CERN-81-04 (1981).
While we shall follow this reference, the anticipated physics programme was also much discussed in BNL reports, in connection with the Isabelle project, and in FNAL reports, in connection with the Tevatron project.
For a rapid overview, see:
M. Jacob, "$p\bar{p}$ from Very Low to Very High Energies", Los Alamos Workshop 1979, LA8335-C, Vol. III (1980).

8) C. Lattes, Y. Fujimoto and S. Hasegawa, Physics Reports 65 (1980), No 2.

9) The Tevatron I will operate at 1.6 to 2 TeV centre-of-mass energy. The CERN-SPS Collider will operate up to 620 GeV centre-of-mass energy.

10) K. Alpgard et al., Phys.Letters 115B (1982) 71;
G. Arnison et al., Phys.Letters 122B (1983) 189.

11) J.D. Bjorken and L.D. McLerran, Phys.Rev. D20 (1979) 2353.

12) T. Gaiser and G. Yodh, Ann.Rev.Nucl.Sci. 30 (1980) 475;
N. Arata, Comparison of C-Jet Events with Accelerator Results, CBPF, Rio de Janeiro (1982).

13) For a general review of physics at the ISR, see:
G. Giacomelli and M. Jacob, Physics Reports 55 (1979) No 1, and
G. Bellettini, Physics Reports, in preparation.

14) For recent jet results at the ISR, see the report of D. Lissauer quoted in Ref. 2).

15) For a detailed presentation of the key features of particle production at high energy, see:
D. Horn, Physics Reports 4 (1972) No 1;
L. Foà, Physics Reports 22 (1975) No 1.

16) K. Alpgard et al., Phys.Letters 107B (1981) 315, UA5.

17) G. Arnison et al., Phys.Letters 123B (1983) 103, UA1.

18) T.T. Chou and C.N. Yang, Phys.Rev. 170 (1968) 1591;
T.T. Chou and C.N. Yang, Phys.Letters 116B (1982) 301;
S. Barshay, Phys.Letters 42B (1972) 457.

19) G. Ekspong, Third Topical Workshop on $p\bar{p}$, Op.Cit in Ref. 6).

20) U. Amaldi et al., Ann.Rev.Nucl.Sci. 26 (1976) 187;
U. Amaldi and K. Shubert, Nuclear Phys. B145 (1978) 367.

21) R.N. Cahn, "Expectation for Old and New Physics at High Energy Colliders" LBL 15469 (1983), SLAC Summer Institute 1982.

22) R. Battison et al., Phys.Letters 117B (1982) 126, UA4.

23) G. Arnison et al., Phys.Letters, to be published, UA1.

24) R. Battiston et al., Phys.Letters 127B (1983) 472, UA4.

25) A. Donnachie and P.V. Landshoff, DAMTP Preprint (1983).

26) For a comparison between ISR pp and $p\bar{p}$ results, see:
M. Jacob, Physics in Collision No 2, Stockholm, 1982 (Plenum, 1983);
N. Amos et al., Phys.Letters 120B (1983) 460.

27) R. Battiston et al., Phys.Letters 115B (1982) 333, and Refs. 22 and 24, UA4.

28) G. Arnison et al., Phys.Letters 121B (1983) 77, UA1.

29) G. Arnison et al., Phys.Letters 118B (1982) 167, UA1.

30) A. Breakstone et al., Contribution to the High Energy Physics Conference, Brighton (1983).

31) M. Jacob, Third Topical Workshop on $p\bar{p}$, Op.Cit. in Ref. 6).

32) A. Bassetto, M. Ciafaloni and G. Marchesini, Physics Reports, to be published (1983);
L. Gribov, E. Levin and M. Ryuskin, Physics Reports, to be published (1983).

33) M. Colvetti, Third Topical Workshop on $p\bar{p}$, Op.Cit. in Ref. 6);
C. Conta, Ibid;
D. Ward and G. Ekspong, Ibid.

34) See Ref. 7) and F.E. Paige and S.D. Protopescu, Isajet Program BNL 29777 (1981) for estimates in the leading log approximation;
See also the early parton model calculation of C. Quigg, Rev.Mod.Phys. 49 (1977) 297.

35) The mean value of $\cos\theta$, where θ is the angle between the electron and the proton direction in the W frame, should be $\langle\cos\theta\rangle = \langle\lambda\rangle\langle\mu\rangle/J(J+1)$, with $\langle\lambda\rangle = \langle\mu\rangle = -1$ and $J = 1$ for a spin 1 W with V-A couplings. The general formula is derived in M. Jacob, Nuovo Cimento 9 (1958) 826. Angular distributions for e are given in G. Goggi, Physics in Collisions I, 1981 (Plenum, 1982).

36) F. Halzen, A.D. Martin and D.M. Scott, Phys.Letters 112B (1982) 160;
P. Aurenche and J. Lindfors, Nuclear Phys. B185 (1981) 274.

37) LEP Summer Study, Les Houches and CERN (1978), CERN 79-01 (1979).

38) M. Jacob and P.V. Landshoff, Phys. Rep. 48, No. 4 (1978);
P. Darriulat, Ann. Rev. Nucl. Part. Sci. 30, (1980) 159;
Jets in High Energy Collisions, Physicia Scripta 19 (1979) K. Hansen and P. Hoyes, Ed.

39) R.P. Feynman, Photon-Hadron Interactions, Benjamin (1972).

40) S.M. Berman, J.D. Björken and J.B. Kogut, Phys.Rev. 4D (1971) 3388.

41) S.M. Berman and M. Jacob, Phys.Rev.Letters 25 (1970) 1683.

42) G. Altarelli, Third Topical Workshop on $p\bar{p}$, Op.Cit. in Ref. 6).

43) R. Horgan and M. Jacob, Nuclear Phys. B179 (1981) 441; see also Ref. 7);
R. Field, La Jolla Summer Institute, 1978, AIP Conference Proceedings 53 (1979). This paper reviews in particular the important work of R.P. Feynman, R. Field and G. Fox on large p_T particle and jet production.

44) G. Arnison et al., Phys.Letters 123B (1983) 115, UA1, and report of A. Honma, Ref. 2).

45) M. Banner et al., Phys.Letters 118B (1982) 203, UA2, and report of J.P. Repellin, Ref. 2).

46) N.G. Antoniou et al., Phys.Letters 128B (1983) 257;
W. Furmanski and H. Kowalski, Nuclear Phys. B, to be published;
Z. Kunszt and E. Pietarinen, CERN Preprint TH. 3584 (1983), and Ref. 43) for predictions.

47) T. Akesson et al., Phys.Letters 123B (1983) 133, and report by D. Lissauer, Ref. 2).

48) G. Wolf, Rapporteur talk, Proceedings International Conference on High Energy Physics, Paris (1982);
R. Hollebeck, Lecture Notes, SLAC Summer Institute (1983), these Proceedings.

49) S. Ellis et al., Nuclear Phys. B108 (1976) 93;
M. Jacob and P.V. Landshoff, Nuclear Phys. B113 (1976) 395;
See also: R. Field, Ref. 43).

50) P. Bagnaia et al., CERN-EP/83-94 (1983), Z.Phys.C., to be published.

51) A.P. Contogouris and M. Sanielevici, CERN Preprint TH. 3656 (1983).

52) See the reviews on ISR Physics by:
L. Camillieri, Madison Topical Conference, Op.Cit. in Ref. 3) and Third Topical Conference on $p\bar{p}$ Collider Physics, Op.Cit. in Ref. 6). Recent results from R806/R807 and R108/R110 at the ISR.

53) Ref. 50) (UA2) and C. Rubbia, Third Topical Conference on $p\bar{p}$ Collider Physics, Op.Cit. in Ref. 6 (UA1).

54) For jet yields, see Ref. 47). For single particle yields, see:
A. Angelis et al., Phys.Letters 79B (1978) 505;
A. Clark et al., Phys.Letters 74B (1978) 267;
C. Kourkoumelis et al., Phys.Letters 84 (1979) 271.

55) C. Bromberg et al., Phys.Rev.Letters 38 (1977) 1447; Nuclear Phys. B134 (1978) 189;
J. Rohlf, Caltech Thesis (1980).

56) K. Pretzl, Madison Topical Conference, Op.Cit. in Ref. 3);
J. Seyboth, Proceedings International Conference on High Energy Physics, Madison, WI (1980).

57) Z. Kunszt and E. Pietarinen, Ref. 46).

58) B. Humpert, Private communication, to be published.

59) P.V. Landshoff and J. Polkinghorne, Phys.Rev. D12 (1975) 3738;
N. Power and D. Treleani, Trieste Preprints (1982);
B. Humpert, Phys.Letters, to be published (1983).

60) D. Scott, Madison Topical Conference, Op.Cit. in Ref. 3);
R. Horgan and M. Jacob, Kupari Lecture Notes (1981).

61) S. Pakvasa et al., Phys.Rev. D20 (1979) 2862.

62) J. Ellis et al., Phys.Letters 127B (1983) 233;
R. Barbieri et al., Phys.Letters 127B (1983) 458;
J. Ellis et al., Supersymmetry Confronting Experiment, Physics Reports, to be published.

63) D. Scott in Ref. 60);
A. Martin, Contribution to the Moriond Meeting (1983), and references therein;
R. Horgan and M. Jacob, Phys.Letters 107B (1981) 395;
D. Denegri, Private communication.

64) The electron from b decay can reach the limit of phase space whereas the positron from c or t decay cannot. This results from the V-A nature of the coupling. Hence b quarks are particularly efficient at giving prompt leptons at high p_T.

65) R. Horgan and M. Jacob, CERN Preprint TH. 3682 (1983).

66) J. Ellis et al., First Ref. 62).

67) J. Stroughair, C. Bilchok and R.W. Brown, Case Western Reserve Preprint, to be published;
B. Humpert, Private communication, to be published.
The curves in Fig. 22 are those of B. Humpert.

68) See Ref. 5). One event in each (small) sample corresponds to $Z^o \; e^+e^-\gamma$ decay with a large momentum γ ray corresponding to a bremsstrahlung probability at the per cent level only! One thus cannot exclude yet a peculiar electromagnetic coupling of the gauge bosons though such a departure from the standard model looks very unlikely in view of the present successes. I am indebted to T.D. Lee for a discussion on that point.

69) R. Brown, K. Kowalski and S. Brodsky, Fermilab Pub 82/102, to be published. I am indebted to S. Brodsky for a discussion on that point.

70) I am indebted to M. Peskin for a discussion on that point. The signal of today will be the background of tomorrow!

71) L. Van Hove and M. Jacob, Physics Reports 62 (1980) No 1.

SLAC SUMMER INSTITUTE PARTICIPANTS

1983

R. Akhoury
Department of Physics
University of California
Los Angeles, California 90024

Dan Amedei
Trilling-Goldhaber Group
Bldg. 50A, Rm. 2160
Lawrence Berkeley Laboratory
One Cyclotron Road
Berkeley, California 94720

Dikran Antreasyan
SLAC, Bin 98
Stanford University
Stanford, California 94305

Hideaki Aoyama
SLAC, Bin 81
Stanford University
Stanford, California 94305

David Aschman
Physics Department
University of Capetown
Capetown, SOUTH AFRICA

William Ash
SLAC, Bin 94
Stanford University
Stanford, California 94305

Victor Ashford
SLAC, Bin 62
Stanford University
Stanford, California 94305

William Atwood
SLAC, Bin 96
Stanford University
Stanford, California 94305

Naoki Awaji
SLAC, Bin 62
Stanford University
Stanford, California 94305

Kaladi Babu
Department of Physics
University of Hawaii at Manoa
Honolulu, Hawaii 96822

Joe Ballam
SLAC, Bin 78
Stanford University
Stanford, California 94305

Henry Band
SLAC, Bin 94
Stanford University
Stanford, California 94305

Gregory Baranko
SLAC, Bin 20
Stanford University
Stanford, California 94305

Phillip Baringer
SLAC, Bin 20
Stanford University
Stanford, California 94305

Alan Barnes
Bldg. 50, Rm. 137
Lawrence Berkeley Laboratory
One Cyclotron Road
Berkeley, California

Michael Barnett
SLAC, Bin 81
Stanford University
Stanford, California 94305

Gabor Bartha
SLAC, Bin 95
Stanford University
Stanford, California 94305

Alfred Bartl
Institut fuer Theoretische Physik
der Universitat Wien
A-1090 Wien, Boltzmanngasse 5
AUSTRIA

Fernando Bazan
552 Everett Avenue Apt. 3
Palo Alto, California 94301

Jeff Becker
SLAC, Bin 65
Stanford University
Stanford, California 94305

I. Beltrami
SLAC, Bin 37
Stanford University
Stanford, California 94305

Dave Bennett
SLAC, Bin 81
Stanford University
Stanford, California 94305

Didier Besset
SLAC, Bin 98
Stanford University
Stanford, California 94305

Johan Bijnens
California Institute of Technology
Lauritsen Lab
256-48
Pasadena, California 91125

H.H. Bingham
301 Le Conte Hall
University of California
Berkeley, California 94720

Fred Bird
SLAC, Bin 62
Stanford University
Stanford, California 94305

Guy Blaylock
SLAC, Bin 65
Stanford University
Stanford, California 94305

David Blockus
SLAC, Bin 43
Stanford University
Stanford, California 94305

Horst Blume
SLAC, Bin 43
Stanford University
Stanford, California 94305

Kersten Braune
SLAC, Bin 78
Stanford University
Stanford, California 94305

Marty Breidenbach
SLAC, Bin 95
Stanford University
Stanford, California 94305

Stan Brodsky
SLAC, Bin 81
Stanford University
Stanford, California 94305

John S. Brown
SLAC, Bin 43
Stanford University
Stanford, California 94305

Charles Buchanan
Physics Department
UCLA
405 Hilgard Avenue
Los Angeles, California 90024

Adriaan Buijs
SLAC, Bin 43
Stanford University
Stanford, California 94305

Fatin Bulos
SLAC, Bin 98
Stanford University
Stanford, California 94305

Kirk Bunnell
SLAC, Bin 65
Stanford University
Stanford, California 94305

Patricia Burchat
SLAC, Bin 61
Stanford University
Stanford, California 94305

David Burke
SLAC Bin 61
Stanford University
Stanford, California 94305

Toby Burnett
SLAC, Bin 65
Stanford University
Stanford, California 94305

Frederick Butler
Trilling-Goldhaber Group
Bldg. 50A, Rm. 2160
Lawrence Berkeley Laboratory
One Cyclotron Road
Berkeley, California 94720

John Butler
SLAC, Bin 78
Stanford University
Stanford, California 94305

Kevin Cahill
SLAC, Bin 81
Stanford University
Stanford, California 94305

Robert Cahn
Bldg. 50A, Rm. 3115
Lawrence Berkeley Laboratory
One Cyclotron Road
Berkeley, California 94720

Michael Cain
SLAC, Bin 43
Stanford University
Stanford, California 94305

Terry Carroll
SLAC, Bin 78
Stanford University
Stanford, California 94305

Mark Carter
SLAC, Bin 80
Stanford University
Stanford, California 94305

Ron Cassell
SLAC, Bin 65
Stanford University
Stanford, California 94305

Matteo Cavalli
SLAC, Bin 98
Stanford University
Stanford, California 94305

Selcuk Cihangir
Department of Physics
University of Illinois
1110 W. Green Street
Urbana, Illinois 61801

Bob Clare
SLAC, Bin 98
Stanford University
Stanford, California 94305

Daniel M. Coffman
SLAC, Bin 65
Stanford University
Stanford, California 94305

Robert Cousins
Department of Physics
UCLA
Los Angeles, California 90024

Ray Cowan
SLAC, Bin 98
Stanford University
Stanford, California 94305

David Coward
SLAC, Bin 65
Stanford University
Stanford, California 94305

John D'Amore
SLAC, Bin 62
Stanford University
Stanford, California 94305

Farhad Daghighian
Physics Department
University of California at Irvine
Irvine, California 92717

Denny Dahl
SLAC, Bin 81
Stanford University
Stanford, California 94305

Manuel Delfino
SLAC, Bin 43
Stanford University
Stanford, California 94305

Kevin Derby
50B-5239
Lawrence Berkeley Laboratory
One Cyclotron Road
Berkeley, California 94720

Malcolm Derrick
SLAC, Bin 78
Stanford University
Stanford, California 94305

Herbert De Staebler
SLAC, Bin 96
Stanford University
Stanford, California 94305

Jonathan Dorfan
SLAC, Bin 95
Stanford University
Stanford, California 94305

Yi-shi Duan
SLAC, Bin 81
Stanford University
Stanford, California 94305

Richard DuBois
SLAC, Bin 96
Stanford University
Stanford, California 94305

Ian Duck
Department of Physics
Rice University
Houston, Texas 77251

Alan Duncan
SLAC, Bin 43
Stanford University
Stanford, California 94305

William Dunwoodie
SLAC, Bin 62
Stanford University
Stanford, California 94305

Marsha Duro
SLAC, Bin 63
Stanford University
Stanford, California 94305

Stan Ecklund
SLAC, Bin 60
Stanford University
Stanford, California 94305

Chad Edwards
358-48
CALTECH
Pasadena, California 91125

Richard Ehrlich
c/o Wilson Laboratory, CESR
Cornell University
Ithaca, New York 14853

Estia Eichten
Theory Group
Fermilab
P.O. Box 500
Batavia, Illinois 60510

Kevin Einsweiler
SLAC, Bin 65
Stanford University
Stanford, California 94305

John Ellis
CERN- TH
CH-1211, Geneva 23
SWITZERLAND

Steve Ellis
Department of Physics, FM-15
University of Washington
Seattle, Washington 98195

Eckhard Elsen
SLAC, Bin 96
Stanford University
Stanford, California 94305

Paul Ensign
University of Colorado
Physics Department
Boulder, Colorado 80309

Steve Errede
SLAC, Bin 37
Stanford University
Stanford, California 94305

Gregory Eyink
Ohio State University
Department of Physics
Columbus, Ohio 43210

Enrique Fernandez
SLAC, Bin 43
Stanford University
Stanford, California 94305

R. Clive Field
SLAC, Bin 78
Stanford University
Stanford, California 94305

Curt Flory
SLAC, Bin 81
Stanford University
Stanford, California 94305

Geoffrey Forden
SLAC, Bin 20
Stanford University
Stanford, California 94305

Thomas A. J. Frank
Massachusetts Institute of Technology
Laboratory of Nuclear Science
Room 408, 575 Tech Square
Cambridge, Massachusetts 02139

Dieter Freytag
SLAC, Bin 51
Stanford University
Stanford, California 94305

John Gaiser
SLAC, Bin 98
Stanford University
Stanford, California 94305

Peter Galison
Lyman Laboratory of Physics
Harvard University
Cambridge, Massachusetts 02138

K. K. Gan
SLAC, Bin 37
Stanford University
Stanford, California 94305

Margaret Garnjost
50B - 5239
Lawrence Berkeley Laboratory
One Cyclotron Road
Berkeley, California 94720

Lynn Garren
Wilson Laboratory
Cornell Univesity
Ithaca, New York 14853

Bill Gary
50B- 5239
Lawrence Berkeley Laboratory
One Cyclotron Road
Berkeley, California 94720

Roger Gearhart
SLAC, Bin 20
Stanford University
Stanford, California 94305

David Gelphman
SLAC, Bin 98
Stanford University
Stanford, California 94305

Murdock Gilchriese
Department of Physics
Cornell University
Ithaca, New York 14853

Fred Gilman
SLAC, Bin 80
Stanford University
Stanford, California 94305

Larry Gladney
SLAC, Bin 95
Stanford University
Stanford, California 94305

Tom Glanzman
SLAC, Bin 78
Stanford University
Stanford, California 94305

Gary Godfrey
SLAC, Bin 98
Stanford University
Stanford, California 94305

Lawrence Godfrey
Department of Physics
SUNY, Stony Brook
Long Island, New York 11794

Jack Goldberg
SLAC, Bin 78
Stanford University
Stanford, California 94305

Bill Goldstein
SLAC, Bin 80
Stanford University
Stanford, California 94305

Richard Gonsalves
Department of Physics and Astronomy
State University of New York at Buffalo
Buffalo, New York 14260

Steve Gray
SLAC, Bin 37
Stanford University
Stanford, California 94305

Joe Gress
Physics Department
Kansas University
Lawrence, Kansas 66044

Paul Griffin
SLAC, Bin 61
Stanford University
Stanford, California 94305

Howard Haber
SLAC, Bin 81
Stanford University
Stanford, California 94305

Traudl Hansl-Kozanecka
CERN
Ch-1211, Geneva 23
SWITZERLAND

Gail Hanson
SLAC, Bin 61
Stanford University
Stanford, California 94305

Hirofumi Hayashi
Department of Physics
Faculty of Education
Shizuoka University
Shizuoka 422
JAPAN

Kenneth Hayes
SLAC, Bin 61
Stanford University
Stanford, California 94305

Brian Heltsley
SLAC, Bin 94
Stanford University
Stanford, California 94305

Werner Hofmann
Bldg. 50B, Rm. 6208
Lawrence Berkeley Laboratory
One Cyclotron Road
Berkeley,California 94720

Robert Hollebeek
SLAC, Bin 95
Stanford University
Stanford, California 94305

Alan Honma
EP Division
UA1 Experiment
CERN
CH-1211, Geneva 23
SWITZERLAND

Roland Horisberger
Hansen Labs
Stanford University
Stanford, California 94305

Kent Hornbostel
SLAC, Bin 81
Stanford University
Stanford, California 94305

James Horstkotte
SBU Group
Wilson Laboratory
Cornell University
Ithaca, New York 14853

David Hutchinson
SLAC, Bin 65
Stanford University
Stanford, California 94305

Jim Hylen
SLAC, Bin 43
Stanford University
Stanford, California 94305

Walter Innes
SLAC, Bin 61
Stanford University
Stanford, California 94305

Achim Irion
SLAC, Bin 98
Stanford University
Stanford, California 94305

George Irwin
SLAC, Bin 63
Stanford University
Stanford, California 94305

Maurice Jacob
Theory Division
CERN
CH-1211, Geneva 23
SWITZERLAND

John Jaros
SLAC, Bin 61
Stanford University
Stanford, California 94305

Abolhassan Jawahery
Wilson Laboratory
Cornell University
Ithaca, New York 14850

Chueng Ryong Ji
SLAC, Bin 80
Stanford University
Stanford, California 94305

Kenneth Johns
Bonner Laboratories
Rice University
P.O. Box 1892
Houston, Texas 77251

Jim Johnson
SLAC, Bin 94
Stanford University
Stanford, California 94305

Robert Johnson
SLAC, Bin 96
Stanford University
Stanford, California 94305

M. Jonker
SLAC, Bin 95
Stanford University
Stanford, California 94305

C. Jung
SLAC, Bin 37
Stanford University
Stanford, California 94305

Ivanna Juricic
Bldg. 50A, Rm. 2160
Lawrence Berkeley Laboratory
One Cyclotron Road
Berkeley, California 94720

Vadim Kalmeyer
SLAC, Bin 96
Stanford University
Stanford, California 94305

Vadim Kaplunovsky
SLAC, Bin 81
Stanford University
Stanford, California 94305

Dean Karlen
SLAC, Bin 95
Stanford University
Stanford, California 94305

Inga Karliner
Department of Physics
University of Illinois
Urbana, Illinois 61801

Steve Kaye
SLAC, Bin 94
Stanford University
Stanford, California 94305

Lew Keller
SLAC, Bin 20
Stanford University
Stanford, California 94305

David P. Kelsey
SLAC, Bin 78
Stanford University
Stanford, California 94305

Robert Kenney
Bldg. 50A, Rm. 6141
Lawrence Berkeley Laboratory
One Cyclotron Road
Berkeley, California 94720

Ian Kirkbride
Hansen Labs
Stanford University
Stanford, California 94305

Jasper Kirkby
SLAC, Bin 63
Stanford University
Stanford, California 94305

Spencer Klein
SLAC, Bin 61
Stanford University
Stanford, California 94305

Daniel Klem
SLAC, Bin 96
Stanford University
Stanford, California 94305

Jürgen Koerner
SLAC, Bin 81
Stanford University
Stanford, California 94305

P. Kooijman
SLAC, Bin 78
Stanford University
Stanford, California 94305

Dale Koop
SLAC, Bin 63
Stanford University
Stanford, California 94305

Hermann Kuester
DESY
Notkestrasse 85
D-2000, Hamburg 52
GERMANY

Paul Kunz
SLAC, Bin 62
Stanford University
Stanford, California 94305

Klaus Lackner
SLAC, Bin 81
Stanford University
Stanford, California 94305

Karol Lang
M.S. 210, E-701
Fermilab
P.O. Box 500
Batavia, Illinois 60510

Andrew Lankford
SLAC, Bin 95
Stanford University
Stanford, California 94305

Rudolf Larsen
SLAC, Bin 95
Stanford University
Stanford, California 94305

Ken Lassila
Department of Physics
Iowa State University
Ames, Iowa 50011

Kwong Lau
SLAC, Bin 94
Stanford University
Stanford, California 94305

Ted Lavine
SLAC, Bin 94
Stanford University
Stanford, California 94305

Jacques Layssac
SLAC, Bin 80
Stanford University
Stanford, California 94305

Paul Lebrun
Fermilab, MS 219
P.O. Box 500
Batavia, Illinois 60510

Bruce LeClaire
SLAC, Bin 95
Stanford University
Stanford, California 94305

Roger Lee
SLAC, Bin 98
Stanford University
Stanford, California 94305

Juliet Lee-Franzini
c/o Wilson Laboratory
Cornell University
Ithaca, New York 14853

John (Steve) Leffler
SLAC, Bin 98
Stanford University
Stanford, California 94305

David W.G.S. Leith
SLAC, Bin 62
Stanford University
Stanford, California 94305

Georg Lenzen
EP Division
CERN
CH-1211, Geneva 23
SWITZERLAND

Michael Levi
SLAC, Bin 95
Stanford University
Stanford, California 94305

Steve Linn
Department of Physics
SUNY, Stony Brook
Long Island, New York 11794

David Lissauer
c/o William Willis
EP Division
CERN
CH-1211, Geneva 23
SWITZERLAND

Alan Litke
SLAC, Bin 98
Stanford University
Stanford, California 94305

Bill Lockman
SLAC, Bin 98
Stanford University
Stanford, California 94305

Nigel Lockyer
SLAC, Bin 95
Stanford University
Stanford, California 94305

Erich Lohrmann
DESY
Notkestrasse 85
D-2000, Hamburg 52
GERMANY

Stewart Loken
Bldg. 50, Rm. 137
Lawrence Berkeley Laboratory
One Cyclotron Road
Berkeley, California 94720

Sherwin Love
Department of Physics
Purdue University
West Lafayette, Indiana 47907

Steve Lowe
SLAC, Bin 98
Stanford University
Stanford, California 94305

Bin Lu
SLAC, Bin 43
Stanford University
Stanford, California 94305

Vera Luth
SLAC, Bin 95
Stanford University
Stanford, California 94305

Usha Mallik
SLAC, Bin 37
Stanford University
Stanford, California 94305

Aneesh Manohar
Lyman Laboratory of Physics
Harvard University
Cambridge, Massachusetts 02138

Bruno Mansoulie
CEN-SACLAY
CEN-S DPh-PE-See
91191 Gif-sur-YVETTE CEDEX
FRANCE

Emil Martinec
SLAC, Bin 81
Stanford University
Stanford, California 94305

Takashi Maruyama
SLAC, Bin 94
Stanford University
Stanford, California 94305

John Matthews
SLAC, Bin 43
Stanford University
Stanford, California 94305

Clara Matteuzzi
SLAC, Bin 61
Stanford University
Stanford, California 94305

Michael Mattis
SLAC, Bin 81
Stanford University
Stanford, California 94305

Hugh McCann
DESY F22
Notkestrasse 85
Hamburg 52
WEST GERMANY

Roger McNeil
SLAC, Bin 43
Stanford University
Stanford, California 94305

Brian Meadows
SLAC, Bin 62
Stanford University
Stanford, California 94305

K. Meier
DESY-F11
Notkestrasse 85
D-2000 Hamburg 52
WEST GERMANY

Robert Messner
SLAC, Bin 94
Stanford University
Stanford, California 94305

Adolf G. Minten
CERN
CH-1211, Geneva 23
SWITZERLAND

Akiya Miyamoto
SLAC, Bin 62
Stanford University
Stanford, California 94305

Michiko Miyamoto
11-2, 1-chome
Yamate, Nakasuji
Takarazuka City
Hyogo Prefecture
JAPAN 665

Paul Mockett
Department of Physics
University of Washington
Seattle, Washington 98195

Ken Moffeit
SLAC, Bin 78
Stanford University
Stanford, California 94305

Akbar Mokhtarani
Department of Physics
University of California at Davis
Davis, California 95616

W.R. Moreau
Department of Physics
University of Canterbury
Christchurch 1
New Zealand

Robert Mozley
SLAC, Bin 65
Stanford University
Stanford, California 94305

James Mueller
SLAC, Bin 78
Stanford University
Stanford, California 94305

Itsuo Nakano
University of Tsukuba
Institute of Physics
Ibaraki, 305
JAPAN

Aniello Nappi
SLAC, Bin 43
Stanford University
Stanford, California 94305

Marissa Nappi
SLAC, Bin 78
Stanford University
Stanford, California 94305

Paolo Nason
SLAC, Bin 81
Stanford University
Stanford, California 94305

Mark Nelson
Trilling-Goldhaber Group
Bldg. 50A, Rm. 2160
Lawrence Berkeley Laboratory
One Cyclotron Road
Berkeley, California 94720

C. Ray Ng
SLAC, Bin 37
Stanford University
Stanford, California 94305

Carol Nichols
Department of Physics
University of California at Davis
Davis, California 95616

Allen Odian
SLAC, Bin 65
Stanford University
Stanford, California 94305

Arthur Ogawa
SLAC, Bin 96
Stanford University
Stanford, California 94305

Harold Ogren
SLAC, Bin 20
Stanford University
Stanford, California 94305

Chong-Leong Ong
SLAC, Bin 80
Stanford University
Stanford, California 94305

Rene Ong
SLAC, Bin 61
Stanford University
Stanford, California 94305

Mark Oreglia
Enrico Fermi Institute
University of Chicago
5630 S. Ellis Avenue
Chicago, Illinois 60637

Albert Osterheld
Hansen Labs
Stanford University
Stanford, California 94305

Hitoshi Ozaki
Nagoya University
Physics Department
Chikusa-ku
Nagoya 464
JAPAN

Trivan Pal
California Institute of Technology
Lauritsen Laboratory
High Energy Physics
Pasadena, California 91125

Wolfgang K. H. Panofsky
SLAC, Bin 80
Stanford University
Stanford, California 94305

Vittorio Paolone
Department of Physics
University of California at Davis
Davis, California 95616

Sherwood Parker
SLAC, Bin 43
Stanford University
Stanford, California 94305

Hossein Partovi
Physics Department
California State University
Sacramento,California 95825

Giampiero Passarino
SLAC, Bin 80
Stanford University
Stanford, California 94305

Martin Perl
SLAC, Bin 61
Stanford University
Stanford, California 94305

Jacques Perrier
SLAC, Bin 65
Stanford University
Stanford, California 94305

Ida Peruzzi
SLAC, Bin 94
Stanford University
Stanford, California 94305

Michael Peskin
SLAC, Bin 81
Stanford University
Stanford, California 94305

Thomas Phillips
P.O. Box 3431
Park City, Utah 84060

Marcello Piccolo
INFN
Lab. Nazionali di Frascati
Casella Postale 13
I-00044 Frascati (ROMA)
ITALY

W. Rainer Pitthan
SLAC, Bin 96
Stanford University
Stanford, California 94305

Scott Plaetzer
SLAC, Bin 65
Stanford University
Stanford, California 94305

David L. Pollard
SLAC, Bin 63
Stanford University
Stanford, California 94305

Brian Pollock
Hansen Labs
Stanford University
Stanford, California 94305

Jean Potvin
University of Colorado
Department of Physics
Boulder, Colorado 80309

Christian Preitschopf
Physics Department
Varian Building
Stanford University
Stanford, California 94305

Giuliano Preparata
Dipartiment di Fisica
Universita di Bari
Via Amendola 173
BARI-ITALY

Richard Prepost
SLAC, Bin 94
Stanford University
Stanford, California 94305

Charles Prescott
SLAC, Bin 96
Stanford University
Stanford, California 94305

John Price
SLAC, Bin 61
Stanford University
Stanford, California 94305

L. Price
SLAC, Bin 78
Stanford University
Stanford, California 94305

Giovanni M. Prosperi
Dip. Di Fisica
University Di Milano
ITALY

Nading Qi
SLAC, Bin 43
Stanford University
Stanford, California 94305

Sijin Qian
Department of Physics
Illinois Institute of Technology
Chicago, Illinois 60616

Helen Quinn
SLAC, Bin 81
Stanford University
Stanford, California 94305

Jeff Ransdell
EP Division
CERN
CH-1211, Geneva 23
SWITZERLAND

Blair Ratcliff
SLAC, Bin 62
Stanford University
Stanford, California 94305

Peter Ratoff
SLAC, Bin 98
Stanford University
Stanford, California 94305

Bharat Ratra
SLAC, Bin 81
Stanford University
Stanford, California 94305

Alex Read
SLAC, Bin 43
Stanford University
Stanford, California 94305

Zbigniew Rek
SLAC, Bin 81
Stanford University
Stanford, California 94305

Fernand Renard
SLAC, Bin 81
Stanford University
Stanford, California 94305

Mary Reno
SLAC, Bin 81
Stanford University
Stanford, California 94305

Jean Paul Repellin
EP Division
UA2 Experiment
CERN
CH-1211, Geneva 23
SWITZERLAND

Sun-Hong Rhie
SLAC, Bin 81
Stanford University
Stanford, California 94305

J.A. Richardson
CERN
Laboratorie 1
CH-1211, Geneva 23
SWITZERLAND

Jeff Richman
SLAC, Bin 65
Stanford University
Stanford, California 94305

Burton Richter
SLAC, Bin 7
Stanford University
Stanford, California 94305

Keith Riles
SLAC, Bin 95
Stanford University
Stanford, California 94305

David Ritson
SLAC, Bin 94
Stanford University
Stanford, California 94305

Leon S. Rochester
SLAC, Bin 96
Stanford University
Stanford, California 94305

Natalie Roe
SLAC, Bin 61
Stanford University
Stanford, California 94305

Francesco Ronga
SLAC, Bin 94
Stanford University
Stanford, California 94305

Mark Ross
SLAC, Bin 95
Stanford University
Stanford, California 94305

Ron Ross
50B - 5239
Lawrence Berkeley Laboratory
One Cyclotron Road
Berkeley, California 94720

Forest Rouse
Bldg. 50A, Rm. 5123
Lawrence Berkeley Laboratory
One Cyclotron Road
Berkeley, California 94720

Peter Rowson
50A-2160
Lawrence Berkeley Laboratory
One Cyclotron Road
Berkeley, California 94720

Chris Sachrajda
SLAC, Bin 81
Stanford University
Stanford, California 94305

M. H. Saffouri
International Center for
Theoretical Physics
P.O. Box 586
34100 Trieste, ITALY

Makoto Sakuda
Department of Physics
256-48
Cal Tech
Pasadena, California 91125

Rudolf Saly
Department of Physics
Carleton University
Ottawa, Canada K1S 5B6

Bruce Sawhill
SLAC, Bin 81
Stanford University
Stanford, California 94305

Theo Schaad
SLAC, Bin 95
Stanford University
Stanford, California 94305

Heidi Schellman
SLAC, Bin 95
Stanford University
Stanford, California 94305

Bert Schwarzchild
Physics Today
335 East 45th Street
New York, New York 10017

Roy Schwitters
Department of Physics
Harvard University
Cambridge, Massachusetts 02138

Sally Seidel
University of Michigan
The Harrison M. Randall Lab.
Ann Arbor, Michigan 48109

Paul Sheldon
SLAC, Bin 95
Stanford University
Stanford, California 94305

Dave Sherden
SLAC, Bin 60
Stanford University
Stanford, California 94305

Toshiro Shimomura
SLAC, Bin 62
Stanford University
Stanford, California 94305

Joel Shurkin
Campus Report
Stanford University
Stanford, California 94305

Constantine Simopolous
SLAC, Bin 65
Stanford University
Stanford, California 94305

Pekka Sinervo
SLAC, Bin 62
Stanford University
Stanford, California 94305

Paul Singer
Department of Physics
TECHNION-Israel Institute of Technology
Haifa, ISRAEL

John Slate
Department of Physics
Michigan State University
East Lansing, Michigan 48824

John Sleeman
SLAC, Bin 65
Stanford University
Stanford, California 94305

Arthur Snyder
Wilson Laboratory
Cornell University
Ithaca, New York 14853

Mark Soldate
SLAC, Bin 81
Stanford University
Stanford, California 94305

Amarjit Soni
Department of Physics
University of California
Los Angeles, California 90024

Anthony Spadafora
SLAC, Bin 65
Stanford University
Stanford, California 94305

Thomas R. Steele
SLAC, Bin 95
Stanford University
Stanford, California 94305

Lynn Stevenson
Bldg. 50B, Rm. 5239
Lawrence Berkeley Laboratory
One Cyclotron Road
Berkeley, California 94720

David Stoker
Bldg. 50, Rm. 137
Lawrence Berkeley Laboratory
One Cyclotron Road
Berkeley, California 94720

Ryszard Stroynowski
248-56
Department of Physics
Cal Tech
Pasadena, California 91125

Lawrence Sulak
Department of Physics
Unversity of Michigan
Ann Arbor, Michigan 48109

Giora Tarnopolsky
SLAC, Bin 62
Stanford University
Stanford, California 94305

Richard Taylor
SLAC, Bin 80
Stanford University
Stanford, California 94305

Jon Thaler
SLAC, Bin 65
Stanford University
Stanford, California 94305

Nobukazu Toge
50B-6208
Lawrence Berkeley Laboratory
Berkeley, California 94720

Walter Toki
SLAC, Bin 65
Stanford University
Stanford, California 94305

John Tompkins
Hansen Labs
Stanford University
Stanford, California 94305

Thomas Trinko
SLAC, Bin 78
Stanford University
Stanford, California 94305

Yung-Su Tsai
SLAC, Bin 81
Stanford University
Stanford, Californmia 94305

Gary Tupper
Department of Physics
Oklahoma State University
Stillwater, Oklahoma 74078

Kumataro Ukai
SLAC, Bin 62
Stanford University
Stanford, California 94305

Eric Umland
Bonner Nuclear Laboratory
Rice University
Houston, Texas 77251

Rem Van Tyen
50A, Rm. 5123
Lawrence Berkeley Laboratory
One Cyclotron Road
Berkeley, California 94720

John Venuti
SLAC, Bin 94
Stanford University
Stanford, California 94305

Hans Von Der Schmitt
Physikalisches Institut
Der Universitat Bonn
53 Bonn, Nussallee 12
GERMANY

Anthony Waite
SLAC, Bin 62
Stanford University
Stanford, California 94305

Henry Wald
SLAC, Bin 43
Stanford University
Stanford, California 94305

Albert Walenta
Department of Physics
University of Siegen
D-5900 Siegen 211
WEST GERMANY

Alan Weinstein
SLAC, Bin 98
Stanford University
Stanford, California 94305

Marvin Weinstein
SLAC, Bin 81
Stanford University
Stanford, California 94305

Stefi Weisburd
Campus Report
Stanford, California 94305

Jeffrey Weiss
SLAC, Bin 78
Stanford University
Stanford, California 94305

Christopher Wendt
SLAC, Bin 61
Stanford University
Stanford, California 94305

Norbert Wermes
SLAC, Bin 65
Stanford University
Stanford, California 94305

Kerry Whisnant
Department of Physics
Iowa State University and Ames Lab
Ames, Iowa 50011

Hans Willutzki
SLAC, Bin 65
Stanford University
Stanford, California 94305

David Wiser
SLAC, Bin 94
Stanford University
Stanford, California 94305

Bill Wisniewski
SLAC, Bin 65
Stanford University
Stanford, California 94305

Stanley Wojcicki
SLAC, Bin 63
Stanford University
Stanford, California 94305

Zach Wolf
50B-Rm. 5239
Lawrence Berkeley Labortory
One Cyclotron Road
Berkeley, California 94720

Jorg Wotschack
EP Division
CERN
CH-1211, Geneva 23
SWITZERLAND

Rong-Sheng Xu
Physics Department
University of California
Santa Cruz, California 95064

John Yelton
SLAC, Bin 95
Stanford University
Stanford, California 94305

Edward Yen
National Tsing Hua University
855 Kuang Fu Road
Hsinchu, TAIWAN

Bing-Lin Young
Department of Physics
Iowa State University
Ames, Iowa 50011

Charles C. Young
SLAC, Bin 96
Stanford University
Stanford, California 94305

David Yount
Department of Physics & Astronomy
University of Hawaii
Honolulu, Hawaii 96822

Carl Zaiser
SLAC, Bin 61
Stanford University
Stanford, California 94305

Vasilis Zambetakis
Department of Physics
University of California,Los Angeles
Los Angeles, California 90024

THE SLAC SUMMER INSTITUTES ON PARTICLE PHYSICS

1973 - 1982

1973 DEEP INELASTIC ELECTROPRODUCTION

"Hadron Production in Deep Inelastic Processes"	J. D. Bjorken
"Hadron Production in the Collision of Virtual Photons with Nucleons – and Experimental Review"	M. Perl
"Phenomenological Analysis"	F. J. Gilman
"Asymptotic Behavior and Short Distance Singularities"	Y. Frishman

WEAK CURRENTS AND INTERACTIONS

"Raw Notes of Lectures on Current Algebra and PCAC"	S. Drell
"Experimental Phenomenology"	M. Schwartz S. Wojcicki
"Gauge-Theories of Weak and Electromagnetic Interaction"	T. Appelquist
"How to Transform Current Quarks to Constituent Quarks and Try to Predict Hadron Decays"	J. Primack M. Kugler

1974 THE STRONG INTERACTIONS

"Diffractive Processes"	D.W.G.S. Leith
"Amplitude Structure in Two- and Quasi-Two-Body Processes"	M. Davier
"Resonances: Experimental Review"	R.J. Cashmore
"Resonances: A Quark View of Hadron Spectroscopy and Transitions"	F. J. Gilman
"Lectures on Inclusive Hadronic Processes"	D. Sivers
"Large Momentum Transfer Processes"	R. Blankenbecler
"Hadron Dynamics"	H.D.I. Abarbanel

1975 DEEP HADRONIC STRUCTURE AND THE NEW PARTICLES

"Leptons as a Probe of Hadronic Structure"	F. J. Gilman
"Lepton Scattering as a Probe of Hadron Structure"	E. D. Bloom
"High $p_\perp$ Dynamics"	J. D. Bjorken
"Hadronic Collision and Hadronic Structure (An Experimental Review)"	M. Davier
"The New Spectroscopy"	H. Harari
"The New Spectroscopy (An Experimental Review)"	G. H. Trilling

1976 WEAK INTERACTIONS AT HIGH ENERGY AND THE PRODUCTION OF NEW PARTICLES

"Weak Interaction Theory and Neutral Currents"	J. D. Bjorken
"Weak Interactions at High Energy"	S. G. Wojcicki
"ψ Spectroscopy"	G. J. Feldman
"A New Lepton?"	G. J. Feldman
"Lectures on the New Particles"	J. D. Jackson
"New Particle Production"	D. Hitlin

1977 QUARK SPECTROSCOPY AND HADRON DYNAMICS

"Quarks and Leptons"	H. Harari
"Quark Confinement"	S. D. Drell
"Hadron Spectroscopy"	F. J. Gilman
"Lectures on the Quark Model, Ordinary Mesons, Charmed Mesons, and Heavy Leptons"	M. L. Perl
"Quarks and Particle Production"	K. C. Moffeit

1978 WEAK INTERACTIONS – PRESENT AND FUTURE

"Accelerator Neutrino Experiments"	D. H. Perkins
"Weak Interactions at High Energies"	J. Ellis
"Gauge Theories of the Weak Interactions"	H. Quinn
"Weak Decays"	S. Wojcicki

1979 QUANTUM CHROMODYNAMICS

"Lepton Nucleon Scattering"	W. G. Atwood
"Massive Lepton Pair Production"	R. Stroynowski
"QCD Phenomenology of the Large P_T Processes"	R. Stroynowski
"Perturbative Quantum Chromodynamics"	S. J. Brodsky
"Elements of Quantum Chromodynamics"	J. D. Bjorken

1980 THE WEAK INTERACTIONS

"Gauge Theories of Weak Interactions"	M. J. Veltman
"Neutrinos and Neutrino Interactions"	F. J. Sciulli
"Weak Decays of Strange and Heavy Quarks"	D. Hitlin
"From the Standard Model to Composite Quarks and Leptons"	H. Harari
"Physics of Particle Detectors"	D. M. Ritson
	J. Jaros
	J. Marx
	H. A. Gordon
	R. S. Gilmore
	W. B. Atwood

1981 THE STRONG INTERACTIONS

"Quark-Antiquark Bound State Spectroscopy and QCD"	E. D. Bloom
"Meson Spectroscopy: Quark States and Glueballs"	M. S. Chanowitz
"Quantum Chromodynamics and Hadronic Interactions at Short Distances"	S. J. Brodsky
"Untangling Jets from Hadronic Final States"	G. Fox
"Heavy Flavor Production from Photons and Hadrons"	C. A. Heusch
"Design Constraints and Limitations e^+e^- Storage Rings"	J. LeDuff
"Linear Colliders: A Preview"	H. Wiedemann

1982 PHYSICS AT VERY HIGH ENERGY

"Expectations for Old and New Physics at High Energy Colliders"	R. N. Cahn
"Beyond the Standard Model in Lepton Scattering and Beta Decay"	M. Strovink
"Grand Unification, Proton Decay, and Neutrino Oscillations"	H. H. Williams
"e^+e^- Interactions at Very High Energy: Searching Beyond the Standard Model"	J. Dorfan
"The Gauge Hierachy Problem, Technicolor, Supersymmetry, and All That"	L. Susskind
"Composite Models for Quarks and Leptons"	H. Harari
"Electron-Proton Colliding Beams: The Physics Programme and the Machine"	B. H. Wiik